

IFMBE Proceedings

Dössel • Schlegel (Eds.)

Volume 25/9

World Congress on Medical
Physics and Biomedical
Engineering

7–12 September 2009

Munich, Germany

Neuroengineering, Neural
Systems, Rehabilitation and
Prosthetics



Series Editor: R. Magjarevic

11th International
Congress of the IUPESM

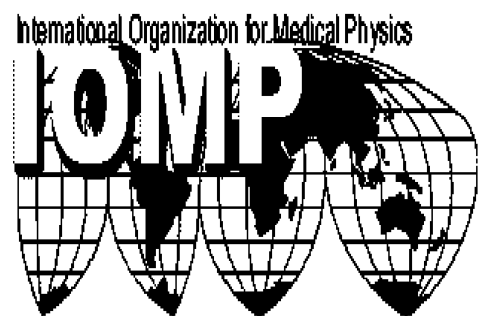
**MEDICAL
PHYSICS AND
BIOMEDICAL
ENGINEERING**

**WORLD
CONGRESS
2009**



For the benefit
of the Patient.

Sept 7–12, 2009
Munich, Germany



The International Federation for Medical and Biological Engineering, IFMBE, is a federation of national and transnational organizations representing internationally the interests of medical and biological engineering and sciences. The IFMBE is a non-profit organization fostering the creation, dissemination and application of medical and biological engineering knowledge and the management of technology for improved health and quality of life. Its activities include participation in the formulation of public policy and the dissemination of information through publications and forums. Within the field of medical, clinical, and biological engineering, IFMBE's aims are to encourage research and the application of knowledge, and to disseminate information and promote collaboration. The objectives of the IFMBE are scientific, technological, literary, and educational.

The IFMBE is a WHO accredited NGO covering the full range of biomedical and clinical engineering, healthcare, healthcare technology and management. It is representing through its 58 member societies some 120.000 professionals involved in the various issues of improved health and health care delivery.

IFMBE Officers

President: Makoto Kikuchi, Vice-President: Herbert Voigt, Former-President: Joachim H. Nagel

Treasurer: Shankar M. Krishnan, Secretary-General: Ratko Magjarevic

<http://www.ifmbe.org>

Previous Editions:

IFMBE Proceedings WC 2009, "World Congress on Medical Physics and Biomedical Engineering",
Vol. 25, 2009, Munich, Germany, CD

IFMBE Proceedings SBEC 2009, "25th Southern Biomedical Engineering Conference 2009",
Vol. 24, 2009, Miami, FL, USA, CD

IFMBE Proceedings ICBME 2008, "13th International Conference on Biomedical Engineering"
Vol. 23, 2008, Singapore, CD

IFMBE Proceedings ECIFMBE 2008 "4th European Conference of the International Federation for Medical and Biological Engineering", Vol. 22, 2008, Antwerp, Belgium, CD

IFMBE Proceedings BIOMED 2008 "4th Kuala Lumpur International Conference on Biomedical Engineering",
Vol. 21, 2008, Kuala Lumpur, Malaysia, CD

IFMBE Proceedings NBC 2008 "14th Nordic-Baltic Conference on Biomedical Engineering and Medical Physics",
Vol. 20, 2008, Riga, Latvia, CD

IFMBE Proceedings APCMBE 2008 "7th Asian-Pacific Conference on Medical and Biological Engineering",
Vol. 19, 2008, Beijing, China, CD

IFMBE Proceedings CLAIB 2007 "IV Latin American Congress on Biomedical Engineering 2007, Bioengineering Solution for Latin America Health", Vol. 18, 2007, Margarita Island, Venezuela, CD

IFMBE Proceedings ICEBI 2007 "13th International Conference on Electrical Bioimpedance and the 8th Conference on Electrical Impedance Tomography", Vol. 17, 2007, Graz, Austria, CD

IFMBE Proceedings MEDICON 2007 "11th Mediterranean Conference on Medical and Biological Engineering and Computing 2007", Vol. 16, 2007, Ljubljana, Slovenia, CD

IFMBE Proceedings BIOMED 2006 "Kuala Lumpur International Conference on Biomedical Engineering",
Vol. 15, 2004, Kuala Lumpur, Malaysia, CD

IFMBE Proceedings WC 2006 "World Congress on Medical Physics and Biomedical Engineering",
Vol. 14, 2006, Seoul, Korea, DVD

IFMBE Proceedings BSN 2007 "4th International Workshop on Wearable and Implantable Body Sensor Networks",
Vol. 13, 2006, Aachen, Germany

IFMBE Proceedings ICBMEC 2005 "The 12th International Conference on Biomedical Engineering",
Vol. 12, 2005, Singapore, CD

IFMBE Proceedings EMBEC'05 "3rd European Medical & Biological Engineering Conference, IFMBE European Conference on Biomedical Engineering", Vol. 11, 2005, Prague, Czech Republic, CD

IFMBE Proceedings ICCE 2005 "The 7th International Conference on Cellular Engineering",
Vol. 10, 2005, Seoul, Korea, CD

IFMBE Proceedings NBC 2005 "13th Nordic Baltic Conference on Biomedical Engineering and Medical Physics",
Vol. 9, 2005, Umeå, Sweden

IFMBE Proceedings Vol. 25/IX
Olaf Dössel · Wolfgang C. Schlegel (Eds.)

World Congress on Medical Physics
and Biomedical Engineering
7–12 September, 2009
Munich, Germany

Neuroengineering, Neural Systems,
Rehabilitation and Prosthetics

 Springer

Editors

Prof. Dr. Olaf Dössel
Univ. Karlsruhe
Inst. Biomedizinische Technik
Kaiserstr. 12
76128 Karlsruhe
Germany
E-mail: olaf.doessel@ibt.uni-karlsruhe.de

Prof. Dr. Wolfgang C. Schlegel
Deutsche Krebsforschungszentrum (DKFZ)
Abt. Medizinische Physik in der
Strahlentherapie
Im Neuenheimer Feld 280
69120 Heidelberg
Germany
E-mail: w.schlegel@dkfz-heidelberg.de

ISSN 1680-0737

ISBN 978-3-642-03888-4

e-ISBN 978-3-642-03889-1

Also available as set Vol. I–XIII ISBN 978-3-642-03897-6

DOI 10.1007/978-3-642-03889-1

Library of Congress Control Number: 2009934297

© International Federation for Medical and Biological Engineering 2009

This work is subject to copyright. All rights are reserved, whether the whole or part of the material is concerned, specifically the rights of translation, reprinting, reuse of illustrations, recitation, broadcasting, reproduction on microfilm or in any other way, and storage in data banks. Duplication of this publication or parts thereof is permitted only under the provisions of the German Copyright Law of September 9, 1965, in its current version, and permissions for use must always be obtained from Springer. Violations are liable to prosecution under the German Copyright Law.

The use of general descriptive names, registered names, trademarks, etc. in this publication does not imply, even in the absence of a specific statement, that such names are exempt from the relevant protective laws and regulations and therefore free for general use.

The IFMBE Proceedings is an Official Publication of the International Federation for Medical and Biological Engineering (IFMBE)

Typesetting: Data supplied by the authors

Production & Cover design: Scientific Publishing Services Pvt. Ltd., Chennai, India.

Printed on acid-free paper

9 8 7 6 5 4 3 2 1

springer.com

Preface

Present Your Research to the World!

The World Congress 2009 on Medical Physics and Biomedical Engineering – the triennial scientific meeting of the IUPESM - is the world's leading forum for presenting the results of current scientific work in health-related physics and technologies to an international audience. With more than 2,800 presentations it will be the biggest conference in the fields of Medical Physics and Biomedical Engineering in 2009!

Medical physics, biomedical engineering and bioengineering have been driving forces of innovation and progress in medicine and healthcare over the past two decades. As new key technologies arise with significant potential to open new options in diagnostics and therapeutics, it is a multidisciplinary task to evaluate their benefit for medicine and healthcare with respect to the quality of performance and therapeutic output.

Covering key aspects such as information and communication technologies, micro- and nanosystems, optics and biotechnology, the congress will serve as an inter- and multidisciplinary platform that brings together people from basic research, R&D, industry and medical application to discuss these issues.

As a major event for science, medicine and technology the congress provides a comprehensive overview and in-depth, first-hand information on new developments, advanced technologies and current and future applications.

With this Final Program we would like to give you an overview of the dimension of the congress and invite you to join us in Munich!

Olaf Dössel
Congress President

Wolfgang C. Schlegel
Congress President

Preface

Welcome to World Congress 2009!

Since the first World Congress on Medical Physics and Biomedical Engineering convened in 1982, medically and biologically oriented engineers and physicists from all continents have gathered every three years to discuss how physics and engineering can advance medicine, health and health care and to assess the clinical, scientific, technical and professional progress in their fields. In the tradition and the mission of our professions, which are the only ones involved in the whole loop of health and health care from basic research to the development, assessment, production, management and application of medical technologies, the theme of WC 2009 is "For the Benefit of the Patient". Thus, in addition to scientific aspects, the Congress will focus on all aspects of safe and efficient health technology in both industrialized and developing countries, including economic issues, the perspectives that advanced technologies and innovations in medicine and healthcare offer for the patients and the development of societies, the progress of MBE and MP, including health policy and educational issues as well as the need for the regulation and classification as health professionals of those biomedical/clinical engineers and medical physicists who are working in the health care systems.

The World Congress as the most important meeting of our professions, bringing together physicists, engineers and physicians from all over the world, including the delegates of the 138 constituent organizations of the IUPESM representing some 140,000 individual members, is the best place to discuss these issues, thereby contributing to the advancement of the physical and engineering sciences, our professions and thus to global health.

It gives me great pleasure to welcome you to this important event. I wish you a rewarding and enjoyable congress and a most pleasant time in Munich, the 'metropolis with heart' that has so much to offer.

Joachim H. Nagel
President of the IUPESM

Preface

Let's talk!

Is our level of communication between Medical Physics, Biomedical Engineering, Clinical Engineering, Medical Informatics, Tissue Engineering, etc. and Medicine good enough? We would like to answer: yes, we are quite good, but not good enough! There is a lot of room for improvement. Let' start right on the spot - on the World Congress on Medical Physics and Biomedical Engineering 2009. And please remember: communication is 50% talking and 50% listening.

Let's work together!

Do we have a perfect level of collaboration in our field? OK, we are quite good, but we can do better. Just to give an example: there should be no funded project in Medical Physics or Biomedical Engineering where there is no medical partner. And vice versa: medical doctors should join their forces with physicists and engineers if they are aiming at improvements on medical devices or healthcare systems. Let's start right here in Munich, September 2009, with innovative projects and innovative ways of cooperation.

Let's get to know each other!

It's known for more than thousand years: people who know each other personally and from face to face can talk with better mutual understanding, collaborate with less friction losses, are much more successful and have much more fun. Plenty of chances to make new friends and to refresh old relations on World Congress on Medical Physics and Biomedical Engineering 2009!

And here are the numbers:

More than 3000 scientists working in the field of Medical Physics and Biomedical Engineering meet in September 2009 in Munich. They come from more than 100 nations. They submitted about 2800 contributions. 10 plenary talks and 46 keynote lectures bring us to the top level of science in our field. 75 companies show their latest achievements in the industrial exhibition. It's definitely the largest market place of ideas and innovations in Medical Physics and Biomedical Engineering of the year 2009.

August 2009

Olaf Dössel

Table of Contents

Study on a High Performance Shoes by Using Silicon Rubber Elements with Human Compatibility	1
<i>Yasuhiro Hayakawa and Naoki Nishida</i>	
Paraplegic Using a Reciprocating Gait Orthosis (RGO) with Functional Electrical Stimulation	5
<i>J.-C. Hsieh, S.-C. Chen, C.-C. Chen, Y.-L. Chen, Walter -H. Chang, Y.-C. Li, and Y.-Y. Shih</i>	
Habilitation Aid for Children with Balance Disorders	9
<i>B. Jantek, Á. Jobbágy, J. Szemán, J. Schultheisz, and P. Bacsó</i>	
Prototype Walker for Children with Cerebral Palsy	13
<i>P. Jureczko, T. Łosień, M. Sottys, K. Jochymczyk, A. Głowacka-Kwiecień, and M. Gzik</i>	
Analysis of Joint Movements and Muscle Length during Sit-to-Stand at Various Sitting Heights in the Korean Elderly Daily Life	17
<i>S.J. Hwang, J.S. Son, J.Y. Kim, H.D. Kim, D.H. Lim, and Y.H. Kim</i>	
Haptic Robot for Arm and Wrist Rehabilitation	20
<i>Jakob Oblak, Imre Cikajlo, and Zlatko Matjačić</i>	
Movement Analysis by Accelerometry of Newborns for the Early Detection of Movement Disorders due to Infantile Cerebral Palsy	24
<i>F. Heinze, N. Breitbach-Faller, T. Schmitz-Rode, and C. Disselhorst-Klug</i>	
Patient-Specific Finite Element Models of Transtibial Amputation in Several Prosthetic Users: The Inter-Subject Variability	28
<i>S. Portnoy, I. Siev-Ner, N. Shabshin, A. Kristal, Z. Yizhar, and A. Gefen</i>	
Development of a Corrugated Polyimide-Based Electrode for Intrafascicular Use in Peripheral Nerves	32
<i>T. Boretius, D. Zimmermann, and T. Stieglitz</i>	
Analysis of Gait Rhythm Variability in Patients with Amyotrophic Lateral Sclerosis	36
<i>Yunfeng Wu and Sridhar Krishnan</i>	
Anatomy of the Human Cochlear Nucleus in Relation to Auditory Brainstem Implants	40
<i>S.K. Rosahl and S. Rosahl</i>	
Estimation and Evaluation of Upper Limb Endpoint Stiffness and Joint Torques for Post-stroke Rehabilitation	44
<i>P.R. Wang, Y.H. Chiu, M.S. Tsai, and K.C. Chung</i>	
Neuroelectronic Interfaces with the Central Nervous Systems – Ethical Issues	48
<i>S.K. Rosahl</i>	
Ultrasound Pre-study of the Kinematics of the Residual Tibia within a Trans-Tibial Socket during Gait	52
<i>S. Klasen, C. Uplegger, S. Rensch, T. Bächle, and U. Schneider</i>	

Development of Unconstrained Rigidity Measurement System for Quantitative Diagnosis of Parkinson’s Disease	55
<i>R. Okuno, T. Endo, M. Yokoe, S. Sakoda, and K. Akazawa</i>	
Measurement of Eye and Head Position in Neurological Practice	57
<i>J. Charfreitag, J. Hozman, and R. Cerny</i>	
Virtual Reality and Robotics for Neuro-Motor Rehabilitation of Ischemic Stroke Patients	61
<i>M. Steinisch, B.M. Guarnieri, J. Hauelsen, A. Serio, and S. Comani</i>	
ARMassist: A Low-Cost Device for Telerehabilitation of Post-stroke Arm Deficits	64
<i>Joel C. Perry, Haritz Zabaleta, Aitor Beloso, and Thierry Keller</i>	
Application of 3D Modeling and Modern Visualization Technique to Neurosurgical Trigonoccephaly Correction in Children	68
<i>M. Gzik, W. Wolański, D. Tejszerska, B. Gzik-Zroska, M. Koźlak, D. Larysz, and M. Mandera</i>	
Peripheral Inductive Stimulation: Physical Issues and Advanced Technological Solutions	72
<i>S.M. Goetz and Th. Weyh</i>	
A Neuronal Network Model with Plasticity for Tinnitus Management by Sound Therapy	76
<i>H. Nagashino, Y. Kinouchi, A.A. Danesh, and A.S. Pandya</i>	
Modular Prosthesis of the Larynx for Application in Laryngectomees – A Theoretical Approach	80
<i>Fridun Nazaradeh, Denis Nazaradeh, Marc André Dupré, and Claus Eckermann</i>	
A Novel Method Exploiting the Nociceptive Withdrawal Reflexes in Rehabilitation of Hemiplegic Gait	84
<i>J. Emborg, J.D. Bendtsen, E.G. Spaich, and O.K. Andersen</i>	
Compact Assistive Rehabilitation Devices– Concept and Preliminary Function Test	88
<i>O. Ivlev, D. Baiden, A. Wilkening, C. Koch, and H.-D. Haas</i>	
Feasibility of Selective Robotic Support of Foot Clearance with Continuously Adapting Impedance Levels	92
<i>E.H.F. van Asseldonk, B. Koopman, C. Simons, J. Buurke, and H. van der Kooij</i>	
Diffusion Limited Tapered Coating with Parylene C	96
<i>R.P. von Metzen, D. Egert, P. Ruther, and T. Stieglitz</i>	
Electrical Characterization of Platinum, Stainless Steel and Platinum/Iridium as Electrode Materials for a New Neural Interface	100
<i>C. Henle, W. Meier, M. Schuettler, T. Boretius, and T. Stieglitz</i>	
Position Decoding of Hippocampal Place Cells	104
<i>S. Schaffelhofer, C. Guger, M.V. Sanchez-Vives, J. Brotons-Mas, and T. Gener</i>	
A Novel Assembly Method for Silicon-Based Neural Devices	107
<i>S. Kisban, J. Kenntner, P. Janssen, R.v. Metzen, S. Herwik, U. Bartsch, T. Stieglitz, O. Paul, and P. Ruther</i>	
Gait Posture Estimation by Wearable Acceleration and Gyro Sensor	111
<i>R. Takeda, S. Tadano, A. Natorigawa, M. Todoh, and S. Yoshinari</i>	

Automobile, Which Can Control an Autonomic Nervous System	115
<i>T. Yambe, Y. Shiraishi, M. Takashima, T. Seki, and R. Kawashima</i>	
Polymer-Based Approaches to Improve the Long Term Performance of Intracortical Neural Interfaces	119
<i>C. Hassler and T. Stieglitz</i>	
Development of a Neural Interface for Artificial Limbs	123
<i>Todd Kuiken</i>	
Orthopedic Testing – A Device for Sagittal and Transversal Knee Stability Detection	124
<i>R. Boos, H. Telles, J. Richter, A. Keim, F. Stegmaier, and U. Schneider</i>	
ARMin - Exoskeleton Robot for Stroke Rehabilitation	127
<i>Tobias Nef, Marco Guidali, Verena Klamroth-Marganska, and Robert Riener</i>	
Comparative Study on the Posture of Individuals With and Without Cervical Pain	131
<i>S.R.G.P. Galera, L.F.C. Nascimento, E.C.M. Teodoro, and J.E. Tomazini</i>	
Functional Assessment of Orthopedic Aids Using Open Vertical MRIs	135
<i>M. Tettke, R.C. Bittner, and M. Kraft</i>	
Bioelectric Source Localization in the Rat Sciatic Nerve: Initial Assessment Using an Idealized Nerve Model	138
<i>José Zariffa, Mary K. Nagai, Zafiris J. Daskalakis, and Milos R. Popovic</i>	
Development of a New Wearable Monitoring System for Posture Changes and Activities and Its Application to Rehabilitation	142
<i>K. Motoi, Y. Kuwae, S. Taniguchi, M. Wakugawa, T. Yuji, Y. Higashi, T. Fujimoto, M. Ogawa, S. Tanaka, and K. Yamakoshi</i>	
An Improved Method for Dipole Modeling in EEG-Based Source Localization	146
<i>Fredrik Edelvik, Björn Andersson, Stefan Jakobsson, Stig Larsson, Mikael Persson, and Yazdan Shirvany</i>	
Machines to Support Motor Rehabilitation after Stroke	150
<i>S. Hesse and C. Werner</i>	
FEM-Based Investigation of Spatial Stimulation Properties of a Multi-electrode Probe with Micrometer-Size Electrodes for Cortical and DBS Applications	154
<i>W. Eberle, A.S. Mecheri, S. Musa, G. Gielen, G. Borghs, and C. Bartic</i>	
Silicon Microprobe Systems for Neural Drug Delivery: Experimental Characterization of Liquid Distribution	158
<i>S. Spieth, A. Schumacher, S. van de Moosdijk, S. Haeberle, and R. Zengerle</i>	
A Measurement Set-Up to Determine the Charge Injection Capacity of Neural Microelectrodes	162
<i>W. Poppendieck, K.P. Koch, S. Steltenkamp, and K.-P. Hoffmann</i>	
Patient-Cooperative Control: Providing Safe Support without Restricting Movement	166
<i>Heike Vallery, Marco Guidali, Alexander Duschau-Wicke, and Robert Riener</i>	
Estimation of Physical Performance for Elderly People via Markerless Sit to Stand Analysis ...	170
<i>M. Goffredo, R. Muscillo, M. Gneo, M. Schmid, S. Conforto, and T. D'Alessio</i>	
Using a P300 Brain Computer Interface for Smart Home Control	174
<i>C. Holzner, C. Guger, C. Grönegress, G. Edlinger, and M. Slater</i>	

The Use of Muscle “Creep” as Opposed to Relaxation in Stretching Braces: A Pseudoelastic Device	178
<i>S. Pittaccio and S. Viscuso</i>	
Customizable Neuro-mechanical Model of a Hemiplegic Elbow Interacting with a Pseudoelastic Dynamic Orthosis	182
<i>S. Pittaccio and S. Viscuso</i>	
The Use of Radio Frequency Identification System for Wheelchair Security System	186
<i>W.Md. Azhar Wan Ibrahim and Md. Shuhaibul Fadly Mansor</i>	
A Lightweight Approach for Activity Classification on Microcontrollers	190
<i>M. Rulsch, M. Benz, C. Arzt, C. Podolak, J. Zhong, and R. Couronné</i>	
Field Applications of a Prosthetic Mobile Measuring System	194
<i>S. Oehler, D. Hochmann, and M. Kraft</i>	
Force Fluctuations in a Simulated Motoneuron Pool	197
<i>A.F. Kohn</i>	
Effect of Passive Stepping on the H-Reflex in the Wrist Flexor	201
<i>T. Kitamura, T. Nakajima, K. Kamibayashi, S.-I. Yamamoto, M. Akai, and K. Nakazawa</i>	
On the Efficacy of Haptic Guidance Schemes for Human Motor Learning	203
<i>Volkan Patoglu, Yvonne Li, and Marcia K. O’Malley</i>	
Design and Development of Acrylic Die for Hip Bone Joint Casting	207
<i>S. Norbahiyah and M.M. Haque</i>	
Pupillary Responses during Learning of Inverted Tracking Tasks	211
<i>Satoshi Kobori and Yosuke Abe</i>	
Instantaneous Gaze-Target Detection by Empirical Mode Decomposition: Application to Brain Computer Interface	215
<i>Chi-Hsun Wu, Hsiang-Chih Chang, and Po-Lei Lee</i>	
Using Virtual Reality for an Autonomous Navigation with Electric Wheelchairs	219
<i>I. Randria, P. Abellard, P. Ramanantsizehena, M. Ben Khelifa, and A. Abellard</i>	
Design of a New Prosthetic Mechanical System Used in Human Ankle Joint Disarticulation ...	223
<i>C. Copiluşî, N. Dumitru, M. Marin, and L. Rusu</i>	
Development of a Telemetric Goniometer	227
<i>G.T. Laskoski, L.D.L. Martins, S.F. Pichorim, and P.J. Abatti</i>	
Artificial Prehension and the Detection of Object Slip	231
<i>S.A. Ahmad and P.H. Chappell</i>	
Influence of Base Material of TRUCT Braille on Readability of TRUCT Braille	235
<i>Kouki Doi, Hiroshi Fujimoto, and Tsutomu Wada</i>	
Functional Evaluation of a Micro-fabricated Planar Multielectrode Probe for in Vivo Neuronal Recording	239
<i>D. Prodanov, M. Welkenhuysen, S. Musa, W. Eberle, T. Dresselaers, U. Himmelreich, C. Bartic, G. Borghs, and B. Nuttin</i>	

Table of Contents	XIII
Research on the Perceptual Size of Tactile Dots and Bars	243
<i>Wataru Toyoda, Kouki Doi, Hiroshi Fujimoto, and Tsutomu Wada</i>	
A Consideration of the Expanded Partial Differential Equations and the Compartment System as the Background of the ABR System	247
<i>Masahiro Aruga, Kiyotaka Takagi, Sinwu Liu, and Shuichi Kato</i>	
Development of the Gait Training System Controlled by Pressure Feed-back	251
<i>Y. Shibata, M. Takagi, T. Miyoshi, and S. Yamamoto</i>	
Regional Absolute Quantification in Neurochemical Profile of the Canine Brain: Investigation by H Nuclear Magnetic Resonance Spectroscopy and Tissue Extraction	255
<i>D.-C. Woo, C.-B. Choi, S.-H. Lee, E.-J. Bang, S.-S. Kim, H.-S. Rhim, S.-Y. Kim, K.-H. Kim, and B.-Y. Choe</i>	
A Potable System for Foot-Drop Correction using Electrical Stimulation	259
<i>R.H. Sohn, S.W. Park, S.H. Hwang, A.R. Ko, Y.H. Lee, S.H. Lee, K.H. Ryu, and Y.H. Kim</i>	
An Implantable Epiretinal Vision Prosthesis for Retinitis Pigmentosa Patients	261
<i>Th. Schanze, U. Thomas, and The EPIRET-Group</i>	
Development of System for Estimating Muscle Force in Real-Time	265
<i>Jongsang Son and Youngho Kim</i>	
Sensitivities of Bipolar Subcutaneous and Cortical EEG Leads	267
<i>J. Väisänen, K. Wendel, G. Seemann, J. Malmivuo, and J. Hyttinen</i>	
Patient-Cooperative Control: Adapting Robotic Interventions to Individual Human Capabilities	271
<i>Alexander Duschau-Wicke, Thomas Brunsch, Simon Felsenstein, Heike Vallery, and Robert Riener</i>	
H-MRS Study of Depressive Animal Model for Assessment of Antidepressant Effects	275
<i>Sang-Young Kim, Chi-Bong Choi, Sung-Ho Lee, Dong-Cheol Woo, Hyun-Sung Lee, Sung-Tak Hong, Hwi-Yool Kim, and Bo-Young Choe</i>	
Improving BCI Performance by Modified Common Spatial Patterns with Robustly Averaged Covariance Matrices	279
<i>M. Kawanabe and C. Vidaurre</i>	
Enhanced Perception for Visually Impaired People Evaluated in a Real Time Setting	283
<i>K. Möller, J. Möller, K.O. Arras, M. Bach, S. Schumann, and J. Guttmann</i>	
A Preliminary Study of a Power Assist System for Toe Exercise Using a Metal Hydride Actuator	287
<i>S. Ino, M. Hosono, M. Sato, S. Nakajima, K. Yamashita, and T. Izumi</i>	
Rehabilitation Robotics for Outpatient Clinical and Domestic Use	291
<i>Thierry Keller and Joel C. Perry</i>	
Seizure Control in an <i>In-Silico</i> Model of Epilepsy Using Backstepping Technique	295
<i>N. Mostofi, M.R. Jahed-Motlagh, C. Lucas, Gh. Montaseri, and A.B. Farjadian</i>	
Walkaround[®] Assisted Walking of Stroke Patients	299
<i>M. Đurić-Jovičić, I. Milovanović, N. Jovičić, and D.B. Popović</i>	

Vision and Distance Based Control of Prehension	302
<i>D.B. Popović, S. Došen, and M.B. Popović</i>	
‘InfoCane’ Based on Wireless Technology for the Visually-Handicapped People	306
<i>Dong-Seok Cho and Jong-Mo Seo</i>	
To Feedback or Not to Feedback? Some Open Questions for Brain-Computer Interfaces Use ...	309
<i>R. Carabalona and P. Castiglioni</i>	
Calculation of Systemic Aerobic Capacity without Contact Using Pattern Light Projection	312
<i>H. Aoki, S. Ichimura, T. Fujiwara, S. Kiyooka, and K. Koshiji</i>	
Functionality of Neuronal Networks Derived from Human Embryonic Stem Cells	316
<i>T.J. Heikkilä, J. Mikkonen, J.M.A. Tanskanen, L. Ylä-Outinen, R. Lappalainen, S. Narkilahti, and J.K. Hyttinen</i>	
Pneumatic Test Device for the Accurate Assessment of Pressure Sensors	319
<i>C. Giacomozzi, G. De Angelis, M. Paolizzi, S. Silvestri, and V. Macellari</i>	
Design and Fabrication of an Ultra-Flexible Electrode System for Invasive Continuous Monitoring during Surgery	323
<i>S. Kraemer, T. Doerge, M. Hanauer, K.-P. Hoffmann, W. Kneist, S. Steltenkamp, Ch. Ulmer, and W. Lamadé</i>	
Prototyping All-Polymer Bioelectrical Signal Transducers	327
<i>A. Blau, A. Murr, S. Trelenkamp, C. Dautermann, S. Wolff, M. Heuschkel, J. Wuesten, C. Ziegler, and F. Benfenati</i>	
Patient-Specific Models and Simulations of Deep Brain Stimulation for Postoperative Follow-Up	331
<i>Mattias Åström, Elina Tripoliti, Irene Martinez-Torres, Ludvic U. Zrinzo, Patricia Limousin, Marwan I. Hariz, and Karin Wårdell</i>	
Robot-Amplified Manual Exploration Improves Load Identification	335
<i>F.C. Huang, J.L. Patton, and F.A. Mussa-Ivaldi</i>	
A New Lightweight, Robust and Forceful Finger for an Artificial Limb	339
<i>M. Franke and M. Bogdan</i>	
Leg Muscles Motion during Whole Body Linear Frequency Sweep Vibration	343
<i>A. Fratini, A. La Gatta, P. Bifulco, M. Cesarelli, and G. Pasquariello</i>	
Motion Capture of Patients with Neurological Disorders by HD Digital Cameras	347
<i>R. Krupicka, P. Janda, and Z. Szabo</i>	
Peripheral Arm Nerve Injury Rehabilitation by Means of “Virtual Sensibility”	351
<i>S. Amsüss, R. Schmidhammer, and H.Redl</i>	
Realization of Constant Phase Element in Metallic Electrodes for Interference Reduction in Neural Recording Tripoles	353
<i>I. Pachnis, A. Demosthenous, and N. Donaldson</i>	
Comparison of Sensor Systems for Gait Phase Detection in Hemiplegic Gait	358
<i>S.W. Park, R.H. Sohn, S.H. Hwang, and Y.H. Kim</i>	

Table of Contents	XV
8-Channel Electrotactile Stimulation System for Auditory Information Substitution	362
<i>R.V. Cendon and P. Nohama</i>	
Intraoperative Neural Electrode for Continuous Monitoring of Nerve Function	366
<i>K.P. Koch, W. Poppendieck, Ch. Ulmer, D.W. Kauff, T. Doerge, P. Osypka, W. Kneist, and W. Lamadé</i>	
Density Distribution of Denervated Degenerated Rectus Femoris Muscle in Electrical Stimulation Treatment	370
<i>T. Helgason, P. Gargiulo, B. Vatnsdal, S. Yngvason, V. Gudmundsdottir, S. Knútsdóttir, and P. Ingvarsson</i>	
Application of the ACT^{3D} Robot in the Evaluation of Functional Reaching Performance and the Administration of Experimental Interventions	374
<i>Michael D. Ellis and Julius P.A. Dewald</i>	
Application of Electrode Matrix to Locate Stimulation Sites for Hand Functions of SCI Patients	377
<i>A. Oskarsdottir and T. Helgason</i>	
Force Field Compensation Can Be Learned without Proprioceptive Error	381
<i>A. Melendez-Calderon, L. Masia, M. Casadio, and E. Burdet</i>	
Implantable Wireless Cortical Recording Device for Primates	384
<i>D.A. Borton, Y.-K. Song, W.R. Patterson, C.W. Bull, S. Park, F. Laiwalla, J.P. Donoghue, and A.V. Nurmikko</i>	
Is Posturography a Candidate for a Vigilance Test?	388
<i>T. Schnupp, A. Schenka, D. Edwards, J. Krajewski, and M. Golz</i>	
Aspects of Weight-Support Mechanisms in Rehabilitation Robotics	392
<i>Arno H.A. Stienen, Edsko E.G. Hekman, Herman van der Kooij, Michael D. Ellis, Jules P.A. Dewald</i>	
Studying Mechanisms Underlying Stroke Induced Movement Disorders Using 3-D Robotics ...	395
<i>Julius P.A. Dewald, Albert Chen, and Jun Yao</i>	
Use of Artificial Neural Networks for Classification Intracranial EEG Signals from Epileptic Patients	398
<i>P. Marchena, M. Díaz, R. Esteller, I. Martínez, and A. Zambrano</i>	
Electrical Network for Emulation of Saccadic Eye Movements	402
<i>O. Terán and E. Suaste</i>	
Study toward a Motion Sickness Assessment with Bio-signal Indices on Korean Tilting Train eXpress	406
<i>Yongsoo-Song, Seongho-Han, and Myounggho-Lee</i>	
Kinematics Analysis of Chopsticks Manipulation	410
<i>S.W. Chen, J.I. Liang, K.Y. Lai, Y.T. Ting, Y.C. Peng, H.Y. Hsu, K.H. Lai, and F.C. Su</i>	
ZigBee-Based Wireless Neuro-stimulator for Improving Stroke Recovery	414
<i>Y. Yang, G. Kim, H. Yun, Y. Shin, H. Kim, and M. Ryu</i>	
The Effect of Clearance upon Friction of Large Diameter Hip Resurfacing Prostheses Using Blood, Clotted Blood and Bovine Serum as Lubricants	418
<i>S. Afshinjavid and M. Youseffi</i>	

Comparison of k-Means and Bayes Classifiers for Human Body Motions Classification	421
<i>J. Havlik, J. Uhlir, and Z. Horcik</i>	
The Effect of Computer Use on Carpal Tunnel Syndrome	425
<i>M.F. Donoghue, D. O'Reilly, and M.T. Walsh</i>	
Automated Vigilance Classification Based on EOG Signals: Preliminary Results	428
<i>S. Hanke, J. Zeitlhofer, G. Wiest, W. Mayr, and D.C. Moser</i>	
A Lexicon Driven P300 Speller	432
<i>S.T. Ahi, H. Kambara, and Y. Koike</i>	
Repositioning Precision of EEG-Caps – A Preliminary Study	436
<i>S. Hemm, E. Schkommodau, and M. de Wild</i>	
Pick to Place Trajectories in Human Arm Training Environment	440
<i>J. Zihlerl and M. Munih</i>	
Subretinal Microelectrode Arrays Implanted into Blind Retinitis Pigmentosa Patients Allow Recognition of Letters and Direction of Thin Stripes	444
<i>E. Zrenner, R. Wilke, H. Sachs, K.U. Bartz-Schmidt, F. Gekeler, D. Besch, H. Benav, A. Bruckmann, U. Greppmaier, A. Harscher, S. Kibbel, A. Kusnyerik, T. Peters, K. Porubská, A. Stett, B. Wilhelm, W. Wrobel, and Subret Study Group</i>	
Investigation of the Adaptation to Artificial Damping in Cerebellar Ataxia Using the Myohaptic Technology	448
<i>M. Manto, N. Van Den Braber, J. Meuleman, P. Lammertse, and G. Grimaldi</i>	
Analysis of Parkinson Gait Based on Wavelet Packet Entropy	452
<i>Yang Han, Zhanhong Ma, Ping Zhou, and Zhicheng Liu</i>	
Medium-Cost Electronic Prosthetic Knee for Transfemoral Amputees: A Medical Solution for Developing Countries	456
<i>R.R. Torrealba, L.A. Zambrano, E. Andara, G. Fernández-López, and J.C. Grieco</i>	
Human Gait Data Mining by Symbol Based Descriptive Features	460
<i>V. Ergovic, S. Tonkovic, and V. Medved</i>	
Novel Control for Ambulation Function Restoration in a Non-invasive Functional Electrical Stimulation System	464
<i>J.-C. Hsieh, C.-C. Chen, S.-C. Chen, Y.-L. Chen, Y.-C. Li, Y.-Y. Shih, and T.-S. Kuo</i>	
Design of a Hybrid Powered Upper Limb Orthosis	468
<i>S. Schulz, C. Pylatiuk, A. Kargov, I. Gaiser, O. Schill, M. Reischl, U. Eck, and R. Rupp</i>	
Electrodeposition and Characterization of Iridium Oxide as Electrode Material for Neural Recording and Stimulation	472
<i>W. Hasenkamp, S. Musa, A. Alexandru, W. Eberle, and C. Bartic</i>	
Design and Modeling of an Upper Extremity Exoskeleton	476
<i>S. Moubarak, M.T. Pham, T. Pajdla, and T. Redarce</i>	
Detection of Steady-State Visual Evoked Potentials for Brain-Computer Interfaces Using PCA and High-Order Statistics	480
<i>S. Pouryazdian and A. Erfanian</i>	

Intensive FES Therapy and Its Effect on the Upper Limb Motor Recovery After Stroke	484
<i>N. Kawashima, V. Zivanovic, and M.R. Popovic</i>	
Dynamics of the Seizure Engine	488
<i>O.C. Zalay and B.L. Bardakjian</i>	
Skin Properties and the Influence on Electrode Design for Transcutaneous (Surface) Electrical Stimulation	492
<i>Thierry Keller and Andreas Kuhn</i>	
Estimation Method of Consumption Energy in Human Activities for Daily Living	496
<i>T. Sugimoto, Y. Yoshida, and I. Yoshida</i>	
A Test of Stride Length Measurement with an Accelerometer and a Gyroscope Attached on the Foot	502
<i>T. Watanabe and Y. Minegishi</i>	
Ankle and Knee Joint Angle Measurements during Gait with Wearable Sensor System for Rehabilitation	506
<i>Hiroki Saito, Takashi Watanabe, and Achmad Arifin</i>	
Performance of Novel Dry Electrode EEG Cap for Evoked Potential and Band-Power Activity Detection	510
<i>C. Grozea, G. Nolte, and F. Popescu</i>	
Development of a Shoe-Type Device for Collecting Gait Information	514
<i>Yukinobu Sugimura, Futoshi Wada, Kenichiro Makino, Taishi Oda, Kenji Hachisuka, Takafumi Ienaga, Zhimei Yang, Yoshihiko Kimuro, Takenori Otawa, Naoto Yukitake, Futoshi Koriyama, Takuro Tsuji, and Chikamune Wada</i>	
Optical Measurements for Guidance during Deep Brain Stimulation Surgery	516
<i>Karin Wårdell, Johannes Johansson, Johan Richter, and Patric Blomstedt</i>	
Trial Study of a Power Presentation Method for Upper-Limb Orthoses	518
<i>Chikamune Wada, Futoshi Wada, Hirotaka Iwata, Naoki Chidiwa, Akio Tsutsumi, and Kenji Hachisuka</i>	
Movement of Lower Extremity – Development of a Portable System for Movement Analysis ...	520
<i>H. Grip, O. Gustavsson, F. Öhberg, U. Edström, C. Häger-Ross, and R. Lundström</i>	
The Role of the sEMG Signal Processing in the Field of the Human Movement Analysis	523
<i>S. Conforto</i>	
Effects of Acupuncture in the Ischemic Model of Diabetes Mellitus Rats	527
<i>S. Choi, G.-J. Lee, C.-S. Yin, S.-K. Choi, S.-W. Kang, S.-J. Chae, J.-H. Park, K.-S. Kim, Y.-H. Park, and H.-K. Park</i>	
The Mechanism of Electro-Acupuncture (EA) Treating Cerebral Ischemia: Whether EA Administered to Mobilization of EPCs?	529
<i>S.X. Cai, S.J. Chen, W.J. Yu, and Y. Zhao</i>	
PERFORM: Building and Mining Electronic Records of Neurological Patients Being Monitored in the Home	533
<i>R. Greenlaw, M. Garcia Robledo, J.J. Estrada, M. Pansera, S. Konitsiotis, D. Baga, P. Maziewski, M. Pastor, A. Papsava, D. Chaloglou, and F. Zanichelli</i>	

Real-Time Adaptive Neural Predictors for Upper Limb Gestures Blind Recognition	536
<i>M. Gneo, R. Muscillo, M. Goffredo, S. Conforto, M. Schmid, and T. D'Alessio</i>	
The European R&D Project RISE - Use of Electrical Stimulation to Restore Standing in Paraplegics with Long-Term Denervated Degenerated Muscles (DDM)	540
<i>Winfried Mayr, Christian Hofer, Helmut Kern, Manfred Bijak, Hermann Lanmüller, Dietmar Rafolt, Ewald Unger, and Hans Stöhr</i>	
Modulation of Stimulation Frequency of Spinal Cord Afferents with Unchanged Intensity and Electrode Site Can Induce a Variety of Movements	543
<i>Winfried Mayr, Christian Hofer, Karen Minassian, Ursula Hofstötter, Helmut Kern, Manfred Bijak, Ewald Unger, Frank Rattay, and Milan Dimitrijevic</i>	
A Biofeedback Based Portable Device to Support Elderly Mobility in the Home Environment	546
<i>M. Mancini, E. Farella, L. Rocchi, C. Tacconi, L. Benini, and L. Chiari</i>	
Measurement System of Hand Tapping Capacity for Quantitative Diagnosis of Parkinson's Disease	550
<i>Sang Kyong Kim, Hyo Seon Jeon, Jonghee Han, Yoon Jae Choi, Beom Seok Jeon, Won Jin Yi, and Kwang Suk Park</i>	
Optimization of Sensomotoric Insoles	554
<i>J. Subke, S. Kolling, J. Griesemann, P. Kleinau, and M. Staudt</i>	
Modeling the Dynamics of Recovery in Robot-Assisted Rehabilitation	558
<i>M. Casadio, P. Morasso, and V. Sanguineti</i>	
Position of the Head Measured by Digital Photograph Analysis	562
<i>R. Cerny, J. Hozman, J. Charfreitag, and P. Kutilek</i>	
Is the Bottleneck in Multitasking of Cognitive Origin? Tapping as an Experimental Assessment Tool	566
<i>M.T. Tarata, C.K. Dung, D. Georgescu, D. Alexandru, G. Staude, and W. Wolf</i>	
Superimposition of 2D Pressure Data and 3D Surface Data to Optimize Seat Shells in Rehabilitation	570
<i>J. Subke, P. Mischke, and J. Griesemann</i>	
Spatiotemporal Pixelization Method Based on Vertical Sub-sampling to Improve Reading Ability for Visual Prosthesis	573
<i>H.S. Kim, J.H. Shin, and K.S. Park</i>	
Optimizing Visual Cues for Brain-Computer Interfaces	576
<i>L.R. Jacinto, N.S. Dias, and J.H. Correia</i>	
Video Game-Based Exercise for Improvement of Calf Muscle Properties: A Case Study	580
<i>D.G. Sayenko, M. Milosevic, K. Masani, E.G. Sanin, K.M. McConville, and M.R. Popovic</i>	
Implanted Myo-neural Interface for Upper Limb Prosthesis	584
<i>N.R. Prabhav, S.R. Devasahayam, and R. Ojha</i>	
Closed-Loop Control of Epileptic Seizures via Deep Brain Stimulation in a Rodent Model of Chronic Epilepsy	588
<i>L.D. Iasemidis, S. Sabesan, L.B. Good, K. Tsakalis, and D.M. Treiman</i>	

**Recognition of Arm-Movement Electroencephalography (EEG) Using Motor-Related
Intrinsic Mode Functions Filtering and Cross Mutual Information** 592
C.F. Lu, C.Y. Hung, P.J. Tseng, L.T. Lin, Z.Y. Wang, and Y.T. Wu

Author Index 597

Study on a High Performance Shoes by using Silicon Rubber Elements with Human Compatibility

Yasuhiro Hayakawa¹ and Naoki Nishida¹

¹Department of Electrical and Control Engineering, Nara National College of Technology, Nara, Japan

Abstract— It is reported that the rate of elderly person in the total population of Japan is about 21.5% in 2007. Thus, the recent society of Japan is called as “Elderly Society”. In the society, many elderly people work or enjoy walking to keep health. However, some problems with respect to stumble over of elderly people are occurred. That is to say, in recent years, accidents of bone fracture with elderly people increase because of tendency to fall by a little step in a house. As one of this cause, it is considered that a center of gravity position with foot parts is changed.

Therefore, in order to solve this problem, we propose a new type of high performance insole by making use of sponge-core-soft rubber actuator (SCSRA). In this study, we indicate the structure of the insole. Further, the basic characteristics of the insole are clarified through some experimental results.

Keywords—High Performance Insole, Pneumatic, Care Prevention, Walking, Soft Rubber Actuator

I. INTRODUCTION

In Japan, the number of elderly people increases. On the other side, the number of young people decreases. As the result, it is reported that elderly people have to care another elderly person. In order to solve this problem, many kinds of support machines have been developed. However, with respect to an elderly person who is not physically handicapped, the bone fracture in tendency to fall sometimes becomes a big issue. For example, when the elderly people fall in a little step, some of them sometimes have trouble of bone fracture. Especially, the number of aged person who comes to keep bed increases by reason of the bone fracture of thighbone cervix in the tendency to fall.

With respect to this problem, it is reported that the main cause of tendency to fall is change of gravity position with each foot[1]. That is to say, when elderly people walk on the road, the center of gravity position moves to edge side of the sole as shown in Fig.1. This is because that the angle between the innominate bone and the thighbone is decreased by the muscle force depression of lower extremities. As the result, the elderly people are easy to stumble over.

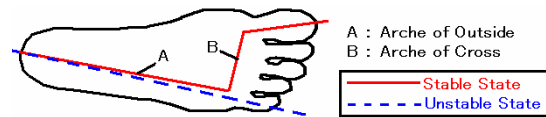


Fig. 1 Trajectory of Center of Gravity

Therefore, in order to solve this problem, we propose a new type of insole. The insole is constructed with compound rubber elements that a sponge rubber is covered with silicon rubber[2]. With respect to the element, since the sponge is coated with silicon rubber, air can be charged into the sponge chamber. As the results, it is possible to control the stiffness of the actuator by controlling pressure in the sponge chamber. Therefore, when some actuators are arranged in parallel, the actuators can estimate the distribution of external force that acts on the actuators. Thus, by making use of control of inner pressure of each actuator, the actuator can adjust torque that acts on the insole.

In this paper, we explain about the structure of insole that is constructed with the elements. Further, a test device to clear the effectiveness of the proposed insole is explained. Moreover, by using the test device an adaptive shape of the insole to distinguish between a roll motion and a pitch motion of the foot part is cleared. This is because that the walking motion is mainly constructed with the pitch motion and the roll motion. From these experimental results, basic characteristics of the proposed insole are clarified.

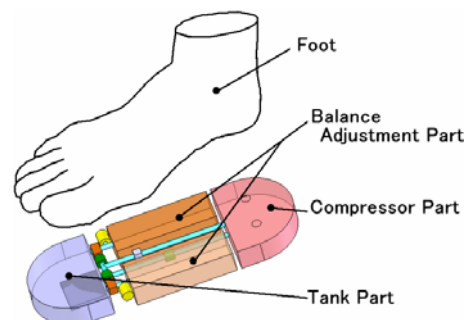


Fig. 2 Structure of High Performance Insole

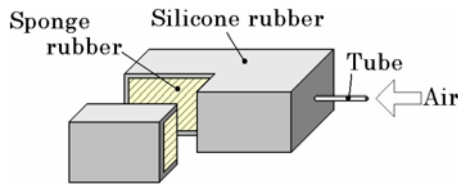


Fig. 3 Schematic View of Pneumatic Rubber Element

II. HIGH PERFORMANCE INSOLE

A. Structure of the Insole

The structure of proposed insole is shown in Fig.2. The insole is constructed with compound rubber elements, a rubber compressor and a tank chamber.

When a subject walks on a road with shoes that has the proposed insole, air is compressed by the deformation of rubber compressor according to the motion of heels. Further, the compressed air is charged into the air chamber of the tiptoe part in the insole. Since pressure in the rubber element is measured by a small size pressure sensor, the stiffness of each rubber element can be controlled by pressure in the air chamber.

B. Rubber Element

In order to develop a new type of insole, we consider a pneumatic rubber element. The structure of the element is shown in Fig.3.

The actuator is made of two materials. One is silicon rubber and the other is sponge rubber. The sponge is coated with silicon rubber, and air can be charged into the sponge chamber. As the results, it is possible to control the stiffness of the element by controlling pressure in the sponge chamber.

III. INSOLE TEST DEVICE

A. Structure of the Insole

When a person uses the shoes that has a high performance insole, the shape of the soft rubber element (SCSRA) is changed by external forces to the insole. This is because that the foot consists of a tiptoe, heel and the arch of a foot. Therefore, in order to clear the performance of the proposed insole, we developed a test device for an insole as shown in Fig.4. Figure 4(a) indicates a whole device and Fig.4(b) shows a foot plate (Ground) whose angles (a pitch angle and a roll angle) are controlled by pneumatic rotary actuators.

Further, a foot model is attached to the 6 axis force sensor that are set to the tip of the cylinder rod to drive in the direction of z axis as shown in Fig.4(c).

In the experiment, two pairs of SCSRA are put on the floor (Fig.4(b):Ground). Further the floor is driven by each rotary actuator. Thus, the inner pressure in the actuator is measured by a pressure sensor and the both torque and force in the direction of each axis that acts on the ankle part is measured by the 6 axis force sensor (Fig.4(c)).

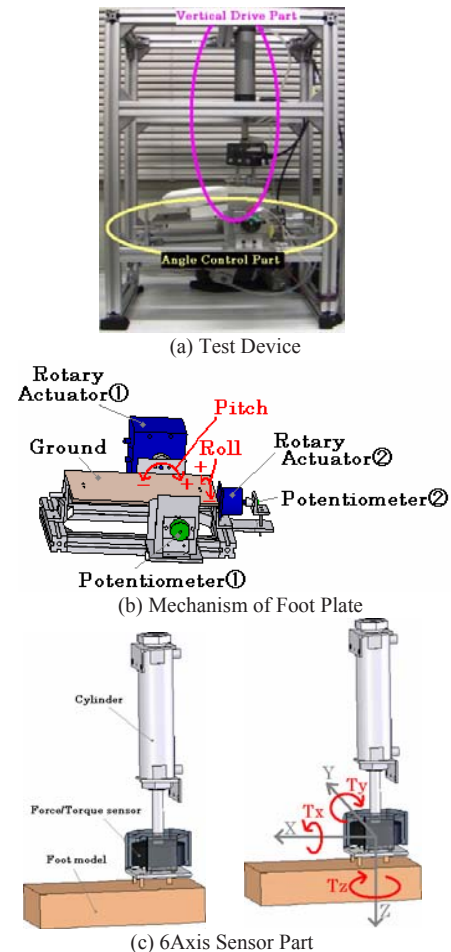


Fig. 4 Structure of Test Device

By using the insole test device, we investigate an adaptive shape of the insole to distinguish the difference between a roll motion and a pitch motion of the foot. This is because that the main motion of falling down is a roll motion of the foot as shown in Fig.1. Therefore, we measure difference pressure between each element by using pressure sensors in the elements. Thus, we clarify the adaptive shape that the difference pressure does not be changed by a pitch

motion but changes just only by a roll motion of the foot part.

B. Suitable Shape of the Element

In order to clear the adaptive shape of the element to distinguish between a roll motion and a pitch motion of the foot by value of pressure in the elements, we investigate the shape of the rubber element that the difference pressure between each rubber element is almost zero when the foot rotates in the direction of pitch motion. That is to say, variation of the inner pressure of the rubber element is measured by making use of the device that is shown in Fig.4.

In the experiment, we use 2 types of rubber element. Figure 5 shows each shape of the element. Figure 5(a) is a symmetric type and Fig.5(b) is an one side inclination type. By using these elements, we clear variation of the difference pressure between each element with respect to both a pitch angle and a roll angle.

Figure 6 shows the result with the symmetric type and Fig.7 is the result with the one side inclination type. The condition of each experiment is as follows.

[Condition]

- (a): Force(60N), Pitch Angle (θ : -10° - 10°)
Roll Angle(ϕ : 0°)
- (b): Force(60N), Pitch Angle (θ : 0°)
Roll Angle(ϕ : -10° - 10°)

From these results, it is cleared that in the case of the symmetric type, the difference pressure changes as the foot rotates in the direction of the pitch angle. On the other hand, in the case of one side inclination type, the value of difference pressure hardly changes when the foot rotates in the direction of pitch angle. As the result, it is clarified that the one side inclination type element can distinguish the motion of the foot by the change value of difference pressure between each element.

Further, the torque variation of the ankle part with respect to the one side inclination type element is shown in Fig.8. In this experiment the foot model is rotated in the direction of pitch motion. From this result, it is cleared that the variation of torque with roll motion is almost zero. Thus, by using the proposed element, the ankle is hardly damaged regardless of the shape of the one side inclination type.

IV. EFFECTIVENESS OF THE ELEMENTS

In this chapter, we indicate the effectiveness of balance motion of the proposed element by adjustment of the pressure in each element. Figure 9 show torque values of ankle

under each parameter (F: Pushing Force [N], R: Roll Angle of the Ground Plate [Deg], P: Settling Pressure [kPa]).

With respect to Fig.9 (a), when the inclination angle between foot and ground (where, the inside point of the right side foot is a base point) increases, the sign of roll angle becomes positive. That is to say, the inside point of foot back (Arch of foot) comes in contact first with the ground. At this time, it is cleared that by the apophysis of the foot, the torque becomes positive at the latter half part of the torque result (latter half of walking motion).

Further, from Fig.9 (b), we verify that as the initial pressure of the outside element in the insole increases, the sign of torque in the direction of roll rotation becomes negative. That is to say, the elements of insole generate torque to the inside direction of the foot.

Moreover, through Fig.9 (c), it is confirmed that when the pushing force of the foot to the ground increases, the roll torque in the direction of negative increases (Where negative sign means inside direction of the foot).

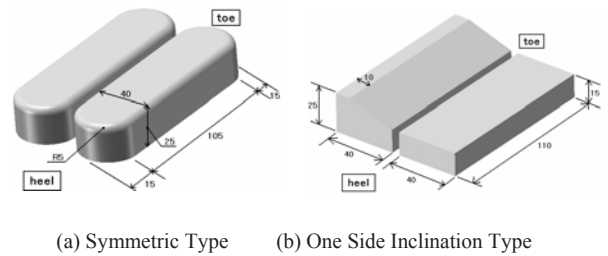


Fig. 5 Rubber Element (Right Side)

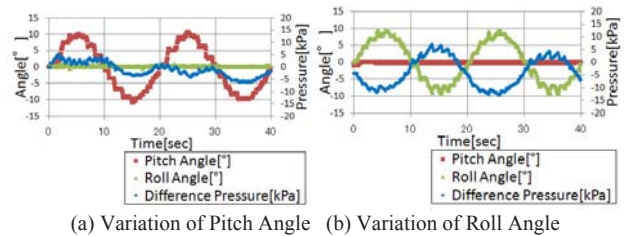


Fig. 6 Difference Pressure of Symmetric Type

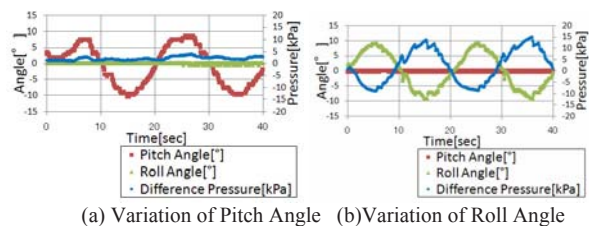


Fig.7 Difference Pressure of One Side Inclination Type

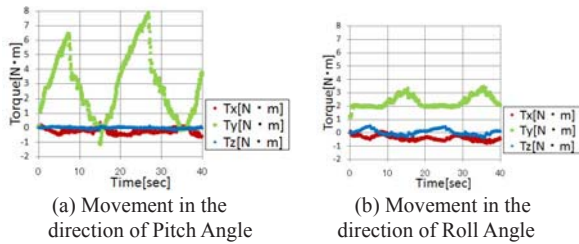


Fig. 8 Torque of Ankle Part (One Side Inclination Type)

V. HIGH PERFORMANCE SHOES

Finally we show a sample of shoes with the high performance insole in Fig.10. The shoes are constructed with rubber elements (SCSRA), pressure sensors, valves, a control circuit and an acceleration sensor. In the experiment, air is compressed by CP (Fig.10). Further the compressed air is charged into TP (Fig.10). Thus the charged air is used to control stiffness of the rubber elements (SCSRA).

VI. CONCLUSIONS

In this paper, we proposed a new type of insole using rubber elements. From some experimental results, we cleared performance of the proposed insole.

ACKNOWLEDGMENT

This research was partially funded by Grant-in-Aid for Scientific Research (c)(Project Number: 20500498). Additional support for this research was provided in part by SMC Co., Ltd.

REFERENCES

[1] M.P. Murray, et al. Walking Patterns of Healthy Old men, *J. Gerontology*, **24**, pp169-178, 1969

[2] Y. Hayakawa, H. Morishita, M. Aichi and R. Tsuda. Development of a Silicone Outer Fence Mold Actuator, *Journal of JSME, Series C*, **70**, pp. 433-439, 2004

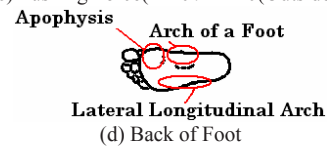
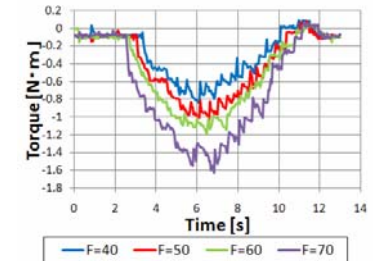
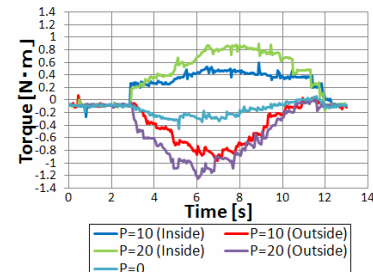
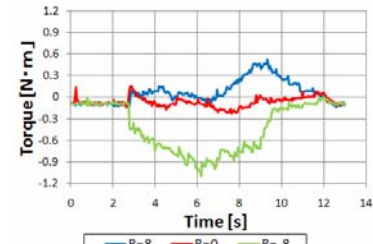


Fig.9 Experimental Results and Back of Foot

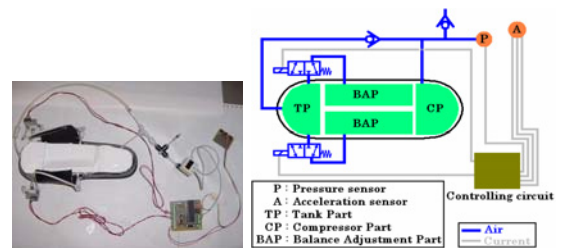


Fig.10 Sample of High Performance Shoes

Author: Yasuhiro Hayakawa
 Institute: Nara National College of Technology
 Street: 22 Yata-cho
 City: Yamato-Koriyama, Nara
 Country: Japan
 Email: hayakawa@ctrl.nara-k.ac.jp

Paraplegic Using a Reciprocating Gait Orthosis (RGO) with Functional Electrical Stimulation

¹J.-C. Hsieh, ²S.-C. Chen, ¹C.-C. Chen, ^{3,*}Y.-L. Chen, ⁴Walter -H. Chang, ⁵Y.-C. Li, ⁵Y.-Y. Shih

¹Department of Information Management, Hwa-Hsia Institute of Technology

²Department of Rehabilitation Medicine, Taipei Medical University

³Department of Computer Science, National Taipei University of Education (*correspondence)

⁴Department of Biomedical Engineering, Chung Yuan Christian University

⁵Department of Rehabilitation Medicine, Chang Gung Memorial Hospital

Abstract— In this study, we used latest reciprocating gait orthosis (RGO) and combined the use of functional electrical stimulation (FES). The combination provides larger support range and applies features of mechanical structures in walking assistant. The coordination of FES especially helps to restore the walking abilities that paralyzed patients lost.

Keywords—spinal cord injury, long leg brace, reciprocating gait orthosis, functional electrical stimulation

I. Introduction

Many studies of nowadays related to the use of mobility aids in spinal cord injured patients have demonstrated that when taking comfort and abandonment rates into consideration, RGO is a better choice than other kinds of walking aids. [1, 2] At present, there is an ongoing trend in other countries to substitute traditional braces with RGO in paraplegic patients. On the other hand, among the mobility aids used by native paraplegic patients, traditional Long Leg Brace (LLB) still plays a dominant role. [3, 4]

Therefore the main purpose of this study was to develop a walking aid equipped with FES device. We hoped the FES device could give electrical stimulations on specific muscles (quadriceps muscle, hamstring muscle) in paraplegic patients.

II. Materials and Methods

Equipments

In this study, we developed a walking aid equipped with FES device. This walking aid can be used by paraplegic patients to help them rehabilitate or walk on their own. The composition of this newly developed walking aid is shown in Figure 1: (a) the principal structure of the walker; (b) a pair of control buttons on the walking aid; (c) the FES device and its control circuit. The principal structure of the walking aid consists of supporting poles made up of rigid frames, including braces, handles and protective bars. The walking aid is convenient to use in the sense its height can be adjusted through design to accommodate the heights of different users.

The FES device and its control circuit are located at an appropriate place on the walking aid. The system control circuit consists of a FES circuit, an input circuit and an output drive circuit. The FES device is actually a four-channel electrical stimulator developed by our laboratory in former studies. The stimulator has an output

frequency $f=10\sim 1\text{kHz}$ and an output current $I=0\sim 140\text{mA}$. The pulse width of the output ranges from $50\mu\text{s}$ to $500\mu\text{s}$. Pressing down either one of the two buttons on the walking aid would trigger the FES device through the control circuit, and the drive circuit in the FES device would subsequently act to transmit stimulatory currents from the electrodes to specific muscles in the lower limbs of the patients. The left button is responsible to stimulate the quadriceps muscle in the left leg and the hamstring muscle in the right leg, while the right button is responsible to stimulate the quadriceps muscle in the right leg and the hamstring muscle in the left leg. The intensity of the stimulation can be determined by physical therapist on the basis of the assessment of the patient's illness so as to achieve an optimal function of the muscle.

Case report

After an initial assessment, our study included one patient as the subject. The subject was a 25-year-old female with a weight of 48kg and a height of 158cm. The subject was suffering a complete injury in the first section of the lumbar cord (L1) which had been diagnosed as the L1 Frankel C type. At the beginning of our study, the patient's spinal cord injury had lasted for 7 months. She received a walking training in our study for 5 weeks.

During the study, we have conducted measurements to collect basic data in relation to the patient's walking activities, such as time spent in a round of walk, the patient's steps, her heart rates and blood pressures before and after a walk, and volume of oxygen consumed (VO₂) during the walking. Using these basic data, we then calculated a few useful parameters which include: walking velocity (cm/sec), step length, difference between heart rates before and after a walk (HRdifference), difference between blood pressures before and after a walk (MBPdifference), oxygen consumption in each minute (ml/min) and oxygen consumption in each minute for each kilogram (ml/min-kg).

Experiment Design

Grouping: After one patient was chosen as our subject, we divided the patient's activities into three sections on the basis of the rehabilitation therapies she received: the control section, the A section and the B section.

Control section: The walking training included traditional physical therapy, specifically speaking, the patient used

Long Leg Brace for the rehabilitation therapy.

A section: The patient used Reciprocal Gait Orthosis for the rehabilitation therapy.

B section: The patient used Functional Electrical Stimulation along with Reciprocal Gait Orthosis for the rehabilitation therapy.

The spinal cord injured patient took different rehabilitation therapies at different hours of the day. First she would receive the specific training in control section, then the specific training in A section, at last the specific training in B section. She received the training on five days of the week; each day she has a two-hour training period both in the morning and in the afternoon. The whole training had lasted for about one month. At the end of the experiment, tests were conducted on the performances of the three sections respectively.

Statistical Analysis

After the patient had received the training in all three sections, a 10-meter walking test was conducted for each section. The test results could be divided into several categories of physiological parameter. Through individual statistical analysis on each category of data, we were able to understand the differential effects of the three walking aids on paraplegic patient.

We had employed a self-comparison method in this study and as a result the samples were not independent from each other. In addition, there were more than two normal state matrixes in the test results. We therefore conducted an ANOVA (Analysis of Variance) to test if any differences exist between three normal state matrixes, repeated measures ANOVA to investigate if the differences between the effects of the three walking aids on paraplegic patients are remarkable and a Newman-Keuls Multiple Test to explore the correlations between these three walking aids.

III. Results

Test Results of the Three Walking aids

On the basis of the above measurements and the data calculated, we were able to make comparisons between the effects of the three walking aids on the paraplegic patient.

A. HRdifference: Difference between heart rates measured before and after a walk. The HRdifferences of the three walking aids are shown in Table 1(A). The heart rate of the patient is easily influenced by various physiological or environmental factors, such as the mood and the habit of the patient or the air temperature. Therefore it is specified that the heart rate measured before a walk should be within a range of ± 5 beats/min compared to that measured before a last walk. From the test results we know that the average HRdifference of LLB (38.6 ± 4.4 beats/min) is 10 beats/min more than that of RGO (29 ± 5.9 beats/min), while the average HRdifference of RGO is 8 beats/min more than that of RGO&FES (21 ± 5.9 beats/min). Using ANOVA we find the P-value is $0.006 < 0.05$, indicating the differences between the three walking aids are significant.

- B. MBPdifference: The mean difference between blood pressures measured before and after the repeated walks. The MBPdifference of the three walking aids are shown in Table 1(B). From the test results we know that the difference between the MBPdifference of LLB and that of RGO is 5 mmHg, and the MBPdifference of RGO&FES is 1.5 mmHg more than that of RGO. Though the differences between the three walking aids seem not evident, using ANOVA we find the P-value is $0.001 < 0.05$, indicating the differences between the three walking aids are actually significant.
- C. Steps: The total steps of the subject for a specific walking distance. The steps of the three walking aids are shown in Table 1(C). Rather than walking in an urgent manner, the patient was admitted to walk in a natural manner when the measurements were being taken since the visible walking performances could readily reflect the effects of different walking aids. Table 1(C) clearly shows the differences between the three walking aids. The average difference between LLB and RGO is 18 steps; while compared to RGO&FES, RGO has a surplus of 7 steps on average. Using ANOVA we find that significant differences do exist between the three walking aids.
- D. Step Length: The average length of each step during a walk. The average step lengths of the three walking aids are shown in Table 1(D). The step length is calculated on the basis of the steps recorded for a given distance. It can serve to suggest if the walking aid is of any help for paraplegic patients during the walking. The test results clearly shows that the average step length of RGO&FES is bigger than that of RGO, while the average step length of RGO is bigger than that of LLB. The results also reflect significant differences between the three walking aids.
- E. Velocity: The walking speed of the subject during a 10-meter walk. The velocities of the three walking aids are shown in Table 1(E). The velocity of LLB is evidently slower than those of other two walking aids. The average velocity of LLB is 3 cm/sec slower than that of RGO, while the difference between RGO and RGO&FES is no more than 1 cm/sec. Using ANOVA we find the P-value is < 0.05 , indicating the differences between the three walking aids are still significant.
- F. Volume of Oxygen Consumed (VO_2): The volume of oxygen consumed by the patient for a given walking distance. It can be converted to oxygen consumption in each minute for each kilogram (ml/min-kg). The VO_2 of the three walking aids are shown in Table 1(F). The labor cost of the patient during a walk can be judged by the volume of oxygen consumed through respiration, in other words, VO_2 can be used as an indicator to assess the energy consumption of the patient during a movement. The average difference of VO_2 between LLB and RGO is 2.4, and the average difference of VO_2 between RGO and RGO&FES is 3.1. Using ANOVA we find that significant differences do exist between the three walking aids.

Statistical Analysis on Test Results

After a preliminary statistical analysis, the categories of data do suggest some characteristics of the three walking aids, though such suggestion is far from our objectives. Further analysis is needed so as to get information out of these data as much as possible. In the six categories of parameter above, the ANOVA results are a unanimous $P < 0.05$, which means in a 95% confidence interval, significant differences exist between the three walking aids for each category of data. In order to get an in-depth understanding of the differences between the three walking aids, we also conducted a Newman-Keuls Multiple Test on each category of parameter:

- a. HRdifference: We made the comparison on the basis of a critical q-value 0.05. The results of the statistical analysis are shown in Table 2(a), it serves to illustrate the comparison between the statistical results of the three walking aids. From Table 2(a) we can see that significant differences do exist between LLB, RGO and RGO&FES. As for the difference between RGO and RGO&FES, the calculated Q-value (2.90) is slightly smaller than critical q-value (3.26), indicating although the difference is small, it is statistically significant.
- b. MBPdifference: The results of the statistical analysis are shown in Table 2(b), it serves to illustrate the comparison between the statistical results of the three walking aids. From the comparison of Q-value and q-value in Table 2(b), we can see the differences between LLB and RGO/RGO&FES are evident. Meanwhile the difference between RGO and RGO&FES is not significant.
- c. Steps: The results of the statistical analysis are shown in Table 2(c), it serves to illustrate the comparison between the statistical results of the three walking aids. In this category of data, the calculated Q-value is much bigger than critical q-value, meaning the differences between the three walking aids are significant.
- d. Step Length: The results of the statistical analysis are shown in Table 2(d), it to illustrate the comparison between the statistical results of the three walking aids. From Table 2(d) we can see that the average step lengths of the three walking aids are in a descending order of RGO&FES, RGO and LLB. Significant differences exist between the three walking aids.
- e. Velocity: The results of the statistical analysis are shown in Table 2(e), it serves to illustrate the comparison between the statistical results of the three walking aids. We can see the difference between RGO and RGO&FES is not evident, and from Table 2(e) we know the difference between these two is insignificant. Significant differences do exist between LLB and other two walking aids.
- f. Unit Oxygen Consumption ($VO_2/\text{min}\cdot\text{kg}$): The results of the statistical analysis are shown in Table 2(f), it serves to illustrate the comparison between the statistical results of the three walking aids. The

statistical results of this energy consumption indicator show that significant differences exist between the three walking aids. RGO&FES has the best energy efficiency, and RGO comes next. Meanwhile LLB presents the highest energy consumption for the patient.

IV. Discussion and Conclusion

This study provides us an insight into the utility of traditional Long Leg Brace and new Reciprocal Gait Orthosis. We also get some knowledge about the beneficial use of Functional Electrical Stimulation. For most of the native spinal cord injured patients, their walking aids are limited to Long Leg Brace and wheelchair. Wheelchair is most popular due to the fast speed and labor saving property it provides. On the other hand, the combined use of RGO&FES will not only serve as a walking aid, but also bring forward other advantages such as preventing osteoporosis and bedsores, improving cardiopulmonary function, kidney function and circulatory function, as well as improving body posture and daily-life habits. Such combined use is also conducive to patients' psychological construction. RGO has already become a prevailing walking aid in foreign countries, but it is hardly used by native patients. Perhaps it is because RGO is newly introduced into the country and its price is frightening high. In the future, improvements should be made in the bulky and complex auxiliary system near the hip joints, as well as in the hard back tubes and chest staffs. There is also a need to reduce the weight of the orthosis. In the meantime, further studies such as going on to explore the long-term effect of these walking aids are essential. Such studies may act to bring more convenient mobility aids to paraplegic patients, with an expectation the patients could become more independent and be able to integrate into society again.

Acknowledgements

This work is supported by the National Science Council, ROC, under Grants 97-2221-E-152-001-MY3.

V. References

1. E.K. Donald, H. Nasreen, W. Phil, Comparative Study of Conventional Hip-Knee-Ankle-Foot Orthoses Versus Reciprocating-Gait Orthoses for Children with High-Level Paraparesis. *J Pediatr Orthop* 1997;3:333-340.
2. H. Shunji, G. Matthew, L. Thanj, M. Solomonow, et al. Energy Consumption in Paraplegic Ambulation Using the Reciprocation Gait Orthosis and Electric Stimulation of the Thigh Muscles. *Arch Phys Med Rehabil* 1990;71:687-693.
3. P.H. Peckham, G.H. Creasey, Neural Prostheses: Clinical Applications of Functional Electrical Stimulation Spinal Cord Injury. *Paraplegia* 1992;30:96-101.
4. L. Vodovnic, B.R. Bowman, P. Hufford, Effects of Electrical Stimulation on Spinal Spasticity. *J Rehabil Med* 1984;16:29-34.

Table 1. The ANOVA test results of the LLB, RGO 及 RGO&FES

	(A) HRdifference	(B) MBPdifference	(C) steps	(D) step length	(E) velocity	(F) VO2/min-kg
LLB	38.6±4.4	14.8±2.3	67.6±2.3	14.8±0.5	6.2±0.4	12.7±0.4
RGO	29.0±5.9	10.1±3.6	49.4±1.5	20.3±0.6	9.4±0.6	10.3±0.5
RGO&FES	21.0±5.9	8.6±2.4	42.6±1.9	23.5±1.1	10.1±1.4	7.2±0.3
ANOVA	0.006*	0.001*	0.008*	0.003*	0.002*	0.001*

*: p<0.05

Table 2. The Newman-Keuls Multiple test results of LLB, RGO and RGO&FES

	Mean Difference	P	Q	q (0.05)
(a) HRdifference				
LLB-RGO&FES	17.6	3	6.39	4.04*
LLB-RGO	9.6	2	3.49	3.26*
RGO-RGO&FES	8.0	2	2.90	3.26
(b) MBPdifference				
LLB-RGO&FES	6.2	3	8.20	4.04*
LLB-RGO	4.7	2	6.22	3.26*
RGO-RGO&FES	1.5	2	1.98	3.26
(c) steps				
LLB-RGO&FES	25.0	3	34.89	4.04*
LLB-RGO	18.2	2	25.40	3.26*
RGO-RGO&FES	6.8	2	9.49	3.26*
(d) step length				
LLB-RGO&FES	8.7	3	29.40	4.04*
LLB-RGO	3.3	2	10.99	3.26*
RGO-RGO&FES	5.5	2	18.40	3.26*
(e) velocity				
LLB-RGO&FES	3.9	3	10.37	4.04*
LLB-RGO	0.7	2	1.85	3.26
RGO-RGO&FES	3.2	2	8.52	3.26*
(f) VO2/min-kg				
LLB-RGO&FES	5.5	3	14.06	4.04*
LLB-RGO	2.3	2	5.96	3.26*
RGO-RGO&FES	3.2	2	8.10	3.26*

* : significant difference, Q value > q value

LLB : long leg braces

RGO : reciprocating gait orthosis

RGO & FES : reciprocating gait orthosis & functional electrical stimulation (FES)

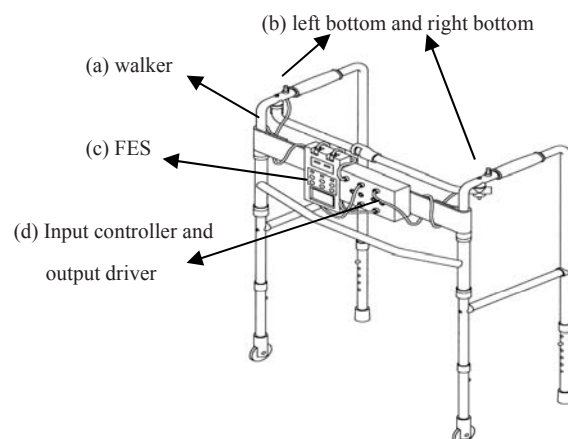


Figure 1 A novel walker (a) walker, (b) bottom, (c) FES , (d) Input controller and output driver

Habilitation Aid for Children with Balance Disorders

B. Jantek¹, Á. Jobbágy¹, J. Szemán¹, J. Schultheisz² and P. Bacsó²

¹ Budapest University of Technology and Economics/Dept. Measurement and Information Systems, Budapest, Hungary

² Gézengúz Alapítvány, Budapest, Hungary

Abstract— Gézengúz Foundation for Children with Birth Injuries offers a complex habilitation-rehabilitation therapy. The patented hemisphere-like tool, Huple[®], can improve the balance ability of affected children. The reported research work focused not only on objectively and quantitatively assessing the balance ability but also increasing the devotion of children to take part actively in the habilitation. Based on a 3D accelerometer sensor children can control simple PC games with the hemisphere. This preoccupies them for quite a long time. Quantitative assessment of balance ability is based on the evaluation of the output signal of two sensors (one on the head and one on the Huple[®]). Inclination angle of the head to upright position of healthy subjects is close to zero even when tilting their trunk. For children with birth injuries this angle can be as high as 50 degrees.

Keywords— habilitation, balance ability, objective assessment, Huple.

I. INTRODUCTION



Fig. 1 The Gézengúz hemisphere, Huple[®].

The Gézengúz Foundation was established in 1990. The purpose of the foundation has been to provide early intervention and complex therapy to children with birth injuries. To aid the complex therapy for these children – and also to help healthy children improve their balance ability –, a

special therapeutic tool, the Huple[®] (Figure 1) was developed and patented [1], [2], [3].

The hemisphere shaped tool helps instructors in playfully assessing and improving the balance ability of children. Sitting in the Huple[®] is a complex task requiring the coordinated movement of the trunk and muscles around the pelvic grindle. This task in itself has beneficial effect. Nevertheless, this is boring for the children. New games are needed to preoccupy them. If they can control PC games by moving the hemisphere (Figure 2) a new game can always attract them. This helps the habilitation process. Attaching a sensor to the head and one to the petal of the hemisphere makes possible to measure the tilting angle of the head as a function of the tilting angle of the tool.



Fig. 2 Controlling PC game by moving the Gézengúz hemisphere.

II. MATERIALS AND METHODS

A. The sensor hardware

The 3D acceleration sensor (MMA7260QT) was interfaced to the rapid prototyping environment (mitmót, [4]) of the Department of Measurement and Information Systems of Budapest University of Technology and Economics. A simple board (4 x 8cm) was assembled that is plugged into the connector of the mitmót mainboard. This made possible

a short development time. The complete sensor together with the local processor and batteries weighs 150g. The full scale value of the sensor is programmable, $\pm 1.5g$, $\pm 2g$, $\pm 4g$ or $\pm 6g$ can be selected. During the research work full scale value was set to $\pm 1.5g$. This sensitivity was found to be sufficient both for using the sensor as an input device for PC games and for measuring the tilting angles. The resolution is 12 bit, the sampling frequency was set to 100Hz.

B. The model for using the sensor for control

For the habilitation very simple PC games are needed as most children concerned are below 6 years and have movement disorders. The 3D acceleration sensor was attached to the Huple[®] (see Figure 2), the movement of the object on the screen can be controlled by moving the hemisphere. There are three possibilities for control. The tilting angle can determine the *position* of the object. In this case measurement noise – even after low-pass filtering – causes annoying vibration of the object on the screen. The second possibility is to move the object on the screen *as if a steel ball was moving on a tilted tray*. The third model is when the tilting angle determines the *velocity* of the object. All three possibilities were tested at the Gézengúz Foundation, and the third was found to fit best to the application.

C. Simple PC games for habilitation

The children participate in habilitation with pleasure if they have success experience. Therefore the operator can set the difficulty level of the games, even while the child is playing. The variable parameters are: the velocity of the moving object, the dependence of its speed on tilting angle, the size of the objects. The simplest game requires moving an object (a hedgehog) in one dimension, along a straight line. Apples are falling from trees along a line and the apples must be gathered by the hedgehog by moving it either to the left or to the right. The tilting angle of the sphere in the frontal plane determines the direction and the velocity of the hedgehog. The next game requires the movement of a hand in two dimensions, along the whole screen, see Fig. 3. Ladybirds are crawling along the screen and they should be caught by the hand. The tilting angle in the frontal as well as in the sagittal plane determines the position of the hand. Figure 2 shows a child playing with this game. There are eight ladybirds on the screen, the hand is actually in the middle.

Children can also control the PC games by moving their head when the sensor is attached to a helmet they are wearing.

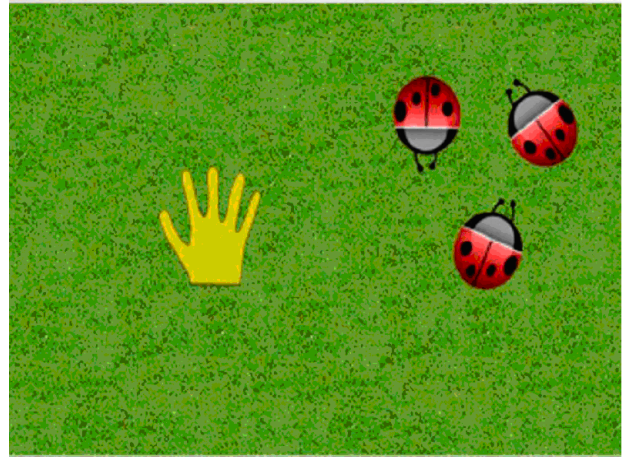


Fig. 3 Ladybirds are gathered by the hand. Objects are big enough not requiring too fine control.

III. MEASURING THE BALANCING ABILITY

A second sensor was embedded into a helmet. The helmet was covered with a textile mouse so that children do not object to wearing it. The output signals of the two sensors are collected while the Huple is tilted several times in both directions by the therapist. Subjects with healthy balancing ability hold their head in the upright position independent of the tilting angle of the hemisphere.

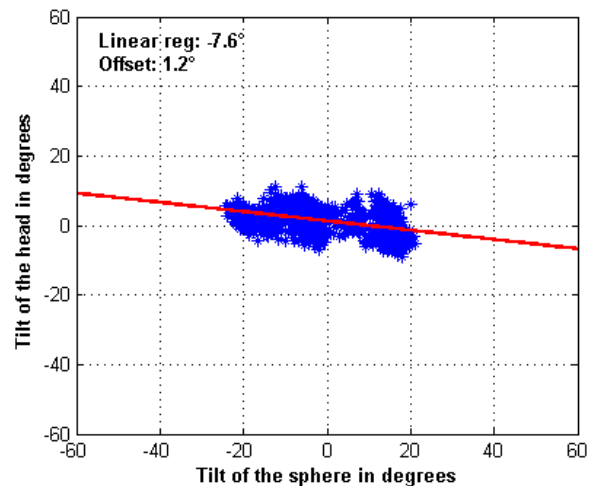


Fig. 4 Angle of the head and of the hemisphere, healthy subject.

Figure 4 shows the head angle versus tilting angle of the hemisphere for a young healthy adult (43 year old female). Less than 10 degrees is the maximum angle, when the hemisphere is tilted by 20 degrees. A slight overcompensation can be observed as well.

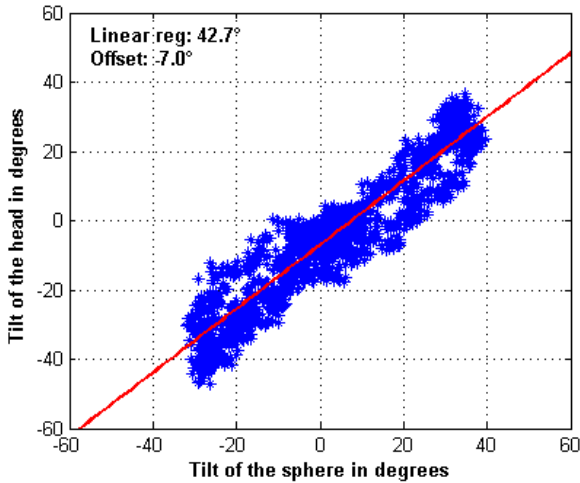


Fig. 5 Angle of the head and the hemisphere; child with balance disorders.

This is not the case for children with balance disorders. Figure 5 (10 year old male) shows that the head is practically moving together with the trunk, showing no activity of the vestibular compensation mechanism. The minimum recording time was 20s. The time function of the tilting angle during sitting in the Huple (healthy control subject, the sensor kept in hand) and the frequency spectrum corresponding to the marked part of the time function are given in Figure 6.

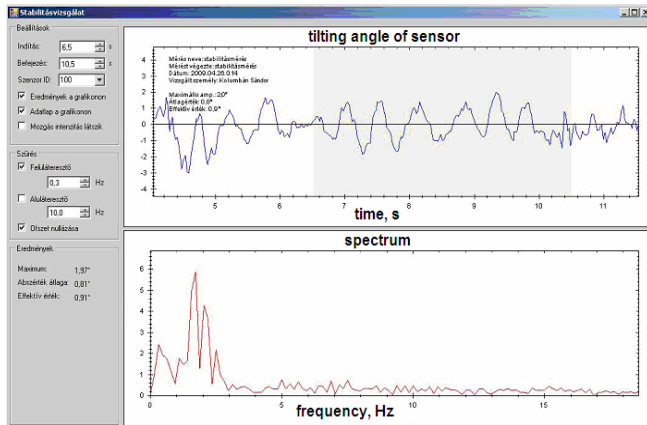


Fig. 6 The angle-time function (top) and its frequency spectrum (bottom) during balance measurement, the sensor is held by tested subject.

Balancing ability is characterized by three parameters. The simplest parameter is the maximum value of the tilting angle (after bandpass filtering), Θ_{max} , see Fig. 6. Usually, the smaller is the swaying of the subject sitting in the Huple, the smaller is the maximum tilting angle. Nevertheless, the maximum can derive from a single unskillful movement. Thus the mean value (I_{abs}) of the absolute value of the tilting angle - time function, $\Theta(t)$, over a given time interval (from T_0 to T_1) is a better estimate.

$$I_{abs} = \frac{1}{T_1 - T_0} \int_{T_0}^{T_1} |\Theta(t)| dt$$

The third possible parameter is the effective value (P) of the tilting angle - time function for the same (from T_0 to T_1) time interval.

$$P = \sqrt{\frac{1}{T_1 - T_0} \int_{T_0}^{T_1} \Theta^2(t) dt}$$

Θ_{max} , I_{abs} , and P are calculated after each test and displayed on the screen.

Balancing ability was tested under different circumstances. The simplest test is when the subject is sitting still in the Huple. Another test is when the subject is asked to stretch upwards for different objects (most frequently a plastic fruit) handed over by the physiotherapist. All these parameters have been found to be helpful during the habilitation process resulting in an objective assessment of the subjects' actual state.

Further testing situations can be easily realized using the above described measurement set-up. Neither the testing procedure nor the parameters to determine the subject's actual state are to be standardized before gathering measurement data from enough subjects at different habilitation centres.

IV. CONCLUSIONS

A simple sensor has been developed that greatly helps not only the quantitative assessment of the balancing ability but also the habilitation process. Children with birth injuries were found to be motivated and they played with pleasure when the level of the game was set to their ability. Further PC games can be offered that are controlled by the Huple[®]. Although the connection wire did not bother the children sensors using wireless transmission are under development. The wireless sensor together with the local processor and battery weighs only 24g. This will make the very effective everyday use, even at home, much simpler.

REFERENCES

1. www.huple.org
2. HUPLE movement and coordination improving tool. Hungarian patent HU/CA01/2184/07
3. Schultheisz J, Bacso P: The The Huple program and hydrotherapy for premature babies. Conf. proc. Eurlyaid 2008/Szeptember- Norway- Early Childhood Intervention in Europe. p. 22.
4. Tóth Cs, Scherer B, Kádár L, Bakó T: "Implementation possibilities of networked smart transducers", ICCCI2003, International Carpathian Control Conference, Tatranska Lomnica, Slovak Republic, 26-29 May 2003, pp. 198-201.

Address of the corresponding author:

Author: Ákos Jobbágy
Institute: Budapest University of Technology and Economics
Street: Magyar Tudósok krt. 2.
City: Budapest
Country: 1521 Hungary
Email: jobbagy@mit.bme.hu

Prototype Walker for children with cerebral palsy

P. Jureczko¹, T. Łosień², M. Sołtys¹, K. Jochymczyk¹ and A. Głowacka-Kwiecień¹, M. Gzik¹

¹ Silesian University of Technology, Faculty of Mechanical Engineering, Department of Applied Mechanics,
ul. Konarskiego 18A, 44-100 Gliwice, Poland

² Medical University of Silesia, The School of Health Care, ul. Medyków 16, 40-752 Katowice, Poland

Abstract— In this study, a model walker for children with cerebral palsy, (poliomyelitis) is presented. It was designed in Inventor environment. Ansys software is used for durability calculation. A prototype of this walker was also constructed and is currently being clinically tested on patients.

Keywords— Rehabilitation, Ansys, Inventor, cerebral palsy.

I. INTRODUCTION

Persons with gait disorder are not able to function normally by themselves in an upright position. They constantly need rehabilitation exercises, as lack of movement not only worsens their physical condition, but also has a negative effect on their mentality, causing depression. Therefore, in order to carry out exercises properly with patients, it is very important to use appropriate devices [1].

Designed and constructed walker enables patients to move self-dependently and overcome flexible resistance. A patient who is suspended on a hip harness is adequately relieved and protected from collapsing. The framework enables movement in sagittal plane as well as enables erect position of the patients with flaccid paralysis. Simple operation of the device and smooth adjustment of load during exercising (smooth adjustment of the pull of rubber bands) is a big trump. No such device was designed in Poland so far, thus its' effectiveness will be verified and confirmed by patients during everyday rehabilitation.

Patients with neurological disorders constitute to the enormously growing group of people permanently immobilized. The development of medicine allows us to save somebody's life in cases in which not so long ago it would have been impossible. Perinatal mortality has decreased, survival after a stroke also improved, as well as survival after congenital and acquired circulatory system disorders and many other disorders. Unfortunately, it is connected with the increasing number of disabled people who have considerably limited motor activity. And lack or deficiency of motor activity affects negatively all human body systems often life threatening [2].

II. DESIGN OF THE DEVICE

A. Structural Guidelines

The principal function of the device is to support and assist children with cerebral palsy during walking but not only. The walker also acts as an artificial framework with flexible resistance (similarly to Therasuit method) [3]. The use of the flexible resistance influences the relief and supporting of weakened muscles. It develops not only muscles responsible for walking but also abdominal and spine muscles (owing to proper spacing of elastic strings). There is a wide selection of strings, so they can be easily adjusted to each and every patient.

There is also an option of passive erect positioning of a patient.

Owing to the possibility of blocking the turning of joints (knees, ankles, and turning of the trunk) and also the precise fixing of the patient's body thanks to special bands and hip harness, even persons with flaccid paralysis can be brought up to erect position using the designed walker.

The presented device is made out of stainless steel, which makes the supporting frame stiff and resistant (Fig.1). At the same time, stainless steel is relatively easy to treat and very light [4].

The following structural guidelines were assumed:

- construction simplicity,
- easy assembly and disassembly,
- stiff and compact structure,
- exploitation safety,
- assurance of appropriate patient's body amortization and stabilization,
- possibility of selection of individual flexible resistance.



Fig. 1 Prototype Walker

B. Device model

The project of the device was designed in Autodesk Inventor 11. 3D visualization was prepared in order to confirm the assumed geometrical parameters and for analysis of frame durability. For the purpose of selecting appropriate device dimensions, a model was constructed taking into consideration size of a 5 year old child and on the basis of this model, dimensions of the walker were finally chosen.

The Prototype was constructed on the basis of the above mentioned model and the earlier prepared technical documentation.

The device can be split into the following:

- riding unit;
- framework unit with hip clasp.

The riding unit consists of a supporting frame, so designed as to obtain as much as possible space for legs, so that one does not interrupt the child during walking. The frame is made out of stainless steel welded with TIG method. A set of rocking levers together with shock absorbers which muffle vibrations that are transferred onto the rear axis, the front turning wheels and the rear

directional wheels are also included in the riding unit of the device.

The framework unit itself is a stabilization system of the patient's body suspended on a special hip harness. It acts as limbs separator, forming a skeleton allowing them to move in sagittal plane, thus leveling any bending or contracture. The framework was also designed to act as a "flexible orthosis" which relieves weakened muscles and at the same time creates resistance for other muscles, causing increased nervous system impulses which results in more efficient rehabilitation.

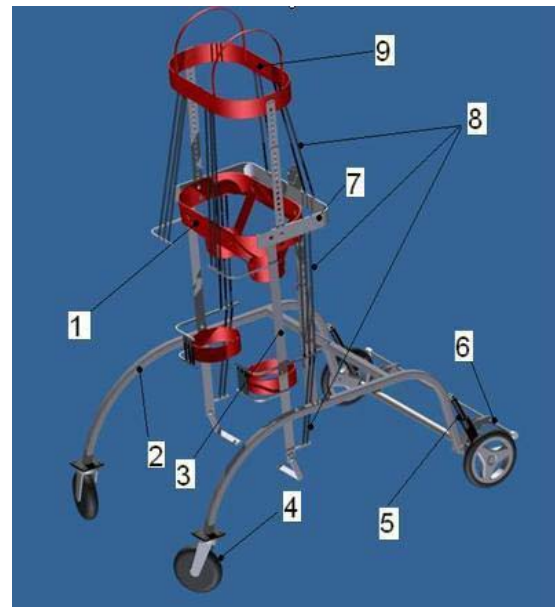


Fig. 2 Project the Walker (front)

The Walker consists of the following elements (Fig.2, 3)

1. hip harness,
2. main frame,
3. orthosis which stabilizes the limbs,
4. front turning rubber wheels,
5. rear shock absorber,
6. brake,
7. hip clasp,
8. elastic strings,
9. thorax harness,
10. knee pad,
11. a post for clasp height adjustment,
12. places indicating mounting of elastic strings,
13. rear pneumatic wheels.



Fig. 3 Project the Walker (back)

The shape of the frame was so designed as to obtain as much as possible space for the legs and so that no other part of the frame would interfere while the child is walking. That's why the square profile is protruding by the means of angular profiles, so that the legs would not be in the way of the distance profile.

The retaining beam acts as a bumper to protect the legs from coming into contact with any other objects. It also gives additional crosswise stabilization and stiffness to the frame. An element – the “top lug” is used to mount the shock absorber and sheet metal is used to mount front wheels.

The rocking lever connects the rear axis with the supporting frame by means of a swivel. The top part of the rocking lever the fork is connected with the supporting frame by means of a screw (M8) and a cap.

Rocking lever suspension together with the shock absorber ensures greater comfort during exploitation and prior, the shock absorber transfer most of the dynamic load, thanks to which, permanent frame deformation is avoided.

The adjustment mechanism of the hip clasp span is based on the action of a flat head countersunk screw. The whole system is hidden in the clasp profile (Fig.4), thanks to which it is discreetly secured and a better visual effect is obtained. The screw is located centrally owing to flanges which are screwed onto the clasp profile, thereby the screw does not move and adjustment is possible.

The flat head countersunk screw, i.e. its end with its right thread directly cooperates with the right sleeve and the end with left thread cooperates with the left sleeve. Both sleeves are screwed onto the profile, respectively to the right one and to the left one.

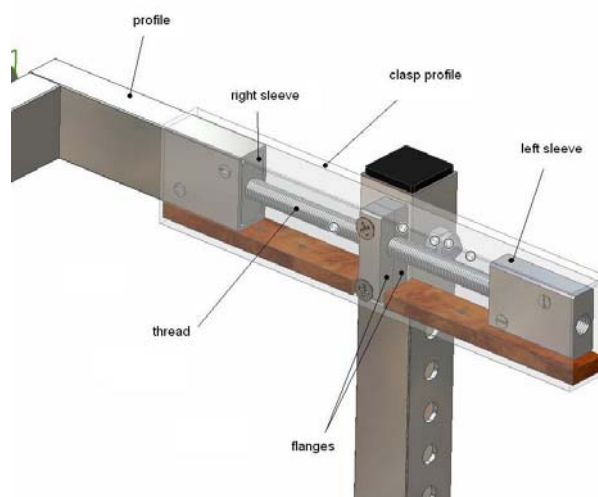


Fig. 4 The adjustment mechanism of the hip clasp span

The functions of the leg framework:

- stabilization and correction of legs during walking,
- it acts as a flexible orthosis (elastic strings of different thickness) which facilitates gait,
- it relieves patient’s body,
- it enables gait in sagittal plane,
- the use of elastic strings facilitates gait, the rubber bands support weakened muscles,
- flexible resistance does not burden the joints,
- bands hold patient’s upper and lower legs in one place in the framework,
- it is possible to block the turning of the framework knee joint, what gives possibility for a passive erect positioning of a patient with flaccid paralysis.

C. Durability Calculations

Frame durability calculations were conducted. The model was divided into 23 765 completed parts (Fig.5).

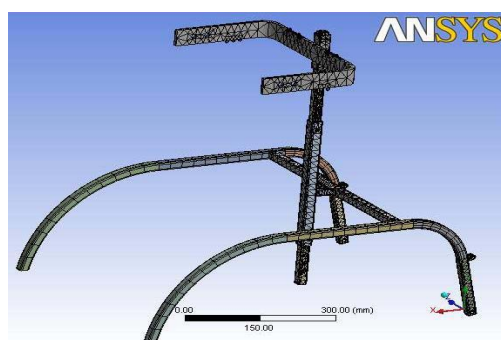


Fig. 5 The mesh model

Then it was firmly mounted onto four fulcrums. Obtained as a result of simulation equivalent stress values did not exceed 200 MPa in case of loading the frame in its maximum span. The stress values are therefore quite small in view of liminal stresses of selected steel, which are 740 MPa (Fig.6).

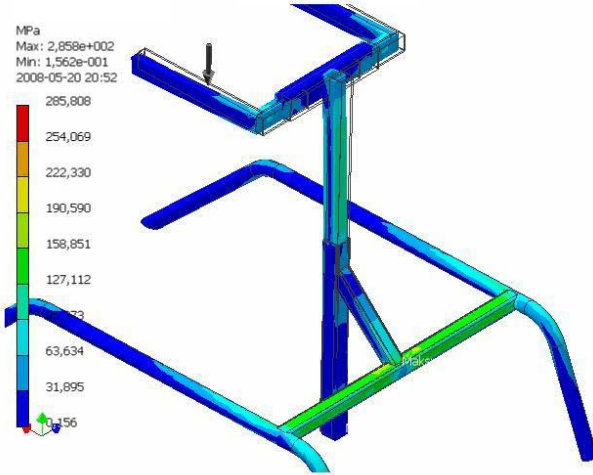


Fig. 6 Maximum equivalent stresses

Maximum principal stresses obtained in the analysis did not exceed 190 MPa (Fig.7).

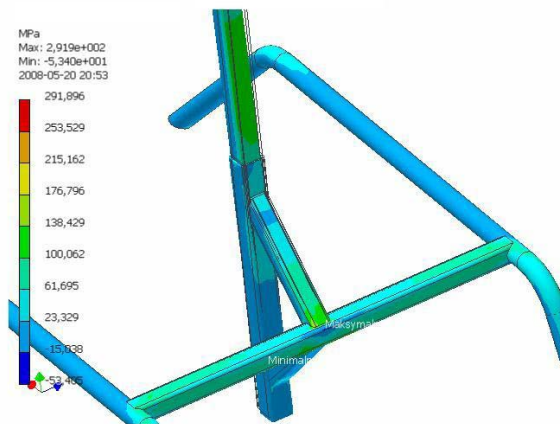


Fig. 7 Maximum principal stresses

Deformations obtained as a result of loading the frame at its maximum span are 21,4 mm (Fig.8). Although, it must be remembered that the analysis didn't take into consideration the activity of shock absorbers, which take

over most of dynamic loads, thus it can be supposed that such deformations will not occur.

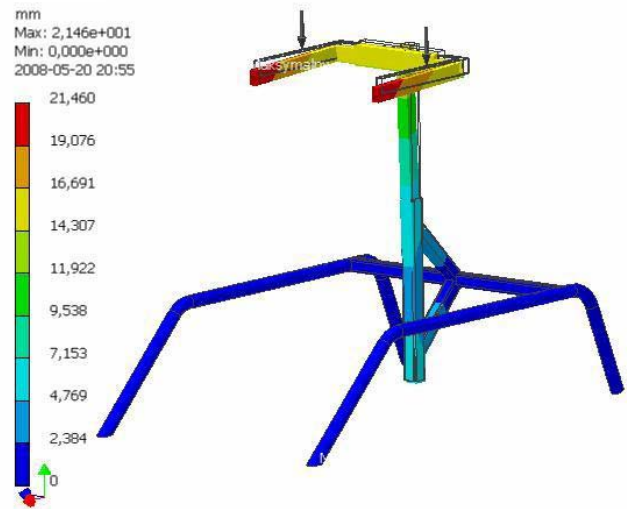


Fig. 8 Deformations obtained

III. CONCLUSIONS

The device ensures appropriate amortization and stabilization giving additionally sense of security to the patient. Its structure enables to hold a weight over twice as big as permissible, at the same time, the shock absorbers taking over most of the dynamic loads. Modular structure ensures easy assembly and disassembly. Operation is very simple and intuitive. The scope of different movements which can be carried out on this device enables one to be properly rehabilitated.

REFERENCES

1. Kiewski J. (2006) Rehabilitacja medyczna. Wydawnictwo Lekarskie PZWL, Warszawa
2. Nałęcz M. et al. (2004) Biocybernetyka i inżynieria biomedyczna. Biomechanika i inżynieria rehabilitacyjna. Akademicka Oficyna Wydawnicza Elit, Warszawa
3. <http://www.olinek.com.pl>
4. PN-EN/10088-2
Author: PhD Ing. Paweł Jureczko
Institute: Silesian University of Technology,
Street: ul. Konarskiego 18A
City: 44-100 Gliwice
Country: Poland
Email: pawel.jureczko@polsl.pl

Analysis of Joint movements and muscle length during sit-to-stand at various sitting heights in the Korean elderly daily life

S.J. Hwang¹, J.S. Son¹, J.Y. Kim¹, H.D. Kim¹, D.H. Lim² and Y.H. Kim¹

¹ Department of Biomedical Engineering, Institute of Medical Engineering, Yonsei University, Wonju, South Korea

² Korea Institute of Industrial Technology, Cheonan, South Korea

Abstract— In this study, we analyzed the elderly joint movements and changes in muscle length during STS at various sitting heights through the motion analysis and the musculoskeletal modeling. Five elderly and five young were participated in this experiment. Three heights of sitting posture which could represent typical sitting in Korean daily life were chosen as table seat (42cm), bath seat (21cm) and bottom (0cm). As the results, the elderly showed both smaller knee/hip flexion and larger trunk flexion relatively in comparison to the young during table seat STS. The elderly also showed larger dorsiflexion and smaller ROM of knee, hip, trunk compared to the young during bath seat STS. Additionally, the elderly showed larger plantarflexion, hip flexion, smaller knee flexion and trunk flexion during the first half of bottom STS and larger knee flexion, hip flexion and trunk flexion during the second half of bottom STS. In addition, we could know contraction and relaxation characters of major muscles in lower limb during various STS through the analysis of changes in muscle length by musculoskeletal modeling.

Keywords— Sit-to-stand, Joint movements, Muscle length, Korean elderly, Sitting heights

I. INTRODUCTION

Sit to stand (STS) movement is one of the most common activities in daily life. Sit to stand movement is a complex activity: it requires an adequate postural control during the motor transfer from a stable 3-points base, the sitting position, to a 2-points base, the standing position[1]-[3].

With aging, the deterioration of the ability to rise from a chair contributes a major source of disability and handicap. It accentuates the risk of falling, the dependence level in daily living activities and can lead to institutionalization[4]-[6].

In addition, Korean traditionally stands up from various sitting heights in one's daily life compared to other foreigners. As Korea enter rapidly to the aging society, needs of the elderly independent life are increasing. Therefore the importance of research about the analysis of elderly activity in daily life is rapidly increasing. In this study, we analyzed joint movements and changes of muscle length during STS(sit-to-stand) at various sitting heights(table seat, bath

seat, bottom) in the Korean elderly daily life by using the motion analysis and musculoskeletal modeling.

II. MATERIALS AND METHOD

A. Subjects

Ten elderly (69.4±6.3years, 161.6±6.1cm, 60.9±4.7kg) and ten young (24.4±1.3years, 173.3±3.3cm, 65.5±5.9kg) were participated in this experiment(Table 1).

Table 1 Characters of subjects

	Elderly	Young
Age(yr)	69.4±6.3	24.4±1.3
Height(cm)	161.6±6.1	173.3±3.3
Weight(kg)	60.9±4.7	65.5±5.9

B. Motion analysis

Joint movements(ankle, knee and hip) in sagittal plane during STS were measured by using six infrared cameras (VICON, U.K.) and thirty nine reflective markers which were attached on the body as the plug-in gait marker set(Fig. 1).

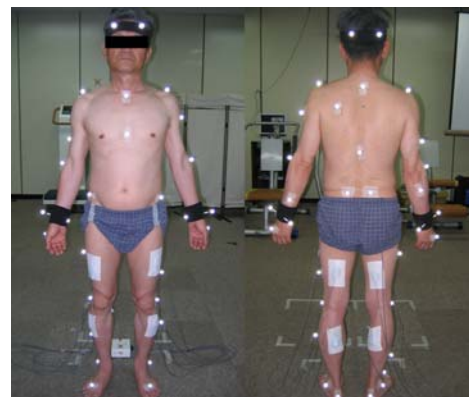


Fig. 1 Marker set for the motion analysis

Three heights of sitting posture which could represent typical sitting in Korean daily life were chosen as table seat (height from bottom: 42cm), bath seat (21cm) and bottom (0cm) as shown in Fig. 2.

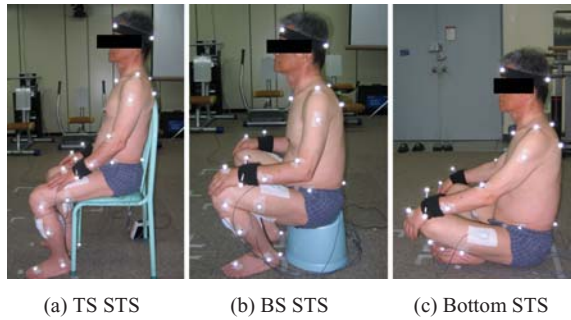


Fig. 2 Three heights of sitting posture for the experiment

All subjects were requested to keep the posture as close as possible to situations of their actual life. Every subject's feet were initially placed flat on the floor at a fixed location. The hands were also initially positioned on the knees. One cycle of STS was defined as from once the motion of standing started to when the motion of standing finished. In order to allow the assessment of trials consistency, subjects were asked to perform five trials with a break after each trial.

C. Musculoskeletal modeling & dynamic simulation

The musculoskeletal modeling and dynamic simulation were also performed to analysis changes of the length of major muscle in lower limb during STS using SIMM(Musculographics, U.S.A.) as shown in Fig. 3. Gastrocnemius, tibialis anterior, biceps femoris, rectus femoris, gluteus maximus and psoas were selected for major muscles of lower limb. We defend the muscle length in natural position as 100%, the muscle length was increased when the muscle relaxed and the muscle length was decreased when the muscle contracted.

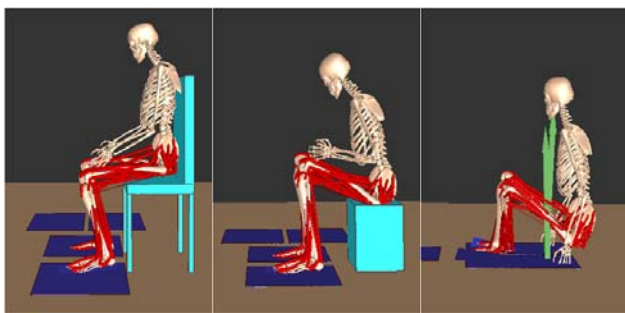


Fig. 3 Musculoskeletal modeling during STS

III. RESULTS & DISCUSSION

Fig. 4, Fig. 5 and Fig 6 were joint angles of during TS STS, BS STS and Bottom STS. The elderly showed both smaller knee/hip flexion and larger trunk flexion relatively in comparison to the young during table seat STS. The elderly also showed larger dorsiflexion and smaller ROM of knee, hip, trunk compared to the young during bath seat STS. Additionally, the elderly showed larger plantarflexion, hip flexion, smaller knee flexion and trunk flexion during the first half of bottom STS and larger knee flexion, hip flexion and trunk flexion during the second half of bottom STS. In addition, we could know contraction and relaxation characters of major muscles in lower limb during various STS through the analysis of changes in muscle length by musculoskeletal modeling(Fig. 7, Fig. 8).

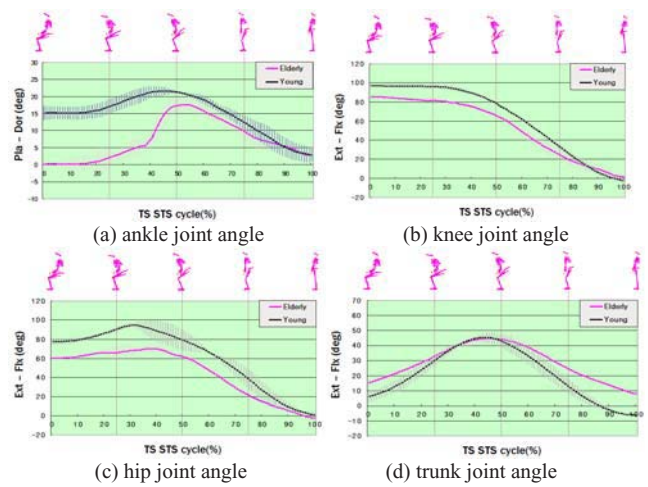


Fig. 4 Joint angles during table seat sit-to-stand(TS STS)

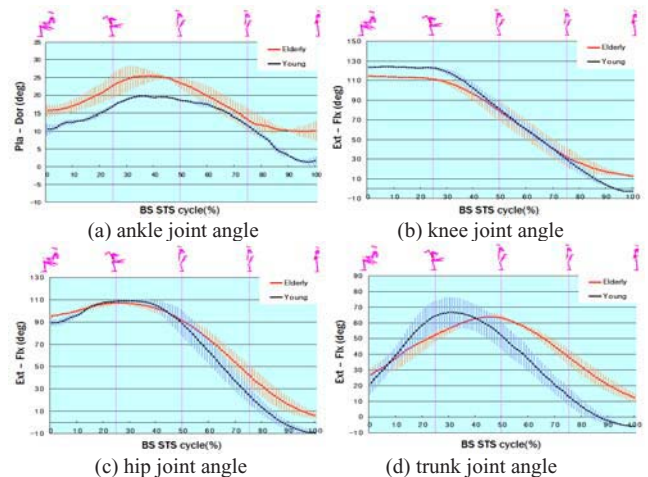


Figure 5 Joint angles during bath seat sit-to-stand(BS STS)

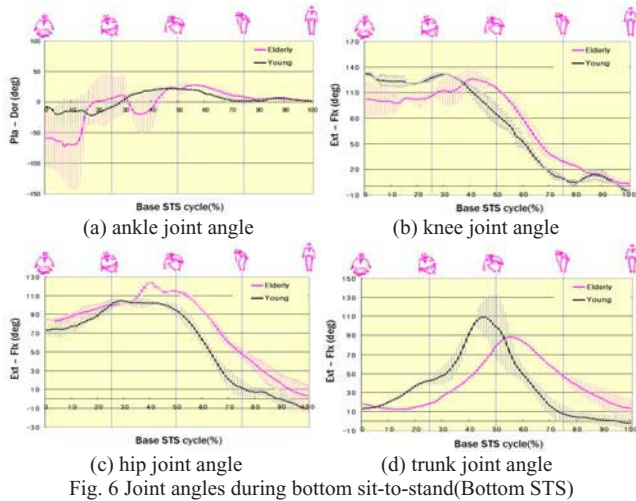


Fig. 6 Joint angles during bottom sit-to-stand(Bottom STS)

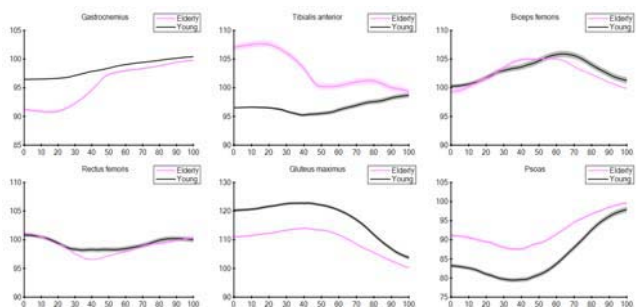


Fig. 7 Changes of the muscle length during TS STS

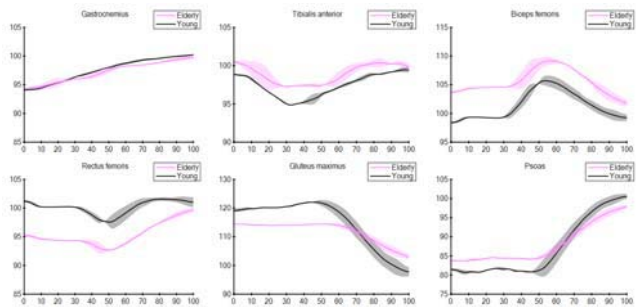


Fig. 8 Changes of the muscle length during BS STS

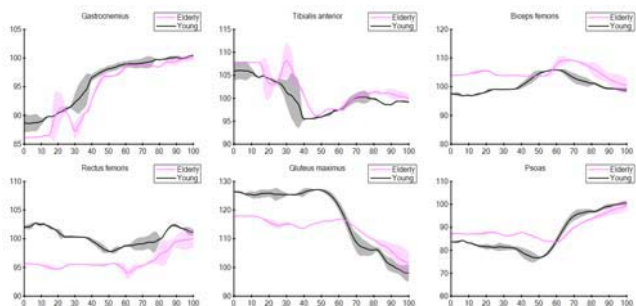


Fig. 9 Changes of the muscle length during Bottom STS

IV. CONCLUSIONS

Joint movements and changes of muscle length during STS(sit-to-stand) of various sitting heights(table seat, bath seat, bottom) in the Korean elderly daily life were analyzed by using the motion analysis and musculoskeletal modeling in this study. We expect results of this study could be useful information to design chairs for the elderly. In addition, those also could be helpful to train and strengthen proper muscles for the sit-to-stand.

ACKNOWLEDGMENT

This research project was supported by the Sports Promotion Fund of Seoul Olympic Sports Promotion Foundation from Ministry of Culture, Sports and Tourism and also was financially supported by the Ministry of Education, Science Technology (MEST) and Korea Industrial Technology Foundation (KOTEF) through the Human Resource Training Project for Regional Innovation

REFERENCES

1. Roebroeck ME, Doorenbosch CA et al. (1994) Biomechanics and muscular activity during sit-to-stand transfer. *Clin Biomech* 9:235-244.
2. Vander Linden DW, Brunt D et al. (1994) Variant and invariant characteristics of the sit-to-stand task in healthy elderly adults. *Arch Phts Med Rehabil* 75:653-660
3. Galli M, Cimolin V et al. (2007) Quantitative analysis of sit to stand movement: Experimental set-up definition and application to healthy and hemiplegic adults. *Gait & Posture* doi:10.1016/j.gaitpost.2007.10.003
4. Janssen WG, Bussmann HB et al. (2002) Determinants of the Sit-to-Stand Movement: A Review. *Physical Therap.* 82:866-879
5. Dehail P, Bestaven E et al. (2007) Kinematic and electromyographic analysis of rising from a chair during a ‘‘Sit-to-Walk’’ task in elderly subjects: Role of strength. *Clin Biomec.* 22:1096-1103
6. Weiner DK, Long R et al. (1993) When older adults face the chair-rise challenge: a study of chair availability and heightmodified chair-rise performance in the elderly. *J AM Geriatr Soc* 41:6-10

Author: Young-Ho Kim
 Institute: Yonsei University
 Street: 234 Maeji, Heungup
 City: Wonju
 Country: South Korea
 Email: younghokim@yonsei.ac.kr

Haptic robot for arm and wrist rehabilitation

Jakob Oblak¹, Imre Cikajlo¹ and Zlatko Matjačić¹

¹Institute for rehabilitation, Linhartova 51, SI-1000 Ljubljana, SLOVENIA

Abstract—Robot-mediated rehabilitation is rapidly advancing field. However, robots that are used for rehabilitation purposes are usually single task oriented. This paper presents the design of a universal haptic device (UHD) for arm and wrist rehabilitation. The essence of the developed device is in mechanical design, which enables the rehabilitation of the upper limb in two different modes; “ARM” and “WRIST” mode. By simple mechanical reconfiguration it is possible to switch between both modes, which enables gradual rehabilitation of complete upper limb. Device is actuated by 2-DOF haptic drive based on Series Elastic Actuation (SEA). The performance of the developed robot and impedance controller were tested in different regimes of operation: simulation of empty space and “high impedance” simulation. The results show that the developed haptic device may be used in robot - assisted rehabilitation.

Keywords— rehabilitation robotics, stroke, functional restoration, haptics.

I. INTRODUCTION

In order to increase the ratio between the outcome and cost of rehabilitation, robotic devices are being introduced into clinical rehabilitation [1-3]. Besides the cost-effective aspect, robotic devices introduce a higher accuracy and repeatability in performing rehabilitation exercises. Precise measuring of quantitative parameters by means of robotic instrumentation ensures objective monitoring of patient’s recovery. So far, many robotic devices have been successfully introduced into clinical rehabilitation of the upper limb. However, robots such as MIT-MANUS [4], GENTLE/S [5], Pneu-WREX [6] and NEREBOT [7] are designed to assist in arm reaching exercises, but lack the ability to assist in wrist and forearm motions. On the other hand, CRAMER [8], RICE WRIST [9], HAND MENTOR [10] and HWARD [11] robots are specifically designed to perform forearm and wrist movement exercises, but do not allow arm reaching exercising. An approach to overcome aforementioned limitations would be in designing of an universal device that could be used in different modes, which would allow alternating rehabilitation of the complete upper limb.

We propose a universal haptic device (UHD) based on 2-DOF haptic drive and mechanical design, which enables the

rehabilitation of the upper limb in two different modes; “ARM” and “WRIST” mode. In “ARM” mode, the UHD can perform planar arm-reaching exercises focusing on shoulder and elbow movements. On the other hand, “WRIST” mode ensures performing tasks where forearm and wrist movements are involved.

In this paper we outline the proposed concept and the first results of system performance evaluation.

II. DEVICE DESCRIPTION

The photography of the actual system and schematic of the universal haptic device (UHD) is presented in Fig. 1. The device is based on the 2-DOF haptic drive, which actuates the handle bar via uniquely designed mechanical construction of the UHD. The patient’s hand is attached to the handle bar, which can be adequately positioned or oriented, depending on the mechanical mode of the UHD. In “ARM” mode, the handle bar can be moved in a desired position, which ensures arm-reaching exercises. On the other hand, in “WRIST” mode, the handle bar is not moving but orientating instead, which allows forearm and wrist exercising, see Fig. 1(b).

A. Universality

By simple mechanical reconfiguration we can easily switch between both modes. For instance, if we want to perform exercise in “ARM” mode we lock the universal joint, see Fig. 2. In “ARM” mode UHD allows patient to perform reaching exercises in backward, forward, left and right direction. On a contrary, in “WRIST” mode, the universal joint should be unlocked and forearm fixed which enables turning the hand in a desired orientation, see Fig. 3.

The orientation of the handle bar can be easily adjusted. The advantage of that option is that the same handle bar can be used for both right and left arm rehabilitation, by simply re-orientating the offset position of the handle bar. Besides that, 3-DOFs are needed for complete wrist and forearm exercising: flexion/extension, radial/ulnar deviation and pronation/supination. However, the UHD allows only 2-DOF actuated movements. By setting the offset orientation of the handle bar in horizontal or vertical position, we can achieve alternating activation of all 3-DOF, see Fig. (3).

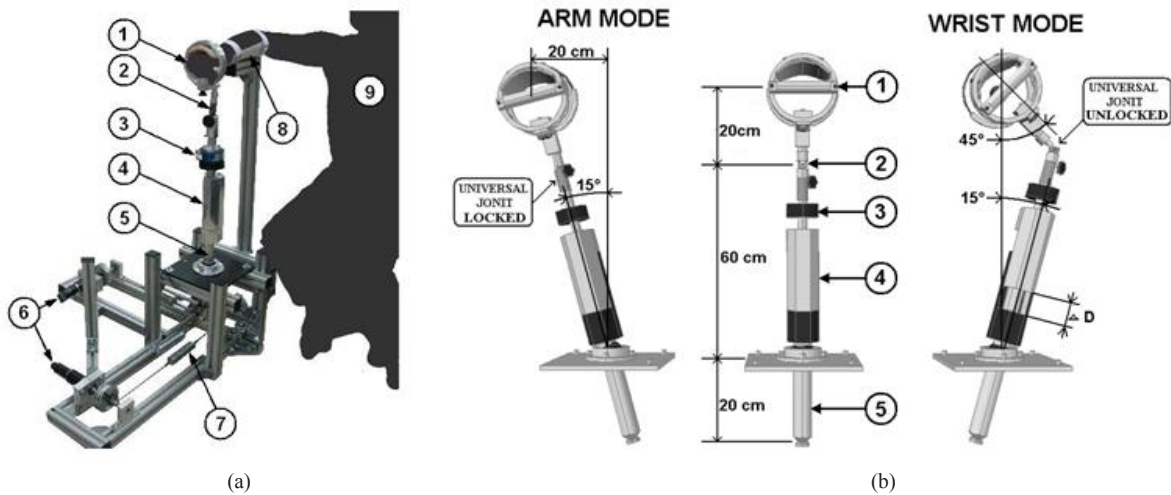


Fig. 1. (a) Overall view of the UHD prototype: 1-handle bar, 2-universal joint, 3-force sensor, 4-sliding mechanism, 5-actuated bar, 6-2 sets of DC motors with gears and encoders, 7-elastic springs, 8-forearm support (“WRIST” mode) and 9-patient. (b) Switching between “ARM” and “WRIST” mode can be easily achieved by locking or unlocking universal joint on the actuated bar. In “WRIST” mode, the length difference ΔD of the bar under the universal joint is compensated with sliding mechanism.

The range of motion of the UHD is limited by the angle ($<15^\circ$) of the spherical joint, which is inserted between the base and actuated bar, see Fig 1(b). In “ARM” mode range of motion is approximately ± 20 cm in all directions. On the other hand, in “WRIST” mode, the range of the handle bar rotation is approximately $\pm 45^\circ$. That can be achieved, if the lengths of the actuated bar above and below the unlocked universal joint are in ratio 1:3, (see Fig.1(b)).

B. Actuation

The actuation of the UHD is presented in Fig. 4(a). It consists of two sets of DC motors with gears and encoders, which are connected in series with elastic springs by means of string wires and pulleys. The string wires are connected to the actuated bar perpendicularly one to another.

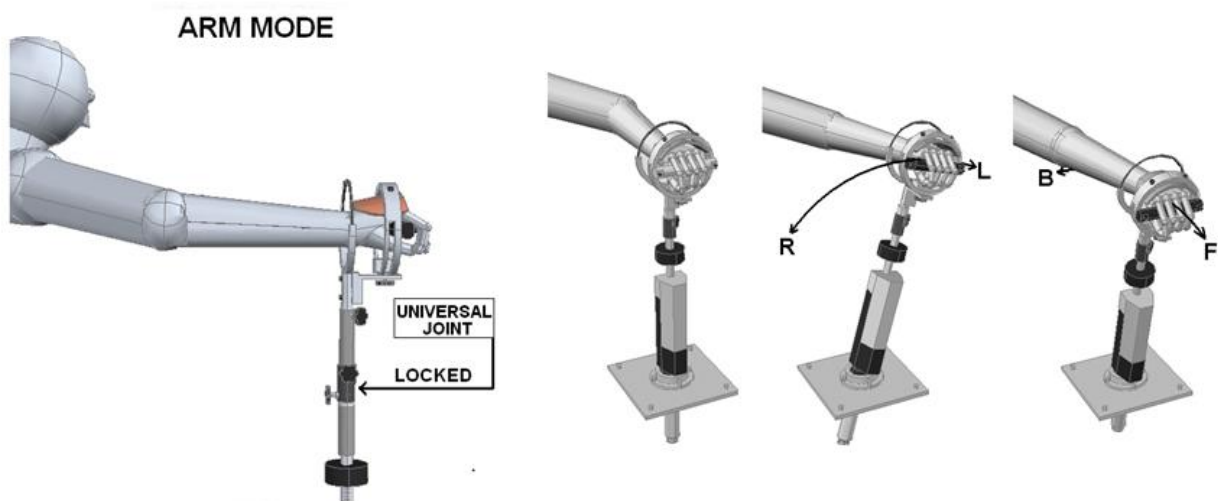


Fig. 2. Mechanical configuration in “ARM” mode; universal joint is locked. Patient arm can be moved in R-ight, L-ef, B-ackward and F-orward directions.

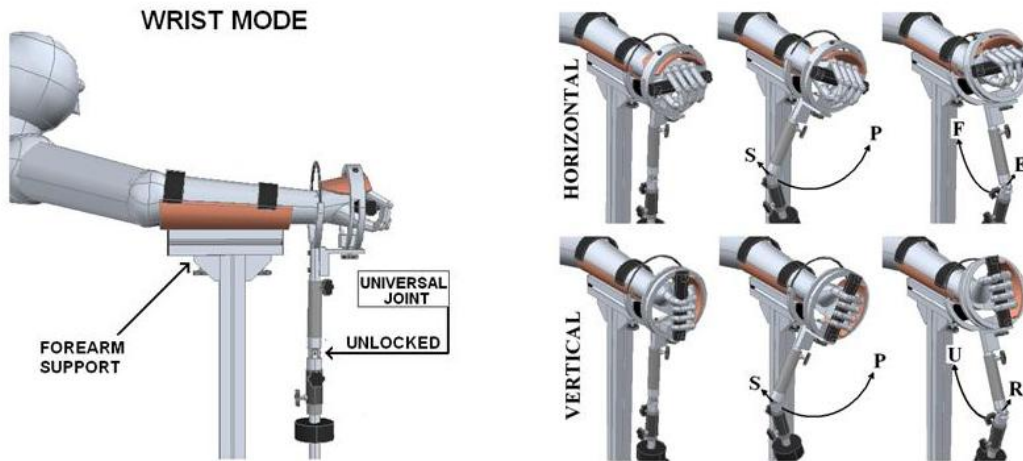


Fig. 3. Mechanical configuration in “WRIST” mode; universal joint is unlocked and forearm is supported to fix the centre of wrist joint rotation. When handle bar is set in HORIZONTAL position, S-upination/P-rotation and F-flexion/E-tension can be exercised. Setting the handle bar in VERTICAL position enables to exercise S-upination/P-rotation and U-Inar/R-radial deviation.

There are two reasons for utilization of series elastic elements in the actuation. The first reason is in geometrical design of the UHD actuation. The distance from the motor through the actuated bar to the pulley changes by moving the bar in perpendicular direction according to the string wire. The situation is demonstrated in Fig. 4(b) where $D+d \neq R+r$. That's why, it would be impossible to move the bar, if there was no elastic element inserted in series to compensate the length difference. In this regard the springs should be as compliant as possible, which would minimize mutual influence on both perpendicular directions of actuation. The second reason to use springs relates to the effect that, by introducing an elastic element in series with the motor we have actually designed a Series Elastic Actuator (SEA), which provides many benefits in force control. These benefits include greater shock tolerance, lower reflected inertia, more accurate and stable force control and the capacity for energy storage [12]. However, these benefits come with one shortcoming, which relates to reduction of achievable bandwidth. The stiffer the spring, the larger bandwidth of actuation system can be achieved. Therefore, selection of suitable spring stiffness requires a compromise between the above two contradicting requirements. We have experimentally determined spring stiffness to be 4000N/m, which enables actuator bandwidth of 2 Hz.

The maximal continuous torque of Maxon (Maxon, Sachseln, Switzerland) DC Motor (RE 40,150W) with Planetary Gearhead (GP 52 C, 81:1) is approximately 15Nm. Therefore, the maximal continuous force we can apply on the handle bar is 75N and the maximal continuous torque provided in “WRIST” mode is 20 Nm.

C. Impedance Control

Impedance control strategy, which is based on a principle: “measure position and display force” was

implemented. The force feedback signal is measured by means of JR3 (JR3, Woodland, USA) force sensor, which is mounted on the actuated bar, see Fig. 1(a,b). The desired/virtual force is calculated from impedance parameters and position of the actuated bar. The position of the actuated bar * , see Fig 3(b), is determined by the position of the encoders (θ_1, θ_2) on DC motors and the length of the springs (L_1, L_2), which are measured with linear potentiometers. The control algorithm is built in Simulink (MATLAB) and runs in real time on xPC target with the frequency of 1 KHz. All the signals from the sensors are assessed with National Instruments 6025 Data Acquisition Card (National Instruments, Texas, USA).

III. DEVICE PERFORMANCE EVALUATION AND DISCUSSION

The principal function of the UHD is to ensure a haptic interface between a patient and computer simulation based training task. Therefore, the device performance can be estimated by measuring how precisely, the UHD can exert required force on a patient. Because we are using an impedance control strategy, the required force we want to exert on the patient's hand is set by selection of the virtual impedance of the UHD. However, there are two “extreme” situations. The first situation is when we want to simulate “LOW IMPEDANCE” environment. In other words, a patient should not feel any force while performing movements in UHD workspace. That situation is typical for patient-in-charge oriented exercises. Another “extreme” situation occurs, when we want to simulate the biggest possible resistive force, to prevent the patient from moving in a certain direction. That situation is common for robot-in-charge mode or when we want to simulate “HIGH IMPEDANCE” environment.

The UHD performance was verified in an experiment with an able-bodied subject. Because the UHD allows performing exercises in “ARM” and “WRIST” modes, we measured forces/torques for both modes. The experiment was carried out by moving the handle bar in a single direction for approximately $\pm 8\text{cm}$ (“ARM” mode)/ $\pm 30^\circ$ (“WRIST” mode) with a frequency of 1Hz and simultaneously measuring the force/torque interaction between the patient and the device. This frequency was selected as being close to the upper bound of expected frequency range in upper limb movement rehabilitation. The maximal force that a tested subject felt in “LOW

IMPEDANCE” simulation was approximately 2.5 N (ARM)/ 0.5 Nm (WRIST), which is much smaller than in the case when the motors are switched off, where the maximal force can be up to 10N (ARM)/ 2 Nm (WRIST). On the other hand the maximal force that appeared in “HIGH IMPEDANCE” simulation was approximately 45 N (ARM)/ 8 Nm (WRIST), which corresponds to a virtual stiffness of 500 N/m (ARM)/ 0.33 Nm/ $^\circ$ (WRIST).

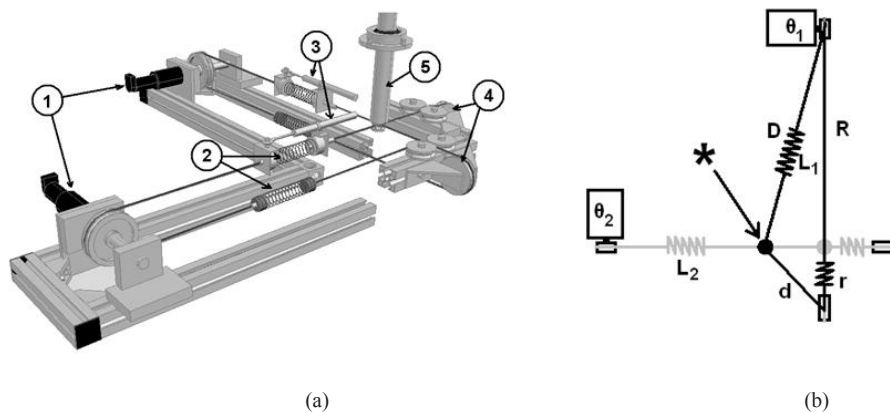


Fig. 4. (a) Actuation of the UHD consists of: 1-DC motors, 2-elastic springs, 3-linear potentiometers, 4-pulleys and 5-actuated bar. Motors, springs and actuated bar are connected with string wires. (b) By moving actuated bar in horizontal direction (*), the geometry of the actuation in vertical direction changes from $R+r$ to $D+d$.

REFERENCES

- [1] W.S. Harwin, J. Patton, and V.R. Edgerton "Challenges and opportunities for robot mediated neurorehabilitation," *Proceedings of the IEEE Special issue on medical robotics*, vol. 94, no. 9, pp. 1717 – 1726, September 2006.
- [2] J. M. Hidler, D. Nichols, M. Pelliccio, and K. Brady, "Advances in the understanding and treatment of stroke impairment using robotic devices," *Top Stroke Rehabil*, vol. 12(2), pp. 22-35, 2005.
- [3] H.I. Krebs, J.J. Palazzolo, L. Dipietro, M. Ferraro, J. Krol, K. Rannekleiv, B.T. Volpe, and N. Hogan, "Rehabilitation robotics: Performance-based progressive robot-assisted therapy," *Autonomous Robots* vol. 15, no. 1, pp. 7-20, 2003.
- [4] H. I. Krebs, B. T. Volpe, D. Williams, J. Celestino, S. K. Charles, D. Lynch, and N. Hogan, "Robot-aided neurorehabilitation: a robot for wrist rehabilitation," *IEEE Transactions on Neural Systems and Rehabilitation Engineering* vol. 15, pp. 327-335, September 2007.
- [5] F. Amirabdollahian, W. S. Harwin, and R. C. V. Loureiro, "Analysis of the Fugl-Meyer Outcome Measures Assessing the Effectiveness of Robot-Mediated Stroke Therapy," *Proceedings of the 2007 IEEE 10th International Conference on Rehabilitation Robotics* pp. 729 – 735, 2007.
- [6] R.J. Sanchez Jr., E. Wolbrecht, R. Smith, J. Liu, S. Cramer, T. Rahman, J.E. Bobrow, and D.J. Reinkensmeyer, "A pneumatic robot for re-training arm movement after stroke: Rationale and mechanical design," in *Rehabilitation Robotics, 2005. ICORR 2005, 9th International Conference on*, pp. 500-504, 2005.
- [7] G. Rosati, P. Gallina, and S. Masiero, "Design, Implementation and Clinical Tests of a Wire-Based Robot for Neurorehabilitation," *IEEE Transactions on Neural Systems and Rehabilitation Engineering* vol. 15(4), pp. 560–569, 2007.
- [8] S. J. Spencer, J. Klein, K. Minakata, V. Le, J. E. Bobrow, and D. J. Reinkensmeyer, "A low cost parallel robot and trajectory optimization method for wrist and forearm rehabilitation using the Wii," *Proceedings of the 2008 IEEE Conference on Biorobotics* pp. 869-874, 2008.
- [9] A. Gupta and M. K. O'Malley, "Design of a haptic arm exoskeleton for training and rehabilitation," *Mechatronics, IEEE/ASME Transactions on*, vol. 11, pp. 280-289, 2006.
- [10] E. J. Koeneman, R. S. Schultz, S. L. Wolf, D. E. Herring and J. B. Koeneman, "A pneumatic muscle hand therapy device," *Conf. Proc. IEEE Eng. Med. Biol. Soc.* vol. 4, pp. 2711-2713, 2004.
- [11] C. D. Takahashi, L. Der-Yeghiaian, V. H. Le and S. C. Cramer, "A robotic device for hand motor therapy after stroke," in *Rehabilitation Robotics, 2005. ICORR 2005, 9th International Conference on*, pp. 17-20, 2005.
- [12] G. Pratt, and M. M. Williamson, "Series Elastic Actuators," *Proceedings of the IEEE International Conference on Intelligent Robots and Systems I* pp. 399-406, 1995.

Author: Jakob Oblak
 Institute: Institute for rehabilitation
 Street: Linhartova 51
 City: Ljubljana
 Country: SLOVENIA
 Email: jakob.oblak@ir-rs.si

Movement Analysis by Accelerometry of Newborns for the Early Detection of Movement Disorders due to Infantile Cerebral Palsy

F. Heinze¹, N. Breitbach-Faller², T. Schmitz-Rode¹, and C. Disselhorst-Klug¹

¹ Chair of Applied Medical Engineering, RWTH Aachen University, Germany

² Social Pediatric Centre, Klinikum Esslingen, Germany

Abstract— The most frequent cause of handicap in children is infantile cerebral palsy (ICP). To limit the consequences of ICP, physiotherapy should start as early as possible. Seemingly effective, the developed diagnostic strategies are not easily applicable in a clinical setting, possibly due to its subjective character. The objective approaches are too expensive and too complex to be established in pediatric offices to be used in daily routine. The developed methodology allows the objective diagnosis of developing movement disorders in newborns due to ICP and is able to be established in the daily routine of pediatric clinics. Features as low expenses, less time consuming and manageability make this system available for the screening of large numbers of infants. With an early diagnosis of ICP it is possible to minimize follow-up problems and thus to relieve the health care system and above all to significantly improve the quality of life for both the patients and their families.

Keywords— accelerometry, movement analysis, infantile cerebral palsy, movement disorders.

I. INTRODUCTION

In the field of biomedical technologies, deployment of accelerometers is increasing. Since in the 1990s, it benefits from accelerometers research in other fields as for example the airbag release system development for the automotive industry [1]. Accelerometers provide even now sufficient quality and reliability for accessing the characteristics of movement disorders. Additionally they are inexpensive and sufficiently miniaturized for portable assessment [1,2]. Therefore, the accelerometers technology improves faster than other typically used tools for movement assessment [2]. There is a wide range of accelerometers application in assessing and quantifying human movements. Most implementations have concerned gait analysis. Furthermore, accelerometers have been successful introduced for reflex quantification and the monitoring of tremor in Parkinson's disease [1]. Summarizing the employment of accelerometers leads to improvements in the objective quantified assessment of movement disorders, their development, and therapy efficacy.

The most frequent cause of handicap and especially of movement disorders in children is infantile cerebral palsy (ICP). Approximately one out of 400 newborns is affected

and the risk increases significant for pre-term newborns, depending on gestational age it can reach up to 10%. Today, diagnosis is based on visual observation of the spontaneous movements performed by the infant by physicians [3]. The so-called general movement assessment (GMA) has been described by Prechtl and colleagues in detail [4]. GMA is a subjective procedure based on the observer's acquired expertise and as such is influenced by subjective impressions. Although seemingly effective, GMA is not necessarily easily applicable in a clinical setting, possibly due to its subjective character [5], and there is an incipient demand for more objective methods [5, 6].

Meinecke et al. developed a full diagnosis support system to assist physicians with less experience in GMA. The existing diversity between healthy children and children with ICP can be described objectively by mathematical parameters, which are calculated out of the movement data gained from an optical motion analysis system. Basing on these parameters, it is possible to separate reliable the healthy from the affected group and to give a diagnosis support to untrained physicians [6]. But optical systems [5, 6] are too expensive to introduce them in pediatric practices for regularly use. In addition, the systems are not portable and still have the optical line-of-sight restrictions. The most of the extracted parameters of Meinecke and colleagues depend on acceleration or velocity of the newborns extremities. For example, out of the optimal parameter combination of eight parameters five parameters are concerning acceleration or velocity. Based on the prior observations and the improvements in accelerometers' technology, the aim of our study, was the development of a methodology which allows the objective and quantitative description of unconstrained spontaneous movement in newborns as described by Meinecke and additionally is able to be established in pediatric offices to be used in daily routine. Within the study, the relevant movement parameters have to be ascertained which can be obtained out of accelerometers signals of the infant limbs. These parameters quantitatively describe the differences between healthy and affected subjects. Together with the extracted movement parameters, the developed accelerometer system permits a reliable prediction of patients at risk for developing movement disorders even at the age of newborn babies.

II. METHODES

A. Measurement system

The established assembly technology for accelerometers in human motion application is micromachining. The acceleration signal is generated by a physical method. Simplified, on a micro machined spring platform applied movable mass deflects in the presence of acceleration, which produces a measurable signal. The developed accelerometers based on the three axis micromachined accelerometer integrated circuit with a $\pm 10g$ maximum range and a 120 mV/g sensitivity. With a measurement chain disposed downstream including high-pass filtering (cut-off frequency = 0.16 Hz) and AC/DC conversion (100 Hz sampling rate) the system achieves a resolution of 0.01g. Due to the high-pass filter the measurements are not affected by the gravity. The whole sensor weighs with cover only 0,001 kg and has a 12 mm diameter with a height of 8 mm (Figure 1). The cable, witch connects the sensors with the AC/DC converter, is light, high flexible and tear proof. The whole device of sensor and cable is water proof and sterilizable.



Fig. 1 Developed accelerometer

B. Participants

Twenty-three infants, nineteen healthy full-term (mean gestational age 39,6 weeks, standard deviation 1,4 weeks, 10 female, 9 male) and four high-risk pre-term (mean gestational age 29,25 weeks, standard deviation 4,2 weeks, 2 female, 2 male) infants took part in the study. All infants were clinically and neurologically examined. Pathology of the “at-risk” patients was ensured through ultrasound-based detection of cerebral haemorrhage or periventricular leukomalacia. Additionally, a few of the patients were screened using computer or magnetic resonance tomography. The healthy subjects of the control group were separated from “at-risk” patients by the criteria mentioned in [6]. To ensure, that subjects in the two groups, healthy children and children with ICP, were allocated correctly with respect to

their diagnoses, all subjects’ diagnoses were confirmed by a follow-up examination after 1 year in the run-up to this study. All affected children developed ICP; all healthy children were without pathological findings. Hence, all children were allocated correctly and the consistency of the two groups can be considered to be reliable. In the infants’ first six months of life the development of spontaneous movements in healthy newborns and infants is divided into three post-natal phases: the writhing movements in the first eight weeks, the fidgety movements starting around six weeks after birth lasting till the twentieth week and finally the voluntary movements starting around the thirteenth post-natal week [4]. Therefore, measurements were carried out around the first, the third and the fifth months of life, calculated with respect to the target date of delivery.

C. Measurement Procedure

The agreement of the Ethical Commission regarding the entire measurement procedure was secured in advance. The parents of the subjects also gave their informed consent prior to starting the measurements. Furthermore, the measurements were stopped at any point at the request of the parents. The measurements took place approximately 1 hour after the last feeding and about 1-2 hours before the next feeding of the infants. This was to assure that the infant would be awake and unagitated as required for general movement assessment [4]. Prior to starting the measurement, the infant’s bodily dimensions and weight were registered. The room temperature was set at 29°C. As shown in Figure 2, accelerometers were affixed with skin friendly adhesive strips to the child’s extremities in defined orientation. The unclothed infant was then placed supine upon a blanket on the floor. Each child performed spontaneous movements for about 15 minutes which were recorded by the measurement system in segments of about 2.5 minutes. If any sensor dropped off during a measurement the dataset was cut at the point of disturbance before the parameters are calculated.



Fig. 2 Example of sensor placement.

D. Parameter extraction

The velocity was computed using the least squares fitting algorithm by The MathWorks (Matlab System Identification Toolbox). The movement trajectory was not calculated because the most of the parameters described by Meinecke depend on acceleration and velocity, as described in the introduction section. Additionally, due to noise effects, the calculation of the trajectory out of acceleration is very imprecise and unstable. So, with the extracted acceleration and velocity data of each sensor it is possible to calculate 32 parameters of the 53 described in [6]. A schedule of the used parameters can be found in the result section. The calculation is exactly equivalent to those used by [6].

E. Optimization of the parameter combination

To identify the optimal parameter combination to separate the best between the affected and healthy group and to contain the expenditure of time a dedicated algorithm had to be used. The optimization method has to search not only the best parameter combination but also the best size of the combination. A convenient solution is a genetic algorithm. Hence the genetic algorithm operates parallel with several possible solutions it is well faster than the complete search done by [6] with comparable reliable results. Furthermore, the genetic algorithm preserves the meaning of the parameters, so that the link to the physiological meanings as described in [6] persists. By dint of this method optimal combinations of parameters and optimal sizes of the combinations were found for each measurement date. Both, size of combination and parameters vary between the three measurement points as also expected by Prechtel and colleagues [4].

F. Classification

After finding the optimal parameter combination for each measurement date a classification system to evaluate the qualification of the parameter combination to distinguish between “healthy” and “at-risk” infants is necessary. To achieve good and comprehensible results as well as preferably low computing time, a decision tree was chosen. Additionally, the possibility of knowledge extraction is the key benefit of decision trees against other classification systems and especially useful in medical applications. In this application the tree uses the extracted parameters to minimize from node to node the impurity, i.e. to separate more and more between healthy and affected children. To evaluate the extracted parameter combinations and the classification measurement data was allocated in an evaluation database and a training database.

III. RESULTS

The preliminary results described below comprise the measurements of newborn babies within their first five month of life. Compared to [6] in this study visibility of the sensors is not a problem, but accelerometers are only fixed on extremities, the calculated parameters contain characteristics only of the hands and feet. The detection rates achievable by the use of chosen parameter combination are predicated on so far unclassified data. Table 1 shows sensitivity (correct classification of affected participants), specificity (correct classification of healthy participants) as well as overall detection rate for all measurement dates reached with the evaluation database.

Table 1 Classification results

Measurement	1st	2nd	3rd
Sensitivity	100%	100%	100%
Specificity	83%	86%	89%
Overall detection rate	89%	88%	92%

IV. DISCUSSION

Particularly with regard to the disadvantages of optical motion analysis systems as high expense, measurements are confined to a restricted volume, and the optical line of sight to the markers can easily be obscured [6], this study shows it is possible to obtain valid kinematic values for quantifying spontaneous motor activity in newborns using accelerometers. As the results published by Meinecke et al. [6] are limited to the movements of the feet due to the measurement system used and were determined only for the first measurement date the extracted parameter combinations are not comparable in respect of content. However, regarding the classification results Table 2 compares the results from Meinecke et al. with the results of this study at the first measurement date.

Table 2 Classification results at the first measurement date from Meinecke et al [6] vs. this study

Measurement	Meinecke et al.	This study
Sensitivity	100%	100 %
Specificity	70%	83 %
Overall detection rate	73%	89 %

Aside from the equal high sensitivity the classification system in this inquiry delivers better results. This was already expected by Meinecke as the consideration of the hand movements provides important information for the separation of healthy and affected infants [4]. Basing on these values comparable classification results can be

achieved as in optical motion analysis systems, but with less expense, and without volume and line-of-sight restrictions. The differences in between spontaneous movements of healthy and ICP-affected infants are highest during the third to fifth months, which correspond to fidgety movements and the absence of fidgety movements [4]. This tendency can be observed in the determined sensitivities and specificity (Table 1) as well. It becomes increasingly easier to classify children from the first to the third measurement date. The minor decrease in the overall detection rate from the first to second measurement date is due to the fuzzy age dependency of the spontaneous motor activity described by Prechtl and colleagues. Due to weak phase transitions between the developmental steps this age group is the inhomogeneous one. Apart from this, a high sensitivity is regarded to be the more important parameter as the non-detection of affected children would have a much worse consequence than an incorrect prediction for a healthy infant.

V. CONCLUSIONS

In combination with the low costs, reduced screening time, manageability, portability and the light weight of the measuring device the method presented is able to analyse the movements of newborns using accelerometry for the early detection of movement disorders due to infantile cerebral palsy. Overall detection rates of 89%, 88% and 92% for new patients were achieved. Essentially, this is a better result than that which most physicians, who are not specially trained in evaluating spontaneous motor activity, would be able to reach during visual examination and it is quite comparable to the results of trained physicians [5]. Since the method presented is objective, quantitative and easy to apply, it is suitable for helping to support early diagnosis and quantify therapy success in the daily routine of pediatric clinics. Moreover, the measurement system developed is an important step towards an easy to use, payable, computer-based movement analysis system for newborns with and without ICP. These are essential requirements in order to make this system available for the screening of large numbers of infants. With an early diagnosis of ICP it is possible to minimize follow-up problems and thus to relieve the health care system and above all to significantly improve the quality of life for both the patients and their families.

ACKNOWLEDGMENT

The authors gratefully acknowledge the financial support provided by the German Research Council (Deutsche Forschungsgemeinschaft DFG, DI 596/5-1).

REFERENCES

1. LeMoyne, R., Coroian, C., Mastroianni, T., & Grundfest, W. (2008). Accelerometers for quantification of gait and movement disorders: a perspective review. *Journal of Mechanics in Medicine and Biology*, 8(2): 137–152.
2. Culhane, K. M., O’Conner, M., & Lyons, G. M. (2005). Accelerometers in rehabilitation medicine for older adults. *Age Ageing*, 34: 556–60.
3. Stahlmann, N., Härtel, C., Knopp, A., Gehring, B., Kiecksee, H., & Thyen, U. (2007). Predictive value of neurodevelopmental assessment versus evaluation of general movements for motor outcome in pre-term infants with birth weights < 1500g. *Neuropediatrics*, 38: 91–99.
4. Prechtl, H. F. R. (2001). General movement assessment as a method of developmental neurology: new paradigms and their consequences. *Dev Med Child Neurol*, 43: 836–842.
5. Berge, P. R., Adde, L., Espinosa, G., Stavadahl, Ø. (2008). ENIGMA - Enhanced interactive general movement assessment. *Expert systems with applications*, 34: 2664–2672.
6. Meinecke, L., Breitbach-Faller, N., Bartz, C., Damen, R., Rau, G., & Disselhorst-Klug, C. (2006). Movement analysis in the early detection of newborns at risk for developing spasticity due to infantile cerebral palsy. *Hum Mov Sci.*, 25: 125–144.

Author: Franziska Heinze
 Institute: Chair of Applied Medical Engineering,
 RWTH Aachen University, Germany
 Street: Pauwelsstrasse 20
 City: 52074 Aachen
 Country: Germany
 Email: heinze@hia.rwth-aachen.de

Patient-Specific Finite Element Models of Transtibial Amputation in Several Prosthetic Users: The Inter-Subject Variability

S. Portnoy¹, I. Siev-Ner², N. Shabshin³, A. Kristal², Z. Yizhar⁴, A. Gefen¹

¹Department of Biomedical Engineering, Tel Aviv University, Ramat Aviv, Israel

²Department of Orthopaedic Rehabilitation, Chaim Sheba Medical Center, Israel

³Department of Diagnostic Imaging, Chaim Sheba Medical Center, Israel

⁴Department of Physical Therapy, Tel Aviv University, Ramat Aviv, Israel

Abstract— Active transtibial amputation (TTA) patients are at risk for developing pressure ulcers and deep tissue injury (DTI) while using their prosthesis. It is therefore important to obtain knowledge of the mechanical state in the internal soft tissues of the residuum, as well as the mechanical state upon its surface. For this purpose we employed patient-specific MRI-based non-linear 3D finite element models to quantify the internal mechanical conditions in 3 residual limbs of TTA prosthetic users during load-bearing. The geometrical characteristics of the residuum of the TTA participants varied significantly between patients, e.g. the residuum lengths were 7.6, 9.2 and 13.3cm. We generally found that internal strains were higher in the bone proximity than in the muscle periphery. The highest strains were found in the 7.6cm-long residuum. Correspondingly, the lowest strains were found in the 13.3cm-long residuum, which had the thickest muscle flap. Yet even in the case of a long residuum, a third of the distal tibial proximity area was occupied by internal principal compression strains above 5%. For both patients with shorter residual limbs, the internal principal compression strains above 5% occupied almost the entire distal tibial proximity area. We conclude that the wide variability between residual limbs necessitate quantitative analysis of internal mechanical state in the TTA individual to assess the risk for DTI onset.

Keywords— Deep tissue injury, finite element modeling, pressure ulcer, rehabilitation

I. INTRODUCTION

Deep tissue injury (DTI) is a life-threatening complication that initiates in a muscular tissue underlying a bony edge [1]. This injury is most common in wheelchair bound patients but also occurs in bed-ridden patients and lower limb amputees while using their prostheses. Transtibial amputation (TTA) dictates a new loading state in the severed limb via the posterior calf muscles, now folded under

the truncated bones. The gastrocnemius muscle flap and fat tissue cushioning the truncated tibia and fibula may precariously undergo large deformation and ischemia during load bearing, which may lead to cell death in the internal soft tissues. Even at a critical state of tissue necrosis, visual detection of the DTI on the skin of the patient will frequently result in a wrongful diagnosis as a pressure ulcer (PU) type I, i.e. superficial skin-deep wound. Most TTA occur due to vascular diseases, which are sometimes coupled with a certain level of peripheral neuro-deficiency. The TTA residuum inside the prosthetic socket is therefore endangered by the lack of sensorial alert to the formation of DTI. While laboring to avoid hazardous falls and maintain stability and symmetrical gait during daily activities, an internal ulcer may spread to surrounding tissues, inevitably resulting in hospitalization of the patient and possibly death.

Previous researches quantified surface skin-prosthetic socket stresses and temperatures using various sensors and computational modeling of the residuum as a first step in achieving socket optimization. These studies utilized interface stresses to evaluate socket alignment, different foot components, socks, liners and so on, while disregarding the internal mechanical condition of the residuum. Unfortunately, there is little correlation between interface stresses in the TTA socket and internal stresses in the bone proximity, where DTI initiates. Depending on the unique geometry of the individual TTA residuum, we hypothesize that the mechanical condition of internal soft tissues is significantly different, separating between a healthy and a frail residuum.

The purpose of this study is therefore to apply patient-specific magnetic resonance imaging (MRI) based non-linear finite element (FE) models to quantify the internal mechanical states in multiple residual limbs of TTA prosthetic users during load-bearing.

II. METHODS

In a recent study [2] we introduced a patient-specific FE three-dimensional (3D) modeling technique of the TTA residuum using MRI. The FE model was used to quantify internal strains and stresses in the confined residual limb during load-bearing. In order to obtain the geometry of the bones, muscle and fat tissues during upright standing position, the TTA patient donned a plaster cast, prepared before the trial and stood inside an open-MRI ("Signa SP" model, General Electric Co., CT, USA). Two scans were performed: the first taken while no pressure was applied to the residuum and the second scan was taken while the patient applied partial body weight to the residuum, against the MRI table. During the second trial we used thin force sensors (FlexiForce, Tekscan Co. MA, USA) to verify load bearing in this posture.

Three traumatic unilateral TTA patients participated so far in our ongoing research. All the patients chosen for this study are active individuals, who use their prosthesis for several hours on a daily basis. Helsinki approval (#4302/06 from Sheba Medical Center, Ramat-Gan, Israel) and informed consents were obtained before the trials. Table 1 lists patient information for the participating subjects.

Table 1 Patient information for the participants

Patient #	#1	#2	#3
Gender	Female	Male	Male
Age (years)	32	44	63
Amputated limb	Right	Left	Right
Weight (kg)	50	82	64
Years post-amputation	2	4	41
Illnesses	-	Diabetes	-

The transversal MRI scans of the unloaded residuum were uploaded to a solid modeling software (SolidWorks 2009, SolidWorks, MA, USA). Then, a 3D solid model of the truncated bones, muscle flap, fat and plaster cast was exported to an FE modeling software (ABAQUS v. 6.8, SIMULIA, RI, USA) for non-linear large deformation analyses. A 2mm skin layer was configured in the FE software. We measured the downward displacement of the tibia and fibula, relative to the most distal point of the limb at the scans with and without load-bearing. This displacement was used as a boundary condition applied to the FE bones. The exterior surface of the plaster cast was constrained for all translations. A friction coefficient of 0.7 was set between the skin and the cast. All the internal surfaces, i.e. fat/muscle and muscle/bones, were tied together.

By imposing the downward displacements of the bones, measured in the MRI trials for each patient, we were able to calculate 3D distributions of soft tissue strains per each model. Since the patient-specific mechanical properties of the muscle, fat and skin tissues of the individuals were unknown, we refrained from further calculating stresses from

the strain tensors. However, since ABAQUS formally requires definitions of constitutive laws and properties for each model component, these were defined as follows. The bones were assumed to be rigid. The cast was assumed to be a homogeneous, isotropic and linear-elastic material, with elastic modulus of 1GPa and Poisson's ratio of 0.3. All the soft tissues were assumed to be hyperelastic, homogeneous and isotropic, and were modeled using the Generalized Mooney-Rivlin Solid strain energy function [3]:

$$W = C_{10}(I_1 - 3) + C_{11}(I_1 - 3)(I_2 - 3) + \frac{1}{D_1}(J - 1)^2 \quad (1)$$

where the invariants of the principal stretch ratios λ_i are $I_1 = \lambda_1^2 + \lambda_2^2 + \lambda_3^2$ and $I_2 = \lambda_1^{-2} + \lambda_2^{-2} + \lambda_3^{-2}$, the relative volume change is $J = \lambda_1 \lambda_2 \lambda_3$, and C_{10}, C_{11}, D_1 are the constitutive parameters. Values for the constitutive parameters C_{10}, C_{11}, D_1 were adopted from the literature for all soft tissues, and are specified in Table 2.

Table 2 Material parameters for soft tissues of the transtibial residuum represented using eq. (1)

Soft tissue	C_{10} [kPa]	C_{11} [kPa]	D_1 [MPa^{-1}]
Fat	0.143	0	70.2
Muscle	4.25	0	2.36
Skin	9.4	82	0

The bones were meshed with 4-node quadrilateral surface elements ("SFM3D4" in ABAQUS). The muscle flap, fat tissue and plaster cast were meshed with second-order 10-node modified quadratic tetrahedron elements ("C3D10M"). The skin tissue was meshed with 6-node quadratic triangular membrane elements ("M3D6").

We calculated distributions of principal compression and tension strains, maximal shear strain and strain energy density (SED). Strains are reported here as engineering strains. We defined two separate muscular volumes of interests (VOI; Fig 1b): The first VOI is a layer of all the elements contacting the third distal end of the tibia, i.e. the bone proximity layer (BPL) and a second VOI of all the elements contacting the fat/skin tissues, that are under the projection of the distal third of the tibia, and that are located not higher than the height of the distal third of the tibia, i.e. fat proximity layer (FPL).

III. RESULTS

The geometrical characteristics of the transtibial residual limbs measured on the 3D patient-specific solid model are specified in Table 3. According to our measurements, patient #2 had the longest residuum, manifesting in longer tibia and fibula. Additionally, the soft tissue bulk of patient #2 was thicker as the muscle cushioning the distal tibial end

was 2.5-fold and 10-fold thicker than the flap muscle under the tibias of patients #3 and #1, respectively (Table 3). The volume of the muscle flap of patient #2 was more than 3-fold greater than the volumes of the muscle flap of patients #1 and #3. Patient #1 is very thin so that no fat tissue could be isolated from her MRI scans for the solid model. The limb of patient #3 was amputated at the most proximal location compared to patients #1 and #2, resulting in the shortest tibial length (Table 3). The residuum of patient #3 had a conical shape as opposed to the more cylindrical shapes of the residuum of patients #1 and 2.

Table 3 Geometrical characteristic of the residual limbs

Patient #		#1	#2	#3
Length [cm]	Tibia	9	11.2	6.8
	Fibula	5.1	8.9	5.3
	Muscle flap under the tibia	0.2	2.1	0.8
Bevelment [°]	Tibia	12.5	52.3	18
	At the tibial tuberosity	10	14.9	14.5
	Central tibia	5.8	8.1	10.5
Cross-sectional area [cm ²]	Distal tibia	1.3	1.5	2.1
	Central fibula	0.65	0.6	0.64
	Distal fibula	0.3	0.2	0.1
	Central muscle	39.2	58.8	43.8
	Distal muscle	9.2	33.6	5.0
	Muscle	196.3	702	183.3
Volume [cm ³]	Fat	0	90.2	13.7
	Skin	38.1	92.4	39.6

Vertical displacements of 1, 1.6 and 1.8mm of the bones towards the MRI table were measured on the loaded and unloaded coronal MRI scans of patient #1 to #3, respectively. The mean principal compression and tension strains, maximal shear strain and SED are presented in Table 4 for the three TTA patients. Generally, mean internal strains at the tibial proximity were higher than mean strains at muscle tissue near the skin of the residuum. Mean strains found in the residual limb of patient #2 were one magnitude of order lower than mean strains found in the residual limbs of patients #1 and 3.

Table 4 Mean principal compression and tension strain, maximal shear strain and SED for the three TTA patients. Values in parentheses are standard deviations from the mean.

Patient #		#1	#2	#3
Mean principal compressive strain [%]	BPL	12.8 (9.7)	3.1 (1.3)	14.2 (9.1)
	FPL	6.2 (8.8)	2.5 (1.1)	13.7 (11.8)
Mean principal tensile strain [%]	BPL	11.1 (7.1)	2.8 (1.4)	12.6 (7.7)
	FPL	5.0 (7.0)	2.0 (0.7)	11.1 (10.2)
Mean maximal shear strain [%]	BPL	12.6 (9.9)	2.9 (1.3)	14.9 (10.4)
	FPL	6.1 (9.1)	2.5 (0.8)	13.1 (11.4)
Mean strain energy density [kJ/m ³]	BPL	734 (1844)	47.4 (43.4)	734 (1228)
	FPL	370 (1483)	14.8 (12.2)	863 (1168)

Figure 1 depicts the principal compression and tension strains, maximal shear strain and SED in the flap muscle of the three TTA patients in a sagittal view through the tibia. Since the fat tissue of patient #3 was embedded in the muscle tissue, it is included in the representation of strains in Figure 1.

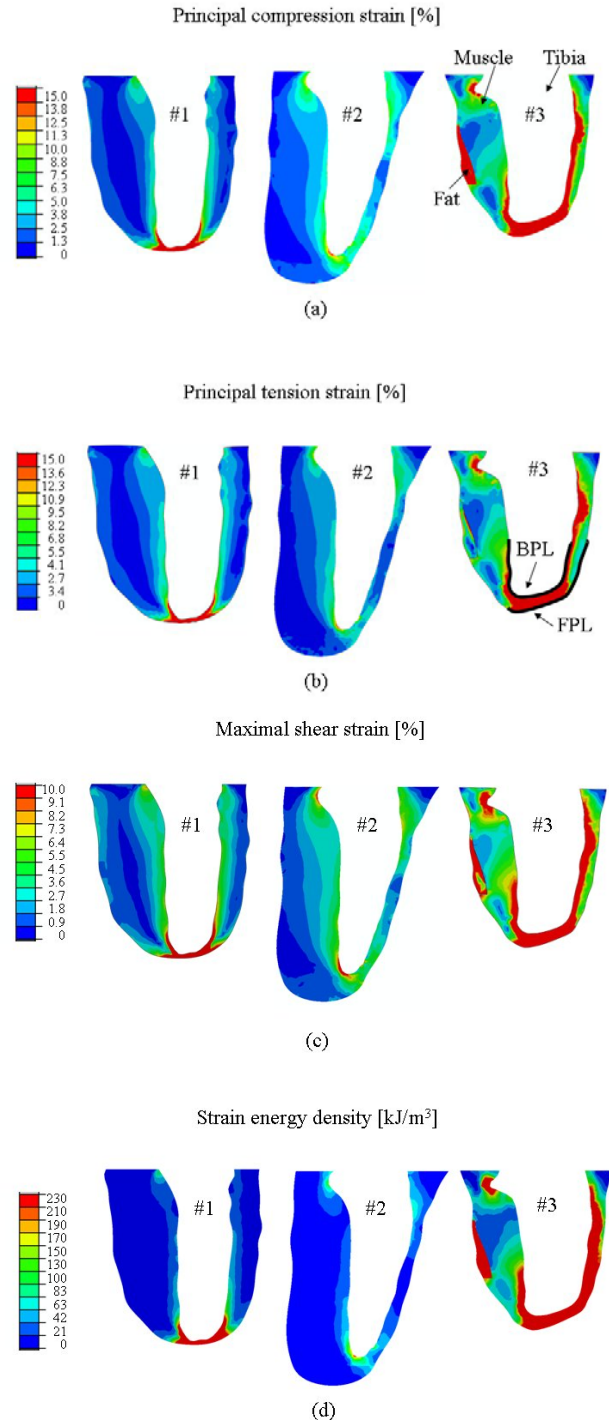


Fig. 1 The (a) principal compression [%] and (b) tension strain [%], (c) maximal shear strain [%] and (d) strain energy density [kJ/m³] in the muscle tissues of the three transtibial amputation patients.

The percentage of volume of the muscle tissue at the BPL and FPL that holds principal compression strains above 5% (i.e. large strains) are presented in Fig 2. These results clearly show low compression strains in the longer residuum of patient #2 and higher compression strains in the shorter residual limbs of patients #1 and 3.

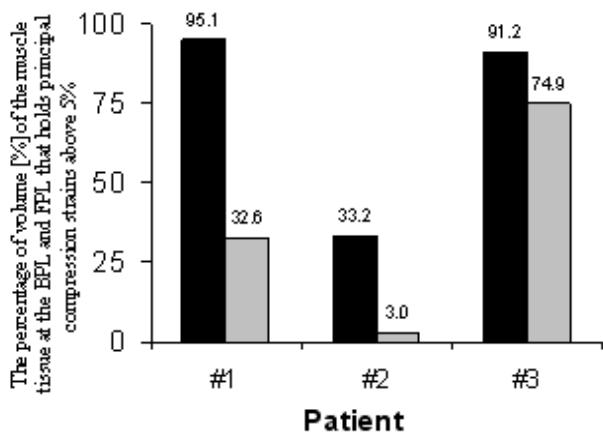


Fig. 2 The percentage of volume [%] of the muscle tissue at the BPL and FPL that holds principal compression strains above 5%

IV. CONCLUSIONS

In this study, we used patient-specific 3D FE modeling of the residual limbs of TTA patients during standing in an open MRI setting while applying body weight to their residual limb. We found high strains in the BPL rather than in the FPL (Table 4; Figs 1,2). This finding alerts to the sus-

ceptibility of the TTA muscle flap to DTI in the proximity of the distal end of the tibia.

The highest strains were found in the shortest residuum of patient #3. This is partially because the vertical movement of the bones found on the MRI scans of this patient was the greatest between the three patients. Correspondingly, the lowest strains were found in the longest residuum with the thickest muscle flap. Yet even in the case of a long residuum, a third of the distal tibial proximity area was occupied by internal principal compression strains above 5%. For the two TTA patients with shorter residual limbs, the internal principal compression strains above 5% occupied almost the entire distal tibial proximity area.

We conclude that the wide variability between TTA residual limbs necessitate quantitative analysis of the internal mechanical state in the TTA individual to assess the risk for DTI onset.

REFERENCES

1. Agam L, Gefen A (2007) Pressure ulcers and deep tissue injury: a bioengineering perspective. *J Wound Care* 16:336-342.
2. Portnoy S, Yizhar Z, Shabshin N, Itzhak Y, Kristal A, Dotan-Marom Y, Siev-Ner I, Gefen A (2008) Internal mechanical conditions in the soft tissues of a residual limb of a trans-tibial amputee. *J Biomech* 41:1897-1909.
3. Mooney MA (1940) Theory of large elastic deformation. *J Appl Phys* 11:582-592.

Author: Prof. Amit Gefen
 Institute: Tel Aviv University
 Street: Klauzner
 City: Ramat Aviv
 Country: Israel
 Email: gefen@eng.tau.ac.il

Development of a Corrugated Polyimide-Based Electrode for Intrafascicular Use in Peripheral Nerves

T. Boretius, D. Zimmermann and T. Stieglitz

Laboratory for Biomedical Microtechnology, Department of Microsystems Engineering – IMTEK, University of Freiburg, Freiburg, Germany

Abstract—This paper presents the first design of a corrugated polyimide-based electrode with the intention to improve the neuro-technical interface. The corrugation is achieved through tempering the polyimide substrate within a moldform, which is fabricated via precision mechanics. Mechanical properties, load-displacement and strength of shape measurements before and after corrugation are examined and evaluated for three different dimensions of moldforms.

Keywords— Electrode, corrugation, polyimide, intrafascicular, neural interface

I. INTRODUCTION

In recent years many different concepts for neural electrodes arose, like cuffs, sieves, slowly penetrating intrafascicular electrodes (SPINEs), longitudinal intrafascicular electrodes (LIFEs) or transverse intrafascicular multichannel electrodes (TIMES) [1-5]. Beneath the distinctions in spatial selectivity and implantation procedure, all these designs suffer from the relative motion of tissue and device, commonly called micromotion [6;7]. To reduce this particular problem and to obtain an increased contact with the targeted fascicles, a corrugation may be applied to the thin-film substrate. This corrugation is meant to (1) stabilize the structure along its implanted direction and (2) to yield a good liaison between the electrodes' sites and the nerves' fascicles. First preliminary studies were conducted where shape memory alloys (SMA) were used to add micro-actuation to the structure. These actuated intraneural electrodes (ACTIN) consist of a polyimide substrate, gold tracks and active sites and a 7 μm thick layer of TiNi alloy [8]. The SMA pads can be individually activated to achieve a corrugated deviation of about 10 μm , which is sufficient for the rats' allocation of fascicles [9]. But beneath these promising results, several problems occur like the increased thickness of the device and, most of all, the need for high temperatures or rather currents to activate the shape memory alloy.

Henceforth, our group decided to go one step back and to develop a device which incorporates a static corrugation of the thin-film substrate without any increase in thickness or additional cleanroom processing steps. Similar to cuff elec-

trode manufacture, this can be achieved through a temper process which comprises a moldform and the already cured polyimide substrate. Since the moldform is solely fabricated via precision mechanics, variable dimensions can easily be obtained, yielding in low-cost and rapid prototyping.

II. MATERIALS AND METHODS

A. Moldform Layout

Three moldforms were designed using conventional CAD software followed by the fabrication through precision mechanics. The forms comprise a medical grade steel mold (1.4541 by Goodfellow GmbH, Bad Nauheim, Germany) and an aluminum housing. The mold was manufactured by wire-cut electrical discharge machining (EDM) and the housing was afterwards individually trimmed to fit the mold.

The three forms of different dimensions were fabricated in this first trial. All comprise a sinusoidal form defined by a wavelength λ , an amplitude h which gives the final corrugated deviation, the radius r , and the number of wavelengths n (Fig. 1, Table 1). The external dimensions are the same for all moldforms, namely 5 cm in length, 4 cm in height (i.e. 2 cm for upper and lower part) and 1.3 cm in thickness, whereas the steel mold is 3 mm thick.

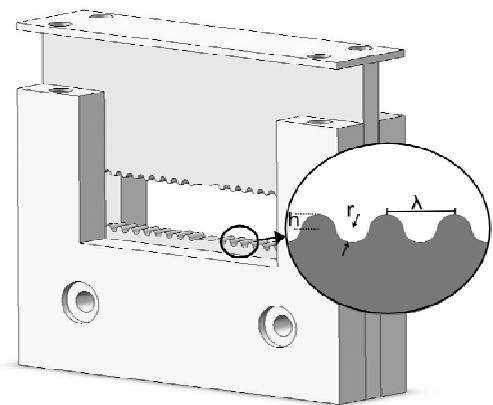


Fig. 1: Schematic view of the moldforms' design. For dimensions see Table 1.

Table 1: Dimensions of the three molds in use.

Dimension	Small Mold	Mid-Size Mold	Large Mold
Wavelength λ (μm)	501	1.832	4.000
Amplitude h (μm)	91	401	716
Radius r (μm)	130	450	1.050
# of Wavelengths n	40	16	8

B. Manufacturing Process

The manufacturing of the electrodes was done using standard thin-film processes in a class 1000 cleanroom. The devices were made from two 5.5 μm layer of polyimide (U-Varnish-S by UBE Europe GmbH, Duesseldorf, Germany) between which a patterned platinum layer is sandwiched. Perimeter and openings were etched via reactive ion etching (RIE) in oxygen plasma. An extensive description of the overall process can be found in [4]. The finished electrodes have a width of 580 μm , an overall thickness of 11 μm and a length (without interconnections) of 6 cm.

The devices were mechanically peeled off the wafer using tweezers and inserted into the mold. In these first attempts, no high value was set to place the active sites exactly onto the turning points of the sinusoidal form. The mold was closed afterwards and fixed via screws. The complete form was transferred into an oven (PEO-601, ATV Technologie GmbH, Vaterstetten, Germany) and tempered in an inert nitrogen atmosphere at 300 °C for 90 minutes. Subsequent to the cooling period the mold was opened again and the corrugated electrode retrieved.

C. Mechanical Characterization

Mechanical characterization was done via a tensile testing machine (zwicki TC-FR2.5TS.D09 by Zwick GmbH, Ulm, Germany), whereas the sample size was 10 ($n=10$) for all experiments. Young's modulus and tensile strength were measured using non-corrugated electrodes as reference. Additionally, corrugated devices were stored for 2 weeks in saline solution (0.9 % NaCl) at 37, 60 and 85 °C, respectively, and were tested afterwards for decorrugation and their mechanical properties.

To determine the contour accuracy and strength of shape of the polyimide substrate in respect to the original mold-form, amplitudes and wavelengths were optically measured using a light microscope (MZ75, Leica Microsystems CMS GmbH, Wetzlar, Germany) in combination with imaging software (IM500 ver. 4.0 by Leica Microsystems Imaging Solutions Ltd., Cambridge, UK). The moldforms' dimensions were set to 100 % and the yielded corrugation of the electrodes was percentaged to this value.

Load-displacement diagrams were measured with a custom build measuring setup, which comprises a force sensor

(SS2 by Sherborne Sensors, Basingstoke, Hampshire, UK) and a linear precision actuator (M230.25 by Physical Instruments, Karlsruhe, Germany). The corrugated electrode was clamped taut at the lower end and connected with the force sensor in a 180 ° angle on the other side. From this free-length position, the z-drive moved the sensor and electrode up until the corrugation was compensated. The starting position was the same for all measurements within handling tolerances and data was gathered online through a custom made LabView program (National Instruments Corp., Austin, Texas, USA). To verify the experimental setup for load-displacement measurements, a simulation was done for corrugated devices using Comsol Multiphysics ver. 3.4 by Comsol Multiphysics GmbH, Goettingen, Germany. For a first approximation the layer of platinum was neglected in these simulations, since the ratio of overall thickness (11 μm) to platinum (300 nm) suggests an evanescent influence on these experiments. Young's modulus and Poisson's ratio were extracted from literature, i.e. 7.04 GPa and 0.33 respectively, whereas the geometry was adopted from optical measurements of the devices after tempering. As model served a 3-dimensional static analysis for elastoplastic materials.

III. RESULTS

Electrodes have been fabricated and successfully corrugated (Fig. 2). Mean and standard deviation of Young's modulus and tensile strength for non-corrugated electrodes was determined to be 5.2 GPa (± 0.2 GPa) and 499 MPa (± 66.3 MPa) respectively. After tempering the substrates within the mid-sized and largest mold, no significant change could be observed and Young's modulus remained stable at 5.2 GPa (± 0.2 GPa) and 4.9 GPa (± 0.1 GPa), while the tensile strength decreased slightly to 437 MPa (± 24.5 MPa) and 427 MPa (± 57.0 MPa), respectively. Those devices tempered in the smallest mold yielded a modulus of 3.9 GPa (± 0.6 GPa) and 450 MPa (± 48.6 MPa) of tensile strength. Devices stored for two weeks in saline solution showed no alteration in their mechanical properties.

Load-displacement curves were measured for electrodes corrugated in all three dimensions. Additionally, devices corrugated within the mid-sized and largest mold were simulated to verify the experimental setup (Fig. 3). Note that the values of displacement on the x-axis are normalized to four wavelengths for comparison purposes. The first linear region in Fig. 3 represents the decorrugation of the devices, followed by an exponential increase which transfers the graph into the elastic region of stress-strain analysis. The maximum force F_{max} for a complete decorrugation was henceforth set to 95 % of the beginning of this asymptotic

region. The electrodes with the largest corrugation exhibited a mean force of $F_{max}=4.5$ mN, the mid-sized and smallest versions had a maximum force of 17.5 mN and 21 mN, respectively.

Contour accuracy and strength of shape of corrugated devices was optically obtained and percentaged to the original moldforms' dimensions. Amplitude and wavelength were separately measured for tempered electrodes, yielding the contour accuracy, and for devices stored for two weeks in saline solution at 37, 60 and 85 °C, respectively, which gives the strength of shape. The mean values are summarized in Table 2. Regarding the amplitude, between ~91 % and ~51 % of the moldforms' dimension could be transferred into the polyimide substrate after the temper process, whereas the strength of shape decreased (~3.3 to 24.8 %) with the storage at different temperatures. The transferred wavelength was more accurate with ~98 % to 90 % for the small and large mold, respectively. In this case, only 0.32 % to 9.4 % strength of shape was lost while stored at 85 °C for two weeks. Fig. 4 represents a typical strength of shape diagram for electrodes tempered within the mid-size mold (dashed line) in respect to the molds' dimensions (straight line) and after a storage time of two weeks in saline solution at 85 °C (dotted line). After the temper process 80 % of the amplitude and 98.5 % of the wavelength was transferred into the substrate. The storage time decreased the wavelength about 4.61 % and the amplitude about 13.4 % further.

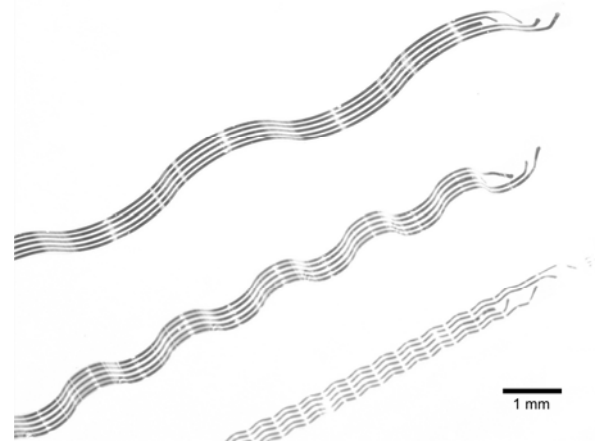


Fig. 2: Prototypes of corrugated electrodes.

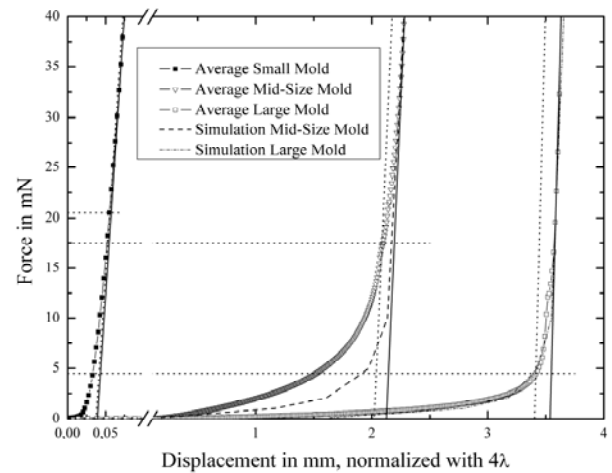


Fig. 3: Load-displacement diagram for electrodes corrugated in three different molds. Curves are mean values (n=10) and simulations, respectively.

Table 2: Values of contour accuracy and strength of shape for corrugated electrodes percentaged to the original moldform. Measurements were taken after the temper process and storage of two weeks at 37, 60 and 85 °C, respectively.

	Small Mold	Mid-Size Mold	Large Mold
Amplitude h			
After Tempering	-48.35 %	-19.95 %	-8.62 %
2 Weeks at 37 °C	-48.35 %	-23.26 %	-24.92 %
2 Weeks at 60 °C	-50.55 %	-23.82 %	-26.12 %
2 Weeks at 85 °C	-51.65 %	-35.35 %	-33.44 %
Wavelength λ			
After Tempering	1.63 %	1.54 %	9.48 %
2 Weeks at 37 °C	1.47 %	3.23 %	14.80 %
2 Weeks at 60 °C	1.30 %	4.39 %	14.55 %
2 Weeks at 85 °C	1.95 %	6.15 %	18.88 %

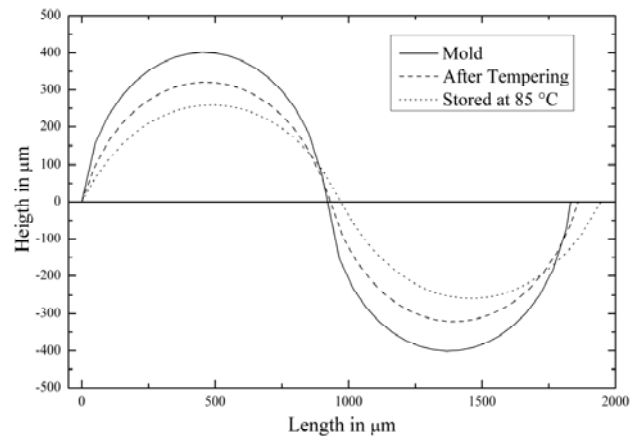


Fig. 4: Strength of shape diagram for electrodes tempered within the mid-sized mold in respect to the mold itself and after two weeks of storage time in saline solution at 85 °C. Reproduced from microscopic images.

IV. CONCLUSIONS

The first prototypes of corrugated thin-film electrodes were successfully produced and tested on their mechanical properties. The process of corrugation via tempering in moldforms was implemented and showed good manageability and low-cost in respect to the shape memory technique. Young's modulus and tensile strengths were measured and, regarding the largest two molds, no significant influence of the tempering process on the material properties could be observed. Within the smallest form Young's modulus and tensile strength decreased by 25 % and 10 % respectively, due to yet unknown influencing factors. A possible explanation could be found in the measurement of decorrugation and Young's modulus itself, since these two regions are somewhat merged together and could not be separated satisfactorily. Devices stored for two weeks in saline solution showed no alteration in their material properties which is in accordance with another study of our group [10].

Load-displacement measurements were done and the maximum force for a complete decorrugation was determined for all three dimensions in use. Additionally, devices tempered in the largest two molds were simulated and, although these appear more flexible, the overall characteristics are the same as for the experimental setup which serves us as secondary verification. To impede forces which are situated within the elastic region of the material, a safety threshold of 95 % of the maximum force was introduced. Staying within this region should ensure that the strengths of shape of the devices are not affected by handling purposes or implantation procedure.

The contour accuracy, i.e. the dimensions of the polyimide substrates after corrugation in respect to the mold, was optically determined for all forms in use. We found that the larger the mold the more accurate the contour could be transferred into the substrate. The strength of shape, however, which is the ability to maintain the form over time, showed just a contrary behavior. Here, the smallest form was the one most stable over the two week period of storage in saline solution at different temperatures. These results are, though, to handle with care given that the time period is still low for a quantitative conclusion. It is to expect that, given a broader period of time, the strength of shape decreases further to a final degree, which is then more comparable within the different mold dimensions.

Further studies are in progress to estimate this degree of shape strength and the limits of achievable moldform dimensions with the precision mechanics technique. Furthermore, influences of the molding process on the platinum

layer and active sites are under research, regarding electrochemical and potential field distribution measurements.

ACKNOWLEDGMENT

The authors would like to thank the European Union for funding the TIME project (Transverse, Intrafascicular Multichannel Electrode system for induction of sensation and treatment of phantom limb pain in amputees) in the 7th Framework Program (grant CP-FP-INFSO 224012/TIME).

REFERENCES

1. X. Navarro, S. Calvet, F. J. Rodriguez, T. Stieglitz, C. Blau, M. Buti, E. Valderrama, and J.-U. Meyer (1998) Stimulation and Recording from Regenerated Peripheral Nerves Through Polyimide Sieve Electrodes. *J Peripher Nerv Syst*, vol. 3, no. 2, pp. 91-101.
2. D. J. Tyler and D. M. Durand (1997) A Slowly Penetrating Interfascicular Nerve Electrode for Selective Activation of Peripheral Nerves. *IEEE T Rehabil Eng*, vol. 5, no. 1, pp. 51-61.
3. K. H. Polasek, H. A. Hoyen, M. W. Keith, and D. J. Tyler (2007) Human Nerve Stimulation Thresholds and Selectivity Using a Multi-Contact Nerve Cuff Electrode. *IEEE T Neural Syst Rehabil Eng*, vol. 15, no. 1, pp. 76-82.
4. Boretius, T., Badia, J., Pascual-Font, A., Navarro, X., Yoshida, K., and Stieglitz, T., Concept of a transversal intrafascicular multichannel electrode (TIME) to interface with the peripheral nerve, submitted
5. D. Farina, K. Yoshida, T. Stieglitz, and K. P. Koch (2008) Multichannel Thin-Film Electrode for Intramuscular Electromyographic Recordings. *J Appl Physiol*, vol. 104 pp. 821-827.
6. K. K. Lee, A. Singh, J. He, S. P. Massia, B. Kim, and G. B. Raupp (2004) Polyimide Based Neural Implants with Stiffness Improvement. *Sensor Actuat B-Chem*, vol. 102 pp. 67-72.
7. J. Subbaroyan, D. C. Martin, and D. R. Kipke (2005) A finite-element model of the mechanical effects of implantable microelectrodes in the cerebral cortex. *J Neural Eng*, vol. 2, no. 4, pp. 103-113.
8. S. Bossi, A. Menciassi, K. P. Koch, K. P. Hoffmann, K. Yoshida, P. Dario, and S. Micera (2007) Shape Memory Alloy Microactuation of tf-LIFEs: Preliminary Results. *IEEE T Bio-Med Eng*, vol. 54, no. 6, pp. 1115-1120.
9. N. Lago, K. Yoshida, K. P. Koch, and X. Navarro (2007) Assessment of Biocompatibility of Chronically Implanted Polyimide and Platinum Intrafascicular Electrodes. *IEEE T Bio-Med Eng*, vol. 54, no. 2, pp. 281-290.
10. B. Rubehn, S. Kisban, and T. Stieglitz (2006) Mechanical Characterization of Flexible Substrates for Neural Microimplants, *Proc of the 11th Ann Conf of the IFESS Soc* pp. 106-108.

Author: Tim Boretius

Institute: Department of Microsystems Engineering-IMTEK

Street: Georges-Koehler-Allee 102

City: Freiburg

Country: Germany

Email: boretius@imtek.de

Analysis of Gait Rhythm Variability in Patients with Amyotrophic Lateral Sclerosis

Yunfeng Wu and Sridhar Krishnan

Department of Electrical and Computer Engineering, Ryerson University
350 Victoria Street, Toronto, ON, M5B 2K3, Canada

Abstract—Gait rhythm patterns in neurodegenerative diseases could become abnormal due to deterioration of motor neurons. In the present study, we used the turns count (TC) method to measure the variability of gait rhythm (swing interval) in amyotrophic lateral sclerosis (ALS). The number of turns detected with the threshold of 0.06 s in the swing-interval time series exhibits a significant difference ($p < 0.001$) between 16 healthy control subjects and 13 patients with ALS. The pattern classification experiments were implemented using the linear discriminant analysis (LDA) and the least-squares support vector machine (LS-SVM), with the input features of TC and averaged stride interval (ASI, $p < 0.0001$). The results showed that the TC and ASI features may serve as excellent indicators to characterize the gait variability in ALS. The LS-SVM with sigmoid kernels was able to provide 89.7% classification accuracy and an area of 0.9568 under the receiver operating characteristic curve, which were superior to the diagnostic performance of the LDA.

Keywords— Amyotrophic lateral sclerosis, gait dynamics, linear discriminant analysis, support vector machine.

I. INTRODUCTION

Motor neurons in the brain stem and spinal cord control voluntary muscle movement. Degeneration of motor neurons will result in neurological pathologies and lead to motor skill dysfunction. Amyotrophic lateral sclerosis (ALS) is a progressive neurodegenerative disorder caused by the degeneration of motor neurons or their myelin sheath [1]. With the ALS disorder, muscles cannot receive the sensory information in the central nervous system. Early clinical symptoms of ALS include twitching and cramping of the arms or legs, muscle fatigue, difficulty speaking, and swallowing or breathing [2]. The patient may gradually lose the ability to initiate and control voluntary movement [3, 4].

Analysis of gait dynamics in neurodegenerative diseases can assist the neurologist to develop computer-aided tools in order to monitor the progression of a specific neurological pathology. Sekine *et al.* [5] used a maximum likelihood estimation method to compute the fractal parameters in the acceleration signals recorded during climbing stairs and walking along a corridor. The results of their study showed that the fractal dimensions of the gait rhythm present in the

acceleration signals recorded from patients with Parkinson's disease tend to be higher than those of healthy elderly subjects [6]. Hausdorff *et al.* [7] estimated the variation of gait cycle duration, also referred to as stride interval, in healthy elderly subjects and patients with Huntington's disease. Their study suggested that the coefficient of variation is associated with the degree of severity of Huntington's disease. Hausdorff *et al.* [8] studied the gait fluctuation in patients with ALS, by using the detrended fluctuation analysis method. Their results showed that the temporal gait-rhythm variability parameters (stride-to-stride fluctuation magnitude and fractal dimensions) of patients with ALS are significantly different from those of healthy subjects. In addition to stride interval, it is hypothesized that the gait patterns extracted from swing-interval time series of ALS patients might become abnormal as well. In the present study, we applied the turns count method to study the swing-interval variability in ALS patients, and also carried out the linear and nonlinear classification experiments to analyze the ALS gait patterns.

II. METHODS

A. Data Description

The gait database used in the present study was the same as used in the previous study of Hausdorff *et al.* [8], and can be downloaded via PhysioNet (<http://www.physionet.org>) [9]. The database consists of the time series of stride interval (along with its two subphases: swing and stance intervals) recorded from 16 healthy control (CO) subjects, including 2 men and 14 women aged 20-74 years (39.3 ± 18.5 years, mean \pm standard deviation, thereafter), and 13 patients with ALS, including 10 men and 3 women aged 36-70 years (55.6 ± 12.8 years). The duration of the neurological pathology since diagnosis of ALS ranges from 1 to 54 months (18.3 ± 17.8 months). These ALS patients were free from other pathologies that might affect the gait. Height and weight of the CO subjects was not significantly different from those of the ALS patients.

According to the experimental protocol [8], each subject was instructed to walk at his or her normal pace along a 77-

m-long straight hallway for 5 min. The force applied to the ground for each stride was recorded using ultrathin force-sensitive switches placed inside each subject's shoes and a small and lightweight recorder worn with a wallet on the ankle. The signal from the foot switches was digitized by an on-board analog-to-digital converter at the sampling rate of 300 Hz with 12-bit resolution per sample. Each subject provided informed consent as approved by the Institutional Review Board of the Massachusetts General Hospital.

B. Median Filtering

In order to minimize start-up effects, the stride-interval and swing-interval samples recorded in the first 20 s were excluded. We applied a median filter to remove the stride-interval samples that were 3 standard deviations (SDs) greater or less than the median value over the entire time series. These stride-interval outliers had very large values because the subject had to turn around at the end of the hallway during the 5-min walking. In addition, the corresponding swing-interval samples in the time series associated with the hallway turns were also removed for the variability analysis and the further pattern classification experiments. Fig. 1 shows the stride-interval time series of a 50-year-old ALS patient. Two stride-interval outliers detected by the median filter are marked with diamonds in Fig. 1.

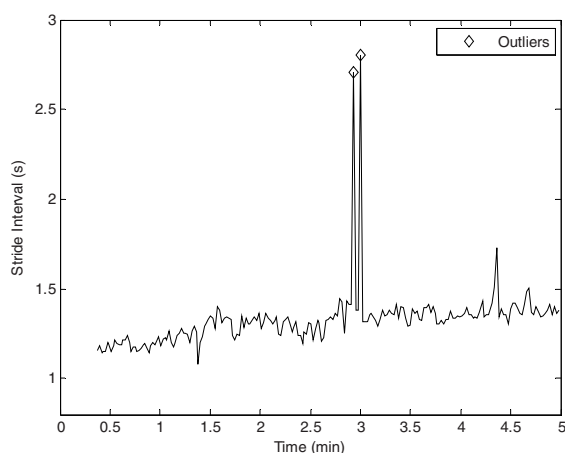


Fig. 1 An example of the raw stride-interval time series of a 50-year-old male subject with amyotrophic lateral sclerosis (ALS). Outliers were 3 SDs greater than the median stride interval over the entire time series.

C. Turns Count

The turns count (TC) can be used to characterize the degree of signal variability in a time series [10]. According to Rangayyan and Wu [11], the TC feature extracted from the

knee-joint vibroarthrographic (VAG) signal analysis may serve as one of the useful indicators for the screening of articular cartilage disorders.

A signal sample in the time series can be identified as a "turn" if it satisfies the following two conditions: 1) it represents a change in direction in the signal; 2) the difference between its amplitude and that of the preceding sample should be over a certain threshold.

In the present work, the threshold used to detect the number of the signal turns in the swing-interval time series was varied from 0.05 to 0.1 s, increased by a step of 0.01 s. The Student's *t*-test was used to check whether or not the TC numbers of the ALS patients were different from those of the healthy CO subjects. Fig. 2 plots the *p* values of the Student's *t*-test on the TC numbers determined by different thresholds. It can be observed that the TC numbers present a significant difference ($p < 0.01$) between the ALS patients and the healthy CO subjects. With the threshold of 0.06 s, the lowest *p* value (0.0002) of the Student's *t*-test was obtained, which indicated that the TC numbers determined with such a threshold was the best choice in the detection procedure. The mean and SD values of the TC numbers for the healthy CO subjects and the ALS patients were 4.69 ± 4.59 and 28.77 ± 22.18 , respectively.

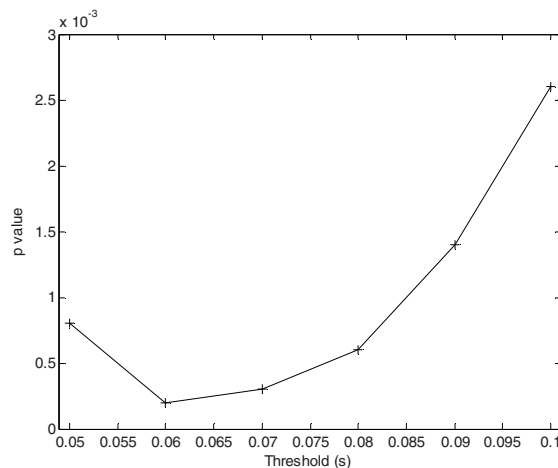


Fig. 2 The *p* values with regard to different thresholds that were used to determine signal turns in the swing-interval time series recorded from the healthy control and amyotrophic lateral sclerosis (ALS) subjects.

Hausdorff *et al.* [8] reported that the gait cycle duration, also referred to as the stride interval, is usually longer for patients with ALS, compared with that of healthy subjects. Thus we considered the averaged stride interval (ASI) as the other dominate feature for classification of the ALS gait patterns. In the feature extraction procedure, the ASI value

was averaged over the entire stride-interval time series. The mean and SD values of the ASI feature for the healthy CO subjects and the ALS patients were 1.09 ± 0.09 s and 1.36 ± 0.21 s, respectively. And the p value of the ASI evaluated with the Student's t -test was lower than 0.0001, which indicated high statistical significance of separability between the healthy CO subjects and the ALS patients.

In the ASI-TC feature space, depicted in Fig. 3, the gait patterns of the healthy CO subjects and the ALS patients are marked with circles and crosses, respectively. It is clear that the TC numbers of the healthy CO subjects congregate in the range from 0 to 20, and the ASI values concentrate in the range from 0.9 to 1.2 s, except for a 74-year-old healthy CO subject who possesses an ASI of 1.14 s. And the gait patterns associated with the ALS patients are dispersive in the feature space. In addition, we may also observe that the gait patterns of the healthy CO subjects exhibit distinct characteristics compared with those of the ALS patients.

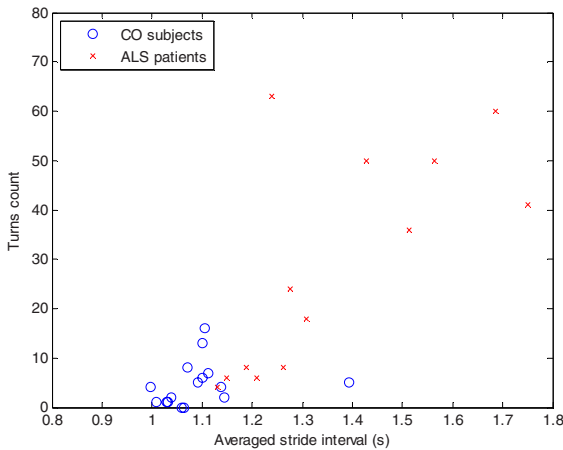


Fig. 3 Scatter plot of the averaged stride interval (ASI) and turns count (TC) features of the healthy control (CO) subjects, marked as circles, and of the patients with amyotrophic lateral sclerosis (ALS), marked as crosses.

D. Classifiers

The computer-aided analysis of the ALS gait patterns was implemented using the linear and nonlinear classifiers with the ASI and TC features. The linear classification was performed with the linear discriminant analysis (LDA), a commonly used statistical technique to find the linear combination of features which best separate two or more classes [12]. The nonlinear classifier used in the gait pattern analysis was the least-squares support vector machine (LS-SVM) proposed by Suykens *et al.* [13].

The LS-SVM is a reformulation to the standard support vector machine (SVM). The learning is implemented by

minimizing a regularized least-squares cost function with equality constraints, and a subset of training data is selected as the support vectors. By choosing a specific type of nonlinear inner-product kernels in the hidden layer, the LS-SVM is able to perform the same function as the polynomial learning machine, radial-basis function network, or multi-layer perceptron [14]. The major advantage of the LS-SVM is that the network has moderate complexity, which makes the training process become more efficient than the standard SVM. The detailed theoretical framework of the LS-SVM is described in the work of Suykens *et al.* [13]. In the experiments, we compared the performance of the LS-SVM with the polynomial, sigmoid, and Gaussian kernels, which were assigned with different model parameters. The classification performance was evaluated with the leave-one-out (LOO) cross validation method [15]. By checking the accuracy results of the LS-SVM with different kernels, we chose the sigmoid kernel function with the zero bias, unity scale parameter, and the regularization parameter equal to 5, which were well suited for the gait classification task.

III. RESULTS

The classification performance was measured in terms of overall accuracy in percentage and the area (A_z) under the receiver operating characteristic (ROC) curve. The ROC curve is commonly used in clinical applications to depict the patterns of sensitivities and specificities observed when the performance is evaluated at different diagnostic thresholds [16]. The ROC results were implemented using the ROCKIT software tool provided by Metz *et al.* (University of Chicago, Chicago, IL, USA) [17].

The LDA was able to provide 82.76% overall accuracy, and an A_z of 0.9315 with the standard error (SE) of 0.0470. One healthy CO subject and four patients with ALS were misclassified, that is, the sensitivity and specificity were 0.6923 (11/13) and 0.9375 (15/16), respectively. On the other hand, the LS-SVM with the sigmoid kernels was able to provide higher percentage accuracy (89.66%) and a larger A_z value (0.9568, SE: 0.0388), compared with the LDA. Although the LS-SVM cannot distinguish the same healthy CO subject as done by the LDA, only two ALS patients were misclassified by the LS-SVM. The sensitivity and specificity of the sigmoid-kernel-based LS-SVM evaluated with the LOO method were 0.8462 (11/13) and 0.9375 (15/16), respectively. Such results were superior to those obtained with the LS-SVM based on other kernels, such as the polynomial or Gaussian kernels.

Fig. 4 plots the ROC curves provided by the LDA and the LS-SVM, respectively. It can be observed that the LS-SVM improved the diagnostic performance, and its ROC

curve was consistently over that provided by the LDA. Such results demonstrated that the nonlinear classifier performed better than the linear classifier for the analysis of ALS gait patterns based on the ASI and TC features.

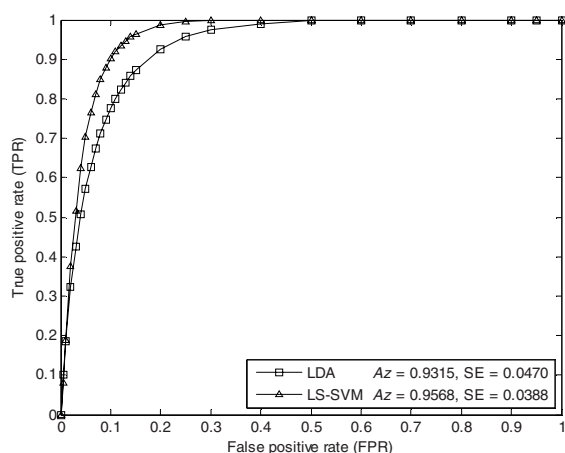


Fig. 4 ROC curves of the linear discriminant analysis (LDA) and the least-squares support vector machine (LS-SVM) evaluated with the leave-one-out (LOO) cross valuation method, respectively.

IV. CONCLUSION

ALS is a common neurodegenerative disorder in the central nervous system [18]. With the ALS, the gait rhythm from one gait cycle to the next would be affected due to deterioration of motor neurons in the central nervous system. Computer-assisted tools may help the neurologist better interpret and characterize a specific neurological degenerative pathology. Analysis of gait patterns based on signal processing and machine learning techniques is able to provide important diagnostic information that can be used to distinguish particular disorders of motor or sensory function, and to monitor the progression of a particular neurodegenerative disorder.

In the present work, we studied the variability of swing interval with the turns count (TC) method, and also measured the averaged stride interval (ASI). Two dominant statistical features, i.e., the TC numbers ($p < 0.001$) and the ASI ($p < 0.0001$), extracted from the swing- and stride-interval time series present significant differences between the healthy CO subjects and the patients with ALS. Both of the LDA and the LS-SVM were able to provide excellent diagnostic performance, in terms of the overall classification accuracy and the A_z under the ROC curve. The pattern classification results obtained in our experiments showed the advantages of the TC and ASI features, as well as the nonlinear LS-SVM classifier, for the analysis of the ALS

gait-rhythm patterns.

REFERENCES

- Hirano A (1996) Neuropathology of ALS: an overview. *Neurology* 47(S2):63–66
- Brooks BR (1996) Natural history of ALS: symptoms, strength, pulmonary function, and disability. *Neurology* 47 (S2):71–81
- Hausdorff JM, Alexander NB (2005) *Gait disorders: evaluation and management*. Informa Healthcare, New York, NY
- Leigh PN, Meldrum BS (1996) Excitotoxicity in ALS. *Neurology* 47(S4):221–227
- Sekine M, Akay M, Tamura T et al. (2004) Fractal dynamics of body motion in patients with Parkinson's disease. *J Neural Eng* 1:8–15
- Akay M, Sekine M, Tamura T et al. (2003) Unconstrained monitoring of body motion during walking. *IEEE Eng Med Biol* 22:104–109
- Hausdorff JM, Mitchell SL, Firtion R et al. (1997) Altered fractal dynamics of gait: reduced stride-interval correlations with aging and Huntington's disease. *J Appl Physiol* 82:262–269
- Hausdorff JM, Lertratanakul A, Cudkowicz ME et al. (2000) Dynamic markers of altered gait rhythm in amyotrophic lateral sclerosis. *J Appl Physiol* 88:2045–2053
- Moody GB, Mark RG, Goldberger AL (2001) PhysioNet: a web-based resource for the study of physiologic signals. *IEEE Eng Med Biol* 20:70–75
- Rangayyan RM (2002) *Biomedical signal analysis: a case-study approach*. IEEE and Wiley, New York, NY
- Rangayyan RM, Wu YF (2009) Analysis of vibroarthrographic signals with features related to signal variability and radial-basis functions. *Ann Biomed Eng* 37:156–163
- Duda RO, Hart PE, Stork DG (2001) *Pattern classification*, 2nd ed. Wiley, New York, NY
- Suykens JAK, Van Gestel T, De Brabanter J et al. (2002) Least squares support vector machines. World Scientific Publishing, Singapore.
- Herbrich R (2002) *Learning kernel classifiers*. MIT Press, Cambridge, MA
- Theodoridis S, Koutroumbas K (2006) *Pattern recognition*, 3rd ed. Academic Press, New York, NY
- Marques de Sa JP (2003) *Applied statistics using SPSS, STATISTICA, and MATLAB*. Springer, Berlin, Germany
- Metz C, Herman B, Shen J (1998) Maximum-likelihood estimation of ROC curves from continuously-distributed data. *Stat Med* 17: 1033–1053
- Brown RH, Meininger V, Swash M (1999) *Amyotrophic lateral sclerosis*. Martin Dunitz Publishers, London, UK

Author: Sridhar Krishnan
 Institute: Ryerson University
 Street: 350 Victoria Street
 City: Toronto, ON
 Country: Canada
 Email: krishnan@ee.ryerson.ca

Anatomy of the human cochlear nucleus in relation to auditory brainstem implants

S.K. Rosahl and S. Rosahl^{1,2}

¹Department of Neurosurgery, HELIOS Klinikum Erfurt, Germany

²University of Freiburg, Germany

Abstract— OBJECTIVE: The performance of auditory brainstem implants is significantly inferior to that of cochlear implants with respect to auditory perceptions in profoundly deaf patients. Inconsistencies in the electrode-tissue-interface may contribute to this issue. The study fills in essential data on the anatomical variability of the human cochlear nucleus complex (CNC) that have never been systematically analyzed before.

METHODS: The location and the size of 33 CNC (17 right-sided, 16 left-sided) were examined in cross-axial sections of 20 formalin-fixed specimens with the aid of a light microscope. Length, size, width, and the relationship to the intramedullary portion of facial nerve have been assessed for both the ventral (VCN) and dorsal portion (DCN) of the nucleus on either side. All measurements were corrected by a factor of 1.13 (12%) for transverse and 1.21 (17%) for longitudinal shrinkage.

RESULTS: The shape of the cochlear nuclei is complex, creating a distorted X-shaped silhouette in a sagittal view of the brainstem. Mean maximal dimensions (anteroposterior x mediolateral x rostrocaudal; \pm standard deviation) obtained for the VCN were $4.59 \pm 0.89 \times 1.53 \pm 0.64 \times 3.18 \pm 0.69$ mm, and $3.42 \pm 1.21 \times 0.68 \pm 0.20 \times 1.90 \pm 0.66$ mm for the DCN. Interindividual differences were highly significant and there was considerable overlap between VCN and DCN in the sagittal plane. While the outer posterolateral surface of the DCN runs almost parallel to the surface of the brainstem in a mean depth of about 0.3 mm, the VCN gradually dives into the depth in the rostroventral direction, ending up at a mean minimum of 7 mm off the surface.

CONCLUSION: The complex morphology of the CNC, its interindividual variability, and its varying location with respect to the surface of the brainstem and outer landmarks constitute a major challenge in designing auditory brainstem implants.

Keywords— auditory brainstem implant, cochlear nucleus, neural electrode interface, anatomy, landmarks

I. INTRODUCTION

The anatomy of the cochlear nucleus (CN) as well as its neighboring and landmark anatomical structures have become of interest for auditory brainstem implantation. In addition to the classical surface electrodes placed into the lateral recess of the fourth ventricle since the 1980ies, penetrating brainstem electrodes have now also been implanted to interface the cochlear nuclei with a speech processor in order to partially restore hearing [1].

In an attempt to guide surgical approaches for the purpose of implanting electrodes at this site, a number of authors have described the complex histological structure of the cochlear nucleus complex [3,5,6,11]. While the outline of the ventral and dorsal cochlear nuclei have also been investigated with a few studies designed to measure the size of the nucleus based on surface formations [2,3,8,10], the internal dimensions, the depth, and the orientation of the nuclei inside the human brainstem have not been studied systematically before. Knowledge about these parameters largely stems from individual cases [7]. Surface electrodes for CN stimulation are implanted into a small “tube” that is called the “lateral recess” of the fourth brain ventricle, so that the portion of the CN that can be electrically stimulated is mostly determined by the size of the electrode carrier and the spacing of the electrode contacts. Penetrating electrodes have to be injected into the brainstem tissue itself. Entry point, trajectory and length of electrode shafts are important variable for the efficacy and safety of penetrating auditory brainstem implants (PABI) than for the classical surface implant.

The present study examines size, spatial orientation, and surface depth of the ventral and dorsal cochlear nucleus in histological cross-sections of human brainstem specimens.

II. METHODS

Size and location of 33 CNC (17 right-sided, 16 left-sided) obtained from 20 formalin-fixed specimen taken from autopsies of 11 male and 9 female patients were examined in cross-axial brainstem sections with the aid of a light microscope (Leica[®], magnification x2.5, Neubauer ocular scale, resolution 4 μ m). Mean age of the patients at death was 57.5 (48-83) years. Brain weight varied between 1100g und 1600g (mean 1362g). The brains were fixed in Formalin for at least 6 weeks to balance for swelling and shrinkage. All measurements were corrected by a factor of 1.13 (12%) for transverse and 1.21 (17%) for longitudinal shrinkage caused by histological preparation.

Length, width, and height have been measured for both the ventral (VCN) and dorsal portion (DCN) of the nucleus on either side (Fig. 1, 2). The relationship of the

nuclei to the intramedullary portion of facial nerve was determined.

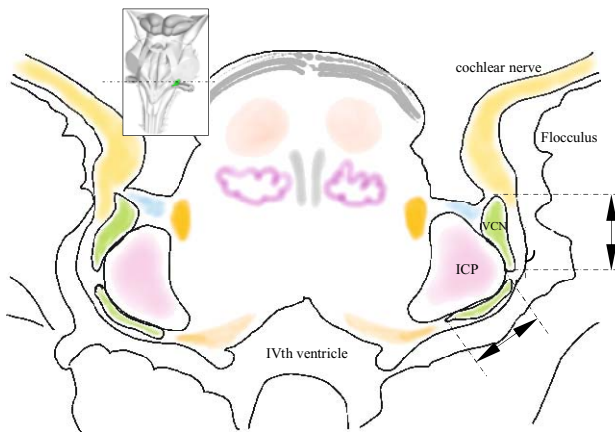


Fig. 1 Longitudinal section of the brainstem at the level of the entry zone of the cochlear nerve. The variable “length” of VCN and DCN is indicated by the arrows. ICP...inferior cerebellar peduncle VCN...ventral cochlea nucleus

The most rostral section of the intramedullary segment of facial nerve was used for an anatomical referencing of the height, i.e. the sagittal extension of the nuclei, (Fig. 2).

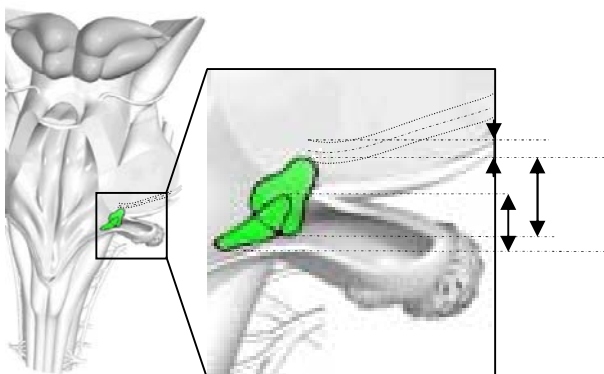


Fig. 2 Coronal section through the brainstem at the level of the cochlear nuclei. Arrows indicate the height of the nuclei and the distance to the intramedullary facial nerve. Note the regular anatomical overlap between VCN and DCN. The overall height of the CNC accessible to electrodes therefore is smaller than the combined height of the VCN and DCN.

Data were analyzed using the SPSS PC+ statistical package. Chi-Squares and Kolmogorov-Smirnov tests did not reveal significant derivations of the data from the normal distribution.

A univariate ANOVA was performed for left/right side differences. Pearson correlations have been obtained for grouped variables like diameters of the cochlear nuclei in axial, coronal and sagittal planes.

III. RESULTS

The cochlear nucleus complex has an overall extension of 8.01 x 1.53 x 3.76 mm (length x width x height) in respect to the intrinsic axis of the complex was with standard deviations ranging between 1-2 mm (see Table 1).

Table 1. Mean (± standard deviation) of the maximum measured dimensions in each histological slice of the DCN, VCN, and the complete nucleus (CNC)

	Length		Height
	anteroposterior	mediolateral	rostrocaudal
DCN	3.42 ± 1.21	0.68 ± 0.20	1.90 ± 0.66
VCN	4.59 ± 0.89	1.53 ± 0.64	3.18 ± 0.69
CNC	8.01 ± 1.05	1.53 ± 0.64	3.76 ± 0.89

While for the DCN maximum length and width fell together at one single level, the VCN was longer in lower section but wider in more superior slices.

There was an inter-individual variability with a factor of 3 between extremes in all data. This is best illustrated by the smallest and largest dimensions that have been encountered (Table 2a&b).

Table 2. Variability of the extension of the human cochlear nucleus

a. Smallest mean maxima of the dimensions of the cochlear nuclei. Because the measurements have been carried out in transverse sections, there is only one composite value per case for the variable “height”.

	Length		Height
	anteroposterior	mediolateral	rostrocaudal
DCN	1.46 ± 1.00	0.29 ± 0.19	0.77
VCN	1.92 ± 1.11	0.78 ± 0.31	2.32
CNC	3.38 ± 1.05	0.78 ± 0.31	2.32

b. Largest mean maxima of the dimensions of the cochlear nuclei

	Length		Height
	anteroposterior	mediolateral	rostrocaudal
DCN	4.24 ± 1.67	0.81 ± 0.19	3.10
VCN	5.42 ± 1.75	2.10 ± 0.91	4.26
CNC	9.66 ± 3.42	2.10 ± 0.91	7.36

No single CNC has been found to be smallest or largest in *all* measured dimensions.

Sizes of the ventral and the dorsal cochlear nuclei correlated well with each other.

Except for the length of the dorsal cochlear nucleus, which has been found slightly greater on the 4.14mm left side (4.14 mm versus 2.80 mm on the right side, F=5.52, p=0.38) there were no significant side differences. To the contrary, most parameters including the distance of the nuclei from the surface (depth) correlated well between right and left sides.

The ventral cochlear nucleus reached its maximum diameter (width) either at the level of the first (most rostral) transverse section of the facial nerve or 320µm

below that level. Because the axis of the VCN is obliquely orientated to the sagittal plane, the outer surface of the VCN was buried in a mean depth of at least 7 mm from the surface of the brainstem at this location (Fig. 3).

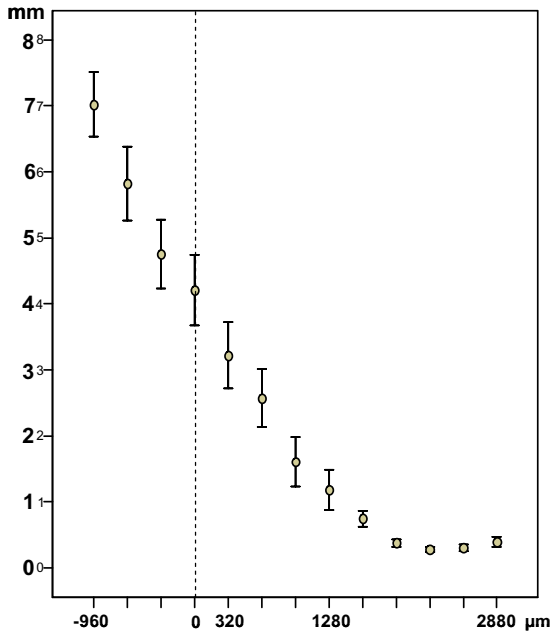


Fig. 3 Minimal surface depth (mean ± standard error) of the VCN. The broken line represents the first section of the facial nerve.

The outer surface of the DCN was located almost parallel to the surface of the brainstem with a mean minimal depth of about 0.3 mm (range 0.09 – 0.9 mm).

The spatial orientation of the CNC is most complex. Its shape resembles a distorted X-shaped silhouette in a sagittal view of the brainstem. The upper portion of the VCN is also curving in towards the midline of the medulla oblongata (Fig. 5).

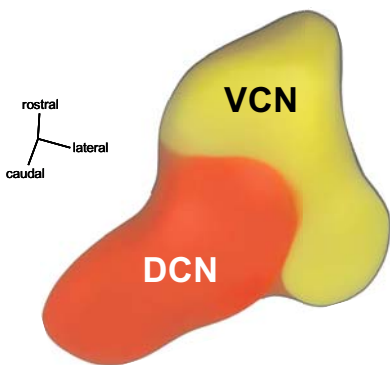


Fig. 5A Three-dimensional rendering of the CNC (lateral view)

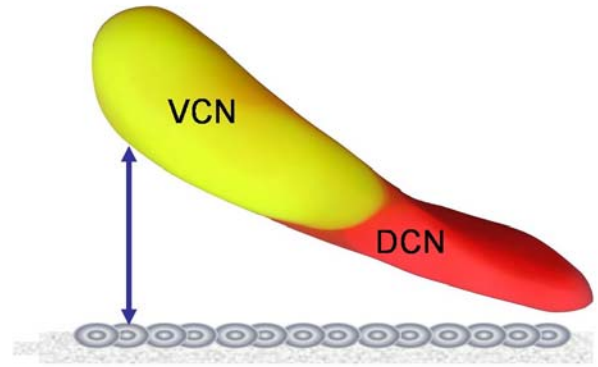


Fig. 5B Three-dimensional rendering of the left CNC (view from above). The arrow indicates the distance of the rostral part of the VCN to a surface electrode (see also Fig. 3).

IV. DISCUSSION

Because of the anatomical overlap of the dorsal and ventral cochlear nuclei in the rostrocaudal axis, the overall “height” (y-axis) of the cochlear nucleus complex (CNC) in this plane is lower than the sum of the height of DNC and VNC combined. Further, because of the inward rotation of the whole complex with respect to the brainstem axis, the projected area for electrode contact at the outer surface does not match the reachable parts of the CNC by electrical stimulation with common surface electrodes. Especially the neurons that are connected to the primary afferents of the cochlear nerve probably do not receive appropriate current to be activated. For a PABI, the entry area for insertion of penetrating electrodes to the cochlear nucleus is no larger than 8 x 3 mm. While these extensions compare relatively well with data from measurements at the surface of the brainstem published in previous studies [2,3,8,10], intrinsic brainstem measurements reveal other dimensions of the challenge to place electrodes inside the nucleus. The diameter DCN is only 1 mm and this part of the CNC is located just under the surface of the brainstem. Electrodes that are longer than 2 mm over a length of about 3.5 mm (the DCN’s mean length) will penetrate through the DCN and lose efficacy. Moreover, the upper portion of the VCN can only be reached by electrodes that are as long as 7mm.

Successful surface electrodes reach the CNC mostly at its caudal half, sharply above the exit zone of the ninth cranial nerve, which is located 4.5 mm (2.5-6.5 mm) caudal to the exit zone of the facial nerve [4]. Penetrating electrodes for the upper VCN therefore have to be inserted above the lateral recess in the zenith of the brainstem. The length of the electrode shafts would have to incrementally extend (over a distance of just 3 mm) -

from 2 mm to 7mm. Spacing of the electrodes would have to be narrow – probably as small as 0.75mm which in turn may cause more problems with tissue damage and channel crosstalk.

The PABI implanted by the House Ear Institute in Los Angeles comes close to complying with these constraints and further clinical results should be awaited [1,9].

V. CONCLUSION

The small dimensions of the CNC, its inter-individual variability, and its varying location with respect to the surface of the brainstem and outer landmarks will continue to constitute a major challenge at the electrode-tissue-interface for these implants.

ACKNOWLEDGMENT

The authors express their gratitude to Prof. Gerhard Franz Walter, M.D. and his former team at the Department of Neuropathology of the Medizinische Hochschule Hannover, Prof. Madjid Samii, M.D. (International Neuroscience Institute Hannover, Germany), Prof. Cordula Matthies, M.D. (Neurosurgery, University of Würzburg), Prof. Thomas Lenarz, M.D. (ENT, Medizinische Hochschule Hannover, Germany), Prof. Wolf Sollmann, M.D. (Neurosurgery, Klinikum Braunschweig, Germany), and Prof. Roland Laszig, M.D. (ENT, University of Freiburg, Germany).

REFERENCES

1. Fayad,J.N., Otto,S.R., and Brackmann,D.E. (2006): Auditory brainstem implants: surgical aspects. *Adv.Otorhinolaryngol.*, 64:144-153.
2. Jacob,U., Mrosack,B., Gerhardt,H.J., and Staudt,J. (1991): [The surgical approach to the cochlear nucleus area]. *Anat.Anz.*, 173:93-100.
3. Klose,A.K. and Sollmann,W.P. (2000): Anatomical variations of landmarks for implantation at the cochlear nucleus. *J.Laryngol.Otol.Suppl*, 8-10.
4. Lang,J. (1995): Skull base and related structures. Schattauer, Stuttgart, New York.
5. McElveen,J.T., Jr., Hitselberger,W.E., and House,W.F. (1987): Surgical accessibility of the cochlear nuclear complex in man: surgical landmarks. *Otolaryngol Head Neck Surg*, 96:135-40.
6. Mobley,J.P., Huang,J., Moore,J.K., and McCreery,D.B. (1995): Three-dimensional modeling of human brain stem structures for an auditory brain stem implant. *Ann.Otol.Rhinol.Laryngol.Suppl*, 166:30-31.
7. Moore,J.K. and Osen,K.K. (1979): The cochlear nuclei in man. *Am.J.Anat.*, 154:393-418.
8. Quester,R. and Schroder,R. (1999): Topographic anatomy of the cochlear nuclear region at the floor of the fourth ventricle in humans. *J.Neurosurg.*, 91:466-476.
9. Schwartz,M.S., Otto,S.R., Shannon,R.V., Hitselberger,W.E., and Brackmann,D.E. (2008): Auditory brainstem implants. *Neurotherapeutics.*, 5:128-136.
10. Terr,L.I. and Edgerton,B.J. (1985): Three-dimensional reconstruction of the cochlear nuclear complex in humans. *Arch.Otolaryngol.*, 111:495-501.
11. Terr,L.I., Fayad,J., Hitselberger,W.E., and Zakhary,R. (1990): Cochlear nucleus anatomy related to central electroauditory prosthesis implantation. *Otolaryngol.Head Neck Surg.*, 102:717-721.

Corresponding Author:	Steffen K. Rosahl, M.D.
Institute:	HELIOS Department of Neurosurgery
Street:	Nordhaeuser Str. 74
City:	Erfurt
Country:	Germany
Email:	steffen.rosahl@helios-kliniken.de

Estimation and Evaluation of Upper Limb Endpoint Stiffness and Joint Torques for Post-stroke Rehabilitation

P.R. Wang¹, Y.H. Chiu¹, M.S. Tsai² and K.C. Chung³

¹ ICT-Enabled Healthcare Program, Industrial Technology Research Institute – South, Tainan, Taiwan

² Potz General Hospital, Department of Health, Executive Yuan, Chai Yi, Taiwan

³ Institute of Biomedical Engineering, National Cheng Kung University, Tainan, Taiwan

Abstract—This research was aimed to investigate biomechanical properties via estimation of upper limb endpoint stiffness and joint torques during force targeting tasks. Sixteen able-bodied subjects were recruited in the study. A 10-N force task was conducted at right and left force directions for three upper limb postures. Hand endpoint trajectories and the response forces were recorded simultaneously for each trial. The 2x2 endpoint stiffness matrix and corresponding stiffness ellipse were determined by least squares error method. Resultant shoulder and elbow torques were also calculated by inverse kinetics. Mann-Whitney U test and Kruskal-Wallis test was used to analyze the effect of movement directions and postures on endpoint stiffness and joint torques. The results indicated that the force directions and postures have significant effects on endpoint stiffness ellipse of upper limb, the shoulder and elbow joint torques during force production tasks ($p < 0.05$). These results demonstrate the importance of the force directions and posture during performing force targeting tasks. The future work of clinical implementation suggests that upper-limb endpoint stiffness and viscosity can be measured and compared with able-bodied subjects and post-stokes.

Keywords— Stroke, upper-limb, endpoint stiffness, rehabilitation

I. INTRODUCTION

Stroke is an acute onset of neurological dysfunction when blood flow to the brain is impaired by infarction or hemorrhage of cerebral arteries [1]. The most common motor deficits are characterized by hemiparesis or hemiplegia, typically on one side of the body opposite the site of the lesion [1]. The illness stages of stroke usually accompany the development of abnormal muscle tone, flexion and extension synergistic patterns [1]. Functional impairments of upper limb are always more severe than those of lower limb for deteriorated activities of daily living (ADL). It has been reported that 88% of the post-strokes suffer from paretic upper limbs in acute stages and 55-75% ones remain the paretic deficits after six months or more [2].

According to equilibrium-point control hypothesis, the neuromuscular system conducts a control mechanism based on the mechanical stability of viscoelastic properties [8].

Particularly, viscoelastic muscle properties, length-tension and force-velocity relationship, lead to joint translation and rotation. Previous researches have suggested the spring-like properties of muscles determine the individual joint stiffness. Endpoint stiffness, defined as the relationship between externally imposed displacements of the hand and the respond force generated, stabilizes the hand position. [3,4]. The resultant elastic resistance is not only due to joint stiffness, but depends on the posture-dependent joint angles and respective limb segment lengths [4, 5]. Furthermore, stability of hand can be characterized by endpoint stiffness ellipse. The major axis of the ellipse is oriented along the direction of the maximal stiffness; the minor one is oriented along the minimal stiffness, and the orientation indicated the direction of the maximal stiffness [6]. The capability to control maximum and minimum stiffness orientation could permit adjustable flexibility during tasks with direction-dependent constraints such as ball-catching, where increased joint stiffness is only required along the line of impact of the ball with the hand, or during object manipulation [7].

This research is to investigate the effects of force directions and postures on endpoint stiffness and joint torques during performing voluntary force task. More specifically, this research is aimed to:

1. Investigate the effects of voluntary force directions and postures endpoint stiffness of upper limb during force production tasks.
2. Apply endpoint stiffness ellipse to quantify stability of hand.
3. Develop a feasibility study on normal subjects.

II. MATERIALS AND METHODS

A. Endpoint stiffness modeling

The two-link and open kinematic chains was conducted to simulate the kinematic model of upper limb in this research. The upper-limb system assumes that endpoint inertia is invariant across every trail. The resulting parameterized system is shown as follows [7]:

$$H_{ij}(s) = I_{ij}s^2 + B_{ij}s + K_{ij}; \quad (1)$$

where $s = 2\pi f\sqrt{-1}$ and I_{ij} , B_{ij} , and K_{ij} represents the endpoint inertia, viscosity, and elasticity matrices, respectively. Eq. 2 shows the endpoint stiffness matrix that indicates the effects of restoring force opposite to the displacement.

$$[I_{end}] \begin{bmatrix} \ddot{x} \\ \ddot{y} \end{bmatrix} + [B_{end}] \begin{bmatrix} \dot{x} \\ \dot{y} \end{bmatrix} + [K_{end}] \begin{bmatrix} x \\ y \end{bmatrix} = \begin{bmatrix} f_x \\ f_y \end{bmatrix}; \quad (2)$$

$$\text{where } I_{end} = \begin{bmatrix} I_{xx} & I_{xy} \\ I_{yx} & I_{yy} \end{bmatrix}, B_{end} = \begin{bmatrix} B_{xx} & B_{xy} \\ B_{yx} & B_{yy} \end{bmatrix}, K_{end} = \begin{bmatrix} K_{xx} & K_{xy} \\ K_{yx} & K_{yy} \end{bmatrix}$$

indicates inertia, viscosity, and elasticity matrices, respectively.

Eq. 3 shows joint stiffness matrix related to shoulder and elbow joint torques is determined by inverse dynamics, as shown in, where the Jacobian, J , is a function of the limb segment lengths and joint angles [7]. The orientation of the endpoint stiffness ellipse is determined by the direction of the eigenvector associated with the maximum eigenvalue of the endpoint stiffness matrix. The ratio of endpoint stiffness ellipse is determined from the long axis divided by short axis and means to the shape of the endpoint stiffness ellipse.

$$\begin{bmatrix} TQ_s \\ TQ_e \end{bmatrix} = J^T K_{end} \begin{bmatrix} dx \\ dy \end{bmatrix} \quad (3)$$

where TQ_s indicates shoulder joint torque, TQ_e indicates elbow joint torque.

$$J = \begin{bmatrix} -l_h \sin(\theta_s) - l_f \sin(\theta_s + \theta_e) & -l_f \sin(\theta_s + \theta_e) \\ l_h \cos(\theta_s) + l_f \cos(\theta_s + \theta_e) & l_f \cos(\theta_s + \theta_e) \end{bmatrix}$$

where l_h refers upper arm length, l_f refers forearm length, θ_s refers shoulder joint angle, θ_e refers elbow joint angle.

B. Subjects and protocol

Sixteen subjects (nine male and seven female) ranging from 23 to 28 years-old with no history of neurological impairments were participated in this study. The protocol was approved by human experiment and ethics committee of National Cheng Kung University Hospital, ROC. The informed consent was signed by subject prior to study. Total two force directions and three seating positions for this study: D0 and D4 was right and left force direction, central position was defined subject's hand located 40 cm far in front of sternum, left and right position were defined apart one-thirds shoulder girdle width from central position, respectively. Subject accomplished with right arm 10N exertion. Table 1 shows demographic and anthropometric data

for all subjects included:

1. L_h measured from right acromion process of scapula to lateral epicondyle of humerus,
2. L_f measured from the right lateral epicondyle of humerus to styloid process of radius,
3. shoulder joint angle at right position (RSangle), central position (CSangle), left position (LSangle)
4. elbow joint angle at right position (REangle), central position (CEangle), left position (LEangle).

Table 1 Demographic datas of subjects

Item	Mean	Standard Deviation
Age (y/o)	25.3	1.3
Height (cm)	167.1	6.1
Weight (kg)	61.4	8.2
L_h (cm)	30.4	1.8
L_f (cm)	26.7	1.7
RSangle (deg)	97.1	11.6
REangle (deg)	31.9	10.3
CSangle (deg)	72.3	5.0
CEangle (deg)	51.5	8.6
LSangle (deg)	51.8	13.7
LEangle (deg)	52.5	7.2

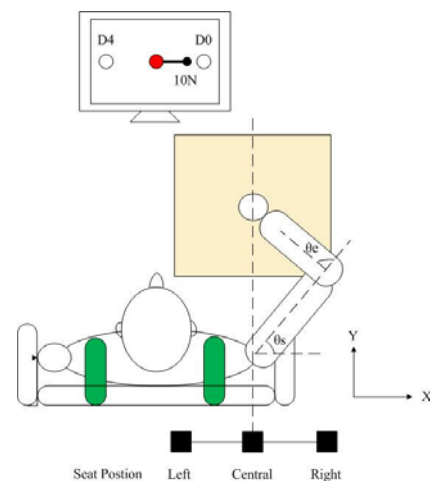


Fig. 1 Experimental setup.

There were totally 6 conditions (2 direction targets \times 3 sitting position) in the experiment (Fig.1) [8]. Experiment procedures were:

1. Initial endpoint position on the screen was centered on the start window.
2. Subjects were instructed to push the robotic manipulum according to the appearing target.

3. As subject exerted with 10-N for 6 seconds, displacement perturbation with 1cm was applied .
4. There were 8 perturbation directions from 0° to 360.

There were three trials in a set of the force production task, and every trial contained four times of the random perturbations. The subject took a rest about 30 to 60 seconds between trials for avoiding muscle fatigue.

C. Statistical analysis

Kruskal-Wallis test was used to analyze the effect of postures on endpoint stiffness and joint torques. Mann-Whitney U test was used to analyze the effect of voluntary force direction on endpoint stiffness and joint torques. The significance level was at a 0.05 level.

III. PRELIMINARY RESULTS AND DISCUSSION

This research has designed and developed a 2-D platform system for objectively endpoint assessment and training through conceptual and functional design [8], hardware selection and integration, calibration and performance testing. The hardware included 2 servo-motor and encoders (SV4835, King Right Motor Corporation, Taiwan), two force transducers (RVQ16YN, Cosmos, Jin Hua Electronic CO.LTD., Taiwan), and two slide mechanisms, one stainless steel manipulandum and iron frame. There are two mainly operating modes of this system: active and passive movement modes. The passive movement mode contains two evaluation and training functions: relaxation and force target functions. This research selects the force target function from the passive movement mode to investigate the biomechanical properties of upper-limb endpoint stiffness and joint torques during tasks.

Table 2 shows the median of endpoint stiffness matrix estimated from 6 conditions . Table 3 shows the median of long axis, orientation, and ratio of the endpoint stiffness ellipse. Table 4 shows the median of shoulder and elbow joint torques. Fig. 2 shows the endpoint stiffness ellipse of one subject (No. 12) at force direction D0 for various postures.

The results of statistical analysis have revealed that :

1. The force directions have significant effects on endpoint stiffness of upper limb except long axis length ($p<0.05$) , shown in Table 5.
2. The postures have significant effects on endpoint stiffness ellipse of upper limb, the shoulder and elbow joint torques ($p<0.05$) , shown in Table 6.

The limitations of research may include the variations in the individual limb configuration, movement velocity and small sample sizes.

Table 2 Median of endpoint stiffness matrix

Positions	Force direction	N	Endpoint stiffness matrix (N / m)	
Left	D0	16	$\begin{bmatrix} -36.67 & 4.50 \\ 21.29 & 274.61 \end{bmatrix}$	
	D4	16	$\begin{bmatrix} -68.03 & 9.19 \\ 26.17 & -241.59 \end{bmatrix}$	
Central	D0	16	$\begin{bmatrix} -101.71 & 40.62 \\ 126.06 & -302.90 \end{bmatrix}$	
	D4	16	$\begin{bmatrix} -163.09 & 56.88 \\ 141.48 & -246.81 \end{bmatrix}$	
Right	D0	16	$\begin{bmatrix} -106.00 & 66.79 \\ 149.62 & -270.09 \end{bmatrix}$	
	D4	16	$\begin{bmatrix} -159.67 & 75.14 \\ 147.76 & -197.66 \end{bmatrix}$	

Table 3 Median of parameters of endpoint stiffness ellipse

Position	Target direction	N	Long axis (m)	Orientation (deg)	Raito
Left	D0	16	642.2	128.6	9.1
	D4	16	506.2	132.0	7.6
Central	D0	16	797.0	122.7	10.9
	D4	16	910.1	129.6	9.3
Right	D0	16	868.4	103.5	4.9
	D4	16	754.1	109.1	5.2

Table 4 Median of the shoulder and elbow joint torques

Position	Target direction	TQs (Nm)	TQe (Nm)
Left	D0	-3.39	-1.14
	D4	3.39	1.14
Central	D0	-2.11	0.77
	D4	2.11	-0.77
Right	D0	-0.98	2.05
	D4	0.98	-2.05

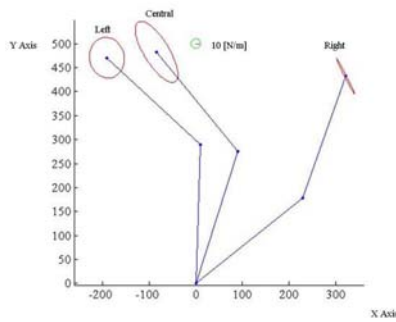


Fig. 2 Result of endpoint stiffness ellipse for subject No.12.

Table 5 Mean ranks of endpoint stiffness parameters .

	D0	D4
Long axis (m)	147.72	141.28
Orientation (deg)	147.72	141.28 *
Shape	155.92	133.08 *
TQs (Nm)	173.82	115.18 *
TQe (Nm)	74.20	214.80 *

*p< 0.05

Table 6 Mean ranks of endpoint stiffness parameters.

		Centel	Right	Left
Long axis	D0	28.38	28.69	16.44 *
	D4	29.50	27.88	16.13 *
Orientation	D0	26.06	34.38	13.06 *
	D4	27.88	33.00	12.63 *
Shape	D0	27.34	16.47	29.69 *
	D4	29.38	17.13	27.00 *
TQs	D0	25.13	38.75	9.63 *
	D4	23.88	10.25	39.38 *
TQe	D0	25.09	39.00	9.41 *
	D4	23.91	10.00	39.59 *

*p< 0.05

IV. CONCLUSIONS

The results have revealed that the endpoint stiffness model of upper-limb shows the potential advantage for

functional test and evaluation in force production tasks. The upper-limb system may provide more equilibrium state due to the more isotropic endpoint stiffness ellipse, as the force direction and endpoint position are closer to shoulder joint. More subjective and objective experiments will be developed to:

1. Investigate the endpoint viscosity of the multi-joint system.
2. Compare the endpoint stiffness and viscosity variations between able-bodied subjects and post-strokes.

REFERENCES

1. O'Sullivan SB, Schmitz TJ (2003) Physical Rehabilitation: Assessment And Treatment. FA Davis, Philadelphia.
2. Cirstea MC, Pfito A, Levin MF et al (2003) ,Arm reaching improvements with short-term practice depend on the severity of the motor deficit in stroke. *Exp Brain Res* 152: 476-488.
3. Milner TE (2002) Contribution of geometry and joint stiffness to mechanical stability of the human arm. *Exp. Brain Res* 143:515-519
4. Perreault EJ, Kirsch RF, Crago PEL. (2001) Effects of voluntary force generation on the elastic components of endpoint stiffness. *Exp Brain Res* 141(3), pp. 312-323
5. Perreault EJ, Kirsch RF, and Crago PE. (2004) Multijoint dynamics and postural stability of the human arm. *Exp Brain Res* 157(4): pp. 507-517
6. Zatsiorsky VM. (2002) *Kinetics of Human Motion*. Human Kinetics, Leeds , Champaign
7. Mussa-Ivaldi FA, Hogan N, et al. (1985) Neural, Mechanical, and Geometric Factors Subservng Arm Posture in Humans. *J Neurosci* 5(10), pp.2732-2743
8. PR Wang, JY Chang, KC Chung (2008) Effects of Upper-Limb Posture on Endpoint Stiffness during Force Targeting Tasks, IFMBE Proc. vol. 23, 13th International Conference on Biomedical Engineering, Singapore, 2008, pp 1862-1865

Author: Pei-Rong Wang
 Institute: Industrial Technology Research Institute- South / ICT-Enabled Healthcare Program, Tainan
 Street: Bldg. R1, Rm. 304, No. 31, Gongye, 2nd Rd., Annan District, Tainan City 70955
 City: Tainan
 Country: Taiwan, R.O.C
 Email: PR_Wang@itri.org.tw

Neuroelectronic interfaces with the central nervous systems – ethical issues

S.K. Rosahl^{1,2}

¹ Department of Neurosurgery, HELIOS Klinikum Erfurt, Germany

² University of Freiburg, Germany

Abstract— Public debate about electronic implants for the restoration or modulation of disturbed neural function has controversial aspects and it is loaded with baseless expectations and probably unwarranted fears.

Neural prostheses work in one of two ways, either (1) by delivering electrical stimulation that excites or inhibits neural tissue or (2) by picking up electricity generated by the brain and using it to control computer cursors, electromechanical devices or even paretic limbs. They have a general disadvantage over other methods employed to restore or even enhance neural function: they typically involve an invasive surgical procedure. On the other hand, these implants restore neural function where all other methods fail, and function continuously without the patients having to attend to them or interrupt or alter their normal behaviour. Implants are hidden under the skin and can be turned off easily.

While placebo-controlled studies are problematic whenever surgery is involved, intelligent study designs like crossover paradigms can make up for this drawback.

In expert hands, i.e. with profound knowledge of the indications, risks and current limitations of therapeutical implants, ethical issues do not significantly differ from those related to any other routine medical intervention. The benefits of today's clinically applied neuroelectronic devices to restore function clearly outweigh their risks to the individual.

Microtechnology will definitely improve these interfaces to the nervous system in the future. Ethical analysis should strive to separate realistic forecasts from the more speculative ones. An early and thoughtful discussion of potential benefits and risks will lay the ground for a responsible application of this very promising technology. To date, there is little real technological background for the use of implant technology to improve the physical, cognitive or psychological capabilities of an individual beyond what is considered "normal".

Keywords— Medical ethics, biotechnology, neural implants, central nervous system electrical stimulation, neuroelectronic interfaces, neurosurgery

I. INTRODUCTION

Several electronic implants have been introduced into medical practice in order to restore lost neural function. Scientists, engineers and medical doctors are clearly at the forefront of the technological development and it is their responsibility to establish not only scientific but also

ethical standards that will serve as arguments in an ongoing discussion.

At first glance, the criteria for assessment of electrical interfaces to the central nervous system that could potentially influence psyche or even affect society as a whole appear to be different from those applied for other medical treatment modalities like pharmacological remedies or radiotherapy. After all, some of these interfaces require a direct contact between electrodes and the human brain. Does it take a completely new variety of ethical assessment for these interfaces? Do we need some sort of "implant ethics"[9]?

The question implies that there may be more to the emotional adversity of a large number of people to these implants. It also implies that a change of social normative values and ethical judgment might be necessary to arrive at appropriate recommendations for proceeding with this kind of research. It even implies that regulative measures might be necessary for this kind of research that go beyond the regulations for other biomedical explorations. Finally, it reflects public worries (or hopes, respectively, depending on the juror's point of view), that central nervous system implants may not just be employed for treatment but also for "enhancement" of human capacities beyond "normality", resulting in a "trans-human" society[3].

This paper attempts to provide a few basic criteria for the ethical evaluation of research studies involving neuroelectronic interfaces with the human central nervous system. At the same time, it will be shown that these basic ethical criteria, including non-maleficence, beneficence, respect for autonomy, and justice - often referred to as the Belmont principles [16] - do not differ significantly from those applied to medical research in general.

II. ETHICAL PRINCIPLES

A. Non-maleficence

Placing electrodes in eloquent areas of the central nervous system is not exactly a risk-free procedure. With such implants, however, the surgical risk is not what really causes significant concern. Of course, a direct intervention into the human brain will have to be monitored with extreme caution. Neurosurgery has come

a long way since its beginnings at the turn of the 19th century. We have learnt what there is to avoid to leave a patient's brain function intact during such procedures. What we often do not exactly know yet is the reaction of specific neural tissue to chronic electrical input, but this gap in ultimate knowledge is something that is encountered in research on other medical products or pharmaceutical compounds as well.

Therefore, there is no qualitative difference in the ethical evaluation of brain implants to any other new method or technology interfering with the CNS. It should be monitored systematically, and research designs and protocols have to be carefully tuned to rule out expected and non-expected side effects. Perhaps these monitoring methods have to be quantitatively more extensive, since subtle side effects pertaining to personality and those mental capacities related to personhood are more likely to be missed especially in chronic applications like deep brain stimulation. Electrical stimulation delivered to highly sensitive central nervous structure at a functional level that is critical for complex behavior (e.g. the limbic system) requires more extensive research protocols and monitoring, sometimes affording a multidisciplinary team.

When implants advance into the next generation, incorporating microfluidic devices to deliver drugs, neurotransmitters or other neurohumoral substances, systemic neural responses will have to be considered and monitored rather closely for complex side effects.

Still, being extremely cautious and vigilant with respect to the first and most basic moral principle – the obligation not to inflict harm on others - does not mean that with technology acting on basis of brain-electrode-interfaces this first basic ethic principle needs to be replaced or in any way extended beyond its application in other fields of medical research.

B. Beneficence

I have no doubt that a biomedical technology that does not result in a benefit for the patient will be off the market very quickly. So why do we even have to consider the ethical principle of beneficence in this context?

It is the triangle constructed of risks, side-effects, and benefit that justifies a closer look. Without going too much into detail, there are electronic implants interfacing the brain that have the potential to ease some of the burden that the loss of specific neural function has caused for a patient. Still the same implant may impede the personal range of motion that this patient had before the implant was placed. For example, when wiring was crucial to contact the electrodes in the past, a brain-computer-interface might have establish new channels of communication for the patient, but at the same time have

limited his mobility. Such a patient might not consider the implant beneficial on the long run, even though it might enable him to move a cursor on a computer screen.

On the other hand, if it can safely be assumed that a direct interface to the human central nervous system is a legitimate treatment option, i.e. it is in positive accord with the common criteria of weighing its intended primary effects against its unwanted, but foreseeable, side effects, it is by definition beneficial.

Again, there is nothing new on the ethical front: New types of neuroelectronic interfaces are subject to the general principle of beneficence - just as any other new medical treatment option.

C. Respect for autonomy

Autonomy is a complex, multi-faceted concept. In human research, respecting the autonomy of a patient or any other research subject mandates obtaining that patient's (subject's) *informed consent* in advance. In order to arrive at a decision, the patient has to *know* what he or she consents to. Informing the person on the nature, method, benefits and possible side-effects of a planned medical or research intervention obviously is an indispensable obligation and certainly a principle that is strictly adhered especially in the field of neuroelectronic interfaces. These interfaces, aimed at alleviating diseases and restoring central functions, in themselves do not raise specific normative problems in this context.

However, they do have a specific tone to them, because some of the effects and side effects of direct electrical stimulation of the brain may be hard to grasp for the patient; at times even for the researcher or to the treating physician. Such effects are likely to be underestimated (if not downplayed). While changes of personal identity or dissociative behavior would seem exotic and represent an extreme (probably resulting in switching off the stimulator), mere personality changes may also be liable to underestimation as possible side effects. It would appear crucial to describe their potential manifestations as detailed as possible to a person reasoning about whether to undergo a certain intervention.

Another problem in this realm is the pressure that weighs on a patient who suffers from a brain disease. It has been argued that, to relief his suffering, such a patient would accept almost any treatment option that is offered to him. His suffering would compromise his ability to freely exercising his autonomy at all. Exemplary speaking: A tetraplegic patient confronted with the alternative of never being able to move a limb again or have a direct (however still fictitious) CNS implant to make him walk, will most probably choose the latter.

Lack of alternatives, however, has nothing to do with coercion and the patient's consent to the implant surgery would doubtlessly be autonomous and valid. In practice,

the example of the “deaf community” refusing to be restored to “species-typical functioning” by cochlear implants illustrates the range of possibilities. [2]

The topic of autonomy in third party cases and in cases, when parents have to decide for their children, extends beyond the limits of this paper.

D. Justice

There is consensus that medical services are a socially distributed good that is destined to preserve or restore health as a precondition for any reasonable life plan of any rational person. Yet the scope of human conditions these medical services should be allocated to will remain a matter of constant debate. With western and eastern societies facing a severe lack of resources in health care, problems of distributive justice are among the most pressing issues today. The ever widening scope of treatment options in medicine, e.g. by central nervous system interfaces like double-sided cochlear implants, will probably command a stricter regime of rationing under current health care systems.

The less severe the functional loss which can be restored by a neural prosthesis, the more likely health insurance companies and other financial providers will compare its implantation to cosmetic surgery and other interventions at the borderline between treatment and “enhancement”. However convincing economical and political prudence may be, public awareness will have to single out cases where such reasoning might override the principles of justice.

Apart from the societal context given by issues of distributive justice, on a more individual level researchers and physicians should strive to allocate new treatment options to all patients who will benefit from these new technologies. On the other hand, the selection of research participants needs to be constantly monitored to exclude abuse of participants who primarily chosen because they are easily available or vulnerable or easy to manipulate.

All that involves efforts in appropriate and honest publication of the results of basic and clinical research studies in scientific journals, but it also includes the often forgotten field of public education and the delivery of scientific information in a manner that can be understood by the general public. Only an informed society will be able to justly allocate resources for new biomedical technologies such as neuroelectronic implants.

Up to now, I see no reason to expect that just allocation of resources would necessitate a change of normative values with respect to neural prostheses. This may change on a technological level where it might be considered beneficial for humans to extend their

capabilities beyond what is deemed “normal”, in other words, when we move from treatment to “enhancement”.

III. Enhancement

While the distinction between treatment and enhancement may be difficult in borderline cases [10], it can safely be assumed that enhancing healthy human beings is not part of the responsibility of health care professionals, which is to treat and prevent diseases and to restore function that is normal for an individual of a given age and sex. [1,4-6,8,15] When looking ahead from current neural prosthesis to possible enhancement with electronic devices directly coupled to the human brain, what comes to my mind primarily is not the question whether there should be regulatory limits to enhancements in order to remain a human society. [14,18]

On a personal level, the first question I would consider is: Do I really want to be “enhanced” by surgically implanted devices when I can acquire the profits and benefits provided by such an implant with noninvasive technology or by simply taking a pill? Infrared vision, perception of radio-frequency signals, ultrasound hearing, and even invisible communication can all be accomplished by small external devices today. Enhanced well-being, motivation and cognition by administering drugs—in other words “doping”—are well established.

On the other hand, devices like the “artificial hippocampus” [7] to extend human “memory capacity”, “co-processors” to the human brain that boost cognition or implanted gadgets that let us communicate “by thought alone” sound not just a little far-fetched when I look at the current state of technology.

Still, with every new step on the way a new technology is taking, there is a potential for abuse. [11,12] Moreover, enhancement by connecting electronic devices to the human body and brain to many appears morally suspect, at least at the first glance. Others have argued that these enhancement technologies offer an opportunity to make life even more worthwhile, provided that society responds appropriately to the implicit social challenges, including that posed by distributing these technological interventions justly.

Last but not least, a variety of science fiction scenarios involving cyborgs and the imminent transformation of the human race into a semi-electronic species have left the public rather perplexed. [13] These scenarios have also provoked counter-reactions against scientific progress in the field of neuroelectronic devices and neural prosthetics.

While I hold company to those authors who argue that that concerns about an enhanced “trans-human” race can be put off until later as long as technology does not

progress to the point where implants have advantages unsurpassed by other, less-invasive means [17], the ethical debate about these issues should not be postponed. To the contrary, it should be bolstered by arguments based on scientific research and scientific reason that can only come from experts who oversee the current state and trends in the field. It is their responsibility to express their highly specific knowledge in terms that can be understood not only by experts in other scientific fields involved in technology assessment, but also by large parts of society and the general public. Only then we will be able to inject reason into an ongoing public debate that to date is mainly fueled by Hollywood scenarios and highly exaggerated campaigns in the World Wide Web, and the tabloid press.

While there is certainly no point in trying to stop or ban the development of new central neural implants, an early and thoughtful discussion of their potential benefits and risks must lay the ground for a responsible application of this very promising technology.

4 Literature

1. Caplan,A.L. (2003): Is better best? A noted ethicist argues in favor of brain enhancement. *Sci.Am.*, 289:104-105.
2. Crouch,R.A. (1997): Letting the deaf be deaf. Reconsidering the use of cochlear implants in prelingually deaf children. *Hastings Cent.Rep.*, 27:14-21.
3. Daly,B.M. (2004): Transhumanism: toward a brave new world? *America.(NY)*, 191:18-20.
4. Daniels,N. (2000): Normal functioning and the treatment-enhancement distinction. *Camb Q Healthc Ethics*, 9:309-322.
5. Elliott,C. (2003): Making us better. *Ment.Health Today*, 20-23.
6. Evans,J.H. (2005): Bioethical consensus and the force of good ideas. *Hastings Cent.Rep.*, 35:3
7. Gabrieli,J.D. (2004): Memory: Pandora's hippocampus? *Cerebrum.*, 6:39-48.
8. Garreau,J. (2005): Perfecting the human. *Fortune.*, 151:101-2, 104, 106.
9. Hansson,S.O. (2005): Implant ethics. *J.Med.Ethics*, 31:519-525.
10. Merkel,R., Boer,G., Fegert,J., Galert,T., Nuttin,B., and Rosahl,S.K. (2007): *Intervening in the Brain: Changing Psyche and Society*. Springer, Berlin - Heidelberg - New York.
11. Moreno,J.D. (2003): Neuroethics: an agenda for neuroscience and society. *Nat.Rev.Neurosci.*, 4:149-153.
12. Moreno,J.D. (2004): DARPA on your mind. *Cerebrum.*, 6:91-99.
13. Rosahl,S.K. (2007): Neuroprosthetics and neuroenhancement: can we draw a line? *Virtual Mentor - American Medical Association Journal of Ethics*, 9:132-139.
14. Rubin,C.T. (2004): Man or machine? *New Atlantis*, 4:31-37.
15. Sandel,M.J. (2004): The case against perfection: what's wrong with designer children, bionic athletes, and genetic engineering. *Atl.Mon.*, 292:50-60, 62.
16. The National Commission for the Protection of Human Subjects of Biomedical and Behavioral Research (1979): *The Belmont Report - Ethical Principles and Guidelines for the Protection of Human Subjects of Research*. Office of the Secretary of the U.S. Department of Health, education, and welfare.
17. White,R.J. (1999): Brain chips: postpone the debate. *Hastings Cent.Rep.*, 29:4
18. Wickelgren,I. (2004): Neuroprosthetics. Brain-computer interface adds a new dimension. *Science*, 306:1878-1879.

Corresponding Author:	Steffen K. Rosahl, M.D.
Institute:	HELIOS Department of Neurosurgery
Street:	Nordhaeuser Str. 74
City:	Erfurt
Country:	Germany
Email:	steffen.rosahl@helios-kliniken.de

Ultrasound Pre-study of the Kinematics of the Residual Tibia within a Trans-Tibial Socket during Gait

S. Klasen, C. Uplegger, S. Rensch, T. Bächle, and U. Schneider

Fraunhofer Institute for Manufacturing Engineering and Automation IPA,
University of Applied Sciences Münster, Stuttgart, Germany

Abstract— The motion of the residual-tibia within a trans-tibial socket was examined so far only by X-ray. In this pre-study now the motion of the residual tibia is to be described during gait using ultrasound data. The results of measurement raised here are to serve as input for later simulation work, in order to be able to adapt socket fit individually.

So far, this procedure of ultrasound measurement during gait cycle was used only related to the femur.

In the first part the structure of the test rig and the integration into the socket is described, as well as the calibration of the system. In the second part, the results of measurement are represented and discussed afterwards.

Keywords— ultrasound, trans-tibial, relative motion, prosthesis, gait.

I. INTRODUCTION

Eriksson and Lemperg (1969) [1], Grevsten and Eriksson (1975) [2] and Lilja et al. (1993) [3] all used radiographic techniques to analyse residual tibial movement within trans-tibial sockets. Mayfield et al. (1977)[4], Sabolich (1985)[5] and Long (1985)[6] also used radiographic techniques to the analysis, however they were occupied with the motion of the residual femur within the trans-femoral socket. The use of radiographic technique is possible only temporarily because of the risk of ionising radiation. Furthermore these studies were restricted to static analysis at simulated instants of the gait cycle.

Convery and Murray (2000) [7] used the ultrasound for the examination of the residual femur motion within a trans-femoral socket during gait cycle for the first time.

The ETH Zurich developed in 2006 a „moving-video-fluoroscope“, a C-arm-x-ray unit, which is carried with the patient. Thus it permits recordings of the knee-TEP during a complete gait cycle [8, 9]. This procedure was used only to analyse TEP knee joints so far.

This pre-study measured the motion of the residual tibia within a trans-tibial socket during gait using ultrasound for first time.

Four 9MHz linear array transducer were selected in order to provide an optimal image of the tibia. The field of view

of all four transducers is 39mm and each transducer was connected to a separate diagnostic ultrasound scanner EchoBlaster128 (Teleded, Lithuania).

By mounting the ultrasound transducers on the outside wall of the socket it is possible to set the movement of the Tibia within the socket direct in connection to the socket. However, overruns may occur due to poor contact at the interface between transducer and stump during gait cycle. This can be prevented and/or minimized by exact positioning of probes in forward, an optimal socket fit and the use of “Sonar Aid” (Geistlich Pharma, Switzerland), aqueous coupling medium for diagnostic ultrasound.

Also out of this the necessity can be derived that for each measurement an individually manufactured and adapted prosthesis socket will be required.

II. SUBJECT

The subject is a 27-year-old male whose left trans-tibial amputation was a result of an osteogenic sarcoma. He is 1,82 meter tall and weights 72 kilogram. The subject was amputated for 11 years at the time of the preliminary study. He carries his prosthesis daily about 16 hours, is vocationally main sitting actively and is due to its private activities assigned to the activity class IV.

III. METHODOLOGY

For the production of the measuring socket at first a test socket was manufactured out of „Thermoflex solid“ (Bauerfeind, Germany) within a 3mm soft wall interior socket out of „Extrafoam“ (Leder Scheben, Germany).

At the measuring socket, four ultrasound transducers were positioned in such a way that the Tibia is on target during the entire gait cycle. Subsequently, two points of reference were specified: proximal the Tuberositas tibiae and distal at the end of the tibia, to those in each case two ultrasonic probes were anterior and laterally aligned. For stabilization serves a metal-rack, which fix the probes by means of cube caps. Threaded rods and axial pivots connect

the mounting plates and thus avoids the change in angle of the probes among themselves.

According to this model the measuring socket could be manufactured. As placeholder for the ultrasound transducer dummies from gypsum were manufactured. Armoring consisted of four layers stockinette, four layers glass, carbon fiber amplification, and the whole was filled up with carbon acrylic resin. The finished measuring socket with the integrated ultrasound transducers and the metal-rack is to be seen in fig. 1.

In each case the four ultrasound transducers were assigned to an IPC (Bressner, Germany). These IPCs contain an Intel Core2Duo processor with 1,6GHz and 2GB DDR II RAM main memory. USB 2.0 connect the diagnostic ultrasound scanner with the IPCs. The four IPCs are interlaced over a SWITCH among themselves. All devices of the measurement setup are supplied via a voltage supply with 12VDC.

The four measuring systems were appointed before beginning of each measurement with the help of DCF77-receiver for accuracy in the same time. This time serves for the synchronisation of the measurements.

The entire ultrasound measuring system is on a trolley, which was motor driven over a belt drive beside the subject.

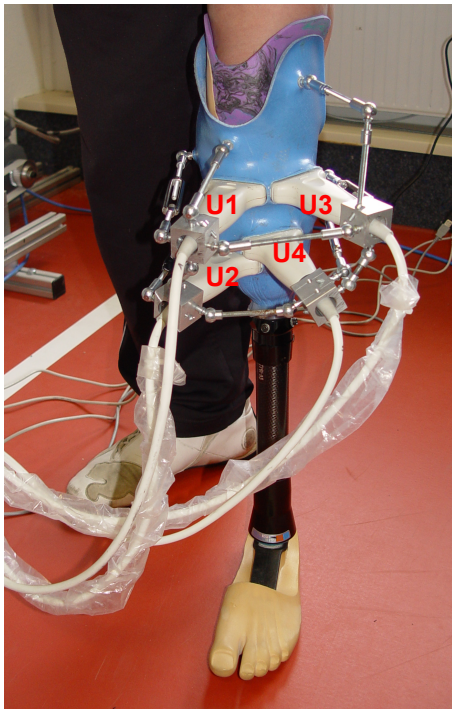


Fig. 1 Measuring socket with integrated transducers

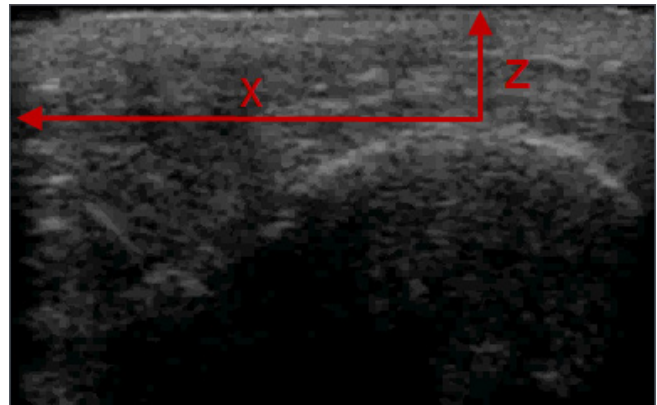


Fig. 2 Ultrasound measurement of the Tibia with the transducer 2

For calibration of the measuring system three long parallel rods with 5mm targets were incorporated centrally in the socket, parallel to the socket axis. The socket was filled with water and the position of the rods in the socket was compared with the values of the ultrasound measurement.

A 3-dimensional x, y, z co-ordinate system was adopted for measurement purposes. The z distance was measured perpendicular from the transducer surface to the measuring object. The x distance was measured parallel to the transducer, from the lateral border of the field of view to the measuring object. The distance y indicates the measurement from the deepest point of the Patella support, the relative depth of the measuring object within the socket. It was measured using a height gauge. Figure 2 illustrates the ultrasound image of the residual tibia-end within the socket as a semicircular arc and the transducer surface as the horizontal line across the top of the screen. The x and z co-ordinates lie at the apex of the arc.

The ultrasound transducers 1 and 2 lie approximately parallel to the posterior brim of the socket. Tibia motion perpendicular to the sensing surface of the transducers 1 and 2 was considered to be flexion/extension relative to the anterior socket wall. Tibia motion parallel to the sensing surface of the two transducers was considered to be abduction/adduction relative to the anterior socket wall. The measured ultrasound data was transferred to spreadsheets.

By the knowledge about the orientation of all ultrasound transducers to each other and these, again to the axle center of socket, the angle changes of the Tibia movement can be computed. The flexion/extension of the Tibia on each moment of the gait cycle was computed over the formula 1.

$$\tan \alpha = \frac{(zU2 - zU1)}{(yU2 - yU1)} \tag{1}$$

Abduktion/adduktion of the Tibia was computed over the formula 2. The ultrasound transducers 3 and 4 were evaluated as check measurement.

$$\tan \beta = \frac{(xU1 - xU2)}{(yU1 - yU2)} \quad (2)$$

A Qualisys Motion Capture system (Qualisys, Sweden) seizes „the outside“ kinematic data. Thirteen retro-reflective markers were placed after the Oxford Foot Model on both sides of the subject. Two parallel hall-effect-force-plates (AMTI, USA) and the NOVEL pedarX system (NOVEL, Germany) supply kinetic data. The Qualisys program as well as the NOVEL system and the force-plates serve the momentary gait phase as reference values for the clear regulation.

The pre-study was accomplished in the gait-laboratory of the department of Orthopaedics and movement systems of the Fraunhofer Institute for Manufacturing Engineering and Automation in Stuttgart.

The patient moved in a self-chosen and pleasant cadence and speed for him. In ten going attempts by four measuring transducers the distances between bone edge and socket wall, as well as the kinetic and kinematic parameters were determined.

IV. RESULTS

Further the measurements take place at present, results up to the expiration of the term are supplied later.

V. DISCUSSION

Discussion is supplied later.

VI. CONCLUSIONS

Conclusions are supplied later.

ACKNOWLEDGMENT

Sanitätshaus Bächle, Deutschland

REFERENCES

1. Eriksson U, Lemperg R (1969) Roentgenological study of movements of the amputation stump within the prosthesis socket in below-knee amputees fitted with a PTB prosthesis. *Acta Orthop Scand* 40:520–529
2. Grevsten S, Eriksson U (1974) Stump-Socket Contact and Skeletal Displacement in a Suction Patellar-Tendon Bearing Prosthesis. *J Bone Joint Surg* 56:1692–1696
3. Lilja M, Johansson T, Oberg T (1993) Movement of the tibial end in a PTB prosthesis socket: a sagittal X-ray study of the PTB prosthesis. *Prosthet Orthot Int* 17:21–26
4. Mayfield GW, Scanlon J, Long I (1977) A new look to and trough the above-knee socket (abstract). *Orthop Trans* 1:95
5. Sabolich J (1985) Contoured adduction trochanteric controlled alignment method (CAT-CAM). *Clin Prosthet Orthot* 9:15-26
6. Long I (1985) Normal shape Normal Alignment (NSNA) above-knee prosthesis. *Clin Prosthet Orthot* 29:53-54
7. Convery P, Murray KD (2000) Ultrasound study of the motion of the residual femur within a trans-femoral socket during gait. *Prosthet Orthot Int* 24:226–232.
8. Meier, Christoph (2006): Das bewegte Knie. *Mobiler Röntgenapparat. ETH Life.* at <http://archiv.ethlife.ethz.ch/articles/tages/mobilroentg.html>
9. Foresti M, Gerber H et al. (2008) A novel set-up for the automation of a video knee joint kinematics during level walking. *Laboratory for Biomechanics.* at <http://www.univ-valenciennes.fr/congres/3D2006/Abstracts/149-Foresti.pdf>

Use macro [author address] to enter the address of the corresponding author:

Author: Urs Schneider
 Institute: Fraunhofer IPA
 Street: Nobelstr. 12
 City: Stuttgart
 Country: Germany
 Email: Urs.Schneider@ipa.fraunhofer.de

Development of Unconstrained Rigidity Measurement System for Quantitative Diagnosis of Parkinson's Disease

R. Okuno¹, T. Endo², M. Yokoe², S. Sakoda², and K. Akazawa³

¹ Department of Electrical and Electronics Engineering, Setsunan University, Neyagawa, Japan

² Graduate School of Medicine, Osaka University, Suita, Japan

³ Department of Biomedical Engineering, Osaka Institute of Technology, Osaka, Japan

Abstract—The purpose of this study was to develop unconstrained rigidity measurement system by using small force sensors for quantitative diagnosis of Parkinson's Disease (PD). The developed measurement system was composed of two compact three-axis force sensors, a gyroscope, and surface electrodes. The force sensors were attached by sandwiching the wrist joint. The force along the Z-axis was measured to estimate elbow joint torque during flexion and extension movements. The elbow joint angle was calculated by the gyroscope attached between the two force sensors. The measurement experiments were conducted. The subjects were 25 PD patients and 20 healthy elderly volunteers. The examiner applied the measuring system to the wrist joint of the subject with the other hand and performed passive flexion and extension movements of the elbow joint. The relationships between elbow joint torque and elbow angle were calculated from the obtained data. It was shown that the slope of the relationships in the PD patients was larger than that in the healthy subjects and the bias of elbow joint torque in flexion was larger than that in extension.

Keywords— Parkinson's disease, rigidity, torque, angle, UPDRS, measurement.

I. INTRODUCTION

Rigidity was one of significant clinical symptoms in Parkinson's disease (PD). Neurologists utilized passive flexion and extension movements of major joints to detect the rigidity. In order to evaluate of the severity, Unified Parkinson Disease Rating Scale (UPDRS) was widely used scale [1]. However, the scores were somewhat variable from examiner to examiner, and may not be as reproducible as one would like. It was, therefore, necessary to develop a quantitatively evaluating system.

Many researchers have evaluated quantitatively it and characteristic indices have been proposed, concerning to elasticity and mechanical impedance for rigidity during the cycle of flexion and extension movements [2-9]. However, these reported studies, a large-scale device were used or physical stresses were imposed on subjects due to difficulty in applying a measuring device. The purpose of this study was to develop a noninvasive and unconstrained rigidity

measurement system by using small force sensors for quantitative diagnosis of the rigidity.

II. MEASUREMENT EXPERIMENTS

A. Measurement system

Figure 1 shows the developed measurement system. This system was composed of two compact three-axis force sensors (USL06-H5-50N, Keitech System), a gyroscope (CRS03-04S, SILICON SENSING SYSTEMS JAPAN), and surface electrodes (Vitrode Bs-150, NIHON KOHDEN, Japan). The force sensors were attached by sandwiching the wrist joint and measured the force along the Z-axis during flexion. The elbow joint torque was computed by multiplying arm length by the difference between the force sensors. The gyroscope was attached between the two force sensors and the elbow joint angle was calculated by integrating the monitored angular velocity. The surface electrodes were attached to Biceps Brachii muscle and Triceps Brachii muscle to record myoelectrical activity. The angular velocity, forces and electromyogram (EMG) were measured and collected using a Personal Computer at a sampling frequency of 1 kHz, and then noise was reduced with a low pass filter (15 Hz).

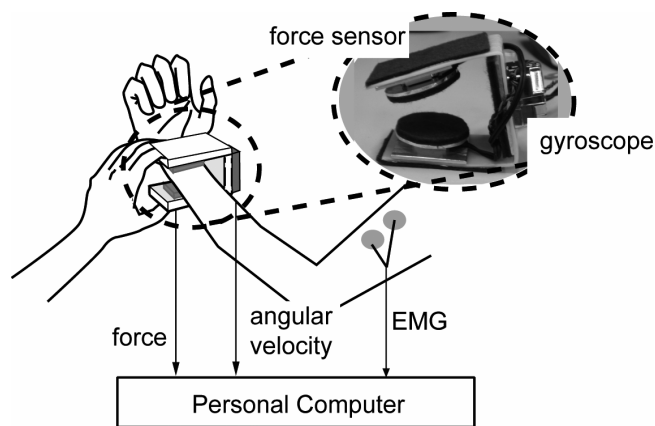


Fig. 1 Rigidity measurement system

B. Protocol

The study subjects consisted of 25 patients diagnosed with PD (mean age of 70.0 ± 7.4 years) and 19 healthy elderly volunteers (mean age of 67.6 ± 9.0 years). The measurement in this study was approved by the Institutional Review Board of Osaka University Hospital, and written informed consent was obtained from subjects. The subject was instructed to remain relaxed in a sitting position, and an examiner held the elbow joint of the subject with one hand to keep the forearm horizontal. The examiner applied the measuring device to the wrist joint of the subject with the other hand and performed passive flexion and extension movements of the elbow joint. The measurement was made by instructing the subjects to repeat the following four-phase movement: (1) holding the elbow in maximal extension for at least 3 s, (2) passive flexion for 2 s, (3) holding the elbow in maximal flexion for at least 3 s, and (4) passive extension for 2 s (ramp-and-hold). Data collection continued for 60 s. This measurement was executed at each of the left and right upper limbs per subject.

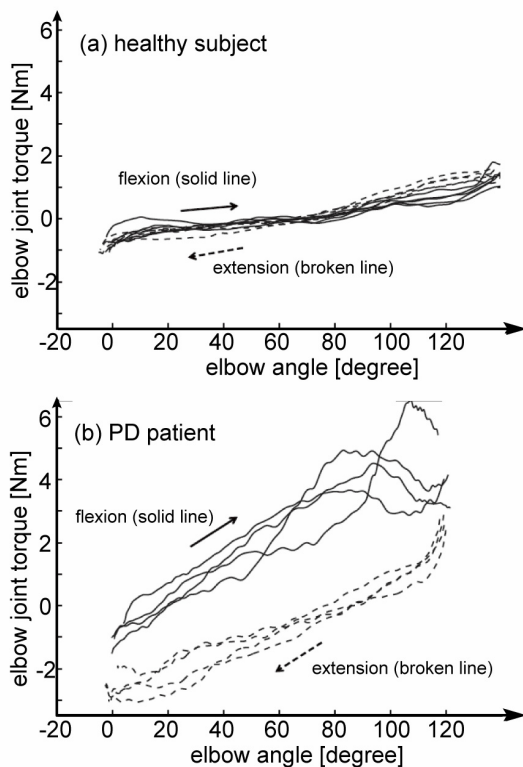


Fig. 2 Relationships between elbow angle and torque. (a) Relationships in healthy subject, (b) relationships in PD patient (UPDRS score:3)

III. EXPERIMENTAL RESULTS

Figure 2 shows relationships between the elbow joint angle and the torque. Figure 2 (a) shows the result of the healthy subject. The slope of the relationship was represented elastic coefficients in extension and flexion movements. The slopes in both extension and flexion were small and almost same. Figure 2(b) shows the results of the PD patient. The slope was larger than that in the healthy subjects. This result was corresponding to the stiffness the neurologists felt in the PD patients. Additionally, it was shown that the bias of elbow joint torque in flexion was larger than that in extension. It was held forth the possibility that the severity of the rigidity could be diagnosed quantitatively by using these features.

ACKNOWLEDGMENT

This study was supported by the Program for Promotion of Fundamental Studies in Health Sciences of the National Institute of Biomedical Innovation (NIBIO).

REFERENCES

1. Fahn S et al. (1987) Unified Parkinson's disease rating scale in Resent Developments in Parkinson's disease, vol. 2, Fahn S, Marsden CD, Goldstein M, Calne DB, Ed. Florham Park, New Jersey, pp.153-63.
2. Lee HM et al. (2002) Quantitative analysis of the velocity related pathophysiology of spasticity and rigidity in the elbow flexors. *J Neurol Neurosurg Psychiatry*;72:621-629.
3. Caligiuri MP (1994) Portable device for quantifying parkinsonian wrist rigidity. *Mov Disord*;9:57-63.
4. Fung VS, et al. (2000) Objective quantification of resting and activated parkinsonian rigidity: a comparison of angular impulse and work scores. *Mov Disord*;15:48-55.
5. Webster DD. (1960) Dynamic measurement of rigidity, strength, and tremor in Parkinson patients before and after destruction of mesial globus pallidus. *Neurology*;10:157-163.
6. Prochazka A et al. (1997) Measurement of rigidity in Parkinson's disease. *Mov Disord*;12:24-32.
7. Patrick SK et al (2001) Quantification of the UPDRS Rigidity Scale. *IEEE Trans Neural Syst Rehabil Eng*;9:31-41.
8. Teravainen H et al. (1989) Optimal indices for testing parkinsonian rigidity. *Can J Neurol Sci*;16:180-183.
9. Kirolos Cet al. (1996) Objective measurement of activation of rigidity: diagnostic, pathogenetic and therapeutic implications in parkinsonism. *Br J Clin Pharmacol*;41:557-564.

Author: Ryuhei Okuno
 Institute: Setsunan University
 Street: 17-8 Ikeda-Nakamachi,
 City: Neyagawa
 Country: Japan
 Email: okuno@ele.setsunan.ac.jp

Measurement of Eye and Head Position in Neurological Practice

J. Charfreitag¹, J. Hozman¹, and R. Cerny²

¹ Czech Technical University in Prague, Faculty of Biomedical Engineering, Kladno, Czech Republic

² Charles University in Prague, Clinic of Neurology (2nd Faculty of Medicine), Prague, Czech Republic

Abstract— The base of this work is an analysis and design of specialized glasses usaging the basic available parts and makings with the goal to create an experimental machinery with a possibility of eye movement research. The aim of this work was to describe a „Design and Construction of Specialized Glasses for Neurology Investigation“. The motivation for this work is to implement a system usaging primary 2D and 3D HMD (Head-Mounted Display) projection displays for eye stimulation. The result is a set of experimental models describing specialized glasses which are used to verify the proposed solution of eye movement and for measurement of the dynamic position of the head in 3D space. Modified Starburst algorithm for recognition centre pupil and calibrated scene for repeated measurement were used to detect eye movements. Created specialized projection displays for neurology investigation can perform measurements in different luminous conditions (method based on both infra red and a visible light spectrum) and stimulation with measurement of the dynamic position of the head based on programmed software.

Keywords— HMD, eye measurement, head measurement, videoculography, eye tracker, head posture

I. INTRODUCTION

The measurement of eye position is an important investigative tool in the understanding of a human vestibular system. As well, the measurement of head position could contribute to diagnosis of vestibular system. These relations have not been systematically studied and the both measurement methods have been separately examined.

Monitoring eye movements and their imaging plotting have a long tradition in the medical practice. It is used as a diagnostic tool in neurology and psychology. More information about used methods of eye measurement can be found in [1], [2] and [3]. We measure eye movements using a VOG (videoculography) method that is based on the principle of scanning eye using a set of video cameras and consequently, this data is post-processed to a different result in IR (infra red) or visible light spectrum (e.g. nystagmogram, fixing the eye to the projected area et al.).

First possibility is to scan the eye moving using the IR spectrum created by a LED (light emitting diode) diode with a wavelength approximately $\lambda = 880 - 940$ nm. Looking to the eye we can see its elements – outer filamentous layer with title sclera, further is cornea, iris and

eye pupilla [4]. The VOG method in the IR spectrum detects the pupil using an appropriate light that makes it completely black. Advantage of this method is a relatively easy pupil detection and a well known directive light, most often using an IR LED diode. Disadvantage and limitation is a need to make measurements without access of visible light, i.e. in conditions that do not correspond with patient's real situation.

Eye analysis in the visible light spectrum is far more complicated. The method is called passive, because the eye is scanned in the visible light spectrum due to the diffused visible light. The method without the IR supplementary light will not be only safer for the patient (undesirably warms up the eye), but also much more preferable, because does not necessarily needs to suppress background light. Detection can be done due to the sclera and iris interface. Disadvantage of these methods is the uncontrolled lighting from scattered sources, considerable luminous artefacts and high computational power. Also accuracy of these methods is rather poor, because in contrast to the pupil of the eye that is over measuring time visible, the interface between sclera and iris is often hidden.

II. BACKGROUND AND RELATED WORKS

Horizontal and vertical eye movements can be measured from an image of the eye by detecting the edges of the pupil (iris) and fitting an ellipse them. The video system PAL (NTSC) record video with frequency 50 Hz (60 Hz) non - interlace. In the medical practice were documentary eye movements with frequency approximately 200 – 250 Hz. These movements present angular change approximately 400 – 450°/s. These video systems are too slow for capture images of the eye movements, e.g. torsion iris description. The main analysis of eye movements is obtaining centre of the pupil or the iris. The torsion measurement needs high quality iris description. We used the detection method which search for the interface points between the pupil and the iris or between the iris and the sclera. The points are base on the mathematical function (e.g. circle or ellipse). We used algorithm RANSAC (Random Sample Consensus) [5] for higher accuracy. It is an iterative method to estimate parameters of a mathematical model from a set of observed data which contains outliers.

In many cases, the head position can be small and hard to be observed. Despite the fact that an accurate method for measuring the head position and the eye position could contribute to diagnosis of vestibular system, this issue has not been systematically studied [13].

III. PROBLEM SOLUTION

A. Eye movement analysis

We applied modified Starburst [5, 6] algorithm [9], which we used in the IR spectrum or in the visible spectrum. Goal of our solution is using eye movements' detection [7] in comparison with the stimulation scene. The scene can be showing on the LCD screen or through the special HMD display unit in 2D or 3D space. Thanks the special 3D HMD projection displays [9] we used Starburst algorithm for measuring in the IR spectrum and appropriate LED diode to illumination the eye. The method is called active, because the eye is scanned in the infra red light spectrum. Goal of the eye movements' measurement is location the centre of the pupil area. We used a new system based on finding the outline pupil of the eye. The system and algorithm was the first time published on Iowa University in 2006 [9] and the name of the project is Starburst [5]. Method finding the margins of the pupil (IR spectrum) or the iris (visible spectrum) along limits quantity of the rays. The rays are visible on Fig. 3. The starting point shoots the rays to generate candidate pupil points. The candidate pupil points shoot rays back towards the start point to detect more candidate pupil points. This two-stage detection method takes advantage of the elliptical profile of the pupil contour to preferentially detect features on the pupil contour.



Fig. 1 Location of the pupil center with the rays

The blue circle (Fig. 1) shows the centre of the pupil after the second iteration (and after the next iteration) includes determine points. The Fig. 1 show red and blue circles quickly converge to the actual centre of the pupil. The iteration was stopped when the detected centre of the new points turn less than $d = 10$ pixels. Thanks to exponential calculation is error of the pupil centre about ± 10 pixels whole circle bearing and it is important from found points' fit resulting ellipse. At the end, we can find centre of the pupil from the resulting ellipse.

There are more possible methods how we can put together resulting ellipse. We chose method [9] Random Sample Consensus (RANSAC [10]) to solving the problem with large error points. The method RANSAC is efficient technique for completion model in the presence of large, but unknown percentage outlines in sample measurement. In our case are all internal found points' probable points that correspond with outline of the pupil. RANSAC algorithm was used to estimate parameters of the mathematical model from a set of observed data which contains outliers. On the basis of the MATLAB documentation we used optimal mathematical model to create the ellipse - *Nelder-Mead's* algorithm. The final result of the RANSAC algorithm and the *Nelder-Mead* ellipse model is on Fig. 2.

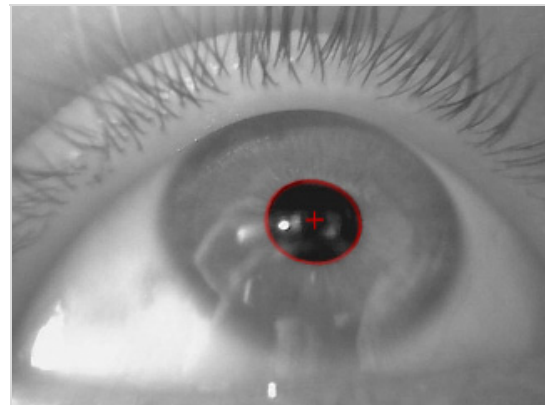


Fig. 2 Use the RANSAC and the Nelder-Mead algorithm together

B. Head position measurement

The headtracker in the eMagin Z800 3DVisor® personal display can measure head position in the 3D space. For the acquisition of the head motion we programmed software FBMI SPH in C# language based on Z800 3DVisor® SDK 2.2. The SW (software) retrieves position of the head from the build-in headtracker through the USB connection and save the measured results in to the CSV (comma-separated values) file. The result of measurement can be representing graphically as a graph of the head position (Fig. 3). The first

measured values were used as initial, i.e. zero and were used as correction for all subsequent values. Head position was measured with precision of 1.0° in three planes (rotation -yaw, flexion-pitch and inclination-roll).

The main result is that the accuracy of the method alone is in eights of degree per the ten measurements. This is the dynamic error thanks the low-cost headtracker which has long stabilize time after the previous measurement.

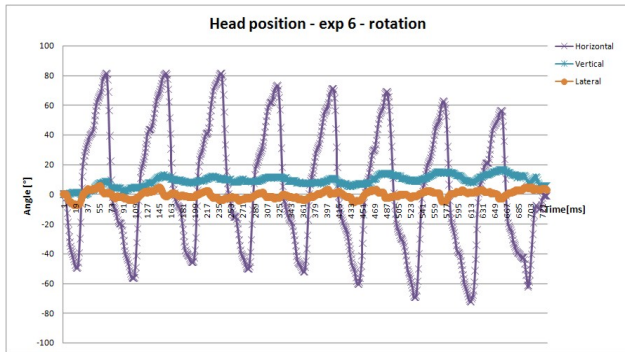


Fig. 3 Rotation of a patient's head for the X-, Y-, Z- axis

C. Displays units - specialized glasses

We made the first type of projection displays (Fig. 4), which used PAL cameras, supplementary IR LED diode, projection displays, control appliance, video capture appliance and laptop computer with appropriate software equipment.

For the eye stimulation we used commercial HMD system Z800 3DVisor® from eMagin Company or LCD monitor. The HMD displays eMagin Z800 3DVisor's integrated headtracker uses MEMS (micro-electro-mechanical system) accelerometers and gyroscopes to detect motion. The headtracker features three gyroscopes, one each for the X-, Y-, and Z-axis. In addition, the headtracker contains corresponding compasses and accelerometers to ensure performance over varying forms of motion. We used the headtracker for the measurement of head position. The Z800 3DVisor® is the personal display system to combine two OLED (organic light-emitting diode) micro displays with stereovision 3D capabilities. Stereo vision refers to the human ability to see in three dimensions and most often refers to depth perception (the ability to determine the approximate distance of objects). Stereovision 3D provides this experience by delivering two distinct images simultaneously on two separate screens, one for each eye. The Z800 3DVisor® personal display is used to stimulate the eye in 2D or 3D space. The position of eye and the position of head can be recorded simultaneously by the video camera and integrated headtracker to the laptop.

We found during the measurement problematic parts which were necessary solve for the next biomedical tests. The problems were to be with weight, sharp edges on the semi-permeable mirrors and minimal place between personal display Z800 3DVisor® and the eyes. Another problem was measuring with the glasses.

On the previous base type we made the new projection displays, which allowed trace projection on the LCD monitor or the projection screen in visible spectrum. We used the special projection displays (Fig. 5) to control principle function and detection algorithm. Detection algorithm can measure the eye position and the scene position. The video files of positions are merging into the date file. The second version of projection displays has lower weight, does not contain any sharp edges and include the cameras, which are connect by the help of USB (Universal Serial Bus) interface and does not using any special recorder. Power supply is solving over the USB port. We used record software TVideoGrabber. The software TVideoGrabber can set capture parameters (30 FPS – Frames Per Second, 640 x 480 pixels, RGB24, data format AVI). We used for the synchronization between two cameras external flash from photographic apparatus (In the future we will use the TVideoGrabber component with more threads. The threads will start record from several video sources at the same time).



Fig. 4 Displays units - specialized glasses with eMagin 3DVisor®

The next type of our projection displays is designated for measuring in the IR spectrum. The third projection displays using the IR USB cameras which record eye movements. The type of this projection displays must using cameras which are support scan the eye movements in the IR spectrum because lighting is already poor. This type of projection displays combines a unique system for measuring eye movements and head position with 2D or 3D stimulation.



Fig. 5 The eye tracker unit with the measurement cameras

The specialized glasses - projection displays for neurology investigation can be using without the LCD monitor thanks build-in HMD 3D projections displays eMagin Z800 3DVisor® and can be using as a mobile system. We usaging experimental machinery for monitoring eye movements with different luminous conditions (in the visible spectrum or in the IR spectrum) or using different stimulation sources (e.g. record eye movements at specific activities - „eye Holter”, long time eye movements record, 2D and 3D stimulation et al.).

IV. CONCLUSIONS

We designed the specialized projection displays for neurology investigation which can perform measurement in the different luminous conditions and stimulations with measurement of the dynamic position of the head. The solution combines the unique system for measurement of the eye movements and the head posture in the 3D space with 2D or 3D eye stimulation. We come to the conclusion that is possible joining together of the two important and closely related methods for the measurement of the human vestibular system. A result of this study is a recommendation to use the video cameras with higher frequency (approximately 200 Hz) for the measurement of eye movements and the headtracker with lesser dynamic error (less than 0.3°/s) for the measurement of head position. The whole accuracy of the method could be this way markedly increased.

ACKNOWLEDGMENT

This is the work of the Department of Biomedical Technology, Faculty of Biomedical Engineering, Czech Technical University in Prague in the frame of the research

program No. MSM 6840770012 "Transdisciplinary Biomedical Engineering Research II" of the Czech Technical University sponsored by the Ministry of Education, Youth and Sports of the Czech Republic. The study has been supported by grant GACR 102/08/H018.

REFERENCES

1. Halswanter T., Measurement and Analysis Techniques for Three-Dimensional Eye Movements. Tubingen: Neurologische Universitätsklinik Tubingen,
2. Snopek J., Methods of preprocessing and analysis of eye movement's data. Prague: CTU FEL in Prague, 2003
3. Charfreitag J., Design and Construction of Specialized Glasses for Neurology Investigation. Kladno: CTU FBMI in Prague, 2006
4. Rokyta R., Fyziologie pro bakalářská studia v medicíně, přírodovědných a tělovýchovných oborech. Prague: ISV, 2000
5. Dongheng, Li., Low-cost eye-tracking for human computer interaction. Ames, Iowa: Iowa State University, 2006
6. Duchowski A., 3D Eye Movement Analysis In Behavior Research Methods. Instruments and Computers, 2002
7. Knox P. C., The Parameters of Eye Movement. Liverpool: The University of Liverpool, 2003
8. Moore, Steven T., - Curthoys, Ian S. - Haslwanter, Thomas G. – Halmagyi, Michael Measuring Three-Dimensional Eye Position Using Image Processing – The VTM System. Sydney: Department of Psychology, University of Sydney, NSW, 2006
9. Ruian L., Shijiu J., Xiaorong W., Single Camera Remote Eye Gaze Tracking Under Natural Head Movements. Tianjin: College of Physics and Electronic Information Science, Tianjin Normal University, 2006
10. Eui C. L., Kang R. P., A robust eye gaze tracking method based on a virtual eyeball model. Seoul: Electronic Engineering of Yonsei University, 2007
11. Stampe D. M., Heuristic filtering and reliable calibration methods for video-based pupil tracking systems. Behavior Research Methods, Instruments and Computers, 1993
12. Lee J. J., Park K. R., Kim J. H., Gaze detection system under HMD environments for user interface. Istanbul: ICANN/ICONIP, 2003
13. Hozman, J., Zanchi V., Cerny, R., Marsalek P., Szabo Z., Precise Advanced Head Posture Measurement, In: The 3rd WSEAS International Conference on Remote Sensing. Venice, Italy, November 21-23.2007. Venice, Italy, pp. 18-26.

- Author: Jaroslav Charfreitag
- Institute: FBMI CTU in Prague
- Street: Sq. Sitna 3105
- City: Kladno
- Country: Czech Republic
- Email: jaroslav.charfreitag@fbmi.cvut.cz

Virtual Reality and Robotics for Neuro-Motor Rehabilitation of Ischemic Stroke Patients

M. Steinisch¹, B.M. Guarnieri², J. Haueisen³, A. Serio², and S. Comani^{1,2}

¹ BIND – Behavioral Imaging and Neural Dynamics Center, University “G. d’Annunzio”, Chieti, Italy

² Institute for Clinical Research Villa Serena, Via L. Petruzzi 42, 65013 Città S. Angelo (Pescara), Italy

³ BMTI – Institute of Biomedical Engineering and Informatics, Ilmenau University of Technology, Ilmenau, Germany

Abstract— It is well known that patients undergoing a cerebrovascular attack often experience a partial recovery of the motor function of the upper limbs, despite the application of manual motor therapy. Therefore, several research studies have recently focused on improving the rehabilitation process by using robotic devices and virtual reality. Robot-aided therapy may be capable of overcoming some of the limitations of manual therapy, such as the lack of exact repeatability of the movements and the objective measurement of training progresses. On the other hand, embedding the patient in a virtual environment, which might be personalized not only to his spared abilities but also to his interests, could be more motivating and could provide online bio-feedback about his performance, hence reinforcing the effect of the therapy. Although the preliminary results of those studies are encouraging, they have been limited to small groups of chronic patients. In this project, robot-aided rehabilitation in combination with virtual environments will be used on sub-acute and chronic stroke patients for the first time. This allows not only the evaluation of effectiveness of the advanced treatment and comparison to traditional motor therapy, but will also supply information about the retention of benefits over time. In order to explore the temporal evolution of cortical activity in relation to the degree of functional recovery, functional Magnetic Resonance Imaging (fMRI) will be conducted before, during and after the new rehabilitation therapy. Combined with Electroencephalography (EEG) and Electromyography (EMG) studies, which will be recorded online during treatment, the collected data will provide a basis for a better understanding of the neurobiological and neurophysiological mechanisms that underlie the changes in brain pattern activation after stroke.

Keywords— Virtual Reality, Robotics, Rehabilitation, Ischemic Stroke.

I. INTRODUCTION

Stroke is a leading cause of permanent disability in the industrialized countries. In Italy about 30% of persons who undergo a cerebrovascular attack report disabling outcomes, mainly disability of the upper limbs (UL). Functional recovery of motor abilities is fundamental for enhancing the patients quality of life. Unfortunately, despite the continu-

ous exercise required by conventional therapies, recovery of the motor function is often only partial.

Several research studies have recently focused on the development of novel robotic interfaces and on the use of Virtual Reality (VR) for more efficient rehabilitation of stroke patients. The combination of these advanced technologies seems to be a promising way to improve the effectiveness of the stroke patient’s training and recovery.

The use of haptic devices may overcome some of the major limitations related to manually assisted movement training, such as the lack of repeatability, the high dependence on the availability of specialized therapists and the lack of objective estimation of the rehabilitation progress.

On the other hand, a unique feature of VR is that the patient is embedded in an evocative virtual environment that is more stimulating than a traditional rehabilitation therapy setting. Virtual environments tailored to the patient’s preferences can be produced and adjusted to his needs and spared abilities. Moreover, a typical VR set up may permit to provide the patient with online feedback about his performance, enhancing his awareness of deficits and improvements, hence maximizing the effectiveness of the rehabilitative process.

II. WHAT IS ALREADY KNOWN?

The current evidence on the effectiveness of robotic interfaces and VR environments for the upper limbs rehabilitation in stroke patients is limited to small groups of chronic patients, where an improved recovery has been observed in tasks of reaching of visual targets with the arm [1] and of object manipulation with the hand [2]. Although preliminary, those results are sufficiently promising to justify additional clinical trials on chronic stroke patients’ population, and new studies on acute and/or sub-acute stroke patients. Until present, no study has been performed on these patients for a number of reasons, mainly practical, despite the importance of assessing the effectiveness of the robots & VR therapy when administered from the very early stages after stroke.

Furthermore, cross-sectional and longitudinal neurophysiological studies have demonstrated that the damaged adult brain is able to reorganize in order to compensate for motor deficits. To date, the most common pattern of functional reorganization observed in patients with focal injury is a dynamical reorganization of the topography of task-related functional responses. Involvement of non-motor and contra-lesional motor areas has been consistently reported, but the emerging notion is that the greater the involvement of the ipsi-lesional motor network, the better is the recovery [3]. Recently, a strong and task-specific increase of sensorimotor cortical activity after robot-based therapy combined with VR games has been described [2].

Besides task-related functional activation, more recent measures of intrinsic functional connectivity (FC) between cortical regions during resting wakefulness are providing important clues on the large-scale functional reorganization that the injured brain undergoes during recovery from stroke. However, changes in FC during motor recovery following rehabilitation have not been explored yet.

III. DESCRIPTION OF THE PROJECT

In this project the conjoint use of robotic interfaces and non-immersive Virtual Reality scenarios, successfully employed in few studies on chronic stroke patients, will be employed for the first time in sub-acute patients. The same treatment will be used on a larger population of chronic patients than before, in order to verify the validity of positive results already obtained by the few studies present in the clinical literature. Both sub-acute and chronic stroke patients' groups will be also administered traditional rehabilitation therapy. In this manner, we will be able to compare the effectiveness of the innovative treatment in two different populations of stroke patients (sub-acute and chronic), we will be able to evaluate the retention of benefits over time, and we will also gather information sufficient to perform a comparative study on the outcomes of rehabilitation therapy when it is administered following a traditional procedure only, or when it is accompanied with treatments based on the use of technologically advanced systems.

Another important feature of this project is that it will provide new information on the neurophysiological correlates of motor recovery and rehabilitation training. The neural correlates of robot-based therapy combined with Virtual Reality have been explored only by a recent study restricted to chronic patients and to manipulation of objects with the hand [2]. A high temporal resolution EEG and functional neuroimaging data will be used to significantly improve current knowledge because they will be collected

before, during and after a treatment based on robot-aided rehabilitation and VR, involving the arm during movements of reaching, not only at chronic stage but also on sub-acute stage. Moreover, the longitudinal study will allow to collect missing information on the dynamic temporal evolution of the neural reorganization following the innovative treatments. Furthermore, we will study the functional connectivity in stroke patients suffering from motor deficits of the upper limbs.

Collected data will also provide useful information for reproduction and generalization of previous findings. These are important issues, given that primarily very small patient samples have been studied, which furthermore may not represent the entire spectrum of deficit and recovery.

The present project will provide also missing information on the comparison between simple motor tasks, used in the literature on motor recovery, and more elaborate paradigms employed in cognitive neuroscience, including reaching, action observation and action imagination.

Finally the project will add new insights on the effects of VR environment manipulation on the motivation and psychological well-being of stroke patients affected by disability of the upper limbs.

IV. PROJECT AIMS

The main purpose of the present research project is to evaluate the effectiveness of new motor rehabilitation treatments for the upper limbs of hemiparetic patients affected by ischemic stroke. The treatments will make use of VR systems and dedicated robots (haptic devices) to exploit the combination of robot-aided rehabilitation and VR at the sub-acute and chronic stage. The treatment will be administered in addition to traditional motor therapy (MT), and the obtained motor functional outcome will be compared with that of patients being administered only MT.

The second aim is to assess if the positive effects of innovative therapies on motor recovery are more persistent in time compared to those deriving from traditional MT, and if the repetition of such treatments from sub-acute to chronic stage can reinforce the initial effects.

The third aim of the research project is to achieve a better understanding of the neurobiological and neurophysiological mechanisms underlying the changes in brain activation patterns after stroke. Indeed, to devise better therapeutic strategies for the rehabilitation of patients with hemiparetic stroke, it is important to understand the mechanisms that underlie the neuroplasticity induced by skills training and exercise programs. This will be achieved by combining high temporal resolution techniques such as electroencephalography (EEG) with functional imaging. High-resolution

EEG studies, together with EMG measures, will be conducted online during the innovative rehabilitation treatments. In addition functional magnetic resonance (fMRI) studies will be conducted at the beginning, after 3 weeks and at the end of the same rehabilitation training, exploring the temporal evolution of cortical activity and functional connectivity between cortical regions in relation to the degree of functional recovery.

A further aim of the project is to increase the patients' motivation and well-being by creating different virtual environments and scenarios which may be of particular interest for them. Personal scenarios may be presented ad hoc according to the patient, following an interview with each of them, in order to introduce familiar elements in the scene. Motivation and positive disposition are critical aspects to maintain a constant exercise and to obtain the maximal final motor outcome.

V. POTENTIAL IMPACT OF RESULTS

Task-oriented repetitive movements can improve muscular strength and movement coordination in patients with movement disabilities due to neurological impairment. Particularly in stroke patients, several studies prove that movement therapy of the upper limbs has positive effects on the rehabilitation progress, which include the recovery of motor function along with the prevention of muscle atrophy, and also a large-scale functional reorganization of the brain.

However, manually assisted movement training is labor-intensive and therefore, the training duration is usually limited by personnel shortage and fatigue of the therapist and patient. The disadvantageous consequence is that the training sessions are shorter than required to gain optimal therapeutic outcome.

In contrast, new therapies for upper limb rehabilitation that are based on robot-assisted devices and VR environments have several advantages, such as the fact that they can be used in an either active or passive manner, hence reducing patient's and therapist's fatigue and consequently permitting to afford longer sessions, or that they allow an objective estimation of rehabilitation progress. Therefore, robot-assisted and VR therapies permit to envisage an intensive and controlled training program without increasing the time dedicated by the therapist to each patient.

If the outcome of this research project will confirm the expected effectiveness and advantages of these novel rehabilitation treatments, five potential and highly important impacts can be foreseen:

1. an increase of the number and duration of training sessions per patient

2. the possibility to objectively document and evaluate the rehabilitation process through quantitative measures
3. an overall improvement of upper limb rehabilitation and a better restoration of the related brain functions, also in patients for whom traditional movement therapy is ineffective
4. a reduction of the therapist-hours devoted to each patient
5. an overall decrease of the costs for specialized personnel

REFERENCES

1. Frisoli A, Borelli L, Montagner A et al (2007) Arm rehabilitation with a robotic exoskeleton in Virtual Reality. IEEE Proc., Intern. Conf. on Rehabilitation Robotics, Noordwijk, Netherlands, 2007, pp 631-642
2. Takahashi C, Der-Yeghiaian L, Le V et al (2008) Robot-based hand motor therapy after stroke. *Brain* 131:425-437
3. Calautti C, Baron J.C. (2003) Functional neuroimaging studies of motor recovery after stroke in adults: a review. *Stroke* 34:1553-1566

Address of the corresponding author:

Author: Steinisch, Martin
 Institute: University "G. d'Annunzio"
 BIND – Behavioral Imaging and Neural Dynamics Center
 c/o Dept. of Human Movement Sciences
 Street: Via dei Vestini 31
 City: 66013 Chieti
 Country: Italy
 Email: martin.steinisch@web.de

ARMassist: A low-cost device for telerehabilitation of post-stroke arm deficits

Joel C. Perry, Haritz Zabaleta, Aitor Beloso, and Thierry Keller

Fatronik Foundation, Mikeletegi Pasealekua, 7, Donostia-San Sebastian, Spain
<jperry, hzabaleta, abeloso, tkeller>@fatronik.com

Abstract— Motor deficits in the growing population of stroke survivors are creating a pressing need for new strategies and new tools to provide efficient and effective delivery of patient care. A summary of existing devices for upper-limb rehabilitation is presented, including the modes of feedback provided and whether the intended market is clinical or personal use. The design requirements for a new portable device are outlined from both patient and therapist viewpoints. Embodiments of the device combine planar gravitational support of the arm, low-cost sensors, passive or active movement assistance, visual and haptic feedback, and wireless communication protocol to produce an affordable but effective device for in-home therapy. The device targets the treatment of upper-limb motor deficits resulting from conditions such as stroke, traumatic injury, and disuse. The development of a passive first prototype ARMassist device is presented.

Keywords— Arm rehabilitation, stroke, upper-limb impairment, telerehabilitation, home health care.

I. INTRODUCTION

New technologies to address arm deficits from stroke, traumatic injury, and other sources of motor impairment and disuse are needed. Considering (1) the increasing trends in stroke, (2) the known benefits of training duration, and (3) the existing devices in rehabilitation, it is expected that simplified, low-cost solutions hold the key. The aim of this research is to develop a simple human interface device that is portable, modular, easy to use, and includes only the essential components necessary to enable effective telerehabilitation. It is believed that a basic, low-cost system will produce the greatest outcome in terms of the number of patients treated while producing functional gains comparable to more complex systems. As background information, a brief review of the impact of stroke, past and present treatment methods, and existing rehabilitation robotics are presented.

A. Significance of Stroke

Prevalence: Stroke is one of the leading causes of long-term disability in Europe, The United States, and Australia. Each year in US, 780,000 persons sustain a new or recurrent stroke, and nearly 6 million persons are currently living with the long-term effects of a prior stroke [1]. Improved medical treatment of the complications caused by acute stroke has contributed to decreased mortality, but 90% of the survivors have significant neurological deficits.

Symptoms: The most common consequence of stroke is hemiparesis of the limbs contralateral to the brain lesion [2].

Hemiparesis can range from mild weakness to complete paralysis. Impairments in the upper limb tend to persist long-term with only 14-16% of stroke survivors with upper extremity hemiparesis regaining complete or nearly complete motor function [3]. Although the effects of stroke depend largely on the location of the obstruction and the extent of the brain tissue affected, movement disorders and stereotypic muscle synergies affect most individuals with stroke [4, 5].

Cost of stroke: The combined direct and indirect costs of stroke in the US in 2005 were estimated at over 56 billion US dollars. Furthermore, the demand for physical and occupational therapy for stroke survivors is expected to increase by a factor of three over the next 3 decades given the steady increase in life expectancy of the population and the high incidence of stroke in older adults [6].

B. Conventional vs. Robot-Assisted Rehabilitation

While there is no one standard technique that occupational and physical therapists use to improve upper extremity function, many of the techniques that are used require some manual assistance from the therapist to position, guide, and/or support all or some of the weight of the limb [7]. When provided with at least partial compensation of gravitational forces, it is possible for patients to perform controlled movements that could not otherwise be performed without assistance [8].

Using robot-mediated approaches, previous studies have shown that patients who performed progressive resistance exercises with adequate motor control for as little as 3-4 times per week for 6-12 weeks improved both strength and functional activities [9]. Furthermore, recently published research work confirms that better results in terms of rehabilitation outcome are obtained in specialized care centers where patients receive more therapy per day for extended periods of time [10].

C. Literature Review of Upper-Limb Devices

Commercial: A small number of systems for upper limb rehabilitation have only recently made their appearance on the market (Table 1). The most well-known device is the InMotion² (Interactive Motion Technologies, Inc.), the commercial successor to the academic MIT-MANUS, a 2-dof high-powered parallel manipulator. Hocoma has developed an upper limb product, Armeo®, based on the academic T-WREX device, a 5-dof passively counterbalanced exoskeleton. A third approach was taken by Motorika with the ReoRobot, now known as the ReoGo, a 2-dof mobile-robot-mounted joystick with an attached laptop. Additionally, there exists one portable commercial orthosis that

provides powered assistance in response to measured EMG signals (Myomo e100). However, none of the above devices are sold for personal use.

Table 1 Commercial upper-limb rehabilitation devices

Device Name	Company (Location)	Feedback Provided	Clinical / Personal Use
InMotion2	Interactive Motion Technologies (Boston, MA)	V, H, A	Clinical
Armeo®	Hocoma AG, (Switzerland)	V, P	Clinical
ReoGo	Motorika (Mount Laurel, NJ)	V, H, A	Clinical
Myomo e100	Myomo, Inc. (Boston, MA)	A	Clinical

Note: Feedback provided: visual (V), haptic (H), active force (A), or passive force (P).

Academic: Despite a large and growing number of academic robotics research aimed at upper-limb therapy, the research is overwhelmingly focused on the clinical setting (Table 2). Only two devices to our knowledge are under study for therapy in the home. The MEMOS device is a 2-dog Cartesian platform that rests on a table and is currently involved in clinical trials through the end of 2009. RUPERT is a lightweight exoskeleton that uses pneumatic muscles as the driving actuators to provide 4-dof assistance. Both devices remain relatively large and cumbersome for regular in-home use by the patient population. Additionally, the question of true affordability remains a concern.

Table 2 Academic upper-limb rehabilitation devices

Device	Institution	Feedback Provided	Clinical / Personal Intended Use
MIT-MANUS	Massachusetts Institute of Technology (Boston, MA)	V, H, A	Clinical
ACT3D	Northwestern U. (Chicago, IL)	V, A	Clinical
MIME	VA Palo Alto (Palo Alto, CA)	V, H, A	Clinical
GENTLE/s	U. Reading (Reading, UK)	V, H, A	Clinical
ARMin	Swiss Federal Institute of Technology (Zurich, Switzerland)	V, H, A	Clinical
ARM Guide	Rehabilitation Institute of Chicago (Chicago, IL)	V, A	Clinical
Haptic Drive	Institute for Rehabilitation (Ljubljana, Slovenia)	V, H, A	Clinical
EXO-UL7	UC Santa Cruz (Santa Cruz, USA)	V, H, A	Clinical
MGA	Georgetown U. (Washington DC, USA)	V, H, A	Clinical
MEMOS	Scuola Superiore Sant'Anna (Pisa, Italy)	V, H, A	Clinical / Personal
RUPERT	Arizona State (Mesa, AZ)	A	Clinical / Personal

Note: Feedback abbreviations are provided in Table 1.

From the review of existing rehabilitation systems, it is clear that the inclusion of an engaging visual feedback coupled with actively powered assistance are considered vital aspects of robotic therapy. However, there are also studies indicating that passive compensation of gravitational forces is sufficient to enable users to regain movement coordination, at least in low levels of impairment severity [8]. Of the devices listed in the above tables, Armeo® is the only device that takes advantage of this simplification.

II. METHODS

The proposed system will first be developed as a passive prototype. A later active version will follow, building from the lessons learned in the passive development phase. The envisioned system will be a portable unit (Figure 1 - left) that straps to the user's forearm and can be operated in the patient home on a standard table (Figure 1 - right). As a first step in the process, a set of system requirements were outlined in order to direct the further development of system hardware and software. These requirements are outlined and discussed below.



Figure 1. The ARMassist (left) is a wireless human interface device that connects to the user forearm and is operated on a standard table (right).

A. System Requirement

Affordability: The target production cost for the passive unit is 100 Euros, such that it can be sold a price comparable to other computer peripherals. The target production cost for the active unit is 500 Euros. Maintaining affordability requires the use of inexpensive stock parts (motors, sensors, raw material) and standard processes (basic machining, high-volume manufacturing practices).

Simplicity: Utilizing a simple robust design with minimal moving parts plays a role in both ultimate affordability (price) and product life cycle (value).

Portability: The unit should be small enough to be carried easily from a store in a standard grocery bag, and should weigh less than 4 kg.

Usability: For a system to be easy to use, it should be intuitive and clearly understandable without explanation. It should allow simple one-handed donning and doffing. Considering use in a virtual environment, mappings between actual and on-screen motions that are not readily intuitive should be avoided.

Functionality: From a functional standpoint, the design should (1) provide a large workspace for user, (2) ensure repeatable movement tracking, (3) store a log of movement trajectories and performance information for therapists to review, and (4) be able to run on a single charge for up to 3 hours per day over a 1 week duration.

Modularity: The human-machine-interface should be adjustable in terms of relative position with the device, user fit, and should be removable to accommodate different end-effectors, forearm or wrist, for example. A separate module for the hand should also be attachable in conjunction with the forearm support.

B. Telerehabilitation Architecture

As the ultimate deployment of this technology will be in the home, the relationship between this new training modality and the expertise provided by medical staff should be considered. The concept for use in a telerehabilitation environment is that the prototype will communicate wirelessly with a local pc that is connected by internet to a care center or medical professional. While this model should be considered, it is important to note that even before such tele-health networks are established, portable devices can serve a valuable purpose. In addition to allowing greater amounts of training, data can be stored locally and sent periodically to health providers for analysis and periodic treatment updates.

III. RESULTS

The hardware of a first prototype of the ARMassist was developed using low-cost components for motion and force sensing and for passive gravitational support of the limb.

In order to fulfill the above requirements, the design of the device was divided into two component assemblies: the forearm support and the main structure. The two-component design makes the unit easy to assemble and feasible for different patients, in addition to increasing portability.

The forearm support is composed of a foam liner inside of a 3mm thermoplastic shell. The shell attached to a stiffening aluminum rib provides rigid support against longitudinal bending while providing flexibility in the radial direction for a secure fit with the arm when fastened by two Velcro straps. The straps are oriented such that the user can secure by pulling toward the user with the intact limb.

The main structure is a square module where the following components have been integrated:

- **Ball transfers:** Three ball transfer units allow for a large planar workspace with sufficient device stability and low friction motion. Both load ball and minor balls of each transfer unit are made of nylon in order to reduce the noise of operation.
- **Movement sensors:** Two Logitech Value optical USB mice boards provide position data.

- **Processing and communication unit:** A portable computer processes position and force data and provides the communication with the user computer through Bluetooth, and connects to the sensors through a USB hub.
- **Force sensor:** A load cell is incorporated in the center of the structure providing force data to the micro-processor.
- **Battery:** A 6000mAh 5V battery powers the sensors and the processing and communication unit.
- **Forearm rocker:** A single-axis pivot with interchangeable forearm springs allows the stiffness of the forearm support to be varied depending on the user's support needs.

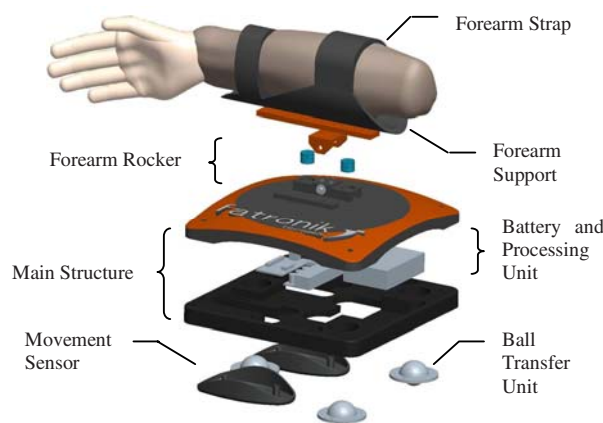


Figure 2. Exploded CAD view of first prototype design.

In order to monitor movements and forces exerted by the arm, the prototype (Figure 3) is equipped with two types of low-cost sensors: 2-axis position and 1-axis force.

Position Sensors: Two Logitech Value optical scroll USB mice boards have been attached to the base of the device. The mice are based on the ADNS-2610 optical mouse sensor which processes 1512 frames per second. Each frame contains a rectangular array of 18 x 18 pixels, and each pixel senses up to 64 shades of gray. The mice provide information about displacement in the X and Y directions with a maximum resolution of 400 counts per inch.

Force Sensor: To measure the vertical (Z-axis) force exerted by the forearm, the main structure is also equipped with a low-cost 1-axis force sensor with a 10 kg capacity in both positive and negative directions. The analog output of the load cell is connected to an Analog Devices AD727 instrumentation amplifier and read by the 10 bit A/D converter of the processing and communication unit at 1 kHz. The signal is low pass filtered using a simple moving average filter. It was found that using a window frame of 20 ms obtained the optimum tradeoff between the stability of the signal and the delay from buffering.



Figure 3. First ARMassist prototype (left) during initial testing (right).

IV. CONCLUSIONS

From the trends of aging populations throughout the world, and the increasing prevalence of stroke with age, it is clear that more treatment modalities must be extended beyond the borders of the in-patient setting to locations outside of the hospital. We believe that the combination of requirements outlined in this paper and used in the development of this first prototype ARMassist device are sufficient to successfully meet this need.

Current efforts are being devoted to the development of fundamental movement strategies in using the ARMassist in simulated 3D training environments. It is anticipated that the measure of X and Y position and Z force will be sufficient to control three dimensional reach tasks in the on-screen virtual environment for the purposes of functional motor relearning in patients with motor impairment of the upper limb.

Additionally, future development will produce an actively driven prototype for planar motion assistance, as well as modular device add-ons for hand training.

ACKNOWLEDGMENT

The authors would like to thank David Valencia for his contributions to the project.

REFERENCES

1. The American Heart Association, (2008). Heart Disease and Stroke Statistics – 2008 Update, *Circulation*. 2008;117:e25-e146
2. Taub E, Uswatte G, & Pidikiti R, (1999). Constraint-induced movement therapy: A new family of techniques with broad application to physical rehabilitation—a clinical review. *Journal of Rehabilitation Research and Development*, 36, 237-251.
3. Nakayama, H, Jorgenson, HS, Raaschou, HO, & Olsen, T, (1994). Compensation in recovery of upper extremity function after stroke: The Copenhagen study. *Archives of Physical Medicine and Rehabilitation*, 75, 852-857.
4. Beer RF, Ellis MD, Holubar BG, Dewald JP. (2007) Impact of gravity loading on post-stroke reaching and its relationship to weakness. *Muscle Nerve*. 2007 Aug;36(2):242-50.
5. Dewald JP, Beer RF, (2001). Abnormal joint torque patterns in the paretic upper limb of subjects with hemiparesis. *Muscle Nerve* 24:273-283.
6. Krebs HI, Volpe BT, Aisen ML, Hogan, N, (2000). Increasing Productivity and Quality of Care: Robot-Aided Neurorehabilitation, *VA Journal of Rehabilitation Research and Development* 37:6:639-652.
7. Woodson AM, (2002). Stroke. In C. A. Trombly, & M. V. Radomski (Eds.), *Occupational Therapy for Physical Dysfunction* (5th ed., pp. 817-853). Baltimore: Lippincott Williams & Wilkins.
8. Sanchez RJ, Liu J, Rao S, Shah P, Smith R, Rahman T, Cramer SC, Bobrow JE, Reinkensmeyer DJ. (2006) Automating arm movement training following severe stroke: functional exercises with quantitative feedback in a gravity-reduced environment. *IEEE Trans Neural Syst Rehabil Eng*. 2006 Sep;14(3):378-89.
9. Patten C, Loxell J, Brown HE, (2004). Weakness and strength training in persons with poststroke hemiplegia: rationale, method, and efficacy. *J Rehabil Res Dev* 2004;41:293-312.
10. De Wit L, Putman K, Schuback B, Komárek A, Angst F, Baert I, Berman P, Bogaerts K, Brinkmann N, Connell L, Dejaeger E, Feys H, Jenni W, Kaske C, Lesaffre E, Leys M, Lincoln N, Louckx F, Schupp W, Smith B, De Weerd W, (2007). Motor and functional recovery after stroke: a comparison of 4 European rehabilitation centers. *Stroke*. 2007;38:2101

Corresponding author:

Author: Joel C. Perry
 Institute: Fatronik Foundation
 Street: Paseo Mikeletegi, 7
 City: Donostia-San Sebastian
 Country: Spain
 Email: jperry@fatronik.com

Application of 3D modeling and modern visualization technique to neurosurgical trigonocephaly correction in children

M. Gzik¹, W. Wolański¹, D. Tejszerska¹, B. Gzik-Zroska, M. Koźlak¹, D. Larysz² and M. Mandra²

¹ Silesian University of Technology, Department of Applied Mechanics, Gliwice, Poland

² Medical University of Silesia, Katowice, Poland

Abstract— The attempt to a new methodology creation, supported neurosurgical correction of trigonocephaly by engineers is presented in this paper. Trigonocephaly is an example of skull deformity, that wrong influence on child physical and psychological development. Conventional procedures in such cases are connected with invasive operation. Up to now neurosurgeons during pre-operation planning of bones correction, based on their own knowledge and experience. Modeling in biomechanics connected with modern visualization methods give new possibilities of engineer support for medical procedures. Three-dimensional model of deformed skull was created on the basis of CT scans with use of Mimics software. The model was transformed to FEM and used for suitable shape of forehead bone determination. Material properties of modeled bones were assumed on the basis of experimental researches. The geometrical model was presented in 3-dimensional virtual reality. It helps to better imagine about the real shape of skull hidden under head skin and take the best decision how to operate the example of trigonocephaly.

Keywords— 3-D modeling, FEM analysis, trigonocephaly, visualization technique

I. INTRODUCTION

Contemporary medicine owes a lot to technology development. Collaboration between medical doctors and engineers contributes to new treatment methods creation. Biomedical engineering is increasingly becoming very important also in pediatric neurosurgery [7].



Fig. 1 Skull defect – trigonocephaly [1]

Trigonocephaly is an example of children skull defects demanding invasive surgical operation (fig.1). Several different factors (primary fusion of a cranial vault suture, abnormal tensile forces acting on the cranial sutures, genetic control and fetal constraint) may be responsible for the malformation. In spite of many research, pathogenesis is still poorly understood. Conventional procedures include flattening of the forehead and straightening of the supraorbital bar by multiple osteotomies. Surgical correction is generally considered to be ideally performed at the age of 3 to 6 months [2,3,4,5,6].

This article describes an example of neurosurgical applications of modeling in biomechanics and modern method of visualization. The applied technology supported decision process during preoperation planning of surgical approach.

II. MODELING RESEARCH

A. Analyzed example of trigonocephaly

The research was concerning a 3 - months old boy with prominent trigonocephaly. His condition was evaluated using CT scans fig.2.

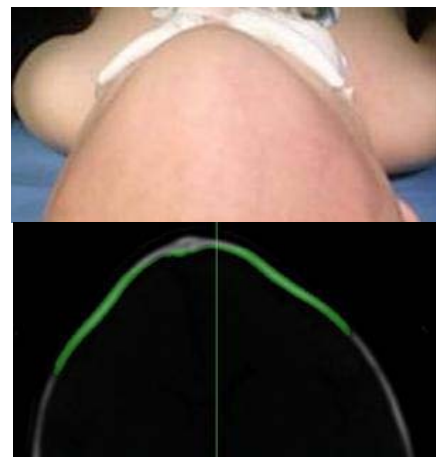


Fig. 2 A 3 - months boy with trigonocephaly

On the basis of CT scans geometrical 3 – dimensional model was created with use of MIMICS software fig.3.

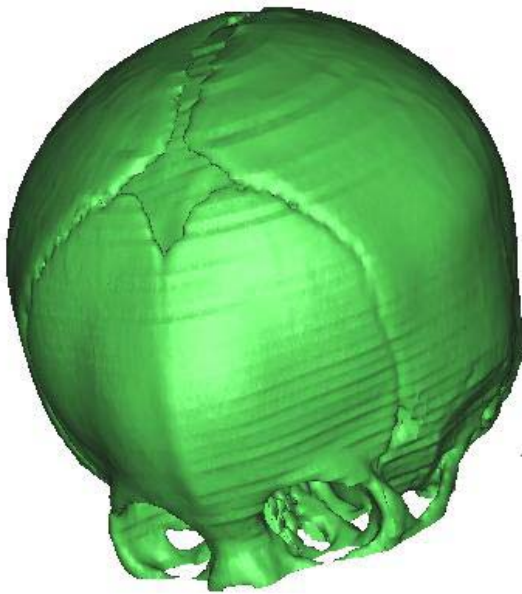


Fig. 3 A geometrical model of deformed skull

The modeling researches were carried out for two aims realization: first for neurosurgeons support during preoperation planning process, second in order to estimate best method of defect correction limited range of forehead bone invasion.

B. FEM model of forehead bone

Mimics software allowed crating finite element models FEM of forehead bone in several variants fig.4. The models were used for best variants of osteotomies determination.

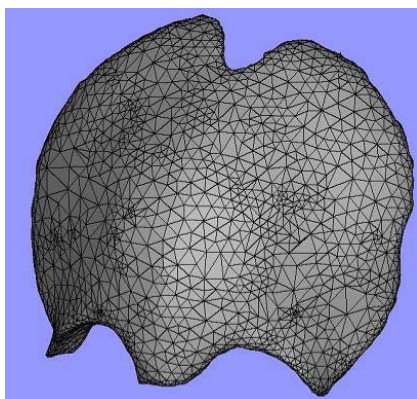


Fig. 4 FEM model of deformed forehead bone

C. Experimental researches

Modeling process demanded materials properties identification. Material of bone was treated as isotropic. Necessary parameters were determined during tests on skull bone specimens received during previous operation.



Fig. 5 Experimental stand - MTS Insight 10 kN

Fig. 6 Bone specimen separately and fixed by machine holders

Average value for ten tests is presented in table 1 whereas curve of bone stiffness in fig 7.

Table 1 Material properties

Material	Young modulus [MPa]	Peak load [N]
bone of 3 months child	380	55

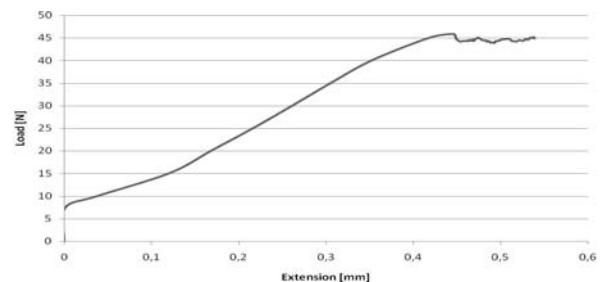


Fig. 7 Characteristics of 3-months old children skull bone

III. MODEL OF DEFORMED SKULL IN VIRTUAL REALITY

3D image stereography gives new possibility of visualization. Virtual model of analyzed skull was created in EON software. Geometry from MIMICS was exported as 3-dimensional model.



Fig. 8 Reconstruction of deformed skull in virtual reality

Virtual model helped to medical doctors better imagine the case of trigonocephaly. The model played important role during preoperating planning of neurosurgical operation fig.8.

IV. RESULTS OF NUMERICAL SIMULATIONS

3-D models of forehead bone created in MIMICS program in 5 variants were exported to ANSYS software: intact bone, flattened, 5 osteotomies, 6 osteotomies, 8 osteotomies (fig.9). In order to achieve flat bone it should be deflected 20mm. Relations between bone deflection and load are presented in table 2.

Table 2 Type of finite element model and results of simulation

Type of correction	Size of deformation [mm]	Load [N]
Intact	20	52
flattened	20	37
5 osteotomies	20	15
6 osteotomies	20	10
8 osteotomies	20	4

Shapes of deformed bones after deflection are presented in fig. 10.

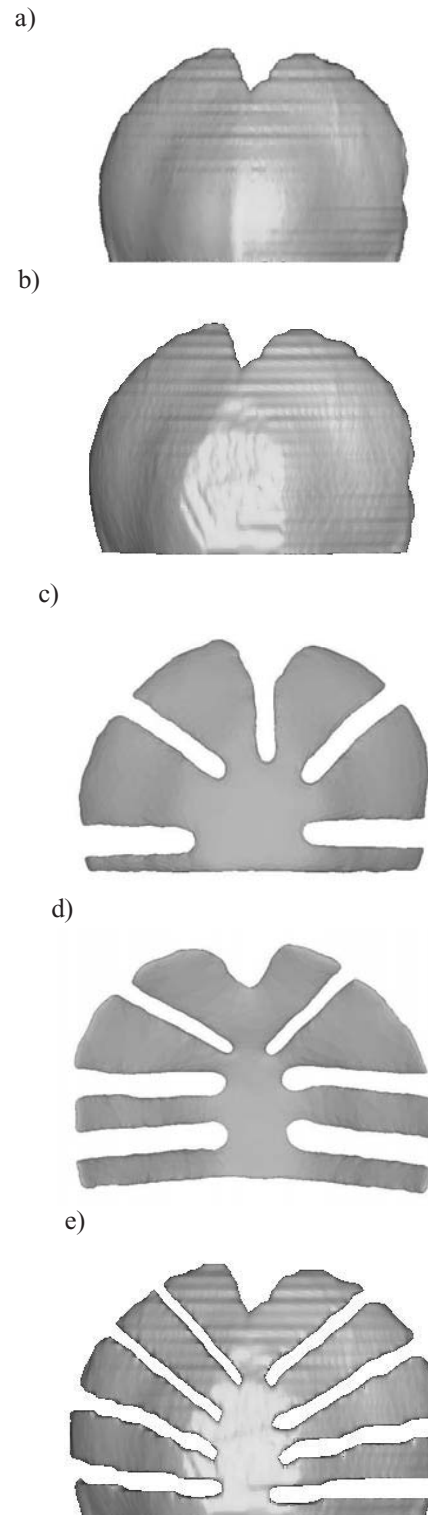


Fig. 9 Variants of analyzed forehead bone osteotomies: a) intact bone, b) flattened, c) 5 osteotomies, d) 6 osteotomies, e) 8 osteotomies

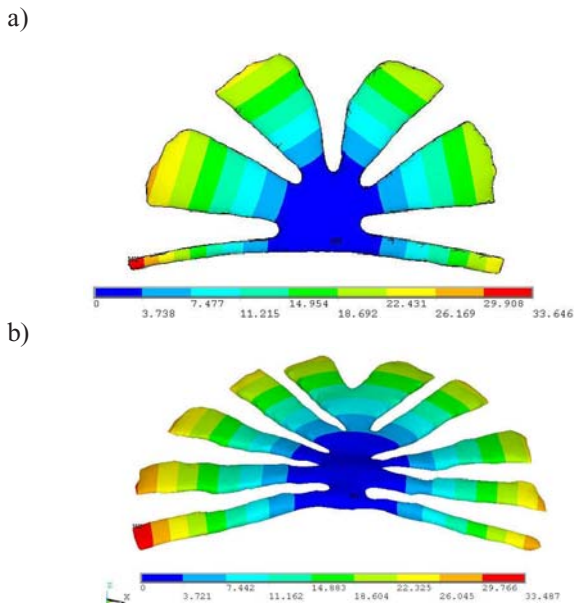


Fig. 10 Bones deformation after deflection: a) 5 osteotomies, b) 8 osteotomies

V. CONCLUSIONS

The presented methodology based on latest bioengineering technology. After carried out researches neurosurgeons decided about method of trigonocephaly correction. Results of numerical simulations proved that in analyzed case 8 number osteotomies give best skull correction conditions. Stiffness of bone prepared in this way guarantee safe load for neighbor anatomical structure. The research revealed very important factor of age on correction methods. 3 months age child has so stiff skull that need many bone osteotomies in order to achieve satisfy correction. Operation in earlier age time could much limit skull invasion process.

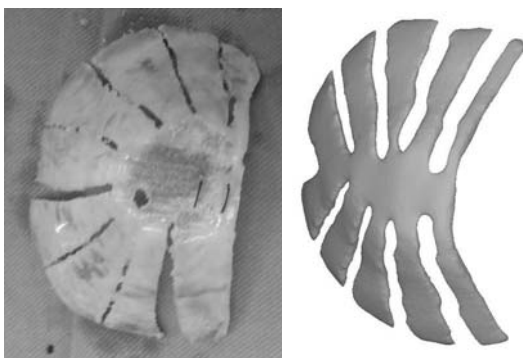


Fig. 11 Forehead bone during operation



Fig. 12 Photo of skull during correction.

REFERENCES

1. David J. David. Advances in the management of the craniosynostoses, ANZ J. Surgery, 2003, 73, 949-957.
2. Littlefield TR, Kelly KM, Pomatto JK, Beals SP. Multiple-birth infants at higher risk for development of deformational plagiocephaly: II. is one twin at greater risk? Pediatrics. 2002 Jan;109(1):19-25.
3. Losee JE, Mason AC, Dudas J, Hua LB, Mooney MP. Nonsynostotic occipital plagiocephaly: factors impacting onset, treatment, and outcomes. Plast Reconstr Surg. 2007 May;119(6):1866-73.
4. Miller RI, Clarren SK. Long-term developmental outcomes in patients with deformational plagiocephaly. Pediatrics. 2000 Feb;105(2):E26
5. Murad GJ, Clayman M, Seagle MB, White S, Perkins LA, Pincus DW. Endoscopic-assisted repair of craniosynostosis. Neurosurg Focus. 2005 Dec 15;19(6):E6.
6. Sloan GM, Wells KC, Raffel C, McComb JG. Surgical treatment of craniosynostosis: outcome analysis of 250 consecutive patients. Pediatrics. 1997 Jul;100(1):E2.
7. Virtanen R, Korhonen T, Fagerholm J, Viljanto J. Neurocognitive sequelae of scaphocephaly. Pediatrics. 1999 Apr;103(4 Pt 1):791-5.

Author: PhD. Eng. Marek Gzik
 Institute: Silesian University of Technology,
 Street: ul. Konarskiego 18A
 City: 44-100 Gliwice
 Country: Poland
 Email: marek.gzik@polsl.pl

Peripheral Inductive Stimulation: Physical Issues and Advanced Technological Solutions

S. M. Goetz^{1,2}, Th. Weyh²

¹ Fachgebiet Energiewandlungstechnik, TU München, Munich, Germany

² Lehrstuhl für Medizinische Elektronik, TU München, Munich, Germany

Abstract—Since its invention in the early 1980s magnetic stimulation has established itself especially in the field of transcranial application, the first purpose. But in recent times the perspective successively widens also to the periphery with neuronal rehabilitation, muscular training and a wide range of diagnostic applications. Thereby certain problems have been heritages from the use concerning the brain, whereas the different micro-anatomical and physical conditions require fundamental reorientation for prosperous methods, which will introduce our arguendo.

The discussed applications as well as peripheral stimulation in principle necessitate different parameters for an experimental setup compared to a system for transcranial stimulation. These comprise the high voltage oscillator, the magnetic coil and, as a matter of course, likewise the protocols. Repetition plays obviously an important role, but also questions concerning carrier frequency, energy efficiency, coil conception as well as design rules for the latter—which alter radically—will be discussed further.

The last part of our pleadings will relate the basic understanding of occurring processes, which is still characterised by a race of different methodology. In this context we present anew some aspiring details of our own original work.

Keywords—Inductive neuro-stimulation, periphery, biophysics, neural engineering, rehabilitation.

I. INTRODUCTION

The history of inductive neurostimulation is highly linked with the desire to influence the processes inside the human body. Especially the hardly understood neuronal system including the brain provided huge attraction and induced the ardent wish to take over control of the biologic information processing [3]. The function of a modern stimulation setup can be summed up roughly as an alternating current in a magnetic coil inducing a certain distributed current inside the tissue. The latter stimulates for example neuronal axons via channel proteins. The parallels to electric stimulation are patently obvious, but the differences, in contrast, lie covert. Exemplarily, body currents generated by inductive stimulation lack any contact transition through the skin, often referred to as being the main cause for pain in electric stimulation [12].

The application of inductive neurostimulation has been mainly focused to the cortex, yet. The advantages compared to other stimulation techniques that led to this triumph as a routine diagnostic instrument are the absence of pain, the capability to stimulate brain areas non-invasively and the possibility to create well defined foci by a convenient coil design. Especially the latter is known to be a problem of electrical attempts [5].

In recent times also the periphery of the body has been added to the domain of interest. But the consequences and differences adjunct to this step have been pointed out no more than roughly. The technical modifications—as will be revealed—are notably higher than apparent from a first glance. All parts of the setup, namely the spatial field profile as well as the generation of the temporal pulse, will play a prominent role in presented and future adaptations.

II. PASSING REMARK ON THE INFLUENCE OF THE SPECIFIC APPLICATION

At this stage it seems important to envision possible aims of a peripheral stimulation more precise. Diagnostics of lesions of any type of nerve fiber based on conduction velocity measurements and alike wave analysis [4,9,13] for instance need a short and rather local stimulus, thus very similar requirements compared to transcranial magnetic stimulation.¹ The needed energy thereby keeps within reasonable limits. In other fields of application the interest is directed towards specific fiber types, exemplary motor neurons. When a large amount of fibers should be firing after an inductive pulse, relatively high power is needed, thus the efficiency of the process becomes a fundamental issue. For optimization we have uncovered at least three possible side conditions: The activation of a certain portion of cells (P_{ap}) could be achieved with minimizing the related pain, with a low fatigue rate or also with best physical/technical conditions. One degree of freedom to achieve this is the pulse

¹ The only difference has mainly influence on the coil design. The nerve fibers studied with these methods are usually straight and relatively long compared to the complex geometric cell structures in the brain, respectively the cortex.

waveform of a stimulation setup, especially the carrier frequency of the high voltage oscillator, which provides the current pulse in the coil. But from electric stimulation is for example known that all these mentioned conditions do not naturally agree [3,14,7]. But this is not necessary. For muscle formation fatigue of the single activated muscle fiber types (I, IIa or IIb) plays a fundamental role, whereas in rehabilitation pain is of inestimable importance, as distress was found to counteract the attendance and even the success of a treatment [8]. Elaborating the physical side conditions for inductive stimulation devices, we find again three different optima that shall be discussed further:

A minimum voltage peak in the stimulator waveform aims not only at the semiconductor switches with their specific dielectric strength, but also at patient safety. Typical system designs of the authors work with voltage levels around 3000 volts for an adequate effect like muscle torque and require high insulation efforts as well as failure detection complexity. One approach for reducing the high voltage was recently suggested by Peterchev et al. [11].

Another limiting factor, especially for application in rehabilitation—that will be highlighted from an alternative perspective later—is the short treatment time due to heating of the magnetic coil and its cable due to their finite conductance [15]. High expectations regarding this issue are linked with better adaptations of the stimulators' pulse properties and also the coil design.

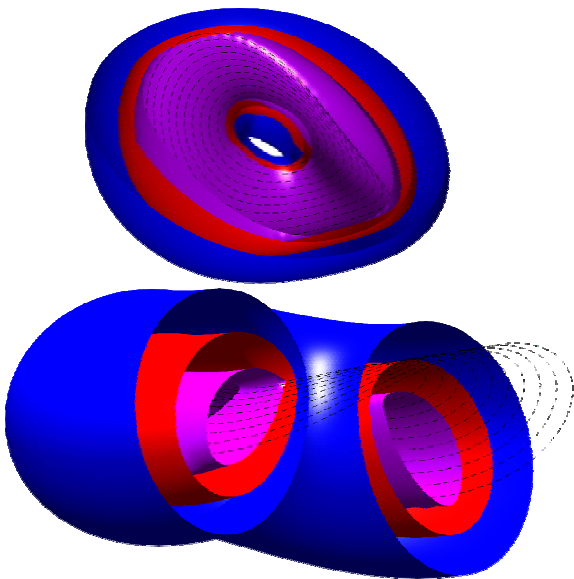


Figure 1: Simple peripheral coil design for muscle training: The electric field (displayed in isosurfaces around the single wire turns) is deliberately “anti-focal” and widespread. The data have been calculated with a finite integration method.

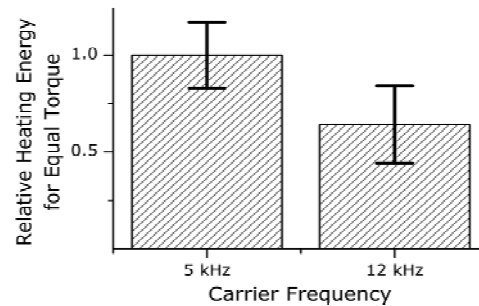


Figure 2: Reduction of coil heating by switching to higher carrier frequencies in experiments at the musculus quadriceps femoris.

The last interesting optimization condition is driven by the wish to design smaller and maybe even portable stimulation systems that are mainly limited by the supply with power for operation. The minimum condition for the power consumption should explicitly not be equated with minimal coil losses or the voltage level in the device. Especially the latter can outbalance linearly the reduced efficiency by a quadratic reduction of the pulse energy by changing the carrier frequency. Our own investigation showed possible optimization potential via the waveform here (unpublished results). It can be shown very easily that in the case of harmonic waveforms the pulse energy is direct proportional to the pulse capacitance (for a constant inductance of the magnetic coil), whereas the heat losses in the coil shows approximately a square-root dependency.

III. LIMITATIONS OF PERIPHERAL MAGNETIC STIMULATION

A. Pulse Energy

All commercially available devices meet several grave problems currently. Some of these problems are indeed a matter of principle, but the prevailing part bears promising challenges for the scientific community. An unwelcome heritage from classical transcranial magnetic stimulation is the incredibly huge power consumption of inductive stimulation setups (see e. g. [6]).² Whereas this can be narrowly ignored in brain stimulation, the desire for high muscle forces over long periods renders that hardly acceptable. The reason for the energy demand lies not in the stimulation device, but the body, more precisely in the electric properties of biologic tissue. The low conductivity, but relatively high dielectricity of the latter circumscribes the inductive coupling of the primary magnetic field to the tissue. Neglecting the feedback from the induced currents to the coil, a second consequence of the above mentioned context, the induced

² The massive size of the systems is just a consequence of that.

current density j is not only widely dependent on, but even approximately proportional to the local conductance σ in the body. Directly from the Maxwell Equation one derives the desire for a high time derivative of the magnetic flux Φ . This leads to the intuitive relation of $j \sim \sigma d\Phi/dt \sim \sigma dI_{coil}/dt \sim \sigma V_{coil}$, with the current I_{coil} and the voltage V_{coil} in the stimulation circuit. For harmonic functions (all biphasic full- or half-wave devices for example) one can add even the proportionality to the coil current itself. As a consequence one needs extremely high pulse powers in the megawatt range. But in this context it should be emphasized that this does not necessarily mean that the power consumption cannot be reduced. The key is an appropriate system of energy recovery. One needs extremely high energy, but due to the low coupling the transfer to the body is negligible.

Measures to counteract the energy problem contain the use of higher oscillation frequencies for the pulse. Our experimental studies showed that the neurons' threshold rises with carrier frequencies higher than 10 kHz, but the losses falling with $1/\omega$ outweighed this effect obviously. A with a factor of 1.4 higher efficiency was observed as a consequence of doubled carrier frequency (see Figure 2). The second presented remedy is based on a better exploiting the field energy and affects the coil design discussed later.

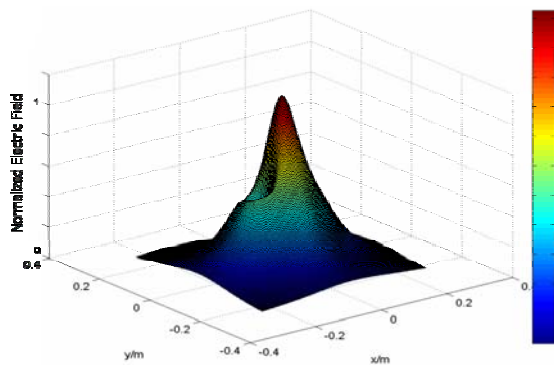


Figure 3: Normalized induced electric field of a commercial figure-of-eight coil local stimulation in a plain five centimeters below the coil. Very salient is the peak defining the focus in the center. But typical measures like the higher order moments of such field distribution (e. g. $(\sigma_x, \sigma_y, \sigma_z) = (10, 9.4, 5.7)$ cm here) are no longer applicable for peripheral demands.

B. Thermal Issues—Operation Time

The second limitation must be attributed to thermal problems in the magnetic coil. Legal requirements often restrict the maximal temperature of a medical device that touches a patient to values around 40° C. The high currents lead, even for extremely low resistances in the circuitry, to a high loss power. A typical commercial system dispenses per pulse a thermal energy up to $T_{pulse}/2 R I_{peak}^2 = 80 \mu s 30 m\Omega = 5.6$

$(kA)^2 \approx 75$ Joule. A repetition rate of 30 stimuli per second for tetanic muscle contraction leads to more than 2000 W heating power. In another configuration this value would not attract attention, but the low maximum temperature also limits the driving gradient needed for effective heat transport out of the coil ($J = -\kappa \text{ grad } T$). Compensating the low temperature difference with a high thermal conductivity fails, as electronic heat conduction (e. g. in metals) would also lead to huge eddy currents linked with high energy losses. Closed cooling circuits with a liquid medium are still the only alternative until now.

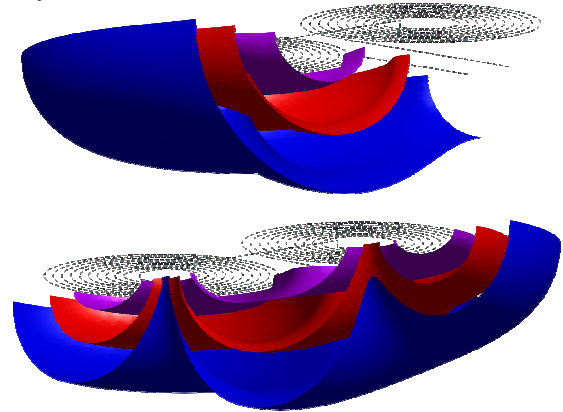


Figure 4: Isosurfaces of the electric field of the commercial figure-of-eight coil from figure 1: The focus can be recognized here by the convexity of the three envelope levels underneath the center. Because of the short ranging outer wings this design is totally unapt for applications like muscle stimulation.

IV. COIL DESIGN RULES FOR PERIPHERAL STIMULATION

The most important change in the periphery concerns the spatial use of the magnetic field namely via the coil design. For an effective activation of a muscle for instance the fine specificity desired in cortical stimulation is absolutely inappropriate. Admittedly all muscles are innervated by single locally confined nerve cords, but these lie usually with far distance too deep in the body [1,10]. Therefore it is much easier to reach the threshold of the axons already within the muscle in branches of higher order. Accordingly, the spatial requirements of the alternating magnetic field demand a widespread behaviour.

Figure 1 shows a simple, but rather effective exemplary design of a peripheral muscle coil. Despite typical cortical devices (fig. 3, 4) a focus can no longer be observed. The key issue is an optimal use of the field energy for the target to be stimulated and therefore in a sort of smoothness.

The distance is a very important factor we want to add to the design rules separately for special emphasis. Without any distortion by higher tissue inhomogeneities the induced

electric field exhibits a one-over-d-decay perpendicular to a single wire segment, as can be derived very easily from the Maxwell Equations. The field of a whole coil as a superposition behaves similarly. This very sharp profile brings to mind, what important role the distance of the coil conductor to the treated region plays. In the direct surrounding of the coil even the thickness of the insulation layer has a notable and detectable influence on the obtainable muscle torque.

The last passage should be dedicated to accentuate the functional chain. Although muscle activation is often the desired effect of peripheral stimulation, of course, the design of the field profile should be oriented towards the nerve shape rather than the more imposing muscle body. Meanwhile several good studies of mammalian nerve branching inside the muscle are available for such optimization [1,10] and await application.

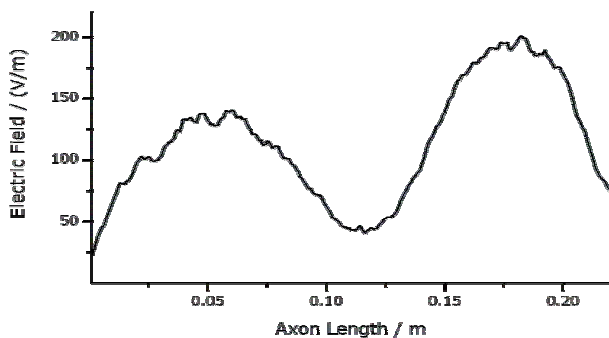


Figure 5: Projection of the electric field generated by the magnetic coil of figure 1 onto an exemplary branch of an innervating nerve tree. Analysis of the field projection onto a whole axon tree is a rather complex, but although the most promising tool for optimizations.

V. CONCLUSIONS

With the step of inductive neurostimulation towards the periphery several physical as well as physiological issues lead to new technological challenges as a matter of principle. In this context also the physical pitfalls to be avoided have been discussed shortly. The attempt to compensate the weak effects by brute power—leading to extreme heating losses—to achieve the desired impact is just one example. Whereas the coil design was identified as being a central issue with huge influence, also the high voltage circuitry is a component it should not be lost sight of. For the optimization of magnetic coils several quite elaborate steps with personalized design as the end of the flagpole. Important is finally still that the nervous system has to define the target.

REFERENCES

1. Arakawa T, Sekiya S, Kumaki K and Terashima T (2006) Intramuscular nerve distribution pattern of the oblique and transverse heads of the adductor hallucis muscles in the human foot. *Anatomical Science International* 81:187–196.
2. Basser PJ, Wijesinghe RS and Roth BJ (1992) The Activating Function for Magnetic Stimulation Derived from a Three-Dimensional Colume Conductor Model. *IEEE Transactions on Biomedical Engineering* 39(11):1207–1210.
3. Binder-Macleod SA and Snyder-Mackler L (1993) Muscle Fatigue: Clinical Implications for Fatigue Assessment and Neuromuscular Electrical Stimulation. *Physical Therapy*, 73(12):902–910.
4. Cioni R, Passero S, Paradiso C, Giannini F, Battistini N and Rushworth G (1989) Diagnostic specificity of sensory and motor nerve conduction variables in early detection of carpal tunnel syndrome. *J Neurol* 236:208–213.
5. Datta A, Elwassif M, Battaglia F and Bikson M (2008) Transcranial current stimulation focality using disc and ring electrode configurations: FEM analysis. *J Neural Eng* 5:163–174.
6. Davey K, Kalaitzakis KC and Epstein C (1988) Transcranial Magnetic Stimulation of the Cerebral Cortex. 10th IEEE EMBS, 1988, pp. 922–923.
7. Emrich D, Fischer A, Altenhöfer C, Weyh T, Helling F, Gatteringer N, Goetz S, Schmahl W, Schmidt J, Schlegel J and Matiasek K (2009) Muscle force development after low-frequency magnetic burst stimulation of the femoral nerve in dogs—implications for neurorehabilitation, submitted.
8. Griffin A and Bernhardt J (2006) Strapping the hemiplegic shoulder prevents development of pain during rehabilitation: a randomized controlled trial. *Clin Rehabil* 20:287–295.
9. Kleinrensink GJ, Stoeckart JM, Kaulsar Sukul DMKS, Vleeming A, Snijders CJ and van Noort A (1994) Lowered motor conduction velocity of the peroneal nerve after inversion trauma. *Medicine and Science in Sports and Exercise* 877–883.
10. Liu J, Kumar P, Shen Y, Lau H-K, Pereira BP and Pho RWH (1997) Modified Sihler's Technique for Studying the Distribution of Intramuscular Nerve Branches in Mammalian Skeletal Muscle. *The Anatomical Record* 247:137–144.
11. Peterchev AV, Jalinous R and Lisanby SH (2008) A Transcranial Magnetic Stimulator Inducing Near-Rectangular Pulses with Controllable Pulse Width (cTMS). *IEEE Transactions on Biomedical Engineering* 55(1):257–266.
12. Prausnitz MR (1996) The effects of electric current applied to skin: A review for transdermal drug delivery. *Advanced Drug Delivery Reviews* 18:395–425.
13. Tackmann W, Vogel P, Kaeser HE and Ettlin Th (1984) Sensitivity and localizing significance of motor and sensory electroneurographic parameters in the diagnosis of ulnar nerve lesions at the elbow. *J Neurol* 231:204–211.
14. Ward AR and Robertson VJ (2000) The variation in fatigue rate with frequency using kHz frequency alternating current. *Medical Engineering & Physics* 22:637–646.
15. Weyh Th, Wendicke K, Mentschel C, Zantow H and Siebner HR (2005) Marked differences in the thermal characteristics of figure-of-eight shaped coils used for repetitive transcranial magnetic stimulation. *Clinical Neurophysiology* 116:1477–1486.

Author: S. M. Goetz
 Institute: TU München
 Street: Arcsistr. 21
 City: Munich
 Country: Germany
 Email: sgoetz@tum.de

A Neuronal Network Model with Plasticity for Tinnitus Management by Sound Therapy

H. Nagashino¹, Y. Kinouchi², A. A. Danesh³ and A. S. Pandya⁴

¹ Department of Biomedical Information Science, The University of Tokushima, Tokushima, Japan

² Department of Biological Functions Engineering, The University of Tokushima, Tokushima, Japan

³ Department of Communications and Disorders Florida Atlantic University, Boca Raton, USA

⁴ Department of Computer Science and Engineering, Florida Atlantic University, Boca Raton, USA

Abstract—A perception of hearing sounds in the ear or head without any external source is referred to as tinnitus. There are many therapeutic approaches for tinnitus and sound therapy techniques for its treatment has been proposed. In order to investigate mechanisms of tinnitus generation and the clinical effects of sound therapy from the viewpoint of neural engineering, we have proposed a computational model using a neural oscillator. In the present paper, we propose another model that is composed of model neurons described by simplified Hodgkin-Huxley equations. By computer simulation it was detected that this model also has a bistable state, i.e., a stable oscillatory state and a stable equilibrium (non-oscillatory) state coexist at a certain parameter region. It was also noticed that the oscillation can be inhibited by supplying constant or pulse train stimulus, which is hypothesized as an afferent signal that is employed as an acoustical stimulus for tinnitus treatment. By hypothesizing that the oscillation and the equilibrium correspond to generation and inhibition of tinnitus, respectively, these phenomena could explain the fact that the habituated human auditory system temporarily halts perception of tinnitus following sound therapy.

Keywords— tinnitus, sound therapy, neuronal network model, plasticity, oscillation

I. INTRODUCTION

A perception of hearing sounds in the ear or head without any external source is referred to as tinnitus. Mechanism of tinnitus generation has been hypothesized from the viewpoint of neurophysiology [1, 2]. Contribution of neural plasticity to tinnitus has been discussed [3, 4]. Tinnitus has many subclasses and attempts has been made to categorize tinnitus based on its characteristics which in turn can facilitate the selection of treatment method [5]. Sound therapy techniques for tinnitus have been proposed. This kind of treatment has the clinical effect that tinnitus disappears or reduce in its loudness after the sound presentation [6]. The mechanisms of tinnitus and its management by sound therapy, however, are not clear. To account for those mechanisms from the viewpoint of neural engineering, we constructed a computational model using a neural oscillator [7-

9]. It was attempted to reproduce conceptually tinnitus generation and its inhibition using sound stimuli. It was detected that by providing the model with sinusoidal or noise stimulus that is hypothesized as sound for treatment of tinnitus we can inhibit the oscillation changing the parameter value by introducing plasticity to the model. By hypothesizing that the oscillation and the equilibrium correspond to generation and inhibition of tinnitus, respectively, we reported that these phenomena could explain the fact that the habituated human auditory system temporarily halts perception of tinnitus following sound therapy [6]. Our model is built by a somewhat conservative simplification of the central auditory pathways and associated central nervous system areas that are relevant to tinnitus.

In the present paper, we propose a different model composed of model neurons described by simplified Hodgkin-Huxley equations [10, 11]. This model is still conceptual since it consists of only three neurons, but more realistic than the previous one because it shows time series of firings of neurons. We show here that inhibition of the oscillation can be observed in this model as well by constant or pulse train stimuli. Through numerical simulations we found out that adequate intensity of stimulus is required for inhibition of the oscillation.

II. METHODS

We propose a neuronal network model shown in Fig. 1 in which firing sequences in the nervous system are simulated. This model of tinnitus generation network is conceptually simplified and composed of two excitatory neurons and one inhibitory neuron as shown in Fig. 1 (a). The two excitatory neurons, E_1 and E_2 , are mutually coupled forming a positive feedback loop. The excitatory neuron E_1 and the inhibitory neuron I are also mutually coupled forming a negative feedback loop. The positive feedback loop brings sustained firings. The negative feedback loop controls the firing rate. The coupling strength between neurons is denoted by C_{ij} ($i, j \in \{1, 2, I\}$). The neuron E_1 receives external stimuli S that is afferent signal due to the acoustic stimuli that are

employed in sound therapy. We express the dynamics by a simplified version of Hodgkin-Huxley equations (HH) [10, 11]. We employed it instead of HH because of reduction of the number of state variables for each neuron from four to two.

External stimuli S by pulse train stimulus are given by multiple input neurons E_1, \dots, E_P as shown in Fig. 1 (b). Because cortical neurons receive input from a number of neurons, and the simulation with the stimulus of a wide range of firing rate is impossible from a single neuron model. The number of input neurons and the stimulus to input neuron E_{S_j} is denoted by P and S_j , respectively.

A. Formulation of the model without plasticity

We describe the basic dynamics of the model as

$$\frac{dv_1}{dt} = \frac{G(v_1, m^\infty(v_1), 0.8(1-h_1), h_1) + C_{12}z_2 + S}{C_m}, \quad (1)$$

$$\frac{dh_1}{dt} = \alpha_h(v_1)(1-h_1) + \beta_h(v_1)h_1, \quad (2)$$

$$\frac{dv_2}{dt} = \frac{G(v_2, m^\infty(v_2), 0.8(1-h_2), h_2) + C_{21}z_1 - C_{21}z_I}{C_m}, \quad (3)$$

$$\frac{dh_2}{dt} = \alpha_h(v_2)(1-h_2) + \beta_h(v_2)h_2, \quad (4)$$

$$\frac{dv_I}{dt} = \frac{G(v_I, m^\infty(v_I), 0.8(1-h_I), h_I) + C_{I2}z_2}{C_m}, \quad (5)$$

$$\frac{dh_I}{dt} = \alpha_h(v_I)(1-h_I) + \beta_h(v_I)h_I, \quad (6)$$

where v is the membrane potential and h is the variable associated with activation of potassium ion channel in the neuron E_1 , E_2 or I . The functions $G(v, m, n, h)$ and $m^\infty(v)$ are expressed as

$$G(v, m, n, h) = \bar{g}_{Na} m^3 h (V_{Na} - v) + \bar{g}_K n^4 (V_K - v) + \bar{g}_I (V_I - v) \quad (7)$$

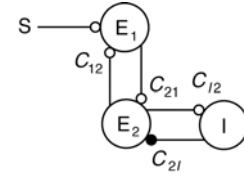
and

$$m^\infty(v) = \alpha_m(v) / \{\alpha_m(v) + \beta_m(v)\} \quad (8)$$

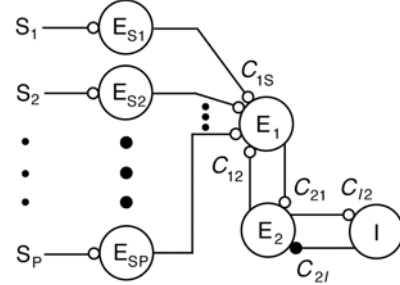
respectively. The functions $\alpha_m(v)$ and $\beta_m(v)$ in Eq. (8) are expressed respectively as

$$\alpha_m(v) = 0.1(25-v) / \{e^{(25-v)/10} - 1\} \quad (9)$$

and



(a) Basic structure of the present model



(b) Model structure with pulse train input

Fig. 1 Neuronal network model structure

$$\beta_m(v) = 4 e^{-v/18} \quad (10)$$

Functions $\alpha_h(v)$ and $\beta_h(v)$ in Eq. (2), (4), (6) are expressed respectively as

$$\alpha_h(v) = 0.07 e^{-v/20} \quad (11)$$

and

$$\beta_h(v) = 1 / \{e^{(30-v)/10} + 1\}. \quad (12)$$

The parameters of the neuron model were fixed as

$C_m = 1[\mu\text{F}/\text{cm}^2]$, $\bar{g}_{Na} = 120[\text{mS}/\text{cm}^2]$, $\bar{g}_K = 36[\text{mS}/\text{cm}^2]$, $\bar{g}_I = 0.3[\text{mS}/\text{cm}^2]$, $V_{Na} = 115[\text{mV}]$, $V_K = -12[\text{mV}]$, $V_I = 10.6[\text{mV}]$, based on the values in Hodgkin-Huxley model. The output of the neuron is denoted by z_j and expressed as function of the membrane potential v_j as

$$z_j = \begin{cases} 1 & (v_j \geq 1) \\ 0 & (v_j < 1) \end{cases}. \quad (13)$$

B. Formulation of plasticity

To reproduce the effect of sound therapy, we assume that the coupling strength from the neuron E_1 to the neuron E_2 , C_{12} , has plasticity in such a way that it increases when the neurons E_1 and E_2 fires simultaneously, and decreases when the firings of the neurons E_1 and E_2 are not synchronized. This assumption is based on Hebbian hypothesis regarding synaptic plasticity [12]. We describe the dynamics of C_{12} as follows. When both z_1 and z_2 are 0,

$$\frac{dC_{12}}{dt} = 0, \quad (14)$$

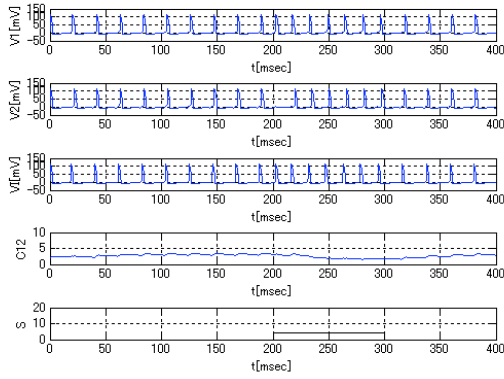
and otherwise

$$\frac{dC_{12}}{dt} = \frac{-C_{12} + b(z_1 - 0.5)(z_2 - 0.5) + C_0}{\tau}, \quad (15)$$

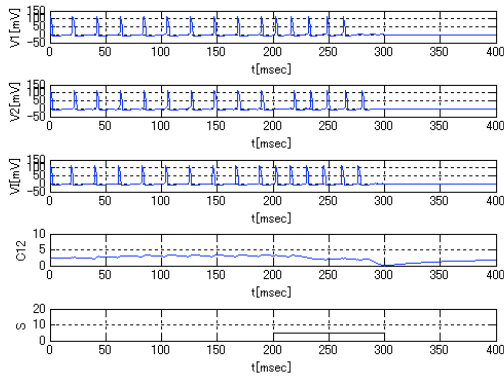
where C_0 , b and τ are positive constants. The constant C_0 is associated with the equilibrium of C_{12} . The constants b and τ denote the efficacy of synaptic plasticity and the time constant of C_{12} , respectively.

III. RESULTS

Throughout the simulation the parameter values except C_0 were given as $C_{21} = 10$, $C_{2l} = 10$, $C_{l2} = 20$, $b = 40$ and $\tau_c = 50$ [ms].



(a) An unsuccessful result. $I = 4$ [$\mu\text{A}/\text{cm}^2$].



(b) A successful result. $I = 5$ [$\mu\text{A}/\text{cm}^2$].

Fig. 2 Inhibition of oscillation by constant input. $C_0 = 2$.

Without stimulation or plasticity, the model has two stable solutions, an oscillatory state by sustained firings and a non-firing state, which are bistable for a parameter region. The larger C_{12} brings the larger basin of the oscillatory solution in the state space of the model in the region.

A. Constant stimulus

First the inhibition of oscillation by constant stimulus to neuron E_1 was examined with plasticity. The amplitude I of the stimulus was increased one by one [$\mu\text{A}/\text{cm}^2$]. Stimulation period is 100ms. Fig. 2 shows an unsuccessful result (a) and a successful result (b) when $C_0 = 2$. The amplitude I not less than 5 [$\mu\text{A}/\text{cm}^2$] was required for inhibition of oscillation.

B. Pulse train stimulus

Next the inhibition of oscillation by pulse train stimulus to neuron E_1 was examined. To simulate the input by neurons in the brain, the stimulus S to neuron E_1 was formulated as

$$S = \sum_{j=1}^P C_{1S} z_{Sj}, \quad (16)$$

where z_{Sj} is the output of neuron E_{Sj} . The membrane potential v_{Sj} and the variable h_{Sj} is given as

$$\frac{dv_{Sj}}{dt} = \frac{G(v_{Sj}, m^\infty(v_{Sj}), 0.8(1 - h_{Sj}), h_{Sj}) + S_j}{C_m} \quad (17)$$

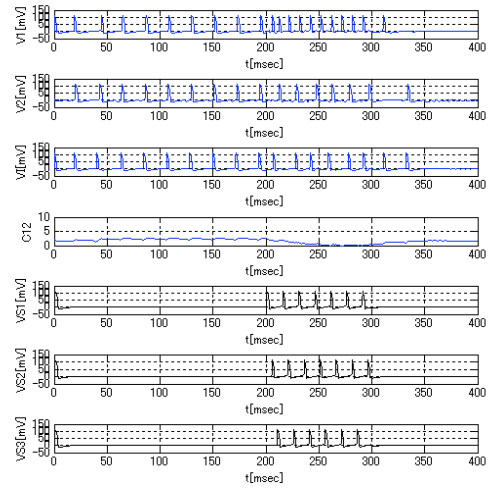


Fig. 3 Inhibition of oscillation by pulse train input. $C_0 = 2$, $I = 10$ [$\mu\text{A}/\text{cm}^2$].

and

$$\frac{dh_{S_j}}{dt} = \alpha_h(v_{S_j})(1 - h_{S_j}) + \beta_h(v_{S_j})h_{S_j}, \quad (18)$$

respectively. The stimulus S_j to input neuron E_{S_j} was expressed as

$$S_j = \begin{cases} I & (200 + 5(j-1) \leq t \leq 300 \text{ [ms]}) \\ 0 & (\text{other time}) \end{cases}, \quad (19)$$

so that firing instances of each input neuron E_{S_j} are different from others. The amplitude I of stimulus to input neurons E_{S_j} is constant with time. The number of input neurons P is three in the present simulation. The amplitude I was increased one by one [$\mu\text{A}/\text{cm}^2$] as case for constant stimulus. Fig. 3 shows a successful result when $C_0 = 2$ and $I = 10[\mu\text{A}/\text{cm}^2]$. The amplitude I not less than $10[\mu\text{A}/\text{cm}^2]$ was required for inhibition of oscillation.

IV. DISCUSSION

The reason why inhibition of oscillation occurs is as follows. When no stimulus is provided, the firings of neurons E_1 and E_2 are synchronized. When constant or pulse train stimulus is provided, those firings are not synchronized. It makes the coupling strength C_{12} decrease according to Eq. (15). Once C_{12} is decreased to the value in which only non-oscillatory solution exists and the stimulus stops, the model neurons stop firing.

In order to investigate the characteristics of the model in more detail, simulation with different values of C_0 was performed. It was observed that there is a threshold of the amplitude I for each C_0 . In order to inhibit the oscillation, larger I than the threshold is required. Moreover, the larger the value of C_0 is, the larger value of I is necessary to inhibit the oscillation. The reason is speculated as follows. The larger C_0 brings the larger stationary value of C_{12} . It additionally brings the larger basin of the oscillatory solution in the state space of the model equations. In order to reduce the value of C_{12} a stronger stimulation is required.

V. CONCLUSIONS

In this study a conceptual and computational neuronal network model with plasticity in the human auditory system was proposed to explain the mechanisms of tinnitus and its management by sound therapy. Through analysis of this model, it was shown that, similar to the previous neural

oscillator model, oscillation can be inhibited due to the change of coupling strength between neurons in the model by supplying constant or pulse train stimulus to the model.

Our future work will expand this model so that it can more effectively relate to the underlying physiology of tinnitus, and explore better stimulation for its inhibition. This in turn will result in improvement in designing sound therapy techniques and stimuli.

ACKNOWLEDGMENT

Authors thank Shota Hattori for his help with computer simulation.

REFERENCES

1. Axelsson A and Ringdahl A (1989) Tinnitus—a study of its prevalence and characteristics. *Br J Audiol* 23(1):53–62
2. Jastreboff P J (1990) Phantom auditory perception (tinnitus): mechanisms of generation and perception. *Neurosci Res* 8(4):221–254
3. Eggermont J J and Roberts L E (2004) The neuroscience of tinnitus, *Trends Neurosci* 27(11):676–682
4. Moller A R (2006) *Neural plasticity and disorders of the nervous system*, Cambridge University Press, Cambridge
5. Tyler R, Coelho C, Tao P et al. (2008) Identifying tinnitus subgroups with cluster analysis. *Am J Audiol* 17(2):S176–S184
6. Henry J. A., Schechter M. A. et al. (2006) Outcomes of clinical trial: tinnitus masking versus tinnitus retraining therapy. *J Am Acad Audiol* 17(2):104–132
7. Fujimoto K, Nagashino H, Kinouchi Y et al. (2006) Analysis of a neural oscillator model with plasticity for treatment of tinnitus. *IFM-BE Proc., World Congress on Med. Phys. & Biomed. Eng., Seoul, Korea, 2006*, 3413–3416
8. Fujimoto K, Nagashino H, Kinouchi Y et al. (2007) A plastic neural network model for sound therapy of tinnitus. *IEEJ Trans on Electrical and Electronic Engineering* 2(4):488–490
9. Fujimoto K, Nagashino H, Kinouchi Y et al. (2007) Dynamical properties of a plastic neural network model for tinnitus therapy and inhibition of oscillation using noise stimulus. *Proc. of the 29th Annual International Conference of the IEEE EMBS, Lyon, France, 2007*, 2408–2411
10. Kawakami H (2001) Dynamics of biological rhythmic phenomena—Nonlinear dynamics applied to ME. *Corona, Tokyo*, ch. 7
11. Hodgkin A L and Huxley A F (1952) A quantitative description of membrane current and its application to conduction and excitation in nerve. *J Physiol* 117:500–544
12. Hebb D O (1949) *The Organization of behavior: A neuropsychological theory*. John Wiley & Sons, New York

Address of the corresponding author:

Author: Dr. Hirofumi Nagashino
 Institute: The University of Tokushima
 Street: 3-18-15 Kuramoto
 City: Tokushima
 Country: Japan
 Email: nagasino@medsci.tokushima-u.ac.jp

Modular Prosthesis of the Larynx for Application in Laryngectomees – A Theoretical Approach

Fridun Nazaradeh¹, Denis Nazaradeh², Marc André Dupré³, and Claus Eckermann⁴

¹ Consultant radiologist and engineer for electronics and computer science, Bottrop, Germany

² Engineer for information technology and project and process auditor ISO 9001, Dusseldorf, Germany

³ Architect and expert for descriptive geometry, Essen, Germany

⁴ Phonation and psychoacoustics, Dorsten, Germany

Abstract— Purpose: A total laryngectomy which usually is carried out after the diagnosis of a laryngeal carcinoma of the stages T3/T4 is leading to dissatisfying results in the postoperative rehabilitation of the patient. The postoperative consequences include the loss of the native voice, the loss of the regular air ways via mouth and nose, the loss of the sense of smell, and the inability to build up an abdominal pressure. This paper deals with the feasibility of a modular larynx prosthesis which enables the laryngectomy patient to talk with his native voice, to breathe via the regular air ways, and to build up abdominal pressure.

Materials and methods: The autonomous prosthesis consists of a device to reproduce the natural human voice, a device to reproduce the natural air ways including an artificial epiglottis to avoid choking, and a system of valves to build up an abdominal pressure e.g. to cough. An additional device is required to analyze, conserve and manage voice characteristics before laryngectomy. The prosthesis consists of two modules: a stationary module and an exchangeable module. This is necessary to avoid a destruction of the electronics during possible radiation therapies and to easily replace the module in case of maintenance.

Conclusions: Regarding the actual possibilities of rehabilitation the modular prosthesis of the larynx for application in laryngectomees means a medical and ethical benefit for the postoperative course in rehabilitation of laryngectomees.

Keywords— Laryngeal carcinoma, laryngectomy, *nervus laryngeus recurrens*, larynx prosthesis, rehabilitation.

I. INTRODUCTION

A. Pathology

The laryngeal carcinoma is one of the most common malignant tumors of the head-neck region. The incidence of laryngeal carcinoma worldwide is approx. 160.000 individuals per year and the worldwide mortality is approx. 90.000 individuals per year [1]. Incidence and mortality are slightly decreasing since the 1990s in male individuals

while incidence and mortality in women are increasing. Incidence peaks in the 5th to 7th decade of life and recently is showing an increase in persons younger than 40 years [2].

A fundamental risk factor for laryngeal carcinoma is smoking, often combined with alcohol ingestion, and work-related exposure to dust and chemicals like halogenated hydrocarbons [3].

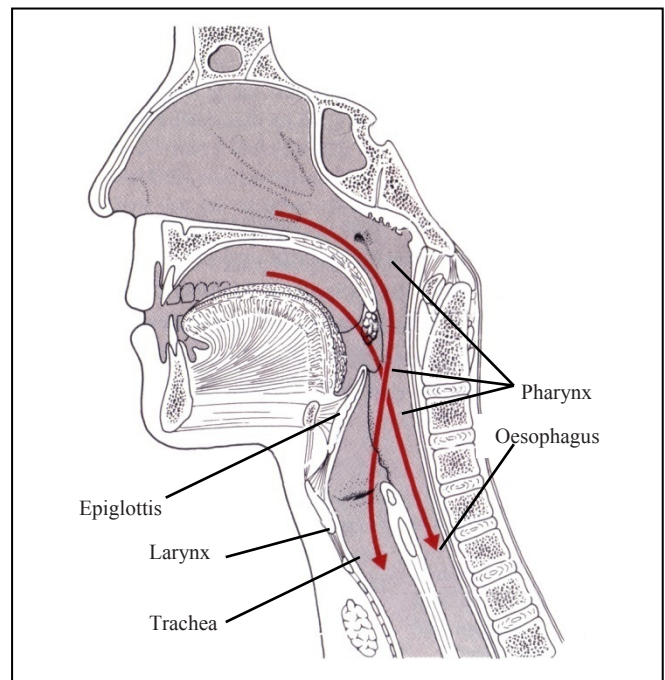


Fig. 1 Anatomy

B. Anatomy

The larynx is an organ of phonation which is located at the upper end of the trachea (Fig. 1). It consists of a skeleton of cartilages which are connected to multiple muscles. The rima glottis, located in the middle of the

larynx, is formed by two opposing plicae vocales, the vocal cords. This complete organ of phonation is called glottis. According to the length of the vocal cords the voice pitch is high or low. The resilience of the vocal cords, which is influenced by specific groups of muscles, is used to change the pitch of tones produced by air which streams through the narrowed glottis. While multiple muscles are included in closing the glottis, only one pair of muscles can significantly open the glottis. This pair of muscles, *M. crycoarytenoideus* (in short “Posticus”), has the major influence on the pitch. Thus, according to the degree of contraction, the muscles are able to open the glottis maximally for forced inspiration or slightly for minor changes of the pitch [4]. The pair of muscles is innervated by the *N. laryngeus recurrens*, a nerve which arises from the 10th cranial nerve, *N. vagus* [5].

C. Present therapy and ways of rehabilitation

Depending on the cancer stage an adequate therapy is initiated. Therapy includes laser treatments, partial resection of the larynx in early stages and total resection of the larynx in advanced stages as well as radiation therapy. Cancer stages T3 and T4 are usually treated by laryngectomy and lead to the permanent loss of the voice and the regular air ways by placement of a tracheostoma [6].

The present state of rehabilitation includes the training of the esophageal voice using the gullet for phonation, the implantation of a vocal fistula using valve vocals, or the use of electrolaryngeal speech aids. Depending on the valve and electrolarynx the synthetically produced voice sounds either rattling or monotonous (robot voice). Artificial valves used in vocal fistulas are often colonized by fungus and bacteria which lead to local infections [7].

To summarize, the state of rehabilitation is dissatisfying to the patient: the consequences of therapy mean the loss of the voice, the loss of the regular air ways, and the inability to smell and to build up an abdominal pressure.

II. MATERIALS AND METHODS

A. Electronics and information technology

This paper presents a modular prosthesis of the larynx which gives the laryngectomee the continuing ability to talk with his native voice. The prosthesis of the larynx includes a device to reproduce human voices, a neural interface to receive the impulses on the laryngeal recurrent nerve, a processing unit to decode the neural impulses and to translate them into the individual voice characteristics of the

laryngectomee, a voice output, and the prosthesis’ power supply.

The customized prosthesis is placed between the pharynx and the trachea during laryngectomy [8, 9]. It is made up of a biocompatible, fungicidal and bactericidal material, that adheres, once sutured with the trachea [10]. The processing unit consists of a microprocessor and the audio component. The audio component’s main circuitry consists of a filter-component with multiple fixed and adjustable filter coefficients to determine the voice characteristics dynamically within a given range. The given range of the fixed filter components is defined by preoperative voice recordings and analyses of the laryngectomee’s native voice. The audio component’s adjustable filter components can be dynamically altered by the microprocessor in real-time for the generation of situational voice characteristics. The audio component’s main circuitry is a vocoder chip comparable to the vocoders used in digital cellular phones [11, 12].

Therefore the prosthesis contains the neural interface to connect the laryngeal recurrent nerve, a programmable microprocessor using Fuzzy logic, a RAM, an EEPROM containing the firmware, and the audio component [13, 14, 15]. The prosthesis also contains a preamplifier to amplify the neural impulses, an audio signal amplifier, and a speaker. The power is supplied by lithium polymer batteries which are charged by an inductive collar [16]. A transponder unit is used for bidirectional communication between the prosthesis and a service computer (e.g. firmware updates, adjustment of fixed filter values, status information of the prosthesis etc.) using technologies like low power RF.

B. Conserving and administration of voice characteristics

The system to digitally conserve and administrate the voiced and unvoiced portions of the patient’s native voice characteristics contains a digital recording unit, an analyzing unit including the identical filter components as the prosthesis, and an audio database [12]. After being digitally recorded, the patient’s voice is analyzed by frequency, structure and range of voiced portions, in particular the tessitura.

The analyzing unit uses Fast Fourier Transform (FFT) to transform the voice signal from the time domain into the frequency domain. After spectrum analysis the analyzing unit compares the digitally recorded native voice with the output of its digital filter units to approach the highest similarity in the input signal and the reproduced signal. A regular computer with specific software controls the recording unit, the analyzing unit and its digital filters. Audible control is provided by loudspeakers connected to

the system. The generated data for filter settings of the voiced portions will be transferred to the prosthesis via the transponder unit after the implantation.

C. Epiglottis prosthesis

The epiglottis prosthesis is located on the cranial part of the laryngeal prosthesis which is sutured with the pharynx and trachea (Fig. 2). The epiglottis prosthesis is made up of a biocompatible, fungicidal and bactericidal material and replicates the anatomic features and sizes of the native epiglottis. The epiglottis prosthesis protects the cranial aperture of the trachea from chyme being choked and is pressed down by the tongue during swallowing. When the chyme has passed a coil spring puts the artificial epiglottis back into its home position [8, 17, 18, 19].

In case of an emergency intubation of the patient the coil spring of the artificial epiglottis gives way to the laryngoscope, thus facilitating access to the trachea.

D. Valve engineering

The valve appliance replicates the natural air way functionality and is located in the caudal part of the laryngeal prosthesis (Fig. 2). The valve appliance's width is that of a regular trachea's inner diameter from 1,0 to 1,5 cm, and its height is from 1,0 to 1,5 cm. It is made up of titanium and covered by a biocompatible, fungicidal and bactericidal material [9, 10]. The valve appliance consists of a device to build up air pressure and a pressurizing device.

The hatches of the air pressure device will suddenly be hermetically closed in forced expiration. When air pressure abruptly exceeds a defined limit the pressurizing device opens a pressure relief valve explosively. In the opposite case of falling air pressure - during inspiration - the hatches of the air pressure device return to their home position by pivot bearings.

The air pressure device's hatches can be pushed in caudal direction to allow intubation by a tubus if the laryngectomee needs to be mechanically ventilated [9, 19].

E. Stationary and exchangeable module

A radiation therapy can be necessary to destroy remaining tumor cells after laryngectomy. The implantation of the laryngeal prosthesis is not possible after radiation therapy as the tissue is harmed by ionizing radiation (radiation fibrosis, ulcerations) which impedes the engraftment of the laryngeal prosthesis [20, 21]. Implantation of the laryngeal prosthesis before radiation therapy is not advisable, either, as the doses used for

radiation therapy vary from 30 – 70 Gray which will severely damage electronic components made up of doped silicon. Further damaging solid-state physical effects include the Compton effect and the generation of high currents in the circuitry during radiation [22]. A permanently implanted electronic device can become useless by aging or component failure. In the case of component failure or the necessity of a hardware update, or in the case of a mechanical failure the whole prosthesis had to be explanted.

The laryngeal prosthesis which gives the laryngectomee continuing ability to talk with his native voice therefore needs to be divided into a stationary and an exchangeable module (Fig. 2). Stationary and exchangeable module are made up of a biocompatible, fungicidal and bactericidal material. The stationary module has at least one interface connecting the laryngeal recurrent nerve to the prosthesis and at least one contact to the exchangeable module's electronic devices. The exchangeable module is inserted into the stationary module by a plug-and-turn connector. The exchangeable module contains the valve appliance, the electronic devices with their power supply, the contact to the stationary module, and the epiglottis prosthesis. After the resection of the larynx the stationary module is placed permanently between pharynx and trachea. A dummy module 'B' which excludes the electronic devices and power supply but includes the valves and the artificial epiglottis is inserted into the stationary module for radiation therapy.

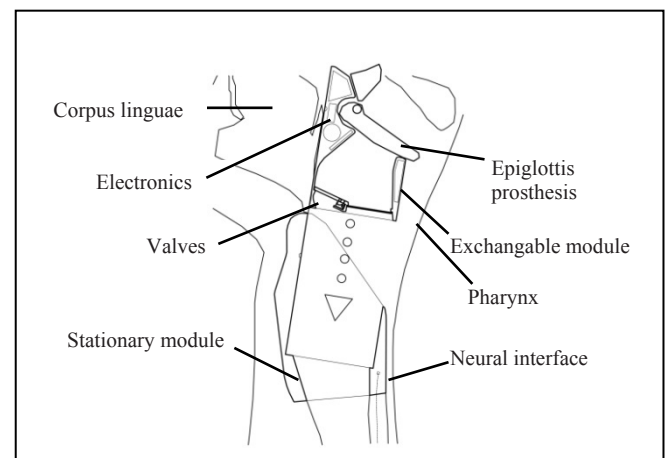


Fig. 2 Modular prosthesis of the larynx

After the radiation therapy the dummy module 'B' is replaced by the fully equipped module 'A'. In the case of a mechanical or electronic component failure or if hardware

update is required, the defected or serviced module ‚A‘ is replaced by a functional module ‚A‘. The replacement is done via the opened mouth of the sedated patient without the requirement of an operation.

This modular solution minimizes the complexity of servicing and replacing the laryngeal prosthesis and avoids the danger of a damage to the laryngeal prosthesis by ionizing radiation.

III. CONCLUSIONS

The further development of the laryngeal prosthesis requires research in the fields of neurophysiology, neural interface design and the implantation and durability of foreign material in the head-neck region.

The mentioned materials and methods, namely the neural interface, the audio component, the transponder unit, the system to digitally conserve and administrate the voiced and unvoiced portions, the epiglottis prosthesis, and the valve appliance represent capable state-of-the-art technology.

Having said that, the comparison of the capable state-of-the-art technology with the actual ways of rehabilitation leaves a disappointing and dissatisfying mark as the rehabilitated laryngectomee still is vastly hindered after his therapy and rehabilitation [6, 7].

Due to the benefits of the modular prosthesis of the larynx the so far severely disabled laryngectomee will be adequately rehabilitated by the continuing ability to talk with his natural voice, to breathe via his regular air ways, and to build up an abdominal pressure.

REFERENCES

1. Ferlay J, Bray F, Pisani P et al. (2004) Globocan 2002: Cancer Incidence, Mortality and Prevalence Worldwide IARC CancerBase No. 5. version 2.0. IARC Press, Lyon
2. Giersipen K, Brünings-Kuppe C, Lehmann C (2004) The Bremen Mortality Index. Bundesgesundheitsblatt Gesundheitsforschung Gesundheitsschutz 47(5): 451 - 456
3. Righini CA, Karkas A, Morel N et al. (2008) Risk factors for cancers of the oral cavity, pharynx (cavity excluded) and larynx. Presse Med. 37(9): 1229 - 1240
4. Schiebler T, Schmidt W, Zilles K (2005) Anatomie: Zytologie, Histologie, Entwicklungsgeschichte, makroskopische und mikroskopische Anatomie des Menschen – 9. Auflage. Springer, Berlin Heidelberg New York, 435 – 441
5. Schiebler T, Schmidt W, Zilles K (2005) Anatomie: Zytologie, Histologie, Entwicklungsgeschichte, makroskopische und mikroskopische Anatomie des Menschen – 9. Auflage. Springer, Berlin Heidelberg New York, 463 et seq.
6. Hudson WR, Cavanaugh PJ (1965) Combined surgical and radiation management of carcinoma of the laryngopharynx. Laryngoscope 75: 1123 - 1138
7. Pawar PV, Sayed SI, Kazi R et al. (2008) Current status and future prospects in prosthetic voice rehabilitation following laryngectomy. J Cancer Res Ther. 4(4): 186-191
8. Eckel HE, Sittel C, Zorowka P et al. (1994) Dimensions of the laryngeal framework in adults. Surg Radiol Anat 16(1): 31 – 36
9. Selbie WS, Gewalt SL, Ludlow CL et al. (2002) Developing an anatomical model of the human laryngeal cartilages from magnetic resonance imaging. J Acoust Soc Am 112 (3 Pt 1): 1077 – 1090
10. Prasad CK, Muraleedharan CV, Krishnan LK (2007) Bio-mimetic composite matrix that promotes endothelial cell growth for modification of biomaterial surface. J Biomed Mater Res A. 80(3): 644 – 654
11. Ivanov VN, Lanne AA, Moroz IV et al. (1996) Implementing vocoder and HF modem algorithms using the TMS320C31 DSP. Digital Signal Processing Solutions: 7 – 23
12. Saito S, Nakata K (1985) Fundamentals of speech signal processing. Academic Press: 31 – 41
13. Kovacs GT, Hentz VR, Rosen JM (1994) The nerve chip: technology development for a chronic neural interface. Rehabilitation R&D Center Progress Report
14. Fromherz P (2002) Electrical interfacing of nerve cells and semiconductor chips. Chemphyschem 3: 276 – 284
15. Roark RM, Li JCL, Schaefer SD et al. (2002) Multiple motor unit recordings of laryngeal muscles: the technique of vector laryngeal electromyography. Laryngoscope 112: 2196 – 2203
16. Yamamoto T, Koshiji K, Homma A et al. (2008) Improvement in magnetic field immunity of externally-coupled transcutaneous energy transmission system for a totally implantable artificial heart. J Artif Organs 11(4): 238 – 240
17. Schiebler T, Schmidt W, Zilles K (2005) Anatomie: Zytologie, Histologie, Entwicklungsgeschichte, makroskopische und mikroskopische Anatomie des Menschen – 9. Auflage. Springer, Berlin Heidelberg New York, 433 – 436
18. Storey AT (1968) Laryngeal initiation of swallowing. Experimental Neurology 20(3): 359 – 365
19. Tayama N, Chan RW, Kaga K et al. (2001) Geometric characterization of the laryngeal cartilage framework for the purpose of biomechanical modeling. Ann Otol Rhinol Laryngol. 110(12): 1154 – 1161
20. Budach W (1998) Das chronische Larynxödem als Spätreaktion nach Radiochemotherapie. HNO 46(8): 708 – 711
21. Adelstein DJ (2005) Squamous Cell Head and Neck Cancer Recent Clinical Progress and Prospects for the Future. Humana Press: 79 – 92
22. Messenger GC, Ash MS (1992) The Effects of Radiation on Electronic Systems. Van Nostrand Reinhold, New York

Author: Dr. med. Dipl.-Ing. Fridun Nazaradeh
 Institute: Katholische Kliniken Essen-Nord-West gGmbH –
 Akademisches Lehrkrankenhaus der Universität Essen-Duisburg.
 Street: Lindhorststr. 215
 City: 46242 Bottrop
 Country: Germany
 Email: dr.nazaradeh@yahoo.com

A novel method exploiting the nociceptive withdrawal reflexes in rehabilitation of hemiplegic gait

J. Emborg¹, J. D. Bendtsen², E.G. Spaich¹, O.K. Andersen¹

¹ Center for Sensory-Motor Interaction (SMI), Aalborg University, Denmark

² Department of Electronic Systems, Automation and Control, Aalborg University, Denmark

Abstract—A novel closed loop method for improving gait in hemiplegic patients by supporting the production of the swing phase using electrical stimulations to evoke the nociceptive withdrawal reflex was developed and evaluated in one chronic hemiplegic subject. Electrical stimulations were delivered to 4 locations on the sole of the foot at 3 different times between heel-off and toe-off. The system exploits the modular organization of the nociceptive withdrawal reflex and its stimulation site- and gait phase-modulation in order to evoke optimal flexion of the hip, knee and ankle joints in the early swing phase. A Rule-based Model Reference Adaptive Controller (MRAC) was designed to select the optimal stimulation parameters. It was hypothesized that the MRAC-system would result in a better walking pattern compared with a pre-programmed fixed stimulation pattern controller. Based on the unperturbed gait and withdrawal strategies of the patient, an individual controller target for hip, knee and ankle flexion was set. The patient walked 10 min with the MRAC-system, 10 min with the fixed pre-programmed stimulation pattern, and 10 min with no-stimulation. The results indicate that both stimulation paradigms resulted in a more functional gait compared with no-stimulation and that the control strategy in the MRAC system is superior suggesting that it will be able to adapt better to the varying needs during rehabilitation therapy.

Keywords— Nociceptive withdrawal reflex, Reflex modulation, Human locomotion, Automated Control, Model reference adaptive control.

I. INTRODUCTION

Patients who have suffered a cerebral stroke often have problems controlling the lower limbs, leading to a compromised gait pattern. In the swing-phase, the patients typically exhibit decreased hip flexion, decreased knee flexion, decreased knee extension at heel strike and decreased ankle dorsiflexion throughout the swing-phase [1]. To support the production of the swing phase, the withdrawal reflex can be evoked as a synergistic contraction of flexor muscles resulting in hip and knee flexion in combination with ankle dorsiflexion (Figure 1A). Recent studies on lower limb nociceptive withdrawal reflexes in humans elicited by painful electrical stimulation of the sole of the foot indicate that the reflex response is dependent on the stimulation site [2], intensity [3], and frequency [3]. Moreover, the site

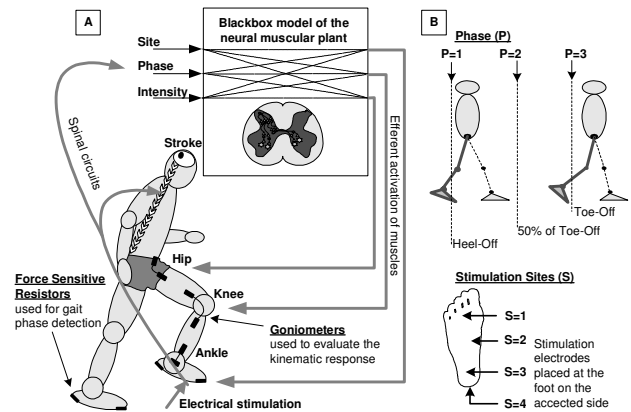


Figure 1A: The neuro-muscular plant from stimulation to kinematic response. Painful electrical stimulations lead to afferent input to spinal circuits which respond with activation of the muscle groups controlling the stimulated limb. This removes the affected site from the stimulus by activation of muscles controlling the hip, knee and ankle joints depending on the stimulation parameters and posture. B: Stimulation is delivered to 4 locations of the sole of the foot at 3 different time points between heel-off and toe-off.

dependent reflex responses are modulated by posture [4] and the gait cycle [5].

The efficiency of two schemes for controlling the withdrawal reflex in a system for improving the hemiplegic gait by supporting the swing phase was examined in this study. The system exploited the differences in withdrawal strategies depending on stimulation site and stimulation onset during gait to tailor the desired movement for the individual patient. An open loop system and a novel method for closed loop control were designed and tested. The focus of this paper is primarily on the development of a method for closed loop control; however, a full paper describing the test of the system on a larger group of patients is in preparation.

A. Modeling and control

A precise parametric model of the kinematic reflex response for hip, knee and ankle joint is difficult to establish because the knowledge about the neural pathways from afferent activation to the kinematic response is not com-

plete. Furthermore, due to substantial changes that may occur in the muscle and nervous system after a stroke, an adaptive model is required to characterize this highly individual and plastic system.

The neuro-muscular plant can be characterized as a Multiple Input Multiple Output (MIMO) dynamical system (Figure 1A). The inputs *Site* and *Phase* are assumed to be categorical variables without any intrinsic ordering but evoking different withdrawal strategies, while *Intensity* is a continuous variable mainly affecting the amplitude of the reflex response. In this study it was chosen to fix the intensity at one level and develop a method for controlling only the categorical variables. The outputs are coupled, highly time variant, stochastic and nonlinear. Furthermore there are significant latencies in the system, since the mechanical response typically occurs 140-360ms from stimulation onset [6]. Considering that a normal swing phase lasts approximately 400ms, it is obvious that only one stimulation train can be delivered and evaluated in each swing phase. Further, adaptation between every step is required in the controller design to handle reflex habituation (gradually lower reflex responses) and gradual improvement in walking performance during therapy.

The control system was designed as a rule-based Model Reference Adaptive System (MRAC) [7] [8]. Conventional MRAC concepts are associated with parametric models [7], but in this application neither model structure nor parameter values are known. Instead, a modified MRAC was introduced, in which a model of the entire kinematic trajectories within the swing phase was recursively derived from input-output data for the three joint angles. Based on this model the controller compared the deviation from each trajectory to a pre-defined target trajectory.

The advantage of the MRAC scheme (Figure 2) is that even though the system is very poorly known the desired output can still be designated to follow the output of a reference model with specified dynamics. The error (e_2) is defined as the difference between the estimated outputs of the system (\hat{Y}) and the reference model (Y_m , Figure 3B). The regulator has parameters that are changed in such a way that the error e_2 is minimized

$$e_2 = \int_{T_0}^{T_H} (\hat{Y} - Y_m)^2 dt \quad (1)$$

Here t denotes time, $t \geq 0$, T_0 describes the start of the push-off phase (*heel-off*) and T_H describes the end of the swing phase (*heel-on*).

The desired closed loop system is described through the target trajectory Y_m

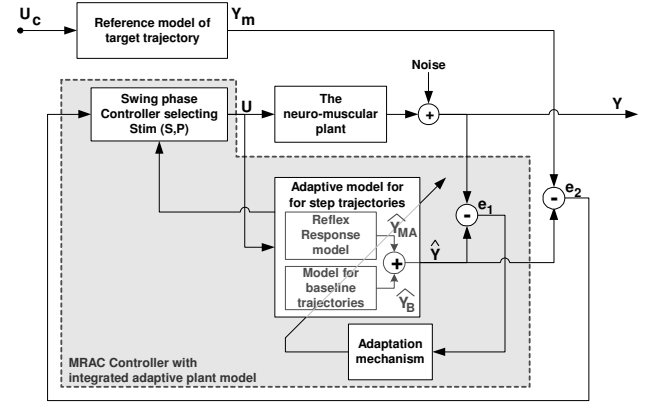


Figure 2: Block-diagram for the rule-based Model Reference Adaptive Control System.

$$Y_m(t) = \begin{bmatrix} \mathcal{T}_{HIP}(t) \\ \mathcal{T}_{KNEE}(t) \\ \mathcal{T}_{ANKLE}(t) \end{bmatrix} \text{ for } T_0 \leq t \leq T_H \quad (2)$$

and the neuro-muscular plant model is described by \hat{Y}

$$\hat{Y}(S, P, t) = \begin{bmatrix} \mathcal{T}_{HIP}(S, P, t) \\ \mathcal{T}_{KNEE}(S, P, t) \\ \mathcal{T}_{ANKLE}(S, P, t) \end{bmatrix} \text{ for } T_0 \leq t \leq T_H \quad (3)$$

Where S denotes the *Site*, P the *Phase*, \mathcal{T} symbols the *trajectories* and $S \in \bar{S} = \{1,2,3,4\}$, $P \in \bar{P} = \{1,2,3\}$. The characteristics of S and P are defined in Figure 1B.

The dynamics of the outer loop which adjusts the controller parameters is normally assumed to be slower than the inner loop [7] and the adjustments are often based on a gradient approach. However, since a parametric model was not available for the present system the gradient approach was not feasible. Instead a simple moving average (MA) approach for modeling the trajectory was introduced and the length of the MA-algorithm reflected the adaptation rate.

The hypothesis of this study was: A rule-based MRAC-system that exploits the modular organization of the nociceptive withdrawal reflex and the site and phase modulation of the reflex during gait is superior to a pre-programmed fixed stimulation pattern for swing phase support in hemiplegic gait. This was tested in a case study on one chronic hemiplegic subject.

II. METHODS & MATERIALS

The hemiplegic subject: One hemiplegic subject participated in the study (Male, age 50, left body side affected, time since stroke: 2 years). Informed consent was obtained and the Helsinki Declaration was respected. The study was approved by the local Ethical committee, approval number N-20070026.

Electrical stimulation: The method for evoking the reflex has been described in earlier publications [3;6;9]. In short, the nociceptive withdrawal reflex was elicited by transcutaneous electrical stimulation delivered to one of four sites on the sole of the foot on the affected side (Figure 1B). Each stimulus consisted of a constant current pulse burst of five individual 1ms pulses delivered at 200 Hz. This stimulus train was repeated four times at a frequency of 15 Hz. The stimulus could be delivered at three phases of the gait cycle between heel-off and toe-off on the affected side (Figure 1B).

Gait analysis: Three goniometers (type SG150 and SG110/A, Biometrics Ltd, Gwent, U.K.) were mounted on the affected limb across the ankle, knee, and hip joints to monitor the kinematic response (Figure 1A). Timing of heel and toe contact with the ground was measured by Force Sensitive Resistors (FSR). All data was sampled at 4 kHz, and stored for later analysis.

Experimental protocol: The experiment was split in two sub-sessions:

Part-I: An initial assessment of baseline gait and measurements of reflex responses to stimulation were performed in order to build an initial model of the patients reflex responses to be used in Part-II. Stimulation was delivered in a random sequence, repeating each combination of stimulation site and phase five times.

Part-II: Test of the closed loop system. The patient walked 10 min with the MRAC-system, 10 min with a pre-programmed fixed stimulation pattern, and 10 min without stimulation. Stimulation was delivered in four out of five steps.

The adaptive neuro-muscular plant model: This plant model, \hat{Y} , consisted of two parts: A MA-model for the kinematic reflex responses, \hat{Y}_{MA} and a model for the trajectory of the unperturbed gait (baseline trajectory), \hat{Y}_B (Figure 2)

$$\hat{Y}(S, P, t) = \hat{Y}_{MA}(S, P, t) + \hat{Y}_B(t) \quad (4)$$

In Part-I \hat{Y}_{MA} was calculated as the difference between the post-stimulation goniogram and the corresponding goniogram recorded in the step cycle immediately prior to the stimulation (unperturbed gait) (Figure 3A).

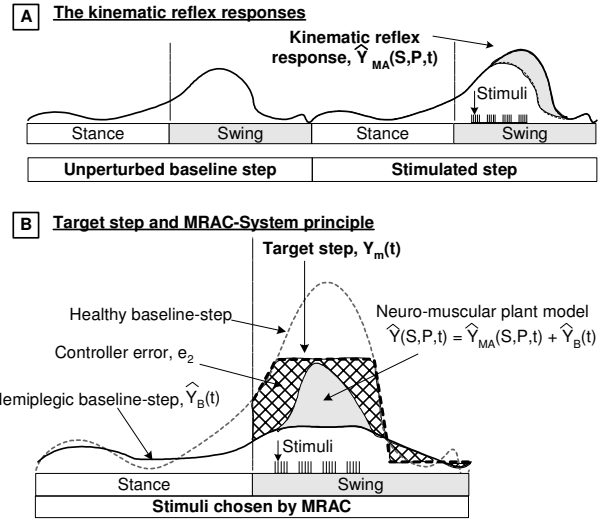


Figure 3A: The kinematic reflex response. B: A sketch of the MRAC-system principle.

The baseline model (\hat{Y}_B) was extracted as an average of all unperturbed control steps.

In Part-II, both models were continuously updated adaptively. The stimulation was disabled every fifth step and the acquired *baseline-step* was used to update (\hat{Y}_B). In the other four *controller-corrected-steps*, the reflex response model (\hat{Y}_{MA}) was updated using a simple MA approach to estimate \hat{Y}_{MA} at time t , where the MA of the last 5 steps corresponding to the same input parameters was calculated:

$$\hat{Y}_{MA}(S_v, P_v, T_{0,v} + \Delta t) = \frac{1}{n} \sum_k \begin{bmatrix} \mathcal{J}_{HIP}(S_k, P_k, T_{0,k} + \Delta t) \\ \mathcal{J}_{KNEE}(S_k, P_k, T_{0,k} + \Delta t) \\ \mathcal{J}_{ANKLE}(S_k, P_k, T_{0,k} + \Delta t) \end{bmatrix} \quad \Delta t \in [0; T_H - T_0] \quad (5)$$

Here v denotes the *step-number*, the model adaptation rate was adjusted by the length of the MA filter, $n=5$ and k denotes the last n steps where $S_k=S_v$ and $P_k=P_v$.

MRAC swing phase controller: At the end of each swing phase, the present step was extracted

$$Y(t) = \begin{bmatrix} \mathcal{J}_{HIP}(S, P, t) \\ \mathcal{J}_{KNEE}(S, P, t) \\ \mathcal{J}_{ANKLE}(S, P, t) \end{bmatrix} \quad \text{for } T_0 \leq t \leq T_H \quad (6)$$

If the acquired step was a controller-corrected-step, the reflex response model was updated based on the subtraction of the latest baseline-step from the present step, $\hat{Y}_{MA} = Y - \hat{Y}_B$. Otherwise the baseline model \hat{Y}_B was updated to be

equal to the present step, $\hat{Y}_B = Y$. The predicted step (\hat{Y}) was calculated for all input options based on the adaptive neuromuscular plant model (Figure 2). A weight matrix with a value for each joint (W_j) enabled prioritizing between joints in the control system

$$W_j = \begin{bmatrix} W_{HIP} & 0 & 0 \\ 0 & W_{KNEE} & 0 \\ 0 & 0 & W_{ANKLE} \end{bmatrix} \quad (7)$$

A weighted sum of the squared error (Figure 2, e_2) was calculated using

$$e_2(S, P) = \frac{1}{T_H - T_0} \int_{T_0}^{T_H} [Y_m(t) - \hat{Y}(t)]^T W_j [Y_m(t) - \hat{Y}(t)] dt \quad (8)$$

The input that minimized the weighted squared error was chosen for the subsequent stimulus and delivered within the subsequent swing phase

$$[S, P]_{v+1} = \underset{S \in \mathcal{S}, P \in \mathcal{P}}{\operatorname{argmin}} \{e_2(S_v, P_v)\} \quad (9)$$

Reference model of target step: To define a realistic target, the unperturbed gait of the hemiplegic patient was compared to a normal healthy reference. This resulted in an individual controller target for each joint, $Y_m(t)$ (Figure 3B). The primary problem for the present subject was lack of knee flexion secondarily insufficient ankle dorsiflexion. Target trajectories that counteracted this was constructed and the weight matrix was set to: $W_{HIP} = 0$, $W_{KNEE} = 0.6$, $W_{ANKLE} = 0.4$.

Fixed pattern of stimulation (FPS): The open loop system delivered stimulation to the arc of the foot at heel-off.

III. RESULTS

Both stimulation paradigms resulted in an improved gait pattern of the patient with additional knee flexion and ankle dorsiflexion. The FPS-system added on average 3.2° knee flexion and 1.7° ankle dorsiflexion while the MRAC system added 6.1° knee flexion and 2.0° dorsiflexion.

IV. DISCUSSION AND CONCLUSION

Two online, real-time, swing phase controllers that exploit the modular organization of the nociceptive withdrawal reflex were designed, implemented, and tested. Both resulted in improved gait pattern compared with no-stimulation. However, as hypnotized, the MRAC-system

was more efficient to provide both knee flexion and ankle dorsiflexion. This suggests that the MRAC system will probably be able to adapt better to the varying needs during rehabilitation therapy.

The novelty of the rule-based MRAC-system system is the use of moving average models of whole trajectories to allow control of the categorical variables *Site* and *Phase*.

The MRAC-system alternates stimulation parameters. This might help maintaining sufficient reflex response by minimizing reflex habituation. Dishabituation by changing stimulation site has been demonstrated by Dimitrijevic et. al. [10] who observed that stimulation at sites 3-4cm from a habituated stimulation site still evokes a full response.

REFERENCES

1. S. Moore, K. Schurr, A. Wales, A. Moseley, and R. Herbert, "Observation and analysis of hemiplegic gait: Swing phase," *Aust. J. Physiother.*, vol. 39, no. 4, pp. 271-278, 1993.
2. O. K. Andersen, F. A. Sonnenborg, and L. Arendt-Nielsen, "Modular organization of human leg withdrawal reflexes elicited by electrical stimulation of the foot sole," *Muscle Nerve*, vol. 22, no. 11, pp. 1520-1530, Nov. 1999.
3. E. G. Spaich, T. Collet, L. Arendt-Nielsen, and O. K. Andersen, "Repetitive painful stimulation evokes site, phase, and frequency modulated responses during the swing phase of the gait cycle: preliminary results," *In: Gantchev, N., (ed.) From Basic Motor Control to Functional Recovery IV. Sofia: Marin Drinov Academic Publishing House*, pp. 136-140, 2005.
4. O. K. Andersen, F. Sonnenborg, Z. Matjacic, and L. Arendt-Nielsen, "Foot-sole reflex receptive fields for human withdrawal reflexes in symmetrical standing position," *Exp. Brain Res.*, vol. 152, no. 4, pp. 434-443, Oct. 2003.
5. E. G. Spaich, L. Arendt-Nielsen, and O. K. Andersen, "Modulation of lower limb withdrawal reflexes during gait: a topographical study," *J. Neurophysiol.*, vol. 91, no. 1, pp. 258-266, Jan. 2004.
6. E. G. Spaich, H. H. Hinge, L. Arendt-Nielsen, and O. K. Andersen, "Modulation of the withdrawal reflex during hemiplegic gait: effect of stimulation site and gait phase," *Clin. Neurophysiol.*, vol. 117, no. 11, pp. 2482-2495, Nov. 2006.
7. K. J. Astrom and B. Wittenmark, *Adaptive Control* Addison-Wesley, 1989. ISBN: 0-201-09720-6
8. I. D. Landau, "Survey of Model Reference Adaptive Techniques - Theory and Applications," *Automatica*, vol. 10, no. 4, pp. 353-379, 1974.
9. J. Emborg, E. G. Spaich, and O. K. Andersen, "Withdrawal reflexes examined during human gait by ground reaction forces: site and gait phase dependency," *Med. Biol. Eng. Comput.*, Oct. 2008.
10. M. R. Dimitrijevic and P. W. Nathan, "Studies of spasticity in man. 5. Dishabituation of the flexion reflex in spinal man," *Brain*, vol. 94, no. 1, pp. 77-90, 1971.

Author: Jonas Emborg
 Institute: Center for Sensory-Motor Interaction
 Street: Fredrik Bajers Vej 7 D3
 City: DK-9220 Aalborg
 Country: Denmark
 Email: jemborg@hst.aau.dk

Compact Assistive Rehabilitation Devices— Concept and Preliminary Function Test

O. Ivlev^{1,2}, D. Baiden¹, A. Wilkening^{1,2}, C. Koch³, and H.-D. Haas³

¹ FWBI Friedrich-Wilhelm-Bessel-Institute Research Company, Bremen, Germany

² University of Bremen, Institute of Automation, Germany

³ Dr. Paul Koch GmbH, Frickenhausen, Germany

Abstract— Conceptual design of compact light-weight devices for lower extremity motion therapy and rehabilitation is presented. The core of these devices are new inherent compliant (soft) fluidic actuators of rotary type, which generally provide safe and gentle treatment. The actuator compliance can be varied by pressure regulation, which makes soft fluidic actuators very suitable for making the transition from continuous passive motion to active (assistive) behavior during the therapy depending on patient activity. The assistive behavior can be realized without force measurements by means of expensive sensors.

Keywords— Assistive motion therapy, rehabilitation robots, soft actuators.

I. INTRODUCTION

The patient-cooperative or assistive rehabilitation robots have obvious therapeutic advantages in comparison with conventional motion therapy devices like continuous passive motion (CPM) machines. It is assumed that patient-cooperative strategies will maximize the therapeutic outcome [1], the treatment period can be reduced and the medical costs will decrease. A recent study confirms the effectiveness of the robot assisted therapy in neurorehabilitation [2].

In fact rehabilitation robots are currently barely used in praxis as the less effective, but more simple and budget CPM-machines. By using of inherent compliant, or “soft” actuators, which allow slight deviations from the given position, the human-machine interaction can occur in a gentle and more comfortable manner. Between a variety of existing inherent compliant actuators the soft fluidic (pneumatic) actuators occupy a unique position. In addition to an inherent safety this kind of soft actuators have extremely low weight combined with high force amounts, therefore soft fluidic actuators are predestinated for safe human-machine interaction, particularly with devices of motion therapy. Instead of elaborate force measurements the working forces can be estimated [3, 4], which makes these devices really simple and cost-efficient.

With soft fluidic actuators of rotary type, which are currently being developed [5], compact and light-weight assistive devices for motion therapy and rehabilitation can be

designed. In comparison with the previously developed actuators with pleated rotary elastic chambers (pREC-actuator) [6, 7], destined for soft robotic joints, the new (patent pending) actuators utilize other techniques for forming of working chambers. These new types of rotary chambers – “buckled” chamber (bREC) and “coiled” chamber (cREC) – allow construction of “slim” REC-actuators in shape of a flat cylinder, whose diameter is larger than their height. With pREC such slim design is not possible. The initial tests of new “slim” REC-actuators show partly better performances (working torque and angle) as pREC-actuators and they are undoubtedly better suitable for integration in rehabilitation devices. The conceptual design of such devices is presented in the following sections.

II. MOTION THERAPY DEVICES FOR LOWER EXTREMITY – STATE OF THE ART

The majority of today existing patient-cooperating rehabilitation devices for lower extremity are designed for gait training [1, 2, 8, 10]. The ranges of motion in each joint are restricted according to the task requirements, i.e. about 65° in knee and about 50° in hip.

For full-range joint mobilisation, i.e. about 130° in knee and about 100° in hip, as it is often required for immediate post-operative treatment after surgical intervention, various CPM splints are mainly in the use [11]. Compact and portable assistive lower-limb devices for single joints are still missing.

There are generally two possibilities to couple a motion therapy device, to be it a rehabilitation robot or a CPM-machine, with a human limb:

- a) using free linkage or end-point based solution,
- b) using jointed (motorized) splint or exoskeleton-like solution.

The main difference is that in the first case the moving mechanism, i.e. a kinematic chain, and the human limb have only one contact spot, while in the second case a kinematic chain is attached at several points along the user’s limb. The advantages and disadvantage of both solutions are well known and detailed discussed in literature [2, 8, 10, 11]. The end-point systems provide an excellent adjustability to

the user's size as well as a long-term comfort and allow multi-axis motion. However the joint stability as well as the control precision of individual joints is very poor. The exoskeleton-like systems can be distinguished in anatomic (kinematically equivalent to the human limb) and non-anatomic, kinematically different with respect to the human limb. The anatomic exoskeletons allow a precise control of individual joints provided that the mechanical axes coincide with the limb axes. Though the long-term comfort for anatomic exoskeletons is better, the user size adjustability is poorer than in non-anatomic systems.

III. CONCEPTUAL DESIGN

Unlike most of conventional CPM, equipped with linear electrical drive affecting the foot, the soft REC-actuator provides directly the rotational movement in the knee joint. Such mechanical scheme (with the actuated knee joint) is implemented in the Otto Bock Lower Limb CPM L4D/L4KD, although using standard – not soft – electric motors with gears. According to the product flyer, treatment benefits of such mechanics include constant angular velocity over the entire range of motion and minimized anterior tibial translation and joint compression.

Conceptual design of two new modular motion therapy devices for lower extremity using slim-line REC-actuators are shown in Fig. 1 (the “full-leg”-concept) and in Fig. 2 (the “free-knee”-concept). Both concepts utilize the constrained (i.e. splint or exoskeleton-like) anatomic solution, whereby the complex leg movement is restricted to only the sagittal plane. Compactness, portability and a low weight should make these devices suitable for hospital use as well as for application at home.

A. “Full-Leg”-Concept

The simultaneous movement in knee and hip joints is ensured due to mechanical linkage with two passive sliders. The actuation of the hip joint with separate actuators is also possible but not applied because of cost reasons.

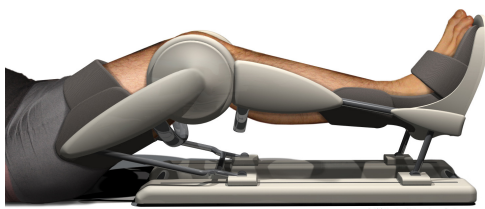


Fig. 1 “Full-Leg”-Concept

With the REC-actuators producing considerable torques in the angle area from 0 to 130° the full ranges of motion in knee as well as in hip are achievable.

B. “Free-Knee”-Concept

If only knee mobilization without hip movements is requested, the device shown in Fig. 2 can be applied. The range of knee motion is admittedly restricted to about 90°, however the nature of lower leg movement is similar to the gentle approach taken by a physiotherapist when manipulating the limb manually immediately after surgical intervention.



Fig. 2 “Free-Knee”-Concept

In the device shown in Fig. 2 the disposition of thigh tilting can be adjusted manually; in the more comfortable version the adjustment in the area of required tilt angles from 0 to 60° can be automated by using of additional REC-actuators with buckled chambers. This kind of REC can be easily integrated directly under the thigh.

Both therapy devices can be applied due to their symmetrical design with two slim REC-actuators sideways for treatment of right or left leg without adaptation. The direct-drive soft actuators in the knee joint care for safe physical interaction. The ankle mobilization in both devices can be realized either with separate actuators or through a mechanical linkage as it is usual in CPM-machines. However this cost-saving solution does not allow the immediate ankle-centred assistive therapy.

IV. FIRST EXPERIMENTAL RESULTS

A. The preliminary test bed

To perform the preliminary functional tests and to investigate the patient-centred (assistive) control strategies in parallel with development of “slim-line” REC-actuators the proof-of-concept prototype with two (non-slim) pREC-actuators have been used (Fig. 3). As a passive load a leg dummy filled with a synthetic material to get a realistic weight of the lower leg is applied. The thigh and the lower

leg are connected through a single-axis mechanical knee joint from Otto-Bock. The active forces occurring while patient activities (contributing or disturbing) have been simulated manually.

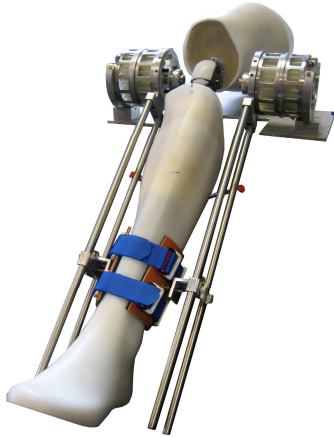


Fig. 3 Test-bed with artificial knee joint and pREC-actuators

B. Control unit

To allow a rapid prototyping of control algorithms, the “hardware-in-the-loop” concept is followed by using the real time development environment of *MATLAB/Simulink* and *dSPACE*-equipment. Implemented control strategies are compiled to run on the *dSPACE* digital signal processor card which is installed in a standard *Windows PC*. *ControlDesk* software is a tool to adjust model parameters and to display the actual operating status. The technical look is transformed into an intuitive graphical user interface by merging additional program code as a combination of *C* and *Python* language.

According to the current state of the art a touch screen monitor is used to permit a versatile configuration of the interface. The monitor is mounted on top of a mobile rack which contains the IPC (Industrial-PC) and offers room for power supplies, I/O connector panel and a 10 litre pressure reservoir which serves as air buffer.

The touch-sensitive interface was designed to be self descriptive and easy to use even for untrained users. The buttons are large, finger friendly and clearly labeled so elderly people could handle the device also by themselves, possibly even at home. Every section is separated by an own frame with associated help buttons which call a pop-up window with detailed instructions. Lots of attention was paid to catch wrong user inputs i.e. starting the device without pressure approval or typing in parameters out of range. Every inappropriate input is notified by an acoustic feedback respectively a text message. One of the two interfaces

serves for default settings (see Fig. 4.b). Here the user can adjust the operation range or record the end positions of a given motion by moving the device manually. By setting up the patient’s body weight and leg length the weight of the lower leg is calculated and therefore gravitation compensation (see section V) works more precisely. Furthermore there is the opportunity to set a therapy timer for stopping the device automatically. The main menu (see Fig. 4.a) only contains the most important buttons for setting motion controls as well as assistive force and velocity by a slider bar. An analogue gauge shows the actual position and the limits of motion while the desired moving direction is indicated by an arrow to give the patient an orientation.

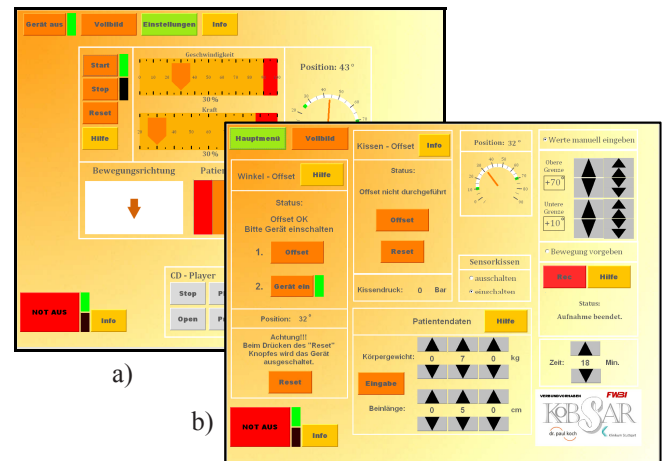


Fig. 4 Graphical user interface; a) main menu, b) settings menu.

Visual feedback shall motivate the user to provide more own muscle activity to improve the healing process. The patient’s efforts are detected and interpreted before showing them as a colour bar.

V. “ASSIST-AS-NEEDED” CONTROL CONCEPT

To ensure an assistive behaviour the “Assist-as-Needed” (AaN) model-based force controller suggested in [3] for conventional pneumatic actuators was adapted and implemented for REC-actuators. Due to the fact, that the inherent compliance of REC-actuators is provided by air compressibility as well as by chamber elasticity, a really comfortable assistive behaviour has been achieved in the experiments. The experimental results reported in this section describe the results using the developed AaN controller.

The control scheme has a cascade structure with a non-linear model-based torque control in the inner loop. By

applying this concept an assistive force of the robot will only be generated if the patient's strength is insufficient to accomplish the desired motion. The implemented control concept is based on a point to point movement, thus no strict desired trajectory is given. The patient just needs to reach a desired target point in a specific time. If a target is reached the next target point will be defined. Consequence of a movement against the target course will be a smooth increasing of force to bring the patient gently to right direction. Sufficient patient's movement, i.e. enough human strength, will decrease the assistive force of the robot to zero. By means of the subordinate model-based torque control a gravitation compensation of the patient's lower leg and the mechanics is achieved. Thus, even in case of enough patient's strength the weight of his lower limb and of the device will be compensated. Fig. 5 shows the experimental results using the AaN controller, with a passive continuous motion in the first and the AaN motion in the second segment, whereby the patient's strength has been simulated manually.

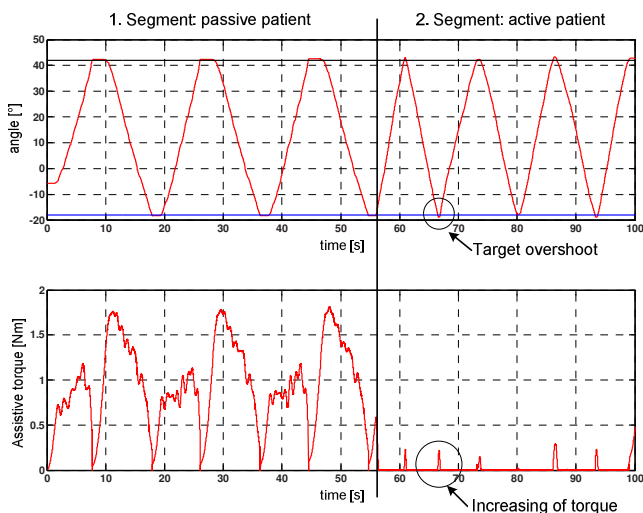


Fig. 5 Experimental results using the AaN controller; patient behaves passive in the first and active in the second segment.

In the first segment (before approx. 55 s) no active strength of the patient was generated and due to that a passive continuous motion is incidental. One can see that the assistive torque is increasing until the desired target point is reached. A sufficient strength in the second segment (after approx. 55 s) causes a decreasing of torque, i.e. assistive force of the robot. Target overshoot leads to a smooth increasing of torque and consequence is a patient's motion to the new correct direction.

ACKNOWLEDGMENT

The concepts of new motion therapy devices with REC-actuators were detailed discussed with the cooperation partner Dr. P. Reize and M. Mahner from Clinical Centre Stuttgart within the cooperative research project KoBSAR "Compact assistive/restorative motion therapy devices of new generation, based on fluidic soft actuators with rotary elastic chambers". Product design renderings are produced by :i/i/d Institute of Integrated Design, Bremen.

REFERENCES

1. Riener R. Patient-Interactive Robots for Arm and Gait Rehabilitation, Technical Aids for Rehabilitation – TAR 2007, Berlin, 2007, pp.29-30
2. Waldner A., Werner C., Hesse S. Robot assisted therapy in neurorehabilitation. Europa Medicophysica, Vo. 44, Suppl.1 to Nr. 3, 2008, pp.1-3
3. Wolbrecht E.T., Leavitt J., Reinkensmeyer D.J., Bobrow J.E. Control of a Pneumatic Orthosis for Upper Extremity Stroke Rehabilitation. Proc. 28th IEEE EMBS Ann. Int. Conf., Aug.30-Sept.3, NYC, 2006, pp.2687-2693
4. Vanderniepen I., Van Ham R., Naudet J., Van Damme M., Vandenberght B., Versluys R., Lefeber D. Novel Compliant Actuator for Safe and Ergonomic Rehabilitation Robots - Design of a Powered Elbow Orthosis. IEEE 10th Int. Conf. on Rehab. Robotics (ICORR'07), 2007, pp. 790 – 797
5. Ivlev O. Soft Fluidic Actuators of Rotary Type for Safe Physical Human-Machine Interaction. Technical Aids for Rehabilitation – TAR 2009, Berlin, March 18-19, 2009
6. Ivlev O., Mihajlov M., Gräser A. Modular Multi-Sensory Fluidic Actuator with Pleated Rotary Elastic Chambers; 4th IFAC Symposium on Mechatronic Systems, Sept. 12 - 14, Heidelberg, Germany; 2006.
7. Kargov A., Breitwieser H., Klosek H., Pylatiuk C., Schulz S., Bretthauer G. Design of a modular arm robot system based on flexible fluidic drive elements. IEEE 10th Int. Conf. on Rehabilitation Robotics (ICORR'07), Noordwijk, NL, June 12-15, 2007
8. Wearable Robots: Biomechatronic Exoskeletons. Edited by J. L. Pons, 2008, 338p.
9. Knestel M., Hofer E.P., Klee B. S., Rupp R. The Artificial Muscle as an Innovative Actuator in Rehabilitation Robotics. Proc. 17th IFAC World Congress (IFAC), Seoul, Korea, July 6-11, 2008
10. Dollar A.M., Herr H. Lower Extremity Exoskeletons and Active Orthoses: Challenges and State-of-the-Art. IEEE Trans. on Robotics, Vol. 24, 1, 2008, pp.144-158
11. Salter R. Continuous Passive Motion: A Biological Concept for the Healing and Regeneration of Articular Cartilage, Ligaments, and Tendons: From Origination to Research to Clinical, 1992, 419p

Author: Dr. Oleg Ivlev
 Institute: Friedrich-Wilhelm-Bessel-Institute Research Company
 and University of Bremen, Institute of Automation
 Street: Otto-Hahn-Allee, NW1
 City: Bremen
 Country: Germany
 Email: ivlev@fwbi-bremen.de; ivlev@iat.uni-bremen.de

Feasibility of selective robotic support of foot clearance with continuously adapting impedance levels

E.H.F. van Asseldonk¹, B. Koopman¹, C. Simons², J. Buurke², H. van der Kooij^{1,3}

¹ Institute for Biomedical Technology (BMTI), University of Twente, Enschede, The Netherlands

² Roessingh Research and Development, Enschede, The Netherlands

³ Department of Biomechanical Engineering, Delft University of Technology Institution, Department, Delft, The Netherlands

Abstract— Encouraging stroke survivors to actively participate in robot aided gait training is critical for optimizing the outcome of this intervention. In this respect, it is of crucial importance that the timing of the provided assistance and the amount of assistance is in accordance with the subjects needs. We tested the feasibility of a control algorithm for a powered exoskeleton that selectively supports foot clearance and adapts its support to the performance of the subject. This was done in five chronic stroke survivors with stiff knee gait. Foot clearance was selectively supported through a virtual spring between the desired and actual ankle height of the paretic leg. The virtual spring stiffness was automatically adapted based on the experienced movement error in the previous step and a forgetting factor. The results showed that the virtual spring stiffness profile converged to a steady state pattern in about 20 steps. The pattern was subject specific and was roughly shaped to the deviation of the actual ankle trajectory from the reference trajectory before the assistance was turned on. The assistance resulted in an increased foot clearance through increased knee flexion, whereas it left other aspects of gait unaffected. The presented algorithm turned out to be effective in providing appropriately timed assistance according to the subjects needs.

Keywords— Adaptive control, stroke, rehabilitation robots, gait training.

I. INTRODUCTION

Robot aided treadmill training is an emerging intervention to regain walking ability in stroke survivors. Robot aided training allows task specific and intensive training while it does not place a high physical demand on the therapists like in manually assisted treadmill training. As it is a relatively new technology, a lot of research effort is put in improving the design and control of the robotic devices. In first instance, the devices were used to move the legs of the subjects through prescribed patterns by using position control. The major limitations of this approach were that the subjects were not required to actively contribute to the movements and that they did not experience any movement errors. Active participation and making errors have been shown to be crucial in motor learning.

To increase the active participation of the subjects and encourage them to self generate activity, different research groups have opted to utilize interactive control schemes that control the interaction forces between the robot and patient. These interactive schemes open many possibilities but also introduce new challenges, like determining the appropriate level and timing of the provided assistance for each specific subject.

A possible solution for the appropriate timing is to split up gait in different subtasks that need to be accomplished during specific phases of the gait cycle and to selectively control these subtasks during the corresponding phase. For instance, subjects need to accomplish appropriate foot clearance during the swing phase of walking. This can be achieved by controlling the vertical ankle height during the pre swing and the swing phase. By using a gait event detection algorithm, the support can be switched on and off with the appropriate timing. This assures that the control of the support is always in synchrony with the gait events of the subject. We recently showed that using this approach enables us to selectively influence the step height and length of healthy subjects walking in the gait trainer LOPES [1].

A possible solution for determining the appropriate level of support was put forward by Emken and colleagues [2]. They proposed an automated method to adjust the amount of support to the capabilities of the subject, a so called “assist-as-needed” algorithm. This algorithm consists of an error-based learning law with a forgetting factor. It adapts the amount of support on a step-by-step basis such that it reduces the assistance when errors are small and increases its assistance when errors are large, effectively bounding these errors. They showed, in a group of spinal cord injury subjects, that the amount of support was adapted in a subject specific way such that the robot only provided support in those regions of the step cycle where the subject consistently made large errors.

In this study we combined the above described selective subtask control and the adaptive control algorithm. The purpose of the study was to demonstrate the feasibility of this combined algorithm in selectively supporting the foot clearance and adjusting the support to the requirements of the subject.

II. METHODS

A. Subjects

Five male chronic stroke survivors (age: 57.2 ± 4.2 years, length: 1.82 ± 0.04 , weight: 89.2 ± 11.7) volunteered to participate in this experiment. All stroke survivors had a left hemi paresis secondary to a single and first ever unilateral stroke. They were at least half a year post-stroke and were all independent ambulators. Their walking pattern was characterized as stiff knee gait.

B. Experimental apparatus and recordings

For the experiments the prototype of the gait rehabilitation robot LOPES was used. LOPES is an exoskeleton type rehabilitation robot with 8 actuated Degrees of Freedom: pelvic horizontal translations and hip abduction/adduction, hip flexion/extension and knee flexion /extension of both legs. It is lightweight and actuated by Bowden cable driven series elastic actuators [3]. The robot is impedance controlled, which implies that the actuators are used as force (torque) sources.

Applied torques and measured joint angles of LOPES are sampled at 100 Hz. The joint angles and segment lengths are used to calculate the ankle position at each instant of time. Four force sensors integrated in the treadmill measured the vertical forces and were used to calculate the centre of pressure (CoP). The CoP velocity and position were analyzed in real time to detect heel contact (HC) and toe off (TO) events. HC and TO were used as the triggers to switch on and off the robotic support.

The forces, torques and joint angles were stored for off-line analysis. From the data we determined different gait parameters and kinematic metrics for each individual step.

C. Protocol

Subjects were strapped into LOPES, such that the hip and knee rotation centers of the exoskeleton lined up with those of the subjects. After being acclimated to walking in the robot, the preferred walking velocity was assessed by systematically varying the treadmill velocity. During these trials the robot was operated in zero impedance mode, meaning that the robot did not apply any support torques. Subsequently, the subjects first walked at this self selected speed for about 1 minute, after which the robotic support was turned on and the subjects continued walking for several minutes. The provided support was solely aimed at increasing the foot clearance (that is the vertical ankle position) of the paretic leg. The support was switched on at heel contact of the non paretic leg and switched off at heel con-

tact of the paretic leg. We defined a reference vertical ankle trajectory, based on a parameterized reference trajectory obtained from measurements with healthy subjects. This pattern was scaled for each subject such that the maximum of this pattern was 5 cm higher than the measured maximal ankle position during walking without support.

D. Adaptive foot clearance support

In controlling the robot we adopted an approach in which the high level control is at a (sub)task level instead of the generally used control at the level of the joints. The used controller is based on the Virtual Model Control (VMC) framework [13]. The basis of this control method is to define physical interactions with the subject that would aid the patient with the concerned gait task. In this case, we define a virtual spring between the actual ankle height and the reference ankle height. If the actual ankle height (Z) deviates from the reference ankle height (Z_{ref}) a “virtual force” is exerted at the ankle which mimics a therapist pulling up the foot at the ankle. The exerted force is dependent on 1) the current deviation of the reference pattern that is movement error, 2) the virtual spring stiffness and 3) on the performance during preceding steps through step to step adaptation of the stiffness of the virtual spring.

In mathematical terms:

$$F_z = K_z(Z - Z_{ref}) \quad (1)$$

where F_z is the desired virtual force and K_z the virtual spring stiffness. The desired forces are delivered by knee and hip joint torques, transferred from the robotic exoskeleton to the human endoskeleton. The virtual force is projected to joint torques by using the Jacobian of the kinematic structure.

The stiffness of the virtual spring was adapted from cycle to cycle according to:

$$K_z^i(t) = f * K_z^{i-1}(t) + g * (Z_{ref}^{i-1}(t) - Z^{i-1}(t)) \quad (2)$$

Where the subscript i denotes the i^{th} step cycle, f is a forgetting factor set to 0.9, g is an error based gain set to 1800 and t indicates the % gait cycle. The stiffness was constrained to positive values. This scheme to adapt the stiffness is adopted from [2]. The idea behind the scheme is that when the desired ankle height is attained by the subject the support will be reduced, since the forgetting factor (always smaller than one) will reduce the stiffness of the virtual spring for each subsequent step. If the subject is unable to follow the desired ankle height trajectory the virtual spring stiffness will be increased in the next step cycle, proportional to the tracking error and weighed by the error based gain.

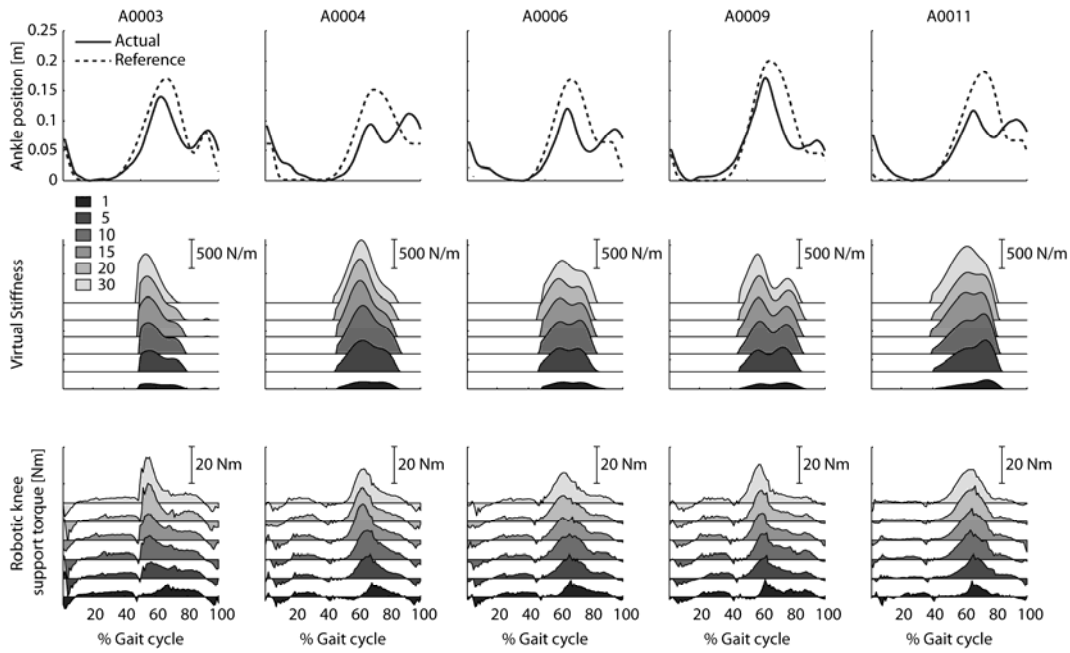


Fig. 1. Shaping of the impedance during the swing phase based on the difference between the actual and the reference ankle trajectory for five chronic stroke survivors. Upper row of graphs indicate the reference and actual ankle trajectory for a step in which no support was provided. The difference between the actual and the reference trajectory is indicative for where robotic support is needed. The middle row of graphs indicates the adaptive virtual stiffness during selected steps (at 1, 5, 10, 15, 20 and 30) after the robotic support was turned on. The virtual stiffness is adapted in every step, based on the error in the previous step and a “forgetting” factor. The lower row of graphs shows the exerted robotic support at the knee. The knee and hip torque (not depicted) are calculated from the virtual stiffness and the deviation between the actual and reference ankle trajectory using a Jacobian transformation.

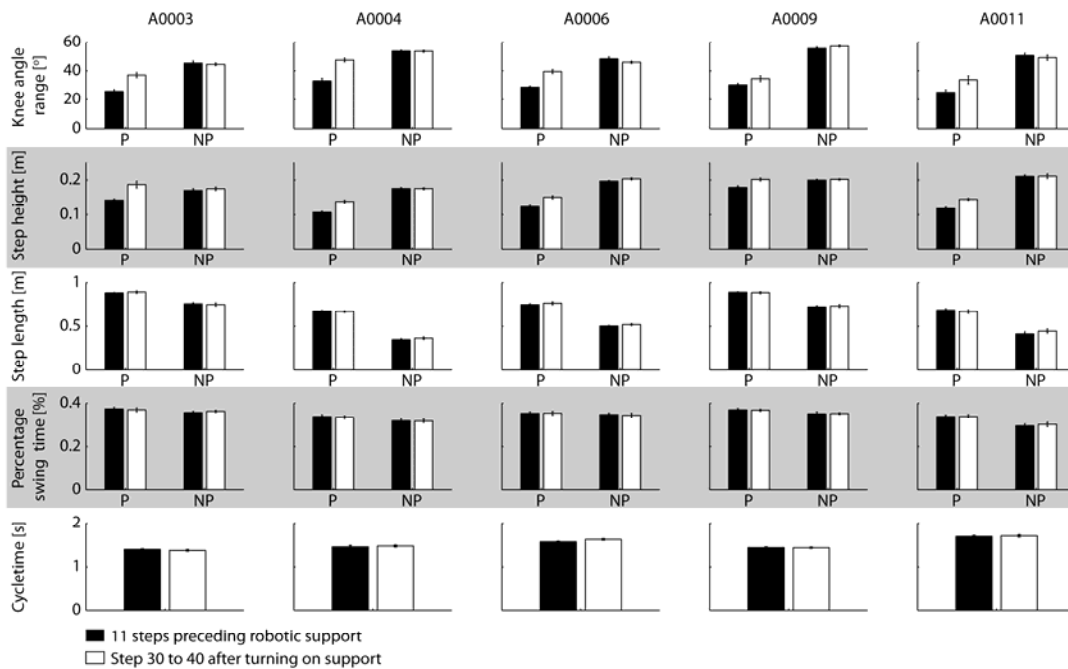


Fig. 2. Assorted kinematic metrics and gait parameters for the different stroke survivors for their paretic (P) and non paretic (NP) leg. The bars represent averages over 11 steps preceding the exposure to robotic support (black) and after the robotic support converged to a “stable” pattern (light grey).

III. RESULTS

The ankle height trajectory of the stroke survivors all deviated in a different way from the scaled reference trajectory (Fig. 1). However, they had in common that the actual ankle height was below the reference ankle height in most of the swing phase (starting from 60%) except the terminal swing phase (>90%). The virtual stiffness gradually increased during the first steps of exposure to the robotic support. Yet, it only increased in the part of the gait cycle where the ankle position was below the reference trajectory, so where the support was needed. In general, the virtual stiffness converged to a steady state pattern in approximately 20 steps. The “steady state” pattern of the virtual stiffness reflected roughly the pattern of the initial deviation between the reference and actual vertical ankle position. The changes in the virtual stiffness were reflected in the applied robotic support at the knee and at the hip joint (not depicted).

The applied robotic support resulted in a significant increase of the knee flexion during swing (see Fig. 2) for all subjects (separate paired t-test for every subject to assess whether the parameter values from the eleven steps prior to applying robotic support differed from those of the eleven steps when a steady state was achieved). The increase in knee flexion resulted in a significant increase of the maximal ankle height during swing. The other parameters were fairly unaffected. Although some parameters showed a significant change in some of the subjects, the relative changes were generally smaller than 3%.

IV. DISCUSSION

In this study we showed the feasibility of combining a control algorithm that specifically supports subtasks of walking with an algorithm that automatically adapts its support to the performance of the subject. The combination of these algorithms resulted in a robot control algorithm that provided support on that part of the swing phase where support was required while it left the other parts of the swing phase and the remaining walking pattern unaffected. The reported results are in agreement with those of Emken and colleagues [2]. They combined an adaptive algorithm with a manual teach and replay algorithm and supported the complete step (step height and step length). Their results, obtained in spinal cord injury subjects, also showed that the stiffness was adapted in a subject specific way. Furthermore they also showed that the convergence to a steady state pattern took about 20 steps.

In the current study we focused on the “convergence” property of the adaptive algorithm. Yet, another advantage of the algorithm is that it keeps adapting the stiffness every step after this initialization phase. In doing so it allows variability in performance and the occurrence of errors. These properties are essential to promote motor (re) learning.

We assessed the instantaneous effects of providing robotic support in a single session. We are currently conducting an effect study in which the presented algorithm is applied in a six week training program aimed at improving the foot clearance in chronic stroke patients during overground walking. Although in a single session the algorithm selectively influence the foot clearance, on the long term the support might also result in beneficial changes of other aspects of the walking pattern, like the asymmetry in step length. Like the majority of stroke survivors, all subjects exhibited a clear asymmetric walking pattern while walking overground. This pattern was also observed while walking in LOPES. This was reflected in the difference between the paretic and non paretic step length. The non paretic foot was placed less far forward with respect to the paretic foot than vice versa (Fig. 2). Difficulties in attaining enough foot clearance are widely regarded as a reason for this asymmetry in step length. Improvements in the foot clearance as a result of the robotic support could therefore also result in less selective effects on the long run.

ACKNOWLEDGMENT

This study was supported by a grant of the Royal Dutch Society for Physical Therapy (KNGF). We want to thank Joelle van den Hoek and Marjanne Folkersma for their help in planning and running the experiments.

REFERENCES

1. Emken J, Harkema S, Beres-Jones J et al (2008) Feasibility of manual teach-and-replay and continuous impedance shaping for robotic locomotor training following spinal cord injury. *IEEE Trans Biomed Eng* 55:322-334
2. Van Asseldonk E, Ekkelenkamp R, Veneman J et al (2007) Selective control of a subtask of walking in a robotic gait trainer (LOPES). *Proceedings of ICORR 2007 - IEEE International Conference on Rehabilitation Robotics*. Noordwijk, pp 841-848
3. Veneman J, Kruidhof R, Hekman E, et al (2007) Design and Evaluation of the LOPES Exoskeleton Robot for Interactive Gait Rehabilitation. *IEEE Trans Neural Syst Rehabil Eng* 15:379-386

Author: Edwin H.F. van Asseldonk
 Institute: University of Twente
 Street: PO box 217 City: Enschede
 Country: The Netherlands Email: e.h.f.vanasseldonk@utwente.nl

Diffusion Limited Tapered Coating with Parylene C

R.P. von Metzen¹, D. Egert¹, P. Ruther², and T. Stieglitz¹

¹ Laboratory for Biomedical Microtechnology,

² Microsystem Materials Laboratory,

Department of Microsystems Engineering – IMTEK, University of Freiburg, Freiburg, Germany

Abstract— A novel process for the fabrication of tapered Parylene C coatings is presented. This method is capable of realizing nearly edgeless transitions from coated to uncoated regions on needle-like structures. The tapering is generated during deposition by positioning the needles in a container through openings that are a few microns larger than the needles' cross sections. Due to the limited diffusion of the Parylene C monomers through the narrow gaps between needles and openings the film thickness declines from 10 μm outside to less than 2 μm inside the container within less than 120 μm along the probe.

For the proof of principle, silicone-based neural probes for intercortical recording are coated and their electrical functionality is verified using a H_2O_2 -test.

Keywords— Parylene C, neural interface, encapsulation, non-hermetic, implant, neural prostheses, MEMS.

I. INTRODUCTION

Neural implants to investigate fundamental processes in the brain benefit from the miniaturization in microelectromechanical systems (MEMS). Silicon-based, needlelike probes to record single unit activity are object of research since the late 1960s [1]. Probes with up to 100 shafts [2] and integrated electronics for signal amplification, multiplexing, and signal processing are widespread in neuroscience [3].

However, encapsulation remains a challenge since hermetic approaches with metallic or ceramic housings are too large and do not allow up to 1024 feedthroughs at a volume of few mm^3 . Non-hermetic encapsulations serve as an alternative for medium term implantation.

In this work we investigate the possibility of depositing Parylene C in a way to selectively encapsulate a defined part of a silicon-based probe without covering the recording electrodes and without the use of photolithographic process steps.

A. Parylene

Poly-para-xylylene (Parylene) is a commonly used polymer for the encapsulation of medical implants. It has

various advantages against other frequently used polymers, which make it especially interesting for the fabrication of biomedical microdevices. Parylene C has an extremely low permeability of moisture and gases and it is compatible to MEMS-processes while being a stable electrical insulator. This allows the fabrication of micro-scaled flexible implants [4-11]. Parylene C as well as the related polymers Parylene N and HT have a USP class VI certified biocompatibility for chronic implantation.

Parylenes are deposited in a vapor deposition polymerization (VDP) process. Gaseous monomers are led into the recipient where they condense and polymerize on all exposed surfaces [12,13]. This allows a deposition on any three-dimensional structures with a conformal and contiguous film.

The deposition rate depends on the pressure inside the chamber, the substrate temperature, the specimen's position in the recipient, the area of surfaces where condensation can occur and the gas flow velocity and direction over the substrates [14-18].

The advantage of this conformal coating turns into a drawback when openings in the encapsulation are needed, e.g. for an electrochemical contact between an electrode site and the biological surrounding. The established techniques to produce openings in Parylenes like cutting and peel off, laser ablation [19], oxygen plasma [4,6,20,21] or reactive ion etching (RIE) [11,20], masking [22] and local heating [16] are either not compatible with a three-dimensional implant, not reliable enough, or lead to abrupt edges in the Parylene where delamination may occur and electrolyte can be soaked in.

B. Neural Probe Shafts

The probe shafts used in this study are fabricated in a silicon-based MEMS process based [23,24] and under development in the framework of the EU-funded project NeuroProbes [25]. These probes are available in different layouts for single shaft, comb shaft and 3D-arrays in various shaft lengths up to 8 mm. Each shaft comprises 9 platinum electrode sites 20 μm in diameter. For this pilot experiment

only the comb like probes with four shafts and 8 mm length are used. Each shaft has a rectangular cross section with a thickness of 100 μm and a width of 120 μm . The pitch between the shafts is 550 μm . They originate from a common bar-like structure where the connection pads are located. A micromachined, polyimide-based flat ribbon cable leads the conductive paths to the next stage.

The presented process enables the encapsulation of the combs with Parylene C including the connection area while keeping the shafts uncoated for a guaranteed electrochemical contact of the electrode sites with the brain tissue and a smooth transition between these two regions.

C. Process principle

The basic approach is to combine the limited diffusion path length of Parylene with masking of probe sections. The taper is realized by precisely positioning the comb shafts in a container through rectangular openings that are several square microns larger than the shafts' cross sectional area. The density of monomers inside the container is zero at the beginning of the deposition, while the concentration is much higher in the coater recipient. Limited diffusion through the gaps around the shafts leads to a higher deposition rate outside the container.

The combs are fixated in polyethylene glycol (PEG) in the container for a safe temporary positioning and masking of the electrode sites as illustrated in Figure 1.

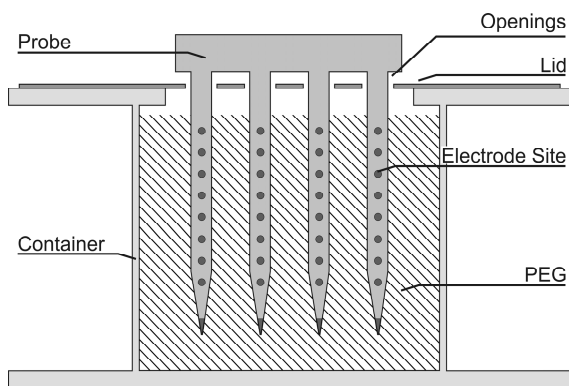


Fig. 1 Sketch of the setup for the tapered deposition of Parylene C on electrode shafts. The needles are immersed in solid PEG, thus being fixated and masked. The shafts reach through openings in a covering lid that are a few microns larger than the shafts, allowing the declining layer thickness in these areas. The sketch is not true to scale.

II. MATERIALS AND METHODS

A. Container

The container consists of an aluminum cap made of a 9 mm long tube with an inner diameter of 10 mm, fixed upon a base plate and a planar covering with a circular aperture with a diameter of 8 mm. On top of that is a lid with the rectangular openings for the probe shafts.

Standard kitchen-type aluminum foil (13 μm thick) is used for the lid. The openings are cut into the foil with a Nd:YAG marking laser (DPL Genesis Marker, cab Produkttechnik GmbH, Karlsruhe, Germany), which operates at 15 % of its cw-power of 7 W, scanning at a velocity of 1.5 mm/s. The laser pulses are generated at a frequency of 900 Hz, while the Q-switch is opened for 12 μs . It requires 4 passes to completely cut through the foil. The use of aluminum foil allows the fabrication of a large number of lids for single use. Vacuum grease is utilized to glue the lids to the container (high vacuum grease, Dow Corning Corporation, Midland, MI, USA).

To investigate the influence of the spacing between the needles and the lid different sizes of the openings are designed to realize gap widths of 35, 40, 45 and 50 μm , respectively.

B. Assembly

The container is filled to 80% with PEG, which is solid at room temperature and melts at 70°C. It is heated on a hotplate to 80°C, then the comb is positioned using a flip chip bonder (Fineplacer Model FD55, Finetech, Berlin, Germany). The comb's bar remains outside the container and the tips and parts of the shafts are immersed in the PEG. The depth and the position of the comb with respect to the lid are adjusted while the PEG is liquid. While cooling the container and thus the PEG, the comb is held by the flip chip bonder until the PEG becomes solid, thus holding the needle array exactly in its centered position. The shafts do not touch the lid.

C. Parylene Coating

The container with fixed combs are stable enough to withstand handling and the air flow caused by the vacuum pumping inside the Parylene coater recipient (Labcoater 2010, Specialty Coating Systems SCS, Indianapolis, IN, USA). Silane A174 adhesion promoter (Merck KGaA, Darmstadt, Germany) is used to enhance the bond between Parylene C and silicon. 1 ml of the liquid promoter is applied to the inside walls of the recipient and evaporates

when the pressure in the chamber is lowered. The specimens are placed on a turntable that rotates relative to the Parylene vapor source, thus improving the homogeneity of the film. The recipient stays at room temperature during deposition.

The amount of dimer used is between 10 g and 16 g to achieve a film thickness of 10 μm , the initial pressure is 19 mTorr and two deposition pressures (24 and 64 mTorr) are investigated.

D. Measurements

The thickness and the shape of the Parylene coatings are measured using a profilometer (P11, KLA-Tencor, Tucson, AZ, USA), an interferometer (NV5000, Zygo Cooperation, Middlefield, CT, USA) and a scanning electron microscope (DSM 962, Zeiss, Jena, Germany).

To test whether the platinum electrodes are free of Parylene after the deposition process the combs are immersed into a 30 % H_2O_2 solution. The platinum works as a catalyst and makes oxygen dissolve out of the H_2O_2 and form visible bubbles if the electrodes are open.

III. RESULTS AND CONCLUSION

Independent of the opening size and deposition pressure all needles exhibited tapered coatings that gradually changed from approx. 10 μm to 1-2 μm within a range of 120 μm over the probe shafts, cf. Figure 2.

The Parylene C thickness on areas between the transition and the PEG-masked regions was constant, ending in a sharp edge with a step height of 1-2 μm . All masked electrode sites passed the H_2O_2 -test successfully.

So far, the applied deposition process of Parylene C does not allow an exact prediction of deposited layer thicknesses, i.e. neither outside the container nor for the thinner film inside the container. The only forecast is that the thickness will be dramatically reduced (by a factor of approx. 5) with respect to the outer layer thickness.

The results are reproducible within large tolerances and independent from parameters which are expected to be crucial. The achieved results from these pilot experiments are promising and will be continued with more accurate setups and a larger number of specimens.

Although the layer thickness could not be eliminated completely inside the container, the layer thickness is thin enough to prevent delamination of the Parylene from the underlying substrate. Cohesion forces in the thin Parylene films are smaller than the Parylene-to-silicon adhesion forces.

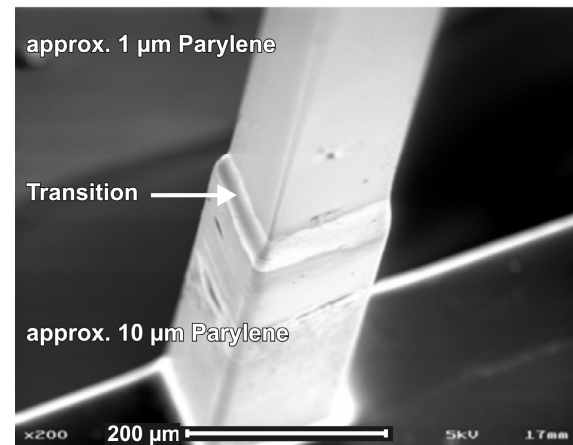


Fig. 2 SEM micrograph of a silicon needle electrode covered with approx. 10 μm Parylene C at the bottom, a tapered transition in the middle of the picture and an approx. 1 μm thick Parylene C layer on the upper part

ACKNOWLEDGMENT

The authors acknowledge S. Herwik providing silicon-based probe combs. The work described in this paper was performed in the frame of the Information Society Technologies (IST) Integrated Project *NeuroProbes* of the 6th Framework Program (FP6) of the European Commission (Project number IST-027017).

REFERENCES

1. K. D. Wise, J. B. Angell, and A. Starr (1969) An Integrated Circuit Approach to Extracellular Microelectrodes, *Digest of the 8th ICMBE*, 1 ed p. 14.
2. C. T. Nordhausen, E. M. Maynard, and R. A. Normann (1996) Single Unit Recording Capabilities of a 100 Microelectrode Array. *Brain Res*, vol. 726, no. 1, pp. 129-140.
3. K. D. Wise, D. J. Anderson, J. F. Hetke, D. R. Kipke, and K. Najafi (2004) Wireless Implantable Microsystems: High-Density Electronic Interfaces to the Nervous System. *Proc of the IEEE*, vol. 92, no. 1, pp. 76-96.
4. J.-M. Hsu, L. Rieth, R. A. Normann, P. Tathireddy, and F. Solzbacher (2008) Encapsulation of an Integrated Neural Interface Device with Parylene-C. *IEEE T Bio-Med Eng*, vol. 55, no. 11, pp. 1-7.
5. R. Huang, C. Pang, Y.-C. Tai, J. Emken, C. Ustun, and R. A. Andersen (2008) Parylene Coated Silicon Probes for Neural Prosthesis, *Proceedings of the 3rd IEEE Int. Conf. on Nano/Micro Engineered and Molecular Systems, Jan. 6-9, 2008, Sanya, China, 2008* pp. 947-950.
6. A. J. H. Spence, K. B. Neeves, D. Murphy, S. Sponberg, B. R. Land, R. R. Hoy, and M. S. Isaacson (2007) Flexible Multielectrodes Can Resolve Multiple Muscles in an Insect Appendage. *J Neurosci Meth*, vol. 159 pp. 116-124.
7. T. Stieglitz, W. Haberer, C. Lau, and M. Goertz (2004) Development of an Inductively Coupled Epiretinal Vision Prosthesis, *Proc of the 26th Ann Internat Conf of the IEEE EMBS* pp. 4178-4181.

8. T. Stieglitz, S. Kammer, K. P. Koch, S. L. Wien, and A. A. Robitzki (2002) Encapsulation of Flexible Biomedical Microimplants with Parylene C, *Proc 7th Ann Conf of the IFESS* pp. 231-233.
9. T. Suzuki, K. Mabuchi, and S. Takeuchi (2003) A 3D Flexible Parylene Probe Array for Multichannel Neural Recording, *Proc of the 1st Internat IEEE EMBS Conf on Neural Eng*, 1 ed pp. 154-156.
10. S. Takeuchi, D. Ziegler, Y. Yoshida, K. Mabuchi, and T. Suzuki (2005) Parylene Flexible Neural Probes Integrated with Microfluidic Channels. *Lab Chip*, vol. 5 pp. 519-523.
11. C. Pang, J. G. Cham, Z. Nenadic, S. Musallam, Y.-C. Tai, J. W. Burdick, and R. A. Andersen (2005) A New Multi-Site Probe Array with Monolithically Integrated Parylene Flexible Cable for Neural Prostheses, *Proceedings of the 2005 IEEE, Engineering in Medicine and Biology 27th Annual Conference, Sept.1-4, 2005, Shanghai, China, 2005* pp. 7114-7117.
12. J. B. Fortin and T. M. Lu (2002) A Model for the Chemical Vapor Deposition of Poly(para-xylylene) (Parylene) Thin Films. *Chem Mater*, vol. 14, no. 5, pp. 1945-1949.
13. H. Lee and J. Cho (2005) Development of Conformal PDMS and Parylene Coatings for Microelectronics and MEMS Packaging, *Proceedings of IMECE 2005, 2005 ASME International Mechanical Engineering Congress and Exposition*.
14. S. Ganguli, H. Agrawal, B. Wang, J. F. McDonald, T. M. Lu, G. R. Yang, and W. N. Gill (1997) Improved Growth and Thermal Stability of Parylene Films. *Am Vacuum Soc*, pp. 3138-3142.
15. G. P. Spellman, J. F. Carley, and L. A. Lopez (1999) Vacuum Deposition of Parylene Films: Influence of Process Factors and Baffling on Film-Thickness Distribution. *J Plast Film Sheet*, vol. 15, no. 4, pp. 308-328.
16. Y.-C. Tai, Y. Xu, and Y. Tai (2003) Selective Deposition of Parylene C for Underwater Shear-Stress Sensors, *12th International Conference on Transducers*, 2 ed pp. 1307-1310.
17. M. C. Demirel (2008) Emergent Properties of Spatially Organized Poly (P-Xylylene) Films Fabricated by Vapor Deposition. *Colloid Surface A*, vol. 321, no. 1-3, pp. 121-124.
18. S. Pursel, M. W. Horn, M. C. Demirel, and A. Lakhtakia (2005) Growth of Sculptured Polymer Submicronwire Assemblies by Vapor Deposition. *Polymer*, vol. 46 pp. 9544-9548.
19. J. D. Weiland, D. J. Anderson, C. C. Pogatchnik, and J. J. Boogaard (1997) Recessed Electrodes Formed by Laser Ablation of Parylene Coated, Micromachined Silicon Probes, *Proc of the 19th Ann Internat Conf of the IEEE EMBS*, 5 ed pp. 2273-2276.
20. E. Meng, P.-Y. Li, and Y.-C. Tai (2008) Plasma Removal of Parylene C. *J Micromech Microeng*, vol. 18, no. 4, pp. 1-13.
21. H. Lo, Y.-C. Tai, and . (2007) Characterization of Parylene as a Water Barrier Via Buried-in Pentacene Moisture Sensors for Soaking Tests, *NEMS ' 07, 2nd IEEE International Conference on Nano/Micro Engineered and Molecular Systems, 2007* pp. 872-875.
22. P.-L. Lu, C.-L. Fan, L.-J. Yang, C.-W. Lin, Y.-J. Yang, and F.-S. Jaw (2007) Completely Parylene-Coated Neuroprobe for Chronic Recording, *Proceedings of the 2nd IEEE International Conference on Nano/Micro Engineered and Molecular Systems, January 16-19, 2007, Bangkok, Thailand, 2007* pp. 223-226.
23. S. Herwik, S. Kisban, K. Seidl, T. Stieglitz, O. Paul, and P. Ruther (2007) Microelectrode Array Combining Silicon Probes with Flexible Polyimide Ribbon Cables for Neural Recording, *Biomed Tech*, 52 ed p. 2 pages.
24. S. Kisban, P. Janssen, S. Herwik, T. Stieglitz, O. Paul, and P. Ruther (2008) Hybrid Microprobes for Chronic Implantation in the Cerebral Cortex, *30th Annual International IEEE EMBS Conference, August 20-24, 2008, Vancouver, British Columbia, Canada, 2008* pp. 2016-2019.
25. P. Ruther, A. Aarts, O. Frey, S. Herwik, S. Kisban, K. Seidl, S. Spieth, A. Schumacher, M. Koudelka-Hep, O. Paul, T. Stieglitz, R. Zengerle, and H. Neves (2008) The NeuroProbes Project-Multifunctional Probe Arrays for Neural Recording and Stimulation, *Biomed Tech*, 53 ed pp. 238-240.

Author: René Patrick von Metzen
 Institute: University of Freiburg, Department of Microsystems Engineering – IMTEK, Laboratory for Biomedical Microtechnology
 Street: Georges-Koehler-Allee 102
 City: Freiburg im Breisgau
 Country: Germany
 Email: metzen@imtek.uni-freiburg.de

Electrical Characterization of Platinum, Stainless Steel and Platinum/Iridium as Electrode Materials for a New Neural Interface

C. Henle, W. Meier, M. Schuettler, T. Boretius, and T. Stieglitz

Laboratory for Biomedical Microtechnology, Department of Microsystems Engineering - IMTEK, University of Freiburg, Freiburg, Germany

Abstract— This paper describes the design and fabrication of a 48-channel microelectrode, based on laser-patterned silicone rubber (polydimethylsiloxane, PDMS) and different metal foils. Samples with platinum, platinum/iridium and stainless steel as electrode materials were fabricated and electrochemically characterized. The electrochemical performance was investigated by electrical impedance spectroscopy. Supplementary, pulse tests were carried out, in order to calculate the charge injection capacities. All samples have the same contacts sizes, what allows a comparison between the three different metal foils.

Keywords— Microelectrode, laser-patterning, platinum, platinum/iridium, stainless steel.

I. INTRODUCTION

The laser-fabrication technology of the presented micro electrode was described by Schuettler et al. for the first time in 2005 [1]. Since that time, process steps were more and more optimized so as we have nowadays a fully established technology for manufacturing microelectrodes based on PDMS as encapsulating material.

These implantable neural interfaces offer a wide range of applications. The spectrum ranges from presurgical epilepsy monitoring to providing brain computer interfaces or stimulation of peripheral nerves in patients, suffering from spinal cord injury or other neural diseases [2, 3].

These various applications make different demands on the mechanical and electrochemical properties of the used electrode material. In this paper, electrode arrays with three different metal foils – platinum, platinum/iridium and stainless steel – were manufactured and investigated, regarding their electrochemical properties in Ringer's solution. Electrical impedance spectroscopy and pulse tests were carried out to estimate the recording and stimulating qualities.

II. MATERIALS AND METHODS

A. Design

Basically, the microelectrode array consists of interconnection pads, insulated metal tracks and active electrode

sites made out of metal foil which is sandwiched between two layers of silicone rubber (PDMS). Fig. 1 shows the design of the electrode array.

The area covered by the 48 electrode sites, is about 18x8 mm². The electrode sites have a diameter of 0.78 mm, an inter-electrode distance of 1.68 mm, and are hexagonally arranged.

The tracks have with a width of 0.07 mm and a distance of 0.07 mm to adjacent tracks, yielding a track pitch of 0.14 mm, which is not the smallest possible track pitch [4].

The connection pads are prepared for micro-spot-welding cables to the tracks. The ending tracks, with a width of 0.14 mm are arranged in a circle, what simplifies the joining of the cables in a flexible silicone tube, and saving the welding points against torsion stress. The metal tracks at the connection sites are exposed within a length of 0.6 mm.

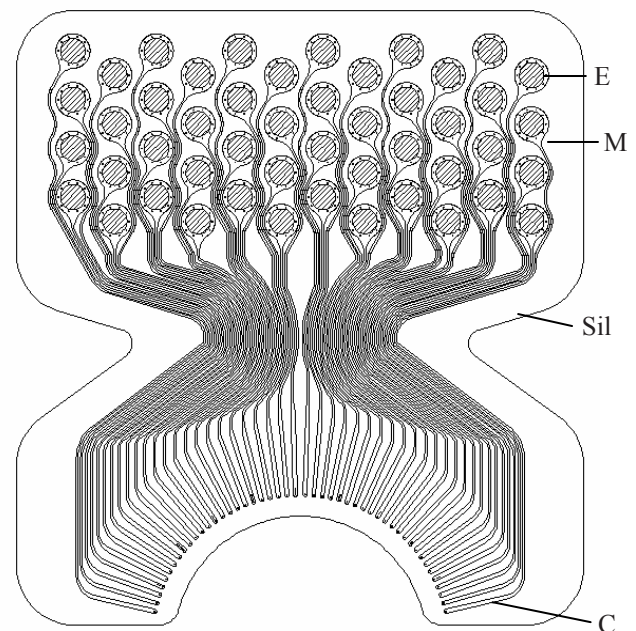


Fig. 1 Design of the 48-Channel-Array; E: electrode site; M: metal foil; Sil: silicone rubber substrate; C: connection site.

B. Manufacturing Process

The manufacturing process, using the example of platinum foil, is shown in Fig. 2 (a-i). As substrate material a

standard glass microscope slide is used. A self-adhesive tape (No 4124, tesa AG, Hamburg, Germany) is laminated, and acts as release layer for the electrode array at the end of the process. N-heptane diluted silicone rubber (MED-1000, NuSil, Carpinteria, CA, USA) is spun on the substrate. After laser-structuring the silicone layer for future connection pads with a Nd:YAG laser (DPL GenesisMarker, cab, Karlsruhe, Germany), platinum foil is laminated. After laser-patterning the platinum foil and removal of the excess material, tape (type 5413 Kapton® Tape, 3M, Neuss, Germany) is laminated to mask the future connection pads. A second layer of diluted silicone rubber is spun-on, and the masking tape is removed in a lift-off process. After curing the silicone rubber, electrode sites are opened, and the boundary is patterned by the laser. As a last step, the entire electrode is removed from the carrier.

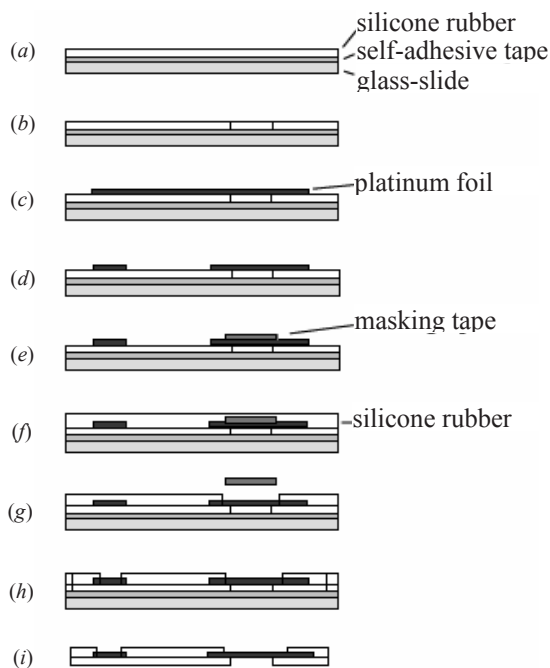


Fig. 2 Step-by-step diagram of the fabrication methodology. (a) Lamination of self-adhesive tape and spin-coating of silicone rubber on a glass microscope slide. (b) Patterning of silicone rubber for future connection pads. (c) Lamination of platinum foil. (d) Structuring of platinum foil and excess material removal. (e) Placing masking tape for future connection pads. (f) Second spin coating of silicone rubber. (g) Removal of masking tape. (h) Patterning of silicone rubber (opening electrode contacts and creating the boundary of the electrode). (i) Removal of complete array without excess material of silicone rubber.

C. Choice of Metals

For the electrochemical characterization, following different metal foils were used: 12.5 μm thin, high purity platinum foil (Goodfellow, Friedberg, Germany), 25 μm thin

platinum/iridium foil (Pt:Ir; 90:10 wt%), (Alfa Aesar, Karlsruhe, Germany), and 12.5 μm thin stainless steel foil (Fe/Cr18/Ni10), (Goodfellow, Friedberg, Germany).

D. Electrochemical characterization

Electrical impedance spectroscopy

Impedance spectroscopy was carried out in 100 % Ringer's solution (Merck, Darmstadt, Germany) at room temperature (22°C). The impedance measurement setup was designed as a three electrode configuration, consisting of the working electrode (device), an Ag/AgCl reference and a platinum counter electrode, connected to the SI 1287 Electrochemical Interface and the SI 1260 Frequency Response Analyzer (Solartron Analytical, Farnborough, United Kingdom) which delivered the alternating voltage and measured the impedance. The setup was controlled by the software Zplot (Scribner Associates Inc., Southern Pines, North Carolina, USA). An excitation amplitude of 10 mV was set in the form of a sine wave. The impedance magnitudes were measured within a range of 10^{-1} - 10^5 Hz.

Pulse Test

The pulse test carried out, basically should show the different charge injection capacities C of the used materials, which is an important parameter in case of electrical stimulation of nerves.

The applied current causes a voltage drop V_a across the access resistance R_a , followed by a voltage ramp caused by charging the phase boundary capacitance. The peak of the voltage ramp V_c is used to calculate the charge injection capacitance with equation

$$C = Q_{inj} / (V_c - V_a) \quad (1)$$

The applied current pulses were rectangular shaped, symmetrically biphasic, positive first and had an amplitude of 0.5 mA and a frequency of 30 Hz. The pulse width was set to 200 μs , and is used to calculate the charge injection ($Q_{inj}=100$ nC) with the formula

$$Q_{inj} = I \times t_{pulse} \quad (2)$$

The pulse test was carried out in Ringer's solution at room temperature. The circuit consists again out of a three electrode arrangement, namely a Ag/AgCl reference electrode, a working, and a platinum counter electrode, which closes the electrical circuit. The difference between reference electrode and the voltage response of the working electrode caused by the current pulses was amplified and recorded through an oscilloscope. The DC offset of the

achieved data was offline removed and mean values of 7 measured curves for each material were calculated.

III. RESULTS

First, optimal laser-parameters for each metal had to be ascertained, which are listed in Table 1.

Table 1 Laser-parameters for cutting metal foils

Metal foil	Platinum	Platinum/Iridium	Stainless steel
Thickness (μm)	12,5	25	12,5
Passes (1)	3	4 / 1 ³	2
Power ¹ (%)	15,8	16 / 16 ³	10
Speed (mm/s)	1	2 / 1 ³	1
Pulse Width (μs)	1	1 / 1 ³	1
Frequency (kHz)	1	1,5 / 1,5 ³	2
Measured Power ² (mW)	170	225 / 225	160

¹ The continuous wave power P_{cw} , in % of the maximum output of 7 W at 100 %.

² The average power measured with the laser power meter.

³ Second step for cutting platinum/iridium foil.

Altogether, 3 electrode arrays were fabricated for the tests. The platinum and the platinum/iridium electrode array were connected to silicone-isolated copper wires ($\varnothing=0.15$ mm), whereas for the stainless steel electrode, trimel-coated platinum wires ($\varnothing=0.07$ mm) were used. Fig. 3 shows the platinum electrode array, spot-welded to isolated copper cables. Afterwards, the connection sites were encapsulated in silicone rubber (MED-1000, NuSil, Carpinteria, CA, USA).

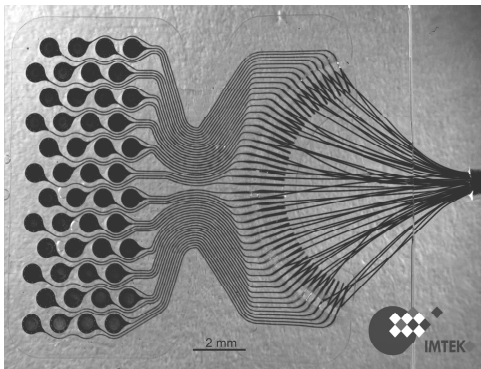


Fig. 3 48-Channel-Array with platinum electrodes and spot-welded silicone-isolated copper wires.

Electrical impedance spectroscopy

Impedance magnitude (Fig. 4) and phase (Fig. 5) are the averages over 7 measured curves for each metal foil. The access resistance for the platinum and the platinum/iridium

foil is 393Ω , whereas the stainless steel electrode has a higher access resistance of about 504Ω . The increased access resistance can be explained with the different wire materials, since the specific resistance of copper is much lower than that of platinum. Cut-off frequencies were measured as follows: $f_{\text{stainless steel}} = 3.2$ kHz, $f_{\text{platinum}} = f_{\text{platinum/iridium}} = 1.2$ kHz. As expected, the impedance magnitude of the stainless steel electrode is definitely higher. Following impedance magnitudes were measured at frequencies at minimal phase: platinum: 4.2 k Ω at 71 Hz platinum/iridium: 5 k Ω at 80 Hz and stainless steel: $11,4$ k Ω at 33 Hz.

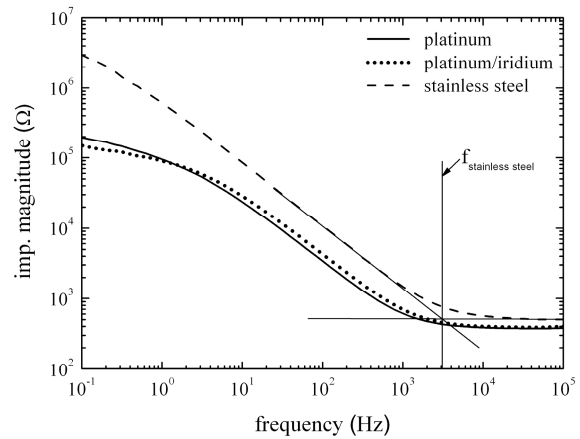


Fig. 4 Impedance magnitude of platinum, platinum/iridium and stainless steel electrodes.

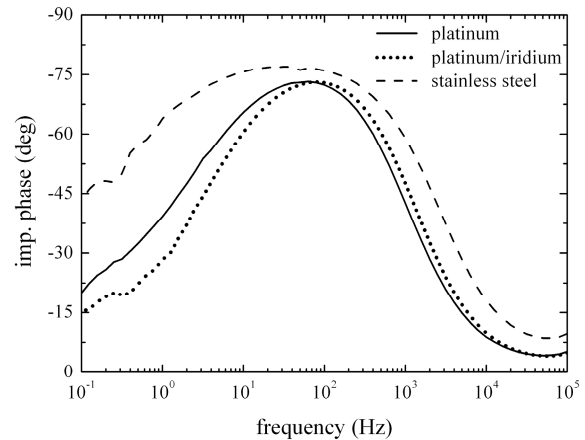


Fig. 5 Impedance phase of platinum, platinum/iridium and stainless steel electrodes.

Pulse test

The voltage responses for the 0.5 mA, $200 \mu\text{s}$ rectangular and biphasic pulses of the 3 different electrode materials are shown in Fig. 6.

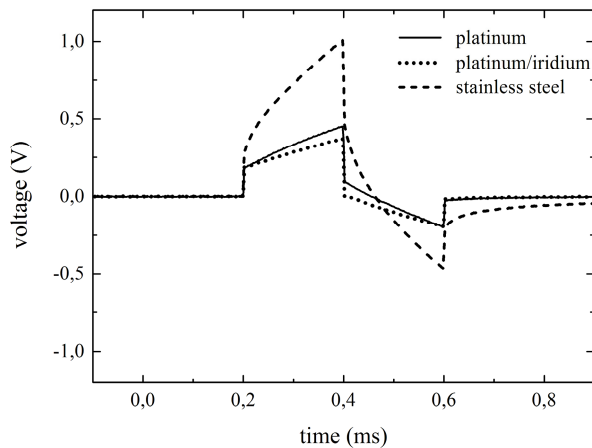


Fig. 6 Voltage responses for 0.5 mA, 200 μ s rectangular, biphasic pulses of platinum, platinum/iridium and stainless steel electrodes.

The stainless steel electrode shows a voltage drop over the access resistance of 250 mV, whereas both other electrodes have a voltage drop of 187 mV, what confirms the results of the impedance spectroscopy. The peak of the voltage ramp V_c is crucial for charge injection capacitance. The higher the peak, the smaller is the capacitance. The best performance for the charge injection capacitance shows the platinum/iridium electrode with a capacitance of 572 nF. The poorest performance demonstrates the stainless steel electrode with 126 nF. The voltages and the derived capacitances are listed in Table 2. The capacitance density was calculated with a geometric electrode area of $4.54 \times 10^{-3} \text{ cm}^2$ for all electrodes.

Table 2 Access resistance, voltage V_c and the derived capacitance

Material	V_a (mV)	$V_c - V_a$ (mV)	C (nF)	Cd ($\mu\text{F}/\text{cm}^2$)
Platinum	187	262	382	84
Platinum/Iridium	187	175	572	126
Stainless steel	250	797	126	28

IV. DISCUSSION AND CONCLUSIONS

A new design for a 48-channel microelectrode array, based on silicone rubber (PDMS) and metal foil was presented. The laser-technology was modified to prepare the electrode for micro-spot-welding interconnection. It was shown, that the laser process for different electrode materials is possible with this fabrication technology. Micro-spot-welding as interconnection technology could be well integrated in the whole fabrication process. Though, spot welding of the copper wire and the stainless steel electrode was not possible. However, medical grade materials, e.g.

stainless steel 316 LVM or MP35N will be used for chronic implants.

Electrical impedance spectroscopy showed definitely higher impedances for stainless steel. The relation between the impedance magnitude and the access resistance is decreasing with decreasing frequencies and at a frequency of 300 Hz it is already down to 1.2 %.

Platinum/iridium electrodes showed the best performance in pulse test. Already a dotted percentage of 10 % iridium results in a rising of the charge injection capacitance of 66 % in respect to pure platinum. At least for platinum and platinum/iridium it is ensured, that there are no irreversible reactions, what is not the case with the stainless steel foil [5]. The better capacitive properties of platinum/iridium predestine it for stimulating electrodes. Neuronal recording results would be also qualitatively better with platinum/iridium or pure platinum foil, however it must be kept in mind that stainless steel is much cheaper. Therefore, it is still a proper alternative for large recording electrodes.

ACKNOWLEDGMENT

This work was supported by the German Ministry for Education and Research (BMBF Grant: ExistGo Bio)

REFERENCES

- Schuetzler, M., Stiebs, S., King, B., Suening, G.: Fabrication of Implantable Microelectrode Arrays by Laser-Cutting of Silicone Rubber and Platinum Foil. *J Neural Eng*, Vol. 2, 2005, pp. 121-128.
- Leuthardt, E.C., Schalk, G., Wolpaw, J. R., Ojemann, F. G., Moran, D. W.: A brain-computer interface using electrocorticographic signals in humans. *J Neural Eng*, Vol. 1, 2004, pp. 63-71.
- D. R. Nair, C. C. McIntyre, and H. Lueders, "Chronic Subdural Electrodes in the Management of Epilepsy," *Clin Neurophysiol*, vol. 119, no. 1, pp. 11-28, 2008.
- Henle, C., Schuetzler, M., Ordonez, J., Stieglitz, T.: Scaling Limitations of Laser-Fabricated Nerve Electrode Arrays. 30th Annual International Conference of the IEEE Engineering in Medicine and Biology Society (Canada, Vancouver) (2008).
- N. d. N. Donaldson and P. E. K. Donaldson, "Performance of Platinum Stimulating Electrodes, Mapped on the Limit-Voltage Plane. Part 2: Corrosion In vitro," *Med Biol Eng Comput*, vol. 24, pp. 431-438, 1986.

Author: Dipl.-Ing. Christian Henle
 Institute: IMTEK, Department for Microsystems Engineering, Laboratory for Biomedical Microtechnology
 Street: Georges-Koehler-Allee 102
 City: 79110 Freiburg i. Breisgau
 Country: Germany
 Email: christian.henle@imtek.de

Position Decoding of Hippocampal Place Cells

S. Schaffelhofer¹, C. Guger¹, M.V. Sanchez-Vives², J. Brotons-Mas², and T. Gener²

¹ g.tec medical engineering GmbH, Schiedlberg, Austria

² Institut d'Investigacions Biomèdiques August Pi i Sunyer, Barcelona, Spain

Abstract— Place cells are pyramidal neurons located in the hippocampus of rats which action potential activities are in correlation with the position of the animal. The fact that different place cells are active at different locations (place fields) allows the reconstruction of the animal's position by the use of its brain waves. In the first step of this process the firing fields are localized by recording and merging action potentials (spikes) and position of the animal. In the second step the activity of unseen parts of the recording are compared with the data of step 1 and the position was reconstructed with the Bayesian 2-step algorithm. The decoded position agreed well with the real position of the animal.

Keywords— Place cells, position reconstruction, Bayesian 2-step;

I. INTRODUCTION

One of the most investigated neurons, the so-called place cells [1], are located in the Hippocampus [2], an important brain region for navigational skills. Place cell neurons have a background firing rate of about 0.1 Hz, but when the animal enters the neurons responsible location, the so-called place field, the firing rate goes up to about 10-20 Hz. These local fields can be stable of up to 150 days [3]. Recordings of place cell neurons of the hippocampus show their firing fields at different locations in space. The correlation of different neurons to different positions allows the reconstruction of the animal's position from their brain waves. The goal was to reconstruct the positions of rats in square open fields with sizes between 0.5 m x 0.5m – 1 m x 1 m.

II. METHODS

A pre-condition of neuronal decoding is the technology for single cell recordings. To be able to distinguish superimposed spikes [4] of different neurons, recordings were made with tetrodes [5]. These multiple wired electrodes dispose of four different channels with an inter-electrode distance of less than 40 μm . Every time the signal exceeds a given threshold the signals was recorded for 1 ms (200 μs before and 800 μs after the spike event) with a sampling rate of 48 kHz. Since the relative distance of each electrode-tip to the recorded cell will be different, the amplitude and

spike duration differ. This allows the assignment of spike activities to specific neurons. For this purpose manual spike-sorting [4] was applied on the recordings. To be able to assign spike activities to the positions of the animal the trajectory of the rat was tracked with a video-tracking-system. After the action potentials and position were recorded two steps are necessary to reconstruct the position: encoding and decoding (see Figure 1). In the encoding step the arena is divided by software into 64 bins in X- and 64 bins in Y-direction. Every recorded spike is then assigned to the position (bin) the rat was at the moment of activity. The results of this process are matrices including the total amount of spikes of a neuron for every bin. The amount of spikes in each bin gets then normalized with the time the animal spent in this bin. This normalization leads to the so-called firing rate map – a map which represents the firing rate of a neuron over all bins the rat has visited during the recording. The firing rate maps of all neurons were then used to train three different algorithms.

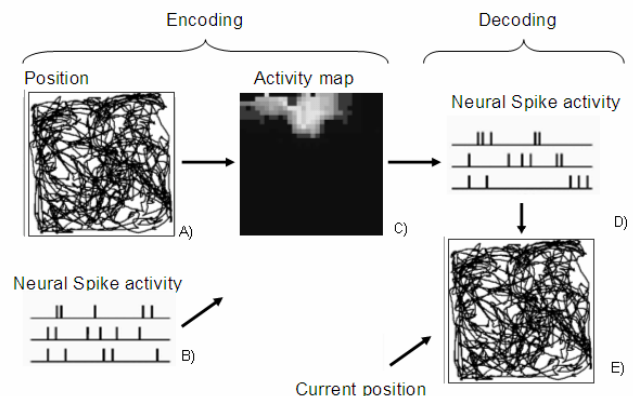


Fig. 1 Encoding and Decoding. The spikes of different neurons (B) are assigned to the position (A) of the animal acquired with a video tracking system. A shows the trajectory of the rat within the recording arena. B shows the spike activity over time for three different neurons. The result is a firing rate map (C) representing the individual firing rates of a neuron over position. Bright pixels are representing positions of high neuronal activity whereas dark pixels represent position of low or no activity. In the decoding step the firing rates within a time window of unseen recording parts (D) are compared with the positions of the firing rate maps and the position gets reconstructed (E).

In the decoding step a time window with a length between 1 s and 8 s was moved along time of unseen recording parts in 500 ms steps. For every step the firing rates of all neurons within the this time-window was calculated and compared with the normalized spike frequencies of the firing rate maps to find the best fitting position. For the reconstruction process ‘template matching’, ‘Bayesian 1-step’ and ‘Bayesian 2-step’ algorithm were used [6]. The reconstruction results were calculated for unseen recording parts with cross validation and for the hole recording (100% of the recording was used for encoding and 100% recording were used for decoding). The reconstruction was calculated for six different rats.

III. RESULTS

The Bayesian 2-step algorithm showed the best results for all rats (Figure 2). The median error of unseen recordings were calculated with a 3 x 3 cross validation and were 9 cm in a 50 cm x 50 cm arena in best case (brain region: CA1) and 45 cm in a 100 cm x 100 cm arena in worst case (brain region: Subiculum). Window lengths of 4000 ms brought the best results.

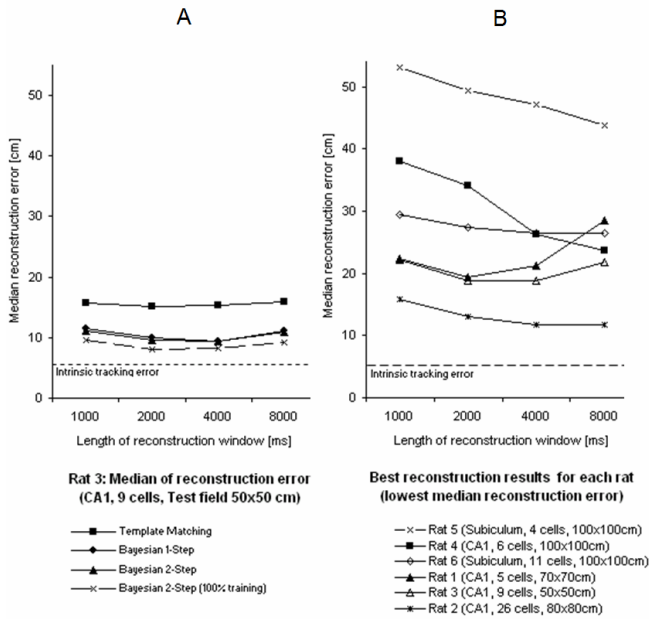


Fig. 2 (A) shows the position reconstruction results of rat 3 for different reconstruction window sizes and all three reconstruction algorithms. (B) shows the best reconstruction results for each rat.

Figure 3 shows the reconstruction results of rat 3 over 160 seconds. The reconstruction error was 1 cm in the best

and 35 cm in the worst case for Bayesian 2-step. The median reconstruction error was 9 cm. The running speed of the rat was between 0 and 42 cm/s. The spiking frequency of the neurons was between 0 and 38 Hz.

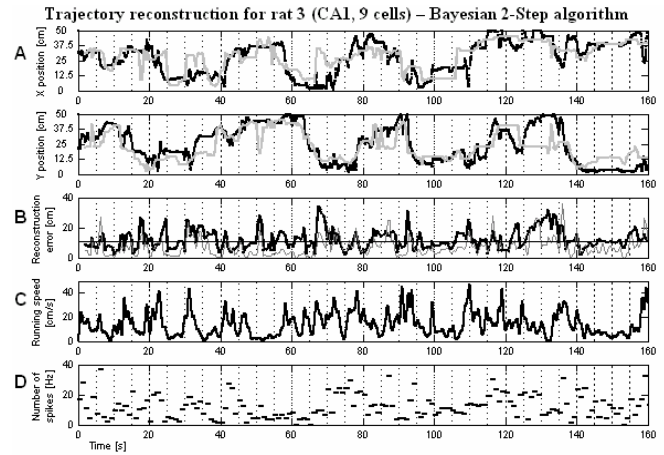


Fig. 3 (A) shows the x- and y-position of the rat tracked with a video system (black) and the reconstructed position (grey). (B) Reconstruction error in cm (horizontal dark line shows median error). (C) Running speed (D) Firing rate

IV. DISCUSSION

The study of six different rats demonstrated that the position of rats in open fields can be reconstructed by the use of place cell recordings. The median error of the Bayesian 2-step algorithm was 9 cm and was achieved with only 9 neurons. In total six different rats were investigated and errors between 9 cm and 45 cm could be found. The accuracy increased significantly with the number of neurons. Furthermore different brain regions were compared. Place cells from CA1 region showed higher accuracies than cells in the subiculum. In future the position reconstruction is planned to be realized in real-time. Therefore automatic sorting algorithms instead of offline manual cluster sorting have to be implemented. However, the ability of encoding neuronal activities holds great promise for the development of neuroprosthetics that rely on control signals from single neurons.

ACKNOWLEDGMENT

The work was funded by EU IST project PRESENCIA.

REFERENCES

1. O'Keefe J, Dostrovsky J (1971) The hippocampus as a spatial map: preliminary evidence from unit activity in the freely moving rat. *Brain Research* 31: 573-590
2. O'Keefe J, Nadel L (1978) *The hippocampus as a cognitive map*. Clarendon Press, Oxford.
3. Thompson LT, Best PJ (1990) Long-term stability of the place-field activity of single units recorded from the dorsal hippocampus of freely behaving rats. *Brain Res* 509:299-308
4. Lewicki MS (1998) A review of methods for spike sorting: the detection and classification of neural action potentials. *Network: Computation in Neural Systems* 9:54-78
5. Gray CM, Maldonado PE, Wilson M et al (1995) Tetrodes markedly improve the reliability and yield of multiple single-unit isolation from multi-unit recordings in cat striate cortex. *Journal of Neuroscience Methods* 63: 43-54
6. Zhang K, Ginzburg I, McNaughton BL (1998) Interpreting neuronal population activity by reconstruction: unified framework with application to hippocampal place cells. *J Neurophysiol* 79:1017-1044

A Novel Assembly Method for Silicon-Based Neural Devices

S. Kisban¹, J. Kenntner¹, P. Janssen², R. v. Metzen³, S. Herwik¹,
U. Bartsch¹, T. Stieglitz³, O. Paul¹ and P. Ruther¹

¹Microsystem Materials Laboratory and ³Laboratory for Biomedical Microtechnology
Department of Microsystems Engineering (IMTEK), University of Freiburg, Germany
²Laboratory for Neuro- and Psychophysiology, University of Leuven, Belgium

Abstract— This paper reports on a novel interconnection technology for silicon-based neural devices used in extracellular recording. It is based on a flip-chip bonding process establishing the electrical connection of the silicon specimen and a highly flexible polymer cable via electroplated contact structures. This process makes possible the parallel connection of multiple bonding pads with high integration density. By the integration of a structurable fluoropolymer on the cables as an adhesion layer the mechanical connection is improved simultaneously. Further, the adhesion layer inherently encapsulates the bonding sites and allows omitting the application of an additional underfill. Test structures were characterized with respect to the electrical and mechanical reliability of this interconnection approach. The storage in Ringer's solution for 12 days minimally affected the cable connection and its inherent encapsulation capability. Furthermore, a neural device was assembled with this technology and its capability for intracortical neural recording was demonstrated.

Keywords— Microprobe, neural device, flip chip, silicon, extracellular recording

I. INTRODUCTION

In the field of neural recording and functional electrical stimulation, silicon-based microprobes have propagated over the last decades [1] and lead to various commercially available systems (NeuroNexus Technologies, Ann Arbor, Michigan, USA and Blackrock Microsystems, Salt Lake City, Utah, USA). Major advantages of these systems in comparison to wire electrodes are the increased number of recording sites and their precise and reproducible fabrication. In terms of chronic application, most of these electrode arrays are connected to the external instrumentation using flexible cables. As an example, 96 electrodes are individually connected in the Utah array via 25- μm -thick insulated Pt/Au wires ultrasonically bonded in a serial process to the rear of the microprobe [2]. In case of the Michigan probes, a thin ($\sim 4\ \mu\text{m}$) silicon substrate with insulated polysilicon leads interconnects the silicon-based electrode comb with a connector [3]. As claimed by the authors however, the relatively high Young's modulus and brittle character of the applied cable materials, i.e. silicon and polysilicon, are responsible for the reduced cable flexibility and robustness

required for some implant applications [3]. To overcome this situation, polymer cables have been introduced that can be fabricated monolithically together with the microprobes [4,5]. Alternatively, cables can be fabricated on a separate wafer using simplified process sequences. As a result, cables with sufficiently high flexibility are obtained that minimize tethering forces applied on the implant. However, one drawback of the latter solution is the need of an additional assembly process which combines the flexible polyimide ribbon cable with a microprobe by means of the so-called *MicroFlex Technology* [6-8]. This technology applies individual rivet-like bumps to create an electrical as well as mechanical connection between cable and electrode array. Although advantageous in the development of prototypes, this technology is a tedious serial process which requires an additional mechanical strengthening and encapsulation of the interconnect areas after assembly.

This paper presents a novel approach that combines the advantages of the modular fabrication of silicon microprobes and flexible polymer cables with a rapid parallel assembly technique that inherently enables a mechanical strengthening and encapsulation of the electrical interconnect. To investigate this novel assembly process, dedicated test structures were realized, assembled and characterized with respect to mechanical strength and reliability.

II. MATERIALS AND METHODS

A. Test specimen fabrication

To characterize the electromechanical reliability of the assembly process, a dedicated test-structure comprising a silicon-based rectangular chip representing the microprobe and a flexible cable are fabricated sharing an identical mask set. As illustrated in Fig. 1(a), silicon chip and flexible cable comprise bonding pads connected through 7.5- μm -wide leads to contact pads for electrical characterization. A two-point resistance measurement between individual bonding pads to test the electrical connectivity is enabled using any of the contact pad pairs #1-#11, #2-#12, #5-#7, or #6-#8. A corresponding four-point contact resistance measurement injects a probing current between pads #4 and #9 and meas-

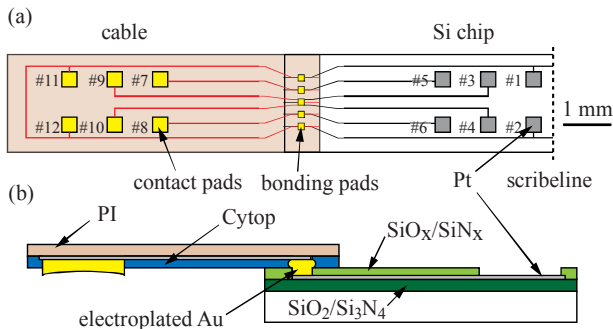


Fig. 1. (a) Test structure layout and (b) schematic cross-section of connected silicon chip and cable.

ures the respective voltage drop between pads #3 and #10. While the cable and chip size is fixed to $2.5 \times 10 \text{ mm}^2$, the edge length L_p of individual bonding pads and the spacing d_p between them is varied from $30 \mu\text{m}$ to $200 \mu\text{m}$.

The fabrication of the cables summarized in Fig. 2 starts with the deposition of a first $5\text{-}\mu\text{m}$ -thick polyimide (U-Varnish S, UBE, Tokyo, Japan) layer using spin-coating. This is followed by the definition of a 300-nm -thick Pt metallization using a lift-off process shown in Fig. 2 (b). Figures 2 (c1-f1) and (c2-f2) illustrate two different versions whereas a fluoropolymer layer, i.e. Cytop[®] (CTL 809M, Asahi Glass, Tokyo, Japan), with a thickness of $4.5 \mu\text{m}$ is spin-coated directly on top of the metallization or on a second $5\text{-}\mu\text{m}$ -thick polyimide (PI) layer, respectively. This fluoropolymer serves as a functional layer to increase the mechanical strength of the interconnect and inherently

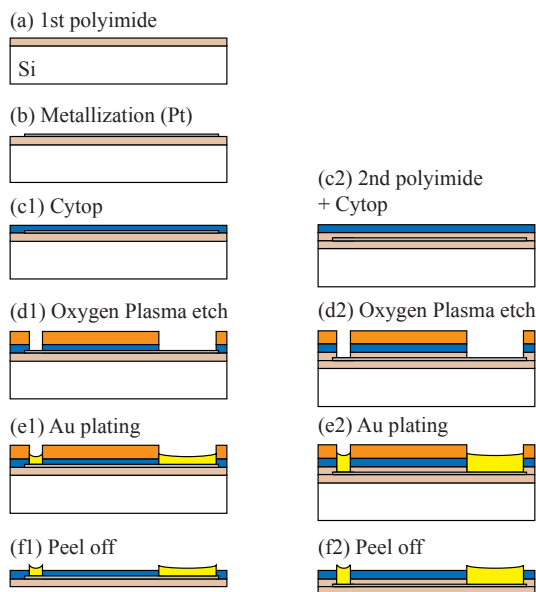


Fig. 2. Fabrication process of the polymer cable with electroplated gold pads and an adhesion layer.

creates an encapsulation of the bonding sites. Cytop[®] is reported to be biochemically stable [9] and shows a minimal water uptake of less than 0.01% at 60°C [10] which is beneficial in terms of reduced stress applied on the bonding sites during water exposure and subsequent swelling. The moisture permeability of Cytop[®] is reported to be in the range of $1.1 \times 10^{-12} \text{ (cm}^3\text{cm)/(cm}^2\text{sPa)}$ [10]. In addition, the ability of Cytop[®] for low-temperature bonding has been demonstrated earlier [11] which makes the material ideally suited for use in this specific application.

The fluoropolymer layer and the underlying PI layers are structured using reactive ion etching (RIE) in an oxygen plasma as shown in Fig. 2 (d). Electrical contact structures, i.e. the bonding sites, are realized using a galvanostatic electroplating process shown in Fig 2 (e). Thick gold is deposited protruding the cable surface by $2\text{-}10 \mu\text{m}$ with the remaining photo resist preventing lateral growth. For electroplating purposes all bonding pads and leads of the test structure are connected to an annular electrode via feeding wires connected to the current source. Finally, the photo resist is removed and the cables are separated from the wafer by peeling them off as shown in Fig. 2 (f). For comparison with the *MicroFlex Technology*, conventional cables [8] are fabricated as illustrated in Figs. 2 (a1)-(f1) with the Cytop layer substituted by a second PI layer.

The fabrication of the silicon chip starts with the deposition of a stress compensated layer stack of SiO_2 and Si_3N_4 using low pressure chemical vapor deposition (LPCVD) on a $525\text{-}\mu\text{m}$ -thick 4-inch wafer. The Ti/Pt/Ti metallization with thicknesses of $20/300/20 \text{ nm}$ is patterned using a lift-off process. A second passivation layer comprises a $\text{SiO}_x/\text{SiN}_x$ layer stack deposited using plasma enhanced chemical vapour deposition (PECVD). It is opened at the bonding and contact pad locations using RIE.

B. Assembly process

The assembly of the test system components, i.e. silicon chip and flexible PI cable, is performed using a commercial flip-chip bonder (Finetech Fineplacer 96 λ , Berlin, Germany). In this way, a simultaneous connection of all bonding sites is achieved. In a first step, the PI cable is positioned on a pick-up tool and aligned with respect to the silicon chip. The electrical and mechanical connection is established at a temperature of 160°C , well above the glass transition temperature $T_{g,\text{Cytop}} = 108^\circ\text{C}$ of Cytop[®] and at a pressure of 4.83 MPa applied for 120 s . Additionally an ultrasonic pulse is applied for 1 s after 100 s of bonding time. In case of the PI cables without Cytop[®] an additional n-butyl cyanoacrylate (Vetbond, 3M, St. Paul, USA) underfill is applied to mechanically strengthen the connection. Figure 1 (b) shows a

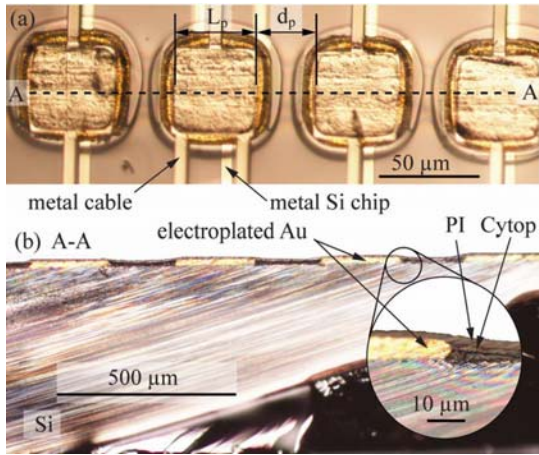


Fig. 3. Top view on the connection between silicon chip and the polymer cable with PI/Pt/Cytop layer stack (a) and a micrograph of the cross-section.

schematic cross-section of an assembled PI cable and silicon chip.

III. RESULTS

A. Test specimen fabrication

Figure 3 (a) shows a top view on the established connection between a PI/Cytop cable {cf. Fig. 2 (f1)} and the silicon chip. The edge length L_p of the pads and the spacing d_p between were $50 \mu\text{m}$ each with the electroplated Au bumps protruding $8 \mu\text{m}$ above the surface. Visible edges around the bonding sites suggested a tight mechanical connection of the remaining area. A cross-sectional view of the connection obtained by wafer dicing is given in Fig. 3 (b). It shows a convolution of the cable after assembly.

We successfully assembled interconnects comprising bonding pads with a minimal edge length and spacing of $L_p = d_p = 40 \mu\text{m}$. The four-wire resistance of individual bonds between PI cable and silicon chip was found to be $1.01 \pm 0.42 \text{ m}\Omega$. The reliability of the mechanical connection is evaluated in tensile shear tests using a tensile testing machine (zwicki TC-FR2.5TS.D09, Zwick GmbH, Ulm, Germany). Test specimens of PI cables without Cytop[®] layer and underfill assembled using the described flip-chip bonding process showed a maximal shear force of $990.46 \pm 0.30 \text{ mN}$ compared to $902.07 \pm 268.33 \text{ mN}$ for the cable reference with the connection established using five *MicroFlex* bumps.

The introduction of Cytop[®] lead to maximal shear forces of $6.76 \pm 1.34 \text{ N}$ compared to $6.80 \pm 1.57 \text{ N}$ of specimens where the connection was strengthened by a cyanoacrylate underfill. In both cases the maximal shear forces were most-

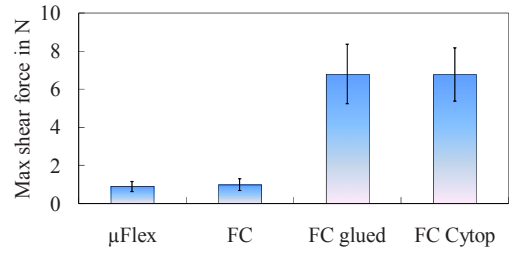


Fig. 4. Results of the tensile shear tests for a *MicroFlex* (μFlex) connection with 5 bumps, a flip-chipped (FC) connection, a FC connection with additional cyanoacrylate underfill (FC glued) and a FC connection with Cytop (FC Cytop). The bonding area is 2.9 mm^2 .

ly limited by the mechanical strength of the cable. The maximal shear forces of the four different interconnects with corresponding standard deviations obtained from minimal four samples per type are summarized in Fig. 4.

Furthermore the specimens were exposed to thermal cycling tests according to MIL standard 883 with temperature bounds of -65°C and 150°C . After 500 temperature cycles no significant influence on the electromechanical performance of the interconnects was observed.

B. Neural device

Neural devices for intracortical applications as developed within the NeuroProbes project [11] have been assembled using the novel assembly technology. The silicon microprobes with 36 bonding sites covering 0.76 mm^2 were fabricated as described previously [8]. The PI cables were processed as mentioned before. The impermeability of the Cytop insulation under harsh conditions comparable to an in vivo application was tested using silicon microprobes with non-functional electrodes exposed to Ringer's solution for 288 h. The impedance spectra covering the frequency range from 10^2 Hz to 10^6 Hz measured between two adjacent bonding sites are shown in Fig. 5. These spectra are taken from a test structure directly after assembly (dry), after immersion to the Ringer solution (0 h), and after 288 h. A slight reduction in impedance was observed after immersion

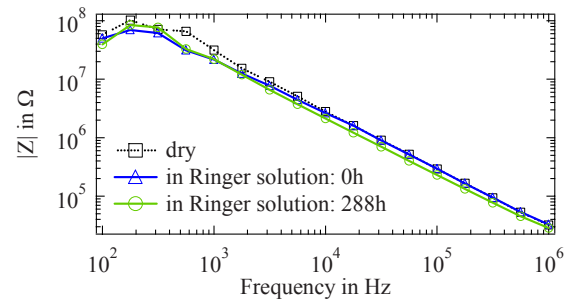


Fig. 5. Impedance spectra between 2 bonded sites after assembly, after immersion into Ringer's solution and after 288 h in Ringer solution.

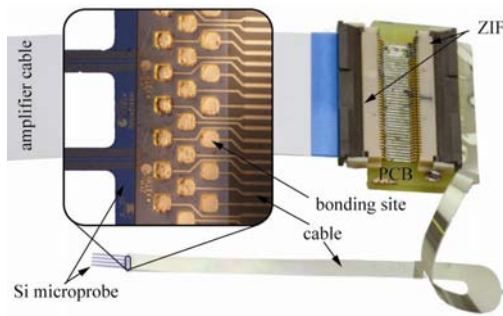


Fig. 6. Photograph of the neural device and the connection between Si microprobe and the polymer cable.

into the electrolyte and after the total duration of 288 h, which however would not affect the functionality of a neural device in terms of recording quality.

First devices, as illustrated in Fig. 6, have been implanted sub-chronically into the anterior intraparietal area of a Rhesus monkey (pursuant to Directive 86/609/EEC). For this purpose a chamber was attached to the skull as shown in Fig. 7 (a). The probe insertion was performed as described in [8]. Single unit activity was observed on multiple channels. Exemplarily sorted spikes with a peak-to-peak signal amplitude of $220 \mu\text{V}$ are shown in Fig. 7 (b).

IV. CONCLUSIONS

Hybrid neural devices were fabricated with a novel interconnection technology, creating an electrical and mechanical connection simultaneously with an inherent encapsulation. The presented process makes possible the parallel connection of multiple electrical contacts and thereby acce-

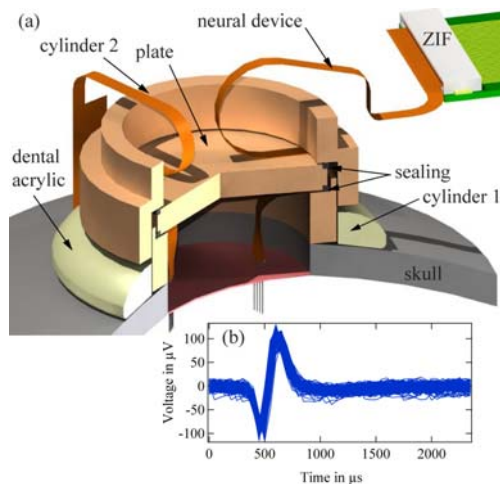


Fig. 7. Schematic of a protection chamber with two neural devices implanted (a) and sorted spikes of one electrode (b).

lerates the assembly process significantly. A minimal pitch of $80 \mu\text{m}$ of the bonding sites was achieved. *In vitro* test showed stable electrical behavior. First neural devices were fabricated and implanted successfully.

ACKNOWLEDGMENT

Special thanks go to Kay Steffen for electroplating. The work described in this paper was performed in the frame of the Information Society Technologies (IST) Integrated Project *NeuroProbes* of the 6th Framework Program (FP6) of the European Commission (Project number IST-027017).

REFERENCES

1. K. D. Wise *et al.*, Wireless Implantable Microsystems: High-Density Electronic Interfaces to the Nervous System, *Proc. IEEE Biomed. Appl. for MEMS and Microfluidics*, vol. 92, pp. 423-426, 2004
 2. P. K. Campbell *et al.*, A Silicon-Based, Three-Dimensional Neural Interface: Manufacturing Processes for an Intracortical Electrode Array, *IEEE Trans. Biomed. Eng.*, pp. 758-768, 1991
 3. J. F. Hetke *et al.*, Silicon Ribbon Cables for Chronically Implantable Microelectrode Arrays, *IEEE Trans. Biomed. Eng.*, vol. 41, pp. 314-321, 1994
 4. C. Pang *et al.*, A New Multi-Site Probe Array with Monolithically Integrated Parylene Flexible Cable for Neural Prostheses, *Proc. 27th Annual Int. Conf. of the IEEE Eng. in Med. and Bio. Soc.*, pp. 7114-7117, Shanghai, China, 2005
 5. Y. Yao *et al.*, Silicon microelectrodes with flexible integrated cables for neural implant applications, *Proc. 3rd Int. IEEE EMBS Conf. on Neural Eng.*, pp. 398-401, Kohala Coast, USA, 2007
 6. J. U. Meyer *et al.*, „High Density Interconnects and Flexible Hybrid Assemblies for Active Biomedical Implants“, *IEEE Trans. on Advanced Packaging*, 24, pp. 366-374, 2001
 7. J. F. Hetke *et al.*, 3-D silicon probe array with hybrid polymer interconnect for chronic cortical recording, *IEEE EMBS Conf. on Neural Engin.*, Capri, Italy, pp. 181-184, 2003
 8. S. Kisban *et al.*, Microprobe Array with Low Impedance Electrodes and Highly Flexible Polyimide Cables for Acute Neural Recording, *Proc. 29th Annual Int. Conf. on the IEEE Eng. in Medicine and Biology Soc.*, Lyon, France, pp. 175-178, 2007
 9. A. Han *et al.*, A Low Temperature Biochemically Compatible Bonding Technique Using Fluoropolymers for Biochemical Microfluidic Systems, *13th Annular Int. Conf. on MEMS*, Miyazaki, Japan, pp. 414-418, 2000
 10. Cytop product datasheet, Asahi Glass Co., Ltd, Japan
 11. U. Bartsch *et al.*, Low-Temperature Adhesive Flip-Chip Bonding Using Cytop combined with Electrical Stud Bump Interconnects, *19th MicroMechanics Europe Workshop*, Aachen, Germany, pp. 411-414, 2008
 12. P. Ruther *et al.*, The NeuroProbes project - Multifunctional probe arrays for neural recording and stimulation, *Biomed. Tech.*, vol. 53, no. 1, pp 238-240, 2008
- Author: Sebastian Kisban
 - Institute: Department of Microsystems Engineering (IMTEK) University of Freiburg
 - Street: Georges-Koehler-Allee 103
 - City: 79110 Freiburg
 - Country: Germany
 - Email: kisban@imtek.de

Gait Posture Estimation by Wearable Acceleration and Gyro Sensor

R. Takeda¹, S. Tadano¹, A. Natorigawa², M. Todoh¹ and S. Yoshinari³

¹ Division of Human Mechanical Systems and Design, Graduate School of Engineering, Hokkaido University, 060-8628, Sapporo, Japan

² Formerly Master Course Student, Graduate School of Engineering, Hokkaido University, Sapporo, Japan

³ Hokkaido Industrial Research Institute, Sapporo, Japan

Abstract— A method for gait analysis using wearable acceleration sensors and gyro sensors is proposed in this work. The volunteers wore small sensor unit that included a tri-axial acceleration sensor and three mono-axis gyro sensors. The angular velocity data measured by gyro sensors were used to estimate the translational acceleration during gait. The translational acceleration was then subtracted from the acceleration sensor measurements to obtain the gravitational acceleration, giving posture of lower limb segments. Segment posture along with body measurements were used to obtain the three dimensional positions of joint centers for hip, knee and ankle during gait. Experiments were carried out on normal gait of three healthy volunteers. As a result, the flexion-extension and the adduction-abduction angle of the hips and the flexion angle of knees were calculated and compared with a camera. The correlation coefficients were 0.888 for the flexion-extension angle of hip, 0.721 for the internal-external rotation angle of hip, 0.924 for the flexion angle of knee. In addition, knee and ankle joint trajectories in the horizontal plane showed that the both right left and legs were bilaterally symmetric.

Keywords—gait analysis, acceleration sensor, gyro sensor.

I. INTRODUCTION

Gait analysis is a clinical tool for obtaining quantitative information of a person for diagnosing walking disabilities. Common methods for gait analysis are placing reflective markers on a person and record the trajectories of the markers by infrared digital cameras, such as the Vicon motion analysis system (Vicon Motion Systems, Inc.). However, such systems are large, expensive and sophisticated to handle. Therefore, most measurements are restricted to indoor laboratories and are not suited for monitoring daily human life.

An alternative method for measuring human motion is by placing small acceleration sensors on the body to obtain acceleration data [1]. However, compared to conventional camera based systems, sensors systems can not provide three dimensional position data, but only information such as the acceleration of a body segment. Therefore, many works in the past have proposed methods to calculate three dimensional human positions from sensor data.

A popular method for estimating body segment posture is by integrating angular velocity data measured by gyro sensors worn on segments [2]. However, small errors included in angular velocity accumulated with integration, thus resulted in inaccuracies in body segment posture calculation. Another interesting method used the displacement of acceleration sensors and gyro sensors on the thigh and shank to estimate three-dimensional knee joint angles during walking [3] [4]. High accuracy was reported for estimating the relative knee joint angles but the actual body posture in the base coordinate system was not reported.

In theory, it is possible to estimate posture of segments by using the gravitational acceleration measured by acceleration sensors. However, during dynamic states such as gait, noise and translational acceleration component gets included. The authors [5] used the cyclic patterns found in acceleration data during gait to create an algorithm to obtain optimal gravitational acceleration pattern. Though, an optimal three dimensional representation of a person in the base coordinate system was reported, differences in joint angle were found with camera. In addition, the method was only applicable to constant motion such as gait.

Since using only acceleration sensors resulted in joint angle differences, this study used angular velocity in addition to acceleration data to calculate lower limb body posture during gait. The angular velocity was used to calculate the translational acceleration during gait. The estimated translational acceleration was then subtracted from the data measured by acceleration sensors to obtain the gravitational acceleration. The gravitational acceleration provided the inclination angle of the segments and consequently the three dimensional posture of lower limb segments. To test our method, gaits of three healthy volunteers were measured during walking on a flat floor. As a result, the hip joint flexion-extension, hip joint abduction-adduction and knee joint flexion angles were estimated. The characteristic three-dimensional walking established in this method could be visualized by the expression using a stick figure model in a base coordinate system and the knee and ankle joint trajectories in the horizontal plane were calculated.

II. METHOD

A. Sensor System

The sensor system used in this investigation consisted of small wearable sensor units, each containing a data logger and a sensor head. The sensor head has a tri-axial acceleration sensor (H34C, Hitachi Metals, Ltd.) and three gyro sensors (ENC-03M, muRata Manufacturing Co., Ltd.). One sensor unit can measure the acceleration and the angular velocity along three orthogonal axes simultaneously. The data logger can record the acceleration and angular velocity data for a maximum of 160 seconds at a sampling rate of 100Hz. Sensors were placed on four segments (left and right thigh (LT, RT), left and right shank (LS, RS)) as shown in Fig. 1.

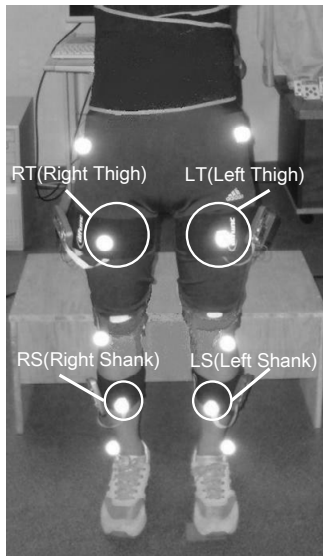


Fig. 1 Sensor attachment location. Sensors are attached to both thighs (LT, RT) and both shanks (LS, RS).

B. Calculating Inclination from Acceleration Sensors

The three-dimensional position of lower body joints can be calculated from inclination angle and length of each body segment. We presumed that the inclination angle of the segment is equal to the inclination angle of the attached acceleration sensor. And the inclination angle of a sensor can be expressed using the following Eq. (1).

$$\theta^\alpha = \sin^{-1}\left(\frac{a_x^\alpha}{g}\right) \quad (1)$$

Here, a_x^α is the gravitational acceleration measured along x axis direction of segment α (LT, RT, LS, RS). During static

state the gravitational acceleration is the only acceleration measured, therefore the inclination angle is the inclination against the direction of gravity.

C. Measurement of Hip Joint Angle

Figure 2 shows the gait analysis model used for this study in the sagittal plane. Sensor S^{RT} (or S^{LT}) is placed on the thigh and sensor S^{RS} (or S^{LS}) is placed on the shank. The distances between; sensor S^{RT} (or S^{LT}) and hip joint (r_{HT}), sensor S^{RT} (or S^{LT}) and knee joint (r_{KT}), S^{RS} (or S^{LS}) and knee joint (r_{KS}) are measured.

The hip joint angle can be calculated if the inclination angle of the thigh segment can be obtained. The acceleration and angular velocity data from the thigh segment, LT and RT, are used to estimate the segment inclination. When there is no translational acceleration at the hip joint the only acceleration that the sensor S^{RT} (or S^{LT}) measures are the gravitational acceleration and rotational acceleration around the hip joint. The rotational acceleration around the hip joint can be obtained from $\dot{\omega}$, the differential of the angular velocity ω at S^{RT} (or S^{LT}), and the distance from RH (or LH) to S^{RT} (or S^{LT}). By using Eq. (2) the rotational acceleration can be subtracted from the measured acceleration \mathbf{O} to give the gravitational acceleration \mathbf{g} . This gravitational can be used to calculate the joint angle of the hip.

$$-\mathbf{g} = \mathbf{O} - \dot{\omega} \times \mathbf{r}_{HT} - \omega \times (\omega \times \mathbf{r}_{HT}) \quad (2)$$

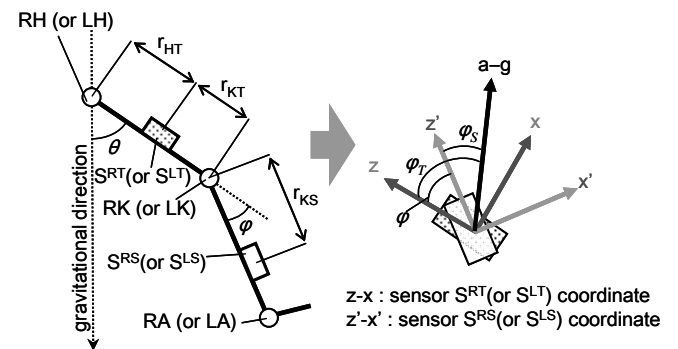


Fig. 2 Gait analysis model using sensors on thigh and shank .

D. Knee Joint Angle Measurement

When the knee joint is in motion with acceleration \mathbf{a} , and angular velocity ω , the acceleration measured from a sensor at distance \mathbf{r}_{Kj} (j is either S (shank: S^{RT} or S^{LT}) or T (thigh: S^{RS} or S^{LS})) from the knee joint is \mathbf{O} (Fig. 2). The following Eq. (3) can be established.

$$\mathbf{a} - \mathbf{g} = \mathbf{O} - \dot{\omega} \times \mathbf{r}_{Kj} - \omega \times (\omega \times \mathbf{r}_{Kj}) \quad (3)$$

Since $(\mathbf{a} - \mathbf{g})$ is the same whether it is measured from S^{RT} (or S^{LT}) or S^{RS} (or S^{LS}), the angle between z-axis of S^{RT} (or S^{LT}) and z'-axis of S^{RS} (or S^{LS}) φ can be calculated by the following Eq. (4).

$$\varphi = \varphi_T - \varphi_S \tag{4}$$

The knee joint flexion angle can then be calculated by $(180^\circ - \varphi)$.

E. Stick Figure Model

A stick figure representation of a volunteer was created to visually confirm the lower limb segments during walking. To convert the position of joints in the relative coordinate system into base coordinate system, the time of heel contact was used. This work used the acceleration at the shank, RS and LS, to determine the leg set on the ground. Once the leg set on the ground is determined, ankle joint, RA or LA, is defined as the origin in the base coordinate system (Fig. 3).

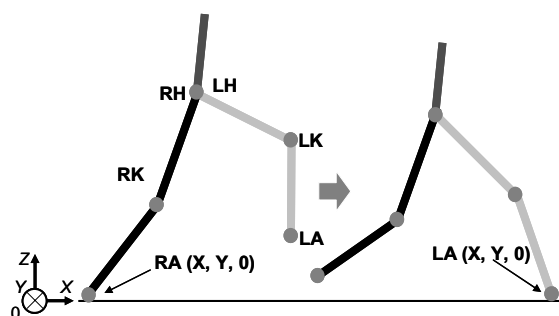


Fig. 3 Stick figure representation of volunteer during heel contact.

F. Experimental Procedure

Three healthy volunteers participated in the experiment. Along with the sensor units on four locations, reflective markers were placed on the volunteers and captured with camera. Volunteers were asked to walk for 5 meters on a flat floor inside a laboratory. The walking velocity was at the discretion of the volunteers, and gait was commenced with the right foot. Body measurements of each volunteer were taken to obtain distances between lower limb joints.

To countermeasure sensor attachment errors, measurements of each sensor unit were taken before and after trials of the volunteer. In addition, measurements of each sensor were taken for two postures, standing upright and sitting flat on the floor. The measurements of the two different postures were used to calibrate the three orthogonal axes of the sensor units. The calibration aligned one axis to the longitudinal direction of the segment, one

axis to the anterior direction and one axis to the left lateral direction.

III. RESULTS AND DISCUSSIONS

Figure 4 and 5 shows an example of the joint angles calculated from this method and those measured from a camera. The vertical axis represents the angles in degrees and the horizontal represents one gait cycle in percentage. The joint angles calculated using this method is shown by dark line and camera by light line. The RSME and correlation coefficient is shown in Table 1. The joint angles of both hip and knee are almost consistent with the results provided by the camera. The slight phase lag in the peak flexion joint angle could be caused by the moving average used to remove noise from the raw acceleration and angular velocity data. The relative displacement in the hip abduction-adduction seems large but this is because the absolute abduction-adduction during walking is actually a lot smaller compared to the hip and knee flexion angles.

The knee and ankle joint trajectories in the horizontal plane were obtained and are shown in Fig. 6. The vertical and horizontal axes represent the measurement in the x and y coordinates respectively, with (0,0) as the center of the right and left hip joint. Knee and ankle joint trajectories were symmetric for both right and left leg.

Table 1 RSME and correlation coefficient of joint angles for each subject.

	Hip Angle (Flexion-Extension)		Hip Angle (Abduction-Adduction)		Knee Angle (Flexion-Extension)	
	RMSE (deg)	CC	RMSE (deg)	CC	RMSE (deg)	CC
Subject (a)	10.34	0.918	5.24	0.892	6.69	0.928
Subject (b)	6.45	0.902	4.10	0.628	6.58	0.954
Subject (c)	9.38	0.845	5.55	0.644	7.10	0.892

IV. CONCLUSIONS

This work showed that the acceleration and angular velocity measured during gait can be used to estimate lower limb body posture. The angular velocity was used estimate translational acceleration, and by subtracting this from the measured acceleration the gravitational acceleration was calculated. The thigh segment posture was measured using the inclination angle against the gravitational acceleration. The knee joint angle was measured using the sensors on the thigh and shank.

There are some limitations to this work. This method assumed that the walking was at a constant velocity, meaning no acceleration was generated. Therefore it might cause errors for measuring movements that are not at constant velocity. However, this work showed that it can provide quantitative information, such as joint angles and joint trajectories, which are important for gait diagnosis.

ACKNOWLEDGMENT

The authors would like to express their thanks to H. Miyagawa, master course student of Laboratory of Biomechanical Design (Division of Human Mechanical Systems and Design, Hokkaido University), for his support and cooperation to experiment and computer data analysis of this study.

REFERENCES

1. Morris J.R.W. (1973) Accelerometry - A technique for the measurement of human body movements. *J Biomech* 6: pp729-736.
2. Tong K. and Granat M. H. (1999) A practical gait analysis system using gyroscopes. *Med Eng Phys* 21, pp87-94.
3. Dejnabadi H., Jolles B.M., Casanova E., et al. (2006) Estimation and visualization of sagittal kinematics of lower limbs orientation using body-fixed sensors. *IEEE Trans Biomed Eng* 53, pp1385-1393.
4. Favre J., Jolles B.M., Aissaoui R. et al. (2008) Ambulatory measurement of 3D knee joint angle. *J Biomech* 41, pp1029-1035.
5. Takeda R., Tadano S., Todoh M. et al. (2009) Gait analysis using gravitational acceleration measured by wearable sensors. *J Biomech* 42, pp223-233.

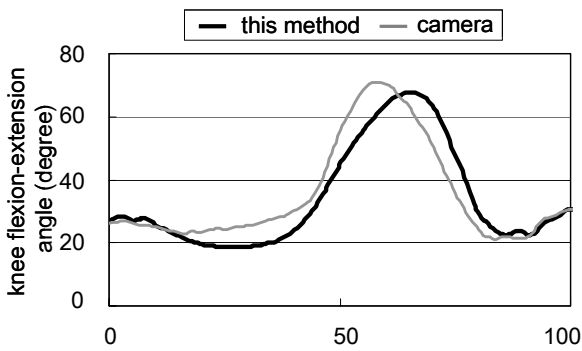


Fig. 4 Knee joint flexion-extension angle comparisons between this method and camera.

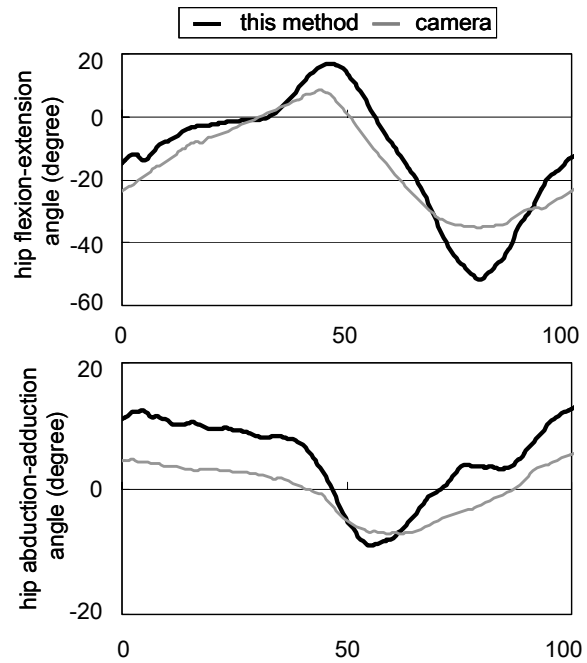


Fig. 5 Hip joint (a) flexion-extension angle and (b) abduction-adduction angle comparisons between this method and camera.

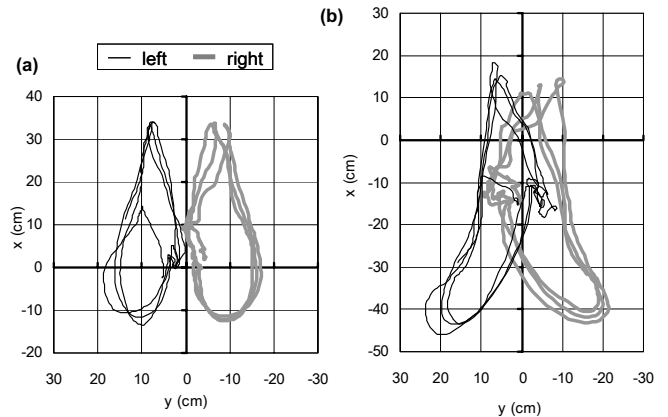


Fig. 6 Joint trajectory of the (a) knee and (b) ankle in the horizontal plane.

Author: Ryo Takeda
 Institute: Hokkaido University
 Street: Kita 13 Nishi 8, Kita-ku
 City: Sapporo
 Country: Japan
 Email: takeda@mech-me.eng.hokudai.ac.jp

Automobile, which can Control an Autonomic nervous system

T.Yambe¹, Y.Shiraishi¹, M.Takashima¹, T.Seki², and R. Kawashima¹

¹ Institute of Development, Aging and Cancer, Tohoku University, Sendai, Japan

² Tohoku University Hospital, Sendai, Japan

Abstract— By the use of the vehicle, function of the Human body has been expanded more and more in the history. If human body will be connected to the vehicle, the vehicle will become a part of a human body. In the previous reports, several investigators have been studying about the man-machine interface. Furthermore, we added the therapeutic effect for the autonomic nervous system during driving in this study. ECG and pulse wave recording system was added to the handle and drive console in the experimental system. Air pressure sensors to detect the respiration and aortic pulse wave were inserted into the drive seat. By the evaluation of the ECG and pulse wave, we can evaluate the circulation dynamics, and furthermore, we can evaluate the pulse wave velocity and fluctuations in hemodynamic derivatives. By the use of this information, several kinds of Aroma, Massage to the Acu-point or the Moxibustion were added to the driver. So, the automobile can control the autonomic nerve condition during driving. After ethical committee allowance we evaluated the effect of aroma and moxibustion therapy on driver. Hemodynamics, HRV and baroreflex system was tended to altered depending of the kinds of Aroma, acupuncture point stimulation with massage and moxibustion. These results suggest that vehicle can become artificial automatic nerve controller in future.

Keywords— automobile, autonomic nervous system, aroma, acupuncture, moxibustion .

I. INTRODUCTION

In the history, function of the Human body has been expanded with vehicles like automobile, ship and plane. If human body will be connected to the vehicle, the vehicle will become a part of a human body (1-5).

Several investigators have been studying about the man-machine interface. In this study, we added the therapeutic effect for the autonomic nervous system during driving. ECG recording system and pulse wave recording system was added to the handle and drive console in the experimental system. Air pressure sensors to detect the respiration and aortic pulse wave were inserted into the drive seat. By the evaluation of the ECG and pulse wave, we can evaluate the circulation dynamics, and furthermore, we can evaluate the pulse wave velocity and fluctuations in hemodynamics. By the use of these information, several kinds of Aroma,

Massage to the Acu-point or the Moxibustion were added to the driver. So, the car can control the autonomic nerve condition during driving.

II. MATERIAL AND METHOD

Concept diagram of the automobile, which can control an autonomic nervous system was shown below.

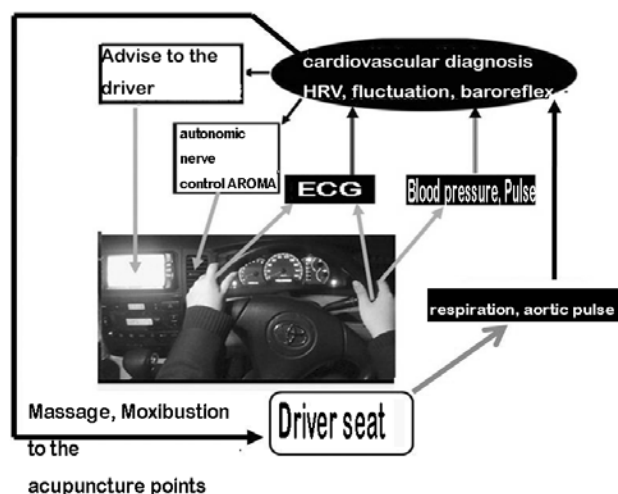


Fig.1 Schematic diagram of the automobile, which can control autonomic nervous system

In the concept, the automobile detected the ECG, pulse wave, blood pressure, and respiratory wave and aortic pulse wave from driver seat.

Respiration and pulse wave were detected by the air pressure sensor shown below.

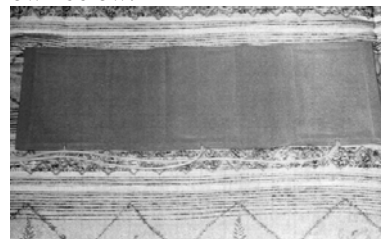


Fig.2 Air bag sensor for detecting respiration and pulse in driver seat

Respiration and pulse wave were detected as we shown below.

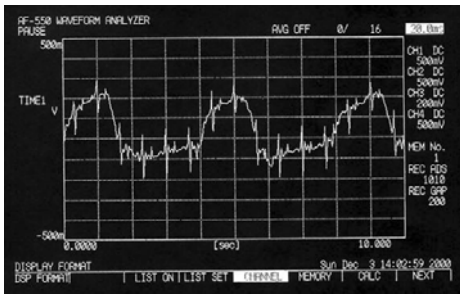


Fig.3 Respiration and aortic pulse wave signals recording from driver seat

So, we can evaluate the respiration and circulation of the driver with air bag sensor in driving seat. From the data line of ECG and pulse wave, we can also calculated the pulse wave velocity.

Based on the quantitative evaluation, HRV, fluctuations in the hemodynamic derivatives, pulse wave velocity calculated from the ECG and pulse wave, baroreflex sensitivity calculated from the time series data of the hemodynamic parameters were quantitatively evaluated and Driver's autonomic nerve condition was diagnosed.

Based on the driver's condition, driving advise and advise for the driver's health was shown in the car navigation system and voice message. Autonomic Nerve control aroma was supplied from the air conditioner based on the information like sympathetic and parasympathetic balance in HRV or baroreflex sensitivity.

Furthermore, stimulation to the acupuncture points based on the oriental medicine was started in the driver's seat with automatic massage and moxibustion with electric devise.

After ethical committee allowance we evaluated the effect of aroma, acupuncture points stimulation with massage and Moxibustion on driver during the cognitive test simulated the driving behavior in the experimental room. Hemodynamic parameters, HRV and baroreflex system were evaluated in this study. Healthy male volunteers were used in this study after informed consent.

III. RESULTS

After ethical committee allowance, examination was started in the experimental room of Institute of Development, Aging and Cancer, Tohoku University. During cognitive test simulating automobile driving, aroma was added to the healthy volunteers and hemodynamic parameters were recorded as we shown in Fig.4.

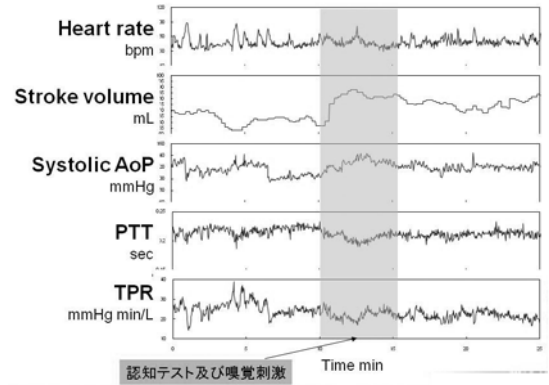


Fig.4 Time series data of the hemodynamic parameters with cognitive test and aroma inhalation.

HR during aroma inhalation with lemon and rose was compared with HR without aroma. HR tended to be altered depending on the kind of aroma.

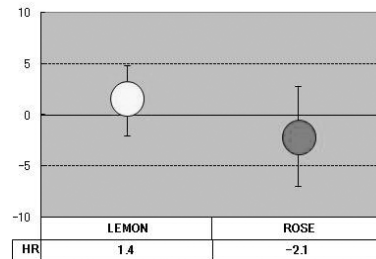


Fig.5 HR during aroma inhalation compared with HR without aroma

Furthermore, cognitive test response time was altered according to the response of the hemodynamic change, suggesting that improvement of the driving behavior can be able to be expected.

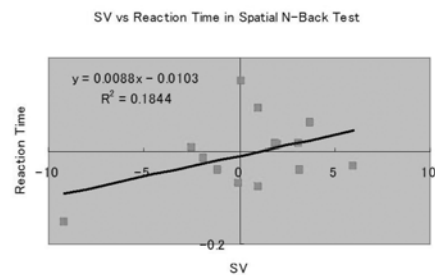


Fig.6 Responses of the stroke volume and alteration of the reaction time in cognitive test simulating driving behavior.

LF/HF during aroma inhalation with lemon and rose was compared with LF/HF without aroma. LF/HF tended to be altered depending on the kind of aroma. Furthermore, cognitive test response time was altered according to the response of the hemodynamic change, suggesting that improvement of the driving behavior can be able to be expected.

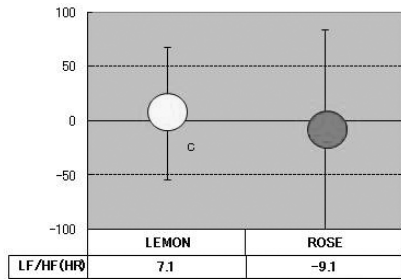


Fig.7 LF/HF during aroma inhalation compared with LF/HF without aroma

Arousal level of the driver was evaluated and the alteration of the arousal level was shown below. Depending on the kinds of Aroma, arousal level of the driver were tended to be altered, suggesting that driving behavior can be able to be controlled by the motorcar.

If the driving behavior will be able to be diagnosed by the motorcar, this information may be useful when we consider the safety driving.

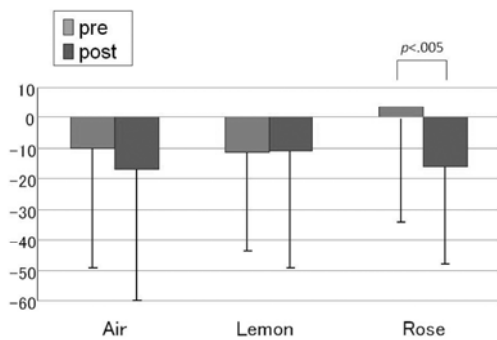


Fig.8 Arousal level with various kinds of Aroma

Based on the quantitative evaluation of an automatic nerve function, stimulation was added to the acupuncture points of the driver by the use of massage and the Moxibustion.

LH/HF before and after automatic acupuncture massage system stimulation in the driver seat was shown below.

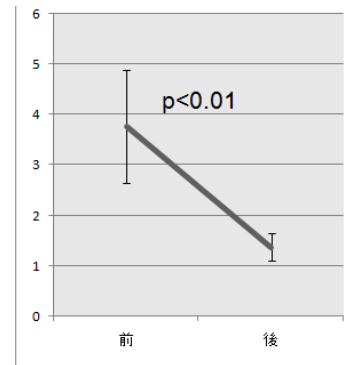


Fig.9 LF/HF before and after the automatic massage system to the acupuncture points

After the automatic massage stimulation of the acupuncture points of the whole body, LF/HF was tended to decrease suggested that autonomic nerve condition can be able to be controlled.

In the Moxibustion stimulation to the Ten-su acupuncture points by the use of the safety belt of driver seat, superior mesenteric artery was tended to altered as we shown below. So, we can control the organ circulation by the use of drive seat and safety belt.

Change of SMA Blood Flow Volume

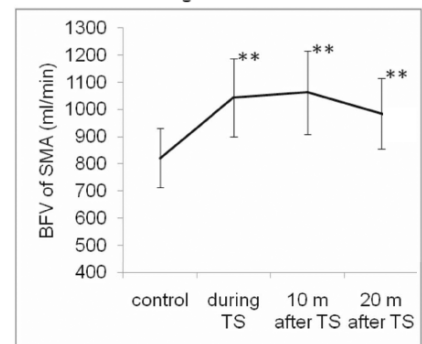


Fig.10 Change of superior mesenteric arterial flow with automatic Moxibustion in the safety belt in the drive seat

So, the cardiovascular hemodynamic parameters and the autonomic nervous system were tended to altered depending of the kinds of Aroma like Rose or Lemon, automatic massage and Moxibustion to the acupuncture points, furthermore, the Arousal and driving behavior were tended to altered.

These results suggest that motorcar can become artificial cardiovascular and automatic nerve controller based on the quantitative evaluation of the hemodynamic system.

IV. DISCUSSION

Various investigators have been studying about the man machine interface for the computer system. Especially, in the field of brain science, many kinds of brain-machine interface system have been under development till now in all over the world. However, a few reports studied the man machine interface in the vehicles.

In this paper, feasibility study had been carried out for the development of the automatic control system of the cardiovascular function and an autonomic nervous system of the driver. For the purpose, effect of the several kinds of Aroma, Massage of the acupuncture points, and Moxibus-tion were evaluated in this study.

Our results suggest the possibility of the embodiment of the cardiovascular dynamics and automatic nerve control system in motorcar based on the information of precise diagnosis of the human body. Of course, further examination may be needed especially cooperation with motor car company. So, we had started the cooperative study.

Control of the human body in the automobile may be able to be embodied in near future.

V. CONCLUSIONS

Embodiment of the cardiovascular dynamics and automatic nerve control system in motorcar based on the information of precise diagnosis of the human body during driving may be achieved in near future based on the cooperative study of academic side and industrial side.

ACKNOWLEDGMENT

This work was supported with Smart aging program in Tohoku University and a lot of supporting company in this program, Tohoku University Global COE Program "Global Nano-Biomedical Engineering Education and Research Network Centre". And 21st century COE program: Future Medical Engineering based on Bio Nanotechnology, Research Grant for Cardiovascular Diseases from the Ministry of Health and Welfare, Research Grant from the Ministry of Education, Culture, Science and Technology, and Program for Promotion of Fundamental Studies in Health Science of Organizing for Drug ADR Relief, R&D Promotion and Product Review of Japan. And Research Grant from Mitsui Sumitomo Insurance Welfare Foundation, Nakatani Electronic Measuring Technology Association of Japan, Japan Epilepsy Research Foundation, Naito Founda-tion

REFERENCES

1. Jpn Pt.Appl. 2008-326215
2. Jpn.Pt.Appl. 2006-271105
3. Osaka M, Murata H, Fuwamoto Y, Nanba S, Sakai K, Katoh T. Application of heart rate variability analysis to electrocardiogram recorded outside the driver's awareness from an automobile steering wheel. *Circ J.* 2008 Nov;72(11):1867-73.
4. Yamaguchi M, Deguchi M, Wakasugi J, Ono S, Takai N, Higashi T, Mizuno Y. Hand-held monitor of sympathetic nervous system using salivary amylase activity and its validation by driver fatigue assessment. *Biosens Bioelectron.* 2006 Jan 15;21(7):1007-14.
5. Li Z, Jiao K, Chen M, Wang C. Effect of magnitopuncture on sympathetic and parasympathetic nerve activities in healthy drivers--assessment by power spectrum analysis of heart rate variability. *Eur J Appl Physiol.* 2003 Jan;88(4-5):404-10. Epub 2002 Nov 15.

Author: Tomoyuki YAMBE
 Institute: Institute of Development, Aging and Cancer, Tohoku University
 Street: 4-1 Seiryō-machi, Aoba-ku
 City: Sendai
 Country: Japan
 Email: yambe@idac.tohoku.ac.jp

Polymer-Based Approaches to Improve the Long Term Performance of Intracortical Neural Interfaces

C. Hassler^{1,2} and T. Stieglitz^{1,2}

¹ Laboratory for Biomedical Microtechnology, Department of Microsystems Engineering – IMTEK, University of Freiburg, Freiburg, Germany

² Bernstein Focus Neurotechnology – Freiburg/Tuebingen, Freiburg, Germany

Abstract— This paper describes different polymer-based approaches to improve the long term performance of intracortical neural interfaces. The advantages of these modified interfaces compared to the commonly used interfaces are identified and possible problems which can arise with these modifications are discussed. Furthermore, some new ideas which will be implemented within the framework of the recently founded Bernstein Focus Neurotechnology – Freiburg/Tuebingen are presented.

Keywords— neural interface, conducting polymers, hydrogels, flexible substrate, long term performance.

I. INTRODUCTION

Neural interfaces to the CNS offer new opportunities to treat several diseases like Parkinson's disease, depression, epilepsy or chronic pain and they can even help paralyzed patients to communicate with their environment [1;2]. To realize this, it is necessary to selectively interface a high quantity of neurons over years to allow selective and stable recording and stimulation.

While planar epicortical arrays are in use for pre-surgical epilepsy diagnostics [3] and tubular depth electrodes interface with deep brain structures [4], micromachining techniques have been developed for penetrating electrodes with a large number of electrode sites. The "Michigan Probe" [5;6] and the "Utah Array" [7] are without doubt the best known penetrating electrode arrays. However, new arrays are under development, which also integrate microfluidic channels [8]. They all have in common a fabrication that is based on silicon technology, which provides the possibility for microscale precision, batch fabrication and on-chip circuitry. These arrays work successfully in acute in vivo experiments, but they lose their ability to record and stimulate neurons effectively over time. A possible reason for this disappointing behavior is assumed to be the stiffness of the silicon shanks [9]. There is a large mismatch in the Young's modulus of the stiff silicon shanks (~200 GPa) and the soft brain tissue (~6 kPa). The silicon shanks cannot adapt to the mechanical conditions of the brain tissue and hence micro-

motion of the brain due to breathing and the heart beat constantly injures the brain tissue. These injuries result in an increased tissue response, which benefits the formation of a glial scar and a "kill zone" for neurons around the probe [10-12]. The glial scar avoids the contact between the probe and the neurons and hence recording and stimulation is no longer possible. In this study we describe and discuss some new approaches to circumvent this problem with the use of polymers, in order to find a possibility to fabricate neural interfaces with a prolonged lifetime that can be used to treat the mentioned diseases effectively.

II. CURRENT RESEARCH

There are several approaches to improve the long term stability of intracortical neural interfaces. One way is to find new materials for electrode sites, which are able to transfer more charge at small geometric areas, to overcome the glial scar. Since the amount of safely transferable charge is limited with the commonly used electrode site materials, many groups focus on the development of tailored conducting polymers to increase the charge transfer. Cui *et al.* mainly dealt with the polymer polypyrrole (PPy) [13-16]. They started with the electrochemical deposition of PPy, doped with polystyrene sulfonate (PSS), onto electrode sites of the "Michigan Probe". With this technique they were able to decrease the magnitude of impedance of the electrode sites compared to the flat gold electrode sites [13] as a result of an increased effective surface area. Furthermore, they showed that the charge delivery capacity (Q_{CDC}) of this PPy/PSS film was with 186 mC/cm^2 much higher than that of iridium oxide (30 mC/cm^2). Another approach to improve the long term performance of intracortical neural interfaces is to enhance the attachment of neurons to the electrode sites, since a strong mechanical connection between the electrode surface and the neurons may prevent the formation of a non-conductive boundary layer. Hence, Cui replaced PSS with biomolecules like fibrinogen or laminin fragments [14], which led to a preferred and selective attachment of human neuroblastoma cells and rat glial cells in

vitro. The research of Kim *et al.* [17] covered another relevant aspect in improving the long term stability of intracortical neural interfaces. They used a hydrogel scaffold as a buffering layer between the stiff electrode and the soft brain tissue. They demonstrated that the impedance of the hydrogel coated electrode was only slightly higher than the impedance of the uncoated gold electrode and in acute in vivo recordings from the cerebellum of guinea pigs it was shown that the coated probes could transport charge as efficiently as the uncoated probes. With PPy/PSS grown into this scaffold onto the electrode sites, the impedance could even be decreased and the charge delivery capacity was increased to 560 mC/cm². Since in vivo studies of PPy/peptide coated neural probes showed that PPy undergoes subtle changes in chemical structure, what results in a decreased conductivity [15], research focused on another conducting polymer called poly(3,4-ethylenedioxythiophene) (PEDOT). Cui and Martin showed that PEDOT coatings have a much better electrochemical stability than PPy, but are also able to decrease the electrode impedance and to integrate bioactive peptides to improve the attachment of neurons [18]. In stimulation experiments it was also shown, that PEDOT films have a charge injection capacity much better than that of thin film platinum and comparable to that of IrO_x and TiN [19]. Furthermore, it was found out that PEDOT coated electrode sites provide suitable signal-to-noise ratios due to the reduced impedance [20].

Aside from the use of conducting polymers to overcome the glial scar through an increased charge transfer, there are other approaches, which try to reduce the tissue response and hence the formation of a glial scar or try to attach neurons onto the electrode sites. Winter, Cogan and Rizzo investigated the use of biodegradable, neurotrophin-eluting hydrogels made of poly(ethylene glycol)-poly(lactic acid) (PEGPLA) to improve the neuron-electrode proximity [21]. They had promising results in vitro with neurotrophin eluting over four weeks and hence increased attachment of neurons without changing the electrochemical properties of the electrodes too much.

The concepts mentioned above all have one thing in common. They try to solve the problem of increased tissue response induced by the stiffness of the silicon substrate. A completely different approach is to use flexible substrate materials like polyimide or parylene C instead of silicon. The use of flexible materials would minimize the injury of brain tissue due to micromotion and hence may minimize the formation of a glial scar [9]. The technology to fabricate flexible thin film polyimide electrodes is already established [22]. However, the use of this kind of substrate material is accompanied by further challenges. It is difficult to insert flexible probes into the cortex. In particular cases this is possible [23;24], but the insertion is limited to a certain

depth and not easy to handle. A possibility to simplify the insertion is to bend the electrodes [25] to improve the stiffness but to have electrodes that are flexible enough to adapt to the mechanical conditions of the brain tissue. Takeuchi *et al.* [26] used a parylene C based probe with integrated microfluidic channels, which were filled with polyethylene glycol (PEG) before insertion. PEG is solid at room temperature and dissolves in contact with water. With this method they were able to insert the probe into a rat's cortex. Lee *et al.* [27] used polyimide as substrate material and attached a 5-10 μm thick silicon backbone layer to the tip of the electrode to simplify the insertion of the probe. This stiff segment was followed by a flexible one without a silicon backbone layer, which was intended to accommodate the micromotion between brain tissue and skull. This probe was robust enough to penetrate the rat's pia without buckling.

III. DISCUSSION

The approaches described above offer promising possibilities to improve the long term stability of intracortical neural interfaces. However, most of them were tested only in vitro or in short term in vivo experiments. It is still not known how these newly developed electrodes behave when they are chronically implanted into the human brain. Table 1 lists the different approaches with respect to their advantages and the problems which can arise with them.

PPy does not seem to be suitable for long term use in intracortical neural interfaces. In spite of the fact that it has some interesting properties like a high conductivity, good biocompatibility and controllable surface properties, its electroactivity is not stable long term, as it was shown in cyclic voltammetry experiments [18]. PEDOT is more stable than PPy, but it still undergoes chemical changes over time and hence the good recording and stimulation properties got lost. It is not known how these chemical changes influence the biocompatibility of the conducting polymer. Delamination of the electrochemically deposited PEDOT to the underlying metal electrode sites seems to be an additional problem [19]. Hydrogel coatings onto the whole electrode shanks can serve as buffering layers between the stiff shank and the soft brain tissue and they offer the opportunity to integrate bioactive species, which may provide the cell attachment. However, the increased thickness of a hydrogel coated electrode can result in further problems. A thicker electrode means the damage of more neurons during insertion and it was shown in different studies that the tissue response to an implanted electrode depends on its size [28;29]. Furthermore, a coated electrode shank can result in impaired charge transfer properties due to the additional impedance of the coating.

Table 1 Comparison of different approaches

Approach	Advantages	Problems	Reference
Coating of the electrode sites with conducting polymers	Improved charge transfer properties and improved signal-to-noise ratio through a lowered electrode impedance	Stability of conducting polymers Delamination of the coatings Loss of selectivity through increased charge transfer	[13-16;18-20]
Coating of the whole electrode shank with polymers/polymer hydrogels	Mechanical buffer between stiff silicon shanks and soft brain tissue	Damaging more neurons due to increased electrode thickness Possible impairment of charge transfer properties	[17]
Coating with biodegradable drug eluting hydrogels	Improved neuron-electrode connection	Possible impairment of charge transfer properties	[21]
Flexible substrate material	Less damage due to micromotion	Insertion into the brain tissue is difficult	[23;24]
Flexible substrate with integrated microfluidic channels	Simplified insertion into brain tissue (PEG) Possibility of drug delivery	Damaging more neurons due to increased electrode thickness	[26]
Flexible substrate with silicon backbone	Simplified insertion into brain tissue	Impaired flexibility	[27]

The overall problem of porous surfaces, which appear in electrochemically deposited conducting polymers or hydrogel coatings, is that bacteria can settle in the pores and because these pores are too small for macrophages to penetrate, this may lead to a specific response of the immune system with chronic inflammation around the implant.

The use of flexible thin film substrate materials like polyimide instead of silicon would solve the problem of increased tissue damage due to micromotion of the brain, but the methods mentioned above to simplify the insertion of such a flexible probe have yet to be refined, because they are accompanied with an impaired flexibility after implantation or an increased probe thickness. A possible approach to solve this problem would be the application of probes with variable stiffness, either by active actuation principles [30] or by resorbable polymer coatings, which improve the stiffness for insertion and degrade with time, when the probe is already implanted. Within the framework of the recently founded Bernstein Focus Neurotechnology – Freiburg/Tuebingen we intend to develop such probes and try to combine and refine the concepts mentioned above to receive long term stable electrodes, which can be used to treat several diseases in the future.

IV. CONCLUSIONS

There are a lot of promising approaches to improve the long term performance of intracortical neural interfaces. However, their effectivity was tested only in short term experiments in the most cases and it is not known how these newly developed probes behave when they are chronically implanted in the brain. There remains much work to do to

understand the basic principles and to engineer the interface. Existing concepts must be refined and new ones have to be developed to ensure that intracortical neural interfaces will work reliably to treat several diseases in the near future.

ACKNOWLEDGMENT

This work is supported by the German Federal Ministry of Education and Research (BMBF grant 01GQ0830).

REFERENCES

1. L. R. Hochberg, M. D. Serruya, G. M. Friehs, J. A. Mukand, M. Saleh, A. H. Caplan, A. Branner, D. Chen, R. D. Penn, and J. P. Donoghue (2006) Neuronal Ensemble Control of Prosthetic Devices by a Human with Tetraplegia. *Nature*, vol. 442, no. 7099, pp. 164-171.
2. J. P. Donoghue (2002) Connecting Cortex to Machines: Recent Advances in Brain Interfaces. *Nat Neurosci*, vol. 5 pp. 1085-1088.
3. S. Fauser and A. Schulze-Bonhage (2006) Epileptogenicity of Cortical Dysplasia in Temporal Lobe Dual Pathology an Electrophysiological Study with Invasive Recordings. *Brain*, vol. 129, no. 1, pp. 82-95.
4. A. L. Benabid (2003) Deep brain stimulation for Parkinson's disease. *Curr Opin Neurobiol*, vol. 13 pp. 696-706.
5. K. D. Wise, J. B. Angell, and A. Starr (1970) An Integrated-Circuit Approach to Extracellular Microelectrodes. *IEEE T Bio-Med Eng*, vol. BME-17, no. 3, pp. 238-247.
6. K. Najafi and K. D. Wise (1986) An Implantable Multielectrode Array with On-Chip Signal Processing. *IEEE J Solid-St Circ*, vol. 21, no. 6, pp. 1035-1044.
7. P. K. Campbell, K. E. Jones, R. J. Huber, K. W. Horch, and R. A. Normann (1991) A Silicon-Based, Three-Dimensional Neural Interface: Manufacturing Processes for an Intracortical Electrode Array. *IEEE T Bio-Med Eng*, vol. 38, no. 8, pp. 758-768.

8. P. Ruther, S. Herwik, S. Kisban, K. Seidl, S. Spieth, B. Rubehn, N. Haj Hosseini, J. Steigert, M. Daub, O. Paul, T. Stieglitz, R. Zengerle, and H. P. Neves (2007) NeuroProbes - Development of Modular Multifunktional Probe Arrays for Neuroscience, *Proc of the Mikrosystemtechnik Kongress 2007* pp. 739-742.
9. J. Subbaroyan, D. C. Martin, and D. R. Kipke (2005) A Finite-Element model of the mechanical Effects of Implantable Microelectrodes in the Cerebral Cortex. *J Neural Eng*, vol. 2 pp. 103-113.
10. V. S. Polikov, M. L. Block, J. M. Fellous, J. S. Hong, and W. M. Reichert (2006) In Vitro Model of Glial Scarring around Neuroelectrodes Chronically Implanted in the CNS. *Biomaterials*, vol. 27 pp. 5368-5376.
11. V. S. Polikov, P. A. Tresco, and W. M. Reichert (2005) Response of Brain Tissue to Chronically Implanted Neural Electrodes. *J Neurosci Meth*, vol. 148, no. 1, pp. 1-18.
12. J. N. Turner, W. G. Shain, D. H. Szarowski, M. D. Andersen, S. Martins, M. S. Isaacson, and H. G. Craighead (1999) Cerebral Astrocyte Response to Micromachined Silicon Implants. *Exp Neurol*, vol. 156 pp. 33-49.
13. X. Cui, J. F. Hetke, J. A. Wiler, D. J. Anderson, and D. C. Martin (2001) Electrochemical deposition and characterization of conducting polymer polypyrrole/PSS on multichannel neural probes. *Sensor Actuat A-Phys*, vol. 93 pp. 8-18.
14. X. Cui, A. L. Lee, Y. Raphael, J. A. Wiler, J. F. Hetke, and D. J. Anderson (2001) Surface modification of neural recording electrodes with conducting polymer/biomolecule blends. *Biomed Mater Res*, vol. 56 pp. 261-272.
15. X. Cui, J. Wiler, M. Dzaman, R. A. Altschuler, and D. C. Martin (2003) In vivo studies of polypyrrole/peptide coated neural probes. *Biomaterials*, vol. 24 pp. 777-787.
16. X. Cui and D. C. Martin (2003) Fuzzy gold electrodes for lowering impedance and improving adhesion with electrodeposited conducting polymer films. *Sensor Actuat A-Phys*, vol. 103 pp. 384-394.
17. D. H. Kim, M. R. Abidian, and D. C. Martin (2004) Conducting Polymers Grown in Hydrogel Scaffolds Coated on Neural Prosthetic Devices. *J Biomed Mater Res-A*, vol. 71 pp. 577-585.
18. X. Cui and D. C. Martin (2003) Electrochemical deposition and characterization of poly(3,4-ethylenedioxythiophene) on neural microelectrode arrays. *Sensor Actuat B-Chem*, vol. 89 pp. 92-102.
19. X. T. Cui and D. D. Zhou (2007) Poly (3,4-Ethylenedioxythiophene) for Chronic Neural Stimulation. *IEEE T Neural Syst Rehabil Eng*, vol. 15, no. 4, pp. 502-508.
20. K. A. Ludwig, J. D. Uram, J. Yang, D. C. Martin, and D. R. Kipke (2006) Chronic Neural Recordings Using Silicon Microelectrode Arrays Electrochemically Deposited with a Poly(3,4-Ethylenedioxythiophene) (PEDOT) Film. *J Neural Eng*, vol. 3 pp. 59-70.
21. J. O. Winter, S. F. Cogan, and J. F. Rizzo (2007) Neurotrophin-Eluting hydrogel Coatings for Neural Stimulating Electrodes. *J Biomed Mater Res-B*, vol. 81 pp. 551-563.
22. T. Stieglitz, M. Schuettler, and K. P. Koch (2005) Implantable Biomedical Microsystems for Neural Prostheses. Flexible, Polyimide-Based, and Modular. *IEEE Eng Med Biol*, vol. 24, no. 5, pp. 58-65.
23. K. C. Cheung, P. Renaud, H. Tanila, and K. Djupsund (2007) Flexible Polyimide Microelectrode Array for in Vivo Recordings and Current Source Density Analysis. *Biosens Bioelectron*, vol. 22 pp. 1783-1790.
24. P. J. Rousche, D. S. Pellinen, D. P. Pivin Jr, J. C. Williams, R. J. Vetter, and D. R. Kipke (2001) Flexible Polyimide-Based Intracortical Electrode Arrays with Bioactive Capability. *IEEE T Bio-Med Eng*, vol. 48, no. 3, pp. 361-371.
25. N. Haj Hosseini, R. Hoffmann, S. Kisban, T. Stieglitz, O. Paul, and P. Ruther (2007) Comparative Study on the Insertion Behavior of Cerebral Microprobes, *Proc of the 29th Ann Internat Conf of the IEEE EMBS* pp. 4711-4714.
26. S. Takeuchi, D. Ziegler, Y. Yoshida, K. Mabuchi, and T. Suzuki (2005) Parylene Flexible Neural Probes Integrated with Microfluidic Channels. *Lab Chip*, vol. 5 pp. 519-523.
27. K. K. Lee, A. Singh, J. He, S. P. Massia, B. Kim, and G. B. Raupp (2004) Polyimide Based Neural Implants with Stiffness Improvement. *Sensor Actuat B-Chem*, vol. 102 pp. 67-72.
28. P. Stice, A. Gilletti, A. Panitch, and J. Muthuswamy (2007) Thin Microelectrodes Reduce GFAP Expression in the Implant Site in Rodent Somatosensory Cortex. *J Neural Eng*, vol. 4, no. 2, pp. 42-53.
29. J. P. Seymour and D. R. Kipke (2007) Neural Probe Design for Reduced Tissue Encapsulation in CNS. *Biomaterials*, vol. 28, no. 25, pp. 3594-3607.
30. J. R. Capadona, K. Shanmuganathan, D. J. Tyler, S. J. Rowan, and C. Weder (2008) Stimuli-Responsive Polymer Nanocomposites Inspired by the Sea Cucumber Dermis. *Science*, vol. 319 pp. 1370-1374.

Author: Christina Hassler
 Institute: University of Freiburg, Department of Microsystems Engineering – IMTEK, Laboratory for Biomedical Microtechnology
 Street: Georges-Koehler-Allee 102
 City: Freiburg
 Country: Germany
 Email: hassler@imtek.de

Development of a Neural Interface for Artificial Limbs

Todd Kuiken

Institution: Rehabilitation Institute of Chicago and Northwestern Univ., Chicago, Illinois, USA
Address for correspondence: RIC Rm 1309, 345 E Superior St, Chicago, Illinois, 60611, USA

Providing adequate control of a powered artificial arm is difficult, especially with high levels of amputation where the need is greatest. In this presentation we will describe a new technique to create a bi-directional neural interface for artificial limbs.

We have developed a technique to provide additional motor control commands called targeted reinnervation that takes the residual nerves to in an amputated limb and transfers them to spare muscle in or near the limb. The nerves grow into this muscle, and then the surface EMG over this muscle can be used as an additional control signal. Since physiologically appropriate neural pathways are used, the control is intuitive, thus easier and faster for the amputee. Similarly, sensory nerves can be transferred to the

residual nerves so that skin of the chest or arm is reinnervated. Then when the amputee is touched on this reinnervated skin, it feels like he or she is being touched in the missing arm or hand. This provides a pathway for true sensory feedback of light touch, graded pressure, sharp/dull, and thermal feedback.

With conventional prosthesis using simply the amplitude of the EMG for control, functional testing has shown marked improvement in all tests. Pattern Recognition computer algorithms have been added to greatly increase the degrees of freedom that can be intuitively operated. Early research is all presented showing how the skin of residual limbs has been reinnervated by hand afferents and our early attempts to provide closed loop feedback.

Orthopedic Testing – A device for sagittal and transversal knee stability detection

R.Boos¹, H.Telles², Dr. J.Richter³, A.Keim¹, F.Stegmaier¹ and Dr. U.Schneider¹

¹ Fraunhofer Institute for Manufacturing Engineering and Automation IPA, Stuttgart, Germany

² Bort Medical GmbH, Weinstadt-Benzach, Germany

³ Orthopädische Klinik Markgröningen gGmbH, Markgröningen, Germany

Abstract— There are no measuring devices which can measure the rotational stability after anterior cruciate ligament rupture. It is only possible to measure the sagittal stability clinically or via KT-1000, X-ray and other devices. To measure the rotational stability becomes more important because of new operation methods like the double bundle technique. This technique reconstructed the rotational stability very good. Up to now no device can measure this criterion. For this reason Fraunhofer IPA and Bort Medical developed with assistance of the clinic Markgröningen a measurement device which can measure the sagittal and transversal knee stability during the Lachman- and Pivot-Shift-Test.

Keywords— Lachman-Test, Pivot-Shift-Test, ACL, orthopaedic measurement, knee stability

I. INTRODUCTION

The cruciate surgery is a very major segment of the accident surgery and orthopaedics. In this context the anterior cruciate ligament rupture (ACL) is the most common ligament rupture at the knee joint. [1]

Permanent improvement in minimally invasive surgery and better understanding in biomechanics enables to enhance operation techniques. These aspects require better pre- and post operative diagnostic methods.

Currently no method is available, providing objective examination for sagittal and transversal knee stability during ACL treatment. This is essential for diagnosis of the knee stability, post-operative treatment and quality assurance of surgery and rehabilitation. Regarding to the special needs and the rising standards in operations and clinical treatment the quality assurance gets a more and more important factor.

Therefore the Fraunhofer Institute for Manufacturing Engineering and Automation (IPA) division Orthopaedics and Motion Systems (OBS), specialised on motion tracking and sensor systems, developed a system to measure the sagittal and transversal knee stability during the procedure of standard Lachman- and Pivot-Shift-Test (Figure 1).



Figure1: Measurement device

II. METHODS

A. Function

- Detection of the degree of injury through Lachman- and Pivot-Shift-Test
- Lachman Test is detected through translation between tibia and patella with a high precision optical sensor
- Acceleration and turn rate in 3D are detected with a inertial sensor system
- Automatic recognition and assignment of Lachman- and Pivot-Shift-Test

B. Sensors

The measurement device consists of an optical sensor and 3-D acceleration and turn rate sensor system. The resolution of the used optical sensor for distance measurement at the patella is less than 0.1 mm. Since more than 8 years the Fraunhofer IPA is specialist in developing algorithms for sensor fusion in inertial navigation systems (INS). The core of the measurement system is a sensor unit measuring acceleration and turning rate. This information is computed to relative orientation and velocity in relation to a reference system (in most cases the three room directions of the earth).

C. Handling and result view

- Fast and easy mounting at the lower leg
- Implementation in a standard Lachman- and Pivot-Shift-Test examination
- No changes in examination procedures
- Readout of the measurement data with display or PC

D. Characteristics of Lachman-Test

The Lachman-Test is an established test to examine sagittal knee stability after ruptures of the crucial ligaments.

The patient lays relaxed in dorsal position. For analysis of the posterior cruciate ligament the examiner flexes the knee of the patient to an angle of about 30 degrees. The examiner places dorsal to the patient and pulls the tibia anterior. The difference of the dislocation between tibia and femur condyle of the injured knee in comparison to the healthy knee is an indicator for the severity of the injury. With the data of the INS the flexion angle of the knee (figure 2, middle, magenta) is calculated. The examiner can see the flexion angle during measurement optionally displayed on directly in a display or on a PC. This feedback has very high importance for a better and more objective comparability between injured and normal knee. The optical sensor measure the distance between a layer parallel to the anterior tibia crest and the patella plateau. The device detects the minima and maxima of the distance signal and calculates

the difference to get the dislocation distance in sagittal direction. For a better accuracy the algorithm builds the median of five or more minima/maxima and eliminates outliers.

E. Characteristics of Pivot-Shift-Test

The Pivot-Shift-Test gives information about the rotational knee stability. This test is compared to the Lachman-Test a dynamic examination. Indicator for a rupture in this test is a subluxation of the knee joint. [1, 2]

At this test the patient lays also in dorsal position. The examiner stands lateral to the patient. The lower leg and ankle is hold in internal tibia rotation. The knee adept a valgus rotation in cause of the legs weight. The examiner flexes the knee and at a flexion angle between 27 and 45 degree [3] he feels the subluxation. Very strong subluxations are also directly visible. Anatomical the Pivot-Shift means that the lateral femur condyle moves forward in relation to the lateral tibia condyle. This generates a subluxation and is an indicator for an anterior cruciate ligament rupture (ACL). The severity of this test has four degrees (0-III).

For detection of the Pivot-Shift degree the device detects mainly the sagittal dislocation distance accomplished by acceleration and the rotational turn rate. As an example data of a measurement process is shown in figure 2.

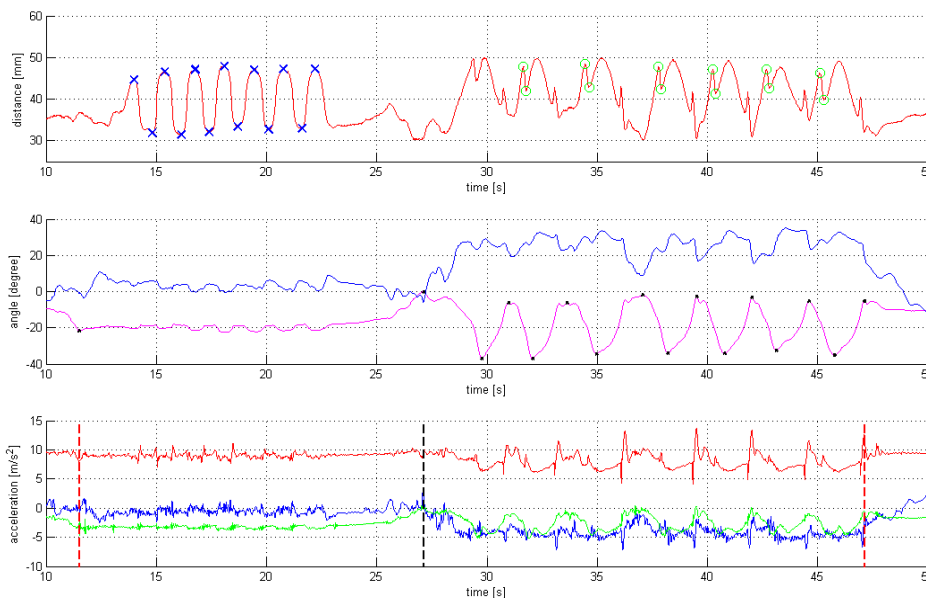


Figure 2: Measurement data

Top: distance between patella and tibia (red)
 Middle: flexion (magenta) and rotation (blue) angle
 Bottom: accelerations

III. RESULTS

A first test with the measurement device at Fraunhofer IPA and Orthopaedic Clinic Markgröningen with normal and injured knees has ended very positive. The handling and fixation is very comfortable and reliable. The examiner has marginal limitations in diagnostic procedure of Lachman- and Pivot-Shift-Test. Because of the similar measuring principle at the Lachman-Test of KT-1000 and the new measurement device, the accuracy should be alike. An advantage is the optical sensor which measures contactless and with a resolution smaller 0.1 mm. The complete device is smaller and lighter as comparable systems on the market. The most important source of error is the therapists handling. Compared to other systems for ligament rupture this will be the first system on the market which provides a reliable and quantitative detection of the Pivot shift test. First tests at patients with anterior cruciate ligament rupture were made and show very reliable and repeatable results at Lachman-Test and different levels at the Pivot-Shift-Test.

IV. CONCLUSIONS

It is possible to measure the distance during the Lachman-Test very reliable and repeatable with assistance of the displayed flexion angle.

First tests of the Pivot-Shift detection show that it is possible to identify a Pivot-Shift but it seems also that the detected effects are related to the examination process. For a better classification in different Pivot-Shift levels there are more tests necessary to get a wider statistic base.

REFERENCES

1. Kohn D (2004) Orthopädie und Orthopädische Chirurgie. Knie. Thieme, Stuttgart
2. Kapandji I (2001) Funktionelle Anatomie der Gelenke. Hippokrates Verlag, Stuttgart
3. Bull A, Earnshaw P, Smith A et al. (2002) Intraoperative measurement of knee kinematics in reconstruction of the anterior cruciate ligament. JB&JS Vol. 84-B No.7:1075-1081

ARMin - Exoskeleton Robot for Stroke Rehabilitation

Tobias Nef^{1,2}, Marco Guidali^{3,4}, Verena Klamroth-Marganska^{3,4}, and Robert Riener^{3,4}

¹ Department of Biomedical Engineering, The Catholic University of America, Washington DC, USA

² Center for Applied Biomechanics and Rehabilitation Research, National Rehabilitation Hospital, Washington DC, USA

³ Sensory-Motor Systems Lab, Institute of Robotics and Intelligent Systems, ETH Zurich, Switzerland

³ Spinal Cord Injury Center, Balgrist University Hospital, University of Zurich, Switzerland

Abstract— Rehabilitation robots are becoming an important tool in rehabilitation of stroke, SCI and other neurological pathologies. Compared to manual arm training, robot-supported training can be more intensive, of longer duration, repetitive and task-oriented. Therefore, such devices have the potential to improve the rehabilitation process in stroke patients. Whereas a majority of previous work in upper limb rehabilitation robotics has focused on end-effector based robots, a shift toward exoskeleton robots is taking place because they offer a better guidance of the human arm, especially for movements with large range of motions. One of the first actuated exoskeleton robot that is ready for deployment in clinics is the ARMin III robot. This paper gives a short overview of the ongoing clinical application and evaluation process of the ARMin III robot.

Keywords— Arm rehabilitation robotics, exoskeleton, stroke rehabilitation.

I. INTRODUCTION

Stroke is the neurological disease with the highest prevalence and it is the leading cause of disability. Recent studies estimate that it affects more than 1 million people in the EU [1,2] and more than 0.7 million in the U.S. each year [3]. One major symptom of stroke is hemiparesis that affects the upper extremities. Several studies show that sensorimotor arm therapy has positive effects on the rehabilitation process of stroke patients (see [4] for review). The goal hereby is to induce long-term brain plasticity to improve functional outcomes. The critical factors of the treatment are that the therapy is intensive [5], of long duration [6], repetitive [7] and task-oriented [8]. Regarding these criteria, one-to-one manually-assisted arm training has several limitations. The training is labor-intensive and, therefore, expensive. The disadvantageous consequence is that the rehabilitation period and the single training sessions are often shorter than required for a maximal therapeutic outcome.

Part of these shortcomings can be solved by introducing robotic technology. Robotic training as such can obviously be repetitive and of long duration. Using patient-cooperative

control algorithms [9,10] that detect the patient's contribution and support the patient only as much as needed can be used to make sure that the patient participates actively to the training and that the robotic intervention becomes intensive. Since it seems that patient-motivation [11] is a key factor for an intensive training, audiovisual displays with game-like scenarios [10,12] can be used to enhance patient-motivation and active participation. The requirement to allow task-oriented training that is based on Activities of Daily Living (ADL) is however, more challenging to achieve with a robotic device. Since ADL movements in general require large range of motions (RoM) [14], many degrees of freedom (DoF) and sophisticated control algorithms [9], most robotic devices allowing ADL-training are complex and expensive [10,15,16,17]. Therefore, some groups are working with non-motorized devices that provide weight compensation to the affected arm only [18,19]. Other groups are focusing on end-effector based robots. While in exoskeleton robots, the human is connected to the robotic device at several points, in endeffector-based robots (also called endpoint-type robots) the human is connected to the robot at one point only [10]. As consequence, endeffector based robots are easier to use but do not allow single joint torque control and, in general, provide less guidance and support than exoskeleton devices [20,21,22,23].

The ARMin III device is the 3rd generation of arm exoskeleton robots that have been developed during the last six years [10,13]. This paper gives a short overview of the evaluation of the device in healthy test persons and consecutively in chronic stroke patients.

II. METHODS

A. The ARMin III Arm Rehabilitation Robot

Figure 1 shows a picture of the ARMin III device. It is equipped with six motors moving the shoulder joint in three DoF, the elbow joint, lower arm pro/supination and wrist flexion/extension. The mechanics is symmetric and the robot can be used for the right- or the left arm. Advanced control algorithms allow controlling not only the position of

the device, but also the interacting force between the robot and the patient [10,12].



Fig. 1: ARMin III exoskeleton robot with a healthy subject. The device has six actuated DoF and connects to the most affected arm. A computer monitor shows different graphical scenarios to the patient.

A graphical display (Figure 2) presents different training scenarios to the patient. The scenario varies with the selected training mode. These are passive mobilization, active game therapy and active ADL-training. In passive mobilization, the patient's limb is moved by the robot on a previously recorded trajectory. The purpose of this therapy mode is to prevent secondary complications, to increase blood circulation and to reduce joint and muscle stiffness.

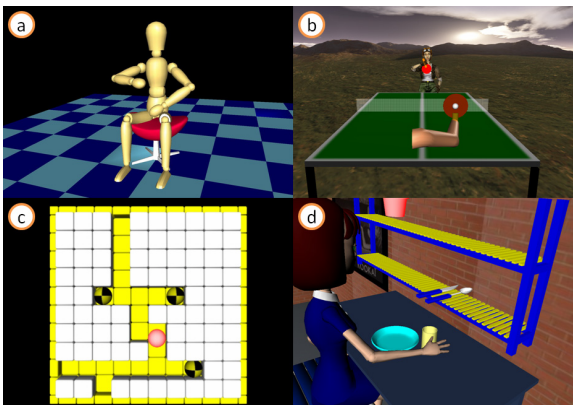


Fig. 2: Graphical display for the ARMin training [10]. The computer screen (a) is shown during passive mobilization, screen (b) and (c) during game training, and screen (d) during ADL-training.

In the game therapy mode, a game-like scenario is presented to the patient. The patient tries to fulfill the task while he is supported by the robot. The device detects how much the patient contributes to the movement and delivers support as much as needed [12]. One example for the game-supported therapy is a ping-pong game (Figure 2b) where a virtual arm with a racket is used to hit a ball. In this particular case, the robot detects how much the user can do and supports if necessary by pulling the racket towards the expected location of the impact with the ball. Other therapeutic games are a labyrinth (Figure 2c) and simple ball games. In most cases, the patient plays against the computer, but recently we implemented a tele-rehabilitation application where the patient can play against another patient from a different hospital [24].

In the third therapy mode, patients can train ADLs such as eating, cooking, table setting, to brush one's teeth and others. Also here, the audiovisual display shows a virtual representation of the patient's arm and the given task environment (Figure 2d).

B. Evaluation

The evaluation of the ARMin device included tests with healthy persons, with stroke survivors and with some spinal cord injured patients (SCI). The consecutive order of the tests was:

- I. Tests with healthy persons
- II. Tests with chronic stroke and some SCI patients
- III. Pilot tests in chronic stroke
- IV. Randomized clinical trial (RCT) in chronic stroke

In phase I, healthy volunteers tested the robotic device with respect to functionality, safety, stability and performance. In phase II, the very same questions as in phase I have been investigated with patients. The dosage of the training was low (1-10 training sessions arbitrarily distributed over several weeks), therefore no improvement in the motor performance of these patients was expected. Phases I and II only served to investigate the functionality of the robot and the feasibility of single training sessions. Phase III tests aimed to investigate whether long-term ARMin training is feasible and whether it has *some* beneficial effect onto the motor performance of these patients. Therefore, an A-B design with baseline measurements (A), vs. intervention (B) has been selected for these tests. Therefore, the results are specific to single cases only and they cannot be generalized to a larger patient-population. Thus, these results cannot be used to compare ARMin training with other interventions. However, these pilot tests are prerequisite and pre-indicator for the larger RCT. In other words, only if the pilot tests

show encouraging results, it makes sense to start the RCT. In the phase IV RCT, 88 chronic stroke patients will be included. A randomized set of 44 patients will receive 8 weeks ARMin training (three one hour training sessions per week) and 44 patients will receive the same amount of conventional therapy. Main outcome measure is the upper limb section of the Fugl-Meyer (FMA) score [25]. Secondary outcome measures include the Wolf Motor Function Test to test for transfer to ADL, maximum voluntary torques, passive and active RoM and others.

III. PRELIMINARY RESULTS

To current date, phases I, II and III have been completed. In phases I and II, we could show that the device works reliable and safe with both healthy test persons and with patients [10]. In phase III, eight chronic stroke patients (6-131 months post stroke) received 24-32 hours ARMin training, equally distributed over 8 weeks. The trainings have been performed either with ARMin II or with ARMin III. The changes in FMA between baseline and discharge, where in four patients above 6 points (6-18 points) and in four patients between 2 and 3 points. The FMA changes were in agreement with improvements in secondary assessments.

Besides possible beneficial effects, also the feasibility of intensive ARMin training has been investigated as part of phase III. We looked at the reliability of the ARMin device and at the motivation of the patient, since both are required for an eight-week intervention. To summarize, we observed that the patients were very motivated to participate and not a single training lesson has been canceled.

IV. DISCUSSION AND CONCLUSION

Phases I-III of the ARMin evaluation have been completed. The results of the phase III single case studies are highly promising and some patients showed very pronounced improvements with respect to FMA. These improvements must be seen in the context of selected single cases, which cannot be generalized due to the limited sample size. However, the promising results so far definitely justify the start of the RCT. Consequently, five ARMin III devices have been deployed in clinics in Switzerland and in the US and the phase IV RCT has recently been started in a multicenter setting.

ACKNOWLEDGMENT

We thank Patricia Staubli and Mark Schmiedeskamp from ETH and University Zurich for their contributions to

the clinical evaluation. We furthermore also thank Andreas Brunschweiler and Alessandro Rotta from the ETH Zurich and the occupational therapists and Prof. Dr. Volker Dietz of the Balgrist University Hospital, Zurich for their contributions to this work. Furthermore, we thank Dr. Gery Colombo from Hocoma AG, Volketswil, Switzerland and Dr. Peter Früh, from the University of Applied Sciences Winterthur for their contributions.

This work was supported in part by the Hans-Eggenberger Foundation, by the ETH Foundation, by the Swiss Research Foundation NCCR on Neural Plasticity and Repair, by the Gottfried and Julia Bangerter-Rhyner Foundation and by a fellowship from the Swiss National Science Foundation.

REFERENCES

1. Thorvaldsen P, Asplund K, Kuulasmaa K, Rajakangas AM, Schroll M. 1995. Stroke Incidence, Case Fatality, and Mortality in the WHO MONICA Project. *Stroke*, 26:361-367.
2. Brainin M, Bornstein N, Boysen G, Demarin V. 2000. Acute neurological stroke care in Europe: results of the European Stroke Care Inventory. *European Journal of Neurology*, 7:5-10.
3. Wayne R et al. 2007. Heart Disease and Stroke Statistics – 2007 Update. A Report from the American Heart Association Statistics Committee and Stroke Statistics Subcommittee. *American Heart Association*.
4. Platz T. 2003. Evidenzbasierte Armrehabilitation: Eine systematische Literaturübersicht. *Nervenarzt*, 74:841-849.
5. Kwakkel G, Wagenaar RC, Twisk JWE, Langkhorst GJ, and Koetsier JC. 1999. Intensity of leg and arm training after primary middle-cerebral artery stroke: a randomized trial. *Lancet*, 35:191-196.
6. Sunderland A, Tinson DJ, Bradley EL, Fletcher D, Langton HR, and Wade DT. 1992. Enhanced physical therapy improves recovery of arm function after stroke. A randomised clinical trial. *J Neurol Neurosurg Psychiatry*, 55:530-535.
7. Butefisch C, Hummelsheim H, Denzler P, and Mauritz KH. 1995. Repetitive training of isolated movements improves the outcome of motor rehabilitation of the centrally paretic hand. *J Neurol Sci*, 130:59-68.
8. Bayona NA, Bitensky J, Salter K, and Teasell R. 2005. The role of task-specific training in rehabilitation therapies. *Top Stroke Rehabil*, 12:58-65.
9. Mihelj M, Nef T and Riener R. 2007. A novel paradigm for patient-cooperative control of upper limb rehabilitation robots, *Advanced Robotics*, 21(8):843-867.
10. Nef T, Mihelj M and Riener R. 2007a. ARMin: a robot for patient-cooperative arm therapy. *Medical & Biological Engineering & Computing*, 45:887-900.
11. Riener R, Wellner M, Nef T, von Zitzewitz J, Duschau-Wicke, A, Colombo G, Lünenburger L. (2006) A View on VR-Enhanced Rehabilitation Robotics. Virtual Rehabilitation, 2006 International Workshop on. New York, NY, pp149-154.
12. Nef T, Guidali M and Riener R (2009) ARMin III – Arm therapy exoskeleton with an ergonomic shoulder actuation. *Applied Bionics and Biomechanics*, in press.
13. van Andel CJ, Wolterbeek N, Doorenbosch CA, Veeger DH, Harlaar J. 2008. Complete 3D kinematics of upper extremity functional tasks. *Gait Posture*. 27(1):120-7.

14. Carignan C and Liszka M. 2005. Design of an arm exoskeleton with scapula motion for shoulder rehabilitation. In: *Proceedings of the 12th International Conference on Advanced Robotics*; 18-20 July, Seattle, USA; pp. 524- 531.
15. Bergamasco M, Borelli L, Carboncini MC, Frisoli A, Marcheschi S, Montagner A, Procopio C, Rossi B, Salsedo F and Tolaini M. 2007. Arm rehabilitation with a robotic exoskeleton in Virtual Reality. In: *Proceedings of the IEEE 10th International Conference on Rehabilitation Robotics*; June 13-15; Noordwijk, The Netherlands; pp.631-642.
16. Rosen J, Perry JC, Manning N, Burns S and Hannaford B. 2005. The human arm kinematics and dynamics during daily activities - toward a 7 DOF upper limb powered exoskeleton. In: *Proceedings of the 12th International Conference on Advanced Robotics*; 18-20 July, Seattle, USA; pp. 532-539.
17. Sanchez RJ, Liu J, Rao S, Shah P, Smith R, Rahman T, Cramer SC, Bobrow JE and Reinkensmeyer DJ. 2006. Automating arm movement training following severe stroke: Functional exercises with quantitative feedback in a gravity-reduced environment. *IEEE Trans Neural Syst Rehabil Eng*, 14(3):378-389.
18. Stienen AHA, Hekman EEG, Van der Helm FCT, Prange GB, Jannink MJA, Aalsma AMM and Van der Kooij H. 2007. Dampace: dynamic force-coordination trainer for the upper extremities. In: *Proceedings of the IEEE 10th International Conference on Rehabilitation Robotics*; June 13-15; Noordwijk, The Netherlands; pp. 820-826.
19. Riener R, Nef T, Colombo G. 2005b. Robot-aided Neurorehabilitation for the Upper Extremities. *Medical & Biological Engineering & Computing*, 43:2-10.
20. Krebs HI, Ferraro M, Buerger SP, Newbery MJ, Makiyama A, Sandmann M, Lynch D, Volpe BT and Hogan N. 2004. Rehabilitation robotics: pilot trial of a spatial extension for MIT-Manus. *J Neuroeng Rehabil* 1:5.
21. Lum PS, Burgar CG and Shor PC. 2004. Evidence for improved muscle activation patterns after retraining of reaching movements with the MIME robotic system in subjects with poststroke hemiparesis. *IEEE Trans Neural Syst Rehabil Eng*, 12(2):186-94.
22. Dewald J, Ellis MD, Holubar BG, Sukal T, Acosta AM. (2004). The robot application in the rehabilitation of stroke patients. *Neurol Rehabil*, (4):S7
23. Hesse S, Werner C, Pohl M, Rueckriem S, Mehrholz J, Lingau ML. (2005). Computerized Arm Training Improves the Motor Control of the severely Affected Arm After Stroke. *Stroke*, 36:1960-1966.
24. Nef T, Riener R (2007). Arm Therapy Robot ARMin: A Tele-Game to Increase Patient Motivation. Proceedings of the Automated Conference, October 19-21, Munich, Germany.
25. Fugl-Meyer AR, Jääskö L, Leyman I, Olsson S, Steglind S. The post-stroke hemiplegic patient: A method for evaluation of physical performance. *Scand J Rehabil Med* 1975;7(1):13-31.

Comparative Study on the Posture of Individuals with and without Cervical Pain

S.R.G.P. Galera¹, L.F.C. Nascimento², E.C.M. Teodoro¹, and J.E. Tomazini¹

¹ Graduate student. São Paulo State University. Campus of Guaratinguetá., Brazil

² Department of Medicine – University of Taubaté. Taubaté, Brazil

Abstract — Posture can be defined as the overall position and spatial orientation of the human body and its members relative to each other. The study of posture can be applied either static, with the subject standing still. Objectives: to identify and quantify the static posture alignment of individuals who were either symptomatic or asymptomatic for cervical pain. Methods: A cross-sectional study was carried out on subjects with cervical pain and individuals with no complaints of pain. The procedure consists in placing markers on specific points. Several views, following the protocol of the Posture Assessment software, regarding the measurement of angles (in degrees) and differences in lower leg lengths (in centimeters). Angles were analyzed through the comparison of averages between the groups using test *t* Student, ($\alpha=5\%$). Results: There enrolled 27 subjects. There were differences in horizontal alignment of head (3.37x1.33), acromia (2.60x1.18), iliac spines (2.91x0.67), vertical alignment of head (25.70x18.26) and in length of lower limbs (1.36x0.75) in respect to cervical and asymptomatic subjects. Conclusions: Was possible identify and quantify the static posture alignment of individuals with and with no cervical pain. The data obtained suggest the presence of asymmetry in all the symptomatic individuals studied. The data obtained suggest the presence of overall asymmetry in all the symptomatic individuals studied.

Keywords— posture, assessment, spinal column, cervical pain.

I. INTRODUCTION

As the support for the body, having to withstand considerable impact and load, the spine is generally involved in bodily disorders of a postural nature [1]. Posture can be defined as the overall position and spatial orientation of the human body and its members relative to each other [2].

Human posture has been studied in its biomechanical aspects. Structural and functional disorders cause imbalances and compensatory behavior that could cause important alterations. The study of posture is applied, which can be

either static or dynamic [3]. Static posturography addresses erect, undisturbed posture, with the subject standing still [4].

To quantify posture assessment methods, a large number of diagnostic instruments have been used in the physiotherapy field, such as the isokinetic dynamometer and computerized posturography. These devices are currently considered the most precise, objective manner to perform posture assessments [5]. Photography is a common and quite effective procedure, as it allows analysis through the recorded image. Thus, visualization becomes more detailed, with a lower margin of error, which cannot be said for methods that depend upon the subjectivity of the evaluator.

The aim of the present study was to identify and quantify the positioning of body segments of subjects with cervical pain in an erect posture from the anterior, posterior, right lateral and left lateral views and compare these subjects with asymptomatic individuals using posture assessment software.

II. WRITING THE PAPER

A. Methods

A cross-sectional study was carried out with individuals who were either symptomatic or asymptomatic of spine cervical pain. Subjects were divided into two groups: asymptomatic individuals and those with cervical pain. The following were the inclusion criteria for the two groups: sufficient cognitive level to understand the procedures, following orientations, and answer questions related to patient history; no use of prosthetics or braces; no lasting effects of any accident that cause limitations in active movement; and no history of neurological disease or syndrome.

The following materials were used: Digital camera; tripod; polystyrene passive markers; blackboard; white chalk; non-extendable millimeter scale; digital scale (Filizola);

plumb line marked with two polystyrene balls. The protocol for the subject history was provided by the SAPO postural assessment computational software program, available at <http://sapo.incubadora.fapesp.br>.

Following the localization of the anatomic demarcation points, subjects were photographed in anterior, posterior, right lateral and left lateral views. Small polystyrene foam balls cut in half were used as markers. The balls were previously prepared with double-face adhesive tape and placed over the specific anatomic points. A blackboard was used in order to assure the same base in the four photographs. Subjects positioned themselves freely atop the blackboard for the first photograph and the outline of their feet was traced. Subjects were instructed to position themselves directly upon the same mark for the subsequent photographs. The camera was positioned three meters from the subject. A plumb line marked with two polystyrene balls placed one meter apart was used for the calibration of the photo.

Anatomic points were marked on the head, trunk and lower limbs. The choice of anatomic points was made based on criteria regarding relevant clinical analyses. Such points were chosen for their importance to scientific research and for the possibility of minimizing errors in localization through knowledge regarding palpatory anatomy [6].

The photographs were transferred to a computer using a USB interface and analyzed on the SAPO program. These points are part of the computational program employed. As the present study did not take into consideration the sides referring to the inclinations of the segments, the angle measurements were considered in module.

Analysis of variance (Test *t* Student) was used in the statistical analysis for the comparison of averages between the two groups. Data were compiled on the Microsoft Excel and Epi-Info 6.04 software programs.

B. Results

Twenty-seven subjects participated in the study, 13 (48%) with neck pain and 14 (52%) with no complaints of pain. Thirteen subjects (48%) were male and fourteen were female (52%). The age of the participants ranged from 35 to 55 years, with an average of 40.42 years of age. Tables 1 and 2 display the results of the ANOVA test.

In the anterior view, horizontal alignment of the head was different between the two groups ($p = 0.004$). In the trunk region, the angle measurement between the two acromia and the two anterior superior iliac spines exhibited the greatest significant difference between the groups ($p < 0.001$). Subjects with cervical pain exhibited difference in length between the lower limbs when compared to the other

group ($p < 0.04$). There was a significant difference between groups regarding the vertical ($p = 0.04$) and horizontal ($p = 0.07$) alignment of the head in the right lateral view. All subjects with cervical pain exhibited forward lean from the center of gravity. No significant difference between groups was observed in the posterior and left lateral views.

Table 1: Average angle values in degrees, assessed in the anterior and posterior views, with respective standard deviation (sd) for 27 subjects pertaining to the cervical pain (CA) and asymptomatic (AA) groups.

Anterior view	CA (sd)	AA (sd)
Head		
Horizontal alignment of head #	3.37 (1.72)	1.33 (1.19)
Trunk		
Horizontal alignment of acromia	1.89 (1.14)	1.05 (1.11)
Horizontal alignment of anterior superior iliac spines #	2.60 (1.59)	1.18 (0.70)
Angle between the two acromia and the two anterior superior iliac spines #	2.91 (1.78)	0.67 (0.48)
Lower limbs		
Frontal angle of lower right limb	3.55 (2.54)	2.45 (1.98)
Frontal angle of lower left limb	2.97 (2.05)	2.37 (2.18)
Difference in length of lower limbs (R-L)	1.36 (1.29)	0.75 (0.46)
Horizontal alignment of tuberosity of tibias	3.29 (3.11)	2.77 (1.93)
Right Q angle	23.63 (9.46)	19.26 (12.84)
Left Q angle	18.47 (11.24)	19.70 (11.52)
Posterior View		
Trunk		
Horizontal asymmetry of scapula in relation to T3	13.76 (13.15)	16.20 (14.71)
Lower limbs		
Right leg/hindfoot angle	7.32 (5.63)	9.58 (6.87)
Left leg/hindfoot angle	10.71 (5.39)	12.97 (8.10)

p-value <0.01

Table 2: Average angle values in degrees, assessed in the right and left lateral views, with respective standard deviation (sd) for 27 subjects pertaining to the cervical pain (CA) and asymptomatic (AA) groups.

Right Lateral View	CA (sd)	AA (sd)
Head		
Horizontal alignment of head (C7)	44.21 (4.99)	47.19 (3.40)
Vertical alignment of head (acromion) #	25.70 (5.31)	18.26 (7.47)
Trunk		
Vertical alignment of trunk	6.11 (3.26)	5.68 (2.67)
Angle of hip (trunk and lower limb)	11.22 (4.91)	11.47 (3.94)
Vertical alignment of body	1.01 (1.25)	1.26 (0.83)
Horizontal alignment of pelvis	15.45 (21.41)	11.25 (6.39)
Lower limbs		
Angle of knee	6.21 (3.97)	4.52 (2.67)
Angle of ankle	86.80 (4.05)	86.63 (2.04)
Left Lateral View		
Head		
Horizontal alignment of head (C7)	46.27 (2.93)	45.66 (4.05)
Vertical alignment of head (acromion)	21.61 (7.63)	21.87 (7.91)
Trunk		
Vertical alignment of trunk	4.70 (2.72)	3.99 (2.67)
Angle of hip (trunk and lower limb)	11.52 (4.03)	10.69 (4.28)
Vertical alignment of body	2.08 (1.25)	2.52 (1.19)
Horizontal alignment of the pelvis	10.21 (4.82)	11.21 (7.84)
Lower limbs		
Angle of knee	5.61 (3.75)	5.96 (3.51)
Angle of ankle	85.52 (2.18)	85.80 (2.82)

p-value < 0.01

C. Discussion

The present study evaluated individuals who were either symptomatic or asymptomatic of spinal cervical pain from a postural perspective according to the angles obtained from the posture assessment program. The same methodology was used for all subjects and applied by the same evaluator. This minimized the margin of error of the results and enabled the obtainment of a single standard of assessment, as intra-evaluator reliability is greater than inter-evaluator reliability [7].

The SAPO postural assessment computational software program was used to determine the coordinates of the anatomic points marked in photographs by the passive markers and to perform the measures of the angles analyzed. This program also offers scientific tutorials and the creation of a

databank. It is easy to use and offers image calibration functions, which help to correct any errors that may have occurred during image capture as well as a zoom feature, simultaneous visualization of various photos, *Wizard* support protocol, manual or default point demarcation, and the measuring of angles and distances [6]. The measurement protocol provides reference values for some measurements, but the values obtained from symptomatic subjects were compared to the group without pain (control group), which exhibited values close to the references provided by the program for many angles.

The anterior assessment of the horizontal alignment of the head revealed values other than zero in the entire sample of the group with cervical pain; exhibited significant differences in comparison to the asymptomatic individuals. It can be stated that all the cases with spinal cervical pain exhibited alterations in the horizontal alignment of the head for one of the two sides. This deviation may be related to muscle shortening on the side corresponding to the alteration, linked to symptoms of pain [8,9].

In the trunk region, the angle formed by the acromia and anterior superior iliac spines exhibited deviations in subjects with cervical pain when compared to asymptomatic subjects. Chronic musculoskeletal pain is considered the major cause of posture alterations in various segments of the spinal column [10].

The two groups exhibited differences in the right lateral view for the vertical and horizontal alignment of the head. In the case of the subjects with cervical pain, the entire sample exhibited forward lean from the center of gravity. One of the most common problems found in individuals with cervical pain is the forward lean posture of the head. This posture places the head in front of the line of gravity and may generate different problems of a postural nature, including pain [11].

Another point observed is an overall bilateral asymmetry in the subjects from the two groups studied. As Ferreira [6] also found, the results of the present study demonstrate that there is a standard of similarity for postural alignment among the subjects. Nonetheless, it cannot be affirmed that postural symmetry is this standard. This proves that the evolution of deviations and compensation mechanisms obeys the individuality of the subject and presents globally throughout the body. Human posture control is a complex function that includes components such as the detection of movement as well as voluntary coordinated control and muscle reflex response [12], thereby justifying the need to study posture through an analysis of the entire body [13].

Despite some possible limitations, such as the fact that the incorrect localization of anatomic points may generate measurement errors as well as the fact that some measurements are vulnerable to anthropometric characteristics and

the evaluation method, the present study allowed the discussion of the results to have an objective, less personal focus. From the analysis of the data regarding the variables used, it was possible to identify and quantify the positioning of body segments according to situations of pain located in the cervical region. The data obtained proved satisfactory, without the need to complement the study with more sophisticated, costly methods. Significant differences were also found between the three groups studied with regard to the measurements of the angles evaluated.

III. CONCLUSIONS

Was possible identify and quantify the static posture alignment of individuals with and with no cervical pain. the data obtained suggest the presence of asymmetry in all the symptomatic individuals studied. the data obtained suggest the presence of overall asymmetry in all the symptomatic individuals studied.

REFERENCES

- Occhipinti E, Colombini D. (2000) Aging at work and musculoskeletal disorders. *Med Lav* 4: 342-353.
- Massion J, Woollacott MH. (1996) Posture and Equilibrium. In: Bronstein A. M., Brandt T., Woollacott MH, eds. *Clinical Disorders of Balance, Posture and Gait*. London: Arnold Publishers. 1-19
- Mochizuki, L, Amadio, AC. (2003) Aspectos biomecânicos da postura ereta: a relação entre o centro de massa e o centro de pressão. *Rev Port de Ciênc do Desporto* 3: 77-83.
- Collins JJ, Deluca CJ. (1993) Open-loop and closed-loop control of posture: a rondon-walk analysis of center-of-pressure trajectories. *Exp Brain Res* 95: 308-318.
- Clark S; Rose DJ; Fujimoto K. (1997) Generalizability of the limits of stability test in the evaluation of dynamic balance among older adults. *Arch Phys Med Rehabil* 78: 1078-1084.
- Ferreira EAG. (2005) **Postura e controle postural: desenvolvimento e aplicação de método quantitativo de avaliação postural**. 80f. Tese (Doutorado em Ciências) Faculdade de Medicina da Universidade de São Paulo, 2005.
- Fedorak C; Ashwoth N; Marshall J; Paull H. (2003) Reliability of the visual assessment of cervical and lordosis: How good are we? *Spine* 16: 1857- 1859
- Borghouts JA, Koes BW, Bouter LM. (1998) The clinical course and prognostic factors of non-specific neck pain: a systematic review. *Pain*. 77: 1-13.
- Sobel J; Sollenberger P; Robinson R; Polatin P; Gatchel R. (2000) Cervical non-organic signs: a new clinical tool to assess abnormal illness behavior in neck pain patients. A pilot study. *Arch Phys Med Rehabil*. 81: 170-175.
- Manchikanti L, Staats PS, Singh V. et al. (2003) Evidence- based practice guidelines for interventional techniques in the management of chronic spinal pain. *Pain Physician*. [<http://www.asipp.org/documents/Guidelines%202003.pdf>].
- Gross A, Aker P, Goldsmith Ch, Peloso P. (2007) Withdrawn: Physical medicine modalities for mechanical neck disorders. *Cochrane Database Syst Rev*. 3: CD000961.
- Fransson PA; Johansson R; Hafstrom A et al. (2000) Methods for evaluation of postural control adaptation. *Gait Posture* 12: 14-24.
- Descatha A, Roquelaure Y, Evanoff B, et al. (2007) Predictive factors for incident musculoskeletal disorders in an in-plant surveillance program. *Ann Occup Hyg*. 3: 337-344.

Author: Sandra Regina De Gouvêa Padilha Galera
 Institute: Department of Mechanics – Sao Paulo State University
 Street: Av. Ariberto Pereira da Cunha, 333 – 12.516-410
 City: Guaratinguetá
 Country: Brazil
 Email: sandragalera@vivax.com.br

Functional Assessment of Orthopedic Aids Using Open Vertical MRIs

M. Tettke¹, R.C. Bittner², and M. Kraft¹

¹ Technical University of Berlin, Institute for Construction, Microtechnology and Medical Technology
Department of Medical Engineering, Berlin, Germany

² Helios-Clinic Emil-von-Behring, Department of Diagnostic and Interventional Radiology, Berlin, Germany

Abstract— This paper presents – using the examples “knee orthosis” and “patellar stabilizing braces” – a method which delivers an insight into the “patient - orthopedic aid” system using an open low-field MRI, adapted MRI-sequences, MR compatible measurement techniques and self-build software. The basic principle is a consistent three-dimensional image acquisition and reconstruction of bony structures.

Created in Matlab¹, our software is able to segment, reconstruct and register objects, to determine the principle axes, and to calculate translational and rotational components (a. e. movements and tilts of the patella proportional to the femur) as well as joint axes using the helical axes method.

A previously acquired structured light 3D-scan of the orthopedic aid and the application of 3D-MRI-markers during the MRI scan allow a mapping of the orthopedic device on the scanned anatomy, thus a. e. giving the possibility of comparing joint axes with those of the orthopedic device.

Keywords - functional MRI, segmentation, registration, functional assessment, orthopedic aid.

I. INTRODUCTION

There is still some uncertainty concerning the parameters describing the influence of orthopedic aids on the human anatomy, as well as their effectiveness. As the mode of operation often is not yet known, methods to describe and quantify the interaction of aid and human are needed. A characterization of an aid without the understanding of its function principles is not adequate, as it does not shed light on the achievable therapeutic or rehabilitative effect to a patient or a patient collective sharing the same pathology.

So far methods like gait analysis or fluoroscopy were often used for kinematic studies. While gait analysis yields the big problem of migration of soft tissue, fluoroscopy uses ionizing radiation and is therefore unsuitable for ongoing evaluation of therapeutic effects. There are some studies using kinematic MRI, but acquisition is always two-dimensional. 2-D approaches cause a big problem because measurements are only comparable when the slices are always acquired at the exact same position without any

rotation. Even the occurrence of relative movements in the anatomy, a. e. a movement or tilt of the patella relative to the femur, has to be eliminated as it is not possible to compare 2-D routes on differently rotated objects – a precondition that is virtually unable to achieve in the understanding of the author.

In this paper, we will introduce a consistent three-dimensional method using horizontal aligned, low-field open MRI, MRI-compatible measurement technique and self-developed software.

New findings on knee kinematics give evidence for a three dimensional course of the physiologic knee axes with differences between medial and lateral [1]. Substantial individual differences make it nearly impossible for the joints of pre-fabricated knee orthoses to follow this individual movement. Because there are different types of joints for orthoses available, the grade of congruence between anatomic and orthotic joint axes and the influence of the orthosis on the anatomic joint axes are interesting to know.

Patellar stabilizing braces are often used in patients with patellofemoral pain syndrome. There is some evidence, that adequate tracking of the patellar helps to decrease the level of pain in these patients, if an adequate compensation of mediolateral patellar displacement and patellar tilt is achieved. ([2], [3])

II. MATERIAL AND METHODS

We used a modern low-field MRI with 0,25 T (ESAOTE G-Scan, Fig. 1) which allows to acquire data on upright patients under physical loading conditions in different angles of flexion [4]. As the patient’s position should be as physiological as possible, we used no guiding techniques but constructed a measurement device consisting of two platforms to measure the load difference between the two feet. The compliance with a preassigned condition was calculated and displayed to the patient using a green (correct load), red (overload) and blue (underload) light. When the loading condition was not in the predefined state, the lights started to flash – as faster, the bigger the difference between the actual and the preassigned condition was.

¹ Matlab is a trademark of The MathWorks, Inc.

Rubber sheets under the patient's feet were used to get the patient into flexion (Fig. 2).



Fig. 1 ESAOTE G-Scan MRI (left)

Fig 2 Flexion trial with rubber sheets and measurement device (right)

We used knee orthoses and patellar stabilizing braces as examples for orthopedic aids and developed measurement procedures for both of them.

Dealing with acquisition under loading conditions, there is always the problem of finding a compromise of image quality (which rises with longer acquisition times) and the physical stress on the patient while holding a position without having the possibility to do small movements. We found an acquisition time of up to four minutes is possible without causing too much stress for the patient.

The type of image acquisition differed between the two kinds of aids:

- Measuring the knee orthosis we acquired a sagittal volume of 200 x 200 x 120 mm with a slice thickness of 1,9 mm using a SSFE sequence. The acquisition time was 1:28 min. We used a short GE sequence with three transversal slices to plan the acquisition.
- For the Patellar stabilizing braces a sagittal volume of 240 x 240 x 58 mm with a slice thickness of 1,1 mm using a "turbo 3D T1"-sequence was acquired in 3:12 min. Again, we used a short transversal GE sequence, but here to align our FOV to the structure of the patella. So, we acquired the whole structure of the patella, but only a subvolume of femur and tibia.

Subsequently, we transferred the MRI data of both orthopedic aids (using exported DICOM3 data) to our software to do the segmentation tasks using combined methods like regions of interest, grey-based thresholds, morphological operations (erosion, dilation), live-wire guidance [5], and three-dimensional object reconstruction while keeping all DICOM metadata intact. In the next step, the objects of different flexion angles were transferred to one coordinate system using a femur-registration based on a combination of a genetic algorithm and a gradient based method (see [6]).

We used different cost functions for the registration when dealing with the data from the patellar stabilizing braces, as we didn't have complete femur-objects. After selecting the method the process of registration was running without user interaction and without the need of manually placed points.

Once again, the mode of evaluation differed for both kinds of orthopedic aids:

- For the knee orthosis, the femur was defined as fixed and the tibia as moving part of the joint. Using the helical-axes method ([7], [8]) it was possible to calculate the functional knee axis from a rigid transformation matrix (results are shown in Fig. 6), which results in a rotation about an axis and a translation along this axis.

The position of the knee orthosis was acquired using two attached MR sensitive coordinate systems (Fig. 3). These acquired marker positions allowed the shaping of the orthosis on the MRI data, using the known marker coordinates from a previous generated structured light 3D-scan (Fig. 4).

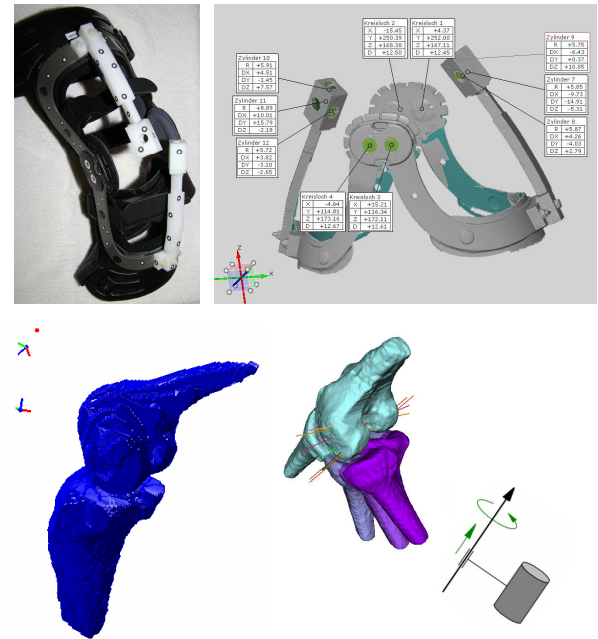


Fig. 3 Knee orthosis with attached coordinate systems (upper left)

Fig 4 Result of the structured light 3D-scan (upper right)

Fig 5 Reconstructed MRI image with coordinate systems (lower left)

Fig 6 Combined helical knee and orthosis axes (lower right)

- As described in the introduction, the position of the patella in relationship to the femur as well as the mediolateral and proximodistal tilt of the patella is important when dealing with patellofemoral pain syndrome. Both can be calculated using the center of gravity and the principal axes method [9] of patella and femur.

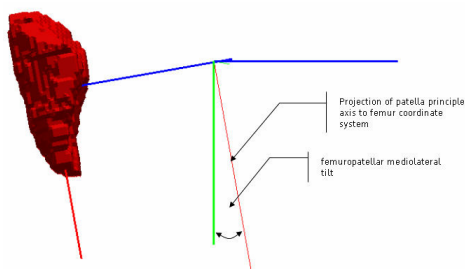
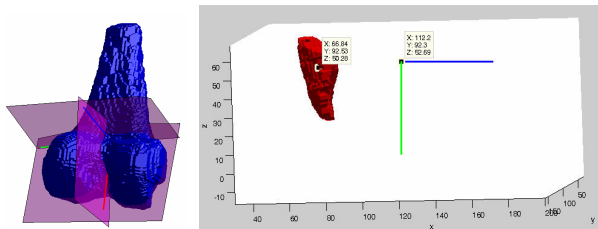


Fig. 7 Principle axes of femur (upper left)

Fig 8 Coordinate calculation of patella and femur (upper right)

Fig 9 Calculation of mediolateral patella-tilt (lower)

III. RESULTS

The method described in this document was proven in a pilot study. Looking at first results, a comparative assessment of orthopedic aids using this method is possible, if adequate parameters are chosen.

In a nutshell, it is possible for the first time to compare the influence of orthopedic aids to human anatomy using three-dimensional low-field MRI. Especially an assessment of patients with different pathologies and with and without orthopedic aid can lead to new results about the effectiveness of orthopedic aids, giving valuable impulses for product development.

IV. DISCUSSION

As measurements show, the chosen MRI parameters (such as positioning, slice thickness) have a big influence on the accuracy of our method. Actually, work in progress studies are underway to establish validation process and to develop optimal MRI parameters.

ACKNOWLEDGMENTS

The authors wish to thank the Stiftung Oskar-Helene-Heim, the Otto Bock Stiftung and the Helios Clinic Emil-von-Behring in Berlin, Germany for their support.

REFERENCES

- Wetz H H, Jacob H A C. (2001) Funktionelle Anatomie und Kinematik des Femurotibialgelenks - Forschungsergebnisse von 1836-1950. Orthopädie, 30: 135-144
- Baker V et al (2002) Abnormal knee joint position sense in individuals with patellofemoral pain syndrome. J Orthop Res 20, 208-214
- Powers C M et al (2004) The effect of bracing on patella alignment and patellofemoral joint contact area. Med Sci Sports Exerc 36, 1226-1232
- Marin F. et al (2006) Can a finite set of knee extension in supine position be used for a knee functional examination? Journal of Biomechanics 39: 359-363
- Chodorowski A et al (2005) Color Lesion Boundary Detection Using Live Wire. Proceedings of SPIE Medical Imaging: Image Processing, vol. 5747, 1589-1596.
- Niesche A et al (2008) Numerical evaluation and comparison of instantaneous anatomical knee joint axes and orthotic joint axes using MRI data under weight-bearing condition. ECIFMBE 2008, IFMBE Proceedings 22: 522-525
- Spoor C W, Veldpaus F E (1980) Rigid body motion calculated from spatial co-ordinates of markers. J Biomechanics 13:391-393
- Woltring H J, Huiskes R, et al. (1985) Finite centroid and helical axis estimation from noisy landmark measurements in the study of human joint kinematics. J Biomechanics 18:379-389
- Alpert N M et al (1990) The Principal Axes Transformation - A Method for Image Registration. J Nucl Med 31: 1717-1722

Bioelectric Source Localization in the Rat Sciatic Nerve: Initial Assessment Using an Idealized Nerve Model

José Zariffa^{1,2,3}, Mary K. Nagai^{1,3}, Zafiris J. Daskalakis⁴ and Milos R. Popovic^{1,2,3}

1. Institute of Biomaterials and Biomedical Engineering, University of Toronto, Canada

2. Edward S. Rogers Sr. Department of Electrical and Computer Engineering, University of Toronto, Canada

3. Toronto Rehabilitation Institute, Canada

4. Schizophrenia Program, Centre for Addiction and Mental Health, Department of Psychiatry, Faculty of Medicine, University of Toronto, Canada

Abstract—Our goal is to determine the spatial origin of bioelectric activity within a peripheral nerve using recordings from a multi-contact nerve cuff electrode. This task is a bioelectric source localization problem, and a natural question is whether or not algorithms developed for the similar problem of EEG source localization can be applied in the peripheral nerve context. This technique requires a model of the nerve, and the present study aims to determine if using an idealized nerve geometry in the finite-element model is sufficient to achieve acceptable localization performance. Using a leadfield derived from the idealized model, the sLORETA algorithm was applied to recordings from a 56-channel “matrix” nerve cuff electrode placed around the rat sciatic nerve. The results show that the method was not able to reliably estimate the number and combination of active fascicles. A summary of the issues that need to be addressed before source localization techniques can be applied to peripheral nerves is provided.

Keywords: bioelectric source localization; multi-contact nerve cuff electrode; rat sciatic nerve; sLORETA; finite-element modeling.

I. INTRODUCTION

Monitoring the electrical activity of specific pathways in a peripheral nerve is a crucial goal in the development of better neuroprostheses. Several types of neural interfaces have been proposed to accomplish this goal, but each of them has limitations. Longitudinal intrafascicular electrodes [1, 2] are very spatially specific, at the cost of monitoring activity only in a limited region of the nerve. Micro-electrode arrays [3, 4] provide both good spatial selectivity and good spatial coverage of the nerve, but are the most invasive of the proposed technologies and can therefore damage the nerve. Nerve cuff electrodes [5], on the other hand, are less invasive and can monitor a whole nerve but have poor spatial selectivity. Improvements in manufacturing technology have made increasingly sophisticated multi-contact nerve cuff electrodes possible [6, 7], raising the possibility of increasing the selectivity of these devices and

obtaining an effective and versatile type of neural interface. Determining the spatial origin of electrical activity recorded at multiple contacts in a nerve cuff is fundamentally a bioelectric source localization problem. Algorithms that have been developed for other similar problems, most notably EEG/MEG source localization, have not been applied in the peripheral nerve context and are just starting to draw attention [8, 9]. These algorithms require a model of the nerve’s anatomy, and the accuracy of this model influences the performance of the source localization. The level of detail needed in this model will have important implications for the applicability of peripheral nerve source localization techniques in practice. In the present study we consider the task of identifying active fascicles in a rat sciatic nerve and investigate the performance of an EEG source localization algorithm in conjunction with an idealized nerve model.

II. METHODS

A. Data Collection

Five old male Long-Evans breeders (640 g to 850 g) (Charles River Laboratories Inc., Wilmington, MA) were used. All rats were acclimatized for one week prior to use in the experiment, with food and water provided *ad libitum* and a 12 hour lights on/off cycle. All animal care and use procedures conformed to those outlined by the Canadian

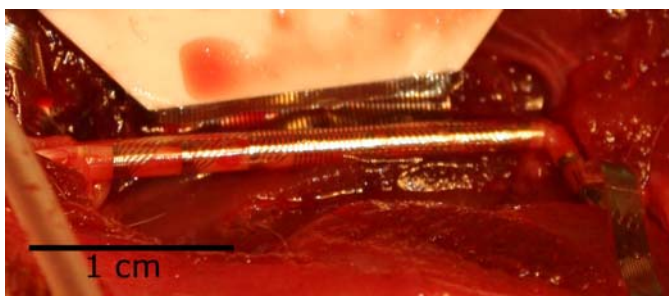


Fig. 1: 56-channel “matrix” nerve cuff placed on the rat sciatic nerve.

Council on Animal Care (CCAC). Animals were anesthetized with a single bolus injection of pentobarbital (60 mg/kg, intraperitoneal), and their lower backs and legs were shaved and treated with povidone-iodine. The sciatic nerve was exposed as far proximally as possible, then followed distally, where three branches were identified: the sural nerve, peroneal nerve, and tibial nerve. The soft tissue surrounding each of these nerves was carefully blunt dissected to allow a nerve cuff to be applied to each nerve.

A “matrix” design polyimide spiral nerve cuff electrode [10] was placed on the sciatic nerve, just proximal to its division into its peroneal and tibial branches (Fig. 1). This cuff was 23 mm long, 1 mm in diameter and contained 56 contacts, arranged in 7 rings of 8 contacts. This electrode was used to record the nerve activity during the experiments. In addition, three tripolar stimulating polyimide spiral nerve cuffs (8 mm long and 1 mm in diameter) were placed around the tibial, sural, and common peroneal nerves. The measurements from the cuff on the sciatic nerve were acquired using a SynAmps2 64-channel amplifier (Neuroscan Inc., Herndon, VA, USA), with a sampling rate of 20 kHz and a gain of 2010. The signals were bandpassed filtered between 300 Hz and 3 kHz (which was the highest cutoff permitted by the amplifier). The reference for the recordings was a contact included in the electrode design and located just outside the cuff. A needle electrode in the calf was used as the ground. The tibial, peroneal, and sural nerves were stimulated one at a time and in every combination using the 8 mm cuff electrodes. The stimulation pulses were generated using Compex Motion stimulators (Compex SA, Switzerland). The intended stimulation parameters consisted of 10 μ s 2 mA pulses, but technical difficulties noticed only after the fact resulted in pulses with an estimated duration of 2-4 μ s and with amplitudes in the 0.7 to 3.8 mA range approximately. Fortunately, these pulses were still able to reliably produce action potentials in the nerve (as indicated by muscle twitches and the fact that the matrix cuff recordings showed a temporal progression of activity along the cuff consistent with action potential propagation). 100 trials were conducted for each fascicle, at a frequency of 2 Hz. The recorded data was converted to a common-average reference in order to reduce interference from the stimulation artifact.

B. Source Localization

A finite-element (FE) model of an idealized unifascicular section of a rat sciatic nerve was built, consisting of concentric cylinders representing the endoneurium, perineurium and epineurium layers, an encapsulation tissue layer, a saline layer, the nerve cuff, and a saline bath. The dimensions and conductivities of the various part of the nerve model are

given in Table I. 56 contacts were placed on the inside of the nerve cuff, in positions corresponding to those in the matrix cuff used in the experiments. Although much more accurate models can be constructed if information about the anatomy of the nerve is available, the goal here is to evaluate the performance of the method using a model that is idealized and hence will not need to be tailored to each patient. The FE analysis was conducted using the SCIRun computing environment [11], and the leadfield computed according to the procedure described by Weinstein et al. [12]. The number of variables in the leadfield was reduced according to the method in [13].

The source localization was performed by applying the standardized low resolution brain electromagnetic tomography (sLORETA) algorithm [14] to the 56-channel data recorded from the matrix cuff. Preliminary studies had determined that sLORETA is more appropriate for this task than existing alternatives [15]. The regularization parameter was chosen by means of the cross-validation error function [14, 16]. For each trial, the source localization was applied to a small time interval delimited by the peaks of the action potential recordings at a contact in the first ring and a contact in the last ring, plus 0.1 ms before and after this interval.

III. RESULTS

In order to view a convenient summary of the results, an estimate of the activity of each “pathway” (longitudinal column in the FE model) was obtained by summing the absolute values of the estimated activities in all the elements

Table 1 Finite Element Model Parameters

Parameter	Value
Nerve length	5 cm
Endoneurium radius	360 μ m
Perineurium width	25 μ m
Epineurium width	35 μ m
Encapsulation tissue layer width	40 μ m
Saline layer width	40 μ m
Cuff length	2.3 cm
Cuff width	30 μ m
Cuff radius	500 μ m
Cuff starting height	1.35 cm
Saline bath length	5 cm
Saline bath radius	0.48 cm
Endoneurium conductivity (radial)	8.26×10^{-2} S/m
Endoneurium conductivity (longitudinal)	0.571 S/m
Perineurium conductivity (all directions)	2.1×10^{-3} S/m
Epineurium conductivity (all directions)	8.26×10^{-2} S/m
Encapsulation tissue conductivity (all directions)	6.59×10^{-2} S/m
Saline conductivity (all directions)	2 S/m
Cuff conductivity (all directions)	1×10^{-7} S/m

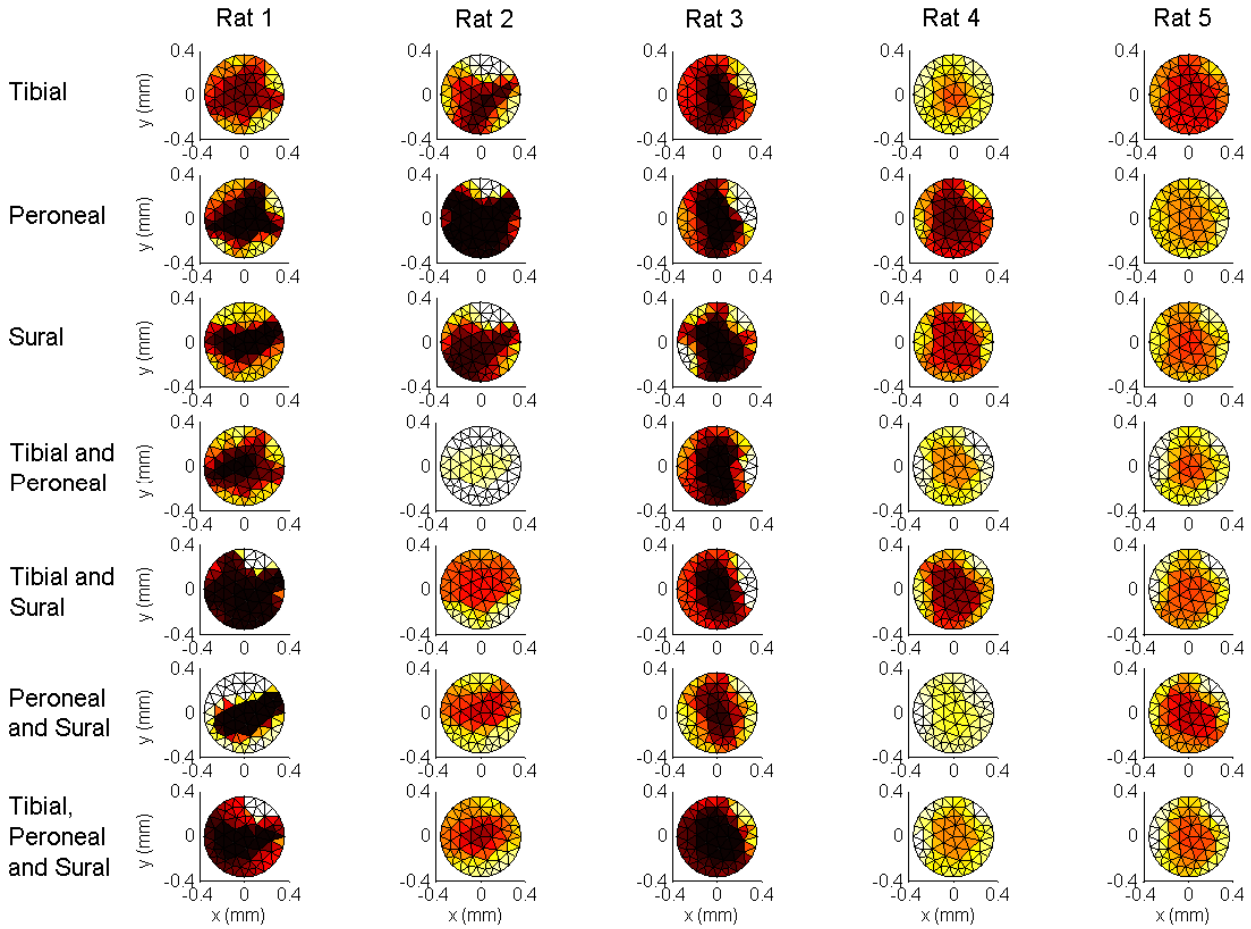


Fig. 2: Summary of the source localization results, for each combination of stimulated branches and each rat. See text for the meaning of the values in the 2-dimensional projections. Lighter colours represent higher levels of activity.

of that column over the time interval. Pathways with levels of activity that were equal to at least 50% of the maximum level of activity in that trial were considered active pathways. The results are compiled in Fig. 2, where the intensity of a mesh element in this figure is determined by the number of trials in which that pathway was judged to be active.

Because the position of the contacts with respect to the nerve varied from one animal to the next, the images in Fig. 2 should be interpreted not by using the absolute location of the activity, but rather by examining whether stimulating the different nerve branches generated activation at distinct locations and whether the number and combination of active branches could be identified from the results. According to these criteria, the source localization was not successful.

Indeed, in all animals, several of the possible combinations yielded patterns of activity that were effectively indistinguishable from one another. These results suggest that the differences between the nerve model and the actual anatomy were simply too great for the source localization algorithm to be able to interpret the recordings correctly.

IV. DISCUSSION AND CONCLUSIONS

Our experiments indicate that applying a source localization algorithm to multi-contact nerve cuff recordings based on an idealized nerve model is a strategy unlikely to lead to a reliable and highly selective neural interface, at least in the case of a spiral cuff on a small nerve. Difficulties encoun-

tered during the experiments included slight movement of the cuff and a stimulation artifact. While these factors mean that we are not testing the source localization under ideal conditions, they are representative of realistic conditions (i.e., a moving nerve, and interference from bioelectric sources outside the cuff), such that our results are indicative of the expected performance in practice. Previous theoretical and simulation work by our group had anticipated these difficulties and indicated that, like in other ill-posed inverse problems, performance in the peripheral nerve bioelectric source localization problem can be improved by employing more realistic nerve models, by constraining the problem in physiological meaningful ways, and by ensuring that noise is reduced as much as possible [8]. It is the authors' opinion that any readers interested in exploring the peripheral nerve source localization problem should focus their efforts on developing such constraints and noise reduction strategies, as well as techniques that can be used to estimate a nerve's precise anatomy *in vivo*.

ACKNOWLEDGMENT

This work was supported by the Natural Sciences and Engineering Research Council of Canada (grant #249669), the Ontario Graduate Scholarship program, and the Walter C. Sumner Foundation. The authors would like to thank Dr. Thomas Stieglitz and Dr. Martin Schuettler for providing us with the cuff electrodes, as well as Lori Dixon, Ashlie Soko and Dr. Dimitry Sayenko for their help with the experiments.

REFERENCES

- Dhillon GS, Lawrence SM., Hutchinson DT, Horch KW (2004) Residual function in peripheral nerve stumps of amputees: implications for neural control of artificial limbs. *J. Hand Surg.* 29(4):605–15; discussion 616–8.
- Micera S et al. (2008) On the use of longitudinal intrafascicular peripheral interfaces for the control of cybernetic hand prostheses in amputees. *IEEE Trans Neural Sys Rehab Eng.* 16(5):453–472.
- Warwick K et al. (2003) The application of implant technology for cybernetic systems. *Arch. Neurol.* 60(10):1369–1373.
- Branner A, Stein RB, Fernandez E, Aoyagi Y, Normann RA (2004) Long-term stimulation and recording with a penetrating microelectrode array in cat sciatic nerve. *IEEE Trans. Biomed. Eng.* 51, 146-157.
- Stein RB et al. (1975) Principles underlying new methods for chronic neural recording. *Canadian J. Neurol. Sci.* 2(3):235–244.
- Stieglitz T, Beutel H, Schuettler M, Meyer JW (2000) Micromachined, polyimidebased devices for flexible neural interfaces. *Biomed. Microdev.* 2:283–294.
- Yoo PB, Durand DM (2005) Selective recording of the canine hypoglossal nerve using a multicontact flat interface nerve electrode. *IEEE Trans. Biomed. Eng.* 52(8):1461–1469.
- Zariffa J, Popovic MR (2008) Localization of active pathways in peripheral nerves: a simulation study, *IEEE Trans Neural Sys Rehab Eng.* 17(1):53-62.
- Durand DM, Park HJ, Wodlinger B (2008) Localization and control of activity in peripheral nerves. *Proc. 30th Ann. Int. Conf. IEEE EMBS*, pp. 3352–3354.
- Schuettler M, Triantis IF, Rubehn B, Stieglitz T (2007) Matrix cuff electrodes for fibre and fascicle selective peripheral nerve recording and stimulation. *Proc. 12th Ann. Conf. IFESS.*
- SCIRun: A Scientific Computing Problem Solving Environment. Scientific Computing and Imaging Institute (SCI), <http://software.sci.utah.edu/scirun.html>.
- Weinstein D, Zhukov L, Johnson C (2000) Lead-field bases for electroencephalography source imaging. *Ann. Biomed. Eng.* 28(9):1059–1065.

Please send correspondence to:

- Author: José Zariffa
- Institute: University of Toronto
- City: Toronto
- Country: Canada
- Email: jose.zariffa@utoronto.ca

Development of a New Wearable Monitoring System for Posture Changes and Activities and its Application to Rehabilitation

K. Motoi¹, Y. Kuwae², S. Taniguchi², M. Wakugawa², T. Yuji², Y. Higashi²
T. Fujimoto², M. Ogawa³, S. Tanaka¹ and K. Yamakoshi¹

¹ Graduate School of Natural Science and Technology, Kanazawa University, Kanazawa, Japan

² Fujimoto Hayasuzu Hospital, Miyakonojo, Japan, ³yu.sys Corporation, Kanazawa, Japan

Abstract— In order to evaluate the efficacy of rehabilitation for persons with hemiplegia, a therapist usually makes judgment by directly observing posture changes, walking speed, activities not only in hospital, but also during daily living. Therefore, quantitative assessment of activities is most desirable. From this viewpoint, we have developed a device for ambulatory monitoring of posture changes, walking speed and activity scenario and evaluated its measurement accuracy by simultaneous recordings of a digital video camera. In order to investigate its applicability to a patient's activity monitoring, we have further developed a new monitoring system which can display static and dynamic motion pictures as well as detailed angle changes of the trunk, thigh and calf. This system makes a therapist to easily understand the patient's motion during training in rehabilitation center and activities during daily living. By evaluation on 6 patients with hemiplegia, the patients' motions were successfully monitored during walking in the rehabilitation center and daily living at their own home. The results clearly demonstrated that the system could detect detailed motion characteristics, indicating that the system appears useful for evaluating quantitatively the efficacy of rehabilitation.

Keywords— Wearable monitoring system, Posture changes, Activities, Walking speed, Rehabilitation

I. INTRODUCTION

Importance of activity monitoring is well recognized in the fields of health care, gerontology and rehabilitation. For example, in the field of gerontology, it is one of the key subjects for the elderly to maintain their activity in daily life in high condition to avoid becoming bedridden. Therefore, an objective measurement of activity is essential [1].

Activity monitoring is also well recognized as being useful in the field of rehabilitation. In order to evaluate the efficacy of rehabilitation, a therapist must evaluate motion characteristics during standing-up, walking, and so on. However, the therapist must usually make assessments subjectively using direct observation. Therefore, quantitative assessment of activities is most desirable. One method employed is to make recordings using a 3D motion capture, but the range over which such recording is possible is usu-

ally limited and data analysis is complicated. Therefore, these methods are generally not useful in rehabilitation.

Some wearable instruments capable of monitoring activity using accelerometer, gyro-sensor, and so on, have been developed [2~8]. But, it is difficult for the therapist to evaluate the patient's posture changes from the data obtained from these devices. Therefore, the wearable system has not yet become practical in rehabilitation field.

On the other hand, we developed a portable device measuring the trunk, thigh and calf angle to the gravitational direction to improve of quality of life for the elderly persons [9]. At the beginning of development, we used miniature electromagnetic inclinometers to measure angles, but had problems with limited measurement range and inertial artifacts of the weight built in the sensor. To solve these problems, we used the accelerometer and gyro-sensor for angle measurement [10], and developed our system to measure the posture changes together with walking speed including the slowness of elderly persons (50 cm/s or less) with high precision ($r=0.99$) [11~13].

In order to investigate its applicability to a patient's activity monitoring, we have been carrying out the clinical evaluation in rehabilitation center [11~13]. In this study, we have further developed a new monitoring system which can display motion pictures as well as detailed angle changes. By evaluation on 6 patients with hemiplegia, the patients' motions were monitored during walking in rehabilitation center and daily living at their own home.

II. SYSTEM OVERVIEW

Fig. 1 shows the outline of the sensor system for monitoring posture changes on sagittal plane together with walking speed. Lower part shows the block diagram of sensor unit. The accelerometer, gyro-sensor, amplifier, Micro SD card, transmitter, Battery, CPU, and so on, are installed in the sensor unit, and this unit is attached on the subject's trunk, thigh and calf, respectively. The patient's motion in the rehabilitation center is monitored using the telemetering system and their activity during daily living at home is recorded using micro SD card.

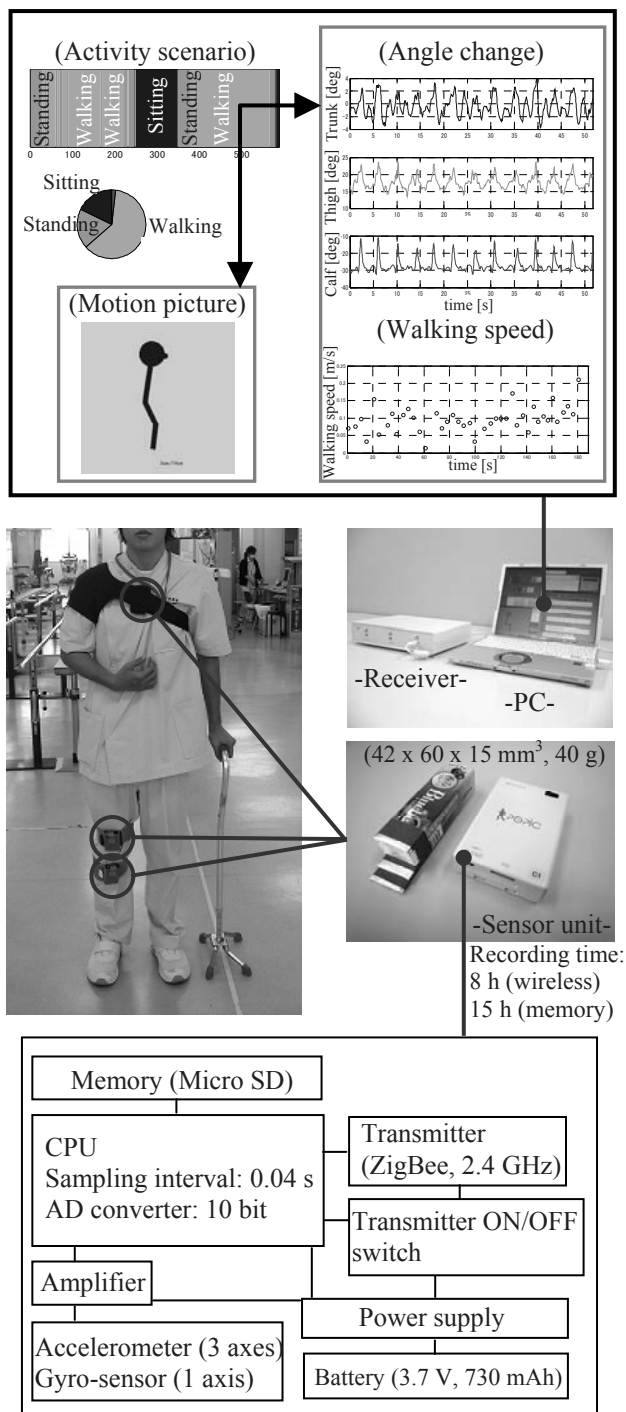


Fig. 1 Outline of the monitoring system

Firstly, it discriminates among postures from walking, sitting, lying and standing using the angle changes on the sagittal plane calculated from low frequency signals

(DC~0.5 Hz) of the accelerometers of each part. Specifically, each posture is determined using the angle thresholds. In the static posture such as standing, sitting and lying, the angle to the gravitational direction of each part is obtained from these low frequency signals of the accelerometers. On the other hand, to calculate the angle changes in the trunk, thigh and calf during dynamic posture such as walking with high precision, angular velocity outputs (0.1~10 Hz) of the gyro-sensors of each part are integrated. The initial angle value is obtained from the sensor signal of accelerometer just before walking. Using the thigh and calf angles in heel contact and off and subject's leg length, walking speed for one walking cycle is calculated using the two link gait model. We previously reported details of calculation methods described above and its measurement accuracy [10~13].

Upper part of Fig. 1 shows the outline of data display for the therapist. Firstly, activity scenarios are displayed as 5 color bars (standing, walking, sitting, lying and standing-up and sitting down). The detailed angle changes, walking speed and motion pictures can be displayed by clicking the bar of activity scenario. These make a therapist to easily understand the patient's activity and motion characteristics.

III. SUBJECTS AND METHODS

4 subjects with hemiplegia (50~85 yrs) had measurements of posture changes during walking in the rehabilitation center. Posture change and walking speed were measured during 10 m-walking. The posture changes of subjects were also recorded using a digital video camera.

2 subjects with hemiplegia (80, 84 yrs) had measurements of activities during daily living at home after leaving the hospital. The measurement are carried out for two hours after home visiting rehabilitation, and activity scenarios, posture changes, walking speed were evaluated. The lower limb sensors were fixed on the paralyzed side.

Before measurement, we acquired permission from the ethical review board at the hospital and the informed consent had been obtained in each patient.

IV. RESULTS AND DISCUSSION

Fig. 2 shows typical recordings of the angle changes of trunk, thigh, knee and calf before and after rehabilitation in male patient using T-cane and MAFO (62 yrs, paralyzed side: right, rehabilitation: 21 days). The patient had measurement during 10 m-walking before and after rehabilitation program. From these results, the range of knee angle changes obtained after rehabilitation became larger than those obtained before rehabilitation, and cyclic angle

changes of trunk, thigh and calf were also detected. These results show that the subject could control the gait by flexion and extension of the knee after rehabilitation, indicating that the efficacy of rehabilitation program could be evaluated by the quantitative data obtained from the system.

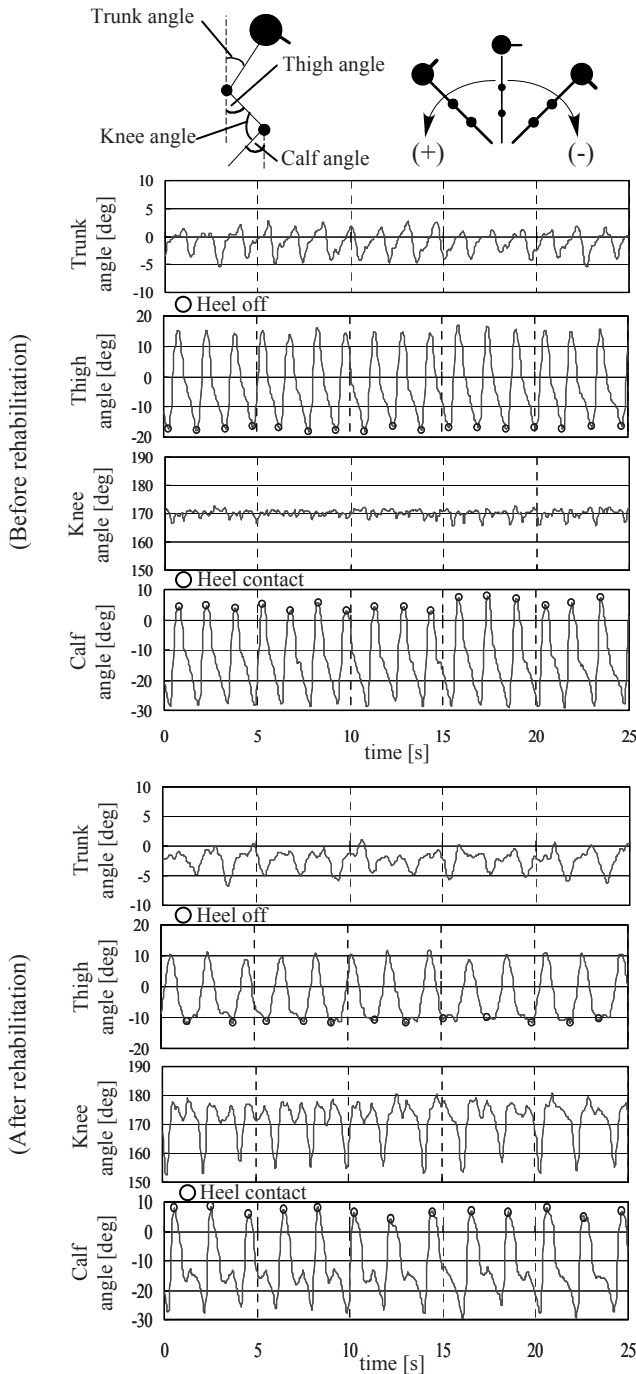


Fig. 2 Typical recordings of the angle changes of trunk, thigh, knee and calf during walking before and after rehabilitation

Fig. 3 shows analytical results for a long-term rehabilitation in male patient with non-cane and non-brace (56 yrs, paralyzed side: right). Each plot denotes the average value during 10 m-walking after rehabilitation. Each plot denotes the average value during 10 m-walking after rehabilitation. 20 walking cycles were accumulated in standard deviation: SD of the thigh angle in heel contact.

From these results, the walking speed became faster by 57 rehabilitation days and then keeping about 0.7 m/s. Therefore, the performance of walking could improve and keep by the rehabilitation. The range of thigh angle changes became larger by the rehabilitation, therefore joint motion improved. SD of the thigh angle in heel contact, i.e., repeatability of motion was getting worse by 57 days while the walking speed was increasing, but those were improving with keeping walking speed by 71 days. It is demonstrated that the present system appears useful for quantitative evaluation of the efficacy for a long-term rehabilitation.

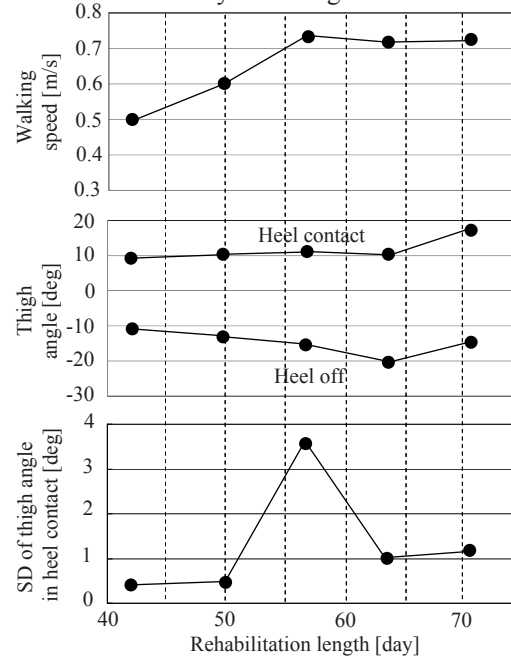


Fig. 3 Analytical results for a long-term rehabilitation

Fig. 4 shows typical recordings of the activity scenario, stick picture during sitting, and the thigh angle change and walking speed during walking in female subject with hemiplegia (84 yrs, paralyzed side: right), in 13 and 34 days after leaving the hospital. From these results, the subject was almost living with sitting and lying position. In 13 days after leaving the hospital, cyclic thigh angle change and walking speed were not detected, showing that the subject's gait was unstable. But, in 34 days, cyclic angle changes and stable speed-up and slowing-down in walking speed, were

detected. From stick pictures, detailed posture in sitting position could be evaluated, indicating that the system appears useful for evaluating activities during daily living and the efficacy of home visiting rehabilitation.

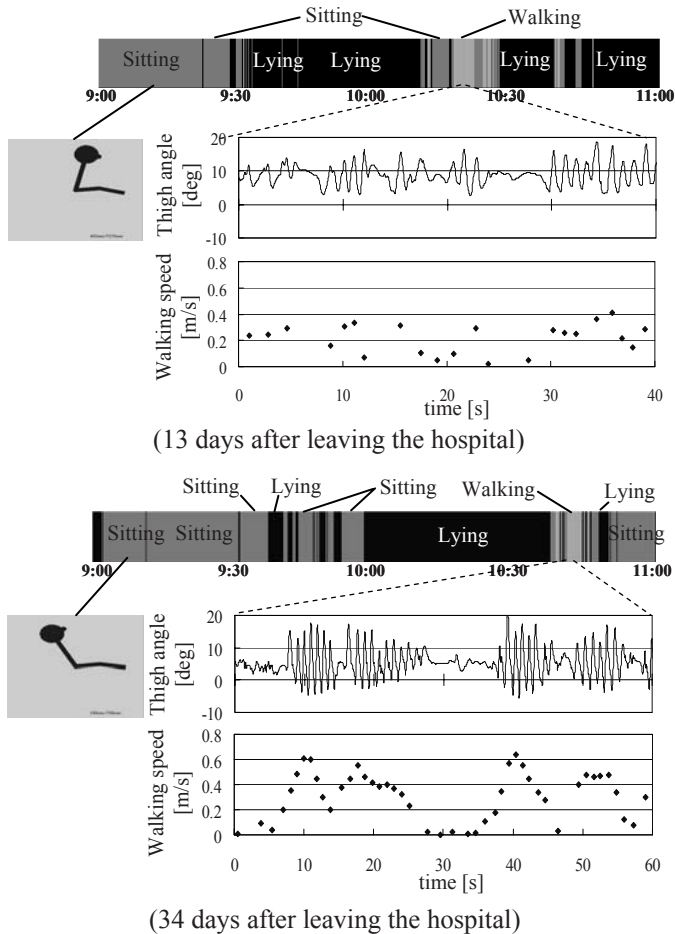


Fig. 4 Typical recordings of the activity scenarios and the thigh angle change and walking speed during walking in daily living at patient's home

V. CONCLUSIONS

In this study, we have developed a new monitoring system which can display motion pictures as well as detailed angle changes of the trunk, thigh and calf. By evaluation on 6 patients with hemiplegia, the patients' motions were successfully monitored not only in rehabilitation center, but also during daily living. These results clearly demonstrated that the present system could detect detailed motion characteristics, indicating that the system appears useful for evaluating the efficacy of rehabilitation using quantitative data. Further investigations will be needed through measurements for a longer period of time in many patients.

ACKNOWLEDGMENT

This research was funded in part by Grants-in-Aid for Scientific Research (No. 19700469), Ministry of Education, Culture, Sports, Science & Technology. For this, we express our appreciation.

REFERENCES

1. A. Hendry, W. Gilchrist G. Duncan, A. L. Evans and D. C. Smith (1990) Measurement of walking speed in elderly inpatients. *Med. Biol. Eng. Comput.*, vol. 28(6), pp. 602-604
2. R. E. Mayagoitia, J.C. Lotters, P. H. Veltink and H. Hermens (2002) Standing balance evaluation using a triaxial accelerometer. *Gait and Posture*, vol. 16, pp. 55-59
3. M. Sekine, T. Tamura, M. Akay, T. Fujimoto, T. Togawa and Y. Fukui (2002) Discrimination of walking patterns using wavelet-based fractal analysis. *IEEE Trans. Rehab. Eng.*, vol. 10(3), pp. 188-196
4. M. Makikawa and H. Izumi (1995) Development of an ambulatory physical activity memory device and its application for the categorization of actions in daily life. In *Proc. Medinfo. '95*, pp. 747-750
5. B. Najafi, K. Aminian, A. Paraschiv-Ionescu, F. Loew, C.J. Bula and P. Robert (2003) Ambulatory system for human motion analysis using a kinematic sensor: Monitoring of daily physical activity in the elderly. *IEEE Trans. Biomed. Eng.*, vol. 50(6), pp. 711-723
6. S. Miyazaki (1997) Long-term unrestrained measurement of stride length and walking velocity utilizing a piezoelectric gyroscope. *IEEE Trans. Biomed. Eng.*, vol. 44(8), pp. 753-759
7. R. Williamson and B.J. Andrews (2001) Detecting absolute human knee angle and angular velocity using accelerometers and rate gyroscopes. *Med. Biol. Eng. Comput.*, vol. 39, pp. 1-9
8. H. Dejnabadi, B. M. Jolles, E. Casanova, P. Fua and K. Aminian (2006) Estimation and visualization of sagittal kinematics of lower limbs orientation using body-fixed sensors. *IEEE Trans. Biomed. Eng.*, vol. 53(7), pp. 1385-1393
9. S. Tanaka, K. Yamakoshi and P. Rolfe (1994) New portable instrument for long-term ambulatory monitoring of posture change using miniature electro-magnetic inclinometers. *Med. & Biol. Eng. & Comput.*, vol. 32, pp. 357-360
10. K. Motoi, S. Tanaka, M. Nogawa and K. Yamakoshi (2003) Evaluation of a new sensor system for ambulatory monitoring of human posture and walking speed using accelerometers and gyroscope. *SICE Annual Conference 2003 Proceedings*, pp. 563-566
11. K. Motoi, Y. Higashi, Y. Kuwae, T. Yuji, S. Tanaka and Y. Yamakoshi (2005) Development of a wearable device capable of monitoring human activity for use in rehabilitation and certification of eligibility for long-term care. *Proceedings of the IEEE Engineering in Medicine and Biology 27th Annual Conference Shanghai*, CD-ROM
12. K. Motoi, K. Ikeda, Y. Kuwae, T. Yuji, Y. Higashi, M. Nogawa, S. Tanaka and Y. Yamakoshi (2006) Development of an ambulatory device for monitoring posture change and walking speed for use in rehabilitation. *Proceedings of the 28th Annual Conference of the IEEE Engineering in Medicine and Biology Society*, CD-ROM
13. K. Motoi, S. Tanaka, Y. Kuwae, T. Yuji, Y. Higashi, T. Fujimoto and K. Yamakoshi (2007) Evaluation of a Wearable Sensor System Monitoring Posture Changes and Activities for Use in Rehabilitation. *Journal of Robotics and Mechatronics*, vol. 19(6), pp. 656-666

Kosuke Motoi (motoi566@staff.kanazawa-u.ac.jp)
Kanazawa University (Kakuma-machi, Kanazawa, 920-1192, Japan)

An Improved Method for Dipole Modeling in EEG-Based Source Localization

Fredrik Edelvik^{#1}, Björn Andersson^{#2}, Stefan Jakobsson^{#3}, Stig Larsson^{°4},
Mikael Persson^{*5}, Yazdan Shirvany^{*6}

*#Fraunhofer-Chalmers Research Centre, Chalmers Science Park
SE-412 88 Göteborg, Sweden*

{¹fredrik.edelvik,²bjorn.andersson,³stefan.jakobsson}@fcc.chalmers.se

*°Department of Mathematical Sciences, Chalmers University of Technology
SE-412 96 Göteborg, Sweden*

**Department of Signals and Systems, Chalmers University of Technology
SE-412 96 Göteborg, Sweden*

{⁴stig,⁵mikael.persson,⁶yazdan.shirvany}@chalmers.se

Abstract— The inverse problem in EEG-based source localization is to determine the location of the brain sources that are responsible for the measured potentials at the scalp electrodes. The brain sources are usually modeled as current dipoles which lead to a singularity in the right-hand side of the governing Poisson's equation. Subtraction methods have been proposed as a remedy and in this paper an improved subtraction method for modeling the dipoles is presented. The accuracy is demonstrated for radial and tangential sources in layered sphere models and is to the best of the authors' knowledge superior to previous methods for superficial sources. An additional advantage is that it produces a right hand side with few non-zeros which is beneficial for efficient solution of the inverse problem.

Keywords— epilepsy; EEG; finite element method; source reconstruction

Introduction

Epilepsy is one of the most common neurological diseases and about 0.5 to 1% of the population suffers from it. Surgical therapy has become an important therapeutic alternative for patients with medically intractable epilepsy. Correct and anatomically precise localization of the epileptic focus is mandatory to decide if resection of brain tissue is possible.

The most important non-invasive diagnosis tool used at epilepsy surgery centers is electroencephalography (EEG). To find the brain sources, which are usually modeled as current dipoles, that are responsible for the measured potentials at the EEG electrodes on the scalp is an inverse problem. Inverse problems are in general more difficult to solve than direct problems mainly due to ill-posedness and non-linearity. In this case the data is perturbed by noise and the potentials measured on the scalp surface do not uniquely determine the location of the dipoles as many different dipole configurations can generate the same distribution of potentials on the scalp.

Methods for solving the inverse problem in EEG-based source localization are based on solutions of the corresponding forward problem, i.e. simulation of the potentials on the

scalp for a given source. The associated differential equations are the quasi-static Maxwell equations, which reduce to a Poisson equation. The sources are electrolytic currents, usually modeled as point dipoles, which are activated during epilepsy. The dipoles introduce singularities in the right-hand side of the Poisson equation that need to be treated.

A major limitation in EEG-based source reconstruction has been the poor spatial accuracy, which is attributed to low resolution of previous EEG systems and to the use of simplified spherical head models for solving the inverse problem. EEG-based source localization is an active field of research[1, 2], but partly due to the mentioned shortcomings the computational techniques are not yet part of the standard pre-surgical diagnostic workup.

Realistic models of the human head are geometrically complex and the tissue conductivity is highly inhomogeneous and even anisotropic, which makes finite element methods (FEM) well suited. The critical issue is how to handle the computational complexity of FEM with regard to the inverse problem. As has been shown in recent publications by Wolters et al.[3, 4] this can be accomplished through the use of algebraic multigrid preconditioners, parallel computing, and not the least the concept of reciprocity which makes it possible to solve the forward problem for each electrode position rather than for each possible dipole position. A so-called lead field matrix can be computed during the preprocessing. The repeated solution of the forward problem in the iterative process is then efficiently accomplished by multiplication of the lead field matrix by the estimated source to produce the electrode potentials.

Source localization is heavily dependent on the choice of dipole model and several different alternatives have been suggested in the literature. According to the survey article[5], the subtraction method[6] is the most accurate. In this paper we present an improved subtraction method that reduces the non-zeros in the right-hand side (RHS) vector and in addition

produces the same non-zero structure of the vector regardless of dipole position. This implies that only part of the lead field matrix needs to be stored and the solution of the inverse problem will therefore be much faster.

Methods

The characteristic frequencies of the signals in the kHz range and below make the capacitive and inductive effects of the tissue negligible. Therefore, the quasi-static approximation of Maxwell's equations for the potential Φ can be used.

If we denote the domain of interest as Ω (with boundary $\partial\Omega$) and let the tissue conductivity be σ , we have Poisson's equation

$$\nabla \cdot (\sigma \nabla \Phi) = \nabla \cdot \mathbf{j}^s \text{ in } \Omega, \quad (1)$$

subject to the conditions

$$\hat{\mathbf{n}} \cdot (\sigma \nabla \Phi) = 0 \text{ on } \partial\Omega, \quad (2a)$$

$$\Phi(\mathbf{x}_{\text{ref}}) = 0. \quad (2b)$$

The source current \mathbf{j}^s is modeled by a mathematical dipole at position $\mathbf{x}_0 \in \Omega$ with the moment $\mathbf{M} \in \mathbf{R}^3$,

$$\mathbf{j}^s(\mathbf{x}) = \mathbf{M} \delta(\mathbf{x} - \mathbf{x}_0). \quad (3)$$

The source has a singularity at \mathbf{x}_0 and is therefore difficult to model with standard finite elements. A subtraction method[6] is used to circumvent this problem, where the total potential is split into two parts,

$$\Phi = \Phi^\infty + \Phi^{\text{corr}}. \quad (4)$$

The first part, Φ^∞ , is the solution to Eq. (1) in an unbounded domain with constant conductivity σ^∞ ,

$$\Delta \Phi^\infty = \frac{\nabla \cdot \mathbf{j}^s}{\sigma^\infty}. \quad (5)$$

The solution can in this case be formed analytically as

$$\Phi^\infty(\mathbf{x}) = \frac{1}{4\pi\sigma^\infty} \frac{\mathbf{M} \cdot (\mathbf{x} - \mathbf{x}_0)}{|\mathbf{x} - \mathbf{x}_0|^3}. \quad (6)$$

An equation for Φ^{corr} can now be formed by subtracting Eq. (5) from (1),

$$-\nabla \cdot (\sigma \nabla \Phi^{\text{corr}}) = \nabla \cdot ((\sigma - \sigma^\infty) \nabla \Phi^\infty) \text{ in } \Omega, \quad (7)$$

subject to the conditions

$$\hat{\mathbf{n}} \cdot (\sigma \nabla \Phi^{\text{corr}}) = -\hat{\mathbf{n}} \cdot (\sigma \nabla \Phi^\infty) \text{ on } \partial\Omega, \quad (8a)$$

$$\Phi(\mathbf{x}_{\text{ref}}) = 0. \quad (8b)$$

This approach to the problem ensures that the RHS of Eq. (7) is non-singular in the case where σ is constant in a small ball around \mathbf{x}_0 [4]. The original RHS of Eq. (1) has support only at $\mathbf{x} = \mathbf{x}_0$, whereas the RHS of Eq. (7) has support where $\nabla\sigma \neq \mathbf{0}$. To obtain a more compact support Ω is divided into two subdomains

$$\Omega = \Omega^c \cup \Omega^t, \quad (9)$$

where Ω^c is the region with constant σ^∞ containing the source. See Fig. 1 for a schematic view in two dimensions. In this region the correction potential is solved for as described above, and in Ω^t the whole solution is sought at once. Using Eqs. (7) and (1) the new formulation reads,

$$-\nabla \cdot (\sigma^\infty \nabla \Phi^c) = 0 \text{ in } \Omega^c, \quad (10a)$$

$$-\nabla \cdot (\sigma \nabla \Phi^t) = 0 \text{ in } \Omega^t, \quad (10b)$$

subject to the conditions

$$\Phi^c + \Phi^\infty = \Phi^t \text{ on } \partial\Omega^c, \quad (11a)$$

$$\hat{\mathbf{n}}^c \cdot (\sigma^\infty \nabla (\Phi^c + \Phi^\infty)) = \hat{\mathbf{n}}^c \cdot (\sigma \nabla \Phi^t) \text{ on } \partial\Omega^c, \quad (11b)$$

$$\hat{\mathbf{n}}^t \cdot (\sigma \nabla \Phi^t) = 0 \text{ on } \partial\Omega^t, \quad (11c)$$

$$\Phi(\mathbf{x}_{\text{ref}}) = 0. \quad (11d)$$

In this formulation the support is only in $\partial\Omega^c$, which can greatly improve efficiency when solving the forward problem multiple times.

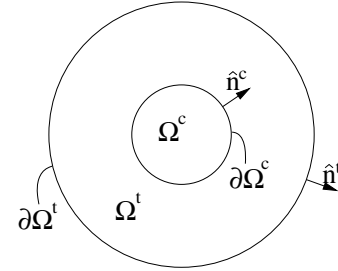


Figure 1: Schematic view of a two layer model.

The discretization of Eq. (10) performed by the piecewise linear FEM with basis functions φ_i centered at the mesh points ξ_i . The solution to this equation, as well as Φ^∞ , is represented in the FE space as

$$\Phi^\infty \approx \sum_{\xi_i \in \Omega^c} u_i^\infty \varphi_i(\mathbf{x}), \quad (12a)$$

$$\Phi^t \approx \sum_{\xi_i \in \Omega^t} u_i^t \varphi_i(\mathbf{x}), \quad (12b)$$

$$\Phi^c \approx \sum_{\xi_i \in \Omega^c \wedge \xi_i \notin \partial\Omega^c} u_i^c \varphi_i(\mathbf{x}) + \sum_{\xi_i \in \partial\Omega^c} (u_i^t - u_i^\infty) \varphi_i(\mathbf{x}). \quad (12c)$$

After applying variational and FEM techniques to Eqs. (10) and (11) we arrive at the system of linear equations

$$\mathbf{K}\mathbf{u} = \mathbf{j}, \quad (13)$$

where \mathbf{u} contains the nodal degrees of freedom in both domains, Ω^c and Ω^t . The stiffness matrix has the entries

$$K_{i,j} = \iiint_{\Omega} (\sigma \nabla \varphi_i) \cdot \nabla \varphi_j \, dV. \quad (14)$$

The vector \mathbf{j} has contributions from Eqs. (11a) and (11b)

$$\mathbf{j} = \mathbf{j}_D + \mathbf{j}_N. \quad (15)$$

The first part can be written as

$$\mathbf{j}_D = \mathbf{K}_D \mathbf{u}^\infty, \quad (16)$$

where the entries in \mathbf{K}_D are given by

$$K_{D,i,j} = \iiint_{\Omega} (\sigma^\infty \nabla \varphi_i) \cdot \nabla \varphi_j \, dV, \quad \xi_i \in \Omega^c \wedge \xi_i \notin \partial\Omega^c, \xi_j \in \partial\Omega^c. \quad (17)$$

The entries in the vector \mathbf{j}_N are given by

$$j_{N_i} = \iint_{\partial\Omega^c} \varphi_i \hat{\mathbf{n}} \cdot (\sigma^\infty \nabla \Phi^\infty) \, dS. \quad (18)$$

The total potential in Ω can then be computed by means of Eq. (4).

As a comparison, if the standard subtraction method[6] is used to discretize Eqs. (7) and (8) on a multilayer isotropic sphere with different conductivity in each layer, the RHS vector would consist of contributions of the type

$$j_i = \iint_{S_k} \varphi_i \hat{\mathbf{n}} \cdot ((\sigma^{k+1} - \sigma^k) \nabla \Phi^\infty) \, dS, \quad (19)$$

for each interface k .

The system of linear equations, Eq. (13), can be efficiently solved iteratively by a conjugate gradient (CG) solver preconditioned by an algebraic multigrid (AMG) method.

Results

The model used for the head is a four layer sphere which has been used in several studies [5]. The parameters are defined in Table 1. The validation and comparison of the method was done by calculating the potential for dipoles with eccentricity from 0 to 97.4%, where the eccentricity of the dipole

is defined as the ratio between the distance from the center of the sphere to the source divided by the radius of the brain compartment, 78mm. Comparisons are made for dipoles directed in the two principal directions, normal and tangential to the surface. Finally, calculations were performed on two tetrahedral meshes of different resolution.

Table 1: Parameterization of the four layer sphere model

	Brain	CSF	Skull	Scalp
Outer shell radius [mm]	78	80	86	92
Conductivity [S/m]	0.33	1.0	0.0042	0.33

The errors are calculated by comparing the solutions to the potential given by an analytic solution[7] at each surface node. The *maximum relative error*, the *relative error*, the *relative difference measure*, and the *magnification factor*, are defined as

$$e_{\max} = \max_i |u_i^a - u_i^n| / \max_i |u_i^a|, \quad (20a)$$

$$e_{\text{RE}} = \frac{\|\mathbf{u}^a - \mathbf{u}^n\|_2}{\|\mathbf{u}^a\|_2}, \quad (20b)$$

$$e_{\text{RDM}} = \sqrt{\sum_i \left(\frac{u_i^a}{\|\mathbf{u}^a\|_2} - \frac{u_i^n}{\|\mathbf{u}^n\|_2} \right)^2}, \quad (20c)$$

$$e_{\text{MAG}} = \frac{\|\mathbf{u}^n\|_2}{\|\mathbf{u}^a\|_2}, \quad (20d)$$

where u_i^a is the value of the analytical solution at surface node i , u_i^n is the corresponding value of the numerical solution. $\|\cdot\|_2$ denotes the Euclidean norm.

To benchmark the method proposed in this paper we compare with the state-of-the-art method in the literature[6] according to the survey article[5]. The errors are shown in Fig. 2 where the two methods are compared on two meshes of different resolution. The upper subfigure shows the result for radial dipoles and the lower the result for tangential dipoles. The newly developed method shows significantly better results for dipoles placed close to the surface of the inner layer. For the coarser mesh the ratio of the RDM error between the two solution methods at eccentricity 97.4% is 5.3 for both radial and tangential dipoles. The corresponding ratios for the finer mesh are 3.3, and 2.6, respectively. The largest improvement is indicated in the relative maximum error. On the coarser mesh the ratio of the errors are 22 and 25 for radial and tangential dipoles, respectively. The corresponding values for the finer mesh are 14 and 13, respectively.

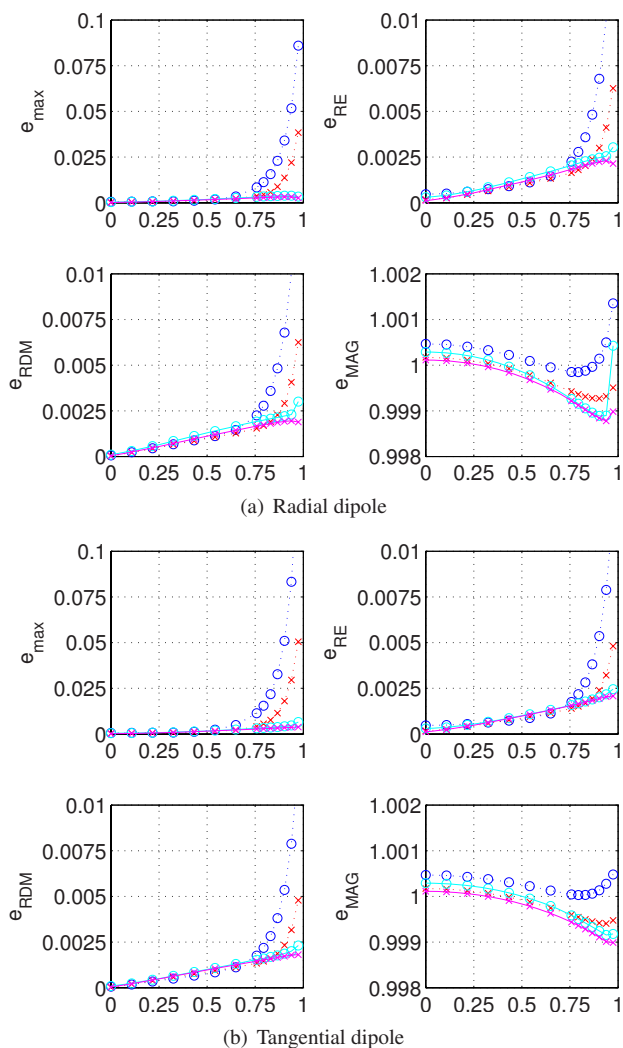


Figure 2: Error as a function of eccentricity. Full lines: method presented here, dotted lines: subtraction method from [6]. \circ markers: mesh with 233k nodes, \times marker: mesh with 991k nodes.

Conclusions

In this paper we have presented an improved method for modeling the dipole in source localization. The proposed method has been shown to be more accurate than the state-of-the-art method in the literature. Additional advantages are that the RHS has fewer non-zeros and the same non-zero structure regardless of dipole position something which in contrast to earlier approaches also holds for anisotropic tissue. This fact will be very beneficial for efficient solution of

the inverse problem. Future work will include development of methods for solving the inverse problem and application to source localization with realistic head models generated from a segmentation of the patient's MRI.

Acknowledgement

This work was supported in part by the Swedish Foundation for Strategic Research (SSF) through the Gothenburg Mathematical Modeling Centre (GMMC).

References

- [1] H. Hallez, B. Vanrumste, R. Grech, J. Muscat, W. De Clercq, A. Vergult, Y. D'Asseler, K. P. Camilleri, S. G. Fabri, S. Van Huffel, and I. Lemahieu. Review on solving the forward problem in EEG source analysis. *Neuroengineering and Rehabilitation*, 46(4), 2007.
- [2] C. M. Michel, M. M. Murray, G. Lantz, S. Gonzalez, L. Spinelli, and R. Grave de Peralta. EEG source imaging. *Clinical Neurophysiology*, 115(10):2195–2222, 2004.
- [3] C. H. Wolters, M. Kuhn, A. Anwander, and Reitzinger S. A parallel algebraic multigrid solver for finite element method based source localization in the human brain. *Computing and Visualization in Science*, 5(3), 2002.
- [4] C. H. Wolters, H. Köstler, C. Härdtlein J. Möller, L. Grasedyck, and W. Hackbusch. Numerical mathematics of the subtraction method for the construction of a current dipole in EEG source reconstruction using finite element head models. *SIAM J. Scientific Computing*, 30(1):24–45, 2007.
- [5] P. H. Schimpf, C. Ramon, and J. Haueisen. Dipole models for the EEG and MEG. *IEEE Trans. Biomedical Engineering*, 49(5):409–418, May 2002.
- [6] S. van den Broeh, H. Zhou, and M. Peters. Computation of neuromagnetic fields using finite-element method and Biot-Savart law. *Medical and Biological Engineering and Computing*, 34(1):21–26, 1996.
- [7] M. Sun. An efficient algorithm for computing multi-shell spherical volume conductor models in EEG dipole source localization. *IEEE Trans. Biomedical Engineering*, 44(12):1243–1252, Dec. 1997.

Machines to support motor rehabilitation after stroke

Hesse S, Werner C

Medical Park Berlin Humboldtmühle/Charité University Hospital, Department of Neurological Rehabilitation, Berlin

Correspondence: Stefan Hesse, MD, Medical Park Berlin Humboldtmühle, An der Mühle 2-7, 13507 Berlin, Germany, email:s.hesse@medicalpark.de

Abstract

Following the introduction of treadmill training with partial body weight support, our group designed and developed an electromechanical gait trainer (GT) based on movable footplates to relieve the strenuous effort of the therapists, and to intensify the patient's gait training. Results of a multicentre trial of 155 acute stroke patients showed its effectiveness in promoting gait ability and competence in activities of daily living (ADL). The "HapticWalker" was the next step, a robotic walking simulator with freely programmable footplates, so that patients could, for example, additionally train stair climbing and perturbations.

For the severely affected upper extremity, the computerized arm trainer "Bi-Manu-Track" enabled the bilateral practice of a forearm pronation/supination and wrist flexion/extension. Compared to an electrical stimulation of the paretic wrist extensors, acute stroke patients with a severe arm paresis (n=44) gained significantly more upper limb muscle strength and control. The REHA-Slide is a purely mechanical device to train the shoulder, elbow and wrist joints bilaterally. The REHA-Slide was in a RCT compared to EMG-triggered electrical stimulation. Patient who trained with the REHA-Slide were able to transport more cubes in the Box and Block test than the control group.

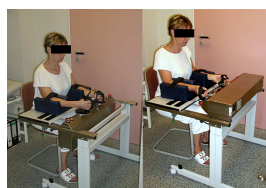
Introduction

Stroke is the leading cause of impairment and disability in the industrialised world. The restoration of gait and arm hand function is crucial for the aspired social and vocational integration. Modern treatment concepts favour a task-specific treatment approach, i.e. "who wants to regain walking has to walk". But an intensive treatment of the upper and lower extremities after stroke collides with the effort for the therapists, e.g. when placing the paretic limb, and general budget constrains. Intelligent machines may offer a solution to this problem, relieving the strenuous effort for the therapists and providing numerous repetitions of a well defined movement cycle. The present article gives an overview of machines designed by our group for this purpose.

Upper extremity

Bi-Manu-Track

The "Bi-Manu-Track" (Fig. 1) is a 2x1DOF robot enabling hemiparetic patients the bilateral practice of two different movement cycles: forearm pronation/supination and a wrist flexion/extension (1), (Fig.1).



Three different control modes are possible: passive – passive, active – passive (the non-affected drives the affected extremity), and active – active (the affected one has to overcome an initial isometric resistance). Amplitude, speed, and resistances can be set individually.

The assumptions made about underlying mechanisms that influenced our design were that (a) the bilateral approach would facilitate the paretic side via intercallosal fibres (2), (b) that the more distal movements have a larger cortical representation of the hand and fingers, and (c) that proximal upper limb segments, if trained, would compete with distal upper limb segments for plastic brain territory (3). The latter advocates starting the treatment distally, as a preferential proximal treatment approach might even impede the restoration of the paretic hand and fingers.

Open clinical studies in severely affected chronic patients could document a muscle tone reduction for the wrist and finger joints and a minor improvement in motor functions without clinical relevance following four weeks of daily training (4). The number of repetitions had to be restricted (800 per session evenly distributed on the four movement directions), otherwise wrist pain and a swollen could have been elicited. Shoulder pain was not a problem.

A subsequent randomized trial of two centers included 44 acute stroke victims, whose first stroke was 4 to 8 weeks before study onset (5). All of them were severely affected with an initial Fugl-Meyer Motor score (FM, 0-66) of less than 18, and had no volitional activity of the wrist and finger extensors. For six weeks, the randomly assigned patients practiced either with the robot or the electrical stimulation of the paretic wrist extensors. The FM was the primary outcome parameter, blindly assessed with the help of a standardized video. Both groups were initially homogenous regarding clinical data. Over time both groups improved their upper limb motor control and power significantly, the between group comparison revealed a superior result in the robot trained group both at study end and at follow-up three months later. The muscle tone did not change, side effects did not occur. Interestingly, the proximal (0-42) and distal (0-24) FM sub-score improved evenly in the robot trained group, i.e. the treatment effect was generalized.

REHA-Slide

With the help of this mechanic device stroke victims can train three bilateral movement cycles: elbow extension/flexion, shoulder abduction/adduction and wrist flexion/extension, either isolated or in combination. The patient grasps two handles (either actively or with help of a Velcro), so the movement of the non-affected side guides the affected hand and arm. An optional extension is the integration of a cordless computer mouse, which can be attached to the REHA-Slide middle bar. Then the 2DOF translatory motion of the user driven bar: forward/backward and sideward (left/right) is transmitted to the attached mouse. The mouse movement can be visualized via any computer game in order to incorporate visual biofeedback into therapy. The initial clinical case studies revealed a significant muscle tone reduction and improvement of upper limb motor control, even in chronic patients, confirming previous reports about the application of the similar custom-made device named BATRAC (**B**ilateral **A**rm **T**raining with **R**hythmic **A**uditory **C**ueing).(6). The REHA-Slide was in a RCT compared to EMG-triggered electrical stimulation. Patient who trained with the REHA-Slide were able to transport more cubes in the Box and Block test than the control group.(7)

Lower extremity

Gait machines are designed to relieve the physiotherapists, e.g. when assisting the paretic limbs or controlling the weight shift manually on the treadmill or on the floor, as well as to intensify patient gait training. So far two different types of machine design have been realized for clinical purposes, (a) a treadmill with a driven gait orthosis (12, 13) or (b) a moving footplate system.

Gait Trainer GT I

The electromechanical gait trainer GT I (Fig. 2) is based on the moving footplate approach (8).

On this machine, the harness-secured patient is positioned on two foot plates, whose movements simulate stance and swing at a fixed ratio of 60% to 40% with the help of a sun gear system. The cadence and step length (ranging from 28 to 48 cm) can be set individually.

A multi-center trial (DEGAS, **DE**utsche **GA**ngtrainer-Studie) included 155 acute, non-ambulatory stroke patients.(9) Following random group allocation, the patients either practiced 20 min GT I + 25 min physiotherapy (PT) (group A; experimental group) or 45 min PT (group B; control group) every workday for four weeks, i.e. a total of 20 sessions. The PT in both groups concentrated on the repetitive gait training on the floor and on the stairs. Both groups were homogeneous regarding the clinical data at study onset. Patients of group A scored significantly higher at the end of the study and at follow-up with respect to both gait ability and Barthel Index. At study end, 41 of 77 (53.2%) in group A vs. 17 of 77 (22.1%) in group B could walk independently, i.e. they had reached an FAC level of either 4 or 5. Experimental group patients practiced 800 to 1,200 steps each session on the machine, while control group patients rarely exceeded 200 steps during their individual 45-min PT sessions.



HapticWalker

The HapticWalker is the latest development for gait rehabilitation by our group (10).

The device is a robotic walking simulator for gait rehabilitation based on the principle of programmable footplates, i.e. it continues the successfully applied approach of movable footplates and allowing patient physiotherapist interaction during training. The machine comprises the following main advantages compared to the GT I: (a) the footplate trajectories are freely programmable, hence patient training is no longer restricted to walking on plane ground, arbitrary foot trajectories, for instance, walking up/down stairs can also be trained, (b) the foot trajectory motion profiles are based on measured free walking foot motion data at normal walking speeds, which can be fully adjusted to individual patients' needs, (c) there are 6DOF force/torque sensors under each footplate, whose readings are the basis for different types of force/compliance control, in addition they are used for diagnostic purposes during the stance (= ground reaction force) and swing phase, (d) motion generation algorithms for different types of artificial foot motions are implemented as well: perturbations such as stumbling or sliding during gait training.

The first HapticWalker prototype was successfully completed and tested with healthy subjects and was approved by the German technical inspectorate for medical devices (TÜV). Clinical trials with hemiparetic subjects are underway. Dynamic EMG revealed a similar activation of lower limb muscles during real and simulated stair climbing up and down stairs in hemiparetic patients.

Lessons learned

Machines open new dimensions in motor rehabilitation after stroke. To promote this new field, more randomized clinical studies are mandatory. In the studies presented here, machines were always used as a supplementary tool to assist the therapist and enable more intensive practice, thereby improving treatment. These studies were also in line with modern concepts of motor rehabilitation of stroke patients. It should be emphasized that no machine can ever substitute the “human touch” of an experienced therapist. We look forward to the future development of this exciting new field of rehabilitation.

References

1. Hesse S, Schulte-Tigges G, Konrad M, Bardeleben A, Werner C. Robot-assisted arm trainer for the passive and active practice of bilateral forearm and wrist movements in hemiparetic subjects. *Arch Phys Med Rehabil* 2003;84:915-20.
2. Förster O, Buhnke O. *Handbuch der Neurologie*, Band 6. Berlin: Springer-Verlag, 1936.
3. Muelbacher W, Richards C, Ziermann U, Wittenberg G, Weltz D, Boroojerdi B, Cohen L, Hallett M. Improving hand function in chronic stroke. *Arch Neurol* 2002;59:1278-82.
4. Hesse S, Schulte-Tigges G, Konrad M, Bardeleben A, Werner C. Robot-assisted arm trainer for the passive and active practice of bilateral forearm and wrist movements in hemiparetic subjects. *Arch Phys Med Rehabil* 2003;84:915-920.
5. Hesse S, Werner C, Pohl M, Rückriem S, Mehrholz. Computerized arm training improves the motor control of the severely affected arm after stroke: a single-blinded randomized trial in two centers. *Stroke* 2005, in press.
6. Whittall J, McCombe Waller S, Silver KHC, Macko RF. Repetitive bilateral arm training with rhythmic auditory cueing improves motor function in chronic hemiparetic stroke. *Stroke* 2000;31:2390-96.
7. Hesse S, Werner C, Pohl M, Mehrholz J, Puzich U, Krebs HI. Mechanical arm trainer for the treatment of severely affected arm after stroke: a single-blinded randomized trial in two centres. *Am J Phys Med Rehabil* 2008;87:779-788.
8. Hesse S, Sarkodie-Gyan T, Uhlenbrock D. Development of an advanced mechanized gait trainer, controlling the movement of the centre of mass, for restoring gait in non-ambulant subjects. *Biomed Tech* 1999;44:194-201.
9. Pohl M, Werner C, Holzgraefe M, Kroczeck G, Mehrholz J, Wingendorf I, Hölig G, Koch R, Hesse S. Repetitive locomotor training and physiotherapy improve walking and basic activities of daily living after stroke: a single-blind, randomised multi-centre trial (Deutsche Gangtrainerstudie, DEGAS). *Clinical Rehabilitation* 2007;1:17:27.
10. Schmidt H, Sorowka D, Hesse S, Bernhardt R. Development of a robotic walking simulator for gait rehabilitation. *Biomed Tech* 2003;48:281-86.

FEM-based investigation of spatial stimulation properties of a multi-electrode probe with micrometer-size electrodes for cortical and DBS applications

W. Eberle¹, A. S. Mecheri^{1,2}, S. Musa^{1,3}, G. Gielen², G. Borghs^{1,3}, and C. Bartic^{1,3}

¹ IMEC, Bioelectronic Systems Group, Kapeldreef 75, B-3001 Leuven, Belgium

² MICAS, Department of Electrical Engineering, KU Leuven, B-3001 Leuven, Belgium

³ Department of Physics and Astronomy, KU Leuven, B-3001 Leuven, Belgium

Contact: wolfgang.eberle@imec.be

Abstract— Deep-brain stimulation (DBS) probes in today’s clinical applications use four to six mm-size contacts to electrically influence the neuronal networking activity in a target brain area. While the treatment is successful for applications such as Parkinson’s disease and tremor, unwanted side effects are observed mainly originating from the non-selective stimulation of a large tissue volume around the electrodes. Micro-fabrication techniques allow a larger number of μm -size contacts which can be used for stimulation and recording enabling closed-loop operation. Starting from a set of fabricated and characterized probes with 10 electrode contacts, we investigate here the spatial stimulation properties for different electrode shapes and topologies in a layered tissue model using a finite-element modeling and simulation approach. Results indicate the potential of μm -size topologies to be used for spatial stimulation patterns.

Keywords— Neural probes, deep brain stimulation, spatial stimulation patterns, modeling.

I. INTRODUCTION

Deep brain stimulation (DBS) has been successfully used in clinical practice for movement disorders and is positively evaluated in other neurological disorders such as obsessive-compulsive disorders (OCD). State-of-the-art implants consist of quadripolar DBS probes (e.g. from Medtronic) and an external current pulse generator. Electrode contact size is in the mm-range (1.5 mm). Despite common use for above mentioned diseases, exact working principles of DBS are not fully resolved [1], partially due to the fact that exact models of probe, electrode-electrolyte interface, and tissue have not been available. A fundamental concern is the poor spatial selectivity due to the large and few electrode contacts which frequently trigger unwanted side effects resulting in emergence of other neurological conditions. Experimental and finite-element model (FEM) based simulations have been carried out mainly for the Medtronic type probes [2,3] or for cortical shank electrodes [4].

With the availability of modern micro-fabrication technologies, we propose the investigation of probes with more and smaller contact sizes in the μm -range. The reconfigura-

tion flexibility in such arrays can be used to create both spatial stimulation patterns as well as combine recording and stimulation functionality, allowing even recording down to single-neuron level such as shown for such 2D planar probes in first cortical recording experiments [5][8]. Note that our current application is in the rat model for novel target and therapy development.

In this paper, we explore the electrical potential distribution for several topologies of fabricated μm -contact size probes in brain tissue surroundings taking into account the peri-electrode space around the inserted probe in acute and chronic conditions. First, we describe how the electrode interface has been measured on manufactured probes. Next, we describe the FEM probe/tissue model. Finally, several topologies are analyzed in this setup regarding their spatial electrical potential distribution.

II. EXPERIMENTAL PROBE CHARACTERIZATION

A. Manufactured probes

Micro-fabrication of implantable, silicon-based single-shank neural probes conceived for both recording and stimulation purposes were reported in [5]. Multiple flavors of probes were fabricated, with dual-row (Fig. 1A), single-row (Fig. 1B), and C-shaped (Fig. 1C) electrode types and several electrode diameters (4, 10, 25, 50 μm). Both 200- μm and 100- μm thinned probes are available.

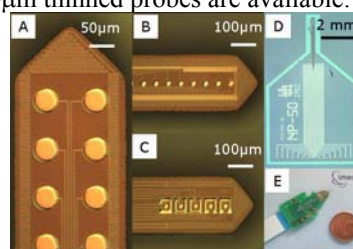


Fig. 1. Optical micrographs of probe tips with different electrode sizes and configurations: tip with electrodes of 50 μm diameter (A), of 25 μm diameter (B) and with C-shaped electrodes (C). Picture of the whole probe (D) and the packaged probe (E).

B. Probe characterization and model extraction

The small-signal behavior of a 50 μ m-diameter Pt electrode was determined with potential-scan electrochemical impedance spectroscopy (PS-EIS) at electrode voltages within the safe potential window for water electrolysis, i.e. between -0.6 and 1.1V versus a Ag/AgCl reference electrode. Measurements were performed in phosphate buffered saline solution (pH=7.4) with an additional Pt counter electrode. Care was taken to perform the EIS at steady-state conditions to prevent changes of the electrode state during measurements and thus obtain inconsistent data values. Therefore, the electrodes were pre-biased for 30 second at the desired potential and kept at this value during EIS.

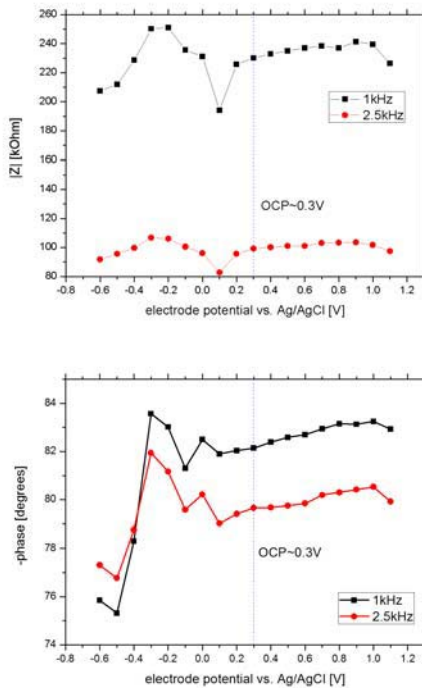
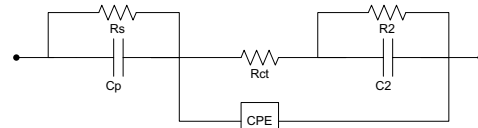


Fig. 2. Amplitude (top) and phase (bottom) diagrams from impedance measurements of a 50- μ m electrode show moderate amplitude and phase dependency on the open circuit potential (OCP) shown for relevant recording frequencies (1 kHz) and stimulation frequencies (2.5 kHz).

Measurement results reveal a safe stimulation voltage range for the electrodes between ± 0.6 V (± 1.0 V) relative to the OCP. For extraction of the potential-dependent small-signal parameters, data were fitted to an equivalent circuit-model (Fig. 3). ZPlot (ScribnerAssociates inc.) was used for fitting the data. The model consists of several parts: interconnect parasitics (R_s , C_p), constant-phase element ($Z_{CPE} = (1/Y)(j\omega)^{-\alpha}$), and charge-transfer path (R_{ct} with parasitic interface-related R_2 , C_2).



Parasitic R-C: $R_s = 4690 \pm 57$ k Ω , $C_p = 135 \pm 4$ pF
 Non-CPE: $R_{ct} = 215 \pm 23$ k Ω , $R_2 = 2.7 \pm 0.2$ G Ω , $C_2 = 78 \pm 4$ pF
 CPE: $Y = 1.1 \pm 0.006$ nF, $\alpha = 0.93 \pm 0.0006$

Fig. 3. 1-port equivalent circuit topology for a single 50- μ m electrode representing the electrode-electrolyte interface (R_{ct} , R_2 , C_2 , CPE) and the parasitic interconnect network (R_s , C_p) with values obtained from fitting of electrode measurements at OCP = 0.3V.

The resulting transfer function (Fig. 4) is used to extract the frequency-dependent electrode impedance for the stimulation waveform. Note that the non-CPE path mainly shapes the phase response while Fig. 4 shows that it has negligible influence on the absolute impedance as the two overlapping curves (o) curves indicate. For the impedance at 1 kHz and the bounds of ± 0.6 V, a maximum current density of $2 \cdot 10^3$ A/m² is derived which is applied to all further experiments.

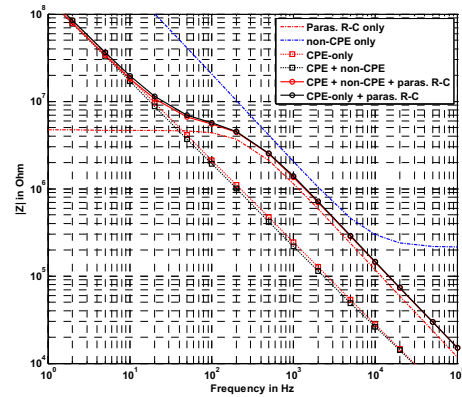


Fig. 4. The absolute impedance $|Z|$ of a 50- μ m electrode is dominated by the CPE element below 100 Hz and shaped by the parasitic R-C network for higher frequencies. 150 kOhm (1 kHz, recording) and 60 kOhm (2.5 kHz, stimulation) are observed at relevant frequencies.

III. FINITE-ELEMENT MODELING OF PROBE AND TISSUE

A 2.5D axial-symmetric cross-section model of the probe is embedded in a surrounding tissue model in the finite-element modeling software COMSOL 3.4 (Fig. 5).

A. Model setup

For the probe substrate, Si with 1- μ m Parylene C coating with an average conductivity $\sigma = 10^{-14}$ S/m is used. Dimensions of the probe, the tissue surroundings, and the three electrode topology types are described in Fig. 6.

We assume a peri-electrode space (PES) around the probe due to insertion [3] which is estimated to about 10-20% of the probe thickness on each side. Tissue parameters from [6] were used for the conductivity of brain tissue. We also model the distinction between acute condition where the PES is filled by extracellular fluid (ECF) and chronic condition where the ECF is replaced by giant cell growth resulting in scar tissue formation [3].

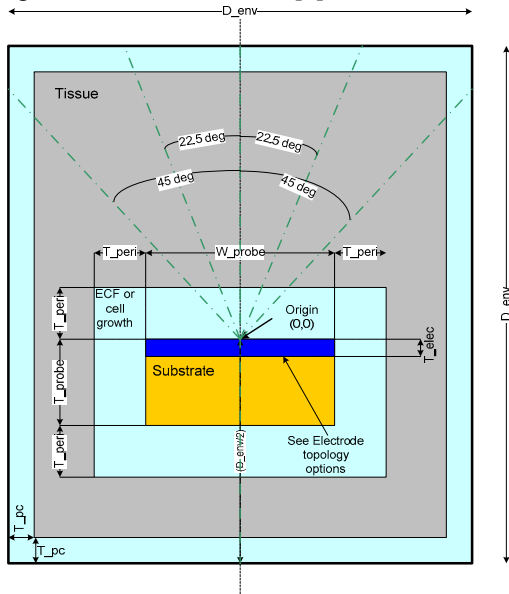


Fig. 5. The model encapsulates a substrate with several electrode topologies on top inside a first encapsulation layer (ECF or scar tissue by cell growth), a second tissue encapsulation layer, and an outer ECF layer. The origin (0,0) for all graphs lies symmetrically in the electrode surface plane.

Tissue	
D_{env}	5 mm
T_{pc}	100 μm
T_{peri}	{1,10,40} μm
Substrate	
T_{probe}	{100,200} μm
W_{probe}	200 μm
Electrodes	
T_{elec}	200 nm
W_{se}	50 μm
W_{de}	50 μm
D_{de}	{50,100} μm
W_{teo}	15 μm
W_{tei}	20 μm
D_{te}	5 μm

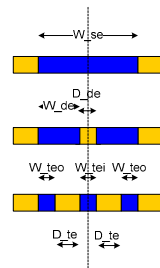


Fig. 6. Model parameters including options to compare (left) and cross-section through three electrode types (right): single electrode (se), two electrodes (de), ring (= approximated C-shaped) electrode (te).

B. Simulation conditions and post-processing

Quasi-DC simulations are carried out with the external ECF boundary set to ground and varying boundary conditions for the electrode topologies: current source (+/-) or grounded. Simulation results are scaled according to the safe current density limits as obtained from measurements

are applied resulting in electrode area-dependent maximum injection currents. Note that for temporal waveform investigation (not considered here) transfer function phase dependency on frequency must be included.

The electrical potential is evaluated along the 0, +/- 22.5, and 45 degree lines (Fig. 5) for which a minimum mesh resolution of (5 mm/10000 pts = 0.5 μm) is chosen.

All topologies have been collected in a modular, parametrized script-based model to automate batch simulation and result extraction. Data post-processing is performed in MATLAB 7. Simulation times are in the sub-minute range per topology.

IV. RESULTS AND DISCUSSION

A. Impact of probe thickness and PES layer thickness

Probe thickness (100 or 200 μm) has no influence on the voltage potential on the active top side. A slower decay in the substrate towards the back-side is observed but voltage levels at the backside are not significantly different. A larger ECF-filled PES leads to lower top side surface voltages due to the larger high conductive fluid volume. A 4 x increase in PES thickness leads to ca. 20% voltage decrease.

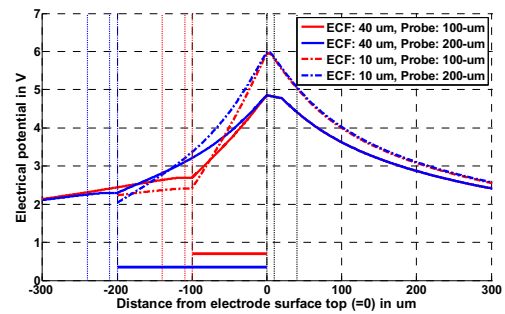


Fig. 7. Simulation case for 100- μm single electrode: Probe thickness has no effect on field distribution on the top side. The dependency on the ECF thickness is only visible on the back-side. The back-side potential drops 1.5-to-2 times faster than at the top with distance to the origin.

B. Spatial selectivity in function of PES layer thickness

Results for different PES layer thicknesses (ECF-filled) for a 100- μm single electrode indicate about 30% peak voltage reduction for the realistic 40 μm PES layer (Fig. 8). However, voltage levels and 2nd derivative relevant for the activation function [7] in the neighborhood of potential neurons (at > 100 μm distance) are comparable between all cases. High-voltage levels close to the surface may lead to unwanted chemical reactions. Spatial selectivity for such a single large electrode is naturally poor.

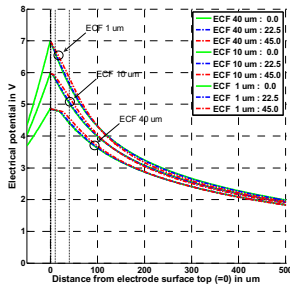


Fig. 8. For a single 100- μm electrode, thicker PES layers result in a lower voltage close to the electrode. Beyond 100 μm distance from the electrode, voltage levels and decay are similar. Angle selectivity is poor.

C. Impact of electrode size in chronic vs. acute conditions

Cell growth replacing the post-implantation ECF filled peri-electrode space results in a 40% increase in voltage due to the reduced conductivity. Two 50- μm electrodes perform insignificantly worse at $>100 \mu\text{m}$ distance than a single 100- μm electrode for the same current density.

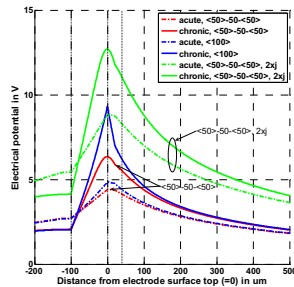


Fig. 9. Far-distance cases are similar. Only a 2 x increase in current density (2xj case) leads to a larger voltage potential at $>100 \mu\text{m}$ distance.

D. Stimulation capability of various electrode topologies

For a 100- μm thick probe in an acute condition with 40- μm thick ECF layer, single electrode, dual electrode (50 and 100 μm spacing), and C-shaped electrodes are compared.

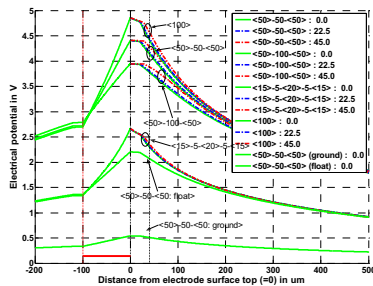


Fig. 10. Intensity depends on topology but has poor angle selectivity except for asymmetric electrodes (last two cases). C-shaped electrodes suffer from low current injection; however, their area can still be increased.

All electrodes inject the same current density except for the last two cases: here, only the left of the 50- μm electrodes injects current, the right is either grounded or floating. Angle selectivity is low but for the 50- μm case, leaving the right electrode floating (recording site) results in a 50% peak voltage reduction down from ca. 4.4V. Grounding this electrode results in local discharging (down to 0.5V), interesting for stimulus artifact reduction at recording sites.

E. Selectivity with C-shaped electrodes

Inner and outer parts of the C-shaped electrodes are used with different combinations of current sourcing (isrc), sinking (-isrc), and grounding. Combining sourcing with sinking or grounding allows for local discharging. A grounded inner electrode appears not interesting since all current from the outer electrode is locally sinked; an outer grounding electrode is more interesting to discharge.

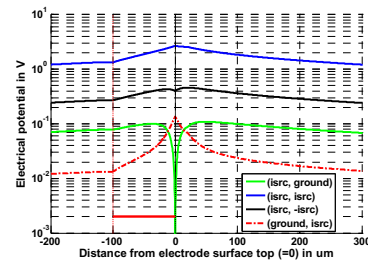


Fig. 11. C-shaped electrodes (outer electrode, inner electrode) effectively combine stimulation, recording, and discharging functions.

V. CONCLUSIONS

Through a combination of electrode interface measurements and FEM, we show that the usage of μm -size arrays with multiple electrodes is promising for introducing more flexibility in DBSR while maintaining stimulation capabilities. Following investigations will combine our full 3D model [8] with the tissue and ECF surroundings described here. Research is continued towards combining these spatial with temporal stimulation patterns [9] and simultaneous stimulation and recording with these electrode arrays.

1. C.C. McIntyre et al., J. Clin. Neurophys., 21(1), 40-50, 2004.
2. C.C. McIntyre et al., Expert Rev. Med. Dev., 4(5), 615-622, 2007.
3. N. Yousif et al., Exp.Rev.Med.Dev., 4(5), 623-631, 2007.
4. M.A. Moffitt et al., Clin.Neurophys., 116, 2240-2250, 2005.
5. S. Musa, M. Welkenhuysen, R. Huys, W. Eberle et al., "Planar 2D-array neural probe for DBSR," Proc. MBEC, Antwerp, Nov. 2008.
6. S. Gabriel et al., Phys. Med. Biol., 41, 2251-2269, 1996.
7. F. Rattay, IEEE Trans. Biomed. Eng., 33, 974-977, 1986.
8. A. S. Mecheri, W. Eberle et al., "Modeling the impact of local and distant electrode configuration on the stimulation pattern in μm -size neural probes," acc. for IEEE NE, Antalya, Turkey, Apr. 2009.
9. C. R. Butson et al., Brain Stim., 1, 7-15, 2008.

Silicon Microprobe Systems for Neural Drug Delivery: Experimental Characterization of Liquid Distribution

S. Spieth, A. Schumacher, S. van de Moosdijk, S. Haeberle, and R. Zengerle

Hahn-Schickard-Gesellschaft, Institute of Micromachining and Information Technology (HSG-IMIT),
Villingen-Schwenningen, Germany

Abstract— Neural drug delivery by microprobes is considered to be one of the most promising methods for treating brain related diseases since the drug liquid can be directly infused into a specific brain region. However, this requires in turn knowledge on the liquid distribution during infusion. This work evaluates the liquid distribution in agarose gel of micro-fabricated silicon probes with two different outlet styles in comparison to a conventional stainless steel capillary. The optical liquid distributions for infusion rates of 0.2, 0.5, and 1.2 $\mu\text{L}/\text{min}$ are determined in a special experimental setup which allows in parallel the measurement of pressure and flow during infusion. Flexible fluidic interfacing to the silicon probes is achieved by small o-rings for easy interchangeability. Since the actual pressure and flow conditions at the outlets of the inserted microprobes cannot be directly measured, a system model of the experimental setup is derived which allows to determine these values. Information on the predominant liquid distributions for the different probe types and infusion rates is qualitatively provided. Finally, actual pressure and flow conditions as well as backflow heights are exemplary presented for an infusion rate of 0.2 $\mu\text{L}/\text{min}$.

Keywords—drug delivery, silicon microprobes, microfluidics, liquid distribution.

I. INTRODUCTION

Whereas silicon-based microprobe arrays with electrodes are meanwhile widely used, multifunctional arrays which combine electrode recording and stimulation with microfluidic drug delivery, biosensing, etc. are currently under development [1]. However, neural recording combined with simultaneous drug delivery at the location of recording is of great importance in neuroscience since liquid drug can be directly delivered to a specific brain region. This could open new perspectives, e.g. in diagnosis and therapy of epilepsy. Recently, we reported on robust microprobe systems for simultaneous neural recording and drug delivery in acute experiments [2]. In this paper we report and compare the spatial distribution of the liquid delivered with these probes.

Generally, it is desired to precisely define and localize the volume area which is finally covered by the drug. Dependent on the infusion rate, two different delivery regimes are typically distinguished: *Low-flow microinfusions* for

infusion rates up to 0.5 $\mu\text{L}/\text{min}$ and *high-flow microinfusions* for infusion rates exceeding 0.5 $\mu\text{L}/\text{min}$ with drug distributions of a few millimeters to more than 10 mm, respectively [3]. One characteristic length of the liquid distribution is the backflow height, i.e. the height of the liquid bubble in probe direction which forms around the fluidic outlet. The backflow height and consequently the liquid distribution has been reported to depend on several parameters, e.g. probe geometry [4,5,6], infusion [4,6] and insertion parameters [5]. However, once microprobes have been inserted into the brain, it is very difficult to monitor the liquid distribution as well as proper operation, e.g. detection of blocked channels. To gain information on the liquid distribution of fluidic probes, different approaches exist, e.g. predictive simulations [4], use of dye or lesioning agents [7], and agarose gel experiments [7]. Detection of blockages is complicated by the fact that an open channel together with a high fluidic resistance in the brain has to be distinguished from an entirely blocked channel.

The approach reported here to characterize liquid distribution combines agarose gel experiments with optical inspection, parallel measurement of pressure and flow, and incorporation of the fluidic system behavior. Typically, system influences of the experimental setup are neglected. However, only by considering the fluidic system behavior it is possible to determine the actual infused liquid and the pressure conditions at the probe outlet during infusion of smallest liquid amounts.

II. MATERIAL AND METHODS

A. Microprobes with Fluidic Channels

In this study, two types of fluidic silicon microprobes (type A and B, Fig. 1) are compared with conventional stainless steel capillaries (type C). The geometrical properties of the probes are compared in table 1. The fluidic silicon microprobes are fabricated using standard 300- μm -thick 4-inch silicon (100) wafers, deep reactive ion etching (DRIE), silicon fusion bonding, wafer grinding, and thin film processing as described in [8]. Each probe comprises two 8-mm-long shafts attached to a common platform. An

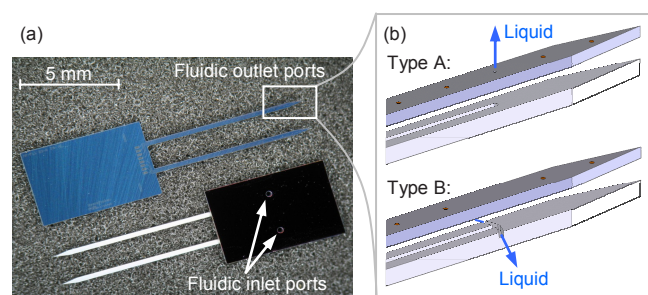


Fig. 1 Silicon microprobes: (a) Front and back side, (b) exploded drawing of the out-of-plane outlet (Type A) and the two in-plane outlets (Type B)

individual probe shaft includes a microfluidic channel with cross-section of $50 \times 50 \mu\text{m}^2$. Type A has an out-of-plane outlet port of $25 \mu\text{m}$ in diameter, whereas type B has two in-plane outlet ports at the probe flanks with cross-sectional area of $50 \times 50 \mu\text{m}^2$ each (Fig. 1b). Type C has a perfectly flat tip outlet with a diameter of $114 \mu\text{m}$.

Table 1 Geometrical properties of probe types A, B, and C

Type	Material	Shaft crosssection	Tip shape	Outlet type	Outlet dimensions
A	Silicon	$250 \times 250 \mu\text{m}^2$	sharp	Out-of-plane	$\text{Ø } 25 \mu\text{m}$
B	Silicon	$250 \times 250 \mu\text{m}^2$	sharp	In-plane	$2 \times 50 \times 50 \mu\text{m}^2$
C	Stainless steel	$\text{Ø } 254 \mu\text{m}$	flat	Tip	$\text{Ø } 114 \mu\text{m}$

The $6 \times 4 \text{ mm}^2$ common platform of the silicon probe types A and B has been specifically designed for characterization purposes. Out-of-plane inlet holes allow flexible fluidic interfacing and easy interchangeability. The microprobe is simply inserted into a special fixture and the inlet holes are sealed by small o-rings (Fig. 2). The fixture provides pluggable access to up to four fluidic channels of the probes by fluidic connectors (here only two in use).

B. Experimental Setup and Procedures

The liquid distribution around the outlet ports is characterized by delivery of $0.2\text{-}\mu\text{m}$ -filtered dye solution (methylene blue) into agarose gel (Merck KGaA) at rates of 0.2, 0.5, and $1.2 \mu\text{L}/\text{min}$. 0.6% agarose gel was reported to be a suitable brain phantom [5]. The complete experimental setup is schematically shown in Fig. 3. The fluidic microprobes are first mounted into a fixture on a micrometer stage (Fig. 2a) and connected to a high precision syringe pump (Cetoni nEMESYS). In-line sensors are used to record flow rate (Bronkhorst μFlow , 0-100 $\mu\text{L}/\text{hr}$) and pressure (Sensortech CTE9000, 0-100 mbar). After priming the fluidic system, the micrometer stage is used to insert the probes into a transparent cuvette filled with agarose gel to

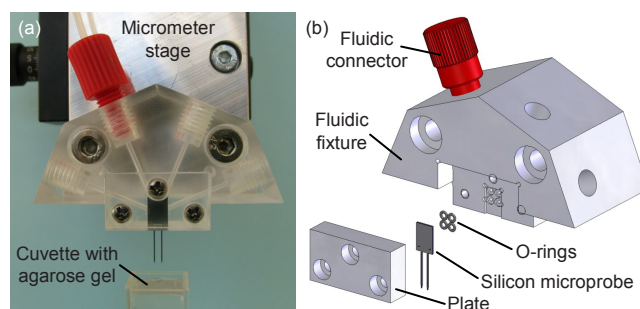


Fig. 2 Fluidic connection to the microprobes: (a) Microprobe mounted into the fluidic fixture together with a cuvette filled with agarose gel, (b) exploded view showing the probe fluidic connection by o-rings

an insertion depth of 6 mm. During the experiment, the liquid distribution within the gel is monitored at a rate of 0.5 frames/s with a digital camera (Moticam 2300) mounted on a microscope (Leica MZ6).

C. Theoretical Description

Ideally, a microfluidic system can be considered as a combination of perfectly rigid tubings with different inner diameters. In laminar flow regime which is often encountered in microfluidics, such a system is solely characterized by its fluidic resistances. However, in reality tubings offer always certain elasticity. Additionally, measurement equipment can introduce deformable elements, e.g. pressure sensors which rely on a deformable membrane. Hence, fluidic capacitances and inductances have also to be taken into account. Due to the analogy between electricity and laminar flow, a microfluidic system may be represented by an electric equivalent circuit. For the experimental setup shown in Fig. 3, a first order model taking into account the most important effects is illustrated in Fig. 4. The constant flow source represents the syringe pump and the fluidic resistances R and capacitances C are defined as:

$$R = \frac{p}{q} \quad \text{and} \quad C = \frac{dV}{dp} \quad \text{with} \quad q = \frac{dV}{dt} \quad (1)$$

with pressure p , flow rate q , volume V , and time t .

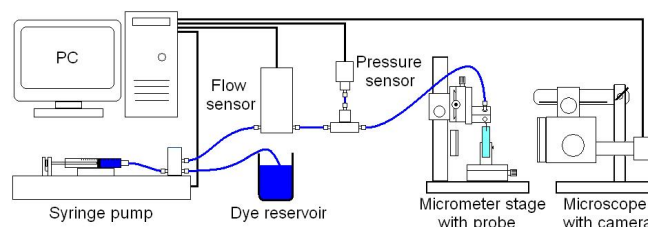


Fig. 3 Schematic of the experimental setup for probe characterization

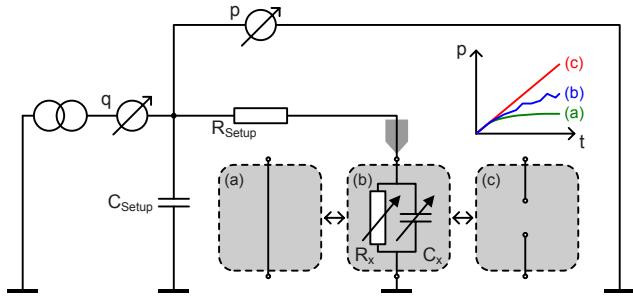


Fig. 4 Electric equivalent circuit: (a) No fluidic resistance, (b) symbolized complex fluid-mechanic interactions, (c) completely blocked microprobe

R_{Setup} summarizes the resistances of tubings, microprobes and sensor elements. Thereby, pressure dependent changes in resistance due to variations of cross-sectional area are neglected. The capacitance C_{Setup} considers the elasticity of tubings and the mechanical flexibility of the pressure sensor membrane. The complex fluid-mechanic interactions between microprobe and agarose gel involve channel flow, porous flow and mechanical elasticity [4]. We symbolize these interactions by the variable fluidic resistance R_x and capacitance C_x as shown in Fig. 4b. Using the equivalent circuit, the boundaries of the pressure characteristic during operation can be determined by two special cases:

Case 1: If the agarose gel opposes no fluidic resistance (Fig. 4a), the transient pressure signal $p(t)$ can be calculated from the constant pump rate q :

$$q = C_{\text{Setup}} \frac{dp}{dt} + \frac{p}{R_{\text{Setup}}} \Rightarrow p(t) = R_{\text{Setup}} q \left(1 - e^{-\frac{t}{R_{\text{Setup}} C_{\text{Setup}}}} \right) \quad (2)$$

Case 2: If the outlet is blocked (Fig. 4c), only the capacitance C_{Setup} has to be considered to determine $p(t)$:

$$q = C_{\text{Setup}} \frac{dp}{dt} \Rightarrow p(t) = \frac{q}{C_{\text{Setup}}} t \quad (3)$$

Consequently, the pressure characteristic during any delivery must fall between these boundaries. Dependent on the

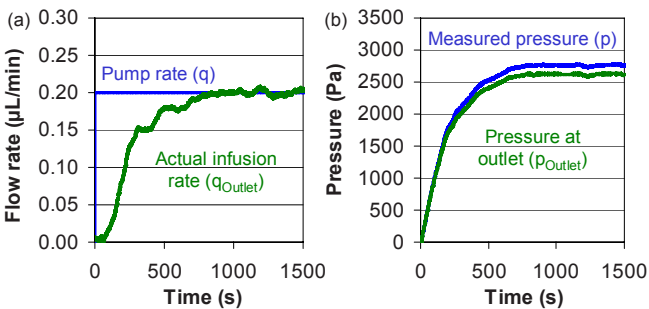


Fig. 5 Probe type B at 0.2 $\mu\text{L}/\text{min}$ inserted into agarose gel: (a) Pump rate and actual infusion rate, (b) Measured pressure and pressure at the outlet

complex fluid-mechanic interactions between microprobe and agarose gel, the pressure curve develops in-between. Additionally, the following two conclusions can be derived:

First, the liquid delivered by the syringe pump is not directly infused by the probe but with some time lag due to the capacitance C_{Setup} of the system. However, having experimentally determined R_{Setup} and C_{Setup} by the two special cases (Fig. 4a,c), the actual real-time flow q_{Outlet} and pressure p_{Outlet} during infusion can be calculated from q and p .

$$q_{\text{Outlet}} = q - C_{\text{Setup}} \frac{dp}{dt} \quad \text{and} \quad p_{\text{Outlet}} = p - R_{\text{Setup}} q_{\text{Outlet}} \quad (4)$$

Second, a blocked channel can only be detected by the transient pressure characteristic rather than by absolute values. However, since the slopes of the pressure curves are very similar at the begin of the delivery, a certain infusion time and volume are required.

III. EXPERIMENTAL RESULTS

The infusion experiments were performed as described in section II. First, R_{Setup} and C_{Setup} were experimentally determined and used to calculate the actual infused liquid and pressure at the probe outlet from the pressure signal and pump rate. Exemplary, these values are shown in Fig. 5 for probe type B and a pump rate of 0.2 $\mu\text{L}/\text{min}$. There is a time-lag of 800 s until the actual infusion rate equals the pump rate. The pressure conditions at the outlet are about 5% lower than measured with the pressure sensor.

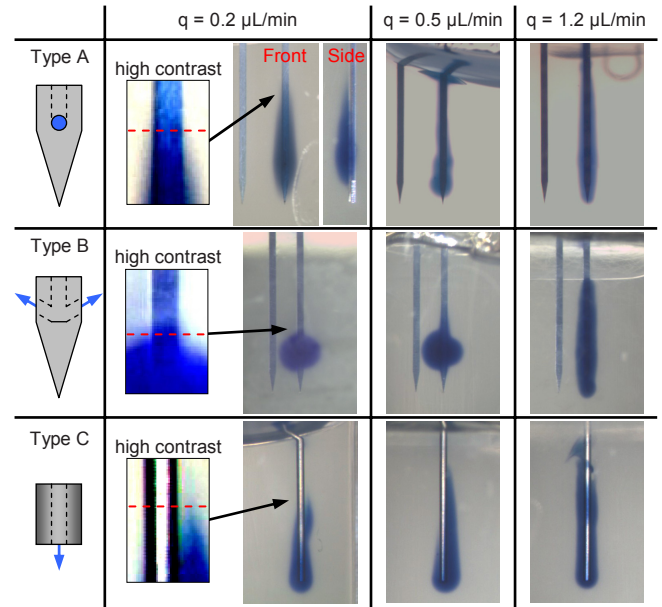


Fig. 6 Predominant liquid distributions for pump rates of 0.2, 0.5, and 1.2 $\mu\text{L}/\text{min}$ after an actual infused volume of 1 μL .

Exemplary microscope images of the predominant liquid distributions of the different probe types after an actual infused volume of 1 μL for different pump rates are shown in Fig. 6. For probe type A, the preferred distribution direction is coincident with the outlet direction in low-flow regime. In average, ten infusion experiments have been performed for each probe type and pump rate.

Additionally, the backflow height was determined by evaluating the images recorded during infusion. The distance between outlet position and top of the color cloud was measured on pixel-level with increased image contrast (Fig. 6). We estimate the preciseness of this approach to $\pm 200 \mu\text{m}$. Exemplary, the average backflow heights versus actual infused volumes for an infusion rate of 0.2 $\mu\text{L}/\text{min}$ are shown in Fig. 7.

IV. CONCLUSIONS

Due to the complex interactions between microprobe and insertion media, infusion experiments cannot reveal 100%-reproducibility. Smallest variations of media or during insertion can already change the run of an experiment. Dependent on the experimental setup, fluidic capacitances can cause a significant time delay between pump and actual infusion rate and complicate the detection of blockages. However, considering the fluidic system behavior, actual infusion rates and infused volumes as well as the actual outlet pressure can be determined. As expected, for increasing pump rates the backflow height of all three probe types is increasing. With respect to backflow height, silicon probe type B performed better and type A worse than the conventional capillary type C. Additionally, probe type B resulted in a concentrated, nearly spherical liquid distribution in low flow-regime, although one would expect that fluid is preferably injected through only one outlet. We attribute all this to the position of the fluidic outlets with respect to the sharp tip blade. During insertion, the tip blade displaces the agarose gel towards the probe flanks, whereas a small crack

forms in blade direction. Hence, backflow is promoted for type A since the crack is next to the outlet, whereas backflow is reduced for type B because the displaced gel increases the contact pressure. The concentrated pressure at the flanks is higher than for type C where the pressure distributes uniformly around the circular circumference. However, one has to keep in mind that agarose gel can only approximate the conditions in real brain. Nevertheless, the presented results suggest that microprobes with rectangular cross section and tip blade can outperform steel capillaries if the fluidic outlets are placed at the probe flanks.

ACKNOWLEDGMENT

The work was performed in the frame of the Information Society Technologies (IST) Integrated Project *NeuroProbes* of the 6th Framework Program (FP6) of the European Commission (Project number IST-027017). The authors acknowledge the support from K. Seidl, P. Ruther, and the cleanroom facility of IMTEK, University of Freiburg. The authors further acknowledge the technical support from the cleanroom and the machine shop facility at HSG-IMIT.

REFERENCES

1. Ruther P, Aarts A, Frey O et al. (2008) The NeuroProbes project – multifunctional probe arrays for neural recording and stimulation, *Biomed. Techn.* 53, Suppl. 1:238-240
2. Spieth S et al. (2008) Robust microprobe systems for simultaneous neural recording and drug delivery, *eMBEC Proc.*, 4th European Biomedical Engineering Congress, Antwerp, Belgium, pp 2426-2430
3. Raghavan R, Brady ML, Rodríguez-Ponce MI et al. (2006) Convection-enhanced delivery of therapeutics for brain disease, and its optimization, *Neurosurg. Focus* 20(3):E12
4. Morrison PF, Chen MY, Chadwick RS et al. (1999) Focal delivery during direct infusion to brain: role of flow rate, catheter diameter, and tissue mechanics, *Am. J. Physiol.* 277: R1218-R1229
5. Chen Z-J, Gillies GT et al. (2004) A realistic brain tissue phantom for intraparenchymal infusion studies, *J. Neurosurg* 101:314-322
6. Chen MY, Lonser RR, Morrison PF (1999) Variables affecting convection-enhanced delivery to the striatum: a systematic examination of rate of infusion, cannula size, infusate concentration, and tissue-cannula sealing time, *J. Neurosurg.* 90:315-320
7. Neeves KB, Lo CT, Foley CP et al. (2006) Fabrication and characterization of microfluidic probes for convection enhanced drug delivery, *J. Control. Rel.* 111:252-262
8. Seidl K, Spieth S, Steigert J et al. (2007) Fabrication process for silicon in-plane probes for simultaneous neural recording and drug delivery, *HARMST Proc.*, 7th Int. Workshop on High-Aspect-Ratio Micro-Structure Technology, Besançon, France, pp 247-248

Author: Sven Spieth
 Institute: HSG-IMIT
 Street: Wilhelm-Schickard-Str. 10
 City: D-78052 Villingen-Schwenningen
 Country: Germany
 Email: sven.spieth@hsg-imit.de

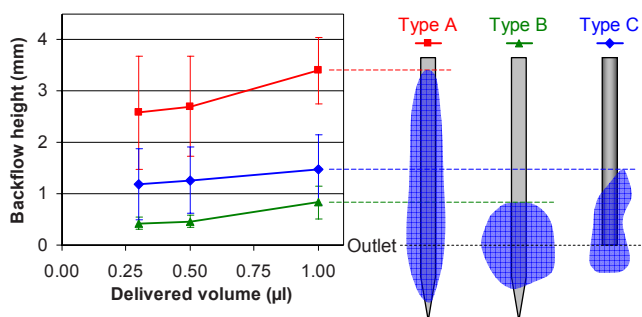


Fig. 7 Average backflow heights with standard deviations of the different probe types after actual infused volumes of 0.3, 0.5, and 1 μL at an infusion rate of 0.2 $\mu\text{L}/\text{min}$. Each average represents 7-25 experimental values

A measurement set-up to determine the charge injection capacity of neural microelectrodes

W. Poppendieck¹, K.P. Koch², S. Steltenkamp¹, K.-P. Hoffmann¹

¹ Fraunhofer Institute for Biomedical Engineering, Department Medical Engineering & Neuroprosthetics, St. Ingbert, Germany

² Fachhochschule Trier, Department Engineering, Trier, Germany

Abstract— A measurement set-up is presented which can be used to determine the charge injection capacity of neural microelectrodes. This value determines the amount of charge that can be reversibly injected during a single stimulation pulse, and is strongly depending on the materials present at the electrode/electrolyte interface. The set-up was used to measure and compare the charge injection capacity of various electrode materials (sputtered platinum, microporous platinum, PEDOT), and for various stimulation pulse widths. It was observed that the charge injection capacity for microporous platinum und PEDOT was significantly higher than for sputtered platinum. Moreover, the charge injection capacity was found to increase with the stimulation pulse width.

Keywords— Neural microelectrodes, charge injection capacity, microporous platinum, PEDOT.

I. INTRODUCTION

In neural prosthetics, electrodes are used to stimulate neural or myogenic tissue, and to record bioelectrical signals. In many cases, the application demands the use of very small structures (implantable microelectrodes), in order to establish a close and selective contact to the nerve, and to keep the implantable device as small as possible [1].

If current with a small amplitude is applied to an electrode (e.g. during recording applications), the electrode potential remains close to the equilibrium potential. Here, charge is essentially transferred only by charging/discharging of the Helmholtz double layer at the interface. However, the capacity of the double layer is limited ($10\text{-}20\ \mu\text{F}/\text{cm}^2$), and thus higher current densities require electrochemical reactions at the interface to allow for charge transfer [2]. These reactions can be reversible (i.e. can be reversed by reversing the current), but if the reaction products quickly diffuse away from the interface, the reactions cannot be reversed. Such irreversible reactions lead to electrode corrosion and damage of the surrounding tissue, and thus have to be avoided.

Hydrolysis is an example for an irreversible electrode reaction. If the current density becomes so high that the potential at the electrode exceeds a certain threshold value, gaseous oxygen is produced at the interface, forming bub-

bles. Analogously, if the electrode potential falls below a certain value, hydrogen evolution is observed. The limiting potentials define the so-called “water window”. During application, the electrode potential should always remain within this window, in order to avoid irreversible reactions and its negative effects on the electrode and the patient.

However, for stimulation, the use of small electrode contacts leads to very high current densities at the interface, as the injected charge has to overcome the threshold which is needed to generate an action potential at the target (in the range of $0.2\text{-}5\ \mu\text{C}$ per pulse for muscle, peripheral nerve or cortical surface [2]).

The amount of charge which can be reversibly injected during a single stimulation pulse (i.e. with the electrode potential remaining within the water window) is defined as the charge injection capacity of the electrode, and is generally related to the geometric electrode area. It is strongly dependent on the materials at the electrode interface.

As electrodes made of platinum metals show good electrochemical properties for stimulation applications, neural microelectrodes are often made of platinum [3]. If the electrode contacts do not become too small, platinum electrodes can reversibly inject enough charge for successful stimulation. However, for a number of applications, the electrode contacts have to be so small that the charge injection capacity of platinum is not large enough to reversibly inject the required charge.

An approach which is frequently used to increase the charge injection capacity of microelectrodes is to coat them with a suitable material, for instance microporous platinum [4] or a conductive polymer such as PEDOT (poly(3,4-ethylenedioxythiophene)) [5]. Due to their porous surface structure, such materials increase the effective (microscopic) surface area of the electrode, while the geometric (macroscopic) area remains constant. Thus, this method provides a good solution to increase the charge injection capacity of an electrode. Layers of microporous platinum and PEDOT can be deposited on platinum microelectrodes using electrodeposition. In previous work, it was demonstrated that such coatings lead to a significant reduction of the impedance at the electrode interface. Moreover, the electrical parameters for electrodeposition were optimized [4,5].

In the following, a set-up is presented which can be used to measure the charge injection capacity of neural microelectrodes. With this method, the charge injection capacity of sputtered (plain) platinum, microporous platinum and PEDOT is determined and compared. Moreover, measurements with platinum are performed using different stimulation pulse widths, in order to demonstrate the dependence of the charge injection capacity on the pulse width.

II. MATERIALS AND METHODS

A. Microelectrode manufacturing

Flexible, polyimide-based microelectrodes were produced by means of a previously described process [6]. For the measurements, structures with round electrode contacts ($d=300\ \mu\text{m}$) made of sputtered platinum were used. The electrodes were divided into three groups:

- Untreated electrodes (sputtered platinum)
- Electrodes coated with microporous platinum from a solution of hexachloroplatinum-(IV)-acid hexahydrate in deionized water at $-0.2\ \text{V}$ vs. Ag/AgCl (charge transferred during deposition: $1\ \text{C}/\text{cm}^2$) [4]
- Electrodes coated with PEDOT/PSS from a solution of 2,3-dihydrothieno(3,4-B)-1,4-dioxin (EDOT) and sodium polystyrene sulfonate (NaPSS) in deionized water at $+0.9\ \text{V}$ vs. Ag/AgCl (charge transferred during deposition: $0.1\ \text{C}/\text{cm}^2$) [5]

Quality of the manufactured electrodes and the prepared coatings was controlled using impedance spectroscopy.

B. Set-up to measure the charge injection capacity

To determine the charge injection capacity, a method similar to the one described by Rose and Robblee was used [7]. The developed measurement station is shown in Fig. 1. The idea is to apply current pulses with various amplitudes to the electrode and to simultaneously measure the potential over the time. By determining the maximum current density for which the electrode potential remains within the reversible range, the charge injection capacity can be calculated by multiplying the current density with the pulse width. For the reversible limits, the following values were applied [8]:

- Platinum: between $-0.6\ \text{V}$ and $+0.9\ \text{V}$ vs. Ag/AgCl
- PEDOT: between $-0.7\ \text{V}$ and $+0.7\ \text{V}$ vs. Ag/AgCl

The stimulation signal is generated by a stimulator (EasyStim, internal development at IBMT), which is synchronized by an external trigger. With the stimulator, biphasic, cathodic-first square pulses with various current

amplitudes between $50\ \mu\text{A}$ and $5\ \text{mA}$ could be generated, as well as pulse widths between $10\ \mu\text{s}$ and $500\ \mu\text{s}$. As trigger, a second EasyStim was used, working in voltage-controlled mode (amplitude $5\ \text{V}$, pulse width $50\ \mu\text{s}$).

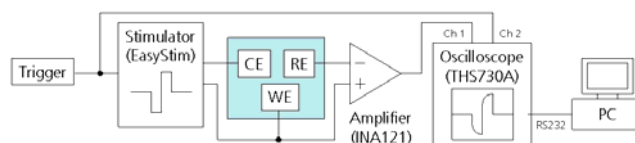


Fig. 1 Set-up to determine the charge injection capacity

For the measurements, a three-electrode set-up with a Pt counter electrode (PT 1800, Schott) and a Ag/AgCl reference electrode (B 2920, Schott) in physiological saline was used. This set-up was connected to the output of the stimulator, such that the stimulation current flowed between the working electrode (WE) and the counter electrode (CE). The potential at the working electrode with respect to the reference electrode (RE) was recorded by an amplifier (INA121, Texas Instruments, Dallas/USA) and displayed by a digital oscilloscope (THS730A, Tektronix, Beaverton/USA). The oscilloscope was externally triggered by the same signal as the stimulator. Via the RS232 interface, the data could be transferred to a PC for further processing.

To compare the charge injection capacity of sputtered platinum, microporous platinum and PEDOT, pulse widths of $200\ \mu\text{s}$ were used. In order to evaluate the influence of the pulse width on the charge injection capacity of sputtered platinum, the pulse width was varied from $10\ \mu\text{s}$ to $500\ \mu\text{s}$.

Finally, the recorded potentials were corrected for the potential drop iR_S in the electrolyte [7]. The solution resistance R_S was calculated by [9]:

$$R_S = \frac{\rho_E}{4r} + \frac{\rho_E h}{\pi r^2} + h_a \frac{\rho_E}{r}$$

Here, r is the electrode radius, h is the height by which the electrode contacts are recessed inside the polyimide structure, ρ_E is the conductivity of the electrolyte, and h_a is a correction factor. For $r=150\ \mu\text{m}$, $h=5\ \mu\text{m}$, $h_a=0,01$ [9] and $\rho_E=72\ \Omega\text{cm}$ [10], a value of $R_S \approx 1300\ \Omega$ was found.

III. RESULTS

A. Preparation of coated microelectrodes

Microporous platinum and PEDOT were successfully deposited on the platinum microelectrodes. The impedance spectra of the three different groups of electrodes are shown in Fig. 2. It is visible that the coating of the electrodes led to a significant reduction of the interface impedance.

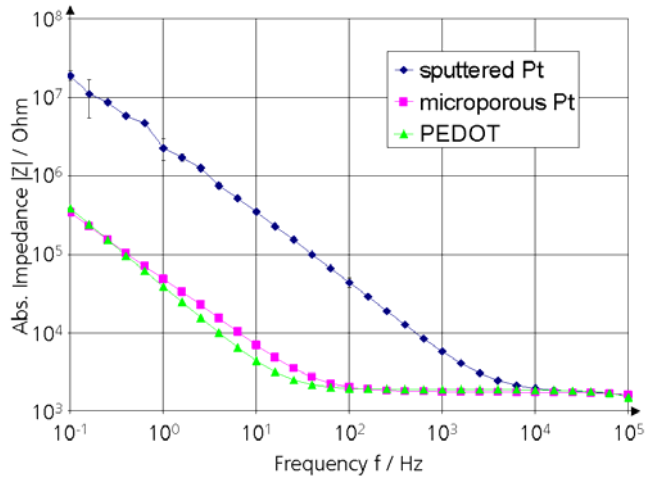


Fig. 2 Impedance spectra of uncoated and coated microelectrodes (n=4)

B. Charge injection capacity for various materials

The electrodes were subjected to biphasic, cathodic-first square current pulses, and the potential response over the time was recorded. As an example, Fig. 3 shows the potential response of a sputtered platinum electrode for current pulses with a pulse width of 200 μ s and various amplitudes. It can be seen that with increasing current amplitude, the potential excursions become larger (the small peaks at $t=50 \mu$ s are artifacts caused by the trigger signal).

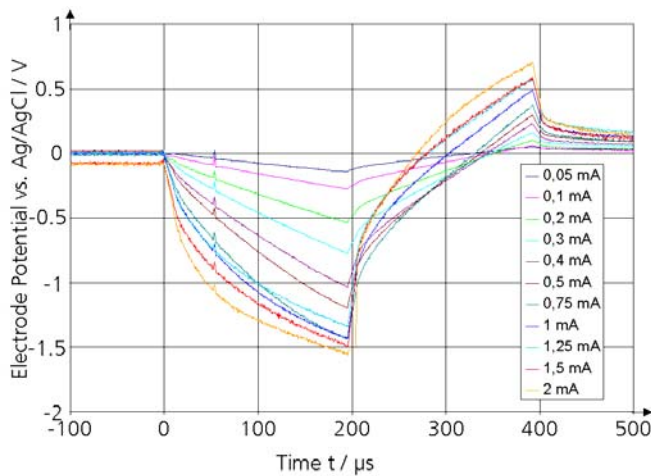


Fig. 3 Potential response measured at an electrode (sputtered platinum) for biphasic current pulses of various amplitudes (pulse width 200 μ s)

In order to determine the charge injection capacity, the maximum and minimum values for the electrode potential (see Fig. 3) were plotted versus the charge injected during a

single pulse (i.e. the applied current amplitude multiplied with the pulse width). For the three different materials tested, these plots are shown in Fig. 4 for a pulse width of 200 μ s. Moreover, the limits of the water window of platinum (dashed) and PEDOT (dotted) are drawn in the diagram.

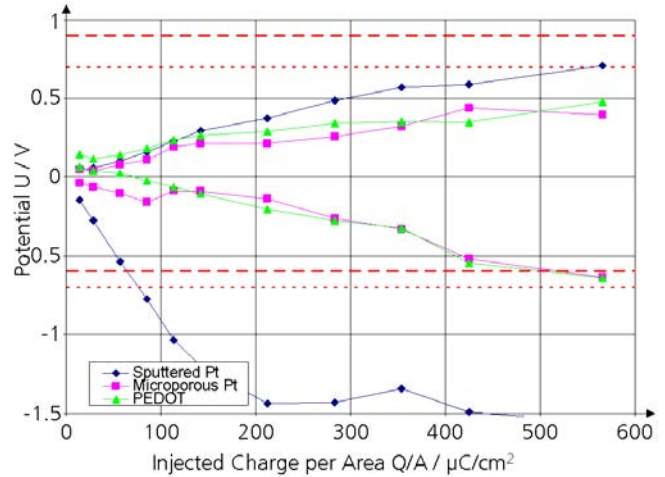


Fig. 4 Maximum and minimum electrode potential for stimulation pulses of various amplitudes (pulse width 200 μ s) versus injected charge (n=4) for sputtered Pt, microporous Pt and PEDOT; the charge injection capacity is the charge where the potential leaves the reversible potential limits

In Fig. 4, the charge injection capacity can be seen as the intersection of the potential lines with the water window. For sputtered platinum, the potential leaves the reversible range at the lower limit, while for microporous platinum and PEDOT, the potential leaves the water window at the upper limit. By linear interpolation, the following values for the charge injection capacity for 200 μ s pulses were found:

- Sputtered platinum: 64 μ C/cm²
- Microporous platinum: 524 μ C/cm²
- PEDOT: 658 μ C/cm²

Thus, for a pulse width of 200 μ s, coating the electrode resulted in an increase of the charge injection capacity by a factor of ~ 8 (microporous platinum) or ~ 10 (PEDOT).

C. Charge injection capacity versus pulse width

For sputtered platinum electrodes, the charge injection capacity was determined for various pulse widths between 10 μ s and 500 μ s, using the same procedure as described above. In Fig. 5, the determined charge injection capacity is displayed versus the pulse width. It can be seen that for larger pulse widths, the charge injection capacity increases.

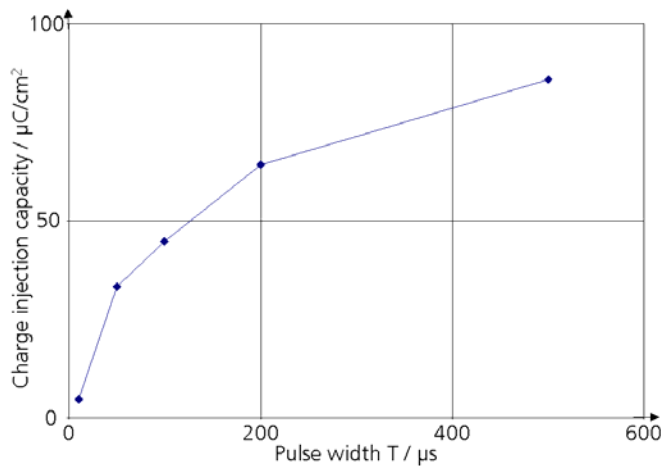


Fig. 5 Charge injection capacity for sputtered platinum electrodes and biphasic square pulses of various pulse widths ($n=4$)

IV. CONCLUSIONS

The charge injection capacity of microelectrodes was successfully determined using a set-up to apply stimulation pulses. For sputtered platinum, a value of $64 \mu\text{C}/\text{cm}^2$ was found, which is in good accordance with values found in the literature ($50\text{-}150 \mu\text{C}/\text{cm}^2$) [7]. Coating of the electrodes with microporous platinum led to a significant increase of the charge injection capacity ($487 \mu\text{C}/\text{cm}^2$). The value found for an electrode coated with PEDOT was even higher ($658 \mu\text{C}/\text{cm}^2$). This increase in the charge injection capacity is generally assumed to be due to the microrough surface structure of the coating materials, which leads to an increase in the effective surface area. The results indicate that the coating of microelectrodes with such materials yields a significant improvement of the electrochemical properties of the electrodes, especially for stimulation applications.

For sputtered platinum electrodes, it could be clearly observed that the charge injection capacity increases with longer pulse widths. The reason for this is the increasing amount of slower reactions contributing to the charge injection for increasing pulse widths. Thus, when giving values for the charge injection capacity of an electrode, the respective pulse width should always be mentioned. The limit of the charge injection capacity for extremely slow pulses corresponds to the charge storage capacity, which can be calculated from cyclic voltammetry experiments. For sputtered platinum, the charge storage capacity of similar electrodes was determined to be $1400 \mu\text{C}/\text{cm}^2$ [4].

The charge injection capacity is a crucial parameter in the process of electrode design. By estimating or determining the amount of charge or current which is needed for stimulation in a certain application, the minimum geometric electrode area which is required for safe stimulation can be calculated using the charge injection capacity. Thus, the presented measurement method is an important tool for the characterization of electrodes and electrode materials.

ACKNOWLEDGMENT

This work was supported by the EU Project NEUROBOTICS (IST-FET Project #2003-001917).

REFERENCES

- Schuetzler M, Doerge T, Wien SL, Becker S, Staiger A, Hanauer M, Kammer S, Stieglitz T (2005) Cytotoxicity of Platinum Black. 10th Ann Conf Int FES Soc, Montreal, Canada, pp 343-345
- Merrill DR, Bikson M, Jefferys JGR (2005) Electrical stimulation of excitable tissue: design of efficacious and safe protocols. *J Neurosci Meth* 141:171-198
- Robblee LD, Rose TL (1990) *Electrochemical Guidelines for Selection of Protocols and Electrode Materials for Neural Stimulation*. Neural Prostheses (ed. Agnew WF, McCreery DB), Prentice Hall, Englewood Cliffs, New Jersey (pp 25-66)
- Poppendieck W, Doerge T, Hoffmann KP (2008) Optimization of microporous platinum coatings for neural microelectrodes. 13th Ann Conf Int FES Soc, Freiburg, Germany, pp 319-321
- Poppendieck W, Hoffmann KP (2008) Coating of neural microelectrodes with intrinsically conducting polymers as a means to improve their electrochemical properties. 4th Europ Congr Int Fed Med & Biomed Eng, Antwerpen, Belgium, pp 2409-2412
- Hoffmann KP, Koch KP, Doerge T (2006) New technologies in manufacturing of different implantable microelectrodes as an interface to the peripheral nervous system. 1st IEEE/RAS-EMBS Int Conf Biomed Robotics & Biomechatronics BioRob, Pisa, Italy, pp 414-419
- Rose TL, Robblee LS (1990) Electrical Stimulation with Pt Electrodes. VIII. Electrochemically Safe Charge Injection Limits with 0.2 ms Pulses. *IEEE T Biomed Eng* 37:1118-1120
- Cui XT, Zhou DD (2007) Poly (3,4-Ethylenedioxythiophene) for Chronic Neural Stimulation. *IEEE T Neur Sys Rehabil Eng* 15:502-508
- West AC, Newman J (1991) Current Distribution on Recessed Electrodes. *J Electrochem Soc* 138:1620:1625
- Kovacs GTA (1994) *Introduction to the Theory, Design, and Modeling of Thin-Film Microelectrodes for Neural Interfaces*. Enabling Technologies for Cultured Neural Networks (ed. Stenger DA, McKenna TM), San Diego, Academic Press (pp 121-165)

Author: Wigand Poppendieck
 Institute: Fraunhofer Institute for Biomedical Engineering
 Street: Ensheimer Strasse 48
 City: 66386 St. Ingbert
 Country: Germany
 Email: wigand.poppendieck@ibmt.fraunhofer.de

Patient-Cooperative Control: Providing Safe Support without Restricting Movement

Heike Vallery^{1,2}, Marco Guidali^{1,2}, Alexander Duschau-Wicke^{1,2,3}, and Robert Riener^{1,2}

¹Sensory-Motor Systems Lab, Institute of Robotics and Intelligent Systems, ETH Zurich, Zurich, Switzerland

²Spinal Cord Injury Center, University Hospital Balgrist, Zurich, Switzerland

³Hocoma AG, Volketswil, Switzerland.

Abstract—Patient-cooperative behavior of a rehabilitation robot can be seen as a tight interplay of three control components: The first and most important is the intervention paradigm, which can for example be assistance, resistance, or error augmentation. The second and third are more related to the underlying properties of the robot: On the one hand the robot should be transparent in “free” movements, and on the other hand it should provide a safe training frame with appropriate virtual constraints for the movement. In this paper, control strategies to enhance transparency and to constrain movement with virtual tunnels are presented using the examples of the ARMin and the Lokomat, which are rehabilitation robots for upper and lower extremities, respectively. Differences and similarities in control of these robots are outlined in terms of the control strategies for transparency enhancement and movement constraints. The control concepts *Generalized Elasticities* and *Path Control* are described, which improve transparency in free movements inside an allowed spatial region, and which impose movement constraints to confine the user to this allowed region. *Generalized Elastic Path Control* unifies both control approaches within a single potential field, and preliminary results of this controller on the Lokomat are shown.

Keywords—Rehabilitation robotics, patient-cooperative control, transparency, motion constraints, potential fields

I. INTRODUCTION

Recent multicenter controlled trials showed that subacute and chronic stroke patients still profit more from conventional manual therapy than from robotic gait training, at least when the robot imposes movements via position control along a fixed reference trajectory [1], [2]. New results on motor learning and neural plasticity can help explain this by the fact that position control does not allow the human to make errors, which is necessary for learning and the formation of an internal task representation [3], [4]. Furthermore, the robot induces motion and does not require active participation of the patient, which is a key element for recovery [5]–[8]. These results encourage patient-cooperative control of rehabilitation robots, which allows the human to make errors. Three components are needed to achieve such patient-cooperative behavior: First, undesired interaction forces between robot and human must be reduced to a minimum in order to give maximum freedom to the human, meaning that the robot must be *transparent*. Second, the robot must provide a safe training frame and prevent injury. Kinematic *constraints* are an important means for this. Third, the robot may assist or perturb the human in performing the motion, which corresponds to the desired *intervention*.

While the first two features are universal requirements for most rehabilitation robots, the third depends on the specific paradigm to induce motor learning. There may of course be some overlap between the three aims. In the following, we will focus only on transparency and constraints.

When talking about transparency, this refers to apparent robot dynamics the user feels in “free space” motion, when the user moves the robot and should not feel it. Forces that need to be overcome when moving a robot are inertia, gravity, Coriolis and centrifugal forces, and friction. A lightweight construction and/or compliant actuation [9], [10] reduce these forces, but this reduction is limited, especially when the robot is supposed to stiffly guide severely affected patients. There are also control strategies available to reduce apparent robot dynamics. However, these strategies cannot fully compensate the robot, where the main problem is generally to hide inertia. The most prominent strategy to reduce inertia is force feedback, realized via admittance or impedance control concepts [11], [12]. However, due to stability limits, the user will always feel some residual apparent inertia [13].

Concerning the second demand, a safe training frame, control approaches are often based on the concept of *Virtual Fixtures* [14], where rigid constraints or walls are introduced that confine the motion to a certain (safe) domain. These constraints can also facilitate correct motion execution, comparable to a ruler that simplifies drawing a straight line. To define an allowed region, virtual tunnels around a prescribed reference motion pattern can be defined. Depending on the width of the tunnel, strategies aiming only at safety or also at assistance [15], [16] can be realized.

This paper gives an overview on current control research activities for the Lokomat lower extremity robot [17] and the ARMin upper extremity robot [18], with focus on transparency and virtual motion constraints. Both the ARMin and the Lokomat are exoskeleton-type robots, and they aim at assisting upper and lower extremity rehabilitation, respectively (Fig. 1). A comparative analysis of differences and similarities is presented from a control engineering point of view. A special focus is on the newly developed method of *Generalized Elasticities* [19] and its extension to *Generalized Elastic Path Control* [20], which can serve two purposes in a unified way: The controller improves robot transparency by hiding the robot’s apparent inertia beyond the capabilities of closed-loop force control, and it can also be used to

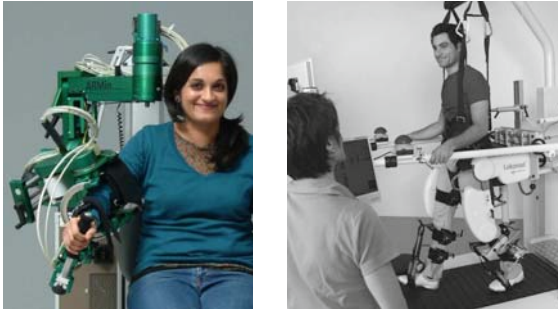


Fig. 1. ARMin and Lokomat upper and lower extremity exoskeletons (Lokomat photo courtesy of Hocoma AG, Switzerland).

enforce motion constraints. The method ensures passive robot behavior, which is a sufficient condition for stability in contact with any other passive environment. Preliminary results with the Lokomat are presented.

II. TRANSPARENCY ENHANCEMENT USING GENERALIZED ELASTICITIES

In arm rehabilitation robots like the ARMin, robot inertia is in general not a serious problem. The patient's reaching movements are rather slow, and gravitational forces are dominant. Therefore, the ARMin is not equipped with force sensors for closed-loop force control, and there is only a feed-forward gravity (and viscous friction) compensation.

In gait rehabilitation robots like the Lokomat, the case is different: Human gait is a very dynamic, even ballistic motion, such that the robot's inertia causes high undesired interaction forces acting on the human's legs. Therefore, mechanisms are necessary that compensate this inertia. Firstly, the Lokomat is equipped with force sensors between actuators and exoskeleton. Closed-loop force control can reduce at least inertial forces caused by the robot's DC motors with high transmission. There is residual actuator inertia, however, and also the dynamics of the exoskeleton legs remain uncompensated by this procedure. The common strategy in robot control would be to tolerate this remaining inertia and to compensate "at least" the other force components, especially gravity of the exoskeleton legs. However, we have shown that gravity compensation of the robot is not always an effective means to reduce interaction forces [19]. On the contrary, gravity compensation of leg exoskeletons during gait is even counterproductive, and it increases interaction forces. This can be explained by the natural dynamics of the robot, which resemble those of a pendulum during the swing phase: The leg swings easily with gravity helping to accelerate and decelerate the inert mass. Without gravity acting on the exoskeleton leg, accelerating and decelerating forces have to be induced by the human to overcome the exoskeleton's inertia, which severely increases interaction forces between human and robot.

Recently, we have proposed the concept of *Generalized Elasticities* as a generic tool to hide robot dynamics, including inertia, during dynamic movements in contact with a human. [19]. This strategy is inspired by the above observation

that the Lokomat's natural dynamics cause less interaction forces than a gravity-compensated Lokomat, meaning that the earth's gravitational field partially compensates robot inertia during gait. Generalized Elasticities go one step further, they represent a potential field that *optimally* compensates robot dynamics during certain types of movement (such as walking). Using a robot model, a cost function that penalizes interaction forces, and a guess for the dynamic movement primitives (in the Lokomat case, a gait pattern), a parameterized potential field is optimized off-line. With the constraint of passivity, the resulting robot behavior is optimal in terms of interaction forces. Instead of compensating gravitational forces of the robot, the outcome of the optimization might even be the opposite strategy. Only as a special case for quasi-static movement, the resulting optimal potential field will once again simply cancel robot gravity.

As it is formulated as a potential, this field leads to passive behavior of the robot, which ensures stability in interaction with the human. Passive behavior means that the same behavior could theoretically be obtained by adding a multitude of mechanical elastic elements, and passivity ensures that the robot will be stable (in a control theoretic sense) when coupled to any other passive environment [13]. Generalized Elasticities can, thus, be imagined as multiple elastic bands spanning one or multiple joints. These elasticities store, release, and transfer energy between joints, such that minimum work needs to be transferred to the robot by the user to perform a given motion.

In the ideal case, the motion that the user performs becomes the "eigenmotion" of the robot, just like a pendular motion would be the eigenmotion of a pendulum. For gait training, this means that the robot requires only very low forces from the human to "oscillate" in a gait-like pattern. This oscillation is highly compliant, meaning that the force field is not intended to guide, support, or even force the human onto the expected trajectory. The robot only optimally compensates its own dynamics along this trajectory. Deviations from the eigenmotion of the robot (smaller or larger steps, different frequency, etc.) should not lead to a large increase in interaction forces, the compensation is only not optimal anymore. Furthermore, different gait patterns can be included during the optimization process, such that the resulting force field represents a very general compromise.

III. MOTION CONSTRAINTS

Both for the ARMin and for the Lokomat, virtual tunnels have been implemented to provide spatial constraints [15], [21]. The tunnels are implemented via a nearest-neighbor search. A predefined trajectory is stored, and the nearest neighbor to the current position on this trajectory is searched. Based on the distance from this nearest neighbor, the defined tunnel width, and the desired stiffness of the virtual walls, a corrective force is generated that pushes the human back towards the reference trajectory in the center of the tunnel. In case the human is capable of executing the movement correctly and stays inside the allowed region, no corrective force is applied.

For the Lokomat, this “Path Control” [15] can be used for two purposes: If the tunnel is wide, its purpose is limited to avoiding dangerous situations such as excessive knee flexion during stance (caused by deficient weight bearing capacity) or deficient knee flexion during swing (leading to the foot touching the treadmill and thus to stumbling). If the tunnel is narrow, assistance can also be provided to the human, comparable to rails that assure motion along the track. The reference trajectory is adapted from the recorded gait pattern of a healthy person. The trajectory is scaled based on the subject’s anatomy, and based on the walking speed. The virtual walls are defined in a unified joint space for both legs, thus in four dimensions (hip and knee flexion/extension left and right leg).

For the ARMin device, the tunnel is mainly intended for assistance, and an additional collision detection prevents the robot arm from colliding with the human’s body. The reference trajectory is calculated dynamically based on the next virtual task to achieve and the current position. The minimum angular jerk method to generate such trajectories has shown to be appropriate for reaching movements with ARMin [21]. The reference trajectory and the virtual tunnels are defined in the task space of the end-effector, and they can be visualized in 3D (Fig. 2).

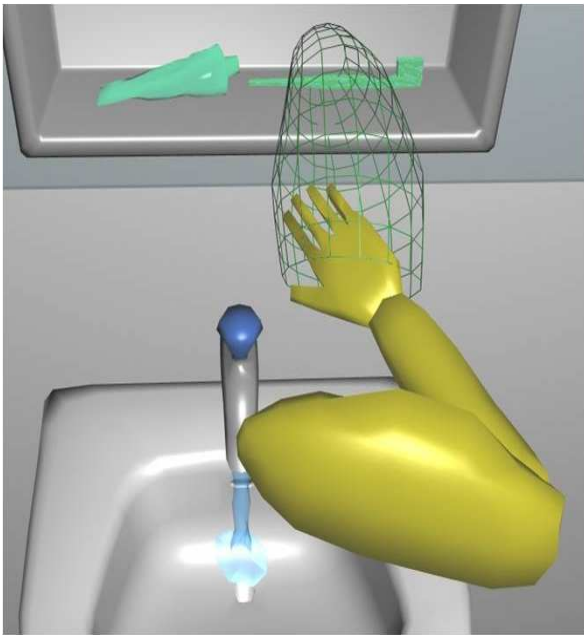


Fig. 2. Virtual tunnel to constrain motion for a reaching task with ARMin.

A main disadvantage of this implementation of Path Control is unproven stability, and cases can be constructed where the control may indeed get unstable. One example is varying tunnel width, with the aim to adapt the amount of freedom to the movement phase. Then, the behavior resulting from the nearest-neighbor-based attraction is not passive. Therefore, a modified approach is presented in the next section, which reformulates Path Control in terms of an intrinsically passive potential field.

IV. TRANSPARENCY AND CONSTRAINTS: GENERALIZED ELASTIC PATH CONTROL

The transparency-enhancing potential field represented by the Generalized Elasticities of Sec. II is optimized based on training data that lies *within* the allowed region. The path controller of Sec. III is only active *outside* the allowed region. Therefore, both strategies can easily be combined to one unified potential field, as a potential field can be used as well to encode virtual walls. To generate additional training data that can be added to the training data of Sec. II, the forces of a simulated nearest-neighbor search are assigned to the region outside the tunnel. The unified concept then still hides robot dynamics inside the allowed spatial region in an optimal way, letting the human move unhindered there, and it includes virtual tunnels to prevent the human from leaving this allowed region. The main advantage is that the potential field approximates the forces of the nearest-neighbor-based controller in an optimal way, preserving as much as possible of its behavior, but ensuring passivity. This combined strategy of Generalized Elasticities and Path Control is called “Generalized Elastic Path Control”. Until now, it has only been implemented for the Lokomat.

V. PRELIMINARY RESULTS

In direct comparison with closed-loop force control with and without gravity compensation, Generalized Elasticities showed to be most effective in terms of transparency for healthy subjects walking in the Lokomat [19]. Experiments with Generalized Elastic Path Control [20] show that the described effect in transparency is maintained, and that the conservative force field also provides a safe training frame, because it prevents dangerous movements.

To illustrate the selective effect of Generalized Elastic Path Control, the results of one healthy subject are shown, who walked with Generalized Elastic Path Control in the Lokomat under two conditions: The subject walked once normally, and once simulating an isolated deficiency (in weight bearing during stance). A rather wide tunnel was used, only preventing dangerous situations.

When the subject walked normally, i.e. without weight bearing deficiencies, average interaction torques were low over the whole gait cycle (considering the high inertia of the robot) (Fig. 3). When the subject showed deficient weight bearing capacities, it can be seen that the interaction torques between robot and human at the knee joint are still low for all movement instances expect for stance. Then, the knee weakness leads to excessive knee flexion, which leaves the range of allowed movements within the tunnel, and supportive forces are generated to help the subject extend the knee.

VI. DISCUSSION

The results show that optimizing passive behavior of a rehabilitation robot can be effective to enhance transparency, and that the concept of Path Control provides a safe training frame that only generates forces when needed. Using these two fundamental components of patient-cooperative behavior

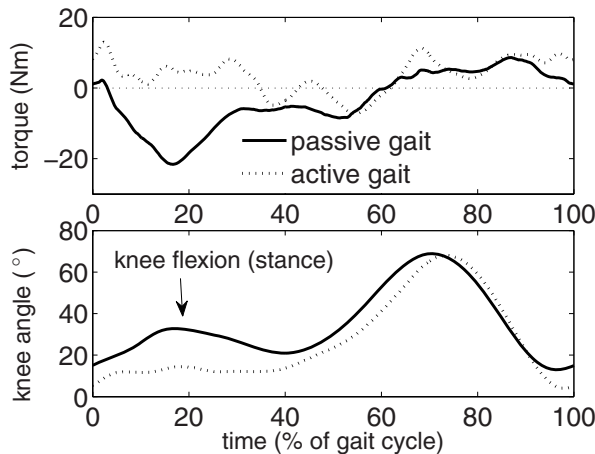


Fig. 3. Torque in response to an active gait style, and to gait with deficient weight bearing. The gait cycle begins at heel strike.

as a basis, the third control component, which encodes the individual intervention (such as assistive forces, error augmentation, etc.), can be superimposed.

VII. CONCLUSION AND OUTLOOK

In this paper, three fundamental components of patient-cooperative training have been distinguished: Transparency, constraints, and intervention. Focusing only on the first two issues, control concepts both for upper and lower extremity rehabilitation robots have been compared on the examples of the upper extremity exoskeleton ARMin and the lower extremity exoskeleton Lokomat. The control concept of Generalized Elasticities has been described, which hides robot dynamics when interacting with a human, as well as the Path Control concept, which confines the human to an allowed region. Furthermore, Generalized Elastic Path Control has been described, which unifies both transparency enhancement and movement constraints. The method is based on potential fields. Preliminary results with the Lokomat indicate that both transparent behavior and motion constraints can be realized effectively. This means that the robot provides a safe training environment while still leaving maximum freedom to the subject.

Future work will aim to incorporate Generalized Elasticities also in ARMin, in order to allow more generic and dynamic arm movements with improved transparency. A further focus will be on developing superimposed controllers for both robots that realize individually tailored interventions for each patient to maximize rehabilitation outcome.

ACKNOWLEDGMENTS

The contents of this publication were developed in part with support of the National Center of Competence in Research (NCCR) on Neural Plasticity and Repair of the Swiss National Science Foundation and in part under a grant from the US Department of Education, NIDRR grant number H133E070013. However, those contents do not necessarily represent the policy of the US Department of Education, and you should not assume endorsement by the Federal Government of the United States of America.

REFERENCES

- [1] T. G. Hornby, D. D. Campbell, J. H. Kahn, T. Demott, J. L. Moore, and H. R. Roth. Enhanced gait-related improvements after therapist- versus robotic-assisted locomotor training in subjects with chronic stroke: a randomized controlled study. *Stroke*, **39**(6):1786–1792, 2008.
- [2] J. Hidler, D. Nichols, M. Pelliccio, K. Brady, D. D. Campbell, J. H. Kahn, and T. G. Hornby. Multicenter randomized clinical trial evaluating the effectiveness of the lokomat in subacute stroke. *Neurorehabilitation and Neural Repair*, **23**(1):5–13, 2009.
- [3] R. Shadmehr and F. A. Mussa-Ivaldi. Adaptive representation of dynamics during learning of a motor task. *Journal of Neuroscience*, **14**:3208–24, 1994.
- [4] R. A. Scheidt, J. B. Dingwell, and F. A. Mussa-Ivaldi. Learning to move amid uncertainty. *Journal of Neurophysiology*, **86**:971–85, 2001.
- [5] E. Taub, G. Uswatte, and R. Pidicki. Constraint-induced movement therapy: a new family of techniques with broad application to physical rehabilitation: a clinical review. *Journal of Rehabilitation Research & Development*, **36**(3):237–51, 1999.
- [6] L. L. Cai, A. J. Fong, C. K. Otoshi, Y. Liang, J. W. Burdick, R. R. Roy, and V. R. Edgerton. Implications of assist-as-needed robotic step training after a complete spinal cord injury on intrinsic strategies of motor learning. *Journal of Neuroscience*, **26**(41):10564–8, 2006.
- [7] N. Hogan, H. I. Krebs, B. Rohrer, J. J. Palazzolo, L. Dipietro, S. E. Fasoli, J. Stein, R. Hughes, W. R. Frontera, D. Lynch, and B. T. Volpe. Motions or muscles?: Some behavioral factors underlying robotic assistance of motor recovery. *Journal of Rehabilitation Research & Development*, **43**(5):605–18, 2006.
- [8] H. I. Krebs, J. J. Palazzolo, L. Dipietro, B. T. Volpe, and N. Hogan. Rehabilitation robotics: Performance-based progressive robot-assisted therapy. *Autonomous Robots*, **15**:7–20, 2003.
- [9] G. A. Pratt, M. M. Williamson, P. Dillworth, J. Pratt, K. Ulland, and A. Wright. Stiffness Isn't Everything. In *International Symposium on Experimental Robotics (ISER)*. 1995.
- [10] H. Vallery, J. Veneman, E. van Asseldonk, R. Ekkelenkamp, M. Buss, and H. van der Kooij. Compliant Actuation of Rehabilitation Robots - Benefits and Limitations of Series Elastic Actuators. *IEEE Robotics and Automation Magazine (RAM)*, **15**(3):60–69, 2008.
- [11] N. Hogan. Impedance control: An approach to manipulation. Part I - Theory, Part II - Implementation, Part III - Applications. *ASME Journal of Dynamic Systems, Measurement, and Control*, **107**:1–24, 1985.
- [12] B. S. und O. Khatib (ed.). *Handbook of Robotics*. Springer, 2008.
- [13] E. Colgate and N. Hogan. An analysis of contact instability in terms of passive physical equivalents. In *Proceedings of the IEEE International Conference on Robotics and Automation (ICRA)*, pp. 404–409. Scottsdale, AZ, USA, 1989.
- [14] L. Rosenberg. *Virtual fixtures: Perceptual overlays enhance operator performance in telepresence tasks*. Ph.D. thesis, Stanford University, CA, 1994.
- [15] J. v. Zitzewitz, A. Duschau-Wicke, M. Wellner, L. Lünenburger, and R. Riener. Path control: a new approach in patient-cooperative gait training with the rehabilitation robot Lokomat. In *Tagungsband der BMT 3-Länder-Tagung*. Zrich, 2006.
- [16] S. Banala, A. Kulpe, and S. Agrawal. A Powered Leg Orthosis for Gait Rehabilitation of Motor-Impaired Patients. In *Proceedings of the IEEE International Conference on Robotics and Automation (ICRA)*, pp. 4140–4145. 2007.
- [17] G. Colombo, M. Wirz, and V. Dietz. Driven gait orthosis for improvement of locomotor training in paraplegic patients. *Spinal Cord*, **39**(5):252–255, 2001.
- [18] T. Nef, M. Mihelj, and R. Riener. ARMin: a robot for patient-cooperative arm therapy. *Medical & Biological Engineering & Computing*, **45**(9):887–900, 2007.
- [19] H. Vallery, A. Duschau-Wicke, and R. Riener. Optimized Passive Dynamics Improve Transparency of Haptic Devices. In *Proceedings of the IEEE International Conference on Robotics and Automation (ICRA)*. 2009, to appear.
- [20] H. Vallery, A. Duschau-Wicke, and R. Riener. Generalized Elasticities Improve Patient-Cooperative Control of Rehabilitation Robots. Submitted for the IEEE International Conference on Rehabilitation Robotics (ICORR), 2009.
- [21] M. Guidali, M. Bchel, V. Klamroth, T. Nef, and R. Riener. Trajectory Planning of ADL Tasks for an Exoskeletal Arm Rehabilitation Robot. In *Proceedings of European Conference on Technically Assisted Rehabilitation (TAR)*. 2009, to appear.

Estimation of Physical Performance for Elderly People via Markerless Sit to Stand Analysis

M. Goffredo, R. Muscillo, M. Gneo, M. Schmid, S. Conforto, T. D'Alessio

Applied Electronics Department, University of "Roma TRE", Rome, Italy

Abstract— We propose a novel system for automatically assessing physical performance in elderly people. We concentrated on the kinematic analysis of the Sit-to-Stand (STS) task since it is widely recognised that the inability to rise from a seated position is associated with physical impairment and risk of falling. The approach implements a markerless kinematic analysis by applying a method working on the Gauss-Laguerre transformed domain. Limbs' pose is analysed and compared with a normality trend, obtained from young subjects. A parameter representing the strategy used for raising from the chair, and correlated to the physical assessment, is extracted. Experimental tests on a population of elderly people are conducted and results are compared with scores from the Short Physical Performance Battery and the Tinetti's Test.

Keywords— Physical Performance, Sit to Stand, Markerless Movement Analysis.

I. INTRODUCTION

Balance maintaining and mobility controlling are critical factors for decreasing the risk of disability and mortality in elderly people. Recently, scientific community increases interest in the use of physical performance assessment tools for objectively evaluating physical conditions [1]. The possibility of objectively assessing physical ability and disability is particularly appealing since it traditionally relied on self-report and clinician's qualitative visual observations. Several studies demonstrated that physical performance measures are reliable source of information on elderly subjects' conditions and that they can predict outcomes such as falls [2]. Physical Performance batteries generally do not require special equipment, are low-cost and relatively quick to perform [1][3][4]. However, technical trained staff is required to obtain an objective and reliable assessment.

In this context, we present a novel system for automatically assessing physical performance. The method does not require technical human intervention and it is based on the markerless kinematic analysis of Sit-to-Stand task (STS). It is widely recognised, in fact, that the inability to rise from a seated position is associated with an increased risk of falling and hip fracture [5][2] and

clinical tests for STS movement performance are highly correlated with physical functioning in elderly people [6]. STS analysis is part of performance batteries, such as [1], but scores are defined by means of the time spent to execute the task, while no information regarding limb's pose and the way the movement is performed are included. To this extent, it is widely recognised that elderly people with mobility problems present larger trunk oscillations while maintaining their legs almost still during the execution of STS ("fully forward" strategy) [7][8]. For this reason, we propose a method that is able to assess physical condition by means of the quantitative kinematic analysis of STS.

The markerless approach introduced by the authors in [9] will be used because of the need of executing the test without any markers or devices applied on the body, rapidly and in the most natural conditions. The method is based on the Gauss-Laguerre transformed (GLT) domain, which allows estimating both the translations and the rotations of some relevant anatomical points with a matching pattern algorithm. After the kinematic analysis is performed, the limbs' orientation trend will be analysed: a specifically designed approach, based on Dynamic Time Warping (DTW) [10], will extract a normality reference trend from young subjects. A parameter describing the strategy used for raising from the chair, and therefore the physical performance, will be extracted from the kinematic data.

Experimental tests on a large number of elderly people are conducted and results are compared with scores from two physical performance batteries: the Short Physical Performance Battery (SPPB) [1] and the Tinetti's Test (TIN) [3].

II. MATERIALS AND METHODS

The proposed method for automatic physical performance assessment is based on the markerless kinematic analysis of STS manoeuvre. The physical performance parameter is extracted by using a 2D human body model. The physical performance is then evaluated by applying a specifically designed method which compares the STS strategy parameter value with the normality reference

value obtained from the analysis of healthy young subjects. Figure 1 summarizes the approach.

A. Markerless Analysis and 2D Body Model

The kinematic analysis of STS task is achieved by applying the markerless method for joints' tracking described in a previous work of the authors [9]. The approach transforms the video frames at every instant $\mathbf{t}=[t_1, t_2, \dots, t_p, t_{i+1}, \dots, t_T]$ by using an orthogonal family of Circular Harmonic Functions, the Gauss-Laguerre polynomials, with order n and degree k :

$$I_k^{(n)}(t) = \frac{t^{-n} e^t}{k!} \frac{d^k}{dt^k} [t^{k+n} e^{-t}] = \sum_{h=0}^k (-1)^h \binom{n+k}{k-h} \frac{t^h}{h!} \quad (1)$$

In order to extract the joints' trajectories, relevant points at the shoulder, waist, knee, and ankle level ($s(t_i)$, $w(t_i)$, $k(t_i)$, $a(t_i)$) have been selected on the first frame of the video sequence. The estimation is obtained by means of GLT application on pairs of consecutive frames \mathbf{I}_i and \mathbf{I}_{i+1} . The estimated position $s(t_{i+1})$, $w(t_{i+1})$, $k(t_{i+1})$, $a(t_{i+1})$ is obtained with a Maximum Likelihood (ML) solution.

Considering a point of interest ξ in the frame \mathbf{I}_i , the ML functional is:

$$\ln \Lambda[\mathbf{I}_i(\mathbf{x}); \boldsymbol{\theta}] = -\frac{2}{N_0} \iint w(\mathbf{x} - \xi)^2 \cdot \left| \mathbf{I}_i(\mathbf{x}) - \mathbf{I}_{i+1} \left(R_\varphi \left(\frac{\mathbf{x} - \mathbf{b}}{a} \right) \right) \right|^2 d\mathbf{x} \quad (2)$$

where \mathbf{x} are the coordinates of a generic point in the image plane \mathbf{R}^2 , $\mathbf{b}=[b_1, b_2]^T$ is the displacement vector, a the scaling factor, φ the rotation angle, R_φ the rotation operator, $w(\mathbf{x})$ an appropriate weighting window that defines the region of interest, $\boldsymbol{\theta}=[b_1, b_2, a, \varphi]$ and $N_0/4$ is the power density spectrum of a white, zero-mean Gaussian Random field modelling all those effects that cannot be captured by a planar rigid motion approximation between frames.

The collection of ML maxima for each point defines the Gauss Laguerre Likelihood Map, whose absolute maximum indicates the pattern location along with the associate scale and orientation. By iterating the ML procedure to every point of interest and every frame of the video sequence, the matrix

$$\begin{bmatrix} \mathbf{S}(\mathbf{t}) \\ \mathbf{W}(\mathbf{t}) \\ \mathbf{K}(\mathbf{t}) \\ \mathbf{A}(\mathbf{t}) \end{bmatrix} = \begin{bmatrix} s(t_1) & s(t_2) & \dots & s(t_i) & \dots & s(t_T) \\ w(t_1) & w(t_2) & \dots & w(t_i) & \dots & w(t_T) \\ k(t_1) & k(t_2) & \dots & k(t_i) & \dots & k(t_T) \\ a(t_1) & a(t_2) & \dots & a(t_i) & \dots & a(t_T) \end{bmatrix} \quad (3)$$

is thus estimated.

Since STS movement mainly involves the anterior-posterior trunk, thighs and shins flexion-extension [8]

[11], it can be analyzed by using a 2D human body model which considers body segment displacements only in the sagittal plane. Therefore, a model of the human body composed of 4 body segments has been applied, as used in [8][9], and the trunk and shin flexion/extension ($\alpha(\mathbf{t})$ and $\gamma(\mathbf{t})$) have been extracted over time.

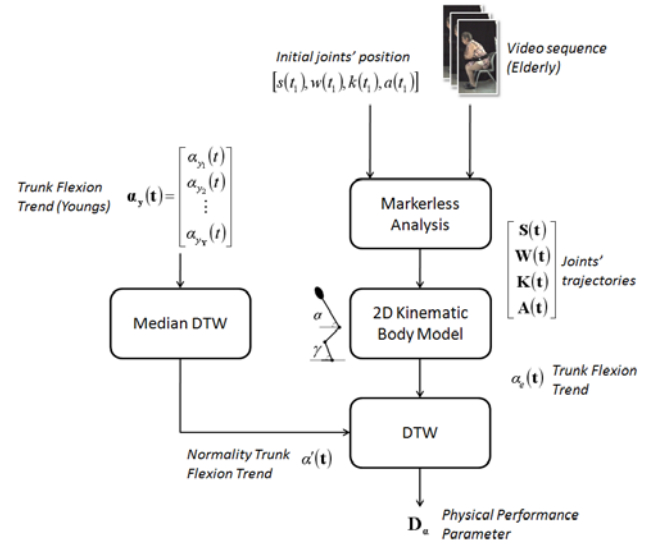


Fig. 1. Overview of the proposed approach.

B. Normality Trunk Flexion and Physical Performance Parameter

The subject can use two different strategies for rising from a chair: the “fully forward” strategy, which is characterised by large trunk flexions with increased peak trunk flexion angular velocity; or the “limited flexion” strategy, which is defined by a limited torque on the lumbar back and thus by larger ankle and hip flexions [8]. Studies demonstrated that elderly people with mobility problems use the “fully forward” strategy and present signs of countermovement phase ($\alpha(t_i) > 90^\circ$), similar to the one exerted by young adults when facing high power tasks, such as vertical jumping, which allows them to attain greater joint moment [1]. For this reason, the trunk flexion/extension angle $\alpha(\mathbf{t})$ has been chosen as a variable characterizing the STS strategy and thus subject's physical performance. In particular, the proposed method allows to extract the normality reference trunk flexion trend from the analysis of healthy young subjects.

The algorithm is based on the Dynamic Time Warping algorithm (DTW) that preserves signal's shape and is more robust with respect to misalignments and distortion effects with respect to classic average techniques and shape distance measures. The DTW algorithm is based on

the principle of signal comparison on the basis of waveform similarities. The extraction of the point to point correspondence between two time series (i.e. warping path, W) is achieved by finding the positions (i_w, j_w) of the minima in the matrix \mathbf{D} defined as:

$$\mathbf{D}(i, j) = \mathbf{d}(i, j) + \min[\mathbf{D}(i-1, j-1), \mathbf{D}(i, j-1), \mathbf{D}(i-1, j)] \quad (4)$$

where $\mathbf{d}(i, j)$ represents the distance between the i^{th} element of the first time series and the j^{th} element of the second one (Figure 2).

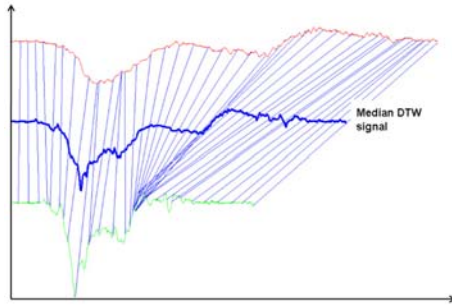


Fig.2 Graphical representation of the median DTW signal construction.

In order to estimate the normality trunk flexion trend $\dot{\alpha}(\mathbf{t})$, the time series $\alpha_Y(\mathbf{t})$, from the analysis of \mathbf{Y} young healthy subjects, is calculated through (4) by considering the median point between each point-to-point correspondence extracted from the warping path.

Given a trunk flexion trend $\alpha_e(\mathbf{t})$, obtained from the markerless analysis of the e^{th} elderly subject, the physical performance parameter $\mathbf{D}_\alpha(e)$ is extracted as the sum of $\mathbf{D}(i_w, j_w)$ distances on the warping path obtained between $\alpha_e(\mathbf{t})$ and $\dot{\alpha}(\mathbf{t})$. The \mathbf{D}_α value can be interpreted as an integrated parameter representing different features related to the way STS is performed such as the execution time, the minimum flexion angle and possible signs of counter-movement phase.

III. EXPERIMENTAL TESTS

A sample of $\mathbf{Y}=6$ healthy young (27 ± 4 years) and $\mathbf{E}=18$ elderly subjects (73 ± 7 years) participated to the tests. The subjects were recruited in the local community and provided written consent prior to participation.

To assess balance and movement disorders, two standardized physical performance batteries have been used according to Guralnik [1] and Tinetti [3]. Testing involves assessments of standing balance, walk, rising from a chair and sitting down. All timings were measured to the nearest 0.1s using a stopwatch. SPPB performance is scored between 0 and 12, while TIN values are between 0

and 24.

A digital camera (Silicon Imaging MegaCameras SI-3300RGB) fixed on a tripod was used to capture the STS sequences in an indoor environment. The video camera was set at a height of 1.2m and at 3.5m from the chair, with image plane parallel to subjects' sagittal plane. The video sequences (image resolution 1000x1400pixels, resolution about 1.72mm/pixel after rectification and calibration) were acquired with a time resolution of 25fps. The subjects sat in an armless chair (seat height 43cm) positioned perpendicularly to the video camera. The starting position of the knee was set at approximately 90° of flexion before each trial by adjusting initial foot placement. Each subject was then asked to execute the movement with the arms folded on the chest at a self-selected comfortable speed.

The video sequences have been analysed by applying the proposed markerless method to the points of interest $s(t_l)$, $w(t_l)$, $k(t_l)$, $a(t_l)$. As in [9], the generalized Laguerre polynomial used for the GLT of each portion of frame has been truncated at order $n=2$ and degree $k=7$.

Once the trajectory of each joint has been obtained, the corresponding human body model was run and the trunk flexion trends of young and elderly subjects, $\alpha_Y(\mathbf{t})$ and $\alpha_E(\mathbf{t})$ respectively, were extracted over time.

The normality trunk flexion trend $\dot{\alpha}(\mathbf{t})$ has been extracted from $\alpha_Y(\mathbf{t})$: since the obtained values are in accordance with [7], the young subjects that participated to the study can be considered as representative sample. The application of the DTW-based method on $\alpha_E(\mathbf{t})$ allowed to estimate the physical performance parameters $\mathbf{D}_\alpha(e)=[\mathbf{D}_\alpha(1), \mathbf{D}_\alpha(2), \dots, \mathbf{D}_\alpha(e), \dots, \mathbf{D}_\alpha(\mathbf{E})]$.

Comparative tests have been conducted by extracting the physical performance parameters \mathbf{D}_α both with the proposed method and with the classic Euclidean distance. Moreover, \mathbf{D}_α s have been compared with SPPB and TIN scores.

IV. RESULTS

In this section, results are shown. Figure 3 depicts the estimated trajectories obtained with the markerless analysis of a sample video sequences of the elderly subject D. The GLT algorithm allows to estimate the joints' position and appears particularly robust with respect to the human body deformation.

Figure 4 shows the normality trunk flexion trend $\dot{\alpha}(\mathbf{t})$ obtained from the \mathbf{Y} video sequences of young subjects. Moreover, $\alpha_D(\mathbf{t})$ from subject D is plotted. Figures show that the elderly subject presents a wider trunk oscillation,

a lower minimum value, a greater time to execute the movement, in accordance with [7][8].

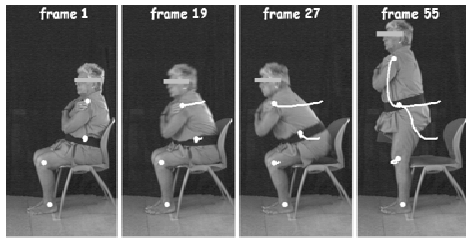


Fig. 3 Example of the markerless analysis (elderly subject D).

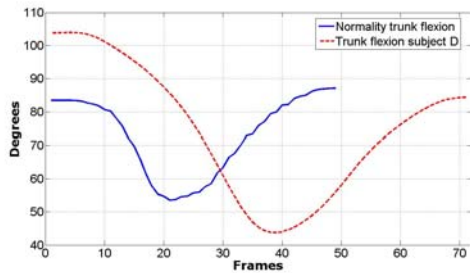


Fig. 4 Normality trunk flexion trend from the analysis of the young subjects (blue solid line) and example of elderly trunk flexion trend (red dot line).

Videos from all the E elderly subjects have been processed and the physical performance parameters $D_{\alpha}(e)$ have been extracted both with the proposed DTW-based approach and the Euclidean distance. $D_{\alpha}(e)$ s have been compared with SPPB and TIN scores in terms of correlation coefficient and p-values. Results in table 1 confirm that the proposed DTW method is more robust to shape deformation and length difference and is more reliable in the extraction of the physical performance parameter.

Table 1 Correlation coefficient and p-values between D_{α} -SPPBscore and D_{α} -TINscore

D_{α} extraction method	R_{SPPB}	p_{SPPB}	R_{TIN}	p_{TIN}
Euclidean distance	-0.757	0.0003	-0.368	0.1328
DTW method	-0.798	0.0001	-0.702	0.0011

Figure 5 depicts the relationship between $D_{\alpha}(e)$ and SPPB and TIN scores with the corresponding regression line. Results shows an acceptable correspondence with high correlation coefficients (>0.7) and low p-values (<0.001).

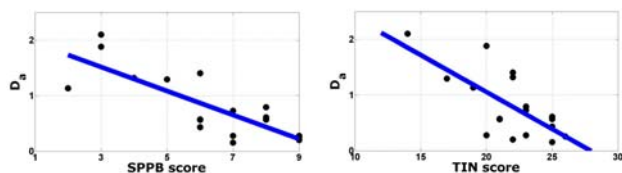


Fig.5 Relationship between D_{α} and SPPB and TIN scores with the corresponding regression line.

V. CONCLUSIONS

A novel approach for automatically assessing physical performance in elderly people has been presented. The method is based on the markerless kinematic analysis of Sit-to-Stand movement by applying a method based on the Gauss-Laguerre transformed domain. The analysis of limbs' orientation with a DTW-based approach extracts a normality trunk flexion trend from data of young healthy subjects and a parameter describing the physical assessment. Experimental tests on a large population of elderly people have been conducted. Our results, compared with scores from performance batteries, present high correlation coefficients (>0.7) and low p-values (<0.001). Further results on a larger population should confirm the reliability of the proposed method as tool for the automatic assessment of physical condition in elderly people.

REFERENCES

- Guralnik JM, Simonsick EM, Ferucci L et al. A short physical performance battery assessing lower extremity function: Association with self-reported disability and prediction of mortality and nursing home admission. *J Gerontol* 1994;49:M85–M94.
- B. Najafi, K. Aminian, F. Loew, Y. Blanc, P.A. Robert, Measurement of stand-sit and sit-stand transitions using a miniature gyroscope and its application in fall risk evaluation in the elderly *IEEE Trans TBME*, vol.49, pp.843-851, 2002.
- M. E. Tinetti, "Performance-oriented assessment of mobility problems in elderly patients," *J. Amer. Geriatr. Soc.*, vol. 34, pp. 119–126, 1986.
- Berg K. Measuring balance in the elderly: Validation of an instrument. *Can J Public Health*. 1992;83:S7-S11 .
- K. M. Kerr, J. A. White, D. A. Barr, R. A. B. Mollan, "Analysis of the sit-stand-sit movement cycle in normal subjects" *Clinical Biomech.*, vol.12, no.4, pp.236-245, Jun.1997.
- Shubert TE, Schrodtt LA, Mercer VS, Busby-Whitehead J, Giuliani CA., Are scores on balance screening tests associated with mobility in older adults?, *J Geriatr Phys Ther*. 2006;29(1):35-9.
- Papa E, Cappozzo A., Sit-to-stand motor strategies investigated in able-bodied young and elderly subjects., *J Biomech*. 2000 Sep;33(9):1113-22.
- M. Gross, P. Stevenson, S. Charette, G. Pyka, R. Marcus, "Effect of muscle strength and movement speed on the biomechanics of rising from a chair in healthy elderly and young women" *Gait Posture*, vol.8, no.3, pp.175-185, Dec. 1998.
- Goffredo, M., Schmid, M., Conforto, S., Carli, M., Neri, A., D'Alessio, T., Markerless Human Motion Analysis in Gauss-Laguerre Transform Domain: Application to Sit-to-Stand in Young and Elderly People, *Information Technology in Biomedicine, IEEE Transactions on*, Dec. 2008.
- R. Muscillo, S. Conforto, M. Schmid, P. Caselli, T. D'Alessio, Resolving ADL Activities Variability through Derivative Dynamic Time Warping applied on Accelerometer Data. *Proceedings of the 29th International Conference of the IEEE EMBS 2007*: 4930-33.
- D. W. Vander Linden, D. Brunt, M. McCulloch, "Variant and invariant characteristics of the sit-to-stand task in healthy elderly adults" *Arch Phys Med Rehabil.*, vol.75, no.6, pp.653-660, Jun.1994.

Using a P300 Brain Computer Interface for Smart Home Control

C. Holzner¹, C. Guger¹, C. Grönegress², G. Edlinger¹, M. Slater²

¹ g.tec medical engineering GmbH, Guger Technologies OEG, Graz, Austria

² Centre de Realitat Virtual, Universitat Politècnica de Catalunya, Barcelona, Spain

Abstract— An electroencephalogram (EEG) based brain-computer interface (BCI) was connected with a Virtual Reality system in order to control a smart home application. Therefore special control masks were developed which allowed using the P300 component of the EEG as input signal for the BCI system. Control commands for switching TV channels, for opening and closing doors and windows, for navigation and conversation were realized. Experiments with 12 subjects were made to investigate the speed and accuracy that can be achieved if several hundred of commands are used to control the smart home environment. The study clearly shows that such a BCI system can be used for smart home control. The Virtual Reality approach is a very cost effective way for testing the smart home environment together with the BCI system.

Keywords— EEG, BCI brain computer interface, P300, smart home, Virtual Reality

I. INTRODUCTION

An EEG based Brain-Computer Interface (BCI) measures and analyzes the electrical brain activity (EEG) in order to control external devices. BCIs are based on slow cortical potentials [1], EEG oscillations in the alpha and beta band [2, 3], the P300 response [4] or steady-state visual evoked potentials (SSVEP) [5]. BCI systems are used mainly for moving a cursor on a computer screen, controlling external devices or for spelling purposes [2, 3, 4].

BCI systems based on slow cortical potentials or oscillatory EEG components with 1-5 degrees of freedom were realized up to now. However, high information transfer rates were reached based on 2 degrees of freedom as otherwise the accuracy of the BCI systems dropped down. SSVEP based systems allow selecting up to 48 different targets and are limited by the number of distinct frequency responses that can be analyzed in the EEG. P300 response based BCIs typically used a matrix of 36 characters for spelling applications [4].

In a previous BCI study three subjects participated in a spelling experiment and were trained firstly in spelling characters and numbers based on their P300 EEG response [6]. Therefore, the characters of the English alphabet (A, B,...Z) and Arabic numbers (1, 2,...9) were arranged in a 6

x 6 matrix on a computer screen. Then the characters were highlighted in a random order and the subject had the task to concentrate on the specific character he/she wanted to spell. All experiments were undertaken in 2 modes: (i) the row/column speller – all items of one row or column are highlighted at the same time, (ii) the single character speller – only one character is highlighted. For the single character speller each character was highlighted 15 times. For the row/column speller each row and each column was also highlighted 15 times. This results in a speed up of 3 for the row/column speller. Therefore the BCI system was trained based on the P300 response of 42 characters of each subject with 15 flashes per character (about 40 minutes training time). All 3 subjects needed between 3 and 10 flashes (mean 5.2) per character to reach an accuracy of 95 % for the single character speller and between 4 and 11 flashes (mean 5.4) for the Row/Column speller. This resulted in a maximum information transfer rate of 84 bits/s (60 ms per character flash time) for the single character speller and 65 bits/s (100 ms per character flash time) for the row column speller.

Based on this previous study this work shows the usage of a P300 based BCI system to control a smart home environment. The usability of the BCI implementation will be tested to control many different elements of a house. Of special interest was to test the accuracy of different control masks in the smart home application.

II. METHODS

The smart home was implemented in XVR (extreme VR, University of Pisa) as virtual representation of a real one. Through a UDP interface the P300 based BCI system was connected to it. A bird's eye view of the virtual 3D representation of a smart home with different control elements is shown in Figure 1.

In the experiment it should be possible for a subject to switch on and off the light, to open and close the doors and windows, to control the TV set, to use the phone, to play music, to operate a video camera at the entrance, to walk around in the house and to move him/herself to a specific location in the smart home. Therefore special control masks



Figure 1: Virtual representation of a smart home

for the BCI system were developed containing all the different necessary commands. In total 7 control masks were created: a light mask, a music mask, a phone mask, a temperature mask, a TV mask (see Figure 2), a move mask and a go to mask (see Figure 3).

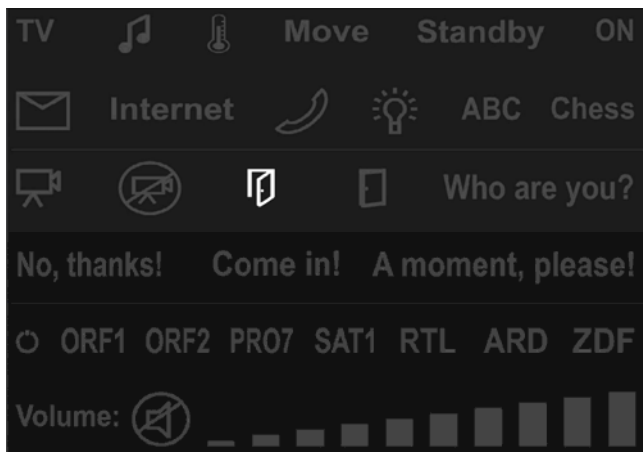


Figure 2: Control mask with the main menu in the first 2 rows, the icons for the camera, door control and questions in the 3rd and 4th row and the TV control in the last 2 rows.



Figure 3: Control mask for going to a specific position in the smart home. The mask gives a bird's eye view of the apartment with characters at specific positions.

12 subjects participated in the experiments and were trained firstly on selecting specific commands from the P300 matrices. Each person had to select 7 icons of each of the 7 control masks for training the computer system on its individual EEG data. Therefore the characters were highlighted in a random order and the subject had the task to concentrate on the specific character he/she wanted to spell. All experiments were undertaken in a so called single character speller mode where only one character is highlighted at one specific time point. In order to increase the recognition accuracy it is necessary to highlight each character several times. In this experiment we tested the system with 8, 4 and 2 flashes of each character to test the accuracy and speed that can be achieved.

Another important parameter in the P300 experiment is the flash time (character is highlighted) and the dark time (time between 2 highlights). Both times should be as short as possible to reach a high communication speed, but must be long enough so that the subject can detect the flash and that the single P300 responses are not overlapping.

The training with 7 characters per mask took about 45 minutes and based on this data the BCI system was trained to recognize the specific EEG response. The experiment for the P300 smart home control was divided into 23 decisions involving all 7 control masks. One task was e.g. to go to the living room, to switch on the TV and to select a specific channel, ...

III. RESULTS

Table 1 shows the results of the 12 subjects averaged over all decisions for 8, 4 and 2 flashes and the mean for the three flash rates. The best result was achieved for subject 6

with 100 % accuracy for 8 and 4 flashes. The worst results had subject 3 with only 30 % accuracy for 2 flashes. Except for subject 1 and 2, which have a constant success rate, there is an identifiable difference between the flash rates.

Table 1: Classification results of the BCI based system for all subjects and all decisions. Column 2 gives the result for 8 flashes, column 3 the result for 4 flashes and column 3 the result for 2 flashes. The last row shows the average success of every subject.

Flashes	8	4	2	Mean
Subject1	82,61%	86,96%	78,26%	82,61%
Subject2	86,96%	78,26%	78,26%	81,16%
Subject3	65,22%	43,48%	30,43%	46,38%
Subject4	65,22%	56,52%	43,48%	55,07%
Subject5	91,30%	73,91%	65,22%	76,81%
Subject6	100,00%	100,00%	69,57%	89,86%
Subject7	69,57%	60,87%	39,13%	56,52%
Subject8	95,65%	82,61%	47,83%	75,36%
Subject9	82,61%	60,87%	56,52%	66,67%
Subject10	69,57%	69,57%	34,78%	57,97%
Subject11	60,87%	60,87%	47,83%	56,52%
Subject12	82,61%	60,87%	52,17%	65,22%
Total	79,35%	69,57%	53,62%	67,51%

Therefore it is interesting to compare the different masks for all subjects. Figure 3 shows the accuracies for all 7 masks. The light mask was used in the experiment for example 4 times and the total accuracy was 65,28 %. The best accuracies were achieved for the Music, Move and Temp masks. Clearly the worst accuracy had the GoTo mask.

Mask	Light	Music	Phone	Temp	TV	Move	GoTo
1	80,56%	75,00%	63,89%	75,00%	58,33%	86,11%	27,78%
2	58,33%	77,78%	63,89%	75,00%	63,89%	69,44%	25,00%
3	63,89%	80,56%		83,33%	75,00%	72,22%	
4	58,33%	69,44%		72,22%			
5		77,78%					
Total	65,28%	76,11%	63,89%	76,39%	65,74%	75,93%	26,39%
# Icons	25	50	30	38	40	13	22

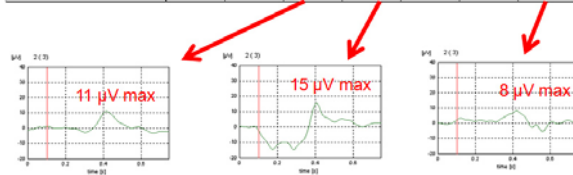


Figure 3: Accuracy for different masks for all subjects and number of icons on each mask. The last row shows the grand average for the P300 evoked potentials for three masks.

Therefore the P300 component was inspected for three masks. The P300 response of the Temp mask reaches amplitudes of about 15 µV, the P300 response of the Phone mask reaches amplitudes of 11 µV and the GoTo mask only 8 µV.

From figure 4 it can be seen that the accuracy for all masks is rather constant for a specific flash rate. However, the accuracy for the Goto Mask was the clearly the worst for all flash rates.

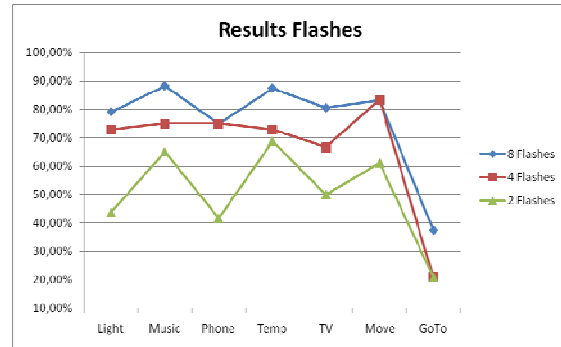


Figure 4: Accuracy for all masks as function of 8, 4 and 2 flashes.

IV. DISCUSSION

The P300 based BCI system was successfully used to control a smart home environment with an accuracy of 79 % for 8 flashes, an accuracy of 70 % for 4 flashes and 54 % for 2 flashes for all subjects. The accuracy was of course higher if each item flashed up more often. But it was necessary to test the achievable speed since we already knew that the P300 BCI system can be controlled with very high accuracy using 15 flashes [6].

Subject 6 was able to control the system with 100 % accuracy even with only 7 training icons per mask. Even the worst subject 11 still achieved an accuracy of 61 % with 8 flashes. It must be noted that 7 training icons require only about 5 minutes of training time and this is really a very short time compared to other BCI realizations. But the goal of this study was not to achieve the best accuracy and fastest time, it was to show the performance of different mask types.

Interesting is that three masks with different numbers of icons (Music mask with 50 icon, Temp 38 and Move just 13) were the best masks with around 75 % accuracy. Typically the amplitude of the P300 potential increases if more icons are used because the likelihood that the specific icon is highlighted is smaller resulting usually in a higher P300 response. However, even the Move mask was as good controlled as the other two mask with only 13 icons. Of

special interest is the GoTo mask which appears to be quite similar to all the other masks. The mask had 22 icons and therefore more than the Move mask but achieved only a total accuracy of 26 %. Also the P300 analysis shows that the resulting amplitude is smaller than for the other masks. The reason for that could be the layout of the mask itself which will be investigated in further studies.

The experiment yielded 2 important new facts: (i) instead of displaying characters and numbers to the subject also different icons can be used, (ii) the BCI system must not be trained on each individual character. The BCI system was trained with EEG data of the 7 randomly selected icons and the subject specific information was used for all other commands. This allows using icons for many different tasks without prior time consuming and boring training of the subject on each individual icon. This reduces the training time in contrast to other BCI implementations where hours or even weeks of training are needed [1, 2, 3]. This reduction in training time might be important for locked-in and ALS patients who have problems with the concentration over longer time periods. The P300 concept works also better if more items are presented in the control mask as the P300 response is more pronounced if the likelihood that the target character is highlighted drops down [4]. This results of course in a lower information transfer rate, but enables control of almost any device with such a BCI system. Especially applications which require reliable decisions are highly supported. Therefore the P300 based BCI system is an optimal tool for the smart home control. The virtual smart home acts in such experiments as a testing installation for real smart homes. Also wheelchair control, which many authors identify as their target application, can be realized with this type of BCI system in a goal oriented way. In a goal oriented BCI approach it is then not necessary e.g. to move a robotic hand by thinking about hand or foot movements and controlling right, left, up, down commands. Humans just think "I want to grasp the glass" and the real command is initiated by this type of BCI implementation.

V. CONCLUSIONS

A P300 based BCI system is optimally suited to control smart home applications with high accuracy and high reliability. Such a system can serve as an easily reconfigurable and therefore cheap testing environment for real smart homes for handicapped people.

ACKNOWLEDGEMENT

The work was funded by the EU projects PRESENCIA and SM4ALL.

REFERENCES

- [1] Birbaumer N, Ghanayim N, Hinterberger T, Iversen I, Kotchoubey B, Kübler A, Perelmouter J, Taub E, Flor H (1999) A spelling device for the paralysed, *Nature*, vol. 398, pp. 297- 298.
- [2] Guger C, Schlögl A, Neuper C, Walterspacher D, Strein T, Pfurtscheller G (2001) Rapid prototyping of an EEG-based brain-computer interface (BCI), *IEEE Trans. Rehab. Engng.*, vol. 9 (1), pp. 49-58.
- [3] Vaughan T M, Wolpaw J R, Donchin E (1996) EEG-based communication: Prospects and problems, *IEEE Trans. Rehab. Engng.*, vol. 4, pp. 425-430.
- [4] Krusienski D, Sellers E, Cabestaing F, Bayouth S, McFarland D, Vaughan T, Wolpaw J (2006) A comparison of classification techniques for the P300 Speller, *Journal of Neural Engineering*, vol. 6, pp. 299 – 305.
- [5] McMillan G R, Calhoun G L et al (1995) Direct brain interface utilizing self-regulation of steady-state visual evoke response, in *Proceedings of RESNA*, June 9-14, pp.693-695.
- [6] Guger C, Holzner C, Groenegress C, Edlinger G, Slater M (2008) Control of a Smart Home with a Brain-Computer Interface, *Proc. 3rd BCI workshop at University of Technology Graz*.

Author: Clemens Holzner
 Institute: Guger Technologies OEG
 Street: Sierningstrasse 14
 City: 4521 Schiedlberg
 Country: Austria
 Email: holzner@gtec.at

The use of muscle “creep” as opposed to relaxation in stretching braces: a pseudoelastic device

S. Pittaccio and S. Viscuso

Italian National Research Council, Institute for Energetics and Interphases, Lecco, Italy

Abstract— Traditional orthoses reduce muscle contractures by constraining limbs in increasingly more extended positions in which muscles and tissues relax. This paper proposes a new approach to achieve muscle stretching by applying a quasi-constant force without constraining any particular position. This is possible by exploiting the wide deformation range and peculiar mechanical response of pseudoelastic NiTi, which was utilized to build an elbow brace (EDGES). Per-clinical tests on two hemiplegic patients showed that improvement of resting elbow angle can be achieved in a week’s application and that this type of orthosis is much more easily accepted by patients than traditional ones. Further tests will address the possibility of stabilizing elbow posture through plastic tissue remodeling.

Keywords—Pseudoelasticity, Ni-Ti, rehabilitation, remodeling

I. INTRODUCTION

Nearly 17% of post-stroke patients develop spastic contractures within the first 6 months after stroke [1]. Spastic muscles management commonly includes the use of static orthoses which achieve muscle relaxation through a sequence of constrained positions more and more stretched. This approach causes a number of problems: first of all, the spastic response elicited at every stretching step provokes great pain to the patients. Furthermore, static splinting does not allow for any movement of the constrained joint, which is not good for functional rehabilitation on the basis of patho-physiological considerations such as the insurgence of contractures and of learned non-use [2]. Moreover, post-stroke patients commonly show involuntary jerks or contraction patterns involving the spastic limbs, thus constraining movement causes further pain during these pathological episodes. That is also the reason why traditional static orthoses are not very well accepted by the patients, who usually can tolerate splinting for only few hours a day.

The present study suggests a different approach to passive muscle stretching and splinting therapy. It also investigates the use of smart materials to provide the appropriate combination of loading and positioning to match the requirement of such new approach. In particular, a pseudoelastic device for treating (or preventing) elbow contractures was designed. Evidence from technical characterization and pre-clinical tests is presented.

II. BACKGROUND

A. Muscle plastic remodeling and lengthening therapy

In the practice of physical therapy methods of lengthening muscle groups to improve articularity are widespread for the treatment of several neuromuscular pathologies, among which some sequelae of stroke. The basic idea is that a maintained stretch of contracted muscles will cause them to increase in length, so that wider articular ranges of motions can become functionally available to the patient. The means by which such stretch is provided is traditionally through fixation of the joint angle in an extended position. Subsequently a “relaxation” in the set posture is expected. In fact, this “relaxation” is a viscoelastic, but mainly *plastic*

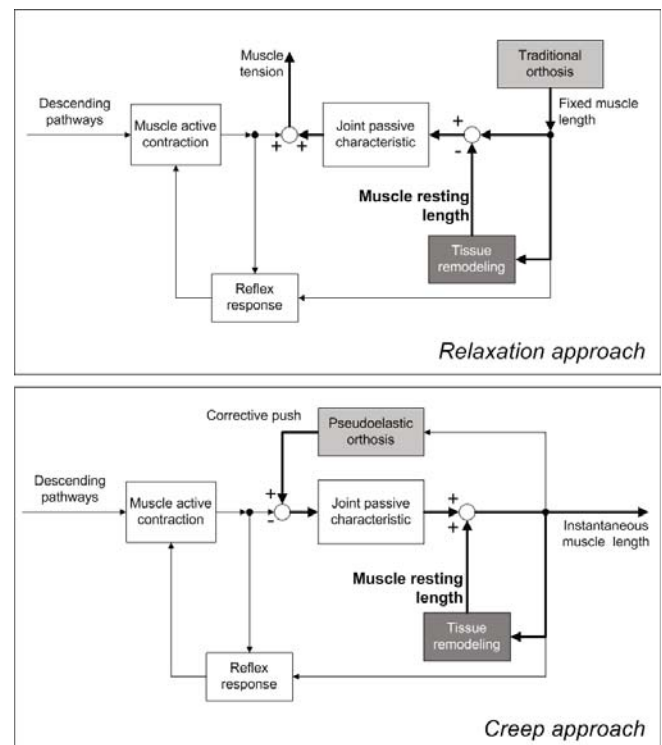


Fig. 1 Schematics of the “relaxation” and “creep” approaches in comparison. Bold lines represent principal directions along which muscle lengthening is achieved by bracing. Also additional outputs of interest are shown.

process, as it should be, since permanent muscle remodeling is required. Holding on to a viscoelastic metaphor, it could be argued that muscle lengthening might be achieved by “creep” instead, which the present work suggests.

B. “Visco-elasto-plastic creep”

The principle that a *plastic creep* can be envisaged in biological terms is drawn from the observation that a permanent force acting along a muscle would impart sufficient stretch to promote remodeling and lengthening even though joint position is not directly controlled. The virtue of such an approach lies in the following considerations:

1. as the definition of creep includes change in length or position, it is implicit that there will be no need for adjustments in orthosis angle, as that parameter is bound to evolve;
2. the fact that position is not fixed *a priori* implies that freedom of movement is preserved in principle;
3. the fact that a force (rather than position) leads the lengthening process makes freedom of movement practically possible provided that that force is not too large (e.g. lower than active muscular force);

From considerations 2 and 3 descend some important ideas for a different approach to therapy: first, the fact that joint position is never fixed implies that immobility as a cause of worsening paresis is shunned; second, the fact that the corrective force can be surpassed by muscular strength entails that in dystonia or myoclonus less pain is expected to arise as compared to the case of (in)voluntary movements initiated against unyielding constraints (such as with braces that fix a joint angle); third, that as position depends on the equilibrium between instantaneous muscular and corrective forces, improvement is likely to be more naturally linked to the current conditions of the patients and pace would partially self-adjust (Fig.1).

This framework inevitably leads to the practical issue of devising an efficient device to carry out this treatment, in much the same fashion as traditional orthotics are appropriate for imparting step-wise elongations pointing at “relaxation”. It is believed that a pseudoelastic device could be used to exert the required maintained force for creep.

C. Pseudoelastic alloys

Pseudoelasticity is the unique ability of some alloys (typically Ni–Ti alloys, with nickel content more than 50.6%at) of recovering up to 8% of deformation fully. This behavior is due to crystallographically reversible phase transformations occurring in the solid state [3], from austenite to martensite during loading and vice versa on unloading. Deformation and shape recovery occur in a pseudo-plastic

manner, through extended plateaux along which stress remains constant. Besides their peculiar mechanical characteristics, pseudoelastic Ni–Ti is very biocompatible and thus it is commonly utilized in biomedical applications such as cardiovascular stents and orthodontic wires. This unusual behavior could be exploited to apply to contracted muscles the quasi-constant stress required to induce tissue remodeling through *creep*. Alternative solutions (e.g. electromechanical actuators, hydraulic systems...) would generally be quite bulky and probably not practical to develop a wearable device, especially in certain anatomical contexts.

III. MATERIALS AND METHODS

A. Pseudoelastic orthosis

A pseudoelastic brace for treating the contracted elbow was designed taking inspiration from traditional splints and it was given the name of EDGES (Fig. 2). The interface to the patient’s skin is implemented using padded thermoplastic shells, which are easily customized to fit individual arm sizes. The main difference with respect to traditional orthoses is in the shell coupling. EDGES mounts two polycentric hinges that can be aligned to the anatomical elbow joint pivot, but cannot be fixed at any particular angle. In contrast, they are equipped with four pseudoelastic bars, which are mounted with a bending pre-load exerting an extensional torque, so that the resting position of the orthosis is straight.

For the present study Ti–Ni50.7%at alloy bars (2mm in diameter) were chosen. They were thermally treated at 673K for 1 hour and water quenched to set straight shape. Tensile tests on samples of the bars are displayed in Fig. 3. The graph shows the typical hysteretic behavior in the stress-strain plane. A similar feature can be also recognized in the bending test curves obtained for the assembled orthosis, as depicted in Fig. 4. For the present application, it can be noticed that the lower plateau (associated to shape

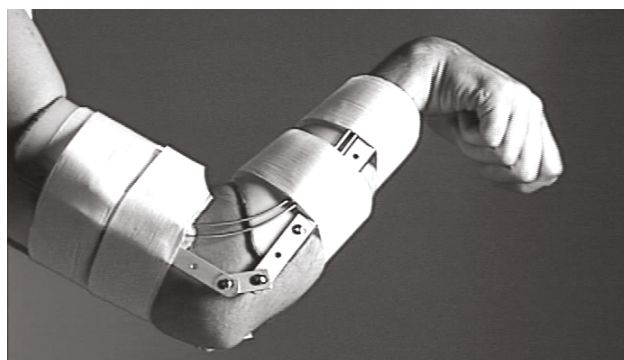


Fig. 2 The EDGES orthosis.

recovery) represents the level that can be exploited to produce muscle creep. Bending loads the material cross section in an inhomogeneous way, and this results in a different curve shape with respect to tensile trials. In particular, the pseudoplastic plateaux are mingled with the linear domains and the overall behavior is a slanted relatively-low force hysteresis loop in the torque-angle plane. In spite of this observation, the principle of creep holds quite robustly valid, as, even though force is not strictly constant with angle, it will be quasi-constant in time, provided arm extension evolve slowly, which is expected during this type of therapy.

B. Clinical protocol

EDGES was tested in a clinical setting on two stabilized post-stroke patients (more than 6 months from the ischemic event). They were both chronically affected by contracture and spasticity at the elbow following stroke. Their characteristics are presented in Table 1. Patients were treated ac-

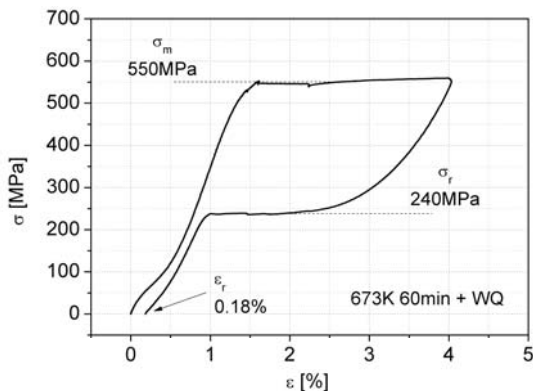


Fig. 3 Stress-strain characteristic of the chosen pseudoelastic Ni-Ti alloy. A small residual deformation is present at the end of the cycle.

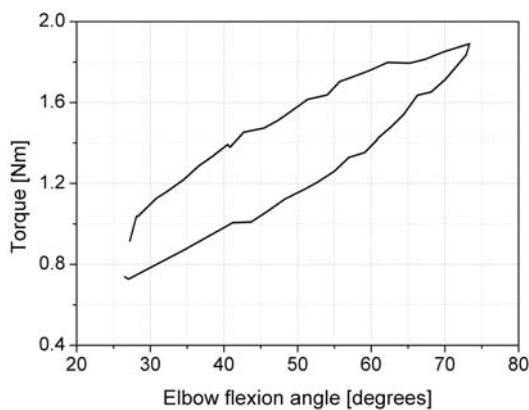


Fig. 4 Torque-angle response of the EDGES orthosis mounting four 2-mm diameter NiTi bars. Full extension is at 0 degrees.

Table 1 Patients' characteristics

Patient	Age	Sex	Time since event	Spasticity Flex(ext)	ROM
A	62	M	6 years	Ashworth 3 (3)	Full PROM No AROM
B	64	F	9 years	Ashworth 2 (0)	Full PROM No AROM

cording to ethical principles as approved by the hospital ethical committee (Ospedale Valduce - Clinica Villa Beretta, Costamasnaga, Italy) and gave informed consent to undergo a period of treatment with EDGES.

Patients underwent general clinical assessment prior to the start of the treatment, which consisted in wearing EDGES continuously for the first 24h and as long as possible for the following week. A number of measurement were scheduled at T0 and 3h, 24h and 1 week after the initiation of the therapy. These included active and passive range of motion, spasticity on the Ashworth Scale, resting elbow position while sitting, standing and standing after walking. Elbow angles were assessed also via optoelectronic measurements, which allowed dynamical evaluation of patient-orthosis interaction. The same protocol was also repeated 1 week after discontinuation of the therapy. Visual clinical assessment was carried out routinely every time an optoelectronic measurement was scheduled. Optoelectronic measurement protocol was based on 100Hz acquisition of the position of three IR reflecting markers (fixed on the shoulder, elbow and forearm) to track the elbow angle by eight IR cameras (Elite Gait Eliclinic - BTS, Garbagnate Milanese, Italy). During this trial the patient (initially sitting with the affected limb resting on his/her lap) was cued to relax the arm down along the side of the body, then stand up, relax the arm down again and finally start walking along the gangway. Acceptability of EDGES was also investigated by means of a visual scoring questionnaire proposed by Gracies et al [4].

IV. RESULTS

Optoelectronic measurements show very nicely the time-course of elbow angle during the proposed clinical trials (Fig. 5). The quantitative analysis of movement confirms the general trend towards an increased elbow extension during therapy. Furthermore it is very interesting to observe that, while EDGES allows for wide movement of the elbow and does not impede flexing synergies during standing-up and walking, it is capable of reducing the amplitude of this pathological movement. Variations of clinical conditions during the follow-up period were recorded and the most relevant results are as in Table 2. In both patients an im-

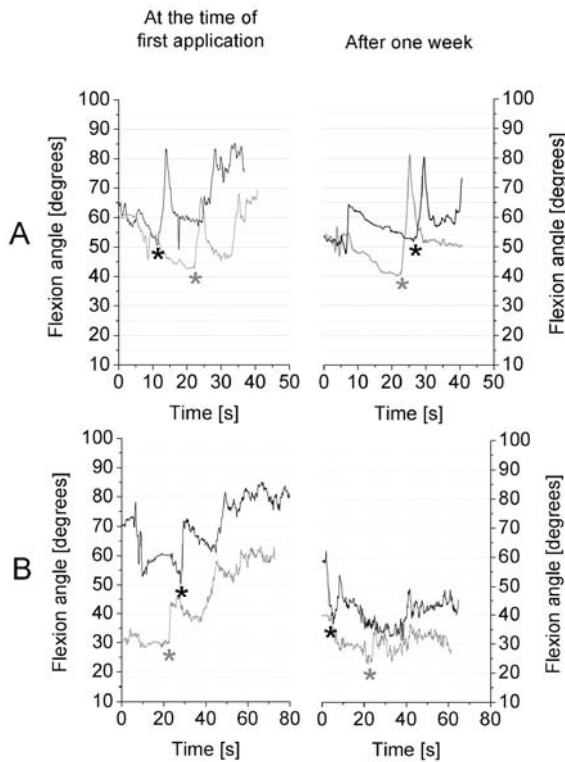


Fig. 5 Optoelectronic measurements on both patients wearing EDGES (gray line) and on removing it (black line). Star marks the “stand up” command. Elbow flexion following this point is a typical flexor synergic contraction. EDGES does not constrain this involuntary movement.

Table 2 Elbow resting angle and spasticity at T0 and after 1w

	A		B	
	T0	1w	T0	1w
Resting position	50°	40°	60°	20°
Ashworth	3	2	2	1

provement of the resting elbow posture can be noted. Moreover, the decrease in spasticity observed in both subjects is indeed a very interesting datum, since traditional orthotics were never reported to produce that result [5]. This is even more striking considering the short duration of treatment. All improvements appear to regress within 1 week of discontinuation. Patients’ acceptance of EDGES was generally good after both 24 hours and 1 week of therapy. They both wore EDGES more than 12h every day, which is an important result considering that traditional orthoses can hardly be tolerated for more than 4h a day. Only minor problems were observed, among which some light skin rash, that could possibly be avoided by a better lining than the present one. It is also interesting to notice that both patients reported

walking better when they are wearing this elbow splint, possibly suggesting that improved confidence and decreased flexor synergies bring about greater stability.

V. DISCUSSION & CONCLUSIONS

The presented results show that an orthotic treatment aiming at producing viscoelastoplastic creep of muscles can be effective in improving limb posture in such a smooth way that is very well accepted by the patients. Therapy was sufficiently long to produce some reduction of contractures, as the decrease of spasticity suggests, but not enough to achieve permanent plastic remodeling of the tissues. In fact, all the improvements were lost in the week following treatment discontinuation, which was expected since tissue remodeling is reported to takes place with a time constant of 22days [6]. Further tests will investigate if a longer application of EDGES could stabilize a more extended elbow posture through plastic remodeling of tissues.

AKNOWLEDGEMENTS

The authors are grateful to the HINT@Lecco Project for partially funding this study, to Mr. M. Caimmi, Dr. G. Gasperini, Mr. S. Pirovano and Dr. F. Molteni for the pre-clinical trials and to Dr. E. Villa for the tests on EDGES.

REFERENCES

1. Lundström E, Teréntb A, Borg J (2008) Prevalence of disabling spasticity 1 year after first-ever stroke. *Eur J Neurol* 15:533–539 DOI 10.1111/j.1468-1331.2008.02114.x
2. Gracies JM (2005) Pathophysiology of spastic paresis I: paresis and soft tissue changes. *Muscle Nerve* 31:535–551 DOI 10.1002/mus.20284
3. Duerig TW, Melton KN (1990) Engineering aspects of shape memory alloys. Butterworth-Heinemann Ltd, London
4. Gracies JM, Marosszeky JE, Renton R et al. (2000) Short-term effects of dynamic Lycra splints on upper limb in hemiplegic patients. *Arch Phys Med Rehabil* 81:1547–1555 DOI 10.1053/apmr.2000.16346
5. Lannin NA, Novak I, Cusick A (2007) A systematic review of upper extremity casting for children and adults with central nervous system motor disorders. *Clin Rehabil* 21:963–976 DOI 10.1177/0269215507079141
6. Wren TAL (2003) A computational model for the adaptation of muscle and tendon length to average muscle length and minimum tendon strain. *J Biomech* 36:1117–1124 DOI 10.1016/S0021-9290(03)00107-6

Author: Simone Pittaccio
 Institute: CNR-Institute for Energetics and Interphases
 Street: Corso Promessi Sposi, 29
 City: Lecco
 Country: Italy
 Email: s.pittaccio@ieni.cnr.it

Customizable neuro-mechanical model of a hemiplegic elbow interacting with a pseudoelastic dynamic orthosis

S. Pittaccio and S. Viscuso

Italian National Research Council, Institute for Energetics and Interphases, Lecco, Italy

Abstract— This paper presents a clinically-oriented mathematical model of the elbow, capable to simulate treatment scenarios, particularly in the case of orthotic therapy by pseudoelastic stretching braces. The model is divided into two patient-customizable lumped-parameter subsystems to include spinal mono- and poly-synaptic reflexes, joint contracture, muscle co-contraction, dystonia and spasticity on one side; plastic remodeling and therapeutic variables, on the other. An example of simulation is presented mimicking application of the NiTi-based brace EDGES during 1 month, 12h/day on a mock chronic hemiplegic subject. The model can be used to plan brace prescription and foresee patient-specific results.

Keywords— Spasticity, Ni-Ti, reflex, rehabilitation, remodeling

I. INTRODUCTION

Neuromuscular rehabilitation of stroke survivors is based on multidisciplinary approaches aiming at preventing or contrasting the detrimental sequelae of paresis, contracture and spasticity. Besides pharmacological therapy, physical methods are employed in the form of manual or robotic mobilization, stretching and application of orthoses on the affected limbs. Due to the high individual variability of patients' conditions and impairments it is generally difficult to have a quantitative grasp of the appropriate line of action to prescribe bracing in the most effective manner. This is an even more complex task when testing new therapeutic principles and using non-standardized devices. To this end, it is important to evaluate both instantaneous interaction (orthosis compliance to patient's movement, localized pressure on the skin, reflex responses, etc.) and mid-long term evolution of the ill-posture (resting angle, reflex adaptation, range of motion, etc.). Accordingly, the current paper presents a model devised to obtain prescription guidelines and foresee results of the application of a Ni-Ti based orthosis for the extension of the chronically spastic elbow in hemiplegic patients. This device (EDGES) was already described in previous works where its design and working characteristics are outlined alongside the preliminary results of its use on selected subjects [1]. In order for predictions to be patient-specific and suitably clinically-oriented, a measurement protocol was written to acquire the necessary modeling parameters individually.

II. METHODS

A. Modeling strategy and assumptions

The model is based on systems of ordinary differential equations describing, by lumped parameter blocks, the neural conduction between the spinal interneuron and the muscle end-plate; the stretch reflex and tension-mediated autogenic inhibition; the power-generation properties of two articular motors accounting for the ensemble of the flexor muscles and that of the extensor muscles, respectively; the viscoelastic properties of the elbow joint; the pseudoelastic orthosis; the orthosis-skin interface; the muscular remodeling. The role of the Renshaw cells was considered marginal in connection to the pathophysiology of spasticity, (spastic) dystonia, co-contraction or muscular contracture [2], and was therefore neglected. Reciprocal inhibition was also not included as not directly relevant for the aims of this particular study. All modulations (e.g. supraspinal, pain-dependent, sensorial, cutaneous, etc.) to the neural responses were not included.

The general model is divided into two sub-models simulating the elbow/orthosis system during instantaneous (INST, timescale: seconds) and long-term (THER, timescale: days) interaction. These two sub-models are integrated separately but a file-system is generated during their respective runs producing result datasets which can be partially utilized to generate cross input files for subsequent or composed runs.

B. Pseudoelastic orthosis model

The dynamic orthosis EDGES is made up of two hinged thermoplastic shells to be strapped onto the arm and forearm. A mild corrective torque around the elbow joint is provided by 2, 4 or more pseudoelastic NiTi bars connected in parallel to the polycentric hinges. These bars undergo bending during elbow flexion and respond with a nonlinear hysteretic characteristic as in Fig. 1.

For the scopes of modeling, this characteristic was mimicked by discrete functions of the elbow angle such as:

$$T_k = \begin{cases} f_k(\theta_k) & \text{for } \dot{\theta}_k \geq 0 \\ g_k(\theta_k) & \text{for } \dot{\theta}_k < 0 \end{cases} ; \quad \dot{\theta}_k = \frac{\theta_k - \theta_{k-1}}{\Delta t} \quad (1,2)$$

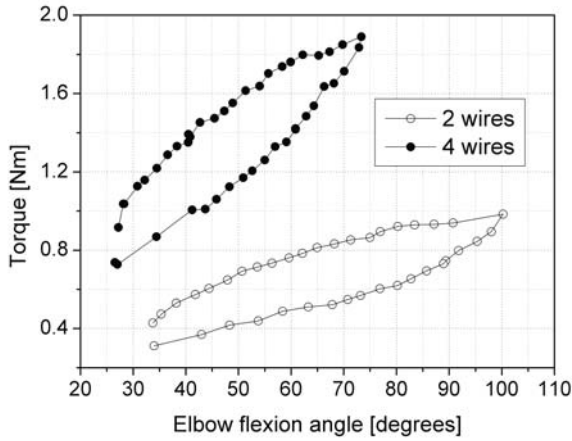


Fig. 1 Measured (dots) and interpolated (piecewise linear curves) torque-angle characteristics for EDGES with 2 and 4 NiTi bars

with f_k and g_k two piecewise linear functions, and Δt the simulation timestep.

C. The instantaneous interaction model (INST)

This sub-model was devised to describe the effects of putting-on the orthosis, wearing EDGES during involuntary jerks or synergetic movements of the elbow, and to study the muscle response to passive mobilization at different therapeutic milestones. As such, it includes all the above-listed properties, apart from plastic muscular remodeling, which is not likely to occur in time-spans of seconds or minutes. On the contrary, the main focus of INST is on reflex responses.

α - and γ -motoneurons, and neuromuscular end-plate: The “activation” of the α -motoneuron is obtained by weighted composition of the firing rates of the supraspinal, Ia and Ib fiber contributions. Weighting is based on the type and number of synapses as from the literature [3], while the composition is obtained by normalization to 1 of the sum of firings r by an $\text{erf}(r - r_0)$ function, wherein r_0 is a firing threshold. The muscle activation is mediated by the endplate dynamics implying rising (τ_r) and falling (τ_f) time constants, as in [4]. The γ -motoneuron and spindle contraction are treated in much the same way, with only the supraspinal inputs.

Articular motor torques: The active torque is computed based on the level of activation and the current elbow angle. This approach takes into account an articular-motor version of Starling’s law. The maximal torque vs. angle characteristic is approximated by fitting second-degree polynomials to torque values measured during isometric maximal voluntary contraction at different angles of the flexors and extensors, respectively.

Viscoelastic properties: the global passive response of the elbow muscles and joint is modeled as a 2-pole transfer function taking into account the forearm inertia (I) and the viscoelastic characteristics of the limb (η, K), as obtained from torque-angle measurements during low-speed passive mobilization.

Stretch reflexes: The measurement protocol requires obtaining of passive torque-angle curves during isocinetic mobilization at increasing speeds. The lowest-speed tracing (below stretch-reflex threshold) is subtracted from the remaining ones and then the recorded curves are fitted to a suitable continuous two-variable “spasticity” surface of the form:

$$\tilde{T}_s = \begin{cases} g \left\{ 1 - \left(\frac{\dot{\theta}}{\dot{\theta}_0} \right)^p \right\} \cdot \left\{ \frac{1}{2} \left[1 + \text{erf} \left(\frac{\theta - (\theta_0 + \delta)}{\delta} \right) \right] \right\}, & \dot{\theta} \geq \dot{\theta}_0 \\ 0, & \dot{\theta} < \dot{\theta}_0 \end{cases} \quad (3)$$

where θ_0 is the reflex threshold angle and $\dot{\theta}_0$ reflex threshold speed. p is an exponent in the (0,1) range and g is a gain. 2δ is the angular range across which reflex torque undergoes steep rising from quasi-zero to approaching its maximum value. This we modified from an appropriate model in the literature [5]. The actual value of reflex torque is then obtained by evaluating

$$T_s(\theta, \dot{\theta}) = \tilde{T}_s(\theta(t - \tau_s) - \Delta\theta_\gamma, \dot{\theta}(t - \tau_s)) \quad (4)$$

wherein $\Delta\theta_\gamma$ is a correction on measured threshold angle due to the dynamically estimated effects of γ -motoneuron-mediated spindle contraction. τ_s is the transmission delay between the muscle spindles and the α -motoneuron. The same procedure is repeated for the flexors and the extensors.

Tension-mediated inhibition: The effect of tension on the Golgi tendon organs is modeled as a linear relationship between the voluntary muscle torque and the Ib fiber firing rate. A delay and low pass-filtering by a transfer function mimic the polysynaptic transmission to the α -motoneuron via an interneuron. The parameters are taken from the literature [6,7] and are not considered patient-dependent.

Skin interface: An average pressure on the forearm skin can be obtained by dividing the algebraic sum of torques by the distal shell padding surface and the shell centroid lever arm to the elbow flexion axis. An approximated estimate of localized pressure scales linearly with distance from the elbow.

D. The mid-long term model of orthotic therapy (THER)

With timescales in the order of days, all events occurring with time constants in the order of seconds or less become negligible. That is why THER does not include spinal reflex

Table 1 List of parameters taken from literature (*deduced)

	Description	Value	Ref.
τ_s	Spindle transmission time constant (ms)	20	[4]
τ_g	GTO transmission time constant (ms)	44	[6]
τ_r, τ_f	Activation, de-activation time const (ms)	20; 200*	[4]
τ_m	Remodeling time constant (days)	22	[8]
r_θ, r_s	M-N activation threshold; saturation (pps)	58; 108*	[4]
τ_I	Interneuron transmission time constant (ms)	5	[3]
g_{GTO}	GTO gain (pps)	200	[7]
g_I	Interneuron gain	0.8857*	[3]

blocks, or the inertial and viscous parts of passive joint characteristics, while only an average voluntary activation can be assigned to account for dystonia or co-contraction. The focus of THER is on the daily application of EDGES and on plastic remodeling of the muscle tissue.

Muscle remodeling: The assumptions on which the modeling of muscle lengthening therapy is based rest on literature findings [7]. If a particular elbow angle is maintained, while tendon length tends not to vary, the joint resting (neutral) position evolves to match that angle by lengthening (or shortening) of the muscles. This evolution occurs with a muscle remodeling time-constant (τ_m). Referred to the neutral angle, also the angle of optimal torque generation and the spindle threshold angle change proportionally. Even if the spindle reflex is not modeled in THER, during a THER run, spindle threshold angle evolution is written in a file alongside the neutral angle changes.

Therapy adjustments: Therapy parameters are controlled by the timing of daily wearing of the EDGES orthosis (putting-on and taking-off times), and by the overall therapy duration (weeks, months,...). Furthermore the resting elbow position during the time of not wearing the orthosis can be chosen independently.

E. Setting-up and running of INST-THER simulations

Setting-up of the models is conducted by obtaining specific biometric (upper limb dimensions), biomechanical (e.g. maximal isometric torques, passive/reflex behavior, initial resting angle, range of motion) and bioelectric characteristics (dystonia/contraction reset time, degree of co-contraction,...) of a particular patient. Appropriate input files are automatically generated from the raw data. Based on these input files, specific runs of INST can be launched. For instance, the effect of passive mobilization across a defined articular range can be simulated for the initial condition prior to therapy initiation. Or, the effect of voluntary/involuntary supraspinal volleys on elbow mobility with or without the orthosis can be studied. Subsequently a THER run can be carried out. The predicted evolution of

informative parameters (neutral elbow angle, maximum extension angle,...) can be observed with varying prescription parameters (e.g. timing and duration of application, number of pseudoelastic bars, material properties). During a THER simulation, specific files are updated with evolving set-up parameters. These can be used as input files for a post-therapy simulation with INST to check important predicted indices (e.g. stretch reflex activation during passive mobilisation or limb mobility under supraspinal excitation).

III. SIMULATED PATIENT

The results obtained so far refer to a simulated patient, whose characteristics are based on typical features of hemiplegic subjects affected by contracture, spasticity, (spastic) dystonia, co-contraction, involuntary jerks or myocloni, or combinations of these traits. Relative measurements are abundant in the scientific literature, so suitably paired examples of those symptoms could be chosen to investigate various scenarios. Although this step is considered by the authors as an intermediate one before application on real patients, it is believed that the present results are interesting *per se* and worth sharing. The results in this paper refer to a simulated patient of the following initial conditions:

1. Maximal isometric torque vs. angle as in Fig. 2;
2. Stretch response torque vs. angle and speed as in Fig. 2;
3. Additional parameters as in Table 2.

Such patient could be described as a chronicized hemiplegic with mild-severe spasticity of the flexors and relative muscle shortening, dystonic, with co-contraction of the flexo-extensors and flexorial synergies of the elbow resulting in slow-resetting jerks.

IV. RESULTS

Simulations of INST were carried out with an optimized $\Delta t = 10^{-4}$ s while $\Delta t = 15$ min was selected for THER. Among others, passive extension-flexion across 40° - 160° at 120° /s and therapy for 30 days 12h/day were simulated.

As an initial hypothesis it was decided to use four bars, so that the resulting corrective push might be insufficient to block elbow movements and immobilization be prevented. The waveforms in the top graph of Fig. 3 show that, according to INST simulations, stretch reflex due to passive mobilization decreases in intensity due to therapy. The reason for this can be understood by analyzing the evolution of postural angles, as displayed in bottom of Fig. 3. The fact that the neutral angle (muscle length) increases (with the remodeling time constant of 22 days) also results in a progressive lengthening of the muscle spindles. This, in turn, has the

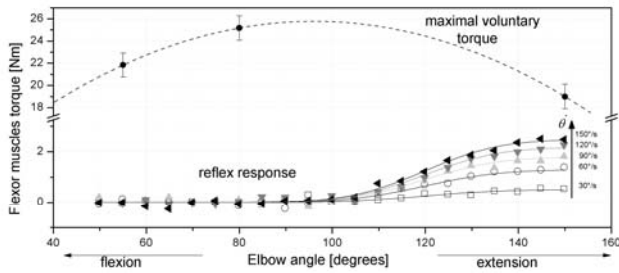


Fig. 2 Simulated biomechanical measurements (dots) and automatic fitting of the raw data (lines) for the flexor muscles maximal isometric torque and stretch response to passive mobilization at increasing speed (\square 30°/s; \circ 60°/s; \triangle 90°/s; ∇ 120°/s; \blacktriangleleft 150°/s) as in [5].

Table 2 Main characteristics of the simulated patient and therapy settings

Parameter	Value
I (Ncm·s ² /rad); η (Ncm·s/rad); K (Ncm/rad)	8.6; 50; 126.05
Maximal flexion/extension (°)	35 / 160
Initial resting angle (°)	102
Dystonia-affected τ_f (s)	1
Baseline of supraspinal firing rate (pps)	10
Co-contraction ratio (-)	0.1

functionally-favorable effect of off-setting the angular threshold for stretch reflex, thus making passive mobilization less hindered by involuntary reaction. This result can at least partially explain the practical observation in our previous pre-clinical trial, that 1 week’s application of EDGES seemed to bring about a decrease in the level of spasticity in two chronic hemiplegic patients [1]. That decrease was cancelled by one following week of not wearing the orthosis, which is consistent with the simulation of therapy discontinuation and persistent habit of resting the arm on the patient’s lap (imposed resting angle $\sim 100^\circ$).

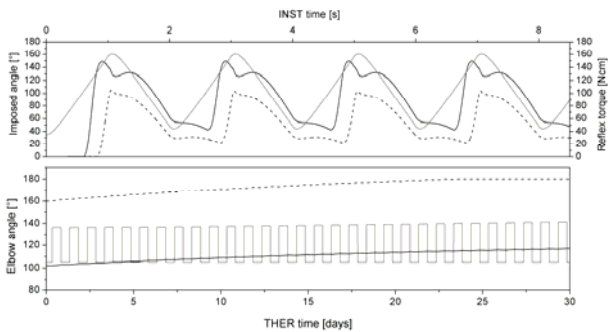


Fig. 3 Top: Sawtooth passive mobilization (gray) with instantaneous response prior to (bold) and after 1 month of simulated therapy (dashed). Bottom: elbow position during therapy (gray – wearing EDGES 12h/day) with evolution of the neutral angle (bold) and maximum extension limit (dashed).

V. DISCUSSION & CONCLUSIONS

This preliminary work proposes a protocol and a mathematical instrument to customize the use of a novel type of braces promoting posture improvement in stroke survivors. The aims of the present study, albeit ambitious, respond to a paramount principle of employing quantitative information to make more substantiated decisions in the clinical practice. The main advantage is the relatively direct use of clinically-obtainable parameters in the simulation set-up. A drawback lies in the fact that some important simplifications were introduced in order to include both the effects of pathological neuromuscular activity and mechanically-induced tissue remodeling, while still keeping the model easy to handle. It is hoped that, with the first trials on real patients, this model will demonstrate effective in providing realistic outcomes and guiding prescription of a by now little-known device, such as the pseudoelastic EDGES orthosis.

REFERENCES

1. Viscuso S, Pittaccio S, Caimmi M et al (2008) Pseudoelastic alloy devices for spastic elbow relaxation, IFMBE Proc. vol. 23, 13th International Conference on Biomedical Engineering, Singapore, 2008, pp 1584–1587
2. Gracies JM (2005) Pathophysiology of spastic paresis I: paresis and soft tissue changes. *Muscle Nerve* 31:535–551 DOI 10.1002/mus.20284
3. Stienen AH, Schouten AC, Schuurmans J et al (2007) Analysis of reflex modulation with a biologically realistic neural network. *J Comput Neurosci* 23:333–348 DOI 10.1007/s10827-007-0037-7
4. Koo TKK, Mak AFT (2006) A neuromusculoskeletal model to simulate the constant angular velocity elbow extension test of spasticity. *Med Eng Phys* 28:60–69 DOI 10.1016/j.medengphy.2005.03.012
5. Schmit BD, Rymer WZ (2001) Identification of static and dynamic components of reflex sensitivity in spastic elbow flexors using a muscle activation model. *Ann Biomed Eng* 29:330–339 DOI 10.1114/1.1359496
6. Hidler JM, Schmit BD (2004) Evidence for force-feedback inhibition in chronic stroke. *IEEE Trans Neural Syst Rehabil Eng* 12:166–176 DOI 10.1109/TNSRE.2004.828428
7. Mileusnic MP, Loeb GE (2006) Mathematical models of proprioceptors. II. Structure and function of the Golgi tendon organ. *J Neurophysiol* 96:1789–1802 DOI 10.1152/jn.00869.2005
8. Wren TAL (2003) A computational model for the adaptation of muscle and tendon length to average muscle length and minimum tendon strain. *J Biomech* 36:1117–1124 DOI 10.1016/S0021-9290(03)00107-6
9. Given JD, Dewald JP, Rymer WZ (1995) Joint dependent passive stiffness in paretic and contralateral limbs of spastic patients with hemiparetic stroke. *J Neurol Neurosurg Psychiatry* 59:271–279

Author: Simone Pittaccio
 Institute: CNR-Institute for Energetics and Interphases
 Street: Corso Promessi Sposi, 29
 City: Lecco
 Country: Italy
 Email: s.pittaccio@ieni.cnr.it

The Use of Radio Frequency Identification System for Wheelchair Security System

W. Md. Azhar Wan Ibrahim and Md. Shuhaibul Fadly Mansor

1. Introduction

Wheelchair plays an important role in hospital. Disable patients use wheelchair to travel around the hospital for treatments or for recreation purposes. There is an indication that large amount of wheelchair be stolen from the hospital. There are some common reasons for why the wheelchair often gets stolen. The most common case is the thefts seem like an innocent acts. For example, a family member wheels a discharged patient to the parking lot and transfers the patient into the car and left the wheelchair at that compound or takes the wheelchair home. Eventually the wheelchair got lost. Therefore frequent trips to health care facilities can result in patients taking home more than one hospital wheelchairs. There also a case where the outsider stole the wheelchair and sold at the market. A large amount of cash could be earned as the wheelchair is still in good quality. The missing wheelchair problem may also the result of the patients who came with an older and outdated wheelchair but went home with a newer one. Therefore, missing and unorganized wheelchair may cause inconvenient to the hospital staff's when there is an emergency needs of wheelchairs.

There are several wheelchair security system have been used by many hospital. Some hospital required the discharged patients' to be escorted out of the hospital by a worker pushing the wheelchair however the hospital staff not always available at all time to associate the discharged patient out off the hospital in order to make sure the wheelchair is returned. Sometimes the use of a long metal stick that attached to the handle of the wheelchair is being used. It is to make sure that the wheelchair cannot be feed into the vehicle so that the patients cannot take the wheelchair

home. However the metal stick is easily to be broke. Some hospital assigns the security department to take care of the wheelchair. The security officer may ask to leave the identity card from borrower to make sure the wheelchair is returned after used. This system is only suitable practiced at the main entrance of the hospital and specific for the out-patients only. It is seen to be very tedious for the application at the ward.

Some of the hospital began to tag their wheelchairs with transmitters that communicate with sensor placed throughout the hospital. The computer system tracks the last sensor that the wheelchair has passed. Baxter Healthcare makes a similar tracking product which its system can either activate a security camera or alert the security guard when a tagged wheelchair went through an exit point.

This paper is to discuss a design of a new security system for wheelchairs by using RFID technology. The objective of the new security system is to cope with the problems of missing wheelchair and to trace the wheelchair movement

2. Radio-Frequency Identification System (RFID)

Radio-frequency identification (RFID) is an automatic identification method, relying on storing and remotely retrieving data using devices called RFID tags or transponders. The RFID tag is an object that can be attached to or incorporated into a product, animal or person for the purpose of identification by using radio waves. Chip-based RFID tags contain silicon chips and antennas. Transmitter of interrogation signals which is contained within an interrogator communicates via

electromagnetic waves with an electronically coded label which contained data characteristic of the object to which the label is attached. The reply signal from the label is detected by a receiver in the interrogator and made available to a control system.

RFID Tags

RFID systems carry data in suitable transponders generally known as tag. It retrieved data via reader which is can be fixed or handheld. Each tag has a discrete memory capacity that varies from a small license plate with only a few characters to a memory with thousands of records. Data within a tag may provide any level of identification for an item during manufacture, in-transit, in-storage, in-use or in-maintenance. With additional data, the tag may support applications that require item-specific information. There are three type RFID tags i.e active, passive, and semi-active RFID tag. Passive RFID tag has no power supply. It draws power from the reader. They are usually cheaper than other types of tag and maintenance free. This tag can operate at low, high and ultra-high frequency. On board of an active RFID tag have a battery which is used to run the microchips and to broadcast a signal to a reader. Usually operate at 455MHz, 2.45 GHz or 5.8 GHz and have a read range of 60 to 300 feet. This tag is usually used on large assets such as cargo containers, rail cars and large reusable containers. It can be always on alert or can be "awakened" when needed. Semi-active RFID tag contains some combining traits of both active and passive tags. This tag uses a power from a battery to run the chip's circuitry but communicate by drawing power from the reader. Often in a sleep mode until awakened by a specific reader signal.

The characteristic of RFID tag are can be read in a wide variety of circumstances, the tag need not be on the surface of the object, it reading time is typically less than 100 milliseconds, and a large numbers of tags can be read at once.

RFID Reader, Detector and Sensor

The RFID reader powers an antenna to generate a radio frequency (RF) field. When a tag object passes through the RF field, the information stored on the chip in the tag is decoded by reader and sent the information to the server which in turn communicates with the Hospital Information System (HIS) when the RFID system is interfaced with it. There is software in each reader to facilitate communication with the server and/or with other system. Reader functioning detect and read an RFID tag passage for purposes of determining whether it is a charged (authorized/no alarm) discharged (non-authorized/alarm) event.

A reader has several components. They are a transmitter, a receiver, a microprocessor, a RAM memory, input/output channels, a controller, a communication interface and a power source. The reader's transmitter is used to transmit AC power and the clock cycle via its antennas to the tags within its read zone. This is a part of the transceiver unit, the component responsible for sending the reader's signal to the surrounding environment and receiving tag responses back via the reader antenna. The antenna ports of a reader are connected to its transceiver component. One reader antenna can be attached to each antenna port. Currently some readers can support up to four antennas.

Receiver is also part of transceiver module. It receives analog signals from the tag via the reader antenna. It then sends these signals to the reader microprocessor, where it is

converted to its equivalent digital form. The microprocessor is responsible for implementing the reader protocol to communicate with compatible tags. It performs decoding and error checking of the analog signal from the receiver. In addition, the microprocessor might contain custom logic for doing low-level filtering and processing of read tag data.

RAM Memory is used for storing data such as the reader configuration parameters and a list of tag reads. Therefore, if the connection between the reader and the controller/software system goes down, not all read tag data will be lost. Depending on the memory size, however a limit applies as to how many such tag reads can be stored.

Readers do not have to be turned on for reading tags at all times. After all, the tags might appear only at certain times in the read zone, and leaving readers perpetually on would just waste of the reader's energy. Input/output channels for external sensors, actuators, and enunciators' provide a mechanism for turning a reader on and off depending on external events. A sensor of some sort, such as a motion or light sensor, detects the presence of tagged object in the reader's read zone. This sensor can then set the reader on to read this tag. Similarly, this component also allows the reader to provide local output depending on some condition via enunciators (for sounding an audible alarm) or an actuator (for opening and closing a security gate).

A controller is an entity that allows an external entity, either a human or a computer program, to communicate with and control a reader's functions and to control enunciators and actuators associated with the reader. The communication interface component provides the communication instructions to the reader

that allows it to interact with external entities via a controller. Its transfer the stored data and accept commands and sent back the corresponding responses.

The power supply component supplies power to the reader. The power source is generally provided through a power cord connected to an appropriate external electrical outlet.

3. Implementation of RFID on Wheelchair System

The implementation of RFID wheelchair management system can be divided into a few phases i.e registration and tagging of wheelchair, registration of patients, and installing parallel RFID gate (reader) in the entrance and exits of the ward.

The wheelchairs are tagged with a passive RFID tag at hidden place. The tag contains specific ID number (probably odd numbers) that also registered into the system. The information system can be build for storing the data and it can be a web based system. The wheelchair's information is entered into the system together with RFID id tag number. The information such wheelchair ID, RFID tag ID, owner (belong to which ward), date of purchase etc can be stored in the system's database.

The second phase for implementation of this system involved the registration and tagging of ward patients. Each of the patients can be tagged with a passive RFID tag that contains even ID number and register into the system database. Since the patients have to wear an identity paper around the wrist, so the RFID tag can be attached at the back of this patient identity tag. Each patient must has unique RFID tag identification. The RFID ID is a part of the

patient's information that is stored in the database.

The third phase of the implementation of the system is to install RFID gate at the entrance and exits of the ward. The measurement of the wheelchair to be taken because the distance between the gates has to be set according to the width of the wheelchair

4. Operation of RFID Wheelchair Security System

When a patient leaves the ward with a wheelchair from the ward, through the gate, it means that the RFID tag passes through the field of the RFID reader antenna. The reader's transmitter which is one of the transceiver units transmits AC power and the clock cycle via its antennas to the tags in its read zone. The radio-frequency signal will be put out in a relatively short range which means it provides a means of communication with the transponder (RFID tag) and also provides the RFID tag with energy to communicate back. This "wakes up" the RFID chip, and it transmits the information on its microchip to be picked up by the reader antenna. The tag response is then received by the transmitter. As the receiver received an analog signal from the tag via transmitter, it sends the signal to the reader microprocessor. Finally the tag data is converted to its equivalent digital form. Next the communication interface component provides the communication instruction to a reader to transfer its stored data to external entities such as computer system via a controller. Computer receives the digital data through the cables or by wireless connections and stored in the database.

If the computer system detects the two even and odd number which mean that the

wheelchair and the patient ID appear at the same time then no instruction will be send back to the controller to trigger annunciations associated with the reader. However if the wheelchair passes the gate without proper patient RFID tag, the computer system will send back response to reader through controller to activate alarm at the gate. This means that the wheelchair cannot leave the ward without permission or clearance from the administrator.

5. Discussions

The main objective is achieved by applying RFID wheelchair security system i.e the wheelchair stolen cases can effectively solved. There always a record on all the wheelchairs that used by the patients. Therefore if the wheelchair is missing, the system can traces the last patient using it as the wheelchair cannot simply leave the ward without the association of the patient tag because this will trigger the alarm. This will alert the hospital staff and immediate action can be taken to stop unauthorized check out of the wheelchair. This system also enables us to reduce the burden of the hospital staff by reducing their work load. Therefore they can pay more attention in taking care of the patients and consequently give quality service.

This system can be applied to any ward. Apart from a low cost system, the RFID tag can last long and the passive tag is maintenance free and it does not need for a battery supply. So the battery life time is not a concern. Besides that, the used patients RFID tag can be recycle in order to save the cost. The wheelchair must be returned together with patient RFID tag and the patient account is cleared for using this RFID ID.

A Lightweight Approach for Activity Classification on Microcontrollers

M. Rulsch¹, M. Benz¹, C. Arzt¹, C. Podolak¹, J. Zhong¹, and R. Couronné¹

¹Fraunhofer Institute for Integrated Circuits IIS, Erlangen, Germany

Abstract— A lightweight activity classification algorithm suitable for microcontrollers is presented, which is intended to be used on activity monitors. Therefore it focuses on five daily activities: inactivity, walking, cycling and walking up- and downstairs. This algorithm includes a novel approach for detecting cycling, which relies on properties of the power spectrum. Classification parameters are extracted from accelerometer and barometer data streams.

Resources on activity monitors are usually short. The algorithm is able to cope with these limitations and was implemented on our demonstration activity monitor.

Classification results were obtained from two test trials. The first trial consisted of consecutive sequences of basic activities. In the second trial a complex daily activity was executed. Twelve persons participated in each trial. Classification rates in the first trial were very promising: inactivity (97.3 %), walking a straight plane (92.6%), cycling (82.2%), walking upstairs (66.8%) and downstairs (65.7%). However trial two depicted that a supplementary class should be introduced, which requires further research.

Keywords— accelerometer, barometer, activity classification, activity monitoring, microcontroller.

I. INTRODUCTION

Quantifying reliably physical activity and predicting the energy expenditure (EE) is a topic of increasing interest with a broad range of applications: for example the knowledge of a quantitative measure of physical activity is essential in scientific studies concerning the prevention and treatment of obesity [2,3,4]. Furthermore persons suffering from obesity or diabetes are advised commonly to increase their physical activity [5,6]. Therefore another important application is to motivate these persons to be physically active by providing them information about their activity level in an adequate way.

The investigation of an activity sensor addressed to the above mentioned applications comprises mainly three tasks: firstly the development of a sensor module for the data acquisition, secondly algorithms for signal processing and quantifying physical activity are needed and finally an user interface providing feedback has to be realized.

The key measuring module of common activity sensors are accelerometers, which provide information about intensity and frequency of activities [1,10,11]. Beside they are

small, energy efficient and relatively cheap. Oftentimes these algorithms are based on averaged accelerations along several or all measurement axes as input for a regression equation. However relying on one equation is prone to fit only a limited range of activities and under- or overestimate others [1,8,9]. The accuracy of activity monitors could be significantly improved if they could identify some important activities like cycling or stairs climbing. Therefore we present an approach for classifying several activity classes including cycling and stairs climbing.

Another advantage of the developed system is that all algorithms are implemented on a microcontroller directly placed on the sensor module.

II. MATERIALS AND METHODS

A. Measurement System

A wireless sensor module, recording acceleration in three directions and altitude, was built in our lab. It is intended to be worn on the hip.

Data is measured with a three-axial accelerometer (MMA7260Q) and a barometer (SCP1000-D01). These sensors are connected to a microcontroller (MSP430F1611) which performs the signal processing. Using a Bluetooth module, the sensor can transmit its results wirelessly to a mobile, notebook or PDA.

Acceleration is measured in multiples of g. Measurement range for the accelerometer lies between -1.5g and 1.5g. This range offers a high sensitivity for light movements and is adequate for most daily activities e.g. walking and cycling. Sampling frequency was set to 32 Hz.

The barometer sensor module also contains an onboard temperature sensor. Pressure and temperature combined are used to compute absolute altitude in meter. Sampling rate was set to 9 Hz.

B. Data preprocessing

Measurements from accelerometer consist of two components: gravity and acceleration. For further activity classification the contribution of the gravity to the measuring sig-

nal has to be deducted. The gravity component is removed from signal in x- and z-direction with an elliptical highpass filter. Its cutoff frequency is at 0.25 Hz [12]. The signal in y-direction will also be used in the computation of a Fast Fourier Transformation (FFT). Therefore we combined highpass and antialiasing filter in an elliptical bandpass with cutoff frequencies at 0.25 Hz and 15 Hz.

Also the measuring signal of the barometer is preprocessed as the computed altitude is subject to considerable variations due to noise. To suppress noise we use a lowpass FIR-filter with a cutoff frequency of 0.35 Hz. In contrast natural fluctuations in barometric pressure are usually too small to influence our algorithm.

C. Parameter Extraction

The classification algorithm is based on four parameters which are extracted from the measured data using a four seconds window:

- SMA_{tot} (signal magnitude area)
- $E_{<3}$ (mean power in frequency band less than three Hz)
- $E_{\geq 3}$ (mean power in frequency band greater or equal than three Hz)
- Δh (change in altitude)

Each of them reflects a different property of the observed movement.

SMA_{tot} contains information about the underlying movement, its intensity and frequency. It is computed from the magnitude of acceleration vector $a=(a_x, a_y, a_z)^T$ and is normalized with respect to time window Δt :

$$SMA = \frac{1}{\Delta t} \sum_{t_0}^{t_0+\Delta t} \sqrt{a_x^2 + a_y^2 + a_z^2}$$

Thus it is independent from the orientation of the sensor module.

Characteristics of the power spectrum are different for certain movements, e.g. walking and cycling. It is assumed, that the sensor's y-axis is parallel to the direction of gravity. While walking, a peak at the step frequency can be observed on the y-axis due to ground contact (figure 1). In contrast frequencies are nearly equal distributed for cycling (figure 2).

For exploiting this observation, mean powers in two frequency bands are computed. The first band with frequencies less than three Hz will contain the peak at walking frequency. Its mean power is denoted with $E_{<3}$. The second band with frequencies equal or larger than three Hz will contain other movement related parts and noise. Its mean power is denoted with $E_{\geq 3}$.

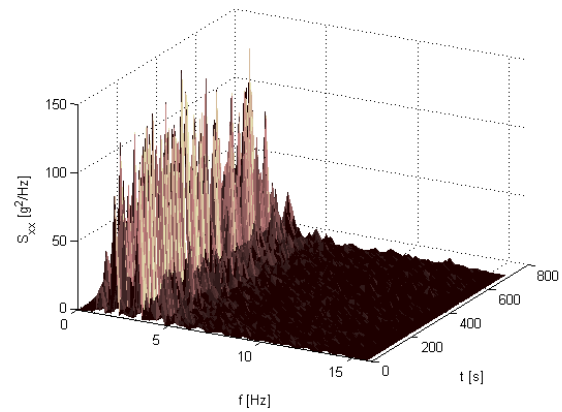


Fig. 1 Power spectrum of y-axis for walking

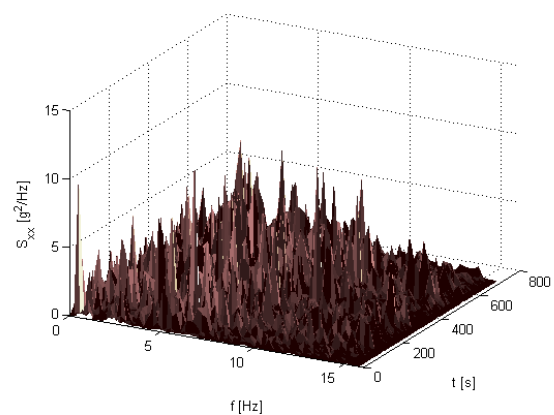


Fig. 2 Power spectrum of y-axis for cycling

Power spectrum is computed using the Fast Fourier Transformation. This is the most computationally intensive task for the microcontroller. Processing a FFT with the whole data from four seconds would require a 128 point FFT. Fortunately space and time complexity can be reduced because the acceleration values are real numbers [13]. Half of the data can be put in the imaginary part of the input. Thus a 64 point FFT is sufficient for computing the power spectrum.

Knowledge about change in altitude (Δh) supports classification of stairs up and down. It is computed from data at beginning (t_0) and end (t_1) of the four second interval using the barometric formula [14].

D. Cycling Detection

Cycling is a common movement, which is often not detected by existing activity monitors [1]. An algorithm which

classifies motion as cycling could greatly improve their performance.

The cycling detection part of the classification algorithm is based on the parameters $E_{<3}$ and $E_{\geq 3}$. As mentioned before, they differ for movements with and without ground contact. Parameter $E_{<3}$ is usually much smaller for cycling than for walking due to a peak at walking frequency. Thus a simple threshold approach is appropriate for distinguishing between walking and cycling. In addition the ratio between $E_{<3}$ and $E_{\geq 3}$ is evaluated. This comparison incorporates the frequency distribution in our algorithm. Comparing walking and cycling, $E_{<3}$ is usually much larger than $E_{\geq 3}$ for walking. Summarizing the observations, a movement is classified as cycling if $E_{<3}$ is in a given range and the ratio between $E_{<3}$ and $E_{\geq 3}$ is small.

The heuristic will not fit all the time, but a person's movement usually does not change every fourth second. It is useful to apply a hysteresis approach and classify a movement as cycling if the criterion is matched multiple times. On the other hand the criterion for cycling should fail a few times before changing the classification result.

E. Classification

The classification algorithm distinguishes between five classes: inactive, walking, cycling, stairs up and stairs down. The decision rules are modeled with a decision tree:

0. Check SMA_{tot} , if it is below an acceleration of 0.1g, the person is inactive.
0. Apply cycling criterions, if they are fulfilled, the person is cycling.
0. If cycling criterions do not match, the person is walking.
0. At last check the change in altitude (Δh), if it is below -75 cm or above 75 cm, the person is walking stairs up or down.

III. RESULTS AND DISCUSSION

The classification algorithm was implemented on our sensor module. Computing and processing SMA, $E_{<3}$, $E_{\geq 3}$ and Δh every fourth second turned out to be computationally practicable.

It was calibrated and validated with data from six male and six female persons. Six of these data sets were used for setting thresholds of the decision rules. Classification results were obtained from the other half.

The test course for each person consisted of 3.7 km cycling, 1.5 km walking, going up and downstairs three times, using a lift, driving car and office work. During the trial, the

sensor was fixed on the test person's trousers with a belt clip. Hence the y-axis of the sensor is aligned with the y-axis of the world coordinate system. Ground truth was annotated by a staff member, who observed the execution of the trials.

Under these conditions, the classification algorithm was able to distinguish between inactivity (driving car, using a lift, doing office work), going stairs up and down, walking and cycling. In total, from 14.8 hours of data 13359 parameter sets were computed, one set of SMA_{tot} , $E_{<3}$, $E_{\geq 3}$ and Δh for each four second time slice. Inactivity dominates our datasets, due to activities like driving car and doing office work. A comparison between classification results for this trial and the annotations is shown in table 1. Classification rates for each movement class are highlighted in table 2. The algorithm performed best for detecting inactivity and walking.

Beside our heuristic for cycling detection turned out to work well. Table 3 shows results for applying the heuristic and relying only on SMA_{tot} . The recognition of cycling could be improved by using the parameters $E_{<3}$ and $E_{\geq 3}$ in addition to SMA_{tot} , while the rate of false classifications could be reduced.

Table 1 Classification Results

		Annotation				
		Inactivity	Walking	Cycling	Upstairs	Downstairs
Classification	Inactivity	35404s	272s	704s	28s	16s
	Walking	480s	10440s	44s	160s	128s
	Cycling	424s	272s	3452s	60s	100s
	Upstairs	48s	144s	0s	596s	48s
	Downstairs	24s	144s	0s	48s	560s

Table 2 Classification Rate

Activity	Classification Rate
Inactivity	97.3%
Walking	92.6%
Cycling	82.2%
Upstairs	66.8%
Downstairs	65.7%

Table 3 Benefit of Cycling Detection Algorithm

		Cycling	
		SMA, $E_{<3}$ and $E_{\geq 3}$	SMA
Classification	Inactivity	704s	804s
	Walking	44s	348s
	Cycling	3452s	2992s
	Upstairs	0	24s
	Downstairs	0	32s

Table 4 Classification Results for Clearing Dishwasher

		Clearing Dishwasher
Classification	Inactivity	860s
	Walking	56s
	Cycling	2892s
	Upstairs	0s
	Downstairs	0s

In a second trial, the same persons performed a more complex movement. They were asked to clear a dishwasher. It was suspected to observe a mixture of inactive and walking classifications. Instead this movement often caused similar parameter constellations like cycling and could not be clearly separated. The classification results are shown in table 4.

IV. CONCLUSIONS

An algorithm for recognizing inactivity, cycling, walking, going up- and downstairs from accelerometer and barometer data was presented.

First classification results are very promising, especially for the classes inactivity and walking. Nevertheless some problems are not solved yet. Some complex motions cause similar parameter combinations like the basic movements. It is necessary to examine further correlations in the data and to add supplementary classes.

Beside the dependence on correct orientation of the sensor's y-axis according to the direction of gravity can be uncomfortable, because it restricts wearing of the sensor. It can even lead to errors in the classification, if the sensor orientation significantly changes, e.g. due to fitful movements. Thus it is desirable to automatically predict the orientation.

ACKNOWLEDGMENT

This work has been mainly funded by the Fraunhofer Personal Health Innovation Cluster which is sponsored by the Fraunhofer Gesellschaft, the German Federal Ministry of Education and Research, the Free State of Bavaria and the European Union.

REFERENCES

1. Crouter S E, Churilla J R, Bassett D R Jr (2006) Estimating energy expenditure using accelerometers. *Eur J Appl Physiol* 98:601-612 DOI 10.1007/s00421-006-0307-5
2. Trost SG, Kerr LM, Ward DS, Pate RR (2001) Physical activity and determinants of physical activity in obese and non-obese children. *Int J of Obesity* 25: 822-829
3. Lovejoy JC et al. (2001) Ethnic differences in dietary intakes, physical activity, energy expenditure in middle-aged, premenopausal women: the Healthy Transitions Study. *Am J Clin Nutr* 74: 90-5
4. Reilly JJ et al. (2004) Total energy expenditure and physical activity in young Scottish children : mixed longitudinal study. *Lancet* 363: 211-12
5. Faber-Heinemann G, Kulzer B, Heinemann L (2008) Effekte von Lebensstiländerungen bei Typ-2-Diabetikern : Diabetes-MOBIL-Studie. *Diabetes, Stoffwechsel und Herz* 4 : 261-266
6. Snowling NJ, Hopkins WG (2006) Effects of Different Modes of Exercise Training on Glucose Control and Risk Factors for Complications in Type 2 Diabetic Patients. *Diabetes Care* 29:2518-2527
7. Bouten C V, Westertep K R, Verduin M, Janssen J D (1994) Assessment of energy expenditure for physical activity using a triaxial accelerometer. *Med Sci Sports Exerc.* 26(12):1516-1523
8. Choi J H, Lee J, Hwang H T, Kim J P, Park J C, Shin K (2005) Estimation of Activity Energy Expenditure: Accelerometer Approach, *IEEE-EMBS Proc., Engineering in Medicine and Biology* 27th Annual Conference, Shanghai, China, 2005, pp 3830-3833
9. Henelman D, Miller K, Baggett C, Debold E, Freedson P (2000) Validity of accelerometry for the assessment of moderate intensity physical activity in the field. *Med Sci Sports Exerc.* 32(9):442-449
10. Swan P D, Byrnes W C, Haymes E M (1997) Energy expenditure estimates of the Caltrac accelerometer for running, race walking, and stepping. *Br J Sports Med.* 31:235-239
11. King G A, Torres N, Potter C, Brooks T J, Coleman K J (2004) Comparison of Activity Monitors to Estimate Energy Cost of Treadmill Exercise. *Med Sci Sports Exerc.* 36(7):1244-1251
12. Mathie M J, Coster A C F, Lovell N H, Celler B G (2003) Detection of daily physical activities using a triaxial accelerometer. *Med Biol Eng Comput.* 41(3):296-301
13. Press W H et al. (1992) Numerical recipes in C: the art of scientific programming. Cambridge University Press, Cambridge
14. Stöcker H. (2004) Taschenbuch der Physik: Formeln, Tabellen, Übersichten. Verlag Harri Deutsch, Frankfurt am Main

Author: Martin Rulsch
 Institute: Fraunhofer Institute for Integrated Circuits IIS
 Street: Am Wolfsmantel 33
 City: 91058 Erlangen
 Country: Germany
 Email: martin.rulsch@iis.fraunhofer.de

Field applications of a prosthetic mobile measuring system

S.Oehler¹, D.Hochmann¹ and M.Kraft¹

¹ Berlin Institute of Technology, Department of Medical Engineering, Berlin, Germany

Abstract— A mobile measuring system was developed to study the mobility and activity of amputees with focus on the applied loads to the metallic structures and therefore the resulting loads to the prosthesis. Equipped with strain gauges, the system had to be applicable to prosthetic adapters and meet certain criteria like limited geometrical - and strength - requirements. The developed portable system is able to record data (3D forces and moments) throughout the daily use of a prosthesis. First results were obtained in a study on transtibial amputees which were then used for the development of testing procedures for knee braces. With the results of an ongoing study on 15 transfemoral amputees over a period of one year a database can be generated to re-evaluate parameters of international standard testing (ISO 10328). Furthermore potentials for safer prostheses and higher functionality can be deduced from this data.

Keywords— gait analysis, prosthesis, knee brace, measuring system, strain gauges

I. INTRODUCTION

In Germany around 150.000 people wear prostheses of the lower limb but there is only little knowledge about how and how frequently they are used. In order to answer this question one needs to develop a system that can easily be integrated into prostheses and is able to measure forces and moments in all three dimensions. Other projects [1, 2] that also addressed this topic had problems to integrate a system into the limited available space which lead to a limited operating range of the patient or they discovered problems with interfering signals while clamping the components. So there was a need for a new approach that would at the same time open a broader field of applications.

Components of prostheses are tested to harmonized standards, e.g. ISO 10328, in order to certify that they are able to withstand the applied loads. The testing parameters defined in these standards should reflect the intended use within a typical time of usage. However, the underlying patient mobility measurements to obtain these parameters were carried out about 30 years ago.

Therefore one essential purpose of the project was to find out what a patient does with his/her prosthesis over a longer period of time and how the structure and the material are stressed during daily usage. Further interesting objectives

were how very heavy people stress the components, and what loads occur during swing phase of a gait cycle etc.

Currently available systems (e.g. microprocessor-controlled knee joints) provide higher functionality so that they can hardly be compared with the prostheses tested in 1976. Due to improved technology patient mobility increases while at the same time the prosthesis strength requirements are growing. Consequently, it is necessary to build up a new database which takes into account new technologies and active patients. The attained results allow to re-evaluate in what respect the new strength requirements and service life differ from previous values. Subsequently, conclusions can be drawn concerning patient mobility and criteria for standard testing.

Furthermore the system aids to compare the performance of different prosthetic knee joints and it can be used as a mobile gait analysis, especially to study loads during swing phase.

II. MATERIALS AND METHODS

In order to investigate loads in prosthesis during every day situations, it was necessary to develop a mobile measuring system that provides the ability to collect, save and analyze forces, moments and angles acting in the prosthetic structure over a representative period of time.

To achieve this, the system needs to meet certain criteria. In order to be easily replaced without major changes in the static alignment of a transfemoral prosthesis - which was one of the main target groups - it may not exceed the dimensions of a rotation adapter; therefore it must not be higher than 22 mm or wider than 45 mm. Furthermore, the bearing structure has to fit the prosthetic standard connectors to be applicable to different prostheses. Depending on the level of amputation the system should be positioned so as to not unnecessarily increase the oscillating weight.

The geometry of the structure was optimized via finite element analyses (Fig. 1) and tested according to ISO 10328. The appropriate position of the strain gauges in specific planes was also calculated by finite element method (FEM) to optimize the signals for measuring 3D forces and moments. Further components of the measuring system are two sensors measuring the absolute angles of thigh and shank, a data storage unit and an energy supply.

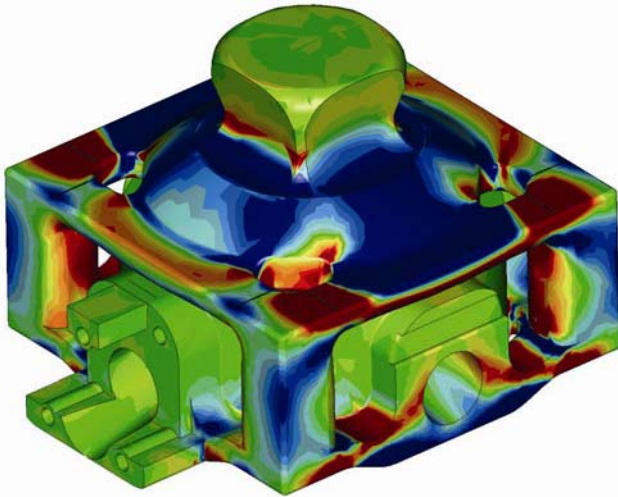


Fig. 1: FE analysis of the CAD-model of the measurement system (strains)

Data acquisition can be operated at various desired sampling rates up to 1024 Hz and a resolution of 12 bit. The memory and battery capacity supports up to 18 h recording time. Furthermore, the system was tested according to EN-60601-1-2. This certifies that the data recording will not be affected by environmental influences and the system will also not affect the function or safety of other electrical devices nearby.

The calibration of the force-moment sensor is carried out via an algorithm that transforms the eight amplified Wheatstone bridge signals into three forces and three moments.

Overall, the acquired signals can be extrapolated to every point in space e.g. hip, knee and ankle joint.

The visualization, data processing and data analysis allows to choose between various applications such as overload detection, histograms for the amplitudes and quantities of all corresponding loads and a gait pattern analysis. All results can be written to a data base and later filtered via different queries.

The system was validated by comparing its results to gait analysis data. There was a very close correlation during stance phase for the relevant forces, moments and angles. Furthermore a validation in a test stand compared the measured data with the data of a six degrees load cell. The variation was within 3% of the measuring range. These results confirm that the system performs accurately.

To get a better understanding how loads change with bodyweight the system was integrated into the prosthesis of ten heavy weight transtibial amputees. Their average weight was 143.5 kg (SD=4.85 kg). The position of the system in relation to the knee and ankle joint was measured. They were then studied walking around a course consisting of

stairs, ramps as well as even and uneven ground. The goal was to determine whether the dynamic proportion of the applied loads correlates with the higher weight during different walking situations and speeds of walking.

III. RESULTS

The results obtained from transtibial amputees using the force-moment sensor can also, with some limitations, provide valuable information for the development and testing of knee braces. As conventional force plate based gait analysis systems can only directly measure forces during the stance phase of gait, they do not provide any information on forces or moments in the swing phase. Moreover, the transformation from a global coordinate system used by optical systems to a local system is subject to errors and not always possible for published results. These limitations are especially important for the examination of the posterior cruciate ligament (PCL), because peak PCL strain occurs during swing phase at high knee flexion [3]. Measurements of anteroposterior shear forces during the complete gait cycle are also needed to validate existing models of anterior cruciate ligament (ACL) strain, which are neglecting centrifugal and inertial forces during swing phase [3]. This information can be provided through measurements on transtibial amputees as their natural knee is still intact, although there are some methodical limitations, like the absence of tibial musculature or the influence of prosthetic alignment. On the other side, knee rotation moments can not be obtained as there is no tibial terminal rotation due to the absence of the subtalar joint.

Fig. 2 shows the mean values of anteroposterior shear force measurements on transtibial amputees. The results show that the contribution of centrifugal and inertial forces to the anteroposterior shear force during swing phase at natural speed is very low with a maximum posterior force near heel strike of 2.3 %BW.

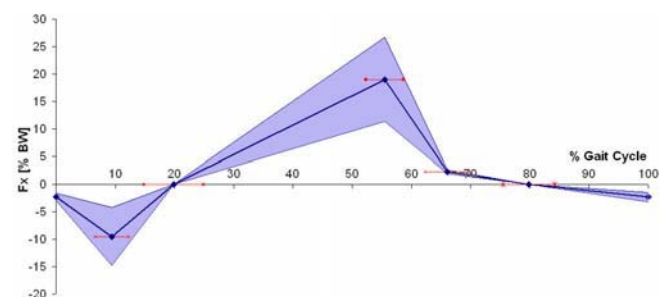


Fig. 2: Anteroposterior shear force in transtibial amputees (mean value and SD). Horizontal bars describe the deviation of characteristic points.

Fig. 3 shows the comparison btw. measured local system values and transformed global system values for one representative patient plus previously reported results in healthy volunteers [4].

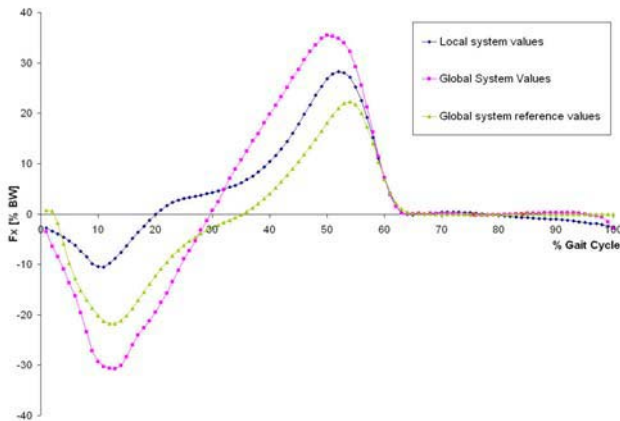


Fig. 3: Comparison of anteroposterior shear force btw. local system values, transformed global system values and previously published data [4]

To analyze the system’s long-term performance, it was tested in the field on different transfemoral amputees over 2 to 20 months.

In the following table (Tab. 1) results of two different subjects measured over a period of two months are listed.

Table 1 two months by two subjects

	Subject A			
	# number	length (h)	% 2 months	% 200 days
Level walking	251761	103.1	12.2	12.1
Stairs down	2154	0.7	0.1	0.1
Stairs up	4176	1.6	0.2	0.2
Standing (load)	58048	242.2	28.7	25.0
Kneeling	1679	29.8	3.5	3.8
Standing (no load)	39915	139.7	16.6	15.4
Sitting	3323	307.3	36.4	41.3
Lying	75	4.7	0.6	0.4
Cycling	0	0.0	0.0	0.0
No match	16782	14.2	1.7	1.7
	317818*	843.3	100	100
	Subject B			
	#number	length (h)	% 2 months	*# periodic load cycles
Level walking	154694	70.6	9.3	
Stairs down	1632	0.6	0.1	
Stairs up	1150	0.5	0.1	
Standing (load)	35185	103.1	13.7	
Kneeling	141	0.7	0.1	
Standing (no load)	14399	27.4	3.6	
Sitting	11200	419.2	55.4	
Lying	683	89.9	11.9	
Cycling	107638	31.8	4.2	
No match	18516	12.1	1.6	
	192802*	755.9	100	

The activity (cyclic loading) in relation to the weekly measured time of subject A is 12.5% and for subject B 13.7% (with cycling). We now have data of 200 days for subject A and there is remarkably little variation within the percentages. From this one can deduce that seasonal changes have no essential influence on this subject’s activity. The total number of cyclic loads also considers standing under load and kneeling because the prosthesis experiences an initial loading of more than 35% body weight. But these patterns are not considered for the activity calculations because the loading time of the prosthesis is at least more the three seconds which makes it a rather static loading.

IV. DISCUSSION

The measurements made so far only allow statements over a short period of time. A study with 15 transfemoral amputees (5 of each mobility grade MOBIS™ 2-4, 10 with C-Leg®, 5 with 3R60®) and a continuous observation time of one year started in April 2008.

The results are i.a. supposed to allow statements concerning the daily activities of the subjects and the consequential loads to the prosthesis. The number of instances (loading cycles) and the kind of gait pattern can help to build up load collectives which take into account principles of cumulative damage analysis. Subsequently the tests for service life of prosthetic components can be carried out according to a model based on experimental data gained from long term field tests.

If based on these findings the standard testing of ISO 10328 will be reviewed also an optimization of the prosthetic construction lies within the horizon of this study. This would improve the mobility and safety of above-knee amputees, and, ultimately of all lower extremity amputees.

REFERENCES

1. M. Nietert et al.: Ein portables Meßsystem zur Erfassung von Belastungswerten in Beinprothesen als Alternative zu stationären Ganganalysesystemen, OT, 1998, S. 13-32.
2. W. Lee et al.: Direct Measurement of 3D Force and Moment on Lower-Limb Osseointegrated Fixation, Proceedings Symposium on the 3D Analysis of Human Movement, Valenciennes, France.
3. K.B. Shelburne et al.: Pattern of anterior cruciate ligament force in normal walking. J Biomech 37 (2004), S. 797–805.
4. D. Waldmann: Biomechanik des Gehens auf verschiedenen Neigungen - eine kinetische, kinematische und elektromyographische Untersuchung. Universität Göttingen, 2006.
 Author: Simone Oehler
 Institute: Fachgebiet Medizintechnik, TU Berlin
 Street: Dovestr. 6
 City: Berlin
 Country: Germany
 Email: simone.oehler@tu-berlin.de

Force fluctuations in a simulated motoneuron pool

A.F. Kohn¹

¹ University of São Paulo, São Paulo, Brazil

Abstract— Force fluctuations, even for maintained isometric force, have many origins and are attributed to noise, errors and variabilities associated with different elements of the sensory-motor system. Part of the random-like fluctuations of the force is due to the motor pathway per se and much work has been focused in quantifying the fluctuations and in determining their dependence on variables such as number of motor units, discharge rate variability of each motor unit, etc. A recently developed simulator of the neuromuscular control system was utilized here to verify stochastic features of the simulated force signal generated by the soleus muscle for different mean force levels. The mean force level increased in a sigmoidal fashion as the intensity of the descending drive increased. The standard deviation of force as a function of mean force level resulted in an approximate parabola, while the coefficient of variation of force decreased monotonically with mean force level. Force power spectrum was strongly concentrated in the 0-5 Hz frequency range. Individual motor unit force signals showed a tendency for decreased force variability as overall muscle force level increased, helping to explain the relation found between muscle force variability and mean muscle force. Comparisons are made with results from the literature of simulations of other muscles and the differences and similarities are discussed.

Keywords— force variability, motor units, neuronal models, neuromuscular system.

I. INTRODUCTION

Normal subjects exhibit fluctuations in force along time (called here force variability for short) when pushing or pulling against a fixed object [1,2]. Excessive force variability, e.g., due to disease, hampers the performance of movements and may lead to difficulties in keeping the appropriate posture to avoid falls. For the few muscles that have been tested, the literature shows that the standard deviation of a force developed against a fixed object exerted with a constant volitional effort increases with the mean value of the force [3]. On the other hand, the force coefficient of variation has usually been found to decrease with the intensity of the exerted force [1,3]. Mathematical modeling and simulation have been important tools in the study of the mechanisms behind the experimental results reported in the literature concerning force variability [3-6]. The objective of the present paper was to investigate how features such as the standard deviation and coefficient of variation of force vary as a function of force in a recently developed comprehensive neuromuscular model of leg muscles and their neural control [7]. Previous investigations in the literature on force variability employed a popular phenomenological model [8]. In this model, the spike trains of each motoneu-

ron have their statistical features appropriately defined to mimic those found in nature. In the new model [7] each motoneuron is modeled as a two-compartment dynamical system with parameters based on biophysical data. The motoneuron pools are driven by several dozens of axons, each carrying a Poisson point process.

II. MATERIALS AND METHODS

A. The simulator

The soleus muscle was controlled in the simulator by 900 motoneurons, 800 being of type S, 50 of type FR and 50 of type FF. The individual motoneurons were represented by two-compartment models with fast and slow dynamics in the soma and a passive dendritic compartment [7]. The Hodgkin-Huxley-like dynamics were approximated by the pulse activation method [9] for computational efficiency. The synaptic inputs activated dendritic conductances according to a two-state kinetic model [10], which provided computational efficiency and good biological reality. The descending drive was enacted by 100 axons, each carrying an independent Poisson process spike train. Each of these axons activated a randomly selected fraction of 20% of the motoneuron pool. A motor unit twitch was implemented as the impulse response of a critically damped second order system. The peak amplitude ranges of the twitches employed in the simulations were the default values given in the simulator: from 10.5 to 12.5 gf for the S type motor units, 12.5 to 30.0 gf for the FR type motor units and 30.0 to 50.0 for the FF type motor units.

B. Procedures

All possibilities of random parameter variations were disabled prior to starting the simulations so that a similar network could be used for every simulation run. The mean interspike interval values of each Poisson process of the corticomotoneuronal pathway were varied from 1 ms to 10ms, which means that the mean rate of each descending axon was varied from 100 Hz to 1000 Hz. This range approximately covered the generation of contraction forces varying from 0 up to about 80% the maximum muscle force (f_{\max}). The value of f_{\max} was measured from a simulation where the nerve to the muscle was stimulated by a 100 Hz train of pulses. In the simulations reported here, no Renshaw cells were included, so the motoneuron pool responded only to the drive from the corticomotoneuronal pathway. In spite of the stochastic nature of the system, only a single

simulation run was used to obtain the force signal corresponding to a given parameter set due to the long times involved in any simulation.

III. RESULTS

Following the activation of the descending Poisson trains the force increased towards a plateau value, around which it oscillated randomly. Fig. 1 shows several force signals in response to different levels of fixed intensity descending drive. The bottom signal was generated in response to a 133 Hz mean rate of Poisson per axon while the uppermost was due to a 1000 Hz Poisson drive per axon.

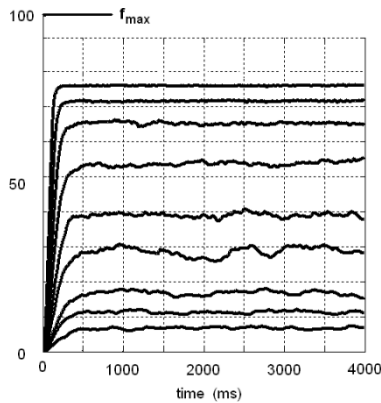


Fig. 1 Muscle force as a function of time for different activation levels, increasing from bottom to top. The ordinate is a percentage of f_{max} .

The two highest levels of force corresponded to the recruitment of the first 800 and 850 motoneurons, respectively. This means that only for the 1000 Hz Poisson descending drive trains did the FR motoneurons get recruited. For all the other mean rates of the Poisson drive trains only the type S motoneurons were recruited. The increase in force level in response to the increase in descending drive intensity followed a sigmoidal-like relation, as shown in Fig. 2.

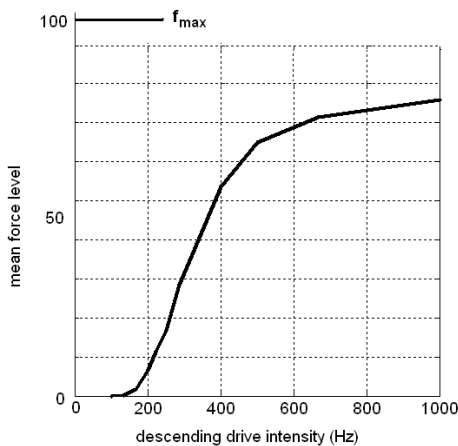


Fig. 2 Mean muscle force level as a function of the intensity of the descending drive (the mean rate of each of its Poisson spike trains).

There was an increase in force variability up to medium levels of force followed by a decrease when the mean force levels were larger. This can be seen qualitatively in Fig. 1, and quantitatively in Fig. 3.

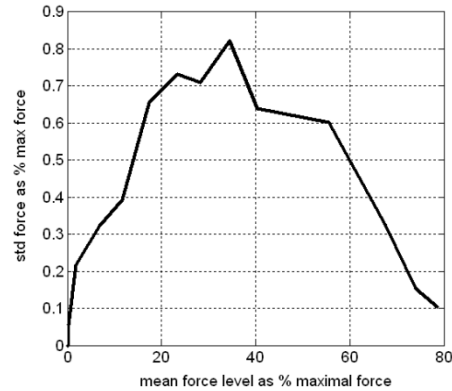


Fig. 3 Standard deviation of force as a function of the mean force, both indicated as a percentage of the maximum force.

On the other hand, the relation between the coefficient of variation ($CV = \text{standard deviation} / \text{mean}$) and the mean force followed a hyperbolic type of relation (Fig. 4).

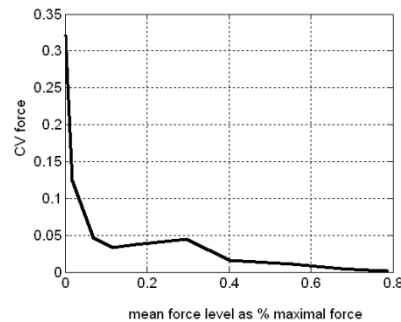


Fig. 4 Coefficient of variation of force as a function of the mean force, the latter indicated as a percentage of the maximum force.

Next, an analysis was made of the CVs of the forces generated individually by the motor units 1, 267, 533 and 800 from the pool. These were chosen equispaced in terms of their mean recruitment thresholds. Two points were chosen arbitrarily on the ascending limb of the curve of Fig. 3 and two on the descending limb. The corresponding descending drive intensities were found to be 200 Hz, 250 Hz, 400 Hz and 500 Hz, respectively. The resulting values of motor unit force CV in percentage may be seen on Table 1. These results suggest that a given motor unit tended to decrease its force variability in the model as the drive intensity increased, or (from Fig. 2) as the muscle mean force level increased. On the other hand, at a fixed drive intensity, the higher threshold MNs tended to command forces with higher CVs.

Table 1 Coefficient of variation (in %) of force generated by individual motor units 1, 267, 533 and 800 for descending drive frequencies shown on the first line (Poisson rate per descending axon). In three cases the motoneuron did not fire, so the CV is not defined.

	200 Hz	250 Hz	400 Hz	500 Hz
MN 1	98.80	4.73	2.50	1.45
MN 267	10.77	11.55	7.18	1.28
MN 533	-----	32.4	12.6	2.21
MN 800	-----	-----	11.41	2.26

Finally, for a mean force level about 60% MVC (point in the descending limb in Figure 3) the power spectrum of the force signal (taken in the 1-4s interval) resulted as shown in Figure 5. Power was concentrated at low frequencies, 73% of the total power being in the range from 0 to 4 Hz.

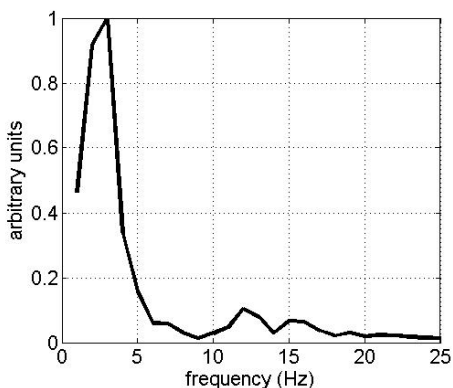


Fig. 5 Force power spectrum estimated by Welch's method for a force level about 60% MVC.

IV. DISCUSSION

Initially, the results will be compared with those described in the literature using the phenomenological model of [8]. The force curves in Fig. 1 resemble those described in [1,5] except for the smaller variability found here for the higher force signals (see below). The sigmoidal-like relationship between force and descending drive intensity shown in Fig. 2 is similar to that described in [1]. Simulations with specific model parameter values reported a monotonic increasing function relating force standard deviation to mean force [1,3] while others reported a peaking or saturation-like effect at higher force levels [5,6]. The result in Fig. 3 is not in accordance with these previous results from the literature. However, Keenan et al [4] ran an extensive Monte Carlo simulation using wide parameter ranges for the phenomenological model and found a large number of curves reminding that in Fig. 3, i.e., showing an initial increase in force standard deviation followed by a decrease. These same authors reported that only for narrow parameter ranges could they find reasonably good agreement between

experimental and simulated data on the basis of functions that related variables such as those in Fig. 3 as well as others. The CV as a function of mean force curve of Fig. 4, resembling a hyperbolic curve, was similar to previous reports [3,1]. Finally, the force power spectrum shown in Fig. 5 was similar to those shown in [5] for experimental data (50% MVC) from a small hand muscle and for a specific computer simulation that included a 1Hz frequency modulation of the descending drive. Here, our power spectrum was obtained without any modulation of the descending drive. In [6] the authors obtained a spectrum with a power concentration as shown in Fig. 5 when the motor units were simulated with a "high" level of synchronism.

It is important to point out that, except for [4], the other papers adjusted the model parameters to yield appropriate fittings to experimental curves relating standard deviation and coefficient of variation of force as a function of mean force. The muscles involved were usually small hand muscles. In the simulations reported here, practically the default values of the simulator were employed, as found in www.remoto.leb.usp.br and in [7].

The results based on the simulations are useful from at least two perspectives: *i* allowing the analysis of the influences of the elements, parameters or variables of the system on the force variability, *ii* giving predictions of how the given muscle should behave if the modeling hypotheses are appropriate. With respect to the latter, an additional important consequence is that if experimental data are not reproduced well by the simulations, new hypotheses are generated, which point to new experiments, to improvements in the modeling and perhaps to conceptual changes.

The results reported here have not dealt with the problem of evaluating the effects of different model features or parameter values on force variability. There were some efforts in the literature to study the influence of different parameters of the neuromuscular system on force variability [1,3-6] based on the phenomenological neuromuscular model of [8]. Number of motoneurons in the pool, the relation between twitch peak of the largest motor unit and that of the smallest motor unit, the level of discharge irregularity of the motoneurons and the degree of synchronism between the motoneurons were all shown to have significant effects on force variability. A similar effort seems worthwhile using the new model proposed in [7] but is outside the scope of the present paper. However, from some of the data presented here, one can grasp why the standard deviation versus mean force curve showed a falling limb (Fig. 3). In Table 1 one sees that for increased muscle force level (i.e., higher descending drive) the force variability of each motor unit decreases. One reason is that the motoneurons tend to fire more regularly (not shown). In addition, at higher descending drives, the motor units tend to show a fused force signal near to its maximum (saturated) level (not shown), which also yields a lowered force variability. The difficulties of a mathematical approach to predict the muscle force variability in terms of the various elements of the neuro-

muscular system stem from the fact that the system is of high dimensionality, nonlinear and stochastic.

On the issue (*ii*) of the usefulness of simulation results in predicting an experimental outcome, the results presented here stand as a conjecture. This is so, because, to the author's knowledge, there is no experimental data available on the force variability behavior of the human soleus muscle. However, if the experimental results should indicate an increasing relation between the standard deviation of force and the mean force level (as has been found in other muscles with a less homogeneous fiber-type composition), then the present neuromuscular model would have to be changed either in terms of its parameter values (e.g., larger ranges of twitch peaks along the motoneuron pool as in [1]) or in its structure. Hence, the results shown in the present paper are a point of departure for future research that will try to integrate experimental and simulation data to further our understanding of motor control of the lower limbs in humans.

ACKNOWLEDGMENT

This work was financed by grants from CNPq and Fapesp (from Brazil).

REFERENCES

1. Jones KE, Hamilton AFC, Wolpert, DM (2002) Sources of signal-dependent noise during isometric force production. *J Neurophysiol* 88:1533-1544
2. Moritz CT, Barry BK, Pascoe MA, Enoka RM (2005) Discharge rate variability influences the variation in force fluctuations across the working range of a hand muscle. *J Neurophysiol* 93:2449-2459
3. Hamilton AFC, Jones KE, Wolpert DM (2004) The scaling of motor noise with muscle strength and motor unit number in humans. *Exp Brain Res* 157:417-430
4. Keenan KG, Valero-Cuevas J (2007) Experimentally valid predictions of muscle force and EMG in models of motor-unit function are most sensitive to neural properties. *J Neurophysiol* 98:1581-1590
5. Taylor AM, Christou EA, Enoka RM (2003) Multiple features of motor-unit activity influence force fluctuations during isometric contractions. *J Neurophysiol* 90:1350-1361
6. Yao W, Fuglevand RJ, Enoka RM (2000) Motor-unit synchronization increases EMG amplitude and decreases force steadiness of simulated contractions. *J Neurophysiol* 83: 441-452
7. Cisi RRL, Kohn AF (2008) Simulation system of spinal cord motor nuclei and associated nerves and muscles, in a Web-based architecture. *J Comput Neurosci* 25:520-542
8. Fuglevand AF, Winter A, Patla AE (1993) Models of recruitment and rate coding organization in motor-unit pools. *J Neurophysiol* 70: 2470-2488
9. Destexhe A (1997) Conductance-based integrate-and-fire models. *Neural Comput* 9:503-514
10. Destexhe A, Mainen ZF, Sejnowski TJ (1994) An efficient method for computing synaptic conductances based on a kinetic model of receptor-binding. *Neural Comput* 6:14-18

Author: Andre Fabio Kohn
 Institute: Universidade de Sao Paulo, EP, PTC
 Street: Cidade Universitaria
 City: Sao Paulo
 Country: Brazil
 Email: andfkohn@leeb.usp.br

Effect of passive stepping on the H-reflex in the wrist flexor

T. Kitamura¹, T. Nakajima², K. Kamibayashi³, S-I. Yamamoto¹, M. Akai² and K. Nakazawa²

¹ Graduate School of Engineering, Shibaura Institute of Technology, Saitama, Japan

² Department of Rehabilitation for Movement Function, National Rehabilitation Center for persons with Disabilities, Saitama, Japan

³ Graduate School of Systems and Information Engineering, University of Tsukuba, Ibaraki, Japan

Abstract— It is possible for patients with spinal cord injury and stroke to regain locomotor-like activity with intense step training on a treadmill. However, the neural mechanisms underlying the reattainment of locomotor activity are unknown. In particular, the principles governing interlimb coordination is not known. Therefore, we investigated modulation of the H-reflex in the flexor carpi radialis (FCR) of 10 subjects during passive stepping of the leg. Passive stepping tasks were performed with the aid of a robotic gait trainer system (Lokomat). The H-reflex in the FCR was elicited by electrical stimulation of the median nerve at the elbow level and recorded during 10 different phases of the walking cycle and static standing condition. The results showed that passive stepping significantly suppresses the FCR H-reflex amplitude as compared with static standing condition. These results suggest that movement-related afferent leg feedback mediates suppression of forearm H-reflex during passive stepping.

Keywords— H-reflex, passive stepping, interlimb coordination.

I. INTRODUCTION

Rehabilitation techniques involving unloading the body weight and assisted leg movements during walking by the physiotherapist or with the aid of robotic orthosis are useful for regaining the function of walking after spinal cord injury or stroke [1][2]. However, the process or mechanism underlying the reattainment of locomotor activity is still unknown.

In this study, we focused on the interlimb coordination between the upper and lower limbs. Previous studies have described the functional connection between the upper and lower limbs. Dietz et al. investigated the locomotor pattern in subjects who had suffered from complete or nearly complete spinal cord injury with lesions at different levels in the spinal cord. The subjects were made to walk on the treadmill when their body weights were partially unloaded with support [3]. They reported that a more normal locomotor pattern was observed in subjects with lesions at a higher level in the spinal cord, which is responsible for upper and lower limb functions, than in those with lesions at a lower level in the spinal cord, which is responsible for only lower limb functions. This suggests that the segment of the spinal cord responsible for upper limb function is important during walking, and further studies of this region may provide

considerable insights in understanding the mechanism underlying walking in humans.

Recently, it has been reported that voluntary leg cycling interfered with the segment innervating the forearm muscle [4]. However, it is still unknown whether this phenomenon was ascribed to the afferent feedback related to leg movement. Therefore, we investigated the modulation of the H-reflex in the flexor carpi radialis (FCR) during robotic passive stepping.

II. MATERIALS AND METHODS

A. Subjects

Ten neurologically intact volunteers aged 22–32 years (8 male and 2 female subjects) participated in this study. All the subjects provided their informed consents according to the declaration of Helsinki before participating in the experimental procedures. This study was approved by the local ethics committee.

B. Protocol

We used the driven gait orthosis system (Lokomat; Hocoma AG, Volkeltswil, Switzerland) mounted on a treadmill to produce passive stepping. Subjects were positioned on the Lokomat and their right forearm was fixed on the platform to reduce unwanted movement.

The H-reflex was recorded in the FCR muscle of the right side at 2 different conditions: (1) static standing position on the Lokomat, which was used as a control and (2) passive stepping using the Lokomat system. The treadmill speed was set to 2.0 km/h (0.56 m/s) during passive stepping. The subjects were asked to keep the FCR and the whole body relaxed throughout the experiment.

C. Recordings

Surface-active electrodes were used to record electromyographic (EMG) signals from the FCR, extensor carpi radialis (ECR), tibialis anterior (TA), soleus (Sol), rectus femoris (RF), and biceps femoris (BF) muscles on the right side of the body. EMG signals were amplified and band-

pass filtered from 15 Hz to 1000 Hz, except for the FCR in which the EMG signal was filtered from 15 Hz to 3000 Hz by using a bio-amplifier system (MEG-6108, Nihon Kohden, Tokyo, Japan).

Kinematics data of the hip and knee joints were obtained from potentiometers embedded in the Lokomat system, and ankle joint data were recorded using an electrogoniometer (DLK800, Biometrics Co. Ltd, Newcastle upon Tyne, UK) placed over the ankle joint.

D. Nerve stimulation

In order to evoke the H-reflex in the FCR, electric stimulation was delivered to the median nerve at the elbow with a single rectangular pulse using a constant current stimulator (SS-100, Nihon Kohden, Tokyo, Japan). During passive stepping, stimuli were pseudo-randomly delivered at every 10% of one step cycle on the basis of the heel strike. The stimulus intensity was set to 10% of the maximum M-wave (M_{max}) just before each trial and adjusted to maintain the M-wave amplitude during trials.

E. Data and statistics analysis

The peak-to-peak amplitude of the H and M-waves was calculated from the single sweeps of EMG. These data were normalized to corresponding M_{max} values to reduce the inter-subject variability and averaged for comparison of trials. The background EMG (BG EMG) was root mean squared for 50 ms before stimulus.

To identify the significant effects of passive stepping or the stepping phase on the H-reflexes, repeated one-way ANOVA was performed for passive standing and each phase of passive stepping. Tukey's honestly significant difference (HSD) test was used to post hoc significant main effects.

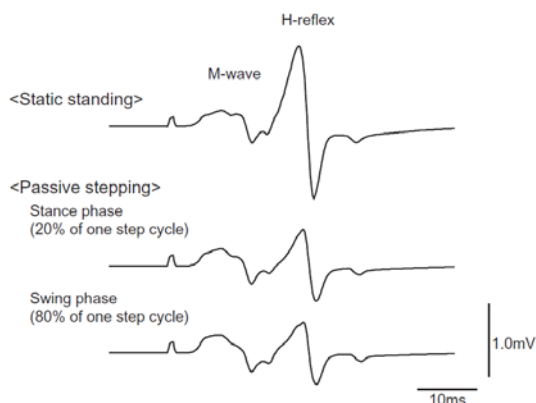


Fig. 1 The averaged waveform of the FCR H-reflex and M-wave during static standing and the stance phase (20% of 1 step cycle) and swing phase (80% of 1 step cycle) of passive stepping in 1 subject.

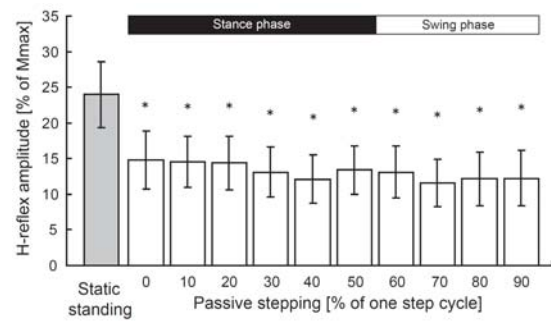


Fig. 2 H-reflex modulation during passive standing and stepping. The grey bar represents the mean amplitude \pm SE during passive standing. White bars represent the mean amplitude \pm SE during passive stepping. * $p < 0.05$.

III. RESULTS AND DISCUSSION

The averaged waveform in a single subject during static standing and passive stepping is shown in Figure 1. The H-reflex amplitude during passive stepping was significantly suppressed as compared with that during passive standing ($p < 0.001$; Figure 2), although the M-wave and background FCR EMG activity did not differ over the course of the stepping phase (M-wave: $p = 0.245$, BG EMG: $p = 0.143$; data not shown). Furthermore, these comparable suppressive effects of the H-reflex were observed at all phases of passive stepping; there was no phase-dependence.

These results were similar to those of a previous study that recorded the FCR H-reflex during voluntary leg cycling [4]. In this study, it was shown the forearm H-reflex was suppressed by passive leg movement as compared with static standing. These results suggest that movement-related afferent feedback mediates suppression of forelimb H-reflex pathways during passive stepping.

REFERENCES

1. Wernig A, Müller S, Nanassy A et al. (1995) Laufband therapy based on 'rules of spinal locomotion' is effective in spinal cord injured persons. *Eur J Neurosci* 7: 823–829
2. Hesse S (2008) Treadmill training with partial body weight support after stroke: A review. *Neuro Rehabilitation* 23: 55–65
3. Dietz V, Nakazawa K, Wirz M et al. (1999) Level of spinal lesion determines locomotor activity in spinal man. *Exp Brain Res* 128: 405–409
4. Zehr E.P, Klimstra M, Johnson E.A et al. (2007) Rhythmic leg cycling modulates forearm H-reflex amplitude and corticospinal tract excitability. *Neurosci Lett* 419: 10–14

Author: Taku Kitamura
 Institute: Shibaura Institute of Technology
 Street: 307 Fukasaku Minuma-ku
 City: Saitama 337-8570
 Country: Japan
 Email: t.kitamura.bpe@gmail.com

On the Efficacy of Haptic Guidance Schemes for Human Motor Learning

Volkan Patoglu¹, Yvonne Li², and Marcia K. O'Malley²

¹ Faculty of Engineering and Natural Sciences, Sabancı University, İstanbul, Turkey

² Department of Mechanical Engineering and Material Science, Rice University, Houston, USA

Abstract—This article investigates the efficacy of different haptic guidance schemes on human motor learning. In particular, the performances of four training protocols, virtual practice, virtual fixtures, fixed-gain error-reducing shared control, and progressive error-reducing shared control, are compared. The experimental results indicate that, if not designed carefully, haptic guidance protocols may be detrimental on motor learning, since such schemes actively interfere with the coupled system dynamics and cause participants to experience task dynamics that are altered from those of the real task. Results also show that the amount of assistance is an important factor, and fixed-gain assistance schemes may cause subjects to gain dependence on the existence of the guidance. Adjusting the amount of haptic guidance based on performance, utilizing progressive gains, is shown to increase the training effectiveness when compared to fixed gain controllers. Key parameters that influence the principles of motor learning in healthy human subjects may guide the design of more effective rehabilitation training protocols.

I. INTRODUCTION

Assistance of repetitive and physically involved rehabilitation exercises using robotic devices not only helps eliminate the physical burden of the movement therapy for the therapists, but also enables safe and versatile training with increased intensity. Robot assisted therapy can be used to treat patients with all levels of injury, allows for quantitative measurements of patient progress, and can be tailored to induce patient specific treatment protocols. With the addition of virtual environments and haptic feedback, these devices can be used to realize new treatment protocols; hence, promise to improve the efficacy of treatment.

In the literature, beneficial effects of robot assisted rehabilitation over conventional therapy have been demonstrated. However, the magnitude of benefits achieved over conventional therapy in terms of functional outcome has only been modest. The limited success of early implementations of rehabilitation systems is attributed to the human-machine interface established by the controller design of these devices that does not allow for active involvement of patients. Specifically, many of these devices employ robots as non-accommodating trajectory generators, while the patients are expected to behave as passive subjects. Recent studies suggest that intervention methods that emphasize the active involvement of patients in the physical therapy routine and provide assistance to the patient *as needed* in order to render the task completion feasible, possess the potential to have positive influence on the efficacy of the rehabilitation therapies.

Unfortunately, only a limited amount of clinical evidence is available on how to optimally engage patients. The relationship between many of the proposed intervention

protocols and their clinical outcomes is yet to be studied. The design of effective treatment schemes is not a trivial task and the investigation of the optimal intervention scheme through trial and error techniques is prohibitive due to time consuming nature and high cost of clinical trials. Hence, a more effective framework is necessary to study rehabilitation protocols.

Since it is the plasticity of CNS that enables injured people to recover and healthy people to learn new motor skills, the principles of motor learning in healthy subjects may guide the design of effective treatment protocols. Even though one cannot assume that the damaged CNS learns in the same manner as the intact one, the key parameters that influence acquisition of skill may be relevant for both cases.

This article investigates the efficacy of different haptic guidance schemes on human motor learning. In particular, the performance of four training protocols, virtual practice, virtual fixtures, fixed-gain error-reducing shared control, and progressive error-reducing shared control, are compared with a long-term human subject experiment. The possible detrimental influence of haptic guidance schemes on learning is demonstrated. The importance of the amount of assistance is discussed and the efficacy of progressive gains over fixed gains is shown. These results are relevant to the rehabilitation literature, since the principles of motor learning in healthy subjects may guide the design of more effective treatment protocols.

To date, several performance-based assistance schemes have been implemented in the field of rehabilitation robotics. In [1], a performance-based progressive robot-assisted therapy for stroke patients was implemented. The patients were provided with haptic guidance during a reaching task by means of a virtual spring pulling them towards the target. The spring coefficient, hence the amount of guidance, was adjusted based on the performance of the patients. Unfortunately, no conclusive training results are reported for this study. In another study for gait training, human motor adaptation to dynamic environments was modeled as an error corrective learning process and the control gains of the guidance robot were adjusted at each trial based on the error [2]. The results from the interaction simulations of this study suggest that providing guidance as needed is more effective than always assisting with a fixed amount. Similarly, in [3] assist-as-needed protocols have been proposed and tested for gait training. The results of our study provide further experimental evidence on the positive efficacy of progressive gains over fixed gains while assisting task completion and supports use of assist-as-needed protocols in the rehabilitation literature.

II. METHODS

A. Task

The task for the training experiment is a target-hitting manual control task. Participants view a virtual double-mass spring system on a computer monitor and are asked to control the motion of mass m_1 via a two DoF haptic device, a joystick. Through the two-mass system's dynamics, the participants are able to indirectly control mass m_2 to alternately hit a fixed pair of targets. The targets are equidistant from the origin; therefore, the participants need to move the joystick, directly coupled to m_1 , rhythmically, along the sloped path (referred to as the target axis), to cause m_2 to alternately hit the target pair. The task objective, as presented to each participant, is to hit as many targets as possible in each 20 second trial.

B. Participants

Thirty-two participants (8 females, 24 males, ages 18–33, 1 left-handed), primarily undergraduate students in engineering, participated in the experiment.

C. Performance Measures

Two performance measures were analyzed to assess participant performance for the target-hitting task, namely normalized hit count and average error. Normalized hit count is the total number of target hits within one trial normalized by the natural frequency of the corresponding dynamic system. Average error is the average of the instantaneous trajectory errors of mass m_2 . Together, these performance measures capture the features of the task, where normalized hit count gives an assessment of speed of execution, while average error monitors the ability of the participant to maintain a trajectory along the target axis. Average error is treated as a secondary performance metric, since participants are not specifically instructed to reduce the deviation of m_2 from the target axis. Nevertheless, these two measures provide a means for the proposed haptic guidance schemes to be objectively compared.

D. Haptic Guidance

The four different haptic guidance schemes presented and subsequently compared in this experiment are virtual practice, akin to no assistance (N), virtual fixtures (V), fixed-gain (S) and progressive error-reducing (P) shared controllers. In the virtual practice (N) mode, participants felt the forces generated solely due to the internal dynamics of the 2 DoF system. In contrast, for the virtual fixtures (V) and shared control cases (P and S), participants felt the forces due to both the internal dynamics of the system and the guidance forces intended to assist.

In the virtual fixtures (V) guidance mode, virtual walls were used to encourage users, in a passive manner, to move mass m_1 along the target axis, thereby causing m_2 to settle along the same path. The virtual walls generated forces proportional to the deviation and velocity of mass m_1 normal to the x -axis. In the error reduction implementation of shared control (P and S), the dynamics of the (state dependent) shared controller are designed such that the coupled (closed loop) dynamics of the system are simpler to manipulate than

the system dynamics without the controller in place. In particular, this training scheme differs from the virtual fixtures in that perceptual constraints are not implemented on user input but on user output, and are reflected to the user through the inverse dynamics of the system to be controlled. The detailed implementation of error reducing shared controller is described in the authors' previous works [4].

The performance-based progressive algorithm was employed to determine the gains of the controller during assistance sub-sessions for progressive shared control (P). The input performance measurement for the algorithm was the normalized hit count since it is the primary goal of the task. The progressive shared controller (P) started with the same control gains as fixed-gain shared controller (S). The progressive shared control gain update law was controlled by a rolling average of three consecutive trials. Once the average of the current trial and two previous trials (average 2) is larger than the average of previous three trials (average 1), the control gain decreases. On the other hand, if average 2 is smaller than average 1 for three consecutive trials, control gain increases. Furthermore, if the absolute value of average 1 is above a certain threshold, 30 normalized hit counts, the control gain decreases. The control gain was adjusted based on the ratio of difference between average 1 and average 2 over average 1. This update law, similar to the one-up three-down scheme described by Levitt [5], aims to decrease the haptic guidance, thereby decreasing the dependence on the guidance while the participant's performance still increases. In this way the progressive shared control scheme approaches virtual practice toward the end of training. Figure 1 depicts the decaying progressive shared control gain of a typical participant.

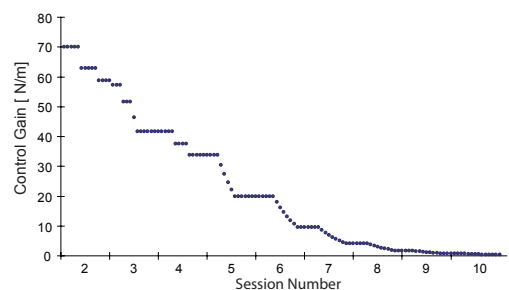


Fig. 1. Progressive shared control gain of a participant during assistance sub-sessions #2-10 illustrates the typical decaying trend. Decreasing gain is indicative of improving performance in terms of normalized hit count.

E. Experiment Design

The experiment was composed of 11 sessions, including an evaluation session, nine training sessions, and a retention session. Each training session contained three sub-sessions: pre-assistance baseline, assistance, and post-assistance baseline. Each sub-session consisted of 14 trials, with each trial lasting 20 seconds. Details of the experiment design are schematically represented in Figure 2.

F. Procedure

Before the experiment, each participant was given a maximum of five minutes to become familiar with the haptic joystick and the virtual task. In order to control for individual differences in performance, each participant was asked to

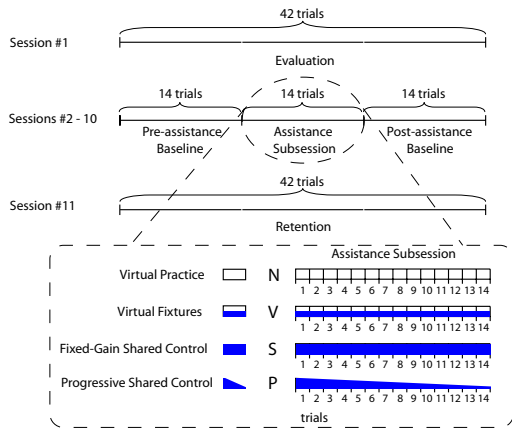


Fig. 2. Experiment consists of one evaluation, nine training and one retention session. Each training session contains three subsessions: pre-assistance baseline, assistance, and post-assistance baseline.

perform the task in an evaluation session, administered without haptic guidance. Then, participants were assigned to one of four training protocols based on their initial performance of the target-hitting task.

All groups completed one evaluation session, nine training sessions, and one retention session. The virtual practice (N) group served as the control set with no haptic guidance provided during assistance subsessions of the protocol. In order to assess the improvement of participants across the nine training sessions, baseline subsessions of 14 trials administered without guidance were completed before and after each assistance subsession. One assistance subsession and its corresponding pre- and post-assistance baseline subsessions took place in one 30 minute session. The nine training sessions were separated by two to three days, such that the participants completed all the sessions in no less than three but no more than four weeks. One month after the final training session, all participants were recalled to complete one retention session. In the evaluation and retention sessions, no haptic guidance was provided to any participants.

G. Data Analysis

Repeated measure ANOVAs were utilized to determine significance of results. The guidance mode was between-subjects, with levels virtual practice (N), virtual fixtures (V), fixed-gain (S) and progressive (P) shared control. The session factor was within-subjects, with levels of evaluation, training (9 in all), and retention, for a total of 11 levels. Difference of least square means is used as the multi comparison strategy.

III. RESULTS

Figure 3 shows the results for all four groups in the post-assistance baseline subsession in order to compare the efficacy of different haptic guidance schemes. The performance of all groups improved significantly in terms of both performance measures (normalized hit count and average error) and saturated near the end of training. A repeated measures ANOVA with between-subject factors (group as between-subject factor, session as within-subject factor) was carried out to determine significance of results for these four groups. The results revealed a significant main effect of group and session for the post-assistance subsessions in terms of both normalized hit count and average error.

Summaries of ANOVA and all pertinent multi comparisons at post-assistance are listed in Tables I and II, respectively. Figure 3, Tables I and II reveal that S group exhibits

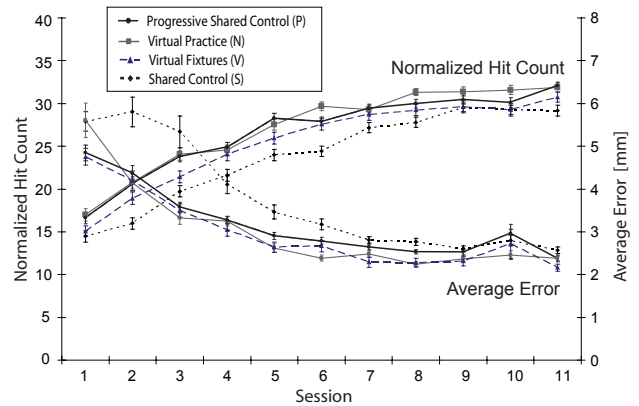


Fig. 3. Post-assistance baseline normalized hit count and average error plots for different haptic guidance groups over eleven sessions of the training protocol.

TABLE I

SUMMARY OF SIGNIFICANCE OF FACTORS		
Measure	Effect	post-assistance
Normalized Hit Count	Group	$F(3, 444) = 13.29, p < 0.0001^*$
	Session	$F(8, 437) = 182.58, p < 0.0001^*$
	Interaction	$F(24, 1268) = 2.28, p = 0.0004^*$
Average Error	Group	$F(3, 444) = 19.67, p < 0.0001^*$
	Session	$F(8, 437) = 67.16, p < 0.0001^*$
	Interaction	$F(24, 1268) = 3.33, p < 0.0001^*$

TABLE II

SUMMARY OF SIGNIFICANCE FOR MULTI COMPARISON		
Group Comparison	Average Error	Normalized Hit Count
S vs. N	$p < 0.001^*$	$p < 0.001^*$
S vs. V	$p < 0.001^*$	$p < 0.001^*$
S vs. P	$p < 0.001^*$	$p < 0.001^*$
N vs. V	$p < 0.001^*$	$p > 0.05$
N vs. P	$p > 0.05$	$p > 0.05$
V vs. P	$p = 0.003^*$	$p = 0.042^*$

the worst performance among all the groups in terms of both normalized hit count and average error. V group is significantly worse than N and P groups in terms of average error, while is not significantly different from N group in terms of average error. P group exhibits performance at least as good as N group in terms of both normalized hit count and average error.

IV. DISCUSSION

Among all the haptic assistance training paradigms tested in this study, P group is the only training protocol that has comparable overall performance to N group (virtual practice). This result indicates that fixed-gain guidance schemes (V and S) in fact have negative training efficacy and these paradigms are less effective for training of motor skill than practicing without assistance forces.

To further explore the negative efficacy of S and V groups, learning trends within a session and across sessions are analyzed in Figure 4 for the hit count performance. Figure 4 consists of two plots: a line plot displaying absolute task performance improvement within a session, with each line segment corresponding to one training session, and a bar plot representing the percent change of performance within a session. For both plots, the data represents a comparison

of the average performance of the last three trials of the pre-assistance baseline subsession to the average performance of the first three trials of post-assistance baseline subsessions. These values characterize within session performance of a group just before and just after the assistance subsession, quantifying the amount of learning that occurred within the assistance subsession. As depicted in Figure 4, all groups

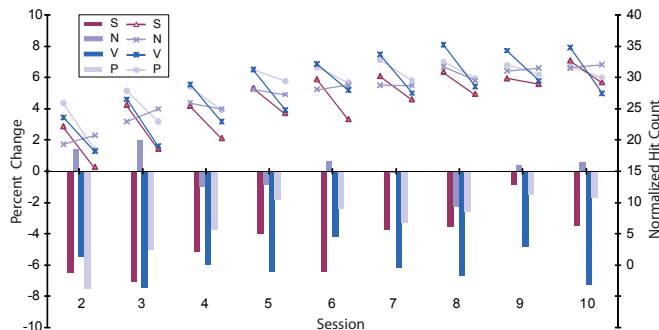


Fig. 4. Absolute task performance (line) and performance change percentage (bar) plots in terms of normalized hit count for all groups over nine training sessions (sessions #2-10).

start from approximately the same performance level in terms of normalized hit count at session #2; however, the slope of the within session learning curve becomes negative for the S and V groups after the first assistance subsession and remains negative during early subsessions. The existence of negative learning in early sessions of training for S and V groups indicates that guidance provided during the assistance subsessions significantly interferes with learning. The interference exists since the haptic guidance modifies and augments the system dynamics in order to assist task completion and the assisted task becomes a secondary task to be learned.

The existence of interference is a major concern that results in negative learning efficacy of fixed-gain guidance paradigms that are designed to improve task performance. Even though all three groups exhibited approximately the same amount of interference at the beginning of training, for P group this interference decreased progressively as the training proceeded (see Figure 4). In the case of V group, the performance difference fluctuated and remained at the similar level throughout the training, while for S group, the difference experiences an overall decreased but still maintained at a relatively higher level when compared to P group. The different trends among these three groups indicate that each training paradigm results in different interference characteristics.

The normalized total guidance force provided during the assistance subsession is introduced as a way to investigate how much the human participants depend on the existence of the haptic guidance. The normalized measure for each assistance subsession is calculated as the percentage change of the total guidance force provided within the session, compared to the total guidance force provided during the first session. This measure serves as an indicator of the amount of guidance provided by each of the haptic guidance methods and is recorded in Figure 5 for all three haptic guidance groups. Figure 5 shows that P group decreasingly depended

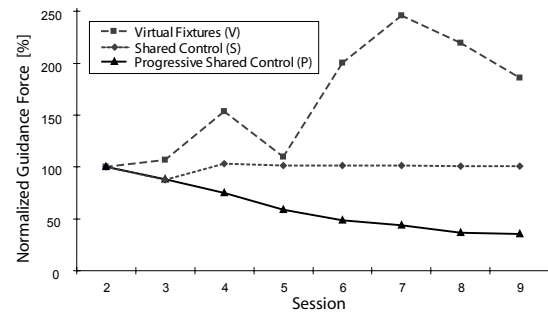


Fig. 5. Total guidance force during the assistance subsessions for all three haptic guidance schemes demonstrates that the progressive shared control (P) group depended decreasingly on the guidance while the other two groups throughout the training protocol continued to depend on the guidance provided. Results are normalized based on the amount of guidance force incurred in the first session of training.

on the guidance throughout the protocol. With less and less assistance provided from the haptic guidance paradigm, the performance of P group kept increasing. Therefore, the increasing performance of the P group is *not solely* due to the existence of assistance, but due to the skills the participants acquire during training. Contrary to S and P groups, V group exhibited an increasing trend in terms of total assistance force experienced. This fluctuating yet increasing average trend indicates the heavy reliance of V group on the assistance.

These results indicate that the performance-based progressive algorithm has a positive effect in reducing interference and dependency over the other forms of fixed-gain haptic guidance that assist task completion. However, P group does not necessarily exhibit better performance than virtual practice. One possible reason for this result maybe due to the incomplete design of the shared controller. According to [6], during training, a task should be simplified only if the important perceptual invariants of the task are preserved. In the current implementation, the shared controller assists position control perpendicular to target axis, but neglects the temporal aspect of the control task: exciting the system near its resonant frequency along the target axis. A redesign of the progressive shared controller to capture all critical aspects of the manual control task may lead to significantly better training performance than virtual practice.

REFERENCES

- [1] H. Krebs, J. Palazzolo, L. Dipietro, M. Ferraro, J. Krol, K. Ranekleiv, B. Volpe, and N. Hogan, "Rehabilitation robotics: Performance-based progressive robot-assisted therapy," *Autonomous Robots*, vol. 15, no. 1, pp. 7–20, 2003.
- [2] D. Reinkensmeyer, D. Aoyagi, J. Emken, J. Galvez, W. Ichinose, G. Kerdanyan, J. Nessler, S. Maneeakobkumwong, B. Timoszyk, K. Vallance, R. Weber, J. Wynne, R. de Leon, J. Bobrow, S. Harkema, and V. Edgerton, "Robotic gait training: Toward more natural movements and optimal training algorithms," in *Proceedings of the 26th Annual International Conference of the IEEE EMBS*, 2004, pp. 4819–4821.
- [3] E. H. F. van Asseldonk, R. Ekkelenkamp, J. F. Veneman, F. C. T. van der Helm, and H. van der Kooij, "Selective control of a subtask of walking in a robotic gait trainer (LOPES)," in *IEEE International Conference on Rehabilitation Robotics*, 2007, pp. 841–848.
- [4] Y. Li, V. Patoglu, and M. K. O'Malley, "Negative efficacy of fixed gain error reducing shared control for training in virtual environments," *ACM Transactions on Applied Perception*, vol. 6, no. 1, pp. 1–21, 2009.
- [5] H. Levitt, "Transformed up-down methods in psycho-acoustics," *Journal of the Acoust. Soc. of America*, vol. 49, no. 2, pp. 467–477, 1970.
- [6] G. Lintern, "An informational perspective on skill transfer in human-machine systems," *Human Factors*, vol. 33, no. 3, pp. 251–266, 1991.

Design and Development of Acrylic Die for Hip Bone Joint Casting

S. Norbahiyah and M. M. Haque.

Department of Manufacturing and Materials Engineering, Faculty of Engineering, International Islamic University Malaysia (IIUM)
P.O. BOX 10, 50728 Kuala Lumpur, Malaysia.

Abstract - The hip joint is one kind of joints that is very important to human being, which controls the movements of daily activities of human body. Failure of hip bone joint is commonly caused by injuries, arthritis or aging factor. Currently, the total hip bone replacement operation has been done to overcome the hip bone joint problem. Investment casting process can give optimum properties of the product having complex geometry with biocompatible material. In order to perform this casting, a die or mould is needed to produce wax pattern, which will be used to make ceramic investment for the hip joint. This study includes the modification of design together with fabrication of a typical hip joint casting dies with acrylic. The modulus of casting and riser has been calculated and accommodated with the main hip joint die design. The hip-bone joint design has been generated using CATIA V5 software before it is converted into numerical control (NC) codes for machining purpose. Two acrylic slabs of the acrylic dies were machined using Vertical Machining Center (VMC). The acrylic dies for hip bone joint are now ready for making wax pattern intended to produce ceramic investment for casting the required joint with biocompatible material.

Keywords - Human, arthritis, biocompatible, investment, fabrication.

I. INTRODUCTION

Recent years, solution selected for hip joint problems are; lifestyle modifications, hip resurfacing and hip replacement. Today, total hip replacement has become a common and predictable procedure since it gives pain relief and improved function [1]. Hip replacement surgery is to remove two damaged and worn parts of a hip joint (hip socket acetabulum, the ball, femoral head) and replace them with smooth and artificial implants (prosthesis) [2]. Fig. 1 shows various parts of the hip bone implantation and their positions [3].

Over the past years, the hip bone joint can be made by using four manufacturing processes such as machining, forging and casting and powder metallurgy of biocompatible material [4]. Machining and forging processes have some limitations to produce such complicated item, especially in terms of production cost, freedom of alloy selection, time consumption and to sustain functioning with complex properties that a hip bone joint requires [5]. Investment casting has been selected as an appropriate casting method in the present study to produce a typical hip joint. For investment casting, a die or mould is required to produce wax pattern, which will be used to make ceramic investment for the hip joint [6]. Thus, this study includes the design and fabrication of a typical hip

joint casting dies with acrylic to produce wax pattern for making the ceramic investment.

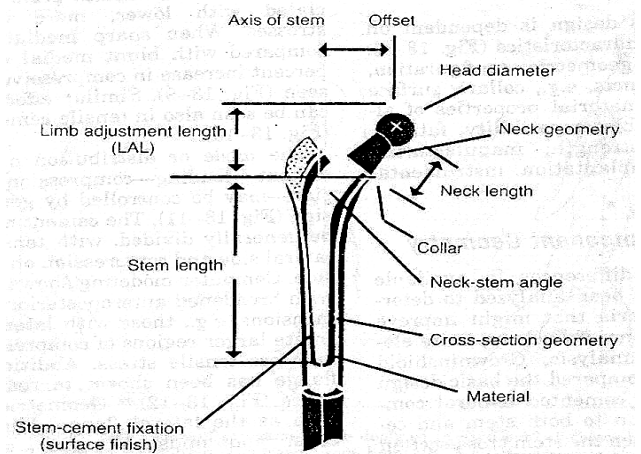


Fig. 1, Nomenclatures and positions of various parts of hip-bone implantation.

II. EXPERIMENTAL PROCEDURES

The design of a typical human hip joint was first configured from previous designs [7, 8] and modified to accommodate better and wider flexibility. Throughout the project, modulus of the casting and the riser has been calculated and provided with the main hip bone joint cavity design in order to avoid shrinkage porosity during solidification. These are elaborated in following sub-sections:

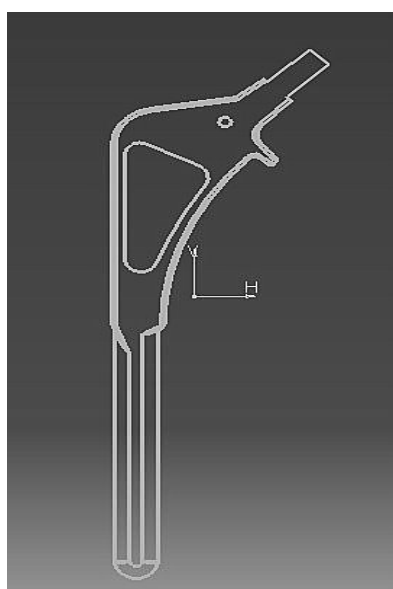
The hip-bone joint design has been generated using CATIA V5 software before it is converted into numerical control (NC) codes for machining purpose. In this study, a transparent cast acrylic sheet purchased accordingly to the hip joint design dimensions. Both acrylic sheets were then milled for surfacing to be smooth so that the contact between the two moulds is maximum thus causing the error while casting will be minimum. By using computer numerical control (CNC) vertical milling machine (VMC), two acrylic slabs with similar thickness and sizes have been machined. The required die cavity fabricated using carbide ball head cutting tools with diameters 10 mm and 4 mm [9].

Design of hip-bone joint

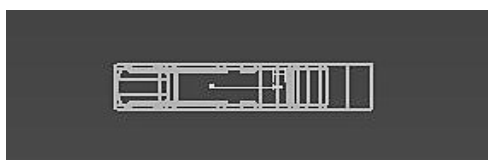
Design taken from previous investigators [7, 8] was analyzed and improved in this study. The neck stem plate is

designed without smooth surface to improve the performance of fixation by providing good bonding capability at the interfaces. Stem shapes without smooth surfaces may reduce stress concentration and increase fatigue life of the prosthesis [10]. Improving from previous design, a notch shaped gripping mechanism is designed and added at the stem angle. This is created to reduce sliding of the implant in the bone cement and fix securely [10]. Cross-section of stem is important in hip joint design and it evaluates amount of total displacement. In this study, the hip stem is designed with circle type cross section. Circle designs distribute stress evenly around the implant when only small change in stress found from one point to another [11]. Finally a model of the femur of a typical patient is constructed using CATIA V5.

In this process, using the CATIA software, the axis of stem, the geometry of the neck, the offset, the limb adjustable length (LAL), the stem length and the neck length are constructed. The design is then placed on the 2D form (Fig. 2) before it was converted into 3D form (Fig. 3) without the head using dress-up features in the software. To construct smooth and continuous surfaces, a chamfering and edge fillet tool in Boolean Operation has been used.



(a)



(b)



(c)

Fig. 2, Drawing of the implant in 2D, (a) Front view, (b) Top view, (c) Side view.

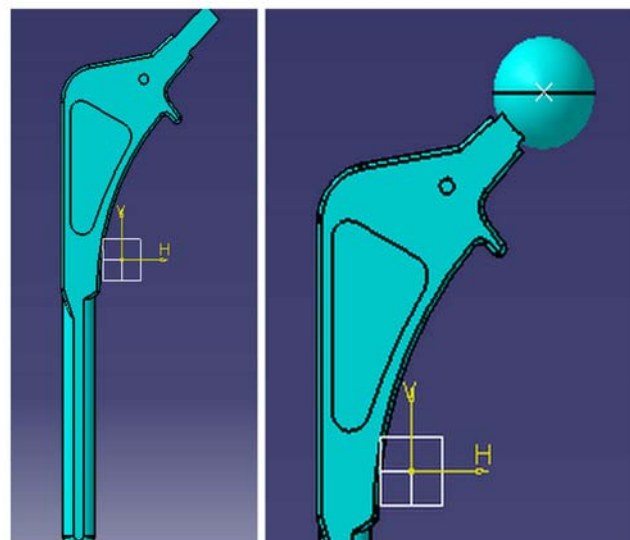


Fig. 3, Design of hip joint before and after sphere construction.

The head of the hip joint implant was then added using sphere-wire frame tool and finally, the whole product design was combined using solid-combine tool.

Modulus calculation

In order to determine the appropriate dimensions for riser and sprue, modulus of the casting needs to be determined. Modulus of the casting was calculated by using volume of the casting divided by its surface area through which heat is dissipating.

Thus, modulus of casting, $M_c = V_c / SA_c$ where V_c = Volume of the casting and SA_c = Surface area of the casting

To avoid shrinkage in the casting during solidification, riser must feed the molten metal to the main casting. In order to do so, modulus of the riser must be greater than the modulus of the casting and it is usually taken about 20% greater [12].

Thus, modulus of riser, $M_r \approx 1.2 M_c$. Using this relationship, the riser design has been finalized and adopted in making the die halves.

Die construction

In order to produce the wax pattern, acrylic was chosen as a suitable material for fabricating the die halves. Acrylic is stronger than glass, making it much more impact resistant and safer. Cast acrylic rivals glass with transparency of 92% light transmission and exhibits outstanding weather ability. It also insulates better than glass and it has a great advantage i.e., it is found to be $\frac{1}{2}$ the weight of glass and fabricated wood. Furthermore, post polishing can produce a crystal clear surface on acrylic [4]. The acrylic used in the present study can withstand a temperature up to 130°C , which is quite higher than the melting temperature of the wax used in making pattern in

the present study. At the same time, the acrylic slab or block with required thickness was cheaply available in the local market.

Blueprint design of the hip joint created using CATIA V5 design software following the values of sprue and riser as calculated earlier. The hip joint design is shown in Fig. 4 with all dimensions.

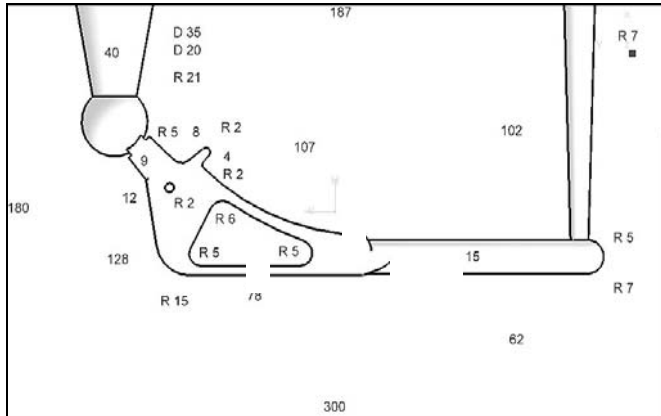


Fig. 4, Hip bone joint design with sprue and riser (dimensions are given in mm).

From the hip joint design created, NC codes generated by converting the design into G codes by using CATIA V5 software. Actual cutting/machining operations took place when two blocks of acrylic were placed horizontally under milling machine, after making sure that the both die halves had correct and equal thicknesses. Then the blocks were put under the vertical machining centre (VMC) one after another to do the necessary contour and the engineering details of the cavity. Automatically, the CNC vertical milling machine controller reads the codes for cutting operation and the machined hip joint cast die halves.

However, machining, polishing and finishing of the die halves had been performed by using various grades of emery paper to improve the smoothness of the surface. Fig. 5 shows one of the polished die halves containing the cavity of a typical hip-bone joint and is now ready for wax patterning.



Fig. 5, Finished die half (1 side) after polishing.

III. PRODUCTION OF WAX PATTERN

The combination of paraffin and microcrystalline waxes with 56°C melting temperature was used as the pattern material. This type of wax is widely used for making pattern as the combination properties tend to be complementary [4]. However, the wax was melted in Pyrex beaker and superheated up to 110° C and poured into the acrylic die cavity. The die halves were tightly fixed by shear pins and heated up to 110° C in an oven before pouring the wax into it. This permits slow cooling of the wax so that it maintains the fluidity to cover all the intricate details of the die cavity. The wax is solidified and hardened under room temperature for a few minutes and then die opened to take out the pattern. One of the wax pattern produced using the acrylic die halves is shown in Fig. 6.

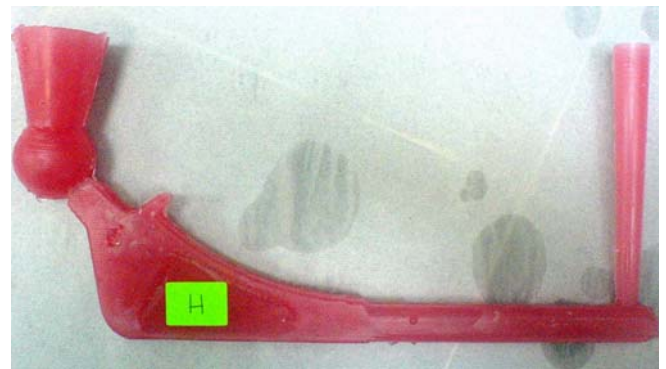


Fig. 6, Showing the wax pattern just after casting.

IV. CONCLUSIONS

The following conclusions can be drawn from the works of the present investigation:

- (i) A typical hip-bone joint has been designed successfully using software like CATIA V5.
- (ii) Acrylic die halves have been constructed by using VMC to produce wax pattern for hip-bone joint.
- (iii) Wax patterns for hip-bone joint have been successfully produced for making ceramic investment in which biocompatible material can be cast to manufacture hip joints.

ACKNOWLEDGEMENTS

The authors are grateful to the Research Management Centre (RMC) of IIUM for sanctioning the Research Fund (Grant No. IFRG 0702-59) to carry out the project. The authors are also indebted to the Dean, Faculty of Engineering for providing the necessary facilities in the Faculty without which, the various jobs of the present study would not be performed smoothly.

REFERENCES

1. Art and Craft Supplies. Retrieved on February 19, 2007 at www.suppliers online.com.
2. Hungerford D, Baltimore M. D (2003) Total Joint Replacement: The Last Frontiers, Maryland. Retrieved on December 20, 2007 www.aboutjoints.com/patientinfo/topics/tjrlastfrontier/tjrlastfrontier.htm
3. Petty W (1990) Prostheses for Total Hip Arthroplasty, Prentice Hall, New York
4. Kalpakjian S, Schmid S (2006) Manufacturing Engineering and Technology. Prentice Hall, Pearson Education South Asia Pte Ltd, Singapore
5. Ruyu M, Wendong X, Dongmei W, Kerong D, Chengtao W (2005) Design and manufacture of custom hip prostheses based on standard X-ray films, International Journal Advanced Manufacturing Technology, 27.70-74
6. ASM International Handbook Committee (1996) Metals Handbook – Investment Casting, ASM International, pp. 253-266
7. Mischke C. R, Shigley J. E, Budynas R. G (2004) Mechanical Engineering Design, Mc Graw Hill
8. Haque, M. M, Irzal, K. H, Azdy , M. A (2005) An Integrated Approach of Computer Aided Design, Rapid Prototyping and Investment Casting, The 2nd Int. Conf. on Mechatronics (ICOM 2005) Proc. vol. 2, Kuala Lumpur, Malaysia, 2005, pp. 864-870
9. The Plastics Distributor and Fabricator Industry Magazine (2008) vol. 20, Issue 6, Article no. 2332. Retrieved on December 20, 2008 at www.plasticsmag.com
10. Senalp A. Z, Kayabasi O, Kurtaran, H (2007) Static, Dynamic and Fatigue behavior of newly designed stem shapes for hip prosthesis using finite element analysis, Materials and Design, 28.1577 - 1583
11. Sabatini A. L, Goswami, T (2008) Hip Implants VII: Finite Element Analysis and optimization of cross sections Materials and Design, 29.1438 - 1446.
12. Beeley, P (2001) Foundry Technology, 2nd Edition., Butterworth – Heinemann, Oxford, U. K.

Corresponding Author: Prof. Dr. Md. Mohafizul Haque
 Institute: International Islamic University Malaysia (IIUM)
 Street: Jalan Gombak
 City: Kuala Lumpur
 Country: Malaysia
 Email: mohafizul@iiu.edu.my

Pupillary Responses during Learning of Inverted Tracking Tasks

Satoshi Kobori¹, Yosuke Abe¹

¹ Department of Electronics and Informatics, Ryukoku University, Otsu, Japan

Abstract— We used visuomotor tracking as our motor task and studied how subjects learn to adjust for inversion of the relation between joystick movement and target movement. This task requires learning a novel sensorimotor transformation. We have measured tracking performance and pupil dilation simultaneously. We have used pupil dilation as a measure of cognitive load, since the diameter of the human pupil increases with task difficulty across a wide range of cognitive tasks. Subjects observed a target moving at constant velocity along a clockwise circular trajectory on a computer screen. Subjects held a joystick in their hand, and moved it so that a cursor tracked the target as closely as possible. 60 normal subjects participated in the experiment. During 6 blocks of learning, inversion-evoked tracking error and inversion-evoked pupil dilation both decreased significantly. This finding suggests increasing automatization of the to-be-learned sensorimotor transformation. Pupil measures were not correlated with tracking error on individual trials, suggesting that the inversion-evoked cognitive load reflects changes in motor task, and is not merely a response to high errors. Our results thus suggest a relatively direct physiological measure of the processes of motor-skill automatization.

Keywords— inverted tracking task, pupil dilation, sensorimotor transformation, cognitive load, automatization

I. INTRODUCTION

Motor learning is a fundamental feature of all motor performance, and so it has been a central interest throughout the history of psychology. Motor learning has traditionally been associated with the concept of automaticity. Automaticity refers to the reduction of the cognitive effort required to perform a task, as learning progresses [1]. However, there is little consensus about how automaticity develops, about how to measure it, or about what neural processes are involved in automatization [2].

In order to discuss these points, we have used visuomotor tracking as our motor task and studied how subjects learn to adjust for inversion of the relation between joystick movement and cursor movement. This task requires learning a novel visuomotor transformation. We have measured tracking performance and pupil dilation simultaneously. We have used pupil dilation as a measure of cognitive load [3, 4], since the diameter of the human pupil increases with task difficulty across a wide range of cognitive tasks [5]. Though we used one-dimensional tracking task in our pre-

vious study [6], here we have adopted 3 types of two-dimensional tracking in order to study the relation between tracking performance and pupil dilation at different task difficulties.

II. METHODS

A. Apparatus

The experimental apparatus consisted of a computer and joystick for tracking measurement, and a pupillary measurement system. Tracking and pupil data were synchronized by digital signals transmitted by the tracking computer at the start of each trial. The apparatus is shown in Fig. 1.

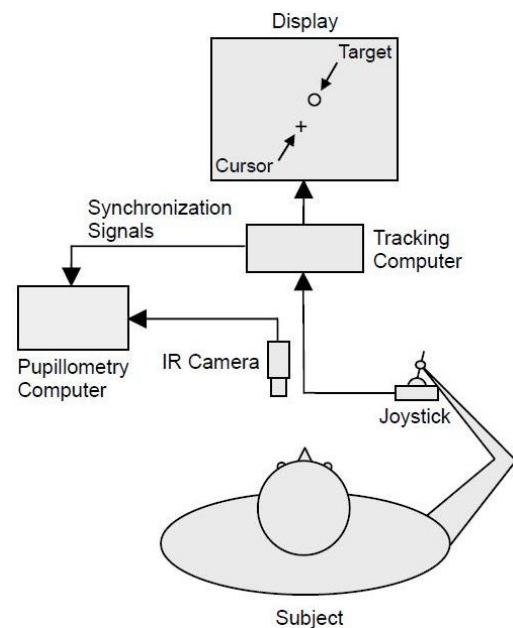


Fig. 1 Experimental apparatus.

B. Tracking

Subjects observed a circular target moving at constant tangential velocity along a clockwise circular trajectory on a computer screen. The target cycle was 5 s. Each trial lasted 20 s. Subjects held a modified joystick in their right hand,

and moved it so that a visual cross hair cursor tracked the target as closely as possible. Target and cursor positions were digitized and stored on the computer at 30 Hz.

Inverted tracking trials were of 3 types, horizontal inversion, vertical inversion and bidirectional inversion. In inverted trials, the relation between joystick movement and cursor movement was inverted at an unpredictable time during the trial. For instance, in horizontal inversion, the subject had to move the joystick rightward to produce leftward movement of the cursor, and had to move the joystick leftward to produce rightward movement of the cursor. The inversion occurred at an unpredictable time between 11.5 and 12.5 s. The inverted relation remained for the rest of the tracking trial.

Tracking error data from inverted trials were aligned to the time of inversion, and epoch from 4 s before inversion until 6 s after was selected for display. Tracking error traces were then made for each subject in each block of the experiment.

C. Pupillometry

Pupil diameter was measured at 60 Hz using an infrared video eye-tracking system (NAC Image Technology Inc., EMR8B-NL). The subject sat comfortably with their head on a chin rest. The IR sensitive video camera was positioned to view the dominant eye for each subject. The pupil diameters were calculated from the pupil images and stored for later analysis.

Pupil diameter data were analyzed using the same way as tracking data. Traces were baseline-corrected by subtracting the mean pupil diameter on each trial during the 1 s before inversion.

D. Experimental design

All experimental blocks consisted of 5 trials. The experiment began with a pretest block of normal non-inverted tracking trials. Next, subjects performed 6 learning blocks of inverted trials each. Then, subjects performed a posttest block of normal trials similar to the pretest block. The subjects were instructed to continue tracking as accurately as possible even if the inversion happened.

60 subjects were recruited. Subjects' ages ranged between 18 and 24 years. We divided the subjects into 3 groups, horizontal inversion group, vertical inversion group, and bidirectional inversion group. Each group included 10 males and 10 females. The horizontal inversion group performed horizontal inverted trials, the vertical inversion group performed vertical inverted trials, and the bidirectional inversion group performed bidirectional inverted trials in the learning blocks.

III. RESULTS

A. Tracking data

The grand average unsigned tracking error for each block is shown in Fig. 2. The inversion occurred at time 0. Several features of this figure deserve comment.

First, the error caused by inversion varies across the learning blocks. The tracking error is higher for block 1 than for the other blocks of the experiment. The learning effect between blocks is very clear in each group.

Second, regarding earlier blocks, the error in horizontal inversion group is higher than in vertical inversion group, but the error for block 6 is not differ among these groups.

Third, the tracking error in bidirectional inversion group decreases earlier than in the other groups, and the waveform is different from the others.

To draw learning curves, we measured mean tracking error during 4 s after inversion, and subtracted tracking error during the 1 s before inversion as a baseline.

Fig. 3 also shows the clear learning effect in each group and the difference among these groups. The differences between horizontal inversion group and vertical inversion group are significant ($p < 0.05$) for all blocks but block 6. On the other hand, the differences between vertical inversion group and bidirectional inversion group are not significant for all blocks.

B. Pupil data

The pupil data were analyzed as an indirect measure of the cognitive processes associated with skilled tracking. The grand average pupil diameter traces for each block is shown in Fig. 4. This figure shows several features.

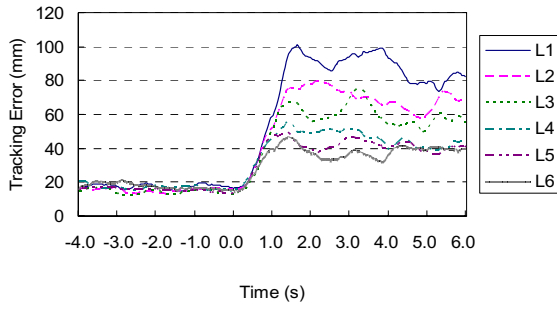
First, the waveforms show a clear pupil dilation related to inversion. Pupil diameter begins to increase some 500 ms after inversion, and does not return to the level before inversion.

Second, the amplitude of pupil dilation evoked by the inversion varies across learning blocks. In general, inversion-evoked pupil dilation decreases during learning.

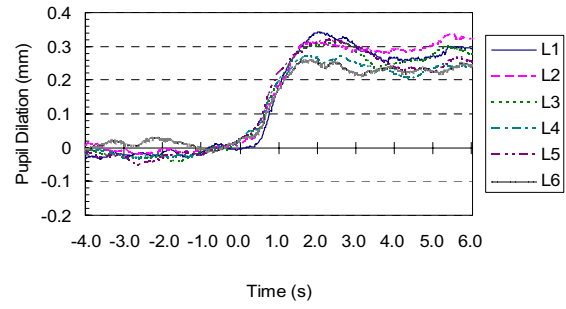
Third, the pupil dilation in horizontal inversion group is much higher than in vertical inversion group for all learning blocks.

Fourth, the pupil dilation in vertical inversion group is higher than in bidirectional inversion group for all blocks but block 1.

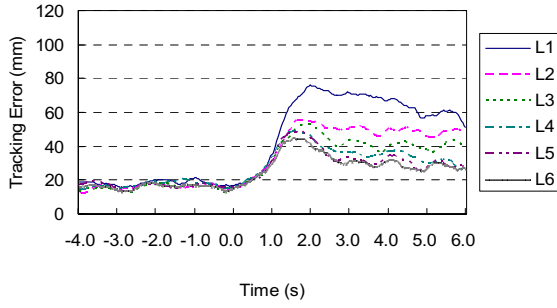
Fifth, the pupil dilation in bidirectional inversion group decreases earlier than in the other groups, and the waveform is different from the others.



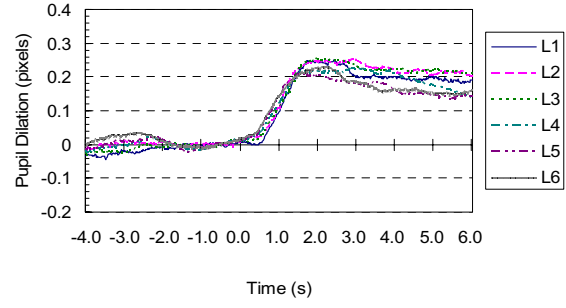
(a)



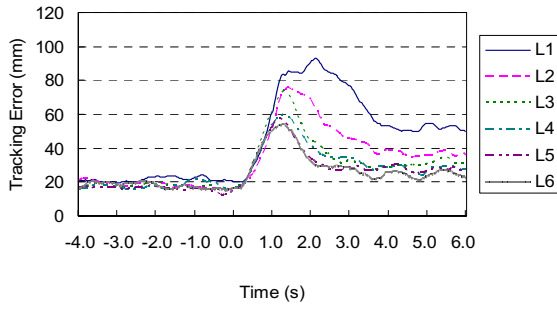
(a)



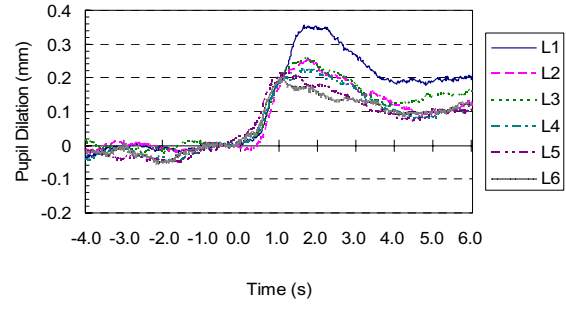
(b)



(b)



(c)



(c)

Fig. 2 The waveform of grand average tracking error arranged by learning block. (a) Horizontal inversion group, (b) Vertical inversion group, (c) Bidirectional inversion group. Ln refers to nth learning block.

Fig. 4 The waveform of grand average pupil dilation arranged by learning block. (a) Horizontal inversion group, (b) Vertical inversion group, (c) Bidirectional inversion group. Ln refers to nth learning block.

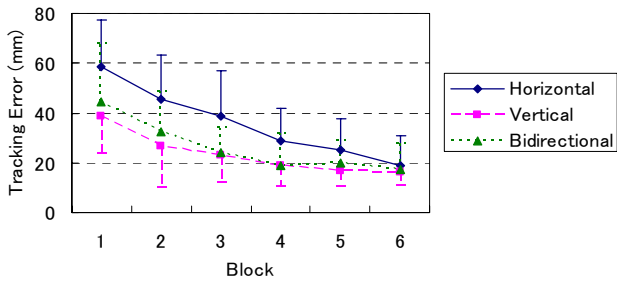


Fig. 3 Learning curve of tracking error for each learning block.

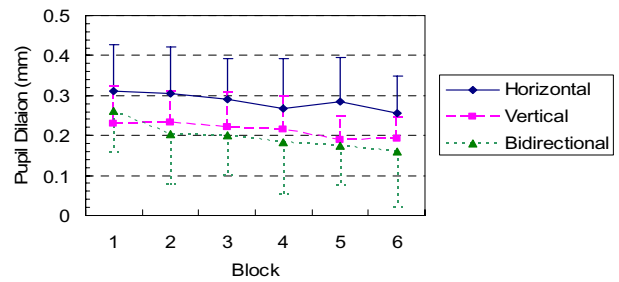


Fig. 5 Learning curve of pupil dilation for each learning block.

To draw learning curves, we calculated the mean pupil diameter from 0.5 to 4.5 s after inversion, and subtracted the pupil diameter during the 1 s before inversion as a baseline.

Fig. 5 also shows the learning effect in each group and the difference among these groups.

We compared the pupil dilation in block 1 and in block 6 in each group, the learning effects are all significant ($p < 0.05$ for horizontal inversion group and vertical inversion group, $p < 0.01$ for bidirectional group).

The differences between horizontal inversion group and vertical inversion group are significant ($p < 0.05$) for all blocks but block 2 and block 4. On the other hand, the differences between vertical inversion group and bidirectional inversion group are not significant for all blocks.

C. Relation between tracking error and pupil dilation

We also calculated the correlation coefficients between tracking error and pupil dilation on a trial-by-trial basis in each group. These are 0.16, 0.22 and 0.23 in horizontal inversion group, vertical inversion group and bidirectional inversion group. Tracking error and pupil dilation correlate very lowly across trials in all groups.

The relation between tracking error and pupil dilation is shown in Fig. 6. This figure shows the clear learning effects in tracking error and pupil dilation. It also shows the difference among the experimental groups. The pupil dilations in these groups are quite different in each block, though the tracking errors in the groups are similar in block 6.

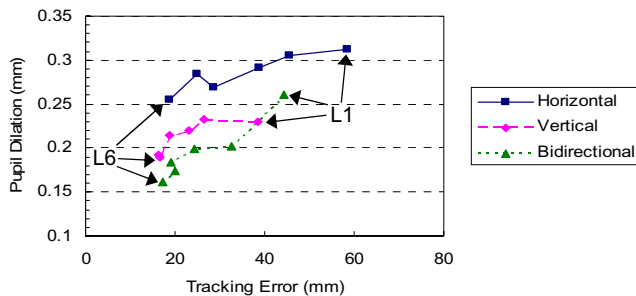


Fig. 6 Relation between tracking error and pupil dilation.

IV. DISCUSSION

The findings are summarized below. First, subjects can learn a novel sensorimotor mapping when tracking unpredictably inverts. Second, tracking inversion evokes pupil dilation, suggesting that engaging the new sensorimotor transformation involves a cognitive load. Third, inversion-

evoked pupil dilations decrease with learning, implying a gradual reduction in this cognitive load, or an automatization of inverting tracking. Fourth, this cognitive load is not merely driven by tracking performance, since tracking error and pupil dilation do not correlate across trials.

Our data extend previous studies of automatization of motor learning in many ways. We have developed pupil dilation as a new and relatively direct physiological measure of cognitive effort during learning. Although pupil dilation is known to correlate with task difficulty, and thus presumably with cognitive effort, in many different tasks [5], we are not aware of any previous use of pupil data to describe processing changes during learning. Our pupil measures provide psychophysiological evidence for a reduction in cognitive effort during learning inverted tracking, directly supporting an automatization theory of motor learning.

ACKNOWLEDGMENT

This work was supported in part by a grant from High-tech Research Center of Ryukoku University. This paper was partially written at Institute of Cognitive Neuroscience, University College London, thanks to Professor Patrick Haggard and the Research Abroad Program of Ryukoku University.

REFERENCES

1. Schneider W, Shiffrin R M (1977) Controlled and automatic human information processing: I. Detection, search, and attention. *Psychological Review* 84: 1-66
2. Brown T L, Carr T H (1989) Automaticity in skill acquisition: mechanisms for reducing interference in concurrent performance. *Journal of Experimental Psychology: Human Perception and Performance* 15: 686-700
3. Sirevaag E J, Stern J A (2000) Ocular measures of fatigue and cognitive factors. In: Backs R W, Boucsein W eds, *Engineering psychophysiology*. Lawrence Erlbaum Associates, New Jersey, pp 269-287
4. Matthews G, Davies D R, Westerman S J, Stammers R B (2000) Divided attention and workload. In: *Human performance: Cognition, stress and individual differences*. Psychology Press, East Sussex, p 97
5. Beatty J (1982) Task-evoked pupillary response, processing load, and the structure of processing responses. *Psychological Bulletin* 91: 276-292
6. Kobori S, Haggard P (2003) Cognitive Load during Learning of Tracking Task. *Proc of European Cognitive Science Conference 2003*, Cognitive Science Society, Osnabrueck, pp 119-204

Author: Satoshi Kobori

Institute: Department of Informatics and Electronics, Ryukoku University

Street: Seta

City: Otsu

Country: Japan

Email: kobori@rins.ryukoku.ac.jp

Instantaneous Gaze-Target Detection by Empirical Mode Decomposition: Application to Brain Computer Interface

Chi-Hsun Wu¹, Hsiang-Chih Chang¹, Po-Lei Lee^{1,2,3,*}, Ph.D

¹Department of Electrical Engineering, National Central University, Jhongli, Taiwan

²Laboratory of Integrated Brain Research, Department of Medical Research and Education, Taipei Veterans General Hospital, Taipei, Taiwan

³Institute of Brain Science, National Yang-Ming University, Taipei, Taiwan

Abstract— This paper presents an Empirical mode decomposition (EMD) approach for achieving high-speed frequency-tagged steady state visual evoked potential (SSVEP) brain computer interface (BCI) system. Empirical mode decomposition (EMD) has been demonstrated as a local and fully data-driven technique for the data processing of nonlinear and non-stationary time-series. It allows the frequency and amplitude of a time-series to be evaluated with excellent time resolution. The proposed system utilized flickering sources with high flickering rate acting as cursor system for the purpose of alternatively communication system. Induced EEG signal were decomposed into different scale of oscillation components namely intrinsic mode functions. In order to find out the SSVEP-related IMFs, instantaneous frequency were computed by generalized zero crossing (GZC). After identification of the frequency power by quadrature detection, the result shows the proposed system achieved 51.46 bits/min of average ITR. Compare with FFT approaches, EMD method provide better temporal and frequency sensitivity in detection of cognitive state of neuron activities.

Keywords— Brain computer interface (BCI), Empirical mode decomposition (EMD), Steady-state visual evoked potential (SSVEP).

I. INTRODUCTION

The steady state visual evoked potentials (SSVEPs) are resonantly neural responses mainly evoked by the visual cortex that can be investigated via noninvasive surface electroencephalography (EEG), when a subject is attentively focusing on a flashing light source with flickering frequency above 4 Hz[1]. Recently, the SSVEP oscillation has been widely used in a new application in so-called brain-computer interfaces (BCIs). A SSVEP based brain computer interface based on the detection of amplitude increasing that evaluates the focus of the subject's gaze. Since SSVEP is an inherent response of the brain, very little training is required of a person before using the BCI system. Compared to other types of BCIs, SSVEP based BCIs provide higher information transfer rates (bitrate) with minimal user training, and require fewer EEG channels. Different methods and techniques have been

developed in this promising field and are evolving toward practicability.

Several SSVEP BCI system have been proposed. Cheng [2] and colleagues demonstrated a multiclass SSVEP based BCI to select ten numbers and two control buttons. The mean information transfer rate was 27.15 bits/min. Another application shown by Lalor et al[3], was the control of a computer game. Participants were able to play this game with the help of a two-class BCI with an accuracy of 89.5%. Although Fourier Transform works well in current BCI systems, it has its shortages. The disadvantage of FFT based approach is that we have to ensure that the data within the time window is stationary and the spectrogram method has an additional problem of having a trade-off in time and frequency resolution. The current SSVEP-based BCI systems require long stimulation time to achieve satisfactory classification (3.5~ 6 sec), To obtain an acceptable speed of the BCI, correct decisions must be made based on short signal segments, usually between 0.5 and 4. We propose a frequency recognition approach based on empirical mode decomposition (EMD), which extract SSVEP signal in short time segment of EEG.

Empirical mode decomposition method was firstly proposed by Huang et al.[4] as an efficient method for analyzing nonlinear and non-stationary data, which has been demonstrated as an powerful data-driven approach for extracting meaningful stochastically modulated signals in many applications, such as blood pressure measurements, heart-rate variability in electrocardiogram (ECG), pulmonary hypertension etc.

In the present study, EMD-based method was proposed to extract SSVEP-related oscillatory activities during gazing at flickering LEDs as a mouse controller. Since the SSVEP could be modulated by cognitive and physiological states, this study extracts oscillatory activities in an adaptive manner without a pre-defined basis or prior information of statistical model. Our investigation indicates that the method is more sensitive to SSVEP than Fast Fourier Transform measures, and therefore, it was proved to be useful in a cursor control brain-computer interfaces applications.

II. MATERIALS AND MATHEDS

A. System configuration

The architecture of this cursor control system was shown in figure 1. It includes visual stimulus generator, EEG acquisition equipments, signal processing algorithms, and device control unit. 6 virtual cursor control pad including 4 direction buttons surrounding about a LCD monitor and two buttons located on the top of left side and right side acted as mouse left and right clicks. The moving cursor was controlled by alteration of the user's gaze direction.

The flickering sequences were generated by dsPIC (dsPIC30F4011, Microchip Technology Inc., USA). Using MPLAB IDE software with MPLAB C30 compiler to program the internal timer and interrupt of the dsPIC chip to generate 30 31 32 33 34 35 Hz with 50/50 on-off duties for all frequencies. These LED flickers stand for six functions (cursor to left, cursor to up, cursor to down, cursor to right, right button click and left button click).

B. Subjects and tasks

Four healthy subjects, aged between 23 and 29, participated in this study. All subjects had normal or correct-to-normal vision. All participants are instructed to gazed at these flicker LEDs one-after-one to complete sequential commands, which were "L ↑ R → ↓ ← L ↑ R → ↓ ←". When gaze-target was detected, one monotonic beep was feedback to inform subject to go next command.

c. Empirical mode decomposition

The empirical mode decomposition [5] separates a time series into a finite number of its individual characteristic oscillations. In comparison with other signal processing methods, the EMD method does not need a prior knowledge

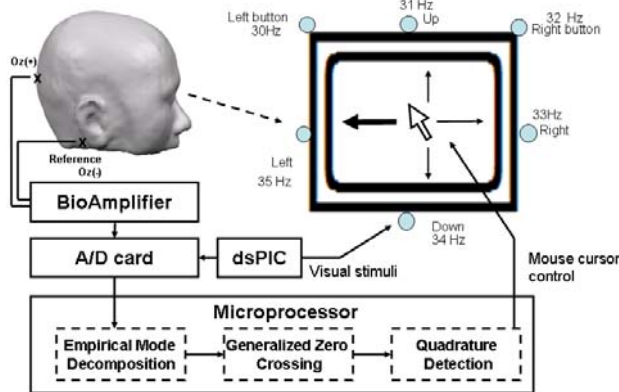


Figure 1 the architecture of the SSVEP-based BCI system.

or a pre-defined statistical model for data decomposition. The EMD attempts to sequentially decompose a signal into the sum of a finite number of intrinsic mode functions (IMFs), which allows the amplitudes and frequencies varying with time and is especially beneficial to present local characteristics of nonstationary signals. Each IMF represents a simple oscillation with the following definitions: (1) the number of local extrema (including local maxima and local minima) and the number of zero-crossings must either equal or differ at most by one, and (2) the mean value of the envelope defined by the local maxima and the envelope defined by the local minima are zeros. For a M-channel EEG data, B, one epoch, \vec{x} , in the longitudinal gradiometer at the designated sensorimotor-related sensor unit is decomposed by the following EMD steps:

- (1) identifying all the local extrema in \vec{x} , including local maxima and local minima;
- (2) connecting all the local maxima/minima by a cubic spline to generate the upper/lower envelope;
- (3) generating a local mean curve, \vec{m} , by averaging the upper and lower envelopes;
- (4) calculating the pre-IMF, $\vec{h}^{(1)}$, by subtracting the local mean, \vec{m} , from \vec{x} , i.e., $\vec{h}^{(1)} = \vec{x}^{(1)} - \vec{m}$;
- (5) continuing steps from (1) to (4) for k iterations until

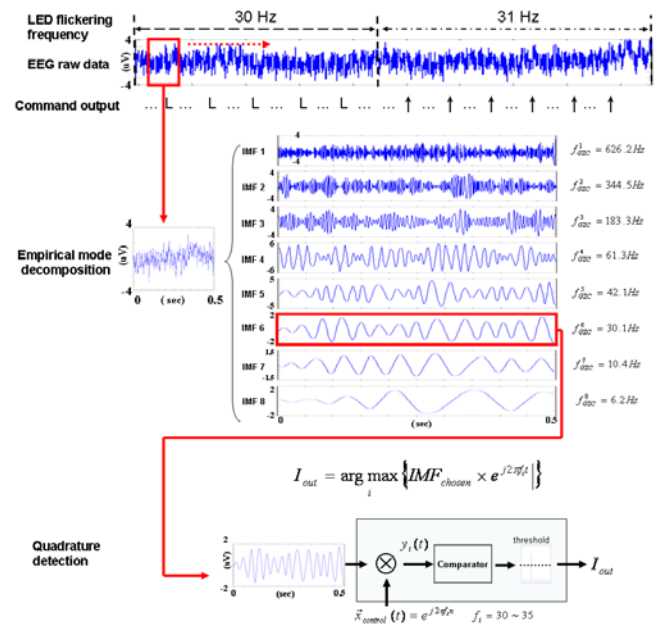


Figure 2 diagram of signal processing method for the proposed SSVEP-based BCI system. Three steps were applied (1) decomposed the EEG signal within the sliding window into IMFs. (2) choose SSVEP related IMF by generalized zero crossing (3) compute and compare the power of the chosen IMF by quadrature detection method.

the difference of two continuing pre-IMFs, SD_k , reaching a user-defined stoppage criterion, ε , i.e.,

$$SD^{(k)} = \frac{\|\vec{h}^{(k+1)} - \vec{h}^{(k)}\|^2}{\|\vec{h}^{(k)}\|^2} < \varepsilon$$

where $\|\cdot\|$ denotes the Euclidean distance;

- (6) setting $\vec{c}_1 = \vec{h}_k$ as the first IMF;
- (7) calculating $\vec{r} = \vec{x} - \vec{c}_1$;
- (8) replaced \vec{x} in step (1) by \vec{r} and repeating steps from (1) to (7) (sifting process), to find other IMFs, $\vec{c}_2, \vec{c}_3, \dots$, and \vec{c}_J ;
- (9) stopping the sifting process until the residue function $\vec{r} = \vec{x} - \sum_{j=1}^J \vec{c}_j$ becomes a monotonic

function which no more IMFs can be extracted.

After applying the EMD process to a single MEG epoch, the signals, $x(t)$, can be represented by a monotonic residue function, $r(t)$, plus a set of posteriori-defined IMF basis, $\vec{c}_1, \vec{c}_2, \dots$, and \vec{c}_J , where J is the number of IMFs extracted from \vec{x} and each \vec{c}_k , $1 \leq k \leq J$, is a $1 \times n$ vector. The IMFs can be arranged into a $J \times N$ matrix, \mathbf{C} , where each row \vec{c}_k represents the k^{th} IMF:

$$\mathbf{C} = \begin{bmatrix} \vec{c}_1 \\ \vec{c}_2 \\ \vdots \\ \vec{c}_J \end{bmatrix}_{J \times N} \quad (4)$$

C. Generalized zero crossing

Criteria for identifying SSVEP components in practice were based on time-domain features. In this study, Generalized zero crossing (GZC) [6] was utilized to find out the SSVEP related component, computing the dominant oscillation for each IMF and recruited the dominant oscillation which was closest to determined stimulation frequency.

D. Identification of user intention by means of Quadrature detection method

To compute the frequency power of the SSVEP related component. Quadrature detection method was used in this study. In quadrature detection the transmitter frequency is in the centre of the observed frequency range. Taking absolute

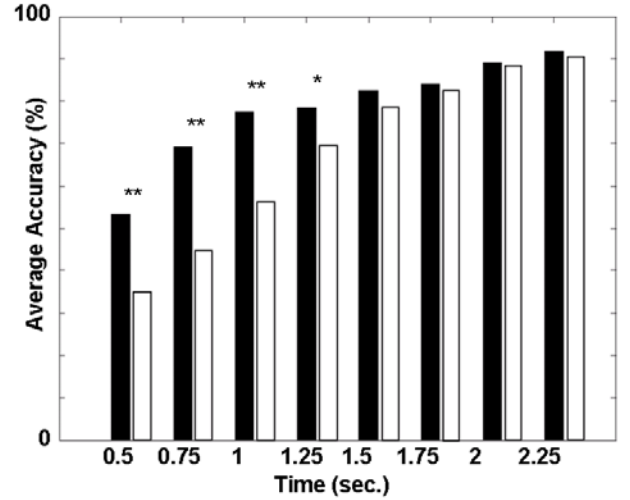


Figure 3 Comparison of average accuracy between EMD and FFT approach. Black and white bars represent the result of EMD and FFT approach, respectively. The asterisks shows the significance of paired t-test, where ** stands for $p < 0.01$. The result demonstrate the EMD approach is better than FFT at relatively short time

value to measure the energy of transmitter frequency, which was stimulus frequency.

$$I_{out} = \arg \max_i \left\{ IMF_{chosen}(t) \times e^{j2\pi f_i t} \right\}$$

III. RESULTS

The System performance is evaluated by ITR. The measurement of ITR is obtained through the task of completing 12 commands. The standard method for measuring BCI performance is information transfer rate. It is the amount of information communicated per unit time. The bit rate of each selection can be expressed as

$$B = \log_2 N + P \log_2 P + (1-P) \log_2 \left[\frac{(1-P)}{(N-1)} \right]$$

In the serial input study, all subjects could finish the requested command. Table 1 presents the result from four subjects. Subject YL completed the task without errors. The average ITR was 51.46 bits/min (range from 18.35-90 bits/min).

Figure 3 indicates that our method attains higher recognition accuracy at various time window lengths for most subjects and also presents the paired t-test significant test results. The asterisk marks significance (* : $p < 0.05$; ** : $p < 0.01$). The result shows that the EMD-based QD approach is significantly better than the FFT approach at most time window lengths.

Table 1 Results of consequential inputs for mouse control application

Subject	Input Results (wrong input)	Total time (sec)	Seconds per corrected selection (Max/Min/Average:std) (sec)	ITR (bits/min)
Y.L.	L ↑ R → ↓ ← L ↑ R → ↓ ←	19.8	1.94 / 1.55 / 1.65 ± 0.15	90
C.H.	L ↑ R → ↓ (L) ← L ↑ R → ↓ (↓) ←	29	2.5 / 1.5 / 1.83 ± 0.36	54.5
L.W.	L ↑ R (R) → ↓ ← L ↑ R (↓) → (L) ↓ ←	34	2.36 / 1.57 / 1.95 ± 0.31	43
K.S.	L ↑ R → (←→) ↓ (L ↓) ← L ↑ R → (R) ↓ (LL ↓) ←	50.9	2.9 / 1.76 / 2.24 ± 0.44	18.35
Average		33.4		51.46

* Note: ←: cursor left, ↑: cursor up, ↓: cursor down, →: cursor right, R: right button, L: left button; wrong input was denoted as brackets.

IV. DISCUSSION

For the current SSVEP-based BCIs, Fourier analysis is mostly used method for the purpose of flickering frequency detection. However, it has some shortages that were (1) the utility of Fourier based analysis exist tradeoff situation between system speed and accuracy, (2) SSVEP are modulated by several cognitive process, such as selective attention and working memory. Filters with fixed bandwidth may be too stringent to explain non-stationary (time-varying) signals. In this paper, the EMD approach has been successfully demonstrated for SSVEP-based BCI study in data preprocessing and frequency detection.

EMD is an emerging new technique for adaptively decomposing nonlinear and nonstationary signal into a sum of oscillatory components (e.g. IMFs) which become the basis representing the data. The decomposition technique depends on the local characteristic of the data, without any prior knowledge. This technique has already been applied with success in biology and medicine. In this contribution, we applied the idea of EMD in EEG signal preprocessing and develop strategies to the application of SSVEP-based brain computer interface. The result show this proposed method adaptively extract SSVEP from background noise, e.g., 60 Hz, low-frequency eye-blinking and spontaneous EEG rhythm etc. and demonstrate the better information transfer rate in relatively short data length which might reflect the instantaneous state of cognitive state.

V. CONCLUSIONS

A brain computer interface is an alternatively communication prosthesis for people suffered from severely

motor disabled. Many study have confirmed that SSVEP based BCI systems have well performance with less training and suitable for most people. However, the current SSVEP-based BCI require long stimulus time to achieve satisfactory performance (3.5~5 sec). In this study, a SSVEP based BCI using EMD has been proposed and the result demonstrated that SSVEP-unrelated components could be adaptively removed in relatively short time to improve SNR and increase the information transfer rate.

ACKNOWLEDGMENT

This study was funded by National Central University, the Nation Science Council (95-2314-B-075-118, 96-2628-E-008-070-MY3, 96-2221-E-122-MY3, 96-2221-E-010-003-MY3, 96-2221-008-115-My3, 96-2752-B-010-008-PAE), and Veterans General Hospital University System of Taiwan Joint Research Program (VGHUST96-P4-15, VGHUST97-P3-11).

REFERENCES

1. Regan D (1989) Electrophysiology: Evoked Potentials and Evoked Magnetic Fields in Science and Medicine. Elsevier, New York.
2. Cheng M, Gao X, Xu D et al. (2002) Design and implementation of a Brain-Computer Interface With High Transfer Rates. IEEE T BIOMED ENG. 49:1181-1186
3. Kelly P, Lalor C et al. (2005) Visual spatial attention tracking using high-density SSVEP data for independent brain-computer communication. IEEE Trans Neural Syst Rehabil Eng 13: 172-8
4. Huang E (1971) The empirical mode decomposition and the Hilbert spectrum for nonlinear and non-stationary time series analysis. Proc R Soc A 454:903-995
5. Huang W, Shen Z, Huang E et al. (1998) Use of intrinsic modes in biology: Examples of indicial response of pulmonary blood pressure to ± step hypoxia. P Natl Acad Sci USA 95:12766-12771
6. Huang E (2006) Computing frequency by using generalized zero-crossing applied to intrinsic mode functions US patent 6990436

Use macro [author address] to enter the address of the corresponding author:

Author:
Institute:
Street:
City:
Country:
Email:

Using virtual reality for an autonomous navigation with electric wheelchairs

I. Randria^{1,2}, P. Abellard¹, P. Ramanantsizehena², M. Ben Khelifa¹ and A. Abellard¹

¹ HANDIBIO, Université du Sud Toulon-Var, La Garde, France

² Laboratoire SIG, ESPA – Université d'Antananarivo, Antananarivo, Madagascar

Abstract— The aim of this paper is to present a new autonomous navigation learning tools for disabled people. The main constraints are the material cost, the sense of presence, the human machine interaction and the study of a new promising clue which can be combined with classic decisional information. Apart from the usual systems in clinical and rehabilitation center, we used virtual reality as well as a platform wheelchair to assess the navigation learning and ability in a known virtual environment.

Keywords— Handicap assistance, Simulation, Electric wheelchair, Man-Machine Interaction, Decision-making aid.

I. INTRODUCTION

Despite technological and medical evolutions, mobility and autonomy remain noticeable issues for disabled people. Literatures report on several wheelchair simulation projects and the lack of commercial products. In fact, this lack may come from the design difficulty for a standardized tool for a large range of wheelchairs, from the limited tuning with market software or from the expensive costs These reasons led us to study the possibility and the relevance of a virtual reality based navigation tool design. This task is part of the project ISIDORE (Interface of SIMulation, of Deci-siOn-making aid and to REhabilitation) which aims at:

- Designing and developing the “Simulation” function, i.e. let the user navigate without risk in varied environment, easily and quickly configurable by using (or not) a certain number of assistances (visual, sound, sensory). We have proposed a bibliographical synthesis of this topic and a comparative study of six algorithms chosen in adequacy with the system main constraints [1]. We gave priority to the latency time reduction during the scenarios changes to take into account the user fatigability, the facility of these changes to the prescriber, the therapist, the building designer.... In addition, a special attention was given to the use of genetic algorithms with variable length chromosomes which constitute the originality of our application model.

- Developing a “decision-making aid” function: The adopted solution is based on the use of a fuzzy controller, in order to facilitate:
 1. the work of the doctor prescriber who will be able to validate wheelchair attribution, if necessary by adding specific safety sensors,
 2. the work of the interior designer who will be able to create and navigate in the virtual environment he designed and to make the best choices for each element (distribution, furniture,...).
- Developing a “assistance with rehabilitation” function i.e. providing the ergotherapist qualitative and quantitative data relating to navigation of a potential user. Parameters are numerous and diversified, such as displacements fluidity, obstacles avoidance, number of collisions, execution time... and contribute to the diagnosis related to the progressions/regressions of the user. Section 3 will present our prototype with its original points: execution speed for scenarii changes, interfacing with commercial 2D and 3D CAD products, supervision mode ensuring the automatic changes of modes of manual navigation, assisted or automatic according to the situation of the patient and the possibility of controlling its wheelchair with head, foot, voice or breath.

II. RELATED WORKS

Several international teams show work results in the field of wheelchair simulation. However one can notice that many of these approaches are subjective and thus give priority to the therapist while not using numerical tools that could provide quantitative evaluation for the control capacity. Moreover, some projects are rather advanced whereas others are simple in their approach but quite as interesting considering the design profit and material costs. For instance, the use of isometric levers would have almost the same impact in navigation as the usual lever of the electric wheelchairs but they are much more expensive since they are very specific [2]. Other projects use a 6 degrees-of-freedom platform in order to reduce discomfort and to have

more realism [3]. However, the benefit of a better realism is not important as regards to the material cost [4]. Others use stereoscopic vision to have a better 3D perception [5], but these systems are expensive and did not provide notable improvement of navigation as their use quickly leads to the establishment of a visual embarrassment and even a persistent eyestrain.

From these observations, we developed a new tool named ISIDORE, centered on the patient [6] and the expert. It was studied with the aim of offering the best cost-performance compromises satisfying medical teams and observing the particular conditions related to the current narrowness of the market [7,8,9].

This tool is useful for the training and the evaluation of the control capacity for electric wheelchair prescription. It helps the medical therapist in a quantitative way with decision-making depending on the progression of the user, as well as the minimal safety instrumentation necessary to its control. It integrates behavioral information of reference with a fuzzy approach. To obtain a reference trajectory, ISIDORE uses a genetic or deterministic approach according to the requested fluidity in rehabilitation and the users' fatigue. It processes some other behavioral information for better evaluation and to provide more relevant information to the decision makers. The simulator can be used in an autonomous way (lever and screen of computer) or be integrated in a complete system using a platform of virtual reality with a fixed wheelchair and using the wheels speed (Fig. 1).

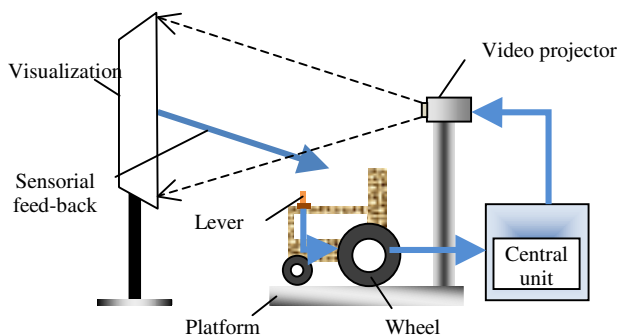


Fig. 1. Virtual reality platform

Moreover, the simulator also has a supervision module of hand-drive operation, semi-automatic order and automatic control. This module is interesting for the user because it helps to avoid collisions, to solve delicate problems of navigation and to acquire and gradually reinforce the will and the capacities to autonomy. Finally, information feedbacks that ISIDORE offers are in various forms (stereo sounds, visual returns in the form of guide, traffic lights, 2D and 3D

global or local sights...) in order to provide to patients the information they consider the most useful to navigate.

III. PROPOSITION OF AN INTERFACE ASSISTANCE WITH SIMULATION, DECISION AND REHABILITATION

A. Context

This state-of-art in the electric wheelchair simulation field encompasses a large variety of work these last three decades. Generally, the main goal is to prescribe an autonomy tool appropriated to the disabled person by respecting the characteristics of a motorized or robotized technical assistance. Thus, flexibility is an important character to facilitate collaboration between humans (doctor-patient) and the human machine co-operation (less apprehension).

Fault tolerance of the system enables the man-machine couple to cooperate in a symbiotic way, in spite of dysfunctions, thanks to the tool's additional capacities. Besides, the effectiveness in degenerated mode is a desirable criterion so that the system remains exploitable in contexts of unavailability of all the resources (for example, navigation with the sound returns if the visual information is not provided).

Moreover, it is advised to integrate, in the design of a technical assistance, the notion of science evolution, particularly when considering data processing, in order to benefit from it. Finally, the realization step generally follows a certain development plan on the basis of the reliability phase, going from the study of mobility, to the human-machine interface, towards the phase of exploration [10].

If such are the qualities desired for a technical assistance in general, in this work, we mainly focused on:

- the fatigability of the handicapped person,
- the financial costs of the material,
- the risks for the handicapped person and the environment (accident, collision...).

These choices aim at achieving a set of objectives :

- the contribution of a solution to safety issues,
- the experiments diversification so as to dissociate the user trajectories memorization,
- the evaluation of the wheelchair control capacities within the user progressions/regressions for the purpose of an adequate help prescription,
- the requirements quantification in terms of functionalities to ensure a protected autonomous displacement and lower costs.

B. Basic functions

ISIDORE is the acronym of Interface of assistance to Simulation, the DecisiON and REhabilitation. This tool enables a quantitative evaluation of the capacity of a person to operate an electric wheelchair. Fig. 2 shows the general organization of this evaluation.

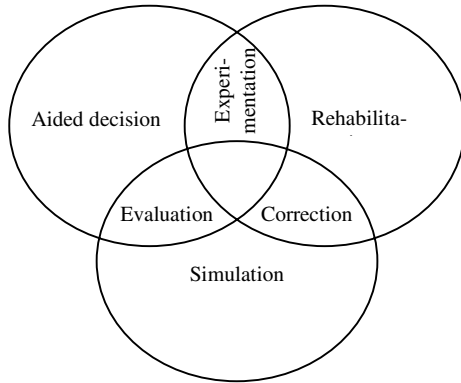


Fig. 2. ISIDORE basic functions

This simulator is part of rehabilitation process so as to make autonomy recovering possible for a disabled person. It takes part in three phases: simulation, decision-making aid and rehabilitation. The necessary details in each function are given hereafter.

i) Simulation

Simulation is a stage that let the user evolve safely without any physical accident risks, with the aim at directing the training towards the tasks [11] and to concentrate on the progressions

To facilitate the man-machine cooperation, the elements of the system must be tunable with the user specificities such as residual capacities.

It is then materially possible to implement the simulator on a computer with signal processing software and visual and sound feedback, or on a equipped platform.

ii) Evaluation

Navigation exercises help the prescriber doctor to evaluate user capacities and training progression and thus, the wheelchair attribution.

To carry out the evaluation, the doctor must have information which can contribute to decision-making. These informations, such as the navigation behavior of the patient, can be used as visual clues and be quantified.

The capacities of the handicapped person to operate an electric wheelchair can also be evaluated by a comparison of the trajectory adopted during simulation with a reference trajectory. The latter can come from the navigation of a healthy person tested or calculated by the component trajectory planning of the ISIDORE system.

iii) Decision-making aid

ISIDORE aims at helping the prescriber doctor to make a decision considering technical questions for wheelchair attribution. This attribution may be done under some security conditions (i.e. by adding safety sensors). Information resulting from simulation, used in this procedure, can be rough or synthetic according to the needs for the therapist.

iv) Experimentation

During training and rehabilitation process, it is important to be able to test the impact of a navigation clue. Thanks to virtual reality, ISIDORE has this modification capacity to cope with the nearest configuration that would offer patient autonomy with minimal cost. Improvement can also be declined in a collaborative help to go from a point to another, with automatic or semi-automatic drive.

v) Rehabilitation and engineering

In order to minimize the accident risks during electric wheelchair navigation, it is paramount to control it the best possible. ISIDORE system enables a progressive training. The progression can be done using assistance such as a geometrical form guide. This guide shows the way to follow and is put in front of the virtual wheelchair and always on the reference trajectory. These elements of assistance are interesting for the user and contribute to rehabilitation. Besides, another form of assistance (sound messages) can inform the presence of obstacles in the environment and facilitates their avoidance.

vi) Correction towards realism and low cost

This stage is necessary to approach as much as possible the version of the real electric wheelchair to be prescribed and to minimize its cost. Moreover, it is possible to sophisticate navigation in ISIDORE, at least on the level of realism so as to come as closer as possible to the navigation in real-world. That means for example, suppressing purely virtual assistance such as the guide mentioned in the previous paragraph.

IV. RESULTS

The following result comes from tests on 12 users. The target is to assess the computer human interaction to ease the electric wheelchair navigation learning. The evaluation criteria are the reference and adopted trajectories deviations, and the user felts depending on feedback combination (Fig. 3-4). The legend is clarified as follows:

- 2D: global view in 2D of the navigation environment,
- G: guide (green cone) for navigation,
- L: tricolour fires,
- S: sound feedback,
- ‘ – ‘: without feedback.

Fig. 3 shows the sum of the average deviations of each user for any combination of the information feedbacks. Indeed, for subjects 3 and 7, one notes an important cumulated variation. It means that they may have to learn to navigate much more before operating a real electric wheelchair. Fig.4 shows the users level of satisfaction is non negligible (over 60%=80/140). This quite high level of satisfaction shows the good acceptability of the Computer Human Interaction between ISIDORE system and the users. This appreciation still stands even for those with important navigation problems.

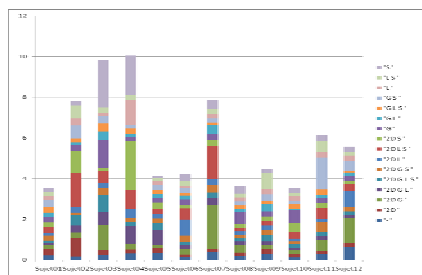


Fig. 3 Sum of the average deviations

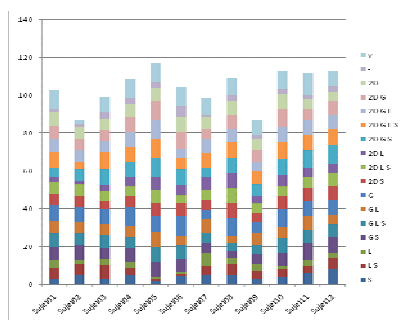


Fig. 4 Sum of user satisfactions depending on provided assistance

V. CONCLUSION

This paper reports the results of the use of a low cost virtual reality based tool for navigation learning and rehabilitation to help decision makers in prescribing electric wheelchair with the minimum safety instrumentation. The ISIDORE System offers interesting evaluation capacities also, thanks to its configurability a good level of acceptability among the users. Deeper analysis on the specificities of each user afterward would certainly give more accurate clue to adapt the machine to the needs of an eventual new user. It would also help medical care professional conduct refined classification upon disabilities of patients. These perspective works are in progress in our two partner laboratories.

REFERENCES

1. Randria I., Ben Khelifa M., Bouhouicha M. et al (2007) A Comparative Study of Six Basic Approaches for Path Planning Towards an Autonomous Navigation. in The 33rd Annual Conference IECON of the IEEE Industrial Electronics Society, Taipei, Taiwan
2. Cooper R, Spaeth DM, Jones DK et al. (2002) Comparison of virtual and real electric powered wheelchair driving using a position sensing joystick and an iso-metric joystick. Medical Eng. & Phys., 24(10):703-708 DOI: 10.1016/S1350-4533(02)00111-X
3. Niniss H, Inoue T (2005) Electric Wheelchair Simulator for Rehabilitation of Persons with Motor Disability. Simpósio Brasileiro de Realidade Virtual, Belém, Brazil.
4. Mestre D (2004) Activités sensori-motrices : Apports de la Réalité Virtuelle à la Psychologie Ergonomique. In Psychologie ergonomique: tendances actuelles (Hoc JM, Darses F Eds), Presses Universitaires de France, Paris
5. Swan E, Stredney D, Carlson W et al. (1994) The determination of wheelchair user proficiency and environmental accessibility through virtual simulation, Proc. of Virt. Real. and Persons with Disabilities Conf., Northridge, CA, USA.
6. Pruski A, Morere Y, Horn O et al. (2007) Approche centrée utilisateur pour la conception d'un fauteuil intelligent, STH – Sc. et Tech. Handicap, Lavoisier, Paris, 1(1):9-32
7. Abellard A, Randria I, Franceschi M et al. (2006) Étude de faisabilité d'une plateforme technique d'aide à la conduite d'un fauteuil roulant électrique, Lett. Méd. Phy. et Réadapt., Springer, Paris, 22(1)
8. Franceschi M, Randria I, Abellard A et al. (2006) A virtual reality based simulator project to train wheelchair navigation, VRIC Virtual Reality International Conference, Laval, France
9. Randria I et al. (2007) A Virtual Reality application to disabled transportation simulation, in Virtual Reality International Conference, Laval, France
10. Ben Khelifa MM (2001) Vision par Ordinateur et Robotique d'Assistance, Université du Sud Toulon-Var. PhD Thesis.
11. Fuchs P (2006) Le traité de la réalité virtuelle : Volume 4, Les applications de la réalité virtuelle, Presses de l'École des mines, vol. 4.

Author: Patrick Abellard
 Institute: HANDIBIO / Université du Sud Toulon-Var
 Street: Avenue de l'Université
 City: La Garde
 Country: France
 Email: abellard@univ-tln.fr

Design of a new prosthetic mechanical system used in human ankle joint disarticulation

C. Copiluși¹, N. Dumitru¹, M. Marin¹ and L. Rusu²

¹ Faculty of Mechanics/ Department of Applied Mechanics, University of Craiova, Craiova, Romania

² Faculty of Physical Education and Sport, University of Craiova, Craiova, Romania

Abstract— In this paper we follow to elaborate a new prosthetic mechanical system used in ankle joint disarticulation from the human lower limb structure. The prosthetic system has on base cam mechanisms which assure the angular amplitude corresponding to the one created by the human ankle joint but also assure the damping necessary for plantar or dorsal flexion process fulfilment.

The design of this prosthesis has on base a kinematics and dynamic study of the whole human lower limb in the sight to obtain the connection forces and the motion law developed at the ankle joint level. With this important data will be able to establish some dimensions and to adapt the new prosthetic system in the human lower limb structure.

Keywords— cam mechanism, shank prosthesis, dynamics, kinematics human lower limb prosthesis.

varus motion, due to specific form of the prosthetic foot; special design in order to take over the reaction forces from the ground contact in the concentrated points. This is an advantage because the components are individually stressed, and are fabricated from carbon fiber which posses the shape memory capacity.

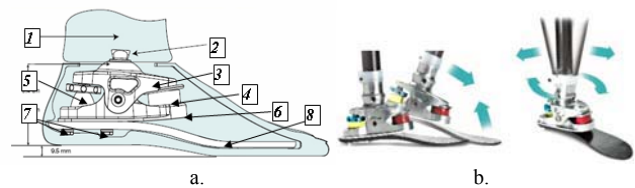


Fig. 1 Prosthetic mechanism structure type Venture used in ankle disarticulation: a – prosthesis structure; b – prosthesis movements [8]

I. ACTUAL STUDY OF THE PROSTHESES USED IN HUMAN ANKLE DISARTICULATION

In the case of shank prosthesis, this are fabricated from materials which posses a capacity to memorize shapes and to store energy developed in different activities. The mobility from the ankle joint level is generated by the deformation of the foot replacement component in elastic field. With this it can be kept the angular amplitude, in order to realize the dorsal or plantar flexion. Also we can find different types of shank prostheses.

In figure 1 a, b, we present a shank prosthesis Venture type used in ankle disarticulations, fabricated by the College Park Industries [8]. This posses the following characteristics: multi-axial rotations, in order to adapt at any type of terrains; energy store capacity in order to minimize the patient effort; adaptable mechanism in the sight of movements adjustment, for any amputees; fixation ability through a cup or a implant; an easy transaction at changing the activities;

The prosthesis components are: shank flare (1); catching device (2); superior component (3); dumper components (4, 5); inferior component (6); fixation elements (7); artificial foot (8).

In figure 2 and 3 we present a shank prosthesis Elite Foot type, fabricated by Blatchford and Sons Ltd England [11].

This type of prosthesis posses the following characteristics: no mechanical systems; permits the ankle valgus or



Fig. 2 Elite Foot prosthesis: 1, 2, 3 – components which are fabricated from composite materials like carbon fiber

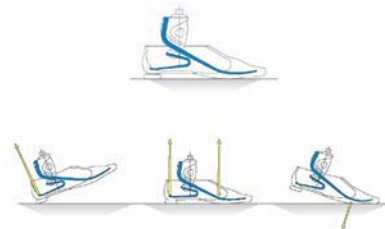


Fig. 3 Aspect regarding the Elite Foot functionality [11]

II. EXPERIMENTAL KINEMATIC HUMAN LOWER LIMB ANALYSIS

We follow to obtain on experimental way the cinematic parameters from the human lower limb in the sight of take over the motion laws developed at ankle joint level.

The experimental research motivation was given by the impossibility to obtain these motion laws on analytical way, because of the human lower limb complexity. And so in order to obtain these motion laws we used an image acquisition system called SIMI Motion, (SIMI Reality Motion Systems GmbH) from Faculty of Physical Education and Sport, University of Craiova. The cinematic parameters were obtained through video capture and image analysis. The process is schematized in figure 4.

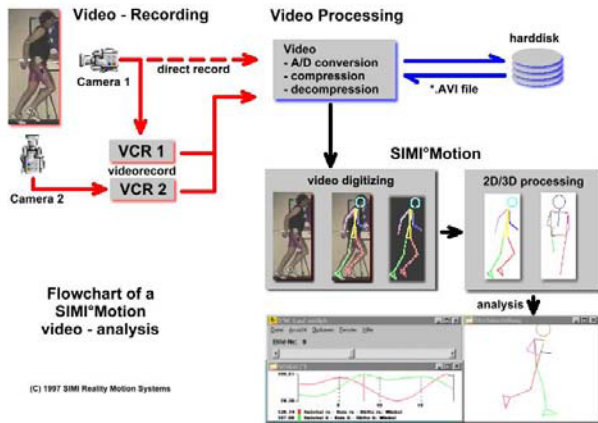


Fig. 4 SIMI – Motion analysis scheme [14]

In order to obtain the motion laws developed at the ankle joint we analyze a human subject without locomotion disabilities (male, age 26, 1, 73 height, 65 kg weight, femur length= 401mm; tibia length =322 mm; foot length = 210 mm). This experiment represents the in-vivo cinematic analysis of the human lower limb for walking process (figure 5). The walking process was performed in a 2D space. The subject walked on x axis direction for a 2, 5 meters distance, in a 4, 2 seconds.

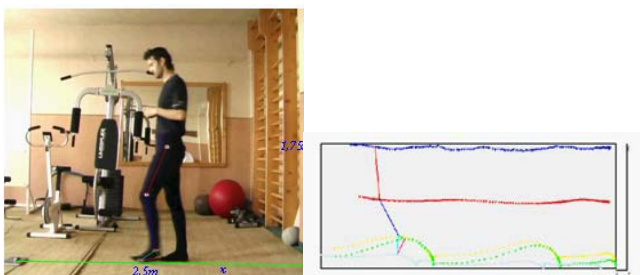


Fig. 5 Aspect regarding the walking process analyzed with SIMI – Motion's aid

We obtain the angular displacements, velocities and accelerations for the ankle joint. As an example we present the angular displacements from the ankle joint in figure 6.

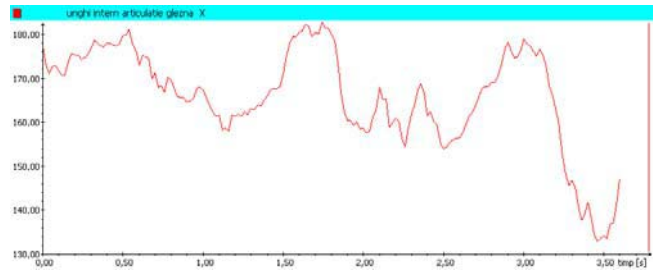


Fig. 6 Angular displacement, – dorsal flexion, angular displacement depending on time

III. DYNAMIC MODEL ELABORATION EQUIVALENT TO HUMAN LOWER LIMB

The mathematic model for the human lower limb inverse dynamic analysis was elaborated by taking in account the experimental cinematic analysis [1]. We consider the foot ground contact as it shows in figure 7. The cinematic constrain equations are:

$$\Phi(q, t) = 0 \tag{1}$$

Where: q - generalized coordinates vector; t - time.

We differentiate (1) by taking in account the time as a variable, and we obtain:

$$J_q \cdot \dot{q} + \frac{\partial \Phi}{\partial t} = 0 \tag{2}$$

The mass forces mechanical work is :

$$\begin{aligned} \delta L &= \delta r_{C_1}^{Tcx} \cdot G_1 + \delta r_{C_2}^{Tcx} \cdot G_2 + \dots + \delta r_{C_8}^{Tcx} \cdot G_8 = \\ &= \sum_{i=1}^8 \delta r_{C_i}^{Tcx} \cdot G_i \end{aligned} \tag{3}$$

The motion equation has the following form:

$$\begin{bmatrix} M & J_q^T \\ J_q & 0 \end{bmatrix} \begin{bmatrix} \ddot{q} \\ \lambda \end{bmatrix} = \begin{bmatrix} Q_a \\ a \end{bmatrix} \tag{4}$$

We know the motion laws for the equivalent ankle joint $q(t)$, $\dot{q}(t)$ and $\ddot{q}(t)$ from the experimental analysis, performed in the dynamic regime. From relation (4) we determine Lagrange multipliers λ , with the aid of an algorithm performed in MAPLE program. And so we compute the connection forces from the cinematic joints of the mathematic model.

The relations which we compute these connection forces, by considering the Lagrange multipliers are:

$$\begin{cases} F_i^{nr(i,j)} = [R_{i,i^n}]^T \cdot [A_{oi}]^T \cdot [\lambda]^{r(i,j)} \\ T_i^{nr(i,j)} = \left[\{S_i^M\}^T \cdot [P_{oi}]^T \cdot [I] - \{S_i^M\}^T \cdot [P_{oi}]^T [\lambda]^{r(i,j)} \right] \end{cases} \quad (5)$$

The variation of the connection force component for the ankle joint is presented in figure 8.

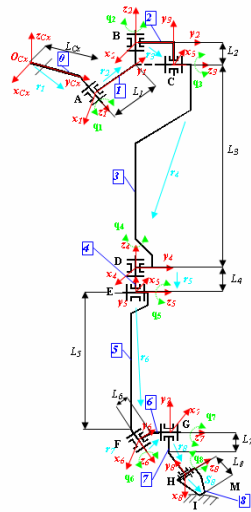


Fig. 7 The human lower limb cinematic scheme

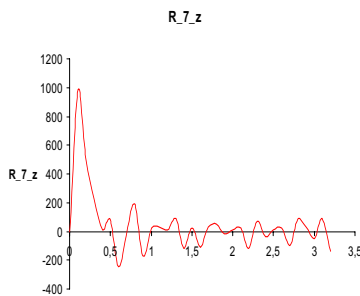


Fig. 8 The variation of the connection force for the ankle joint on z direction

IV. THE NEW PROSTHEISIS SYSTEM DESIGN

The imposed conditions for the new prosthesis system design are: to achieve the motion with an angular amplitude identical with the one which was obtained on human subject without disabilities (55°); to permit the plantar/dorsal flexion without shocks; in the plantar/dorsal flexion phases, the shock absorber must have a minimal displacement of the piston; it must have a minimal clearance – loading gauge, a

simplified construction in such manner that can be respected the imposed dimensional conditions by the ankle joint; the prosthesis components must posses a geometrical form in the sight of ankle motion law achievement, which was developed by the human subject without locomotion disabilities; the shock absorber’s track must be small enough, but the damping coefficient must be high, in order to support the connection force developed at the human ankle joint.

Regarding those imposed conditions and the anterior data, the best mechanism which can be implemented on the prosthesis structure was a cam mechanism. This mechanism is the only one that can fulfil the motion law developed at the human ankle joint. Also the cam was fixed to the artificial foot, and the cam follower was fixed with the shock absorber’s rod (figure 9). The shock absorber was integrated in the resistance structure of the prosthesis and has the possibility to make some axial adjustments in order to establish the alignment of the prosthesis.

The prosthesis virtual model was developed with the CATIA V5 R16 3D modelling software’s aid. The components identified on figure 9 are: tibia component (1), which contain the shock absorber’s body; shock absorber’s support (2); shock absorber’s rod (3); role of the cam follower (4) which slide over the cam profile; bolt (5) which glides over a imposed profile described by the motion law from a human subject without locomotion disabilities; C-Walk foot (6).

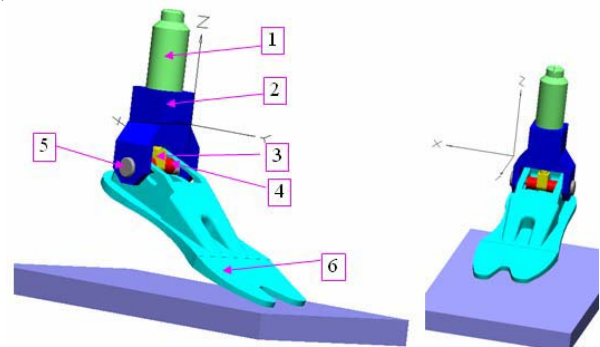


Fig. 9 Virtual model of the prosthesis

After simulating the virtual model and validating through calculus the cam mechanism, this prosthesis was executed and adapted on an amputee (figure 10).

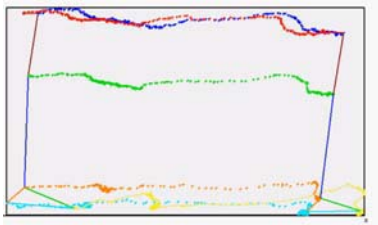
The main objective of the study was to improve this type of prostheses by implementing a mechanism. In order to validate this improvement the adapted prosthesis was analyzed with SIMI Motion software. We made some intermediary experimental tests, and after 14 days, when the amputee began familiar with this, we obtain the results by cinematic laws. In figure 11 we present some aspects from the new prosthesis experimental tests.



Fig. 10 The new prosthesis used in human ankle disarticulations



Fig. 11 Some aspects from the new prosthesis experimental tests achieved with SIMI Motion software



V. CONCLUSIONS

The novelty elements of this prosthesis are the cam mechanism. This mechanism was perfectly adapted onto prosthesis structure and respects the imposed conditions.

The prosthesis experimental tests were achieved in two phases, and the results obtained from the second phase are closer to the ones from the human subject without locomotion disabilities.

The motion law obtained in the experimental tests are different from a human subject to another. The angular displacement variation of the new prosthesis (figure 12) is almost identical with the one from figure 6. The values in the walking process indicate angular displacements over 50...55 degrees.

On the future we want to improve this mechanical system and to keep the cam mechanism in his structure, in

order to obtain better results. Also we want to make other experimental tests such like stairs climbing, dancing, running, etc.

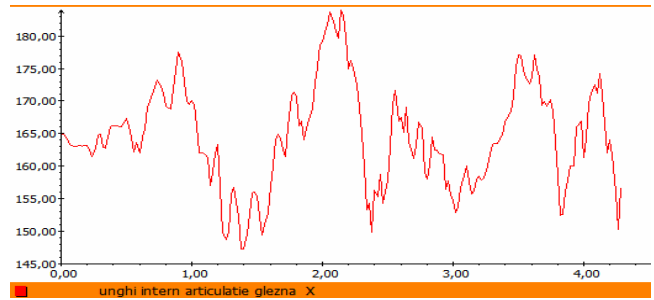


Fig 12 The angular displacement variation of the new prosthesis dorsal flexion, angular displacement depending on time

REFERENCES

1. Dumitru N., Nanu Ghe., Vintilă D (2008) Mecanisme și transmisii mecanice. Tehnici de modelare clasice și moderne. Editura Didactică și Pedagogică. București.
2. Sameer Singh (2004) Intelligent Robotics For Rehabilitation Robotic Lower Limb for Above Knee Prosthesis. Grant type (83/ECE/2000) Department of Electronics and Communication Engineering India.
3. T. McGeer (1990) Passive dynamic walking. International Journal of Robotics Research, vol. 9, no. 2, pp. 62-82.
4. Wilson A.B. (1994) Limb prosthetics, artificial limb. Springer Verlag.
5. J. Moreno, K. Meijer, H. Savelberg, and J. Pons (2004) Characterization of an actuator system for a controllable knee ankle foot orthosis. Proceedings of 8th International Conference ACTUATOR, Bremen.
6. M. Hardt, K. Kreutz-Delgado, J. Helton and O.V. Stryk (1999) Obtaining minimum energy biped walking gaits with symbolic models and numerical optimal control. Workshop - Biomechanics Meets Robotics, Modelling and Simulation of Motion, Heidelberg, Germany. 1999, pp. 1-19.
7. Williams M. (1996) Biomechanics of human motion. W.B. Saunders Co. Philadelphia and London.
8. SouthWest Orthotic Centre <http://www.southwest-ortho.com>
9. Otto Bock Prosthetic Centre <http://www.ottobock.com>
10. Bauerfeind Research Center AG Germany <http://www.bauerfeind.com>
11. Blatchford prosthetics institution <http://www.blatchford.co.uk>
12. Ohio Willow Wood Prosthetic Centre <http://www.owwco.com>
13. SIMI Motion <http://www.simi.com>

Author: Phd student. Eng. Cristian COPILUȘI
 Institute: Faculty of Mechanics. University of Craiova.
 Street: Calea București no.107
 City: Craiova. Dolj
 Country: Romania
 Email: cristache03@yahoo.co.uk

Development of a Telemetric Goniometer

G.T. Laskoski¹, L.D.L. Martins¹, S.F. Pichorim¹, and P. J. Abatti¹

¹ Federal University of Technology - Parana/CPGEI, Curitiba, Brazil

Abstract— This work presents a description of a goniometer with inductive sensors which can be used for medical applications. The goniometer uses the coupling between two coils. The new method is demonstrated that knowing the transmitter signal and the distance between the coils in the same goniometer's arm, the angle between the moving and stationary arms can be easily determined. Preliminary tests indicated that the goniometer has a maximum error of 6° from 20° to 120°.

Keywords— Biomedical Instrumentation, Goniometer, Inductive sensor.

I. INTRODUCTION

Goniometry has been described in the literature since 1914 and it is widely used in clinical practice and scientific research to evaluate the amplitudes of joint motion to determine the most appropriate therapeutic intervention [1].

The most common techniques used to measure joint motion are visual observation, image processing, and through the direct application of goniometers. Visual observation is a subjective method which makes it difficult to achieve a reliable diagnosis. The image processing requires more sophisticated equipment and may be impracticable in small clinics. The goniometer is a simple and low cost equipment and it is widely used to measure the joint motion [2, 3]. The universal goniometer is the most used equipment in goniometry and it is formed by a stationary arm, a moving arm, a central articulation point, and a protractor which allows the measurement of the angle between the arms [4]. However, the universal goniometer has two main limitations: the inability to evaluate the motion in more than one plan and the discrepancy due the change in the relative position between the articulations axis of goniometer axis and limbs [4, 5].

Scientific and technological advances have improved the methods and equipments used to measure joint motion [5]. For instance the use of a goniometer with a potentiometer or an optical encoder at the central point allows the automatic acquisition of amplitude movement. Both of them (optical and potentiometers) have the same disadvantages of the universal goniometer [2, 4, 5].

In 1987 it was developed the flexible goniometer which is formed by a flexible rod coated by a plastic and employing a strain gauge as transducer. The flexible goniometer is less influenced by the misalignment between the articulation axis and the goniometer axis than universal goniometers. However, the coupling between the flexible goniometer and the articulation is still a problem [5, 6].

Another method to measure the joint motion is the use of inertial sensors like accelerometers and gyroscopes. The main advantages of using inertial sensors are the automatic data acquisition, small dimensions of equipment, and the fact that it is not necessary to find the central articulation point. However, such systems usually present a low sensitivity to slow movements and external acceleration may interfere in the final readout [7, 8, 9].

Recently, it has been developed a goniometer using inductive sensors [10]. Specifically, applying a signal to one coil and measuring the induced voltage at a second coil, the angle between them can be calculated, provided the distances between the coils and the central articulation point is known. Thus the accuracy of this method is strongly dependent on the determination of the position of the articulation point, which in biological systems it is not usually easy to determine.

In this work it is demonstrated that it is not necessary to know the distance between the coils and the central articulation point when goniometer with two inductive sensors are employed. Experimental setup is show and corresponding results are disclosed.

II. MATERIAL AND METHODS

A. The goniometer with inductive sensor

The goniometer is formed by two coils in the same plane. Figure 1 shows a graphical representation of goniometer with inductive sensor. A signal applied in the transmitter coil (TX) induces a voltage in the receiver coil (RX), so that knowing the positions of the coils x and y in relation to the central articulation point, it is possible to determine the mutual inductance (M), distance (d), and angle (α).

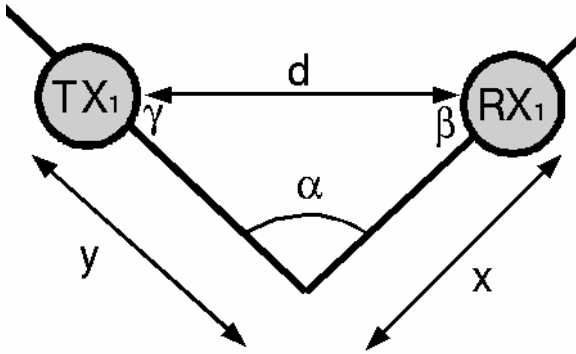


Figure 1 – Graphical representation of the inductive goniometer.

The distance d can be calculated using the law of cosines

$$d^2 = x^2 + y^2 - 2x \cdot y \cdot \cos(\alpha) \tag{1}$$

Pichorim and Abatti [11] describe a simplified method to determine the magnetic flux density (B) in the receiver coil and the mutual inductance (M) between parallel coils. Assuming the coils are coplanar (the distance (d) between the coils occurs in the xy) and the measuring point d is gratter than the transmitter coil radius (a), the magnetic flux density can be expressed by

$$B = \frac{\mu_0 \cdot i \cdot a^2 \cdot n_1}{4d^3} \tag{2}$$

where μ_0 is the magnetic permeability of the medium and n_1 is the number of turns of the transmitter coil. The mutual inductance (M) can be obtained by the product of the area inside the coil and magnetic flux density [10], yielding

$$M = \frac{n_2}{i} \cdot B \cdot \pi \cdot b^2 = \frac{\mu_0 \cdot \pi \cdot a^2 \cdot b^2 \cdot n_1 \cdot n_2}{4d^3} \tag{3}$$

where n_2 is the number of turns of receiver coil and b is the receiver coil radius. Figure 2 shows the circuit used to measure M . The transmitter is formed by a sinusoidal generator and LC circuit while the receiver is constituted by a coil and an amplifier circuit. In this arrangement it can be easily demonstrated that M can be written as

$$M = \frac{L_1 \cdot V}{A \cdot V_g} \tag{4}$$

where V_g is the voltage of generator, L_1 the inductance of transmitter coil and A is the voltage gain of amplifier circuit.

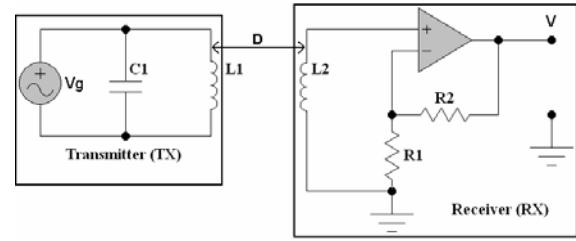


Figure 2 – Circuit to measure the mutual inductance.

The practical value of d is determined by measuring the received voltage in RX. Combining (3) and (4) and isolating d , yielding

$$d = \sqrt[3]{\frac{\pi \cdot A \cdot V_g \cdot \mu_0 \cdot a^2 \cdot b^2 \cdot n_1 \cdot n_2}{4L_1 \cdot V}} \tag{5}$$

Therefore, the angle α can be calculated by substituting (5) in (1). Isolating α is obtained a relation between α and V , expressed by

$$\alpha = \arccos \left[\frac{\left(\frac{\mu_0 \cdot \pi \cdot a^2 \cdot b^2 \cdot n_1 \cdot n_2 \cdot A \cdot V_g}{4L_1 \cdot V} \right)^{2/3} - x^2 - y^2}{-2x \cdot y} \right] \tag{6}$$

B. The goniometer with two inductive sensors

The new method shows, with a controlled variation in x and y , it is possible to calculate the angle α without knowing x and y . Figure 3 shows a graphical representation of the new goniometer which is constituted by two coils in each arm with a fixed distance s between them.

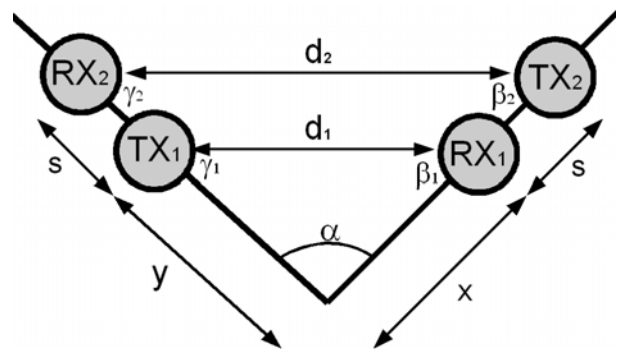


Figure 3 – Graphical representation of the goniometer with two sensors.

The goniometer can be determined by the law of sines

$$\frac{d_2}{\sin \alpha} = \frac{y+s}{\sin \beta_2} = \frac{x+s}{\sin \gamma_2}, \tag{7}$$

$$\frac{d_1}{\sin \alpha} = \frac{y}{\sin \beta_1} = \frac{x}{\sin \gamma_1}. \tag{8}$$

If the distance x is equal or similar to y or there is a high angular value, the angular coefficient of d_1 and d_2 (in relation to axis x) is the same and β_1 can be considered equal to β_2 , a solution can be obtained by equaling α in (7) and (8) and simplifying β_1 and β_2 . Therefore, the distances x and y can be expressed by

$$x \approx y \approx \frac{d_1 \cdot s}{d_2 - d_1} = t. \tag{9}$$

Thus, a new triangle can be found which d_1 and d_2 are parallel and both goniometer's arms have the same distance (t) and the angle between them are very similar to α . This angle α can be calculated by substituting (9) in (1) and isolating α , yielding

$$\alpha = \arccos \left(1 - \frac{d_1^2}{2t^2} \right). \tag{10}$$

Observe that d_1 and d_2 can be determined by (5) and α can be determined by (10) without knowing x and y .

III. TESTS AND RESULTS

Figure 4 shows a photo of the experiment which consists in compare the protractor angle with the angle obtained by measuring voltage in RX_1 and RX_2 .

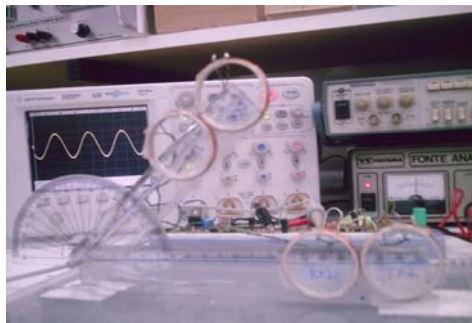


Figure 4 – Photo of the experiment. A scope is used to measure the peak to peak voltage in the receiver coils and a generator is used to apply a signal in the transmitter coils.

The transmitters are formed by a LC circuit which is tuned in 67 kHz. The coils have a circular form with 7 turns in a wire AWG30, 40 mm in diameter, and inductance about 4.7 μ H. The distances x and y are 150 mm and 110 mm, respectively. The distance s is 41mm. It was applied a sinusoidal signal V_g at TX_1 and TX_2 with 13 V peak to peak. In order to avoid interference between the coils, first the signal is applied in TX_1 and the voltage in RX_1 was measured and after the signal is applied in TX_2 and the voltage in RX_2 was measured for the same angle. Figure 5 shows the result of the experiment for an angular range from 20° to 180° with steps of 5°.

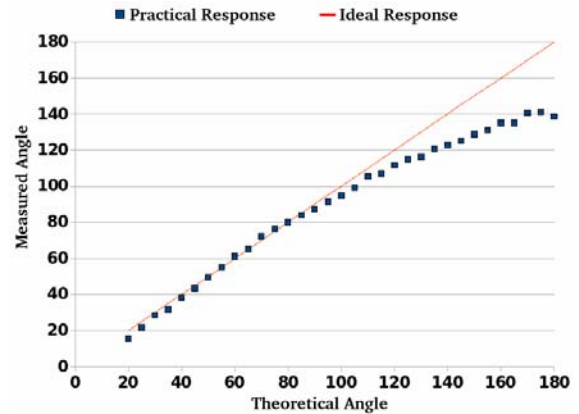


Figure 5 – Result of the experiment.

Table 1 shows maximum standard deviation and correlation between the ideal response and the practical angular value according to the range of the goniometer.

Table 1 – Maximum standard deviation and correlation

Range	Maximum standard deviation (σ)	Correlation
20° to 120°	5.88°	0.99622
20° to 140°	12.05°	0.99434
20° to 160°	17.61°	0.99223
20° to 180°	29.19°	0.99053

IV. CONCLUSIONS

The goniometer with inductive sensor shows functional for angles up to 120° in a plane (σ of 5.88 °). For angles greater than 120° there are discrepancies due to low signal/noise ratio of received signal, resulting in errors to determine the mutual inductance in terms of distance.

In a previously work [10], it was related by analyzing the equation (5) which the distance is inversely proportional to the signal amplitude in the reception. Moreover, for great angles, smaller is the variation of distance depending on the angular variation, reducing the goniometer resolution [10]. Another problem is the discrepancy in the frequency of resonance due to tolerance and the characteristics of capacitors and coils in the transmitter circuit.

This new method demonstrated that it is not necessary to know the distances between the coils and the central articulation point with two sensors. The experiment shows with diferents distances between x (150 mm) and y (110 mm), it is possible to find a good response for lower angles ($\sigma = 3.05^\circ$ to 20°). It is important to point out that errors can be reduced if arm distances x and y are equal. However, this technique can support some variations in x and y during the angular movement.

The goniometer with inductive sensor presents a good response for angles from 20° to 120° . Future works can be developed to improve the coupling between the coils, increasing the resolution of the goniometer and reduce the noise levels.

ACKNOWLEDGMENT

This work was supported in part by CNPq (Brazilian Council for Scientific and Technological Development).

REFERENCES

1. Marques A P (1997) Goniometry Manual, Manole, São Paulo (in Portuguese)
2. Barreiro M S, Frére A F, Theodório N E M, Amate F C (2003) Goniometer based to computer, Engineering in Medicine and Biology Society, Proceedings of the 25th Annual International Conference of the IEEE, v 4, pp 3290-3293
3. Theodório E M, Barreiro, M S, Souza D J M S, Frére A F (2004) Development of a Computed Device for Shoulder Goniometry. Latin American Congress on Biomedical Engineering. João Pessoa (in Portuguese)
4. Vieira E R (2002) Analysis of the reliability of equipment and methods to measure the movement of anterior flexion of the lumbar spine. Federal University of São Carlos, São Carlos. (in Portuguese)
5. Tesio L, Monzani M, Gatti R, Franchignoni F (1995), Flexible electrogoniometers: kinesiological advantages with respect to potentiometric goniometers, Clinical Biomechanics, v 10, n 5, pp 275-277
6. Roduit R, Besse P A, Micalef J P (1998) Flexible Angular Sensor, IEEE Transactions on Instrumentation and Measurement, v 47, n 4, pp 1020-1022
7. Kurata S, Makikawa M, Kobayashi H, Tokue R, Takahashi A (1998) Joint Motion Monitoring by Accelerometers set at both near sides around the joint, IEEE Engineering in Medicine and Biology Society, v 20, n 4, pp 1936-1939
8. O'Donovan K J, Kamnikb R., O'Keeffea D T, Lyonsa G M (2007) An inertial and magnetic sensor based technique for joint angle measurement, Journal of Biomechanics, v 40, n 12, pp 2604-2611
9. Willemsen M T A, Frigo C, Herman B K (1991), Lower Extremity Angle Measurement with Accelerometers - Error and Sensitivity Analysis, IEEE Transactions on Biomedical Engineering, v 38, n 12, pp 1186-1193
10. Laskoski G T, Pichorim S F (2008) Development of a Telemetric Goniometer with Inductive Sensor for Medical Applications, XXI Brazilian Congress on Biomedical Engineering, pp 922-925 (in Portuguese)
11. Pichorim S F, Abatti P J (2004) Design of Coils for Milimeter and Submilimeter-Sized Biotelemetry, IEEE Transactions on Biomedical Engineering, v 5, n 8, pp 921-925

Author: Gustavo Theodoro Laskoski
 Institute: Federal University of Technology - Parana
 Street: Av. Sete de Setembro, 3165.
 City: Curitiba/PR
 Country: Brazil
 Email: gustavo_thl@yahoo.com.br

Artificial Prehension and the Detection of Object Slip

S.A. Ahmad^{1,2} and P.H. Chappell¹

¹ School of Electronics and Computer Science, University of Southampton, Highfield SO17 3AS Southampton, UK

² Dept. of Electric and Electronics, Fac. of Engineering, University Putra Malaysia 43400 Serdang, Selangor, Malaysia

Abstract— An investigation of the fundamental operation of an artificial hand has been carried out with the aim to study the automatic control feedback for this system. The hand is modeled as a simple prehension system with three sensing elements; force, acceleration and slip. This prehension study focused on the object's gripping and slippage processes. An automatic closed loop feedback control algorithm is developed to re-grip the object when it starts to slip which is similar in form to Hooke's Law. The algorithm uses information from the distance of the object has slipped to re-grip the object and control the amount of force required. Also, a method called approximate entropy has been used to analyze and detect when the object begins to slip. This method can be used to prevent the object from slipping.

Keywords— Prosthesis control; prehension system; automatic feedback control; slip detection.

I. INTRODUCTION

The human hand system is a complex biological system with a multitude of muscles and tendons that provide multiple degrees of freedom of movements. It has an array of over 17,000 tactile sensors for sensory feedback mechanisms. For example, when the normal human hand holds a small object and it slips, the person could automatically re-grip the object within a very short time.

The development of hand prosthesis began centuries ago. They have been designed to provide functional replacement for individuals with amputation; a main aim is to design prosthetic hands that could mimic the control and functionality of a human hand. A good and reliable prosthetic hand should have an automatic grip and feedback control between the hand and the control mechanism.

The Southampton Hand, for example is an artificial hand with multiple degrees of freedom [1]. It has four digits and a thumb that is able to do multiple grip postures. This lighter weight hand uses six gearboxes that can flex/ extend the four digits, and the thumb can flex/extend and also rotate. It also has some sensors (slip, force and temperature) placed on each fingertip [2] that add more functionality of the artificial hand.

Prehension is an action of physically grasping or holding something and manipulation within the hand. The most important function of a human hand is prehension. An

example is picking up a ball with a spherical grip posture. Several designs and developments of artificial hands have been reported, but none of them have included the study of prehension [1,3,4,5]. There is growing interest in studying methods to avoid the object from slipping when being held. A robust control solution is needed to overcome this matter where robust sensors are essential for the measurement of variables in a control loop.

Approximate entropy (ApEn) is a method introduced by Pincus [6] to investigate the regularity/irregularity of a signal. It has been used widely to analyze various biomedical signals, such as heart rate variability, surface electromyography and electroencephalography [6,7,8]. In this study, ApEn is used to investigate the slip signal and how it can be used to detect and avoid the object from slipping.

II. EXPERIMENTS

The operation of the prehension system can be explained in the diagram shown in Fig. 1. The system performs a single-degree of freedom operation where an aluminium bar with a 'U' cross section is used as an object. A DC motor/gearbox generates a force, F which increases until the object is gripped securely where the gravitation force, mg equals to the friction force, $2\mu F$. The apparatus arrangement allows for linear and horizontal movement to reflect the pinching action between a finger tip and thumb.

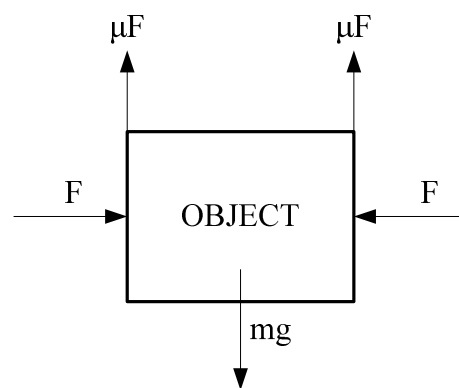


Fig. 1 A diagram of the object gripping of the prehension system

The prehension system has three sensors integrated into the system which are a force sensor, an accelerometer and a slip sensor. The force sensor measures the force required to hold the object. The accelerometer is to measure the acceleration of the object when it slips. Consequently, the velocity and the distance can be obtained by applying double integration to the signal. The slip sensor is to detect when the object starts to slip and will be used to trigger the re-gripping process.

Experimental tests are developed to mimic the behavior of an artificial hand and are focused on an understanding of a hand's operation associated with object's gripping and slippage, and attempt to re-grip the object.

The findings from the experiment are then used to develop the control algorithm for automatic closed feedback control which of a similar form to Hooke's Law:

$$F = k\hat{x} \quad (1)$$

where F is the force, k is a constant and \hat{x} is an estimate of the distance that the object has slipped. The distance, \hat{x} will determine the amount of force required to tighten the object.

III. RESULTS AND DISCUSSION

The experiment on the prehension system was carried out by running an object gripping test. Initially, the force was applied to grip the object. After the object was held, the force was reduced and the object started to slip. The force was applied again to re-grip the object and prevent the object from slipping.

The signals from the three sensors during the gripping and re-gripping processes are shown in Fig. 2. The study focuses on three phases of the object condition which are when it is held, it starts to slip and when it is securely re-gripped. From the top plot, it shows that the average force required to grip the object is about 3.5V which is equivalent to 7N. The value is typical of the finger force required to hold an object. When the object starts to slip, the force dropped at almost 0N and signal responses can be seen from the accelerometer (middle plot in Fig.2) and the slip sensor (bottom plot in Fig.2).

From the acceleration signal, it can be seen that the object accelerates when the force is reduced and it starts to decelerate when there's attempt to re-grip the object. When an object experienced a free fall, it has the acceleration of $1g (= 9.81\text{ms}^{-1})$. From the acceleration plot, it shows that the object dropped under free fall condition. Simpson's rule was used to estimate the velocity and the distance from the acceleration signal.

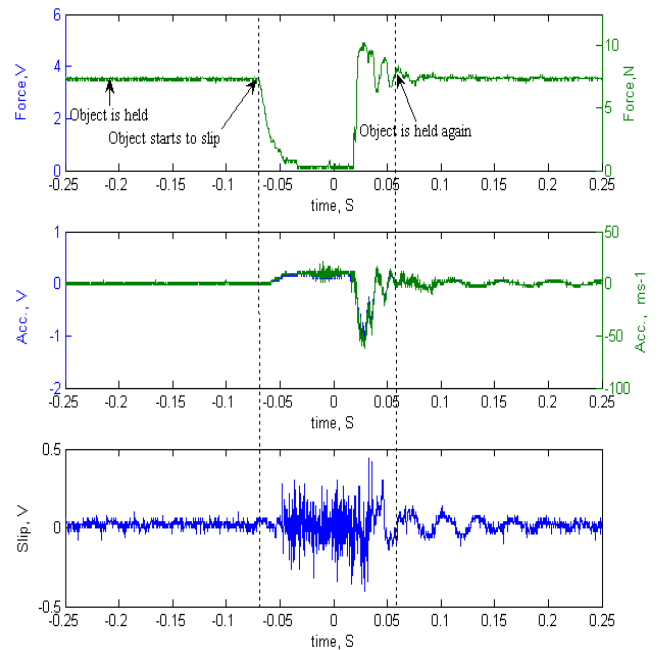


Fig. 2 The signal responses from the three sensors in the prehension system; force (top), acceleration (middle) and slip (bottom)

The results are shown in Fig. 3 where middle and bottom plots are for the velocity and the distance respectively. Label A, B and C in the top plot shows when the object starts to slip, an attempt to re-grip the object and when the object is held again respectively. From the plots, it can be observed that the velocity and the distance of the object start to increase when the object begins to slip. The velocity starts to decrease when attempt to re-grip the object is done. The velocity returns to zero eventually and the distance becomes a constant when the object stops.

For the slip signal, besides detecting when the object starts to slip, the distance of the object's slippage can also be computed. This can be done by applying an approximate integrator to the signal [9]. With this method, a suitable threshold voltage, V_t is chosen. Selection of a good value for V_t will detect the object slippage at the right moment. Three different V_t s were selected in the investigation which are $0.04\text{V} (V_{t1})$, $0.06\text{V} (V_{t2})$ and $0.08\text{V} (V_{t3})$. The result from the approximate integration is the sum of 1's that represent the estimation of the object has slipped.

A further investigation of the slip signal has been carried out using the ApEn algorithm. A detailed explanation on the algorithm can be found in reference [6]. Two parameters are required prior to the calculation of ApEn which are the embedding vector, m and the tolerance range, r and for N data samples, ApEn can be defined as:

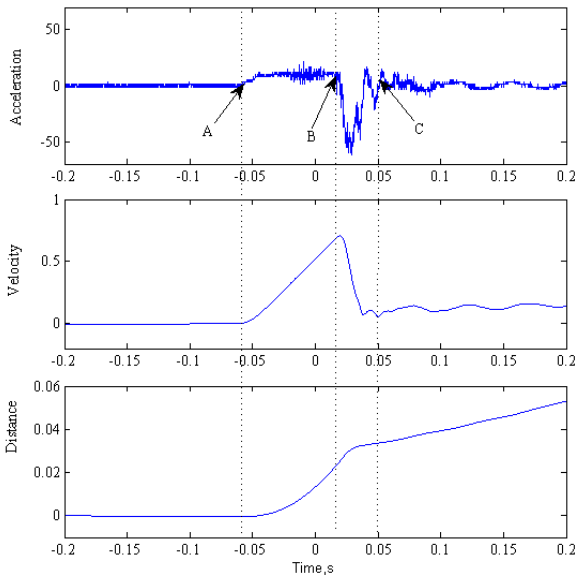


Fig. 3 By applying double integration to the acceleration signal (top), the velocity (middle) and the distance (bottom) are obtained.

$$ApEn(m, r, N) = \phi^m(r) - \phi^{m+1}(r) \quad (2)$$

In this work, $N=200$, $m=2$ and $r = 0.25$ of the standard deviation of the data are used for the ApEn calculation. Fig.4 shows the ApEn analysis when applied to the slip signal. It can be seen that the ApEn drops to a value about 0.4 when the object slips. When there is attempt to re-grip the object, there is an increase in the ApEn before it drops again. The ApEn is then increases again to about 1 when the object is held again (the slip signal is 0V). The analysis shows that ApEn can be used to detect the object's slip.

The information obtained from both, the accelerometer and the slip sensor could be used to estimate the distance that the object has slipped. Fig. 5 shows the relationship between the force and the distance obtained from the acceleration and the slip signals. From the right-axis of the bottom plot, it can be observed that when the object slipped, it has dropped about 0.2m before it was re-gripped again. A force of 8N is required to grip the object securely. The result for three different V_t s of the approximate integration of the slip signal is shown in the bottom plot, left-axis. It can be observed that at higher threshold levels, threshold crossing events are not recorded until later on in the experiment and oppositely, at lower velocities, threshold crossing events are observed much earlier in the experiment. Also, it can be seen that the distance obtained from the acceleration is proportional to the sum of 1's obtained from the approximate integration of the slip signal.

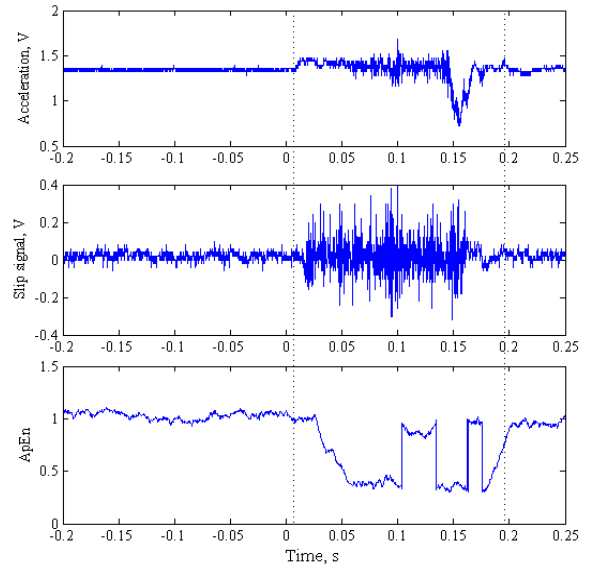


Fig. 4 ApEn analysis of the slip signal. Top: the acceleration signal, middle: the slip signal and bottom: the ApEn of the slip signal

The distance is used to determine the amount of force required to re-grip the object, as described earlier in Equation 1. However, for the proposed algorithm of the automatic control feedback, the slip signal is used to detect the object's slip which will be then used to trigger the processing of the acceleration where the distance will be calculated.

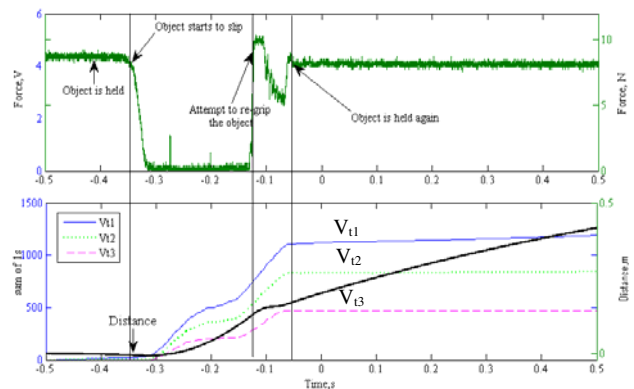


Fig. 5 The relationship between the force and the distance of the object has slipped during the re-gripping process

Prior to the implementation of the algorithm, the scalar 'k' in Equation 1 will be determined. Further analysis between the distance obtained from the acceleration signal and the force during the re-gripping process was carried out. The experiment was repeated twenty times in determining the most appropriate value for 'k'. In the analysis, the

average force when the system tried to re-grip the object until it's being gripped is calculated and the distance of the object has slipped during this period is measured. Fig. 6 shows the range of values the average force (top plot) and the distance (middle plot). Using Equation 1, the scalar 'k' is determined. The range of the 'k' values is between 30 and 107 (bottom plot in Fig. 6). Table 1 shows the statistics of the parameters shown in Fig. 6. The average of the 'k' value is 67.10 with a SD of 19.28.

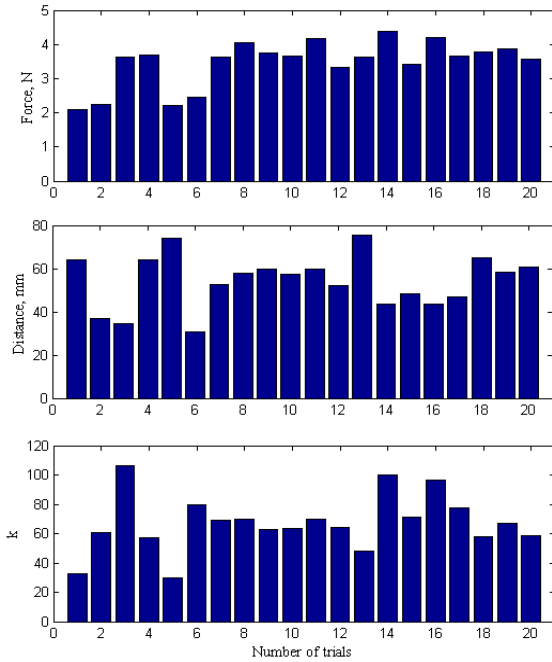


Fig. 6 Distributions of the force, distance and 'k' values over twenty trials

Table 1 Statistics of the force, distance and 'k' values from Fig. 5

	Force, N	Distance, mm	k
Minimum	2.08	30.80	29.69
Maximum	4.37	75.30	106.12
Mean	3.47	54.28	67.10
SD	0.68	12.27	19.28

IV. CONCLUSIONS

Tests and results from the apparatus used to investigate the artificial hand operation have demonstrated that it is suitable to simulate the following: acceleration, object slip-page and gripper force. It has also been observed that a large is de-acceleration is required to obtain a small and acceptable slip distance. Also, an analysis on the slip signal using ApEn has shown when an object begins to slip. During re-gripping, there is a wide variation in the ratio of the applied average force to the object slip-distance.

REFERENCES

1. Light C.M., Chappell P.H., Hudgins B., Engelhart K. (2002) Intelligent multifunction myoelectric control of hand prostheses, *J Med Eng Technol*, 26(4), 139-146.
2. Cotton D.P.J., Chappell P.H., Beeby S.P., Cranny A., White N.M., (2005) Thick film force, slip and temperature sensors for a prosthetic hand, *Meas. Sci. and Tech*, 16, 931-941
3. De Laurentis K.J, Mavroidis M. (2002) Mechanical Design of a Shape Memory Alloy Actuated Prosthetic Hand, *Technology and Health Care*, 10(2), 91-106.
4. Dechev N., Cleghorn W., Naumann S. (2001) Multiple Finger, Passive Adaptive Grasp Prosthetic Hand, *Mechanism and Machine Theory*, 36, 1157-1173.
5. G., Micera G., Edin B., Beccai L., Cipriani C. (2006) Design of a Cybernetic Hand for Perception and Action, *Biological Cybernetics*, 95(6), 629-644.
6. Pincus S.M. (1988) Approximate entropy as measure of system complexity, *Proc. Nat. Aca. Sci. USA*, 88(6), 2297-2301
7. Ahmad S.A. and Chappell P.H. (2008) Moving Approximate Entropy Applied to Surface Electromyographic Signal, *Biomed. Sig. Proc. & Ctrl*, 3, 88-93.
8. Natarajan, K., Acharya, U.R., Alias, F., Tiboleng, T., Puthusserypady, S.K., Nonlinear analysis of EEG at different mental states, *Biomed Eng Online*, 3:7, 2004.
9. Cotton D.P.J., Chappell P.H., Beeby S.P., Cranny A., White N.M., (2007) A novel thick-film piezoelectric slip sensor for a prosthetic hand, *IEEE Sensors Journal*, 7(5), 752-761

Influence of Base Material of TRUCT Braille on Readability of TRUCT Braille

Kouki Doi¹, Hiroshi Fujimoto² and Tsutomu Wada³

¹ Faculty of System Design, Tokyo Metropolitan University, Tokyo, Japan

² Faculty of Human Sciences, Waseda University, Saitama, Japan

³ Universal Design Laboratory, Japan Braille Library, Tokyo, Japan

Abstract— When they are printed together with visual characters, recently transparent-resinous-ultraviolet-curing-type (TRUCT) Braille signs are becoming more and more popular in Japan. These signs are made by screen printing whose technique can be applied to various base materials, such as paper, metal, and plastic. TRUCT Braille signs have begun to be used in public facilities, such as on tactile maps and on handrails. Naturally, it is expected that Braille beginners will utilize these signs. However, it is not easy to read when printed on base material on which it is difficult for the forefinger to slide. The purpose of this study is to examine the influence of base materials on the TRUCT Braille reading. We used fine paper and laminate film as the base material, and measured coefficient of kinetic friction between forefinger and their base materials. The coefficient of kinetic friction for fine paper was one-third that for the laminate film. As the subjects, twelve acquired visual impaired persons of Braille reader were examined. They were asked to read verbally randomly-arranged characters printed on fine paper and laminate film. Reading time was one minute and was repeated twelve times for each subject. As the results, most subjects could read TRUCT Brailles significantly faster and more correctly when they were printed on fine papers than when they were printed on laminate films. We found that base material influenced on TRUCT Braille reading.

Keywords— TRUCT Braille, Base Material, Readability, Screen Printing, Coefficient of Kinetic Friction

I. INTRODUCTION

Transparent-resinous-ultraviolet-curing-type (TRUCT) Braille signs are rapidly gaining popularity in Japan, especially when they are printed together with visual characters. These signs are produced by screen printing and are made using a resinous ink that is cured with ultraviolet radiation. The screen printing technique can be applied to various base materials such as paper, metal and plastic, on which the Braille dots are printed, and TRUCT Braille signs have begun to be used in public facilities, such as on tactile guide maps, ticket vending machines and handrails. Naturally, it is expected that Braille beginners will utilize these signs. The Japan Braille Library has already adopted TRUCT Braille in texts for Braille beginners with acquired

visual impairment[1]. However, it is pointed out that Braille readers find it not easy to read TRUCT Braille which is printed on base material on which their forefingers can not slide easily. The purpose of this study is to examine the influence of base material on the TRUCT Braille reading. Concretely, we conducted an experiment to compare the readability of TRUCT Braille printed on base materials that have different coefficient of kinetic friction.

II. MATERIALS AND METHODS

In this chapter, we introduce base material of TRUCT Braille, the evaluation experiment of characteristics of base material and an outline of the experiment in which the readability of TRUCT Braille printed on two base materials have different coefficient of kinetic friction.

A. Base Material

We used fine paper and laminate film as base material. The laminate film is generally used as base material, because it protects the surface of the visual characters. It is known that laminate film is base material on which the forefinger cannot slide easily. The fine paper is used as most common base material.

B. Measurement of Coefficient of kinetic friction between forefinger and base material

We measured coefficient of kinetic friction between two base materials and forefinger. Two subjects participated in this experiment. They were a 29-year-old male and a 22-year-old female. We developed a friction tester for measuring the coefficient of kinetic friction (Fig 1). First, the participants were asked to put the base material on an aluminium board. Second, they were asked to maintain a 0.39 (N) press force based on press force data obtained during Braille reading [2]. The press force N (N) was measured by a load cell (LM-500GA, Kyowa Electronic Instruments Co., Ltd) under the column. Last, the base material was automatically slid under the subject's

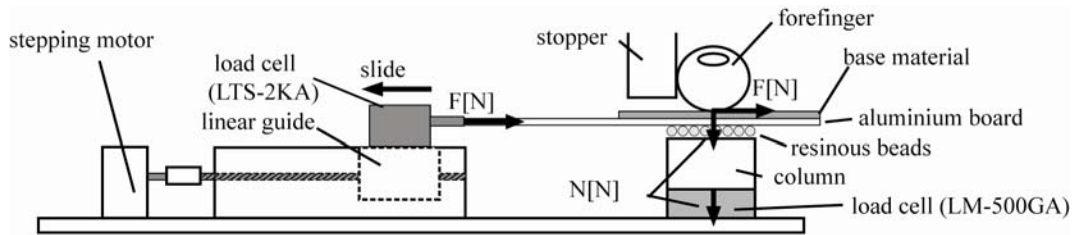
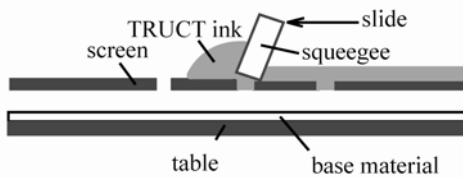
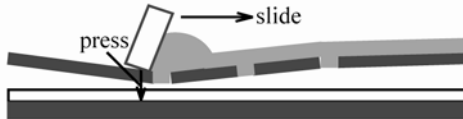


Fig.1 Friction tester for measuring the coefficient of kinetic friction

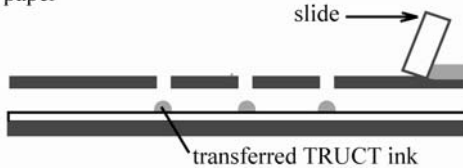
- 1) TRUCT ink is put in unfilled areas of the mesh on the screen by sliding squeegee



- 2) TRUCT ink is forced down through the unfilled areas of the mesh



- 3) TRUCT ink is transferred to base material such as paper



- 4) TRUCT ink is cured by ultraviolet rays

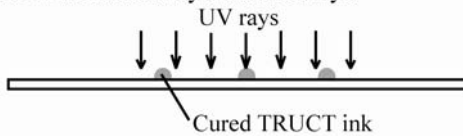


Fig.2 Method of screen printing

forefinger using a stepping motor. The sliding speed was 6.0 mm/s, the same as Braille reading speed [3]. Simultaneously, the friction F (N) was measured by the load cell (LTS-2KA, Kyowa Electronic Instruments Co., Ltd) on the linear guide. Each trial under each condition was conducted 3 times. A total of 6 trials were performed, requiring approximately 0.5 hour.

C. Experiment to compare the readability of TRUCT Braille printed on two base materials have different coefficient of kinetic friction

Based on above the results of measurement of coefficient of kinetic friction between forefinger and base material, we

compared readability of TRUCT Braille. TRUCT Braille characters were printed on fine paper and laminate film by screen printing method (Fig 2). Twelve Braille learners with acquired visual impairment participated as subjects in our experiments. Their average age was 56.4 years. They were asked to read randomly arranged Japanese TRUCT Braille characters both when printing on fine paper and laminate film. The Braille used in this study consisted of two different dot heights, 0.15mm and 0.40mm, with a Japanese standard dot distance of 2.3mm [4]. We set two different dot height. The subjects were asked to read the characters verbally for one minute, both fine paper and laminate film. The reading speed and error rate were recorded, and the reading speed was determined as the number of characters read per minute. The error rate was displayed as the percentage of reading mistakes. In each case, the results were analyzed statistically using two factors (base material and dot-height) between the groups and employing the analysis of the variance (ANOVA) technique with Bonferroni multiple comparison test corrections.

III. RESULTS

Regarding experiment of measuring kinetic friction between forefinger and base material, we calculated the coefficients of kinetic friction in two base materials, and the results are shown in Fig 3. The result of measurement of kinetic friction can be interpreted as follows, The coefficient of kinetic friction of fine paper was about one-third that of laminate film. From above the results, we quantified difference of kinetic friction between the two base materials and forefinger.

The average reading speed and error rate were measured, and the results are shown in Fig 4 and Fig 5.

Reading speed (characters /min): The two-way interaction of two parameters (base material and dot height) was found to be statistically significant ($F(1,11)=25.83, p<.001$). Fig 4 shows result of reading speed. From Fig 4, in the case of the 0.15 mm dot height characters, the reading speed of laminate film was 26.8 characters per minute, and that of fine paper also was 47.1 characters per minutes. In case of the 0.4 mm dot height characters, the reading speed of

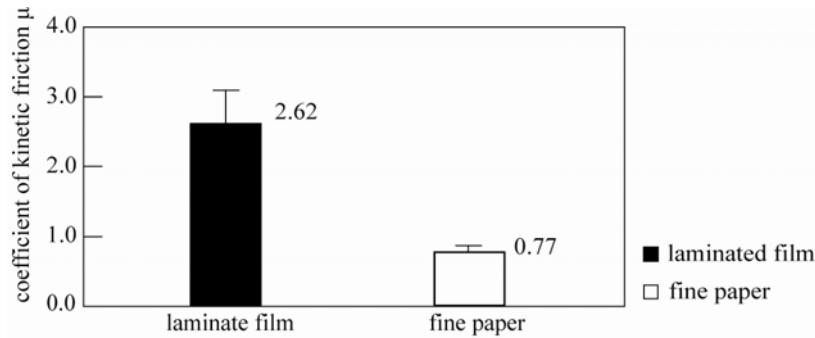


Fig. 3 Results of measurement of coefficient of kinetic friction μ

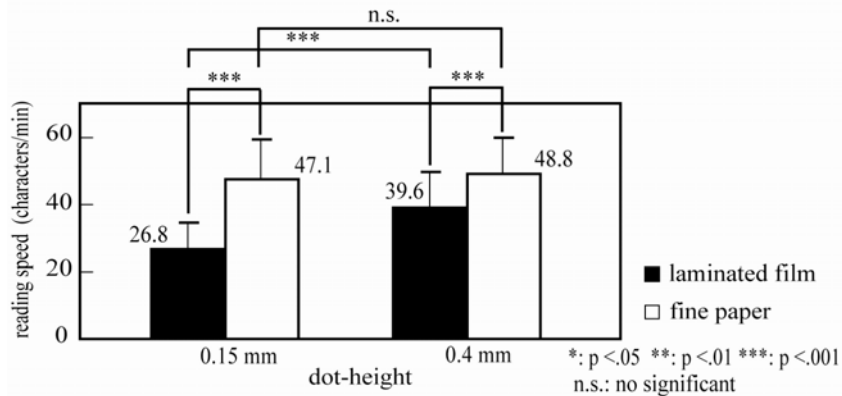


Fig. 4 Results of reading speed during reading TRUCT Braille

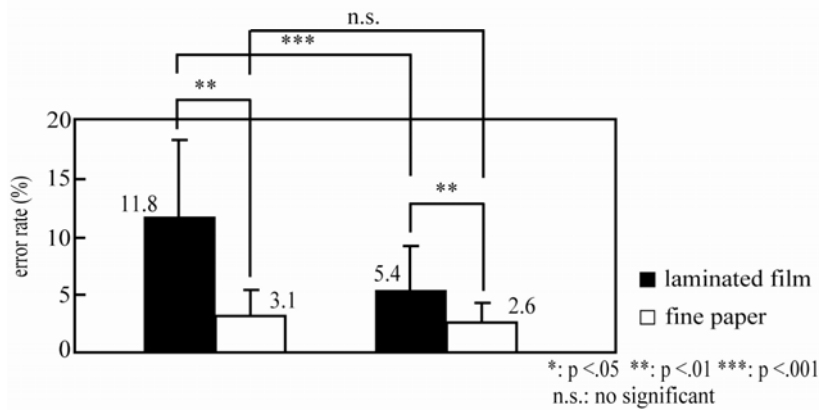


Fig. 5 Results of error rate during reading TRUCT Braille

laminated film was 39.6 characters per minute, and that of fine paper also was 48.8 characters per minutes.

In the case of the 0.15 mm dot height characters, the reading speed of fine paper was about twice that of laminated film. In the case of the 0.4 mm dot height characters, the reading speed was about 1.2 times faster when the base material was fine paper than that was laminated film. Regarding laminated film, the 0.4 mm dot height character reading speed was about 1.5 times faster than the 0.15 mm

dot height character reading speed. In contrast, no significant difference in reading speed between the two dot height characters was observed when the base material was fine paper. These results show that most subjects could read TRUCT Braille significantly faster when the base material was fine paper than that was laminated film.

Error rate (%): The two-way interaction of two parameters (base material and dot height) was found to be statistically significant ($F(1,11)=19.31, p<.001$). Fig 5 shows result of

error rate. From Fig 5, in the case of the 0.15 mm dot height characters, the error rate of laminate film was 11.8 %, and that of fine paper also was 3.1 %. In case of the 0.4 mm dot height characters, the error rate of laminate film was 5.4 %, and that of fine paper also was 2.6 %.

The error rate of fine paper for the 0.15 mm dot height characters was about one-fourth that of laminate film for them. The error rate of fine paper for the 0.4 mm dot height characters was about half that of laminate film for them. Regarding laminate film, the error rate of reading 0.4 mm dot height characters was about half that for reading 0.15 mm dot height characters. Regarding fine paper, there was no significant difference in error rate of reading between 0.4mm dot height characters and 0.15mm dot height characters.

These results show that most subjects could read TRUCT Braille significantly more correctly when the base material was fine paper than that was laminate film.

IV. DISCUSSIONS

The results of this experiment show that most subjects could read TRUCT Braille significantly more correctly and faster than when the base material was fine paper than that was laminate film. Especially, in the case of the 0.15 mm dot height characters, the reading speed of fine paper was about twice that of laminate film, and the error rate of fine paper was about one-fourth that of laminate film. And also, the coefficient of kinetic friction of fine paper was about one-fourth that of laminate film. An interpretation of our results could be that the signal for identifying each dot is not easy to be transmitted in case of base material with high coefficient of kinetic friction, because the noise due to the friction between the base material and the forefinger's skin is larger than signal for identifying each dot. In practice, most subjects claimed that it was difficult to read TRUCT Braille printed on laminate film because their forefingers could not slide easily due to the friction.

Regarding the difference of readability of between 0.15mm dot height characters and 0.4mm dot height characters, in case of laminate film, the 0.4 mm dot height character reading speed was about 1.5 times faster than the 0.15 mm dot height character reading speed. And also, the error rate of reading 0.4 mm dot height characters was about half that of reading 0.15 mm dot height characters. We found that dot height may influence on the readability of TRUCT Braille printed on laminate film. In case of fine paper, no significant differences in both reading speed and error rate between the two dot height characters were observed. It was found that dot height may not influence on the readability of TRUCT Braille printed on fine paper.

From these results, we found that base material influences on TRUCT Braille reading. And also, a lot of friction may obstruct the movement of the forefinger, and so the forefinger may fail to receive sufficient stimuli from the dots to be able to read them.

V. CONCLUSIONS

In this study, we conducted an experiment to compare the readability of TRUCT Braille printed on base materials that have different coefficient of kinetic friction. Twelve persons with acquired visual impairment who were learning to read Braille participated in our experiment. The results of this experiment show that most subjects could read TRUCT Braille significantly more correctly and faster than when the base material was fine paper than that was laminate film. We found that base material influences on TRUCT Braille reading. This knowledge will be very helpful data when printing makers choice the base material.

ACKNOWLEDGMENT

This research was partly supported by two Grant-in-Aids for Scientific Research from the Ministry of Education, Culture, Sports, Science and Technology of Japan (16300187, 18700478), and by the 21st Century Center of Excellence Program in Waseda University (The Innovative Research on Symbiosis Technologies for Human and Robots in the Elderly Dominated Society), Japan Society for the Promotion of Science.

REFERENCES

1. Tachibana, A., Matsutani, U. (2002). Braille text for Braille beginners with acquired visual impairment. Tokyo, Japan Braille Library
2. Kuroda H, Sasaki T, Nakano Y, Kizuka Y, Horigome Y (1995) The Effects of the Reading Efficiency in the Proportions of Braille, Proceedings of the 21st Sensory Substitution Symposium:55-58
3. Otake T, Chu Ting-Liang, Yonezawa Y, Chubachi N (1991) Analysis of Finger Movement during Braille Reading, The Transactions of the Institute of Electronics Information and Communication Engineers Series A, 1.74:1576-1586
4. Doi K, Odawara R, Hayashi M, Fujimoto H (2005) The Influence of the Patterns of Transparent-Resinous-Ultraviolet-Curing-Type Braille on Discriminability, Transactions of the Japan Society of Mechanical Engineers Series C, 70(699):300-305

Corresponding Author: Kouki Doi
 Institute: Faculty of System Design, Tokyo Metropolitan University
 Street: 6-6 Asahigaoka
 City: Hino, Tokyo
 Country: Japan
 Email: doi@sd.tmu.ac.jp

Functional evaluation of a micro-fabricated planar multielectrode probe for *in vivo* neuronal recording

D. Prodanov^{1,2}, M. Welkenhuysen^{1,2}, S. Musa¹, W. Eberle¹, T. Dresselaers³, U. Himmelreich³, C. Bartic^{1,4}, G. Borghs^{1,4}, B. Nuttin^{2,5}

¹Bioelectronic Systems group, IMEC, Leuven, Belgium

²Laboratory Experimental Functional Neurosurgery, Katholieke Universiteit Leuven (KULeuven), Leuven, Belgium

³Biomedical NMR unit/ Molecular Small Animal Imaging Center (MoSAIC), KULeuven, Leuven, Belgium

⁴Department of Physics and Astronomy, KULeuven, Leuven, Belgium

⁵Department of Neurosurgery, KULeuven, Leuven, Belgium

Abstract—Existing commercial Deep Brain Stimulation (DBS) systems are restricted by their limited electrical stimulation selectivity and open-loop approach. As a step towards a closed-loop clinical DBS system we develop silicon-based multielectrode neural probe arrays for *in vivo* selective neuronal recording and stimulation. This paper reports the fabrication and subsequent evaluation of a planar neural probe containing an array of 8 Pt contacts with diameters of 50 μ m. The probe was designed to provide Magnetic Resonance Imaging (MRI) compatibility. The recording selectivity of the probes was tested in acute electrophysiological experiments in the motor cortex of anesthetized rats (n=9). Obtained recordings of action potentials of single neurons demonstrated an acceptable level of interference with the brain function. The *in vivo* MRI compatibility of the probes was validated in a chronic implantation study in rats (n=3; 3 weeks follow-up). The animals did not show signs of pain or distress or other types of abnormal behavior. Obtained results demonstrate the usability of the neural probe both as a prototype of a medical device and as a research tool in fundamental neurophysiological studies.

Keywords—MRI, neurophysiology, multielectrode array, neural prosthesis, deep brain stimulation

I. INTRODUCTION

Electrical stimulation of the nervous system can be used to treat abnormal neural functions. Prominent examples of this approach are the Deep Brain Stimulation (DBS) for Parkinson's disease, dystonia and essential tremor (recent review in [1]). Promising results have been obtained also for other conditions, such as obsessive-compulsive disorder [2]. Contemporary systems for DBS use open-loop stimulation approaches employing a small number of large electrode contacts. This results in a very limited spatial selectivity of stimulation or recording. Due to the open-loop approach, the amount of stimulation can not be adjusted dynamically, which can lead to unwanted stimulation of surrounding brain structures and behavioral side effects. In contrast, development of DBS systems providing high spatial selec-

tivity of stimulation and closed-loop approach (recording-stimulation-recording) would be a major innovation in the clinical practice of DBS. The use of such devices could eventually reduce the occurrence of side effects and broaden current therapeutic options.

Despite its clinical efficacy, the mechanisms of action of DBS are still insufficiently studied and remain a subject of debating (review in [3]). Functional imaging approaches (e.g. functional magnetic resonance imaging) in this perspective, offer the possibility to monitor non-invasively distant brain regions and eventually unravel the neuronal circuits modulated by DBS.

As an initial step towards a closed-loop system combining stimulation and recording capabilities we develop micro-fabricated planar multielectrode probes for *in vivo* neuronal recording and stimulation. In a previous paper [4] we reported on the processing of a neural probe with Au-coated Ni contacts. As those were prone to corrosion resulting in

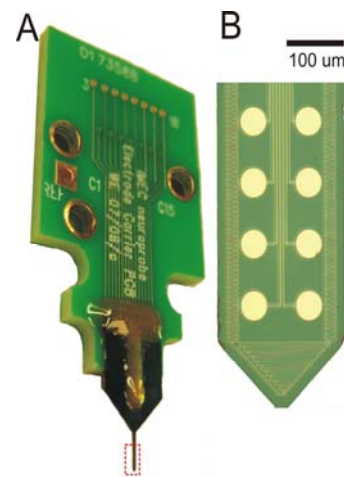


Fig. 1. The fabricated probe assembly. **A** – Photograph of the packaged neural probe. The microfabricated multielectrode array is attached to a printed circuit board (PCB). The probe tip is marked by a dashed rectangle. **B** – Photomicrograph of the probe tip. Contact sizes are 50 μ m.

limited lifespan both *in vitro* and *in vivo*, the electrode material was changed to *Pt*. The work reported here is focused on the optimization of the probe–nervous tissue interaction and the MRI–compatibility of the probe.

II. SUBJECTS, MATERIALS AND METHODS

A. Experimental subjects and Implantations

Reported *in vivo* experiments were approved by the animal ethics committee of the Catholic University of Leuven in accordance with the Belgian national and EU regulations for animal experimentation (Directive 86/609/EEC). Implantations ($n=5$ acute; $n=3$ chronic) were performed in the cortices of anesthetized rats in a stereotactic frame (1.0 mm posterior, 2.0 mm lateral of bregma). The implantation sites corresponded to the hind limb area motor representation. The rats were anesthetized with urethane (1.3 g/kg, i.p. $n=5$) or chloral hydrate (0.5 g/kg i.p. $n=7$). Cranial burr holes were drilled under microscopic control. After resection of *dura mater*, the probes were inserted in the cortex using a motorized micropositioner at a constant velocity of 10 $\mu\text{m/s}$ to the final depth of 1800 μm . In some acute experiments ($n=4$) the neural probes were dipped into methanol solution of the carbocyanine tracer substance DiI (Invitrogen, Carlsbad, CA, USA) to visualize the probe insertion track [5]. In the chronic implantation experiments the probes were fixed permanently to the skull by dental acrylic cement and non-magnetic bone-screws.

B. Recording procedures and MRI

The preparation was shielded with a Faraday cage. Neural activity was recorded with a LeadPoint system (Medtronic, Minneapolis, MN, USA; band-pass filtering 500–5000 Hz; digitization at 24 kHz) or with a Model 3000 AC/CD differential amplifier (A-M Systems Inc, Sequim, WA, USA; band-pass filtering 300 – 20000 Hz) and CED micro-1401 digitization unit (digitization at 20 kHz; Cambridge Electronic Design, Cambridge, UK).

To validate the MRI-compatibility of the probe, 3 animals were implanted with probes and scanned repeatedly before (3 days) and after (24 hrs, 4 days and 17 days) the implantations using a 9.4T small animal MRI scanner (Bruker, Billerica, MA, USA). The images were acquired using the following protocols: 3D T2w MRI (FLASH, 100 μm isotropic resolution, $T_E/T_R=12/150\text{ms}$), 3D Turbo RARE (150 μm isotropic resolution, $T_{E\text{eff}}/T_R/\text{RARE factor}=40/1000\text{ms}/16$), diffusion-weighted MRI and T2-maps (150 μm in plane resolution, 0.5mm slice thickness, $T_R=2500\text{ms}$, 10 echos of 10ms increments). To minimize movement artifacts, the animals were anesthetized with isoflurane and fixed in the coil for the duration of the image acquisition. After every scan one animal was sacrificed for histological investigation.

C. Probe fabrication

The probe fabrication was carried out on 8" silicon wafers using lift-off to define the electrode sites and metal interconnects. *Parylene C* was used as device insulation. The probe assembly is shown in Fig. 1. The electrochemical

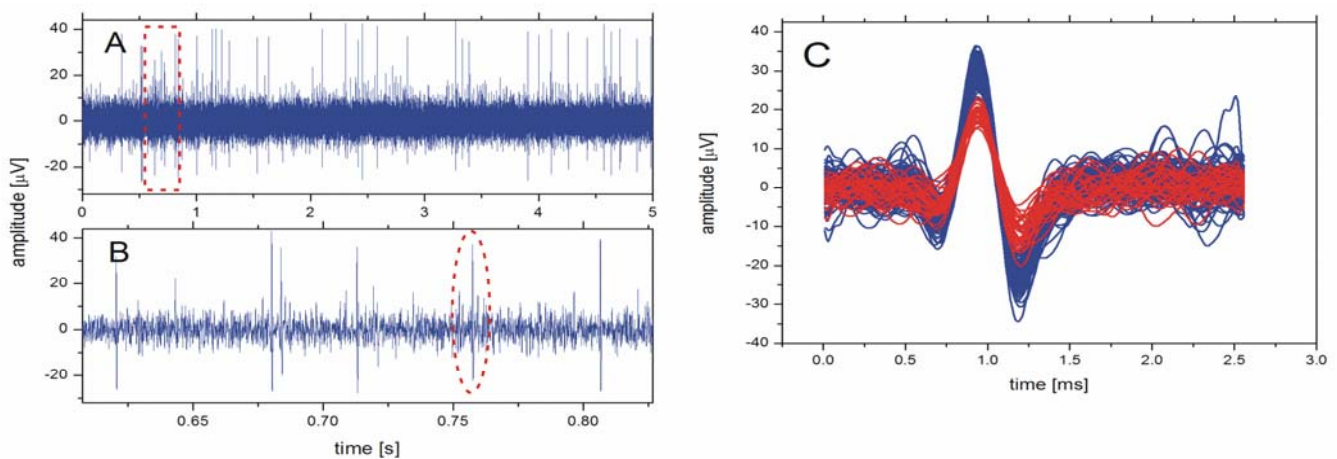


Fig. 2. *In vivo* cortical micro-recording. Representative cortical micro-recording traces performed by a probe with contact size of 50 μm . **A**, **B** – Two traces of band-pass-filtered raw signal (Leadpoint). **A** – 5s recording trace. Neuronal activity showed a regular pattern of ~ 5 Hz intermixed with occasional bursts. **B** – A magnified stripe (see insert in **A**). Nose level is $\sim 20 \mu\text{V}_{\text{pp}}$, while spike amplitudes are 35 – 65 μV_{pp} . One representative spike is outlined with an ellipse. **C** – Neuronal action potentials (spikes) automatically detected using the package Osort [6]. Two different spike waveforms are apparent.

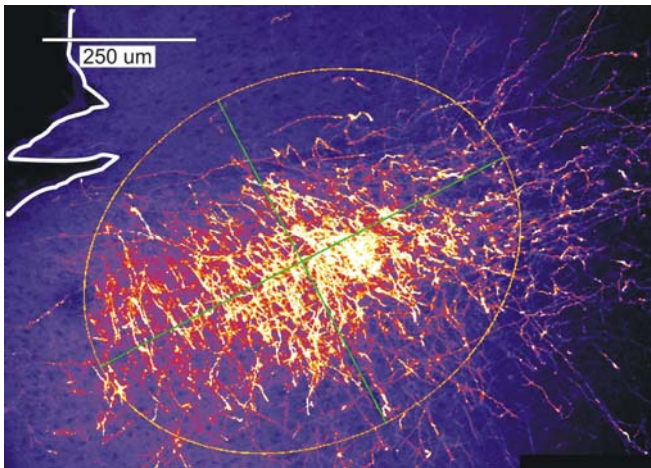


Fig. 3. Reconstruction of the probe insertion track. Composite confocal image of the probe insertion track. Brain tissue appears in shades of purple. Cut axons loaded with DiI (tracing substance) appear in shades of yellow. Orientation of the inserted probe corresponds to the orientation of the mass of injured axons. Principal axes of orientation of the image (green) and the equivalent ellipse of orientation are estimated automatically. Cortical surface border is enhanced by a hand-drawn line (white).

impedance of the contacts was measured in a phosphate-buffered (pH=7.4) 0.9% NaCl solution using a potentiostat combined with a frequency response analyzer (PGSTAT302N, EcoChemie, Utrecht, Netherlands), Ag/AgCl reference and Pt counter electrodes. The impedance at 1 kHz ranged between 200 and 300 kOhm.

D. Tissue processing and microscopy

The animals were euthanized by overdoses of Nembutal i.p. and subsequently perfused transcardially with water solutions of 10% sucrose followed by 4% formaldehyde. The brains were dissected and sectioned on vibratome at 150 μm thickness. The probe insertion tracks were visualized on a Zeiss confocal system at 10x magnification (excitation 543 nm).

III. RESULTS AND DISCUSSION

A. In vivo electrophysiological evaluation of the neural probe

Obtained results validate desired recording selectivity of the neural probe. The cortical activity could be recorded continuously during insertion, while the probe was advanced into the cortex. Representative cortical micro-recordings are presented in Fig. 2. The obtained signal to noise ratio was acceptable (approx. 3:1) and the brain activity was not masked by the noise. Observed spike patterns

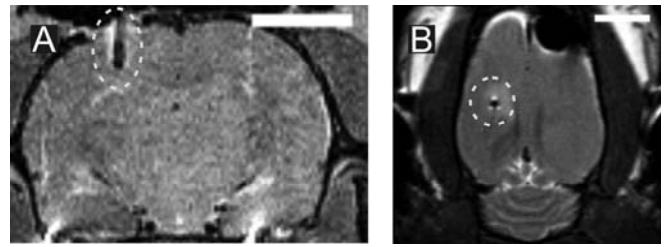


Fig. 4. MRI 24hrs after probe implantation. Implanted probe is represented by hypointensive shadows highlighted by hyperintensive edge (dashed ellipses). **A** – 3D Turbo RARE coronal projection. Probe shadows closely resemble the shape of the fabricated device. **B** – 3D T2* FLASH axial projection. The hyperintensive region around the implantation site indicates the presence of minimal post-operative brain edema. Scale bars – 5 mm.

corresponded to the frequency of the electroencephalographic theta-rhythm in the rat that can be observed during anesthesia (Fig. 2A,B). Therefore, the normal activity of the cortex was relatively undistorted. The action potentials coming from different neurons could be discriminated automatically (Fig. 2C).

B. Histological evaluation of the brain after micro-recording

In the context of an electrophysiological experiment, it is important to correlate observed activity with the neuronal cell distribution around the recording sites. The recording configuration, that is the orientation and final insertion depth of the neural probes, was verified histologically. The technique uses the property of DiI to diffuse passively along the lipid bi-layer of the cell membrane. The probe insertion track was reconstructed from the pattern of DiI deposits, which penetrated the axons cut by the probe during insertion (Fig. 2). The predominant orientation of the axonal mass could be calculated from the image moments¹.

C. MRI of the implanted probe

Contemporary metal DBS electrodes can potentially generate large artifacts in T2/T2*-weighted MRI. Therefore, providing MRI-compatible electrodes could offer a valuable research tool for studying mechanisms of DBS. The MRI-compatibility of the probe was validated *in vivo*. No harmful effects were observed for the duration of the experiments (n=6 scans for up to 17 days). The animals were active and did not show signs of distress or pain.

MRI could precisely demonstrate the position of the implants and the anatomy of the surrounding tissues. The

¹ D. Prodanov, 2008, <http://rsb.info.nih.gov/ij/plugins/image-moments.html>

presence of the probes inside the brain introduced only marginal image distortions (Fig. 3A). This was reflected by a relatively good agreement between the diameter of the probe shank (0.2 mm) with the MRI based determination (3D RARE 0.3mm; 3D FLASH 0.4mm). As expected, artifacts were larger in T2*-weighted MRI (FLASH). There were no signs of large acute hemorrhages or brain edema that may have been caused by the implantations (Fig. 3B). This corresponded well with the observed behavior.

IV. CONCLUSIONS AND OUTLOOK

In this paper we report the functional evaluation of a multielectrode neural probe array designed to provide both recording and stimulation modalities. Obtained single unit neuronal recordings validated the designed level of recording selectivity and demonstrated an acceptable level of interference with the brain function. The MRI compatibility of the probe was validated *in vivo*, which allows using MRI in combined electrophysiological experiments as a complementary non-invasive imaging modality. Taken together, the results demonstrate that the neural probe could be used both as a prototype of a medical device and as a research tool for fundamental neurophysiological studies.

Current implementation of the neural probe targets applications in the cortex. Employed fabrication approach is scalable also for testing of closed-loop stimulation approaches in DBS targets in the rat. Future use of the neural probe in chronic implantation experiments requires more studies on the chronic biocompatibility of the implant and the stability of the recording conditions to be performed.

ACKNOWLEDGMENT

Presented work has been supported in part by the Flemish Institute for Promotion of Innovation by Science and Technology, IWT (project "The Artificial Synapse" SBO-50151). M. Welkenhuysen is a doctoral fellow of IWT (project 61236). Authors would like to acknowledge Dr Danny Jans for help with the confocal microscopy.

REFERENCES

1. Benabid A.L. What the future holds for deep brain stimulation (2007) *Expert Rev Med Devices*, 4(6):895–903
2. Nuttin B, Cosyns P, Demeulemeester H et al. (1999) Electrical stimulation in anterior limbs of internal capsules in patients with obsessive-compulsive disorder. *Lancet*, 354(9189):1526.
3. McIntyre C, Savasta M, Walter B et al. How does deep brain stimulation work? Present understanding and future questions (2004) *J Clin Neurophysiol*, 21(1):40–50
4. Musa S, Welkenhuysen M, Huys R et al. Planar 2D-array neural probe for deep brain stimulation and recording (DBSR). In *Proceedings of the 4th European Conference of the International Federation for Medical and Biological Engineering*, vol. 22, pp. 2421–25, Antwerp, Belgium, 2008.
5. Blanche T, Spacek M, Hetke J et al. Polytrodes: high-density silicon electrode arrays for large-scale multiunit recording (2005) *J Neurophysiol*, 93(5):2987–3000
6. Rutishauser U, Schuman E, and Mamelak M (2006) Online detection and sorting of extracellularly recorded action potentials in human medial temporal lobe recordings, *in vivo*. *J Neurosci Methods*, 154(1-2):204–224.

Author: Dr. Dimiter Prodanov, MD, PhD
 Institute: IMEC vzw
 Street: Kapeldreef 75
 City: Leuven
 Country: Belgium
 Email: dimiter.prodanov@imec.be

Research on the Perceptual Size of Tactile Dots and Bars

Wataru Toyoda¹, Kouki Doi², Hiroshi Fujimoto³ and Tsutomu Wada⁴

¹ Graduate School of Human Sciences & Faculty of Science and Engineering, Waseda University, Saitama & Tokyo, Japan

² Division of Management Systems Engineering (Ergonomics), Faculty of System Design, Tokyo Metropolitan University, Tokyo, Japan

³ Faculty of Human Sciences, Waseda University, Saitama, Japan

⁴ Universal Design Laboratory, Japan Braille Library, Tokyo, Japan

Abstract—Many countries today have rapidly aging populations, and so it becomes increasingly important that standards developers design consumer products that address the accessibility needs of older persons as well as persons with disabilities. The Japanese Standards Association is presently forming several exploratory committees to address the standardization of accessible design. In 2000, Japan enacted a standard (Japanese Industrial Standard, JIS S 0011) regulating the perceptual sizes of tactile dots and bars for use in consumer products. However, these regulations were not based on highly reliable data. Therefore, objective and quantitative data for perceptual sizes of tactile dots and bars is required for revising this JIS and for devising other standards. In this study, we examine the objectively appropriate perceptual sizes for tactile dots and bars. We determine the optimal size for the tactile dot on a cellular-phone button and the optimal relative size and shape that enable a tactile dot and bar to be distinguished from one another.

Keywords—Tactile Dots, Tactile Bars, Customer Products, Cellular Phone, Operability

I. INTRODUCTION

In 2000, “Guidelines for all people including elderly and people with disabilities—Making tactile dots on consumer products” (Japanese Industrial Standard, JIS S 0011) was enacted in Japan. This standard specifies guidelines for the design of tactile dots and bars used on consumer products to improve accessibility for all people, including older persons and persons with disabilities. Tactile dots (dot-shaped tactile symbols) and tactile bars (bar-shaped tactile symbols) are applied to manually operated product keys for two purposes: to provide location information for other functions on the device, and to identify control functions. On the basis of the above JIS, discussion has arisen concerning the creation of international standards for tactile dots and bars. However, the perceptual sizes of the dots and bars recommended in the JIS were not based on objective and quantitative data. Therefore, research on perceptual sizes is required for revision of the JIS and creation of other, including international, standards. In this study, we conduct two experiments to determine the objectively appropriate perceptual size of tactile dots and bars.

Table 1. Tactile dot size conditions

height (mm)	0.0 (without tactile dot), 0.1, 0.3, 0.5, 0.7

II. EXPERIMENT 1

The tactile dot on button 5 of a cellular phone aids sighted and especially visually impaired users. In Experiment 1, we investigated the influence of the height of the dot on the operational performance of a cellular phone.

Procedure

Subject participants included 20 sighted younger (mean age 21.6 years, SD = 1.5 years) and elderly (mean age 67.5 years, SD = 4.0 years) persons. All were without injury, disease, or dermatosis and all used a cellular phone on a regular basis and comprehended the array of the operating panel.

Experimental equipment included mock-ups of cellular phones (Fig. 1). Tactile dots of 5 different heights (0.0, 0.1, 0.3, 0.5, and 0.7 mm) were produced by screen-printing on button 5 of each mock-up using a resinous ink cured with ultraviolet radiation (Table. 1). Participants were blindfolded and asked to operate each phone 4 times at each of the 5 different heights for a total of 20 trials, requiring approximately 2 hours. Practice trials were conducted before starting the experiment.

Participants were asked to push cellular-phone buttons with the thumb of their dominant hand while looking at 50 randomly ordered Arabic numbers one at a time. They were then asked to assess the following using a 5-point scale: sureness of input operation, and pain when pushing button 5 (Table 2).

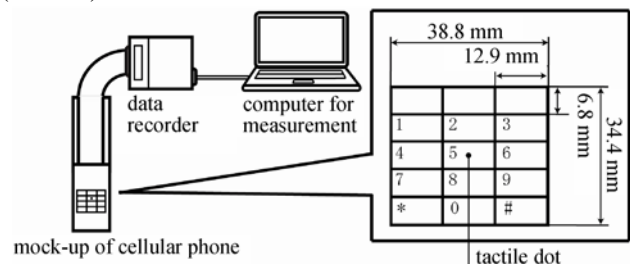


Figure 1. Experimental equipment for evaluating the operability of cellular phone using cellular phone mock-ups

Table 2. Scale of subjective assessment

(1) Sureness of input operation	1, not sure ; 5, very sure
(2) Pain when pushing button 5	1, not painful ; 5, very painful

Results & Discussion

The average time of operation, error rate, sureness of input operation, and pain when pushing button 5 are shown in Figs. 2(a), 2(b), 2(c), and 2(d). In each case, the results were analyzed statically using one factor—the tactile dot height—between the groups and employing analysis of variance (ANOVA).

Overall, the younger group performed much faster and more accurately than the elderly group. Both groups performed better with a tactile dot than without it. In particular, with a dot of height 0.3 mm, both groups performed significantly faster, more accurately, and more confidently with than without a dot. However, with a dot height of 0.7 mm, participants felt significant pain. We therefore determined that a dot height of 0.3 mm improves the operability of a cellular phone and is suitable for localizing the relative position of a button. A dot height of 0.7 mm is unsuitable for both younger and elderly persons.

III. EXPERIMENT 2

In Experiment 2, we examined how the size of tactile dots and bars influence their identification.

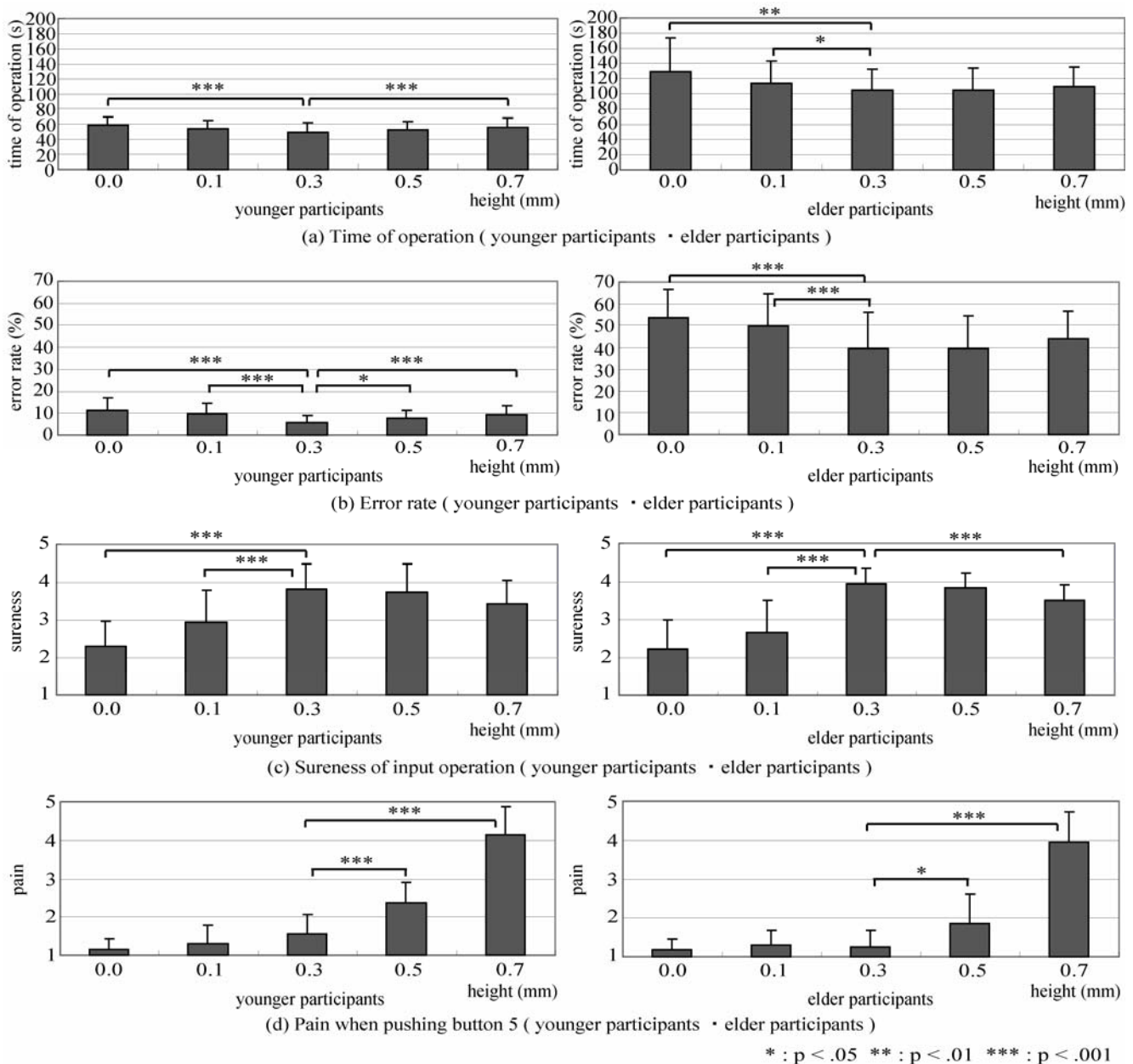


Figure 2. Result of experiment 1: (a) time of operation, (b) error rate, (c) sureness of input operation, (d) pain when pushing button 5

Procedure

Subject participants included 20 sighted younger (mean age 20.8 years, SD = 1.8 years) and elderly (mean age 63.9 years, SD = 3.0 years) persons. Sighted participants were used in order to eliminate any effect of tactile texture experience.

Experimental equipment included test pieces of different sizes, including 30 conditions of width and length (Table 3 and Fig. 3). The various combinations yielded 5 tactile dot conditions and 25 tactile bar conditions. Participants were blindfolded, presented with test pieces one at a time in random order, and asked to state whether what they had touched was a dot or a bar. Each dot condition was presented 15 times and each bar condition was presented 3 times in order to eliminate any order effect. Thus a total of 150 trials were performed (5 dot conditions × 15 times and 25 bar conditions × 3 times), requiring approximately 2 hours. Practice trials were conducted before starting the experiment.

Results & Discussion

Tactile bar conditions

The average discrimination time and accuracy rate are shown in Figs. 4(a) and 4(b). In each case, the results were analyzed statically using two factors—the width and the length of the tactile bar—between the groups and employing ANOVA.

Discrimination time: The longer the length of a tactile bar, the faster each group could distinguish the bar from a dot. Among adjacent group conditions, a significant difference was observed between +2.0 mm and +3.0 mm ($p < .001$) for each group. However, no significant difference was observed between +3.0 mm and +4.0 mm. Thus, participants could identify tactile bars significantly faster when lengths were larger than +3.0 mm.

Accuracy rate: The longer the length of a tactile bar, the more accurately each group could distinguish the bar from a dot. Among adjacent conditions, a significant difference was observed between +1.0 mm and +2.0 mm ($p < .001$) for each group. However, no significant difference was observed between +2.0, +3.0, and +4.0 mm. Thus, participants could identify tactile bars significantly more accurately when lengths were larger than +2.0 mm.

In summary, we found that most subjects could distinguish tactile bars of more than +3.0 mm length from tactile dots with significant speed and accuracy. The width of the bar had no influence. These data indicate that, to be easily distinguishable, a tactile bar should be 3.0 mm longer in length than in width. However, the conditions of tactile bars used in this experiment were very limited. Further experiments are needed to examine the influence on distinguishability of other conditions such as height, cross-sectional shape, and texture.

Table 3. Tactile symbol size conditions

width (mm)	0.5, 0.8, 1.0, 1.5, 2.0
length (mm)	+ 0.0, + 0.5, + 1.0, + 2.0, + 3.0, + 4.0 (The actual length is the size that adds each width to each condition mentioned above.)
height (mm)	0.5

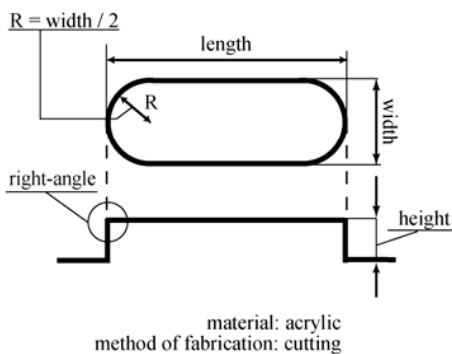
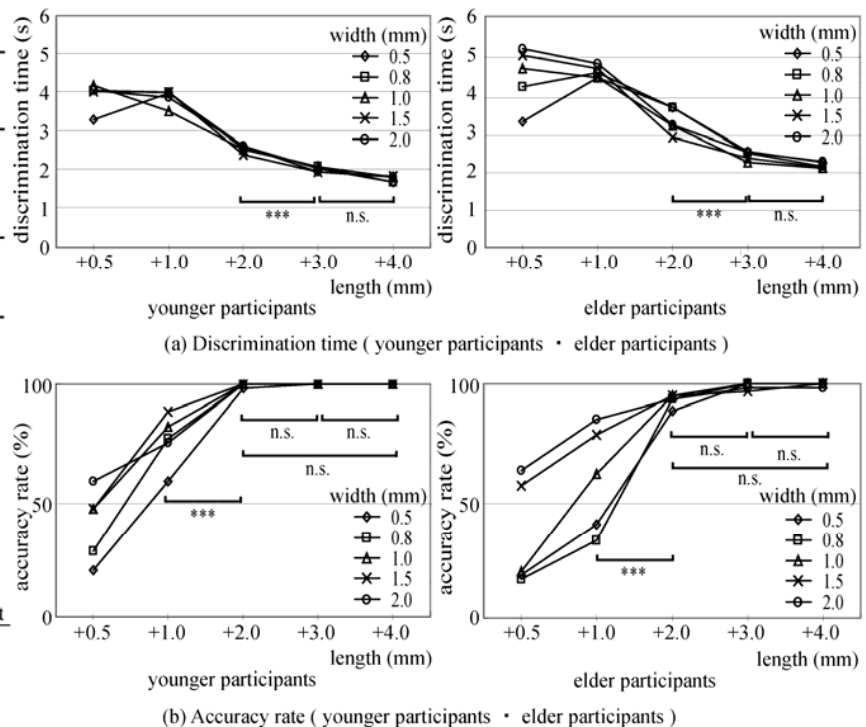


Figure 3. Tactile bars used in experiment 2.



* : $p < .05$ ** : $p < .01$ *** : $p < .001$ n.s. : no significant

Figure 4. Result of experiment 2 regarding tactile bars: (a) discrimination time, (b) accuracy rate

Tactile dot conditions

The average discrimination time and accuracy rate are shown in Figs. 5(a) and 5(b). In each case, the results were analyzed statically using one factor—the diameter of the tactile dot—between the groups and employing ANOVA. The average discrimination time was also measured.

Discrimination time: The smaller the size of a tactile dot, the faster each group could distinguish the dot from a bar. Among adjacent conditions, a significant difference was observed between 0.5 mm and 2.0 mm ($p < .001$) for each group. Thus, participants could distinguish between tactile bars and dots faster when the diameter of the dot was 0.5 mm.

Accuracy rate: The smaller the size of a tactile dot, the more accurately each group could distinguish the dot from a bar. Among adjacent conditions, a significant difference was observed between 0.5 mm and 2.0 mm for each group (the younger group: $p < .05$, the elder group: $p < .001$). Thus, participants could distinguish between tactile bars and dots more accurately when the diameter of the dot was 0.5 mm.

In summary, we found that most subjects could distinguish between tactile bars and dots with significant speed and accuracy when the dots were smaller and markedly different in size from the length of the bar. These results indicate that when tactile dots and bars are used in combination on a customer product, a smaller dot is more suitable.

V. CONCLUSIONS

We conducted experiments to determine the objectively appropriate perceptual sizes for tactile dots and bars. We determined the optimal size for the tactile dot on a cellular-phone button. We also determined the optimal relative size and shape that enable a tactile dot and bar to be distinguished from one another. This knowledge will be helpful when JIS S 0011 is revised and other standards are created.

ACKNOWLEDGMENT

This research was partly supported by a Grant-in-Aid for Scientific Research from the Ministry of Education, Culture, Sports, Science and Technology of Japan (19300205).

REFERENCES

1. JIS S 0011 (Guidelines for all people including elderly and people with disabilities—Making tactile dots on consumer products) (2000) Japanese Standards Association

Address of the corresponding author:

Author: Wataru Toyoda
 Institute: Faculty of Human Sciences, Waseda University, Saitama, Japan
 Street: 2-579-15 Mikajima Tokorozawa, Saitama Pref. 359-1192
 City: Tokorozawa
 Country: Japan
 Email: wataru_toyoda@toki.waseda.jp

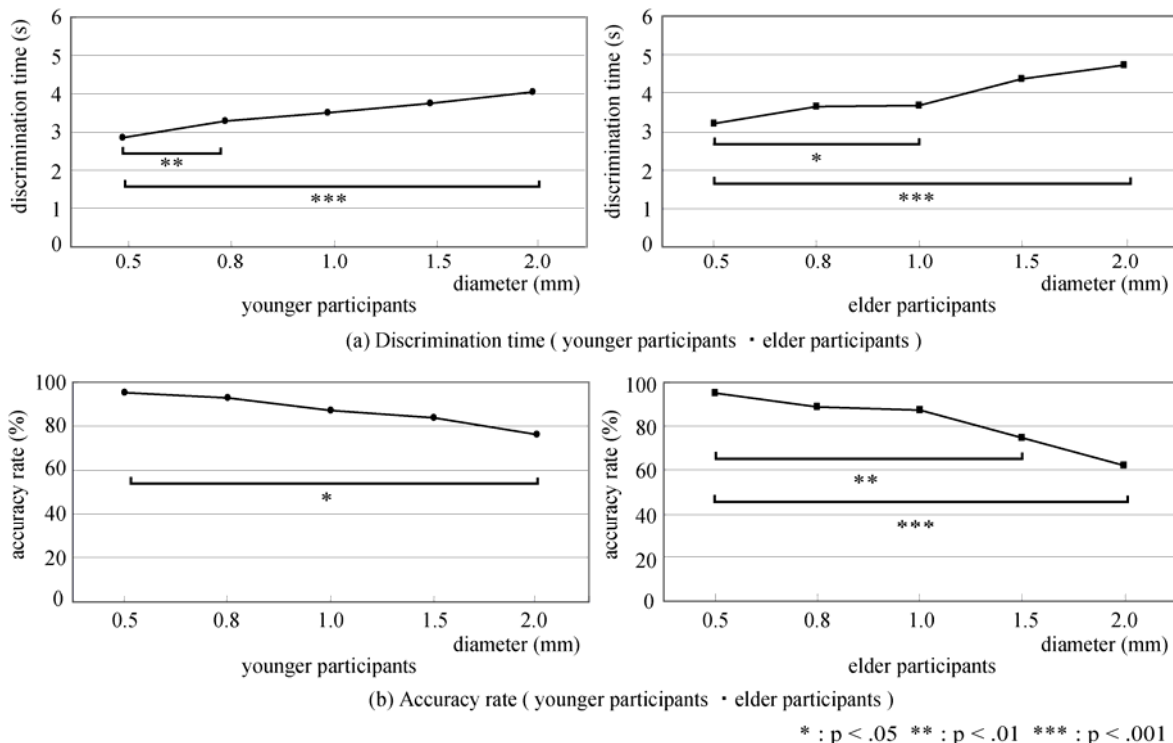


Figure 5. Result of experiment 2 regarding tactile dots: (a) discrimination time, (b) accuracy rate

A Consideration of the Expanded Partial Differential Equations and the Compartment System as the Background of the ABR System

Masahiro Aruga¹, Kiyotaka Takagi², Sinwu Liu³, and Shuichi Kato⁴

¹ Tokai University / Department of Human and Information Science, School of Information Science and Technology
Kitakaname 1117, Hiratsuka-shi, Knagawa-ken, 259-1292 Japan

² Tokai University / Graduate school of Engineering, Kitakaname 1117, Hiratsuka-shi, Knagawa-ken, 259-1292 Japan

³ Tokai University / Research Student, school of Engineering, Kitakaname 1117, Hiratsuka-shi, Knagawa-ken, 259-1292 Japan

⁴ Teikyo Heisei University / Graduate school of informatics, Aza-Otani 2289-23, Uruido, Ichihara-shi, Chiba-ken, 290-01 Japan

Abstract— It is well known that the characteristics of ABR (Auditory Brainstem Responses) have been used widely on many fields, and especially they have been adapted on the medical and clinical fields. For examples their characters are discussed on the fields of inspection of some consciousness levels etc. But the characters of the ABR detail system, especially with regard to their background theories are not sufficiently discussed. And the ABR characteristics derived directly from the experiment data are not sufficiently analyzed too. Therefore the theories of the ABR system and the detail model derived from the experiments must be made to be developed. Especially in order to analyze the ABR system the fundamental background theory and its expanded consideration must be preformed more widely. In this paper, firstly the fundamental partial differential equations are discussed and the consideration of the relation between their fundamental differential equation formulas and their experimental formulas is described. And secondly the meaning of characters among the partial deferential equations is considered and using the estimated improvement method the expanded partial differential equations is derived and proposed as a kind of more generalized formula of the fundamental characters. Especially the high order partial differential equations are considered and the characteristics of the ABR system are discussed considering the compartment system model. And thirdly an analysis method to use the synthesis technique of compartment system by an inverse procedure of a solution of such ABR differential equation models is described. And finally the conclusion and further works are described.

Keywords— the ABR, partial differential equations, compartment system.

I. INTRODUCTION

The ABR (Auditory Brainstem Responses) are the auditory evoked responses which appear as electric potential waveforms. Those responses are induced by sound stimulus from the external ear, and make their specific wave patterns of electric potential. And it is well known for them to have the amplitudes under 1 μ V and the latencies within 10ms from the acoustic stimulus. The whole wave pattern of the

ABR is mainly synthesized by 7 fundamental wave patterns. Now the sources to generate them are about specified, and they are understood to be on the nervous groups along the process of the reaction. But the detail generating mechanism of them are not sufficiently made to be clear yet. From the practical view point, the qualitative ABR characters are now applied for clinical and medical inspection because of their many useful elements. However, although since the first papers of the ABR by Sohmer (1967) and Jewett (1970) were presented many reports of the ABR have been presented until now, the detail of many ABR characteristics and systems is not sufficiently analyzed even today. Therefore the discussion of the ABR system is needed more radically, especially considering many models to reflect such characters. [1]-[4] During authors' having studied such subjects some background theories of the ABR characteristics have been obtained and partly have been analyzed. On such considerations the 5th wave form of ABR has especially been concentrated upon in order to discuss the quantitative characters of the ABR because its data can be recorded comparatively clearly. As a result some differential equation formulas about the latency characters of the 5th wave form have been derived and discussed. In this paper, firstly, a fundamental partial differential equation model of the latency character of the 5th wave of ABR is considered and at the same time an experimental formula of it is derived. Secondly considering the experimental formulas and the solution of the fundamental partial differential equation a meaning of approximation method of the latency character of the 5th wave is proposed. Thirdly as a practical experimental formula the expanded formula is proposed and its approximation meaning is conformed by investigating an example set of parameters of the transformed formula. As a same consideration an expanded partial differential equation formula of the characters of the 5th wave form is discussed and the expanded experimental formula is discussed with regard to the expanded partial differential equation. And it is estimated that such general partial differential equations inherit the fundamental characters of the ABR latency. Furthermore, on the basis of such approximating and ana-

lyzing method an inverse method for synthesizing the ABR system by using the electric circuit theory and some electronic elements and the compartment system theory and its characteristics is described in order to analyze the ABR system more radically and more practically. Finally some conclusions and further works are presented. There the necessity of development of some methods to analyze the ABR system more radically and clearly on the basis of such deriving results is described.

II. AN EXPERIMENTAL FORMULA AND THE FUNDAMENTAL PARTIAL DIFFERENTIAL EQUATION FORMULA

A. The outline of experiment and its backgrounds

As the 5th or the 4-5th wave forms of the whole ABR wave pattern is specified clearly they have been used as an audiometric index. For example, the differences in hearing disorders show the different tendencies in latency characteristics to be responded to the input stimulus. Especially as the 5th wave is clear it is useful that the 5th wave is selected for discussing its characters. In this paper, the latency characters of the 5th wave is considered. The experiment was performed with the acoustic click stimuli to vary the three parameters of click stimuli, that is; intensity, duration, and interval (the reciprocal is called stimulus rate or frequency). And the stimulus parameters are adapted within some practical ranges. The outline of this experiments is as the following. In this experiments the data were taken from thirty adult males, ranging in age from 18 to 22 years, with neither hearing nor neurological complaints. The input click stimulus was used within some practical ranges of the latency character, and its intensity was changed from 30 dB nHL to 90 dB nHL by 10 dB nHL. Here nHL is normal hearing level. Four levels of duration were used within some practical ranges; Namely, 0.1, 0.3, 0.5, 1.0 ms. And as the latency of the 5th wave is well known to be varied under 80 Hz the frequencies (the reciprocal of interval) were selected at 20, 40, 60, 80 Hz. Average counts were 2000 times, as the electrodes (Ag-AgCl) there were used disk electrodes for an electroencephalograph. The potential was recorded as a unipolar recording between an active electrode placed on vertex (Cz) and the reference electrodes placed on both earlobes (A1,A2) to be shorted electrically. The frontal (Fpz) was connected to the ground and both ears were stimulated. Low cut filter was set at 100 Hz and High cut filter at 5 KHz. Headphone was well as the acoustic device for the click stimulus. Responses were recorded by Neuropack Four Mini (of Nihon Koden Co.Ltd.). As a result, Fig.1, Fig.2 were obtained.

B. The fundamental experimental formulas and the fundamental partial differential equation

From the experimental results Fig.1 and Fig.2 are obtained, and an experimental formula has been derived with regard to the changing peak latency character of the 5th wave.

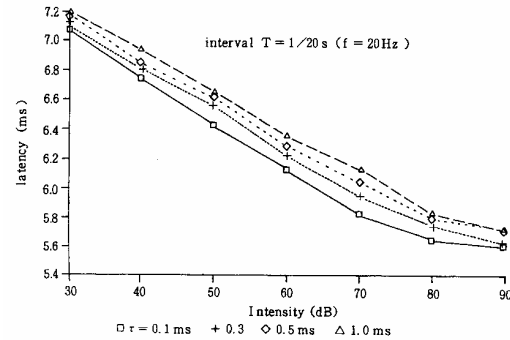


Fig. 1 Intensity-Latency curve (parameter; τ)

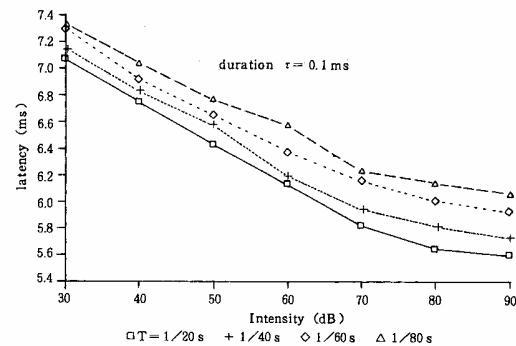


Fig. 2 Intensity-Latency curve (parameter; T)

And according as the acoustic stimulus parameters of ABR change the latency character changes, and the following two experimental formulas are derived.

That is;

$$y = K_0 \exp(-K_1 x T) \quad \tau = \text{const} \tag{1}$$

$$y = K_2 \exp \{-K_3 (x - a) / \tau\} \quad T = \text{const} \tag{2}$$

Here, y is the peak latency, x is the intensity, τ is the duration, the interval is T, and K_0, K_1, K_2, K_3 are positive constant numbers. The formulas (1), (2) are such formulas as their one parameter is constant, therefore from such formulas a new function to have three parameters is derived like formula (3). Here, α, β are constants and the formula

$$y = f(x, \tau, T) = y_0 \exp \{\alpha(\beta - x/\tau)T\} \tag{3}$$

is proposed as an fundamental experimental formula. And the practical values of these parameters are derived by the approximation method which is called the Taylor Series

Method. As a result a practical example of the optimum parameter values (detail is omitted) has been obtained as $\alpha=9.058000 \times 10^{-3}$, $\beta=7.639656$

Here, $T=0.05$ [ms], $\tau=0.1$ [ms].

On the other hand, from natural analogical character the fundamental partial differential equation form (5) is derived. And the experimental formula (3) is shown to satisfy it as a solution.

$$Ay \frac{\partial y}{\partial x} + By \frac{\partial y}{\partial \tau} + C \frac{\partial y}{\partial x} \frac{\partial y}{\partial T} = 0 \quad (4)$$

Furthermore, though making α , β constants the formula (3) satisfies the equation (4) as a solution, the factor β is treated as the function; $\beta = \beta(x, \tau, T)$ in order to analyze the character of the ABR system more radically. [1]-[4]

III. THE EXPANDED EXPERIMENTAL FORMULA AND THE EXPANDED PARTIAL DIFFERENTIAL EQUATION FORMULA AND THE INVERSE SYNTHESIZING METHOD CONSIDERING THE COMPARTMENT SYSTEM THEORY

Considering that α is constant and the compensable term $\beta = \beta(x, \tau, T)$ an expanded formula from the formula (3) is derived as the following.

$$\beta = \beta(x, \tau, T) = C_1 \tau/T + C_2 x/T + C_3 x + C_4 x/\tau \quad (5)$$

As $C_4=C_4-1$, the following expanded formula is obtained.

$$y = y_0 \exp(C_1 \tau + C_2 x + C_3 xT + C_4 xT/\tau) \quad (6)$$

Then with regard to this formula (6) a practical example of coefficients has already been obtained on the practical ranges.

$$\begin{aligned} y_0 &= 8.08 \text{ (ms)} \\ C_1 &= 3.46 \times 10^{-3} \text{ (ms)}^{-1} \\ C_2 &= -3.24 \times 10^{-3} \text{ (dB nHL)}^{-1} \\ C_3 &= -2.68 \times 10^{-3} \text{ (ms.dB nHL)}^{-1} \\ C_4 &= 1.02 \times 10^{-7} \text{ (dB nHL)}^{-1} \end{aligned}$$

Here the detail calculation is omitted. But this practical values show that the expanded experimental formula (6) is derived from the fundamental formula (3) as a properly approximated formula because of the following reasons. That is;

Here the practical experiment parameters are set within the following ranges.

$$\begin{aligned} 0.1 \leq \tau \leq 1.0 \text{ (ms)} \quad 12.5 \leq T \leq 50 \text{ (ms)} \quad 30 \leq X \leq 90 \text{ (dB nHL)} \end{aligned}$$

Therefore, the values $C_3 : C_4/\tau$ are derived as following. From above parameters, $375 \leq XT \leq 4500$ (ms dB nHL) is obtained and the influence of τ appears for the latency mainly, From $0.1 \leq \tau \leq 1.0$ (ms)

$$C_3 + C_4/1.0 \leq C_3 + C_4/\tau \leq C_3 + C_4/0.1$$

$-266.98 \times 10^{-7} \leq (-268 + 1.02/\tau) \times 10^{-7} \leq -257.8 \times 10^{-7}$ and $3.46 \times 10^{-3} \leq C_1 \tau \leq 3.46 \times 10^{-2}$ and the order of XT is $10^2 \sim 10^3$, even the highest of the influence of C_4 is the order of 10^{-3} . This is the lowest order of the term of C_1 and is counterbalanced on calculation. Other terms have one figure higher orders and their influences are able to be understood by discussion of flowing reasons. Considering that C_3 is 10^{-5} order and C_4/τ at most is 10^{-6} order, from the above parameter and coefficient values the order ratio $C_3 : C_4/\tau : 10 : 1$ is obtained. Therefore, it is possible that the experimental formula's tendency is examined from a simple calculation of orders without calculation of real coefficient values. Namely to set $z_1=1, z_2=10^{-1}$ and examine

$$e^{z_2}/e^{z_1} \approx 1.1/e$$

is obtained. This means that the influence of the term of latency tendency C_4/τ is almost negligible, rather it has a meaning of a compensating term calculating the whole tendency of experimental formula. As a result the expanded experiment formula (6) above described has not only a proper meaning, but also in such coefficients the characters involved in the fundamental formula (3) can be shown to be inherited in this expanded formula. Furthermore, this expanded formula satisfies (calculation is omitted) the following partial differential equation (8) expanded from the fundamental differential equation (4). This partial differential equation (8) is derived as the general expanded differential equation form considering the compensable terms as the function of stimulating parameters. And this equation (8) inherits the characteristics of the fundamental equation (4).

As a result it is estimated that such a method as transform constants into the functions of stimulating parameters gives some directions to take the method by which the ABR system is able to be analyzed more radically, and with which the more practical experimental formulas are able to be derived. Therefore as one expanded pattern, the partial differential equation more expanded generally from the formula (4) is derived as following. This formula (7) is expanded on the formula of first order differential equation from the partial differential equation (4). That is;

$$\begin{aligned} &(A_1 \frac{\partial y}{\partial x} + A_2 \frac{\partial y}{\partial \tau} + A_3 \frac{\partial y}{\partial T})y \\ &+ B_1 \frac{\partial y}{\partial x} \frac{\partial y}{\partial \tau} + B_2 \frac{\partial y}{\partial \tau} \frac{\partial y}{\partial T} + B_3 \frac{\partial y}{\partial T} \frac{\partial y}{\partial x} + Cy^2 = 0 \end{aligned} \quad (7)$$

Here, $A_i = A_i(x, \tau, T)$, $B_i = B_i(x, \tau, T)$, $C = C(x, \tau, T)$.

And furthermore using such expanded method, as other expanded pattern, an expanded partial differential equation by the high order derived function is formed as the formula (8). This equation (8) contains not only above mentioned

characteristics of the ABR but also another characters, especially it inherits the characters of the ABR for the high order derived function to have.

$$A \frac{\partial^2}{\partial \tau^2} \left(\frac{1}{y} \cdot \frac{\partial y}{\partial \tau} \right) + B \frac{\partial}{\partial \tau} \left(\frac{1}{y} \cdot \frac{\partial y}{\partial x} \right) \times C \frac{\partial}{\partial \tau} \left(\frac{1}{y} \cdot \frac{\partial y}{\partial T} \right) = 0 \quad (8)$$

Here, A , B , C are the coefficients which are able to be the functions of the ABR parameters. Furthermore, as the inverse synthesis algorithm considered from the above description is useful to understand the ABR system the inverse synthesis method to make the ABR system clear is discussed. And then, the consideration of synthesis algorithm is firstly performed on some assumptions. The detail of them is omitted here, and will be presented in other papers. As a result, when the parameter vector is P , the 5th wave of the ABR as time function can be put as $m(t, P)$, Now when the Laplace Transform of $m(t, P)$ is presented as $M(s, P)$, it means a kind of impulse response. Or if the input time function is $\text{inp}(t) = x \{U(t) - U(t - \tau)\}$,

$$L[\text{inp}(t, P)] = L[x \{U(t) - U(t - \tau)\}] = x(1 - e^{-\tau s})(1/s) \\ = \text{INP}(s, P), \text{ (is presented in a sign)}$$

is obtained. Therefore the system function of the ABR character; $H(s) = M(s, P) / \text{INP}(s, P)$ is presented. Here as the characters of the ABR system can be understood by this $H(s)$, it is very important to find the Laplace Transform $M(s, P)$ and the inverse Laplace Transform $m(t, P)$. Now, if the $m(t, P)$ is approximately $m_a(t, P)$ near the peak point, the following relations are formed.

$$m_a(t, P) = A(P) e^{-\{t - \rho(P)\}^2}$$

$$\rho(P) = y_0 \exp\left(\alpha \left(\beta - \frac{x}{\tau}\right) T\right)$$

$$\rho(P) = y_0 \exp(C_1 \tau + C_2 x + C_3 xT + C_4 xT/\tau)$$

From such an approximate example and the direct synthesis of equivalent circuits about these differential equations it is estimated that the ABR system characters are able to be understood more radically. And at the same time the compartment system theory is considered in parallel in order to synthesize the background system of the ABR derivation. Then along the formula (7) and (8) and from some assumptions above described, for instance the formula $H(s) = M(s, P) / \text{INP}(s, P)$ is expanded into the compartment system forms. In general the compartment system is formed in the formula of the state variable vectors and their differential equations as following forms. That is; Ordinary compartment system is expressed with a transfer matrix A and the state variable vector x and Bu is controllable term and t is time.

$$d x / dt = A x \quad \text{or} \quad d x / dt = A x + B u$$

But here, not only this forms are discussed in order to analyze the ABR background mechanism by the use of expansion of the compartment system, but also this forms are needed to be transformed for the analysis of the ABR background mechanism. And for instance, the transformation function $H(s) = M(s, P) / \text{INP}(s, P)$ is needed to be expanded into such transformed differential forms of the compartment system for the same analysis. As a result it is estimated for the background mechanism that the above described partial differential equations show potentially to be analyzed from such techniques as the use of circuit theory and the use of compartment system theory. [1]-[4]

IV. CONCLUSION AND FURTHER WORKS

From a fundamental experimental formula and a fundamental differential equation the expanded formulas were derived and the method by which the characters of the ABR are analyzed more radically was obtained. And the inverse method was presented to do so. After this the concrete analysis method of the ABR system is needed to be developed by such method involving the compartment system.

ACKNOWLEDGMENT

We appreciate Dr. Masao SAITO of an honorary professor of University of Tokyo.

REFERENCES

1. H. Sohmer and Feinbesser (1967) Cochlear action potentials recorded from the external ear in man. *Ann. Otol*, 76:427-436.
2. D.L. Jewett, M.L. Romano and J.S. Williston (1970) Human auditory evoked potentials possible brainstem components detected on the scalp. *Science*, N.Y., 167:1517-1518
3. Masahiro Aruga, et.al (2005) A Consideration of the Characteristics of ABR on the basis of a Differential Equation Model and the Estimation of Parameters of Its Solution. 27th Annual International Conference of the IEEE Engineering in Medicine and Biology Society (EMBC'05), 6.6.2-10, No.2174.
4. MASAHIRO Aruga (2007) The compartment system taking account of fussy concept. Japan Ergonomics Society 15th System Conference, CD-ROM.

Author: ¹Masahiro Aruga, ¹Kiyotaka Takagi, ¹Shinwu Liu, ²Shuichi Kato

Institute: ¹Tokai University, ²Teikyo Heisei University

Street: ¹Kitakaname 1117, ²Aza-Otani 2289-23, Uruido

City: ¹Hiratsuka-shi, Knagawa-ken, ²Ichihara-shi, Chiba-ken

Country: ^{1,2}Japan

Email: ¹aruga@keyaki.cc.u-tokai.ac.jp

Development of the Gait Training System Controlled by Pressure Feed-back

Y. Shibata¹, M. Takagi¹, T. Miyoshi² and S. Yamamoto¹

¹ Graduate School of Engineering, Shibaura Institute of Technology, Saitama, Japan

² Welfare of Engineering, Iwate University, Iwate, Japan

Abstract— The purpose of this study is to develop a gait training system for elderly and disabled people. The developed gait training system comprises a long-leg brace with trunk support and is driven by pneumatic Mckibben actuators. The gait training system developed in our previous study was controlled by an open-loop circuit. In this study, we attempted to develop a feedback control system which referred difference between inner pressures of actuators set up in an antagonistic arrangement. This system, however, was unable to represent completely natural human walking because the feedback parameter did not include hip and knee joint angle information. We then used a control method wherein the difference between the inner pressures of the agonistic and antagonistic Mckibben actuators was used as the input data and a proportional directional control valve was used to simultaneously activate the actuators. This control method increased the stiffness of the hip and knee joints of the orthosis. Thus, we successfully developed an inner pressure difference control system to drive a gait training system.

Keywords— Gait training, Mckibben actuator, pressure feedback control, agonist and antagonist.

I. INTRODUCTION

Patients bedridden as a result of aging, stroke, or spinal cord injury are extremely susceptible to the disuse syndrome—a condition brought about by a decrease in the function of the cardiorespiratory and musculoskeletal systems. Gait training is effective in preventing the disuse syndrome in patients of bedridden and disabled. Wernig et al. [1] demonstrated that 25 out of 33 persons with incomplete spinal cord injuries were able to walk independently after treadmill training with partial body-weight support. However, in this training process, both legs of the patient have to be stepped manually by two therapists; therefore, for the therapist, this training process is a difficult one. Colombo et al. [2] developed a driven gait orthosis (DGO) that can be used on patients with varying degrees of paresis or spasticity for up to 30 min. Dietz et al. [3] used this DGO on patients with incomplete spinal cord injuries, and they suggested that the afferent input from the hip joints is important for leg muscle activation during locomotion.

In previous studies, we developed a robotic gait trainer that can be used in water (RGTW). We observed that this

orthosis is very effective in reducing enhanced hip extensor muscle activities; this is because of the fact that this orthosis is meant for use in water and consequently, the muscles of the patient undergoing training need to exert propulsive forces against water resistance [4][5]. We also developed a bi-articular muscle model that could successfully reduce hip extensor muscle activities [6]. In another study, we observed that the orthosis could not control the walking trajectory and torque precisely because our gait training system was controlled by an open-loop circuit [7]. In order to represent natural human cadence, it is necessary to develop a system with a closed-loop circuit. Therefore, the purpose of this study is to develop a pressure feedback control system as the first step in the development of a closed-loop circuit.

II. SYSTEM DESIGN

A. Pneumatic Mckibben Actuator

The gait training system (gait training orthosis) developed in this study comprises a long-leg brace with trunk support and it is powered by pneumatic Mckibben actuators, called “Air Muscle,” manufactured by Hitachi Medical Co. (shown in Fig.1). This actuator is safe because if this actuator use into the water, the Air Muscle prevent accidents from short circuits. Then, pneumatic drive is no trouble for oil leak, so air pressure is considered safer than hydraulic pressure.

Similar to a human muscle, the Air Muscle contracts when activated. The Air Muscle is expanded 1.0 [inch] across when Air Muscle is pressurized, and this type of Air Muscle generates a tensional force of approximately 800 [N] at 0.5 [MPa] without a load. This actuator was arranged two pairs of antagonistic mono-articular muscle model of one leg (hip and knee joints). The length of the Air Muscle was calculated geometrically from equation (1) and Fig.2.

The actuators attached to the hip at the anterior and posterior sides had a natural length of 430 mm. The actuators attached to the knee at the anterior and posterior sides had a natural length of 650 mm and 450 mm, respectively. The knee anterior actuator should be longer than the posterior actuator to ensure that the anterior actuator does not interfere when the knee joint is in flexion.

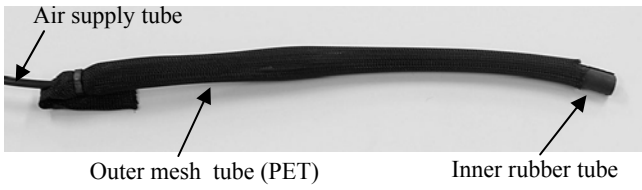


Fig. 1 Air Muscle (cut model). This is a linear-motion-type actuator. It has a 30% modulus of contraction from natural length without load.

$$L_3 = \sqrt{L_1^2 + L_2^2 + 2L_1L_2 \cos\left\{\theta + \tan^{-1}\left(\frac{a_1}{L_1}\right) \tan^{-1}\left(\frac{a_2}{L_2}\right)\right\}} \quad (1)$$

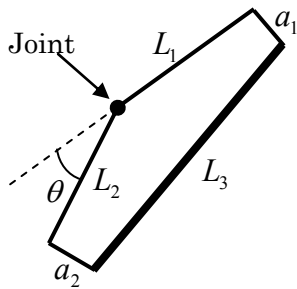


Fig. 2 Geometric model of a mono-articular muscle. L_1 and L_2 are the lengths of the orthosis frame. a_1 and a_2 are the attachment lengths of the Air Muscle. L_3 is the length of the Air Muscle.

Fig.3 provides an overview of the gait training orthosis. We had suspended the orthosis on an experimental frame.



Fig. 3 Overview of the gait training orthosis. 6 actuators were attached to one leg. In the mono-articular model, the actuators were attached to the anterior and posterior of the hip and knee joints.

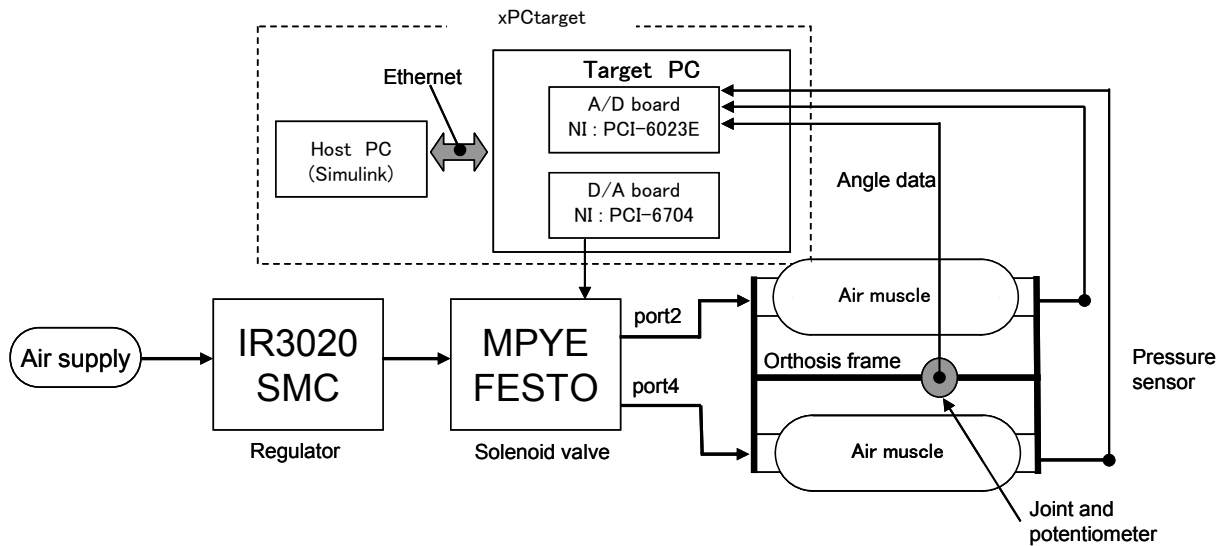


Fig.4 Schematic diagram of the gait training system.

B. Control Program

The pneumatic control devices used in this study were a proportional directional control valve (MPYE5-1/8-HF-010-B, FESTO Co.) and a pressure sensor (PSE540-R06, SMC co.). Fig.4 shows the schematic diagram of the developed gait training system. The compressed air was regulated to pressures between 0.7 MPa and 0.4 MPa by a regulator (IR3020, SMC Co.). The proportional directional control valve controls the supply of air to the two Air Muscle actuators. which were set in an antagonistic arrangement. The inner pressure of each actuator was measured by the pressure sensor. Potentiometers were attached to the axis passing through the hip and knee joints of the orthosis. The control system was programmed in MATLAB/Simulink (The MathWorks Co.) and was connected to devices using xPC Target with Simulink (The MathWorks Co.).

Two actuators were set up in an antagonistic arrangement, and the difference between their inner pressures was applied to the controlled object, which were set in an antagonistic arrangement. Fig.5 shows the block diagram of the feedback control system. Input data applied the inner pressure difference of two actuators as sin wave which peak to peak voltage setup at 0.2 MPa. The proportional directional control valve has two output ports; port 2 and port 4. An output port 2 open within set-point 1 to 4.6 volts, and an output port 4 open within set-point 5.4 to 10 volts.

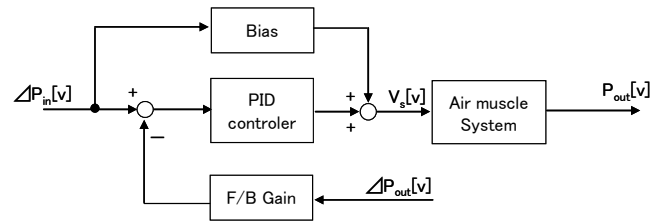


Fig. 5 Block diagram of pressure difference feedback control system. ΔP_{in} : Input data (difference between inner pressures of actuators). P_{out} : Measured inner pressure of the Mckibben actuator. V_s : Control voltage of the proportional directional control valve. ΔP_{out} : Calculated data from P_{out} (Controlled object).

The reference point was approximately 5.0 V. The reference point of the spool valve of the proportional directional control valve was located experimentally by varying the set-point voltage of the proportional directional control valve from 4.5 V to 5.6 V in steps of 0.05 V. However, even if the spool valve was located at the center (reference point), the supply of air did not stop completely. Therefore, each actuator was pressurized. The difference between the inner pressures of the anterior and posterior actuators were calculated by Simulink, and the calculated values were fed back to the PID controller.

In this experiment, the input signals were in the form of sine waves of amplitude 0.4 V (corresponding to 0.1 MPa).

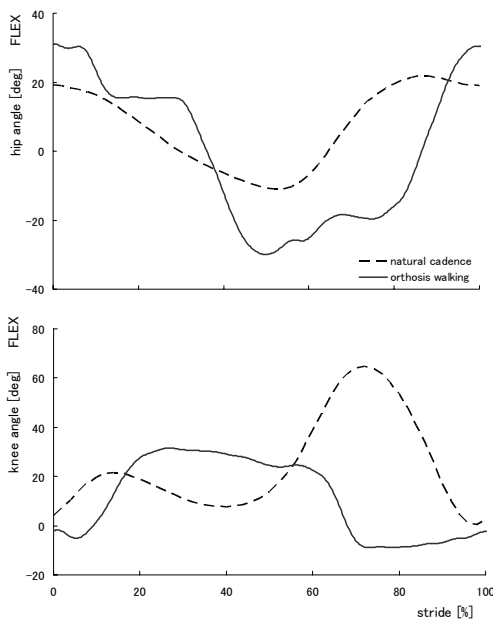


Fig. 6 Compare orthosis walking to natural cadence. Solid line: measurement data of the orthosis. Dashed line: typical angle data of human. Transverse indicate percentage of one step cycle.

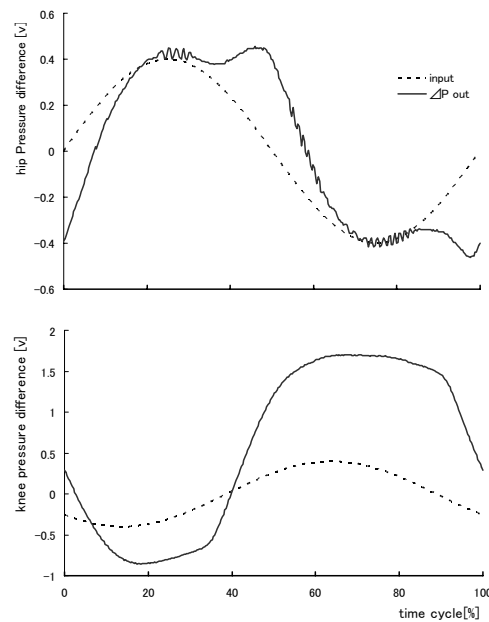


Fig. 7 Compare input data to output data. Solid line; difference of measurement pressure. Dash line; input data. Transverse indicate percentage of one cycle.

III. RESULTS AND DISCUSSION

Fig.6 shows the typical hip and knee joint angle data of the orthosis. Typical data of the natural cadence was obtained from the study of Winter [8]. The gait of the orthosis was different from the natural cadence because the input data did not include hip and knee joint angle data. Since the actuator attached to the posterior of the knee had insufficient contraction length, the angle of knee joint did not reach 60 degrees of flexion. Conversely, the hip range of motion was larger than the natural cadence. Fig.7 shows the input and output data of the difference in the inner pressures of the actuator (The upper graph corresponds to hip data, while the bottom graph corresponds to knee data). Because the length of the actuator attached to the knee on the posterior side was different from the length of the actuator attached to the knee on the anterior side, the controller had to increase the pressure difference and compensate reference point of the proportional directional control valve. The output data of the actuator of the hip joint oscillated that was influenced by inertia force of short leg. Therefore, we have to devise a method that takes into consideration the oscillation of the actuator attached to the hip.

The main objective of this study was to develop a pressure feedback control system as the first step in the development of a closed-loop control system for a gait training system. Kawashima et al. developed a robotic arm driven by antagonistic pneumatic actuators [9]. They demonstrated that the use of a cascade control system for controlling pressure and position enables increased controllability of a robotic arm. In particular, they showed that the movement of the robotic arm could be represented accurately by applying inverse kinematics to the input data. In our study, we were able to control the antagonistic Mckibben actuators attached to a long-leg brace by using the difference in the inner pressures of the actuators as the input data. This control method increased the stiffness of the hip and knee joints of the orthosis because agonistic and antagonistic actuators were activated simultaneously with one proportional directional control valve. However, in this study, the feedback data did not consist of information related to the position of the hip and knee joints of the orthosis. Hence, it is difficult for an orthosis to replicate human cadence when a single pressure control system is used. It is necessary to use a position control system that includes pressure control.

In addition, actuator arrangement was mono-articular muscle model in this experiment. Kumamoto et al. reported that a bi-articular muscle model stabilizes trajectory and increases stiffness [10]. Bi-articular muscles are muscles that work on two joints; the rectus femoris and the ham-

string in humans are two examples of bi-articular muscles. If the bi-articular muscle model is applied to the actuator arrangement of the orthosis, this gait training system may be able to represent behaviors that are more similar to human natural walking, because in such a case, the hip and knee joints of the orthosis will be controlled coordinately.

IV. CONCLUSION

We developed a gait training orthosis powered by a pneumatic Mckibben actuator. By using difference between the inner pressures of the agonistic and antagonistic Mckibben actuators for the controlled object, we were able to control two pneumatic Mckibben actuators with one control valve. We were able to develop a pressure feedback control system as the first step in the development of closed-loop control for a gait training system.

REFERENCES

1. Wernig A, Muller S et al. (1995) Laufband therapy based on 'rules of spinal locomotion' is effective in spinal cord injured persons. *Eur J Neurosci* 7:823-9
2. Colombo G, Joerg M. et al. (2000) Treadmill training of paraplegic patients using a robotic orthosis. *Journal of Rehabilitation Research and Development* 37(6):693-700
3. Dietz V, Müller R, Colombo G. (2002) Locomotor activity in spinal man: significance of afferent input from joint and load receptors. *Brain* 125:2626-2634
4. Miyoshi T, Hiramatsu K et al.. (2008) Robotic gait trainer in water: Development of an underwater gait-training orthosis. *Disability and Rehabilitation* 30:81-87
5. Miyoshi T, Shirota T et al.. (2004) Effect of the walking speed to the lower limb joint angular displacements, joint moments and ground reaction forces during walking in water. *Disability and Rehabilitation* 26:724-732
6. Yamamoto S, Miyoshi T et al.. (2007) Development of pneumatic gait assist system, *Proceedings of the Complex Medical Engineering International Conference on*, 2007, pp1337 - 1340.
7. Shibata Y, Takagi M et al. (2008) Development of gait training system using bi-articular muscle model, *Proceedings of the 7th JFPS International Symposium on Fluid Power, TOYAMA 2008*, pp1-47
8. Winter D (1991) *Biomechanics and Motor Control of Human Gait*, 2nd ed. University of Waterloo Press
9. Kawashima K, Sasaki T et al. (2004) Development of Robot Using Pneumatic Artificial Rubber Muscles to Operate Construction Machinery. *Journal of Robotics and Mechatronics* 16:8-15
10. Kumamoto M, Oshima T, Fujikawa T (2002) Bi-articular muscle as a principle keyword for Biomimetic motor link system, *Microtechnologies in Medicine & Biology 2nd Annual International IEEE-EMB Special Topic Conference on*, 2002, pp 346-351

Author: Yoshiyuki Shibata
 Institute: Shibaura Institute of Technology
 Street: 307 Fukasaku
 City: Minuma-ku, Saitama-City, Saitama
 Country: Japan
 Email: shibata@bpe.se.shibaura-it.ac.jp

Regional absolute quantification in neurochemical profile of the canine brain: Investigation by ¹H nuclear magnetic resonance spectroscopy and tissue extraction

D-C Woo¹, C-B Choi², S-H Lee^{1,3}, E-J Bang⁴, S-S Kim⁵, H-S Rhim⁵, S-Y Kim¹, K-H Kim¹, B-Y Choe¹

¹ Department of Biomedical Engineering, The Catholic University of Korea, Seoul, Korea

² Department of Radiology, Kyung-Hee University of Korea, Seoul, Korea

³ Department of Veterinary Surgery, Konkuk University of Korea, Seoul, Korea

⁴ Metabolome Analysis Team, Seoul center, Korea Basic Science Institute, Seoul, Korea

⁵ Department of Molecular Biology, The Catholic University of Korea, Seoul, Korea

Abstract - The purpose of this study was to characterize the neurochemical profiles of various parts of the canine brain using proton nuclear magnetic resonance spectroscopy (NMRS), tissue extraction, and external simulated phantom concentration quantification. The occipital, frontal, and temporal lobes, thalami, cerebellar cortices, and spinal cords of five pure bred adult beagles were cut, and heavy water solutions for the NMR sample were prepared using the methanol-chloroform-water (M/C) extraction method. The metabolite concentrations in canine brain tissues were measured and compared with those found in human and rat brain tissues. In addition, the cross peaks of Lac, Glu/Gln, and mIns were identified using 2D correlation spectroscopy (2D-COSY) in the canine frontal cortex. The present study demonstrated the absolute quantification of canine neuronal parts using in vitro high resolution MRS, with tissue extraction used to accurately measure metabolite concentrations and provides valuable metabolic information in the various canine neuronal regions.

Keywords— nuclear magnetic resonance spectroscopy (NMR/NMRS), tissue extraction, canine brain, metabolic concentration

I. INTRODUCTION

In vitro high resolution nuclear magnetic resonance spectroscopy (NMR/NMRS) has been used to identify and quantify metabolites of organ tissues and fluids such as brain, breast, urine, articulation, lymph, and others. [1] Although In vitro NMRS is weak to observe longitudinal metabolic change, it is more useful for analyzing metabolites than in vivo NMR is, because the former uses more homogeneous NMR solution samples and higher magnetic field strength. Therefore, the results of in vitro NMR can be used to support pathologic/physiologic analysis. Ex vivo NMR using high resolution magic angle spinning (HR-MAS) technique has been frequently applied in recent times, but in vitro NMRS still provides the

metabolic references for humans and animals because of its high resolution.

Perchloric acid (PCA) and methanol-chloroform (M/C) water extraction are two methods that have been reported in tissue metabolite extraction for NMRS. The two extract solvents differ from each other, and, in NMRS, these methods have differing extraction efficiencies with respect to each metabolite [2].

The present study was designed to characterize the neurochemical profiles of various parts of the canine brain using NMRS, tissue extraction, and external simulated phantom concentration quantification. We further compared these concentrations with the concentrations found in human and rat brains, which have already been reported in other articles.

II. MATERIALS AND METHODS

1. Tissue preparation and extraction

Five adult male beagles (60±2 months, 6~8 kg) were used in this study. Animal experiments were approved by the Institutional Animal Care and Use Committee at the College of Veterinary Medicine, Konkuk University. Animals were maintained according to the 'Guide for the Care and Use of Laboratory Animals' issued by ILAR, USA. Dogs were injected with intravenous propofol (Hana Pharam Co. Ltd., Korea) at a dose of 6 mg/kg. Anesthesia was maintained using 1.5% isoflurane (Rhodia Organique Fine Ltd., Korea) and oxygen (approximately 1.5 l/min) added to room air using an endotracheal tube. After sacrifice, each canine skull was sectioned on the midline and cut around the occipital, frontal, and temporal lobes, thalamus, cerebellar cortices, and spinal cord (C-spine). All tissues were frozen in situ through immediate, direct immersion in liquid nitrogen (-96 °C). This was performed in order to prevent decomposition.

Reagent-grade methanol and chloroform (4°C) were added in a ratio of 2:1 to frozen, ground tissue and to the frozen cell pellets. The tissue-solvent mixture was allowed to thaw before being transferred to centrifuge tubes. The cell pellet-solvent mixture was then sonicated. After approximately 15 min in contact with the first solvents, chloroform and distilled water were added to the samples in a ratio of 1:1 to form an emulsion. The samples were then centrifuged at 13,000 rpm for 20 min. The upper phase (methanol and water) was separated from the lower phase using a glass syringe, and both fractions were dried at freezing state. All dried extract samples were re-dissolved in 90% D₂O water solvent in order to produce the same conditions in the phantom samples [2].

2. 1H-NMR spectroscopy and analyzing spectra

Spectroscopy was performed at 25°C with a Varian 500 MHz FT-NMR spectrometer. One-dimensional NMRS parameters were: proton resonance frequency = 500.384 MHz (Varian spectrometer), Carr-Purcell-Meiboom-Gill (CPMG) spin echo pulse, relaxation/saturation delay time = 0.5/1.5 sec, acquisition time = 1.892 sec, data points = 15146, spectral width = 8000 Hz, number of scans = 256. Two-dimensional correlation spectroscopy (2D-COSY) was performed in a sample made of canine frontal cortex. The 2D-COSY signal was acquired with 4096 data points in the t₂ dimension and 128 increments in the t₁ dimension. The spectral width was 8000 Hz. Solvent suppression was achieved via presaturation by low power water resonance irradiation during the 2 sec relaxation delay.

Tissue and cell metabolite concentrations are expressed per gram millimol (mM) of tissue. The acquired spectra were analyzed using jMRUI 3.0, which calculated the best fit of the experimental spectra as AMARES – Lorentzian fitting, apodization (3Hz). The metabolite concentrations of each tissue sample were measured using the chemical shifts and amplitudes of each metabolite from the ten phantom spectra, as each metabolite peak was subtracted from the original signal.

4. Quantification

Spectral fitting produces an amplitude *A* for each peak, expressed in arbitrary units (au). To standardize this measurement for use in both internal and external referencing schemes, several corrections must be made to account for experimental conditions and the physical properties of each species. The corrected amplitude *A'* is:

$$A' = \frac{A}{f_{gain} f_{coil} f_{T1} f_{T2}} \quad (1)$$

where *f_{gain}*, *f_{coil}*, *f_{T1}*, and *f_{T2}* are correction factors of the receiver gain, coil receiver efficiency, T1, and T2 between a reference and an object. In this study, *f_{coil}*, *f_{T1}*, and *f_{T2}* could be ignored because the same coil, T1, and T2 values were used in all phantoms and samples during NMR.

$$f_{gain} = \frac{gain}{gain_0} = \frac{gain_{sample}}{gain_{phantom}} \quad (2)$$

The gain correction factor (*f_{gain}*) is necessary for external simulated phantom reference quantification, if the receiver gain differs between acquisition of the phantoms and acquisition of the samples. The concentrations of many tissue extraction samples may be low (~μM/ml) in NMR spectroscopy, due to limited amounts of extracted tissue. The concentration (*C_s*) of a metabolite in a tissue sample can be measured as follows:

$$C_s [mM] = \frac{A_s}{A_p f_{gain}} \times \left(C_p [mM] \times \frac{V_s [ml]}{M_{s,t} [gram]} \right) \quad (3)$$

Where *A_s* and *A_p* are the amplitudes of a tissue sample and a phantom, respectively, *V_s* is the volume of sample solution in the NMR tube, and *M_{s,t}* is the wet weight of the tissue used [3].

III. RESULTS

The NMR spectra were obtained from the phantom and the canine tissue samples – occipital, frontal, and temporal lobe, thalamus, cerebellum, and spinal cord (Fig. 1). Huge lactate peaks (1.33 ppm) appeared in all canine tissue sample spectra, but not in the only phantom spectrum. The metabolite concentrations could be measured using external simulated phantom reference quantification and spectral editing technique, which subtracts the peaks of each metabolite from the original signal (Fig. 2). After the subtraction of all metabolites, only residue of the flat baseline level remained. Table 1 shows the spectra and measured metabolite concentrations in the various canine neuronal parts. These concentrations were compared with those found in human and rat brains in other reports. Most metabolite concentrations were higher in the cerebral cortices (occipital, frontal and temporal) than they were in other parts. The data presented in Table 1 demonstrate almost twice the concentration of total creatine (tCr) in the dog cortex as compared to the human cortex. In addition, tCr was higher in the human cerebellum than in the human cortex whereas it was lower in the dog cerebellum than in the dog cortex.

We performed 2D-COSY in the canine frontal cortex (Fig. 3) and noted cross peaks of Lac, Glu/Gln, and mIns, which indicate the presence of three-bond connectivity.

Outside the neuronal metabolites, no other chemical compounds were found.

Fig. 1 Spectra of canine neuronal tissues and phantom. (a) Phantom solution included ten metabolites, (b) spinal cord, (c) cerebellum, (d) thalamus, (e) temporal cortex, (f) frontal cortex, and (g) occipital cortex of a canine.

IV. DISCUSSION

Significantly elevated lactate was observed in all of our NMR spectra (Figs. 1, 2). This was a consequence of anaerobic glycolysis occurring postmortem, prior to freezing of the tissue. Because the warm ischemic period was variable, we did not carry out an analysis of the lactate levels. We previously identified lactate as a contaminant deriving from plastic-ware used during preparation of extracts. Taken together with known problems in freeze-drying samples containing acetate, we decided not to conduct further analysis, although acetate is an interesting metabolite [4].

Numerous studies have shown that the cerebral cortex contains a richer concentration of neurochemical compounds (NAA, tCr, Cho and etc.) compared to most other neuronal tissues in animals and humans, with the notable exception of several metabolites [5,6]. In canine brain, the concentrations of most metabolites tended to be

higher in the cerebral cortex than in other neuronal structures, such as the cerebellum, thalamus, and spinal cord (Table 1).

In general, higher quality spectra can be obtained using the solution NMR system, rather than another in vivo MR spectroscopy system, due to its high magnetic field strength (>10T) and homogeneous solution samples. Many metabolites have been identified in the brains of humans and animals [7]. The coupling effect can cause multiplet peaks when the interaction between the two groups of protons was occurred. These can be split using solution NMR and tissue extraction. In this study, three-bond connectivity was verified using 2D-COSY. When using in vitro NMR spectroscopy, it is possible to perform enhanced identification of neuronal metabolites using two-dimensional nuclear Overhauser effect spectroscopy (2D-NOESY) or hetero-nuclear NMR.

Fig. 2 Example of spectral fitting (canine cerebellum with the same test signal, but superimposed with an artificial baseline). The total test spectrum, the fitted total metabolite spectrum, and the individual simulated metabolite component spectra are overlaid by the fitted spectra, each followed by the residue.

It has been reported that metabolite extraction and sampling are not efficient. M/C water extraction efficiency is reported to be 88~92% during the first extraction, although the efficiency varies based on the metabolite [2].

Table 1. Concentrations of brain metabolites in human, rat, and canine brain tissues (mean±SD, mM)

		tNAA	tCr	tCho	mIns	Tau	Gln	Glu	GABA	Ala
Human adult <i>in vivo</i> , Ref. [16]	Cerebral cortex	9.1±0.7	6.5±0.5	1.2±0.1	4.4±0.6	1.1±0.4	4.1±1.3	8.8±1.1	1.4±0.7	-
	Cerebellum	8.0±0.9	8.3±0.9	2.1±0.3	5.2±0.7	1.8±0.7	5.1±1.2	7.6±1.3	2.2±0.7	-
Rat <i>in vitro</i> , Ref. [10]	Cerebral cortex	7.11	9.35	4.79	2.52	1.57	3.58	4.61	1.71	1.52
	Cerebellum	4.17	9.2	1.62	3.14	0.6	2.71	6.1	1.63	0.74
Canine tissues (Our findings)	Occipital cortex	8.72±1.6	11.08±0.6	2.44±0.9	4.78±0.8	3.16±0.5	3.8±0.9	5.95±0.9	5.00±2.0	1.51±0.2
	Frontal cortex	7.16±1.1	10.27±1.8	2.73±0.4	4.89±0.7	2.86±0.7	3.61±1.0	4.02±1.0	4.91±1.3	1.11±0.2
	Temporal cortex	6.45±0.3	11.31±0.9	3.5±2.0	9.78±2.9	3.89±0.2	8.17±2.2	8.41±3.0	4.7±0.7	2.52±1.3
	Thalamus	3.68±0.4	6.64±0.6	2.15±0.6	3.21±0.7	2.17±0.8	5.22±1.0	3.24±1.7	3.81±0.9	1.12±0.5
	Cerebellum	3.51±0.8	8.77±1.5	1.43±0.4	3.50±1.2	1.89±0.5	3.76±1.2	4.69±1.1	2.24±1.1	0.87±0.3
	Spinal cord	3.63±0.7	6.83±1.5	2.03±0.5	10.30±5.2	4.59±2.5	2.73±2.0	3.39±1.5	3.16±2.3	0.77±0.2

Therefore, it was necessary for us to correct the metabolite concentrations in extracted samples. The results of this study were corrected under the assumption that the extraction efficiency for all metabolites is 90%.

It has been reported that absolute quantification may not be the same for *in vivo* and *in vitro* NMR because of different experimental conditions [7]. In general, the signal of *in vivo* NMR is broader rather than that of *in vitro* NMR because of the lower magnetic field strength and magnetic inhomogeneity in the former. The *in vitro* NMR signal may exhibit an unexpected pattern secondary to unintentional contamination of the NMR sample during preparation. Postmortem metabolic changes can occur, even in a very short time. However, differences in the absolute quantification results for extract and *in vivo* NMR are not statistically significant [7]. Table 1 shows that the metabolic concentrations of canine brain tissue were more closer to those seen in rat brains than to those seen in human brains.

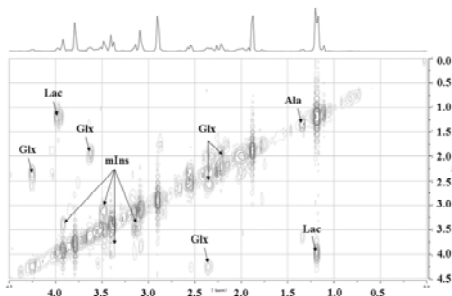


Fig. 3 2D-COSY in frontal cortex shows three-bond coupling connectivity of a metabolite as the cross peak. We found most diagonal peaks corresponding to neurochemical compounds, as well as cross peaks corresponding to myo-inositol, glutamine, glutamate, and lactate.

In the solution NMR experiment, water (H_2O , 4.7 ppm at 25°C) or tetramethylsilane (TMS, 0 ppm) was used as the internal reference. The internal reference quantification method offers several advantages, including insensitivity to inhomogeneities in the B_0/B_1 field and flip angle miscalibration, reduction in experimental time, and independence from magnetic field homogeneity in each sample. However, external simulated phantom reference quantification is superior to internal reference quantification owing to the fact that the chemical shift position for the spectra of a phantom reference and a sample can be precisely matched [8,9]. Although numerous studies have reported the neurochemical profiles of humans and animals using various quantification methods and *in vivo/in vitro/ex vivo* NMR [10], the results have not been identical. There may be individual variations among subjects and individual experimental conditions. In this study, the external simulated phantom reference quantification method was confirmed to show the neurochemical profiles of various

canine tissues. The characteristics of canine brain metabolism can be further elucidated through investigation of phantom reference metabolites such as glucose, glutathione, and acetate, and additional examination of canine brain tissue.

In summary, the present study demonstrated the absolute quantification of canine neuronal parts using *in vitro* high resolution MRS, with tissue extraction serving as the means by which to accurately measure metabolite concentrations. Our findings provide metabolic information for various canine neuronal regions and can be applied in future canine studies.

ACKNOWLEDGMENT

This study was supported by a grant from the Seoul R&BD Program (10550), the Korea Health 21 R&D Project, Ministry of Health & Welfare, Republic of Korea (A081057), a grant (R01-2007-000-20782-0) from the Purpose Basic Research Grant of the KOSEF, the Korea Research Foundation Grant funded by the Korean Government (KRF-2008-313-D01324), and the Seoul Fellowship from the Seoul metropolitan government.

REFERENCES

1. Birken DL, Oldendorf WH (1989) Wiley Interscience. *Neurosci Biobehav Rev* 13:23-31
2. Le Belle JE, Harris NG, Williams SR et al (2002) Wiley Interscience. *NMR Biomed* 15:37-44
3. Bolan JP, Meisamy S, Baker HE et al (2003) Wiley Interscience. *Magn Reson Med* 50:1134-1143
4. Burri R, Bigler P, Straehl P et al (1990) Elsevier. *Neurochem Res* 15(10):1009-1016
5. Florian C-L, Williams SR, Bhakoo KK et al (1996) Elsevier. *Neurochem Res* 21:1065-1074.
6. Pouwels PJW, Brockmann K, Kruse B et al (1999) Lippincott Williams & Wilkins. *Pediatr Res* 46:474-485
7. Barker PB, Breiter SN, Soher BJ et al (1994) Wiley InterScience. *Magn Reson Med* 32:157-163
8. Kreis R, Ernst T, Ross BD (1993) Elsevier. *J Magn Reson B* 102:1-8
9. Kreis R, Ernst T, Ross BD (1993) Elsevier. *J Magn Reson B* 102:9-19
10. Tkac I, Henry P-G, Andersen P et al (2004) Highly resolved *in vivo* 1H NMR spectroscopy of the mouse brain at 9.4T. *Magn Reson Med* 52:478-484

The corresponding author:

Author: Bo-Young Choe
 Institute: Department of Biomedical Engineering, The Catholic University of Korea
 Street: #505 Banpo-dong Seocho-Gu
 City: Seoul
 Country: Korea
 Email: bychoe@catholic.ac.kr

A Potable System for Foot-Drop Correction using Electrical Stimulation

R.H. Sohn¹, S.W. Park¹, S.H. Hwang¹, A.R. Ko², Y.H. Lee², S.H. Lee⁴, K.H. Ryu⁴ and Y.H. Kim^{1,3}

¹ Department of Biomedical Engineering, Yonsei University, Wonju, Republic of Korea

² Wonju College of Medicine, Department of Rehabilitation Medicine, Republic of Korea

³ Institute of Medical Engineering, Yonsei University, Wonju, Republic of Korea

⁴ Hurev, Wonju, South Korea

Abstract— Electrical stimulation (ES) can be used to correct foot drop and toe drag during hemiplegic walking. This study designed to make potable electrical stimulation system according to correct foot drop of hemiplegic walking. A right hemiplegic patient was participated and electrical stimulator was mounted on the motor point of the tibialis anterior (TA) of hemiplegic patient. In order to validate the use of this system, we performed gait analysis of hemiplegic walking with and without electrical stimulation. A potable electrical stimulation system could correct the drag foot successfully.

Keywords — Foot-drop correction, Potable electrical stimulation.

I. INTRODUCTION

Functional Electrical Stimulation (FES) can improve the gait of stroke patients by stimulating the personal nerve in the swing phase of the affected leg, causing ankle dorsiflexion to clear toes from the ground [1-4].

In general, 3-dimensional movement analysis system is widely used in analyzing gait phase, which is very accurate but very expensive. Besides, it is difficult to apply this system in a patient's daily life because it can only be used in the laboratory. Hence, there have been studies on sensors which can be applied effectively and simply to the FES system.

In previous studies, Succeeded in detecting the angular speed of shank and thigh using two gyro sensors, and gait cycles by measuring the gradient to the gyro-sensor's shaft. Gait phase of stroke patients were determined using accelerometers [5]. Gait cycle detecting system was developed using FSR sensors and gyro-sensor [6]. Even though the FSR-gyro sensor system might be more reliable for the gait phase detection in different applications, the simple tilt sensor system is not hindered by cables from the foot and could stimulate limbs at the same places where the detection is made.

In this paper, we developed the potable electrical stimulation system. In order to detect gait cycle, tilt sensor was integrated in this system.

II. MATERIALS AND METHODS

A. System description

The portable electrical stimulator is a micro controller-based system with two stimulation channels. The stimulation channels have pulse amplitude range 0 ~ 100mA, pulse width range 0 ~ 1ms and stimulation frequency 1-100Hz and resolution 1Hz. System voltage range 0 ~ 5V and resolution 20mV [Fig. 1].

A tilt sensor (SCA, 100T, VTI, Finland) was integrated in potable electrical stimulation system for gait event detection. Its measurement range was $\pm 90^\circ$ with sensitivity of 2V/g. Sensor signal can be digitized and transferred to the computer using Bluetooth communication.

B. Experimental procedure

A six-camera 3D motion analysis system (VICON612, UK) was used to record kinematic data at 120 Hz. Temporal-spatial parameter and joint angle were used whether potable electrical stimulation system was useful for correction of foot drop.

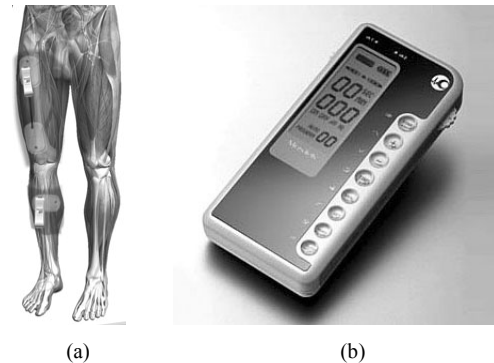


Fig. 1 (a) The placements of potable electrical stimulator. (b) The Potable Electrical Stimulation System

C. Subjects

A right hemiplegic patient was participated in this study. The patient was asked to walk as the convenient speed which was 30cadence without any assistance of potable electrical stimulation system. After that, the subject walking with 30cadence assisted by A potable electrical stimulation system. The potable electrical stimulator was mounted on the motor point of the tibialis anterior (TA) of hemiplegic patient.

III. RESULT

Fig.2 shows the ankle joint angles with and without electrical stimulation. A potable electrical stimulation system could correct the drag foot successfully. In this case, Ankle joint angle were more dorsiflexion then hemiplegic patient's walking without electrical stimulation. And walking speed increased.

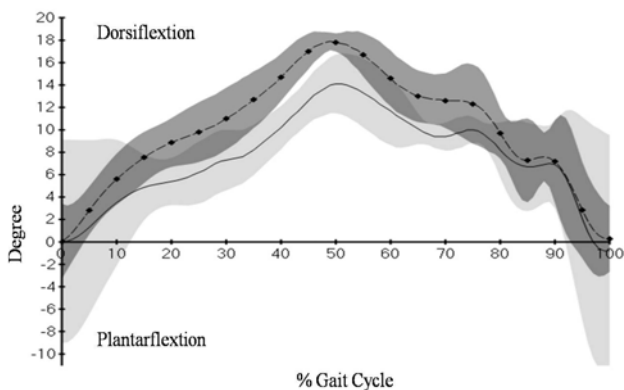


Fig. 2 Right Ankle Joint Angle
(with ES: -▲ - ▲ - ▲ -, without ES: ———)

IV. CONCLUSIONS

For foot drop correction, a potable electrical stimulation system has been developed. A tilt sensor (SCA, 100T, VTI, Finland) was integrated in potable electrical stimulation system for gait event detection.

Foot drop of hemiplegic patients has been corrected using potable electrical stimulator. In the future, we will develop a multi-channel FES walking system for paraplegic patients using complex and wireless sensor system.

ACKNOWLEDGMENT

This research was financially supported by the Ministry of Education, Science Technology (MEST) and Korea Industrial Technology Foundation (KOTEF) through the Human Resource Training Project for Regional Innovation and also was Sports Promotion Fund of Seoul Olympic Sports Promotion Foundation from Ministry of Culture, Sports and Tourism.

REFERENCES

1. Liberson, W. T., Holmquest, H.J., Scott, D., and Dow, M., "Functional electrotherapy, stimulation of the peroneal nerve synchronized with the swing phase of the gait of hemiplegic patients," *Arch. Phys. Med. Rehabil.*, 42, pp. 101-105, 1961.
2. B. R.Brandell, "Development of a universal control unit for functional electrical stimulation (FES)," *Am. J. Phys.Med. Rehabil.*, vol 6, pp. 279-301, 1982.
3. Burridge J, Taylor P, Hagan S, Swain I. (1997) The effect of common peroneal stimulation on the effort and speed of walking. a randomised trial with chronic hemiplegic subjects. *Clinical Rehab*, 11:3, 201-210.
4. Granat MH, Ferguson ACB, Andrews BJ, Delargy M. (1993) The role of functional electrical stimulation in the rehabilitation of patients with incomplete spinal cord injury – observed benefits during gait studies. *Paraplegic*, 31, 207-215.
5. Y. Shimada, S. Ando, T. Matsunaga, A. Misawa, T. Aizawa, T. Shirahata and E. Itoi, "Clinical Application of Acceleration Sensor to Detect the Swing Phase of Stroke Gait in Functional Electrical Stimulation", *The Tohoku Journal of Experimental Medicine*, Vol. 207, no. 3, pp. 197-202, 2005
6. S.C. Ahn, S.J. Hwang, S.J. Kang and Y.H. Kim, "Development and evaluation of a new gait phase detection system using FSR sensor and a gyrosensor", *Journal of the Korean Society of Precision Engineering*, Vol. 21, no. 10, pp.196-203, 2004.

Author: Young Ho Kim
Institute: Medical Engineering, Yonsei University
Street: Meaeji
City: Wonju
Country: Republic of Korea
Email: younghokim@yonsei.ac.kr

An Implantable Epiretinal Vision Prosthesis for Retinitis Pigmentosa Patients

Th. Schanze, U. Thomas, and The EPIRET-Group

EpiRet GmbH, Winchester Straße 8, D-35394 Gießen, Germany

Abstract— Retinal implants are an important neuroprosthetic approach to restore vision in patients that are blind due to photoreceptor loss from retinitis pigmentosa. There are two main approaches. One is the subretinal implant, which is intended to be implanted at the level of the degenerated photoreceptors. The second approach is the epiretinal implant, whose stimulation electrodes are favourably placed from the vitreous side onto the retina of an eye. In this, visual information is captured with an external camera, processed and transmitted to a retinal stimulator that is secured intraocularly and whose electrodes stimulate retinal ganglion cells. As with most electrical prostheses advances are often related to advances in science and technology. Of equal importance are pre-clinical studies and surgical aspects of being able to implant such devices. Recently, the German EpiRet group implanted and tested their epiretinal vision prosthesis in blind human volunteers suffering from retinitis pigmentosa. We present implant's design and results of a clinical study to demonstrate the function and the applicability of the EpiRet vision prosthesis.

Keywords— Blindness, Clinical Study, Retinal Implant, Retinitis Pigmentosa, Vision Restoration.

I. INTRODUCTION

Retinitis pigmentosa is a hereditary blinding disease in which retinal cells of the eye slowly and progressively degenerate. It is estimated that in the Western countries about 5 - 7% of newly diagnosed blindness is due retinitis pigmentosa [1]. However, up to now there is no established method of medical treatment to cure this disease.

Postmortem analyses of retinitis pigmentosa patients have shown that a lot of retinal neurons, e.g. bipolar and especially ganglion cells, are retained compared to the light sensitive photoreceptor cells of the outer nuclear layer [2, 3]. These remaining cells are functionally still intact and may be stimulated with electrical currents to restore vision [4, 5].

Retinal implants are an important neuroprosthetic approach to restore vision in humans that are blind due to photoreceptor degeneration. Two main approaches are currently under development [6-19]. Subretinal implants are implanted between the pigment epithelial layer and the outer layer of the retina and try to stimulate the remaining intact retinal neurons – bipolar or horizontal cells, the initial

stage of neuronal information processing in the retina – with electrical currents. Epiretinal implants have been designed to stimulate retinal ganglion cells – the final retinal processing stage – with an electrode array implanted from the vitreous side onto the nerve fiber and ganglion cell layer of the retina. In short, retinal implants are electronic devices designed to stimulate retinal neurons electrically in order to evoke simplified visual images in the visual system of patients who are blind due to photoreceptor loss.

The challenge of restoring vision is immense and progress in this field is often related to advances in technology, which cross many scientific disciplines, from biology cross over to neurophysics or electrical engineering. Of equal importance are pre-clinical studies and surgical aspects of being able to implant such neuroprosthetic devices. Here, we report on a fully implantable epiretinal vision prosthesis that can be telemetrically activated. We describe its design, implantation and clinical testing in blind volunteers suffering from retinitis pigmentosa.

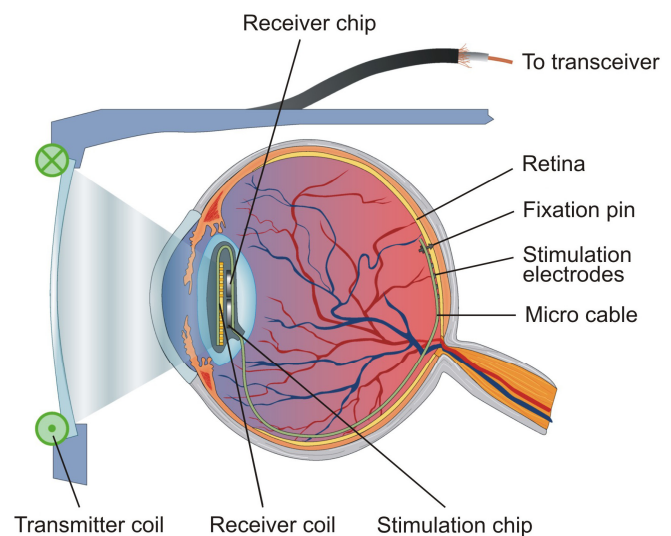


Fig. 1 Notion of the EpiRet retinal implant system for vision restoration. Visual information is captured by a video camera and processed by an external device (not shown). This electronic device transmits the coded visual information and energy inductively to the intraocularly positioned receiver. After signal decoding the stimulation chip activates epiretinally positioned electrodes for stimulation of remaining intact retinal neurons (ganglion cells).

II. EPIRETINAL IMPLANT DESIGN

The notion of the EpiRet epiretinal implant approach is to affix an electrode array onto the retinal surface and to stimulate retinal ganglion cells by physiologically adequate electric current impulses generated by an electronic device (Figure 1). The electronic part of the implant is placed in an artificial intraocular lens and consists of a coil, a receiver and a stimulation chip. The receiver chip is connected to the coil, to receive inductively data signals and energy, and to the stimulation chip. The stimulation chip is finally connected by a micro cable to the epiretinally positioned stimulation electrodes. The implant can be wireless activated by an external transceiver which is also intended to assure an adequate data processing of visual scenes captured by an electronic camera.

The materials for electrodes and for supporting and housing of the electronic chips have to fulfil a variety of requirements and tasks. They have to be highly flexible, smooth, stable, light-weighted, robust, producible, easily implantable, biostable, biocompatible, safe and, as a matter of course, well-performing. In addition, the printed circuit board has to connect the chips and has to be a base for the stimulation electrodes.

We selected polyimide as a basic substrate and housing material for the conductors, the metallic contact pads, required to connect the chips, the micro cable, the electrode array and the galvanically deposited high-Q receiver coil. The electronic circuits were protected against body fluids and other disadvantageous environmental conditions by Parylene C and by silicone rubber. Form and shape of the silicone rubber is like that of an intraocular lens as required for safe implantation and stable fixation (Figures 1 and 2).

Crucial points for low-threshold stimulation in combination with high resolution and information transfer are stimulation current characteristics, e.g. time course, and, especially, the design of the stimulation electrodes [9, 10, 20-24]. Raised or three-dimensional electrodes prospect superior stimulation results compared to flat electrodes. Thus we designed, manufactured and continuously improved stimulation foils with arrays of three-dimensional electrodes (Figure 2). The contact area of each three-dimensional electrode consists of a specially prepared nano-structured oxide-coating. However, this ensures a sufficiently high charge delivery capacity as required for safe and successful local low-threshold stimulation. Some basic details concerning principles of waferlevel production processes, assembly and packaging, as well as electrode design and testing are given elsewhere [10, 14, 18, 26-28].

Implant materials and implants were, of course, tested to be bio- and long term-stable, biocompatible and robust,

especially with respect to sterilization and surgical procedures [10, 29].



Fig. 2 The fully implantable epiretinal EpiRet retina implant. The implant can be telemetrically activated and has 25 electrodes (top side). Each metal-oxide electrode has a three-dimensional shape and was electrically activated and tested. However, this ensures excellent stimulation results. On the right side of the picture are the receiver coil and the electronics protected by parylene C against moisture (ions) and embedded in silicone rubber. Note the picots required for thread-fixation in the eye's lens-capsule. The five-cent coin serves as a ruler.

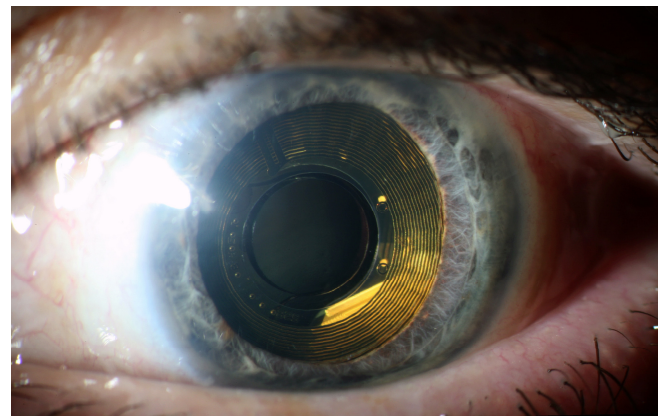


Fig. 3 An implanted epiretinal EpiRet retina implant. The implant's receiver coil, embedded in silicone rubber, shaped as an intraocular lens, is clearly visible. The 'see-through' central sector encircled by the implant's receiver coil allows to observe the posterior inner part of the eye. Thus retina and implant's electrode array can be visually examined during and post surgery.

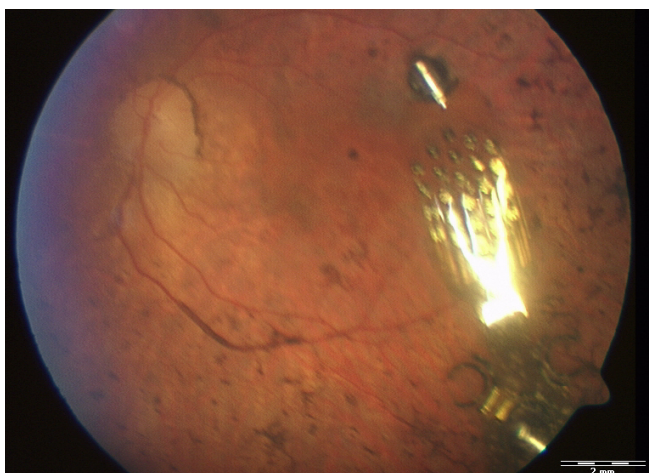


Fig. 4 Fundus photograph of an implanted epiretinal implant's electrode array. The stimulation electrode array was secured safely with a modified retinal fixation pin on the central or foveal area of a human volunteer's inner retinal surface. This fixation approach enables an intimate and thus excellent electrical contact between electrode and ganglion cells as required for stable and successful low-threshold stimulation. The optic nerve disk is in the upper left quadrant. Note that the dark retinal spots are due to retinitis pigmentosa.

III. CLINICAL STUDY

A clinical study was designed and approved by local governments for implantations and implant testings at the Departments for Ophthalmology at RWTH Aachen University and University Essen, Germany. Six blind human volunteers suffering from retinitis pigmentosa received the EpiRet implant (Figures 2, 3, and 4). All implantations were successful and after four weeks the implants were successfully explanted as scheduled. Electrical retinal stimulation and recording of the corresponding volunteers' perceptions proved that vision can be restored with a fully implantable epiretinal vision prosthesis. All volunteers clearly reported visual sensations evoked by electrical stimulation. These perceived sensations, called phosphenes, were related to stimulation parameters like electrode position, stimulation current's amplitude and the duration of the biphasic charge-balanced current impulses.

In correspondence with results and predictions of preceding animal studies (e.g. [9, 20]) we demonstrated for the first time ever that low-threshold electrical stimulation ($< 10 \mu\text{A}$, $< 10 \mu\text{C}/\text{cm}^2$, $< 1 \text{ ms}$ impulse duration) is feasible in blind patients with degenerated retinae due to retinitis pigmentosa. The perception of electrical stimulation was tested over four weeks and showed that important stimulation parameters like threshold, orientation, form, contrast and colour of basic visual objects as well as stimulation resolution and stability can be assessed and optimized.

IV. CONCLUSIONS

The main result of this paper is that with the fully implantable EpiRet epiretinal implant restoring of vision in blind humans with retinitis pigmentosa is feasible. However, it had taken an interdisciplinary approach and more than 15 years to proof this important step in the field of vision restoration. Pre-clinical trials gave direction to epiretinal implant development and were necessary and important for gaining adequate stimulation and design parameters, verification of design, implantation procedures and proof of principle. The clinical trials yielded important knowledge about retinal implant evoked visual sensations or perceptions. These results are the basis to solve the upcoming challenge: the intelligent epiretinal implant with adaptive high resolution and high quality information processing of visual scenes as a medical product to restore vision in blind subjects suffering from retinitis pigmentosa.

ACKNOWLEDGEMENT

The authors greatly acknowledge the participation, the excellent co-operation and the outstanding courage of the six blind human volunteers to render possible the clinical study and their account for medical progress.

Supported by the German Federal Ministry of Education, Science, Research, and Technology, BMBF.

Picture credits (©). Fig. 1: RWTH Aachen, IWE I, 2008; modified. Fig. 2: EpiRet GmbH, 2008. Fig. 3. University Essen, Dept. Ophthalmology, 2008; modified. Fig. 4: RWTH Aachen, Rössler et al., 2009; modified.

REFERENCES

1. Friedman DS, Congdon N, Kempen J, Tielsch JM (2002) Vision problems in the United States. National Eye Institut, <http://www.nei.nih.gov/eyedata/pdf/VPUS.pdf>
2. Stone JL, Barlow WE, Humayun MS, de Juan E, Milam AH (1992) Morphometric analysis of macular photoreceptors and ganglion cells in retinas with retinitis pigmentosa. *Arch Ophthalmol* 110:1634-1639
3. Santos A, Humayun MS, de Juan E, Greenberg R, Marsh MJ, Milam AH (1997) Inner retinal preservation in retinitis pigmentosa: a morphometric analysis. *Arch Ophthalmol* 115:511-515
4. Eckmiller R / Joswig M / Napp-Zinn H / Kreimeier B, Eckhorn R / Schanze T, Ehrfeld W / Schulz C, Gersonde K / Meyer J-U, Heuberger A / Wagner B, Hömberg V / Daunicht WJ, Hostika B / Schwarz M, Jäger D / Buß R, Klar H / Jahnke A, Linke D, Noth J, Samii / Penkert G, Zimmer G / Mokwa W (1994) Neurotechnologie-Report I: Machbarkeitsstudie und Leitprojekt-Vorschlag. Herausgeber: Bundesministerium für Forschung und Technologie, Bonn, April 1994
5. Humayun MS, de Juan E, Dagnelie G, Greenberg RJ, Propst RH, Phillips DH (1996) Visual perception elicited by electrical stimulation of retina in blind humans. *Arch Ophthalmol* 114:40-46

6. Rizzo JF, Wyatt JL (1997) Prospects for a visual prosthesis. *The Neuroscientist* 3:251-262
7. Hesse L, Schanze Th, Wilms M, Eger M (2000) Implantation of retina stimulation electrodes and recording of electrical stimulation responses in the visual cortex of the cat. *Graefe's Arch Clin Exp Ophthalmol* 238:840-845
8. Zrenner E (2002) Will retinal implants restore vision? *Science* 295:1022-1025
9. Schanze T, Wilms M, Eger M, Hesse L, Eckhorn R (2002) Activation zones in cat visual cortex evoked by electrical retina stimulation. *Graefe's Arch Clin Exp Ophthalmol* 240:947-954
10. Schanze T, Hesse L, Lau C, Greve N, Haberer W, Kammer S, Doerge T, Rentzos A, Stieglitz T (2007) An optically powered single-channel stimulation implant as test system for chronic biocompatibility and biostability of miniaturized retinal vision prostheses. *IEEE-TBME* 54:983-992
11. Humayun MS, Weiland JD, Fujii GY, Greenberg R, Williamson R, Little J, Mech B, Cimmarrusti V, Van Boemel G, Dagnelie G, de Juan E Jr (2003) Visual perception in a blind subject with a chronic micro-electronic retinal prosthesis. *Vision Res* 43, 2573-2581
12. Laube T, Akquel H, Schanze T, Goertz M, Bolle I, Brockmann C, Bornfeld N (2004) First time successful epiretinal stimulation with active wireless retinal implants in Göttinger minipigs. *Invest Ophthalmol Vis Sci* 45:4188
13. Dowling J (2005) Artificial human vision. *Expert Rev Med Devices* 1:73-85
14. Walter P, Kisvárdy ZF, Görtz M, Alteheld N, Rössler G, Stieglitz T, Eysel UT (2005) Cortical activation with a completely implanted wireless retinal prosthesis. *Invest Ophthalmol Vis Sci* 46 :1780-1785
15. Javaheri, MJ, Hahn DS, Lakhanpal RR, Weiland JD, Mark S Humayun MS (2006) Retinal prostheses for the blind. *Ann Acad Med Singapore* 35:137-144
16. Hallum L, Tsafnat, G, Lovell NH, and Suaning, GJ (2003) Artificial vision for the blind. *Australasian Science* 24:21-23
17. Yanai D, Weiland JD, Mahadevappa M, Greenberg RJ, Fine I, Humayun MS (2007) Visual performance using a retinal prosthesis in three subjects with retinitis pigmentosa. *Am J Ophthalmol* 143:820-827
18. Mokwa W (2007) Medical implants based on microsystems. *Meas Sci Technol* 18:R47-R57
19. Roessler G, Laube T, Brockmann T, Kirschkamp T, Mazinani B, Goertz M, Koch C, Krisch I, Sellhaus B, Trieu HC, Weis J, Bornfeld N, Röhgen H, Messner A, Mokwa W, Walter P (2009) Implantation and explantation of a wireless epiretinal retina implant in blind RP patients. *IOVS*:in press
20. Schanze Th, Greve N, Hesse L (2003) Towards the cortical representation of form and motion stimuli generated by a retina implant. *Graefe's Arch Clin Exp Ophthalmol* 241:685-693
21. Schanze T, Sachs HG, Wiesenack C, Brunner U, Sailer H (2006) Implantation and testing of subretinal film electrodes in domestic pigs. *Exp Eye Res* 82:332-340
22. Eger M, Wilms M, Eckhorn R, Schanze Th, Hesse L (2005) Retino-cortical information transmission achievable with a retina implant. *BioSystems* 79:133-142
23. Eckhorn R, Wilms M, Schanze T, Eger M, Hesse L, Eysel UT, Kisvárdy ZF, Zrenner E, Gekeler F, Schwahn H, Shinoda K, Sachs H, Walter P (2006) Visual resolution with retinal implants estimated from recordings in cat visual cortex. *Vision Res* 46:2675-2690
24. Eckhorn R (2007) Spatial, temporal-, and contrast resolutions obtainable with retina implants, pp. 5-13. *Ophthalm Res: Visual Prosthesis and Ophthalmic Devices: New Hope in Sight*. Ed: Tombran-Tink J, Barnstable C, Rizzo JF, Humana Press Inc., Totowa, NJ
25. Stieglitz T, Keller R, Beutel H, Meyer J-U (2000) Microsystem integration techniques for intraocular vision prostheses using flexible polyimide-foils. *Proceedings of the MICRO.tec 2000, 25-27th September 2000, Hannover/Germany*, pp. 467-472
26. Mokwa W (2004) MEMS technologies for epiretinal stimulation of the retina. *J Micromechanics and Microengineering* 14 S12-S16
27. Hungar K, Görtz M, Slavcheva E, Spanier G, Weidig C, Mokwa W (2005) Production processes for a flexible retina implant. *Sensors and Actuators A: Physical* 123-124, 23th September 2005, pp. 172-178. *urosensors XVIII 2004 - The 18th European conference on Solid-State Transducers*
28. Mokwa W, Görtz M, Koch C, Krisch I, Trieu H-K, Walter P (2008) Intraocular epiretinal prosthesis to restore vision in blind humans. *Proc. of the 30th Annual International Conference of the IEEE Engineering in Medicine and Biology Society, Vancouver*, pp. 5790-5793
29. Sellhaus B, Schanze T, EPI RET 3 Group (2008) The EPI RET3 wireless intraocular retina implant system: Biocompatibility of the EPI RET 3 device. *ARVO Conference, Fort Lauderdale, 3009/D605*

Author: Dr. Thomas Schanze
 Institute: EpiRet GmbH
 Street: Winchester Straße 8
 City: D-35394 Gießen
 Country: Germany
 Email: info@epiret.de, Th.Schanze@web.de

Addendum

Information concerning EpiRet GmbH, EPIRET-Group, partners and related projects can be found here: <http://www.epiret.de>.
 Some additional information provides: [http://www.pro-retina.de\(/deu/topical/show.php?fetchme=134\)](http://www.pro-retina.de(/deu/topical/show.php?fetchme=134)).

Development of system for estimating muscle force in real-time

Jongsang Son¹ and Youngho Kim^{1,2}

¹ Department of Biomedical Engineering, Yonsei University, Wonju, Korea

² Institute of Medical Engineering, Yonsei University, Wonju, Korea

Abstract— Since insufficient muscle forces mean that people cannot perform some activities well related to roles of the muscle, muscle force have been considered as an important parameter in clinic. Therefore many methods have been introduced to estimate muscle force indirectly. One of the methods is muscle tissue dynamics and it is widely used in commercial software including musculoskeletal model. They, however, need motion data captured from 3-dimensional motion analysis system. In this study, we developed a system for estimating muscle force in real-time by using joint angles. The heel-rise movements were performed for a normal with 3-dimensional motion analysis system, EMG measurement system, and goniometer. Joint angles obtained from goniometers and EMG signals were used to estimate muscle forces. Simulation was performed to find muscle forces using motion data which was imported into musculoskeletal software. As the results, muscle lengths and forces from developed system were similar to those of commercial software in pattern. Results of this study would be helpful to understand and to analyze motion in clinic area on real-time.

Keywords— Muscle force, real-time, 3D motion analysis, Heel-rise

I. INTRODUCTION

Since insufficient muscle forces mean that people cannot perform some activities related to roles of the muscle, muscle force have been considered as an important parameter in clinic or research area. The only way to measure the force of a single muscle directly is to use sensor such as tendon force transducers [1]. However, since people want to avoid to be inserted it into their body, invasive methods are not appropriate for clinical use. Therefore a number of indirect methods have been introduced, one of the noninvasive methods is to use muscle tissue dynamics [2]. However, 3-dimensional (3D) motion analysis should be normally performed first before using commercial software including musculoskeletal model. In the other words, 3D motion analysis system and musculoskeletal modeling software which are too expensive is required and they cannot be performed in real-time.

In this study, we developed a system for estimating muscle force in real-time from joint angles related to muscle that we are interested in.

II. METHOD

A. Motion analysis

A normal was participated for this study. He was required to rise and lower his feet for 5 times. During the experiments, motion analysis was performed with 3D motion analysis system (VICON, U.K.), EMG measurement system (Noraxon, U.S.A.), and goniometers (Biometrics, U.K.). EMG signals were obtained on gastrocnemius medialis (GCM) and tibialis anterior (TA). Goniometers were attached on around knee joint and ankle joint.

B. Joint angle and muscle length

To find relationship between joint angles and muscle lengths, cubic regression analysis was performed using SPSS 12.0 (SPSS, U.S.A.) after muscle lengths were obtained from commercial software SIMM (Musculographics, U.S.A.) including musculoskeletal model.

C. Calculation of muscle force

Muscle model used in this study was designed by Zajac [2]. The model has advantages of cheaper cost than other model and easiness implementation. Estimation of muscle forces was conducted using home-made software written in C# language.

D. Validation

To validate developed system, analysis of correlation coefficient (r) and significance of the correlation (p) were performed between muscle lengths and muscle forces from SIMM and those from developed system.

III. RESULTS

A. Joint angle

Joint angles calculated from marker trajectories were similar to those obtained from goniometers (Fig. 1). Good

correlation was observed in knee joint ($r = 0.879$, $p < 0.01$) and in ankle joint ($r = 0.922$, $p < 0.01$).

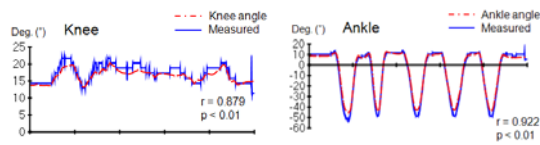


Fig. 1 Comparison of joint angles

B. Muscle length

Muscle lengths obtained from SIMM and those of joint angles using each equation were similar in pattern (Fig. 2). Good correlation was observed in selected muscles (GCM: $r = 0.874$, TA: $r = 0.907$). The correlations were significant in all above muscles at a $p < 0.01$ level.

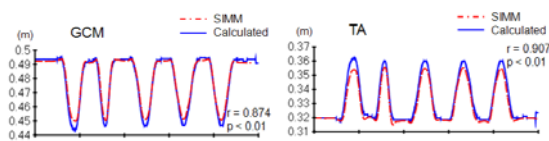


Fig. 2 Comparison of muscle length

C. Muscle force

Muscle forces from developed system had good correlation with those of SIMM in chosen muscles (GCM: 0.913, TA: 0.733; Fig. 3). The significance of correlations was lower than 0.01 in all above muscles.

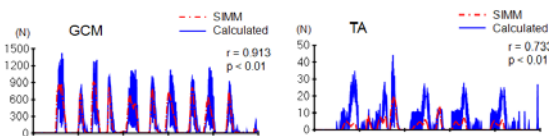


Fig. 3 Comparison of muscle force

IV. DISCUSSION

The results in this study were good at joint angle, muscle length and muscle force. However, low resolution of goniometers resulted in increase of error, especially; noise was generated to differentiate muscle length during calculating muscle force. This problem would be solved by using goniometer which has higher resolution than ours.

Heel-rise movements have been used for manual muscle test and evaluation of functional ability of gastrocnemius muscles with EMG measurement. Normally, EMG signal

could be considered as active force, however, it is not possible to understand EMG signal as muscle force in condition that muscle length is too short or too stretch to generate muscle force (Fig. 4). Since EMG signal could not reflect passive information, it is not reasonable to analyze passive force from EMG signal in condition that muscle length is as long as muscle could generate passive force (Fig. 4). Therefore, those limitations would be covered through developed system in this study.

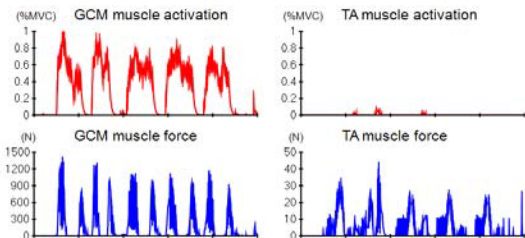


Fig. 4 Comparison between muscle activation and muscle force

V. CONCLUSIONS

In this study, muscle force estimation system was developed to apply in real-time. Muscle length was calculated from joint angle and muscle force was estimated from calculated muscle length. The results had good correlation with those of commercial software including musculoskeletal model at least. Product developed in this study would be expected to apply to research and development or clinic.

ACKNOWLEDGMENT

This research project was supported by the Sports Promotion Fund of Seoul Olympic Sports Promotion Foundation from Ministry of Culture, Sports and Tourism.

REFERENCES

1. Komi P (1990) Relevance of in vivo force measurements to human biomechanics. *J of Biomech* 23:23-34
2. Zajac FE (1989) Muscle and tendon: properties, models, scaling, and application to biomechanics and motor control. In: Broune, J.R. (Ed.), *CRC Critical Reviews in Biomedical Engineering* 17:359-411

Author: Youngho Kim
Institute: Yonsei University
Street: 234 Maeji, Heungup
City: Wonju
Country: Korea
Email: younghokim@yonsei.ac.kr

Sensitivities of Bipolar Subcutaneous and Cortical EEG Leads

J. Väisänen¹, K. Wendel¹, G. Seemann², J. Malmivuo¹ and J. Hyttinen¹

¹ Department of Biomedical Engineering, Tampere University of Technology, Tampere, Finland

² Institute of Biomedical Engineering, Karlsruhe Institute of Technology, Karlsruhe, Germany

Abstract—An ideal bioelectric measurement should be focused on and specific to the target region. Volume conductor effects such as the poorly conducting bones or the moderately conducting skin are known to affect the specificity and accuracy of the surface electroencephalography (EEG) measurements. This paper introduces a modeling study on the effect of bipolar EEG lead implantation on measurement sensitivity. The electrodes were implanted at two depths in the realistic human head, one on the skull and the other on the cortex. The effects on the measurement sensitivity were studied by means of the half-sensitivity volume (HSV) and the region of interest sensitivity ratio (ROISR). The results indicate that subcutaneous implantation notably enhances the accuracy and specificity of EEG measurement compared to the surface measurement. Deeper measurements i.e. implantation on the cortex enables specific monitoring of a small source volume in contrast to partial and whole regions such as the visual cortex. The results of the study imply that in clinical practice the subcutaneous needle electrodes would provide more specific and accurate measurements of cortical activation than scalp measurements.

Keywords—Sensitivity distribution, lead field current density, ROISR, EEG, volume conductor.

I. INTRODUCTION

Clinical electroencephalography (EEG) and visually evoked potentials (VEP) demand high signal-to-noise ratios (SNR), less averaging, minimization of skin artifacts, and high sensitivity and specificity to name a few important criteria. Subcutaneous needle electrodes are commonly used in clinical electromyography (EMG), which are inserted into the muscles of interest. These minimally-invasive measurements offer higher SNRs with lower susceptibility of standard measurement artifacts when compared with traditional surface measurements. We believe that clinical EEG and VEP could adopt the subcutaneous measurement setup, thus placing the lead on the skull bypassing the artifact-prone skin. Our aim is to compare the bipolar subcutaneous EEG measurement with the well-documented surface and cortical electrodes [1, 2].

In the present study we apply the concepts of the half-sensitivity volume (HSV) and region of interest sensitivity ratio (ROISR) in analyzing the effects of EEG electrode im-

plantation on the measurement sensitivity distribution within the brain. Specifically, we aim to identify the measurement sensitivity associated with two implanted electrodes compared to the surface electrode of the same size.

II. METHODS

A. Sensitivity distribution

The sensitivity distributions of measurement leads in an inhomogeneous volume conductor can be illustrated with reciprocal gradient potential fields i.e. current fields, as defined by Plonsey [3]. The lead vectors define the relationship between the measured signal in the lead and the current sources in the volume conductor such that

$$V_{LE}(\mathbf{x}) = - \int_H \nabla \Phi_{LE}(\mathbf{y}; \mathbf{x}) \cdot \mathbf{J}^i(\mathbf{y}) dV, \quad (1)$$

where $V_{LE}(\mathbf{x})$ is the voltage, e.g. measured EEG voltage, in lead \mathbf{x} , H is the volume conductor, $\nabla \Phi_{LE}(\mathbf{y}; \mathbf{x})$ is the sensitivity vector of lead \mathbf{x} in source location \mathbf{y} , $\mathbf{J}^i(\mathbf{y}) [A/cm^2]$ is the impressed current density vector in source location \mathbf{y} .

The sensitivity distribution in the volume conductor can be established by applying the reciprocity theorem of Helmholtz with Poisson's equation applied to describe quasi-static bioelectric source-field problems. A source distribution, $\mathbf{J}^i(\mathbf{y})$, containing only reciprocal source currents at the measurement electrodes raises a gradient potential distribution, $\nabla \sigma(\mathbf{y})$, i.e. measurement sensitivity, according to the following relationship

$$-\nabla \sigma(\mathbf{y}) \nabla \Phi(\mathbf{y}) = \nabla \mathbf{J}^i(\mathbf{y}). \quad (2)$$

B. The Half Sensitivity Volume

In [2] the concept of half-sensitivity volume (HSV) was applied to define the volume in which the sensitivity of the measurement lead is concentrated. The HSV is the size of the volume within the source region of the volume conductor, where the magnitude of the detector's sensitivity is at least half of its maximum density. The smaller the HSV is, the smaller the region from which the detector's signal arises.

Table 1: Tissues and Resistivity values included in our realistic head model

Tissue	Resistivity (Ω m)
Bone marrow	2180
Fat	2500
Skull/Bones	3450
White matter	700
Gray matter	300
Scalp	230
Eye	198
Muscles	900
Blood	100
CSF	65
Other neural tissue	624

Table 2: Results of the 3 bipolar lead cases: the surface i.e. scalp, subcutaneous (SubQ), and the cortical leads.

Leads	Surface	SubQ	Cortical
Max sensitivity [A/cm^3]	0.38	0.72	5.76
HSV [mm^3]	4002	516	63
ROISR	2.06	2.76	5.11

The half-sensitivity volume is thus applied to compare the detector's ability to concentrate its measurement sensitivity.

C. The Region of Interest Sensitivity Ratio

The concept introduced in [4] provides a parameter to analyze the specificity of a measurement system. Eq. 3 defines ROISR as a ratio between the average sensitivity of a predefined region-of-interest (ROI) volume and the average sensitivity in the rest of the source volume, hereafter called as a nonROI volume.

$$\mathbf{ROISR} = \frac{\frac{1}{|H_{ROI}|} \int_{H_{ROI}} \nabla \Phi_{LE}(\mathbf{y}; \mathbf{x}) dy}{\frac{1}{|H_{nonROI}|} \int_{H_{nonROI}} \nabla \Phi_{LE}(\mathbf{y}; \mathbf{x}) dy}, \quad (3)$$

where H_{ROI} is the ROI source volume [cm^3] and H_{nonROI} is the nonROI source volume [cm^3].

In the case of EEG the nonROI volume consists of the entire brain source volume excluding the ROI volume. ROISR thus defines how well the measurement sensitivity is concentrated within the selected ROI, i.e. how specific the measurement is to the signals generated within the ROI. In the present study the brain source volume, B , contains gray and white matter. We define $ROI = B \cap S$, where S is a sphere with a 20 mm radius from the cortical electrode located on the occipital cortex surface (10/20 location, O_Z , Fig. 1). Consequently, our ROI contains both gray and white matter. We selected this location due to its relevance in visually evoked studies [5].

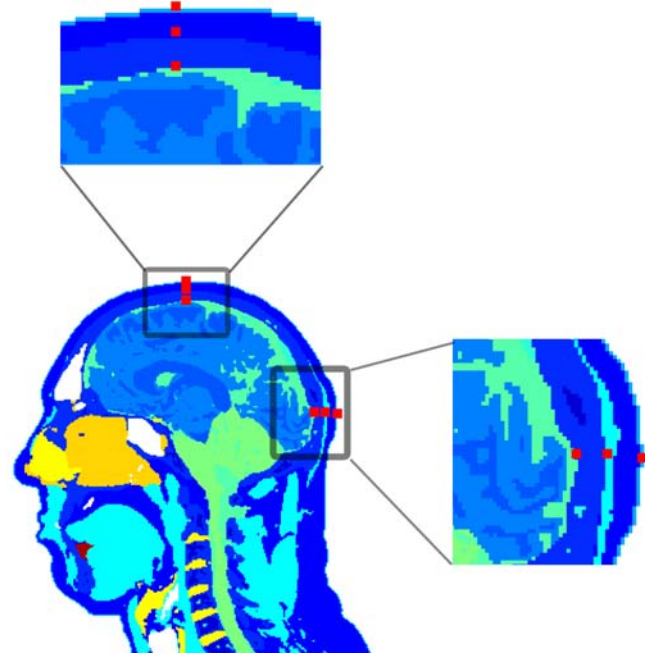


Fig. 1: The sagittal view of the head model showing the bipolar electrode locations. The three red pixels at the apex and occipital cortex are the surface (i.e. on the scalp), subcutaneous (i.e. on the skull), and cortical EEG electrodes of size $1mm \times 1mm \times 1mm$.

D. Model and computations

We calculate the sensitivity distributions in a realistically shaped male head model based on the Visible Human Project man dataset [6]. The tissues and their corresponding resistivities are listed in Table 1 [7]. Calculation of the sensitivity distribution are based on the principle of reciprocity and the numerical FDM solution of EEG electrode sensitivity. In the present study we apply the scalp-to-skull resistivity ratio of 1:15 [8]. We calculate the sensitivity distributions of the brain for three bipolar electrode pairs located on the scalp, the skull, and the cortex. The surface (i.e. scalp), subcutaneous (SubQ), and cortical electrodes all measure $1mm \times 1mm$, which reflects the size of one pixel. Our bipolar leads reflect a visually evoked measurement over the occipital cortex (10/20 location O_Z) referenced against an apex electrode (10/20 location C_Z). A sagittal view of the model (Fig. 1) shows the three bipolar EEG locations: surface i.e. scalp, subcutaneous i.e. skull, and cortex.

III. RESULTS

Clearly, the smearing effect of the scalp and skull disappears with cortical leads since the recording locations are in the target region (Fig. 2 & 3). However, we astonishingly

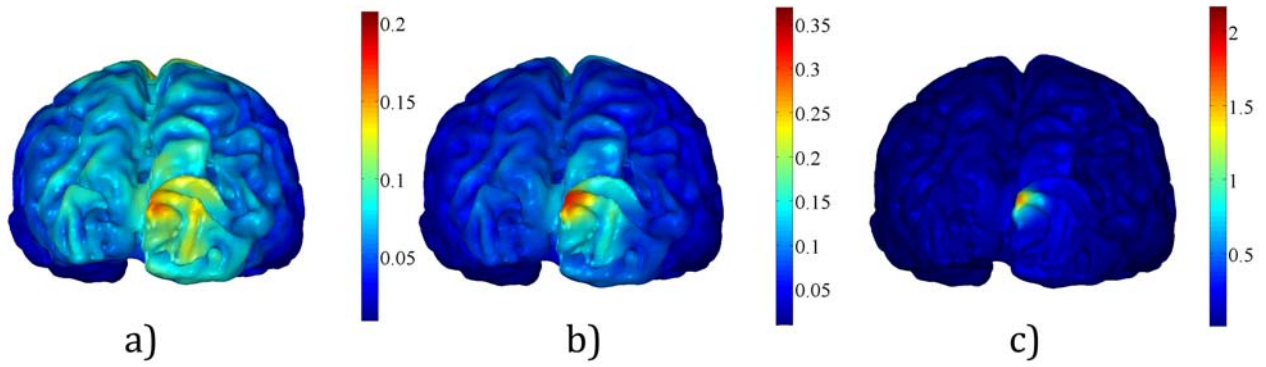


Fig. 2: Measurement sensitivity fields mapped on the brain from a bipolar electrode pair over the apex and occipital cortex. The three subfigures represent different depths of recording: a) surface i.e. scalp, b) subcutaneous i.e. skull, and c) cortex.

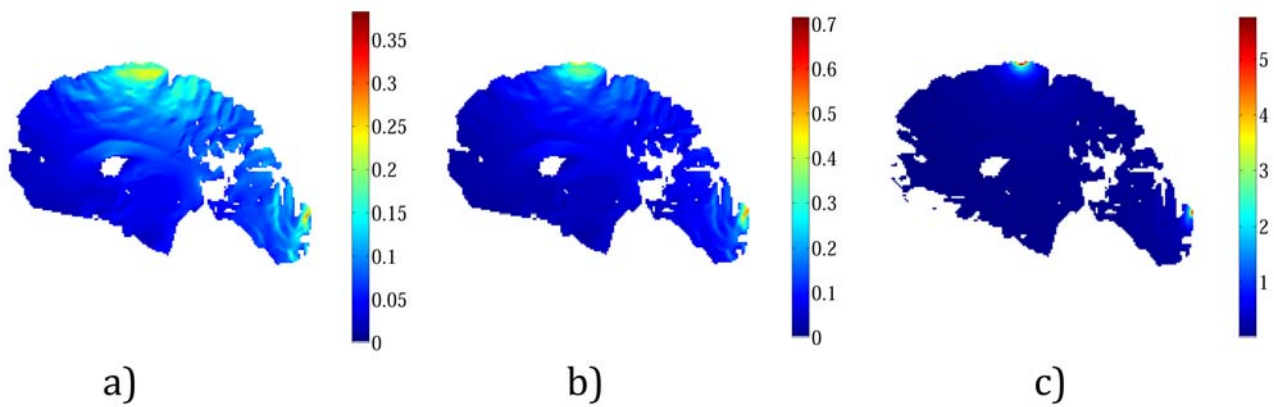


Fig. 3: Sagittal cross sections of the brain compartment depicting measurement sensitivity for the three sets of bipolar electrode pair between the apex and the occipital cortex: a) surface i.e. scalp, b) subcutaneous i.e. skull, and c) cortex.

find the smearing effect is likewise reduced in the subcutaneous sensitivity distributions. Table 2 shows that the subcutaneous lead's HSV decreases to nearly one-eighth the size of the scalp lead's HSV and again by another factor of eight to obtain the cortical lead's HSV. Similarly, we find a 34% improvement in the subcutaneous lead's ROISR over the surface lead's ROISR. Fig 2 and Fig. 3 illustrate that the subcutaneous measurement distributions on the cortical surface looking posteriorly onto the occipital cortex and through the sagittal cross section, respectively, clearly concentrates the measurement sensitivity to the target region as a minimally-invasive measurement and eliminates much of the scalp and skull smearing from the traditional surface measurements. Precisely, the subcutaneous leads measure neuroelectric activity on or near the gyral cortical surface rather than sulcal or deep sources.

IV. DISCUSSION

We analyzed our realistic models to identify the phenomenon of EEG measurement sensitivity. We found that the HSV decreases in volume as the sensors move closer to the bioelectric source i.e. moving from surface to cortical electrodes. This decrease corresponds with an increased ROISR when the ROI is optimally located near the measurement sensor, which means that the sensitivity is more concentrated and higher in the target region. Consequently, the measurements will detect less background activity and require less signal averaging.

Although we find these effects intuitive, we are surprised by the subcutaneous lead almost detecting the median between the sensitivity and specificity of the surface and cortical measurements. Our numerical results indicate that the subcutaneous lead measures a focused volume eight times smaller than the surface electrodes, which would improve the SNR and signal averaging as mentioned above. Suggestively, these SubQ electrodes could avert the need for active scalp electrodes, which aim to eliminate the measurement dependence on the skin-electrode impedance.

Furthermore, the usage of needles significantly reduces the minimum distance required between bipolar electrodes. This benefit allows the clinician to probe around very specifically for foci such as an epileptic focus. These concentrated minimally-invasive measurements will allow clinicians and researchers to obtain more information of the underlying neuroelectric processes without the need for the highly invasive cortical electrodes. Lastly, the subcutaneous leads drastically reduce the effect of the widely debated skull conductivity value and the scalp-to-skull conductivity ratio used on the results of the numerical simulations.

V. CONCLUSION

Implanted electrodes concentrate and focus the measurement sensitivity towards a region of interest (ROI) more so than traditional scalp electrodes. The subcutaneous electrodes sense the area comparable in size to the visual cortex, whereas, the cortical electrodes can focus on neuroelectric activity in the immediate vicinity of the gray matter. We identify the primary benefit of this study as the identification of the concentrated measurement sensitivity of the subcutaneous needle electrodes with respect to traditional surface EEG measurements. These minimally invasive measurements may improve the clinical diagnoses of detecting neuroelectric disorders.

REFERENCES

1. Malmivuo J., Plonsey R.. (1995) Bioelectromagnetism — Principles and Applications of Bioelectric and Biomagnetic Fields. Oxford University Press, New York.
2. Malmivuo J., Suihko V., Eskola H. March 1997 Sensitivity distributions of EEG and MEG measurements. IEEE Trans. on Biomed. Eng. 44:196–208.
3. Plonsey R.. (1963) Reciprocity applied to volume conductors and the EEG. IEEE Trans. Biomed. Electron. 10:9–12.
4. Väisänen J., Väisänen O., Malmivuo J., Hyttinen J.. (2008) New Method for Analysing Sensitivity Distributions of Bioelectric Measurements. Med. Biol. Eng. Comput. 46:101–108.
5. Sörnmo L., Laguna P. (2005) Bioelectrical Signal Processing in Cardiac and Neurological Applications. Academic Press.
6. Sachse F.B., Werner C.D., Meyer-Waarden K., Dössel O.. (1998) Applications of the Visible man dataset in electrocardiology: Calculation and visualization of body surface potential maps of a complete heart cycle. Proc. of the Second Users Conference of the National Library of Medicine's Visible Human Project. :47–48.
7. Ramon C., Schimpf P.H., Haueisen J.. February 2006 Influence of head models on EEG simulations and inverse source localizations. BioMedical Engineering Online .
8. Oostendorp T.F., Delbeke J., Stegeman D.F. December 2000 The Conductivity of the Human Skull: Results of In Vivo and In Vitro Measurements. IEEE Trans. on Biomed. Eng. 47:1487–1492.
9. Wendel K., Narra N.G., Hannula M., Kauppinen P., Malmivuo J.. April 2008 The Influence of CSF on EEG Sensitivity Distributions of Multi-layered Head Models. IEEE Transactions on Biomedical Engineering 55:1454-1456.

Author: J. Väisänen
 Institute: Department of Biomedical Engineering,
 Tampere University of Technology
 Street: Korkeakoulunkatu 3
 City: Tampere
 Country: Finland
 Email: juho.vaisanen@tut.fi

Patient-Cooperative Control: Adapting Robotic Interventions to Individual Human Capabilities

Alexander Duschau-Wicke^{1,2,4}, Thomas Brunsch^{3,4}, Simon Felsenstein¹, Heike Vallery^{1,2}, and Robert Riener^{1,2}

¹Sensory-Motor Systems Lab, Institute of Robotics and Intelligent Systems, ETH Zurich, Zurich, Switzerland

²Spinal Cord Injury Center, University Hospital Balgrist, Zurich, Switzerland

³Control Systems Group, Technical University Berlin, Germany

⁴Hocoma AG, Volketswil, Switzerland.

Abstract—Patient-cooperative control strategies aim at improving the efficacy of current rehabilitation robots. The key aspects of these strategies are the transparency of the robots, constraints for safety and guidance, and individual interventions. Within the frame of transparency and constraints, interventions of challenging or facilitating nature can be applied. In this paper, we propose a way of providing facilitating interventions by force fields or global parameters, which are adapted by iterative learning control. We evaluate this approach in two scenarios with the rehabilitation robot Lokomat; first, to assist knee extension during stance phase, and second, to modulate how actively human subjects participate in bearing their own body weight. Both examples show that iterative learning control algorithms provide a feasible way to allow patients to train at a continuously challenging level according to their individual capabilities.

Keywords—Rehabilitation robotics, patient-cooperative control, assist-as-needed, iterative-learning control

I. INTRODUCTION

Neurological conditions such as stroke and spinal cord injury frequently cause walking disabilities. Body weight supported treadmill training (BWSTT) is successfully applied to the rehabilitation of patients suffering from these conditions [1], [2].

Robotic rehabilitation devices such as the Lokomat (Hocoma AG, Switzerland) [3], the ReoAmbulator (Motorika, USA), and the Gait Trainer (Reha-Stim, Germany) automate BWSTT by moving patients repetitively along pre-defined walking trajectories. However, recent studies indicate that the way in which these devices are currently used in therapy is not optimally effective for all groups of patients [4], [5]. The strong guidance of the robots allows patients to remain completely passive, which leads to reduced activity of muscles and metabolism [6].

Therefore, patient-cooperative control strategies are being developed by numerous research groups [7]–[15]. These strategies aim at empowering patients to influence their movements, while still providing sufficient guidance and support to ensure successful walking. We can summarize the desired properties of cooperative controllers in three key terms: Transparency, constraint, and intervention.

Transparency means the ability of the robot to “get out of the way”: Movements that can be achieved by the patient’s own efforts should not be distorted by the interaction with the robot. This property can be either achieved by very

lightweight mechanical design as e. g. in the LOPES robot [16], or by means of control algorithms such as the recently developed approach of “Generalized Elasticities” [17].

Constraints restrict the possible movements with the robot such that the patient is safe and can only move in physiologically meaningful ways. This concept originates from the idea of “virtual fixtures” [18], and has led to a number of control strategies which provide spatial guidance, but allow free timing of movements [11]–[13].

Transparency and constraints are apparently competing interests: The presence of constraints violates transparency. However, a patient being able to train with a completely transparent rehabilitation robot would not need any therapy at all. Patient-cooperative control needs to find the right balance between transparency and control to provide a safe frame that enables the patient to train.

Within this safe and enabling frame, the robot can apply an individual *intervention* to the patient. Two fundamental types of interventions are possible: challenging and facilitating interventions.

Challenging interventions are e. g. velocity-dependent resistance, which has been shown to increase muscle activity and generate beneficial after-effects [19], or error augmentation, which has led to improved motor learning in upper extremity training of stroke survivors [20].

However, during gait training, patients first and foremost have to be enabled to walk successfully. This aim may be compromised by challenging interventions. Therefore, facilitating interventions are being favored for gait rehabilitation robots.

A direct way to realize facilitating interventions is to immediately reduce movement errors, as with impedance control [8], [21]. Variants of this approach generate reference trajectories which are more individual, e. g. by minimizing interaction forces [7], or by inferring movement intentions from other limbs of the patient [14].

Based on the assumption that patients benefit most from rehabilitation if they participate as actively as possible, there is a general consensus that facilitating interventions should ideally assist only as much as needed [9]. For impedance control, this can be achieved by locally adapting the controller stiffness according to the control errors [15].

In contrast to methods with immediate error reduction,

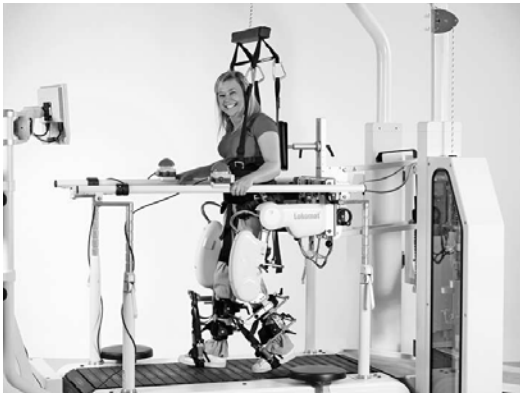


Fig. 1. The Lokomat gait rehabilitation robot with Lokolift body weight support system (Photo courtesy of Hocoma AG, Switzerland)

individual interventions can also be realized by adaptive force fields. An intriguing advantage of this approach is the possibility to read out the adapted force field after the training and interpret it as a model of the patient's weaknesses [22]. To adapt such force fields, we can exploit the highly repetitive nature of rehabilitation training. Iterative learning control [23] algorithms can be used to adapt robotic support from repetition to repetition. This way, all available information from a complete cycle can be taken into account for the adaptation.

In this paper, we propose an adaptive algorithm based on iterative learning control that adjusts the support to the amount needed to maintain walking, but keeps the patient constantly challenged to participate as much as possible in the training. We will demonstrate the use of the algorithm in two different applications for the rehabilitation robot Lokomat: first, to shape an assistive force field applied at the knee joint to assist weight bearing during stance phase, and second, to automatically adjust the amount of body weight support provided to the patient.

II. MATERIALS & METHODS

A. Rehabilitation Robot

Experiments were performed with the gait rehabilitation robot Lokomat (Fig. 1). The robot has been developed to automate body weight supported treadmill training of patients with locomotor dysfunctions in the lower extremities such as spinal cord injury and hemiplegia after stroke [3]. It comprises two actuated leg orthoses that are attached to the patient's legs. Each orthosis has one linear drive in the hip joint and one in the knee joint to induce flexion and extension movements of hip and knee in the sagittal plane. Knee and hip joint torques can be determined from force sensors integrated inside the Lokomat. A closed-loop controlled body weight support system ("Lokolift") relieves the patient from a definable amount of his or her body weight via a harness, which is attached to the patient's trunk [24].

B. Iterative Learning Support

An adaptation algorithm based on iterative learning control (ILC) is used to adjust the amount of support provided to the

patient. The basic idea of ILC is the iterative improvement of an input function for a cyclic process. The input function for the $(k+1)$ th cycle $\mathbf{u}^{(k+1)}(t)$ is determined by adding a correction term to the input function of the k th cycle

$$\mathbf{u}^{(k+1)}(t) = \mathbf{u}^{(k)}(t) + \Gamma(t)\mathbf{e}^{(k)}(t) \quad (1)$$

where $\mathbf{e}^{(k)}(t)$ represents the control error during the k th cycle, and $\Gamma(t)$ is the "learning gain" of the process.

Emken et al. [9] showed that an adaptive controller which is supposed to assist only as much as needed must incorporate a forgetting factor in order to keep patients continuously challenged. Introducing such a factor $k_f \in [0, 1]$ in eq. (1) yields

$$\mathbf{u}^{(k+1)}(t) = (1 - k_f)\mathbf{u}^{(k)}(t) + \Gamma(t)\mathbf{e}^{(k)}(t). \quad (2)$$

Adaptive stance support: When the compliance of the Lokomat is increased to let patients move more freely, many patients are not capable of keeping their knee joints extended during stance phase. Therefore, we applied additional supportive torques to prevent knee buckling. For this particular case, the control error $e^{(k)}(t)$ during the k th cycle is a scalar function of the control deviation in the knee joint during stance phase. Based on this error, a scalar supportive torque for the knee joint is calculated.

$$\tau_{\text{knee}}^{(k+1)}(t) = (1 - k_{f,\text{knee}})\tau_{\text{knee}}^{(k)}(t) + \gamma_{\text{knee}}e^{(k)}(t) \quad (3)$$

This supportive torque is added to the output of the closed-loop impedance controller of the Lokomat [8] as a feedforward term.

Adaptive BWS: To modulate how actively a human subject participates in the Lokomat training, we adapted the body weight support F_{unload} provided by the Lokolift.

With dynamic models of human leg and Lokomat leg during single support stance phase, we can determine the theoretically needed contribution of the subject $\tilde{A}_{\text{needed}}$ and the actual contribution of the subject A_{actual} to the forces the subject needs to bear his/her own body weight [25].

We define the ratio of the actual human contribution to the theoretically needed contribution during the k -th stride as *relative human activity* $A_{\text{rel}}^{(k)}$.

$$A_{\text{rel}}^{(k)} = A_{\text{actual}}^{(k)} / \tilde{A}_{\text{needed}}^{(k)} \quad (4)$$

The error function $\mathbf{e}^{(k)}(t)$ is now replaced by the activity tracking error $\Delta A^{(k)}$.

$$\Delta A^{(k)} = A_{\text{des}} - A_{\text{rel}}^{(k)} \quad (5)$$

with A_{des} being the desired level of relative human activity. Then, the learning law for adapting the body weight support becomes

$$F_{\text{bws}}^{(k+1)} = (1 - k_{f,\text{bws}})F_{\text{bws}}^{(k)} + \gamma_{\text{bws}} \cdot \Delta A^{(k)} \quad (6)$$

with $\gamma_{\text{bws}} > 0$ being the learning gain that determines how much the deviation from the desired activity \tilde{A}_{des} during the current stride affects the update of the unloading force $F_{\text{bws}}^{(k+1)}$ for the next stride.

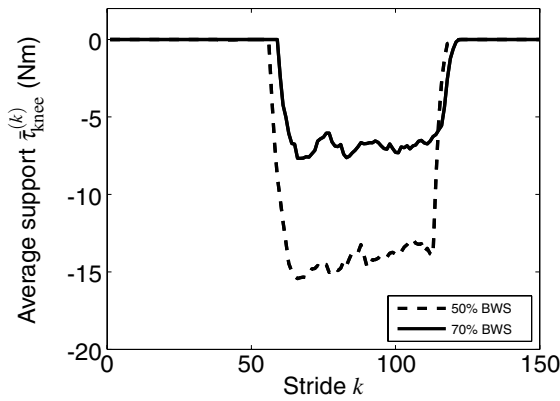


Fig. 2. Adaptive stance support $\bar{\tau}_{knee}^{(k)}$ for a test subject during walking with different levels of BWS. The graph shows the average knee support during stance phase for each step. The subject was active during the first 50 steps (phase A1), passive during the next 50 steps (phase P), and active again during the last 50 steps (phase A1).

C. Experimental evaluation

Adaptive stance support: Three healthy, male subjects were instructed to walk in the Lokomat under 2 different conditions: with 50% body weight support and adaptive support for knee extension, and with 70% body weight support and adaptive support for knee extension. Under each condition, the subjects walked actively for 2 minutes (phase A1), followed by 2 minutes of passive walking (phase P) and another 2 minutes of active walking (phase A2). For phase A1 and A2, the subjects were instructed to actively extend their knees during stance phase. For phase P, they were instructed to simulate not being able to carry their body weight on their own. The resulting support $\tau_{knee}(t)$ was recorded for the left leg, and the average support $\bar{\tau}_{knee}^{(k)}$ was calculated for each stride.

Adaptive BWS: Eight healthy subjects participated in the evaluation. After an acclimation phase of 30 seconds with a BWS level of 30% of the subjects' body mass, the adaptive BWS controller was enabled. The controller modified the provided BWS to make the subjects walk with the desired level of activity. Four different levels of activity were targeted (25%, 50%, 75%, and 100%). The order of the levels of activity was randomized and not revealed to the subjects.

III. RESULTS

Adaptive stance support: When the subjects walked with the Lokomat while adaptive support during stance phase was provided, the support stayed at a minimal level during active walking, increased to a high level during passive walking, and returned back to the initial level when the subjects walked active again (Fig. 2).

During the passive walking phase, the support model adapted to a unimodal output profile with a maximum of support during mid stance phase (Fig. 3).

In all subjects, the knee support during passive walking with 50% body weight support was significantly higher than during passive walking with 70% body weight support.

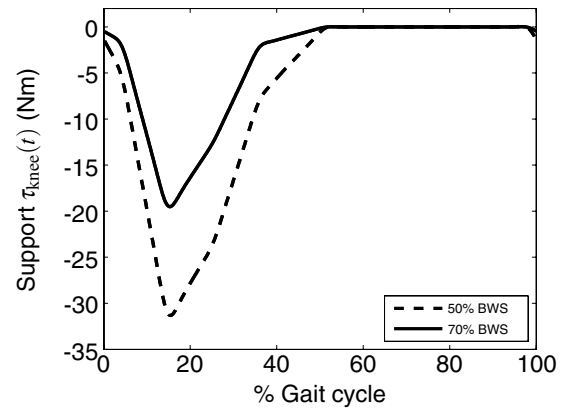


Fig. 3. Output τ_{knee} of adaptive feedforward support component during the 100th stride for a test subject walking with 50% body weight support (dashed line) and 70% body weight support (solid line).

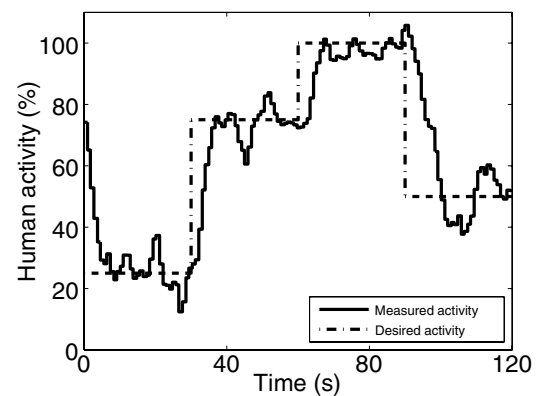


Fig. 4. Activity tracking for one exemplary subject walking with the adaptive BWS controller. The measured human activity $A_{rel}^{(k)}$ (solid line), and the desired level of activity A_{des} (dash-dotted line) are plotted over the time course of the experiment.

Adaptive BWS: The iterative learning algorithm for adapting the body weight support successfully tracked the desired levels of physical activity in the test subjects (Fig. 4).

IV. DISCUSSION

The adaptive stance support for the knee joint reacted as desired to the simulated weakness of the human subjects. The resulting output of the controller can be interpreted as a model of the simulated weakness. The model produced the highest output during mid stance phase when in fact most support is needed. Furthermore, the model output also reflected the changes in environment conditions: When the BWS system took over more body weight, the adaptive feedforward support contributed less.

The latter observation demonstrates that in the presence of other potentially active components of the cooperative controller, the model fitted by the adaptive support component does not necessarily represent the absolute weakness of the patient. Thus, the outputs of the fitted model may only be used as an assessment of patient performance if the contributions of all other components of the system are either

taken into account or kept constant for all measurements that are supposed to be compared.

The example of the adaptive BWS controller shows that it is not only possible to react to the state of a human subject but also to manipulate the state of a human subject in a targeted way. The cycle-to-cycle update of the iterative learning controller makes it possible to use complex model-based calculations which rely on information from a longer time horizon for the update of the adaptive support.

More comprehensive support models may be realized by taking results from the field of “robot learning” into account, where excellent controller performance has been achieved when the controller learned a feedforward model of the—a *priori* unknown—dynamics of a robot even in high-dimensional spaces [26].

V. CONCLUSION

Individual interventions in patient-cooperative control approaches can be realized by supportive force fields or single support parameters, such as the level of body weight support. Iterative learning control algorithms are well suited to adapt these means of support to the individual capabilities of a human subject. Thus, they provide a feasible way to train at a continuously challenging level.

ACKNOWLEDGMENTS

The authors would like to thank all subjects who participated in the evaluation. The contents of this publication were developed in part under a grant from the US Department of Education, NIDRR grant number H133E070013. However, those contents do not necessarily represent the policy of the US Department of Education, and you should not assume endorsement by the Federal Government of the United States of America.

REFERENCES

- [1] K. J. Sullivan, D. A. Brown, T. Klassen, S. Mulroy, T. Ge, S. P. Azen, and C. J. Winstein, “Effects of Task-Specific Locomotor and Strength Training in Adults Who Were Ambulatory After Stroke: Results of the STEPS Randomized Clinical Trial.” *Phys. Therapy*, vol. 87, no. 12, pp. 1580–1602, 2007.
- [2] B. Dobkin, H. Barbeau, D. Deforge, J. Ditunno, R. Elashoff, D. Apple, M. Basso, A. Behrman, S. Harkema, M. Saulino, and M. Scott, “The evolution of walking-related outcomes over the first 12 weeks of rehabilitation for incomplete traumatic spinal cord injury: the multicenter randomized Spinal Cord Injury Locomotor Trial.” *Neurorehabil. Neural Repair*, vol. 21, no. 1, pp. 25–35, 2007.
- [3] G. Colombo, M. Wirz, and V. Dietz, “Driven gait orthosis for improvement of locomotor training in paraplegic patients,” *Spinal Cord*, vol. 39, no. 5, pp. 252–255, 2001.
- [4] J. Hidler, W. Wisman, and N. Neckel, “Kinematic trajectories while walking within the Lokomat robotic gait-orthosis,” *Clinical Biomechanics*, vol. 23, no. 10, pp. 1251–1259, 2008.
- [5] J. Hidler, D. Nichols, M. Pelliccio, K. Brady, D. D. Campbell, J. H. Kahn, and G. T. Hornby, “Multicenter Randomized Clinical Trial Evaluating the Effectiveness of the Lokomat in Subacute Stroke.” *Neurorehabil Neural Repair*, vol. 23, no. 1, pp. 5–13, 2009.
- [6] J. F. Israel, D. D. Campbell, J. H. Kahn, and G. T. Hornby, “Metabolic costs and muscle activity patterns during robotic- and therapist-assisted treadmill walking in individuals with incomplete spinal cord injury.” *Phys. Therapy*, vol. 86, no. 11, pp. 1466–1478, 2006.
- [7] S. Jezernik, G. Colombo, and M. Morari, “Automatic gait-pattern adaptation algorithms for rehabilitation with a 4-DOF robotic orthosis,” *IEEE Trans. Robot. Autom.*, vol. 20, no. 3, pp. 574–582, 2004.
- [8] R. Riener, L. Lünenburger, S. Jezernik, M. Anderschitz, G. Colombo, and V. Dietz, “Patient-cooperative strategies for robot-aided treadmill training: first experimental results,” *IEEE Trans. Neural Syst. Rehabil. Eng.*, vol. 13, no. 3, pp. 380–394, 2005.
- [9] J. L. Emken, J. E. Bobrow, and D. J. Reinkensmeyer, “Robotic movement training as an optimization problem: designing a controller that assists only as needed,” in *Proc. IEEE 9th Int. Conf. Rehabil. Robot.*, Chicago, 2005, pp. 307–312.
- [10] D. J. Reinkensmeyer, D. Aoyagi, J. L. Emken, J. A. Galvez, W. Ichinose, G. Kerdanyan, S. Maneeokkumwong, K. Minakata, J. A. Nessler, R. Weber, R. R. Roy, R. de Leon, J. E. Bobrow, S. J. Harkema, and V. R. Edgerton, “Tools for understanding and optimizing robotic gait training,” *J. Rehabil. Res. Dev.*, vol. 43, no. 5, pp. 657–670, 2006.
- [11] S. K. Banala, S. K. Agrawal, and J. P. Scholz, “Active Leg Exoskeleton (ALEX) for Gait Rehabilitation of Motor-Impaired Patients,” in *Proc. IEEE 10th Int. Conf. Rehabil. Robot.*, Noordwijk, 2007, pp. 401–407.
- [12] E. H. F. Van Asseldonk, R. Ekkelenkamp, J. F. Veneman, F. C. T. Van der Helm, and H. van der Kooij, “Selective control of a subtask of walking in a robotic gait trainer (LOPES),” in *Proc. IEEE 10th Int. Conf. Rehabil. Robot.*, 2007, pp. 841–848.
- [13] A. Duschau-Wicke, J. von Zitzewitz, M. Wellner, A. König, L. Lünenburger, and R. Riener, “Path Control A Strategy for Patient-Cooperative Training of Gait Timing,” in *Proc. 7th Automated Workshop*, Munich, 2007, pp. 1–2.
- [14] H. Vallery, E. van Asseldonk, M. Buss, and H. van der Kooij, “Assuring Functionality of Gait while Minimizing Undesired Interference: Reference Trajectory Generation for Rehabilitation Robots Based on Complementary Limb Motion Estimation,” *IEEE Trans. Neural Syst. Rehabil. Eng.*, vol. In Press, 2008.
- [15] J. L. Emken, S. J. Harkema, J. A. Beres-Jones, C. K. Ferreira, and D. J. Reinkensmeyer, “Feasibility of Manual Teach-and-Replay and Continuous Impedance Shaping for Robotic Locomotor Training Following Spinal Cord Injury,” *IEEE Trans. Biomed. Eng.*, vol. 55, no. 1, pp. 322–334, 2008.
- [16] J. F. Veneman, R. Kruidhof, E. E. G. Hekman, R. Ekkelenkamp, E. H. F. Van Asseldonk, and H. van der Kooij, “Design and Evaluation of the LOPES Exoskeleton Robot for Interactive Gait Rehabilitation,” *IEEE Trans. Neural Syst. Rehabil. Eng.*, vol. 15, no. 3, pp. 379–386, 2007.
- [17] H. Vallery, A. Duschau-Wicke, and R. Riener, “Optimized Passive Dynamics Improve Transparency of Haptic Devices,” in *IEEE Int. Conf. Robot. Aut. (ICRA 2009)*. In Press., 2009.
- [18] L. B. Rosenberg, “Virtual fixtures: Perceptual tools for telerobotic manipulation,” in *Virtual Reality Annual International Symposium, 1993.*, 1993 IEEE, 1993, pp. 76–82.
- [19] T. Lam, M. Wirz, L. Lünenburger, and V. Dietz, “Swing Phase Resistance Enhances Flexor Muscle Activity During Treadmill Locomotion in Incomplete Spinal Cord Injury,” *Neurorehabil Neural Repair*, vol. 22, no. 5, pp. 438–446, 2008.
- [20] J. L. Patton, M. E. Stoykov, M. Kovic, and F. A. Mussa-Ivaldi, “Evaluation of robotic training forces that either enhance or reduce error in chronic hemiparetic stroke survivors.” *Exp Brain Res*, vol. 168, no. 3, pp. 368–383, 2006.
- [21] N. Hogan, “Impedance control - An approach to manipulation. I - Theory. II - Implementation. III - Applications,” *ASME Transactions Journal of Dynamic Systems and Measurement Control B*, vol. 107, pp. 1–24, 1985.
- [22] E. T. Wolbrecht, V. Chan, D. J. Reinkensmeyer, and J. E. Bobrow, “Optimizing Compliant, Model-Based Robotic Assistance to Promote Neurorehabilitation,” *IEEE Trans. Neural Syst. Rehabil. Eng.*, vol. 16, no. 3, pp. 286–297, 2008.
- [23] D. A. Bristow, M. Tharayil, and A. G. Alleyne, “A survey of iterative learning control,” *IEEE Control Syst. Mag.*, vol. 26, no. 3, pp. 96–114, 2006.
- [24] M. Frey, G. Colombo, M. Vaglio, R. Bucher, M. Jörg, and R. Riener, “A novel mechatronic body weight support system,” *IEEE Trans. Neural Syst. Rehabil. Eng.*, vol. 14, no. 3, pp. 311–321, 2006.
- [25] A. Duschau-Wicke, S. Felsenstein, and R. Riener, “Adaptive body weight support controls human activity during robot-aided gait training,” in *IEEE 11th Int. Conf. Rehabil. Robot.*, Submitted, 2009.
- [26] S. Vijayakumar, A. D’Souza, and S. Schaal, “Incremental Online Learning in High Dimensions,” *Neural Computation*, vol. 17, no. 12, pp. 2602–2634, 2005.

¹H-MRS study of a depressive animal model for assessment of antidepressant effects

Sang-Young Kim¹, Chi-Bong Choi², Sung-Ho Lee¹, Dong-Cheol Woo¹, Hyun-Sung Lee³,
Sung-Tak Hong⁴, Hwi-Yool Kim⁵, Bo-Young Choe¹

¹Department of Biomedical Engineering, College of Medicine, The Catholic University of Korea, Seoul, Korea

²Department of Radiology, Kyunghee University Medical Center, Hoekidong, Dongdaemungu, Seoul, Korea

³MRI Team, Korea Basic Science Institute, 804-1 Yangcheon-Ri, Ochang-Myun, Cheongwon-Gun, Choongbuk, Korea

⁴Department of High-Field Magnetic Resonance Center, Max-Planck Institute for Biological Cybernetics, Tübingen, Germany

⁵Department of Veterinary Surgery, College of Veterinary Medicine, Konkuk University, Seoul, Korea

Abstract— The purpose of this study was to evaluate metabolic alterations in the left dorsolateral prefrontal cortex (DLPFC) of depressive rats using proton MRS before and after antidepressant treatment. The acute depressive state was induced by a forced swimming test (FST), which composed of two swimming session. The tricyclic antidepressant (TCA) treatment was administered with a subchronic pattern before last swimming session was started. All ¹H-MRS experiments were performed on a 4.7T BIOSPEC scanner with a 400 mm bore magnet and 150 mT/m actively shielded gradient coils, allowing for acquisition of *in vivo* ¹H PRESS spectra (TR = 3000 ms, TE = 30 ms, 512 acquisitions, the number of data points: 2048, voxel volume: 43 μ l). The ml/tCr ratio of the saline-treated group was significantly higher than that of the normal group (p value: 0.002) and recovered the level similar to that seen in the normal group after desipramine injection (p value: 0.002). The tCho/tCr ratios were increased in FST group treated with saline than normal group, however, no statistical differences were observed. The present study suggests that the higher ml/tCr ratio seen in the left DLPFC in depressive rats could be reversed by injection of desipramine.

Keywords— metabolic alterations, left dorsolateral prefrontal cortex (DLPFC), forced swimming test (FST), tricyclic antidepressant (TCA), ¹H-MRS

I. INTRODUCTION

A forced swimming test (FST) [1] has been evaluated as the most sensitive method for a number of major classes of antidepressant treatments and widely used due to the high reproducibility. However, the evaluations for antidepressant may have limits which the subjects could be intervened, since the procedure for scoring active behaviors was assessed by the experimenters. Magnetic resonance spectroscopy (MRS) can provide biochemical information such as N-acetylaspartate (NAA), total creatine (tCr), choline containing compounds (tCho), myo-inositol (ml), glutamate and glutamine (Glx) as a non-invasive manner with identifications and quantifications of various

metabolites *in vivo*. Our purpose of this study was to assess metabolic changes in the left dorsolateral prefrontal cortex (DLPFC) of rat brain, which plays an essential role in mood regulation and working memory, before and after antidepressant treatment using *in vivo* single voxel spectroscopy.

II. MATERIALS AND METHODS

A. Animals

Study subjects included 32 experimentally naive male Sprague-Dawley rats (Charles River, Yokohama, Japan) weighing 160-180 g, housed in groups of three or four per cage. The 32 rats were divided into three study groups: 11 rats were not exposed to FST, 10 rats were treated with saline as a sham control, and 11 rats were treated with desipramine-HCl as an antidepressant. Rats were acclimated for one week to adjust them to experimental conditions and to remove stress induced during transportation. Colony conditions were controlled by maintaining specific pathogen-free (SPF) environmental conditions in a room kept at a constant temperature (23 \pm 2°C) on a 12-hour/12-hour light/dark cycle. Food and water were available during the entire study. All experimental procedures were conducted in accordance with protocols approved by the Institutional Animal Care and Use Committee (IACUC)

B. Forced swimming test and Drug treatment

The design of the forced swimming test was very similar to that described by Porsolt et al [1], with the exception of the water depth. We conducted the FST by placing rats in individual glass cylinders (height: 40 cm; diameter: 18 cm) that contained 28 cm of water maintained at 25°C. We used greater water depth (Porsolt used cylinders filled with water to 15 cm, a depth in which the rats could touch the bottom with their feet) so the rats could

not support themselves by touching the bottom with their feet. The increased water depth caused considerably more restricted mobility compared to the traditional test [2]. Each rat was left in the cylinder for 15 min and then removed and allowed to dry before being placed back in its home cage. In the second test, each rat was again plunged into the cylinder for 5 min. *In vivo* MRI/MRS scanning was performed one hour later so that the rats could recover the body temperature, that may influence brain metabolism, and the pure effects of the antidepressant could be assessed. The water was replaced between individual tests so any potential toxic substances could be removed. Desipramine-HCl was the antidepressant used in the present study. The drug treatment was administered with a subchronic pattern. Three injections were administered at 24 h, 5 h, and 1 h before the given test was started. The drug was administered subcutaneously (SC) in a volume equivalent to 2 ml/kg. The test dose for the drug was 10 mg/kg. Each injection was dissolved in distilled water in order to enhance solubility. Rats in the sham control group were treated with saline using the same pattern described above.

C. Localized MRS acquisitions and Post-processing

Experiments were performed on a 4.7T BIOSPEC scanner (Bruker Medical GmbH, Ettlingen, Germany) with a 400 mm bore magnet and 150 mT/m actively shielded gradient coils, allowing simultaneous acquisition of ^1H PRESS spectra (TR = 3000 ms, TE = 30 ms, 512 acquisitions, 2048 complex data points, voxel dimensions = 3.5mm \times 3.5mm \times 3.5mm). The position of voxel was visually adjusted in the epicenter of left DLPFC (Figure 1). All ^1H MR spectroscopic data were fitted by using Java-based MR user interface (jMRUI) software. The spectra were filtered for removal of residual water by using the Hankel-Lanczos single-variable decomposition (HLSVD) method and apodized with a 5-Hz Lorentzian function. Metabolite signals were analyzed by using the Advanced Magnetic Resonance (AMARES) fitting algorithm within jMRUI. Five resonances were determined with the assumption of Lorentzian line shapes; (a) NAA at 2.02 ppm (b) Glx at 2.35 ppm (c) tCr at 3.03 ppm (d) tCho at 3.22 ppm (e) mI at 3.55 ppm.

D. Statistical Analysis

Relative concentrations referenced to Cr resonance were compared across the three groups using SPSS (Windows Version 13.0, SPSS Inc., Chicago, IL). All data were analyzed with Student's two-tailed t test, in order to compare significant differences among the three groups. P-

values less than 0.05 were considered statistically significant.

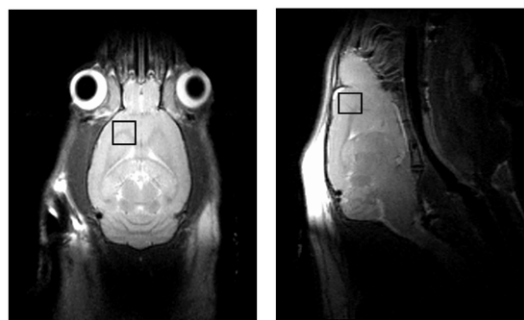


Fig. 1. A T2-weighted MR image of the rat brain indicating voxel position in the left DLPFC. (a) Coronal and (b) sagittal ^1H MR images are shown.

III. RESULTS

Fig. 1 shows a well-defined voxel position in the left DLPFC, which was identified on the set of coronal and sagittal ^1H MR images. There were no morphological differences between the saline- and desipramine-treated rats. Fig. 2 depicts representative spectra obtained from the left DLPFC of rat brains treated with saline or desipramine after induction of depression using FST. We noted a flat baseline in the *in vivo* spectrum and a residue with no spurious signals. Significantly higher mI/tCr ratios were observed in the saline-treated group (Table 1), compared to the normal group (d.f.=19, $t=-3.51$, $p=0.002$). As shown in Fig. 3, individual mI/tCr ratios increased when rats were treated with saline alone after the FST. In desipramine injected rats, the concentration of mI was reduced to a level similar to that seen in normal rats (d.f.=19, $t=3.49$, $p=0.002$). The mean mI/NAA ratio was also significantly higher in rats treated with saline, compared to normal rats (d.f.=19, $t=3.394$, $p=0.003$).

Table 1. Relative concentrations referenced to total creatine resonance in the left DLPFC of rat brain.

	Normal	Saline	Drug
NAA	1.42 \pm 0.14	1.42 \pm 0.21	1.42 \pm 0.18
Glx	0.52 \pm 0.18	0.54 \pm 0.17	0.51 \pm 0.16
tCho	0.61 \pm 0.23	0.73 \pm 0.14	0.64 \pm 0.18
mI	0.11 \pm 0.03	0.16 \pm 0.03	0.12 \pm 0.02

All values are given as means \pm standard deviations (SD). Abbreviations: NAA, N-acetyl-aspartate; Glx, glutamate and glutamine; tCho, choline-containing compound; mI, myo-inositol * Student's two-tailed t test: ns indicates that the value is not significant ($P > 0.05$).

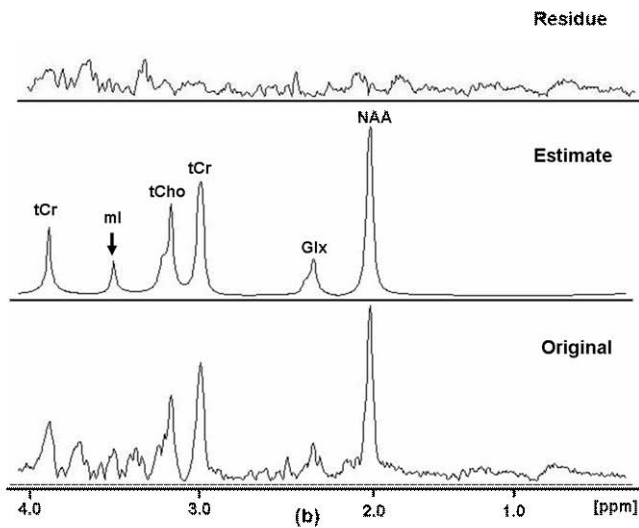
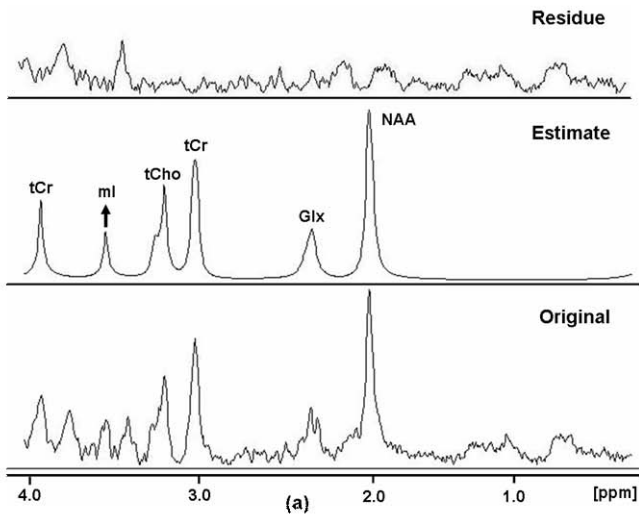


Fig. 2. ¹H MR spectrum fitted by jMRUI AMARES quantification algorithm. All spectra were apodized with a 5-Hz Gaussian function. Each of the spectra was obtained from the left DLPFC of rat brain using a 4.7 T MR scanner. (a) Spectra from a rat treated with saline after FST. (b) Spectra from a rat treated with desipramine-HCl.

After desipramine injection into rats with depression, the mI/NAA ratios were significantly decreased to a level similar to that seen in normal rats (d.f.=19, $t=2.921$, $p=0.009$) (Fig. 4). Relative concentrations of tCho were increased in saline-treated rats when compared to normal control rats, and recovered the level similar to normal rats

due to the desipramine injection. However, no significant differences were noted in the tCho/tCr ratio. There were no significant differences in any other metabolite ratios among the three groups.

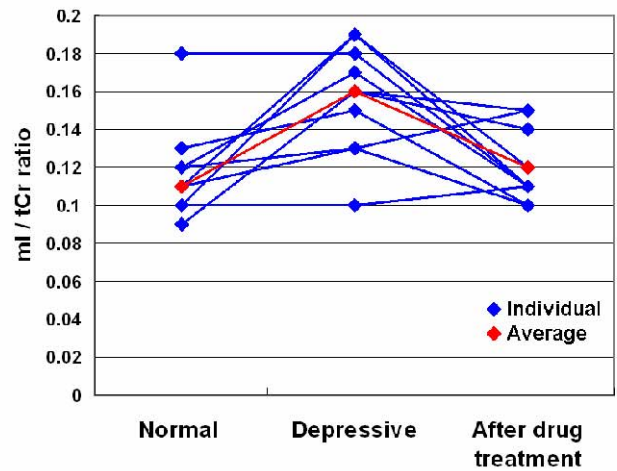


Fig. 3. Individual myo-inositol/total creatine (mI/tCr) ratios in the left dorsolateral prefrontal cortex before and after antidepressant treatment.

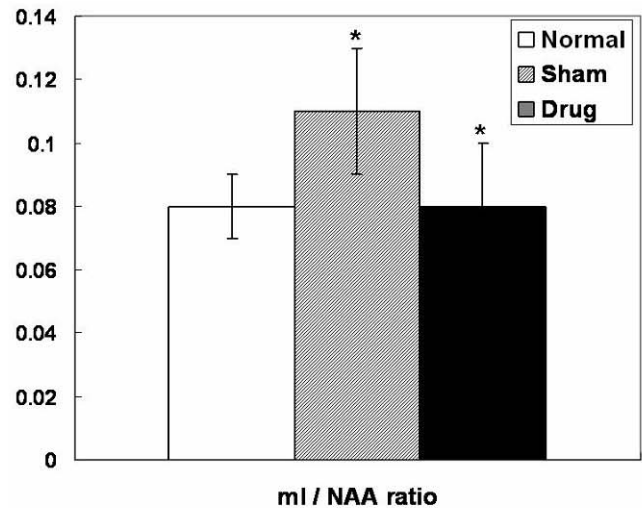


Fig. 4. Myo-inositol/N-acetylaspartate (mI/NAA) ratios in the left dorsolateral prefrontal cortex in controls (white), rats treated with saline (deviant line), and rats treated with desipramine (gray). The error bar indicates a 95% confidence interval. The mI/NAA ratios were compared between normal and saline-injected rats, and between saline-injected and desipramine-injected rats. *P-values less than 0.05 were considered statistically significant.

IV. DISCUSSION

To our knowledge, no previous studies have used proton spectroscopy to assess the effects of desipramine on brain metabolism in animal models of depression. The most striking finding in this study was the reduction in the mI concentration seen after desipramine injection. It is possible that desipramine, which is a tricyclic antidepressant (TCA), could influence the intracellular signaling pathway of the phosphatidyl-inositol second messenger system (PI-cycle), activated by ligand binding with G_q-protein coupled receptors, including adrenergic receptors. Myo-inositol is an important component of the PI-cycle. Abnormalities in this intracellular signaling pathway have been suggested to be involved in the pathophysiology and/or treatment of depression [3]. The increased mI levels we saw in the left DLPFC of depressive rats are consistent with previous clinical studies of major depressive disorder [4]. In contrast, a previous postmortem study reported reduced myo-inositol concentrations in the frontal cortex of depressed subjects, when compared to healthy controls [5]. Therefore, it is not yet possible to definitively confirm if the myo-inositol concentration increases in specific brain regions in depressive patients.

FST is regarded as an acute stress model rather than human depressive symptom in strict pathological mechanism, although this model is feasible to assess the effect of antidepressant drug. Treatments with certain selective serotonin reuptake inhibitors (SSRIs) have been shown to reduce the activity of corticotropin-releasing factor (CRF) neurons, which is the major physiological regulator of the hypothalamic-pituitary-adrenal (HPA) axis system, and may contribute to their therapeutic action [6]. In animal models of depression, it was confirmed that endogenous CRF modulated 5HT transmission [7], meanwhile, TCA treatment decreased hypothalamic CRF mRNA levels [8]. This might explain the decrease of mI/Cr ratio in antidepressant treated rat, since 5HT supposed to stimulate phosphoinositol system.

The present study has some limitations. Our major concern is that the sample size was not large enough to accurately indicate the efficacy of antidepressant treatment. Furthermore, our findings related to acute stress have to be extended to correlate with clinical investigations of depressive symptoms caused by chronic stress. Our investigation should be duplicated with higher field strength in order to yield a higher spectral dispersion and resolution.

Therefore, further study is needed in order to understand the role of DLPFC in the pathophysiology of depression and mechanism of action of antidepressant treatment.

In summary, our findings suggest that the higher mI/Cr ratio seen in the left DLPFC in depressive rats could be reversed by desipramine injection. This reversal appears to be attributable to inhibition of norepinephrine-stimulated inositol phospholipid hydrolysis. Thus, the present proton MRS study could aid our understanding of the pathophysiology of depression and the mechanisms of action of antidepressant treatments.

ACKNOWLEDGMENT

This study was supported by a grant from the Seoul R&BD Program (10550), the Korea Health 21 R&D Project, Ministry of Health & Welfare, Republic of Korea (02-PJ3-PG6-EV07-0002) (A081057), and a grant (R01-2007-000-20782-0) from the Purpose Basic Research Grant of the KOSEF. This study made use of the NMR facility at the Korea Basic Science Institute, which is supported by the Bio-MR Research Program of the Korean Ministry of Science and Technology (E28070).

REFERENCES

1. Porsolt RD, Pichon ML, Jalfre M. (1977) Depression: a new animal model sensitive to antidepressant treatments. *Nature* 266: 730-732.
2. Cryan JF, Markou A, Lucki I. (2002) Assessing antidepressant activity in rodents: recent developments and future needs. *Trends Pharmacol Sci* 23: 238-245.
3. Silverstone PH, McGrath BM, Kim H. (2005) Bipolar disorder and myoinositol: a review of the magnetic resonance spectroscopy findings. *Bipolar Disord* 7: 1-10.
4. Canetano SC, Fonseca M, Olvera RL, et al. (2005) Proton spectroscopy study of the left dorsolateral prefrontal cortex in pediatric depressed patients. *Neurosci Lett* 384: 321-326.
5. Shimon H, Agam G, Belmaker RH, et al. (1997) Reduced frontal cortex inositol levels in postmortem brain of suicide victims and patients with bipolar disorder. *Am J Psychiatry* 154: 1148-1150.
6. Nemeroff CB, Owens MJ. (2004) Pharmacologic differences among the SSRIs: focus on monoamine transporters and the HPA axis. *CNS Spectr* 9: 23-31.
7. Price ML, Kirby LG, Valentino RJ, et al. (2002) Evidence for corticotropin-releasing factor regulation of serotonin in the lateral septum during acute swim stress: adaptation produced by repeated swimming. *Psychopharmacology* 162: 406-414.
8. Aubry JM, Pozzoli G, Vale WW. (1999) Chronic treatment with the antidepressant amitriptyline decreases CRF-R1 receptor mRNA levels in the rat amygdala. *Neurosci Lett* 266: 197-200.

The corresponding author:

Author: Bo-Young Choe

Institute: Department of Biomedical Engineering, The Catholic University of Korea

Street: #505 Banpo-dong Seocho-Gu

City: Seoul

Country: Korea

Email: bychoe@catholic.ac.kr

Improving BCI Performance by Modified Common Spatial Patterns with Robustly Averaged Covariance Matrices

M. Kawanabe^{1,2} and C. Vidaurre²

¹Intelligent Data Analysis group, Fraunhofer FIRST, Kekulestr. 7, 12489, Berlin, Germany

²Machine Learning Group, TU-Berlin, Franklinstr. 28/29 10587, Berlin, Germany

Abstract— EEG single-trial analysis requires methods that are robust against noise and disturbance. In this contribution, based on the framework of robust statistics, we propose a simple modification of Common Spatial Patterns by the robust calculation of covariance estimators against outlying trials caused, for example, by artifacts. We tested the proposed robust filters with EEG recordings from 80 subjects and obtained, not only a significant improvement in performance, but for some subjects, also better neuro-physiologically interpretable filters.

Keywords— Electro-encephalogram EEG, Brain-Computer Interface BCI, robust average covariance, Common Spatial Patterns CSP.

I. INTRODUCTION

Feature extraction is an important prerequisite for analyzing high dimensional real world data. For single-trial EEG classification tasks, spatial filters have become very popular feature extractors. Data driven approaches that optimize spatial filters for each subject individually have been proven useful [1], in particular in Brain-Computer Interfaces (BCIs), which translate the users intent (coded by a small set of mental tasks) into control actions such as computer applications or neuroprostheses [2-4]. In the past years machine learning methods have led to significant advances in the analysis and modeling of neural signals. While early EEG-BCI efforts required neurofeedback training on the part of the user that lasted on the order of days, in ML-based systems it suffices to collect examples of EEG signals in a so-called calibration measurement during which the user is cued to perform repeatedly a small set of mental tasks. This data is then used to adapt the system to the specific brain signals of each user (machine training). After this preparation step, the feedback application can start, allowing the users to actually transfer information through their brain activity to control applications. In this phase, the system is composed of the classifier that discriminates between different mental states and the control logic that translates the classifier output into control signals, e.g., a cursor position or a selection from an alphabet. There are several aspects in which BCI research can profit from improvement,

see the ‘Challenges’ section of [5]. One of them is to make the system more robust against non task-related fluctuations and/or non-stationarity of the measured EEG signals. These fluctuations may be caused by changes in the subject’s brain processes, e.g. change of task involvement, fatigue etc., or by artifacts such as swallowing, blinking or yawning. One of the elements of EEG pre-processing that is very sensitive to artifacts is the Common Spatial Pattern (CSP) approach, which is as well very popular in BCI research [6-9]. In this paper we apply CSP calculated with robust average estimates of trial-wise covariance matrices (rmean-CSP) that can attenuate outlying trials in an automatic way. This rmean-CSP led to significant increases in performance compared to original CSP using BCI data from 80 subjects. Besides, the method revealed filters that were better neuro-physiologically interpretable.

II. MATERIALS AND METHODS

A. Robust average for class-wise covariance estimation in CSP framework

CSP is successful calculating spatial filters for detecting modulations of the sensorimotor rhythm (SMR) or other Event related Des/Synchronization effects (ERD/ERS). Given two distributions in a high-dimensional space, CSP algorithm finds directions (i.e., spatial filters) that maximize variance for one class and simultaneously minimize variance for the other class. Since band-power can be calculated as the variance of band-pass filtered signals, this criterion corresponds to ERD/ERS effects.

Technically CSP analysis works as follows: let Σ_+ and Σ_- be estimates of the covariance matrices of the band-pass filtered EEG signals under the two conditions. These two matrices are simultaneously diagonalized such that the eigenvalues of these matrices sum to 1. Practically, this can be done by calculating the generalized eigenvectors \mathbf{W} :

$$\Sigma_+ \cdot \mathbf{W} = (\Sigma_+ + \Sigma_-) \cdot \mathbf{W} \cdot \mathbf{D} \quad (1)$$

Here, the diagonal matrix \mathbf{D} contains the (generalized) eigenvalues of Σ_+ (defined such that they are between 0 and 1) and the column vectors of \mathbf{W} are the filters for the CSP

projections. By this procedure a full decomposition of the sensor space is determined. Best contrast is provided by those filters with high eigenvalues (large variance for condition 1 and small variance for condition 2) and by filters with low eigenvalues (vice versa). Therefore, the common practice in a classification setting is to use several eigenvectors from both ends of the eigenvalue spectrum as features for classification. For more details, see the CSP tutorial [1].

The averages of the trial-wise covariance matrices under each condition have been used for the matrices Σ_+ and Σ_- in Eq. 1. However, average estimates can be substantially disturbed by outliers i.e., by the covariance matrices from bad trials. In this paper, we propose robust estimates of the class-wise covariance matrices Σ_+ and Σ_- based on the techniques developed by Huber [10].

For simplicity, we will explain our technique for a single class. In this study, the method was applied to each task of BCI experiments separately.

Suppose that we have a set of covariance matrices $\{\Sigma_1, \dots, \Sigma_n\}$. Their average $\bar{\Sigma}^{(av)} = \frac{1}{n} \sum_{i=1}^n \Sigma_i$ is obtained by minimizing the sum of squared distance, i.e.

$$\min_{\bar{\Sigma} \in \text{PD}(d)} \sum_{i=1}^n \left\| \Sigma_i - \bar{\Sigma} \right\|_P^2 \quad (2)$$

where $\text{PD}(d)$ denotes the set of $d \times d$ positive definite matrices and

$$\left\| \Sigma - \bar{\Sigma} \right\|_P^2 = \text{Tr} \left\{ \mathbf{P}^{-1} (\Sigma - \bar{\Sigma}) \mathbf{P}^{-1} (\Sigma - \bar{\Sigma}) \right\}$$

is a (squared) distance between covariance matrices with a positive definite matrix \mathbf{P} .

It is possible to make the average covariance $\bar{\Sigma}^{(av)}$ more robust by reducing the contributions of outlier covariances in Eq. (2). Let ρ be a monotonically increasing function, slower than linear, and consider the optimization problem

$$\min_{\bar{\Sigma} \in \text{PD}(d)} \sum_{i=1}^n \rho \left(\left\| \Sigma_i - \bar{\Sigma} \right\|_P^2 \right)$$

Its solution can be obtained by an iterative procedure: repeating

$$\bar{\Sigma}_{(t+1)} = \sum_{i=1}^n \frac{\rho' \left(\left\| \Sigma_i - \bar{\Sigma}_{(t)} \right\|_P^2 \right)}{\sum_{j=1}^n \rho' \left(\left\| \Sigma_j - \bar{\Sigma}_{(t)} \right\|_P^2 \right)} \Sigma_i \quad (3)$$

until convergence. Examples of the function are $\rho(s) = \sqrt{s}$ and $\rho(s) = \log(1 + \alpha s)$ with an appropriate $\alpha > 0$. The weight function in front of Σ_i in Eq. (3) controls the importance of each covariance depending on the distance from the center.

In our experiments, we used the average covariance $\bar{\Sigma}^{(av)}$ as for the matrix \mathbf{P} in the distance. This measures the

deviations from the center relative to the eigenvalues of $\bar{\Sigma}^{(av)}$. For the function ρ , we employed log loss with normalization by median of squared distances from the average covariance to each of the samples.

B. Experimental setup

Data were recorded in a one-day session from 80 healthy BCI-novices (39m, 41f; age 29.9 ± 11.5 y; 4 left-handed). The subjects were sitting in a comfortable chair with arms lying relaxed on armrests. Brain activity was recorded from the scalp with multi-channel EEG amplifiers using 119 Ag/AgCl electrodes in an extended 10-20 system sampled at 1000 Hz with a band-pass from 0.05 to 200 Hz.

First, the subjects performed a ‘calibration measurement’ in which every 8s one of three different visual cues (arrows pointing left, right, down) indicated to the subject which type of motor imagery to perform: left/right hand or foot. Three runs with 25 trials of each motor condition were recorded. Then, 2 of the classes were selected and the subjects performed a ‘feedback measurement’ with three runs of 100 trials each, although for some subjects only one or two runs were recorded.

C. Data processing

The processing of the calibration data was done on the two classes used during the feedback measurement (and were dependent on the subject). The EEG signals of the calibration measurement were bandpass-filtered in a subject-specific frequency band, temporally filtered in a subject-specific time interval (typically 750 to 3500 ms relative to the presentation of the visual cue) as specified in [6].

In the standard case, the data was spatially filtered with subject-optimized filters determined by original CSP analysis, i.e. by selection of extreme eigenvalues. In the robust case (rmean-CSP), the average matrices were replaced by the robust estimates of the average matrices calculated as described in section II.A. The filters were selected according to extreme eigenvalues, just as in the original case. After spatially filtering the data, the log-variance was calculated in each trial, and a linear discriminant analysis (LDA) trained on those features. The subjects’ performance was calculated by filtering (in frequency, time and space) and classifying the feedback data with the filters and LDA obtained with the calibration measurement.

III. RESULTS

Figure 1 depicts the scatter plot of feedback error rates obtained with original CSP and rmean-CSP filters. To test

whether rmean-CSP performed significantly better than the original CSP, we applied the paired Wilcoxon signed rank test on the error rate of the subjects in the feedback data. The hypothesis test showed that our new robust method is significantly better than original CSP with a p-value of 0.6%.

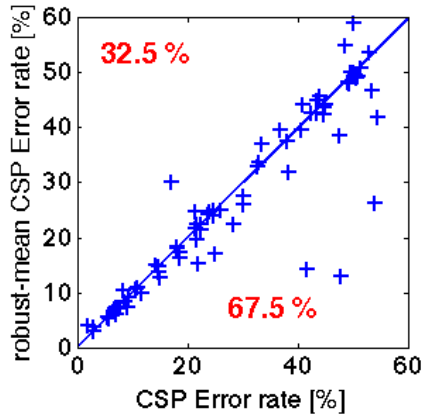


Fig. 1 Scatter-plot of rmean-CSP vs. CSP error rates. All values below the diagonal are examples where rmean-CSP outperforms CSP. This improvement is significant with a p-value of 0.6%.

IV. DISCUSSION

As a result of rmean-CSP, the BCI trials are individually weighted for each subject to construct proper class-wise averaged covariance matrices. Figure 2 illustrates one example, where very low weights indicate those trials as outliers. We could pick up successfully several outlying (i. e. noisy) trials.

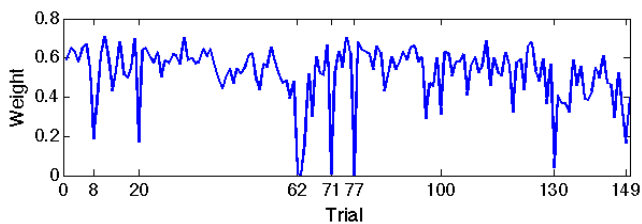


Fig. 2 Trials' weights for the subject in Fig. 3. Trials with low weights are recognized as outlying trials by the method.

By reducing the influence of outlying trials in the calculation of CSP filters, one could expect to extract easier-to-interpret patterns from data contaminated by noise and disturbances. Therefore we explored the selected rmean-CSP

and original CSP filters. Figure 3 presents two filters/patterns, one selected by original CSP and the other with rmean-CSP, of a subject performing left hand versus foot imagery. The data were filtered in the band 16.5-26.5 Hz and then CSP filters were calculated. The original CSP could not find neuro-physiologically interpretable filters/patterns, whereas rmean-CSP revealed a nice foot filter/pattern. The corresponding weighting of trials for this subject is shown in Figure 2.

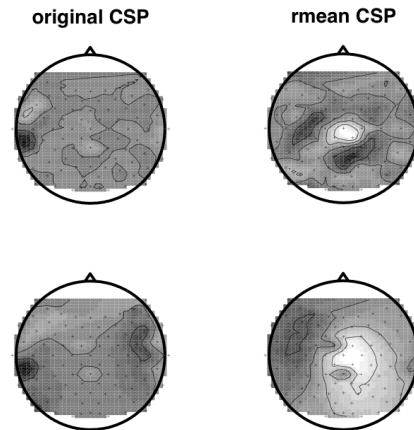


Fig. 3 A pair of filters (first row) and their patterns (second row) selected with original CSP (left column) and rmean-CSP (right column). The subject performed the imagination of left hand and foot. Our rmean-CSP revealed a foot filter/pattern that was not found by the original CSP.

ACKNOWLEDGMENT

This work was supported by the grants MEIF-CT-2006-40666, ICT-2008-224631. This publication only reflects the authors' views. Funding agencies are not liable for any use that may be made of the information contained herein.

REFERENCES

1. Blankertz B, Tomioka R, Lemm S, Kawanabe M and Müller K-R. Optimizing Spatial Filters for Robust EEG Single-Trial Analysis. *IEEE Signal Proc Magazine*, 25(1): 41–56, 2008.
2. Wolpaw JR, Birbaumer N, McFarland DJ, Pfurtscheller G and Vaughan TM. Brain-computer interfaces for communication and control. *Clin Neurophysiol*, 113: 767–791, 2002.
3. Millán J del R. *Handbook of Brain Theory and Neural Networks*. MIT Press, Cambridge, 2002.
4. Dornhege G, Millán J del R, Hinterberger T, McFarland DJ and Müller K-R eds. *Toward Brain-Computer Interfacing*. Cambridge, MA, 2007.

5. Nijholt A, Tan D, Pfurtscheller G, Brunner C, Millán J del R, Allison B, Grainmann B, Popescu F, Blankertz B and Müller K-R, "Brain-Computer Interfacing for Intelligent Systems". *IEEE Intelligent Systems*, 23(3): 72–79, 2008.
6. Blankertz B, Losch F, Krauledat M, Dornhege G, Curio G, Müller KR. The Berlin Brain-Computer Interface: Accurate Performance From First-Session in BCI-Naive Subjects. *IEEE Transactions on Biomedical Engineering*, 55:2452-2462, 2008.
7. Ramoser H, Müller-Gerking J and Pfurtscheller G. Optimal spatial filtering of single trial EEG during imagined hand movement. *IEEE Trans on Rehab Eng*. 8(4):441-446, 2000.
8. Wolpaw JR, McFarland DJ and Vaughan TM. Brain-Computer Interface Research at the Wadsworth Center. *IEEE Trans on Rehab Eng*. 8(2):222-226, 2000.
9. Dornhege G, Blankertz B and Curio C. Speeding up classification of multi-channel Brain-Computer Interfaces: Common spatial patterns for slow cortical potentials. *Proceedings of the 1st International IEEE-EMBS Conference on Neural Engineering*, 591-594, 2003.
10. Huber PJ. *Robust Statistics*. Wiley, New York, 1981.

Author: Carmen Vidaurre
Institute: Machine Learning, TU-Berlin
Street: Franklinstr. 28/29
City: Berlin
Country: Germany
Email: vidcarATcsDOTtu-berlinDOTde

Enhanced perception for visually impaired people evaluated in a real time setting

K. Möller¹, J. Möller², K. O. Arras³, M. Bach⁴, S. Schumann⁵, J. Guttman⁵

¹Furtwangen University, Biomedical Engineering, Germany

²Marie-Curie Gymnasium, Kirchzarten, Germany

³University of Freiburg, Computer Science Department, Germany

⁴University Medical Center, Ophthalmology, Freiburg, Germany

⁵University Medical Center, Exp.Anesthesiology, Freiburg, Germany

Abstract— Many aids have been proposed for the visually impaired or the blind. The regular cane is widely accepted but has known limitations such as its short length. Numerous approaches such as ultrasound enhanced canes have been developed with limited success, the main reason being the information transfer over the auditory system, one of the most important spatial senses.

The AERBUS project proposed to use fast 3D object recognition in conjunction with a priority based information reduction as used in autonomous mobile robotics to generate a virtual velocity map of objects in the surrounding. This information shall be transferred to the cognitive system of the blind via the stimulation of skin receptors. Here we focus on a special belt evaluated in a real time setting.

Up to 8 vibration motors as used in mobile phones were integrated into an elastic belt and were controlled simultaneously via a parallel port of a PC. A simple computer game was developed to obtain the real time performance of test subjects and to evaluate different coding schemes. A direct command mode is compared to a local coding that represents the direction towards an object by the position of the motor in the belt, while distance information is transferred by a pulse coding scheme.

Non-handicapped students were involved as test subjects. They were facing the task of avoiding collisions in the game. The performance of the individuals was determined with respect to the velocity and the number of objects. The subjects were blinded and information, in this case -recommended actions or object distances- is directly transmitted to the subjects via the vibration motors.

With both schemes performance improved significantly. No special training was required and all subjects were able to perform additional tasks while avoiding collisions in the direct command mode.

Keywords— visually impaired, spatial orientation, skin receptor, real time performance, collision avoidance

Further, with a cane, the user can acquire information about the environment only in one dimension simultaneously. Numerous approaches e.g. ultrasound enhanced canes have been proposed but have not found wide acceptance among visually impaired people. One of the main reasons is that these canes typically use the auditory system for information transfer. But the auditory system is one of the primary senses of the blind for many spatial cognitive tasks such as collision detection or wayfinding.

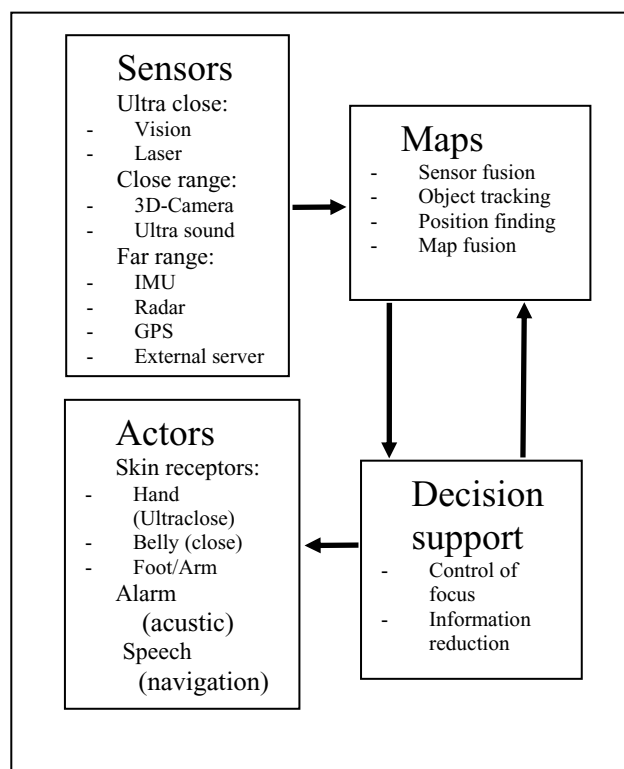


Fig. 1 The AERBUS system architecture

It is proposed to use fast 3D object recognition in conjunction with a priority based information reduction as used in autonomous mobile robotics to generate a virtual velocity map of objects in the surrounding. This information shall be transferred to the cognitive system of the blind via the stimulation of skin receptors. The interaction of the system components are depicted in Fig. 1.

In a prior report [5] we discussed a technique involved in the actors' component: the construction and evaluation of a special belt to communicate object locations and velocities

I. INTRODUCTION

Visually impaired or blind people have a reduced ability to perceive their environment. Guide dogs are most often the best substitute for the missing visual sense but they are expensive, often unavailable and sometimes not sufficient for a task (e.g. where is the nearest phone box?). Thus, many visually impaired people use regular canes. But canes have a small sensory field of "view", constraint by their length.

to subjects. To optimize the bandwidth of the information transfer, a number of influence factors were identified. 1. How should the motors be positioned around the belly to maximize the spatial resolution without introducing crosstalk, 2. Which kind of coding, i.e. the vibration times, or the strength of the vibrations, is appropriate. Now the performance in a real time setting is explored.

II. MATERIALS AND METHODS

A. Hardware

Somehow information about the environment has to be transmitted to the brain of the subject [1,2]. This project focuses on a skin stimulator for the close distance range. A cheap and reliable solution was found on the basis of vibration motors as used in cell phones. A small DC motor with an asymmetric weight at the angle is used to create pulse trains of varying frequency. Up to 15 motors can be integrated into an elastic belt, which is positioned around the belly.

Eight amplifiers, providing the motors with current (150mA) were connected to the parallel port (RS232-DB25) of a laptop. All motors were controlled independently because they have to signal the distance to objects in their receptive fields concurrently. The direction of objects in the environment is represented by the position on the body and additional information e.g. velocity or distance is described by a pulse frequency of the local stimulation.

B. Signal patterns

Frequency modulation is used to code the distance to an object. Variations were realized by pulse trains of different lengths. A sample is given in Fig. 3.

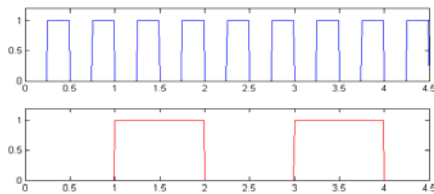


Fig. 3: Voltage signal to vibration motor to generate pulse trains of different length

A short impulse to the motor corresponds to little intensity, signalling a distant object. Longer vibrations mean, "Take care! Something is very close!" The former study [5] revealed a maximum number of distinguishable steps within this setup of about 4-5.

Amplitude variations are used to code velocity information about objects (wall, pedestrian, bicycle, car, train). They were created by Pulse Width Modulation (PWM).

C. Game software

A small game was implemented in Visual C# as a test bed (Fig. 3). A test subject i.e. the player who is represented in

the game as a green dot, has to avoid collisions with a number of red dots. The players' actions are limited to right or left movements (actions) on the base line. A variable number of red dots are falling towards this base line with a preset velocity. It is the goal of the player to minimize collisions with these falling objects. For the control of the parallel port different threads were spawned to ensure "parallel" processing of the game and the vibration motor control.

The game provides a number of custom settings for the user. Especially important are the two parameters VOO (velocity of objects) and NOO (number of objects, spawned at the same time) that are used to control the degree of difficulty (game level).

For several reasons an automatic modus (AI mode) was realized. Though, an optimal strategy could be implemented taking into account exact motion of every red dot on the screen, a reduced approach was taken. A decision strategy was realized that is based on information that can be transmitted via the belt to the test subjects. All potential actions $a \in \{left, right\}$ are evaluated as weighted sum of three factors:

$$E(a) = w_0 T_{coll} + w_1 T_{neighbor} + w_2 D_{lr}$$

$$a^* = \arg \max_{a \in \{left, right\}} E(a)$$

with T_{coll} representing the time until collision, if no action is initiated, $T_{neighbor}$ collision time at neighbor position in the direction of action a , D_{lr} is the relation of the distribution to the left and right of the current position and w_0, w_1, w_2 are weighting factors. Every frame update, the action with the maximal evaluation is selected for execution.

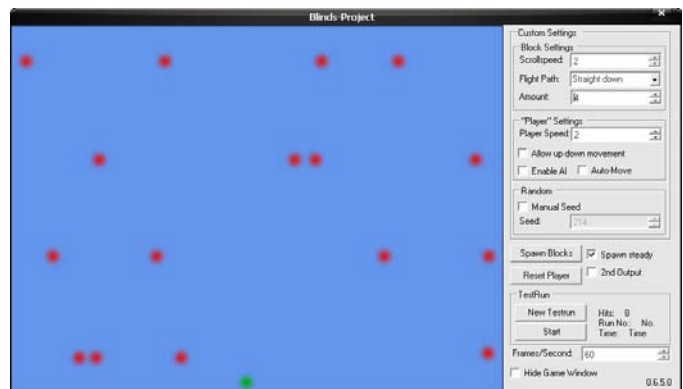


Fig. 3: Game to test real time performance. Red dots are obstacles drifting downwards. Collisions need to be avoided by controlling the green dot.

D. Test experiments

5 different modes were distinguished for evaluation:

- random (RA) mode, in which random movements are applied. The RA mode is used as a baseline for the evaluation
- the game (GA) mode, which is a normal game situation. The test subjects are allowed to visually observe the situation on the screen and are interacting with the game via keyboard.
- an “artificial intelligent” (AI) mode was implemented that evaluates positions and velocities of approaching objects to initiate collision avoiding actions.
- a direct command (DC) mode, where test subjects are blinded to the game situation, i.e. the screen is no longer showing any green or red dots and the motors transmit the recommended actions of the AI mode to the test subjects.
- an object sense (OS) mode, which provides evidence about the objects in the environment to a blinded test subject. Actions are determined by the subject according to the current percepts transmitted via the skin stimulation.

For all modes different levels of complexity were evaluated. The degree of difficulty is quantified by two numbers: the number of objects (NOO) spawned randomly and their velocity (VOO) represented in pixels per frame:

- the more objects on the screen the more complex perception and decision making,
- the faster the objects, the harder time is constrained for the decision process.

In the slowest velocity setting (VOO=1) an object was 8 seconds on the screen and in the fastest applied setting (VOO=10) it appears for 0.8 seconds. In total 12 (NOO,VOO) combinations ranging from (2,1) to (4,10) were evaluated.

For the blinded modes (DC and OS mode) the output of the game to the screen is blocked and navigation is purely based on signals sent to the vibration motors. Two different coding schemes were evaluated. First direct commands (DC mode) i.e. “move right” or “move left” or “stay at current position” are signalled by the skin stimulation. In this case just two motors were placed 15 cm apart on the belly. A vibration on the left side of the belly signals “Move Left” to the test subject, a “Move Right” by running the right motor. If both motors are silent it is safe to stay at the current position. The commands are generated by the AI mode, are coded and sent to the parallel port. In case of the OS mode the information about the environment used by the AI mode is coded and transmitted via the belt, not the decision.

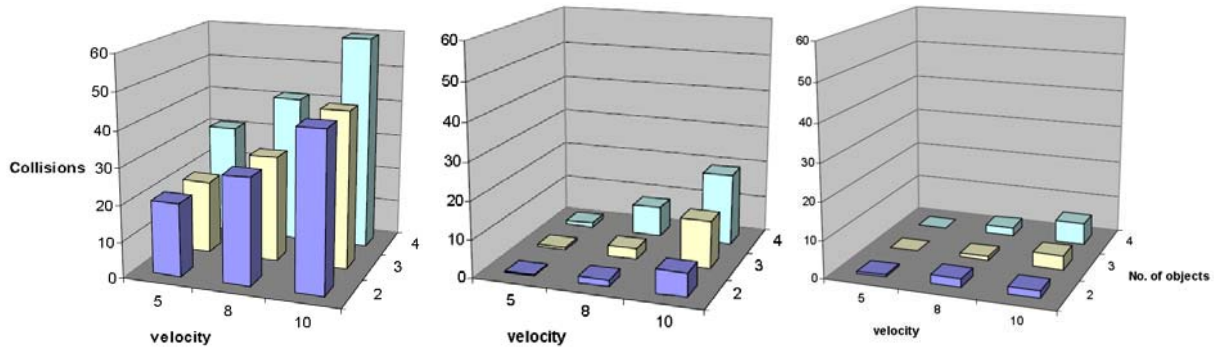


Fig. 4: Number of collisions averaged over 10 runs of 1 min duration. **Left:** Random actions (RA mode), **Centre:** test subjects (GA mode), **Right:** automated approach (AI mode)

III. RESULTS

All experiments were repeated 10 times to reduce the influence of the random number generator. Data was collected and statistically evaluated.

As a baseline for the comparison Figure 4 presents some averages of the collision count in nine different experimental settings. The x-axis represents the velocity setting, the y-axis the number of objects spawned at the same time and the z-axis shows the average number of collisions found for the specific (NOO,VOO) setting. On the left side results of random movements (RA mode) are displayed. In the center the GA mode and on the right the AI mode is shown. Obviously performance of the test subjects was more than five times better than random motion, but exhibited a large variation especially in the demanding task (4,10). The best subjects almost reached the

performance level of the AI mode, which – on the average – performed about three times as good as the test subjects. It seems that familiarity with gaming i.e. individual training largely influences the performance on the challenging levels.

Run	NOO	VOO	Avg	StDev
DC0	2	1	0,4	0,5
DC1	2	3	1,0	1,0
DC2	2	5	4,4	4,3
DC3	3	5	6,1	2,5
DC4	4	5	14,4	5,2
DC5	3	10	29,0	6,5
SUM			55,4	20,1

Table 1. Effect of guiding in a blinded mode (DC mode). Mean and standard deviation of collisions over 10 runs are given. In slow environments the blinded subjects well solved the problem without training or further instructions.

Next the test subjects were facing the game in one of the blinded modes, DC mode. All test subjects were equipped with the belt and were given a short introduction, how they should interpret the signals on the belly. Without any training the screen output of the game was blocked, so that no object positions were accessible by visual perception, while the game was running.

Because of the delay in reaction time the experiments focused on velocities of at most 5 pixels per frame (or approx. 1.5 seconds to cross the game window). With higher velocities the signals sent by the program could not be processed by the subjects in time.

In Table 1 average performance is shown for DC mode.

In Table 2 the average number of collisions is depicted for the OS mode setting.

Run	NOO	VOO	Avg	StDev
OS0	2	1	0,4	0,5
OS1	2	3	2,0	1,6
OS2	2	5	2,2	0,8
OS3	3	5	7,0	2,5
OS4	4	5	12,4	5,9
OS5	3	10	25,4	3,1
SUM			49,4	14,6

Table 2: Effect of object coding in a blinded mode (OS mode). Average collisions over 10 runs are given. A significant effect is found, but due to reaction time delays the result is especially in challenging settings not yet optimal.

IV. DISCUSSION

These first experiments with a real time setting revealed that skin receptor stimulation may lead to significantly improved performance of blind people in navigation tasks. Though the performance of such a guided person is still much worse than those of visually stimulated subjects, a significant improvement was found compared to random i.e. completely blinded people.

Both "blind" modes (DC mode, OS mode) could reduce collisions significantly on all performance levels. Especially in slow settings up to (NOO=2,VOO=5) collisions were reduced to almost zero. The main cause for degrading performance with increasing speed seems to depend on the time delay introduced by the transmission of data via the hardware and the skin receptors to the brain. There is a theoretical limit due to natural reaction times. Thus, the guiding system (DC mode) should adapt to the reaction times of the subjects. Taking this into account an overshoot of the motion that was mainly responsible for collisions could be avoided.

Nevertheless the performance in DC mode was high from the beginning without special training and inter-individual variation is low compared to the normal gaming conditions (GA mode). It may be speculated that individual training may lead to better performance and due to different learning speeds to stronger inter-individual differences as well.

When examining the position and velocity coding of objects (OS mode) leaving decision making completely to the blinded subjects similar results as with DC mode were achieved. On the first glance this was surprising, but OS mode required much more attention and training of the test subjects to achieve these results.

V. CONCLUSION

A first step was presented to provide a better interface for spatial perception and navigation assist to visually impaired people. All involved test subjects came to the conclusion, that this kind of additional information will be useful for helping blind people with orientation and navigation.

REFERENCES

1. P. Bach-y-Rita, K. A. Kaczmarek, M. E. Tyler, and M. Garcia-Lara. Form perception with a 49-point electrotactile stimulus array on the tongue: A technical note. *Journal of Rehabilitation Research and Development*, 1998:427-430, 35
2. Bach-y-Rita P. *Tactile Sensory Substitution Studies* Ann. N.Y. Acad. Sci. 1013: 83-91 (2004).
3. Bostelman R, Russo P, Albus J, Hong T, Madhavan R., "Applications of a 3D range camera towards healthcare mobility aids.", *Proceedings of the 2006 IEEE International Conference on Networking, Sensing and Control*, pp. 416-21, 2006.
4. Bouzit, M. et.al., "Tactile Feedback navigation handle for the visually impaired", *Proceedings of IMECE2004 2004 ASME International Mechanical Engineering Congress and RD&D Expo* November 13-19, 2004, Anaheim, California USA
5. Möller K., Balazs V., Toth F., Schumann S., Arras K., Bach M., Guttmann J., "Enhanced perception of the environment for visually impaired people", In J. Vander Sloten, P. Verdonck, M. Nyssen, J. Haueisen (Eds.): *ECIFMBE 2008, IFMBE Proceedings 22*, Springer Verlag pp. 1624-1627, 2008.
6. van Erp, J. B. F., Presenting directions with a vibrotactile torso display. *Ergonomics*, 48(3):302-313, 2005.
7. J. Schneider, T. Strothotte, „Constructive exploration of spatial information by blind users“, In: *Proceedings of the fourth international ACM conference on Assistive technologies*, Arlington, USA, 2000.

Corresponding author:

- Prof. Dr. Knut Möller
- Biomedical Engineering,
- Furtwangen University
- Jakob Kienzle Str. 17
- 78054 VS-Schwenningen
- Germany
- moe@hs-furtwangen.de

A Preliminary Study of a Power Assist System for Toe Exercise using a Metal Hydride Actuator

S. Ino¹, M. Hosono^{2,1}, M. Sato³, S. Nakajima⁴, K. Yamashita⁵ and T. Izumi⁶

¹ Institute for Human Science and Biomedical Engineering, AIST, Tsukuba, Japan

² Research Center for Advanced Science and Technology, The University of Tokyo, Tokyo, Japan

³ School of Nursing and Rehabilitation Sciences, Showa University, Yokohama, Japan

⁴ Tsukigase Rehabilitation Center, Keio University, Izu, Japan

⁵ Faculty of Healthcare, Tokyo Healthcare University, Tokyo, Japan

⁶ School of Biological Science and Engineering, Tokai University, Sapporo, Japan

Abstract— In an aging society, there is concern that the population of bedridden elderly people will increase due to diseases and injuries such as cerebral strokes and bone fractures. From this social background, we have been developing a power assist system using a soft MH actuator for home health care to help prevent disuse syndromes. The soft MH actuator, which uses a laminate film bellows, has suitable properties for use as home-based motor rehabilitation equipment. To examine the preventive effect on bedsore formation of a passive motion exercise machine, we measured the skin blood flow of the lower limb. Results have shown a significant blood flow increase at sites frequently associated with decubitus ulcers. Thus, passive motion at toe joints may be useful for the prevention of disuse syndromes. Furthermore, we demonstrate a prototype of a power assist system using the soft MH actuators electrically controlled by Peltier devices. This system has performed moderate slow extension and flexion motion for toe joints. The soft MH actuator seems to provide a key solution to develop a human-friendly power assist system for motor rehabilitation and quality-of-life technology.

Keywords— Motor rehabilitation, disuse syndrome, metal hydride actuator, blood flow, continuous passive motion

I. INTRODUCTION

In an aging society with a falling birthrate, there is an increased need for home-based rehabilitation systems and robots. In such an aging society, there is a concern that an increasing percentage of this elderly population will be bedridden, and therefore vulnerable to various diseases. In particular, elderly patients needing to lie in a reclined position due to stroke or bone fracture may suffer from disuse syndromes such as bedsores, joint contracture and muscular atrophy [1]. It is difficult for these elderly patients to actively exercise for preventive rehabilitation. Thus, to manage these disuse syndromes, there is a need to develop a bedside apparatus for continuous exercise of joints to facilitate blood flow in subcutaneous tissues and joints. There are not, however, any commercially available actuators with the

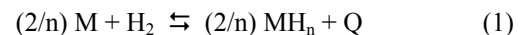
desired characteristics, including human-compatible softness, noiselessness, and a high power-to-weight ratio. These technical issues are an impediment to the development of a robotic rehabilitation system.

To address the above concerns, we designed a novel soft actuator using a metal hydride (MH) alloy, using a rare-earth metal compound as the mechanical power source. The actuator, which we call a MH actuator, generates a high output force, even if its size is small [2]. Moreover, this actuator is soft, noiseless, slow, and environmentally benign. Next, to investigate the preventive effects of toe joint passive motion on bedsore formation, we measured blood flow in the skin of the lower limb before and during passive exercise using a continuous passive motion (CPM) system [3]. Lastly, we developed a power assist system for toe exercise using the MH actuator. This system uses a pair of MH actuators with a soft bellows made of a thin, flexible laminate film.

II. METAL HYDRIDE ACTUATOR

A. Metal hydride alloy

Metal hydride alloys (Fig. 1) have the ability to store a large amount of hydrogen gas [4], approximately 1000 times as large as the volume of the alloy itself. This particular MH alloy can store 100 to 200 ml/g of hydrogen gas. A reversible chemical reaction between a metal (M) and hydrogen gas (H₂) generates metal hydrides (MH_n) as in the following reaction:



where Q is the heat of reaction. If this reaction proceeds at a fixed temperature, it will advance up to an equilibrium pressure, known as the plateau pressure.

The PCT diagram (P: hydrogen pressure, C: hydrogen content, T: temperature) shows the hydrogen-absorbing



Fig. 1. Various styles of metal hydride alloys for a MH actuator.

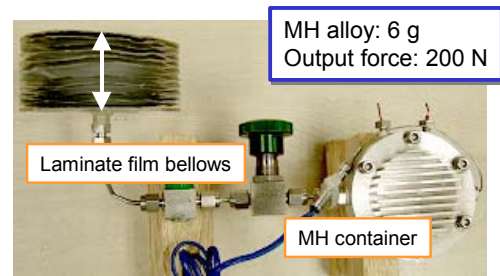


Fig. 3. Photograph of a soft MH actuator using a laminate film bellows.

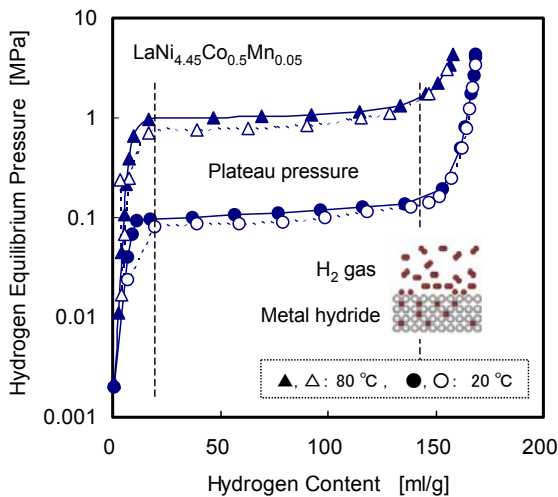


Fig. 2. PCT diagram of a metal hydride (LaNi_5) alloy.

behavior of this MH alloy. As shown in the PCT diagram (Fig. 2), the plateau pressure can be controlled by adjusting the temperature of the MH alloy. Thus, the MH alloy can act as a power source for mechanical actuation.

B. Soft MH actuator

If the reversible reaction of the MH alloy is carried out in a sealed system, heat energy applied to the MH alloy is converted into mechanical energy such as pressure and force. Thus, the MH actuator functions by altering the hydrogen gas pressure via alteration of temperature, which is, in turn, controlled by a thermoelectric Peltier device.

The MH actuator was composed of a solidified MH alloy powder, Peltier elements to electrically control the temperature of the alloy, a MH container to act as a small gas cylinder, and an end-effector to transfer the hydrogen gas pres-

sure into an acting force [2]. The soft laminate film bellows used as an end-effector is better adapted to the human body than is a conventional MH actuator using a metal bellows [5].

The MH actuator using such a soft bellows exhibits flexibility and lightness, critical requirements for rehabilitation equipment. Such an MH actuator, built using a soft bellows, will be referred to as a soft MH actuator. The soft MH actuator (Fig. 3) contained 6 g of the MH alloy. The maximum output force of this actuator was about 200 N. Thus, the power-to-weight ratio of the soft MH actuator is very high, compared to that of commercial actuators such as an electric motor or a pneumatic actuator [2]. The heat drive mechanism of the MH actuator does not produce any noise or vibration. As shown in Fig. 4, the range of stiffness of human muscle [7] was matched by the soft MH actuator [8].

Therefore, we think that the soft MH actuator using a laminate bellows is suitable for use as a human-sized actuator applied to a robotic rehabilitation system and a force-feedback human interface device.

III. EFFECT OF PASSIVE TOE EXERCISE

A. Methods

To assess the usefulness of the passive toe exercise using a robotic rehabilitation system (power assist system) for the purpose of preventing disuse syndromes, we performed some measurements of lower limb blood flow during continuous passive motion of the toe joints. Two DC servomotors and their controller (LEGO, Mindstorm, Denmark) were used to generate the continuous passive motion applied to the subject's toe joints, as in Fig. 5.

Subjects' toe joints were subjected to bending and stretching motions via an attachment connected to the servomotors. This stimulation lasted 2 minutes, and was initiated after

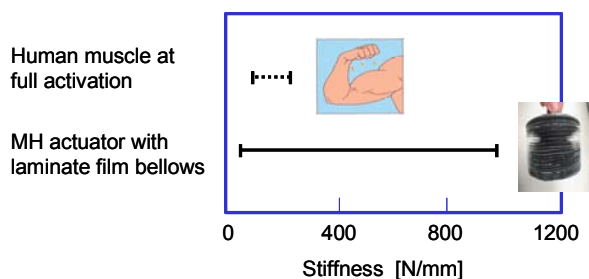


Fig. 4. Comparison between the range of the stiffness of the soft MH actuator and that of the human muscle at full activation.

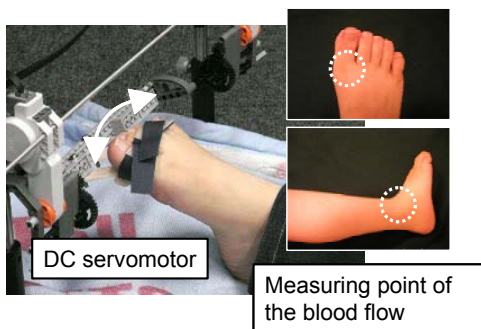


Fig. 5. Setup of continuous passive motion for toe joints using DC servomotors (left) and the measuring site of subcutaneous blood flow (right).

keeping the subjects in a supine position at rest for 5 to 10 minutes. Blood flow was measured at the base of the big toe and at the lateral malleolus using a laser blood flow meter (Advance, ALF21, Japan). Ten healthy subjects from 20 to 80 years of age participated in this experiment after informed consent.

B. Results and Discussion

The average cutaneous blood flow readings at the base of the big toe and the lateral malleolus of the subjects one minute before and two minutes into the toe exercise are shown in Fig. 6. The blood flow readings at the base of the big toe during the toe exercise were significantly larger ($P < 0.02$, Friedman test) than the readings before the exercise, as shown in Fig. 6(a). The blood flow readings at the lateral malleolus exhibited a similar trend ($P < 0.02$, Friedman test), as shown in Fig. 6(b).

The factor responsible for increasing the cutaneous blood flow during passive toe exercise was assumed to be the mechanical deformation of capillaries in the subcutaneous tissue, due to extension and flexion of the toe joints. Alter-

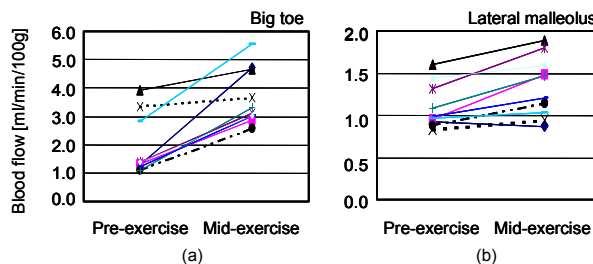


Fig. 6. Average cutaneous blood flow at the base of the big toe and at the lateral malleolus one minute before exercise (pre-exercise) and after two minutes of exercise (mid-exercise).

natively, the effects of the mechanical muscle pump may be due to cyclic passive motion of the toe joints by the power assist system.

From these results, we can conclude that there was a significant blood flow increase at the base of the big toe and the lateral malleolus. Since these are frequent sites of decubitus ulcers, continuous passive motion at toe joints via the power assist system may be a valuable tool to help prevent disuse syndromes such as bedsores and soft tissue contracture induced by ischemia.

IV. POWER ASSIST SYSTEM USING THE SOFT MH ACTUATOR

A prototype of the bedside power assist system for toe exercise consisted of two of the soft MH actuators and a laminate film bellows (soft bellows), pressure sensors (PGM-5KC, Kyowa, Japan), a bipolar power supply (BOP-20-20M, Kepeco, USA), and a PID controller (LabVIEW, NI, USA) using a personal computer. A photograph of the power assist system is shown in Fig. 7. The MH module, composed of a copper-encapsulated powder MH alloy compact (10 g) sandwiched between two Peltier devices, was packed in a discoid, hermetically-sealed duralumin container. The soft bellows (40 g) was made of a trilayer structure film of cast polypropylene (CPP) - aluminum (Al) - polyester (PET). The total thickness of the film was about 0.1 mm. The structure of soft bellows was formed by the thermocompression bonding method in the CPP layer. From former experiments [5], we verified that such soft bellows have high impermeability to hydrogen gas and exhibit flex durability.

A sketch of an antagonistic motion pattern of the soft MH actuators is shown in Fig. 8. The extension and flexion motion of the toe joints is derived from a pair of soft bellows spreading out in a fan-like form in a plastic case. The motion of the toes in the power assist system was properly gentle and slow for joint rehabilitation. During operation of

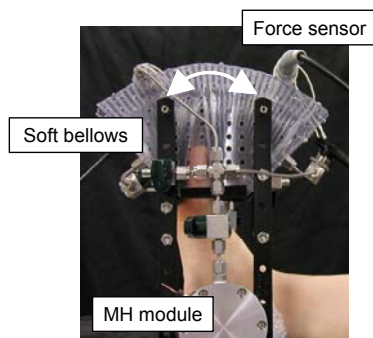


Fig. 7. Overview of the power assist system using soft MH actuators for toe exercise to prevent disuse syndromes.

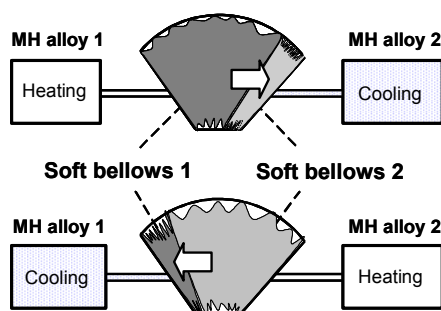


Fig. 8. Sketch of the antagonistic driving mechanism of the power assist system using a pair of soft MH actuators.

the system, the subject's toes constantly fitted in the space between the two soft bellows.

Thus, various joint exercises could be easily actualized by simple pressure control of the soft MH actuator system. These exercises comprise continuous passive motion to adapt joints to passive, and then active motion with moderate resistive force for motor rehabilitation.

V. CONCLUSIONS

This paper has described the framework of a novel power assist system using a MH actuator. This system is designed for home health care in an aging society to prevent disuse syndromes.

The soft MH actuator using a laminate film bellows has suitable properties for use as home-based rehabilitation equipment. To examine the preventive effect on bedsores formation by passive motion exercise, we measured the cutaneous blood flow before and during exercise. Results show a significant blood flow increase at the frequent sites of decubitus ulcers. Thus, passive motion at toe joints may

be useful for the prevention of disuse syndromes. Furthermore, a prototype of the power assist system was described which uses soft MH actuators electrically controlled by Peltier devices. This system has performed moderate slow extension and flexion motion for toe joints. A pair of soft bellows, which have mechanical and design flexibility, can adaptively hold all toes in a proper position for continuous passive motion.

The soft MH actuator seems to provide a key solution to develop a human-friendly power assist system for motor rehabilitation and quality-of-life technology [6].

ACKNOWLEDGMENTS

This work was supported in part by the Grant-in-Aid for Scientific Research (B) 18300191 and (C) 20500489 from JSPS and the Industrial Technology Research Grant Program from NEDO of Japan. The authors would like to thank for H. Ito and H. Kawano of Japan Steel Works Ltd., and H. Kasai, H. Hiyama and T. Miura of Dai Nippon Printing Co., Ltd., for outstanding technical assistance.

REFERENCES

1. Bortz W M (1984) The disuse syndrome. *Western Journal of Medicine* 141(5): 691-694
2. Wakisaka Y, Muro M, Ino S et al. (1997) *IEEE Transactions on Rehabilitation Engineering*, 5 (2): 148-157
3. Salter R B, Hamilton H W, Wedge J H et al (1984) Clinical application of basic research on continuous passive motion for disorders and injuries of synovial joints: A preliminary report of a feasibility study. *Journal of Orthopaedic Research*, 1 (3): 325-342
4. Sakintuna B, Lamari-Darkrimb F, Hirscherc M (2007) Metal hydride materials for solid hydrogen storage. *International Journal of Hydrogen Energy*, 32: 1121-1140
5. Ino S, Sato M, Hosono M, Izumi T (2009) Development of a Soft Metal Hydride Actuator Using a Laminate Bellows for Rehabilitation Systems, *Sensors and Actuators: B. Chemical*, B-136 (1): 86-91
6. Cooper R A (2008) *Quality-of-Life Technology; A Human-Centered and Holistic Design*. *IEEE Engineering in Medicine and Biology Magazine*, 27(2): 10-11
7. Cook C S, McDonagh M J N (1996) Measurement of muscle and tendon stiffness in man. *European Journal of Applied Physiology*, 72 (42): 380-382
8. Ino S, Sato M, Hosono M et al. (2008) Prototype Design of a Wearable Metal Hydride Actuator Using a Soft Bellows for Motor Rehabilitation, *Proc. the 30th Annual International Conference of the IEEE Engineering in Medicine and Biology Society, Vancouver, Canada, 2008*, pp. 3451-3454

Author: Shuichi Ino
 Institute: National Institute of Advanced Industrial Science and Technology (AIST)
 Street: Central 6, 1-1-1 Higashi
 City: Tsukuba
 Country: Japan
 Email: s-ino@aist.go.jp

Rehabilitation Robotics for Outpatient Clinical and Domestic Use

Thierry Keller and Joel C. Perry

Fatronik Foundation, Mikeletegi Pasealekua, 7, Donostia-San Sebastian, Spain
<tkeller, jperry>@fatronik.com

Abstract— Robotic systems for rehabilitation have found acceptance in therapeutic and clinical environment. The main successes are made in support or substitution of manual therapy for locomotion and reaching using stationary multi degree of freedom robotic systems. These systems present a technological complexity that requires constant maintenance and highly qualified operators. They are only affordable by big rehabilitation centers and clinics. On the other hand research results indicate that successful rehabilitation requires more involvement and time of the impaired subjects than the duration of their hospitalization. Outpatient treatments and the continuation of the therapy in local and smaller rehabilitation facilities or at home should follow the clinical rehabilitation. Current challenges are the implementation of affordable rehabilitation robotics in outpatient centers and the development of low cost solutions for domestic environments. This paper presents contributions that use solutions necessary for lower cost rehabilitation robotic systems, i.e. low-cost compliant actuators, sensors, controls, existing gaming controllers, remote support and supervising. New approaches and systems for domestic and tele-rehabilitation, tele-rehabilitation software solutions, low cost training platforms, and workstations are presented and described.

Keywords— Robot rehabilitation, motor impairment, low-cost home rehabilitation systems, telerehabilitation.

I. INTRODUCTION

Rehabilitation is a labor-intensive process involving a physical interaction between a patient and a therapist. Reducing the degree of permanent disability remains the goal of all rehabilitation programs as e.g. post stroke or SCI rehabilitation. Relying on the plasticity of the brain, new approaches to impairment reduction through managing sensorimotor treatment may contribute to a reduction in motor impairment [1]. While there is not one standard technique that occupational and physical therapists use for improving upper or lower extremity motor function within a remediation framework, many of the techniques that are used require some manual assistance from the therapist to position, guide, and/or support all or some of the weight of the limb [2-4]. When provided with at least partial compensation of gravitational forces, it is possible for patients to perform controlled movements that could not otherwise be performed unassisted.

Previous studies have shown that patients who performed progressive resistance exercises with adequate motor control for as little as 3-4 times per week for 6-12 weeks improved both strength and functional activities [5]. Furthermore, recently published research work confirms that better results in terms of rehabilitation outcome are obtained in specialized care centers where patients receive more therapy per day for extended periods of time [6]. However, mean lengths of hospitalization in Spain are on average only 10.2 days followed by less than half of a day in a stroke unit [7]. Similarly in the United States, Medicare coverage policies maintain the current median length of stay in inpatient rehabilitation facilities at only 16 days, and approximately 80% of these inpatients are discharged to their home. In the case of Medicare, in-home services are covered for only the next few weeks following discharge, and then for treatments at an outpatient facility 2-3 times per week for a period of 1-3 months, when the patient reaches a plateau in terms of gains in ADL tasks according to standard assessment tests [8]. There is some belief, however, that these assessment scales are insensitive to further improvement at the point of discharge [9], despite the ability to make further gains. There is evidence that even in stable post-stroke conditions, patients can undergo reduction of sensory-motor impairment if proper therapy is administered [10]. As a method for administering a treatment to this population, robotic assisted rehabilitation has become a major focus in research and for clinical assessment.

However, many of these robotic assisted rehabilitation methods are conducted with stationary, complex high-tech systems and can only be provided and afforded by leading rehabilitation centers. Smaller centers, outpatient facilities or regional hospital cannot afford many of these high end rehabilitation robots, which require technicians and often highly educated researchers to be operated and maintained. Thus, it is evident and necessary that simpler robotic systems, cheaper to maintain and easy to operate need to be developed and tested in its effectiveness. This demand has been recognized and following examples show that lower cost rehabilitation systems can be made. These systems in their limitations are able to perform equally well as their multi-DOF counterparts with no or small limitations in performance, however at the edge to be named robot. Nevertheless, even if passive all these systems share a sensing

part, a human-machine interface and provision of feedback needed for target or goal directed training.

II. REHABILITATION SYSTEMS SUITABLE FOR OUTPATIENT CLINICAL AND HOME USE

A. Gaming based motor-rehabilitation approaches

Gaming consoles associated with customized or adapted controllers have recently been used in rehabilitation of elderly people and disabled. As an example the Nintendo Wii console is installed in numerous therapeutic centers. It provides several controllers (Wii balance board, Wiimote combined with Pilates rubber bands, etc.) that invite active exercising in a motivating gaming like scheme using high scores and gradually increased difficulty levels.

The ElderGAMES project [11,12] works closely with older populations to find the most motivating and enjoyable games for elderly. The combined set of design criteria as collected from the literature is shown in Table 1. Represented in the table are two sets of criteria and the relationship of each criterion to the corresponding gaming classification. The ideal game to be used e.g. for stroke rehabilitation would satisfy all of the listed criteria.

Criteria for Stroke Rehabilitation	Criteria for Elderly Entertainment
<ul style="list-style-type: none"> • Adaptability to motor skill level • Meaningful tasks • Appropriate feedback • Therapy-Appropriate ROM • Focus diverted from exercise 	<ul style="list-style-type: none"> • Appropriate cognitive challenge • Simple objective/interface • Element of social activity • Appropriateness of genre • Creation of new learning • Promotion of cognitive capacities chosen by experts of ElderGames project. • Sensitivity to decreased sensory acuity and slower responses

Table 1. Gaming design criteria for stroke rehabilitation programs serving elderly users

A selection of games reported and used in a rehabilitation environment has been analyzed and scored [13]

UniTherapy [14] applied a fun therapy toolbox consisting of third-party games like Solitaire or Pac-Man together with conventional joysticks and force-feedback steering wheels to stroke therapy. The Joystick (TheraJoy) and steering wheel (TheraDrive) are customized such that they can be

grasped by subjects with impaired arm and hand function. Results in a controlled study supported the potential benefit of robot and computer assisted motivating therapy [14].

B. Low-cost lower extremity motor- rehabilitation systems

Balance trainers

A device called BalanceTrainer has been developed by Z. Matjacic and colleagues at University of Aalborg. It is now commercially available at Medica Medizintechnik GmbH, Germany. The device has two springs that provide an adjustable support in sagittal and coronal planes during standing. In more sophisticated version the vertical support rods are actively driven. Combined with a low-cost COP measurement platform [15], e.g. the Wii balance board and a gaming or virtual reality environment people with balance problems can train stability.

Walkers

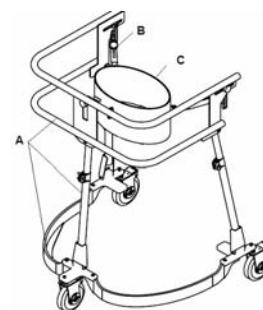
Another commonly used rehabilitation tool is the walker. Simple walkers are passive and have a brake as the only controlled input.



More sophisticated walkers are designed to help the user to stand up and walk. As in [16] the walker can have in addition to the lifting mechanism drives that help to overcome the added weight compared to a standard walker.

Gait trainers

A new category of gait trainers are robotic systems, similar to walkers, that allow ground level walking and provide passive or actuated balance control. An example in the low-cost range of this category is the Walkaround [17]. It provides to the user sufficient stability such that a rehabilitation training can be easily provided by one physiotherapist and the user, e.g. a stroke subject can learn to overcome a static walking with double stance phase and relearn a dynamic walking in a safe manner. A preliminary study has shown that the Walkaround could increase walking speed in acute stroke patients significantly [17].



C. Low-cost upper extremity motor-rehabilitation systems

Hand rehabilitation

The PHANTOM is a small table haptic robot that simulates one or two finger contact to virtual surfaces and deformable objects. The system is based on force feedback and is used to play virtual reality maze games. In therapy it is used for fine finger movements. A standard monitor is used to provide feedback of the gaming environment. its

haptic performance is quite good, however this goes on cost of the prize.

In contrast, the Novint Falcon is a low-cost haptic gaming interface for a few hundreds of US\$. Combining the Falcon with a parallel kinematic construction a small company (Obslap Research LLC) has developed a fine motor rehabilitation system called, MyScrivener. In a pilot evaluation an early prototype showed dramatic visible improvements in handwriting of ADHD children.



The Hand Mentor is an exoskeleton hand rehabilitation system for *Active Repetitive Motion*™. It provides controlled resistive force to the hand and wrist. As actuator the system uses a compliant air muscle actuator. Biofeedback is provided by incorporated EMG electrodes. The system is reported to be well accepted by the patients and has been assessed to work in a clinical setting [18].

Arm rehabilitation

There are numerous workstation like systems for arm rehabilitation. The Rehaslide Duo is a commercially available desk exercising system. It provides resistance to the movement but no active biofeedback. The hand rest can be adjusted in different angles.

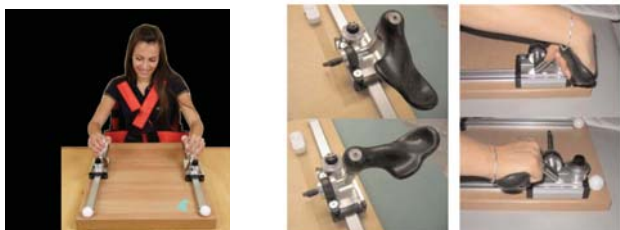


Figure 1: Rehaslide Duo from Reha Technologies s.r.L.

A system that provides low-cost planar arm movement training is called *Armassist*. It measured the lifting force and position and orientation of the arm while the subject performs dual lifting and reaching out tasks.



Figure 2: Armassist therapy and device prototype

The wheels of the table robot can be passive or actuated in order to guide the arm on the table. The system is wirelessly connected to a personal computer and a number of training, gaming and entertainment tasks can be performed.

HapticDrive is a low cost 2-DOF active compliant robot for planar arm movements, wrist movements, and reaching movements. It allows with a simple locking mechanism to select the type of movements. A spring/cable driven actuation principle provides patient safety and a low-cost actuation.



Figure 3: HapticDrive device prototype for arm and wrist training

First results showed great improvements in pro/supination movements in chronic stroke subjects that trained for 10 sessions over three weeks.

III. TELEREHABILITATION

Telerehabilitation according to Jack Winters [19] can be divided in Teleconsultation, Telemonitoring, Telehomecare, and Teletherapy.

Teleconsultation is a standard face-to-face consultation using videoconferencing. Telemonitoring is a clinical application of measuring medical signals and sending the data to a center. Telehomecare is advising and learning ADL tasks over distance using videoconferencing or other means. Teletherapy is conducting therapeutic activities in a home setting using a therapy protocol. When these four telerehabilitation activities are plotted in a two-dimensional plot with intensity and duration as axes then it is clear that teletherapy is the high intensity long duration application [20]. As such it is important that this Tele activity needs to be provided in a cost efficient manner. If not then Telerehabilitation cannot be a solution for the ageing society as it will be too expensive. There are two feasible ways of cost-efficient telerehabilitation: Group therapy and community therapy. Group therapy is a therapy using either videoconferencing or virtual reality together with a closed group at scheduled times, whereas community therapy is a virtual reality therapy in a community space. Currently these concepts are not frequently used for therapy but they are widely applied in gaming and social communities.

In 1998, the US National Institute on Disability and Rehabilitation Research (NIDRR) initiated and established a National center of research for telerehabilitation [21].

NIDRR recognized the potential benefits of telerehabilitation in primary and secondary prevention for people with disabilities.

IV. FUTURE DIRECTION

The trend towards simpler rehabilitation robots that can be applied in outpatient facilities or at home will continue. Telerehabilitation will be needed to facilitate quality service and day-by-day support when needed. It will provide means to increase efficiency in the ageing society. However, to be cost-effective some of the therapist guidance has to come by the rehabilitation robot itself, either by a consequent comprehensive design or by added intelligence. The system at home has to suggest the right grade of difficulty, help in comparing the outcome and guide the user with natural intelligence. It also has to carefully monitor the user, correct wrong posture, motivate or slow down the operator. From a technical point of view lots of artificial cognitive skills need to be added such that a telerehabilitation scenario will provide more than the saving of travel expenses of the customer to clinic.

As a consequence the design of group and community therapy will help at first hand to provide efficient direction of many users by few therapists. Self-learning and see and copy strategies can be performed in such a community setup.

ACKNOWLEDGMENT

This work was supported in part by the FIK Project, San Sebastian, Spain

REFERENCES

- Volpe BT, Krebs HI, Hogan N, (2001). Is Robot-Aided Sensorimotor stroke Rehabilitation a Realist Option, *Curr Opin Neurol*, Dec. 14 (6), pp. 745-752.
- Woodson AM, (2002). Stroke. In C. A. Trombly, & M. V. Radomski (Eds.), *Occupational Therapy for Physical Dysfunction* (5th ed., pp. 817-853). Baltimore: Lippincott Williams & Wilkins.
- Sabari JS, (2002). Optimizing motor control using the Carr and Shepherd approach. In C. A. Trombly, & M. V. Radomski (Eds.), *Occupational Therapy for Physical Dysfunction* (5th ed., pp. 501-520). Baltimore: Lippincott Williams & Wilkins.
- Trombly CA, (2002a). Optimizing motor behavior using the Brunnstrom movement therapy approach. In C. A. Trombly, & M. V. Radomski (Eds.), *Occupational Therapy for Physical Dysfunction* (5th ed., pp. 543-560). Baltimore: Lippincott Williams & Wilkins.
- Patten C, Lexell J, Brown HE, (2004). Weakness and strength training in persons with poststroke hemiplegia: rationale, method, and efficacy. *J Rehabil Res Dev* 2004;41:293-312.
- De Wit L, Putman K, Schuback B, Komárek A, Angst F, Baert I, Berman P, Bogaerts K, Brinkmann N, Connell L, Dejaeger E, Feys H, Jenni W, Kaske C, Lesaffre E, Leys M, Lincoln N, Louckx F, Schupp W, Smith B, De Weerd W, (2007). Motor and functional recovery after stroke: a comparison of 4 European rehabilitation centers., *Stroke*. 2007;38:2101
- Epstein D, Mason A and Manca A, (2008). The hospital costs of care for stroke in nine European countries. *Health Economics* 17: S21-S31
- Ottenbacher KJ, Smith PM, Illig SB, Linn RT, Ostir GV, Granger CV, (2004). Trends in length of stay, living setting, functional outcome, and mortality following medical rehabilitation. *JAMA* 2004;292:1687-95.
- Dobkin BH, (2005). Clinical practice. Rehabilitation after stroke, *Engl J Med*. 2005 Apr 21;352(16):1677-84.
- Byl N, Roderick J, Mohamed O, Hanny M, Kotler J, Smith A, Tang M, Abrams G, (2003). Effectiveness of sensory and motor rehabilitation of the upper limb following the principles of neuro-plasticity: patients stable poststroke. *Neurorehab. and Neural Repair*, Vol.17, No.3, 176-191.
- Fabregat, M., 2006. D1.2 - Game Typologies to be developed and their relationship with the parameters to measure. *ElderGames Project*, final report version.
- Gamberini L., et al., 2006. Cognition, technology and games for the elderly: An introduction to ELDERGAMES Project. *PsychNology Journal*, (December. 2006), 4(3):285 -308.
- Flores E., Tobon G., Cavallaro E., Cavallaro F.I., Perry J.C. , and Keller T., 2008, Improving patient motivation in game development for motor deficit rehabilitation, *Proc ACE Conf*, Yokohama, Japan.
- Johnson, M.J., Feng, X., Johnson, L.M., Winters, J.M., 2007, *J. NeuroEng Rehabil*, 4(6):1-17.
- Cikajlo I, Matjacic Z, (2009) Directionally specific objective postural response assessment tool for treatment evaluation in stroke patients, *IEEE Trans Neural Syst Rehabil Eng*, 17(1):91-100.
- Chugo, D., Asawa, T., Kitamura, T., Jia, S., Takase, K., (2008), A rehabilitation walker with standing and walking assistance, *Proc. I-ROSS Conference*, Nice, France, 260-5.
- Veg, A., Popovic, D.B., (2008) Walkaround: Mobile Balance Support for Therapy of Walking, *IEEE Trans Neural Syst Rehabil Eng*, 16(3):264 – 269.
- Sarakoglou, I., Kousidou, S., Tsagarakis, N.G., Caldwell, D.G. (2007), Exoskeleton-based exercisers for the disabilities of the upper arm and hand, in *Rehabilitation Robotics*, Book edited by Sashi S Kommu, Chapter 27, 499-522, Itech Education and Publishing, Vienna, Austria
- Winters, J. M. (2002). Telerehabilitation research: emerging opportunities. *Annual Review of Biomedical Engineering*, 4, 287-320
- Parmanto, B, Saptono A., (2008) Telerehabilitation: State-of-the-Art from an Informatics Perspective, *J TeleRehab*, Special Issue 1(1):1-11.
- Katherine D. Seelman & Hartman, L.M., (2008) Telerehabilitation: Policy Issues and Research Tools, *J TeleRehab*, Special Issue 1(1):37-48.

Use macro [author address] to enter the address of the corresponding author:

Author: Thierry Keller
 Institute: Biorobotics Department, Fatronik-Tecnalia
 Street: Paseo Mikeletegi, 7
 City: 20009 Donostia – San Sebastian
 Country: Spain
 Email: tkeller@fatronik.com

Seizure Control in an *In-Silico* Model of Epilepsy Using Backstepping Technique

N. Mostofi¹, M.R. Jahed-Motlagh¹, C. Lucas², Gh. Montaseri², and A.B. Farjadian²

¹ Complex lab, Iran University of Science and Technology, Tehran, Iran

² School of Electrical and Computer Engineering, University of Tehran, Tehran, Iran

Abstract— Electrical stimulation is a less-invasive alternative for treating drug-resistant epilepsy compared to surgical resection of the epileptogenic area. Different stimulation protocols have been practiced to suppress seizures either *in-vivo*, *in-vitro* and *in-silico*. In this work we have controlled rapid discharges occurring at electrical onset of seizure in an *in-silico* model of epilepsy using backstepping technique.

Keywords— Epilepsy, *In-Silico* model, Control, Backstepping.

I. INTRODUCTION

Epilepsy is one of the most common disorders of the central nervous system. Almost 1% of the world population is afflicted by this destructive disease. Anti-convulsant prescription is so far the major treatment of epilepsy. Nonetheless almost 1/3 is pharmacoresistant. Surgical resection and electrical stimulation of the epileptogenic zone are two other alternatives for curing the phenomenon. Despite the steady progress in epilepsy research it is accepted by many groups that very few advances have led to efficient beneficial solutions [1]. This is mainly because of the complexity of fundamental neural mechanisms generating seizures.

A variety of experimental and computational models of epilepsy have been elaborated to deal with these restrictions [1-4]. Experimental *in-vivo* and *in-vitro* models have been widely used to expand different stimulation protocols to control and suppress seizures [5]. These protocols include uniform and localized DC fields, single pulses derived from resynchronizations, phase resetting, chaos control and other control techniques besides low and high frequency periodic stimulation.

In-silico computational models with neurophysiologically relevant parameters have also been employed to investigate the characteristics of the epileptic phenomena and its control [6]. It has been suggested that marvelous potential of these models can also be used to build novel therapeutic strategies [1]. As they describe the brain dynamics in different levels from sub-cellular to large scale neural networks by nonlinear systems they offer a mathematical prospective of the epilepsy problem that can be dealt with

by making advantage of nonlinear control techniques. Besides despite experimental models they do not need any special preparations of brain slices and are easily constructed by computers.

In this paper we first explain a modified version of neural population model proposed by Wendling et al. [4]. The transition from background normal activity namely interictal to fast ictal oscillations is accurately visualized by this model. A control strategy is then designed using backstepping technique [7] to steer the oscillations, with beta and low gamma frequency occurring at seizure onset, to the interictal activity, where high amplitude spikes are not observed [8].

II. METHODS

A. Computational model

A modified version of neural mass model proposed by Wendling et al. is used to study the brain dynamics and especially to explore the seizure state. Here we have reduced the model equations from 8 to 10 by some parameter modifications while the results are the very analogous to the main structure [8].

A single neural population is modeled containing four interacting subsets: 1) pyramidal cells, 2) excitatory interneurons, 3) slow dendritic inhibitory interneurons and 4) fast somatic inhibitory interneurons. These subsets ($i=1, 2, 3, 4$) are represented with 8 nonlinear differential equations as shown in Eq.1.

$$\begin{cases} \dot{z}_{11}(t) = z_{12}(t) \\ \dot{z}_{12}(t) = EXCaS(z_{21} - z_{31} - z_{41}) - 2az_{12}(t) - a^2z_{11}(t) \\ \dot{z}_{21}(t) = z_{22}(t) \\ \dot{z}_{22}(t) = EXCa(p(t) + C_2S(C_1z_{11})) - 2az_{22}(t) - a^2z_{21}(t) \\ \dot{z}_{31}(t) = z_{32}(t) \\ \dot{z}_{32}(t) = SDIbC_4S(C_3z_{11}) - 2bz_{32}(t) - b^2z_{31}(t) \\ \dot{z}_{41}(t) = z_{42}(t) \\ \dot{z}_{42}(t) = FSIGC_7S(C_5z_{11} - C_6z_{31}) - 2gz_{42}(t) - g^2z_{41}(t) \end{cases} \quad (1)$$

For each subset an asymmetric sigmoid function $S(v) = 2e_0 / (1 + e^{r(v-v_0)})$ converts the average transmembrane potential to an average pulse density of spikes fired by neurons. The synaptic effect of each subset is modeled by a second order linear transfer function which relates the average presynaptic and postsynaptic action potentials.

$[EXC, SDI, FSI]$ and $[a, b, g]$ are the respective gains and time constants of each synapse. $P(t)$ is a white Gaussian noise input added to the excitatory interneurons representing the effect of the neighboring populations. In the original model this input is subtracted from the excitatory interneurons. Interaction among interneurons are demonstrated via seven connectivity constant C_1 to C_7 . The postsynaptic potential of the pyramidal cells is interpreted as the output EEG signal as in eq. 2.

$$EEG = z_{21}(t) - z_{31}(t) - z_{41}(t) \quad (2)$$

It is shown that the model can simulate different EEG rhythms for different values of population gains: *EXC* (excitation), *SDI* (slow dendritic inhibition) and *FSI* (fast somatic inhibition) [4]. An identification procedure of these three parameters has been developed to reconstruct intracerebral EEG signals recorded from patients with temporal lobe epilepsy [8]. Transition from interictal to fast ictal activity has been divided into four intervals namely interictal, preonset, onset and ictal. The population gains have been identified for each segment consequently. A set of identified parameters have been shown in Table 2 for interictal and onset segments.

Interictal segment is the period during which no high amplitude spikes is observed and is chosen about 1 minute before seizure. This period is proceeded by preonset segment where high amplitude spikes begin to appear while the seizure onset occurs from 10-50 seconds after this period. The main feature of the electrical onset of the seizure is the exhibition of oscillations with beta and low gamma frequency (15-40 Hz). The final period observed in epileptic activity is the ictal period during which the seizure develops and rhythmic activity in theta and alpha band (4-10 Hz) occurs.

B. Control strategy

A control algorithm has been implemented based on backstepping technique to steer the system from seizure onset to interictal activity by adding a control input to each neural subset.

In recent decades recursive methods have been developed to design controller for nonlinear systems. Indeed simplicity of scalar methods motivates designers to use them as starting points for higher-order systems [7].

Backstepping is a Lyapunov-based recursive design procedure that starts with stabilizing a scalar subsystem and moving backward. At each step the dimension of the stabilized subsystem is increased awaiting the last step, where the control input is calculated for the complete system.

Each neural subset can be described as:

$$\begin{cases} \dot{z}_{i1}(t) = z_{i2}(t) \\ \dot{z}_{i2}(t) = W_i w_i f(t) - 2w_i z_{i2}(t) - w_i^2 z_{i1}(t) \end{cases} \quad (3)$$

Where W_i is the respective population gain, *EXC*, *SDI*, *FSI*, and w_i is the time constant, a, b, g , for each population.

In order to apply the backstepping technique to the model (1) and in corresponding to each subset (3), we define the closed loop subsystem (4) as the follows:

$$\begin{cases} \dot{y}_{i1}(t) = y_{i2}(t) \\ \dot{y}_{i2}(t) = W_i w_i h(t) - 2w_i y_{i2}(t) - w_i^2 y_{i1}(t) + u_i \end{cases} \quad (4)$$

Where a control input u_i ($i=1, 2, 3, 4$) is added to each population. Here we set the three population gains according to Table 2 so that the system operates at onset segment. The desired system is described as Eq.5 with parameters selected in interictal period.

$$\begin{cases} \dot{x}_{i1}(t) = x_{i2}(t) \\ \dot{x}_{i2}(t) = W_{id} w_i g(t) - 2w_i x_{i2}(t) - w_i^2 x_{i1}(t) \end{cases} \quad (5)$$

The difference between the closed loop and the desired subsystems construct the following error dynamical system:

$$\dot{e}_{i1}(t) = e_{i2}(t) \quad (6a)$$

$$\dot{e}_{i2}(t) = W_i w_i h(t) - W_{id} w_i g(t) - 2w_i e_{i2}(t) - w_i^2 e_{i1}(t) + u_i \quad (6b)$$

The control objective is to stabilize the above error system at the origin of the (e_{i1}, e_{i2}) plane. In the first step of backstepping technique, the term (6a) is stabilized by choosing the virtual control $e_{i2}(t)$ as Eq.7.

$$e_{i2}(t) = -k_{i1} e_{i1} \quad (7)$$

Where k_{i1} is a positive constant. To back step, the variable q_i is defined as:

$$q_i = e_{i2}(t) + k_{i1} e_{i1} \quad (8)$$

Next, the system (6) is rewritten in the new coordinates (e_{i1}, q_i) and the Lyapunov function is chosen to stabilize the derived system as follows:

$$V = \frac{1}{2}(e_{i1}^2 + q_i^2) \tag{9}$$

Finally, the control input Eq.10, makes the first derivative of the Lyapunov function negative definite in (e_{i1}, e_{i2}) coordinates and the system (6) is thus asymptotically stable.

$$u_i = -W_i w_i h(t) + W_{id} w_i g(t) + (w_i^2 - 1 - k_{i1} k_{i2}) e_{i1} + (2w_i - k_{i1} - k_{i2}) e_{i2} \tag{10}$$

C. Results

Model equations (Eq.1) have been solved by numerical integration methods with fixed time step, equal to 5 milliseconds. Figure 1 shows the simulated EEG activity during (a) interictal and (b) onset periods as they are clearly similar to those reported by Wendling et al. [8]. Model parameters are set according to Table 1.

Table 1 Model parameters

parameter	value
a	100 s ⁻¹
b	30 s ⁻¹
g	350 s ⁻¹
C ₁	135
C ₂ , C ₇	108
C ₃ , C ₄	33.75
C ₅	40.5
C ₆	0.4
v ₀	6 mv
e ₀	2.5 s ⁻¹
r	0.56 mv ⁻¹
p(t)	Mean=90 pulses.s ⁻¹ , SD=900 pulses.s ⁻¹

Control input for each subset has been designed according to Eq.10. Parameters have been set according to Tables 1 and 2.

Table 2 Population gains

period	parameters	value
interictal	EXC _d	3.5
	SDI _d	13.2
	FSI _d	10.76
onset	EXC	7.7
	SDI	4.3
	FSI	15.1

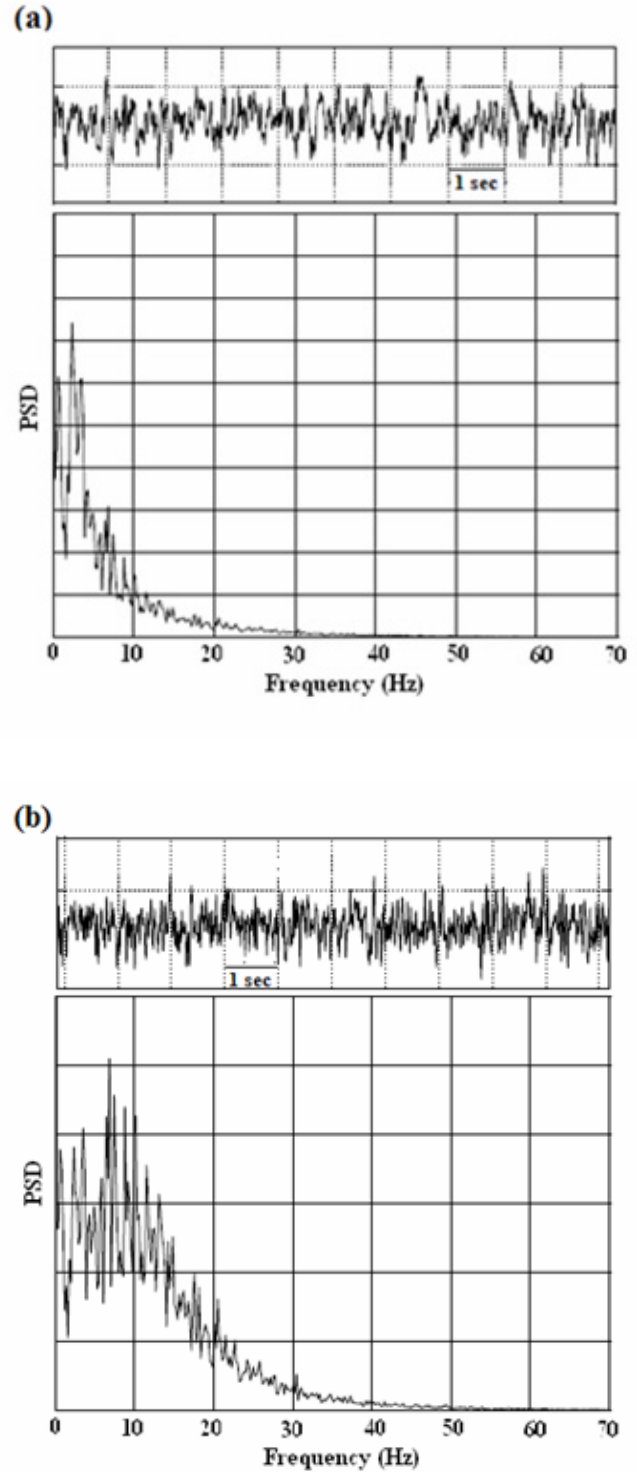


Fig. 1 Simulated EEG activity and power spectral density. (a) Interictal, (b) onset

Note that, the positive k_{i1} and k_{i2} constants are free parameters tuned to achieve desired closed loop response. It has been acquired, through sensitivity analysis, that the quality of closed loop system is more sensitive to the parameters of the control input applied to the excitatory subset. This fact was observed in simulations as well.

The result of applying control signals u_i ($i=1, 2, 3, 4$) to each subset to move the closed loop system from onset period to interictal activity is shown in Figure 2.

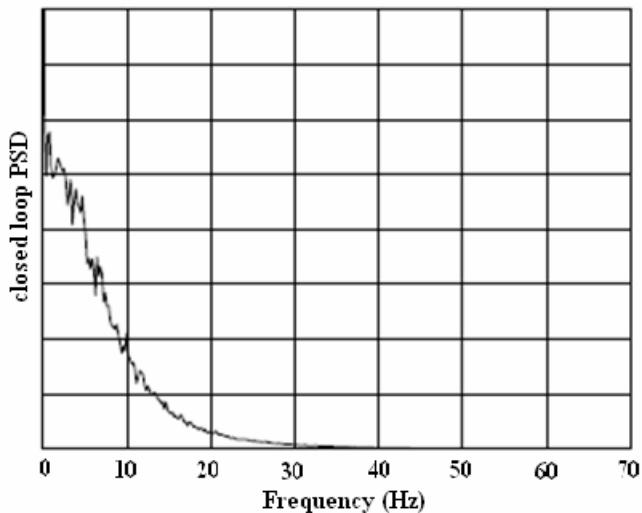


Fig. 2 Response of the controlled onset segment

III. CONCLUSION

In this work we have developed a control strategy on a physiologically relevant model of epilepsy. The results show that by applying a bounded definite electrical signal to each of the main pyramidal cell and three groups of interneurons we can interrupt the state transition from

entering the electrical onset and restore the normal interictal activity. The described algorithm can be validated using in experimental models. The control strategy has the ability to make the model output (EEG activity) move backward from every destructive state.

REFERENCES

1. Wendling F. (2008) Computational models of epileptic activity: a bridge between observation and pathophysiological interpretation. *Expert Rev Neurother* 8(6): 889-896
2. Bardakjian B.L., Diamant N.E. (1994) A mapped clock oscillator model for transmembrane electrical rhythmic activity in excitable cells. *J Theor Biol* 166: 225-235
3. Cosandier-Rimele D., Badier J.M., Chauvel P., Wendling F. (2007) A physiologically plausible spatio-temporal model for EEG signals recorded with intracerebral electrodes in human partial epilepsy. *IEEE Trans Biomed Eng* 54(3): 380-388
4. Wendling F., Bartolomei F., Bellanger J., Chauvel P. (2002) Epileptic fast activity can be explained by a model of impaired GABAergic dendritic inhibition. *Eur J Neurosci* 15:1499-1508
5. Durand D.M., Bikson M. (2001) Suppression and control of epileptiform activity by electrical stimulation; a review. *IEEE proc.* 89: 1065-1082
6. Chiu A.W.L., Bardakjian B.L. (2004) Control of state transition in an in-silico model of epilepsy using small perturbations. *IEEE Trans Biomed Eng.* 51: 1856-1859
7. Krstić M., Kanellakopoulos I., Kokotović P.V. (1995) *Nonlinear and Adaptive Control Design*. John Wiley & sons
8. Wendling F., Hernandez A., Bellanger J.J., Chauvel P., Bartolomei F. (2005) Interictal to ictal transition in human temporal lobe epilepsy: insights from a computational model of intracerebral EEG. *J Clin Neurophysio.* 22: 343-356

Author: Naghmeh Mostofi
 Institute: Iran university of science and technology
 Street: Resalat, Farjam
 City: Tehran
 Country: Iran
 Email: naghmeh.mostofi@gmail.com

Walkaround[®] Assisted Walking of Stroke Patients

M. Đurić-Jovičić^{1,2}, I. Milovanović^{1,2}, N. Jovičić¹, and D.B. Popović^{1,2,3}

¹ Faculty of Electrical Engineering, University of Belgrade, Belgrade, Serbia

² FATRONIK SERBIA, Belgrade, Serbia

³ Department of Health Sciences and Technology, Aalborg University, Denmark

Abstract— We describe here the differences in kinematics, ground force reactions, and temporal parameters of the gait of stroke patients walking assisted by a walking assist (e.g., cane) or therapist, and supported by a powered walking frame termed Walkaround[®]. The Walkaround[®] prevents from falling and supports trunk orientation by means of an ergonomic lumbar belt attached to the rigid wheeled frame by a suspensor system. The term powered relates to the electrical drives on the rear wheels that provide externally controlled mobility. The assessment of walking was done by a wireless system that estimates joint angles and distribution of ground force reactions. Ten stroke patients participated in this study and walked over the level ground over the distance of 6 meters. The Walkaround[®] allows significantly faster walking, improves the symmetry, and increases the range of joint angles. The users felt safer and the therapists were relieved from the physical effort of supporting stroke patients when walking within the Walkaround[®].

Keywords— dynamics, kinematics, stroke, symmetry, training of walking.

I. INTRODUCTION

A stroke is the rapidly developing loss of brain functions due to a disturbance in the blood vessels supplying blood to the brain. As a result, the affected area of the brain is unable to function, leading to the inability to move upper and lower extremity on one side of the body, understand or formulate speech, or the inability to see one side of the visual field. The motor impairment which follows stroke is called hemiplegia. The exercising of the walking is an important component of the rehabilitation. Most stroke patients, especially in the acute phase, need assistance when walking since they have reduced ability to control extensor muscles; thereby assume a crouched position during the stance on the affected leg. In parallel, stroke patients have reduced strength of flexors leading to dragging of the leg during swing, often with the drop foot that prevents the walking. The assistance required to allow walking is labor intensive.

This led to the introduction of robots that drive the legs of stroke patients on a powered treadmill (e.g., Locomat[®] [1], Advanced Gait Trainer[®] [2], Lopes [3]). Today, there is a development of wheeled systems which allow hands-free

walking (e.g., KineAssist [4], Compliant Walker [5], Walkaround[®] [6]). The Walkaround[®] prevents from falling and provides postural stability due to the use of an ergonomic lumbar belt that is attached to the rigid frame through a suspensor system. The Walkaround[®] system used in this study was powered. The power refers to two motor units that drive the Walkaround[®] (controlled speed and direction of walking). The speed and direction of motion can be controlled by a joystick.

The hypothesis that we tested was that the postural control, partial body-weight support, and propulsion provided by a powered Walkaround[®] allow the walking pattern that is more alike healthy walking compared with the pattern when they are assisted by a therapist or use cane, crutch or similar walking assist.

II. METHODS AND MATERIAL

We assessed differences in the walking patterns in ten stroke patients (age: 56±4 years). The inclusion criteria were: ability to stand on the paretic leg with some support, ability to slowly ambulate with the assistance of therapist, no other neurological deficits, cognitively ready to understand the use of the new walking assistive system and the task presented to them. All patients signed the informed consent approved by the local ethics committee. Patients were asked to walk along 8-meters long straight-line path with their natural cadence. Data from the 6 meters in the middle of the walking event were used for assessment. The following types of walking were analyzed: 1) walking assisted by a therapist or using a cane, crutch or similar device, and 2) walking assisted with the powered Walkaround[®] (Fig 1).

The assessment system was a wireless 24 channel device by based on accelerometers and force sensing resistors described elsewhere [7]. The system sends signals via Bluetooth to the host computer, and special software generates information that allows determination of horizontal and vertical components of ground force reactions; and ankle, knee, and hip joint angles from both legs. The same software provides temporal information allowing the estimation of the cadence, symmetry index, and walking velocity.

Accelerometers based sensors were placed on thighs, shanks and feet. Four force sensing resistors (FSRs) per leg were placed in forefoot and heel zones of sole (Fig. 1).

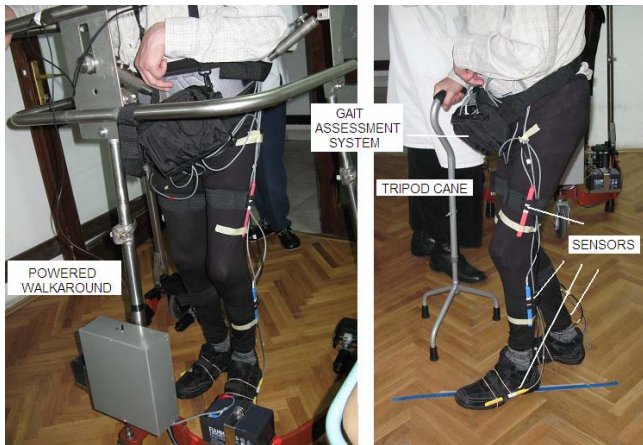


Fig 1 – Stroke patient instrumented with the gait assessment system within the Walkaround® and when walking with the cane

The outcome measures were joint angles, ground reaction forces, and the symmetry index. The symmetry index (SI) was calculated by using the modified formula introduced by Robinson et al. [8]:

$$SI = 2 \frac{T_{parietic} - T_{nonparietic}}{T_{parietic} + T_{nonparietic}} 100$$

$T_{parietic}$ and $T_{nonparietic}$ are the durations of the stride for the parietic and nonparietic leg. SI can be positive or negative, and the ideal symmetry index is $SI = 0$.

III. RESULTLS

Fig. 2 shows a representative set of data for one patient when walking with walking assist and when using the powered Walkaround®. There is a noticeable difference between the duration of the stride when walking with the tripod cane and the stride duration when being supported by the Walkaround®. There are also noticeable differences between the joint angles when walking under two different conditions.

Fig. 3 shows the aggregate result for all ten patients included in the study (white bars). The randomly selected group of patients included two patients who were too good walkers ($v > 0.5$ m/s, without any assistance). When these two patients were excluded from the analysis, since the maximum speed of the powered Walkaround® was set intentionally to about 0.3 m/s the results for the group changed (Fig. 3, filled bars). The data for the eight-patient group has normal distribution.

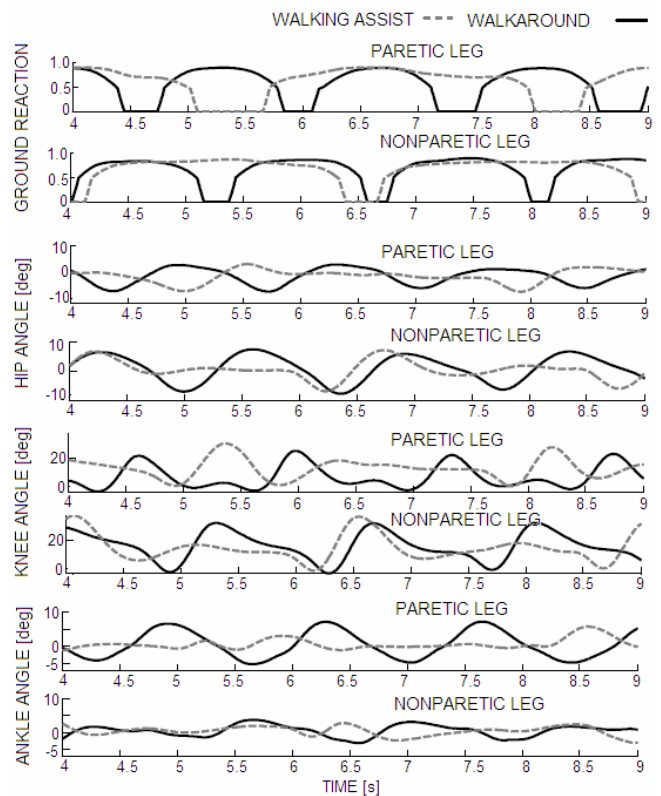


Fig. 2: Vertical ground reaction forces, and hip, knee, and ankle angles recorded during gait assisted by other assists and Walkaround®.

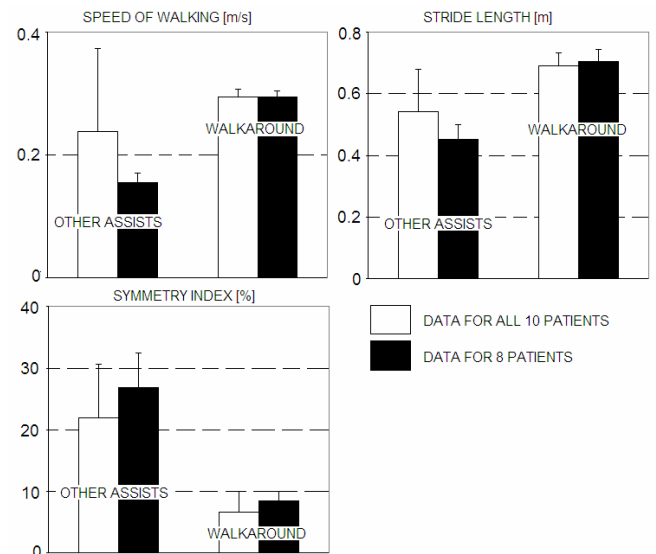


Figure 3: Walking speed, stride length and the symmetry index for all patients (empty bars) and the reduced homogeneous group of eight patients (filled bars)

IV. DISCUSSION

Table I is the summary of analysis of the results for the group of eight subjects that formed the homogenous group.

Table I – t-test (Two sample assuming unequal variances) for walking speed, stride length and symmetry index

Speed of walking [m/s]		
	<i>Variable 1</i>	<i>Variable 2</i>
Mean	0.155847	0.294831
Variance	0.000351	0.000122
P(T<=t) one-tail	7.84E-10	
t Critical one-tail	1.795885	
Stride length [m]		
	<i>Variable 1</i>	<i>Variable 2</i>
Mean	0.451251	0.705698
Variance	0.003257	0.004497
P(T<=t) one-tail	5.33E-07	
t Critical one-tail	1.76131	
Symmetry index [%]		
	<i>Variable 1</i>	<i>Variable 2</i>
Mean	26.82946	8.362369
Variance	39.15874	4.624948
P(T<=t) one-tail	1.23E-05	
t Critical one-tail	1.833113	

The possible conclusion from this small study is that postural control provided with the new assistive system is beneficial. However, it is important to consider only patients who need additional support. Namely, the two patients that were not considered for the statistical analysis are not benefiting from the Walkaround[®] since their ability to walk is above the preset maximum speed of the device. In this study we set the maximum speed of the Walkaround[®] to the value being acceptable by poor walkers which was below the speed of walking of the two good walkers.

One of the findings is that the use of powered Walkaround[®] requires that patients learn how to use the system and develop the “trust” that they will not fall. This led to the definition of the protocol of using the system: 1) initial phase of the use of the system is training of standing and learning of effective use; 2) second phase includes slow walking since the “push” that powered Walkaround[®] generates at the pelvic region is a completely new experience for stroke patients.

V. CONCLUSION

The powered Walkaround[®], when compared to walk assists (cane, crutch) or therapists’ assistance, allows better training of the walking, and potentially could lead to faster and to the higher degree recovery of walking. The powered Walkaround[®] can be programmed to iteratively increase the walking speed and decrease the stiffness of the suspensor based support of the trunk. The overall acceptance of the Walkaround[®] was excellent.

ACKNOWLEDGMENT

We would like to acknowledge valuable suggestions during clinical testing of the Walkaround[®] to Laszlo Schwirtlich, M.D., Aleksandra Dragin, M.D., Aleksandra Stefanović, M.D., and Anđelka Pjanović, P.T. from the Institute for Rehabilitation „Dr Miroslav Zotović“, Belgrade.

The work on this project was partly supported by Ministry for Science and Technology of Serbia, Belgrade, Serbia, Danish National Research Foundation, Copenhagen, Denmark, and Fundacion Fatronik, San Sebastian, Spain.

REFERENCES

1. Colombo G, Joerg M, Schreier R, Dietz V (2000) Treadmill training of paraplegic patients using a robotic orthosis. *J Rehabil Res Dev*, 37(6): 693–700.
2. Hesse S, Uhlenbrock D. (2000) A mechanized gait trainer for restoration of gait, *J Rehabil Res Dev*, 37(6): 701–708.
3. Veneman JF, Kruidhof R, et al. (2007) Design and evaluation of the LOPEX exoskeleton robot for interactive gait rehabilitation. *IEEE Trans Neural Syst Rehabil Eng*, 15(3): 379–386.
4. Patton J, Brown DA et al., (2008) Kineassist: design and development of a robotic overground gait and balance therapy device. *Top Stroke Rehabil*, 15(2): 131–139.
5. Kerley JE Crane B. (1992) Compliant walker, U.S. Patent 5,174,590.
6. Veg A, Popović DB (2008) Walkaround: Mobile balance support for therapy of walking, *IEEE Trans Neu Syst RTNSRE-16(3)*: 264–269.
7. Jovičić NS, Đurić MD, Popović DB (2007) Portable data acquisition system for gait analysis based on Bluetooth communication, In *Telecommunications Forum, TELFOR 2007*, pp. Belgrade, Serbia.
8. Robinson RO, Herzog W, Bigg BM, (1987) Use of platform variables to quantify the effects of chiropractors manipulation on gait symmetry, *J Manipulative Physiol Ther.*, 10:172-176

Author: Prof. Dejan B. Popović
 Institute: Aalborg University, Department of Health Sciences and Technology, SMI
 Street: Fredrik Bajers Vej 7D3
 City: Aalborg
 Country: Denmark
 Email: dbp@hst.aau.dk

Vision and Distance Based Control of Prehension

D.B. Popović^{1,2}, S. Došen¹ and M. B. Popović^{1,2,3}

¹ Department of Health Sciences and Technology, Aalborg University, Denmark

² Faculty of Electrical Engineering, University of Belgrade, Serbia

³ Institute for Multidisciplinary Research, Belgrade, Serbia

Abstract— We present the application of camera and distance sensors for control of prehension (hand orientation and hand opening) that could be integrated into Smarhand, a multi-degree of freedom intelligent artificial hand. The algorithm presented comprises two functions: 1) recognition of the type of grasp based on the comparison of the image of the object that is to be grasped with the previously defined primitives, and recognition of the object size based on the distance to the object and the pixel count, and 2) generation of signals for the wrist and forearm rotations, and thumb and fingers opening. The algorithm was developed by the use of inductive learning, applied to the experimental data obtained in healthy subjects during grasping. The experimental data included prehension and grasping kinematics acquired with motion capture camera based system, and distance and pixel count from the miniature camera and distance sensor mounted on the wrist of the subjects. The objects used in this study were: small and big can requiring palmar grasp, CD and book requiring lateral grasp, and pencil and needle for the analysis of pinch grip. We found reproducible, distinguishable differences in hand orientation and prehension for objects analyzed. The developed computer knowledge was a framework for a rule-base which can be used for real-time control of wrist rotator (pronation/supination), wrist flexion/extension and wrist radial/ulnar rotation, and commands for opening of the thumb and fingers.

Keywords— artificial hand, control, grasping, prehension, vision

I. INTRODUCTION

The aim of the SmartHand project [1] is a new intelligent multi-degree of freedom artificial hand that should enhance the cost/benefit of using a powered assistive system; hence, ultimately improve the quality of life. The SmartHand research focuses on the development of control and new artificial hand with several life-like sensors, advanced EMG control, development of technologies for direct interface with nerves in the stump, integration of tactile feedback, and methodology of assessing the efficacy of the new artificial hand. Here, we present one additional feature suggested as part of the SmartHand project: Coordination of goal-directed movement based on simple vision sensory system mounted on the artificial hand.

Goal-directed movement is a planned change of arm and hand segments positions ultimately leading to a task. The success of goal-directed movement depends on a balance of initial programming and subsequent correction. Initial programming is based partly on visual perception of an object, and partly on proprioception (e.g., a visual cue is used to decide what type of grasp to use). Generating movement requires from the controller to solve the following three problems: multi-modal integration or sensors data intake, complex transformations between different spatial and intrinsic coordinate systems, and motor commands adequate to attain the aim (resolving problems associated with movement dynamics).

The visual information is used to identify a target and its location in space, and also for corrections of ongoing movement. This observation raises the question of how visual guidance is used in the control of the grasping. The grasping comprises the following process: orienting the hand, opening the hand so that the object fits comfortably, contacting the object, and forming a firm grip. The human hand has a variety of ways to grasp objects firmly. The selection of the grasp depends on both the function that has to be achieved and the physical constraints of the object and the hand. Schlesinger [2] suggested a taxonomy that was developed to capture the versatility of human hands for designing functionally effective prosthetic hands. The simplest taxonomy includes set of three grasp postures (Fig. 1).

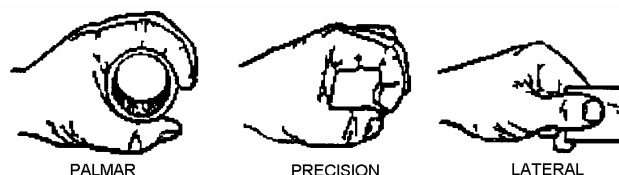


Figure 1: Different patterns of grasping: 1) cylindrical or spherical (palmar); 2) tip (pinch); and 3) lateral (key).

For practical applications one can consider only palmar, lateral, and pinch grasps since those are used for almost 95% of all functions. The pattern of finger movements that arises prior to and during grasping reflects the activity of visuomotor mechanisms for detecting the shape of the object and generating appropriate motor commands. The task is for the motor system of the hand to build an “opposition

space”, which would take into account both the shape of the object and the biomechanics of the hand [3, 4]. Experimental data suggest that there are preferred orientations for the hand opposition space.

The hand posture selected during the preshape defines the optimal opposition space for applying the required forces to the object [5]. Using the term opposition authors described three basic directions along which the human hand can apply forces: 1) pad opposition occurring between hand surfaces along a direction parallel to the palm. The surfaces are typically the volar surface of the fingers and thumb near or on the pads (pinch grasp); 2) palm opposition occurring between hand surfaces along a direction perpendicular to the palm (palmar grasp); and 3) side opposition occurring in the direction generally transverse to the palm (lateral grasp). Paulignan *et al.* [6] showed that the same orientation of the hand was retained during prehension of the same object placed at different positions in the working space, which implies different degrees of rotation of the wrist or the elbow.

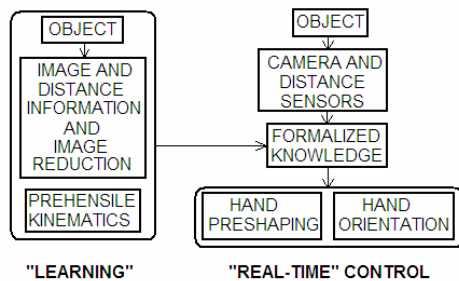


Figure 2: The model of the hand orientation and preshaping controller for the artificial hand. The block on the left is the off-line process which replaces heuristics and provides the knowledge which implemented within a rule-based controller is presented in the right panel.

The stable grasp requires at least three points of contacts that will form three opposition planes, and ensure static equilibrium of the objects. The visual phase of grasping does not imply the use of touch, but it is in direct continuity with the tactile phase and includes preparatory mechanisms for active touch [7-9]. The fingers begin to shape during transportation of the hand at the object location. Preshaping first involves a progressive opening of the grip with straightening of the fingers, followed by a closure of the grip until it matches object size. The point in time where grip size is largest (maximum grip size) is a clearly identifiable landmark which occurs within about 60 to 70 percent of the duration of the reach, that is well before the fingers come in contact with the object [10-12]. The size of aperture during grip formation covaries with object size [13-15]. Marteniuk and colleagues [14] related closure pattern of grip formation to the thumb – finger geometry.

Based on the presented aspects of control found in biological control we suggest an important addition to the controller of the artificial hand for orientation and opening which uses sensors driven rule-based control (Fig. 2). The sensors envisioned are a simple camera and distance sensor mounted on the wrist of the artificial hand.

II. METHODS AND MATERIAL

The experiments were performed in five healthy volunteers who signed the informed consent approved by the local ethics committee. Subjects were comfortably seating in front of the working desk. The height of the chair was adjusted to force subjects to perform movements without sliding their arm on the desk. The following objects were used for the experiments: 0.5 l bottle, 0.3 l soft drink can (palmar grasps), computer CD and 300 pages book positioned on the small post (lateral grasp), and needle and pen (pinch grip). The positions of the objects were varied to test grasping at various distances and directions of movement from the initial (resting) position of the hand. The order of grasping was randomized, and recordings for each combination were collected for at least ten times.

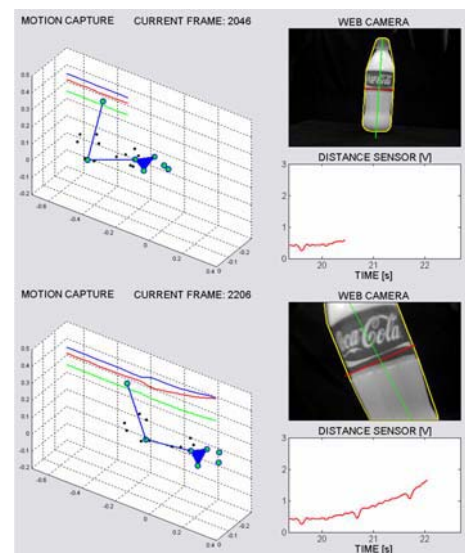


Figure 3: An example image with data used for estimation of distance, objects shape and size. The arm segments in left part of panels are obtained from the reflective sensors, and the right parts of panels show the images from the miniature camera and the voltage output from the distance sensor (inversely proportional to the distance). The signals at the walls are relative Euler angles of the wrist with respect to the forearm (hand orientation).

The experiments were performed at the Center for Sensory-Motor Interaction (SMI), Aalborg University with fixed camera based motion capture system (8 ProReflex MCU240 cameras, Qualisys, SE). Passive retro-reflective markers were placed on the individual's upper arm, forearm, and hand according to recommendations for the human motion analysis software (Visual3D, C-Motion, USA) [16]. In house designed soft wrist holder was instrumented with a miniature web camera and the infrared laser-diode distance sensor (GP2D12, Sharp, JP). The camera and the distance sensor were mounted at positions that allow unobstructed view of the object during the grasping tests (Fig. 3).

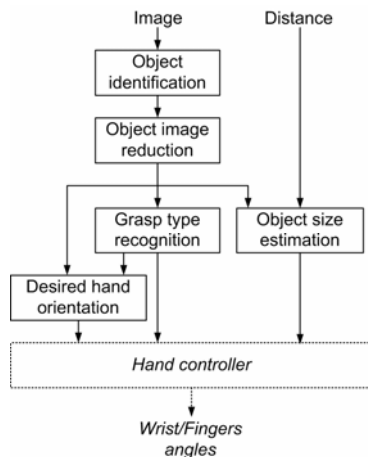


Figure 4: Extracting object properties from the data given by the web camera and the distance sensor.

The method that we developed for extracting object properties from the recorded sensor data is depicted in Fig. 4. The steps are implemented in Matlab 7.4. First, the object, which is the target for grasping, is identified and separated from the background by the application of thresholding and morphological filtering [17]. Then, the image of the object is reduced to a set of simple primitives (features). We selected a set of scale independent and rotation independent image features in order to obtain a classifier that is robust with respect to orientation and/or size of the object [18]. The primitives are input for classification based on machine learning. The classification estimates the type of the grasp.

In this study, the classifier was implemented (trained) by the use of inductive learning [19]. The learning produced a set of decision trees. A separate tree was constructed to recognize each grasping pattern (i.e., palmar, pinch, lateral). Training and testing data sets were formed from the recorded grasping trials. There were two objects for each grasping pattern (e.g., a bottle and a can for the palmar grasp); one was used for the training and the other for the

testing. Furthermore, the testing set included different directions and distances, which were "unseen" during the training.

Based on the type of grasp and description of the object, desired orientation of the hand is determined. In parallel, the information from the distance sensor is used to estimate the size of the object in real world units from the size of the object's image in pixels.

The distance versus voltage characteristics and the ratio of real units to pixels was determined by calibrating the distance sensor and the camera at several distances by using a custom made calibration pattern (e.g., a matrix of black dots on white background). Finally, the estimated object properties are fed into a high-level hand controller. The task of the controller is to integrate these data and calculate the angles for the wrist and fingers of the artificial hand that would orient the hand properly and make the correct aperture for the grasp. The hand controller was not implemented in this study.

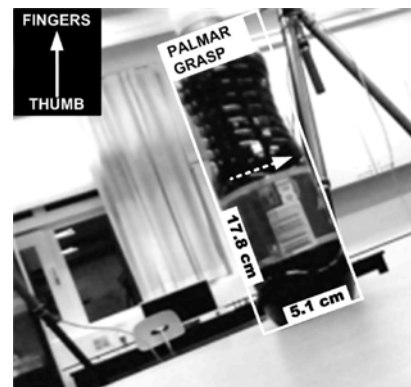


Figure 5: Estimated properties for grasping a 0.5 liter bottle. The recognized grasp type, estimated object dimensions in 2D and target opposition vector are depicted. The orientation of the hand is in the top left corner.

III. RESULTS

A representative result, that is, the output of the processing which is shown in Fig. 4, is given in Fig. 5. The figure shows the object properties estimated in one of the trials when grasping a 0.5 ℓ bottle. The type of the grasp and the estimated object dimensions (height, width) are superimposed to the original image. The orientation of the fingers and thumbs (fixed with respect to the web camera) is shown as the full arrow. The desired orientation of the hand (opposition vector) is shown by the dashed arrow. The actual dimensions of the bottle were 5.9 cm (base diameter), and 19.2 cm (height).

Overall, the classifier for the type of grasp was successful in 85% of the cases from the testing data set. The error in estimation of object dimensions in 2D was between 5-15%. The applicability of the estimation algorithm was limited with the effective working range of the distance sensor (e.g., from 10 to 80 cm). The estimation was more precise for close than for distant objects. In some cases (< 8%) the system failed to register the target object. Subject's hand was blocking the line of sight of the camera and/or distance sensor. Careful system mounting and aligning is important to minimize these misses.

IV. DISCUSSION

In this paper we presented a method for real-time estimation of the shape and the size of the object from the low-resolution, web camera image (frame rate = 15 images per second) and the reflective infrared distance sensor. The size and the shape of the objects are determined with the precision defined with the task: orientation of the hand to allow the appropriate modality of grasping and adequate opening of the hand, which allows the hand to generate the opposition space-ensuring grasp. The actual grasping was assumed to be controlled by a different controller that uses tactical, position and force sensors built into the hand.

The algorithm at this point was implemented within Matlab environment operating on a state of the art PC; yet, the computing needs are relatively low, and the translation to the microcontroller is straight-forward. The update of the image needed for estimation of the size and shape, and necessary corrections during typical daily reaching and grasping is within the time window of 80 ms; hence, the frame rate of 15 images per second is sufficient.

The camera and the distance sensors are assumed to be part of the artificial arm. The use of this system considers the artificial hand that incorporates active control of wrist and forearm. However, the control algorithm for opening can be used in cases where the wrist and forearm are not externally controlled.

The same control method is applicable for control of neural prostheses for restoration of reaching and grasping in stroke and spinal cord injured individuals.

ACKNOWLEDGMENT

The work on this project was supported by the SmartHand - The Smart Bio-adaptive Hand Prosthesis, Contract No: NMP4-CT-206-0033423, FP 6 Strep project, 2006-2009; Danish National Foundation, Copenhagen Denmark, and Ministry for Science and Technology of Serbia, Belgrade.

REFERENCES

1. SmartHand web page. Available online at: <http://www.elmat.lth.se/~smarhand/index.html>
2. Schlesinger G (1919) Der Mechanische Aufbau der kunstlichen Glieder. In: Borchardt M (ed.) Ersatzglieder und Arbeitshilfen fur Kriegsbeschadigte und Unfallverletzte. Springer, Berlin, pp 21-600
3. Arbib MA (1985) Schemas for the temporal control of behavior. *Hum Neurobiol* 4:63-72
4. Iberall T, MacKenzie CL (1990) Opposition space and human prehension. In: Venkataraman ST, Iberall T (eds.) *Dextrous robot hands*. Springer-Verlag, NY, pp 32-54
5. Iberall T, Bingham G, Arbib MA (1986) Opposition space as a structuring concept for the analysis of skilled hand movements. In: Heuer H, Fromm C (eds.) *Generation and modulation of action pattern*.
6. Paulignan Y, MacKenzie CL, Marteniuk RG, Jeannerod M (1991) Selective perturbation of visual input during prehension movements. I. The effects of changing object position. *Exp Brain Res* 83:502-512
7. Jeannerod M (1993) The hand and the object: the role of posterior parietal cortex in forming motor representations. *J Physiol Pharmacol* 72:535-541
8. MacKenzie CL, Iberall T (1994) The Grasping Hand. In: Stelmach GE, Vroom PA (eds.) *Advances in Psychology Series 104*. North-Holland
9. Zong-Ming Li, Latash ML, Zatsiorsky VM (1998) Force sharing among fingers as a model of the redundancy problem. *Exp Brain Res* 119:276-286
10. Jeannerod M (1981) Intersegmental coordination during reaching at natural visual objects. In: Long J, Baddeley A (eds.) *Lawrence Erlbaum Associates, Hillsdale, NJ*
11. Jeannerod M (1984) The timing of natural prehension movements. *J Motor Behav* 16(3):235-254
12. Wing AM, Turton A, Fraser C (1986) Grasp size and accuracy of approach in reaching. *J Motor Behav* 18(3):245-260
13. Marteniuk RG, MacKenzie CL, Jeannerod M (1987) Constraints on human arm movement trajectories. *Can J Psychol* 41:365-378
14. Marteniuk RG, MacKenzie CL, Leavitt JL (1990) The inadequacies of a straight physical account of motor control. In: Whiting HTA, Meijer OG, van Wieringen PCW (eds.) *The Natural-Physical Approach to Movement Control*. Free Univ Press, Amsterdam, pp 95-115
15. Gentilucci M, Castiello U, Corradini ML, Scarpa M, Umilta C, Rizzolatti G (1991) Influence of different types of grasping on the transport component of prehension movements. *Neurophys* 29:361-378
16. Visual 3D on-line documentation. Available online at: <http://cmotion.com/help/>, accessed on December 4th 2008
17. Gonzales ARC, Woods RE (2007) *Digital Image Processing*. 3rd ed., Prentice Hall.
18. Coatrieux JL (2008) Moment-based approaches in imagining part 2: invariance. *IEEE Eng. Med. Biol. Mag.* 27:81-83.
19. Breiman L., Friedman J, Olshen R., Stone C (1993) *Classification and Regression Trees*. Boca Raton: Chapman & Hall.

Author: Prof. Dejan B. Popović

Institute: Aalborg University, Department of Health Sciences and Technology, SMI

Street: Fredrik Bajers Vej 7D3

City: Aalborg

Country: Denmark

Email: dbp@hst.aau.dk

'InfoCane' based on wireless technology for the visually-handicapped people

Dong-Seok Cho¹, and Jong-Mo Seo^{1,2}

¹ School of Electrical engineering, Seoul National University, Seoul, Korea

² Department of Ophthalmology, School of Medicine, Seoul National University, Seoul, Korea
dongsuk0223@hanmail.net

Abstract— Advanced wireless technology can enhance the traditional low-tech devices. We applied RFID and Bluetooth technology to the cane for the visually-handicapped people to provide the additional and useful information.

Small RFID reader is integrated into the 'InfoCane' to read out the information provided by the ground RFID tag, which is embedded into the guiding tile located at specific places.

The received data are transferred to the host device, which converts the data to pre-defined information. And the Bluetooth dongle transfer this to the Bluetooth headset in the type of a voice signal.

InfoCane can provide various information such as obstacles, milestones or landmarks. Also it can be used as commercial purpose with 'opt-in' function, to provide the right of information choice to the user.

Keywords— cane, RFID, Bluetooth

I. INTRODUCTION

As growing RFID technology, its application fields are getting wider and wider. Several groups proposed devices in helping the visually handicapped people using this technique. Japanese group tried this using RFID and small mobile PC. And other groups also provide the solution using similar technique.

Koichi proposes reader-embedded-cane so as to detect the tags which carry specific data [1]. And small mobile PC as host device is carried by user. So in dangerous place like station or crosswalk, the visually handicapped people can be recognized by RFID. It's very innovative and impressive method, but it might be less practical because mobile PC is somewhat heavier to carry, thus user may have troubles in using them. Other method is integrating reader and host device into the cane for the simplicity and the user's convenience. Then, voice signal from cane is transmitted to user's ear by electrical line.

In this paper, we propose the 'InfoCane'. It has reader, host device and Bluetooth dongle in its body. And RFID tag is embedded inside the guiding tile. Data stored in tag are transferred to Bluetooth headset through the reader, host

device and Bluetooth dongle respectively. Unlike existing guiding devices, interface between cane and user is air. Namely it's wireless device. This wirelessness prevents users from being damaged by potential danger.

Through 'InfoCane', the visually handicapped people can detect important messages given RFID tag. Furthermore, they can get useful information, commercials more easily than ever.



Fig. 1(a) Configuration of user with 'InfoCane'

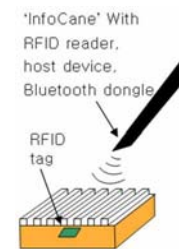


Fig. 1(b) Configuration of 'InfoCane'

II. MATERIALS AND METHODS

The core technologies for the 'InfoCane' are RFID and Bluetooth. To apply RFID technique, frequency band should be determined. In here, 13.56MHz RFID was selected. Because of its small range, data transfer is carried out under the condition that distance between reader and tag is not more than 10cm. Thus visually handicapped people become aware of the data's origin.

We use passive tag as a mean of data storage. Only in resonance between reader and tag, the tag is supplied with power and it transfers data stored in memory to reader. The tags are embedded into the guiding tile. Guiding tiles with the tag are installed in specific locations like crosswalk, subway station, and especially dangerous area to visually handicapped people.

The reader is integrated into the cane. The reader antenna is located on the tip of the cane for the interaction with tag.

And the other part of the reader is apart from antenna about 15cm for the purpose of stability of reader. Because reader is to provide power and process the received data, it is composed of three functional blocks; transmitting block, receiving block, data processing block [2].

Host device plays a role of generating voice signal. The data coming from reader to host device access its memory to find out the voice signal corresponding to its data. Then, it sends a signal to Bluetooth dongle. In here, we realize 'opt-in' function. Naturally, 'InfoCane' is designed to provide essential information and useful commercials for the visually handicapped people. By constituting memory as multilayer, we embody the 'opt-in' function and can filter the unwanted information or commercials. For example, in the 1st layer, most important information related to user's safety is stored. While 'InfoCane' works, data can always access memory's 1st layer. And if user want to receive additional information or commercials, user can switch on to access the 2nd layer. Through the adding 'opt-in' function to cane, we make an improvement of user's right of information choice.

For the more relay to ear, Bluetooth is adopted. Because Bluetooth doesn't need wired contact and doesn't make any crosstalk with RFID, it can be appropriate for our purpose. Once data is converted to voice signals, this voice signals are transmitted directly to Bluetooth headset. Overall system block diagram is shown in Fig. 2 .

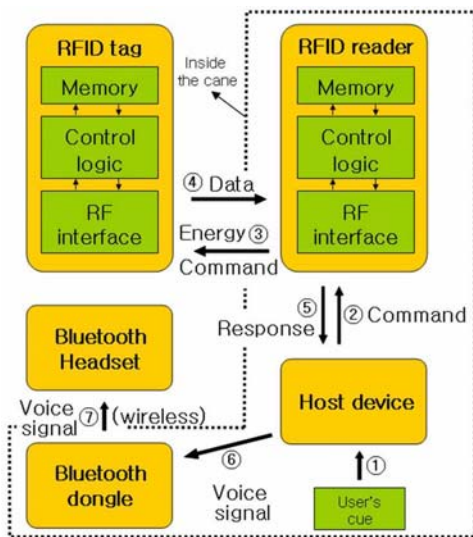


Fig. 2 Overall system configurations

The protocols of RFID follow the ISO. The air interface protocol between tag and reader is defined in ISO18000-3(13.56MHz). ISO 15962 stipulates the protocol about tag driver and logical memory, and ISO 15961 is about the interface between reader and host device. Refer to Fig. 3.

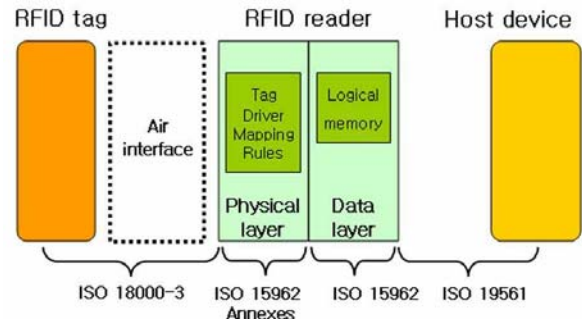


Fig. 3 RFID protocol

Fig. 4 depicts the Bluetooth protocol stacks. The protocols in the stack have been grouped in two categories [3]. The host controller stacks consist of radio, baseband, link manager. Each stack groups together to perform Bluetooth wireless technology. And the host protocol stack links with the Bluetooth module and controls the host controller, then performs the applications. In case of 'InfoCane', HCI, link manger, radio stack are embodied Bluetooth dongle, and other stacks must be realized in host device.

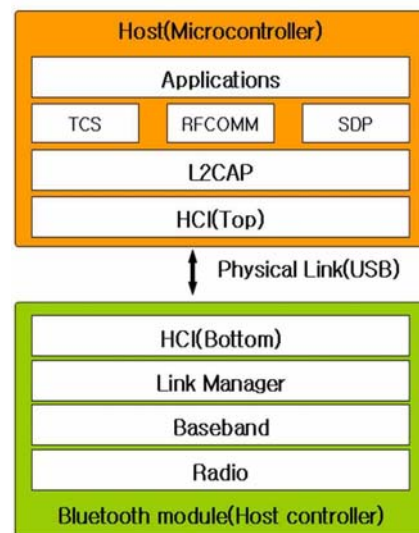


Fig. 4 Bluetooth protocol stack

III. RESULTS

Figure 5 is the proposed system and its installation on the test bed. Patient can use 'InfoCane' like conventional cane for the blind, and by turning on the information function, they can acquire various useful information on tapping over the RFID-embedded 'InfoTile'. Also, because of magnetic coupling between tag and reader, non-magnetic substances cannot interfere with communication. So its performance doesn't depend on weather conditions or other obstacles as long as recognition range maintains.



Fig. 5(a) user with guiding device



Fig. 5(b) Headset



Fig. 5(c) Cane and guiding tile

IV. DISCUSSION

Even though the 'InfoCane' could be a good candidate as the substitute for the conventional cane, there are several things which are needed complement. Because of user's continual tappings, 'InfoCane' must have high durability. Several IC's are embedded with cane, so less impacts must impose on cane. This is worth considering when designing the 'InfoCane'.

It's desirable to design smaller and lighter device. Because users are not robust on the whole, it's harder to stand with cane for a long time. Furthermore, cane looks more compact and nice appearance when embedding small components.

Maybe, it's the most critical point that RFID technique itself cannot identify the direction which data imply. For example, assume that user is heard the message "Five meters in front of you, there is a crosswalk". In this situation,

the visually handicapped people cannot identify the right direction. To solve this problem, it'll be temporal alternatives to block out on side of guiding tile. Unblocked side of guiding tile can be a corresponding direction data imply. See the Fig. 5. Through this method, we anticipate improvement of cane's reliability. However, direction problem of guiding system ultimately must be solved by communication technologies.

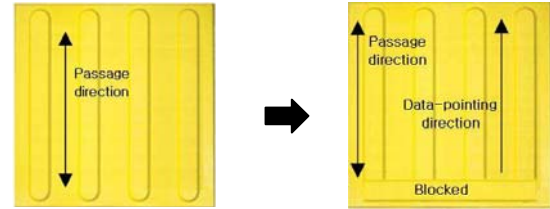


Fig. 5 Direction-enforced guiding tile by blocking one side of them.

V. CONCLUSION

With an 'InfoCane', the visually handicapped people can lead on a safer and more convenient life. Furthermore, they can get useful information like public service advertising or commercials.

ACKNOWLEDGEMENT

This study was supported by a grant of the Korea Health 21 R&D Project, Ministry of Health, Welfare and Family Affairs, Republic of Korea, A050251.

REFERENCES

1. Koichi GOTO et al.(1999) A Mobile Guide System for Visually Disabled Persons
2. Nak-Gwon et al.(2006) Design of a 13.56MHz RFID system
3. Mezo. (2001) Bluestack User's Manual

To feedback or not to feedback? Some open questions for Brain-Computer Interfaces use

R. Carabona¹ and P. Castiglioni¹

¹ Biomedical Technology Department, Santa Maria Nascente Research Hospital, Don Gnocchi Foundation, Milan, Italy

Abstract— Brain-Computer Interfaces (BCI), allowing to operate the environment without muscular activation, can be used as assistive technology as well as neurorehabilitation tool. A BCI exploits brain signal changes induced by event-related potentials (P300) or by voluntary control of the user (Slow Cortical Potentials or Motor Imagery) and this can be achieved using a classifier. A key feature for BCI systems is user-classifier mutual learning, which can be modulated by feedback. There is experimental evidence that feedback can have a positive as well as a negative effect and this is relevant in using BCI both as assistive technology and as neurorehabilitation tool. The aim of this study was to investigate a possible sequence effect on overall accuracy in administering a first training session without feedback and then a second one with feedback. Moreover, we evaluated also a gender effect. We considered a sample of sixteen subjects (ten males), using an EEG-based BCI and executing a Motor Imagery task. Our results, combined with data from literature, indicate the presence of a “cognitive carry-over” effect for continuous feedback in motor imagery, with gender differences not statistically significant. Such a cognitive effect means that the presence or absence of feedback changes the cognitive status of the BCI user and thus the information embedded in the features the classifier uses. Therefore, there should be a sort of cognitive coherence in BCI-training and the assessment of user attitude toward feedback could improve BCI usefulness and effectiveness.

Keywords— Brain-Computer Interface (BCI), feedback, EEG, motor imagery, neurorehabilitation

I. INTRODUCTION

Brain-Computer Interfaces (BCI) rely on brain activity to allow people to operate the environment in a non-muscular way. Therefore, they can serve as assistive technology for severely disabled people as well as neurorehabilitation tool in clinical settings [1].

EEG-based BCI are non invasive interfaces, which use brain signals acquired from the scalp, exploiting EEG changes related to event-related potentials (P300) or to voluntary control (Slow Cortical Potentials, SCP, or Motor Imagery, MI). With respect to SCP and MI, many studies demonstrate that human subjects can voluntarily control their cortical activity, thus inducing changes that can be detected by processing data from EEG acquisitions [2].

A key feature of any BCI system is that there is a form of mutual learning between user, who has to learn to execute a cognitive task, and classifier, who has to be trained in order to achieve high and reliable performances. This mutual learning and adaptation can be mediated by the use of a feedback, which can be either continuous or discrete [3, 4]. Moreover, there is experimental evidence that feedback can have a positive as well as a detrimental effect on the performance of the user [3, 4, 5]. These effects are relevant for BCI usability both as assistive technology and as neurorehabilitation tool. In fact, it can modulate the motivation of disabled people in using BCI as well as the quality of a rehabilitation treatment.

In using BCI as neurorehabilitation tool, there is some new experimental evidence that Motor Imagery could be helpful for stroke patients [6]. Thus, it becomes relevant to study short-term feedback effect for MI paradigms. Moreover, there could be a *sequential* effect, related to the protocol adopted while using BCI. McFarland et al. investigate the short-term feedback effect by considering 12 BCI sessions for the feedback presence (first 10 sessions) versus feedback absence (last 2 sessions) sequence.

The aim of the present study is to investigate the short-term effect of the absence versus presence of continuous feedback on the performance of BCI users, in terms of both overall accuracy and gender related differences in performance.

II. METHODS

Sixteen volunteers, 10 males (median age 33 years, ranging between 21 and 45 years) and 6 females (median age 28.5 years, from 21 to 36 years) participated in this study. Volunteers had no previous experience in BCI sessions and were free of medications. They sat in a comfortable chair, facing a computer screen approximately 1 m away. They were instructed to perform a Motor Imagery task, being relaxed during EEG acquisition. Each session consisted of a *training* phase (without feedback) and a *performance* phase (with feedback).

Subject had to look at a fixation cross displayed in the centre of the monitor. After 3 seconds, an arrow (cue stimulus) pointing to the right or the left, appeared for 1.25s

on the fixation cross and the task for the subject was to imagine a right or left hand movement, according to the direction indicated by the arrow. This trial was repeated 40 times, with the arrow pointing randomly 20 times in each of the two directions. Subjects were aware of the fact that during the training phase there was no feedback. In the performance phase, a continuous feedback overlapped the arrow. The feedback was a horizontal bar indicating the direction of the imagined movement (left or right) as identified by the computer on-line. Its length was continuously updated by means of on-line classification of the features extracted from EEG data.

EEG electrodes are placed according to the 10-20 standard [7] on FC3, FC4, CP3 and CP4. Reference and Ground electrode are placed, respectively, on P8 and Fpz. EEG signals were amplified (g.USBamp, g.tec) and band-pass filtered between 0.5 and 30 Hz. Sampling frequency was 256 Hz. Feature extraction was performed using band power estimation [5] in the 8-12 and 16-24 frequency ranges. Complete experiment set-up, acquisitions, and offline elaborations required 20-40 minutes.

Both in training and performance phase, linear discriminant analysis was used for feature classification and the overall accuracy was defined as the highest accuracy obtained for a series of 40 stimuli presentation for each phase. Weights used for the linear combination of features were updated after the training phase and used for the on-line classification and feedback presentation of the performance phase.

Accuracy change was defined as the difference between the values obtained, respectively, during the performance and the training phase. Those differences were moreover matched within subjects (paired data) and stratified for gender.

Non parametric statistical approach was used in order to test differences in median accuracy (Wilcoxon test) and association between gender and accuracy changes (Fisher exact test, due to small numerosity). Statistical significance was set at 0.05.

III. RESULTS

Results are reported in term of the best overall accuracy reached during, respectively, the training phase and the performance phase (Figure 1). The highest accuracy corresponds to 92.50% and was reached during the training phase (i.e., without feedback). According to the Wilcoxon test, there is no evidence of difference for the median values in the two phases.

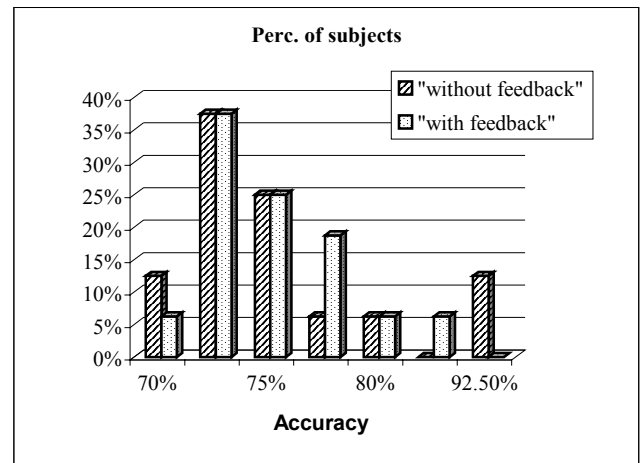


Fig 1 Overall accuracy for training and performance phases

Results for paired data are reported in Table 1 as relative frequencies, for the whole sample as well as for each gender subgroup.

Table 1 Feedback short-term effect on accuracy with respect to gender composition of the sample.

	M (10)	F (6)	All (16)
accuracy unchanged	10%	33.3%	19%
accuracy worsened	50%	17%	37%
accuracy improved	40%	50%	44%
	100%	100%	100%

Paired data for the whole sample (third column in Table 1) indicate that for 56% of the subjects the presence of feedback implies worsened or unchanged accuracy. Moreover, only for a small subgroup the presence of feedback has a "neutral" effect on performance, the other subjects being either facilitated or disturbed by the feedback. With respect to gender differences, Fisher exact test was applied on 2x2 tables (gender being one of the two classification factors) obtained collapsing the "accuracy unchanged" category on the "accuracy worsened" or "accuracy improved" category. In both cases, P-value did not reach statistical significance.

IV. DISCUSSION

Overall accuracy results confirms data previously reported by other investigators [5] with respect to the effect of feedback absence (training phase) and subsequent presence (performance phase) on subject performance.

Results on short-term role of feedback are also reported by McFarland et al. [4]. In their work, they studied feedback

effects the other way around: training with feedback for 10 sessions and then performance without feedback for the remaining two sessions. Although not statistically significant for the whole sample, removal of the feedback seems also to have an effect at the user level.

Combined with our results, experimental evidence indicates a sort of “cognitive carry-over effect”. It means that it is important to consider that the presence or absence of a (whatever) feedback changes the nature of the cognitive experience of a BCI user and thus the information embedded in features submitted to the classifier.

Our results did not show statistical evidence for a gender effect, so the only relevant criterion in training BCI users with respect to feedback is their cognitive reactivity to the feedback itself.

V. CONCLUSIONS

In the present study we considered the short-term role of continuous feedback for an EEG-based BCI, in the framework of a Motor Imagery paradigm. We investigated a sequence effect on overall accuracy (data correctly classified for the whole trial) in administering a first training session without feedback and then a second one (labelled as performance) with feedback. Moreover, we investigated the presence of a gender effect.

Our results did not show any gender significantly relevant effect but, combined with existing experimental evidence, indicate that instead of a sequence effect it is more convenient to think in terms of a “cognitive carry-over” effect of feedback. Thus, it becomes important to assess the user cognitive attitude toward a feedback, in order

select the best setting (with or without feedback) thus improving BCI usefulness and effectiveness both as assistive technology and as neurorehabilitation tool.

REFERENCES

1. Daly J. J., Wolpaw J. R. (2008) Brain-computer interfaces in neurological rehabilitation. *Lancet Neurol* 7: 1032-43
2. Wolpaw J. R., Birbaumer N., McFarland D. J., Pfurtscheller G., and Vaughan T. (2001) Brain-computer interfaces for communication and control. *Clin Neurophysiol* 113: 767–791
3. Neuper C., Schlögl A. and Pfurtscheller G. (1999) Enhancement of left-right sensorimotor EEG differences during feedback-regulated motor imagery. *J Clin Neurophysiol* vol. 16, pp. 373–382
4. McFarland D. J., McCane L. M., and Wolpaw J.R. (1998) EEG-Based Communication and Control: Short-Term Role of Feedback *IEEE Trans Rehab Eng* 6: 7-11
5. Guger C., Edlinger G., Harkam W, Niedermayer I. and Pfurtscheller G. (2003) How Many People are Able to Operate an EEG-Based Brain-Computer Interface (BCI)? *Trans Neural Syst Rehabil Eng* 11: 145-147
6. Buch E., Weber C., Cohen L. G., Braun C., Dimyan M. A. et al. (2008) Think to move: a neuromagnetic Brain-Compute Interface (BCI) system for chronic stroke. *Stroke* 39: 910-917
7. Nuwer M. R., Comi G., Emerson R. et al. (1998) IFCN standards for digital recording of clinical EEG. *International Federation of Clinical Neurophysiology Electroencephalogr Clin Neurophysiol* 106: 259-61

Author: Roberta Carabalona
 Institute: Fondazione Don Carlo Gnocchi
 Street: Via Capecelatro 66
 City: Milan
 Country: Italy
 Email: rcarabalona@dongnocchi.it

Calculation of Systemic Aerobic Capacity without Contact Using Pattern Light Projection

H. Aoki, S. Ichimura, T. Fujiwara, S. Kiyooka, and K. Koshiji

Tokyo University of Science, Noda-si, JAPAN

Abstract— We proposed the calculation method of the systemic aerobic capacity using the noncontact respiration measurement under pedal stroke motion. By the simultaneous measurement with the expiration gas analyzer, we examined the effectiveness of the proposed method. The correlation between the quasi ventilation thresholds calculated by our proposed method and the ventilation thresholds calculated by the expiration gas analyzer is 0.801. And, the gradient of the regression line between two methods is almost 1. This result indicates the possibility of the calculation of the systemic aerobic capacity without contact by the proposed method.

Keywords— respiration measurement, non-contact biomedical measurement, aerobic capacity measurement, motion analysis, image measurement

I. INTRODUCTION

In the evaluation of the systemic aerobic capacity, the anaerobic threshold (AT) by the exercise tolerance test is utilized [1]. The expiration gas analyzer is conventionally used for the measurement of the anaerobic threshold. The expiration gas analyzer is expensive. And, the convenient execution is difficult, because the mask must be mounted on the face of examinee in the measurement.

We have studied the noncontact respiration measurement with the pattern light projection. And, we realized the non-contact measurement of respiration variation under pedaling motion by the recumbent type bicycle ergometer [2]. And, we proposed a method for calculating quasi ventilation threshold (QVT) as the value which corresponded to ventilation threshold (VT). VT is known as a kind of AT, and it is calculated from the change of minute ventilation (VE) in giving the ergometer exercise by the lamp load method [3]. The increasing rate of VE increases at VT. The lactate production is activated by the generation of the anaerobic energy. Therefore, the ventilation volume increases by forming carbon dioxide, when formed lactic acid is buffered in bicarbonate ion [4]. The method for deciding the point where the increasing rate of VE with the increment of the load changes as VT is called V-slope method [5].

We calculated QVT by applying the V-slope method to the respiration variation measured by our noncontact respiration measurement, and compared with VT calculated by

the expiration gas analyzer. As the result, QVT and VT show the near value. However, we were not able to examine those correlation sufficiently, since there was small number of examinees and the difference of the systemic aerobic capacities between the examinees was small [6].

In this study, we carry out the re-examination with sufficient number of measuring data.

II. METHOD

A. Non-contact measurement of respiratory movement

As shown in fig. 1, the pattern light projector and the CCD camera are installed over the examinee, who pedals the bicycle ergometer. The bicycle ergometer is the recumbent type.

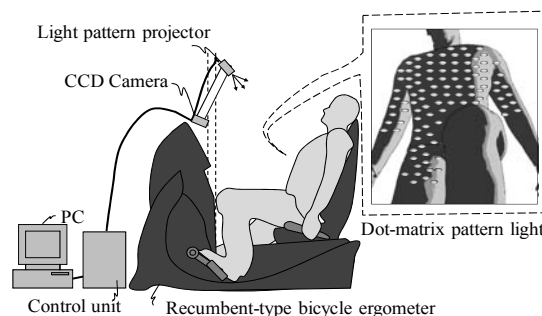


Fig. 1 System configuration

The pattern light projector projects the dot-matrix pattern light on the thorax and abdomen of the examinee, as shown fig. 2. The CCD camera picks up the motion-image of dot-matrix pattern light.

The pattern light projector is composed of two optical elements and a laser source. The optical element, called the fiber grating (FG) element, consists of the optical fiber sheets formed by flatly arranged several hundred optical-fibers. Two optical fiber sheets are orthogonalized. When the laser beam is emitted to the optical elements, the optical elements work as the diffraction grating [7].

As shown in fig. 3, the light dots shift from side to side in the motion-image with the vertical motion of the thorax and

abdomen of the examinee. The movement of light dots in the image is related to the vertical movement of the thorax and abdomen with respiration and pedaling.

In the optical configuration as shown in fig. 3, the relationship between the vertical movement of the thoracoabdominal part, represented by a symbol ΔZ , and the movement of a light dot in the image, represented by a symbol ΔP , is shown by following equation:

$$\Delta P = \frac{\Delta Z}{Z(Z - \Delta Z)} DL \tag{1}$$

where Z is the distance from the segment which connects the pattern light projector with the CCD camera to the dot light on the body surface at last frame, D is the focal distance of the lens, and L is the distance from the center of the lens to the pattern light projector. This equation is based on the principle of the triangulation.

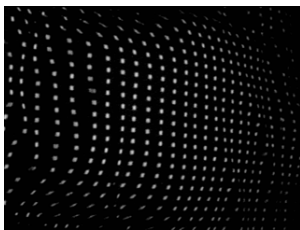


Fig. 2 Image of dot-matrix pattern light

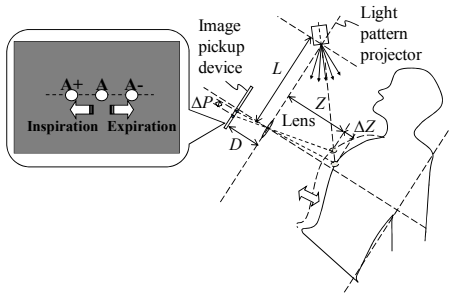


Fig. 3 Optical arrangement

B. Extraction of respiratory movement

The inter-frame movement of each light dot is calculated and the inter-frame movements of all dots are totalized. The total inter-frame movement means the body surface movement in the thorax and abdomen with respiration and pedaling between frames.

When the examinee works the pedal, the inter-frame movement of dot lights originates from not only the respiratory movement but also the pedaling movement. Since the pedaling movement is larger than the respiratory movement,

the pedaling movement is principal component in the waveform of the total movement.

In this study, the examinee pedals the bicycle ergometer at 60 rotations per one minute. By applying the FFT to the waveform of the total movement and removing the higher frequency component of bicycle pedaling, the low frequency component of the respiratory movement is extracted as shown in fig. 4.

Since only the respiratory movement component is contained, the waveform after the low-pass filtering is a sinusoidal wave which vibrates at the respiration frequency. The sign of the sinusoidal waveform has shown the condition of the respiration. That is to say, the examinee exhales the breath in the period when the waveform is the positive value. Reversely, the examinee inhales the breath in the period when the waveform is a negative value. In expiration and inspiration, the sign is reversed.

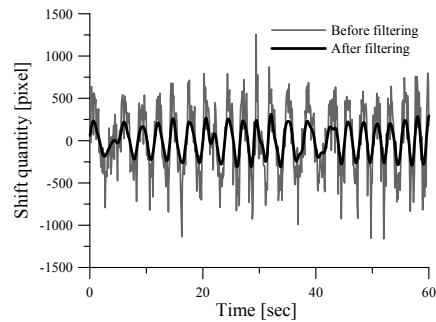


Fig. 4 Filtering of respiratory movement

The integrated value of the waveform in the exhalation interval shows the thorax and abdomen movement with one exhalation. Similarly, the integrated value of the waveform in the inhalation interval shows the thorax and abdomen movement with one inhalation. The integrated value calculated in the exhalation interval is called quasi expiratory flow-rate (QFE). And, the integrated value calculated in the inhalation interval is called quasi inspiratory flow-rate.

C. Calculation of ventilation threshold

It is considered that the product of respiratory rate per one minute and QFE is correspondent to VE , as above-mentioned QFE is correspondent to the tidal volume. Here, the product of respiratory rate per one minute and QFE is called quasi minute volume (QVE).

QVE changes as well as VE , when the lamp load was given to the examinee. Therefore, it is possible to calculate VT from the point where the increasing rate of QVE with the increment of the load changes. In the scatter plot of

QVE-Load as shown in fig. 5, before and behind any point, two regression lines are calculated from the measured value. And, error $E(n)$ between two regression lines and measured values is shown in the following equation:

$$E(n) = \sum_{i=1}^n \{y_i - (a_1x_i + b_1)\}^2 + \sum_{i=n+1}^N \{y_i - (a_2x_i + b_2)\}^2 \quad (2)$$

where measured data set is given by $(x_1, y_1), (x_2, y_2), \dots, (x_N, y_N)$ and x_i is set as the load and y_i is set as QVE ($i=1, 2, \dots, N$). Here, the regression formula of data set $(x_1, y_1)-(x_n, y_n)$ is calculated as $y=a_1x+b_1$ and the regression formula of data set $(x_{n+1}, y_{n+1})-(x_N, y_N)$ is calculated as $y=a_2x+b_2$. The load in which the error $E(n)$ between measured value and regression line becomes a minimum is decided as quasi ventilation threshold (QVT).

It is not possible to apply above-mentioned method for extracting the respiratory movement, when the respiratory rate of the examinee becomes over of 60 breaths per minute. However, VT appears before the respiratory rate exceeds 60 breaths per minute, since the burden to the cardiopulmonary is small in the exercise test with the bicycle ergometer. Incidentally, the respiratory rate of the examinee in the peak load was a maximum of about 40 breaths per minute in the lamp load method by the recumbent-type bicycle ergometer in this study.

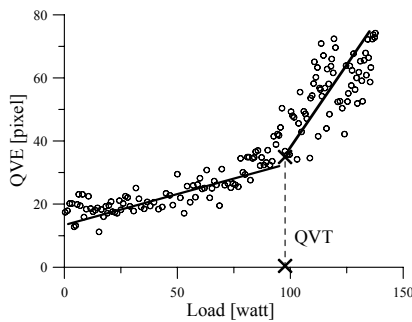


Fig. 5 Determination of QVT

III. EXPERIMENTS AND RESULTS

Our proposed respiration measurement is implemented for the system with the composition. In the system, the distance from the height installed the sensor to seat back is set as 900 mm, and the distance from the center of lens to the FG element is 540 mm.

The pattern light projector uses an infrared semiconductor laser of 804nm wavelength as the laser source. Therefore, projected the dot-matrix pattern light is invisible to the human eye. Also, to lower influence of extraneous light, we mounted an infrared-transmitting band-pass filter with

transmission band 812nm in front of the lens of CCD camera.

The laser source irradiates pulse laser, of which width is 0.1m second, and synchronized the laser irradiation and the electrical shutter of image-pickup device. The pattern light projector is designed in conformance with Class 1 of the laser safety standard defined in IEC 60825-1.

The processing device is composed of a multi-purpose PC (CPU: Intel Pentium 4: 2 GHz, and Memory size: 2 G byte) and an image input board (FDM-PCI IV manufactured by Photoron Limited).

The ergometer exercise test by the lamp load method was carried out, and QVT was calculated. To begin with, the examinee keeps rest condition for one minute. The ergometric load was then increased automatically in 20W/min lamp load from 0W. The examinee continued the pedal stroke motion to the exhaustion. The pedaling rate by the examinee was controlled by the metronome in order to keep 60rpm.

By the simultaneous measurement with the expiration gas analyzer (AEROMONITOR AE-280S manufactured by Minato Medical Science Co., Ltd.), we examined the validity of our proposed method. As mentioned in the above chapter, the expiration gas analysis equipment is the equipment generally used for the evaluation of the systemic aerobic capacity, and it is widely utilized in the medical institution.

Examinees are 16 males (age: 27+/-7 years old, body weight: 68.4+/-7.3 kg). Prior to the measurement, we obtained the consent document on the measurement execution from the examinees. In the measurement, the examinees wear T shirt.

Fig. 6 shows the scatter plots of the normalized VE and the normalized QVE. We calculated the regression line and the correlation coefficient R . Fitted line is a straight line through origin. Two graphs show QVE is highly correlated with VE. There was the high correlation over $R=0.8$ between VE and QVE in all examinees.

As a result of regressing the measurement data to two straight lines, so that the error $E(n)$ may become a minimum, the value of QVT was obtained with 86.1 watt, as shown in fig. 7 and fig. 8.

Fig. 9 shows the scatter plots of the QVT and VT. We calculated the regression line and the correlation coefficient. Fitted line is a straight line through origin. It is considered that the correlation exists between VT and QVT, as the gradient of the regression line is almost 1 and the correlation between both is 0.8. As the exercise load increases, the dispersion occurs for the variation of QVE and the difference between VE and QVE increases. This dispersion is considered as one of the causes of the difference of the QVT calculation. We think that it is necessary to remove the data-spread points in the QVT calculation.

In the future, we will carry out the experiment with more examinees and verify the validity of this experiment result.

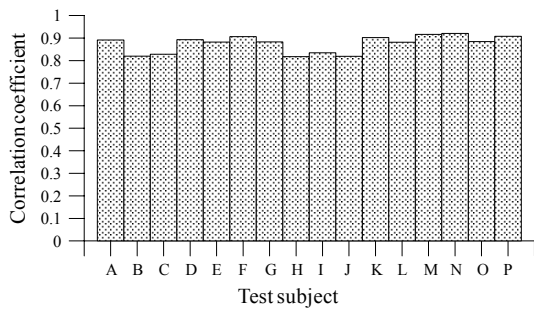


Fig. 6 Correlation between QVE and VE

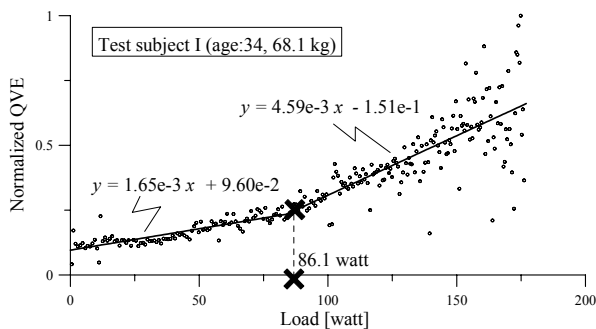


Fig. 7 Result of QVT determination

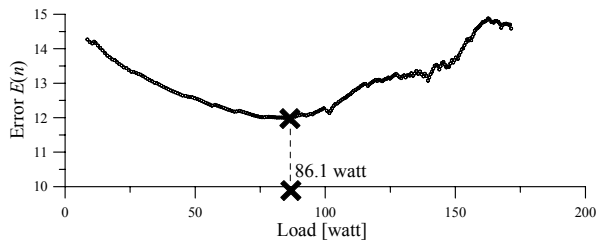


Fig. 8 Minimum value of Error $E(n)$

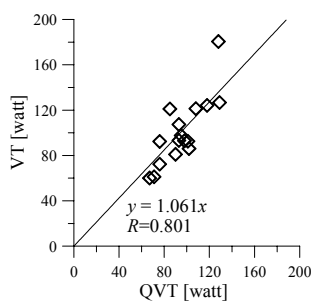


Fig. 9 Correlation between QVE and VE

IV. CONCLUSION

In this study, we proposed the method for calculating the index named QVT, which corresponded to VT, with the noncontact respiration measurement. By expiration gas analyzer and our proposed method, the VT and QVT were measured simultaneously. We calculated the regression line and the correlation coefficient between QVT and VT. Fitted line is a straight line through origin. As the result, it is considered that the correlation exists between QVT and VT, as the gradient of the regression line is almost 1 and the correlation between both is 0.8. This result indicates the possibility of the calculation of the systemic aerobic capacity without contact by our proposed method.

ACKNOWLEDGMENT

This work was supported in part by Research Center for the Holistic Computational Science (HolCS) in Tokyo University of Science.

REFERENCES

1. K. Wasserman and M. McIlroy, "Detecting the threshold of anaerobic metabolism in cardiac patients during exercise", *Am J Cardiol*, Vol.14, 1964, pp 844-852
2. H. AOKI and et al., "Non-contact Measurement Method of Respiratory Movement under Pedal Stroke Motion", *Proceedings of 29th IEEE Engineering in Medicine and Biology Society Annual International Conference, 2007*, pp 374-377
3. R. Robergs and S. Roberts: "Fundamental Principles of Exercise Physiology: For Fitness, Performance, and Health," McGraw-Hill Higher Education, 2000, pp 176-177
4. K. Hirakoba, et al., "Effect of Endurance Training on Excessive CO2 Expiration due to Lactate Production in Exercise," *Eur. J. Appl. Physiol. Occup. Physiol.*, 64, 1992, pp 73-77
5. W. Beaver, and et al., "A New Method for Detecting Anaerobic Threshold by Gas Exchange," *J. Appl. Physiol.*, 60, 6, 1986, pp 2020-2027
6. H. AOKI and et al., "Calculation of Ventilation Threshold Using Noncontact Respirometry", *Proceedings of 30th IEEE Engineering in Medicine and Biology Society Annual International Conference, 2008*, pp 2273 - 2276
7. H. Machida, et al., "High Efficiency Fiber Grating for Producing Multiple Beams of Uniform Intensity," *Appl. Opt.*, 23, 2, 1984, pp 330-332

Author: Hirooki Aoki
 Institute: Tokyo University of Science
 Street: 2641 Yamazaki
 City: Noda-shi
 Country: JAPAN
 Email: haoki@ee.noda.tus.ac.jp

Functionality of neuronal networks derived from human embryonic stem cells

T.J. Heikkilä^{1,2}, J. Mikkonen², J.M.A. Tanskanen¹, L. Ylä-Outinen², R. Lappalainen², S. Narkilahti², and J.K. Hyttinen¹

¹ Department of Biomedical Engineering, Tampere University of Technology, Tampere, Finland

² Regea - Institute for Regenerative Medicine, University of Tampere, Tampere, Finland

Abstract— In this paper, we describe methods for studying the maturation of human embryonic stem cell (hESC)-derived neuronal networks. The production of functional hESC-derived neuronal cells is critical for their application in treating neurodegenerative disorders. Microelectrode array technology allows measuring the electrophysiological activity of the cells while the network matures. Our results indicate that the hESC-derived neuronal networks were spontaneously active and exhibited time dependent maturation in recorded electrical impulse firing patterns starting from spontaneous random spiking and eventually maturing into bursting activity. Immunocytochemical studies revealed that these networks were positive for the neuronal marker microtubule-associated protein 2 (MAP-2) and glial fibrillary acidic protein (GFAP). The formed networks responded to modulation with sodium-ion channel, glutamate and GABA receptors affecting substances, indicating that pharmacologically susceptible neuronal networks with functional synapses had been generated. The findings indicate that hESC-derived neuronal cells can generate communicating networks and are therefore suitable for use in developmental and drug screening studies, and potentially for regenerative medicine in the future.

Keywords— Neuronal network, human embryonic stem cells, hESC-derived neuronal networks, neuronal cell differentiation, microelectrode array (MEA)

I. INTRODUCTION

Human embryonic stem cells (hESCs) are pluripotent cells that have the ability to replicate and differentiate into various cell types even after months in the culture. Their developmental potential makes hESCs a promising source and supply for basic research and cell transplantation therapies for the human nervous system. This requires understanding of the factors that contribute to the generation of functional neuronal networks.

Neuronal network dynamics can be assessed at the network-level *in vitro* using multi-electrode array (MEA) technology [1]. The electrical activity of neuronal network is measured on a growth plate with embedded recording and stimulus electrodes. While the produced network is a 2-D simplification of the 3-D neuronal structure of the central nervous system, the analysis of MEA recordings can pro-

vide valuable information about the spatial and temporal distribution of the activity generated by the network and the basic learning mechanisms of the nervous system. It can also be utilized for pharmacological testing. MEA cultures can be followed for long periods of time while the network passes through the phases of overproduction of synaptic connections and subsequent synaptic elimination and stabilization [2]. Spatiotemporal analyses of multi-channel recordings on dissociated rodent cortical or hippocampal slices [3-4] or mouse embryonic stem cell-derived neurons [5-6] have been reported. Utilizing hESCs open up many avenues for the future applications that cannot be performed with rodents' cells.

In this paper, we describe aspects of functionality that we have observed from hESC-derived neuronal networks. We have investigated expression neuronal and glial markers during the differentiation phase. We have cultured networks for up to 2 months on MEAs. During this time we have followed the development of the network morphology, dynamics of electrical activity and modulated it by electrical stimulation and pharmacologic substances.

II. MATERIALS AND METHODS

The hESC lines 06/015, 06/023, 07/40 derived at Regea (University of Tampere, Tampere, Finland) were used for the neuronal differentiation. The Ethics Committees of the Karolinska Institutet and Pirkanmaa Hospital District, Tampere approved the derivation, characterization, and differentiation of the hESC lines. Neural differentiation of hESCs was performed as previously described [7].

The hESC-derived neuronal cells were cultured (Fig. 1) on PEI/laminin coated MEA dishes (200/30-Ti-gr, Multi Channel Systems, Germany). Electrical activities were recorded using MEA system (MEA60, MCS). At the time of plating, that is, 4 to 8 weeks after the onset of differentiation the cells expressed only neuronal markers [7]. A total of 10 MEA dishes coated with PEI/laminin were measured 3 times/week, 1 to 15 minutes at a time. 20 000 to 30 000 neuronal cells were plated to each MEA. The longest follow-up time was 2 months.

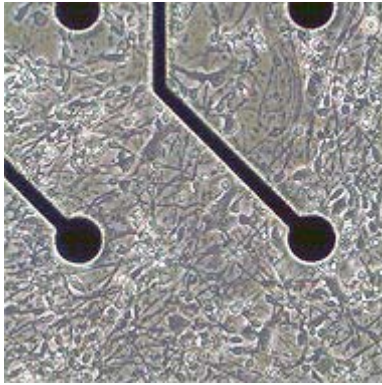


Fig. 1 hESC-derived neuronal cells growing on MEA

Cellular activity was recorded with bandwidth of 200Hz to 10 kHz. Signals were sampled at 20 or 50 kHz using a data acquisition card controlled through MC_Rack software (both from Multi Channel Systems). Same software was used to detect spikes with a threshold of 5.5 times the standard deviation of the noise level. NeuroExplorer (Nex Technologies, Littleton, MA) was used to visualize the processed spike data. An in-house software under Matlab was developed for the spike and burst analysis.

Electrical stimulation was performed on 2 synchronous bursts exhibiting cultures 25 days after plating on MEAs, using STG2004 stimulus generator driven by MC_Stimulus software (both from Multi Channel Systems). An electrode partaking synchronous bursts was chosen for stimulation with the paradigm of a train of 50 biphasic voltage pulses (± 800 mV, 400 μ sec per phase) at 300 msec intervals [2]. The stimulated electrode was blanked for 20 msec after the stimulation in order to reduce the size of the artifacts. Pharmacological responses for sodium ion channel, N-methyl-D-aspartic acid (NMDA), alpha-amino-3-hydroxy-5-methyl-4-isoxazolepropionic acid AMPA, kainic acid (kainite) and γ -aminobutyric acid type A (GABA-A) receptor antagonist were tested.

III. CONCLUSIONS

Our results show that hESC-derived neuronal cells form functional networks *in vitro*. The first spontaneous signals are registered from the networks already on the first culturing week. Gradually, the signaling develops upon maturation of the network towards diversiform high frequency activity and eventually into similar synchronous bursting activity (Fig. 2) described for mESC-derived neuronal networks [6].

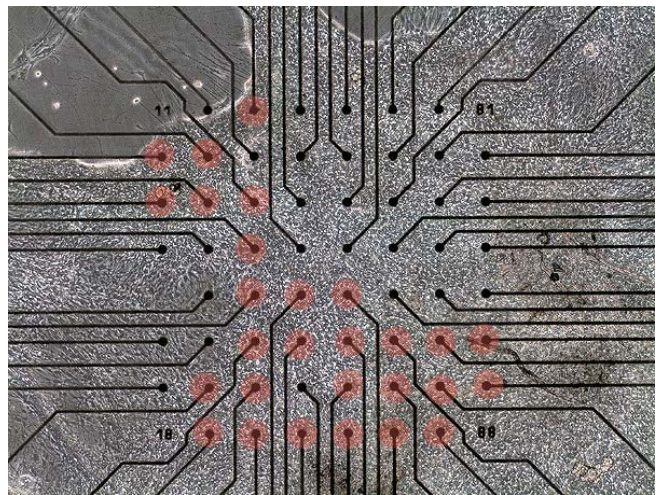
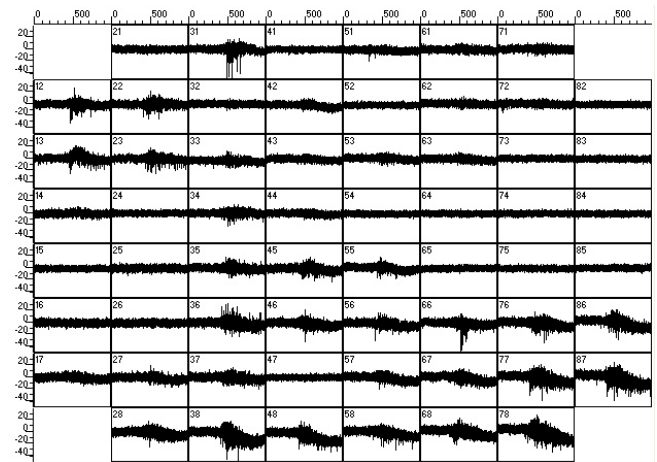


Fig. 2 On the top, synchronous burst recorded simultaneously by multiple electrodes. On the bottom, the culture morphology at 40 DIV, the electrodes registering the burst are indicated in red.

Spontaneous synchronous bursting activity typically appeared 1 month after culturing and varied in frequency and envelope between different cultures. Furthermore, bursting activity was found to be induced by GABA-A antagonist bicuculline.

The hESC-derived neuronal networks responded to the electrical stimulation (Fig. 4). Stimulation induced modulation was observed typically only on areas from which spontaneous activity could be registered. Exogenous electrical stimulation may provide means to study synaptic plasticity as well as its effect to the maturation speed of the network. The network activity was found sensitive to synaptically acting pharmaceuticals, indicating that the typical excitatory and inhibitory receptors are involved in the functional activity of the networks. No morphologic changes were observed following the pharmacologic treatments.

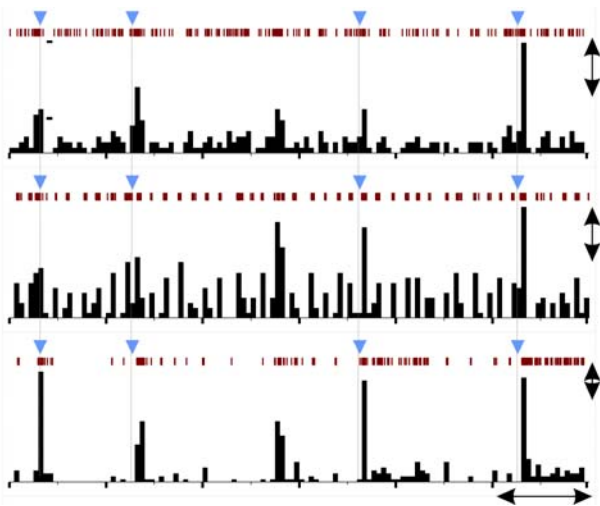


Fig. 4 Response of hESC-derived neuronal network activity to electrical stimulation. Each histogram display the spikes registered from the channel during 1 sec bins. The blue arrow heads denote the time of stimulation. X-axis scale bar = 20 sec, y-axis scale bar = 10 spikes / bin.

The MEA system and the hESC-derived neuronal cells offer a way to study neuronal network formation and dynamics. Our results indicate a clear time dependent formation of the network developing from spontaneous random spiking to high frequency activity, and finally bursting activity. *In vitro* systems are accessible to microscopic imaging and pharmacologic manipulation. In the future, it would be very beneficial to combine the patch clamp and MEA measurements for detailed characterization of specific neuronal phenotypes and the subsequent analysis of the specific neuronal networks.

We aim to control the growth of the networks with mechanic, electric, and chemical cues, barriers, or stimulations. Moreover, by utilizing Ca^{2+} -imaging and advanced image analysis we may gain information about relation of the network activity and its morphology. The process of culturing hESC-derived neuronal networks utilizing the MEA system provides unique opportunities to study the information processing in the human network and the factors affecting its maturation.

ACKNOWLEDGMENT

This work was supported by Competitive Research Funding of Pirkanmaa Hospital District, Finland; The Employment and Economic Development Center for Pirkanmaa, Finland; The Academy of Finland, Arvo ja Lea Ylppö Säätiö, Finland, and BioneXt Tampere, Finland. We want to thank the personnel of Regea for their technical help and support in stem cell research.

REFERENCES

1. Gross G, Rieske E et al (1977). A new fixed-array multi-microelectrode system for long-term monitoring of extracellular single unit neuronal activity in vitro. *Neurosci Lett* 6:101-106
2. Corner M, Van Pelt J et al (2002). Physiological effects of sustained blockade of excitatory synaptic transmission on spontaneously active developing neuronal networks - an inquiry into the reciprocal linkage between intrinsic biorhythms and neuroplasticity in early ontogeny. *Neurosci Biobehav Rev* 26:127-185
3. Madhavan R, Chao Z, Potter S (2007) Plasticity of recurring spatiotemporal activity patterns in cortical networks. *Phys Bio* 4:181-193
4. Wagenaar D, Pine J, Potter S, (2006) An extremely rich repertoire of bursting patterns during the development of cortical cultures. *BMC Neurosci* 7:11
5. Ban J, Bonifazi P et al (2007) ES-derived neurons form functional networks in vitro. *Stem Cells* 25:738-749
6. Illes S, Fleischer W, et al (2007). Development and pharmacological modulation of embryonic stem cell-derived neuronal network activity. *Exp Neurol* 207:171-176
7. Sundberg M, Jansson L, Ketolainen J et al (2008) CD marker expression profiles of human embryonic stem cells and their neural derivatives, determined using flow cytometric analysis, reveal a novel CD marker for exclusion of pluripotent stem cells. *Stem Cell Res.*, in press, available online Sep 16th 2008

Author: Teemu Heikkilä
 Institute: Regea - Institute for Regenerative Medicine, University of Tampere, Tampere, Finland
 Street: Biokatu 12, 6th floor
 City: Tampere
 Country: Finland
 Email: teemu.heikkila@uta.fi

Pneumatic Test Device for the Accurate Assessment of Pressure Sensors

C. Giacomozzi, G. De Angelis, M. Paolizzi, S. Silvestri, and V. Macellari

Istituto Superiore di Sanità/Department of Technology and Health, Rome, Italy

Abstract— Pressure sensors for plantar pressure measurement – either based on resistive or capacitive technology – should guarantee for high accuracy and reliability, since they are increasingly used both in scientific research tools in the field of biomechanics and in diagnostic tools in clinics. The above requirements not only entail a mandatory in-factory calibration, but also periodic in-the-field calibrations to verify the maintenance of an adequate quality level. The present study deals with the design, construction and validation of a valuable pneumatic calibration device suitable both for factory calibration – where each pressure sensor must be wholly characterized over the used pressure range – and for fast, easy in-the-field calibration - where sensor matrices must be tested in their final commercial assembly, and single pressure values are needed as well as force and center of pressure (COP) estimation. The described test device is based on a pneumatic circuit including an on-off valve and a proportional valve for the application of pressure in the range 0-700kPa under static and dynamic conditions over a small squared area, in the frequency range 0.5-1Hz. The test device is also equipped with a special tool to apply a known vertical force through 3 round supports of a graduated round table, to assess accuracy and precision of COP estimation. Correctness of table position is assured by an *ad hoc* positioning system.

The pneumatic test device is relatively light, easily transportable, and adaptable to pressure sensors and platforms of different technology and size.

Keywords— Pressure sensors, biomechanics, test device, pneumatic circuit.

I. INTRODUCTION

The analysis of foot-to-floor interaction by means of measurement devices based on *ad hoc* assembled matrices of pressure sensors is nowadays a consolidated procedure both in biomechanical research and in clinics. The increasing need for accurate and reliable measurements requires to these instruments to be adequately calibrated in the factory and on the field.

To design a proper test device, few concepts should be kept in mind: i) high accuracy of pressure measurements is achieved only if the sensors are wholly characterized in terms of range, linearity, hysteresis, ageing, and so on; ii) pressure transducers commercially used for plantar pressure measurement devices can be arranged as discrete sensors or

in bi-dimensional arrays, and can exploit capacitive or resistive properties of the material. A general purpose test device should allow the assessment of both single sensors and complete platforms of different sizes, spatial resolutions and temporal resolutions; iii) calibration and testing procedures entails pressure sensors to be subjected to a known pressure. Each sensor has an active area that is to be uniformly loaded. This requirement is easily met if the calibration device directly generates a pressure, whereas if a force is generated its uniform distribution over the sensitive area is not easily guaranteed; iv) besides single sensor characterization, the assessment of accuracy in center of pressure (COP) estimation over the assembled sensor matrix is mandatory, since eventual cross-talk, electrical interferences or mechanical construction issues might affect COP accuracy. To this purpose, the simultaneous application of known forces over at least two small areas may represent a reliable and accurate way to assess measured vs calculated COP position; v) calibration and test procedure targets are different in factory and on the field. In factory the sensor response has to be wholly characterized, which requires the application of accurate and varying pressure/time profiles. On the field spot-checks are mainly needed since an easy, fast procedure is sought for. Calibration devices generally used by pressure platform constructors simultaneously impose a specific pressure over the whole sensitive surface of the platform. This calls for heavy structures to sustain the big stresses which are generated in this way; these heavy structures are hardly transportable, and they are not suitable for fast changing the pressure and testing the frequency response of the sensors. Moreover, these devices cannot be easily used with sensor matrices assembled in long platforms. The here described test device, instead, imposes known pressure or force over small areas of the sensitive surface. It is relatively light, easily assembling and transportable, suitable for a complete characterization of both single sensors and platforms, and adaptable to platforms of different sizes.

II. MATERIALS AND METHODS

A first partial prototype of the test device was constructed at the authors' lab and it is described elsewhere [1]. The here described device represents a second generation

prototype, whose main differences from the first are the completely re-designed electronic circuitry and the new designed special tool – graduated round table and accessories – for COP assessment under application of known forces. For the sake of readability, a brief description of the whole test device is here reported anyway.

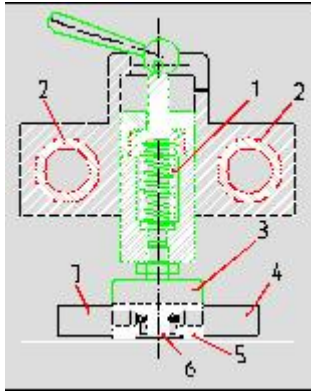


Fig. 1 Cross section of the pressure head. 1: spring; 2: linear bearings; 3: load cell; 4: pneumatic on-off/prop valves; 5: stainless steel element; 6: pressure chamber; 7: miniature pressure transducer

Figure 1 shows a cross section of the main component of the pneumatic test device, namely the **pressure head**. The constructed prototype is showed in Figure 2. The component (Figure 1) is arranged in order to be moved back and forth any point of the platform sensitive surface by means of linear bearings (2) which are coupled with stainless steel cylindrical bars. These 65cm-long bars are supported over the platform with an overall structure similar to an overhead-traveling bridge. Dimensioning of the cylindrical bars and of the anticorodal support base was obtained by taking into account that bar length should allow testing of most commercial plantar pressure platforms but at the same time bar maximum deflection should be limited to 1mm. The stainless steel element (5) is pressed against the surface of the pressure platform by means of a lever that acts on a spring (1), which is a commercial compression spring with elastic constant $k = 50\text{N/mm}$ and preloading equal to 500N (displacement $\sim 3\text{mm}$). The spring was included to compensate thickness differences on the side of sensor matrix and to compensate bar deflection effects. The overall result of the spring action is a good contact between the pressure chamber and the protective rubber of the sensor matrix. The pressure is imposed by inflating pressure-controlled air into the small pressure chamber (6) that is created when the element 5 is in contact with the platform surface. The pressure chamber (Figure 3) has been constructed by using stainless steel. Its squared 25cm^2 base has smoothed edges

to avoid high shear stresses due to the excessive rubber deformation all around the analyzed sensors. Useful surface of the chamber is $2.6\text{cm} \times 2.6\text{cm}$; the number of involved sensors depends on the spatial resolution of sensor matrix. As an example, in order to avoid artifacts due to the border, a total of 4×4 sensors can be accurately analyzed for commercial platforms with spatial resolution of 4sensors/cm^2 . The choice of not using any membrane within the pressure chamber aimed at avoiding possible differences in the pressure distribution due to the contact between the membrane and the protective rubber. A small metallic tooth was instead used, 0.3mm high, all around the border of the pressure chamber. Together with the rubber, it guarantees for an air-tight locking of the examined area. Pressure, which can be rapidly changed thanks to the small volume of the pressure chamber, is managed by two pneumatic valves (4): the on/off electrically actuated pneumatic valve is used to impose pressure in the range 0-700kPa in terms of impulses with rise times up to 1ms, pressure steps with selectable duration in the range 50-150ms, or static pressure; the proportional valve guarantees a sinusoidal pressure with frequency selectable in the range 0.5-1Hz and peak-to-peak amplitude in the range 0-700kPa; both valves are directly screwed onto the element 5.

The imposed pressure is measured by means of a full-bridge miniature pressure transducer (7) with frequency response of 1KHz, mean absolute error $<10\text{kPa}$, relative error $<2\%$, high linearity ($R^2=0.997$). The force exerted onto the platform by the spring is measured by means of a load cell (3); this force has to be always greater than the vertical force generated by the pressure in the above chamber. The device has been designed to sustain a maximum pressure of 1000kPa that is the maximum range for most commercial pressure platforms. The calibrated load cell has mean absolute error $<3\text{N}$, relative error $<1\%$, high linearity ($R^2=0.999$). Signals from both transducers plus a trigger signal to/from the pressure device under test are acquired by means of a BCN NI DaqPad (6024E, 12-bit A/D converter) and a Labview Application.



Fig. 2 Pneumatic test device A: the lever; B: the brass piston (containing the spring); C: the load cell; D: the pressure transducer; E: the stainless steel element (around the pressure chamber); F: the pipe from the valves (connected in parallel).

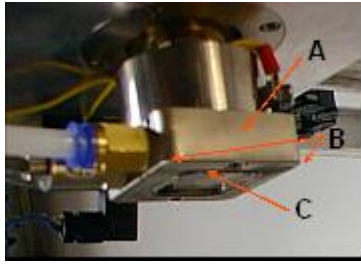


Fig. 3 The pressure chamber. A: stainless steel body; B: smoothed edges (to avoid high stresses); C: metallic tooth.

In order to apply known and well controlled forces through the same test device, an additional tool was designed and constructed which is formed by three components: i) a graduated round table; ii) a graduated positioning system; iii) a protective case to avoid damage to the pressure chamber while applying vertical load (Figure 4). The graduated aluminum round table – diameter 15cm, angular resolution 5° - has three small pylons (diameter 3cm, angular distance 120°, each center being positioned in the vertex of an equilateral triangle) and a central semi-spherical loading point to obtain a correct coupling between the table and the test device. The semi-spherical contact point is removable, and the hole in the center of the table allows the acquisition of theoretical COP coordinates. The table angular resolution allows the execution of up to 24 measurements around the same circumference (namely, COP estimation error may be calculated over 24 values). The mobile positioning system, which is easily fixed to and removed from the test device, has the same angular resolution of the table and was purposely realized to correctly position and reposition it.

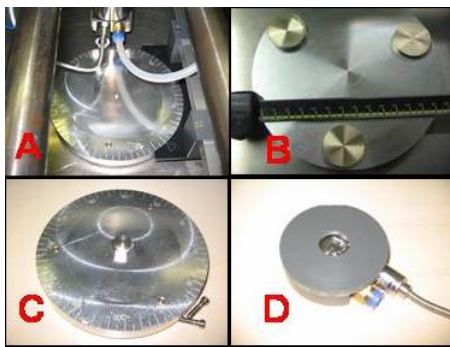


Fig. 4 The graduated round table tool. A: the table and the positioning system inserted in the test device; B: bottom of the table; C: table with the semi-spherical coupling tool; D: protective case for the pressure chamber.

III. RESULTS

The new prototype of the pneumatic test device was constructed and validated. Calibration of pressure and load transducers within the whole pneumatic measuring chain was performed by using higher class reference instrumentations – namely a 1st class reference manometer for the pressure transducer, and a reference load cell previously calibrated with certified loads for the force transducer.

To investigate the feasibility of hypothesized test protocols, the following one was applied to a commercial pressure measurement platform (resistive technology, 1.4sensors/cm²) over 5 randomly selected areas:

- 1) 100kPa steps of static pressure applied through the on-off valve from 0 to 600kPa and down to 0, each step lasting 5s, the area being completely offloaded after each step;
- 2) sinusoidal pressure cycles (0-500kPa; 0.75Hz; at least 10 cycles) applied through the proportional valve;
- 3) constant pressure ((350kPa; 60s) to investigate creep.
- 4) for each area, static load of 500N applied under 6 different angular positions - step 20° - of the round table.

The feasibility test was successful, even though the whole test procedure resulted quite complex and time consuming. Figure 5 shows some relevant results referred to one of the 5 tested areas.

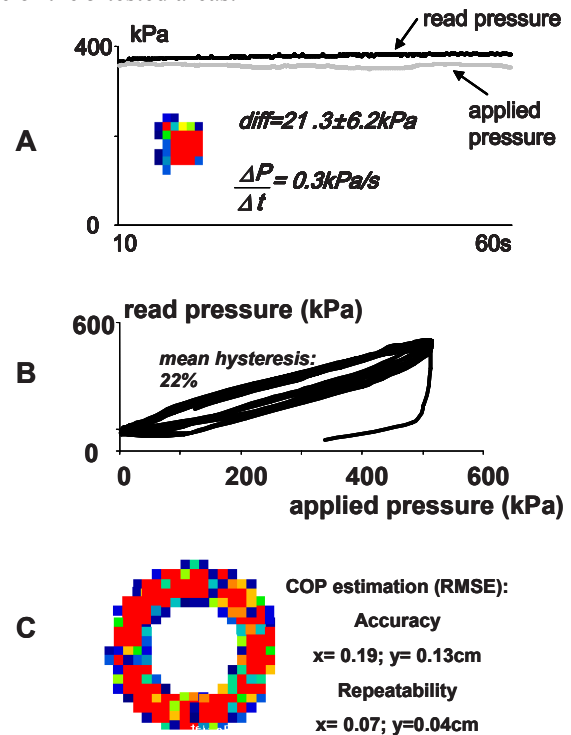


Fig. 5 Test results from one random area of a resistive pressure platform. A: creep; B: sinusoidal pressure cycles; C: COP estimation t (load application through the graduated round table).

IV. DISCUSSION AND CONCLUSIONS

Accurate calibration devices that pressure platform constructors generally use simultaneously impose a uniform pressure over the whole platform. This calls for heavy structures to sustain the big stresses.

The proposed device, on the contrary, is relatively light and suitable for a complete characterization of the pressure sensors both as single transducers and as assembled measuring systems; further, it is easily adaptable to platforms of different sizes.

Among possible measurements, it allows to apply: i) successive sinusoidal pressure cycles, which are useful to quantify each sensor hysteresis, to characterize its response over the whole pressure range of interest, to quantify possible differences in its response due to the frequency, to verify its response repeatability, to quantify the maximum number of cycles before the sensor replacement (mandatory for factory calibration); ii) stable known pressures to be maintained for long periods, which are needed for measurements under static conditions (useful for periodic checks and for creep test); iii) well controlled pressure steps (mandatory for factory calibration); iv) simultaneous, well controlled and uniform application of static load over three areas to assess

accuracy and repeatability of COP estimation (mandatory for factory calibration, useful for periodic checks).

The prototype proved to be robust and reliable, and to allow the implementation of test procedures with accuracy and precision adequate to the assessment of plantar pressure measurement devices. Its main drawback resides in the time-consuming measurement procedure that requires the replacement of the pressure head to check the entire platform sensitive surface. This inconvenient may be partly overcome by automating the displacement of the pressure head and, in any case, it can be tolerated for spot-checks where testing may be limited to a small number of platform sites.

REFERENCES

1. De Angelis G., Giacomozzi C., Maccioni G., Macellari V., Mattia F. (1999) A pneumatic device for the calibration of pressure platforms. Abstracts of the 5th Conference of the European Society for Engineering and Medicine, Barcelona, Spain, 1999, pp 133-134

Design and fabrication of an ultra-flexible electrode system for invasive continuous monitoring during surgery

S. Kraemer¹, T. Doerge², M. Hanauer², K.-P. Hoffmann², W. Kneist⁴, S. Steltenkamp²
Ch. Ulmer³, W. Lamadé³

¹ RheinAhr Campus, Fachhochschule Koblenz, Koblenz, Germany

² Department of Biomedical Engineering and Neuroprosthetics, Fraunhofer Institute, St. Ingbert, Germany

³ Robert-Bosch-Hospital, Department of General, Visceral and Trauma Surgery, Stuttgart, Germany

⁴ University Medical Center of the Johannes Gutenberg University, Department of General and Abdominal Surgery, Mainz, Germany

Abstract— This paper introduces the development, design and characterization of a tube with electrodes for stimulation and recording. This tube can be used as an operative monitoring system for thyroid surgery. In such surgeries damaging of the neural tissue can result in permanently malfunction. Continuous nerve monitoring can reduce significantly this risk.

Keywords— tube electrode, thyroid, operative monitoring, neural stimulation, polyimide, flexible electrodes

I. INTRODUCTION

Nowadays in Germany almost every third person suffers from malfunctions of the thyroid. One common way of curing such diseases is surgery. Unfortunately more than 20% of the cases vocal chords are being badly injured during such a surgery. The problems of such a surgery and therefore the reason of injuries lie in the fact that neural tissue is very similar to the connective tissue. Injuries of patients, who had a thyroid surgery, suffer from hoarseness, paralyse of vocal chords up to the fatal breathlessness [Thomusch1, Petro]. Even slight pressure, inappropriate temperature or shear forces during the surgery can result in such injuries.

Therefore a continuous monitoring system is pivotal for a successful thyroid surgery. Up to date only electro myographical monitoring systems are available [Thomusch2], which are not able to provide a continuously monitoring. The state of the art is an electro physiological identification of the nervous signals with commercially available needle electrodes, which already result in a significant reduction of injuries [Thomusch2]. Unfortunately, in many cases a distortion of the nervous system is reported after the surgery, which is not understood.

Within this, we report a fabrication of a tube like electrode, which can be used for thyroid surgery to reduce injuries. Such a electrode has to be easy to handle, biocompatible and almost invisible during the surgery. It is also mandatory, that such an electrode has to be “immune” to the

wrong placement, when implanting it and during the surgery. This is realized by a multipolar, ultra flexible design of the electrode in combination with and especially develop intelligent-acting software in order to provide all the time the right stimulation and detection parameters for an optimal continuously monitoring.

II. THE KEY IDEA OF THE PROJECT

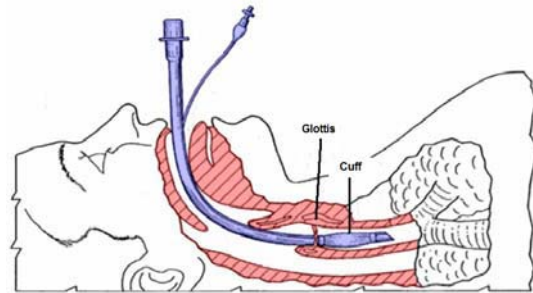


Fig. 1: Schematic draw of the incubated *Endotrachealtubus* into the trachea, including an external airway, cuff balloon and location of the glottis[wiki].

The key idea of a continuous monitoring system during a thyroid surgery is taking advantage of the *Endotrachealtubus*. This tube is usually used to secure the air ways in emergency, during anesthesia or other situation in which persons are not able to breathe on their own.

Especially during surgery this tool always finds its application, where it is injected in the mouth or nose into the air ways (see figure 1). The tube is designed in a special way, so it stays tight in the trachea during surgery.

The purpose of the project is taking advantages of this tool. As such tubes are generally used in surgery; the continuous monitoring systems are placed on such devices. The stimulations unit is attached to the tube balloon, which is sealing the airways and a detection unit for the induced neural signals are placed closed to the glottis (see figure 2).

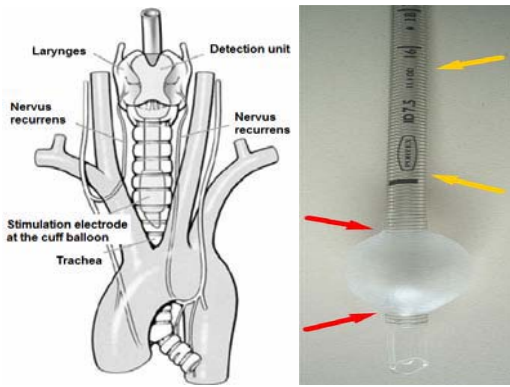


Fig. 2: Location of the neural stimulation and detection units in the trachea (left). Right side the location of the electrodes concerning the *Endotrachealtubus* is shown. The red arrows indicate the stimulations electrode and the yellow the detection unit.

III. DISCIPTION OF THE TUBE ELECTRODES

A. Design and functionality of the electrode system

Such electrodes are made for the purpose of continuously monitoring during surgery and should be place on the *Endotrachealtubus*. During the surgery a undisturbed recording is mandatory for monitoring.

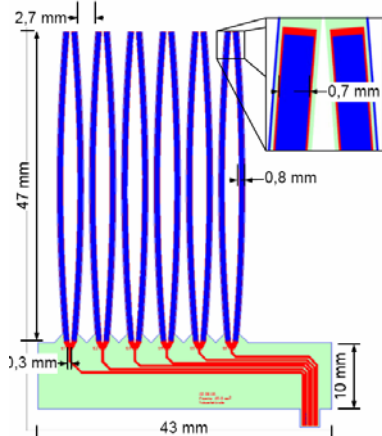


Fig. 3: First design of the stimulation electrode. The oval structure will provide the tight adaption and resist the mechanical stress during an expanded balloon, which an area of 65.8 mm²

Therefore two different designs are tested and presented in this work. For this experiment the stimulation system has to follow and expand with at different capacities of the balloon of the *Endotrachealtubus*. During expansion the electrode is expanded longitudinally and transversally, which cannot be done by usual electrodes made of polyimide [Hoffmann]. Therefore as special design has to compensate the longitudinal and transversal stress.

As a first approach figure 3 shows design which can resist against the mechanical stress during expansion of the balloon. The electrode consists of six single electrodes, called pole. The electrode has an oval structure with 0.7 mm metal paths, which are based on 0.8 mm polyimide. The length of 47 mm corresponds to an expansion of the balloon with 15 ml up to 20 ml. The green area is a 10 mm and 43 mm wide Polyimide layer, which consist of 0.3 mm conduction pathways. The key idea is the oval structure, which will adapt closely to the expanded balloon during the surgery. Also a movement in the center during expansion, which is possible due to the oval structure, supports the adaption even more. The calculated area of electrode-tissue contact is 65.8 mm². Although the electrode design is yielding in a large area, the “straight” electrode-tissue contact might tend to break during inflation. To insure an undisruptive structure a second design was chosen and compared (figure 4).

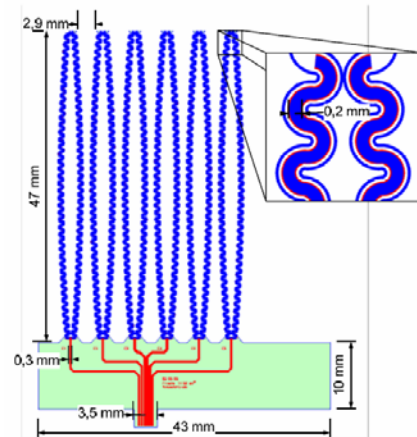


Fig. 4: Electrode design 2. This half ring design is meant to support the resistant of the yield stress during expansion of the balloon, which the cost of a smaller area of 29.18 mm².

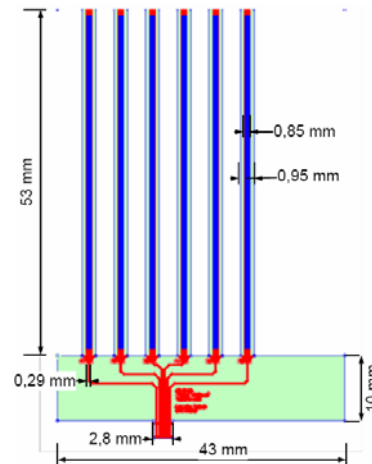


Fig. 5: Electrode system of the detection unit at the upper end of *Endotrachealtubus*.

The second tested design is yielding on a smaller electrode area, which is calculated to 29.18 mm^2 . Here the same dimension are used as before. Only the structure and area of the electrode-tissue contact is significantly changed. Here a half ring structure was chosen with 84 half rings. The half rings like structure has the function of a spring and is meant to provide even more resistant again the mechanical stress during expansion of the balloon.

The design presented in figure 5 is made for the detection unit in the tube close to the glottis. It was only slightly changed to the ones presented before. The main difference of this detection unit lies in the spatial order of each single electrode. The design was chosen to be straight instead of oval as there are no significant transversal and longitudinal forces.

B. Fabrication and processing the electrodes

The electrode system consists of a polyimide substrate with platinum conductive paths. The polyimide (HD Microsystems, PI2611) can be applied by spin coating on a standard 4" silicon wafer. After the curing process of the polyimide a photoresist layer will be applied and structured. The platinum tracks have been manufactured by means of a liftoff-process. The isolation layer on top of the system is also made of polyimide. The electrodes, contact pads and also the geometrical shape of the system were opened by reactive ion etching. After these etching steps the electrode system can be removed from the standard silicon wafer and applied on the tube. More details can be found in [Hoffmann].

C. Connectivity and flexibility

The electrode for the *Endotrachealtubus* requires beside the special specification of the electrode also a unique interface to the peripheral Monitoring System. The requirements of such connectors have to be tiny and very flexible in order to provide an easy implementation on the *Endotrachealtubus*.

The solution of this problem is the fabrication of an ultra flexible adapter with commercially available components from Ilfa (Hannover), DuPont™, where the conductive path are printed and special coated. The final adapter has size of $3 \text{ mm} \times 8.5 \text{ mm}$, including a very small thermal expansion coefficient and excelled electrical properties (see characterization of electrodes). Finally the thickness of 0.05 mm is leading into a good flexibility, which makes the special designed adapter very suitable for the *Endotrachealtubus*.

Unfortunately such an ultra flexible and tiny adapter is not providing the requirements for a biocompatibility. To fulfill the biocompatibility and –stability the adapter was

encapsulated by silicone, which is achieving such requirements.

For the connectivity was further the microflex bonding technique used [Stieglitz], where Cooner Wire (AS, AWG 40 Cooner Wire Inc, CA, USA) were bonded on $2.08 \text{ mm} \times 0.225 \text{ mm}$ bond-pads.

After the complete electrode stimulation and detection system was made, it has to be fixed on the *Endotrachealtubus*. Here various glues and glue technique ranging from commercially available silicon glue, super glue up to UV glue were tested with respect to the bonding properties and biocompatibility.

IV. RESULTS AND DISCUSSION

A. Electrical characterization of the electrodes

The tube electrodes require not only mechanical properties and a special adjusted design, more than that the electrical properties have to be well defined and suitable in order to provide a continuous and excellent monitoring of the neural signals and stimulation. Therefore all electrodes are characterized by impedance spectroscopy. While stimulation electrodes have generally not high requirements, the detection systems has to be well performed in order to provide a high signal the noise ration. Although here the focus is mainly on the stimulation units, as those had to be specially adjusted to resists the mechanical stress. In the following the main focus lies on the stimulation electrodes.

All impedance spectra were tested *in vitro*; 0.9 wt% NaCl solution. Figure 6 shows one typical example of an impedance spectrum for the 6 polar tube electrodes. Clearly visible is the characteristic of the impedance and phase information of all six electrodes from a frequency of 0.1 Hz up to 100 kHz. The uniform and suitability for the project is shown by the overlap of the six poles in one electrode, as the six poles do not have to be calibrated on its own.

To compare the electrode with each other and also different design one usually compares frequencies around 1 kHz. Here good results were achieved for both designs, with impedances around $268 \Omega \pm 5\%$ and for the other tested design $288 \Omega \pm 5\%$; tested over all six electrodes. The error is calculated by the maximal derivation of the mean value and might have its origin sensitive process of fabrication such small electrodes, bonding pads and connectors and can be almost neglected for the purpose of the project. In summary the electrode characterization approved the suitability of the electrode for the project well.

Furthermore one has to take the influence of different size of the cuff balloon on the impedance into account. Table 1 shows such a comparison for different capacity of

the cuff balloon. For the projects the impedance should be constant at all different capacities of the cuff balloon, which is well proofed by table 1.

Within the tested electrical characteristics the both designs fulfill all electrical requirements of an electrical stimulation and the detection of neural activities excelled.

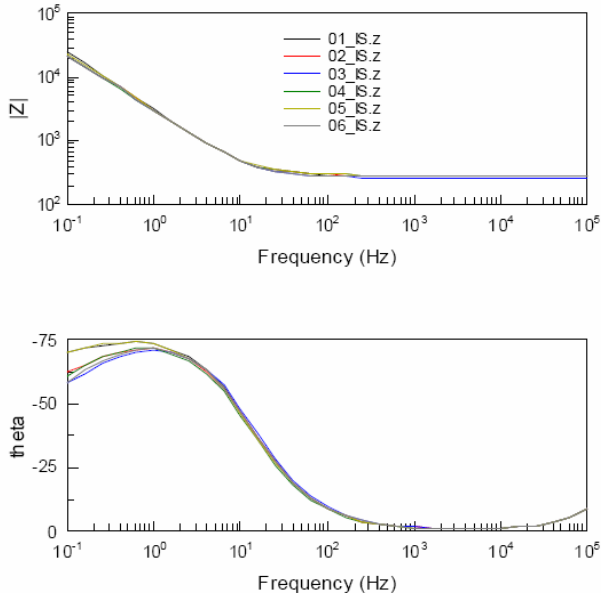


Fig. 6: Typical impedance graph of one six polar electrode. Clearly visible is the characteristic of such electrodes visible. The different poles are plotted in various colors and show nicely the overlap of impedances in one electrode design.

Capacity / ml	Design 1 / Ω	Design 2 / Ω
0	256.86	276.85
5	250.89	274.42
15	255.74	274.93
20	255.32	277.51

Tab. 1: Impedances at 1 kHz for different capacities of the cuff balloon of two tested electrode designs. Clearly visible is the independence of the impedance at different capacities.

V. DISCUSSION AND CONCLUSION

We presented in this paper two designs, fabrications and characterizations of a tube electrode for the pivotal monitoring during a thyroid surgery in order to prevent badly injuries and high follow up costs.

We characterized and discussed the fabrication of the two designs of six-polar electrodes. We could show that the electrical properties of the two designs are similar and af-

flicted with a very small derivation within the six poles as well as within designs and fabrication. The presented electrodes are well performed for recording and stimulation neural tissue, when attached to the *Endotrachealtubus*; especially at different capacities of the cuff balloon.

Both design delivered similar electrical results, although the first design provides slightly better impedances due to the higher electrode area. Nevertheless we have chosen the second design, with a better resistance against the stress and therefore a higher stability during a surgery. The loss of the electrical characteristics can be compensated by intelligent signal processing.

Within this we conclude that the ultra flexible and multi-polar electrode systems suits well for the project. The high requirements of such an electrode, the especially designed adjustment for the tube were respected well. The electrode was designed with high crack resistance due to the double layer of polyimide, which increases the yield of the fabrication as well as the stability on the tube during the surgery. Also the connectivity was improved and well placed, as due to the special developed cable guidance and the ultra flexible connectors, further techniques and additional handling are unnecessary. The next step will be a first check in an animal model.

ACKNOWLEDGEMENTS

The authors would like to thank all members of the IKONA consortium.

This work was supported by the “Bundesministerium für Medizinische Forschung” (BMBF Grand number 01EZ0722).

REFERENCES

- Hoffmann, et al. “New technologies in manufacturing of different implantable microelectrodes as an interface to the peripheral nervous system. IEEE/RAS-EMBS Intern. Conf. on Biomedical Robotics and Biomechatronics, 414-419 (2006)
- Petro ML, Schweinfurth JM, Petro AB. Transcricothyroid, intraoperative monitoring of the vagus nerve. Arch Otolaryngol Head Neck Surg. 2006;132:624-8.
- Stieglitz, et al. “Microflex”-a New AssemblingTechnique for Interconnects”. Journal of Intelligent Material Systemsand Structures (2000)
- Thomusch, et al., “Multivariate Analysis of Risk Factors for Post-operative Complications in Benign Goiter Surgery: Prospective Multicenter Study in Germany. World J. Surg. 24, 2000: 1335-1341
- Thomusch1 et al., Intraoperative neuromonitoring in surgery for benign goiter: decreased rate of recurrent laryngeal nerve palsy after subtotal thyroidectomy. Am J Surg 2002: 183:674–679.
- Wikipedia, www.wikipedia.de (2008)

Prototyping all-polymer bioelectrical signal transducers

A. Blau^{1*§}, A. Murr^{2§}, S. Trellenkamp³, C. Dautermann³, S. Wolff³
M. Heuschkel⁴, J. Wuesten⁵, C. Ziegler² and F. Benfenati¹

¹ The Italian Institute of Technology, Dept. of Neuroscience and Brain Technologies, Via Morego 30, 16163 Genoa, Italy, www.iit.it

² University of Kaiserslautern, Dept. of Physics, Erwin-Schroedinger-Str. 46, 67663 Kaiserslautern, Germany, www.uni-kl.de/physik

³ Nano+Bio Center at the University of Kaiserslautern, Erwin-Schroedinger-Str. 13, 67663 Kaiserslautern, Germany, www.nbc.uni-kl.de

⁴ Ayanda Biosystems SA, PSE Parc Scientifique, Building C, EPFL, 1015 Lausanne, Switzerland, www.ayanda-biosys.com

⁵ Institute for Microtechnique Mainz GmbH, Carl-Zeiss-Str. 18-20, 55129 Mainz, Germany, www.imm-mainz.de

* Corresponding author. E-mail address: axel.blau@iit.it. §These two authors contributed equally to the presented work.

Abstract — For historical reasons, the signal transduction interface of bioelectronic devices is commonly based on metals or inorganic (semi-)conductors. This also applies to application areas where artificial components such as biomedical screening devices, *in vitro* microelectrode arrays and *in vivo* neuroprosthetics come into direct contact with biological tissue. In a proof-of-concept microelectrode array design study, we present an alternative all-polymer approach for the low-cost fabrication of bioelectrical signal transduction devices with adjustable flexibility, electrical impedance and transparency. The fabrication process entailed three steps. Firstly, by means of a replica-moulding strategy, different types of transparent polymers were microstructured by two-level SU-8 masters to create *vias* for contact pads and electrodes, and indentations for interconnecting microchannels. Secondly, recesses in the insulating polymer sheets were filled with conductive polymer composites based on quasi-transparent polystyrenesulfonate doped poly(3,4-ethylenedioxythiophene) (PEDOT:PSS). In a last step, the passive microelectrode arrays were backside-insulated by a second layer of a transparent polymer. The electrical properties of the resulting polymer microelectrode arrays were characterized by impedance spectroscopy, baseline noise measurements and recordings of bioelectrical signals from acute preparations of chicken cardiomyocytes. Biocompatibility was tested with *in vitro* cultures of cortical neurons derived from embryonic chicken.

Keywords — **Neural interfaces, microelectrode arrays, replica moulding, PDMS, PEDOT:PSS electroconductive polymer.**

I. INTRODUCTION

Most bioelectrical transducers are based on metallic (platinum, palladium, gold, iridium) or inorganic (indium-doped tin oxide (ITO), titanium nitride (TiN), iridium oxide, carbon allotropes (nanotubes, graphene, glassy carbon, diamond), silicon) conductors or combinations thereof. Commonly, conductor traces and electrodes are generated and structured by processes such as photolithography, evaporation, etching, screen printing, micromachining or electroplating. Most of these techniques not only require access to special equipment and clean-room infrastructure, but also demand for carrier substrates that withstand the respective processing conditions. These boundary conditions impose limits onto device biocompatibility, bio-stability, flexibility, transparency and exploitation pathways for their mass fabrication [11]. Particularly in the context of designing cochlear, retinal or deep brain implants, various strategies have been suggested to overcome some of these limitations [3, 5, 8]. In addition, there is a steady trend to create more flexible devices because biological tissue is soft [7]. While insulating polymers are already accepted and widely used as elastic electrode carriers, electro-conductive polymers have not yet replaced conventional conductor materials. Although there is proof that they significantly enhance the electrical characteristics of conventional metal-based bioelectric signal transducers [1, 6, 10], there is currently no report on their use as the only transduction element in neuroprosthetics. However, recent advances in polymer material development and processing technologies propose a variety of new design and fabrication possibilities for generating flexible, all-polymeric microelectrode arrays. It can be foreseen that - similar to the recent shift from silicon to organic electronics in consumer devices - conductive polymers will complement if not substitute classical conductor materials in future biomedical and neuroprosthetic transducers.

II. MATERIALS AND METHODS

The individual device fabrication steps for generating a transparent, all-polymer microelectrode array are depicted in figure 1.

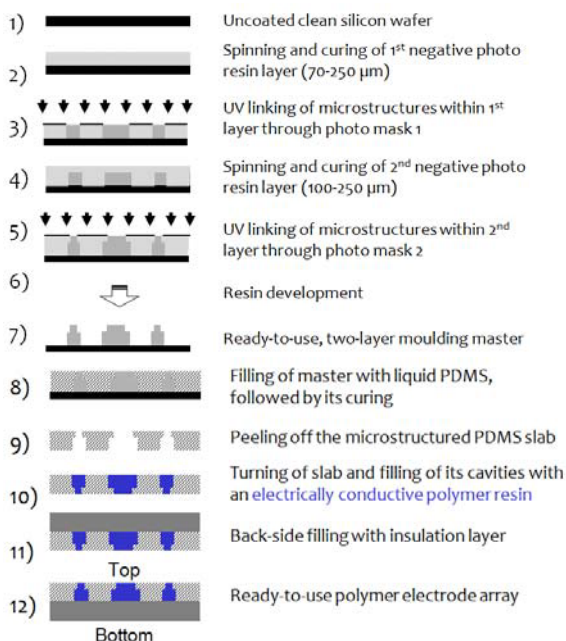


Fig. 1 Fabrication of a moulding master (1-7), replica-moulding of an insulating polymer skeleton (8-9), definition of electroconductive polymer traces (10) and device finalization through backside insulation with a non-conductive polymer (11-12).

A. Master fabrication

Photopolymers such as SU-8 allow the fabrication of high-aspect ratio, multi-level, large-area replica-moulding templates [4]. Based on SU-8 technology, one type of moulding masters was generated in the following way: the negative photoresin SU-8 100 (Microchem) was spun (Delta 80 Gyrset, Suess) onto a 4" silicon wafer with an SU-8 layer thickness of up to 250 μm and soft-baked at 65°C for 20 min, and at 95°C for 55 min. After cool-down, it was exposed to UV (120 s, 15 mW/cm^2 , EVG 620 mask aligner) through the first of two repro-printed photolithography masks (2480 dpi) to define pad, interconnection lead and electrode geometries of a 60-microelectrode array. The SU-8 layer was then post-baked at 65°C for 10 min, followed by 95°C for 25 min, and thereafter allowed to cool down to room temperature. A second SU-8 100 layer was spun onto the first layer with a thickness of up to 250 μm , soft-baked, exposed to UV light through the second mask - this time to define pad and electrode geometries only - and again post-baked using the same parameters as for the creation of the first layer. In a subsequent development step, the non-exposed photoresin was washed away to yield a two-level microstructure with a total height of up to 500 μm .

B. Replica moulding

Degassed poly(dimethylsiloxane) (PDMS) (Dow Corning, Sylgard 184; Wacker, Elastosil RT601) was poured onto the microstructured SU-8, leveled to the highest SU-8 geometries either by spinning (30 s, 1000 – 4000 rpm) or by a laser printer transparency sheet, and allowed to cure for 6 h at 60°C or overnight at room temperature. Thus, the pad and electrode features penetrated the entire PDMS slab, while the interconnection channels between pads and electrodes were only imprinted half-height. With the help of cold ethanol, the microstructured PDMS slab was peeled from the wafer and placed upside-down onto a polytetrafluoroethylene (PTFE) tray, thereby giving access to all of its cavities.

C. Cavity filling with electroconductive polymers

The hydrophobic PDMS was optionally hydrophilized by O_2 plasma exposure (30 s, 50 watt, PICO-UHP, Diener Electronic). The solvent of a conductive polymer nanoparticle dispersion, polystyrenesulfonate doped poly(3,4-ethylenedioxythiophene) (PEDOT:PSS) (Baytron CPP105, H.C. Starck), was partly removed in a desiccator vacuum to increase its viscosity. The cavities in the PDMS slab were filled with the thickened dispersion. Excess dispersion was wiped off from non-cavity areas using the edge of a rubber wiper blade. The dispersion was then tempered at 80-160°C for up to 60 min until completely dried as a thin, transparent, slightly bluish electroconductive film on the cavity walls and the PTFE tray. To increase the thickness and final conductivity of the resulting film, this coating procedure could be repeated several times.

D. Backside insulation

In a last step, the back side of the microstructured PDMS slab with the conductive polymer film in its cavities was electrically insulated by a second PDMS layer. After curing, the sandwich was peeled from the PTFE tray. Due to the “non-stick” properties of PTFE, the electroconductive polymer film of the pads and central microelectrodes was completely transferred onto the PDMS. The rigidity of such soft (\leq shore A 50) all-polymer microelectrode array with a thickness below 1.5 mm could be increased by bonding it to a stiff polymer carrier (e.g. poly(methyl methacrylate) (PMMA)).

E. Electrical characterization

Comparative impedance measurements (100 mHz - 5 kHz) were performed for individual electrode traces of a polymer microelectrode array in phosphate buffered saline (PBS) using a potentiostat (BES, PowerSuite, EG&G Applied Research). An Ag/AgCl wire

served as the reference electrode, a Pt sheet (8 mm²) as the counter electrode. Noise levels on individual electrodes were evaluated using a 60-channel recording station (MEA60, Multi Channel Systems).

F. Testing device performance and biocompatibility

The coordinated firing of cardiac myocytes was recorded from acute preparations of embryonic chicken hearts (E8) in Hanks' Balanced Salt Solution (HBSS). Biocompatibility and biostability of the polymer electrode arrays were evaluated over a period of two weeks on cultures of dissociated cortical chicken neurons (E10) in serum-free medium (NBM/B27, Gibco) using standard cell dissociation and cell culture protocols.

III. RESULTS

Figure 2 depicts a replica-molded PDMS electrode array.

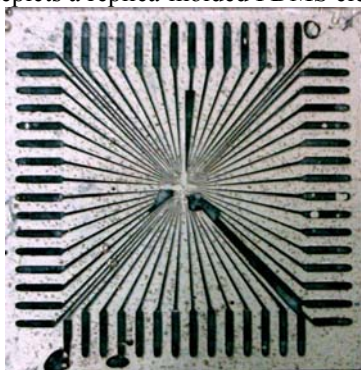


Fig. 2 Prototype of a replica-moulded PDMS microelectrode array (49 x 49 mm²) with a multilayer film of bluish, still somewhat transparent conductive polymer inlays.

The absolute impedance value of the polymer traces with electrode diameters of about 80 μm were almost constant and below 1 MOhm over the range of 0.1 Hz to 5 kHz with an average of 316 ± 176 kΩ (Fig. 3).

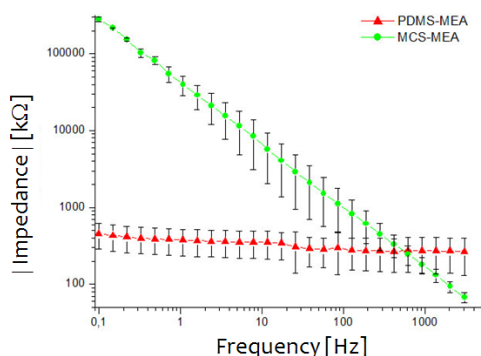


Fig. 3 Comparison of the averaged absolute impedance of Ø 80 μm PEDOT:PSS electrodes (red triangles; n = 8) with that of Ø 30 μm TiN-coated Au electrodes (green circles n = 20) on commercial microelectrode arrays (30/200iR, Multi Channel Systems) measured in phosphate buffered saline (PBS) (Ag/AgCl reference, Pt counter electrode).

For different electrodes, RMS noise varied between ±9 μV to ±50 μV. It is hypothesized that differences in impedance and noise may be attributed to the non-uniformity of the different conducting path geometries and to artefacts resulting from manual fabrication of the prototypes. Electrical characteristics were not affected by normal use (autoclavation, several weeks of cell culturing under standard cell culturing conditions: 5% CO₂ in a humidified incubator at 37°C). However, the conductivity of a PEDOT:PSS film was completely lost when exposed to bleach (hypochlorite). While the scratch and bending stability of the thin conductive PEDOT:PSS films was high, focal pressure exerted by the amplifier contact pins onto the contact pads ruptured them. This was due to the softness of the underlying PDMS insulation layer. Pad film stability could be increased by either substituting the flexible PDMS backside insulation for a more rigid epoxy (UHU plus end-fest 300) or a UVA-polymerizable acrylate-based gel (1-Phasen-Gel, nail-discount-24), or by reinforcing the pads with electroconductive silver-epoxy (ITW Chemtronics) in a post-processing step.

The almost constant impedance over a wide frequency spectrum allowed the recording of low-frequency components in myocardiograms from acute heart preparations; the bioelectric signals (P, Q, R, S and T wave deflections) were clearly visible (Fig. 4).

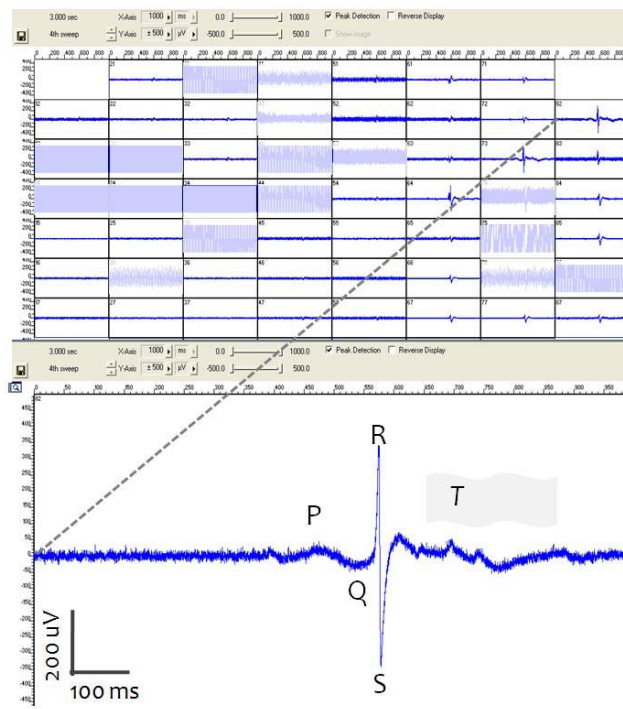


Fig. 4 Acute myocardiogram (chicken E8) picked up on 19 of 60 electrodes of a polymer microelectrode array (MEA60 recording station & software, Multi Channel Systems): Low-frequency components (P, Q, R, S and T deflections) are clearly visible.

IV. CONCLUSIONS

In this proof-of-concept design and validation study, we presented an all-polymer approach for the low-cost fabrication of passive bioelectrical signal transduction devices with adjustable geometry, flexibility, transparency and electrical characteristics. Exemplarily, an electrode array made of a microstructured, electrically insulating PDMS carrier with embedded PEDOT:PSS conductor lines and electrodes was described. The utilized materials were biocompatible [2, 9, 10], optically transparent and thus suitable for concurrent morphology studies by inverse light microscopy. They furthermore tolerated standard sterilization procedures (e.g. autoclavation, 70% ethanol) without noticeable deterioration.

Electrode array geometries were defined by a microstructured SU-8 moulding master. Its two-level design ensured that electrode and pad features within the insulating polymer substrate penetrated through the entire top layer of the array while the interconnection channels for the leads stayed covered by an insulating skin. Conceptually, the design of such moulding masters allows the pattern transfer to a variety of polymers, either along the depicted replica-moulding pathway or by hot-embossing into thermoformable polymer sheets. Furthermore, a given master can be replicated by a two-step pattern transfer to e.g. epoxies without requiring access to clean-room or microstructure processing facilities.

The presented concept allows for variations in the choice of materials and the general production design. Not only can masters with different mechanical properties be fabricated (e.g. by using other microstructuring processes such as high density plasma Advanced Silicon Etching (ASE[®])). Without much effort, the *in vitro* construct may also be translated to fabricating soft, curvature-adaptive *in vivo* probes (e.g. in the context of cortical surface field potential recordings, pacemakers, retinal implants). Array properties such as stiffness, transparency, hydrophilicity and surface chemistry can be tuned through combinations of matrix materials and array post-processing steps. And finally, impedance and capacitive properties of the electrodes can be further enhanced by the addition of other conductor materials (such as graphite, graphene or carbon nanotubes) to the PEDOT:PSS dispersion, however, at the cost of compromising electrode transparency.

In follow-up studies, electrode dimensions will be scaled down to diameters around 10-40 μm to better compare their performance with that of commercially available electrode arrays. While the passive recording capabilities of such devices have already been proven *in vitro*, their performance in different voltage or current stimulation scenarios still needs to be evaluated. Taking into account the critical findings with respect to the electroactive and mechanical long-term stability of conductive polymers under physiological conditions [6], principle parameters such as the charge-injection capacity of a PEDOT:PSS electrode, its change and its degradation over time have to be investigated.

ACKNOWLEDGMENT

The authors would like to thank the team at IMM for their support in converting CAD drawings to photolithography mask layouts. Special thanks to Tanja Neumann, Simone Riedel, Francesca Succol and Marina Nanni for their expert advice and assistance in tissue preparation.

REFERENCES

1. Abidian MR, Martin DC (2008) Experimental and theoretical characterization of implantable neural microelectrodes modified with conducting polymer nanotubes. *Biomaterials* 29:1273-1283
2. Blau A, Neumann T, Ziegler C, Benfenati F (2009) Replica-molded poly(dimethylsiloxane) culture vessel lids attenuate osmotic drift in long-term cell culturing. *J. Biosci.* 34(1)
3. Briggs R, Tykocinski M, Saunders E, Hellier W, Dahm M, Pyman B, Clark G (2001) Surgical implications of perimodiolar cochlear implant electrode design: avoiding intracochlear damage and scala vestibuli insertion. *Cochlear Implants Int* 2:135-149
4. Campo Ad, Greiner C (2007) SU-8: a photoresist for high-aspect-ratio and 3D submicron lithography. *Journal of Micromechanics and Microengineering* 17:R81-R95
5. Cheung KC (2007) Implantable microscale neural interfaces. *Biomed Microdevices* 9:923-938
6. Green RA, Lovell NH, Wallace GG, Poole-Warren LA (2008) Conducting polymers for neural interfaces: challenges in developing an effective long-term implant. *Biomaterials* 29:3393-3399
7. Hosp JA, Molina-Luna K, Hertler B, Atiemo CO, Stett A, Luft AR (2008) Thin-film epidural microelectrode arrays for somatosensory and motor cortex mapping in rat. *J Neurosci Methods* 172:255-262
8. Kim ET, Seo JM, Zhou JA, Jung H, Kim SJ (2004) A retinal implant technology based on flexible polymer electrode and optical/electrical stimulation. 2004 IEEE International Workshop on Biomedical Circuits and Systems, pp S1/8- 12-15
9. Peterson SL, McDonald A, Gourley PL, Sasaki DY (2005) Poly(dimethylsiloxane) thin films as biocompatible coatings for microfluidic devices: cell culture and flow studies with glial cells. *J Biomed Mater Res A* 72:10-18
10. Richardson-Burns SM, Hendricks JL, Foster B, Povlich LK, Kim DH, Martin DC (2007) Polymerization of the conducting polymer poly(3,4-ethylenedioxythiophene) (PEDOT) around living neural cells. *Biomaterials* 28:1539-1552
11. Stieglitz T (2007) Neural prostheses in clinical practice: biomedical microsystems in neurological rehabilitation. *Acta Neurochir Suppl* 97:411-418

Author: Axel Blau
 Institute: The Italian Institute of Technology (IIT)
 Dept. of Neuroscience and Brain Technologies (NBT)
 Street: Via Morego 30
 City: 16163 Genoa
 Country: Italy
 Email: axel.blau@iit.it

Patient-specific models and simulations of deep brain stimulation for postoperative follow-up

Mattias Åström¹, Elina Tripoliti², Irene Martinez-Torres², Ludvic U. Zrinzo², Patricia Limousin², Marwan I. Hariz^{2,3} and Karin Wårdell¹

¹Department of Biomedical Engineering, Linköping University, Sweden

²Institute of Neurology, Queen Square, University College London, UK

³Department of Neurosurgery, University Hospital, Umeå, Sweden

Abstract— Deep brain stimulation (DBS) is an established treatment for Parkinson’s disease (PD). The success of DBS is highly dependent on electrode location and electrical parameter settings. In this study patient-specific computer models of DBS were used for postoperative follow-up in three PD patients who suffered from stimulation induced hypomania, dysarthria, and uncontrollable laughter respectively. The overall aim of the study was to relate the anatomical aspect of the electric field to the effects and side effects of stimulation. The simulations showed the anatomical distribution of the electric field for all the patients and the results were in agreement with previous reports regarding these side effects of stimulation. It was demonstrated that patient-specific models and simulations of DBS may be useful for postoperative follow-up of DBS.

Keywords— Deep brain stimulation, patient specific, finite element method, dysarthria, hypomania

I. INTRODUCTION

Deep brain stimulation (DBS) is used for improving the motor signs in movement disorders such as medically refractory Parkinson’s disease (PD). Despite the effectiveness of DBS there are many unanswered questions regarding the clinical effects and side effects of this therapy. It is well known that significant improvement of motor signs may be accompanied by parallel negative effects on other functions, such as speech. Improved control of the distribution of the electric field is essential for improving the outcome of this therapy. In order to provide a visual feed-back of the anatomical distribution of the electric field we have previously developed a method for setting up 3-dimensional patient-specific finite element computer models of DBS where the electric field can be simulated and visualized [1]. In the present study such patient-specific computer models of DBS were used for postoperative follow-up in three PD patients who suffered from stimulation induced hypomania, dysarthria, and uncontrollable laughter respectively. The overall aim of the study was to relate the anatomical aspect

of the simulated electric field to the effects and side effects of stimulation.

II. MATERIALS AND METHODS

A. Patient-specific models and simulations

Patient-specific finite element computer models of bilateral DBS in the subthalamic nucleus (STN) were set up for each of the three patients. Preoperative T2 weighted stereotactic magnetic resonance images (MRI) was used to create models of each brain, and postoperative stereotactic MRI was used to position the DBS electrodes at their true positions in the brain-models. In order to allot realistic electrical properties to the models, each preoperative MRI voxel was classified into material groups, such as grey matter, white matter, and cerebrospinal fluid. The classified MRI voxels were then allotted isotropic electrical conductivity properties at a frequency of 130 Hz from Andreuccetti’s online database [2]. A random neuronal orientation was assumed, thus isotropic electrical conductivity values were used. Two DBS electrodes with a radius of 0.635 mm and contact lengths of 1.5 mm separated by 0.5 mm (Model 3389 DBS™ Lead, Medtronic, Inc. USA) were modelled and positioned in each brain model. The distribution of the electric potential in the vicinity of the electrodes was calculated using the equation for steady currents [3]:

$$\nabla \cdot J = -\nabla \cdot [\sigma \nabla V] = 0 \quad (\text{A m}^{-3}) \quad (1)$$

where J is the current density (A m^{-2}), σ the electrical conductivity (S m^{-1}), and V the electric potential (V). The electric field was visualized in three dimensions with isolevels at 0.2 V/mm together with the anatomy on two-dimensional colour-coded axial and coronal slices. The contours of the electric field isolevels were traced onto the axial and coronal slices and anatomical structures were identified with help from an atlas presented in Gallay et al. [4].

B. Case 1: Dysarthria

This PD patient was enrolled in a study where speech and movement was assessed during a variety of electrical DBS settings [5]. Speech intelligibility and movement were evaluated during monopolar STN stimulation with an electric potential of 0, 2, and 4 V (off, low and high amplitude stimulation). The evaluation of speech consisted of sustained vowel phonation “ah” for three repetitions, Assessment of Intelligibility for the Dysarthric Speech, and a 60-seconds monologue about a subject of the speaker’s choice. Following the speech recordings, movement was evaluated using the Unified Parkinson’s Disease Rating Scale part three (UPDRS-III). The patient was withdrawn from his anti-parkinsonian medication the night before the day of investigation. The pulse width and frequency remained unchanged at 60 μ s and 130 Hz. Subsequent every change of amplitude the patient rested for 15 minutes before the next evaluation. The electrode contacts located closest to the centre of the STN were used as active electrode contacts. In order to identify the contacts closest to the centre of the STN, the postoperative MRI, where artefacts produced by the electrodes are visible, were studied using the FrameLink Planning Station™ (Medtronic, Minneapolis, MN, USA). The electric field was simulated for 2 V and 4 V electric potential settings which were used during the assessments (Table 1). The frequency and pulse length was kept at 130 Hz and 60 μ s for both electrical settings.

Table 1 Electrical settings and clinical effects

Left contact (Electric potential)	Right contact (Electric potential)	Speech intelligibility	UPDRS-III	Side-effects
0 (2 V)	5 (2 V)	70 %	33	None
0 (4 V)	5 (4 V)	20 %	33	Dysarthria

C. Case 2: Hypomania

This PD patient was treated with bilateral DBS in the STN after unsatisfying medical treatment. Stimulation-induced hypomania appeared a few days after a revisit to the clinical centre where the electrical settings were readjusted for optimization of the clinical effects. After adjustment of the electrical settings, movement as measured by UPDRS-III was slightly improved from 32 to 21. However, introduction of hypomania made these settings unusable. The electric field was simulated and visualized for both the electrical settings that induced hypomania and did not induce hypomania (Table 2). The frequency and pulse length was 145 Hz and 60 μ s before adjustment. After the adjust-

ment the pulse length of the right electrode contact was changed to 90 μ s.

Table 2 Electrical settings and clinical effects

Left contact (Electric potential)	Right contact (Electric potential)	UPDRS-III	Side-effects
1 (3.6 V)	5 (3.5 V)	32	None
0 (3.5V)	4 (3.5 V)	21	Hypomania

D. Case 3: Uncontrolled laughter

This PD patient, who was treated with STN DBS after unsatisfactory medical treatment, was also enrolled in the study where speech and movement was evaluated during a variety of electrical DBS settings, as briefly described in Case 1. When high amplitude stimulation at 4 V was turned on the patient started to laugh uncontrollable. During these electrical settings the patient also experienced stimulation induced dysarthria. The electric field was simulated for 2 V and 4 V electric potential settings which were used during the assessments (Table 3). The frequency and pulse length was kept at 130 Hz and 60 μ s for both electrical settings.

Table 3 Electrical setting and clinical effects

Left contact (Electric potential)	Right contact (Electric potential)	UPDRS-III	Side-effects
2 (2.0 V)	6 (2.0 V)	34	None
2 (4.0 V)	6 (4.0 V)	26	Laughter, Dysarthria

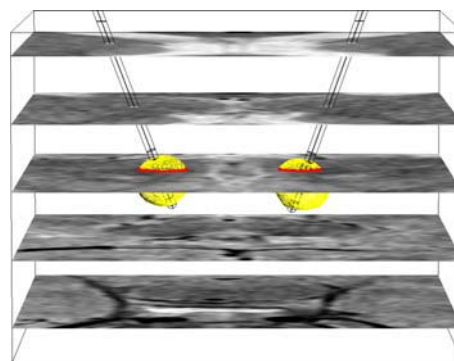


Fig. 1 Patient-specific simulation of DBS. The electric field has been visualized with isolevels at 0.2 V/mm. The isolevels were traced onto the axial and coronal images. This is illustrated with red colour in this figure.

III. RESULTS

The electric field was simulated for all three patients and the electric field isolevel at 0.2 V/mm was traced onto axial and coronal images. The traced isolevels were colour-coded according to the appearance of side-effects where white colour refers to an electric field that did not induce side-effects and red colour to an electric field that did induce side-effects (Fig. 1).

A. Case 1: Dysarthria

The patient suffered from acute stimulation-induced impairment of speech intelligibility during high amplitude stimulation (Fig. 2). This patient had active electrode contacts positioned slightly ventral, posterior and medial to the centre of the STN. The simulations showed that the electric field isolevel covered a major part of the fasciculus cerebello-thalamicus (fct) during high amplitude stimulation. Movement as measured by the UPDRS-III was improved during both low and high amplitude settings compared to off stimulation. In this particular patient the motor score was the same during both high and low amplitude stimulation.

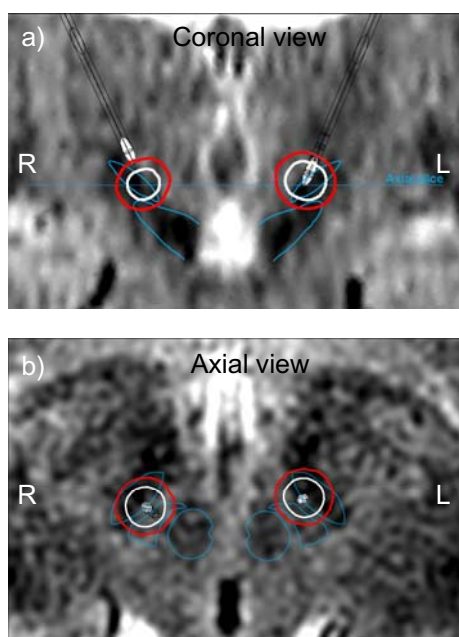


Fig. 2 a) Coronal and b) axial view of the electric field during electrical settings that induced dysarthria (red) and that did not induce dysarthria (white). The approximate boundaries of the red nucleus, the fasciculus cerebello-thalamicus, and the STN have been traced with blue colour.

B. Case 2: Hypomania

This patient suffered from reversible stimulation-induced hypomania. The active electrode contacts that were used during the conditions that induced hypomania were positioned slightly medial and ventral in the STN area. The simulations showed an electric field isolevel that reached down into the substantia nigra (Fig. 3). Movement was slightly improved during the electrical settings that induced hypomania compared to the electrical settings which did not induce hypomania.

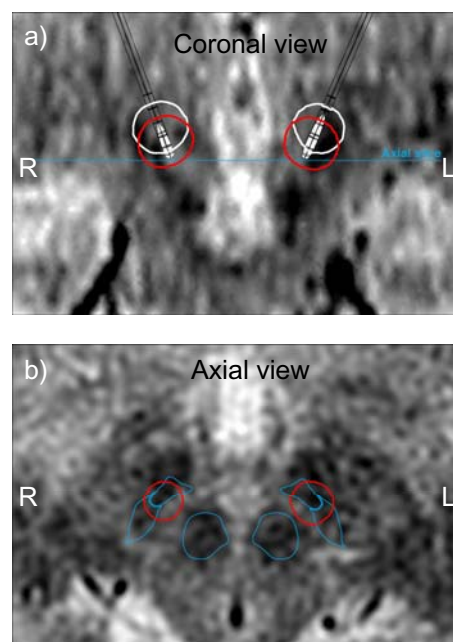


Fig. 3 a) Coronal and b) axial view of the electric field during electrical settings that induced hypomania (red) and that did not induce hypomania (white). The approximate boundaries of the red nucleus, the substantia nigra pars reticulata, and the STN have been traced with blue colour.

C. Case 3: Uncontrolled laughter

Acute uncontrolled laughter was induced during high amplitude stimulation in the STN. In addition to laughter the patient suffered from acute stimulation-induced dysarthria. The simulations showed that the electric field isolevel generated by the right electrode was located far ventral in the STN area and covered part of the substantia nigra. The electric field isolevels generated by both electrodes also covered a major part of the fct during high amplitude stimulation (Fig. 4). There was a greater improvement in movement during high amplitude stimulation than during low amplitude stimulation.

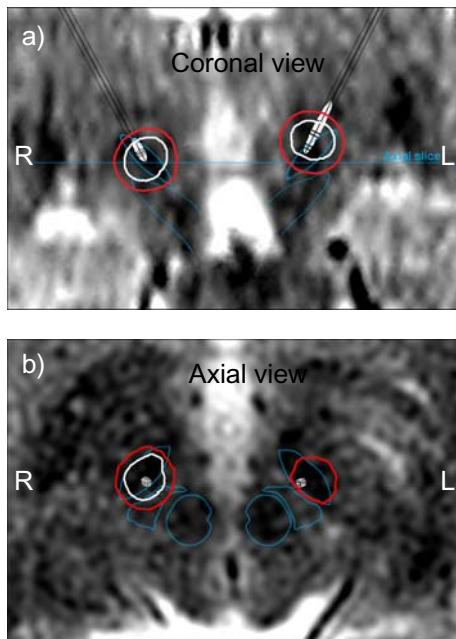


Fig. 4 a) Coronal and b) axial view of the electric field during electrical settings that induced uncontrolled laughter and dysarthria (red) and that did not induce these side-effects (white). The approximate boundaries of the red nucleus, the fasciculus cerebello-thalamicus, and the STN have been traced with blue colour.

IV. DISCUSSIONS

There are several findings of this study. In case 1, speech intelligibility was impaired when the 0.2 V/mm electric field isopleth, from active electrode contacts positioned ventral, posterior and medial to the centre of the STN, covered a major part of the fct. Stimulation-induced speech impairments during STN DBS has often been attributed to lateral stimulation of the motor limb in the internal capsula, the corticobulbar fibers [6]. During stimulation of the corticobulbar fibers there is usually a change of sustained phonation and other acoustical parameters. These characteristics were not seen in this study. In a study by Plaha et al. [7] stimulation related dysarthria were seen in patients with active electrode contacts positioned medially in the STN area. They believed that stimulation of fibres from the fct that control movements of the vocal cords was likely the cause of the dysarthria. This is in agreement with the present study. In case 2, hypomania was introduced during electrical settings that generated an electric field isopleth that reached down into the substantia nigra. Ulla et al. [8] reported that one patient who had benefited from bilateral DBS in the STN for PD, suffered from acute and reproducible manic behavior. They believed their patient was stimu-

lated in the substantia nigra. This is in agreement with the present study where the electric field isopleth covered part of the substantia nigra. Uncontrolled laughter and speech impairments were introduced by the stimulation in case 3. The electric field generated by the right electrode reached down into the substantia nigra, and the electric field isopleths generated by both electrodes covered a major part of the fct during high amplitude stimulation. Mirthful laughter has been reported in a study by Krack et al., 2001 [9] during bilateral stimulation at the most ventral contacts with an electric potential of 3.6 V, a pulse-width of 90 μ s, and a frequency of 160 Hz.

V. CONCLUSIONS

It was demonstrated that the anatomical distribution of the simulated electric field could be visualized and related to the reported effects and side effects of stimulation. Patient specific models and simulations may in the future become a useful tool for postoperative investigations of DBS.

REFERENCES

1. Astrom M, Zrinzo L U, Tisch S et al (2009) Method for patient-specific finite element modeling and simulation of deep brain stimulation. *Med Biol Eng Comput*, 471: 21-8.
2. Andreuccetti D, Fossi R, and Petrucci C (2005) Dielectric properties of body tissue. Italian National Research Council, Institute for Applied Physics, Florence, Italy <http://niremf.ifac.cnr.it/tissprop/>
3. Cheng D K (1989) *Field and wave electromagnetics*. Vol. ISBN 0-201-52820-7. 1989: Addison-Wesley Publishing Company Inc.
4. Galloway M N, Jeanmonod D, Liu J et al (2008) Human pallidothalamic and cerebellothalamic tracts: Anatomical basis for functional stereotactic neurosurgery. *Brain Struct Funct*.
5. Tripoliti E, Zrinzo L, Martinez-Torres I et al (2008) Effects of contact location and voltage amplitude on speech and movement in bilateral subthalamic nucleus deep brain stimulation. *Mov Disord*, 2316: 2377-83.
6. Deuschl G, Herzog J, Kleiner-Fisman G et al (2006) Deep brain stimulation: Postoperative issues. *Mov Disord*, 21 suppl 14: s219-37.
7. Plaha P, Ben-Shlomo Y, Patel N K et al (2006) Stimulation of the caudal zona incerta is superior to stimulation of the subthalamic nucleus in improving contralateral parkinsonism. *Brain*, 129pt 7: 1732-47.
8. Ulla M, Thobois S, Lemaire J J et al (2006) Manic behaviour induced by deep-brain stimulation in parkinson's disease: evidence of substantia nigra implication? *J Neurol Neurosurg Psychiatry*, 7712: 1363-6.
9. Krack P, Kumar R, Ardouin C et al (2001) Mirthful laughter induced by subthalamic nucleus stimulation. *Mov Disord*, 165: 867-75.

Author: Mattias Astrom
 Institute: Linköping University
 Street: Department of Biomedical Engineering
 City: Linköping
 Country: Sweden
 Email: matas@imt.liu.se

Robot-amplified manual exploration improves load identification

F.C. Huang¹, J.L. Patton² and F.A. Mussa-Ivaldi³

¹ Sensory Motor Performance Program, Rehabilitation Institute of Chicago

² Bioengineering, University of Illinois at Chicago

³ Physical Medicine and Rehabilitation, Mechanical and Biomedical Engineering, Northwestern University,

Abstract—We tested how manual exploration with anisotropic loading (*Viscosity-Only* (negative), *Inertia-Only*, or *Combined-Load*) influenced skill transfer to the isolated inertial load. Intact subjects (N=39) performed manual exploration with an anisotropic load before evaluation with prescribed circular movements. Combined-Load resulted in lower error (6.89±3.25%) compared to Inertia-Only (8.40±4.32%) and Viscosity-Only (8.17±4.13%) according to radial deviation analysis (% of trial mean radius). An analysis of sensitivity to load variation in normal and catch trials reveals performance differences were likely due to changes in feedforward mass compensation. Analysis of exploration movement revealed higher average speeds (12.0%) and endpoint forces (22.9%) with *Combined-Load* exploration compared to *Inertia-Only*. Our findings suggest that free movements amplified by negative viscosity can enhance the ability to identify changes in inertial loading.

Keywords— manual control, systems identification, error-augmentation

I. INTRODUCTION

When encountering an unfamiliar manual task, the type of movement pattern itself could influence the efficiency of learning. The motor system evidently exhibits some ability to generalize between prescribed movements[1]. Recent literature suggests that encouraging variability is as effective as repeated practice for generalizing skills in a ballistic task[2]. Other researchers note that practice variability may be especially effective if task parameters are expected to change[3], and can promote more stable performance[4]. Broad sensory-motor experiences associated with free exploration may facilitate the identification of environment dynamics[5]—a process critical for motor planning.

While free exploratory movements might offer richer sensory experiences, it is unclear if the learner necessarily knows how to take advantage of that freedom. Novel forms of human-machine interaction could offer a collaborative process of scaffolding or guiding movement, while enabling the individual to direct their own learning. One promising form of such interaction is movement amplification from robot amplified movement [6]-[7], though learning and generalization of motor skills under these conditions is not

yet well understood. For individuals with motor impairment, negative impedance could reduce workload while providing sensory-motor re-training. For healthy individuals, force fields presented during robotic training have already demonstrated dramatic adaptation in manual coordination with relatively brief exercise [8]-[9]. The challenge with any training paradigm is whether the individual can both learn and generalize learning to unpracticed conditions.

We conducted an investigation into how learning an inertial load might be supplemented with active impedance (negative viscosity). We examined how a period of free manual exploration with both negative viscosity and inertia can benefit performance when the viscosity is removed and only the inertial load remains. We compared the effectiveness of this training to training with an inertial load alone, and also compared it with training with negative viscosity training alone. Our findings demonstrate that exploratory training with negative viscosity improves learning and generalization by facilitating the process of identifying changes in loading conditions.

II. METHODS

A. Apparatus and Implementation of Anisotropic Loads

We asked subjects to control the movement of a two-degree of freedom planar force-feedback device (Fig. 1) described elsewhere [8]. During the evaluation task, the handle responded as if it were a physical mass along one axis, while no load was present in the perpendicular axis. During training for some conditions, we included anisotropic negative viscosity loads aligned with the axis of the inertial load. We selected five orientations for the anisotropic loads: $\theta_m=0, 36, 72, 108, 144$ degrees with respect to the frontal plane. End-point forces $F_x(t)$ and $F_y(t)$ approximating inertial and viscous loads were presented according to:

$$\begin{bmatrix} F_x(t) \\ F_y(t) \end{bmatrix} = R^t \begin{bmatrix} 0 & 0 \\ 0 & m \end{bmatrix} R \begin{bmatrix} \ddot{x}(t) \\ \ddot{y}(t) \end{bmatrix} + R^t \begin{bmatrix} 0 & 0 \\ 0 & b \end{bmatrix} R \begin{bmatrix} \dot{x}(t) \\ \dot{y}(t) \end{bmatrix}$$

$$\text{where } R = \begin{bmatrix} \cos \theta_m & \sin \theta_m \\ -\sin \theta_m & \cos \theta_m \end{bmatrix}. \quad (1)$$

We chose a mass parameter m of 0 or 3 kg and a viscosity parameter b of either 0 or -10 N-s/m. With the rotation matrix R , various anisotropic loads were selected representing orientations of load.

In this study 26 healthy individuals volunteered and were randomly assigned to either the *Inertia-Only* or *Combined-Load* subject groups. We later included a third group with 13 healthy individuals as a part of the *Viscosity-Only*.

Subjects were asked to perform two tasks using the robotic manipulandum: (1) training with free exploratory movements (*free exploration*) followed by (2) performance of a prescribed circular movement (*performance evaluation*). During free exploration, subjects were instructed to move the object at their discretion using various directions, speeds, and positions within a circular region (0.1 m radius centered within the workspace). The computer signaled the user to halt free exploration after 15 meters of handle endpoint total travel. The experiment groups differed in terms of the loading conditions presented during free exploration.

During performance evaluation (2), subjects were instructed to move the robotic interface in three complete counter-clockwise revolutions at about 1 revolution per second. Subjects were told to achieve accurate and smooth performance as much as possible in circular movements about a target track (0.1 m radius). During normal trials, the performance evaluation included the same inertial load as that presented during the free exploration stage. However, the viscosity term (Eq-1) was set to zero during performance for all trials. In some instances, *catch trials* were presented, in which the loading was removed covertly.

III. RESULTS

A. Differences in Evaluation

Results from ANOVA of Evaluation trials indicated influences from each experiment factor: subject group ($F[2, 1800] = 28.57$, $MSE = 0.04037$, $p = 6.12e-13$), load type ($F[4, 1800] = 9.91$, $MSE = 0.01401$, $p = 6.2e-8$), and trial sequence ($F[9, 1800] = 8.81$, $MSE = 0.01245$, $p = 4.5e-13$). Interactions were significant for the group-by-load effect ($F[8, 1800] = 5.15$, $MSE = 0.00728$, $p = 2.3e-6$) and the group-by-trial effect ($F[18, 1800] = 2.88$, $MSE = 0.00408$, $p = 4.6e-3$). These findings indicate that load orientations differed in difficulty, and some performance changes occurred over the course of performance trials following free exploration, though these effects depended on subject group. In contrast, results from ANOVA for catch trials indicated a strong influence only for effects from load type ($F[4, 368] = 20.0$, $MSE = 0.0318$, $p = 6.4e-14$) and trial sequence ($F[1, 368] = 9.5$, $MSE = 0.1511$, $p = 2.2e-3$). Interactions were not significant for catch trials. These results

suggest that subject groups had similar sensitivity to unexpected loads, and that this sensitivity changes between the first and second catch trials.

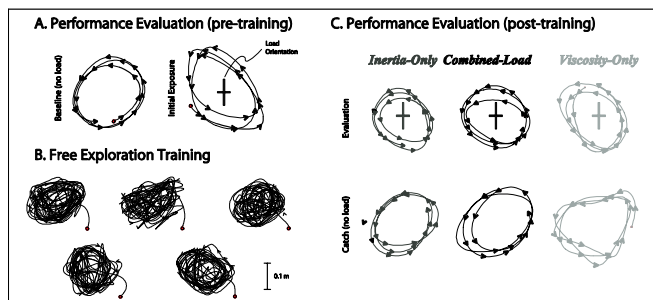


Fig. 1 Typical handle trajectories from one subject during evaluations for one load condition. Coloring (red to blue) indicates time progression. (A) Curvature is most consistent in the Baseline (no load) condition. Systematic distortions arise during Initial Exposure with unexpected anisotropic inertial loading. (B) For each load, subjects were presented with a free exploration stage prior to performance evaluation. Trajectories for each load orientation (indicated by longer black line) of anisotropic inertia reveal wide variability. (C) Trajectories for Evaluation and Catch trials demonstrate error patterns between groups. Errors in Evaluation trials typically were less than Initial Exposure. In contrast, unexpected Catch (no load) trials exhibit systematic errors of similar magnitude with respect to Initial Exposure but with sharply different orientation.

Including free exploration with combined inertia and negative viscosity resulted in lowest overall error. According to the mean radial deviation metric (% of mean trial radius), the *Combined-Load* training group exhibited 18.0% lower error (6.89 ± 3.25 , mean and SD) compared to *Inertia-Only* (8.40 ± 4.32 , mean and SD) and 14.2% lower compared to *Viscosity-Only* (8.03 ± 4.13 , mean and SD). The *Inertia-Only* exhibited 4.64% lower radial deviation relative to *Viscosity-Only*. According to Tukey HSD post-hoc tests, these differences were significant for *Combined-Load* compared to *Inertia-Only* (1.51; CI: 1.00, 2.02; $p = 5.0e-11$) and compared to the *Viscosity-Only* group (1.14; CI: 0.62, 1.65; $p = 5.4e-7$). Differences between *Viscosity-Only* and *Inertia-Only* were not significant (0.37; CI: 0.14, 0.88; $p = 0.20$).

Noting a cyclic pattern of error (see Fig. 2), we fit sinusoids for the radial magnitude as a function of load orientation and observed non-significant amplitude from *Combined-Load* (mean 0.0058, CI: -0.0021, 0.0136, $R^2 = 0.0165$). In contrast, both *Inertia-Only* (mean 0.0166, CI: 0.0062, 0.0270, $R^2 = 0.0725$) and *Viscosity-Only* training (mean 0.0313, CI: 0.0168, 0.0455, $R^2 = 0.1270$) exhibited significant non-zero amplitudes. Low sensitivity to load changes could indicate increased co-contraction or stiffness control. However, analysis of catch-trial results indicates similarity sensitivity to unexpected absence of loading, which suggests that the appropriate feedforward strategy was available for both the *Combined-Load* and *Inertia-only* groups.

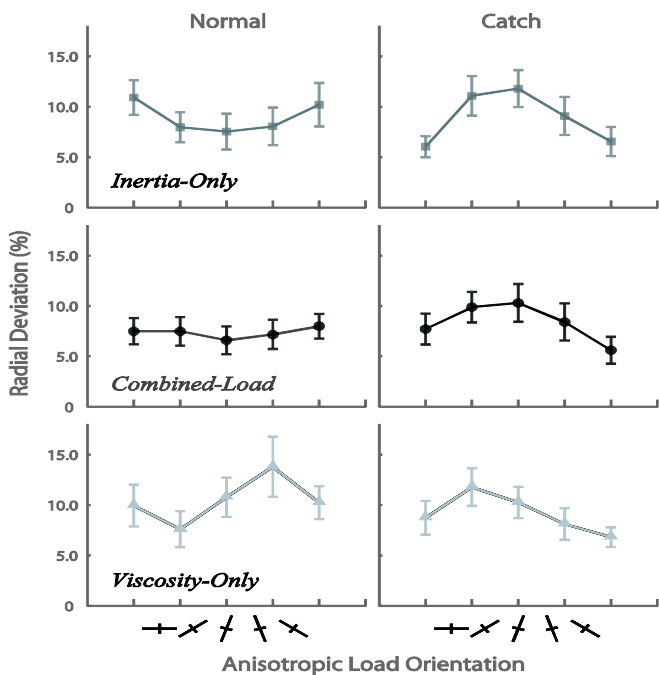


Fig. 2 Radial deviation trends for normal (left) and catch (right) trials reveal differences in sensitivity to load axis (5 conditions, indicated by cross) for each subject group (by rows). The Combined-Load group achieves the lowest error and lowest sensitivity in normal trials and exhibits comparable behavior to Inertia-Only in catch trials. The Viscosity-Only group exhibits larger error overall in normal conditions and lowest error in catch trials, suggesting reduced feedforward mass compensation. Error-bars indicate 95% confidence intervals across subjects and trials (first two trials of normal conditions per load, all two catch trial per load).

B. Analysis of Exploration Behavior

In addition to trends in Evaluation trials, we also observed key differences between the subject groups in free exploration behavior, which show that including negative viscosity promoted a wider range of dynamics. Histograms (Fig. 3, left) of the speed and forces (absolute value of components along direction of anisotropy major axis) averaged over all subjects and trials observed during free exploration showed that the Combined-Load training group exhibited a diminished peak at low values in favor of a wider range of values. Similar trends were observed for acceleration, though the differences were not significant. No differences were observed for position states, indicating similar spatial extents of exploration between groups. Similarly, no differences were observed for movement states and forces in the no-load axis (orthogonal to the inertial load).

A comparison of mean speed and endpoint force data observed during the exploration stages (Fig. 3, right) indicate greatest activity from the Combined-Load group. Using Tukey’s post-hoc tests for significant differences, we found that the average speed was 12.0% larger for the Combined-Load group compared to the Inertia-Only group (0.036 m/s; CI: 0.002, -0.070; $p=0.038$), but was 18.8% smaller with respect to the Viscosity-Only group (-0.077 m/s; CI: -0.111,

-0.042; $p=8.37e-7$). The Inertia-Only group also exhibited 37.9% smaller average speed compared to the Viscosity-Only group (0.112 m/s; CI: 0.078, 0.147; $p=1.24e-12$). In contrast to the trends in speed, we found that the average force was largest for the Combined-Load training group: 22.9% greater compared to the Inertia-Only group (1.27 N; CI: 0.42, 2.11; $p=7.99e-15$) and 179.0% greater compared to the Viscosity-Only training group (4.36 N; CI: 3.51, 5.20; $p=1.46e-3$). The Viscosity-Only group exhibited 55.9% smaller average force compared to the Inertia-Only group (-3.09 N; CI: -3.94, -2.25; $p=4.24e-14$). These trends suggest a greater similarity in training for the two groups that experience inertial loading during free exploration, with a somewhat increased range of exploration for the Combined-Load training group.

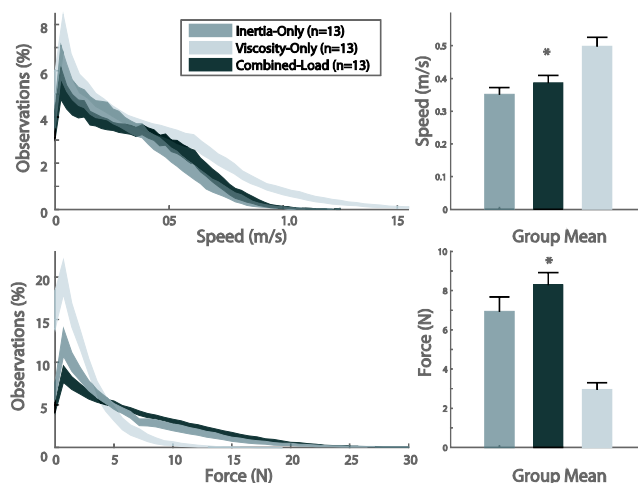


Fig. 3 (A) During free exploration prior to task performance, the Combined-Load (inertia and negative viscosity) training group exhibited modest differences indicating broader distributions (average of all subjects and load conditions) of speed and computed endpoint force (along the axis of the inertial load) compared to Inertia-Only exploration. (B) Quantitative comparisons, however, confirm that the Combined-Load training group exhibited greater increase in average speed (12.0%) and computed endpoint force (22.9%) compared to Inertia-Only exploration. The Combined-Load training group exhibited lower average speed compared to the Viscosity-Only group (18.8%), but the experienced higher average forces (179.0%). Error bars represent 95% CI across all trials.

IV. DISCUSSION

Our findings demonstrate that training with negative viscosity can improve learning of a passive object manipulation task, achieving even better performance than training with the passive conditions alone. These findings suggest a two-part process of improved load identification through enhanced sensorimotor experiences and successful generalization between mechanical environments. Negative viscosi-

ty evidently alters the efficiency of internal model formation of inertial loading by promoting broader exploration during training (See Fig. 3). We argue then that the motor system is able to transfer the enhanced motor scheme to the passive environment by relating the shared features between environments. These findings offer an intriguing new method for facilitating sensorimotor adaptation through augmentation with negative impedance.

Beyond preserving the formation of a feedforward scheme, we argue that including negative impedances can strengthen the learning of passive loading. Negative viscosity effectively introduces a form of error augmentation since it amplifies intended movements. Such environments presumably facilitate learning by strengthening the associations between motor actions and sensory consequences [10-11]. In contrast to perceptual changes, however, altering the force-motion sensitivity through mechanics necessitates changes in the energetic requirements and stability—important factors in promoting motor adaptation. Inertial characteristics of objects and the arm evidently influence preferred movements [12]. Schaal et al. (1996) [13] noted that in ball bouncing, the human motor system seems to autonomously adjust control towards a stable strategy. In these cases, the sensitivity of movement to motor input can be attributed to the impedance at the interface between the arm and environment, which will clearly influence how easily sensory-motor associations are learned.

Our analysis of free exploration movements confirm that including negative viscosity increased the range of experienced speeds and forces—a result that could explain how the *Combined-Load* training group acquired more accurate compensation schemes. The distinct task stages presented in this study may have acted as contextual cues to facilitate switching of strategy elements [14]. Further study is needed to understand how switching between exploratory and prescribed movements influences skill transfer between environments with overlapping mechanical properties.

Enhancing motor learning by including negative impedances could have important implications to rehabilitation and other motor skill training endeavors. Loads that reduce workload [15] may be especially important for individuals with motor impairment who are prone to fatigue or have limited movement capabilities. The current study demonstrates the capacity of the motor system to train with a negative impedance, essentially a form of energetic assistance, and then successfully apply learned skills to a completely passive environment. Further study is needed to determine how training with negative impedance influence long term skill acquisition.

ACKNOWLEDGMENT

This work was supported by NINDS grant NS357673 and by the Coolidge Foundation.

REFERENCES

- [1] MA Conditt and FA Mussa-Ivaldi, "Central representation of time during motor learning," *PNAS*, v. 96, #20, pp. 11 625–11 630, 1999.
- [2] E. L. Shoenfelt, L. A. Snyder, A. E. Maue, C. P. McDowell, and C. D. Woolard, "Comparison of constant and variable practice conditions on free-throw shooting," *Percept Mot Skills*, no. 94(3 Pt 2), pp. 1113–23, Jun 2002.
- [3] C. Shea, Q. Lai, D. Wright, M. Immink, and C. Black, "Consistent and variable practice conditions: effects on relative and absolute timing," *J Mot Behav.*, vol. 33, no. 2, pp. 139–52., Jun 2001.
- [4] C. Giuffrida, J. Shea, and J. Fairbrother, "Differential transfer benefits of increased practice for constant, blocked, and serial practice schedules," *J Mot Behav.*, vol. 34, no. 4, pp. 353–65, Dec 2002.
- [5] F. C. Huang, R. B. Gillespie, and A. D. Kuo, "Visual and haptic feedback contribute to tuning and online control during object manipulation," *J Mot Behav.*, vol. 39, no. 3, pp. 179–93, May 2007.
- [6] Kazerooni, H., "The Human Power Amplifier Technology at the University of California, Berkeley," *Journal of Robotics and Autonomous Systems*, Elsevier, Volume 19, 1996, pp. 179-187.
- [7] Gabriel Aguirre-Ollinger, J. Edward Colgate, Michael A. Peshkin, Ambarish Goswami: A 1-DOF assistive exoskeleton with virtual negative damping: effects on the kinematic response of the lower limbs. *IROS 2007*: 1938-1944
- [8] JL Patton and FA Mussa-Ivaldi, "Robot-assisted adaptive training: custom force fields for teaching movement patterns," *Biomedical Engineering, IEEE Transactions on*, vol. 51, no. 4, pp. 636–646, 2004.
- [9] JL Patton, M Stoykov, M Kovic, and FA Mussa-Ivaldi, "Evaluation of robotic training forces that either enhance or reduce error in chronic hemiparetic stroke survivors," *EBR*, vol.168, pp.368–383, 2006.
- [10] Y. Matsuoka, B. Brewer, and R. Klatzky, "Using visual feedback distortion to alter coordinated pinching patterns for robotic rehabilitation," *J. of NeuroEngineering and Rehabilitation*, v4, #1, p. 17, 2007.
- [11] Wei Y, Bajaj P, Scheidt R, Patton JL: Visual Error Augmentation for Enhancing Motor Learning and Rehabilitative Relearning. In *IEEE Int. Conference on Rehabilitation Robotics*. Chicago, IL; 2005.
- [12] P. N. Sabes, M. I. Jordan, and D. M. Wolpert, "The Role of Inertial Sensitivity in Motor Planning," *J. Neurosci.*, vol. 18, no. 15, pp. 5948–5957, 1998.
- [13] S. Schaal, D. Sternard, and C. G. Atkeson, "One-handed juggling: A dynamical approach to rhythmic movement task," *Journal of Motor Behavior*, vol. 2, no. 28, pp. 165–183, 1996.
- [14] N. I. Krouchev and J. F. Kalaska, "Context-Dependent Anticipation of Different Task Dynamics: Rapid Recall of Appropriate Motor Skills Using Visual Cues," *J Neurophysiol*, vol. 89, no. 2, pp. 1165–1175, 2003.
- [15] S. Housman, V. Le, T. Rahman, R. Sanchez, and D. Reinkensmeyer, "Arm-training with t-wrex after chronic stroke: Preliminary results of a randomized controlled trial," *Proceedings of the 2007 IEEE 10th International Conference on Rehabilitation Robotics, Noordwijk, Netherlands*, pp. 562–568, June 12-15.

A New Lightweight, Robust and Forceful Finger for an Artificial Limb

M. Franke, M. Bogdan

Department of Computer Engineering, Institute for Computer Science, University of Leipzig, Germany

Abstract— Hand prostheses need to be lightweight, robust and forceful and should replace the function and range of performance of the human hand in the best possible way. Furthermore, their look and appearance should turn up as naturally as possible. The prostheses and anthropomorphic robot hands known today often lack one or more of those aspects. In our approach, a new lightweight, robust and forceful finger for an artificial limb is presented. The joints are based on viscoelastic joint capsules instead of fixed axes. The result is an artificial finger of anatomically correct size which provides holding forces up to 100 N. We resume, that these properties are excellent qualifications for applications in the field of future hand prostheses.

Keywords— forceful artificial finger, viscoelastic joint capsule, rheonomic, multibody system, hand prosthesis.

I. INTRODUCTION

Hand prostheses need to be lightweight, robust and forceful. They should replace the functions of the human hand in the best possible way. Furthermore, their look and appearance should be as naturally as possible.

The prostheses and anthropomorphic robot hands known today often lack at least one or more of those aspects. In this approach, a new lightweight, robust and forceful finger for an artificial limb is presented. Anthropomorphic robot hands and hand prostheses known today are commonly based on joints using fixed axes. They can be classified as holonomic ideal skleronomic multibody systems.

Our hypothesis is that the DIP (Distal interphalangeal joint), PIP (Proximal interphalangeal joint) and MCP (Metacarpophalangeal joint) joints of the human finger can be better modeled with viscoelastic joint capsules. Hence, our model is based on a holonomic non-ideal rheonomic multibody system, which is a new approach in this context.

In this study, we use a tension testbed to evaluate the holding force of the artificial finger in the so called hook grasp. We present our experimental results to verify the non-ideal rheonomic properties of our finger model.

II. MOTIVATION FOR AN ARTIFICIAL FINGER BASED ON A NEW KIND OF MULTIBODY SYSTEM

A single finger of an average sized human hand can hold weights up to 100 N and more. In contrast to this, today's known anthropomorphic robot hands and hand prostheses have a largely reduced range of performance with a maximum of 30 N per finger [1].

In medical-anatomical literature [2], [3], [4], [5] the finger DIP and PIP joints are commonly classified as ginglymus or hinged joints with 1 axis which permits flexion and extension. In [4] an additional passive rotation along the finger's longitudinal axis is described. The MCP joint is commonly described as a condyloid joint which permits flexion, extension, adduction, abduction and circumduction which is a combination of the former.

Hence, the DIP or PIP joints of artificial hands are commonly based on joints with 1 degree of freedom (DOF) [1], [6-12] which rotate around a single, fixed joint axis. The MCP joint in hand prostheses with simple kinematics like described in [7], [9], [12] provide 1 DOF for flexion and extension. Artificial hands based on more complex kinematics like [1], [6], [8], [10] provide an additional DOF for abduction and adduction in the MCP joint. They represent holonomic ideal skleronomic multibody systems [13].

Naegerl, Kubein-Meesenburg et al. presented in [14] their hypothesis, that the mechanics of the DIP and PIP joints in the human finger can be described with more than 1 DOF due to elastic properties of the tissue.

Each joint is encapsuled by an articular capsule (or joint capsule) as illustrated in Fig. 1 and has a volar ligament and two collateral ligaments.

We examined a human index finger *in vivo* in a relaxed and a tensed state of the hook grasp using x-ray radiograph images of each state. Figure 2 (a) shows the index finger positioned in a hook grasp in relaxed state. In figure 2 (b) displays the same finger in tensed state holding a weight of 50 N, hanging with a polyethylene slope (width = 2.5 cm) in the flexed finger. The arrows indicate the direction of the tension applied. Detail images 2 (c) and 2 (d) correspond to the rectangled region in fig. 2 (a) and 2 (b).

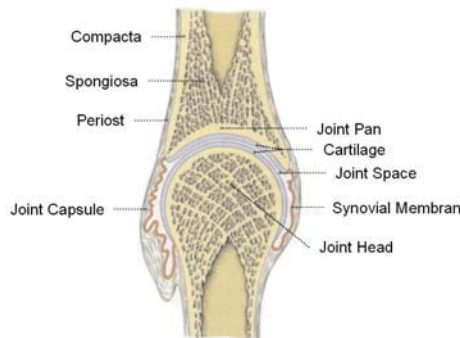


Fig. 1 Illustration of the joint capsule [5]

Image 2 (d) reveals the slight decrease of the joint space in tensed state compared to the relaxed state shown in fig. 2 (c). Our conclusion is, that the joint capsules of the finger's joints are deformed under tension and acting forces. This reveals an additional translational degree of freedom that enables the joint capsule to reconfigure under tension - the articular cartilages of joint head and pan can build a contact surface. Due to the curved morphology of the joint surfaces of the DIP, PIP and MCP joint, the joint space reduction

1. diminishes the passive rotation along the longitudinal axis
2. increases the friction of the joint and
3. stabilizes the joint position.

This change of the dynamic properties is obviously useful to protect the joint and to reduce damages when exposed to large forces. Damages like luxation, rupture or fracture [15] can appear, when the joint is overstressed or inadaequately loaded. After the tension is removed the deformation recedes, the joint space reaches it's former dimension and the joint it's former properties.

III. VIRTUAL REPLICATION AND GENERATION OF THE ARTIFICIAL FINGER

In our approach, we used rapid prototyping models of the human index finger bones derived from MSCT (Multislice Computer Tomograph) images of a human hand. The 3D CAD Data of the bone structures was reconstructed from the MSCT DICOM images. Then the 3D CAD Data has been produced by rapid prototyping. With this method, we gained lightweight but very rugged artificial index finger bones. We call this approach the virtual replication method (VRM).

The joint capsules were constructed by using technical silicone. They stabilize the joint and enable a slight translational deformation, when tension appears. The capsules were filled with synthetic oil of low-viscosity to minimize friction between the joint surfaces. In relaxed state, the joint has a small joint space. Each joint's distal phalanx is connected via 2 nylon cords with 2 linear actors, one for extending and one for flexing the joint. The nylon cords have been attached in anatomically correct regions to the artificial bone. The 6 linear actors are placed in the region corresponding to the location of the forearm.

The result of this is an artificial finger, with a kinematic structure very close to the natural human finger. In addition to this, due to the VRM the anatomic morphology of the artificial bones has been derived *in vivo* from a human hand. To verify the holding force and to measure the rheonomic behavior, the artificial finger was mounted into a testbed like shown in figure 3.

Figure 3 shows the testbed configuration and the artificial finger in an extended pose. In the left Subfigure, a detail view of the artificial finger prototype is given, showing the artificial bones with their tracking marks, joint capsules, the tendon arrangement and mounting parts.

In the following chapter the testbed and the procedure of the tension test will be described.

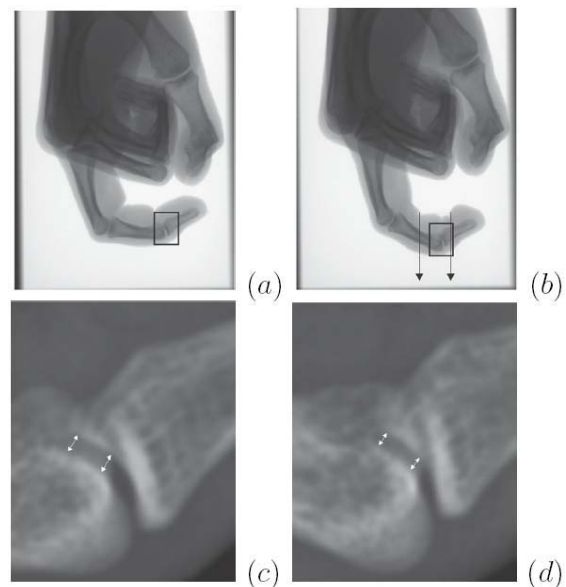


Fig. 2 Reduction of joint space under tension is visible in x-ray images

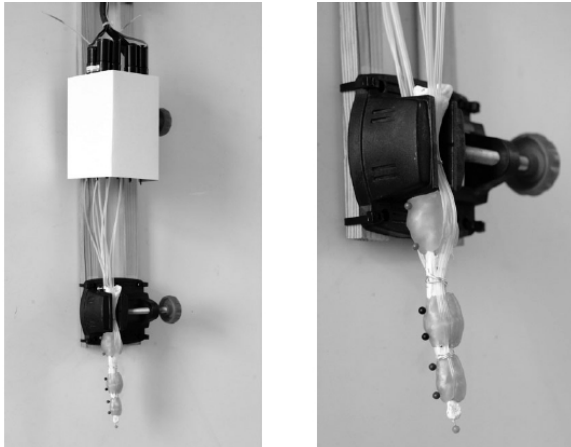


Fig. 3 The tension testbed: Configuration overview (left) and detail view of the artificial finger (right).

IV. DESCRIPTION OF THE TENSION TEST

The artificial finger is mounted top-down with the fingertip to the bottom in extended posture and it can be flexed and extended by the controller. On each phalanx, 2 marks along its center axis are attached to track the kinematic chain of the artificial finger.

Step 1: For the tension test, the artificial finger has been positioned into the hook-grasp posture with the marked tip center point (TCP) in a defined initial position p_0 .

Step 2: Then, different weights (1 N, 5 N, 10 N, 50 N, 100 N, 150 N) have been hung with a polyethylene slope (width = 2.5 cm) into the flexed finger for a tension period of 15 minutes. Each weight has been applied in one separate cycle. The slope fitted very good into the flexed finger and provided a stable hook grasp. Directly after the weight had been applied, the position of the TCP in the initial tensed state p_{t1} has been recorded.

Step 3: At the end of the period, the position of the TCP in the final tensed state p_{t2} has been recorded.

Step 4: After each cycle, the weight was removed and the finger has been positioned into the extended posture. Then, to permit the elastic deformation of the capsule's material to recede, a break of 15 minutes was held.

V. EXPERIMENTAL RESULTS

The tension cycles revealed elastic deformations of the initial hook grasp posture.

The initial position p_0 of the TCP is changed directly by the applied force into the initial tensed state position p_{t1} . During the tension period, the TCP moves to the position p_{t2} . This behaviour can be explained by the elastic

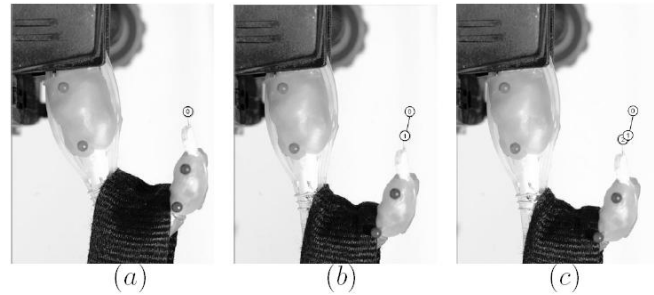


Fig. 4 The flexed artificial finger (a) before, (b) at the beginning and (c) at the end of the tension period.

deformation process called creepage of the viscoelastic material forming the joint capsules due to the applied tension. It results in the variation of the position of the TCP during the tension period.

Figure 4 shows images taken during a tension cycle. Subfigure 4 (a) shows the flexed artificial finger in the initial position during Step 1 in p_0 before the weight was attached. Subfigure 4 (b) was taken directly after the weight had been applied in Step 2. It shows the finger's TCP in initial tensed position p_{t1} . Subfigure 4 (c) was taken at the end of the tension period and shows the TCP in the final tensed position p_{t2} . The test turned out that the finger was capable of holding weights up to 100 N. Yet it was not capable of holding 150 N weight - when applied, the flexed finger was extended by the force and the slope slipped through it.

Fig. 5 shows the movement of the TCP recorded in the different tension cycles. It reveals that the deviation depends on the magnitude of the load applied. The load depending rheonomic behaviour of the TCP revealed in a creepage process during the tension test (Fig. 6).

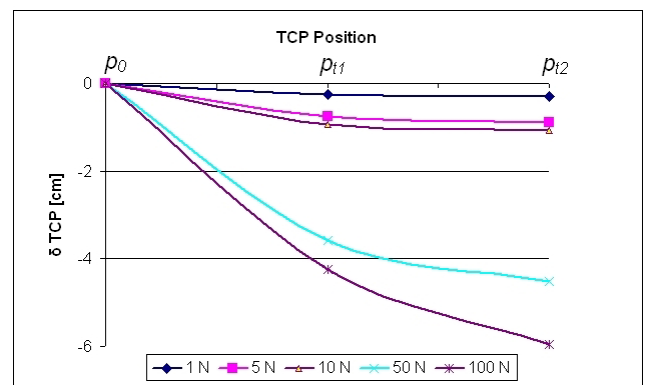


Fig. 5 Movement of the TCP in [cm] during the tension test with different weights applied.

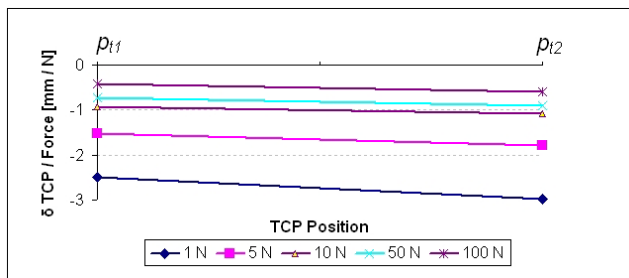


Fig. 6 Load depending rheonomic behaviour of the TCP in [mm / N] during the tension test.

VI. CONCLUSION

In this Investigation we presented a new lightweight artificial finger derived *in vivo* from a human hand by the virtual replication method. In contrast to [1], [6-12] and other known artificial or robot hands, viscoelastic joint capsules have been implemented instead of fixed joint axes.

Our Conclusion is, that viscoelastic joint capsules result in an additional joint space DOF for each DIP, PIP and MCP joint. Hence the DIP and PIP joint provide one rotational (flexion / extension) and one rheonomic translational DOF (joint space reduction / extension). The MCP joint provides two rotational DOF (abduction / adduction, flexion / extension) and one rheonomic translational DOF (joint space reduction / extension). The artificial finger based on viscoelastic joint capsules can be classified as a holonomic non-ideal rheonomic multibody system. It disclosed to be very robust and revealed a holding force of up to 100 N. The delta of the initial position, initial tensed position and final tensed position reveal rheonomic properties and a creepage process of the viscoelastic material, which develops with time.

As a result, the joint space of the joint is reduced and thus the dynamic properties of the joint change depending on the forces exposed. The kinematic chain of the finger reconfigures due to the non-ideal rheonomic property. In detailed kinematic and dynamic models of the human hand these effects should be considered. We conclude, that the non-ideal rheonomic properties of the artificial finger lead to the high holding force of 100 N. This corresponds a weight which is 200 times higher than the weight of the finger itself. Therefore we resume, that these properties are excellent qualifications for applications in the field of future hand prostheses, for example for biologically inspired neural prostheses as described in [16]. Furthermore we conclude, that the artificial finger presented in this work could be used as an anatomical mockup of the human finger due to the similar biomechanical behaviour.

REFERENCES

1. Butterfass J, Grebenstein M, Liu H, Hirzinger G (2001) DLR Hand II: Next Generation of a Dexterous Robot Hand, Proceedings of the 2001 IEEE International Conference on Robotics & Automation, Seoul
2. Dornblueth O, Zink C, Hildebrandt H (1998) Pschyrembel, Klinisches Woerterbuch, Walter de Gruyter, Berlin, in German
3. Rauber A, Kopsch F (1988), Anatomie des Menschen, Band 1, Bewegungsapparat, Toendury, Berlin, in German
4. Frisch H (2007), Programmierte Untersuchung des Bewegungsapparates, Chirodiagnostik, Springer, Berlin, in German
5. Speckmann E J, Wittkowski W (1994) Bau und Funktionen des menschlichen Körpers, Urban & Schwarzenberg, Munich, in German
6. Franke M (2004) Entwurf und Steuerung eines Prototypen einer anthropomorphen Hand, Diploma Thesis, Institute for Robotics and Process Control, Brunswick, in German
7. Lovchik C S, Diftler M A, (1999) The Robonaut hand: a dexterous robot hand for space, Proceedings of 1999 IEEE International Conference on Robotics and Automation
8. Wilkinson D D, Vande Weghe M, Matsuoka Y (2003) An Extensor Mechanism for an Anatomical Robotic Hand, Proceedings of the 2003 IEEE International Conference on Robotics and Automation: 238 – 244
9. Schulz S, Pylatiuk C, Reischl M, Martin J, Mikut R, Bretthauer G (2005) A Lightweight Multifunctional Prosthetic Hand, Robotica, 23(3):293-299
10. Zollo L, Roccella S, Guglielmelli E, Carrozza M C, Dario P (2007) Biomechatronic Design and Control of an Anthropomorphic Artificial Hand for Prosthetic and Robotic Applications, Mechatronics, IEEE/ASME Transactions on , vol.12, no.4, pp.418-429
11. Lee Y K, Shimoyama I, (1999) A skeletal framework artificial hand actuated by pneumatic artificial muscles, Robotics and Automation, 1999. Proceedings. 1999 IEEE International Conference on , vol.2, no., pp.926-931 vol.2
12. Connolly C (2008) Prosthetic hands from Touch Bionics, Industrial Robot: An International Journal 35:290-293
13. Husty M, Karger A, Sachs H, Steinhilper W (1997) Kinematik und Robotik, Springer, Berlin, in German
14. Naegerl H, Kubein-Meesenburg D, Fanghaenel J, Burfeind H, Albus G (1998) Morphology and mechanics of the human finger, Proceedings of NACOB '98: The third North American Congress on Biomechanics:553 – 554
15. Hoffmann R (1999) Checkliste Handchirurgie, Stuttgart, in German
16. Bogdan M, Franke M, Rosenstiel W (2001) Real Time Processing of Nerve Signals for Controlling an Artificial Hand, Proceedings of the IASTED Conference on Applied Informatics 2001, Innsbruck

Author: Marc Franke
 Institute: Institute for Computer Science
 Street: Johannsgasse 26
 City: D-04109 Leipzig
 Country: Germany
 Email: marc.franke@informatik.uni-leipzig.de

Author: Martin Bogdan
 Institute: Institute for Computer Science
 Street: Johannsgasse 26
 City: D-04109 Leipzig
 Country: Germany
 Email: bogdan@informatik.uni-leipzig.de

Leg Muscles Motion during Whole Body Linear Frequency Sweep Vibration

A. Fratini¹, A. La Gatta², P. Bifulco¹, M. Cesarelli¹, and G. Pasquariello¹

¹ Dept. of Biomedical Electronic and Telecommunication Engineering, University of Naples "Federico II", Naples, Italy

² Math4Tech Center, University of Ferrara, Ferrara, Italy

Abstract — Whole body vibration (WBV) aims to mechanically activate muscles by eliciting stretch reflexes. Mechanical vibrations are usually transmitted to the patient body standing on a oscillating plate. WBV is now more and more utilized not only for fitness but also in physical therapy, rehabilitation and in sport medicine. Effects depend on intensity, direction and frequency of vibration; however, the training frequency is one of the most important factors involved. A preliminary vibratory session can be dedicated to find the best vibration frequency for each subject by varying, stepwise, the stimulation frequency and analyzing the resulting EMG activity. This study concentrates on the analysis of muscle motion in response to a vibration frequency sweep, while subjects held two different postures. The frequency of a vibrating platform was increased linearly from 10 to 60 Hz in 26 s, while platform and single muscles (Rectus Femoris, Biceps Femoris – long head and Gastrocnemius Lateralis) motions were monitored using tiny, lightweight three-axial MEMS accelerometers. Displacements were estimated integrating twice the acceleration data after gravity contribution removal. Mechanical frequency response (amplitude and phase) of the mechanical chains ending at the single muscles was characterized. Results revealed a mechanical resonant-like behavior at some muscles, very similar to a second-order system in the frequency interval explored; resonance frequencies and dumping factors depended on subject and its positioning onto the vibrating platform. Stimulation at the resonant frequency maximizes muscle lengthening, and in turn muscle spindle solicitation, which produce muscle activation.

Keywords — whole body vibration, muscle motion, frequency response.

I. INTRODUCTION

Vibratory stimulations transferred to the whole body, i.e. whole body vibrations (WBV) treatments, are studied for their impact on muscular and hormonal activity, neuromuscular and postural control [1-3]. In these treatments, vibrations are often delivered to the whole body by the use of vibrating plates.

Many of these devices produce vertical sinusoidal oscillations (while some other an alternating rotation) of a platform across a frequency range from 10 to 80 Hz and peak to peak displacements from 1 to 10 mm [4, 5]. Vibrations are then transferred to the specific muscle group through the

body; different postural positions of the subject on the platform correspond to different mechanical stimulation at a specific muscle.

When vibration loads are applied, mechanical and metabolic responses arise from the neuromuscular system [1, 2, 6]. Specific WBV frequencies also seem to produce a higher EMG RMS signal than others [6]. According to these findings it became important to discover the proper frequencies for the vibratory stimulation; this kind of training could otherwise result unproductive [4, 5].

Moreover, as reported in a previous study [7], there is a significant correlation between muscle motion and EMG activity; evaluation of muscle motion would be also meaningful in evaluating muscle response to WBV treatment. In particular, the stimulation at opportune frequency can maximize muscles lengthening, and in turn muscle spindle solicitation, which may produce a more effective muscle activation.

This study concentrates on the evaluation and characterization of the local mechanical stimulation of a specific muscle in a subject exposed to Whole Body Vibration treatment. In particular, patients were subjected to a linear vibratory stimulation sweep in a frequency range from 15 to 60 Hz, while motions of the Rectus Femoris (RF), Biceps Femoris - long head (BF) and Gastrocnemius Lateralis (GL) were analyzed.

Furthermore, since most of the experimental system responses resembled those typical of a second-order system, a simple data fitting was performed. A contralateral analysis between both of the lower limbs was also conducted.

II. METHODS

A. Subjects, device and vibratory stimulus

Twenty healthy males (age 22.6 +/- 2.2 years, height 176.7 +/- 8.4 cm, weight 74.0 +/- 10.1 kg - not athletically trained), not affected by any known neurological or musculoskeletal disorders, were voluntarily involved in the study and gave their informed, written consent to participate. Vibrations were impressed by using a vibrating platform (TSEM S.p.A., Padova - Italy). Platform displacement was exclusively vertical, sinusoidal with an intensity (peak-to-peak displacement) set to 1.2 mm. The plate frequency was

controlled from a function generator (Krohn-Hite 5300A) to obtain a linear vibratory stimulation sweep in a frequency range from 15 to 60 in a time interval of 26 s (corresponding to an increase rate of about 1.7 Hz per second). All the subject familiarized with the device before recording; during the test subjects were requested to hold two positions (see figure 1) without the use of any constraint:

- P1: hack squat position (with a 110° knee flexion);
- P2: standing on toes with heels raised (2-4 cm, depending on the subject sensitivity to maximum vibration attenuation to the head).

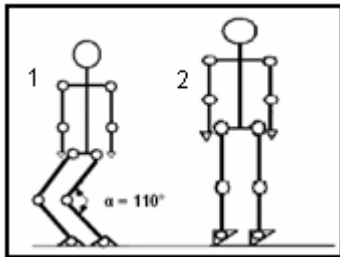


Fig. 1 Body postures selected for the study

These posture are two of the suggested positions for WBV training; they also reduce transmission of vibrations to patient's trunk and head [8].

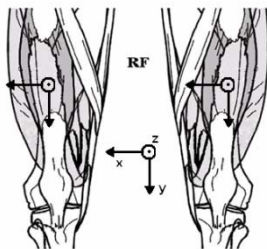


Fig. 2 Example of accelerometer arrangement on muscles for both of the lower limbs. The picture shows the position and orientation of the accelerometer on RF muscles

Tiny and lightweight (less than 10g) three-axial MEMS accelerometers (Freescale Semiconductors) were used to measure accelerations onto patient's skin and on the vibrating platform (the sensors were set to measure acceleration within a $\pm 10g$ range). The accelerometers were placed at 50% on the line from the anterior spina iliaca superior to the superior part of the patella for RF, at 50% on the line between the ischial tuberosity and the lateral epicondyle of the tibia for BF, at 1/3 of the line between the head of the fibula and the heel for GL and at the center of the vibration plate. MEMS accelerometers were stuck onto muscles belly with medical adhesive tape. For each postural position,

signals from the three muscle bellies (both dominant and non-dominant leg) were collected contemporaneously (figure 2).

A PC multi-channel 16-bit data acquisition card (NI-DAQCard 6251) was used to acquire acceleration signals. All signals were sampled at 2048 Hz. Each of the acquisition (one for each posture), spaced with 60 seconds rest intervals, had a duration of 26 s; during this time interval the stimulation frequency, imposed by vibrating plate, raises linearly from 15 to 60 Hz.

B. Accelerometer data processing

Accelerometer signals have been high-pass filtered before the integration in order to exclude the influence of slow accommodation movements and gravity components on motion information. Muscle displacements were estimated integrating twice the acceleration data after gravity (and slow accommodation movements) contribution removal on each axis. Signals have been filtered using a zero-phase 5th order Butterworth with a cut off frequency of 10 Hz.

C. Frequency response of the biomechanical system

Once obtained the displacement signals, they were processed to estimate the frequency response of the biomechanical system. The actual displacement of the vibrating plate (which was substantially invariant in amplitude) was considered as the input signal, while the muscle displacement as system output. Instantaneous frequency was computed for each vibration cycle by estimating two subsequent zero-crossings (with a positive slope) of the signal. Input displacement amplitude, output displacement amplitude and input/output phase difference were estimated for each cycle; gains was obtained by the input/output amplitude ratio. System gain and phase were then plotted against frequency (experimental system response).

D. System identification and data fitting

A simple data fitting was performed supposing the system as a pure second-order given by the equation:

$$G(s) = K_{dc} \frac{1}{\left(\frac{s}{\omega_n}\right)^2 + 2\zeta\left(\frac{s}{\omega_n}\right) + 1} \quad (2)$$

Where K_{dc} is the DC gain, ω_n is the natural frequency and ζ is the damping ratio.

Model parameters (ω_n and ζ) were estimated by utilizing the values of the dominant peak (amplitude and frequency) of the experimental frequency response; K_{dc} coefficient was

chosen minimizing the root mean squared error (RMSE) between model and experimental data.

A contra-lateral analysis on both of the lower limbs was also conducted by comparing:

- muscle motion of dominant and non-dominant leg;
- the estimated resonance frequencies;

In particular we evaluate the symmetry of muscle motion and the similarity of frequency response between lower limbs. For each posture and for all of the muscles analyzed we computed the correlation coefficient (R^2) between the frequency responses (amplitude) of the two limbs muscles.

III. RESULTS

In P1 position RF and BF displacement over frequency showed a resonant-like profile; this was not evident for GL.

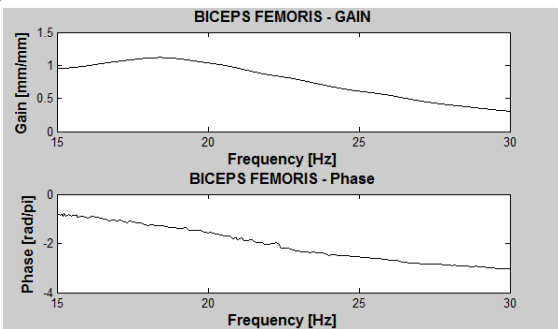


Fig. 3 An example of BF frequency response (amplitude and phase) over frequency with respect to position P1

RF and BF resonance frequencies and dumping factors depended on subject.

In P2 position only the GL muscle showed a resonant-like profile while RF and BF displacements resulted highly damped (mean normalized displacement ≤ 0.4 [mm]/[mm]).

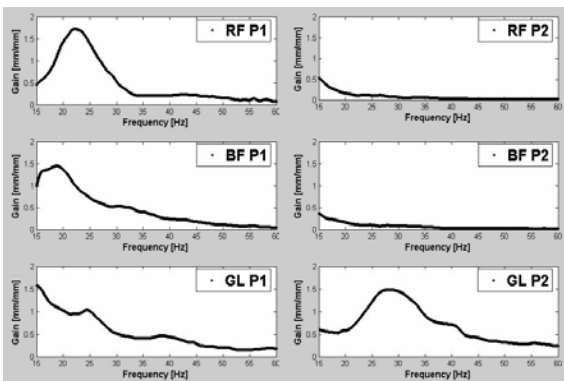


Fig. 4 An example of estimated muscle displacements over frequency with respect to position P1 and P2

In fig.4 is presented an example of the mechanical behavior of the three examined muscles, over the frequency range of interest, for one subject and with respect to each posture.

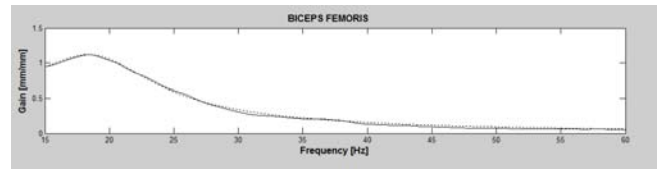


Fig. 5 An example of second order system data fitting: continuous line represent the estimated muscle transfer function while the dotted line shows the second order approximation

For each posture described, the mechanical response of muscles showing a resonant-like profile was very similar to that of second order system (figure 5), as confirmed by the correlation coefficient R_1^2 across the two systems (table 1).

Table 1 Frequency response parameters: mean \pm SD

	Fr [Hz]	Mr [mm/mm]	Q	R_1^2
RF P1	20.50 \pm 1.84	1.42 \pm 0.37	3.49 \pm 1.24	0.95 \pm 0.05
BF P1	19.90 \pm 2.44	1.12 \pm 0.18	2.56 \pm 1.06	0.95 \pm 0.06
GL P2	30.30 \pm 8.27	1.04 \pm 0.36	2.49 \pm 1.02	0.89 \pm 0.11

In general, the contralateral analysis showed that the mechanical behavior of muscles was similar.

In P1, mean difference ΔFr between dominant and non dominant limb resonance frequency was 0.26 \pm 1.85 Hz for RF and 0.39 \pm 2.79 Hz for BF (Table 2). In P2, instead, the mean difference for GL was 0.03 \pm 3.23 Hz.

R_2^2 coefficient resulted very high, suggesting a similar motion of contra-lateral muscles (Table 2).

Table 2 Contra-lateral analysis : mean \pm SD

	ΔFr [Hz]	R_2^2
RF P1	0.26 \pm 1.85	0.95 \pm 0.04
BF P1	0.39 \pm 2.79	0.95 \pm 0.03
GL P1	X	0.94 \pm 0.04
RF P2	X	0.88 \pm 0.09
BF P2	X	0.94 \pm 0.06
GL P2	0.03 \pm 3.23	0.83 \pm 0.12

Besides, only for RF and BF in P1, the phases response is almost identical along Z and Y axes, while displacements along X show a phase difference of π rad. Therefore, the two limbs muscles motion results to be synchronous and symmetric with respect to the sagittal-plane (YZ plane projections).

IV. CONCLUSIONS

As expected, mechanical response of analyzed muscles changes in relation to the posture. Our result, according to the hypothesis of correlation between muscle motion and EMG activity [7], confirm the meaning of a proper positioning onto the vibrating plate during treatments.

Moreover, the transmissibility of vibratory stimulus along the body segment strongly depends on the position held by the subject.

Vibrations, as reported by Harazin and Grzesik [8], result damped from the vibrating plate to the knee, above 25 Hz, in position P1, while is already completely damped above 15 Hz with respect to position P2.

It is therefore reasonable to observe RF and BF resonant behavior below 25 Hz with respect to position P1. Similarly, a GL resonant behavior, with respect to position P2, is observable in the range 30-60 Hz, where the transmissibility of vibrations to the ankle is not reduced.

Results also suggest that BF and RF muscles can receive the maximal stimulus (over the frequency range explored) in position P1 while the for GL muscle may be preferable position P2. Only for this posture/muscle combination the vibratory stimulus is not damped and a resonant-like behavior was clearly visible.

The high correlation coefficient between the experimental frequency response and second order transfer function confirm the validity of the assumption.

Contra-lateral analysis suggested non-significant differences between dominant and non-dominant lower limb.

However, muscles motion in two lower limbs resulted to be synchronous and symmetric with respect to the sagittal-plane (see YZ plane).

ACKNOWLEDGMENT

Author are grateful to TSEM S.p.A. for providing vibrating platform device. Authors are also particularly grateful to F. Di Tora and A. Colonna for their precious collaboration.

REFERENCES

1. Bosco C, Colli R, Introi E. (1999a) Adaptive responses of human skeletal muscle to vibration exposure. *Clin Physiol* 19(2):183-7
2. Bosco C, Iacovelli M, Tsarpela O, Cardinale M, Bonifazi M, Tihanyi J, et al.. (2000) Hormonal responses to whole-body vibration in men. *Eur J Appl Physiol* 81(6):449-54
3. Verschueren S, Roelants M, Delecluse C, Swinnen S, Vanderschueren D, Boonen S. (2004) Effect of 6-month whole body vibration training on hip density, muscle strength, and postural control in postmenopausal women: a randomized controlled pilot study. *J Bone Mineral Res* 19(3):352-9
4. Cardinale M, Wakeling J. (2005) Whole body vibration exercise: are vibrations good for you?. *Br J Sports Med* 39:585-9
5. Mester J, Kleinoder H, Yue Z. (2006) Vibration training: benefits and risks. *J Biomech* 39:1056-65
6. Cardinale M, Lim J. (2003) Electromyography activity of vastus lateralis muscle during whole-body vibrations of different frequencies. *J Strength Condition Res* 17(3):621-4
7. A.Fratini, P. Bifulco, M. Cesarelli, G. Pasquariello, M. Romano, A. La Gatta (2008) Correspondence between Muscle Motion and EMG Activity during Whole Body Vibration IFMBE Proc. vol.22 4th European Conference of the International Federation for Medical and Biological Engineering, Antwerp, Belgium, 2008, pp 2069-2072
8. Harazin B, Grzesik J. (1998) The transmission of vertical whole body vibration to the body segment of standing subjects. *Journal of Sound and Vibration* 215(4):775-787

Author: Antonio Fratini

Institute: Dept. of Biomedical, Electronic and Telecommunication Engineering, University 'Federico II' of Naples

Street: Via Claudio, 21

City: Naples

Country: Italy

Email: a.fratini@unina.it

Motion Capture of Patients with Neurological Disorders by HD Digital Cameras

R. Krupicka¹, P. Janda¹ and Z. Szabo¹

¹ Department of Biomedical Informatics, Faculty of Biomedical Engineering, Czech Technical University, Kladno, Czech Republic

Abstract— Neurological diseases are often exhibited by movement or attitude disorders. These disorders could be recorded and processed by computer. A two or more cameras contactless system is used for capturing 3-dimensional motion of the patients. A high definition (HD) digital camera system was developed for the analysis of the movement of patients with Parkinson's disease and the head posture measurement of patients with neurological disorders. Properties and accuracy of the HD camera system were compared with professional motion capture system LUKOTRONIC. The comparison was based on the deviation of the captured corresponding points.

Keywords— Parkinson's disease, head posture measurement, motion capturing, HD cameras, contactless measurement

I. INTRODUCTION

Different neurological diseases have different movement symptoms, e.g., jerky movements of patients with Parkinson's disease [1] or abnormal head position of patients with cervical dystonia, etc. These disorders could be recorded by cameras and the video is processed by a computer.

It is advantageous to use contactless system for acquisition of the movement. A system with two or more cameras is used for this purpose. It could acquire movement in 3-dimensional coordinating system. The problem of acquiring and processing of the 3D motion is solved at Department of Biomedical Informatics, Faculty of Biomedical Engineering, Czech Technical University in Prague. The research is focused on patients with Parkinson's disease and on processing their arm movement. Parkinson's disease is a degenerative disorder of the central nervous system that often impairs the sufferer's motor skills and causes specific disturbances of hand motor function. The next research region explores the possibilities of accurate measurement of the head position [2]. The main effort in the following research region – craniocorpography – is to create a system which limits the border of patients' movement and marks this border within the image recording. The article is focused on description of the HD camera system, which was developed

for the analysis of the movement of patients with Parkinson's disease and the head posture of patients with neurological disorders. Properties and accuracy of the HD camera system are compared with professional motion capture system LUKOTRONIC. The comparison is based on the deviation of the captured corresponding points.

II. CAMERA CAPTURING SYSTEM

The research is focused on studying the movement of patients. The capturing of the movement in 3-dimensional space requires at least two video cameras. Two video cameras in different positions provide enough data to extract all information needed. We use two independent HD CANON HG10 cameras. The frequency in which the camera gets images in 1080i format [3] is 25 fps. The frame resolution is 1440×1080 , but this image is interlaced and combines two images with a different acquisition time. For capturing the movement, it is advantageous to get two images from the video frame [4]. The images are not interlaced and we get the video in smaller resolution (1440×540) and in double frequency (50 fps).



Fig. 1: Calibration images from two different cameras containing the chessboard.

The cameras are started and synchronized by a remote controller. They are calibrated by checkerboard using closed-form estimation based on planar homographic [5]. We used Camera Calibration Toolbox for Matlab [6] (see Fig.1). The calibrated camera system is one of the conditions for calculating world coordinates of the corresponding points from both cameras and next processing.

III. APPLICATIONS CAMERA CAPTURING SYSTEM

A. Hand motion measurement

We measured the 3D hand motion trajectory of the patients with the Parkinson's disease, when they performed a natural manual transport task (moving an object from one place to another). This task is performed repeatedly by patients with Parkinson disease.

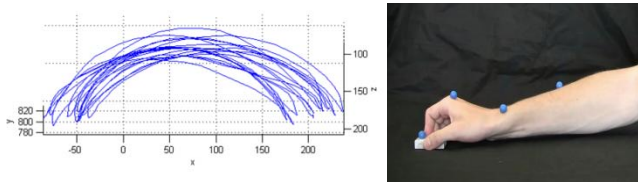


Fig.2: The motion of one marker (left) and markers position on the hand (right).

We capture a position of blue markers by the cameras. The markers are placed on anatomical landmarks of the tracked hand. The movement of the markers in 3D space is captured and saved to the database. The motion could be reconstructed and the simulation could be slowed down and it is possible to see the movement from an arbitrary angle. The trajectory of the movement is processed and features of the motion are evaluated.

B. Head posture measurement

Another application that uses video cameras is head posture measurement. The method is an enhancement of a method developed by Hozman, J. et al, 2004 [2] based on the application of two digital cameras with stands and appropriate image processing software. The main difference is in the use of digital video cameras. Instead of using only few images, the whole video sequences are captured and processed. On the one hand, this leads to greater complexity of the process, but on the other hand, it enhances the applications of the method. Besides measurement of the head position, the record of the head movement can be stored and further analyzed.

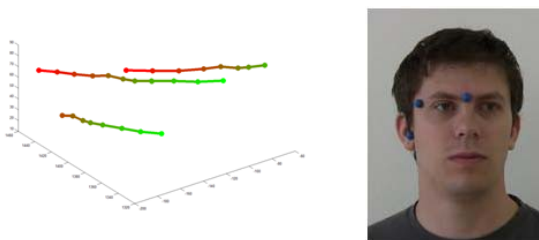


Fig.3: The motion of the markers and their positioning on the head.

This method can use two or more digital video cameras in various positions. Once the system is calibrated, it is prepared to obtain video sequences of the subject. As a result of synchronization, it is possible to determine the corresponding frames correctly. All further processing is performed on the time corresponding frames. Three markers are used to determine the head posture in this method. The 3D coordinates of all three markers provides enough information to calculate the head orientation.

The further development is focused on improvement of the method – markers are not considered to be used. The new method is proposed as a contactless and marker-less – ideal for non-invasive examination. The markers must be detected automatically – significant points on the head (for example, the eyes, the mouth, the nose) or other face features. The computation is very similar and the method should be capable of measuring the exact head posture.

IV. RESOLUTION TEST OF HD CAMERA SYSTEM

We created the HD camera system for capturing of movement. The resolution is 1 mm at distance 1.5 meters. The system was tested by comparison with professional commercial system LUKOTRONIC.

A. LUKOTRONIC

LUKOTRONIC MCU 200 camera capturing system was used for motion capturing. Each camera unit consists of 3 single infrared cameras, that are measuring special movements of active infrared markers in real-time. By means of the three single cameras the motions of the markers are determined in three dimensions. Resolution of the system is 0.1 mm at a distance of 1.5 meter.

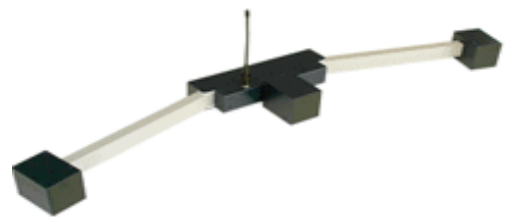


Fig.4: LUKOTRONIC system

B. Comparison of HD camera system with LUKOTRONIC

The comparison of the camera systems is based on the differences between corresponding points. We get 3D coordinates of the points from both systems. The coordinates could be transformed by an affine transformation:

VI. CONCLUSIONS

We created the HD camera motion capture system for the analysis of the movement of patients with Parkinson's disease and the head posture of patients with neurological disorders. We verified its accuracy with professional system LUKOTRONIC. The accuracy of the system is about 1% of the width of the camera covered area. The accuracy of the measurement could be improved by adding more HD cameras to the scene. The HD camera system is sufficiently accurate for analysis mentioned of the neurological diseases mentioned earlier.

The system of acquiring and processing of the 3D motion is still under development at the Department of Biomedical Informatics, Czech Technical University in Prague.

ACKNOWLEDGMENT

Research described in the paper is supervised by doc. RNDr. Ing. M. Jirina, Ph.D., Department of Biomedical Engineering, CTU in Prague and supported by the grant of Ministry of Education, Youth and Sports, Czech Republic, no. MSM6840770012

REFERENCES

1. Stewart A. Factor, William J. Weiner, Parkinson Disease diagnosis, Demos Medical Publishing, LLC 685 pages, 2002, ISBN 1888799501
2. Hozman J., Sturm D., Stoklasa J., Measurement of Head Position in Neurological Practice, In Biomedical Engineering [CD-ROM]. Acta Press, 2004, pp. 586-589.
3. 1080i at <http://en.wikipedia.org/wiki/1080i60>
4. Szabó, Z. - Krupička, R. - Rozinek, O. , Improved Marker Detection for Hand Movement Analysis in Parkinson's Disease In: Analysis of Biomedical Signals and Images; Biosignal 2008 proceedings [CD-ROM]. Brno: VUTIUM Press, 2008, ISBN 978-80-214-3613-8.
5. Milan Šonka, Václav Hlaváč, and Roger Boyle. Image Processing, Analysis and Machine Vision. Thompson Toronto Canada, third edition, 2007
6. Camera Calibration Toolbox for Matlab at http://www.vision.caltech.edu/bouguetj/calib_doc/, Mar 2008

Authors: Eng. Radim Krupicka, Eng. Pavel Janda, Eng. Zoltan Szabo, PhD.,
 Institute: Czech Technical University
 Department of Biomedical Informatics,
 Faculty of Biomedical Engineering,
 Street: nam. Sítna 3105
 City: 272 01 Kladno
 Country: Czech Republic
 Email: krupicka@fbmi.cvut.cz, janda@fbmi.cvut.cz,
szabo@fbmi.cvut.cz

Peripheral Arm Nerve Injury Rehabilitation by means of “Virtual Sensibility”

S. Amsüss¹, R. Schmidhammer¹ and H.Redl¹

¹ Ludwig Boltzmann Institute for Clinical and Experimental Traumatology, Vienna, Austria

Abstract— Peripheral nerve injuries occur with a statistical incidence of 422 new cases per year in Austria ([1], 2005). A new rehabilitation program is presented, which allows patients earlier, faster and better rehabilitation after arm nerve injury compared to current approaches. The “virtual sensibility” method takes advantages of the brain’s capability of creating sensory bypasses.

Keywords— Virtual sensibility, rehabilitation, nerve repair

I. INTRODUCTION

Peripheral nerve injuries are categorized into three main groups [2]:

- Neurapraxia: trauma causing transient nerve conduction inhibition with spontaneous recovery.
- Axonotmesis: trauma causing partial nerve dissection, recovering without surgery after several months.
- Neurotmesis: trauma causing complete transection of the nerve. Surgical repair and nerve grafting are mandatory.

In neurotmesis, the nerve part distal to the injury undergoes Wallerian degeneration, meaning that the distal nerve stump mortifies within the first 24 post traumatic hours [3]. Peripheral nerve fibers however are capable of re-growing into their former tube of Schwann cells at a speed of 1-2mm per day [4]. Thus it can be deducted that e.g. a nerve injury at wrist level leaves the fingers denervated for 100 – 200 days. During this time period no afferent signals from the concerned area reach the brain – provoking a structural remodeling process of the cortical mapping. The sensor neurons of the brain that used to represent the finger tips are seemingly not needed anymore for their original purpose and thus start taking over new functions [2]. This process is generally referred to as learning and can e.g. also be observed in blinded persons, whose visual cortex diminishes making space for a bigger representation of the index fingers.

This process of reorganization starts immediately after an injury and is hard to reverse. Once afferent signals reach the brain again after the peripheral nerve has recovered, the processing and interpretation of these “new” signals has to be relearned. This is a time consuming process and the outcome is always inferior to the original mapping [4].

The best preparation for rehabilitation is thus preventing the cortical maps from dwindling. Using “virtual sensibility” is one approach to realize this task.

Virtual sensibility utilizes the capability of the plasticity of the brain, generating sensory bypasses. A patient, who cannot “feel” touch and pressure with his fingers can still “see” and “hear” such events. Hence a device was developed that generates optical and acoustical signals at the site of no feeling when contact touch of sensors is performed. These acoustic and optical signals at the site of no feeling create a 3 dimensional impression to the brain (transmodal senses) which seems to be crucial in prevention of sensory cortical maps.

By seeing and hearing those signals, the patient gets feedback he can process and correlate with the touch on his fingers. Daily training prevents the brain from “forgetting the fingers”, saving the cortical mapping and facilitating better rehabilitation success [5].

II. METHODS AND MATERIALS

A device has been developed which supplies the characteristics described above. It is equipped with five highly touch sensitive finger sensors that can be positioned individually on different surfaces such as mouldable masses, making the setup adjustable for individual needs of the patients with e.g. splints, casts or wounds.



Fig. 1. Virtual Sensibility device testing

Each sensor has an LED mounted which is triggered by touching the sensor active area. Light touch is signaled by green light and, after surpassing an adjustable threshold, the light switches to red, signaling more pressure. Furthermore touching one of the sensors induces a sound, whose volume is in accordance to the pressure applied to the sensor. The sound characteristic is individual for all five sensors, providing individual sound for each finger. These audio-visual, space correlated signals are referenced as “3D audio-visual signals” [5].

The use of the device is kept fairly simple, permitting the use for a wide spectrum of patients. The training starts as soon as possible for the patient, preferably the first post operative day and is continued until first sensory stimuli of vibration can be perceived. Patients have to train 2-3 times daily with a regular duration of 10-15 minutes. The patient is asked to place the finger gently on the sensor, wait at least one second and then increase the pressure continuously. The time between the first finger contact with the sensor and surpassing the pressure threshold is being measured. If this time is greater than one second, this is interpreted as a well-controlled conduction of the exercise. In case the exercise is conducted too fast, this is interpreted as little controlled movement and therefore taken as unsuccessful execution. The goal for the patient is to have as many successful executions as possible.

An additional feature of the device is the automatic logging of the patients training habit and success. Every event is stored on an SD-card in Microsoft® Excel format. These data can be read out easily once the training is over, allowing easy statistical interpretation of the patients training such as frequency, duration and success of the training sessions.

III. RESULTS AND CONCLUSIONS

The device was used in a clinical trial conducted by the Austrian Cluster for Tissue Regeneration, Ludwig Boltzmann Institute for Clinical and Experimental Traumatology, Research Center of the AUVA, Vienna, Austria with eight adult patients [5]. The results (Fig. 2) revealed significantly better rehabilitation outcomes for patients who trained after the virtual sensibility method compared to a control group treated with classical rehabilitation programs.

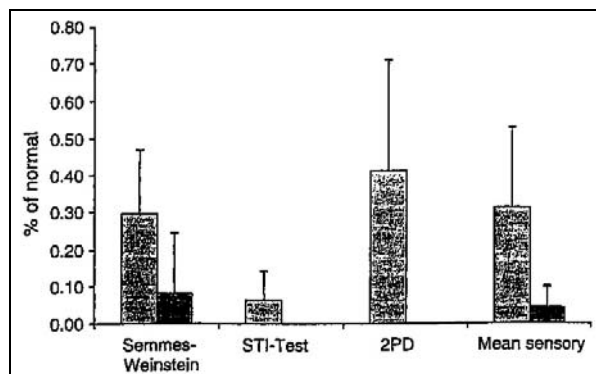


Fig. 2. The sensory enhanced re-learning group showed improved sensory results compared to the normal side in Semmes-Weinstein Monofilament test, STI test (Shape- Texture Identification), and 2-Point Discrimination (2PD). ■: Virtual, ■: Classic. (Schmidhammer, R. et al., 2007, pg. 129)

A similar approach was being followed by Lundborg et al. in a randomized multicentre study [6]. Small microphones were placed on a glove and connected to a mini-stereoprocessor. The recorded sounds were transferred to the patients' ears by headphones. This way, touch on every surface was made audible. The visual component was yet left behind.

The preliminary results strongly support the capability of the virtual sensibility method and further investigations with more subjects will be conducted.

REFERENCES

1. **European Hospital Morbidity Database** World Health Organization Regional Office for Europe. Available at the homepage of the WHO, visited on Feb. 27th 2009
2. Hummelsheim H (1998) Neurologische Rehabilitation. Springer-Verlag, Berlin Heidelberg,
3. Belkas J.S, Shoichet M.S, Midha R (2004) Peripheral nerve regeneration through guidance tubes. *Neurological Research*, 2004(26):151-160
4. Lundborg G, Rosén B (2007) Hand function after nerve repair. *Acta Physiol.* 189, 207-217.
5. Schmidhammer R, Hausner T, Kröpfl A, Huber W, Hopf R, Leixnering M (2007): Enhanced sensory re-learning after nerve repair using 3D audio-visual signals and kinaesthesia – preliminary results. *Acta Neurochirurgica Suppl.* (2007)100:127-129
6. Lundborg G, Rosén B, (2007): Enhanced sensory recovery after median nerve repair using cortical audio-tactile interaction: A randomized multicentre study. *Journal of Hand Surgery (European Volume)* 2007 32E(1):31-37

Author: Sebastian Amsüss, BSc
 Institute: Ludwig Boltzmann Institute for clinical and experimental Traumatology
 Street: Donaueschingenstraße 13
 City: Vienna
 Country: Austria
 Email: sebastian.amsuess@lbitrauma.org:

Realization of Constant Phase Element in Metallic Electrodes for Interference Reduction in Neural Recording Tripoles

I. Pachnis¹, A. Demosthenous¹, and N. Donaldson²

¹ Department of Electronic and Electrical Engineering, University College London, London, UK

² Department of Medical Physics and Bioengineering, University College London, London, UK

Abstract— Recording neural signals using implanted Pt-electrodes in a tripolar arrangement is affected by myoelectric interference present at the interface. In this paper we present a way of realizing the frequency response exhibited by a constant phase element (CPE) of metal electrodes and use this for the removal of interference. Simulation results show that our CPE is very close to the ideal case in the bandwidth we are interested in (i.e. 500 Hz to 10 kHz), while fitting past neutralization data reveals that removing interference now requires no adjustment.

Keywords— EMG, ENG, passive neutralization, CPE, metal electrodes.

I. INTRODUCTION

Metal electrodes are widely used in biological and medical research for stimulating excitable tissue and recording bioelectric events of interest. In this paper we are concerned with the later where non-faradaic (or ideal) polarizable electrodes are used in implanted neuroprosthetic devices for successfully acquiring neural signals (i.e. ENG) and using those towards rehabilitation [1]. Nonetheless, the neural signal needs to be free of interference (e.g. myoelectric or EMG), which we distinguish from electrical noise, since it is due to external sources and not an intrinsic artifact of our system. As it is most likely that our 3-electrode (i.e. tripolar) neural recording system will suffer from such interference, we must be able to compensate against it so the quality of the recorded ENG signal is not degraded.

In a series of previous publications we demonstrated *in-vitro* that it is possible to passively remove myoelectric interference in neural recording tripoles by using resistors and capacitors at the front-end, obtaining satisfactory results in conjunction with reduced power dissipation [2]. A way of making our technique adaptive, by modeling the electrode-electrolyte impedance profile of our recording electrodes then followed [3], albeit with moderate results. The reasons for this were outlined in [4] where we tried to justify the source of poor results in that the constant phase element (CPE) behavior of our electrodes was inadequately represented by a simplistic parallel RC circuit. Additionally, we concluded that the resulted 5-component circuit used to

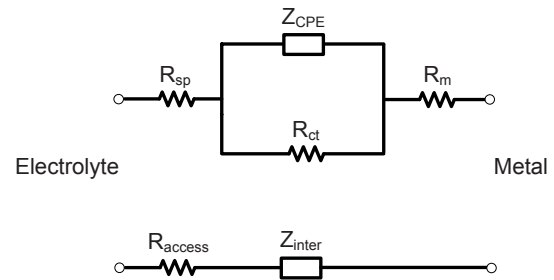


Fig. 1 Small-signal electrical circuit for describing the electrochemical interface impedance of electrodes. The polarisation or diffusion impedance is Z_{CPE} . An alternative representation of the model where $R_{access}=R_{sp}+R_m$ and $Z_{inter}=Z_{CPE}/R_{ct}$, is also shown.

compensate for interference was not easy to tune (i.e. adjust to remove interference) and therefore not practicable.

In this paper we aim to describe qualitatively how to emulate a CPE and, by using it as part of an electrode-electrolyte interface model, to accurately describe the frequency response of electrodes. We approach the problem by first introducing some basic modeling theory of metal electrodes and subsequently present a method of implementing a CPE both in simulation and in a PCB realization. We finally demonstrate that this modeling approach can potentially offer improved results in the way EMG interference is neutralized in tripoles and conclude the paper with an interesting discussion.

II. IMPEDANCE OF METALLIC ELECTRODES

In an attempt to accurately explain and characterize each different process taking place at the electrode-electrolyte interface, many models have been generated that simulate the observed electrode behavior. One such model is the 3-component circuit of Cole [5] shown in Fig. 1, here represented with the access resistance R_{access} broken down in two parts; R_{sp} which is the spreading (or bulk) resistance in the tissue near the electrode, and R_m the series resistance of the electrode conductor (i.e. connecting wires and metallic part – often taken to be of negligible value). The other two

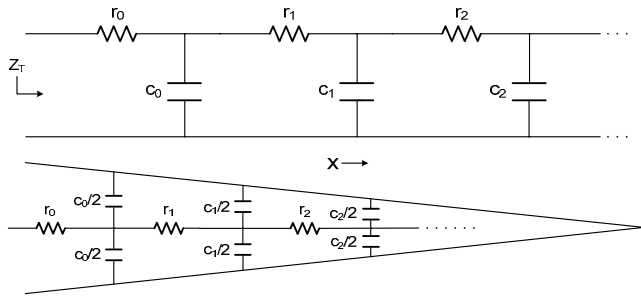


Fig. 2 A non-uniform/tapered RC ladder network used to model a one-dimensional V-shaped pore of infinite length where the specific resistivity of the electrolyte in the pore and the pore cross-section, and the double-layer capacitance at the interface increases and reduces respectively with the distance x down the pore.

components in the model which make the interface impedance Z_{inter} are the charge transfer resistance R_{ct} , and the polarization or diffusion impedance Z_{CPE} . In this paper we will adapt this model in our simulations which, despite its simple structure, it can be used to represent real data of electrodes sufficiently well.

The ideally polarizable (or blocking) small signal AC impedance of metal electrodes, like platinum, is proportional to $(j\omega)^{-a}$ at frequencies below 50 kHz [6] where the polarization impedance Z_{CPE} is dominant and therefore can be successfully described by the following empirical equation:

$$Z(\omega) = K(j\omega)^{-a} \tag{1}$$

where ω is the angular frequency, $j = \sqrt{-1}$, K is a measure of the magnitude of this pseudocapacitive impedance and independent of ω , and finally a takes values between 0 and 1 indicating the departure from pure capacitive behavior. Thinking in terms of the model in Fig. 1, since in polarizable electrodes R_{ct} is very high, it is obvious that Z_{inter} will have a fractional power frequency dependence (FPFD) on ω . Many fellow workers [6, 7] have attempted to explain the physical processes and the observed frequency dispersion exhibited by metal electrodes in solid or aqueous electrolytes and sought to relate the FPFD exponent a to the degree of porosity and roughness of the electrode surface (i.e. a approaches 1 as the electrode surface is made smoother). On the contrary, K depends on the electrode area and the electrolyte conductivity.

III. CONSTANT PHASE ELEMENT REALIZATION

A. Theory

An important part of the circuit model of Fig. 1 is the so-called CPE, named after the fact that metal electrodes exhibit a constant phase angle at low frequencies. There are in

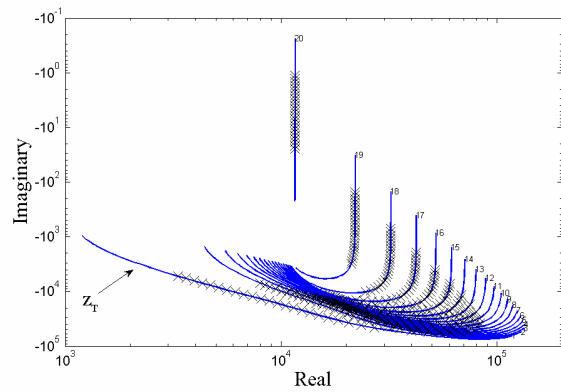


Fig. 3 Argand diagram showing impedance loci for 20 sequentially added stages of Schrama's RC ladder network (from last to first – top to bottom). The input impedance of the ladder Z_T is linear in the 500 Hz to 10 kHz bandwidth of interest (marked with x). A terminating resistive load of 1 k Ω was used.

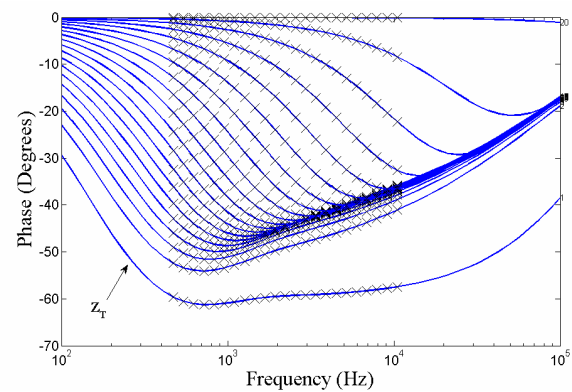


Fig. 4 Phase angle exhibited by Schrama's ladder network. At the input impedance Z_T the phase angle is approximately constant in the bandwidth of interest (marked with x), denoting a CPE with a FPFD exponent $a=0.666$.

general two approaches that someone could follow in emulating the CPE behavior of electrodes; constructing a circuit that will mimic either the frequency behavior, or the geometrical/topological structure of the electrode [8, 9]. For our purpose we have followed the former where we treated the electrode surface as a one-dimensional pore of infinite length and tried to approximate its exhibited CPE frequency response by a semi-infinite RC ladder in which the potential drop along the pore axis is being reproduced by the resistor chain of the ladder, and the equipotential surfaces (i.e. one-dimensional potential distribution) of the pore by the interfacial double-layer capacitance which is reduced as we move down the length x of the pore. A pictorial representation of a one-dimensional pore is shown in Fig. 2 together with its equivalent circuit model. Such circuit offers an input impedance Z_T whose ratio $\text{Im}(Z_T)/\text{Re}(Z_T)$ is independent of ω .

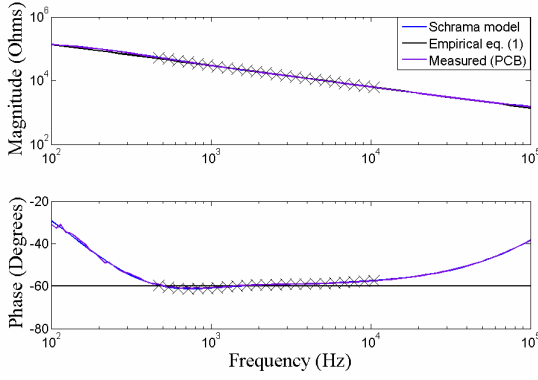


Fig. 5 Comparison of the magnitude and phase of Schrama's input impedance Z_T against Z_{CPE} empirical equation (500 Hz to 10 kHz bandwidth of interest marked with x). Superimposed on the given data are real impedance measurements from a PCB realization of Schrama's ladder network. The same scaling factor $S=10^7$ and FPDF exponent $a=0.666$ were used.

In 1957 Schrama proposed a semi-infinite RC ladder network which had the following generalized impedance based on continued fractions for describing linear relaxation processes [10]:

$$Z_T = \left(h + \frac{1}{z} \right)^a = r_0 + \frac{1}{c_0 j \omega + \frac{1}{r_1 + \frac{1}{c_1 j \omega + \frac{1}{r_2 + \frac{1}{c_2 j \omega + \dots}}}}} \quad (2)$$

$$r_k = 2h^a \frac{\Gamma(1-a)\Gamma(k+a)}{\Gamma(a)\Gamma(k+1-a)} - h^a \delta_{k0} \quad \text{where} \quad \delta_{ij} = \begin{cases} 1, & \text{if } i=j \\ 0, & \text{if } i \neq j \end{cases} \quad (3)$$

$$c_k = h^{1-a} (2k+1) \frac{\Gamma(a)\Gamma(k+1-a)}{\Gamma(1-a)\Gamma(k+1+a)}$$

where k is a stage in the ladder network, a is the same as the FPDF exponent of (1), h is an arbitrary small number, Γ denotes the gamma-function, and δ is the Kronecker delta. Schrama derived (3) such that the resulted impedance Z_T of the RC ladder network is given by $(j\omega)^{-a}$ while we have found that the magnitude K of (1) is also equal to the scaling factor S discussed below. Moreover, by simulating the LHS of (2) for different values of h we also found that in order to obtain a linear impedance locus Z_T , and thus a good CPE behavior at the bandwidth we are interested in (i.e. 500 Hz to 10 kHz), we should set $h=10^{-6}$.

B. Simulation

We subsequently simulated (2) in MatlabTM for $a=0.666$ (i.e. $\varphi_{CPE}=a*\pi/2 \approx 60^\circ$) and $k=20$. Fig. 3 shows the impedance loci from the last stage of the ladder network up to the first (i.e. locus pointed by the arrow), demonstrating the

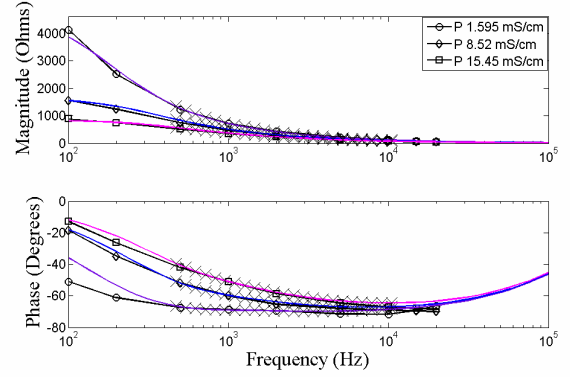


Fig. 6 Fitting past trimming data in [2] using an interface impedance Z_{inter} constructed with a 20-stages of Schrama's ladder network. Both the magnitude and phase are fitted significantly well, particularly in the bandwidth of interest (marked with x). The same electrode tripole was used in all measurements.

Table 1 Values of the interface impedance Z_{inter} , arranged for trimming.

NaCl σ (mS/cm)	1.595	8.52	15.45
S (Ω/s^{-a})	0.8 M	0.61 M	0.45 M
a	0.8	0.8	0.79
R_{ct} (Ω)	12 k	2.2 k	1 k

change in impedance as each stage is sequentially added to the ladder. Fig. 4 is plotted in the same manner but this time for the phase angle. In the former graph the impedance locus of the input stage is linear at mid-frequencies and this is depicted in the later graph as a constant phase angle at the same frequency band. For reasons of simplicity we only show results for a single FPDF exponent value, it is possible nonetheless to acquire a CPE angle for any value in the $0 < a < 1$ range.

Although the chosen number of stages was sufficient to give us a relatively flat phase response at the lower frequency end, the resulted m Ω and mF values of (3) for the r and c components of the ladder network were not practicable. According to Schrama, we can multiply all the resistors and divide all the capacitors in the network by a particular factor; in effect scaling the r and c components (and thus the magnitude of Z_T) but still retaining the same phase angle frequency response. Therefore we multiplied the RHS of (2) by a factor of $S=10^7$ resulting in scaling r up to k Ω (1.01 min, 10.58 max) and c down to pF (375 min, 1488 max), making a potential IC implementation of the design possible.

C. Hardware

The validity of the simulated 20-stages scaled RC ladder network was investigated against actual measured data obtained from a PCB implementation and results are shown in Fig. 5. It is obvious that the measured PCB data match the simulated ones significantly well. Also included in Fig. 5 for

reasons of comparison is the simulated magnitude and phase of (1) for the same frequency span, FPDF exponent, and magnitude K – scaling factor S . It is also apparent that the PCB implementation of Schrama's ladder network is a very good approximation to the (ideal) empirical CPE equation of (1), in the bandwidth of interest.

IV. CPE AND PASSIVE EMG NEUTRALIZATION

Having successfully implemented a CPE we can now arrange it for passively neutralizing EMG interference at the tripole, however, a number of questions rightfully need answering. In particular, how the constructed CPE can be arranged for the purpose of trimming (i.e. reducing) the EMG, and whether the new approach can offer improved performance. We will use Fig. 6 towards aiding our discussion. The figure shows 3 different sets of impedance magnitude and phase angle curves at spot frequencies (denoted by the markers) obtained in [2] for 3 NaCl concentrations, representing a different conductivity on the implantation site upon the degree of tissue growth at the interface. A circuit of equivalent arrangement to Z_{inter} of Fig. 1 was constructed using 20-stages of Schrama's ladder network in an attempt to perform a fit on the past data. As shown in Fig. 6 the fitting is very satisfactory.

The values used for constructing the fitting impedance Z_{inter} are shown in Table 1. The value of the FPDF exponent is the same for all 3 NaCl concentrations, while the fitting values of the scaling factor and the charge transfer resistance did vary significantly. This is something we anticipated since the same electrode tripole was used throughout the experiments in [2], whereas we know that the FPDF exponent is sensitive to the texture of the interface. Concluding, we should emphasize that the proposed trimming impedance technique is now a 3 “degrees of freedom” problem (i.e. 3 components to tune) in comparison to 2 of the previous simplistic parallel RC impedance Z_{trim} used in [2]. The outcome of this is increased performance with only 1 component penalty (i.e. that of the FPDF exponent), which once it is known for a particular electrode tripole, the problem reduces down to 2 again.

V. DISCUSSION

In this paper we have successfully constructed a CPE using Schrama's model. Hence, essentially mimicking the frequency response but not the geometrical/topological structure of an electrode surface. Although this model does not account for the random distribution of pores in a true porous solid, or for a complicated surface topology, it is simple in structure. As such this choice was also based on practical reasons, since a different model-based Z_T would

not be realizable both in terms of application (i.e. easiness of tuning, compensating for changes at the neural interface), as also implementing the idea on silicon. For the later, noise versus the ability to integrate is a tradeoff, since, as we increase the scaling factor S resistance of r increases (and thus the thermal noise), but at the same time capacitance of c reduces. The ladder network that gave Fig. 3 exhibits a calculated RMS voltage noise of 1.02 μV in the 500 Hz to 10 kHz bandwidth of interest. This value is close to the absolute maximum amplitude of ENG which might be of a limiting factor towards using this technique in a fully implantable *in-vivo* preparation.

Schrama's ladder network was realized in a PCB where measurements in Fig. 5 show that it is in a very good agreement with our simulations. Mismatches on the PCB component values, which are certainly present in this discrete implementation, do not seem to have an effect on the frequency response of the PCB. Additionally, component tolerance was investigated in simulation were a variation of up to 10% in various ways (i.e. component value increasing/decreasing at different stages) revealed no significant change in the desired frequency response of the ladder network.

Another matter needs further discussion in Fig. 5. The low-frequency phase angle response of Schrama's network could be further improved (i.e. flattened) by adding more stages to the ladder, nonetheless, this is not the case for the high-frequency end; the double-layer capacitance is shorted resulting in the phase angle tending towards zero. This is however acceptable since this kind of frequency response has been observed with real Pt-electrodes.

Fig. 6 is a very important figure in that it allows us to understand two things; the trimming with the new proposed network is possible and, most importantly, that now tuning is not required. Moreover, arranging for trimming does not require an access resistance R_{access} placed in series with Z_{inter} since the phase angle of the trimming impedance loci in Fig. 6 do not tend towards zero at high frequencies.

In practice, the proposed neutralization technique needs to be used in conjunction with either a negative impedance converter (NIC), or with an audio transformer having a large selection of turns ratios (i.e. for on-bench *in-vitro* ENG recording). The reason for this being that we need to reduce the magnitude of our Z_T down to a value that would be appropriate for trimming. The idea of NIC has been explored in Cadence™ circuit simulator with satisfactory results, while we expect the alternative option of the transformer to offer better signal-to-noise ratio due to its intrinsic ability to reduce noise by the number of the turns ratio.

VI. CONCLUSION

We have presented a new approach where removing the EMG interference in neural recording tripoles is done

passively by appropriately modeling the trimming impedance of our recording electrodes. The improvement lies in the physical interpretation of the trimming impedance by replacing the double-layer capacitance of the parallel RC in [2] with a CPE realized using Schrama's ladder network. As the trimming impedance now adapts to the electrodes' frequency response, no tuning is necessary. Simulation results have demonstrated that this is possible. Experiments using the proposed technique are scheduled to be performed and results will be reported in a future publication.

REFERENCES

1. Donaldson N, Perkins T, Pachnis I, Vanhoest A, Demosthenous A (2008) Design of an implant for preventing incontinence after spinal cord injury, *Artif Organs* vol. 32, no. 8, pp 586-591
2. Pachnis I, Demosthenous A, Donaldson N (2007) Passive neutralization of myoelectric interference from neural recording tripoles, *IEEE Trans Biomed Eng* vol. 54, no. 6, pp 1067-1074
3. Pachnis I, Demosthenous A, Rahal M (2008) Adaptive EMG neutralization using the modified QT, *IEEE Proc ISCAS*, pp 2941-2944
4. Pachnis I, Demosthenous A, Donaldson N (2009) Interference reduction techniques in neural recording tripoles: an overview, in press
5. McAdams E, Jossinet J (1995) Tissue impedance: a historical overview, *Physiol Meas* vol. 16, pp A1-A12
6. Bates J, Chu Y, Stribling W (1988) Surface topography and impedance of metal-electrolyte interfaces, *Phys Rev Lett* vol. 60, no. 7, pp 627-630
7. McAdams E, Lackermeier A, McLaughlin A, Macken D (1995) The linear and non-linear electrical properties of the electrode-electrolyte interface, *Biosens Bioelec* vol. 10, pp 67-74
8. Liu S (1985) Fractal model for the ac response of a rough interface, *Phys Rev Lett* vol. 55, no. 5, pp 529-532
9. Nyikos L, Pajkossy T (1985) Fractal dimension and fractional power frequency-dependent impedance of blocking electrodes, *Electrochim Acta* vol.30, no. 11, pp 1533-1540
10. Schrama J (1957) On the phenomenological theory of linear relaxation processes, PhD thesis, University of Leiden, Netherlands

Author: Ioannis Pachnis
 Institute: Electronic & Electrical Eng., University College London
 Street: Torrington Place, WC1E 7JE
 City: London
 Country: UK
 Email: i.pachnis@ee.ucl.ac.uk

Comparison of sensor systems for gait phase detection in hemiplegic gait

S.W. Park¹, R. H. Sohn¹, S.H. Hwang¹ and Y.H. Kim²

¹ Department of Biomedical Engineering, Yonsei University,
234 Maeji-ri, Heungup-myun, Wonju-si, Gangwon-do 220-710, South Korea

² Department of Biomedical Engineering, Institute of Medical Engineering, Yonsei University,
234 Maeji-ri, Heungup-myun, Wonju-si, Gangwon-do 220-710, South Korea

Abstract— Gait phase detection is important for evaluating the recovering of gait ability in patients with paralysis as well as for determination of stimulation in FES walking. Forceplate in three dimensional system can give the most objective and accurate information about gait phase detection, however it is very expensive and limited in restricted area of laboratory. In this study, three different motion sensors (accelerometer, gyrosensor and tilt sensor) were used for detection of gait events (heel strike, HS; toe off, TO) and they were compared with each other to find out the most applicable sensor for gait phase detection. Four hemiplegic patients (group A : cadence 40 steps/min, group B : cadence 70 steps/min) were volunteered for this study and motion sensors were attached on the shank and heel of subjects. Gait phase detection accuracy of each sensor was assessed using the result of FVA (Foot Velocity Algorithm). Gait phase detection using motion sensors were valid because they all have the reliability more than 95% compared with FVA (objective standard). HS and TO were determined by using FVA and processed motion sensor signal and detection accuracy of motion sensors were assessed by calculation of time interval of HS and TO between FVA and motion sensors. Vertical acceleration from accelerometer could detect the HS most accurately in hemiplegic patients group A. Gyrosensor could detect the HS and TO most accurately in both hemiplegic patients group A and B.

In this study, we could find the most applicable motion sensors to detect the gait phases in patient with hemiplegia. It is respected that this objective and quantitative method could help to decide the motion sensor for gait phase detection in hemiplegic patients.

Keywords— Tilt sensor, Gyrosensor, Accelerometer, Gait phase detection, hemiplegic gait.

I. INTRODUCTION

The gait phase detection acts as an important index for assessing the recovery of the function of the motion by way of providing the space-time gait factor before and after the rehabilitation therapy of the disabled [1] and as the detection is an important standard to determine the accurate operation time of the walking assistive system to prevent the drag foot of the brain damaged patient's walking, various studies have been performed to detect the gait phase. Although the three dimensional motion analysis system

which is the most widely used one can provide accurate gait phase detection and diversified gait analysis, it is very expensive and limited inside the laboratory and also limited to measuring the gait phase within the valid range of the cameras. When the force plates are applied, they are not only expensive but also limited to measuring the gait phase depending on the number of the sensors and they are difficult to be applied to the hemiplegic patients whose step length is shorter than the normal persons because they should put one step only in one force plate. Accordingly other methods for the gait phase detection using various motion sensors have been studied in the direction of having equivalent function like the current expensive and complicated measuring system as well as low cost and convenient in portable and operation. Evans et al. [2] used the acceleration sensor to detect the heel strike and Ju Hyeon Lee et al. [3] analyzed stroke patients' gait cycles using accelerometers. Tong and Grant [4] succeeded in detecting the angular speed of shank and thigh using two gyrosensors, and gait cycles by measuring the gradient to the gyrosensor's shaft. Seung Chan An et al. [5] developed a gait cycle detecting system which uses FSR sensors and gyrosensor. Dai et al. [6] attached tilt sensors on shank and thigh, and analyzed gait cycles by measuring the angle of each volume and Weber et al. [7] did it using the tilt sensor attached to the shank of the hemiplegic patient. Assessment method is required to verify the accuracy and validity of the gait phase detected by the motion sensors.

In this study, we detected the gait phase of the hemiplegic patient using the characteristics of curves of various sensors and examined the validity of using the sensor making use of the time difference of the standard gait phase.

II. METHODS

A. Procedure

This study selected two hemiplegic patients whose cadence is 40 steps/min (group A) and 70 steps/min (group B), respectively. Three motion sensors (tilt sensor, gyrosensor and accelerometer) were applied and the tilt sensor was at

10 Cm below the knee joint marker, the gyrosensor was on the heel marker and the accelerometer was below the tilt sensor. The digital low-pass filter (butterworth, 2nd order) was used as a sensor signal and the greatest power frequency was used for the cutoff when it was analyzed in order for the users could acceptability for the filter.

B. Foot velocity algorithm(FVA)

In this study, we analyzed the accuracy of the gait phase detected by sensors using the time interval between the standard gait phase detected by FVA [8] and the sensor detection. The FVA is to detect the gait phase using the displacement-time data for heel and second metatarsal head markers obtained by the three dimensional motion analysis system. The center of the heel and the second metatarsal head markers were assumed to be the foot center and the vertical velocity was estimated by deriving the vertical displacement of the foot center. The validity of sensor detection methods were examined by Bland Altman plot statistics which can verify the two measuring systems.

III. RESULTS

A. Tilt sensor

Fig. 1 shows the gait phase curve of two gait cycles detected by the tilt sensor in hemiplegic walking. As the group A and B show the characteristics of spinal gait, their foot is on the far front at the time of the heel strike (HS) and it is on the far end just before the toe off (TO). Accordingly the HS was detected using the negative peak of both A and B while TO was done using the positive peak.

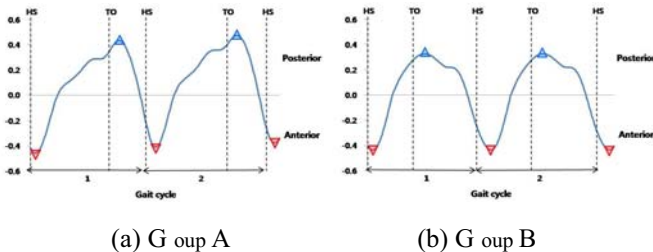


Fig. 1 Gait phase detected by the tilt sensor and sensor output curve

B. Gyrosensor

Fig. 2 shows the gait phase curve of two gait cycles detected by the gyrosensor in hemiplegic walking. Figure 2 show the gait phase curve of two cycles detected by the gyrosensor in hemiplegic walking. The inertia occurs when

the foot turns lateral and throws at the time of heel strike and the heel makes clockwise rotation toward the medial of a body due to the functional loss of the ankle sinews and the heel makes counte clockwise rotation and falls first as the foot lifts making use of the pelvis at the time of toe off. And broad negative winding is generated as the heel turns lateral using the opposite foot and the pelvis to maintain the balance after the heel strike. In case of group A HS was detected by the positive peak generated just before the winding while the TO was detected by the negative peak generated just afterwards. As the negative curve is created among group B even though it is small, HS was detected from the positive peak before the winding on the other hand TO was from the negative peak just after the winding.

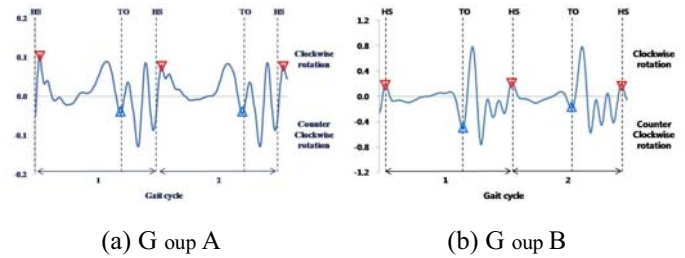


Fig. 2 Gait phase detected by the gyrosensor and sensor output curve

C. Accelerometer

Fig. 3 shows show the gait phase curve of two cycles detected by the accelerometer in hemiplegic walking. The anterior acceleration is reduced rapidly at the time of heel strike both in the anterior-posterior acceleration but the anterior acceleration is increased rapidly at the time of lifting foot of toe off and therefore HS was detected using the positive peak and TO was done by the greatest negative peak generated just before the positive peak. In case of medial-lateral acceleration, at the time of toe off the shank moves lateral and it moves medial rapidly at the heel strike and accordingly HS was detected by the positive peak created just after the largest negative peak and TO was detected by the second negative peak created after the great positive peak. In case of the superior-inferior acceleration as the legs balancing the body keeps vertically like the normal persons without the joint's winding, the acceleration does not change and in the course of lifting the pelvis using reaction at the toe off, the acceleration is reduced to the inferior direction but is increased rapidly to the superior direction. Therefore HS was detected using the negative peak generated just before focusing on the flat area around the reference voltage but the TO was done using the negative peak generated just afterwards.

Table 1 Validity analysis and the time interval between the gait phases detected by each sensor and FVA

	Sensors	Time interval (ms)		Validity (%) (* > 95%)		
		HS	TO	HS	TO	
Group A	Tilt sensor	210.3±12.5	120.9±31.5	100.0*	98.8*	
	Gyrosensor	101.7±55.6	-15.8±79.2	98.0*	98.6*	
	Accelerometer	Anterior-Posterior	136.1±11.0	103.6±95.8	98.8*	100.0*
		Medial-Lateral	243.9±5.3	87.0±103.1	97.6*	100.0*
		Superior-Inferior	-22.2±8.8	-140.0±40.8	100.0*	96.7*
Group B	Tilt sensor	155.6±45.5	114.4±28.6	98.8*	97.6*	
	Gyrosensor	-9.4±20.6	-18.1±20.7	100.0*	100.0*	
	Accelerometer	Anterior-Posterior	122.5±48.0	-53.3±96.4	96.8*	98.2*
		Medial-Lateral	214.7±32.6	133.3±106.1	96.9*	99.1*
		Superior-Inferior	69.4±17.4	-80.0±25.2	96.8*	100.0*

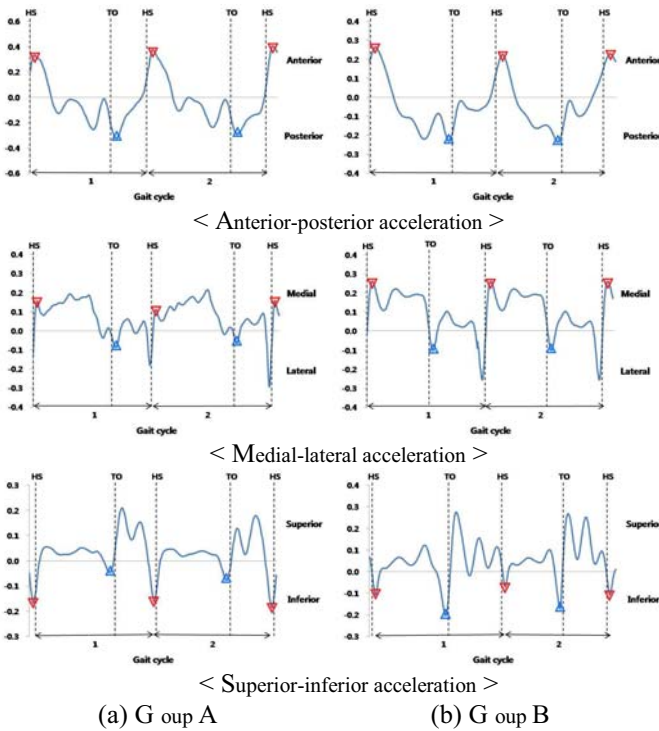


Fig. 3 Gait phase detected by the accelerometer and sensor output curve

D. Validity analysis

Table 1 suggests the result of the validity analysis using Bland Altman plot and the time interval between the gait phases detected by each sensor and the standard gait phase.

As the difference between the two methods is in the range of 95% of valid limit of each sensor, it is judged to be valid.

IV. CONCLUSION

In this study, we detected the gait phase using the characteristic peak of the output curve when the hemiplegic walking of the motion sensors and the time interval from the standard gait phase was derived. In case of hemiplegic walking, the smallest tolerance of HS was detected at the superior-inferior acceleration among group A, while the same of TO was detected at the gyrosensor. As the verification of the validity using the time interval from the standard gait phase is in the range of valid limit of 95% among all the sensors detection method, the verification is judged to be valid. The gait phase detection by motion sensors can possibly replace the three dimensional motion analysis system. As the limited cadences and gait types among diversified gaits of the hemiplegic patients, furthermore, when additional experiments for more various speed and patterns of the gait are investigated, they can be applied to the walking assistive system as well as the gait analysis.

ACKNOWLEDGMENT

This research was financially supported by the Ministry of Education, Science Technology (MEST) and Korea Industrial Technology Foundation (KOTEF) through the Human Resource Training Project for Regional Innovation and also was supported by the Sports Promotion Fund of Seoul Olympic Sports Promotion Foundation from Ministry of Culture, Sports and Tourism.

REFERENCES

1. Sekine M, Abe Y, Sekimoto M, Higashi Y, Fujimoto T, Tamura T, Fukui Y (2000) Assessment of gait parameter in hemiplegic patients by accelerometry. *Engineering in Medicine and Biology Society* 3:1879–1882
2. Evans AL, Duncan G, Gilchrist W (2004) Recording accelerations in body movements. *Med. Biol. Eng. Comput.* 29:102–104
3. Lee JH, Park SW, Kim DA, Jang SJ, Kim YH, Lee JB (2004) Gait analysis using accelerometer in stroke patients. *J. KARM* 28:488–493
4. Tong K, Granat MH (1999) A practical gait analysis system using gyroscopes. *Medical Engineering & Physics* 21:87–94
5. Ahn SC, Hwang SJ, Kang SJ, Kim YH (2004) Development and Evaluation of a New Gait Phase Detection System using FSR Sensors and a Gyro sensor. *J. KSPE* 21:196–203
6. Dai R, Stein RB, Andrews BJ, James KB, Wieler M (1996) Application of tilt sensors in functional electrical stimulation. *Rehabilitation Engineering, IEEE Transactions on* 4:63–72
7. Weber DJ, Stein RB, Chan KM, Loeb G, Richmond F, Rolf R, James K, Chong SL (2005) BIONic WalkAide for Correcting Foot Drop. *Neural Systems and Rehabilitation Engineering, IEEE Transactions on* 13:242–246
8. O'Conner CM, Thope SK, O'Malley MJ, Vaughan CL (2007) Automatic detection of gait events using kinematic data. *Gait & Posture* 25:469–474

Use macro [author address] to enter the address of the corresponding author:

Author: Y.H. Kim
Institute: Institute of Medical Engineering, Yonsei University
Street: 234 Maeji-ro, Heungup-myun
City: Wonju-si, Gangwon-do
Country: South Korea
Email: younghokim@yonsei.ac.kr

8-Channel Electrotactile Stimulation System for Auditory Information Substitution

R.V. Cendon and P. Nohama

Universidade Tecnológica Federal do Paraná / CPGEI, Curitiba, Brazil

Abstract— This paper presents an eight-channel pc-based PAM sensory substitution system with the purpose of investigating information recognition through electrotactile stimulation of patterns based on audio records of spelled words. The system generates the stimulatory patterns and the current intensity on each electrode depends on frequency analysis of audio files. It yields rectangular waveforms bursts, and allows programming its main parameters: pulse width and frequency, biphasic or monophasic type stimuli and maximum current. Voice spectra are grouped on specific ranges and define the stimulatory magnitude on the related electrode. The software that controls the testing protocol procedure has three distinct functions: pattern generation, training and test mode. In the first one the prepared audio files are converted on stimulating intensity for the electrodes array. In training mode, it shows the recorded words in text mode and when a word is clicked the correspondent stimulating pattern is sent to electrodes. Finally, in test mode, the software controls stimulating patterns randomly and presents options to the user selection. The answers are recorded to extract statistical data of the trial.

Keywords— sensory substitution, electrotactile stimulation, voice information, rehabilitation engineering, deaf rehabilitation.

I. INTRODUCTION

Usually deaf communication is made through visual techniques, like lip reading, corporal movements and reference symbols while techniques like Braille and Tadoma are used for deaf-blind subjects [1][2].

As an alternative communication technique was emerged the electrical sensory stimulation that looks for an alternative way to acquire information for people who have deficit or are deprived of their natural channels of communication, as consequence of specific lesion. So the desired information needs to be acquired, processed and displayed to the individual through another sensory channel. This process is known as sensory substitution, where there is the use of healthy ways of transporting information to the central nervous system.

Even with the great development of electrotactile stimulation research, the technique of converting the speech patterns in stimulatory patterns has not been sufficiently

exploited till the point of having a device capable of converting voice signal into an accurate interpretable stimulation pattern. The obstacles to reach that kind of communication are the complexity of stimulation, the difficulty of discrimination and the long time required for training [5]. This is mainly due to the difficulty of transferring such a quantity of information contained in the voice signal through the skin.

The presented scenario shows the need for continuity of the research on electrotactile stimulation on auditory sensory substitution. So, this article describes the design and operation of the developed electrotactile stimulator which defines stimulatory patterns from the spectral analysis and grouping of the speech signal, defining stimuli intensity in each channel.

II. MATERIALS AND METHODS

The developed PAM (Pulse Amplitude Modulation) electrotactile stimulator was designed to operate from 1 to 8 channels simultaneously. The system, illustrated in Figure 1, is composed primarily of four modules: IBM PC, microcontroller processing unit, power supply and eight stimulatory channels.

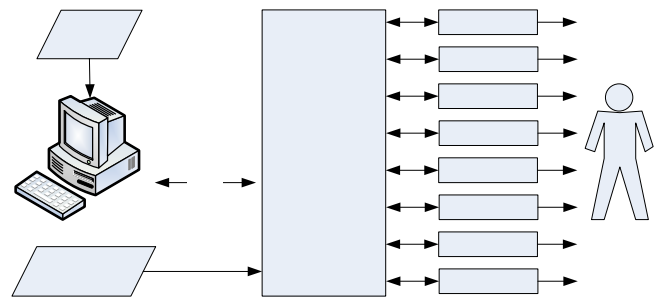


Fig. 1 Block diagram of the designed system.

A. Power Supply

The power supply is designed to provide an intensity current of $\pm 100\text{mA}$ at $\pm 150\text{Vdc}$. Thus, there is no lack of power when stimulating with high magnitudes simultaneously

in more than one channel, since the maximum current for each channel is 18 mA.

For the development of the power supply, we used a switched power supply structure (Figure 2), allowing the use of 12Vdc - batteries as a source of DC current, keeping it isolated from the domestic electrical power net.

For switching technique, there was used the PWM (Pulse Width Modulator) generator SG3525A, configured at 8 kHz, the switching of current is conducted by two IRF530 MOSFETs, which support up to 14A in the transformer primary winding. The transformer was built in the laboratory with 4+4 turns in the primary winding and 60+60 turns in the secondary one. On secondary winding output we used a full-wave rectifier with four schottky diodes MUR1100 and 2.2uF 250V capacitors. Then, it is possible to obtain an output of ± 150 Vdc, from a single 12V-battery.

Beyond the implemented switching circuit, it was also used a PT5062 component from Texas Instruments in order to generate ± 15 Vdc outputs, a 78M33 to generate a 3.3Vdc output and a 7805 to generate 5Vdc.

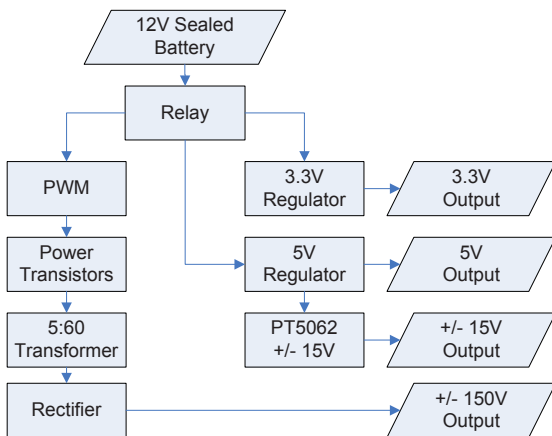


Fig. 2 Block diagram of the developed Power Supply.

B. Microcontrolled Unit

As interface between the stimulatory channel and the computer, it was designed a control board as shown in Figure 3. Communication between the microcontroller and the computer is done via USB port using an USB to Serial converter from FTDI Chip, the FT232BM, which supports serial transfer rates up to 1Mbps with 8-bit TTL data. This interface was the single step of stimulator not electrically isolated from the PC and power grid. The connection of the TTL output of the converter with the microcontroller was done through a pair of optical couplers that support an isolation of up to 2500Vdc.

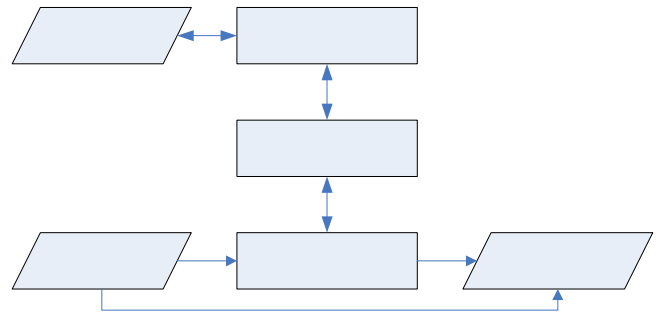


Fig. 3 Block diagram of the digital stage of the stimulator showing the USB communication interface.

The chosen microcontroller was the DSPIC33F that incorporates a modified Harvard architecture and optimized for C-programming. It has an internal structure of 16-bit processing and speed of 40 MIPS. The advantage of using this component is the wide availability of ports (85 programmable i/o ports) allowing the implementation of parallel data buses for DACs. It has TTL serial ports incorporated. The microcontroller provides digital signal processing on-board using an internal DSP core which can be used on the next phase of the project.

C. Stimulatory Channels

The stimulatory channels boards are completely independent, interconnected by a single bus to the control board. Each board, as illustrated in Figure 4, is addressed through a jumper with eight positions.

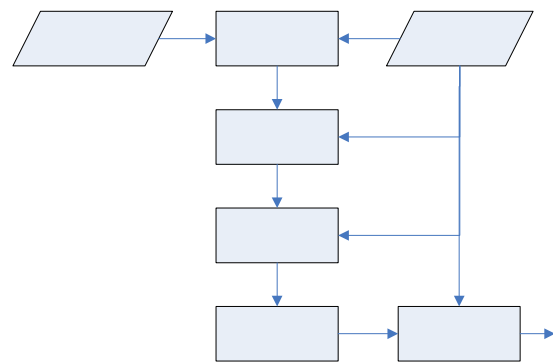


Fig. 4 Block diagram of one stimulatory channel.

Data sent from the bus is received by a 12-bit TLV5619 DAC, from Texas Instruments. The output signal at the DAC voltage was clamped at -1.5 V for a symmetric bipolar output voltage. The signal was converted into current signal,

which modulates the current flow of input of a current mirror, ranging from -22mA to +22 mA.

The current mirror was developed based on Wilson’s current mirror model (Figure 5), where the low-voltage step is controlled by the current output of the voltage to current converter and the high-voltage step is directly fed by ±150 Vdc outputs from the switched power supply.

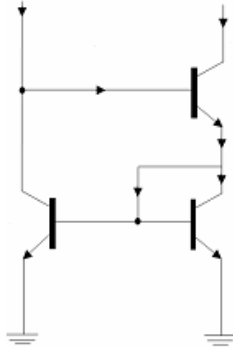


Fig. 5 Simplified model of Wilson Current Mirror.

D. Software

The first step of the system operation is the audio files conversion to WAV standard, 8kHz, 16-bit, mono channel. With the corrected audio file, it is loaded into Matlab Software through the *wavread* function and sent it to a text file. The result of this operation is a file with the values of each sample of the wav file in decimal format, ready to be read in developed software.

With the audio file in text format, it is possible to generate the stimulating intensity for each electrode. The software developed calls as input parameters the file with the audio data in text format, the number of frequency block groups and limits of frequency for each frequency groups.

From those data, the software calculates the Discrete Hartley Transform (DHT) according to Eq. 1 which operates similar to the Discrete Fourier Transform (DFT), but in case of a future optimization of the system, the use of DHT is more advantageous in comparison with DFT, showing a higher speed of processing and a lower computational cost [6].

$$H(f) = \frac{1}{N} \cdot \sum_{t=0}^{N-1} X(t) \cdot \left[\cos\left(\frac{2\pi ft}{N}\right) \cdot \sin\left(\frac{2\pi ft}{N}\right) \right] \tag{1}$$

After DHT application, the resultant vector of real numbers is submitted to Eq. 2, where the assembly of the frequency spectrum of the signal is made.

$$P(f) = \sqrt{[H(f)]^2 + [H((N - 1) - f)]^2} \tag{2}$$

An example of this process can be viewed in Fig. 6, where the algorithm was applied to the word “warning”, pronounced “cuidado” in Portuguese.

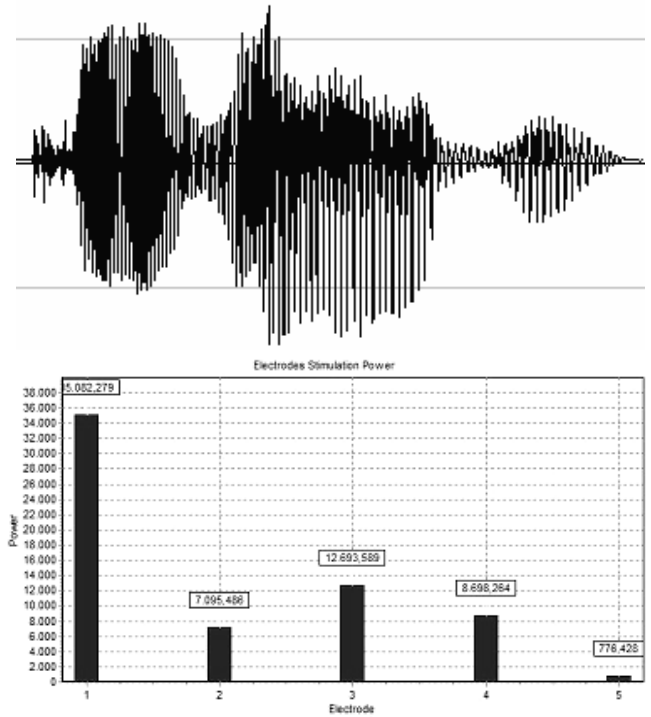


Fig. 6. Example of developed generation pattern software using the word “warning”, pronounced “warning” in Portuguese.

With the intensity values of each frequency bands, we may use the third stage of the software, responsible for training the user, where the person chooses between six different words displayed on the screen. When a word is clicked, the stimulation is performed using the intensity for each electrode pattern corresponding to the selected word.

When the user has been trained through a pre-defined period, the session for learning evaluation is initiated. At this stage, the six options previously trained are presented, and a pattern is applied to the stimulating electrodes. The goal is to evaluate the volunteer recognition rate by choosing the word on the screen corresponding to the effectively presented stimuli.

Data such as hits, errors and response times are stored for each event, leading at the end of the session the statistics of hits and errors and the average response time of the volunteer interpretation.

III. CONCLUSION

The described system is fully functional and ready for *in vivo* testing. Preliminary tests indicate that the patterns are distinct, reproducible and recognizable. With this equipment, we expect to set parameters for the generation of satisfactory stimulatory patterns in order to obtain an increase on the rate of information recognition through electrotactile stimulation compared to previous studies from other researchers.

For *in vivo* researches we will proceed through the following steps: (1) adequacy and configuration of fixed parameters such as pulse width, number of pulses per burst, number of bursts, interphase interval and inter stimulus interval (2) application of a test protocol on volunteers to define recognition rates using this method.

REFERENCES

1. J. L. Northern, M. P. Downs (2002) Hearing in Children. Lippincott Williams & Wilkins, Ed. 5, United States.
2. I. R. Summers (1992) Tactile Aids for the Hearing Impaired. Whurr Publishers, London.
3. M. C. F. de Castro, A. Cliquet Jr. (2001) Estimulação Elétrica Neuromuscular e Estimulação Eletrotáctil na Restauração Artificial da Preensão e da Propriocepção em Tetraplégicos. Acta. Ortop. Bras., vol. 9, no 3, São Paulo, Brazil.
4. J. G. Webster (1998) Medical Instrumentation: Application and Design. John Wiley & Sons Inc., ed. 3, United States.
5. G. Kim, R. Okuno, M. Yoshida, K. Akazawa (2004) Sensory Substitution System of Two-Channel Electrotactile Stimulation for Transmitting Verbal Information. IEEE EMBS Proc. 26th Annual International Conference, San Francisco, United States, 2004, pp 4948-4851.
6. M. Frigo, S. G. Johnson (2005) The Design and Implementation of FFTW3. IEEE Proc. vol. 3, no. 2, pp 216-231.

Intraoperative neural electrode for continuous monitoring of nerve function

K.P. Koch¹, W. Poppendieck², Ch. Ulmer³, D.W. Kauff⁴, T. Doerge², P. Osypka⁵, W. Kneist⁴ and W. Lamadé³

¹ Fachhochschule Trier, University of Applied Science, Department Engineering, Trier, Germany

² Fraunhofer Institute for Biomedical Engineering, St. Ingbert, Germany

³ Robert-Bosch-Hospital, Department of General, Visceral and Trauma Surgery, Stuttgart, Germany

⁴ University Medical Center of the Johannes Gutenberg University, Department of General and Abdominal Surgery, Mainz, Germany

⁵ Dr. Osypka GmbH, Rheinfelden, Germany

Abstract— Nerve damage is still a major concern in all types of surgery and may result in permanent nerve injury. Real time nerve monitoring can reduce the risk of nerve lesions by continuous surveillance of nerve integrity. A stable proximal stimulation of the nerve and recording at the effector organ is essential and the electrodes should not significantly influence the surgical intervention.

This work focuses on the simulation of different electrode designs to compare the results considering the application. Four tripolar electrode designs (cuff, flat, cylindrical and open tube) were simulated by finite-element method. The simulations were performed in 3D and quasi-static electromagnetic case considering the metal-electrolyte interface and the anisotropic conductivity of the nerve.

Highest nerve stimulation efficiency was found for the closed cuff design followed by the open tube design. Flat and cylindrical designs were similar. Nevertheless each design has advantages in relation to implantation method. The advantages and disadvantages of the electrode designs are discussed.

Keywords— finite-element simulation, real time nerve monitoring, electrode design, electrode-electrolyte interface.

I. INTRODUCTION

During surgical intervention there exists a risk of nerve damaging. Especially localization of small nerve branches and their differentiation from other tissue may be difficult. These difficulties are even increased by scraing or tissue edema due to inflammation, reoperation or radiotherapy. By the use of intraoperative neuromonitoring nerves can be identified unequivocally and nerve function can be proven. A standard intraoperative monitoring system consists of electrodes to stimulate the nerve in the operating field and recording electrodes at the effector organ that is directly or indirectly innervated by the nerve. Stimulation pulses are generated and recording signals amplified by an electronic monitoring system.

A variety of systems for intraoperative monitoring has been developed for thyroid surgery. The problem of the conventional systems is that the stimulation electrode has to

be held by the surgeon and therefore no continuous real time monitoring of the nerve is possible. This results in a risk to destroy the nerve during the time interval between the nerve stimulations. This problem could be solved by electrodes that could be placed stably near or at the nerve. One approach is the positioning of recording and stimulation electrodes on a double balloon tube [5]. An alternative concept is the placement of a cuff electrode around the vagus nerve and thereby to stimulate also the fascicles that innervate the larynx [8].

In the lower abdomen pelvic nerve monitoring can be used to control nerve sparing total mesorectal excision. This can reduce damaging of nerves innervating bladder, genitals and anal sphincter [3]. Stimulation takes place at the superior hypogastric plexus, hypogastric nerves, inferior hypogastric plexus and the pelvic splanchnic nerves localized in the pelvic cavity.

A positive stimulation result was identified by increased intravesical pressure. In clinical studies a correlation between the stimulation result and postoperative bladder function could be shown [3].

Aspects for the design of the electrode were time to implant the electrode, invasiveness, stimulation stability, risk of dislocation and selectivity. In this study the electrical field distribution of different electrodes was compared. Thereby the relation between the total current and the current density at the nerve could be investigated. Although the anatomy varies from patient to patient this relation could help to estimate the sensitivity of the different designs.

II. MATERIAL AND METHODS

A. Electrode Designs

The design of the electrodes was based on a tripolar design. Three stripes of electrode material were placed in parallel. The outer electrodes were connected. The technology to produce the first three designs is based on a micro-machining process where platinum electrodes were packaged in a 10 μm thick polyimide foil (Reinhardt Microtech

GmbH, Ulm, Germany) similar to [7]. The polyimide foil was electrically connected by a modified ball-bonding technology via a ceramic adapter to cables. Finally silicone rubber was used to give the electrodes more mechanical stability [4].

Planar electrode: The planar electrode consisted of three parallel platinum stripes with a width of 0.5 mm and a length of 9 mm. The space between the electrodes was 1.6 mm. Electrodes were placed on a flexible sheet of silicone rubber that could be adapted in size during the operation. For the simulation the sheet was assumed to be planar and large in size compared to the electrode geometry. This represents the situation during the operation where the electrode is placed at the surface of the tissue and in the neighborhood of the electrode the tissue is insulated by environmental area.

Cuff electrode: To simulate the cuff electrode the same structure was rolled up with an inner diameter of 1.8 mm. The overlapping electrode area was ignored for the simulation and the cuff sealing was assumed to be perfect.

Open tube electrode: The open tube electrode was designed to be easily placed and removed around the nerve. The structure is similar to a cuff electrode. Instead of overlapping the ends of the sheet were opened to some kind of horn (Fig. 1). The basic structure was produced by silicone rubber (Dr. Osypka GmbH, Rheinfelden, Germany)

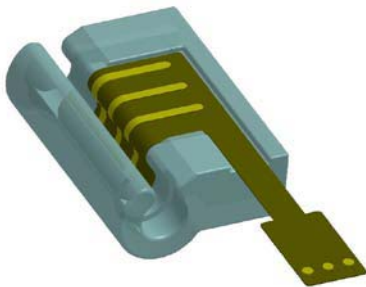


Fig. 1 Open tube electrode

Cylindrical electrode: The geometry of the cylindrical electrode was based on the design of the tripolar electrode for vagus nerve stimulation V3 (inomed Medizintechnik GmbH, Teningen, Germany). The electrode geometry was modified for the simulation to have the same electrode distances and widths as the other electrodes. The radius was 1.8 mm. Original the spacing of the electrodes was 3 mm and electrode was stainless steel in medical grade.

B. Simulation method

Simulations were performed with the finite-element method with FlexPDE Version 5.1.2 3D (PDE-solution). The models were constructed with 3D defining differential equation to quasi-static electromagnetic case under the assumption that magnetic effects are negligible. The equation for the electric complex potential V includes κ as conductivity and ϵ_r as relative permittivity of the materials. j is the imaginary number, $\omega=2\pi f$ is the angular frequency, ϵ_0 is the permittivity of vacuum, and ∇ is the del operator.

$$\nabla \cdot \left((\kappa + j\omega\epsilon_r\epsilon_0) \nabla \cdot V \right) = 0$$

The electrode metal platinum ($\kappa=94 \times 10^5 \text{ S m}^{-1}$ and $\epsilon_r=1$) was simulated with ($\kappa=94 \times 10^2 \text{ S m}^{-1}$ and $\epsilon_r=1$) to improve the numerical performance of the simulation. There is no significant influence by this change to the simulation result because the conductivity of the adjacent materials is still 3 decades smaller. The liquid in the operating field was simulated as physiological saline solution ($\kappa=1 \text{ S m}^{-1}$ and $\epsilon_r=80$). The insulation material ($\kappa=10^{-14} \text{ S m}^{-1}$ and $\epsilon_r=4.2$) was simulated with ($\kappa=10^{-3} \text{ S m}^{-1}$ and $\epsilon_r=4.2$) for the same reason as the approximation for the metal material parameters.

The metal-electrolyte interface was modeled by a 100 nm thick layer similar to the method described by [1]. To find out the impedance of the metal-electrode interface impedance was measured by impedance spectroscopy with potentiostat. The results were modeled by the impedance of the surrounding solution in serial to the impedance of the metal-electrode interface. This was modeled as a parallel circuit of Faradaic resistance and Helmholtz capacitance. These values of Faradaic resistance and Helmholtz capacitance were normalized to the size of the measured electrode and adapted to the thickness of the interface layer in the simulation. This results in simulation parameters for the metal-electrode interface as ($\kappa=4.78 \cdot 10^{-8} \text{ S m}^{-1}$ and $\epsilon_r=7.6 \times 10^6$). Because the current density of the electrodes is relatively low the impedance of the metal-electrode interface was modeled linear.

The model of the nerve was cylindrical with a diameter of 1.6 mm. The distance between the electrode and the nerve was 0.1 mm for all designs. The material parameters for the nerve were anisotropic: $\kappa=0.6 \text{ S m}^{-1}$, $\epsilon_r=80$ parallel to the nerve axis, and $\kappa=0.083 \text{ S m}^{-1}$, $\epsilon_r=80$ orthogonal to the nerve axis [2].

In relation to the stimulation parameters (biphasic pulse, pulse width 200 μs) the simulation frequency was 2.5 kHz. As stimulation current 1 mA was applied to the middle electrode and the outer electrodes were defined as 0 V.

C. Stimulation parameters

A commercial EMG system (NEMO®, Inomed GmbH, Germany) generated stimulation biphasic pulses with pulse width of 200 μ sec. The stimulation frequency was 3 Hz for vagus nerve during thyroid surgery and 30 Hz for pelvic nerve stimulation during total mesorectal excision. The stimulation amplitude was adapted to the need of the application between 0.5 mA and 9 mA

III. RESULTS

As simulation results the absolute values of the electrical field in axial direction of the nerve are shown (Fig. 2). This

field component is mainly responsible for the excitation of the nerve fibers [6]. The highest field strength can be achieved with the cuff electrode design. Also the penetration is the best with cuff electrodes. This is related to the close structure of the electrode and results in a concentration of the field. The next higher field strength could be achieved by the open tube design. The homogeneity of the field strength is less in this configuration compared to the close cuff design. The plane electrode and the cylindrical electrodes are similar in amplitude. Due to the larger surface of the planar electrodes the current density is lower at the electrode surface in relation to the cylindrical electrode. This effect is partly compensated by the lower distance of some parts of the electrode to the nerve.

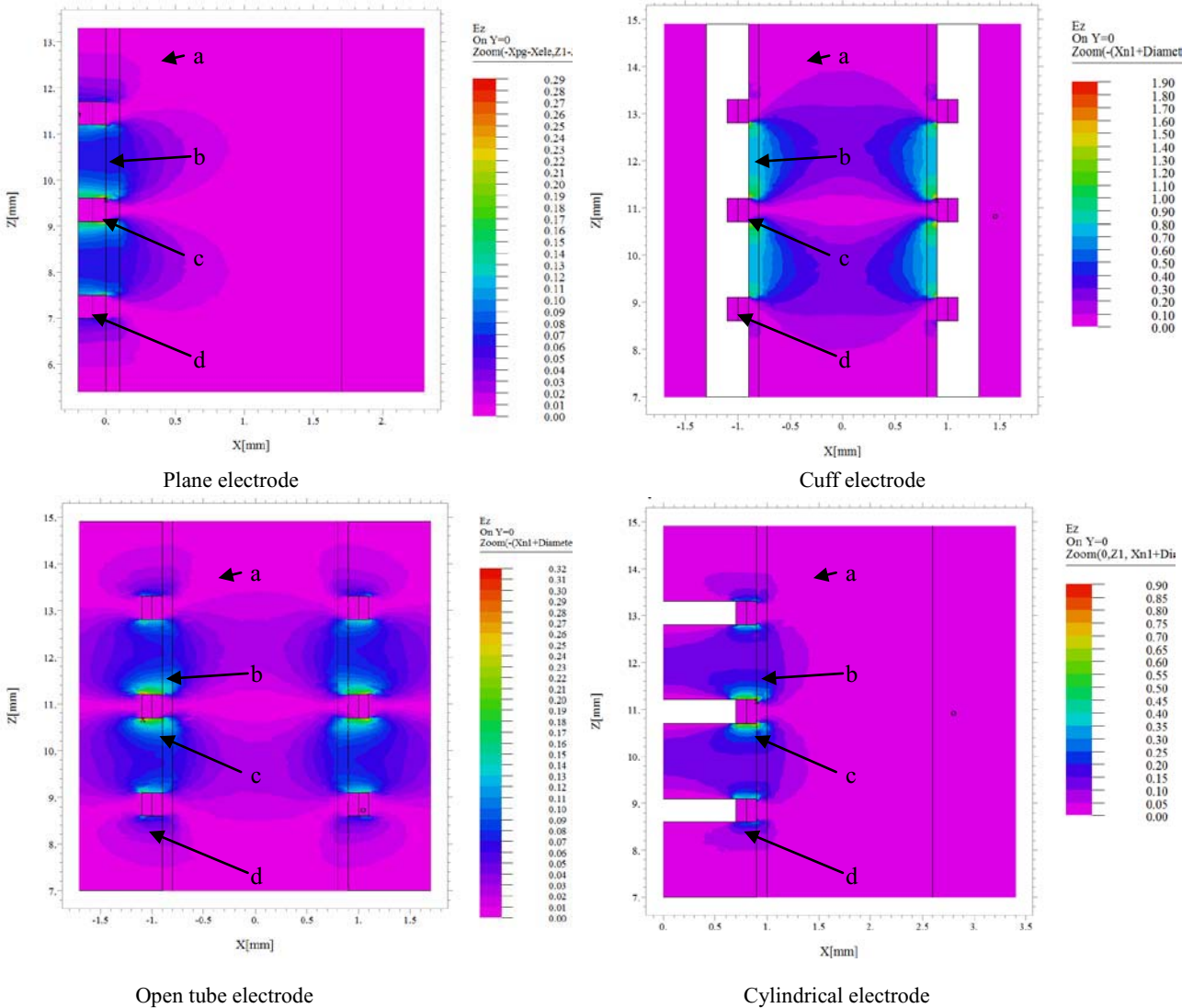


Fig. 2 Absolute value of the electrical field (V/mm) in axial direction to the nerve in x-z plane (note different scale for z and x).
 a) nerve b) physiological solution c) electrode-electrolyte interface d) electrode

IV. DISCUSSION

The four electrode designs generate different field strengths to stimulate the nerve. The good properties for the cuff electrode that were confirmed by the first in vivo experiments are combined with the disadvantage that this electrode has to be wrapped around the nerve. This means that the nerve has to be exposed and that this electrode has the strongest fixation to the nerve. On the one hand the strong fixation has the advantage that the electrode does not significantly move during the operating procedure and stimulation results are highly reproducible. On the other hand an accidental pull on the cable of the electrode results in an unwanted force on the nerve and thereby a risk of damaging the nerve. The problem of unwanted force on the electrode could be mainly avoided by the open tube design. If an accidental pull happens at the cable the electrode can rotate and the nerve can slip out of the electrode without large forces.

The cuff and the open tube design have both the problem that the nerve has to be exposed. By cylindrical design the electrode can be pushed through a small insertion in a tissue layer in parallel to the nerve. Thereby this design is less invasive. However, it is more sensitive against dislocation of the electrode in relation to the nerve. In some applications like pelvic nerve stimulation electrodes are wanted that can be placed at the surface of the tissue because the nerves have a mesh-like geometry. This could be achieved by a planar flexible electrode. The additional advantage of this design is that it is less sensitive against misplacement if the exact position of the nerve is not known.

V. CONCLUSIONS

Electrode design has a high influence on the efficiency related to nerve stimulation. Moreover, the different applications need different electrode geometries related to implantation method and risk for damaging the nerve. In the process of designing an electrode for a certain application,

simulation results can help to decide between different possible solutions with respect to stimulation efficiency and thereby to the capability to stimulate selectively.

ACKNOWLEDGMENT

This work was supported by the German Federal Ministry of Education and Research (“Bundesministerium für Medizinische Forschung”, BMBF Grant number 01EZ0722), Project IKONA.

REFERENCES

1. Cantrell D R, Inayat S, Taflove A, Ruoff R S, Troy J B (2008) Incorporation of the electrode-electrolyte interface into finite-element models of metal microelectrodes. *J. Neural Eng.* 5: 54-67.
2. Geddes L A, Baker L E (1967) The specific resistance of biological material-A compendium of data for the biomedical engineer and physiologist. *Med. & Biol. Eng.* 5: 271-293
3. Kneist W, Junginger T (2007) Intraoperative electrostimulation objectifies the assessment of functional nerve preservation after mesorectal excision. *Int J Colorectal Dis.* 22(6): 675-682
4. Koch K P, Kammer S; Boehler G, Hanauer M, Hoffmann K P (2005) Hybrid Cuff Electrode for Recording Nerve Signals From Sacral Nerves. 39. Jahrestagung der Deutschen Gesellschaft für Biomedizinische Technik, Biomedizinische Technik, Bd. 50, Erg.band 1: 82 – 83
5. Lamadé W, Meyding-Lamadé U, Buchhold C, Brauer M, Brandner R, Uttenweiler V, Motsch J, Klar E, Herfarth C. (2000) First continuous nerve monitoring in thyroid gland surgery. *Chirurg* 71:551-557
6. Rattay F (1989) Analysis of models for extracellular fiber stimulation. *IEEE Trans. Biomed. Eng.* 36: 676-682
7. Stieglitz T, Beutel H, Schuettler M, Meyer JU (2000) Micromachined, polyimide-based devices for flexible neural interfaces. *Bio-med Microdevices* 2: 283–294
8. Ulmer C, Koch K P, Seimer A, Molnar V, Meyding-Lamadé U, Thon K-P, Lamadé W (2008) Real-time monitoring of the recurrent laryngeal nerve - An observational clinical trial. *Surgery* 143 (3):359-365

Author: Klaus Peter Koch
 Institute: Fachhochschule Trier, University of Applied Science
 Street: Schneidershof
 City: 54293 Trier
 Country: Germany
 Email: Koch@Fh-Trier.de

Density Distribution of Denervated Degenerated Rectus Femoris Muscle in Electrical Stimulation treatment.

T. Helgason^{1,3}, P. Gargiulo^{1,3}, B. Vatnsdal^{1,3}, S. Yngvason², V. Gudmundsdottir², S. Knútsdóttir², and P. Ingvarsson²

¹ Department for Research and Development, Landspítali, Reykjavik, Iceland

² Department for Rehabilitation, Landspítali, Reykjavik, Iceland

³ Department for Biomedical Engineering, University of Reykjavik, Reykjavik, Iceland

Abstract— In this work we investigate the density distribution of muscle tissue of denervated and degenerated muscle in electrical stimulation therapy. The muscle tissue mean density is plotted as a graph along the length. The results suggest that the therapy is modulating the muscles density in the way that at locations where there is more frequent stimulation or higher stimulation intensity the muscle tissue is denser.

Keywords— Denervated muscles, degenerated muscles, electrical stimulation therapy, muscle density,

I. INTRODUCTION

Spinal cord injured (SCI) patients with a lower motor neuron lesion suffer from degeneration of muscles below the injury. This is due to inactivity, as the muscles are never contracting. On the contrary, paraplegic patients with an intact lower motor neuron tend to develop spasm, activated through the motor neuron and the muscles do contract but without control. This muscle activity means that they do not degenerate to the same extent, as do the denervated muscles. Blood flow and metabolism are also enhanced. Because of the total inactivity of the denervated and degenerated muscle (DDM) other tissue types suffer. Thinner skin, lower capillary density, lower bone mineral density is the consequence. One side effect of this is decubitus ulcers with a high risk of infection, which in turn is one of the causes for a high mortality in the population of SCI people. Another side effect is bone fracture. Due to lower bone mineral density (BMD) the strength of the bones in the sublesional area is diminished and risk of fracture is increased substantially. The risk is further increased through the absence of sensibility and inability to react on mechanical interrupts. Bone fracture in turn can have severe consequences for the patient's health including inflammatory processes. Since the incidence of SCI is most frequent by young people and the survival rate in accidents has become much higher in recent decades, raising these patients quality of life is highly motivated. Up to now there is no treatment for DDM patients that restore their muscle mass or bone

strength or reverses the process of degeneration of this tissue types. Drug therapies of muscle or of bone remain deficient. Physiotherapeutic treatment also does not stop or reverse the degeneration. The main treatment of these patients addresses the side effects like ulcer or bone fracture. These can be very difficult to treat because of low blood flow and in general low metabolism in the degenerating area. It is not unusual that a decubitus ulcer is open for several years.

In the European RISE project (QLG5-CT-2001-02191) a new method has been developed for DDM patients based on electrical stimulation [3,4]. Since the lower motor neuron is not intact anymore and there is no connection to neural tissue the muscle fibers are directly stimulated. Skeletal muscle tissue is normally not as sensible to electrical stimulation as is the motor neuron and by DDM sensibility is further reduced. The average diameter of the muscle fiber population is reduced, some fibers are seemed to be without contractile elements and need higher current density is needed in order to depolarize the muscle fiber membrane. This requires current intensities that are two or three order of magnitude higher than used by normal neuromuscular stimulation.

The RISE therapy has shown that a DDM can regain its former size and force [HK04]. The capillary density in the skin increases and its appearance becomes healthier. This has a great psychological effect on the patient.

In this work we look at density distribution of a muscle rectus femoris of three subjects that participated in the RISE project and have been in electrical stimulation treatment for six years. The density is measured in Hounsfield (Hu) and reflects the X-ray absorption of the tissue. Since each thigh is stimulated with one stimulation channel using two big electrodes placed on the skin the muscles beneath are not activated in a physiological manner. Therefore the question arises, is the growth of the muscle modified by the unphysiological activation? Can we see the activation on the muscle tissue density? The hypothesis is that it could be higher where the muscle was activated and lower at other places.

II. MATERIAL AND METHODS

A. Subjects

From the 21 DDM patients finishing the RISE projects protocol three were treated in Iceland with electrical stimulation (Table 1). They all are victims of an accident and suffer from spinal cord injury at the lower thoracic or lumbar level, see column two in table 1. They are all males and of different age. Column three gives the degeneration time, that is the time from the accident until the beginning of electrical stimulation therapy. The last column gives the time they have had stimulation therapy. In this time the therapy has been interrupted both because of medical complications and also because of therapy in compliance.

Table 1: Subject overview

Patient/ Born	Lesion	Degen. time [Years, months]	Thera. time [Years, months]
P1/1973	L1	10m	5y, 2m
P2/1979	ThXI- ThXII	4y, 4m	5y, 5m
P3/1949	ThXII-LII	7y, 11m	5y, 5m

B. The therapy

The patients are electrically stimulating for about two hours a day six days a week. The quadriceps muscle group is each stimulated with two electrodes covering most of the skin area of the upper part of the thigh as can be seen in fig. 1. But because of their size the electrodes are close to each other with only about 1 to 2 cm space in between.



Fig. 1 Electrode placement on the thigh. Two big electrodes 12 x 15 cm are used to enable direct muscle fiber stimulation with high currents.

This leads to the suggestion that the highest current density is in the vicinity of the gap between the electrodes. Moreover the muscle rectus femoris is connected to the hip bone and the patella and because the electrodes are not covering either the end of the muscle one is lead to the as-

sumption that muscle fibers that have parts underneath the gap are stimulated more than other parts of the muscle.

CT scan

A spiral CT scan is made three times a year, that is every four months to monitor the tissue changes. The scan starts above the femur head and continues down below the knee joint, with both legs covered by one scan. The scans are taken with a 0,625 slice increment resulting in about 750 slices, depending on the patient's size. Each slice has 512 x 512 pixels, and each pixel has a grey value in the Hounsfield scale of 4096 grey scale values, meaning that it is represented with a 12-bit value. A total data set from a single scan is therefore 512 x 512 x 750 x 12 = 2.36 GBit or around 300 MB. This data set gives a complete three-dimensional description of the tissue, including the muscles and bones in both upper legs.

The scans are made with 140 kV or 120 kV on the X-ray tube. For calibration a phantom was used. It contains hydroxyapatite rods equivalent to 0, 75 and 150 mg/cm³ of calcium.

C. Processing of data

Each spiral CT scan gives one data set showing the tissue situation at the time scanning. From every data set the femur bone, the patella and the muscle rectus femoris are segmented. The result can be seen in fig. 2.

For each CT-slice of the femur muscle the mean density of the muscle tissue is calculated according to the following equation:

$$\overline{Hu} = \frac{1}{n \cdot m} \sum_{i=1}^n \sum_{j=1}^m Hu_{ij} \quad (1)$$



Fig. 2 Muscle rectus femoris, the femur bone and patella are segmented from the spiral CTs. The picture shows the right thigh from patient 2. The growth of the muscle in the period from 2003 to 2008 can easily be seen. The volume of the muscle increases from 88 cm² in the year 2003 to 145 cm² in the year 2008.

The result of this calculation is shown in fig. 3 to 5. The mean density Hu is shown in the figures as a function of muscle length.

III. RESULTS

The results are shown in Fig. 3 to 5. They show at the top a three dimensional picture of the femur muscle, femur bone and patella. Below that is a graph of the mean tissue density in each CT slice of the muscle. The graphs are color coded and marked according to the year the scan was made. The right side of the graph corresponds to the hip end of the femur muscle and the left side to the patella end of the femur muscle.

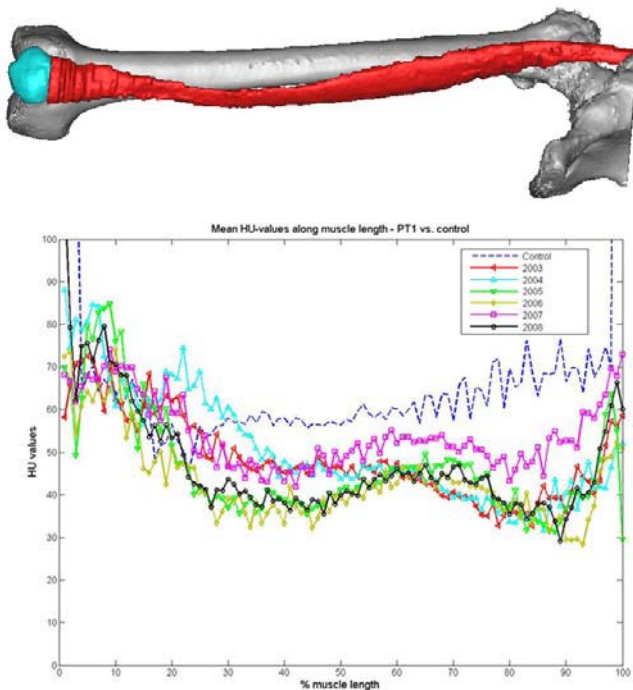


Fig. 3. Patient 1. See text for discussion.

The picture of the muscle is laid the way that each graph value is placed at its location along the length of the muscle. The up most line which is dotted is the mean muscle tissue density of a healthy person with normal muscles. The darkest line shows the latest measurement made in 2008. Figure 3 shows the data from patient 1 who has not been therapy compliant over the whole period from 2003. He was a very muscular person. It can be seen that his mean density lines fluctuate up and down he is not gaining any muscle density.

Figure 4. shows the data from patient 2 who was not therapy compliant in the first one to two years. From that time he has been stimulating. It can be seen that in the middle of the graph, from about 20% of the muscle length and up to about 60% of the length the density of the muscle has been increasing. In the areas above and below that interval there is little or no change in the muscle tissue density. Since the fibers in the femur muscle are organized somewhat like a feather they do not go from the patella all the way up to the hip bone.

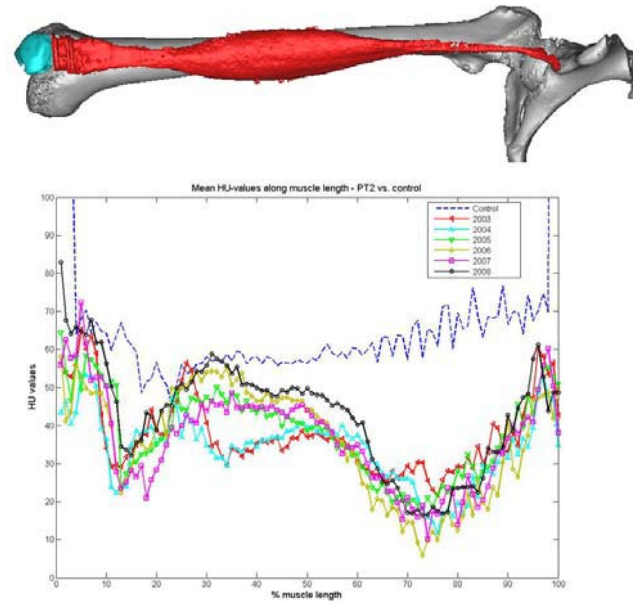


Fig. 4. Patient 2. See text for discussion

Therefore this can be taken as a suggestion that the muscle was stimulated more in the middle area and less at the ends.

Figure 5. shows the data from patient 3 who has been therapy compliant when possible but has had complications leading to longer periods without electrical muscle stimulation. His mean tissue density curves show a continues slow degeneration though there is also less changes in the area between 20 and 60% of the muscle length.

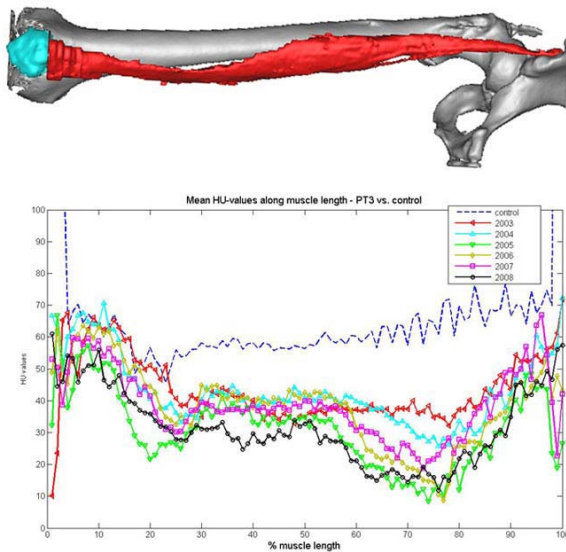


Fig. 5. Patient 3. See text for discussion.

IV. DISCUSSIONS

Our results are from three patients from whom only one was successfully therapy compliant. Therefore the modulation of electrical stimulation on muscle density distribution has to be investigated more. Since there is no nerve fibres in the denervated muscle and the action potential of a single muscle fibre does not go from one fibre to another each and every fibre has to be stimulated to get a contraction. The effect of training is the contraction. Those fibres not contracting will not increase their contractile protein while the contracting will and the muscles not contracting will gather fat between the fibres and the others not. Therefore the less trained muscles show lower density in the CT scan than more trained muscles. This seems also to apply to denervated and degenerated muscle parts. Those parts contracting will have higher density and those not contracting lower density. This leads to the necessity to improve the stimulation method and systems.

V. CONCLUSIONS

We conclude the following: Electrical stimulation of proper intensity can slow down or even builds up muscle density. Our results suggest that the stimulation of the fe-

mur muscle was not homogeneous over the whole muscle and this can be seen in the tissue density distribution along the muscle length.

ACKNOWLEDGMENT

This work was supported by grants from Health Technology Venue, HTV, from The Icelandic Student Innovation Fund, from the Science fund of Landspítali and from Fond for Technological Development and Innovation kept by Icelandic Centre for Research, Rannis.

REFERENCES

1. Kern H, Hofer C, Mödlin M, Forstner C, Mayr W, Richter W.: Functional electrical stimulation (FES) of long-term denervated muscles in humans: clinical observations and laboratory findings. *Basic Appl Myol* 2002;12:291-9.
2. Mayr W, Hofer C, Bijak M, et. al. : Functional electrical stimulation (FES) of denervated muscles: existing and prospective technological solutions. *Basic Appl. Myol* 2002; 12: 287-90
3. Kern H, Boncompagni S, Rossini K, et. al.: Long-term denervation in humans causes degeneration of both contractile and excitation-contraction coupling apparatus, which is reversible by functional electrical stimulation (FES): a role for myofiber regeneration? *J Neuro-path Exp Neurol* 2004; 63: 919.
4. Helgason T, Gargiulo P, Jóhannesdóttir F, Ingvarsson, P, Knútsdóttir S, Gudmundsdóttir V, Yngvason S.: Monitoring Muscle Growth and Tissue Changes Induced by Electrical Stimulation of Denervated Degenerated Muscles with CT and Stereolithographic 3D Modeling. *Artificial Organs* 29(6), 2005 :440-443
5. P. Gargiulo, T. Helgason, P. Ingvarsson, S. Knútsdóttir, V. Gudmundsdóttir, and S. Yngvason "Morphological changes in Rectus Femoris Muscle: Advanced Image Processing Technique and 3-Dimensional Visualization to Monitor Denervated and Degenerated Muscles Treated with Functional Electrical Stimulation." *Journal of Basic and Applied Myology, BAM* 17 (3&4):133-136, 2007
6. P. Gargiulo , B. Vatnsdal, P. Ingvarsson, S.Knútsdóttir, V. Gudmundsdóttir, S.Yngvason and T. Helgason.. Restoration of Muscle Volume and Shape Induced by Electrical Stimulation of Denervated Degenerated Muscles: Qualitative and Quantitative Measurement of Changes in Rectus Femoris Using Computer Tomography and Image Segmentation. *Artificial Organs* (2008) 32(8):609-613.

Corresponding author:

Author: Thordur Helgason

Institute: Dept. for Research and Development, Landspítali/ Department for Medical Engineering, University of Reykjavik
 Street: Eiríksgata 5 / Kringlan 1
 City: 101 Reykjavík / 10
 Country: Iceland
 Email: Thordur@landspitali.is

Application of the ACT^{3D} Robot in the Evaluation of Functional Reaching Performance and the Administration of Experimental Interventions

Michael D. Ellis, PT, DPT¹ & Julius P.A. Dewald^{1,2,3}

¹ Northwestern University, Department of Physical Therapy and Human Movement Sciences, Chicago, USA

² Northwestern University, Department of Biomedical Engineering, Chicago, USA

³ Northwestern University, Department of Physical Medicine and Rehabilitation, Chicago, USA

Abstract— Since the development of the Arm Coordination Training 3D Device (ACT^{3D}, United States Patent No. 7,252,644 B2, Aug. 7, 2007) in 2002, colleagues in the Neuroimaging and Motor Control Laboratory at Northwestern University Department of Physical Therapy and Human Movement Sciences have been studying the administration of therapeutic interventions and the measurement of reaching performance as they relate to the fundamental impairment of abnormal abduction/elbow flexion torque coupling or “flexion synergy” in individuals with chronic hemiparetic stroke. The quantification of reaching work area as a function abduction loading with the ACT^{3D} robot represents the detrimental impact of abnormal joint torque coupling on functional reaching and can be utilized as an outcome measure in clinical research and practice. Furthermore, the ACT^{3D} can be used to initiate and progress a therapeutic intervention meant to reduce the abnormal joint torque coupling impairment and thus increase reaching range of motion under functionally relevant abduction loading conditions. This paper will review the work completed to date utilizing targeted rehabilitation robotics both as a quantitative clinical evaluation tool and also as a rehabilitation device for the administration of quantitatively controlled therapeutic exercise.

Keywords— Stroke, Arm, Rehabilitation, Coordination, Strength.

I. INTRODUCTION

While the post-stroke manifestation of upper extremity *flexion synergy* or coupling of shoulder abduction with elbow/wrist flexion has been qualitatively observed for decades [1-3], the structured quantification of this impairment has only recently been accomplished through the utilization of the ACT^{3D} robot [4]. The recent development in quantifying the expression of *flexion synergy* and its impact on reaching range of motion comes at a critical time in the field of stroke rehabilitation. In its current state, “best practice” in the rehabilitation of individuals with stroke can likely be improved upon through the identification of the operative components of upper extremity rehabilitation [5] and the ability of clinicians to accurately measure the presence of various impairments and their effect on function. The clinical intervention arm of our laboratory is focused on

the growing need in clinical practice to both quantitatively evaluate and subsequently target specific stroke-induced impairments that are most likely leading to activity (functional) limitation. Supplying rehabilitation clinicians with more precise quantitative tools for evaluation and treatment will likely lead to improved movement problem diagnosis and exercise prescription therefore, translating to greater functional gains in individuals with stroke. The following review will describe the efforts to date in our laboratory to validate the measurement of reaching work area by the ACT^{3D} robot as a sound clinical tool and to utilize the device for the delivery of reaching exercise that directly targets the impairment of abnormal abductor/elbow flexor torque coupling or “flexion synergy.”

II. ACT^{3D} AS A CLINICAL EVALUATION TOOL

The ACT^{3D} can be utilized to measure total reaching range of motion in a horizontal plane centered at the shoulder joint (work area). Work area can be measured while the arm is supported by and gliding on a horizontal haptic surface or while the research participant actively lifts the arm just above the haptic surface (see Figure 1).



Figure 1. Measurement of work area with the ACT^{3D} robot.

During the evaluation of work area, participants slowly move the arm through its complete range of motion in the horizontal plane creating a completed circular hand path tracing or envelope. The ACT^{3D} is capable of altering vertical loading forces such that during work area evaluation when the participant is actively supporting the limb above the haptic surface, they are lifting various percentages of limb weight ranging from 0% to 200% of limb weight. During the 0% condition the arm is rendered weightless. An example of work area envelopes from each limb loading condition is illustrated in Figure 2.

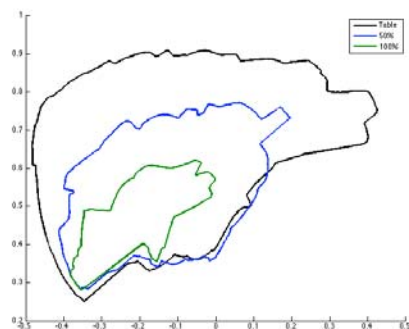


Figure 2. Example of work area envelopes for movement while fully supported by and gliding along the haptic surface (black) and two selected levels of abduction limb loading (50% of limb weight; blue, 100% of limb weight; green). Work area reduces as a function of abduction loading.

From the illustration in Figure 2, the reduction in work area as a function of abduction loading can be appreciated. We have identified a monotonic relationship between work area reductions and increased abduction loading and attributed this to amplified elbow flexor torque coupling during higher abduction loads [4]. Work area therefore, provides a quantitative measurement of “flexion synergy” impairment, importantly, in the context of functional reaching.

The ability of the ACT^{3D} to provide a quantitative measurement of impairment in a functional context positions it to be a powerful clinical evaluation tool. We have recently completed the validation of the work area measure for clinical use [6]. In this work, test-retest reliability was supported in that the measurement of work area could be measured on two separate occasions with little variability. Secondly, the criterion-related validity was supported through significant correlations with existing standardized clinical assessments of impairment, activity and participation limitation. Most importantly, the study demonstrated that, although significant correlations were observed with existing clinical scales, the quantitative measurement of work area proved to provide additional augmentative information readily applied to patient evaluation and intervention prescription. The clinical usefulness of the work area measurement will be apparent

in the following discussion of the application of the ACT^{3D} as a clinical intervention device.

III. ACT^{3D} AS A CLINICAL INTERVENTION DEVICE

Initial intervention work with the ACT^{3D} involved a single group pretest-posttest design addressing the efficacy of directly targeting the “flexion synergy” impairment with progressive abduction loading reaching exercise [7]. The ACT^{3D} was utilized to provide constant vertical loading during the practice of outward reaching to standardized targets. The initial work area assessment provided useful information in determining the abduction loading level at which the intervention was initiated. Individuals in the intervention practiced outward reaching under abduction loading conditions for 3 days per week for 8 weeks. As individuals reached certain performance thresholds, the magnitude of abduction loading was increased by a factor of 25% of limb weight. Following the completion of the 8-week intervention, participants underwent the work area evaluation, isometric strength testing, and clinical assessment. Efficacy of targeting “flexion synergy” with progressive abduction loading reaching practice was supported with the group experiencing significant increases in work area (see Figure 3).

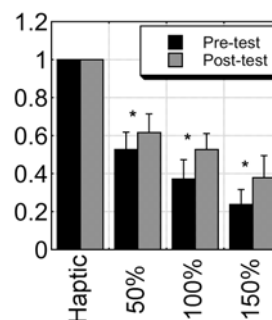


Figure 3. Work area normalized to the work area obtained while supported by the haptic surface for abduction loading levels of 50%, 100%, and 150% of limb weight. Participants showed a significant improvement in work area at all levels.

Interestingly, participants did not show improvements in single-joint strength (Figure 4) indicating that improvements were likely due to a reduction in abnormal abduction/elbow flexion torque coupling or “flexion synergy.” Participants also showed an improvement in clinical evaluation scores demonstrating a modest improvement in impairment and activity limitation in the affected arm. Ultimately, the single-group study demonstrated the beneficial effects of targeting abnormal abduction/elbow flexion torque coupling on function reaching.

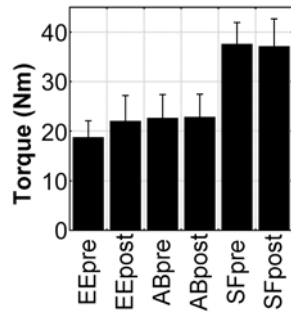


Figure 4. Maximum isometric strength for elbow extension (EE), abduction (AB), and shoulder flexion (SF). There were no changes in single-joint strength for any joint torque direction at both the shoulder and elbow identifying a reduction in abnormal joint torque coupling as the source of improvement.

In a concurrent clinical intervention study utilizing the ACT^{3D}, a randomized control group design was employed to specifically test for the effect of progressive abduction loading during therapeutic reaching exercise [8]. The protocol was identical to the above study however with the addition of a control group who practiced reaching while fully supported by the haptic surface (no progressive abduction loading). The control intervention was matched for repetition and duration. Following 8 weeks of the intervention, the experimental group receiving progressive abduction loading during reaching practice demonstrated significantly greater gains in reaching work area (Figure 5). Importantly, gains were measured at abduction loading levels that were functionally significant. For example, the 150% abduction loading level represented reaching under normal gravitational conditions plus the addition of the weight of an ob-

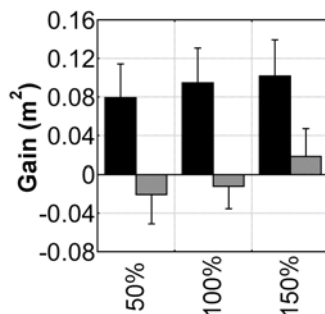


Figure 5. Gain in work area (m^2) for the experimental group (black) and control group (gray) for 50%, 100%, and 150% abduction loading levels. Gain in work area was significantly greater for the experimental group receiving progressive abduction loading reaching practice.

ject. This study demonstrated that progressive abduction loading was a key factor in reaching practice and should be utilized to augment existing clinical interventions.

IV. CONCLUSIONS

The application of the ACT^{3D} robot as both an evaluation tool and as an intervention device has several benefits. First, as an evaluation tool, the ACT^{3D} has the capacity to quantitatively evaluate the impact of abnormal abduction/elbow flexion torque coupling or “flexion synergy” on reaching function. The quantitative nature of the measurement provides rehabilitation specialists with a powerful tool to augment existing qualitative assessments with limited sensitivity and/or specificity. In combination with its evaluation capacity, the application of targeted rehabilitation robotics as an intervention tool provides clinicians with means of prescribing, initiating, and progressing a reaching intervention based on quantitative parameters therefore, optimizing the delivery of care through improved clinical decision making.

ACKNOWLEDGMENT

This work was supported in part by the National Institute of Disability and Rehabilitation Research (H133G030143; J. Dewald), American Heart Association Greater Midwest Affiliate Postdoctoral Fellowship (0520110Z; M. Ellis), National Institutes of Health Loan Repayment Program for Clinical Research (M. Ellis), National Science Foundation Graduate Research Fellowship (T. Sukal), and National Institutes of Health (R42HD049923, J. Dewald/M. Ellis & 2R01HD039343-06A1, J. Dewald).

REFERENCES

1. Brunnstrom S (1970) Movement therapy in hemiplegia: a neurophysiological approach, 1st Edition. New York: Harper and Row.
2. Foerster O (1936) Motorische Felder und Bahnen. In: Handbuch der Neurologie (O. BaO, Foerster, ed), pp 1-357. Berlin: Springer-Verlag.
3. Twitchell TE (1951) The restoration of motor function following hemiplegia in man. *Brain* 74:443-480.
4. Sukal TM, Ellis MD, Dewald JP (2007) Shoulder abduction-induced reductions in reaching work area following hemiparetic stroke: neuroscientific implications. *Exp Brain Res* 183:215-223.
5. Woldag H, Hummelsheim H (2002) Evidence-based physiotherapeutic concepts for improving arm and hand function in stroke patients: a review. *J Neurol* 249:518-528.
6. Ellis MD, Sukal T, Demott T, Dewald JP (2008) Augmenting Clinical Evaluation of Hemiparetic Arm Movement With a Laboratory-based Quantitative Measurement of Kinematics as a Function of Limb Loading. *Neurorehabil Neural Repair* 22:321-329.
7. Ellis MD, Sukal T, Dewald JP (2009) Impairment-Based 3D Robotic Intervention Improves Upper Extremity Work Area in Chronic Stroke: Targeting Abnormal Joint Torque Coupling With Progressive Shoulder Abduction Loading. *IEEE Trans Rob Autom*: In Press.
8. Ellis MD, Sukal T, Dewald JP (2009) Progressive Shoulder Abduction Loading is a Crucial Element of Arm Rehabilitation in Chronic Stroke. *Neurorehabil Neural Repair*: In Press.

Author: Michael D. Ellis, PT, DPT
 Institute: Northwestern University
 Street: 645 N. Michigan Ave. Suite 1100
 City: Chicago, IL 60611
 Country: USA
 Email: m-ellis@northwestern.edu

Application of electrode matrix to locate stimulation sites for hand functions of SCI patients

A. Oskarsdottir¹, and T. Helgason^{1,2}

¹ Department for Medical Engineering, University of Reykjavik, Reykjavik, Iceland

² Department for Research and Development, Landspítali, Reykjavik, Iceland

Abstract— The main topic of this work is to investigate the applicability of electrode matrices for stimulating hand function. Of particular interest is the optimal positioning of electrodes that will elicit some lost hand functions in SCI patients with spinal cord injury at level C6-C7. For this purpose electrode matrices are used. They allow relocation of stimulating sites without moving the electrodes. Various forms are made from different combinations of electrodes in the matrix. Results show that the location of the stimulating site is quicker and the function more selective using electrode matrices with small electrodes.

Keywords— electrode matrix, functional electrical stimulation, hand function, optimal position

I. INTRODUCTION

A spinal cord injury (SCI) at level C6-C7 results in partial or complete loss of sensitivity and motor ability below the level of injury. A patient with this level of injury has movements in head, neck, shoulders, arms and wrists. He can shrug shoulders, bend and straighten elbows, turn palms up and down and extend and flex wrists. He has very little or no strength or movement in fingers which limits the independence of self care tasks [1]

In these cases functional electrical stimulation (FES) can be used to improve grasp capabilities, by reducing the rate of muscle atrophy, and to strengthen muscles which might result in regain of some lost hand functions. Furthermore, hand movements can be elicited by FES. [2]

Electrical stimulation can be applied with surface, percutaneous, or implanted electrodes. [3] Neuromuscular electrical stimulation with surface electrodes is used today for various purposes such as to, decrease pain, strengthen muscles, stimulate paralyzed muscles and stimulate the spinal cord. Researches have shown the need of good knowledge of arm anatomy [4,5] and great patience when placing surface electrodes at a location to obtain the desired hand function. Self adhesive electrodes are commonly used but require complete removal before being accommodated to a better placement. If this is done repeatedly it is not only time-consuming, but also often provokes pain and causes electrodes to wear out quickly. [6]

FES to enhance movements has been known since 1961 when Liberson and colleagues attempted to restore muscle function in dropfoot [7]. Many FES systems have been developed, both implanted system and noninvasive surface stimulation system. The most successful implanted device is The FreehandTM System developed in Cleveland, Ohio[2,3] and marketed in the year 1997[8] when it got FDA approval in the United States. It was implanted in more than 250 individuals with C5 and C6 tetraplegia and has given satisfaction to its users, been noted safe and had few complications during implant years [3,9]. Disadvantages are that it needs surgery, has high cost and limited functional gain.

If implanting is not an option a surface stimulation system can be used. Surface devices that elicit movements for upper extremity have been developed, such as The NESS H200 system, The Bionic Glove and the ETHZ-ParaCare. [3]

A disadvantage of surface stimulation is accuracy of the electrode placement, where few millimeters can affect the muscle response, making it time consuming taking it off and relocating it often more than once. Also because of atrophy of some muscles, electrode placements can vary a great deal from theoretical locations. Even though optimal electrode places are found for some hand functions, electrode position will vary with time as the muscle changes. A new arm pose can change the relative position of muscles to electrodes as well as muscle development from FES among other factors. [10]

Of particular interest in this paper is the optimal positioning of electrodes that will elicit some lost hand functions in SCI patients with spinal chord injury at level C6-C7. For this purpose we use electrode matrices of different forms. They allow relocation of stimulating sites without moving the electrodes. Various combination forms can also be made from different electrodes in the matrix. Can we reliably find the electrode placements for the desired movements? How fast can we find them? Is there a gain in using electrode matrices in this sense?

In this study only one patient is participating. This reduces the complexity of the work and gives the ability to learn from his special situation but has minimal statistical value.

The future vision for this study is to have an arm sleeve with integrated electrode matrices for a SCI patient, search for the optimal electrodes positions for a particular movement and use it functionally in daily life without any additional help. This would tremendously increase his independency and quality of life.

II. MATERIAL AND METHOD

Subject

The SCI patient is a male of age 47. He had an accident in the year 2003 and was diagnosed with a lesion at the C6-C7 level. He has voluntary shoulder and elbow control as well as wrist extension and flexion. He has minimum voluntary finger movements, is not able to grasp and release everyday objects, but can manage to hook for example a cup on his thumb and use his stiffened fingers to some extent. Some of his finger muscles were considered denervated but they seem to be reinnervated at least partly by the time of this work. They can therefore be stimulated with shorter pulses than 1 ms.

The patient has not undergone a tendon transfer or other surgical procedures that might be an alternative to gain finger function.

Equipment

Self adhesive PALS electrodes¹, 2.5 or 3.5 cm in diameters, were aligned up forming an array on the patient arm within the area of interest for each desired function. Programmable stimulator, Actigrip CS^{®2}, was used in connection with a control box, containing switches to select which electrodes are active and which are not. The control box has three 4x4 switch matrices marked with annotations A1 to D4. Three multi-wire cables lie from the box to be plugged into each matrix, which can contain up to 16 electrodes. The stimulator has 4 programmable channels. Current intensity can be controlled for each of the channels digitally on the stimulator from 0 to 50 mA. The current amount adjusted on the stimulator channel is divided between the activated electrodes in the matrix according to their electrical resistance.

Using the control box, by switching single electrodes on or off, different combinations of electrode patterns can be selected from the matrix while approaching the optimal result for each intended functional task. This can be done during stimulation making the difference clear.

The equipment therefore gives us two parameters to adjust, the electrodes activated and the current intensity. The former parameter changes the location and form of the stimulating site and the latter the current intensity inside the arm tissue.

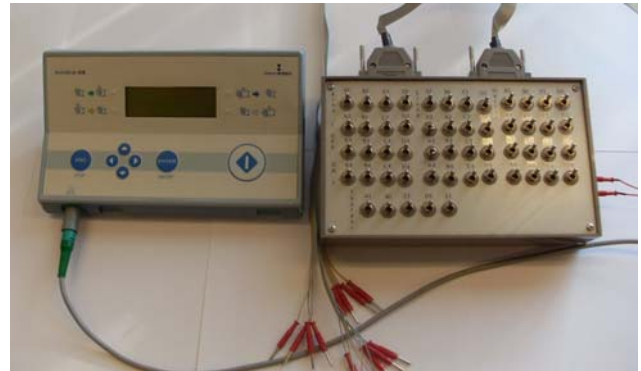


Fig. 1 Actigrip CS[®] stimulator, control box and cables.

Experiment

FES sessions for this research started 70 months after injury. Sessions were one hour of stimulation per day, 5 days a week, with the purpose of finding the optimal stimulation sites and electrodes combinations for some functional hand movements. The main goal is to elicit the five following hand movements for both arms: finger flexion, finger extension, thumb flexion, thumb extension and wrist adduction. The wrist was not stiffened because the patient has fairly good voluntary control of wrist extension and flexion. An electrode matrix (cathode) was located over the muscles that activate each movement. Table 1 lists the muscles needed for each function. One electrode or a small matrix was used to find the anode placement but its location varies, like the cathode placement, between functions.

Each electrode in the matrix was activated, one at a time, and its functional effect considered as a function of stimulating current intensity. Those electrodes capturing a movement closest to the function aimed at were reactivated in combination with others until reaching an optimal pattern. Results from the stimulation patterns were measured visually and documented by two qualified researchers.

¹ Axelgaard Manufacturing Co. Ltd., USA.

² Actigrip CS[®] is a programmable stimulator available from Neuronan A/S, Aalborg, DK.

Table 1 Hand functions

Function	Muscle
Finger flexors	Flexor digitorum profundus Flexor digitorum superficialis
Finger extensors	Extensor digitorum Extensor indicis Extensor digiti minimi
Thumb flexor	Flexor pollicis longus
Thumb extensors	Extensor pollicis longus Extensor pollicis brevis
Wrist adduction	Extensor Carpi Ulnaris Flexor Carpi Ulnaris

One channel was used each time, focusing on gaining one function. Later on all four channels can be combined forming series of four functions. Stimulation parameters were pre fixed and programmed into the stimulator. Frequency was set to 25 Hz, pulse duration 750 μ s and the pulse is asymmetric charge compensated. The pulse intensity was mostly between 10-40 mA.

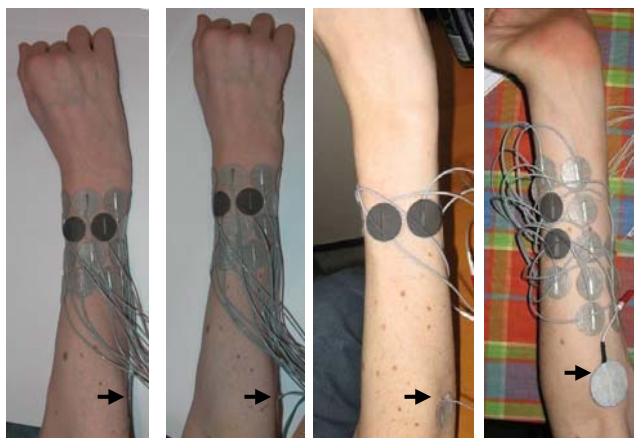


Fig. 2 From left: Wrist adduction before contraction, Wrist adduction after activation of electrodes, Thumb extension, Finger flexion. Active electrodes are shaded dark and arrows point toward anode location.

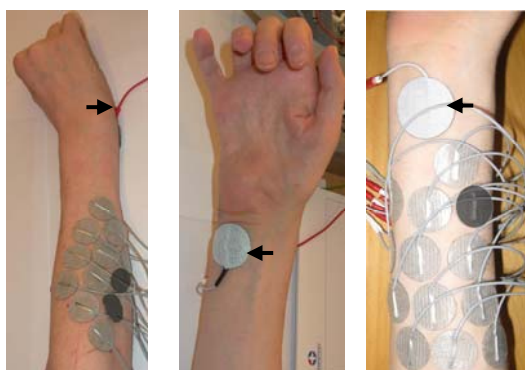


Fig. 3 From left: Electrodes for finger extension, Anode location for finger extension, Thumb flexion.

III. RESULT

The results show that using an electrode matrix, as done in this study, shortens the time used to locate the best stimulation site considerably. The time used to put on all electrodes once in the beginning of the stimulation session is shorter than repeated relocation of an electrode, taking it off and putting it on again. Decrease of the electrode's gel adhesion each time demands moisturizing of the electrode from time to time. In total this adds up and can, depending on how difficult it is to locate the stimulation site, more than double the session time.

Using small electrodes, with a diameter of 2.5 cm, gives a higher spatial resolution than with bigger electrodes but since they are fixed in position the stimulation site is not moved less distance than one electrode diameter each time. This is compensated partly by combining more than one electrode to a single channel of the stimulator. Although the amount of stimulating current going through each single electrode can not be controlled with our equipment and therefore the distribution of current between the electrodes is to some extent random we are able to get more specific movements with a combination, instead of a single electrode. A search for the best combination has to be performed. This does not have to be done by checking through all possible combination of electrodes in the matrix. A comparison showed that doing this search intuitively gives the best combination for a specific movement faster than a systematic search.

Searching for an optimal stimulation site for the same movement, with days or weeks in between, always gave a similar result for an electrode position and similar electrodes combination. This suggests that the geometry of electrical conductivity inside the arm is not changing much from time to time or the positions of the corresponding nerve fibers relative to the electrical field. This stability enables us to start the search next time in a similar setup of electrodes.

Fig. 2 and 3 show the results of electrodes locations and combinations for some finger movements. The dark shaded electrodes (cathode) are the ones that gave the best results, when activated, for each function listed below the figures. The arrows inside the figures point to the location of the anode for a related function.

IV. CONCLUSION

Using an electrode matrix for a single stimulating channel where each electrode can be turned on or off speeds up the search for location of the optimal stimulation site for the movement involved.

Using combinations of electrodes enables a more specific muscle stimulation and hence a more specific movement of the fingers. The smaller electrodes gave a more specific movement where they cover a smaller area, on the patient's arm, and therefore can be located more accurately over a specific muscle.

V. DISCUSSION

The ability to control the current intensity in each electrode separately will enable a more specific stimulation of the muscles and therefore a better movement control. This however will widen the search for the best electrode location where the exact location and the current distribution will be of interest. This will make the search more complicated but generate more accuracy.

ACKNOWLEDGMENT

This work was supported by The Students Innovation Fund and The University of Reykjavik Development Fund. The authors thank them for their support.

REFERENCES

1. Tortora GJ (2002) Principles of Human Anatomy. John Wiley & Sons, Inc, USA
2. O'Dwyer SB, O'Keeffe DT, Coote S, Lyons GM (2006) An electrode configuration technique using electrode matrix arrangement for FES-based upper arm rehabilitation systems. *Medical Engineering & Physics* 28:166-176
3. Ragnarsson KT (2008) Functional electrical stimulation after spinal cord injury: current use, therapeutic effects and future directions. *Spinal Cord* 46:255-274
4. Keller T, Lawrence M, Kuhn A (2007) Textile Neuroprosthesis Garment for Functional Electrical Stimulation. 9th Vienna International Workshop on Functional Electrical Stimulation. Krems, Austria, pp107-110
5. Nathan RH (1979) Functional electrical stimulation of the upper limb: charting the forearm surface. *Med. & Biol. Eng. & Comput.* 17:729-736
6. Bijelic G, Popovic-Bijelic A, Jorgovanovic N, Bojanic D, Popovic D (2004) Actitrode[®]: The New Selective Stimulation Interface for Functional Movements in Hemiplegic Patients. *Serbian Journal of Electrical Engineering* vol 1, no 3:21-28
7. Prodanov D, Marani E, Holsheimer J (2003) Functional Electric Stimulation for sensory and motor functions: Progress and Problems. *Biomedical Reviews* 14:23-50
8. Kilgore KL, Kirsch RF (2004) Upper and Lower Extremity Motor Neuroprostheses, in: *Neuroprosthetics, Theory and Practice*, Horch KW, Dhillon GS, World Scientific Publishing Co., 844-877.
9. Sheffler RL, Chae J (2007) Neuromuscular Electrical Stimulation in Neurorehabilitation. *Muscle Nerve* 35:562-590
10. Bajd T (2006) Surface electrostimulation electrodes, in: *Wiley Encyclopedia of Biomedical Engineering*, Akay M, Hoboken: John Wiley&Sons, 2006, pp 3386-3390

Author: Thordur Helgason
 Institute: University of Reykjavik
 Street: Ofanleiti 2
 City: Reykjavik
 Country: Iceland
 Email: thordurh@ru.is

Force field compensation can be learned without proprioceptive error

A Melendez-Calderon¹, L Masia², M Casadio³ and E Burdet¹

¹Department of Bioengineering, Imperial College London, UK; e.burdet@imperial.ac.uk

²Robotics, Brain and Cognitive Sciences, Italian Institute of Technology, Italy

³Department of Informatics, Systems and Telematics, University of Genova, Italy

Abstract—Robotic devices able to train both reaching and manipulation, involving multiple degrees-of-freedom (DOF), are often large and complex. Could mechanically simpler devices be used to train people, by using only visual feedback and constraining the limb in one or more of the degrees of freedom during task performance? This study examines how this motion guidance influences motor learning in healthy subjects, when virtual kinematic error is provided as visual feedback. The results demonstrate that *i*) virtual learning is possible, though the learning pattern are slightly different than in learning with full proprioception error, and *ii*) the inverse model learned is similar in the two conditions.

I. BACKGROUND OF THE STUDY

Robotic systems have been developed in recent years to train activities of daily living (ADL), e.g. [1]–[3]. To control movements in the space, these systems generally involve a large number of degrees-of-freedom (DOF). For example, ARMin II [3] has six DOF to enable positioning of the hand in the 3D workspace and Gentle/S [2] has 9 DOF to train both reaching and grasping in a reach-grasp-transfer-release sequence. As a consequence, these systems are often large and costly, and hardly compatible with a decentralized use.

Is it possible to train functional tasks using compact robotic devices with limited DOF? To perform arbitrary movements in the 3D space, humans would need at least 6 DOF, even more if hand and fingers movements are considered. However, neuroscience studies have shown that humans generally use regular motion patterns involving few DOF or *synergies* [4], simplifying motion control.

Could we use these motion invariances to simplify the design of dedicated rehabilitation devices? For example, it is well known that, in reaching movements, the hand follows approximately a straight line path from the start to the target [5]. Therefore, ARM Guide [6] has only one active DOF, which considerably simplifies the design and makes the device safer and cheaper relatively to systems moving in 6 DOF.

In a recent study [7], we analyzed typical movements of healthy subjects in three critical ADL: pick-and-place of objects, drinking and eating. The results showed that the hand path remains mainly confined to a vertical plane, and the deviation relatively to this plane is only 5% of the traveled distance [7]. Based on these results, one could assume that lateral deviation is negligible and one could create training devices on which the hand path is constrained to move in a channel. *The question we investigate here is whether/how these lateral constraints influence learning, and if providing*



Fig. 1. Subject performing horizontal arm movements with/without lateral constraint using the *Braccio di Ferro* workstation.

kinematic error is sufficient to promote a reliable feedforward internal model of a real task.

II. LEARNING A VIRTUAL FORCE FIELD

To address this question we let subjects experience both a virtual and a real velocity dependent force field (VF) defined by

$$\begin{bmatrix} F_x \\ F_y \end{bmatrix} = \begin{bmatrix} 0 & 25 \\ -25 & 0 \end{bmatrix} \begin{bmatrix} \dot{x} \\ \dot{y} \end{bmatrix}, \quad (1)$$

where the force applied on the hand \mathbf{F} is in N and the hand velocity $(\dot{x}, \dot{y})^T$ in m/s . In order to compensate for the lack of lateral motion error, our idea is to provide visual feedback of this error, computed from a model of the subject's arm and robot's dynamics.

The paradigm consists in learning the virtual VF while moving along a channel (of stiffness $4000N/m$ and damping $100Ns/m$) when performing horizontal point-to-point arm movements. For this purpose we used the *Braccio di Ferro* (BDF) manipulandum shown in Fig.1 at the Human Behavior Lab of the Italian Institute of Technology.

The channel constrains movement to the y axis, hence proprioceptive feedback on the x deviation is absent, and the VF is basically virtual (vVF). However, the subjects are provided with visual feedback of the estimated hand trajectory as without channel. The simulated trajectory was estimated using a subject-specific arm model (arm dynamics modeled as in [8], [9] and anthropometrical data obtained from tables in

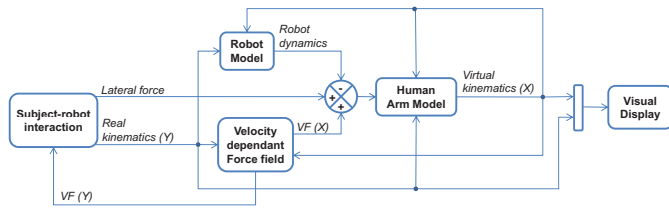


Fig. 2. Diagram of dynamic model implementation.

[10]), a linear second-order robot model, the vVF, the lateral force applied to the channel and the hand position in the y direction, as shown in Fig.2.

Once the subjects have trained in the virtual VF, the channel is removed allowing them to move in the 2D space under a real VF (rVF) and a real Null Field (rNF). This enables us to determine whether subjects learned within the limited DOF conditions, and to observe the after effects of the learning.

III. PROTOCOL

Nine right-handed male subjects, with no history of neurological disease, naive to the device and to the task, were recruited for this experiment. The task consisted in performing unidirectional point-to-point movements of amplitude 20cm in 0.6 ± 0.1 s with the dominant hand from a 2cm diameter origin of to a circular target of the same size. Time started from the moment the subject left the origin and stopped once he reached the target.

Subjects were instructed to perform the movement as straight as possible within the specified time range. Feedback of the trial performance was provided to the subjects indicating them whether they perform “too slow”, “too fast”, or if their movement was successful. A trial was *successful* when the subject moved the hand from the origin to the target within the specified time.

Each subject performed five trials in six phases:

- *Familiarization*: 25 successful movements constrained in a channel and with no vVF but with feedback of the estimated hand trajectory. This, in order to familiarize with the model dynamics without any learning.
- *Learning*: 80 successful movements in a channel and with a vVF, i.e. feedback of the estimated had trajectory with a vVF.
- *Testing real VF*: 25 movements on which 20 were performed in a channel with vVF and 5 pseudo-random catch trials with a rVF.
- *Testing after-effects*: 25 movements on which 20 were performed in a channel with vVF and 5 pseudo-random catch trials with no channel and no rVF.
- *Washout*: 25 successful movements with no channel and no rVF.
- *Baseline (before-effects)*: 25 movements on which 20 were performed with no channel and no rVF, and 5 pseudo-random catch trials with rVF.

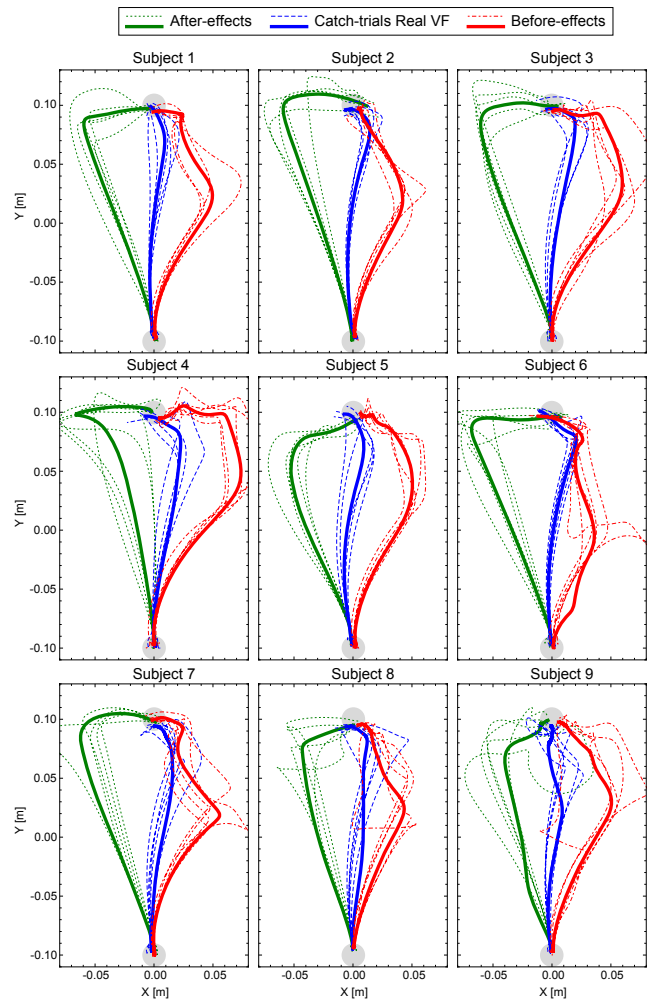


Fig. 3. Comparison between (red) before-effects, (green) after-effects and (blue) catch trials of real VF after learning the virtual VF. The thick lines represent the mean trajectory of each block.

IV. RESULTS

Catch trials on which the channel was removed and a rVF was applied to the subjects after having learned the virtual VF suggest that subjects were able to learn compensating for the VF in a lateral constrained condition. This is shown by the trajectory in rVF after having learned in vVF, which is almost straight as illustrated in Fig.3.

Fig.4 shows the learning phase of a representative subject, and it can be observed that the learning rate is not as fast as it would be when learning in normal conditions (e.g. [11]). Nevertheless, this learning led to a fairly good inverse model of the real task dynamics as suggested by the catch trials during the testing phase (Fig.5).

A comparison between the angular aiming error of the last 10 trials of learning phase and the catch trials of rVF of all subjects showed there was no statistically significant difference ($p=0.17$) between the virtual and the real environments. Subjects reported to be unaware of both rVF catch trials and

of being laterally constrained during the learning phase with vVF.

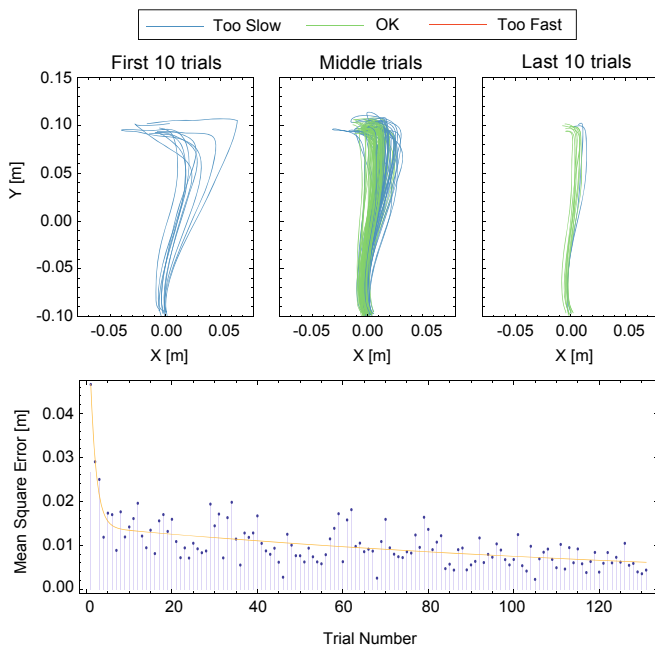


Fig. 4. Learning session of a representative subject in the virtual VF.

Velocity profiles of the all catch trials in rVF conditions showed that in some cases there is slight movement correction at approximately 625ms after initiation of the movement. This happened in approximately 54.54% of all the experiment catch trials in rVF conditions. These could be due to inconsistencies between the model and the real arm-robot dynamics.

We are currently performing complementary experiments for learning in multiple directions using virtual kinematic error as well as the effect of retention of learning when providing kinematic error.

V. ACKNOWLEDGMENT

This work is funded in part by the EU-FP7 grant HUMOUR, IIT and Imperial College. A Melendez doctoral studies are sponsored by CONACYT-Mexico.

REFERENCES

- [1] L. Masia, H. I. Krebs, P. Cappa, and N. Hogan, "Design and Characterization of Hand Module for Whole-Arm Rehabilitation Following Stroke," in *IEEE/ASME Transactions on Mechatronics*, vol. 12, pp. 399-407, 2007.
- [2] R.C.V. Loureiro and W. S. Harwin, "Reach and grasp therapy: Design and control of a 9-DOF robotic neuro-rehabilitation system," *Proc. 10th Int. Conf. on Rehabilitation Robotics*, Noordwijk, The Netherlands, 2007, pp. 757-763.
- [3] T. Nef, M. Mihelj, G. Kiefer, C. Perndl, R. Muller and R. Riener, "ARMin Exoskeleton for arm therapy in stroke patients," *Proc. 10th Int. Conf. on Rehabilitation Robotics*, Noordwijk, The Netherlands, 2007, pp. 68-74.
- [4] N. Bernstein, *The co-ordination and regulation of movements*, Pergamon, London, 1967.
- [5] P. Morasso, "Spatial Control of Arm Movements," *Experimental Brain Research* 42: 223-227, 1981.

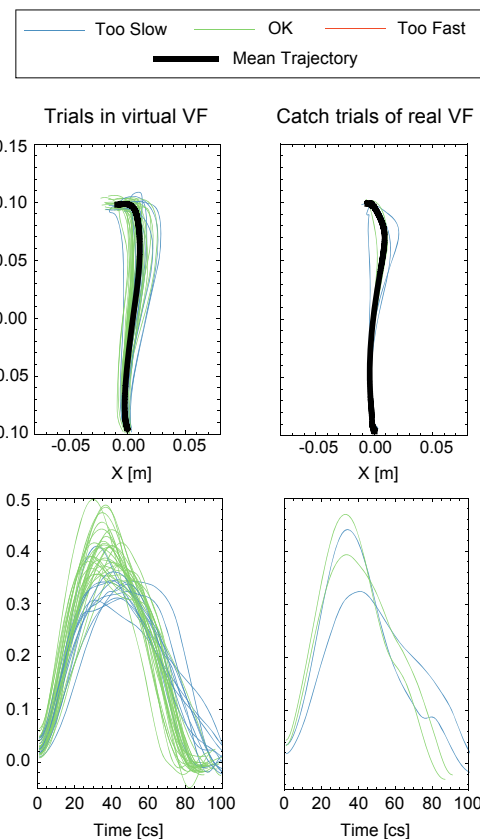


Fig. 5. Comparison between trials in virtual VF and catch trials of real VF of the same subject as in Fig.4 during the testing phase.

- [6] L. E. Kahn, W. Z. Rymer, and D. J. Reinkensmeyer, "Adaptive assistance for guided force training in chronic stroke," in *Proceedings of the 26th Annual International Conference of the IEEE Engineering in Medicine and Biology Society*, San Francisco, CA, USA, pp. 2722-2725, 2004.
- [7] C.F. Yeong, A. Melendez-Calderon and E. Burdet, "Analysis of Pick-and-place, Eating and Drinking Movements for the Workspace Definition of Simple Robotic Devices", submitted to *IEEE International Conference on Rehabilitation Robotics (ICORR)*, 2009.
- [8] Burdet, E., Tee, K., Mareels, I., MILNER, T.E., Chew, C., Franklin, D., Osu, R. and Kawato, M. "Stability and motor adaptation in human arm movements". *Biological Cybernetics*, 94, 20-32, 2006.
- [9] Tee, K. P., Burdet, E., Chew, C.M. and Milner, T.E. "A model of force and impedance in human arm movements". *Biological Cybernetics*, 90, 368-375, 2004.
- [10] Winter, D.A. "Biomechanics and motor control of human movement", John Wiley & Sons, 2004.
- [11] Franklin DW, So U, Burdet E, and Kawato M. "Visual Feedback Is Not Necessary for the Learning of Novel Dynamics". *PLoS ONE*, 2007.

Implantable Wireless Cortical Recording Device for Primates

D. A. Borton¹, Y.-K. Song¹, W. R. Patterson¹, C. W. Bull¹, S. Park¹, F. Laiwalla¹,
J. P. Donoghue², and A. V. Nurmikko¹

¹ Brown University/Division of Engineering, Providence, Rhode Island USA

² Brown University/Division of Neuroscience, Providence, Rhode Island USA

Abstract— We report on the performance of a wireless, implantable, neural recording platform. A multitude of neuroengineering challenges exist today in creating practical, chronic multichannel neural recording systems for primate research and human clinical application. Specifically, a) the persistent wired connections limit patient mobility from the recording system, b) the transfer of high bandwidth signals to external (even distant) electronics normally forces premature data reduction, and c) the chronic susceptibility to infection due to the percutaneous nature of the implants all severely hinder the success of neural prosthetic systems. Here we detail a scalable 16-channel microsystem that can employ any of several modalities of power delivery (wire, radio frequency induction, and a photovoltaic energy converter) and data transmission (wire, and transcutaneous infrared laser transmission). Data is reported from a recent sub-chronic (~30 day) rhesus macaque MI implantation.

Keywords— Neural Interface, Brain Computer Interface, Neural Prosthetics

I. INTRODUCTION

Presently, one demonstrated means to access a collection of single neural cells for deciphering their role in behavior is by using invasive arrays of microelectrodes that pick up the electrical activity of local neural circuits. Based on recent advances, including first preclinical human trials [1], there is now the prospect of direct electronic communication with the brain, motivated by compelling medical rationale e.g. for neuromotor prostheses. Neuroscientists and engineers together have made remarkable progress in unraveling the machinery, and subtlety, of the primate brain. From this has emerged a fascinating contemporary technical and ethical challenge: Can we turn thoughts into actions? Extraordinary work has been done showing that indeed this type of bridge *can* be made, and functional actions *can* be deciphered from limited information extracted from the brain [1], [8], [10]. However, the question remains as to how wide the lanes of this bridge can and should be. Truly understanding the brain will require sensing across a vast range of temporal and spatial scales (low frequency potentials, 1-40 Hz, to action potentials – LFPs to spikes). This

paper selectively highlights our current research, which aims at developing a wireless link to the brain via implantable active microchips.

There are millions of patients who suffer from serious neurological insult and illness whose quality of life is substantially compromised even while the brain itself is completely (or at least mostly) functional. Society, and the individual, stands to have much to gain from the development of devices that can directly record and translate cortical signals into functional output. This translation has been the drive behind the neuromotor prosthesis (NMP) field and is the fundamental reason for the development of the discussed microsystem.

Implantable cortical NMP systems present many challenges, including the development and integration of ultra-low-power microelectronic chips to the sensing multielectrode array (MEA), the modality of on-board broadband telemetry, and power delivery as such a system necessitates active electronics. Almost paramount to these challenges is the encapsulation and biocompatibility of an electrically active, multi-element implant. In this paper, we describe our approach and development status towards these challenges, highlighting design choices and recent results of wireless data transmission from an implanted microsystem in a fully awake rhesus macaque monkey.

II. ARCHITECTURE AND FABRICATION

Substrate: Flexibility, processability, and biocompatibility are of great importance when choosing a substrate to build an implantable microsystem onto. In addition, due to the sensitivity of the cortex to temperature change and intracranial volume constraints (we limited ourselves to 1°C and 1 mm in thickness above cortex), we needed to take into account the distribution of components when designing the substrate. We employ a “two island” concept where the sensing components are separated from the digitizing and telemetry components. The “frontend” (intracranial) section contains only the amplifier and the electrode array. A thin interconnect bridges the frontend to the “backend” (atop the skull), which, is where digitization and telemetry occurs.

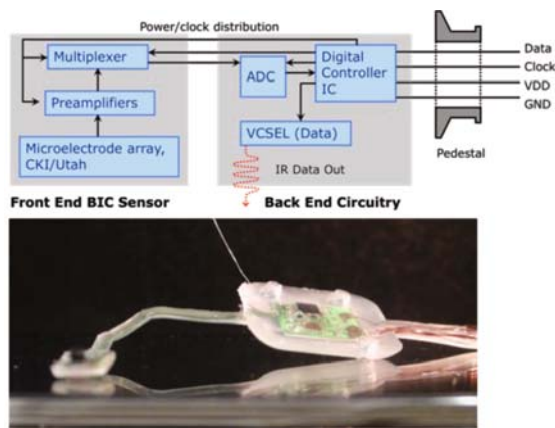


Fig. 1 A Schematic of Brain Implantable Chip with pedestal and image of system encapsulated in PDMS for saline testing. The schematic (top) shows the data flow from the MEA sensor, through the amplifier and digitizer, and eventually bifurcated in the controller to be delivered wirelessly via IR and wired on the data-out line.

For this microsystem substrate itself, we chose to use Kapton (a polyimide – constructed at Microconnex, inc. Seattle, WA). At a thickness of 0.0005”, CuNiAu traces of 0.001”, and double-sided lamination (Kapton) of 0.001” each, the entire substrate achieved a very flexible, as well as durable, structure.

Amplifier and Integration with MEA: We have developed an ultra-low power, easily integrateable CMOS preamplifier array with integral multiplexing and measured noise levels (in saline) of $9 \mu\text{V}_{\text{RMS}}$. This 16-channel, fully scalable CMOS amplifier array has an average gain of 44 dB, bandwidth from 10 Hz to 7.3 kHz, and an average power consumption of $52 \mu\text{W}$ /preamplifier (see **table 1**).

This chip was designed specifically to be integrated directly on the back of the MEA (Blackrock inc., Salt Lake City. UT) in order to minimize the distance raw analog

Table 1 Power consumption of BIC components. Power consumption of components in the BIC microsystem based on 3.3 VDC delivered to the system. The overall amplifier power consumption here is very low, compared to the $80 \mu\text{W}$ per amplifier presented by Harrison [5].

Component	Consumption	Unit
ADC (AD7495)	4.5	mW
Preamplifier (M4b)	52	μW
Amplifier overall	1.3	mW
Controller	5	mW
VCSEL	2	mW
Total	12.32	mW

signals must travel before amplification. We have chosen to use a flip-chip integration strategy based on a specific conductive epoxy (H20E, Epoxy Technology, Inc.) for the electrical interface between the microelectrode array and the CMOS chip. Conductive silver epoxy is applied to the pads ($80 \mu\text{m} \times 80 \mu\text{m}$) of the CMOS chip by a pin stamping technique so that approximately $150 \mu\text{m}$ diameter and $50 \mu\text{m}$ high epoxy dots are deposited with $<10 \mu\text{m}$ placement precision. The 16-element MEAs were bonded to the CMOS chip using a high accuracy, flip-chip bonder (RD Automation, Inc, model M9) with “zero pressure” epoxy bump bonding. The die bonder incorporates an optical auto-collimator, a critical component to ensure absolute parallelism between the entire microelectrode array and amplifier chip during mating.

Infrared Telemetry: The flow of data in the microsystem begins in the amplifier. The output is then multiplexed in the time domain and sent to the backend through metal strip lines on the flexible Kapton substrate (interconnect bridge) connecting the frontend and backend. It is transformed into a serial digital stream by the ADC on the backend circuitry, and then converted into pulses of light by a vertical cavity surface-emitting laser (VCSEL) controlled by the digital controller IC. The light pulses are received in free space by a Silicon PIN photodiode (S6967 from Hamamatsu Inc.), which converts the pulse coded modulated light signal to a digital stream of electrical pulses (a TTL signal) for real-time reconstruction and storage of the neural signal recordings in an PC though a custom designed digital interface. Transmission through primate skin causes scattering, but the photodiode is still able to pick up the digital stream when placed within $\sim 2 \text{ mm}$ of the skin surface.

Encapsulation: The entire microsystem of **fig. 1**(bottom) is presently encapsulated in polydimethylsiloxane (PDMS) for electrical isolation and mechanical flexibility. Surgical implant considerations require careful control of PDMS thickness to maintain flexibility in the interconnect bridge. In addition, we must prevent capillary forces from coating the electrode array with PDMS. For images of the structure after encapsulation, see Refs. [6], [7]. The main functions of the encapsulation are to ensure (i) that electrical leakage current to the adjacent tissue from the system is minimized, and (ii) ionic leakage from the tissue to the electronic components is less than 10pA . For chronic implant applications, this presents a formidable challenge for all researchers in the field of implantable neural prosthetics. We view our initial approach, using PDMS (NuSil R-2188), as a useful starting pathway at least for sub-chronic or short-term (1 – 3 months) in-vivo animal testing. In addition, we have de-

signed and implemented an encapsulation test unit (ETU), which simulates the topographical, thermal, and electrical stresses put on the encapsulant, to test leakage current and component functionality over extended periods of soaking.

Scalability: While the system expressed here attains 16 channels (one channel, 16, carrying the frame synchronization word to align the received data stream), it has been designed from the outset to be expandable without major redesign – specifically for a 100 channel MEA platform (work under way). A 4 x 4 MEA allowed for simpler integration and faster turn-around time of devices. However, it is clear from previous work that more neural units, and in effect, more channels, are required to accurately decode intention in a high-dimensional space, such as in representing wrist and arm joint angles. Beyond increasing the number of channels for a given MEA, the layout of our BIC system also allows, in principle, its extension to a number of cortical ‘frontend’ implants (various recording sites) which are connected to a common subcutaneous backend telemetric units.

III. IMPLEMENTATIONS

Two variations of the microsystem have been fabricated to serve specific tasks. In addition, several iterations of the “implantable primate microsystem” have been used in a rodent model to validate the frontend insertion parameters, which are in fact different than published values for the pneumatic insertion of just a MEA with wire bundle (higher pressure, 25-30 psi).

External Screw-top Microsystem: For the evaluation of the BIC electronics and functionality, it made sense to develop a system that could take input directly from the NeuroPort implant (passive 100 electrode array with pedestal connector – see Refs. [1] and [8]). This would allow us to test the performance of all critical components (signal-noise levels of the amplifier, wireless telemetry, etc.) on signals from a primate with a well-characterized implant. The system we developed is called the Brown Neurocard (BNC) and has been recently detailed in [9]. It has been used on 3 different primates with great success. This device has and will continue to serve as an excellent test platform with direct access to neural signals without reimplantation of the primate.

Implantable Primate Microsystem: As shown in **fig. 1** (bottom), the implantable primate microsystem is encapsulated in PDMS and has an “L” shape, which was designed to fit the cortex of the primate in study. The electrodes of the microsystem frontend were inserted ~1 mm into the arm

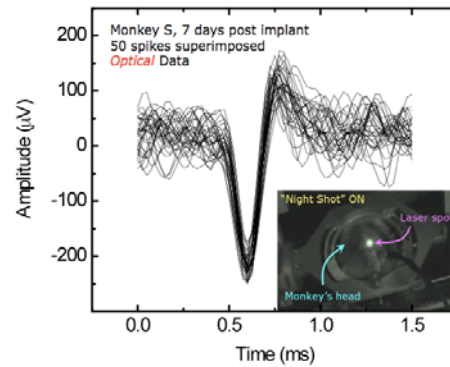


Fig. 2. Superimposed traces recorded from fully implanted neural sensing microsystem with transcutaneous optical data link, 7 days after implantation. A maximum of channels recording occurred on day 11 with 12 of 15 channels showing spikes. Total data above collected over 15 seconds.

region of primary motor cortex (MI). The interconnect bridge was tunneled through the craniotomy, allowing the backend to sit atop the skull where it was fixed with titanium screws. A titanium pedestal was used to allow power, clock and ground lines to enter the system and to allow data lines to exit (data lines used for verification of optical data).

All data reported here was recorded from the primate microsystem and was recorded via transcutaneous optical link from an implanted device.

IV. RESULTS

Seven days after implantation, we began to see spiking activity on several channels (one in particular is shown in **fig. 2**). After the first day of recording, the number of channels with spiking units varied from 8-12 (**fig. 3**). In addition, several channels showed more than one unit on a given

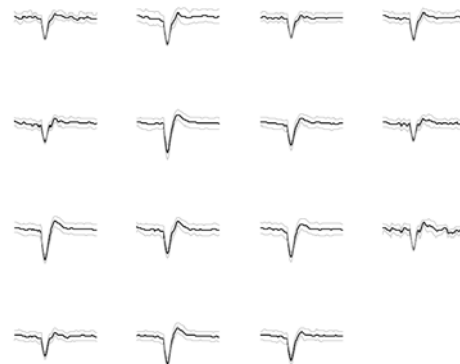


Figure 3 Overlays (from 20-60 spikes) from all 15 channels recorded wirelessly from primate motor cortex while primate performs grasping task.

session. It was unclear and remains unverified if the same units were being recorded on each channel throughout the two-week period. For example, on day 8 channel 14 showed clear activity while on day 9 it presented no activity. This variation is most likely due to settling of the MEA in the cortical tissue

Once initial characterization was completed of the microsystem, the primate was trained to sit in a chair and grasp. During this exercise, we recorded neural activity over 7 trials. The spiking activity correlated well with the timing of the movement – raster plots shown in **fig. 4**. These results show clearly that (i) our system is able to transmit broadband data transcutaneously (wirelessly) out to a receiver, and (ii) that the data being transmitted is in fact neural in origin and movement dependant.

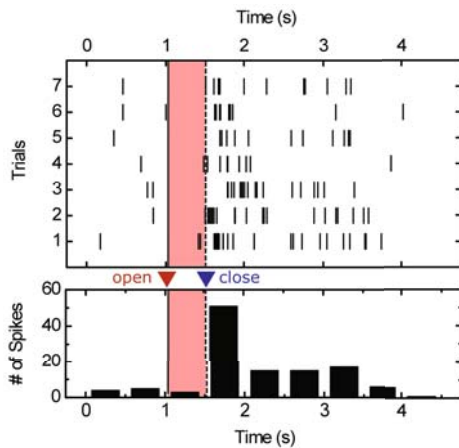


Figure 4 Raster (top) and histogram (bottom) of grasp event (red, shaded if black and white print). This particular neuron appeared to be particularly correlated with grasp relaxation, i.e. when primate released its grip.

V. CONCLUSION AND CONTINUED WORK

While reporting progress where an implantable microsystem has been tested in a non-human primate on the order of 1 month, many challenges remain on the path to a fully implantable, neural processing platform for chronic, long-term human use. Among these are the encapsulation (packaging) of the implantable units to ensure extended animal and patient safety and biocompatibility. Specifically for the BIC microsystem reported here, we are presently developing surgical and post-operation procedures for our tabletop tested device with transcutaneous inductive RF power delivery to complete the truly wireless cortical neural interface in non-human primates and eventually human patients.

ACKNOWLEDGMENT

The authors would like to thank John Mislow M.D., Ph.D. for his surgical and clinical support, Leigh Hochberg M.D., Ph.D. for his guidance, John Simeral Ph.D. and Naveen Rao for their decoding support, as well as James Harper III, V. M. D., and the veterinary staff for their support. Work supported by the National Institute of Health (NIBIB and NCMRR/NICHHD) - Bioengineering Research Partnership Program (1R01EB007401-01), the Office of Naval Research - Neuroengineering Program (N0014-06-0185), and the National Science Foundation - Biophotonics Program (0423566).

REFERENCES

- Hochberg L, Serruya M, Friehs G, Mukand J, Saleh M, Caplan A, Branner A, Chen D, Penn R, Donoghue J (2006) Neuronal ensemble control of prosthetic devices by a human with tetraplegia. *Nature* 442: 164-171.
- Bai Q, Wise K (2001) Single-unit neural recording with active microelectrode arrays. *IEEE Trans. Biomed. Eng.* 48(8):911-920 .
- Mojarradi M, Binkley D et al (2003) A miniaturized neuroprosthesis suitable for implantation into the brain. *IEEE Trans. Neural Syst. Rehabil. Eng.* 11: 38-42.
- Rizk M, Obeid I, Callender S, Wolf P (2007) A single-chip signal processing and telemetry engine for an implantable 96-channel neural data acquisition system. *J Neural Eng.* 4: 309-321 .
- Harrison R, Watkins P, et al (2006) A Low-Power Integrated Circuit for a Wireless 100-Electrode Neural Recording System. *International Solid State Circuits Session 30: Silicon for Biology.*
- Patterson W, Song Y-K, et al (2004) A Microelectrode Microelectronic Hybrid Device for Brain Implantable Neuroprosthetic Applications. *IEEE Trans. Biomed. Eng.* 51:1845-1853.
- Song Y-K, Patterson W, et al (2005) Development of a Chipscale Integrated Microelectrode/Microelectronic Device for Brain Implantable Neuroengineering Applications. *IEEE Trans. Neural Rehabil. Eng.* 13:220.
- Georgopoulos A, Kalaska J, et al (2003) On the relations between the direction of 2-dimensional arm movements and cell discharge in primate motor cortex. *J. Neuroscience*, 2 (11):1527-37.
- Song Y-K, Borton D, et al (*in press*) Active Microelectronic Neurosensor Arrays for Implantable Brain Communication Interfaces. *IEEE Trans. Neural Rehabil. Eng.*
- Chestek C, Kier R, et al (2008) HermesC : RF Wireless Low-Power Neural Recording System for Freely Behaving Primates. *IEEE Circuits and Systems* : 1749-1755.
- Jackson A, Moritz C, Fetz E (2007) Correlations between the same-motor cortex cells and arm muscles during a trained task, free behavior, and natural sleep in the macaque monkey. *J Neurophysiol* vol. 97:360-374.

Author: David A. Borton
 Institute: Brown University
 Street: 182 Hope Street
 City: Providence, Rhode Island 02912 USA
 Email: david_borton@brown.edu

Is Posturography a Candidate for a Vigilance Test?

T. Schnupp¹, A. Schenka¹, D. Edwards², J. Krajewski³ and M. Golz¹

¹ Faculty of Computer Science, University of Applied Sciences Schmalkalden, Schmalkalden, Germany

² Machine Research, Caterpillar Inc., Peoria, Illinois, USA

³ Work and Organizational Psychology, University of Wuppertal, Germany

Abstract— Studies exhibit that between 20 and 40% of traffic accidents in Germany are related to driver's hypovigilance. Hypovigilance, as stated by some authors, effects driver's performance in a similar way as alcohol consumption does. But unlike blood alcohol level testing up to now there is no mobile, non-invasive vigilance test with low test durations. Posturography - a method to assess the balance control system quantitatively - may provide the possibility for such a vigilance test. In this paper we will investigate the discriminatory abilities of posturography using data recorded in conjunction with overnight driving simulation experiments commissioned by Caterpillar Machine Research. A total of 19 young adults volunteered to participate in balance assessment. Experiments included a driving simulation with repetitive assessment of subjective self-rating while driving using Karolinska Sleepiness Scale. As objective vigilance score the standard deviation of lateral position was chosen. Subjective and objective vigilance scores and the Time-Since-Sleep are utilized as labels for discriminant analysis. Two kinds of features were extracted from posturographic recordings. Among others, parameters of diffusion plot and sway density analysis were utilized as features in time domain. As spectral domain features power spectral densities were estimated and averaged in empirically optimized equidistant frequency bands. The usefulness of posturography as vigilance test was evaluated by the mean test set error of computational intelligence algorithms including artificial neural networks and Support-Vector Machines (SVM). These algorithms can be regularized between local and global decision finding. SVM using Gaussian kernel function achieve error rates of 8.8% (leave-one-out cross-validation). Considering some concerns regarding reliability and validity we conclude that it is possible to discriminate patterns of different vigilance levels using posturography.

Keywords— Posturography, Vigilance, Fatigue, Support-Vector Machines, Computational Intelligence

I. INTRODUCTION

Human factors are a major cause for traffic accidents. It is expected, that 93.5% of all incidents are related to human factors. Beside others, hypovigilance - the lack of being capable to maintain attention during monotonous situations and react-

ing properly to weak stimuli - is one of these human factors. It can be deduced from accident reports that hypovigilance plays a role in at least 25% of all accidents. Means to counter hypovigilance in road traffic can be grouped into three types: educational, legal and technical means. Educational means are the most promising approach in order to raise people's awareness concerning the risks of driving impaired. The effort put into these means - besides some commonly event-related medial attention - is limited. From a legal point of view driving within an impaired state is prohibited. But law enforcement needs a quick, mobile and reliable vigilance testing method similar to the (blood) alcohol level testing. Vigilance tests are one possible technical mean supporting legal ones. Up to now no vigilance test suitable for comprehensive field usage is available. Among other reasons usual trial length is too long (e.g. psychomotoric vigilance test, PVT). In addition to enforcing legal means, the development of objective vigilance measures supports educational efforts. Objective measures help justifying subjective awareness. On a wider scope, vigilance testing can support individual alertness management providing circadian pace markers. In recent year's publications have shown that posturography is insensitive to sleep deprivation and hypovigilance [1][2]. Posturography utilizes a force platform for non-invasive body sway measurements, providing one possibility to develop a vigilance test that meets the criteria mentioned. Data recorded in a pilot study aside overnight driving simulation experiments was used for evaluating the discriminatory abilities of posturography. Experiments were commissioned by Caterpillar Machine Research in order to benchmark different Fatigue Management Technologies [3]. Beside the Time-Since-Sleep (TSS), objective and subjective hypovigilance scores were used as class labels. The subjective hypovigilance scores are obtained using Karolinska Sleepiness Scale (KSS) reflecting the level of perceived sleepiness. Whereas both, the standard deviation of lateral lane position (SDLat) and posturography, are measures concerning physiological sleepiness. Benchmarking results are obtained using several classifiers with each discriminatory task, including Support-Vector Machines (SVM) and Learning Vector Quantization (LVQ).

II. EXPERIMENTS

Study Design: Posturography recordings were obtained alongside overnight driving simulation experiments. A total of 19 (13 males, 6 females) young, healthy volunteers, aged 18 to 26 years, mean age 22.0 ± 2.3 years, without known diseases or impairments of their visual, proprioceptive or vestibular system participated in this study. Adherence to an instructed sleep/wake regime prior to experiments was observed by actigraphy. Each subject conducted eight one hour lasting test-sessions. The temporal distribution can be obtained from Fig. 1. Sessions included 40 minutes of night-driving simulation, followed by two vigilance tests. The standard deviation of lateral lane position was utilized as an objective hypovigilance measure [4]. During driving simulation driver's KSS self-rating was assessed in three minute intervals. Driving performance was recorded by different variables including SDLat.

Posturography: In order to differentiate between test-sessions one to eight of the FMT study and sessions of the posturographic experiments latter are labeled A to C. Two posturographic trials were performed each prior to first (session A), between fourth and fifth (session B) and after last FMT test-session (session C, see Fig. 1). In the first trial without any impairment of visual feedback ("eyes open", EO) subjects were instructed to focus a marker on eye level in a distance of approximately two meters. The second trial was performed after a short break where altered instructions were given. With lights turned off subjects had to close the eyes, disabling visual feedback ("eyes closed", EC). In both trials 120 second stabilograms have been recorded. Subjects were instructed to stand upright, hands folded in a way that the tips of thumbs are placed on the navel. This way, a relatively fixed pose for all measurements can be achieved without utilizing Romberg pose. The exhausting effect of Romberg pose was expected to superimpose the effects of hypovigilance, e.g. by causing aversions. Possible implications of this decision will be discussed within the conclusion section. A self-developed 3-point force platform with 1506 Hz sampling rate was utilized. Quality control measurements following an standard procedure were performed and passed.

III. METHODS

Preprocessing: Acquired sensory signals are transformed into stabilograms – a bivariate trajectory representing body sway in anterior-posterior (AP) and medio-lateral (ML) direction. In order to raise the number of patterns available for generalization, stabilograms have been segmented. Based on experience two different segmentation lengths (SL) were benchmarked. Therefore each posturographic measurement

lead to six segments with 20 seconds length or three segments with 40 seconds respectively.

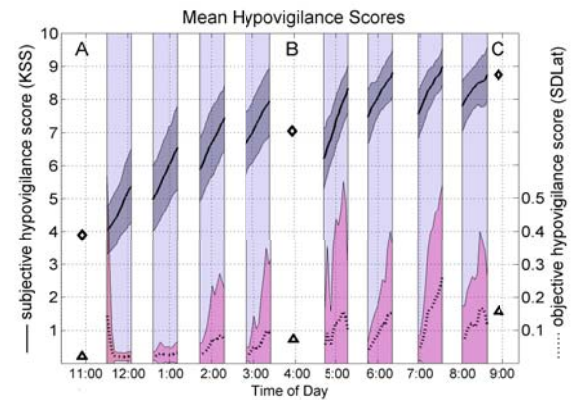


Fig. 1: KSS as well as SDLat values averaged over all subjects show clear Time-On-Task and Time-Since-Sleep effects. Diamonds and pyramids indicate the time of posturographic recording sessions. Marker's ordinate values represent the associated subjective respectively objective hypovigilance scores. Light colored areas indicate ± 1 SD.

Feature Extraction: Two different sets of features have been derived from recorded stabilogram components. The first feature set consists of 23 time-domain features, including global, structural and physical parameters of balance. This set is a well-performing selection evaluated during earlier experiments. Time-Domain features include analysis of diffusion plot [5] and sway density curve [6]. Forsman et. al [2] identified the critical time interval (obtained by analysis of the diffusion plot) to be among the most significant single features for the regression of subject's TSS. The second set contains spectral domain features. In earlier examinations we have shown that time domain features are outperformed by those from spectral domain [7]. Power spectral densities (PSD) have proven to be reliable and robust measures of balance. PSD values are estimated and averaged in equidistant frequency bands. This reduces the dimensionality of the classification problem which is beneficial for some classifiers (e.g. LVQ). The amount of information lost by band averaging can be regarded as low, because adjacent frequency bins correlate significantly. Parameters of band averaging were optimized empirically utilizing OLVQ1 with 25 repetitions of random subsampling validation (80:20 partitioning). An optimal bandwidth was evaluated at 0.1 Hz. A lower cutoff frequency of 0 Hz and an upper cutoff at 11 Hz performed best (e.g. Fig. 3).

Data- & Feature-Fusion: In both trials (EO, EC) stabilograms were recorded. Each stabilogram consists of two components: AP and ML body sway. Best results have been observed by fusing all four sources into a single feature-vector (Fig. 3). Within other fields of biosignal analysis the

fusion of different feature extraction methods show a significant increase in classification performance. Due to the pilot character of this study comprehensive optimization in order to maximize classification performance was not a primary objective of this work. Hence the fusion of time-domain features together with those from spectral domain and the usage of further methods (e.g. wavelet-decomposition or state-space features) was omitted.

Label Generation: Patterns obtained from posturographic recordings were separated into classes by four means. As a first approach three classes according to EO/EC trials, grouped by subject's TSS were defined. Using this separation it is possible to evaluate changes in EO vs. EC discrimination performance over night. A hypovigilance related influence on posturographic data may affect the features supporting discrimination between EO and EC trials. One possible expectation is, that hypovigilance alters the effectiveness of visual feedback interpretation, lowering the influence of visual feedback on postural equilibrium. Therefore the differences between EC and EO recordings is reduced, increasing the difficulty of EO/EC discrimination. This can be regarded as an indication for circadian rhythm based effects on human balance and would therefore endorse posturography as a mean of vigilance testing. In the following steps patterns were classified according to associated vigilance scores. The first approach utilizes TSS as labels. In the second approach SDLat was calculated for each driving session. Session A was linked to subject's SDLat during the first driving simulation task. Session B was associated with the average SDLat value from the fourth and fifth driving session. The last session C was linked to the SDLat measured during the eighth driving session. As expected to be demanded by later users of a vigilance test the associated labels were binarized. Binarization was obtained by applying a threshold of 17.4%. Samples linked to an objective score equal to 17.4% were omitted (less than 4%), leaving two equally sized classes. As a third vigilance score the subjective vigilance rating was used for pattern labeling. Subjective vigilance scores are obtained utilizing KSS prior to posturographic recordings. The binarization threshold was fixed to a KSS value equal 7. For both measures lower values are regarded as "mild hypovigilance", whereas higher values are regarded as examples of "strong hypovigilance". Omitting samples with an KSS score of exactly 7 (less than 4%) lead to two equally sized classes.

Discriminant Analysis: Distribution of values for single features shows a non significant shifting of mean values over night having a high variation and overlapping between different TSS labels (e.g. Fig. 2). Multivariate analysis utilizing soft computing may be able to generalize a function discriminating different levels of hypovigilance. Different methods

were applied. As a representative for global decision finding Fisher's Linear Discriminant Analysis (LDA) was utilized. A purely local decision was obtained by the k-Nearest Neighbor algorithm (kNN) with k set to 1. Regularization between a global and local decision was achieved by varying k, using LVQ (especially OLVQ1) with a empirically optimized number of prototype neurons and by Support-Vector Machines (SVM) with empirically optimized hyper parameters. Testset error rates are obtained utilizing 25 fold random subsampling with an 80:20 separation (LDA, kNN, OLVQ1) and fast leave one out validation estimation (SVM, [8]) respectively.

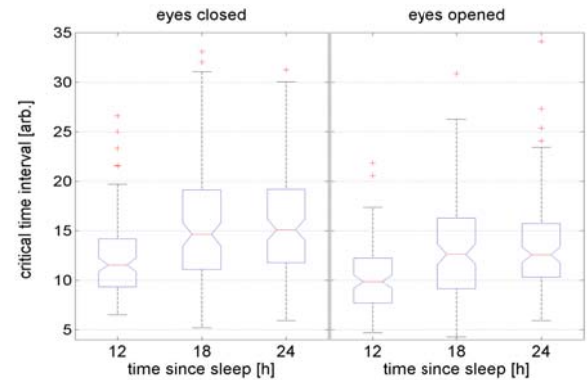


Fig. 2: Box plot of the critical time interval of the change from open-loop to closed-loop control versus Time-Since-Sleep. The increase of mean values between the first and second session is significant.

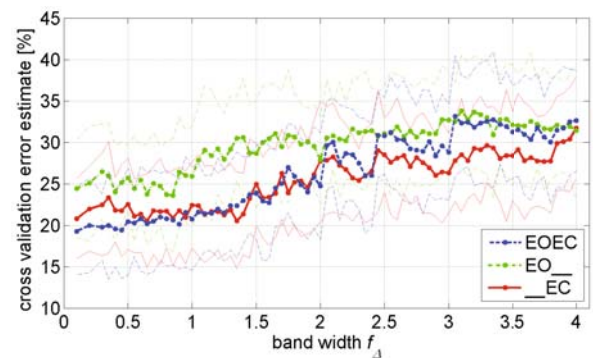


Fig. 3: Mean and standard deviation of test errors versus width of spectral bands. Three different PSD feature sets were used (see text). This is an example of the empirical optimization of free parameters which indicates low values of the band widths are optimal.

IV. RESULTS

Discriminant Analysis - EO vs EC: Results show that the EO vs. EC discriminatory performance reduces between session A and B (e.g. 30.7 ± 6.3 to $35.8 \pm 6.6\%$, PSD features,

SL 20s). From other variables (e.g. SDLat, KSS) can be derived that subjects hypovigilance rises significantly between these sessions. Despite hypovigilance measure values rise significantly between Session B and C, no further drop of classification performance can be observed (e.g. 35.8 ± 6.6 to $36.1 \pm 5.7\%$, PSD features, SL 20s). One possible explanation is that the last session is subjected to different effects. The most prominent ones are circadian rhythm and motivation due to the end of driving experiments. These effects may superimpose those of hypovigilance.

Discriminant Analysis - Hypovigilance Scores: A subset of the final results is shown in Table 1. The most prominent result of discriminatory analysis according labels defined by hypovigilance scores is that LDA fails in all trials indicating that hypovigilance discrimination cannot be regarded a linear separable problem. Finding a general function to discriminate between samples from session A and B was realized with acceptable error rates ($8.8 \pm 0.0\%$, SVM). The difference between subject's hypovigilance level in session A and B is strong, with A being a quite alert state (Time-Since-Sleep: 12 hours, additional activation due to unknown laboratory situation) and B being a state near to the circadian trough. Session C is biased by alerting effects (e.g. end of experiments). All-in-all the obtained error rates are unsatisfying and have to be improved significantly in order to utilize posturography as a vigilance test.

Table 1: Mean and SD of Test Set Error Rates

Results obtained by discriminant analysis regarding different hypovigilance scores (class labels).

Set	Classifier	KSS	SDLat	A vs B
PSD SL 20s	LDA	50.3 ± 6.7	48.3 ± 5.4	48.8 ± 7.2
	OLVQ1 (n)	26.5 ± 3.9 (120)	22.9 ± 4.2 (165)	16.3 ± 5.8 (155)
	SVM (C; γ)	21.9 ± 0.0 (8; -2.25)	18.8 ± 0.0 (0.875; -2.75)	10.1 ± 0.0 (1.0; -2.5)
	kNN (k=opt)	14.0 ± 33.9 (199)	20.0 ± 9.3 (1)	17.2 ± 10.0 (1)
	kNN (k=1)	27.4 ± 8.2	20.0 ± 9.3	17.2 ± 10.0
PSD SL 40s	LDA	49.3 ± 9.6	49.1 ± 8.8	50.5 ± 10.1
	OLVQ1 (n)	18.2 ± 7.6 (185)	16.4 ± 5.9 (155)	11.1 ± 6.6 (170)
	SVM (C; γ)	24.1 ± 0.0 (8; -2.5)	20.8 ± 0.0 (2.0; -2.75)	8.8 ± 0.0 (1.25; -3.125)
	kNN (k=opt)	14.8 ± 10.8 (1)	12.7 ± 11.5 (2)	13.9 ± 15.0 (1)
	kNN (k=1)	14.8 ± 10.8	17.9 ± 14.0	13.9 ± 15.0

V. CONCLUSIONS & OUTLOOK

One of the major disadvantages in this study is the missing baseline measurement for each subject. Despite a baseline depended approach will not be applicable to road side testing, it is essential to estimate the vigilance testing capabilities of posturography on an individual scope. Furthermore it is necessary to obtain more samples during the course of experiments in order to estimate the circadian influence on EO/EC discrimination performance. The decision not choosing Romberg Pose could have lead to less significant stabili-

grams by veering away from the model of an inverse pendulum. Especially model-based features may suffer from that decision. As already mentioned, aversions can emerge from keeping this exhausting pose for too long. The reduction of trial lengths down to 18 seconds has been proposed by Forsman et al. [9]. The application of shorter trial lengths may support acceptance of such kind of vigilance tests, but the demand of a distinct pose may be impractical for field use and remains as a critical matter in dispute.

In order to establish a new vigilance test it is important to validate this test against other measures, like e.g. PVT. Such well accepted tests should be included in future analysis to consolidate results. But it must be emphasized that up to now there exists no gold measure. Many methods of assessing hypovigilance suffer from several drawbacks. One main problem is the large inter-subject variability [4]. Future investigations based on much more data of different experimental sessions, different subjects and utilizing cross validation strategies should reveal intra- and inter-subject variability of our measure. With the discriminant analysis between mild and strong hypovigilance resulting in acceptable error rates, we conclude that posturography can be utilized for vigilance testing.

REFERENCES

- Liu Y, Higuchi S and Motohashi Y (2001) Changes in postural sway during a period of sustained wakefulness in male adults. *Occup. Med.* Vol. 51 No. 8, pp. 490-495
- Forsman P, Hægström E, Wallin A, Toppila E, Pyykkö I (2007) Daytime changes in postural stability and repeatability of posturographic measurements. *J. Occup. Environ. Med.*;49(6):591-6.
- Edwards D, Sirois B, Dawson T et al (2007) Evaluation of fatigue management technologies. *Proc 4th Int Sympos Driving Assessment*, Stevenson WA, USA, pp 146-152
- Ingre M, Åkerstedt T, Peters B, Anund A and Kecklund G (2005) Subjective sleepiness, simulated driving performance and blink duration: examining individual differences. *J. Sleep Res.* (2006) 15, pp. 47-53
- Collins JJ, De Luca CJ, Burrows A and Lipsitz LA (1995) Age-related changes in open-loop and closed-loop postural control mechanisms. *Exp Brain Res.* 1995;104(3):480-92
- Jacono M, Casadio M, Moraso PG, Sanguineti V (2004) The Sway-Density Curve and the Underlying Postural Stabilization Process. *Motor Control*, 8(3):292-311
- Schnupp T, Holzbrecher-Morys M, Golz M (2007) Inter- and Intra-Subject Variability in Posturography. *Proc Ann Conf Biomed Techn, BMT, Aachen, Germany, 2007, CD-ROM*
- Joachims T (2002) *Learning to Classify Text Using Support Vector Machines*. The Springer International Series in Engineering and Computer Science, Vol. 668, ISBN: 978-0-7923-7679-8
- Forsman P, Hægström E and Wallin A (2007) Reducing trial length in force platform posturographic sleep deprivation measurements. *Meas. Sci. Technol.* 18 2893-2897, doi: 10.1088/0957-0233/18/9/019

Author: Thomas Schnupp
 Institute: University of Applied Sciences Schmalkalden
 City: Schmalkalden
 Country: Germany
 Email: schnupp@fh-sm.de

Aspects of Weight-Support Mechanisms in Rehabilitation Robotics.

Arno H.A. Stienen (PhD) and Edsko E.G. Hekman (MSc) and Herman van der Kooij (PhD)
and Michael D. Ellis (PT, DPT) and Jules P.A. Dewald (PT, PhD)

Abstract—Weight support can facilitate upper-limb movements, with which the patients may do more and more meaningful exercises earlier in the rehabilitation process. Most rehabilitation devices support the arm against gravity in one way or the other. Weight support can be realized by limiting vertical displacement or applying constant supportive forces which counteract the gravitational pull. Of these, using constant supportive forces is the most natural way to facilitate natural arm movements as it allows full freedom of movement and the amount of weight support is scalable to the patients needs. To apply the supporting forces to the arm, endpoint mechanisms and exoskeletons are more complex to build and use than cable suspensions, but offer more control over the movements. Finally, passive weight support is inherently safe, but active systems have enhanced control options and the capability to create training conditions beyond limb weight.

I. INTRODUCTION

Supporting the arm against gravity of hemiparetic stroke patients has been shown to result in significant improvements in the arm function of patients [1], [2], [3], [4], [5]. In these training studies, the weight support facilitated functional movement of the patients and was gradually reduced as performance improved. Cross-sectional studies have shown that weight support does not negatively influence the execution of movements and only facilitates them [6], [7]. In these studies, weight support has been provided by exoskeletons [1], [3], endpoint manipulators [8], [2] and cable suspensions [9], [6], [7].

Of these devices, endpoint manipulators have a single connection to the hand, wrist or forearm. Often patients hold onto a handle while making movements in a virtual environment. Exoskeletons are external skeletons placed parallel to the arm and are generally powered by actuators on each of the joints. They control (a subset of) the joints of the shoulder, elbow, and wrist directly, at the cost of more complex mechanics. Cable suspensions support the arm with one or two slings, increasing both control options and complexity with every additional cable linkage. They are simplest to realize but offer the least amount of control of the movements of the arm.

These device types do differ in the resulting implementation of weight support, with each having their own ad-

This work was supported by National Institutes of Health (2R01HD039343-06A1; J. Dewald) and SenterNovem (NL, TSGE2050).

Stienen, Ellis and Dewald are with the Department of Physical Therapy & Human Movement Sciences, Northwestern University, Chicago (IL), USA arnostienen@gmail.com.

Dewald is with the Departments of Physical Medicine & Rehabilitation and Biomedical Engineering, Northwestern University, Chicago (IL), USA.

Stienen, Hekman, and Van der Kooij are with the Laboratory of Biomechanical Engineering, University of Twente, Enschede, NL.

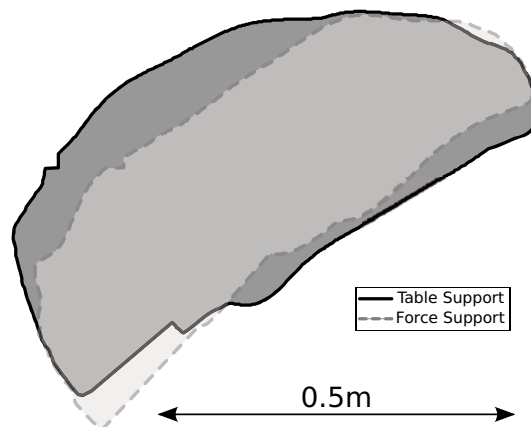


Fig. 1. Difference between table and full weight supports in a single case example. With the table support condition, a stroke patient has a larger range-of-motion (solid black line & dark gray area), whereas with full weight support the reachable area is a lot smaller (stripped gray line & light gray area). Data provided by Mike Ellis and Jacob McPherson.

vantages and disadvantages. In this short report, we wish to highlight these differences and detail the functional consequences.

II. TABLE SUPPORT VERSUS FULL WEIGHT SUPPORT

Weight-support systems function by either restricting vertical displacement or by supporting the arm with constant vertical forces. Planar devices like the MIT-Manus [10] support the weight of the arm by restricting all vertical displacement, which feels like forced sliding of the arm on a smooth horizontal surface. Although this fully supports an arm at rest, the amount of compensation is always equal to the normal force between the arm and the surface and cannot be scaled or externally controlled. Even when such planar mechanisms allow some upward displacements, patients need to fully support their arm themselves before any lift-off is achieved. In none of the aforementioned training studies [1], [2], [3], [4], [5] was a planar device used; for all the slow reduction of weight support was an integral part of the therapy. One of these studies explicitly finds the progressive shoulder abduction loading to be a crucial element of arm rehabilitation in chronic stroke [5].

Secondly, patients can actively press their arm downwards in planar devices, potentially helping their achievements but hindering relearning of normal movement control. For example, using a table-like support artificially increases the range of motion of stroke patients over a fully force-supported arm [8] (see Fig. 1). This rewards patients for the erroneous motor

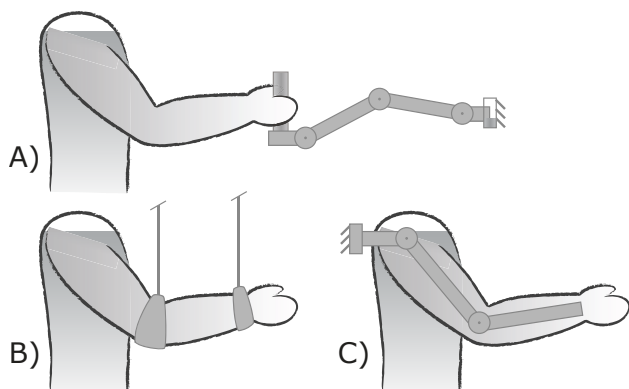


Fig. 2. Device types suitable to provide weight support. A) 3D endpoint manipulators. B) Cable suspension systems. C) Exoskeletons.

pattern of pushing down while wanting to achieve horizontal movements.

For these two reasons, planar endpoint manipulators seems less suitable for restoration of functional movements in stroke rehabilitation therapy. Full 3D endpoint manipulators [11], [12], [8], however, are fully capable of offering weight support through scalable forces.

III. EXOSKELETONS VERSUS ENDPOINT MANIPULATORS

For devices needing close control over the endpoint, exoskeletons or endpoint-manipulators are preferred over cable suspensions (see Fig. 2). Comparing exoskeletons and endpoint manipulators as an application mechanisms for transferring the supporting forces to the arm can be done on the variability of gravity compensation force in the workspace, the achievable range of motion, the movement impedance (mostly inertia and friction), the position and angle measurements, the ease of use, and finally, the ease of construction (including price and maintenance). For generic designs of these two types of rehabilitation devices, the following conclusions can be drawn.

Overall, exoskeletons do not score high marks as a dedicated weight support system. The main problem for the exoskeleton is the need of mechanics for all joint rotations, and the alignment of the exoskeleton joints to the anatomical ones [13], [14], [15]. Misalignment of axes and the additional two translational DOFs in the human shoulder require additional mechanics, making the exoskeleton more complex to construct and use. As an application mechanism, it has a relatively high impedance due to inertia and a limited range of motion. Control of supporting forces depends on the joint orientation. Exoskeletons not directly linked to the limb movements can use better force generating mechanisms with a larger range of movement [1].

Endpoint manipulators are easier to construct than exoskeletons and have a lower movement impedance. Having a mechanical system fully independent of the arm makes a constant force and a large range of motion easier to realize, although the device needs more workspace to operate in. Accurate position and angle measurements require recalculations from manipulator to arm coordinates and assumptions

on the positions of trunk and/or shoulder.

Combination of application mechanisms have been used before. Many partial exoskeleton consist of endpoint mechanisms connection to a forearm cuff [16], often with reduced arm DOFs [8]. Some reduces the gravitational pull on their haptic endpoint device by supporting most of the weight of the arm by cable suspensions [12].

IV. ACTIVE VERSUS PASSIVE DEVICES

Another aspect to consider when providing weight support is whether to use active or passive actuation. All three device types can be fitted with passive mechanisms like counter weights, springs, or spring mechanisms [17], [1], [9], although many rehabilitation robots also have active actuators like electro motors (partly) providing weight support [11], [12], [8], [15]. Advantages of passive weight support are the inherent safety of the device-patient interaction and no need for expensive electronics. Advantage of active support are the availability of fast, computerized control over the amount of weight support and the availability of negative support. With the latter, the training exercises can be made heavier beyond the limb weight, thereby simulating the weight of manipulated objects [8], [4], [5].

V. CONCLUSIONS

To facilitate upper-extremity movements, most rehabilitation devices support the arm against gravity. With weight support, patients may do more and more meaningful exercises earlier in the rehabilitation process.

There is a fundamental difference between weight support by limiting vertical displacement or applying constant supportive forces which counteract the gravitational pull on the arm. Using constant supportive forces is the most natural way to facilitate arm movements as it allows full freedom of movement and the amount of weight support is scalable to the patients needs.

To apply the supporting forces to the arm, endpoint mechanisms and exoskeletons are more complex to build and use than cable suspensions, but offer more control over the movements. This control is useful when combined weight support with other movement manipulation.

Finally, using passive weight support has the advantage of inherent safety, but actively-actuated weight support results in greater control of the support forces and the possibility to extend training environments to beyond limb-weight levels.

REFERENCES

- [1] R. Sanchez, J. Liu, S. Rao, P. Shah, R. Smith, T. Rahman, S. Cramer, J. Bobrow, and D. Reinkensmeyer, "Automating arm movement training following severe stroke: functional exercises with quantitative feedback in a gravity-reduced environment." *IEEE Trans Neural Syst Rehabil Eng*, vol. 14, no. 3, pp. 378–389, 2006.
- [2] M. Ellis, T. Sukal, T. DeMott, and J. Dewald, "ACT-3D exercise targets gravity-induced discoordination and improves reaching work area in individuals with stroke." in *Proc 10th ICORR'07*, B. Driessen, J. Herder, and G. Gelderblom, Eds., Noordwijk, the Netherlands, Jun 13-15 2007.

- [3] S. J. Housman, K. M. Scott, and D. J. Reinkensmeyer, "A randomized controlled trial of gravity-supported, computer-enhanced arm exercise for individuals with severe hemiparesis." *Neurorehabil Neural Repair*, Feb 2009. [Online]. Available: <http://dx.doi.org/10.1177/1545968308331148>
- [4] M. Ellis, T. Sukal, and J. Dewald, "Impairment-based 3d robotic intervention improves upper extremity work area in chronic stroke: Targeting abnormal joint torque coupling with progressive shoulder abduction loading." *IEEE Trans Rob Autom*, vol. in press, 2009.
- [5] —, "Progressive shoulder abduction loading is a crucial element of arm rehabilitation in chronic stroke." *Neurorehabil Neural Repair*, vol. in press, 2009.
- [6] G. Prange, L. Kallenberg, M. Jannink, A. Stienen, H. van der Kooij, M. IJzerman, and H. Hermens, "Influence of gravity compensation on muscle activity during reach and retrieval in healthy elderly." *J Electromyogr Kinesiol*, 2007, epub.
- [7] G. B. Prange, M. J. A. Jannink, A. H. A. Stienen, H. van der Kooij, M. J. IJzerman, and H. J. Hermens, "Influence of gravity compensation on muscle activation patterns during different temporal phases of arm movements of stroke patients." *Neurorehabil Neural Repair*, Feb 2009. [Online]. Available: <http://dx.doi.org/10.1177/1545968308328720>
- [8] T. Sukal, M. Ellis, and J. Dewald, "Shoulder abduction-induced reductions in reaching work area following hemiparetic stroke: neuroscientific implications." *Exp Brain Res*, vol. 183, no. 2, pp. 215–223, 2007.
- [9] A. Stienen, E. Hekman, F. van der Helm, G. Prange, M. Jannink, A. Aalsma, and H. van der Kooij, "Freebal: dedicated gravity compensation for the upper extremities." in *Proc 10th ICORR'07*, B. Driessen, J. Herder, and G. Gelderblom, Eds., Noordwijk, the Netherlands, Jun 13-15 2007.
- [10] N. Hogan, H. Krebs, J. Charnnarong, P. Srikrishna, and A. Sharon, "MIT-MANUS: a workstation for manual therapy and training. i," in *Proc 2th ROMAN'92*, Tokyo, Japan, Sep 1-3 1992, pp. 161–65.
- [11] C. Burgar, P. Lum, P. Shor, and H. van der Loos, "Development of robots for rehabilitation therapy: The Palo Alto VA/Stanford experience." *J Rehabil Res Dev*, vol. 37, no. 6, pp. 663–673, 2000.
- [12] R. Loureiro, F. Amirabdollahian, M. Topping, B. Driessen, and W. Harwin, "Upper limb robot mediated stroke therapy - Gentle/s approach." *Auton Robot*, vol. 15, no. 1, pp. 35–51, 2003.
- [13] A. Schiele and F. van der Helm, "Kinematic design to improve ergonomics in human machine interaction." *IEEE Trans Neural Syst Rehabil Eng*, vol. 14, no. 4, pp. 456–469, 2006.
- [14] A. Stienen, E. Hekman, F. van der Helm, G. Prange, M. Jannink, A. Aalsma, and H. van der Kooij, "Dampace: dynamic force-coordination trainer for the upper extremities." in *Proc 10th ICORR'07*, B. Driessen, J. Herder, and G. Gelderblom, Eds., Noordwijk, the Netherlands, Jun 13-15 2007.
- [15] T. Nef and R. Riener, "Shoulder actuation mechanisms for arm rehabilitation exoskeletons," in *Proc Biorob'08*, J. Desai, D. Meldrum, and O. Khatib, Eds., Scottsdale, Arizona, USA, Oct 19-22, 2008 2008.
- [16] K. Nagai, I. Nakanishi, and T. Kishida, "Design of robotic orthosis assisting human motion in production engineering and human care." in *Proc 6th ICORR'99*, H. van der Loos, Ed., Stanford, California, USA, Jul 1-2 1999, pp. 270–275.
- [17] J. Herder, "Development of a statically balanced arm support: Armon," in *Proc. 9th International Conference on Rehabilitation Robotics ICORR 2005*, 2005, pp. 281–286.
- [18] B. Driessen, J. Herder, and G. Gelderblom, Eds., *Proc 10th ICORR'07*, Noordwijk, the Netherlands, Jun 13-15 2007.

Studying Mechanisms Underlying Stroke Induced Movement Disorders Using 3-D Robotics

Julius P.A. Dewald PT, PhD^{1,2,3}, Albert Chen, PhD^{1,2} & Jun Yao, PhD¹

¹ Northwestern University, Department of Physical Therapy and Human Movement Sciences, Chicago, USA

² Northwestern University, Department of Biomedical Engineering, Chicago, USA

³ Northwestern University, Department of Physical Medicine and Rehabilitation, Chicago, USA

Abstract – When chronic hemiparetic stroke survivors make reaching movements while lifting the paretic arm against gravity, their ability to generate the necessary independent joint movements for reaching degrades dramatically due to abnormal muscle coactivation patterns that couple shoulder abduction with elbow flexion. The neural mechanisms behind the appearance of abnormal coordination patterns during post-stroke recovery are largely unknown, but they are possibly related to a loss in cortical resolution and an increased usage of undamaged, indirect descending motor pathways via the brainstem. In order to investigate the underlying mechanisms responsible for this behavior in chronic stroke survivors, we combine 3-D robotics with the mapping of brain activity during controlled reaching movements with different levels of robot-mediated limb support. Our results provide evidence for changes in cortical activity driving realistic upper-extremity reaching movements as shoulder abduction drive is increased and independent joint control becomes compromised in stroke survivors. The advantage of using robotics to study mechanisms underlying the loss of independent joint control is discussed.

Keywords— Stroke, Upper Limb, Coordination, Brain Imaging, Rehabilitation Robotics.

I. INTRODUCTION

Perhaps the most important cause of upper-extremity motor disability following chronic hemiparetic stroke is due to abnormal joint coordination at the shoulder and elbow. Abnormal movement patterns caused by this discoordination, described by Brunnstrom [1] as flexion and extension synergies, involve the coupling of elbow and shoulder movements, thus severely limiting the ability to make functional movements such as reaching. Previous static [2] and dynamic [3, 4] evidence has shown that independent torque generation, arm workspace and reaching ability can all be seriously impaired when stroke survivors increase the amount of shoulder abduction drive needed to lift the arm

against gravity.

The neural mechanisms behind the appearance of abnormal coordination patterns during post-stroke recovery are largely unknown, but they are postulated to be related to a loss in cortical resolution and an increased usage of undamaged, indirect descending motor pathways via the brainstem [2]. This paper describes an experimental setup consisting of a high-density electro-encephalogram system (EEG), an electro-myographic (EMG) system and a 3D robotic device that allows us to investigate how brain activity changes as shoulder abduction drive is increased during reaching tasks using haptic environments. This study is the first brain imaging study that uses robotics to investigate the spatiotemporal properties of cortical activity simultaneously with muscle and kinematic activity in stroke patients. Results of this study provide evidence for changes in cortical activity driving realistic upper-extremity reaching movements as independent joint control becomes increasingly compromised at the shoulder and elbow in stroke survivors.

II. MATERIAL AND METHODS

2.1 Subject description

Eight able-bodied subjects (7 male, 1 female, 51-62 years old, all with right hand dominance) and 10 chronic hemiparetic stroke subjects (7 male, 3 female, 52-69 years old) participated in our study.

2.2 Experimental setup

Surface EMG signals were recorded from 12 muscles of the arm and trunk using a Delsys EMG system (Delsys, Boston, MA, USA). Electrodes were placed on the dominant limb side of control subjects or the paretic limb of stroke subjects.

Scalp recordings were made with a high-density 160-channel EEG system (Biosemi, Inc., Active II, Amsterdam, The Netherlands). Cortical activity was determined from cortical current density reconstructions computed using a 3D boundary element model from subject-specific anatomical MRIs using the CURRY software (Compumedics Neuroscan Ltd., El Paso, TX, USA).

2.3 Robot mediated motor tasks

Three different reaching tasks were performed using a

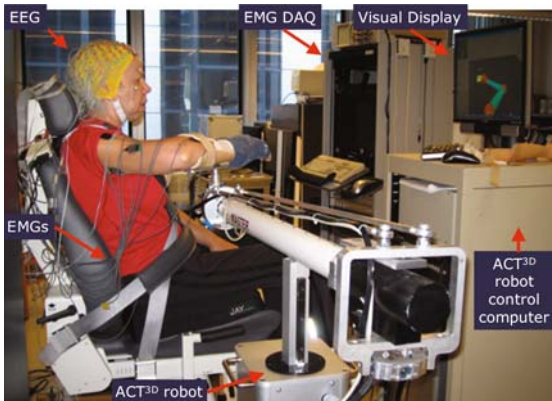


Figure 1 Experimental setup recording kinematics/forces, EEG and surface EMG during movements performed on the ACT^{3D} robot.

3D robotic setup, known as the Arm Coordination Training 3D (ACT^{3D}) robot (Figure 1). The tasks were chosen such that horizontal plane movements would be made with different required levels of shoulder abduction drive in order to deal with different gravitational loads while reaching. The first task (abbreviated as TbRe) involved making a ballistic reaching movement along a haptic planar surface to a target. The second task (0Re) consisted of making the same movement in free space with the robotic setup fully supporting the weight of the limb by pushing up at a constant force. Thus, the arm felt like it was weightless when reaching. The third task (25Re) consisted of the same movement in free space, but subjects had to actively lift 25% of their maximum abduction force (obtained during max effort trials) while reaching. 120 trials were performed for each task.

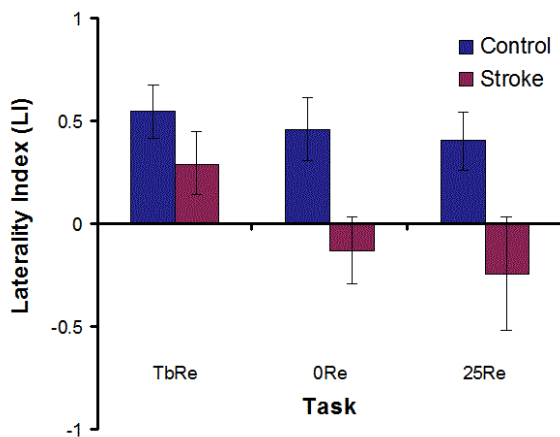


Figure 2 Laterality Indices for both control and stroke subject groups across all tasks.

III. RESULTS

Stroke subjects demonstrated muscle activity consistent with movement synergy patterns during the motor tasks, as well as significant decreases in kinematic performance, as shoulder abduction drive was increased (Figure 2). As deltoid activity increased to abduct the paretic arm of stroke subjects, elbow extensor activity decreased and elbow flexor activity increased as part of the flexion synergy. Both shoulder and elbow joint excursions and velocities also decreased significantly.

An EEG Laterality Index (LI) was computed from the cortical activity, such that an LI of +1 indicated all contralateral activity, and -1 indicated all ipsilateral activity (see Figure 2). Control subjects displayed mean LI values of 0.56, 0.43, and 0.42 for TbRe, 0Re, and 25Re, respectively. Therefore, only slight nonsignificant decreases in value were seen with increasing shoulder abduction loads ($p > 0.05$). Stroke subjects exhibited mean LI values of 0.27 for TbRe, -0.12 for 0Re, and -0.21 for 25Re. These values decreased significantly from TbRe to 0Re ($p < 0.05$) and from TbRe to 25Re ($p < 0.05$), again indicating the shift in lateralization from the contralateral to the ipsilateral hemisphere with decreasing gravitational limb support. However, no significant differences were seen in the LI values from 0Re to 25Re ($p = 0.77$), suggesting that the 0Re and 25Re tasks involved similar levels of ipsilateral activation. For one-way ANOVA statistical comparisons between the two groups, the stroke group had significantly lower LI values than the control group for the 0Re ($p = 0.01$) and 25Re ($p = 0.02$) tasks, but only a strong trend for TbRe ($p = 0.08$). This shows that laterality differences between the two groups in the TbRe were small when stroke subjects were able to perform the task fairly well without clear signs of discoordination. However, these laterality differences were amplified once shoulder abduction load increased and reaching performance degraded for stroke subjects. Furthermore, it was found that the more impaired stroke subjects (as determined by Fugl-Meyer Assessment scores) exhibited more ipsilateral cortical activity than lesser impaired subjects.

Pearson's correlation coefficients were used to determine whether the kinematic measures and maximum EMG values were correlated with the LI values for the stroke subjects. Values for all tasks were grouped together for each of the different measures. They were then tested and confirmed as having normal distributions using the Kolmogorov-Smirnov test. Both joint angular excursions for shoulder flexion (SF) ($r = 0.56$, $p = 0.002$) and elbow extension (EE) ($r = 0.59$, $p = 0.001$) were significantly correlated with LI. SF and EE velocity also showed strong correlations with LI ($r = 0.32$, $p = 0.10$ for SF; $r = 0.37$, $p = 0.06$ for EE). In the case of EMGs, only the long head of the triceps ($r = 0.44$, $p = 0.02$),

the anterior ($r = -0.45, p = 0.02$) and intermediate ($r = -0.47, p = 0.01$) heads of the deltoid muscle correlated significantly with LI. These results show that deficits in kinematic performance and primary muscle activations are directly linked to the ipsilateral shifts in location of cortical activity. In particular, movement excursions and levels of open-loop elbow extensor muscle activity are affected the most by this change in cortical control (see Figure 3).

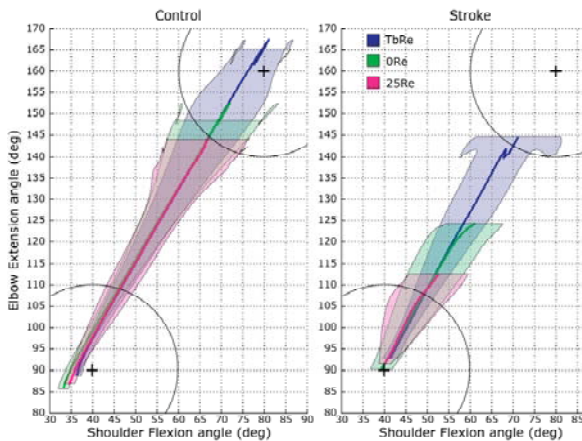


Figure 3. Reductions in reaching from TbRe, 0Re to 25Re can be observed in stroke as opposed to control subjects.

IV. CONCLUSIONS

Our results show differences between control and stroke subjects in quantitative performance of motor tasks implemented using 3D robotics and result in corresponding differences in brain activity. In stroke subjects, as shoulder abduction drive was increased, decreases in speed and distance reached (figure 3) and corresponding increases in secondary EMG activations consistent with movement synergy patterns occurred. This reflected the struggle to break out of the flexion synergy when abducting the arm against gravity. Therefore, differences in muscle activation patterns and kinematics provide evidence for decreases in joint coordination in stroke subjects as shoulder abduction drive is increased.

These motor performance differences then correspond to differences in brain activity. Results from our cortical current density reconstructions give us insight into the underlying mechanisms behind abnormal joint coordination following stroke. The brain has a number of options to choose

from when there is damage to the corticospinal/ corticobulbar tracts after hemiparetic stroke. The increased use of ipsilateral cortical areas and their projections such as uncrossed ventral corticospinal or bilateral ventromedial pathways may be due to the increased requirement of shoulder abduction drive in our tasks. However, ipsilateral cortical areas are likely to be used if there are not enough contralateral resources remaining after brain damage, since previous studies have shown that activity in the ipsilateral hemisphere may correlate with poorer functional recovery [5]. Our results suggest a correlation between the level of shoulder abduction drive and ipsilateral cortical activity, as well as between the level of motor impairment for our stroke subjects and ipsilateral cortical activity.

Finally, this work shows that the effect of shoulder abduction drive on sensorimotor cortical activity can be uniquely studied using 3D robotics. The application of a 3D robot allows for the support of the arm as well as normalized increases of shoulder abduction torques mediated by our admittance controlled ACT^{3D}.

ACKNOWLEDGMENT

The authors would like to acknowledge Carolina Carmona for her assistance with experimental procedures. This study was supported by an American Heart Association Predoctoral Fellowship and National Institutes of Health grant 5R01HD047569-05.

REFERENCES

- [1] Brunnstrom, S., (1970), Harper & Row.
- [2] Dewald, J. P., et al., (2001), *Muscle Nerve*, 24, 273-283.
- [3] Beer, R., et al., (1999), *Prog Brain Res*, 123, 455-460.
- [4] Sukal, T. M., et al., (2007), *Exp Brain Res*, 183, 215-223.
- [5] Ward, N. S., (2004), *Curr Opin Neurol*, 17, 725-730.

Author: Julius P.A. Dewald
 Institute: Northwestern University
 Street: 645 N. Michigan Ave. Suite 1100
 City: Chicago, IL 60611
 Country: USA
 Email: j-dewald@northwestern.edu

Use of Artificial Neural Networks for Classification Intracranial EEG Signals from Epileptic Patients

P. Marchena¹, M. Díaz¹, R. Esteller², I. Martínez³, and A. Zambrano⁴

¹ Simon Bolivar University/Applied Bioengineering and Biophysics Group (GBBA), Caracas, Venezuela

²Neuropace/Mt View, California, USA

³ Simon Bolivar University/Computer Science and I.T, Caracas, Venezuela

⁴ Simon Bolivar University/Electronics and Circuits Department, Caracas, Venezuela

Abstract— An epileptic seizure is an episode of abnormal electrical brain activity that might involve partial or total consciousness loss and/or involuntary movements among others uncomfortable sensations in people who suffer it. At least 1% population worldwide suffer from epilepsy, therefore research aimed to develop new techniques to treat this condition is essential. In the present work an Artificial Neural Network (ANN) implementation is proposed by using the Backpropagation Algorithm (BP) which is used to perform a classification of real Intracranial Electroencephalogram (iEEG) signals into interictal or ictal following these steps: (i) Data reduction by extracting 7 features of the signal, (ii) Implementing the Backpropagation algorithm in a DSP platform with the computed features as input and the signals classification, ictal or interictal as output.

Keywords— Epilepsy, iEEG, features extraction, ANN, BP algorithm, DSP.

I. INTRODUCTION

According to the World Health Organization (WHO) [1], 50 million people worldwide suffer from epilepsy and at least 30% of them do not respond to current treatments available. Although some evaluation systems such as the Magnetic Resonance Imaging (MRI) or Computed Tomography (CT) are used to diagnose brain's structural disorders or to study special lesions, in clinical environments the EEG is more commonly used. Therefore, it is important to develop technology capable of analyzing EEG signals when a seizure occurs in humans. The classification and detection of epileptics patterns in EEG signals have been widely studied using computational methods such as neural networks [2-3-4-5], evolutionary algorithms [6-7] and others signal processing techniques [8-9-10]. Epilepsy diagnosis involves EEG signals classification. Due to the non-stationarity of EEG signals, its classification using the traditional frequency analysis is not highly successful [3]. Artificial neural networks are among one of the most effective learning methods that are known at present, being successfully applied in problems such as: learning of complex data from real

world sensors, visual scenes interpretation, speech recognition and learning control strategies of robots [11]. Thus artificial neural networks have become in an attractive method for signal analysis, one advantage of them is that once the network has been trained satisfactorily and the weights values have been stored, testing and subsequent implementation is rather fast [4].

In this paper a methodology for iEEG signals classification is implemented using a computational method by extracting seven signals features, which are used as input to an artificial neural network by using the Backpropagation algorithm described by Mitchell [11], the network was implemented in a Digital Signal Processor (DSP) and it has as output the signal classification as either interictal or ictal. Figure 1 shows signal classification methodology.

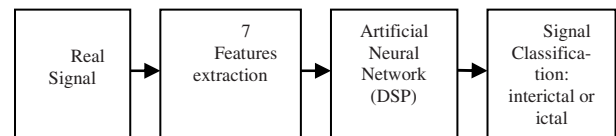


Fig 1. Signal classification methodology

II. METHODS AND MATERIALS

A. Artificial Neural Networks

Learning methods based on neural networks provide a robust approach to approximate functions that could have: real values, discrete values and vectors with real or discrete values.

Multilayer neural networks are based in the BP algorithm and their main learning element is the sigmoid unit [11]. Sigmoid unit computes the linear combination of its inputs and then applies a threshold function to the result leading to, the thresholded output that is a continuous function of its input. The sigmoid unit computes its output o as:

$$net = \sum_{i=0}^n w_i x_i \quad (1)$$

$$o = \sigma(net) = \frac{1}{1+e^{-net}} \quad (2)$$

σ is often called the sigmoid function and its output ranges always are between 0 and 1, n are the number of inputs and weights for each input, x is the input value, w is the weight value and o is the output value.

Backpropagation Algorithm: it is based in the delta training rule, the main idea inside the delta rule is to use gradient descent to search the hypothesis space of potential weights that best fit the training examples [11]. Although it has many applications, the BP algorithm has several limitations as well [5]. First, the hypothesis surface may have false local minima, so the algorithm is not always guaranteed to converge to the best solution. Second, it is difficult to estimate in first instance the exact number of the hidden layer neurons required to represent a problem before the network is trained. Finally, the BP algorithm is often slow. In this paper, the algorithm implemented was the same described by Mitchell [11].

ANN implemented has the following features:

- Inputs number: 7
- Number of sigmoid units or neurons in hidden layer: 20
- Number of neurons in output layer: 1
- η (learning rate): 0.001
- Target output value o_i to ictal signal: 2
- Target output value o_i to interictal signal: -2
- Initial network weights values w_{ji} y w_{kj} : random(-0.05;0.05)
- Iterations number (ending condition): 2000

B. Hardware

The ANN was implemented in an Analog Devices SHARC ADSP-21369 processor, running at 400 MHz. This is a high performance 32-bit processor used for high quality audio, medical imaging, communications, military, test equipment, 3D graphics, speech recognition, motor control, imaging, and other applications [12]. Capable of execute 2400 MFLOPS, programmable in C or C++ language using the VISUALDSP++ environment provided by the manufacturer through the USB port of the computer.

C. Data Set

The iEEG signals classified come from an annotated database of iEEG records obtained during a continuous four-day evaluation for epilepsy surgery of 10 patients suffering mesial temporal lobe. The database was collected in the occasion of the first international collaborative workshop on seizure prediction [13]. From the original seizure records, one-hour segments of signals were selected such as the

seizure onset was at the 3000th second (50th minute). There are 243 signals, 100 signals with seizures containing part of pre-ictal period (at least 50 minutes), the whole ictal period and some portion of post-ictal period. The remaining 143 records are baseline activity (interictal) recorded at least one hour before of the seizures. The data were sampled at 200 Hz and digitized to 12 bits. All records were filtered to eliminate 60 Hz interference, and then bandpass filtered at 0.1 – 100 Hz.

D. Features extraction

Fernandez [14] and Lopes [6] used genetic programming algorithms to classify EMG and EEG signals, respectively. First author used eight EMG signal features, whereas the second one used seven with EEG signals. Both authors performed signals classification with satisfactory results.

The seven features used in this work are detailed below. These were selected because they are easy to compute and have given satisfactory results in signal classification on previous works:

- Mean Absolute Value: MAV.
- Average Value: AV.

$$MAV = \frac{1}{N} \sum_{k=1}^N |x_k| \quad (3)$$

$$AV = \frac{1}{N} \sum_{k=1}^N x_k \quad (4)$$

- Zero-signal cross: ZC

$$ZC = \begin{cases} ZC + 1, & \text{if } (c_1 \vee c_2) \\ ZC & \text{otherwise} \end{cases} \quad (5)$$

where,

$$\begin{cases} c_1 = (x_k \geq 0) \wedge (x_{k+1} < 0) \\ c_2 = (x_k \leq 0) \wedge (x_{k+1} > 0) \end{cases} \quad (6)$$

- Waveform Length: WL

$$WL = \sum_{k=1}^N |x_{k+1} - x_k| \quad (7)$$

- Up Slope : US

$$\begin{cases} US = US + 1, & \text{if } (x_k - x_{k-1}) > 0 \\ US, & \text{otherwise} \end{cases} \quad (8)$$

- Down Slope: DS

$$\begin{cases} DS = US + 1, & \text{if } (x_k - x_{k-1}) < 0 \\ DS, & \text{otherwise} \end{cases} \quad (9)$$

- Slope Sign Changes: SSC

$$SSC = \begin{cases} SSC + 1, & \text{if } (c_4 \vee c_5) \\ SSC & \text{otherwise} \end{cases} \quad (10)$$

where,

$$\begin{cases} c_4 = (x_k > x_{k-1}) \wedge (x_k > x_{k+1}) \\ c_5 = (x_k < x_{k-1}) \wedge (x_k < x_{k+1}) \end{cases} \quad (11)$$

Features were computed in a six-minute time window, taking as starting and ending time the minutes 48th and 54th minute of each record. This window was selected after trial and error, testing with different time windows. For each tested window the features were calculated and then the signals were classified using the ANN. The tested time windows were selected taking into account part of the pre-ictal period, ictal period, and in some cases the post-ictal period. Figure 2 shows an example of two signals from patient 1.

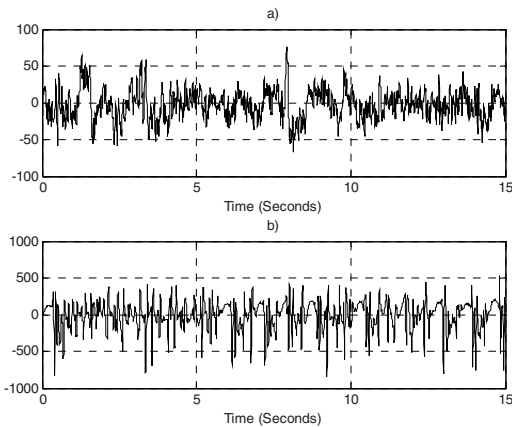


Fig 2. Record 2 of patient 1. a) Interictal. b) Ictal

E. Testing and training sets

Once the features are computed, the training and testing sets are generated and used as inputs to the neural network. Sets were taken randomly from the total of records of interictal and ictal signals. Training set consists of a 80x7 matrix, where 80 is the number of records used in training and 7 the features for each record, therefore each record is composed by the follow data vector {AVM, AV, ZC, SSC, WL, U.S., DS}, 40 of them belong to the ictal signals and 40 to the interictal. The testing set is generated in the same way excluding the data already collected for the training set. It consisted of 120 records, 60 ictal and 60 interictal.

III. RESULTS

To measure the network accuracy four parameters were calculated: true positive (tp), false positive (fp), true negative (tn) and false negative (fn).

The classifier accuracy can be described more precisely by using two indicators: sensitivity (Se) and specificity (Sp) [6]. These indicators take into account not only the number of correct classifications but also the relationship between positive and negative classes. The sensitivity is defined by:

$$Se = \frac{tp}{tp+fn} \quad (12)$$

And specificity as:

$$Sp = \frac{tn}{tn+fp} \quad (13)$$

After running the Backpropagation algorithm with the specifications introduced in section A. *Artificial Neural Networks*, results were obtained for training and testing sets (see Table 1 below)

Table 1 Parameters to measure the classifier accuracy for training and testing sets

Parameter	Training	Testing
true positive (tp)	33	43
false positive (fp)	10	17
true negative (tn)	30	43
false negative (fn)	7	17
Sensitivity (Se)	0.825	0.72
Specificity (Sp)	0.75	0.72

IV. DISCUSSION

The time window of six minutes was selected by trial and error method to compute the features of the signals, with this window satisfactory results were obtained.

The BP algorithm was able to learn satisfactorily. The system was able to classify correctly more than 70% of the testing inputs, therefore the artificial neural networks were applied successfully in this work in the task of iEEG signals classification into: ictal or interictal.

The key factor that allowed the window selection by using a heuristic approach was the implementation of the ANN and the overall system in a DSP platform. Using the DSP processor, it was possible to repeat the training as many times as needed because of its fast computational time. The results presented here required a total of 2000 iterations of the Backpropagation algorithm in the ADSP21369. The training took less than 2 minutes in this

DSP processor. The same training was attempted in a PC with an AMD 1.9 GHz Athlon Dual-Core processor using the DSP emulator software included in the VISUALDSP ++ 5.0 environment, and after 1-hour of training the algorithm had only done 100 iterations.

V. CONCLUSIONS

This work demonstrates the use of ANN in a DSP processor as a classifier for epileptic signals. ANN training is generally very slow, because of the training phase and the weights update of the BP algorithm; which depend on the size of the training set, the number of inputs, the number of neurons in the hidden layer, and the number of outputs. The higher these numbers, the longer is the training phase, as more iterations are required to achieve satisfactory training goal. The DSP platform used, was an independent card connected to the computer. The training time of the ANN was short, in several times less than 1-minute, allowing several testings until satisfactory training results were achieved.

Training an ANN with the Backpropagation algorithm is not an accurate process that must be conducted through trial and error to determine the best configuration in all the parameters required by the algorithm.

Despite that the ANN configuration is a very empirical process, the parameters obtained in this work were satisfactory, due to the majority of the data examples were correctly classified either training or the test sets with the time window selected, moreover, the seven features used as inputs to the ANN demonstrated to be an adequate selection for the implementation of the proposed methodology.

REFERENCES

1. WHO on <http://www.who.int/en/>
2. Akin M, Aserim M.A, Kiyimik M.K and Turkoglu I (2001). A New Approach for Diagnosing Epilepsy by Using Wavelet Transform and Neural Networks. Paper presented at the 23rd Annual Conference IEEE/EMBS, Turkia.
3. Subasi A, Erçelebi E (2005). Classification of EEG signals using neural network and logistic regression. *Computer Methods and Programs in Biomedicine*, 78(2), 87-99.
4. Übeyli E (2009). Combined neural network model employing wavelet coefficients for EEG signals classification. *Digital Signal Processing*, 19(2), 297-308.
5. Weng W, Khorasani K (1996). An Adaptive Structure Neural Networks with Application to EEG Automatic Seizure Detection. *Neural Networks*, 9(7), 1223-1240.
6. Lopes, H. (2007). Genetic programming for epileptic pattern recognition in electroencephalographic signals. *Applied Soft Computing*, 7(1), 343-352.
7. Marchesi B, Stelle A.L, Lopes H.S (1997). Detection of epileptic events using genetic programming. Paper presented at the 19th Annual International Conference of the IEEE, Chicago, IL, USA.
8. Haas S, Frei M.G, Osorio I (2007). Strategies for adapting automated seizure detection algorithms. *Medical Engineering & Physics*, 29(8), 895-909.
9. Subasi A (2007). EEG signal classification using wavelet feature extraction and a mixture of expert model. *Expert Systems with Applications*, 32(4), 1084-1093.
10. Esteller R (2000). Detection of Seizure Onset in Epileptic Patients from Intracranial EEG Signals. Georgia Institute of Technology, Georgia.
11. Mitchell T (1997). *Machine Learning*. MacGraw-Hill.
12. Analog Devices on <http://www.analog.com/>
13. Lehnertz K., Litt B "The first international collaborative workshop on seizure prediction: summary and data description", *J. Clin. Neurophysiol.*, vol. 116, pp. 493-505, Mar. 2005.
14. Fernandez J, Farry K, and Cheatham J (1996). Waveform Recognition Using Genetic Programming: The Myoelectric Signal Recognition Problem. Paper presented at the Genetic Programming 1996: Proceedings of the First Annual Conference, Stanford University, CA, USA.

Author: Pedro Marchena
 Institute: Universidad Simón Bolívar
 Street: Valle de Sartenejas
 City: Caracas
 Country: Venezuela
 EMail: pmarchena@usb.ve

Electrical Network for Emulation of Saccadic Eye Movements

O. Terán and E. Suaste

CINVESTAV-IPN/Department of Electrical Engineering, Bioelectronics Section, D.F., México

Abstract— Based on reciprocal innervation mechanical model for horizontal eye movements, was proposed the design, development and construction of an electronic active model (EAM) to emulate the biodynamic rotatory properties of a human eye plant caused by neurologic activation signals on lateral and medial extraocular muscles. Biodynamic properties as viscosity, inertia and elasticity of the mechanical eye plant were included into the electrical network to obtain a similar response. Apart from these features, were include voltage controlled resistors (VCRs) based on MOSFET to keep the nonlinear of the plant. These active elements altogether with passive components constitute the structure of extraocular muscles, eye ball and tissues around the eye ball. Activation agonist-antagonist signals were generated by two voltage controlled sources to reproduce the neurological activity. In this way, applying the appropriate signals to generate saccadic movements, was obtained a voltage signal proportional to velocity of the eye torque. This signal allows obtain information of acceleration and position in order to validate the EAM. Finally, some of the EAM advantages lie on its response velocity and ease to obtain continues records of the dynamic eyeball response in a signal which features ease recording and application in biomedical areas, specialist as Neuro-ophthalmologists, ophthalmologists and optometrist, and even for medical education.

Keywords— Eye plant, electronic model, saccadic eye movements.

I. INTRODUCTION

Now a day is more frequently found in the biomedical sciences, like ophthalmology, neurology and physiology which are directly linked with the human vision, models and instruments that offer valuable information of the visual system and make possible to reproduce the phenomenological events generally in a particular section of this. One of these sections has been the oculomotor system that is the final stage in the human control of eye movements. Descartes was the first in propose the idea of the conjugate muscles action to produce rotation of the eyeball. This principle of reciprocal innervations open the way to new ideas that pretends to predict the dynamic response of the eye movements [1]. A mechanical model that obtain this results was the presented by Clark and Stark [2] for saccadic hori-

zontal eye movements. Based on Descartes' principle and Hill's model to muscles [3], mechanical model is capable to predict magnitude, velocity and acceleration of saccadic eye movements from the primary position to a new desired position of the eye. This model has probed its efficacy to simulate the eye plant due to consider nonlinear properties of the extraocular eye muscles [4].

In this manner, the importance of the eye plant models, lie in obtain a new form to analyze disorders in people with some class of congenital or pathological disorder in the oculomotor system that most of the times cause a diminution in visual acuity as occurred in the case of Nystagmus that only can be treated to reduce it effects. For this reason, presented design is focus on offer a tool that can be directly applied in diagnostic or research related to the human visual system. In addition, the EAM is a useful tool in medicine or ophthalmologic schools for didactical purposes

II. FUNDAMENTALS

A. Mechanical Model

Sixth order model developed by Clark and Stark [4] has been studied by other authors [5, 6, 7] and results has demonstrated that can reproduce realistic eye position, velocity and acceleration trajectories of human saccades. For this reason our design is based on this nonlinear mechanical model for horizontal eye movements, Fig. 1. The extraocular muscles are based on Hill muscle model. Both contain nonlinear dashpots B_{AG} and B_{AT} which viscosity change as a function of force and velocity on the muscles. Inside each muscle, there is an active-state tension generator (ATG) responsible to produce necessary force to the extraocular muscle contraction [8,9]. This force is the ideal physiological force generated into the muscle and cannot be measure directly, also defines magnitude and duration of saccadic eye movements therefore is important control its properties. In order to simplify this control, the forces produced by the ATGs (F_{AG} , F_{AT}) are obtained from filtering pulse-step signals N_{AG} and N_{AT} with a low-pass filter which change its time constant in the falling edge of the signal. In Fig. 2 are represented the input and output signals of agonist and antagonist extraocular rectus muscle and the moment when occur the time constant change in the filter. This process is

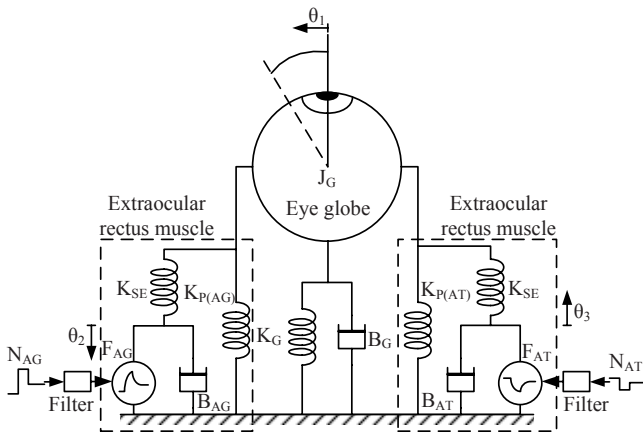


Fig. 1 Sixth order nonlinear eye plant model for horizontal saccadic eye movements [3], B_{AG} and B_{AT} represent the nonlinear force-velocity relationship

$$B_{AG} = \begin{cases} 1.2F_{AG} / (900 + \dot{\theta}_2) & \dot{\theta}_2 \geq 0 \\ 3F_{AG} / 900 & \dot{\theta}_2 < 0 \end{cases} \quad (4)$$

$$B_{AT} = \begin{cases} 3F_{AT} / 900 & \dot{\theta}_3 > 0 \\ 1.2F_{AT} / (900 + \dot{\theta}_3) & \dot{\theta}_3 \leq 0 \end{cases} \quad (5)$$

In (3) the term K_p represents the elements $K_{P(AG)}$, $K_{P(AT)}$ and K_G that was simplified in a only spring connected to the eye globe.

B. Electrical Network

Considering the equations of the system and characteristics of the mechanical model, was obtained directly its analog circuit, Fig 3. According to the terminology of the mechanical model, components on electronic model were named respect to their corresponding electro-mechanical analogies. As a consequence of this, position θ_1 is represented in the circuit by the electrical charge q . Therefore $I_1 = dq/dt$ represent the velocity of the eye movements. The voltage sources V_{AG} and V_{AT} generate the equivalent tension produce by ATGs after filter pulse-step signals.

The eye plant model contains two nonlinear dashpots to satisfy the nonlinear force-velocity relationship in the muscle. In circuit Fig. 3 this mechanical elements are represented by nonlinear resistors (R_1, R_2). Its value are given by the voltage and current in each network, as show the equations of the circuit.

related with the activation and deactivation of cells inside the muscle [4].

The model element J_G represents the inertia due to mass of the eye globe; K_G and B_G are the elasticity and viscosity caused by the tissue that surrounds the eye globe, including the lateral rectus muscles. K_{SE} is related with the instantaneous change of length of the muscle in response an instantaneous change of force. $K_{P(AG)}$ and $K_{P(AT)}$ is the passive elasticity of the muscle.

The equations that govern the entire system are:

$$F_{AG} = K_{SE}(\theta_2 - \theta_1) + B_{AG} \dot{\theta}_2 \quad (1)$$

$$F_{AT} = K_{SE}(\theta_1 - \theta_3) - B_{AT} \dot{\theta}_3 \quad (2)$$

$$K_{SE}(\theta_2 - \theta_1) - K_{SE}(\theta_1 - \theta_3) = K_P \theta_1 + B_P \dot{\theta}_1 + J_G \ddot{\theta}_1 \quad (3)$$

where:

$$V_{AG} = C_{SE}^{-1} \int (I_2 - I_1) dt + R_1(I_2) \quad (6)$$

$$V_{AT} = C_{SE}^{-1} \int (I_1 - I_3) dt - R_2(I_3) \quad (7)$$

$$C_{SE}^{-1} \left[\int (I_2 - I_1) dt - \int (I_1 - I_3) dt \right] = \quad (8)$$

$$C_{EQ}^{-1} \int I_1 dt + R_G I_1 + L_G \dot{I}_1$$

where:

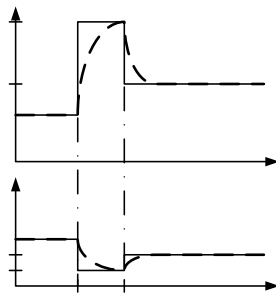


Fig. 2 Controller signals transformed into active tensions by first order filter with the two activation and deactivation constants.

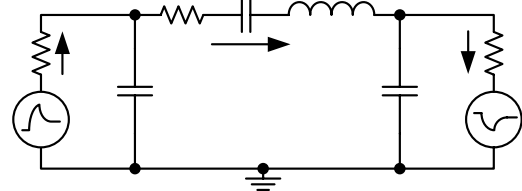


Fig. 3 Simplified electronic model where R_1 and R_2 are nonlinear resistors

$$R_1 = \begin{cases} \frac{1.25 \cdot V_{AG}}{900 + I_2} & I_2 \geq 0 \\ \frac{3 \cdot V_{AG}}{900} & I_2 < 0 \end{cases} \quad (9)$$

$$R_2 = \begin{cases} \frac{1.25 \cdot V_{AT}}{900 + I_3} & I_3 < 0 \\ \frac{3 \cdot V_{AT}}{900} & I_3 \geq 0 \end{cases} \quad (10)$$

R_1 and R_2 are voltage controlled resistors (VCRs) that are circuits capable to emulate an electric resistor changing your resistance with a control voltage. For this reason, a VCR solves the problem of a time-variant resistor present in our EAM (Fig. 4). VCR designed is based on the principle of resistive mirror [10]. This technique linearizes the transimpedance response of common BJT, FET or MOSFET transistor as function as a voltage control. Generate this voltages ($V_{f1}=R_1$ and $V_{f2}=R_2$) for each VCR require independent circuits of control (f_1 and f_2) designed to response according equations (9) and (10). Other important blocks of the circuit are the filters; they change their time constant commuting resistors (τ_{AC} , τ_{DE}) at the same time (Fig. 2). Thus, a microcontroller control amplitude and duration of N_{AT} and N_{AG} and coordinate the electronic switches inside the filters to modifying the time constants according with the pulse-step signals guaranteed the repeatability of input stimulation voltage signals to the EAM.

III. RESULTS

Final circuit of the EAM was probed in a range of movement from 1 to 60 deg with an initial position of 0 deg. Values used in the electronic circuit are: $C_P = 1160\mu F$, $R_G = 15\Omega$, $L_G = 47mH$, $C_{SE} = 560\mu F$, $R_{AC} = 1.8k\Omega$, $R_{DE} = 3.6k\Omega$, $C_{AG} = 2.2\mu F$, $C_{AT} = 2.2\mu F$. All this values where obtained from the original mechanical model multiplied by a factor of 1000 to simplify the design. The electronic ATGs are related with the mechanical muscles force in a scale of $1\text{ gf} = 0.01\text{ V}$. Position (Fig 5), velocity (Fig 6) and acceleration (Fig 7) curves were obtained trough voltage on C_P , R_G , L_G respectively taking advantage of the capable of these components to derivate (L_G), integrate (C_P) or leave the wave form of the current without change (R_P). However, it is necessary that L_G have a high quality factor, to minimize the error caused by electric resistance of the wire.

To obtain appropriate magnitude scale, position voltages need to be multiplied by a factor of C_P , R_G for velocities and $1/L_G$ for acceleration voltage curves and each on multiply

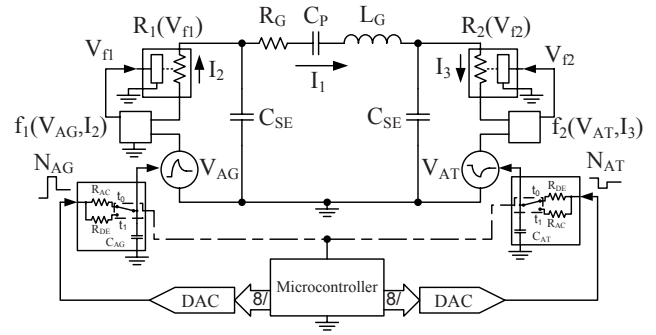


Fig. 4 Block diagram of the EAM where I_1 represents the eye velocity for saccadic movements

by 100000 to compensate reduction in the voltage of ATGs and increments in values of circuit's components.

In order to evaluate the goodness of the EAM results, voltages curves were analyzed according with main-sequence diagrams for human eye movements [1] and compared (Fig. 8) with saccades eye movement signal obtained by high velocity videoculography [11] curves of position an velocity obtained a maximum deviation of $\pm 10\text{ ms}$ for duration of saccades, $\pm 3\text{ deg}$ from desired position, $+100\text{ deg/s}$. Some of this EAM curves not match with experimental curves due to biological variations that modify dynamical responses of human eye plant.

IV. DISCUSSION

The designed EAM is capable to emulate the saccadic eye movements as suggest the comparison with experimental results. According with experimental researches by several authors [1, 5, 6 ,12 13, 14], 10° saccades generated by EAM comply with the 50 ms of duration, peak velocity of 40000° deg/s and acceleration of 50000 deg/s^2 . To ensure that, was design a VCR that experimentally response in a

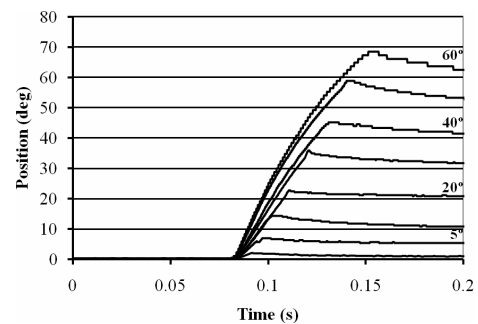


Fig. 5 Position curves obtained by EAM on C_P for saccades with amplitudes of: 1, 5, 10, 20, 30, 40, 50 and 60 degree.

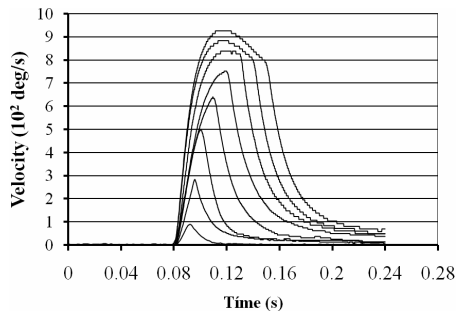


Fig. 6 Velocity curves obtained by EAM on R_G for saccades with amplitudes of 1, 5, 10, 20, 30, 40, 50 and 60 degree

required resistive range and with the more linearity in the saccadic signals bandwidth [15]. The resistive range of the VCR was determinate by the experimental probes in arrange of saccade amplitude of 1 a 60 deg.

Due to amplitude of the saccadic eye movements' signals obtained by EAM, these do not need to be conditioned to be measure by an instrument like an oscilloscope, except that its applications require a great demand of current. The EAM may function completely without the necessity to use a computer because the activation state signals are easily generated and manipulated with aid of a microcontroller or can be used another source to generate desired stimulation signals.

REFERENCES

1. Bahill A. T. (1981) Bioengineering: Biomedical, Medical and Clinical Engineering. Prentice-Hall, Inc., Englewood Cliffs, New Jersey.
2. Clark M. R. and Stark L.(1974) Control of Human Eye Movements: III. Dynamic Characteristics of the Eye Tracking Mechanism. Math Biosci 239:265-20
3. Clark M. R. and Stark, L. (1974) Control of Human Eye Movements: I. Modeling of Extraocular Muscle. Math Biosci 191:211-20

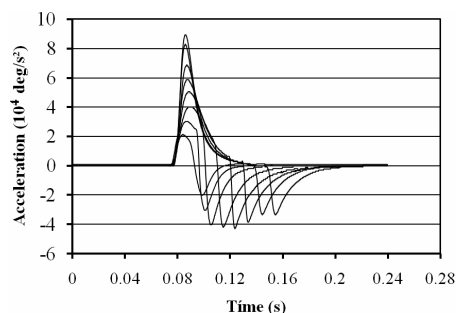
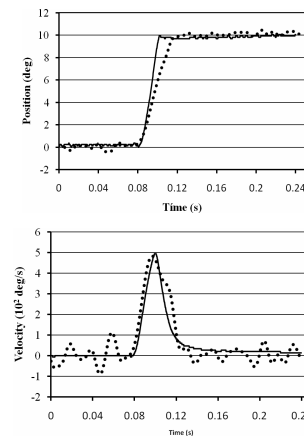


Fig. 7 Acceleration curves obtained by EAM on L_G for saccades with amplitudes of 1, 5, 10, 20, 30, 40, 50 and 60 degree



a) b)

Fig. 8 a) Solid line is the position estimation generated by EAM, dotted line is the position trajectory obtained by high velocity video-oculography, both curves for a 10 deg saccade. b) Solid line is the velocity estimation directly generated by EAM, dotted line is a curve velocity obtained from derive position curve in a), both curves generated from a 10 deg saccade

4. Clark, M. R. & Stark, L. (1974) Control of Human Eye Movements: II. A Model for the Extraocular Plant Mechanism. Math Biosci 213:238-20
5. Enderle J D, Wolfe J W and Yates J T (1984) The Linear Homeomorphic Saccadic Eye Movement Model-A Modification. IEEE Trans Biomed Eng 717:720-31(11)
6. Bahil A T, Latimer J R and Troost B T (1980) Linear Homeomorphic Model for Human Movement. IEEE Trans Biomed Eng 631:639-27(11)
7. Martin C F and Schovanec L (1998) Muscle Mechanics and Dynamics of Ocular Motion. J Math Systems Estim Control 1:15-8(2)
8. Robinson D. A (1964) The Mechanics of human Saccadic Eye Movement. J Physiol 245:264-174
9. Enderle J D, Bronzino J D and Blanchard S M (2005) Introduction to Biomedical Engineering. Academic Press
10. Tadic N. (1998) Resistive Mirror-Based Voltage controlled Resistor with Generalized Active Devices. IEEE Trans Instrum Meas 587:591-42(2)
11. Villamar L A and Suaste E (2008) High Velocity Videoculography to Determination of the Pupil Dynamics, American Institute of Physics Conf. Proc. vol. 1032, Tenth Symposium on Med. Phys., Melville, New York, 2008, pp 276-279
12. Enderle J D and Wolfe J W (1987) Time Optimal Control of Saccadic Eye Movements. IEEE Trans Biomed Eng 43:55-34(1)
13. Clark M R and Stark L (1975) Time Optimal of Human Saccadic Eye Movements. IEEE Trans Autom Control 345:348-20(3)
14. Pfann K D, Keller E L and Miller J M (1995) New Models of the Oculomotor Mechanics Based on Data Obtained with Chronic Muscle Force Transducers. Ann. Biomed. Eng 346:358-23
15. Zuber B L, Semmlow J L and Stark L (1986) Frequency characteristics of the Saccadic Eye Movement. Biophys J 1288:1298-8(11)

Author: Ernesto Suaste
 Institute: CINVESTAV-IPN
 Street: Av. IPN #2508, Ap. Postal 14-740, 07000
 City: D.F.
 Country: México
 Email: esuaste@cinvestav.mx

Study toward a Motion Sickness Assessment with Bio-signal indices On Korean Tilting Train eXpress

YongSoo-Song¹, SeongHo-Han¹ MyoungHo-Lee²

¹ Korea Railroad Research Institute, UiWang-Si, KyungKi-Do, Korea
(Tel : +82-31-460-5000; E-mail: adair@yonsei.ac.kr)

² Department of Electrical Engineering, Yonsei University, Seoul, Korea
(Tel : +82-2-2123-4947; E-mail: mhlee@yonsei.ac.kr)

Abstract— To design a system free from motion sickness, it is required to grade the severity of motion sickness objectively, preferably with the score measured continuously without relating only on subjective judgments. One of the methods expected to be useful is to apply autonomic indices. This report explains the usefulness and a limitation of autonomic indices applied to the assessment of motion sickness and introduces an example of the examination in which bio-signal indices are used to assess the degree and motion sickness.

Keywords— Motion sickness, Tilting train, HRV, Blood pressure.

I. INTRODUCTION

The Train is a popular means of transport for several reasons: (i) it provides better facilities than other transports, for examples, fixed tables, more spaces, separate cabins, bistro, etc.; (ii) it runs through the central of the city where people spend little time to reach to their destinations compared to the aircraft where it arrives several kilometers away from the center of the city; (iii) it is more economical to travel in medium and long-distance range, (iv) it carries several hundred passengers per travel compared to the other means of transports (e.g. buses and domestic aircrafts) and (v) it provides better safety and comfort. Therefore, businessman, students and workers are using trains as a means of their transport back and forth to their jobs in their daily lives. Such types of passengers are using their travelling times as part of their jobs. Both ride comfort and ability to perform sedentary activities are effected by a number of factors such as temperature, noise, vibration, seat design, seated posture, use of backrest, etc. Among them vibration has largest influence on ability to perform sedentary activities [1, 4, 7, 17]. Since the passengers are exposed to vibration and thereby are subjected to reduced ride comfort and consequently they are able to perform less. This is a big issue for passengers who are mostly engaged in sedentary activities while travelling. Hence they are demanding higher comfort level in order to perform sedentary activities efficiently. A number of recent studies gave shown that vibration is signifi-

cantly affecting several types of sedentary activities like reading, writing, etc [10, 15, 19, 20].

Especially, in the development of the Korean high-speed railroad business, the ride comfort enhancement of tilting train is very important problem to be solved.

Currently, Various standards at national and international level such as ISO 2631: 1997[8], BS 6841:1987[1], Sperling's Ride Index [5], ENV-12999: 1999[4] and UIC 513[18] are available to evaluate ride comfort. These standards are often used as a tool to measure the ride comfort where passengers are presumably assumed sitting in idling conditions. This means none of these standards are taking into account the effect of sedentary activities due to the whole body vibration. The transmission of the vibration to the whole body is higher for the seated passengers who are using armrest, backrest and place both feet on the floor. Therefore, the abilities to perform sedentary activities satisfactorily are very much dependent on the vibrations of the seat, table and floor. Many published works are available for measuring ride comfort for railway vehicles [2, 12, 16, 17, and 21]. But studies concerned about motion sickness are rarely available [3, 6, 9-11, 14, 15, 19 and 20].

In Korea case, although it has own standard like KS R9216., it mainly depends on the physical parameter such as vibration and noise. So recently, in the valuation of ride comfort, the movements of living parameter technique introduction are increasing on the base of Japan and many developed countries of Europe techniques In this experiment- the heart rate and Blood pressure change of passengers according to tilting angle change of TTX, the Korean tilting train, we are supposed to know that the extent of tilting on the TTX has influence on the Heart rate and the change of Blood pressure, which are living parameter of heart's blood, HRV.

II. METHODOLOGY

A. Theory

Motion sickness can be induced when humans are exposed to vestibular.

Symptoms may differ according to the vehicles or environment, such as car, sea, train, and air sickness.

Motion sickness can induce symptoms including eye strain, headache, pallor, sweating, vertigo and vomiting. Many previous studies indicate that motion sickness can sometimes impair cognitive and response ability [22, 23]. Thus, numerous studies have attempted to elucidate motion sickness and its symptoms. Two main theories of the cause of motion sickness are the sensory conflict theory [24] and the postural instability theory[25].

Studies have employed various methods of inducing motion sickness, such as rotary chair[26], circular vectio-num[27], and off-axis yaw oscillator. According to the sensory conflict theory, subjects get sick in a virtual environment because of the conflict between the visual and vestibular system.

The goal of the study reported in this paper was tested bio-signal (HRV, blood pressure) for predicting the onset of motion sickness and ride comfort while riding by Korea Tilting Train eXpress(TTX).




Fig 1. Korean Tilting Train eXpress (T.T.X)



B. Experiment Environment

- a) Experiment date : 2008-11~2008, 12
- b) Experiment place: Korean tilting train (Honam line), (Temperature: 23 degree Celsius, Humidity: 43%, maximum noise: 60dB)
- c) The main train experiment was conducted in november 2008 using about 36 test subjects and half of them were femails. Mean age was 25years. The test subjects were instructed to try to read or work during the test ride. They were also instruct to ride either forwards or backwards during all test runs, which meant that they had to change seats and direction before the return trip.

d) Measurement Devices & SW :

<Table1>

category	Device Company	image
Biopac MP150	Acquisition ECG, Blood pressure	

BSL PRO 3.7	Connect on Biopac Real time data(*.acq)	
Complexity 2.8	Analysis program	

e) Data for subject in the test groups: 36 healthy volunteers (18 males and 18 females; aged 22~28 years old; average 25 years old) with no history of gastrointestinal, cardiovascular, or vestibular disorders participated in experiments. All subjects had been instructed to avoid tobacco, caffeine, drugs, or influences on the central and autonomic nervous systems.

<Table 2: 36 healthy volunteers>

	TEST GROUP1	TEST GROUP2	TEST GROUP3	TEST GROUP4	TOTAL
NUMBER OF TEST SUBJECT	8	10	8	10	36
MEAN AGE	24	25	26	25	25
PERCENTAGE FEMALE (%)	50	40	50	60	50

C. Experiment Protocol

a) In order to know about normal condition of Heart rate and Blood pressure change, we recorded the Heart rate change of subjects before riding the experimental installation for 20 minutes. And we checked the fluctuation of Blood pressure before and after measuring the heartbeat to find out the change of Blood pressure.

b) Each experiment started with a 9min period of non-tilting curve diving followed by 7 min of tilting curve diving to induce motion sickness, followed by 4 min of non tilting curve diving for recovery. Data for the first 9 min portion of each experiment were regard as baseline. The subjects were expected to experience ride comfort during and after the 7-min tilting diving session. The physiological signals collected during the “ride comfort” session were then compared with those in the baseline” session.

c) HRV is the common method to analysis human autonomous nervous system. HRV spectrum analysis start form Fourier series, but it is actually adapted as a form of fast Fourier transform (FFT) and auto-regressive (AR) model. For example, power spectrum density is generally used for spectrum analysis, and we can use this spectrum to analysis bio-mechanism according to each own frequency band.

III. RESULT

A. The change of Heartbeat

We calculate LF, HF, and LF/HF values as a comparison reference from each experimental in non-tilting and tilting session.

Table 3 each person's LF/ HF

Person	normal	Tilting section	Person	normal	Tilting section
A1	1.446	1.647	F3	4.823	6.199
B1	5.247	10.038	G3	2.715	2.561
C1	1.434	1.779	H3	5.486	6.136
D1	1.325	3.373	I3	3.347	3.877
E1	0.433	1.641	A4	1.717	2.79
F1	1.509	2.755	B4	2.891	6.994
G1	1.502	2.484	C4	1.347	3.671
H1	2.328	2.503	D4	0.767	4.44
I1	1.479	1.563	E4	1.145	2.842
A2	0.748	1.326	F4	2.528	1.941
B2	1.027	2.335	G4	2.034	2.466
C2	3.507	6.935	H4	1.61	3.427
D2	0.881	1.758	I4	3.804	3.746
E2	3.447	2.889	A3	2.773	3.668
F2	1.338	1.316	B3	2.184	2.147
G2	2.02	4.901	C3	14.991	14.8
H2	3	4.335	D3	4.321	6.386

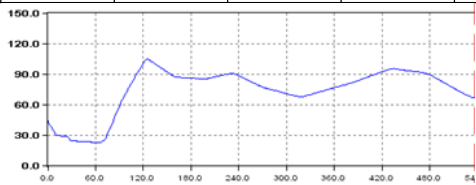


Fig 2 Train speed of non-tilting section

In non-tilting section, average heart rate was 85.3, after tilting; the average heart rate was 87.37, about 2.4% increased. Also, by using the equalized cross correlation, we

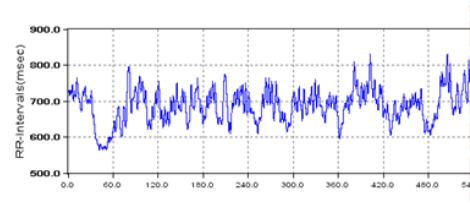


Fig 3 R-R interval in non-tilting section

try to measure the similarity between the change of titling angle and Heartbeat before and after tilting section. As a result, standard deviation increased about 54% from 4.9492 to 7.6305 and we got to know that the change of Heartbeat had effect on the change of tilting angle by increasing of similarity.

It is hard to know numerically about the change of the Heartbeat according to tilting because of differences of individual feature and experiment environment. However, comparing to PSD of each area, the result had definite PSD difference between before and after riding the simulator. And in general, we get to know that environment named tilting has influence on the psychological factor acting, judging from that the wave of wave form occurs a lot.

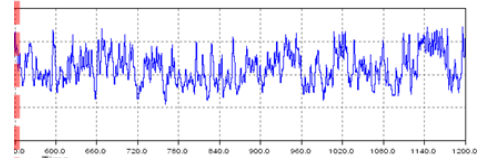


Fig 2 R-R interval in tilting section

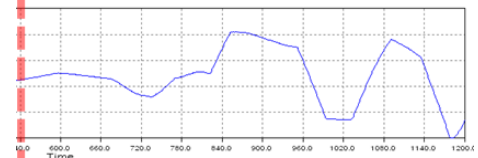


Fig 3 Train speed of tilting section

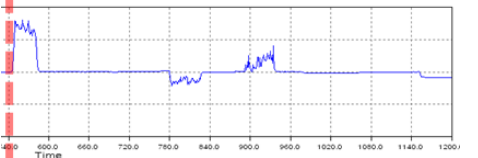


Fig 4 tilting angle

B. The change of Blood pressure

The change of Blood pressure also increased about 2.88% after riding tilting scssion comparing to normal state. Also, standard deviation grew about 0.9.state.

<Table3>

category	Normal State	Riding Tilting
Average	104	107
Standard Deviation	0.8	1.7

IV. DISCUSSION

Judging from this experiment, normal state and tilting section was little bit different. Average heartbeat of 36 Subjects increased about 2.07 and average Blood pressure also increased 1.26%. And considering the relation between tilting angle of tilting section and Heartbeat was high, it seems that tilting section have an effect on the change of Heartbeat. In physiological situation, roll phenomenon which is generated during tilting and the change of the sense of equilibrium from the three semicircular canals in a vestibular organ have effect on the autonomic nervous system of body. Also, it has influence on the heart's blood system. And finally, it is linked by the change of Heartbeat and Blood pressure.

V. CONCLUSIONS

The case of TTX, Korean tilting train which is acknowledged as new technique, was designed differently from other exiting trains and has improved the insufficient elements through the diverse evaluations currently. Especially, ride comfort betterment of tilting train has to be overcome. This thesis estimates riding comfort through two factors of heart's blood; Heartbeat and Blood pressure. And it might be different between the tilting sections and non-tilting, the change of tilting angle was also severe due to the tough scenario. However, it is enable us to know that environment named tilting was one of factors which make passengers react physically. Lastly, standing on the basis of this study, it needs the evaluation of riding comfort on the base of total living body parameter through measuring a variety of living body parameter measure multiply.

ACKNOWLEDGMENT

The authors thank financial and technical supports of Korea Railroad Research Institute, Republic of Korea.

REFERENCES

- BS 6841, 1987. Guide to measurement and evaluation of human exposure to whole-body mechanical vibration and repeated shock. BSI(1987).
- Cleon, L.M. and Lauriks, G., Evaluation of passenger comfort in railway vehicles. *Journal of Low Frequency Noise & Vibration*, 15(2), pp. 53-69(1996).
- Corbridge, C., & Griffin, M.J., "Effects of vertical vibration on passenger activities: writing and drinking", *Ergonomics*, 34(10), 1313-1332(1991).
- ENV12299; 1999: Railway applications: Ride comfort for passengers – Measurements and evaluation(1999).
- Garg, V.K. and Dukkipati, R.V., *Dynamics of railway vehicle systems*. London: Academic Press Inc. Ltd, (1984).
- Griffin, M.J., & Hayword, R. A., "Effects of horizontal whole-body vibration on reading" *Applied Ergonomics*, 25 (3), 165-169, (1994).
- Griffin, M.J., *Handbook of Human Vibration*.(Second printing Ed.) Academic press,(2003).
- ISO 2631-4; 2004 Mechanical vibrations and shock- evaluation of human exposure to whole body vibrations- Part4: guidelines for the evaluation of the effects of vibration and rotational motion on passenger and crew comfort of fixed guide way transport systems. (International organization for Standardization) (2004).
- Jerker Sundstrom and Shafiquzzaman Khan, "Train passengers' ability to read & write during lateral vibration transients", *Proceedings of 13th International Congress on Sound & Vibration*, Vienna, Austria, July 2-6, (2006).
- Jerker Sundstrom, "Difficulties to read and write under lateral vibration exposure" – Contextual studies of train passengers' ride comfort. Doctoral thesis, Royal Institute of Technology, (KTH) Stockholm, Sweden, (2006).
- Jerker Sundstrom, and Shafiquzzaman Khan, "Influence of stationary lateral vibrations on train passengers' ability to read and write", submitted to *Applied Ergonomics*(April 2006).
- Karakasis, K., Skarlatos, D.and Zakinthinos, T., A factorial analysis for the determination of an optimal train speed with a desired ride comfort. *Applied Acoustics*, 66(10), pp.1121-1134, (2005).
- Khan, S.M., "Effects of masking sound on train passenger aboard activities and on other interior annoying noises", *Acta Acustica*, 89 (4), 711-717, (2003).
- M. Shafiquzzaman Khan & Jerker Sundstrom, "Vibration comfort in Swedish inter-city trains – a survey on passenger posture and activities", *Proceedings of 18th International Congress on Acoustics*, (2004).
- Nakagawa, C., and Suzuki, H., "Effects of train vibrations on passenger PC use", *QR of RTRI*, 46 (3), (2005).
- Paddan, G.S. and Griffin, M.J., Evaluation of whole-body vibration in vehicles. *Journal of Sound and Vibration*, 253(1), pp. 195-213, (2002).
- Suzuki, H., Research trends on riding comfort evaluation in Japan. *Proceedings of the Institution of Mechanical Engineers Part F – Journal of Rail and Rapid Transit*, 212(1), pp.61-72, (1998).
- UIC 513R 1994 Guidelines for Evaluating Passenger Comfort in Relation to Vibration in Railway Vehicle. (International Union of Railways) (1994).
- Westberg, J., 2000. "Interference lateral vibration on train passenger activities: an experiment on human ability to perform reading, writing and drinking", Master Thesis TRITA-FKT Report 2000:62, (2000).
- Wollstrom, M., "Effects of vibrations on passenger activities: reading and writing – a literature study", TRITA-FKT Report 2000:64,(2000).
- Yoo, W.S., Lee, C.H., Jeong, W.B. and Kim, S.H., Development and application of new evaluation system for ride comfort and vibration on railway vehicles. *Journal of Mechanical Science and Technology*, 19(7),pp. 1469-1477, (2005).
- Bendat, J. S.; Piersol, A. G. , *Engineering applications of correlation and spectral analysis*, New York, Wiley-Interscience, 1980. 315 p.
- Suzuki,H.,etal., Research Trends on Riding Comfort Evaluation, *Proc. Instn. Mech. Engrs. , Vol.212PartF*, 1998
- Y.K. Kim , 2004, "Ride comfortness Analysis and Estimation using statistical method according to UIC513R", *Korea Railroad Journal*, Vol.7, No. 4, 2004
- Johan Forstberg, "Ride comfort and motion sickness in tilting trains" TRITA-FKT Report 2000,
- 2000Smith J, Jones M Jr, Houghton L et al. (1999) Future of health insurance. *N Engl J Med* 965:325–329
- Smith J, Jones M Jr, Houghton L et al. (1999) Future of health insurance. *N Engl J Med* 965:325–329

Kinematics Analysis of Chopsticks Manipulation

S.W. Chen, J.I. Liang, K.Y. Lai, Y.T. Ting, Y.C. Peng, H.Y. Hsu, K.H. Lai, and F.C. Su

Institute of Biomedical Engineering, National Cheng Kung University, Tainan, Taiwan, ROC

Abstract— Chopsticks are widely used in the Oriental countries. However, people develop their personal holding postures. Two main postures can be identified. One is parallel type, the other is crossed type. The purpose of this study is to compare the kinematics performance in these two holding postures, furthermore, to find out the reasons why the parallel type seems to be more effortless than the crossed type.

Eleven participants were recruited in this study. Six were parallel type, and the others were crossed type. They were asked to manipulate chopsticks in upper and lower positions. The kinematics parameters, including the finger joint flexion-extension angle, the digit-to-digit abduction angle, the finger relative flexion-extension angle, the wrist joint flexion-extension angle as well as radial-ulnar deviation angle, the chopsticks angle, the chopsticks tip distance and the velocity of approaching movement were measured. Whole duration was divided by four time points for a clear comparison.

The results in significance showed that the chopsticks angle was greater in crossed group than in parallel group. Besides, in comparing with crossed group, participants in parallel type seemed to change their movement pattern more often or with more variability.

For the future study, a detailed classification of manipulation patterns should be clarified according to the high variability within two current types. After all, this study has revealed some difference between manipulation patterns in kinematics way. More biomechanics significance needs to be addressed in the future.

Keywords— chopsticks manipulation, kinematics analysis.

I. INTRODUCTION

Hand is a critical part of human owing to its' precise sensation and fine movement coordination [1]. Except the fine function of hand, we can efficiently use chopsticks base on some mechanical mechanism, such as force balance and moment balance. Chopsticks are used as a tool to perform eating, especially for Oriental dwellers. This eating tool must have some kind of benefits for users because it has pass on generations to generations. The hand is considered to be in a grasp pattern When we operating the chopsticks [2], even though different people apparently are in different manipulation ways. In clinical observation, two main hand holding postures are noticed. Firstly, two chopsticks are

hold in a parallel direction [Fig. 1]. The other is that two chopsticks are hold in a crossed direction [Fig. 2]. Both of them are mainly performed by thumb and two former fingers. The ring and the little finger are performed as an assistance role for motion stabilization. However, the rear one is usually regarded as a less efficient posture for performing. On the other hand, we might spend much force to hold the same thing.

According to Figure 1, the fulcrum could be inferred to thumb pad which is contact to the upper chopstick. The effort force is the position which is pressed by index and middle finger. Both of the load forces are presented at the tip position of chopsticks which will help to hold the food. Hence, it can be simply concluded that both postures are the third type lever. To the exclusion of the difference moment arm of effort force between postures, obviously, it can be inferred that type 1 pattern would be more effective than type 2 because the component of load force is inward. Namely, the component of load force in type 1 would help the food to resist the gravity. Then, are there other reasons which can explain type 2 is less efficiency than type 1?

One demographic study divided hand prehension patterns into three main patterns [3]:

- Palmar prehension pattern, was classified when there were obviously one move chopstick and one stabilizing chopstick. The movement was often distributed by IP joints. The prevalence was the highest.
- Lateral prehension pattern was described when the chopsticks were relying on the lateral facet of fingers. A pivotal feature was that CMC joint adducts to clip and stabilize the chopsticks. The prevalence was the lowest.
- Dynamic palmar prehension pattern was classified when the neutral position of chopsticks was crossed. In addition, forearm and palm were usually in pronation when operating. Each main pattern included 3~5 transformations.

The result showed the velocity of palmar prehension pattern and dynamic palmar prehension pattern were significantly greater than lateral prehension pattern. However, the author didn't discuss the kinematics performance between these patterns while their study focused on the functional outcome of each type.

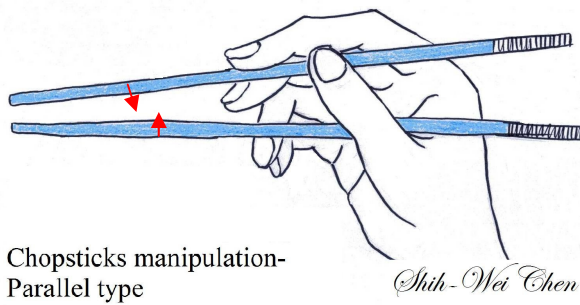


Fig. 1 Type 1: parallel type

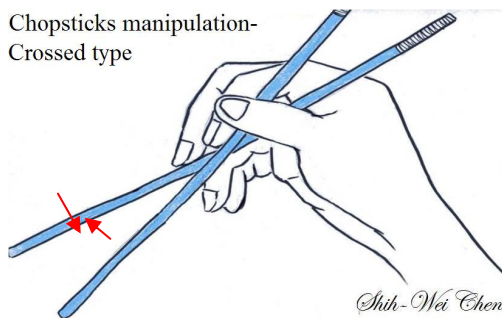


Fig. 2 Type 2: crossed type

Wang [2] tend to separate the chopsticks manipulation into several phases: 1. Approaching phase which involved wrist movement. 2. Tuning phase include fine turning and adjusting movement. 3. Initial contact phase is the period when the contact area is suitable for the minimal load force. 4. Stable grasping phase, there was no relative motion between chopsticks and hand. This classification concept was inherited in our study to analyze the data in different period appropriately. In addition, the contact area of object and chopsticks which provides friction was the determining factor to stabilize the object. The two chopsticks were operated in a single plane, and they were basically parallel while nonparallel case which is inferred as type 2 lead to disequilibrium condition. The author mentioned that the moment equilibrium can only be happened at the midpoint of the line contact. That is to say, even if the force equilibrium is achieved, the object might roll because of the nonparallel pattern. In the contrary, while in pattern1, moment equilibrium was guaranteed as long as the force equilibrium was maintained.

Recent data have verified that chopsticks about 240 and 180 mm in length were optimal for adults and pupils [4]. Moreover, Wu et al [6] also took diameter of chopsticks and the tip angle for significant factors for eating efficiency.

However, previous studies focused on the performance guideline and the chopsticks design. The studies about bio-mechanical analysis of chopsticks manipulation are still deficient. The purpose of this study was to discuss the difference of the kinematical performance between the two holding postures. In spite of the lever and the outward effect force which may cause the awkwardness of type 2 pattern, the other key points about the cause of inefficiency in type 2 pattern would be discussed.

II. MATERIALS AND METHODS

A. Subjects & Marker set

Eleven right-handed participants (age range: 23 – 26 years) were recruited and according to their daily chopsticks manipulation, six participants were in the parallel group and five were in the crossed group.

In the experiment, the kinematic data of thumb, fingers (except for little finger), wrist and chopsticks in these two postures were measured using a video-based passive marker detection system. There were 15 markers on thumb, index finger, middle finger, and ring finger, 3 markers on wrist part, 6 markers on chopsticks and 1 marker on pork ball. The chopsticks using in the experiment were 22.7 cm in length. Figure 3 and Figure 4 showed the marker set and experimental setting.

B. Materials

A three-dimensional optical active marker motion capture system (Motion Analysis Corp., Santa Rosa, CA, USA) was used to collect the movement trajectories of markers, including eight cameras.

C. Procedures

Participants were asked to sit in an upright posture and use the chopsticks to clip up the pork ball which was an unconstrained object [5] from desk top to the determined position in the space. They performed the task in two different holding distances. Two distances conditions were determined by position of tip of thumb, index and middle finger. In the lower position, subjects were holding chopsticks in the former part of chopsticks. On the other hand, when the positions of tips were in the rear part of chopsticks, the condition was considered to be the upper position. Participants were asked to do the task three times in each distance. Eventually, one person totally performed the task 6 times.

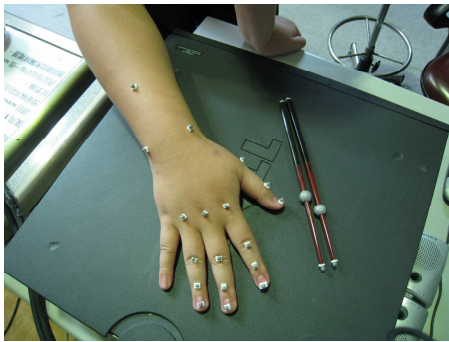


Fig. 3 maker set

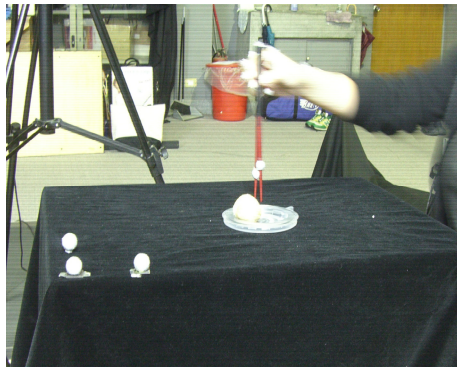


Fig. 4 experimental setting

D. Data analysis

Nonparametric Analysis was used. The performances while subjects hold in different position (e.g. upper & lower positions) were considered as two related samples, whereas the performances of two groups were considered as two independent samples. Software including SPSS 12.0 and Matlab 6.5 (Mathwork, Natick, MA, USA) were used to calculate the data [7]. The kinematic data in the study including:

- IP flexion/ extension angle of thumb
- DIP, PIP & MP flexion/ extension angle of index, middle & ring finger
- Abduction angle between 1-2, 2-3, 2-3, 3-4 fingers
- Relative flexion/ extension angle between 1-2, 2-3, 2-3, 3-4 fingers
- Wrist flexion/extension and ulnar/radial deviation angle
- Chopsticks Angle
- Chopsticks tip distance
- Chopsticks angular velocity of approaching movement.

III. RESULTS

We separated the chopsticks manipulation into four time periods: Time point 1 as the time for chopsticks started directing to the object. Time point 2 was described when the biggest distance between the chopsticks. Time point 3 was described when object was preliminary clipped up. Time point 4 was described when object was stable clipped by chopsticks. In order to avoiding the initial and termination effect, we just show the results in the T2-T3 and T3-T4 period and each time point.

A Time periods

In T2-T3 period, the average maximal ($p=0.011/0.018$) and minimal ($p=0.008/0.007$) chopsticks angle are greater in crossed group than in parallel group regardless in upper or lower position; however, the range of motion of chopsticks is similar in two groups. The ROM of wrist flexion and extension in T3-T4 period is greater in parallel group than in crossed group ($p=0.021/0.019$).

B Time points

Chopsticks angles are significantly greater in crossed group than in parallel group in both positions, except for the time point 1. In the result of relative position of 3th finger compare with 2th finger, we found that the position of index is always below the middle finger in cross type whereas index is always above the middle finger in parallel type in lower position ($p=0.023$).

According the results in parallel group, there is a trend that participants would exact a movement toward radial side in lower position than in upper position at time point 1 ($p=0.031$).

IV. DISCUSSION

For comparing performance between parallel and crossed groups, people in crossed type held the chopsticks in a wider angle. It could be inferred that they might perform more effort to hold the chopsticks. The result supported the previous hypothesis that holding in crossed type might be more inefficient than holding in parallel type. That might also result in some unnecessary force in outward direction or in other directions which might disturb the stability of objects. Furthermore, there was no significant difference in wrist motion between groups except for the T3-T4 period. People in parallel type showed larger wrist ROM than crossed group. That could be inferred that people in parallel

type use more extrinsic muscles to clip up objects in contrast to the crossed group who use more intrinsic muscles to clip objects up.

There were some significant performance differences between upper and lower positions when holding in parallel type while there was no difference in crossed type. It can be inferred as a compensation phenomenon because participants in parallel type were not familiar with the posture in the lower position, whereas the participants in crossed group seems perform the same pattern in different positions. It could be deduced that there are less motor pattern changes with different holding positions in crossed group than in parallel group.

The difficulty that encountered in this project was the data tracking. Since the hand posture was like a fist posture, the markers on the finger tip were not easy to detect. Moreover, we try to use differentiation formula to derive the angular velocity and angular acceleration of each finger segment, unfortunately, the noise interfered with the calculating results. Further, the variability among participants was high. This variance might disturb the results.

V. CONCLUSION

There is lack of studies focus on the biomechanics in chopsticks manipulation. According to this study, we compare the kinematic data of two main operating postures. For the future study, instead of two or three patterns, a more detailed classification in order to decrease the variability within different types. Moreover, in this experiment setting,

the participants were asked to stand by in an unnatural posture which is pretend as the start position. That might also delineate reliability and validity of the experiment. After all, this study has revealed some difference between manipulation patterns. More biomechanical significance needs to be addressed and studied in the future.

REFERENCES

1. Cutkosky M R (1985) *Robotic Grasping and Fine Manipulation*. Kluwer, Norwell, MA, USA
2. Wang G, Stephanou H E. (1988) Chopstick manipulation with an articulated hand: a qualitative analysis. *Proc IEEE Int Conf Robot Autom* 1:94-99
3. Chang J J, Chien T H., Lin Y T. (1985) Comparison of Various Patterns of Chopstick Use and Functional Performance. *Kaohsiung J Med Sci* 9:428-434
4. Hsu S H, Wu S P.(1991) An investigation for determining the optimum length of chopsticks. *Appl Ergon* 22:395-400
5. Chen Y L. (1997) Effects of shape and operation of chopsticks on food-serving performance. *Appl Ergon* 29:233-238
6. Wu S P. (1995) Effect of the handle diameter and tip angle of chopsticks on the food-serving performance of made subjects. *Appl Ergon* 26:379-742
7. MATLAB at <http://www.mathworks.com>

Author: Fong-Chin Su
 Institute: Institute of Biomechanical Engineering
 Street: No.1, University Road
 City: Tainan
 Country: Taiwan (R.O.C)
 Email: fcsu@ncku.edu.tw

ZigBee-Based Wireless Neuro-Stimulator for Improving Stroke Recovery

Y. Yang¹, G. Kim², H. Yun³, Y. Shin⁴, H. Kim⁵, and M. Ryu¹

¹Chonbuk National University/Biomedical Engineering, Jeonju, South Korea

²Korea Institute of Industrial Technology (KITECH), Cheonan, South Korea

³Electronics and Telecommunication Research Institute (ETRI)/Neural Interface, Daejeon, South Korea

⁴Wongwang University Hospital/Rehabilitation, Iksan, South Korea

⁵Presbyterian Medical Center/Neurosurgery, Jeonju, South Korea

Abstract—Stroke is a leading cause of adult disability in the United States, leading to a serious demand for new interventions to improve the quality of life in stroke survivors. To this end, direct cortical stimulation using an epidural electrode has been reported with promising results in animal and human studies, showing the potential for enhancing the recovery in chronic stroke patients. For optimal results, doctors must be able to modify the stimulation pattern as frequently as needed over a period of time for a given patient.

This study aims to develop a prototype of a telemedicine system to enhance stroke recovery by using a ZigBee-based wireless neuro-stimulator. Remote neuro-stimulation treatments was enabled via internet. The system also helps doctors to plan more personalized treatment by analyzing chronic records of the patients. The system can also be beneficial as a common platform for a wide range of brain diseases and clinical care for which electric stimulation is helpful.

Keywords—Electrical brain stimulation, stroke recovery, rehabilitation, ZigBee, neural stimulation.

I. INTRODUCTION

Stroke is a leading cause of adult disability and the third-leading cause of death in the United States. Approximately two-thirds of individuals suffering a stroke survive and require rehabilitation [1]. Medication and physical therapy are common treatments for strokes to facilitate nerve recovery. While early rehabilitation treatment does help patients regain pre-stroke functions, recovery slowly subsides after the first month following the stroke and tends to level off and stagnate in the long term. After about six months, stroke survivors benefit little from rehabilitative training and are left impaired. Long-term interventional strategies to improve the quality of life in stroke survivors are therefore in great demand. Recent studies have shown that electrical currents delivered to the cortex through transcranial magnetic stimulation (TMS) or transcranial direct current stimulation (tDCS) cause cortical stimulation that can modulate the cortical excitability of the human brain noninvasively.

These techniques can also be used as therapeutic interventions to enhance recovery in patients suffering from the long-term aftereffects of stroke. It has been suggested that direct cortical stimulation through an epidural electrode may produce similar effects, possibly with more advantages. [2-4]. The application of direct electric stimulation for stroke recovery is in an early stage, in contrast to the abundant research and clinical studies on commercial deep brain stimulators (DBS) for Parkinson's disease and epilepsy [5]. To directly stimulate the cortical region, an electric stimulator is implanted in the brain and is shielded under the skin, requiring a wireless link for convenient operation of the implanted pulse generator (IPG). The electrical stimulation therapy for stroke implies not just temporary diminishment of symptoms but also gradual recovery of the impaired functions. Ongoing modification of the stimulation pattern is essential during treatment. The stroke patients need intensive administration by doctors for optimal recovery. However, since the commercial DBS systems provide magnetic and proximity RF links for the doctors to configure the IPG and control its operation, the spatial range of control is very limited. What is worse, severe stroke aftereffects often limit patients' activities, making regular doctor visits for treatment difficult.

The stimulator proposed in this study adopts a widely known low-power wireless communication standard ZigBee in order to extend the control range of IPG in space, reaching as far as remote hospitals or clinics through the internet. We aimed to develop a prototype miniaturized electric stimulator for stroke recovery and a wireless control for extended and flexible use of the IPG.

II. MATERIALS AND METHODS

A. IPG model and ZigBee communication system

Two types of pulses were used (anodal and cathodal) in the stimulation of brain tissue in the preliminary animal

experiments [4]. Chronic electrical stimulation of nerve tissue with only a monopolar pulse might damage some tissues and corrode the interfacing electrode, which significantly distorts the stimulation waveform and makes it difficult to deliver the intended electric voltages or currents to the neural tissues concerned. The developed IPG model is capable of charge-balanced bi-phasic pulse generation, which can reduce cell damage and electrode corrosion. We designed an H-bridge circuit to generate biphasic pulses with a single power supply. The amplitude of stimulation is adjustable with a D/A converter, DAC7617 (TI, USA). The IPG model includes the H-bridge, D/A converter, and microcontroller unit (MCU) Atmega128L (Atmel, USA) for accurate generation and adjustment of stimulation. Figure 1 shows the developed stimulation circuit. The IPG model has dimensions of $50 \times 37 \times 8 \text{ mm}^3$ and a weight of 7.4 g. It should be noted that the animal experiments found no remarkable increase in recovery ratio after about 1 month of direct cortical electric stimulation treatment[4]. For humans, it is expected that the implanted system should operate less than about 6 months to cover the period in which functional recovery is most active.

The ZigBee is a standard small, low power radio-frequency communication protocol based on the IEEE 802.15.4 standard, designed for use in wireless personal area networking (WPAN) applications [6]. The low power characteristic is essential to the electrical system implanted in the body because battery replacement requires an additional surgical operation.

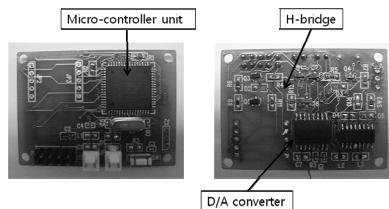


Fig. 1 The miniaturized electrical neuro-stimulator composed of a micro-controller unit, H-bridge and D/A converter. Circuit board of area $50 \times 37 \text{ mm}^2$ and weighing 7.4 g.

A small ZigBee transceiver module was developed using CC2420 ZigBee Development Kit (Chipcon, Norway) with the Atmega128L microcontroller. The developed circuit board is shown in Fig. 2. Its physical dimensions are $45 \times 40 \times 12 \text{ mm}^3$, the size of a small matchbox, and its weight is 12.7 g. In addition to enabling wireless control, the ZigBee can connect the neuro-modulation system to a widespread communication network such as the internet or a mobile network. This network-based neuro-modulation system can

provide a remote or mobile rehabilitation program as shown in Fig. 3.

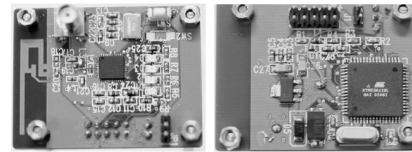


Fig. 2 The ZigBee communication module. Circuit board. Circuit board of area $45 \times 40 \times 12 \text{ mm}^3$ and weighing 12.7 g.



Fig 3 A remote rehabilitation service for stroke recovery using a ZigBee-based neuro-modulation system. The patient's IPG is connected to doctors at a remote site through a) the internet and PC, b) a mobile network and various handheld devices.

B. Remote and wireless configuration of neuro-stimulator

The brain stimulator can be configured by doctors from a remote site selecting ID and several parameters in a graphical user interface (GUI) software shown in Fig. 4.

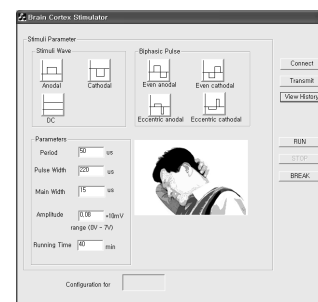


Fig. 4 GUI for configuring the electrical stimulator

The parameters include period, pulse width, amplitude and overall running time. The stimulation waveform can have different polarity modes as shown in Fig. 5. Bipolar stimulations can be even or eccentric shape. The period and the pulse width are in the range of several or tens of microseconds. The amplitude has values of several millivolts. The overall running time is usually about an hour per one day in regular operation. Since there are no commercial standards for neuro-stimulators for stroke, the ranges of

parameters appropriate for neural tissue stimulation were selected based on those used in the preliminary animal experiments clinically available DBS Solettra Model 7426 (Medtronic) used for treating movement disorder like Parkinson's disease and essential tremor.

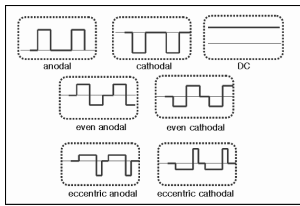


Fig. 5 Various configurations of stimulation

C. Chronic data management for optimal stimulation therapy

A chronic record of the stimulation and the gradual recovery process is a valuable resource in this type of neuro-stimulation therapy. The main objective of the data management system is to provide a visualized history of patient's treatment as illustrated in Fig. 6 to clinical neurosurgeons. Doctors can correlate the condition of parameters with the gradual recovery process of the patient. This will help doctors gain understanding or insight about what conditions improve recovery for a given patient. Though it would be preliminary, doctors can obtain basic information about the patient's language and motor abilities through voice communication over the phone and through question-based scoring methods. Actually, we are developing interactive digital devices in tangible forms like PEG board for on-line evaluation of stroke symptoms and recovery progress based on clinically verified scoring and scaling methods.

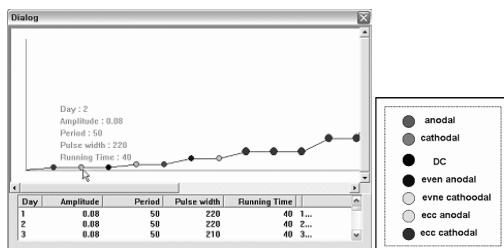


Fig. 6 Graphical visualization of the stimulation parameters. Each color indicates the polarity of stimulation in the amplitude-based display of chronic data.

Multi-parameter display is organized according to the significance of the parameters. Since it is generally accepted that the amplitude of the pulse has the strongest impact on the brain, amplitude is marked on the vertical axis. Each

circle indicates one dose given by the doctor. The radius of the circle corresponds to the duration of each dose. The color shows the polarity and mode of stimulation; red is for anodal stimulation, green for cathodal, black for DC, blue for even anodal, light blue for even cathodal, yellow for eccentric anodal, and purple for eccentric cathodal. Additional details are shown when the mouse cursor moves over the circle. The data mining gives useful information about the principles of stroke recovery accelerated by cortical stimulation. Moreover, since every individual will have different responses to the electrical stimulation, this data collection approach allows for personalized therapy.

III. RESULTS AND DISCUSSION

We verified the remote pulse generation and data management performance of the developed system. Figure 7 shows the controlled output waveforms. The wireless link worked reliably within a radius of about 10 m.

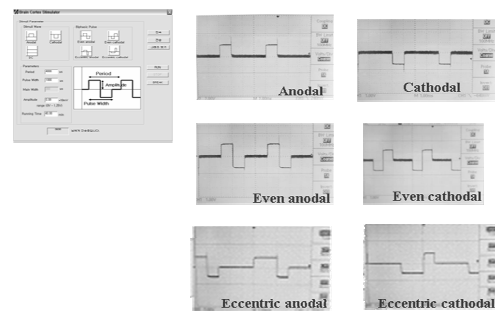


Fig. 7 Wireless configuration of the stimulator and its output waveforms measured by oscilloscope.

For an extended use of a neuro-stimulator implanted in the body, most of the battery power should be concentrated on electrical stimulation of neural tissues rather than on communication. We therefore decided to transmit only the shape parameters of the waveforms instead of all the data points of the waveform. Another drawback to transmitting all the data points is that this requires a long communication time via RF transmission. A complete set of points would allow us to generate arbitrary waveforms; however, there is some potential risk in using high frequency RF transmission through the skin. The parametric transmission needs only about 10 bytes while the entire data point transmission requires about 400 bytes. The proposed method achieved both reduced power consumption and minimal RF exposure time. Table 1 shows the current consumption of the device under various stimulation configurations.

Table 1 Comparison of current consumption under different pulse conditions

Polarity Duty ratio	Mo- nopolar (anodal)	Even bipolar (an- odal)
1/10	47 mA	50 mA
1/40	45 mA	46 mA

Table 2 shows a comparison with the technical specification of the Soletra Model 7426. Although the two systems have different working principles for different diseases and thus cannot be directly compared, Table 2 shows that the developed system might be useful for more precise experiments for research purpose. The output voltage necessary for cortical stimulation for stroke recovery is much lower than 3.3V. Cortical stimulation in animals, which will likely be the first application of the developed system, requires low voltages. Our device meets the requirements for a prototype and animal experiments.

Table 2 Comparison of the developed system with commercial DBS for treating other movement disorder

Symbol	Max. rate	Min. pulse width	Amplitude of stimulation
Soletra Model 7426 (Medtronic)	185 Hz	60 μ s	0 ~ 10.5 V
Our system	500 kHz	1 μ s	0 ~ 3.3 V

IV. CONCLUSIONS

We have developed a novel electrical neuro-stimulator for stroke recovery on the basis of preliminary experimental results. The ZigBee-based RF communication, stimulation output and internet hookup were successfully integrated in the proposed neuro-modulation system. The precise wireless configuration showed promise for applications such as remote rehabilitation, which enables a relatively small number of doctors or certified personnel to manage many stroke patients simultaneously even during their daily activities.

With the help of wireless communication, the developed system will facilitate the study of how electrical stimulations affect neural tissues. Currently, the effective pulse shape parameters for improving stroke recovery are being investigated through animal experiments in collaboration

with experts in neurosurgery and neuro-rehabilitation. The site of stimulation is also an important issue for better efficacy of electric cortical stimulation. Compatibility with magnetic resonance (MR) techniques is another important requirement for the implantable neuro-stimulator because we need to use neuro-imaging systems such as functional MR imaging (fMRI) to study the effect more precisely.

We are also examining additional components, including audiovisual support for better treatment or a user-friendly interface especially for patients with severely impaired motor function. The digitized tools for the more quantitative evaluation of patient recovery are being integrated into the proposed system, which will be a bi-directional interactive platform for a wide range of tele-rehabilitation techniques.

The system developed here can also be used as a common platform for a wide range of brain diseases and clinical care for which electric stimulation is used.

ACKNOWLEDGMENT

This study is supported by Chonbuk National University.

REFERENCES

1. H. T. Hendricks, V. J. Limbeck et al. (2002) Motor recovery after stroke: a systematic review of the literature. *Arch Phys Med Rehabil* 83:1629–1637
2. H. I. Kim, Y. I. Shin, S. K. Moon et al. (2008) Unipolar and continuous cortical stimulation to enhance motor and language deficit in patients with chronic stroke: report of 2 cases. *Surg Neurol* 69:77-80
3. R. Levy, S. Ruland, M. Weinand, D. Lowry et al. (2008) Cortical stimulation for the rehabilitation of patients with hemiparetic stroke: a multicenter feasibility study of safety and efficacy. *J Neurosurg* 108:707-714
4. S. K. Moon, C. Y. Yang, S. E. No et al. (2007) Promotion of motor recovery by anodal continuous and low amplitude cortical stimulation in rat stroke model. *Lab Anim Res* 23:25-30
5. H. O. Luders (2004) Deep brain stimulation and epilepsy. The Cleveland Clinic Foundation USA
6. S. H. Jung, H. I. Jeon (2004) IEEE 802.15.4 and ZigBee Protocol: Active RFID technology for Ubiquitous sensor networking. *J Korean Institute of Communication Sciences* 21:67-88

Author: Yoonseok Yang
 Institute: Chonbuk National University
 Street: 664-14, Deokjin-dong,
 City: Jeonju
 Country: South Korea
 Email: ysyang@gmail.com

The effect of clearance upon friction of large diameter hip resurfacing prostheses using blood, clotted blood and bovine serum as lubricants

S.Afshinjavid and M. Youseffi

School of Engineering, Design and Technology – Medical Engineering University of Bradford,
Bradford, West Yorkshire, BD7 1DP, United Kingdom.

Abstract: Total hip joint implantation is an effective solution for reducing pain and ailing induced by arthritis or other diseases at the hip joint. Hence, a conventional metal on polyethylene (PE) bearing device has been introduced since late 1950's for implantation. However, due to significant release of PE wear debris causing swelling at joints and osteolysis leading to implant loosening and failure in fixation, attempts are made to optimize implant design, manufacturing and surgical procedures for a relatively new metal on metal hip resurfacing prostheses of larger diameters to have lower friction and wear, better fixation and reduced risk of dislocation.

The aim of the present study was to investigate the role of diametral clearance on friction using a large diameter metal on metal hip resurfacing prosthesis and various lubricants including blood, clotted blood and combinations of bovine serum with aqueous solutions of carboxymethyl cellulose (CMC) and hyaluronic acid (HA).

Keywords: Friction, 50mm diameter metal-on-metal hip resurfacing prostheses, Diametral clearances, Blood and Clotted Blood, BS+CMC and BS+HA (+CMC).

I. INTRODUCTION

The major objectives in the design of joint prostheses are the development of stable articulations, low friction and wear, solid fixation into the bone, and normal range of motion. New synthetic replacement materials are being designed by biomedical/medical engineers to accomplish these objectives. Total Hip Joint Replacements (THR) are usually composed of cobalt chrome molybdenum (Co-Cr-Mo) alloys in combination with modern plastic, Ultra-High Molecular Weight Polyethylene (UHMWPE). In recent years, the proportions of younger and more active patients undergoing arthroplasty have increased mainly because of advanced osteoarthritic joints in ~10% of young adults. Due to their higher activity levels compared to the inactive population, the elderly, and the limited survivorship of the conventional replacement, there are still concerns about the use of metal on polyethylene prosthesis for the younger generation. Highly active patients could potentially generate extremely high wear rates, which would in turn result in premature failure of the implant. The most commonly quoted survivorship rates followed by revision for a particular implant or treatment is 10 – 15 years. Hence, it would be advantageous to develop a replacement that could either survive the patients' lifetime, or use a

replacement that would conserve bone stock for the eventual revision. One of the hip replacement procedures in which the head of the femur is retained resulting in minimum bone removal is called hip resurfacing. Instead of removing the head completely, it is shaped to accept an anatomically sized metal sphere. There is no large stem to go down the central part of the femur (or femoral shaft) and the surface of the acetabulum is also replaced with a metal implant, which is wedged directly into the bone.

The modern resurfacing components are made of Co-Cr-Mo metal alloys, which are finely polished to produce a very smooth surface finish giving low friction and wear. There are many other advantages of using hip resurfacing arthroplasty including bone conservation, improved function due to retention of the femoral head and neck and hence better biomechanical restoration, decreased morbidity at the time of revision arthroplasty, reduced dislocation rates and stress-shielding, less infection, and reduced occurrences of thromboembolic phenomena (less blood clotting due to not using any tools/stems in the femur). Typical examples of such devices include the Birmingham Hip Resurfacing prostheses from Smith and Nephew Orthopaedic Ltd. (see Figure 1 [1]), ASR from DePuy International, and DUROM from Zimmer. Following their promising short to medium term clinical results, second-generation metal-on-metal hip resurfacing prostheses have, therefore, been extensively introduced since the 1990's by almost all major orthopaedic companies.

It has been illustrated via both simulator studies and clinical trials that correct manufacturing of the prosthesis will lead to excellent sphericity, tolerances, and an optimum radial clearance which are the main reason for their success. Use of larger diameter bearings (>35-50mm diameter) and hip resurfacing prostheses have the advantages of increased range of motion and decreased incidence of dislocation for younger and more active patients.

The clearance between the articulating components is size-dependent, i.e. the larger the diameter the higher the gap/clearance between the components. The range for the entire family of various diameters is from 90 to 200 microns of diametral clearance, with each bearing size having an optimized gap for maximum fluid film thickness. The diametral clearances between articulation components play a major role in their generation of wear debris which is probably the most influential factor in wear behaviour. Proper clearance is essential for entrapping the synovial fluid between the articulating surfaces. This fluid is largely responsible for separating the surfaces while the joint is in motion and, thereby, reducing wear. If the gap between components is too small or too large there will be a sharp increase in wear rates.

The aim of this work was therefore to investigate the effect of various clearances on friction and lubrication of as-cast Co-Cr-Mo hip resurfacing components with 50mm diameter via hip friction simulator studies which have strongly indicated that clearance plays a major role in generation of high friction and wear, and that wear appears to be relatively insensitive to changes in materials that have similar chemical compositions but different microstructures [2].

II. MATERIALS AND METHODS

Immediately after joint replacement, the artificial prosthesis is bathed in blood and clotted blood instead of synovial fluid. Blood contains large molecules and cells of size ~ 5 to 20 micron suspended in plasma and is considered to be a non-Newtonian fluid with density of 1060 Kg/m^3 . The effect of these properties on friction is not fully understood and, so far, hardly any studies have been carried out regarding friction of metal-on-metal bearings with various clearances in the presence of lubricants such as blood or clotted blood. In this work, therefore, we have investigated the frictional behavior of a group of Smith and Nephew Birmingham Hip Resurfacing devices with a nominal diameter of 50mm and diametral clearances in the range ~ 80 to $300\mu\text{m}$, in the presence of blood (clotted and whole blood).

Five as cast high carbon Co-Cr-Mo MOM 'Birmingham Hip Resurfacing (BHR) devices' (supplied by Smith and Nephew Orthopaedics Ltd, Coventry, UK) with a nominal diameter of 50 mm each and diametral clearances of 80, 135, 200, 243 and $306 \mu\text{m}$ were used in this study. The initial surface roughnesses were in the range ' $R_a=10\text{-}30 \text{ nm}$ ' similar to those of commercial MOM hip prostheses.

Frictional measurements of all the joints were carried out using a Prosim Hip Joint Friction Simulator (Simulation Solutions Ltd, Stockport, UK). Friction measurements were made in the 'stable' part of the cycle at 2000N and thus the loading cycle was set at maximum and minimum loads of 2000N and 100N, respectively. In the flexion/extension plane, an oscillatory harmonic motion of amplitude $\pm 24^\circ$ was applied to the femoral head with a frequency of 1Hz in a period of 1.2s. The load was therefore applied to the femoral head with the artificial hip joint in an inverted position, i.e. femoral head on top of the acetabular component, but with a 12° angle of loading between the two bearings as observed in human's body (12° medially to the vertical). The angular displacement, frictional torque (T) and load (L) were recorded through each cycle. The frictional torque was then converted into friction factor (f) using the equation: $f = T/rL$, where r is the femoral head radius. An average of three independent runs (tests) was taken.

Initially, the test was conducted with non-clotted blood (whole blood with Lithium heparin to prevent clotting) and then clotted blood as the lubricants for each joint. Viscosity

of the non-clotted blood was found to be $\sim 0.01 \text{ Pas}$ and that of clotted blood was $\sim 0.02 \text{ Pas}$. For comparison, combinations of bovine serum (BS, 25%) with aqueous solutions of carboxymethyl cellulose (CMC+75% distilled water) and Hyaluronic acid (HA) as lubricants were also used with viscosities of 0.0136 Pas (BS+CMC) and 0.0132 Pas (BS+HA+CMC). Note that CMC was used as the gelling agent to obtain the required viscosities.

III. RESULTS AND DISCUSSION

Table 1 and Figure 2 show a close comparison between friction factors for various diametral clearances of 80 to $306 \mu\text{m}$ using Blood and Clotted blood as lubricants. It became more obvious that both blood and clotted blood resulted in higher friction factors especially at lower clearances of 80 and $135 \mu\text{m}$. This higher friction in the low clearance bearings may produce micromotion and hamper bony ingrowth immediately after implantation resulting in impaired fixation with long-term implications for survival. The friction factors in Table 1 have also shown that lower clearances do not necessarily reduce the friction factors to a level for the presence of full fluid film lubrication and that the friction factors decrease with increase in diametral clearance. This finding clearly suggests that lower clearances have higher potential for increasing the friction between the articulating joint surfaces using blood and clotted blood as lubricants and thus increase the risk of micromotion due to higher surface contacts, leading to higher risk of joint dislocation. On the other hand, the BS+CMC and BS+HA+CMC lubricants with similar viscosities showed the opposite effect, i.e. caused an increase in friction factor with increase in diametral clearance (see Table 1 and Figure 2). Also notable was that, the friction factors were consistently higher for blood and clotted blood as compared to those of lubricants based on bovine serum.

Table 1: Friction factors for the whole blood, clotted blood, BS+CMC and BS+HA+CMC for different diametral clearances.

Diametral Clearance, μm	Whole Blood, $\eta=0.013 \text{ Pas}$	Clotted Blood, $\eta=0.02 \text{ Pas}$	BS+CMC, $\eta=0.0136 \text{ Pas}$	BS+HA(+CMC), $\eta=0.0132 \text{ Pas}$
80	0.19	0.17	0.08	0.07
135	0.19	0.165	0.09	0.076
200	0.18	0.16	0.12	0.095
243	0.143	0.15	0.125	0.1
306	0.14	0.14	0.132	0.114

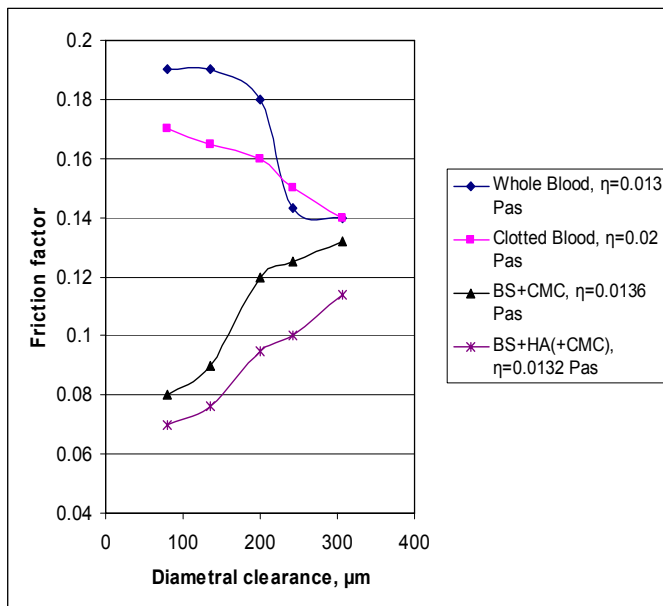


Figure 2. Graph of friction factor versus diametral clearance for the S&N BHR 50mm diameter devices using Blood, Clotted blood and bovine serum as lubricants.

IV. CONCLUSIONS

- The in vitro frictional behaviour of five large diameter (50mm nominal) S & N BHR prostheses with various diametral clearances ($\sim 80\text{-}300 \mu\text{m}$) has been investigated using blood, clotted blood and combinations of bovine serum with aqueous solutions of CMC and Hyaluronic acid as lubricants to understand and mimic the in vivo frictions generated at the articulating surfaces immediately after hip implantation.
- It became clear that the friction factors decreased consistently with increase in diametral clearance for both blood and clotted blood. This therefore suggested that higher clearances will lower the friction (and hence wear) for these large diameter S&N BHR devices depending on the type of lubricant and viscosity.
- On the other hand, the bovine serum based lubricants with similar viscosities showed the opposite effect, i.e. caused an increase in friction factor with increase in diametral clearance and that the friction factors were consistently higher for blood and clotted blood as compared to those of lubricants based on bovine serum.



Figure 1. The Birmingham Hip Resurfacing (BHR) device consists of two parts: an acetabular component (or cup), and a femoral resurfacing component (or head).

REFERENCES

- [1] Javid S.A., Youseffi M., et al., 2007, THE EFFECT OF CUP DEFLECTION ON FRICTION IN METAL-ON-METAL BEARINGS, Abstract presented at the British Hip Society (BHS), Leeds Meeting: 28th February-2nd March 2007, Leeds Royal Armouries, Leeds, UK, Symposium: Biological implications of Metal on Metal Articulation.
- [2] Liu F., Jin Z.M., Roberts P. and Grigoris I., 2006, Importance of head diameter, clearance, and cup wall thickness in elastohydrodynamic lubrication analysis of metal-on-metal hip resurfacing prostheses, Proc. IMechE Vol. 220 Part H: J. Engineering in Medicine, pp 695- 704.

Authors: Mr. Saeed Afshinjavid and Dr M. Youseffi
 Institute: School of Engineering, Design and Technology-
 Medical Engineering, University of Bradford
 Street: Richmond Road
 City: Bradford, BD7 1DP
 Country: United Kingdom
 Email:
S.Afshinjavid@bradford.ac.uk and
m.youseffi@bradford.ac.uk

Comparison of k-Means and Bayes classifiers for Human Body Motions Classification

J. Havlik, J. Uhlir and Z. Horcik

FEE CTU in Prague/Department of Circuit Theory, Technická 2, Prague 6, Czech Republic

Abstract — This paper deals with a comparison of k-Means and Bayes classifiers designed for classification of the human body motions classification. The main task of this paper is to compare the performance and the reliability of classifiers. The presented work is a part of research of relations between brain and muscle activity. The sensing of body motions is based on standard DV camcorders system. The procedures have no negative impact to brain activity (the tracking does not affect the measured EEG signals). Presented paper includes the description of observing, discerning and parameterization procedures and the discussion of motion classification. The results of classification accuracy are the part of this paper.

Keywords — motion analysis, motion classification, k-Means classification, Bayes classification

I. INTRODUCTION

This paper describes the part of research concerning with relations between the brain activity and the human body motions. The main task of presented work is to develop and verify the procedures for observing of muscle activity.

The brain activity is represented by the electro-encephalograph (EEG) signals for this research. The EEG signals are very complex signals reflecting not only intentional motions, but also all vital functions, artifacts from eye motions etc. Due to this complexity it is appropriate to use a small peripheral muscle capable of independent motions to minimize undesirable effects of its neighbourhood. It is possible to presume that the relative simple brain stimulus could be expected for this motion. Due to this reasons the free three-dimensional motions of thumb have been chosen.

The muscle activity is represented by the parameters of the thumb trajectory.

The goal of current research is to assign typical changes of EEG signals to the type of thumb motion. The parameterization and the classification of thumb motions are the aim of presented work.

II. EXPERIMENT

The person under test sits in straight seat. The arm with observed thumb is supported by a rest. The thumb moves

between 3 positions – stationary states. Each movement is triggered by the synchronization pulse. The period of pulses is 6 ± 1 seconds. About 20 % of period is reserved for movement, the rest 80 % of period is the stay on the position.

The recording of motions has to fulfill two necessary conditions:

1. a non-contact sensing,

The sensing has to be non-contact, because any contact between thumb and any part of sensor could affect the EEG signals due to a physiological feedback.

2. a possibility to synchronize the recorded movements and EEG signals.

The recorded movements and the EEG signals are processed separately. The both records have to be synchronized in order to study correlations.

In accord with these conditions the thumb motions are sensed using a pair of standard DV camcorders [1]. The brain activity is sensed using a standard EEG measurement station.

The motions are triggered with LED generated optical pulses, the leading edge of synchronization signal is recorded as a polygraphical signal parallel to EEG signals.

III. PARAMETERIZATION

The sensed thumb is marked by special mark, the black and white concentric circles. The outputs of recording are two video sequences in PAL standard stored on a tape. The main task of the parameterization is to find the parametric description of thumb motion.

The parameterization process could be separated to three parts:

1. the preprocessing of input video-sequences,

The input video-sequences are transformed to B/W images with white background and black regions in places of special marks.

2. the 2–D parameterization,

The recorded sequences are separately processed by 2–D parameterization. The vectors represent the position of special mark projection to the scan plane of camcorder are computed during the 2–D parameterization.

3. the 3–D parameterization.

The obtained 2–D data are stereoscopically combined into 3–D projection. The parameters of thumb motions are computed as space coordinates X , Y and Z of special mark placed on the thumb. A sequence of coordinates X , Y and Z could be represented by the feature vectors [2].

Due to the specifications of experiment the motion classification could be transformed to the classification of stationary states, which is easier to solve.

IV. CLASSIFICATION

The aim of classifiers is to trace the stationary states, the subsequences of vectors. Classification of vectors to R classes, where R is the number of stationary states, has been solved.

The comparison of two classifiers – k-Means classifier and Bayes classifier – is the aim of this paper.

A. k-Means Clustering

The goal of classification is to divide the coordinates vectors into R clusters $\omega_1, \omega_2, \dots, \omega_R$ such that the Euclidian distance relative to the cluster centres $\mu_1, \mu_2, \dots, \mu_R$ is minimized. The clustering algorithm could be described in steps below [3].

Step 1 Set the number of clusters R and generate cluster centers $\mu_1, \mu_2, \dots, \mu_R$ randomly.

Step 2 Assign each input vector to the cluster ω^* , for which

$$!^* = \arg \min_r \| -!_r \|, \tag{1}$$

where $\| -!_r \|$ is the Euclidian distance.

Step 3 Recalculate the cluster centres μ_r using the vectors, which have been assigned into the cluster r (M is the number of vectors assigned into the cluster r).

$$!_r = \frac{1}{M} \sum_{m=1}^M m \tag{2}$$

Step 4 Repeat steps 2 and 3 until the centres μ_r no longer change.

B. Bayes Classifier

The classification of vectors to R classes with classification labels $\omega_1, \omega_2, \dots, \omega_R$ has been solved again.

The prior probabilities $P(\omega_r)$ are known, the sum of prior probabilities is

$$\sum_{r=1}^R P(!_r) = 1. \tag{3}$$

The prior probabilities $P(\omega_r)$ give the likelihood that the vector belongs to the class ω_r . Let's assume that the likelihood functions $p(!_r | \omega_r)$ for given ω_r are also known.

Then the probabilities that the vector belongs to the class ω_r (the posterior probabilities) [4] are

$$P(!_r |) = \frac{p(!_r |)P(\omega_r)}{p()}, \tag{4}$$

where

$$p() = \sum_{r=1}^R p(!_r |)P(\omega_r). \tag{5}$$

The vector belongs to class ω^* , for which

$$!^* = \arg \max_r P(!_r |). \tag{6}$$

Based on the experiment definition, the prior probabilities equals for all classes. It could be written

$$P(\omega_r) = \frac{1}{R} \text{ for all } r = 1, \dots, R. \tag{7}$$

Because denominator of Bayes theorem and the prior probabilities are identical for all classes, the classification of vectors to class ω^* could be realized using the equation

$$!^* = \arg \max_r p(!_r |). \tag{8}$$

Let's assume that the likelihood functions $p(!_r | \omega_r)$ have the normal distribution. It means that the probability density functions $p(!_r | \omega_r)$ could be written as

$$p(\mathbf{x} | \mu_r, \Sigma_r) = \frac{1}{\sqrt{(2\pi)^N |\Sigma_r|}} \exp\left(-\frac{1}{2}(\mathbf{x} - \mu_r)' \Sigma_r^{-1} (\mathbf{x} - \mu_r)\right), \quad (9)$$

where the N is the number of entries in the feature vector \mathbf{x} , the μ_r is the mean of the normal distribution and the Σ_r is the covariance matrix of the distribution [5].

The parameters μ_r and Σ_r have to be determined for each class ω_r before the classification. Let's have a set of M vectors \mathbf{x}_m belonging to class ω_r . Then it could be written the likelihood function

$$p(\mathbf{x}_1, \mathbf{x}_2, \dots, \mathbf{x}_M | \mu_r, \Sigma_r) = \prod_{m=1}^M \frac{1}{\sqrt{(2\pi)^N |\Sigma_r|}} \exp\left(-\frac{1}{2}(\mathbf{x}_m - \mu_r)' \Sigma_r^{-1} (\mathbf{x}_m - \mu_r)\right) \quad (10)$$

for this class [6].

The main task of parameters estimation is to find the parameters μ and Σ , for which the likelihood function is maximal.

The likelihood function is maximal for parameters

$$\mu = \frac{1}{M} \sum_{m=1}^M \mathbf{x}_m \quad (11)$$

and

$$\Sigma = \frac{1}{M} \sum_{m=1}^M \left((\mathbf{x}_m - \mu)(\mathbf{x}_m - \mu)' \right). \quad (12)$$

V. EVALUATION OF THE CLASSIFIERS

Both evaluated classifiers were tested with real data. The efficiency of classifiers has been evaluated using two standard parameters from HTK toolkit - the parameters *%Correct* and *Accuracy*. The parameter *%Correct* is defined as a fraction of correct labels and the total number of labels. The parameter *Accuracy* is defined similarly, but the number of correct labels is decreased by the number of inserted labels [7].

Let assign *Total* the number of all stationary states in reference file which would be classified, *Dels* the number of deleted stationary states, *Subs* the number of substituted stationary states and *Ins* the number of inserted stationary states. Then the evaluation parameters could be defined as

$$\%Correct = \frac{Total - Dels - Subs}{Total} \times 100 \quad (13)$$

and

$$Accuracy = \frac{Total - Dels - Subs - Ins}{Total} \times 100. \quad (14)$$

VI. RESULTS

The classifiers have been tested using the motion database with more than 900 stationary states. More than 550 realizations of stationary states derived from basic experiments with well separable classes (experiments A and B). Next 160 stationary states were recorded in experiment with varying realizations of the same states (experiment C). Rest states were derived from experiment with very short distances between stationary states models (experiment D).

The results of k-Means classifier testing are in Table 1, the Bayes classification results are in Table 2.

Table 1: Results of k-Means classification

Experiment	%Correct	Accuracy	Total	Dels	Subs	Ins
A	95,1 %	95,1 %	243	11	1	0
B	99,4 %	99,4 %	319	2	0	0
C	68,1 %	68,1 %	160	43	8	0
D	75,9 %	68,0 %	203	38	11	16

Table 2: Results of Bayes classification

Experiment	%Correct	Accuracy	Total	Dels	Subs	Ins
A	94,2 %	94,2 %	243	12	2	0
B	99,4 %	99,4 %	319	2	0	0
C	66,3 %	66,3 %	160	47	7	0
D	93,6 %	93,6 %	203	9	4	0

VII. CONCLUSIONS

The results for motions with well separable stationary states (experiments A and B) are fully sufficient for both compared classifiers. The results from experiment with varying realizations of stationary states (experiment C) are almost the same for both classification methods. Not a single classifier gives appropriate result for this experiment. The problems are the changes of stationary states coordinates during the experiment. Neither k-Means classifier nor Bayes classifier can adapt to the new arrange of experiment.

The results from experiment with hard separable stationary states (experiment D) are different for evaluated classifiers. k-Means classification algorithm could not classify some stationary states. There is a big number of deletions, substitutions and especially insertions in the classified states. The results of Bayes classification from this experiment are very good, there are minimal deletions and substitutions and there are no insertions. The Bayes classifier can better classify the hard separable sets of feature vectors than k-Means classifier.

It could be supposed that the well trained Bayes classifier will be more sensitive than the k-Means classifier for the thumb motion classification.

ACKNOWLEDGMENT

This work has been supported by the research program No. MSM 6840770012 of the Czech Technical University in Prague (sponsored by the Ministry of Education, Youth and Sports of the Czech Republic).

REFERENCES

1. Allard, P., Stokes, I., Blachi, J.-P.: Three Dimensional Analysis of Human Movement. Human Kinetics, 1995.
2. Havlík, J., Horčík, Z.: Three-Dimensional Thumb Motion Parameterization. In Applied Electronics 2005, pages 127 – 130. University of West Bohemia in Pilsen, Pilsen, 2005.
3. Moore, A. W.: K-means and Hierarchical Clustering [online]. URL: <http://www.autonlab.org/tutorials/kmeans.html>, [2005-09-14].
4. Kotek, Z. et al: Recognition Methods and Their Applications (*in Czech*). Academia, Prague, 1993.
5. Rektorys, K. et al.: Overview of Applied Mathematics II (*in Czech*). Prometheus, Prague, 2000.
6. Moon, T. K., Stirling, W. C.: Mathematical Methods and Algorithms for Signal Processing. Prentice Hall, 2000.
7. Young, S. et al.: The HTK Book. Cambridge University Engineering Department, 2002.

Author: Ing. Jan Havlík, Ph.D.

Institute: Czech Technical University in Prague
Faculty of Electrical Engineering
Department of Circuit Theory

Street: Technická 2

City: CZ – 166 27 Praha 6

Country: Czech Republic

Email: xhavlikj@fel.cvut.cz

The Effect of Computer Use on Carpal Tunnel Syndrome

M.F. Donoghue¹, D. O'Reilly¹ and M.T. Walsh¹

¹ Center for Applied Biomedical Engineering Research, Department of Mechanical and Aeronautical Engineering & Materials and Surface Science Institute, University of Limerick, Limerick, Ireland

Abstract— Carpal tunnel syndrome (CTS) is the most prevalent of all repetitive strain injuries (RSIs). The Bureau of Labor Statistics [1] determined that there was an average of 26,972 reported cases of CTS annually, between the years 1992 and 2006, in private industry. To understand the effects computer use has on CTS, it is necessary to identify the movements involved in performing everyday tasks such as typing and mouse usage. Motion analysis techniques were employed to determine these movements while performing a computer task. This involved markers being placed on the knuckles, wrists and forearms of the participants. The configuration of the markers allowed for the flexion, extension, radial deviation and ulnar deviation of the wrist to be calculated. The results were categorized in one plane of motion with 20° extension being the most prominent wrist posture. The most common position in two planes was also calculated with an Ext20°Ulnar15° (20° extension and 15° ulnar deviation) accounting for over 3.5% (3.6%) of the total wrist posture during the task. This study determined that the most common wrist positions found in two planes provide an accurate representation of wrist position for computer use. From the results in this study a more exact indication of the wrist positions used in computer tasks have been identified. The results suggest that the wrist position in two planes should be considered when calculating the impact of computer use on CTS as it may have a bearing on the carpal tunnel pressure (CTP) created.

Keywords— Wrist, Computer Use, Carpal Tunnel Syndrome, Motion Analysis, Wrist Position

I. INTRODUCTION

Carpal tunnel syndrome (CTS) is the most prevalent of all repetitive strain injuries (RSIs) and is a common cause of pain, numbness and tingling in the upper extremities [1]. In a survey carried out by the Bureau of Labor Statistics [1] it was determined that there was an average of 26,972 reported cases of CTS annually, between the years 1992 and 2006, in private industry. This made it the leading cause of work absenteeism as CTS results in one of the largest number of median days away from work.

Although the exact cause of CTS is unknown, it is widely believed that computer users are at a high risk of suffering from such a disorder. To determine the effects computer use has, it is necessary to understand the movements in-

involved in performing everyday computer tasks. The most common of these are typing and mouse usage. These activities cause a deviation of the wrist from its neutral position. It has been shown that movement of the wrist away from the neutral position increases the pressure within the carpal tunnel [2-4]. If this pressure exceeds the critical pressure threshold stated by Werner *et al.* and Keir *et al.* [5, 6] for a prolonged period of time, the median nerve may become damaged. However, studies performed to date do not account for a combination of both radioulnar and flexion/extension movement.

Prior to evaluating the effect movement of the wrist in two planes has, the most common wrist positions from performing computer tasks must be identified. Once this is achieved, the impact these movements have on the carpal tunnel and its contents can be analyzed.

II. MATERIALS AND METHODS

Motion analysis techniques were used to determine the movements undertaken by the hands and wrists during the computer task. This involved reflective markers being placed on the knuckle of the middle finger, the wrist and the forearm. From this configuration the flexion/extension and radioulnar deviation of the wrist can be calculated.

20 participants, with no current signs of CTS, were required to open and close a Microsoft Word ® document using the mouse and perform a typing task as per normal. Participants were required to be regular computer users. However, it was not necessary for them to have previously undertaken computer training. The movements undertaken were recorded using Motion Analysis Corporation equipment and software. The typing task, workstation configuration and equipment setup remained constant for all subject. Each subject was allowed to adjust the chair to a comfortable position prior to commencement of the task.

All positions of the wrist were calculated using a specifically written MATLAB program. This program determined the wrist angle by the intersection of two planes. The planes were created from the markers placed along the limbs. This led to the level of extension/flexion and radioulnar deviation of the wrist being categorised. The categories ranged from 0-50° in intervals of 5° with all remaining

values grouped together. The categories were named after the highest attainable value in that range (5 Degrees, 10 Degrees etc.).

The wrist position due to motion in two planes was also obtained. This allowed for the combined extension/flexion and simultaneous radioulnar deviation to be recorded. This was categorized in a similar manner however, for notation purposes a position of 17° extension and 12° ulnar deviation was categorized as Ext20°Ulnar15°.

III. RESULTS

From the angles calculated it was determined that the most prominent wrist angles in extension, flexion, radial deviation and ulnar deviation are 20°, 5°, 15° and 15°, respectively. The breakdown of all wrist positions can be seen in Fig. 1. From this figure it can also be noted that the wrist is not commonly placed in a position of flexion. This corresponds with previous studies which concluded that the wrist is primarily in a position of extension and ulnar deviation of the wrist [7].

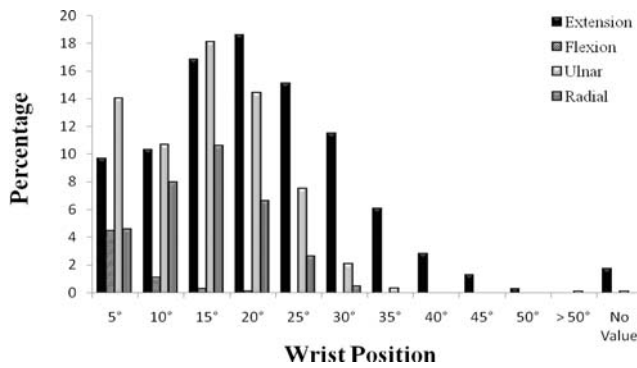


Fig. 1 Breakdown of wrist positions in one plane

To determine the exact wrist position during this task both the flexion/extension and corresponding radioulnar deviation need to be looked at. Fig. 2 shows the ten most frequented wrist positions during the computer task. It was found that an extension of 25° and an ulnar deviation of 20° is the most prominent posture with positions of 20° extension and 15° ulnar deviation and 5° extension and 5° ulnar deviation following close behind. A wrist position including flexion or radial deviation did not feature in the top ten positions.

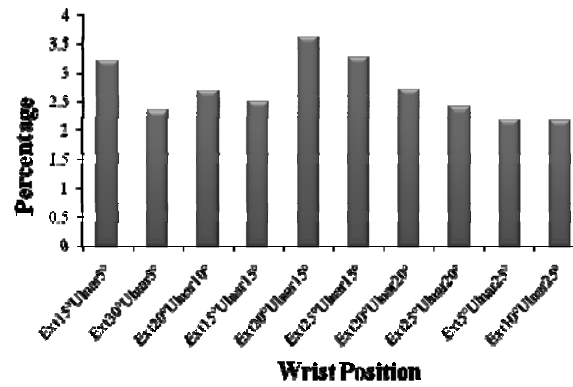


Fig. 2 Ten most prevalent wrist positions during computer use

IV. DISCUSSION

Previous studies have investigated the degree of extension/flexion and radioulnar deviation while carrying out various tasks using a mouse or keyboard. The results determined here correlate closely to that of previous studies. [7](Ref) Although these positions indicate the most prominent wrist position in one plane of motion, they do not account for the simultaneous radioulnar deviation which takes place. This is also the case for the most common radial\ulnar positions ascertained.

The positions indicated in Fig. 2 show the frequency of the most common wrist positions to occur in two planes. A position of Ext20°Ulnar 15° accounts for over 3.5% of total wrist positions during the task. This position could be prominent due to keyboard configuration, typing habit or workstation arrangement. This would also account for positions of similar orientation being among the most prevalent wrist postures.

Evaluating the positions involved while carrying out a computer task is vital in determining the pressures placed on the wrist. The most common wrist position seen in Fig. 1 (20° extension), will create a different pressure within the carpal tunnel depending on the angle of flexion or extension that the wrist is in at that specific time. The impact of this corresponding position has not been included in previous studies measuring carpal tunnel pressure. By determining these angles a more accurate conclusion to the impact computer use has on carpal tunnel syndrome can be found.

V. CONCLUSIONS

In conclusion, this method of categorizing wrist position during computer use demonstrates a more accurate means of determining wrist positions of computer users. The re-

sults found here indicate that wrist position in two planes should be accounted for, as it may have a bearing on the resultant carpal tunnel pressure (CTP). If the wrist positions found here increase the CTP to a value above that of the threshold value, a direct link between the development of CTS and computer use can be made.

VI. ON-GOING WORK

The effect of these wrist positions over a prolonged period of time is being investigated to see the impact they have on the carpal tunnel. Specifically designed supports will be used to maintain the most prevalent wrist postures for up to eight hours. During this period nerve conductivity studies on the median nerve will be regularly assessed. This occurs as nerve conductivity has been shown to alter due to pressure being placed on the nerve [8-10]. This will indicate the wrist positions that induce CTS and in turn determine if computer use is directly linked with the development of the disorder.

ACKNOWLEDGMENT

I wish to acknowledge the funding received from the Irish Research Council for Science, Engineering and Technology.

REFERENCES

1. Bureau of Labor Statistics, 1992-2006. *Lost-Worktime Injuries and Illnesses: Characteristics and Resulting Days Away From Work* [online]. United States Department of Labor. Available From: <http://www.bls.gov/iif/home.htm> [Accessed 12 February 2009].
2. Rempel, D., Keir, P. J., Smutz, W. P. & Hargens, A., 1997, "Effects of Static Fingertip Loading on Carpal Tunnel Pressure" *Journal of Orthopaedic Research*, Vol. 15, pp 422-426.
3. Seradge, H., Jia, Y.-C. & Owens, W., 1995, "In Vivo Measurement of Carpal Tunnel Pressure in the Functioning Hand" *The Journal of Hand Surgery*, Vol. 20, pp 855-859.
4. Werner, R., Armstrong, T. J., Bir, C. & Aylard, M. K., 1997, "Intracarpal Canal Pressures: The Role of Finger, Hand, Wrist and Forearm Position" *Clinical Biomechanics*, Vol. 12, pp 44-51.
5. Keir, P. J., Bach, J. M., Hudes, M. & Rempel, D. M., 2007, "Guidelines for Wrist Posture Based on Carpal Tunnel Pressure Thresholds" *Human Factors*, Vol. 49, pp 88-99.
6. Tittiranonda, P., Rempel, D., Armstrong, T. & Burastero, S., 1999, Workplace Use of an Adjustable Keyboard: Adjustment Preferences and Effect on Wrist Posture. *American Industrial Hygiene Association Journal*, Vol. 60, pp 340 - 348.
7. Serina, E. R., Tal, R. & Rempel, D., 1999, Wrist and Forearm Postures and Motions during Typing. *Ergonomics*, Vol. 42 pp 938-951.
8. Hargens, A. R., Romine, J. S., Sipe, J. C., Evans, K. L., Mubarak, S. J. & Akeson, W. H., 1979, "Peripheral Nerve conduction Block By High Muscle-compartment Pressure" *J Bone Joint Surg Am*, Vol. 61, pp 192-200.
9. Gelberman, R. H., Szabo, R. M., Williamson, R. V. & Dimick, M. P., 1983, "Sensibility Testing in Peripheral-nerve Compression Syndromes. An Experimental Study in Humans" *J Bone Joint Surg Am*, Vol. 65, pp 632-638.
10. Gelberman, R. H., Szabo, R. M., Williamson, R. V. & Dimick, M. P., 1983, "Sensibility Testing in Peripheral-nerve Compression Syndromes. An Experimental Study in Humans" *J Bone Joint Surg Am*, Vol. 65, pp 632-638.

Use macro [author address] to enter the address of the corresponding author:

Author: Maurice F. Donoghue
 Institute: University of Limerick
 Street: Castletroy
 City: Limerick
 Country: Ireland
 Email: maurice.donoghue@ul.ie

Automated Vigilance Classification based on EOG signals: Preliminary Results

S. Hanke¹, J. Zeitlhofer², G. Wiest², W. Mayr³ and D.C. Moser²

¹ Biomedical Systems, Austrian Research Centers GmbH - ARC, Wiener Neustadt, Austria

² Department of Neurology, Medical University of Vienna, Vienna, Austria

³ Center of Biomedical Engineering and Physics, Medical University of Vienna, Vienna, Austria

Abstract— The dramatic increase in the number of traffic accidents associated with sleepiness has stimulated research aimed at identifying behavioural and physiological correlates of alertness in different occupational settings ([1]). The paper describes the first results of a study working on a model for an automated vigilance classification. First measurements of EOG and EEG signals have been performed on persons doing the Mackworth Clock test. In this paper the analysis of the EOG parameters is described and the results concerning the correlation with the reaction time of the Clock test are shown and discussed. The EOG is so far the preferred biosignal because it is relatively easy to measure without too much burden on the user. It is thinkable that a smart device based on EOG recording will serve as an all solution for warning the user in the case of micro sleep events or extreme vigilance decline. In future it would be very important to have models and algorithms available giving the possibility of an automated real time vigilance classification based on biosignals. A device available on the market giving a feedback to the driver when the vigilance is decreasing would contribute to increase the safety in car traffic.

Keywords— EOG, vigilance classification, Mackworth Clock test, drowsiness, sleep onset

I. INTRODUCTION

Limitation of drowsiness and alertness are combined with sleep-awake interferences. These interference symptoms lead to significant subjective constrictions of affected patients. Not only from the scientific point of view but also in practical cases of decision employability or fitness to drive, it would be interesting to estimate the qualitative and quantitative status of vigilance in a subjective as well as objective way ([2]). Eye movements are easy to measure; they represent diverse structures of the central nervous system. Some eye movement parameters were already studied regarding their sensitivity to sleep deprivation. Characteristics are slow rolling eye movements (SEM) in relaxed subjects with closed eyes during sleep onset ([1, 3, 4, 5]). Eye activity is higher during wakefulness than during sleepiness and sleep. That results in a higher frequency and amplitude in the EOG ([5]). During wake, SEMs not only correlate negatively with perfor-

mance and positively with subjective estimates of sleepiness, but also with changes in EEG activity ([1]). An other reliable indicator of sleep onset is a precipitous decline in eyelid movements (ELM) ([3, 1]). Furthermore ([1]) confirmed that ELM density was a better predictor of sleep onset than changes in the time course of either theta or alpha power. They hypothesized that during normal transitions from wake to sleep, eyelid behaviour maybe a more sensitive indicator of changes in arousal systems than are EEG power fluctuations ([1]). Further more the classification of sleep stages based on EEG is in common use but for classifying the stages of vigilance during alertness there are still only suggestions. For instance of sleepiness, changes in variables other than the EEG and the EOG did not follow a consistent pattern other than when sleepiness developed into sleep. EOG has an advantage over EEG since it is a larger signal and less prone to problems with recording artefacts than EEG, and therefore, it is easier to measure ([5]). Studies indicated that computerized scoring systems can perform creditable pattern recognition in EEG and EOG ([6]). As peak velocity of eye movements is not arbitrary controllable, it is a good parameter for fatigue detection ([7]). There is considerable interest in alertness, vigilance and fatigue in safety critical occupational environments, particularly where exacerbating factors such as shift-work and timezone change are present ([5]). Long periods of work often occur against a background of irregular work and rest, which implies that sleep quality and duration are less than optimal.

II. METHODS & MATERIALS

For developing the model and the algorithms we used data based on a data evaluation measured on persons doing a certain vigilance test, the Mackworth Clock test, running on a laptop in an enclosed room in 70 cm distance from the person. The Mackworth Clock test is a common vigilance test simulating a task which should lead to a decline in vigilance. A light illuminating dot moves on a circular path in little hops. On irregular events the dot makes a double hop. This event has to be detected by the proband. The evoked signals to detect occur intermittent and raise no foreseeable attention. Means the frequency of the signals to detect as well as the

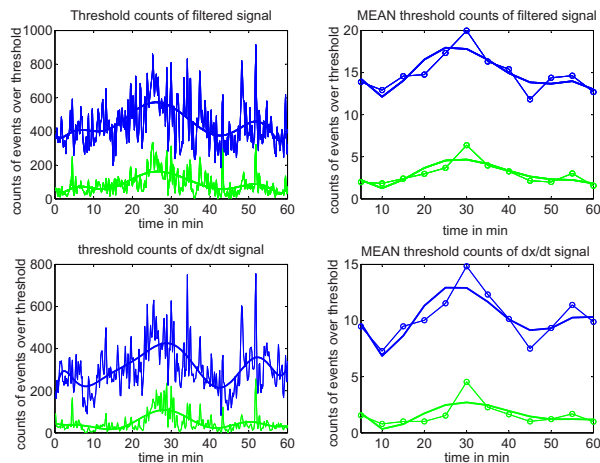


Fig. 1: EOG amplitude and EOG end velocity

intensity of the impulse is low. The duration of the test is 60 minutes and there are 40 events to detect every 10 minutes. The test takes the reaction time to every event. During the test we measured the two channels of the EOG like described by Rechtschaffen and Kales ([8]). In parallel to the EOG signals we measured the central and occipital EEG (C3, O1, C4, O2). These channels have been recommended in literature to monitor activation which can lead to a vigilance state classification. For recording the biosignals we used the alpha-trace 24-h ambulatory polygraphy system from B.E.S.T. medical systems. The sampling frequency of all polygraphic signals was 128 Hz. We used as a preprocessing a digital butterworth filter of 7-th order with the cut-off frequency of 0.5 and 20 Hz. Additionally all remaining windows with high frequency artefacts have been excluded by measuring extremely high amplitudes in the time domain. For analysing the filtered EOG signals in the time and frequency domain we used a 20 seconds time window (2560 samples) with an overlap of 1280 samples. We recorded the EOG amplitude activity by defining a certain threshold which stays the same over the whole 60 minutes signal. The threshold has been set so far to an individual value in ca. 2/3 of the maximal amplitude of the signal. In further evaluation we will make this condition self adapting to the signal. The analysis of the velocity of the signal has been performed similar. We adjusted a threshold to the first derivation of the signal. The frequency attitude of the signal has been analysed with the FFT of the different time windows and also over the whole signal. To differ a high frequency band (HF) and a low frequency band (LF) we defined a 0 - 1 Hz and a 1 - 20 Hz band. These two bands seems to represent the HF and LF signal characteristics, although a clear differentiation of two or more frequency bands was

not evident. We compared all physiological parameters with the parameters obtained in the Mackworth Clock test, which are the reaction time, the right reactions to events, the wrong reactions when no event was occurring and the missed reactions. For intensify the trend of the signal concerning the long time behaviour of the vigilance itself we choose five minutes mean value epochs for the data evaluation. We think this is adequate for a prediction of a relative vigilance change. We also correlated the second deviation of all the physiological signals with the reaction time to get a better correlation of the signal behaviour. We had a closer look at the mean reaction time and the missed events to maybe sort out some unmotivated user.

III. RESULTS

Figure 1 shows the analysis of the end velocity and the amplitude of both EOG channels for one person. The upper figure on the right side shows the distribution of all events over the defined threshold for the amplitude of the EOG over the 60 minutes test. The upper figure on the left side is the appropriate graph with a mean value over every five minutes epochs. The lower right figure shows all threshold counts of the end velocity distribution over the 60 minutes test. The lower left figure shows again the mean values for the end velocity in five minutes epochs. For all graphs the solid line is the regression of the measurement points. It can be clearly seen that there is a dynamic in the amplitude as well as the end velocity behaviour detected in both channels. It can be seen that there is a increase of eye activity followed by a decline of the activity. Around fifty minutes there is again a increase of the activity. This behaviour is typical as it is showing the fighting against of the user against the increasing drowsiness. Normally this behaviour is followed by micro sleep events, which would maybe occur in a longer test trial. Figure 2 shows the regression of the reaction time and all physiological parameters for both EOG channels (left, right) over the 60 minutes trial for one person. What was surprisingly to see is that there is often also a high dynamic in the LF/HF behaviour of the signals which is in correlation of the dynamic of the amplitude and end velocity. The reaction time which is the parameter retrieved from the clock test is negatively correlating with the physiological EOG parameters. The EOG activity in general is higher during phases with a lower reaction time where the user has faster responded to events in the clock test.

In table 1 all subjects are listed with the correlation coefficient of the second derivation with all physiological signals and end velocity of the eye movement (velocity), amplitude of the eye movement (amplitude), the low frequency to high

Table 1: Coefficients of correlation and number of mistakes as well as the mean reaction time over the whole test for each subject

Subject	velocity	amplitude LF/HF	mistakes	RT	
25012008	-0.74	-0.80	-0.97	11	587
18042008	-0.94	-0.97	-0.83	36	731
07032008	0.14	0.36	-0.83	89	746
18012008	-0.51	-0.08	-0.71	29	756
11042008	-0.16	-0.12	0.16	73	708
14032008	NaN	NaN	NaN	108	816
15022008	0.74	0.15	-0.52	17	606
22022008	-0.23	-0.17	0.94	184	507
29022008	-0.78	-0.90	0.07	16	624
08022008	0.51	0.32	-0.95	28	496

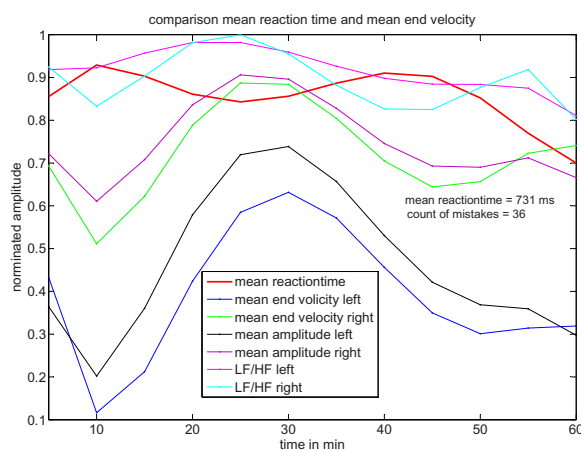


Fig. 2: Reaction time in comparison to physiological parameters

frequency factor (LF/HF) with the reaction time. Also in the table is the mean reaction time (RT) of each user retrieved from all reactions over the 60 minutes as well as the mistakes in the performance including missed reactions and false reactions. One subject (14032008) has to be excluded because he performed a very unmotivated test with no reactions over 30 minutes. In total he did 108 wrong reactions in the whole test. In general it seems that there is mostly a high negative correlation of the described physiological parameters of the EOG with the reaction time. Surprisingly the best indicator seems to be the LF/HF coefficient. Anyway there are a lot of correlation factors and patient not fulfilling the trend. One problem has occurred that it was very hard to retrieve a good fitting correlation with probands where there is nearly no dynamic in the physiological parameters as well as the reaction time.

Actually this problem is also not depending on the account of mistakes or a low mean reaction time (RT). So this two parameters can not be an clear exclusion criteria. Of course the fact of a low motivation and a high number of missed reactions is limiting the variance of the mean reaction time and is therefore difficult to interpret. Anyway this should be analysed in detail in further studies.

IV. CONCLUSION

We think all described parameters extracted from EOG are useful to monitor the eye activity. Although we performed the test under laboratory conditions, where the user has a concentrated gaze on the monitor without any environmental distraction, there is a change in the eye activity which is pointing to a changing vigilance. In later tests at the end of the project we will perform similar measurement in real life scenarios. It could be expected that there the described general trend behaviours of the eye movements is much more present, because the test under clinical conditions is forcing the user to do gaze similar to a tunnel vision. During analysis of the data and screening of papers on application of the Mackworth Clock test for vigilance classification we experienced the problem of having a good correlation parameter which is defining a certain vigilance state. Several papers are using the reaction time on events, measured during the test, for estimating the status of the vigilance. Anyway there are some studies using the amount of missed or false reaction to estimate the vigilance and the test performance ([9, 10]). When analysing the data of the underlying study we experienced that the reaction time and the missed / false reactions, as a performance indicator, are not correlating with each other. This is a problem when searching for a correlation parameter, out of the Clock test, for estimating how much do the physiological biosignals reflecting the trend of the vigilance performance of the subject. Additionally the amount of evaluable reactions to events during the test is very low if the subject is not motivated enough. As described in the methods we got 40 events in 10 minutes epochs. The lower the amount of reactions of the user to the events the vague is the measured mean reaction time. A low variance of the reaction time mostly leads to low dynamic reaction time performance over the 60 minutes. In this cases it is not useful to make a correlation with the physiological parameters. We experiences this problem with some subjects. During further data analysing we will also take a more detailed look in the performance of the amplitude and end velocity like shown in the left side graphs of figure 1. It is promising to detect in this graphs a similar trend of decreasing vigilance alternating with increasing vigilance peaks showing the behaviour of the subject fight to keep awake.

V. DISCUSSION

In next studies we would like to integrate a subjective vigilance test additionally to the Mackworth Clock test. Thinkable would be to superimpose a click-able scale in the corner of the clock test to let the user rate himself, e.g. every 5 minutes, how he is feeling about his vigilance behaviour. Behind the scale there could be a rating to the Karolinska Sleepiness Scale ([11]) or the Stanford Sleepiness Scale ([12]). It would be interesting how this parameter is correlating with the indication of the physiological parameters as well as the reaction time and the missed / false reactions of the Mackworth Clock test. A problem when performing vigilance tests is the different base activity of the persons. Different studies come over this problems when using probands with the same amount of sleep etc. We performed the test on the same time at the day to have the same circadian activation of the vigilance state in every person. Of course normally different probands have different circadian rhythms. Anyway we think this influence factors can be neglected because a different base activation is always expected, also in later applications in real life scenarios. The only think which is possible is a relative assessment of the vigilance state to the beginning of the vigilance monitoring, separate for each subject. In future analysis we will integrate the behaviour of the EEG theta and alpha power to the general model to have a better possibility of classify and predicting the vigilance behaviour in the awaking states.

REFERENCES

1. Atienza M., Cantero J. L., Stickgold R., Hobson J. A.. Eyelid movements measured by Nightcap predict slow eye movements during quiet wakefulness in humans *J Sleep Res.* 2004;13:25-9. DA-11744/DA/United States NIDA MH-13923/MH/United States NIMH MH-48832/MH/United States NIMH Journal Article Research Support, Non-U.S. Gov't Research Support, U.S. Gov't, P.H.S. England.
2. Weess , G. H., Sauter C., et al. Vigilanz, Einschlafneigung, Dauer- aufmerksamkeit, Muedigkeit, Schlaefrigkeit Diagnostische Instru- mentarien zur Messung muedigkeits- und schlaefrigkeitsbezogener Prozesse und deren Guetekriterien: Vigilance, Tendency to Fall Asleep, Sustained Attention, Tiredness, Sleepiness Diagnostic Tools for the Measurement of Sleepiness Related Processes and their Criteria of Quality *Somnologie.* 2000;4:20-38.
3. Rowley J. T., Stickgold R., Hobson J. A.. Eyelid movements and mental activity at sleep onset *Conscious Cogn.* 1998;7:67-84. MH-48832/MH/United States NIMH Clinical Trial Controlled Clinical Trial Journal Article Research Support, Non-U.S. Gov't Research Support, U.S. Gov't, P.H.S. United states.
4. Torsvall L., Akerstedt T.. Sleepiness on the job: continuously measured EEG changes in train drivers *Electroencephalogr Clin Neurophysiol.* 1987;66:502-11. Journal Article Research Support, Non-U.S. Gov't Ireland.
5. Wright N., McGown A.. Vigilance on the civil flight deck: incidence of sleepiness and sleep during long-haul flights and associated changes in physiological parameters *Ergonomics.* 2001;44:82-106. Journal Article Research Support, Non-U.S. Gov't England.
6. Martin W. B., Johnson L. C., Viglione S. S., Naitoh P., Joseph R. D., Moses J. D.. Pattern recognition of EEG-EOG as a technique for all-night sleep stage scoring *Electroencephalogr Clin Neurophysiol.* 1972;32:417-27. Journal Article Netherlands.
7. Zils E.. Auswirkungen von Schlafentzug auf verschiedene Typen sakkadischer Augenbewegungen 2005.
8. Rechtschaffen A., Kales A.. *A manual of standardized terminology, techniques and scoring system for sleep stages of human subjects.* US Government Printing Office, US Public Health Service 1968.
9. Smit A. S., Eling P. A., Coenen A. M.. Mental effort affects vigi- lance enduringly: after-effects in EEG and behavior *Int J Psychophysiol.* 2004;53:239-43. Clinical Trial Journal Article Netherlands official journal of the International Organization of Psychophysiology.
10. Verster J. C., Duin D., Volkerts E. R., Schreuder A. H., Verbaten M. N.. Alcohol hangover effects on memory functioning and vigilance perfor- mance after an evening of binge drinking *Neuropsychopharmacology.* 2003;28:740-6. Comparative Study Journal Article Research Support, Non-U.S. Gov't United States official publication of the American Col- lege of Neuropsychopharmacology.
11. Akerstedt T., Gillberg M.. Subjective and objective sleepiness in the ac- tive individual *Int J Neurosci.* 1990;52:29-37. Journal Article Research Support, Non-U.S. Gov't England.
12. Hoddes E., Zarcone V., Smythe H., Phillips R., Dement W. C.. Quantifi- cation of sleepiness: a new approach *Psychophysiology.* 1973;10:431-6. Journal Article United states.

A Lexicon Driven P300 Speller

S.T. Ahi¹, H. Kambara² and Y. Koike²

¹ Dept. of Comp. Intelligence and Systems Science, Tokyo Institute of Technology, Yokohama, Japan

² Precision and Intelligence Laboratory, Tokyo Institute of Technology, Yokohama, Japan

Abstract— In this paper, we propose a scheme for the integration of a custom-built dictionary into the P300 based speller paradigm in order to reduce the number of required flash repetitions and consequently to boost the information transfer rate. The current system assumes that the misspelling is solely originated from the insufficient performance of the classifier, and users achieve perfect spelling. Under such conditions, the proposed system takes a different form than the conventional spell-correctors, which define the only source of the misspelling as users. The proposed system is evaluated off-line on four subjects trying to spell ten different words of four to five letters length. An 11% increase in the average accuracy rate and a 9.5 bits/min increase in the average communication rate is obtained with the proposed scheme by the incorporation of the dictionary.

Keywords— Brain-Computer Interface, P300, Speller, Spelling Correction, Lexicon Matching

I. INTRODUCTION

P300 Event Related Potentials (ERP) are brain responses occurring in the presence of rare external stimuli [1, 2]. While different types of stimuli have the potential to elicit the response, in an experimental environment usually the so-called *oddball* task is favored. In the oddball task, the subject is randomly presented with two types of stimuli, one of which is frequent. The infrequent or oddball stimulus generates a P300 waveform in the Electroencephalogram (EEG) recordings assuming that the subject reacted to the event by, for example, noticing or silently counting it. This paradigm is a reliable one and relatively easy to detect. Different classification methods, such as Support Vector Machines and Bayesian Linear Discriminant Analysis, have successfully classified the response [3, 5]. However, the low SNR of the acquired EEG signals requires the classifiers to gather more than one instance of the same response type. This, in return, extends the duration of the signal recording and decreases the information transfer rate.

The work presented here attempts to achieve higher accuracies in less number of signal averaging by utilizing a dictionary and combining it with the classifier. The proposed scheme can operate with almost any classifier and therefore represents a substantial improvement to the conventional

speller designs.

II. MATERIALS AND METHODS

A. Subjects

We conducted P300 experiments on 3 male, 1 female able-bodied subjects with a mean age of 26.5 (std=3.5). All subjects, who have little or no previous experience with the BCI systems, were seated in a comfortable chair facing the speller screen (Figure.1).

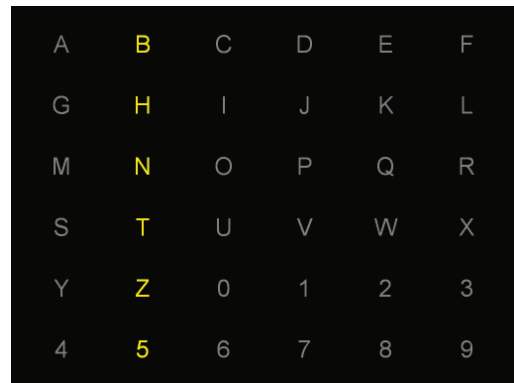


Fig. 1: P300-Speller screenshot, where the second column is flashing.

B. Signal Acquisition

The EEG data is acquired through a 64-channel Biosemi Active Two amplifier. The electrodes are placed according to the international 10-20 system, and the sampling frequency is set to 256 Hz.

C. Experimental Setup

The characters for the speller is placed on a 6x6 matrix, which includes both letters (A-Z) and numbers (0-9). However, the numbers have no significance in this study, since the main concern of the proposed scheme is to decrease the required signal acquisition time for words only.

Trying to generate P300 responses, each of the 6 rows and each of the 6 columns of the matrix is flashed randomly,

and consequently the subject brain is stimulated. The inter-stimulus interval (ISI) is set to 175 ms and the flash duration to 100 ms. Flashing of the 6 rows and 6 columns is called one *trial* [2]. The total duration of one trial is, therefore, $175 \times 12 = 2100$ ms.

The *task* for the subjects is defined as targeting one out of 36 characters and counting silently the number of times the target is intensified. One task is composed of 5 consecutive trials to be able to assess the performance of the proposed system at different levels of signal averaging. Since there is one flash for the corresponding column and one for the corresponding row, there are two flashes per trial and 10 flashes per task for the target letter.

Except for an indication of the target letter before starting with flashes, subjects are given no feedback by the system. Each subject spelled for a total of 15 words (68 letters), among which the first 5 of them (23 letters) were used for training and the remaining 10 (45 letters) were used for testing.

D. Proposed Scheme

Objective of the proposed system is to obtain better performance from P300 spellers by incorporating a custom-built dictionary into the classification process. The system, as seen in figure (2), is composed of three main components: (1) Classifier (2) Dictionary and (3) Recognition unit. Acquired EEG data is initially preprocessed, and the dimensionality of the extracted feature vectors are reduced by a spatial filtering algorithm [4]. The dictionary, which is the major difference between the proposed scheme and current spellers, checks the validity of the classifier's decision, and if no such word exists in the dictionary, the unit suggests a number of alternative words. It is the recognition unit that makes the final decision among the suggestions by the help of classifier's outputs. In the following, you may find more detailed information about the preprocessing, dimension reduction, and the three primary units that complete the system.

(i) Preprocessing:

The raw EEG data acquired through 64 channels is initially passed through a 1-18 Hz bandpass filter, and the amplitudes are mapped into $[-1, +1]$ interval. Then it is downsampled to 32 Hz. Epoch data is extracted by using a time window of 600 ms following the onset of stimuli, corresponding to 20 time samples per epoch. It should be noted that each trial consists of 12 flashes and as a result yields 12 epochs.

(ii) Dimension Reduction:

Extracting epoch data for each flash generates 64×20 dimensional E matrices, whose rows represent individual electrode

data recorded for a duration of T number of time samples, and whose columns represent time instance data recorded by D number of electrodes. The Spatial Filters [4] are vectors that linearly combine all the rows of E and output one T dimensional vector to represent it. In other words, the proposed filters individually map the $D \times T$ dimensional data into $D \times 1$ dimensions. Vectors with the reduced dimensions act as feature vectors in the following training and classification processes. Mathematically speaking:

$$\mathbf{x}_i = E_i^T \cdot \mathbf{f} \quad (1)$$

, where \mathbf{x}_i is the feature vector for i^{th} epoch.

The filters are determined based on Fisher's criteria, where the computed feature vectors of the classes have high inter-class variability and low intra-class variability. Defining the total inter-class variability as \hat{S}_b and intra-class variability as \hat{S}_w , the \mathbf{f} vector that maximize the following criteria is computed.

$$J(\mathbf{f}) = \frac{\mathbf{f}^T \hat{S}_b \mathbf{f}}{\mathbf{f}^T \hat{S}_w \mathbf{f}} \quad (2)$$

Computation of \mathbf{f} through maximizing Eqn. (2) leaves one with the conventional eigenvalue problem. Finding eigenvalues of $(\hat{S}_w^{-1} \cdot \hat{S}_b)$, sorting them, and choosing the eigenvectors corresponding M largest eigenvectors basically completes computation of the spatial filters. In this study, M is set to 5 [7]. Assuming that each eigenvector will map the 64×20 dimensional epoch data into 20×1 dimensions, and employing 5 filters per epoch, the length of each feature vector representing one epoch will be 20×5 . Lastly, please note that such a filtering approach is a supervised one, since the class label of each training epoch is needed during computations.

(iii) Classifier:

In this study, Bayesian LDA (BLDA)¹ [4] is employed as the learning machine, because it applies regularization during the training process, and all the model parameters are automatically estimated from the data, which eliminates the necessity of time consuming cross validation procedure. BLDA receives epoch data, whose dimensionality is reduced for speeding up the training and classification procedures, and ranks each of the 36 characters by how likely a character is the targeted one.

(iv) Dictionary:

9768 words with more than 500 occurrences in the whole 100M-word British National Corpus² are utilized as the core

¹MATLAB source code is available for download from <http://bci.epfl.ch/>.

²The word list can be reached at <http://www.kilgarriff.co.uk/bnc-readme.html>.

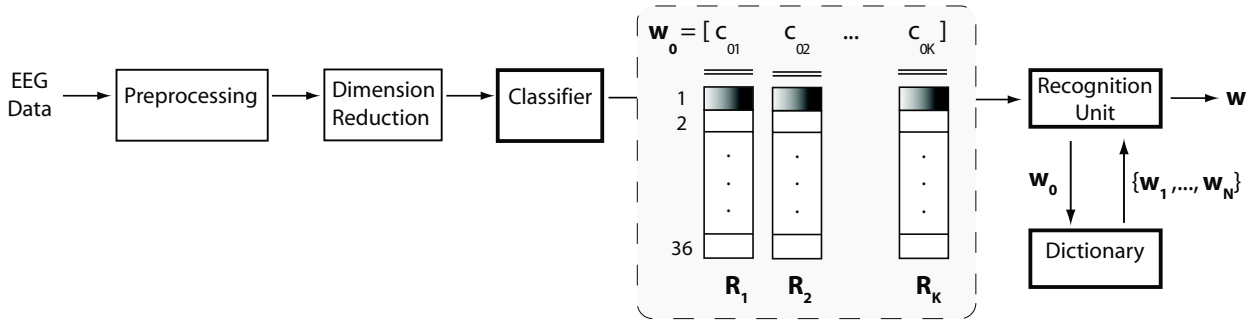


Fig. 2: System flowchart: The classifier outputs K number of rankings, where K represents the number of letters forming the word. Each ranking is composed of 36 elements, and the top candidates from each ranking define the initial estimation, w_0 . Given w_0 , dictionary checks the spelling and makes N number of correction suggestions along with the initial rankings and makes the decision, outputting the final form of the spelled word.

of our custom-built dictionary. We conducted experiments on words with 4 and 5 letters. There were 942 4-letter words and 1324 5-letter words in the dictionary. Therefore, those 942+1324 words constitute the effective core for the experiments. The following 15 words are randomly selected from the effective core: *HOUR, SWEAT, GUEST, ALONG, THIN, WALL, GRANT, MARCH, SIZE, BREAK, PIANO, RICE, CARE, ALARM, TRUE*. Among them, the first 5 words were used for training the classifier, and the remaining 10 were used for testing. The dictionary unit is blind to P300 signals. The unit just receives the candidate word proposed by the classifier, and checks its validity. If the candidate has no match in the core, then it assumes a misspelling has occurred due to the poor performance of the classifier. The degree of the misspelling is selected as half the length of the word, that is, for a given word of n letters, it is assumed that at maximum $n/2$ of them are spelled incorrectly, and the words having $n/2$ common letters with the classifier's candidate are presented to the recognition unit as the candidates of the dictionary.

(v) Recognition Unit:

Almost all classifiers, including BLDA, return a distance value for candidate letters for which P300 response might be present. This metric, which could also be interpreted as a *ranking*, shows how likely other letters contain the response. Given the rankings R_j for $j \in \{1, \dots, K\}$ computed by the classifier, and the candidate words w_i for $i \in \{1, \dots, N\}$ proposed by the dictionary, recognition unit makes the final decision on the spelled word. To this end, the candidates proposed by the dictionary unit are investigated one by one based on the cost function given in equation (3a). As shown in equation (3b), the word with the lowest cost is determined as the final decision.

$$f(w_i) = \sum_{j=1}^K \text{ranking}(c_{ij}) \quad (3a)$$

$$w = \arg \min_{i \in \{1, \dots, N\}} f(w_i) \quad (3b)$$

, where K is the number of letters forming the word, and N represents the number of suggestions made by the dictionary.

III. RESULTS

The final decisions made by the recognition unit are compared with their true form, and a letter-by-letter accuracy and information transfer rate computation [6] is performed. The information transfer rate, B , is computed by equation (4), where N represents the number of total available characters, p denotes the probability that a command is correctly recognized by the system, and t is the time in seconds that is needed to send one command.

$$B = \left(\log_2(N) + p \log_2(p) + (1-p) \log_2\left(\frac{1-p}{N-1}\right) \right) \frac{60}{t} \quad (4)$$

The probability that a command is correctly recognized by the system with or without the incorporation of the dictionary unit is given in figure (3). The change in the information transfer rates (bitrates), on the other hand, are presented in figure (4).

As seen in figure (3), all subjects except for the second one achieves 100% accuracy (a recognition probability of one) with the proposed model. Regarding the information transfer rates, the mean of all subjects increases from 29.7 bits/min to 39.2 bits/min.

The decrease in the bitrate with the increase in the number of trials stems from the accuracy-time tradeoff, and although the best rate is obtained with two trials, at least 3-4 trials are necessary for optimum performance.

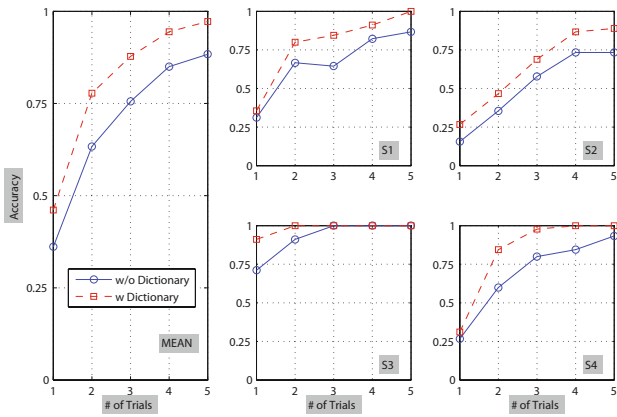


Fig. 3: The probabilities that a command is correctly recognized by the system are presented for 4 subjects with/without the dictionary unit.

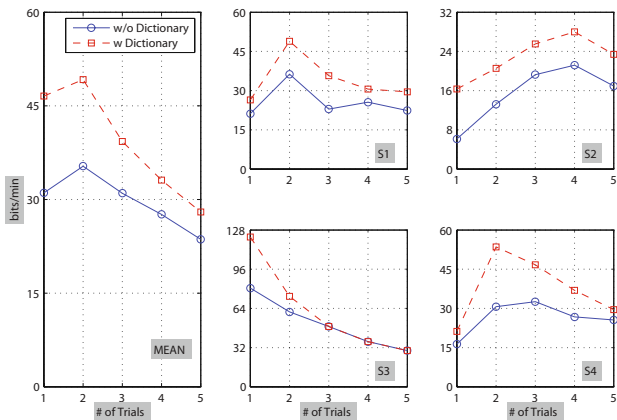


Fig. 4: Bitrates (information transfer rates) obtained for 4 subjects with/without the dictionary unit are given.

IV. CONCLUSIONS

This work proposes a scheme for taking advantage of the lexicon entries in P300 based speller paradigm. To this end, a custom-built dictionary is formed by commonly used English words as specified by the British National Corpus and

connected to the P300 classifier in such a way that the inaccuracy of the classifier due to low SNR margins is tolerated by the help of dictionary entries. This, in turn, reduces the total number of flash repetitions necessary to detect the presence of P300 responses, and the reduced flash repetitions increase the information transfer rate.

Donchin et al. [2] suggests that incorporating sequential structure of the language into the P300 based BCIs might provide significant advantages as well. Focusing on this suggestion and attempting to develop a concrete model will be our future research direction.

V. ACKNOWLEDGMENT

This work was supported with grants by "Strategic Research Program for Brain Sciences" from the Japanese Ministry of Education, Culture, Sports, Science and Technology.

REFERENCES

1. Farwell LA and Donchin E (1988) Talking Off Your Head: Toward a Mental Prosthesis, *Electroencephalography and Clinical Neurophysiology*, 70(6):510-523.
2. Donchin E, Spencer KM and Wijesinghe R (2000) The Mental Prosthesis: Assessing the Speed of a P300-Based Brain-Computer Interface, *IEEE Transactions on Rehabilitation Engineering*, 8(2):174-179.
3. Kaper M, Meinicke P, Grossekhoefer U, Lingner T and Ritter H (2004) BCI Competition 2003-Data Set IIb: Support Vector Machines for the P300 Speller Paradigm, *IEEE Transactions on Biomedical Engineering*, 51(6):1073-1076.
4. Hoffmann U, Vesin JM and Ebrahimi T (2006) Spatial Filters for the Classification of Event-Related Potentials, *ESANN*.
5. Hoffmann U, Vesin JM, Ebrahimi T and Diserens K (2008) An Efficient P300-based Brain-Computer Interface for Disabled Subjects, *Journal of Neuroscience Methods*, 167(1):115-125.
6. Wolpaw JR, Birbaumer N, McFarland DJ, Pfurtscheller G and Vaughan TM (2002) Brain-Computer Interfaces for Communication and Control, *Clinical Neurophysiology* 113(6):767-791.
7. Ahi ST, Kambara H and Koike Y (2009) A Comparison of Dimensionality Reduction Techniques for the P300 Response, *in press*, i-Create 2009.

Repositioning Precision of EEG-Caps – A Preliminary Study

S. Hemm, E. Schkommodau, and M. de Wild

Institute for Medical and Analytical Technologies, University of Applied Sciences Northwestern Switzerland, School of Life Sciences, Muttenz, Switzerland

Abstract— In this study the possibility to mount an EEG cap to a predefined position is investigated and the influence to the measured electrode position and the measured EEG signals was studied in a Brain Computer Interface application. A P300 spelling device was used to compare the performance of 4 probands after replacing the cap with or without tracking by an Optotrak device. We found that the tracking system allows for precise replacement of the cap and the electrodes. The success rates of the spelling experiment correlates well to the mounting accuracy. These findings offer the possibility to continue EEG sessions without the need of reclassification.

Keywords— EEG, cap position, Brain Computer Interface, P300 speller, Optotrak, tracking.

I. INTRODUCTION

Electroencephalographic (EEG) caps are often used today to facilitate the positioning of electrodes, in general following the international 10-20 system. These caps are flexible in order to be adaptable to different head sizes, but in case of repositioning it is not guaranteed that the electrodes are put exactly in the same place as during an anterior session. For conventional EEG recordings where abnormal EEG pattern are looked for, this might be less important, but for brain computer interfaces (BCI) (Wolpaw 2002) for which signal classification is applied and for which in consequence reproducibility is essential, precise repositioning of the electrodes might be a prerequisite. One typical BCI application is the P300-based spelling device. The underlying principle is based on a specific event related potential (ERP) that follows presentation of a rare stimuli as a positive peak at about 300 ms after the stimuli. The use of this stimulus has considerable success in allowing patients with neurodegenerative diseases leading to complete motor paralysis or other peripheral nerve diseases in communication to efficiently communicate with others (Mugler, 2008). The objective of the present work was to analyze the influence of the accuracy of the repositioning of the EEG cap on the functioning of such a P300-based spelling device.

II. MATERIAL AND METHOD

A. P300-based spelling device

Hardware: A gtec EEG cap (Guger Technologies OEG, Graz, Austria) was connected to an amplifier and connected to a computer. We used a 16 channel biosignal acquisition device, gUSBamp with its Simulink Highspeed on-line Processing blocks (version 2.07a, gtec, Graz, Austria) with a sampling frequency of 256 Hz (Highpass: 0.1 Hz, Notch-filter: 50 Hz). 8 gold electrodes were used and fixed over the parietal cortex to the positions F_z , P_3 , P_4 , O_z , C_z , P_z , PO_7 and PO_8 of the international 10-20 System, predefined on the EEG cap. Ground was placed on the forehead and the reference on the right mastoid.

Software: All the applied software is based on Matlab and Simulink Release 2007a. The off-line processing toolbox gbAnalyse (version 3.07a, gtec) was used to present the stimuli and to record the signals: characters are presented to the user of the P300-based spelling device (version 2.07a, gtec) in a 6x6 matrix on a black screen, see figure 1. The characters are then highlighted in a random, flashing sequence (single character speller). Users are instructed to focus their attention on only one character in the matrix, the “targeted character”. This selective attention to one character is then evident due to the presence of the ERP 300 milliseconds after the character was highlighted (Polikoff 1995).

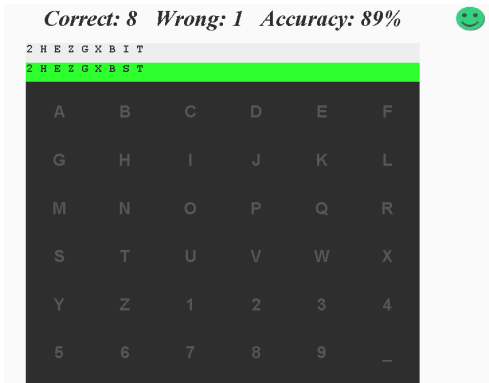


Fig. 1 Screen shot of the g.tec P300-based spelling device showing the 6x6 matrix with the flashing characters, the given word to spell (“2HEZGXBIT”) and the actually identified letters by the classification (“2HEZGXBST”). The number of correct and wrong letters as well as the success is indicated at the upper part.

B. Tracking system



To be able to identify changes in the position of the different markers, we decided to use the Optotrak Certus® motion capture system (Northern Digital Inc. NDI) which is an optical tracking system with active, infrared emitting markers that are recognized by the three cameras. (Koneremann 2003) (Fig. 2). The coordinates of each marker could be registered by the NDI software “First Principles”. The 3D accuracy of the system is of up to 0.15 mm, its resolution of 0.01 mm and its maximum update rate of 4600 Hz (Barnes, 2008).

Fig. 2 Optotrak Certus.

In order to fix the markers to the EEG cap, we produced holders in the form of electrode dummies by rapid prototyping technology (Objet Geometries® System, Israel, Type Eden 250, transparent FullCure acrylic photopolymer material) and fixed the Optotrak markers to them using some screws (Fig. 3).

In order to define a dynamic reference system to which the markers on the EEG cap could be referenced, we introduced a pair of laboratory glasses as rigid body with four markers mounted on the glasses. Repositioning tests of the glasses in relation to a rigid head frame have been

performed for three probands. Therefore, the glasses were mounted and removed ten times and the 3d-coordinates were measured.

To identify the exact spatial situation of the cap, ten markers were fixed into the existing holes of the EEG cap. Finally, five specific connections between these markers and the reference markers on the glasses were defined, see figure 4. We have selected those five important reference distances as a basis to reposition the cap in three dimensions.

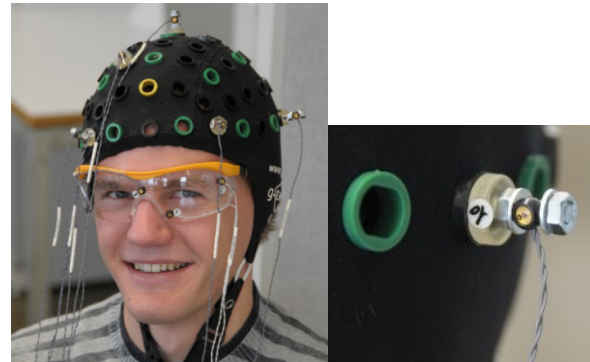


Fig. 3 EEG cap and reference glasses with active, infrared emitting markers that are recognized by the three Optotrak cameras. Details of the marker fixation can be seen in the inset.

C. Protocol

The EEG cap was fixed with its eight electrodes to the proband’s head by trying to keep the impedances between electrode and skin as low as possible (<10 kΩ). Each subject did first of all, after some testing, a classification period with several letters (each character flashing several times; Flash time: 60ms; Dark time: 10ms). In a next step, the test person had to recognize a given number of characters (copy speller) once with the cap in its original position and then after the cap had been removed and some minutes later fixed again to the proband’s head. The protocol of the test persons was as follows:

- a) mounting the EEG cap
- b) wiring the cap
- c) P300 off-line classification
- d) 1st P300 single character spelling session applying online the classifiers defined under c)
- e) identifying the cap position (specific distances between markers on the cap with those on the rigid body, the glasses) with help of the Optotrak system (Fig. 4)

- f) taking-off the cap
- g) remounting the cap with/without navigation control
- h) identifying the cap position with help of the Optotrak system
- i) 2nd P300 single character spelling session applying online the classifiers defined under c)

Our four test persons used following protocols:

First proband: no navigated control of repositioning.

2nd to 4th proband: Optotrak used for repositioning.

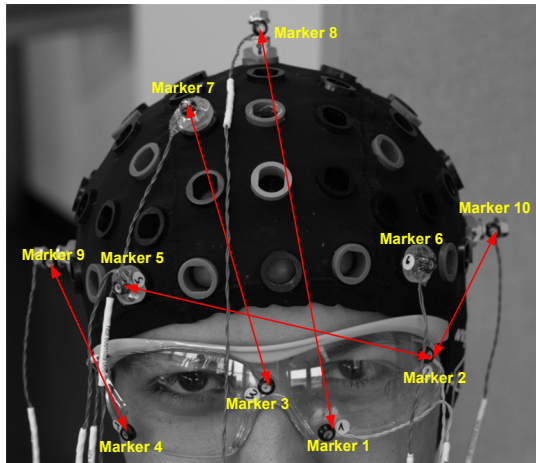


Fig. 4 Definition of the distances that allow the identification of a replacement of the cap in all directions.

D. Data analysis

Mean and standard deviation were determined for all repeated stereoscopic position measurements. For EEG data, individual signal classification was performed offline with a Linear Discriminant Analysis (LDA). Afterwards the defined classifiers were used online for copy spelling. The success rate was expressed as the percentage of correctly identified characters.

III. RESULTS

The repositioning tests of the glasses in relation to a rigid head frame (Table 1) showed that the reproducibility of the positioning of the glasses was satisfying for our EEG cap repositioning tests. The precision of the repositioning was $0.59\text{mm} \pm 0.22\text{mm}$.

Table 1 Repositioning precision of glasses in relation to a rigid head frame

	Displacement Mean \pm STDBW [mm]
Proband 1	0.58 ± 0.33
Proband 2	0.38 ± 0.23
Proband 3	0.82 ± 0.49
Overall precision	0.59 ± 0.22

The influence of the repositioning precision of the EEG cap was measured by comparing the success rate when using the spelling device with and without navigated remounting of the EEG cap. The results of the displacements and the success rates are given in table 2.

Table 2 Repositioning precision of EEG cap

test person	Tracking of reposition	Displacement [mm] Mean \pm STDBW	Success rate after cap replacement [%]
1	no	2.94 ± 1.62	16
2	yes	1.19 ± 1.01	100
3	yes	1.60 ± 1.11	100
4	yes	1.07 ± 0.66	100

Table 2 presents the mean difference of the distances between the markers before and after cap replacement and the P300 speller success rates after the remounting of the EEG cap. The results for the four probands show a clear difference between the one obtained without (proband 1) and those obtained with the support of the Optotrak tracking system for the repositioning (proband 2 to 4). Figure 5 shows the differences for the analyzed marker pairs separately.

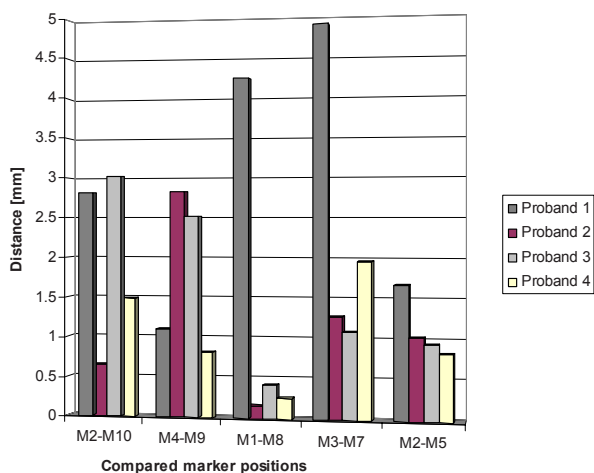


Fig. 5 Displacement of the markers between the first mounting of the EEG cap and a complete new placement. Note that proband 1 did not use navigational control to replace the cap, whereas probands 2 to 4 used the Optotrak system to reposition the cap.

IV. DISCUSSION

The distances between the markers were optimized by the use of the Optotrak, particularly between the sagittal markers 1-8. The position of the EEG cap can be reproduced very well, leading to a high success rate of the spelling experiment.

Not all possible differences between every marker have been taken into account. We have selected five important reference distances as a basis to reposition the cap in three dimensions. In further investigation more reference distances could be considered.

A disadvantage of the selected marker position is that the analysis of marker positions is performed in the front area of the head while the actual electrodes used for the P300 spelling EEG signal are positioned at the back. This lack is the consequence of the fact that the glasses are mounted in front while the visual cortex is opposite. However, in our recent setup the values of the segments 1-8 indicate only a small displacement in the sagittal plane and compensate the suboptimal placement.

V. CONCLUSIONS

Our study showed the importance of the positioning accuracy when replacing EEG electrodes in combination with a predefined classification vector in a BCI application. The navigational support therefore allows the continuation of a session without reclassification.

ACKNOWLEDGMENT

We thank the Foerderverein Fachhochschule Nordwestschweiz Solothurn for their financial support.

REFERENCES

1. Wolpaw JR, Birbaumer N, McFarland DJ, Pfurtscheller G, Vaughan TM (2002) Brain-computer interfaces for communication and control. *Clin Neurophysiol.* 113(6):767-91
2. Mugler E, Bensch M, Halder S, Rosentiel W, Bogdan M, Birbaumer N, Kübler A (2008) Control of an Internet Browser Using the P300 Event-Related Potential. *Int J Bioelectromagnetism* 10(1):56-63
3. Polikoff JB, Bunnell HT, Borkowski WJ (1995) Toward a P300-based computer interface, in Proc. RESNA '95 Annual Conference, RESNAPRESS, Arlington Va. Pp. 178-180
4. Konermann W, Haaker R (2003) Navigation und Robotik in der Gelenk- und Wirbelsäulen Chirurgie, Springer-Verlag, Berlin Heidelberg New York
5. Barnes PJ, Baldock C, Meikle SR, Fulton RR (2008) Benchmarking of a motion sensing system for medical imaging and radiotherapy, *Phys Med Biol.* 53(20):5845-57

Author: Michael de Wild
 Institute: Institute of Medical and Analytical Technologies, University of Applied Sciences Northwestern Switzerland, School of Life Sciences
 Street: Gruendenstrasse 40
 City: 4132 Muttenz
 Country: Switzerland
 Email: michael.dewild@fhnw.ch

Pick to Place Trajectories in Human Arm Training Environment

J. Ziherl¹ and M. Munih¹

¹ Laboratory of Robotics and Biomedical Engineering, Faculty of Electrical Engineering, University of Ljubljana, Ljubljana, Slovenia

Abstract— A new method of trajectory planning in rehabilitation robotics is presented. First were measured in healthy subject the pick to place trajectories while haptic robot was in zero impedance space. B-spline approximation is used to mathematically define the measured paths. This trajectory path serves as a central line for the rounding haptic tunnel. In addition to radial elastic and damping force an optional guidance force can be applied along the tunnel to reach the place point. Finally are presented the pick to place movements with and without tunnel use in stroke hemiplegic patient.

Keywords— trajectory planning, haptic interface, rehabilitation robotics.

I. INTRODUCTION

The demographic structure of population in developed countries shows an increasing number of older people [1]. Among them the stroke is a leading cause of disability [2], to a large extent affecting the activities of daily living [3]. A numbers of controlled trials showed that enhanced physical therapy improves recovery after a stroke [4]. This fact confirms a growing necessity of rehabilitation approaches. In rehabilitation robotics the haptic interfaces combined with virtual reality largely improve the patient's motivation [5].

Several systems have been developed for robotic training of upper and lower extremities. Training systems for upper extremities are divided into two groups: end effectors and exoskeletons [6]. End effector upper extremity devices are more common. MIT-MANUS [7] with SCARA configuration, the MIME [8] system, which uses a Puma 560 robot manipulator, the Gentle/G [9] system based on the Gentle/S rehabilitation robot HapticMASTER, and the robot system for upper limbs rehabilitation developed by Deneve et al. [10] all belong to the class of end-effector based robots.

Human arm movement from point to point is important movement primitive in robotic rehabilitation. Different studies showed the rules that characterize measured human movement [11, 12, 13]. These rules are used as a natural movement bound.

This paper proposes trajectory shape planning using B-splines. The movements measured in healthy subjects are used for trajectory approximation with B-splines [15]. These are used in our case among others for new haptic object, a trajectory tunnel, which enables movement from

pick to place point along a desired trajectory in a virtual haptic environment. The trajectory tunnel is developed as an independent haptic primitive in virtual tasks. Subject's arm is placed in a fixture on the end effector of the haptic robot HapticMaster that is used as a force measurement and position generation device.

II. METHODS

A. Haptic system specification

The rehabilitation system used in the study consists of the haptic interface device HapticMaster (Moog FCS Inc.), a wrist connection mechanism, a grasping device, a lower and upper arm gravity compensation mechanism, a 3D visualization system and a Dolby surround sound display. The robot and the grasping device are shown in Fig. 1.

Two subjects participated in the study. The first subject is a right handed, 24 years old healthy male. This participant had no history of neuromuscular or musculoskeletal disorders related to the upper extremities. The second participant is a right-hemiparetic subject, 40 years old female. Both subjects gave their informed consent to participate.

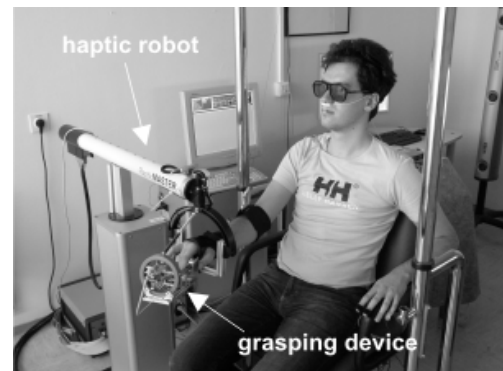


Figure 1: Subject training with haptic system: a grasping device is attached to the HapticMaster end-effector, a 3D projection screen is positioned in front of the subject.

B. Trajectory planning

Pick to place human movement from point to point in 3D space, including pick, transfer and release of the objects is

of outmost priority in everyday life. Studies of the movements measured indicate several rules:

1. The path of the arm is curved from pick to place points and slightly deviates from a straight line. Slight curvature does occur, depending on the area of the arm's workspace [11, 14].
2. The velocity profile is bell-shaped. Human chooses the trajectory with the minimum jerk change of the hand. The acceleration profile of the movement contains no discontinuities [11].
3. The accuracy of the movement is inversely proportioned to the movement velocity. The relationship is known as Fitts' law [12].
4. The path is the most curved, where the velocity is the least [14].

Movements of the arm are becoming smoother and more elegant with exercise and learning. The smoothness of the movements is described [11] using the time derivative of the trajectory.

C. Realization of the pick to place trajectory using B-splines

For the trajectory path measurement was developed a simple task which included a block object on the floor and a table. The healthy subject had to pick the object and place it on the table. After successful placing, the object reappeared at a random starting point on the virtual floor. The movements were made in zero impedance robot mode. This set of the measured movements represents a reference pick to place trajectories.

On the basis of measured reference path trajectory, is generated a mathematically determined path trajectory combined with B-splines, which are used for local approximation and later interpolation of the measured movements with lower degree polynomials. The splines are used as basic functions which are smooth at contact points between segments. Contact points are also known as knots (Fig. 2).

Let $x_0 < x_1 < \dots < x_n$ represent the knots. $b_{i,l}$ marks the i basic spline with l degree on the knots $\{x_j\}_{j=0}^n$. Choosing knots $x_{-l} < x_{-l+1} < \dots < x_0$ and $x_n < x_{n+1} < \dots < x_{n+l}$, a set can be defined:

$$b_{j,0}(x) = \begin{cases} 1, & x \in [x_j, x_{j+1}) \\ 0, & \text{otherwise} \end{cases} \quad (1)$$

$$b_{j,k}(x) = \frac{x - x_j}{x_{j+k} - x_j} b_{j,k-1}(x) + \frac{x_{j+k+1} - x}{x_{j+k+1} - x_{j+1}} b_{j+1,k-1}(x) \quad (2)$$

The defined set $\{b_{j,k}(x)\}$ is the base of the splines vector space with knots x_0, \dots, x_n and degree k . The whole function $s(x)$ is sum of functions

$$s(x) = \sum_{j=0}^{n-k-1} d_j b_{j,k}(x) \quad x \in [x_k, x_{n-k}], \quad (3)$$

where d_j are control points and function $s(x)$ is valid on the interval $[x_k, x_{n-k}]$.

The control points are coefficients of the approximation with basic functions. DeBoor's algorithm [15] is suitable and simple for calculating the function $s(x)$. DeBoor's algorithm enables fast calculation and is numerically stable. Different number of control points can be used to describe the path of the arm from pick point to place point, depending on the complexity of the trajectory. Fig. 2 shows five basic functions when the trajectory is defined by five control points. An example of a healthy person measured movement and its corresponding approximation interpolated with B-splines are shown on Fig. 3.

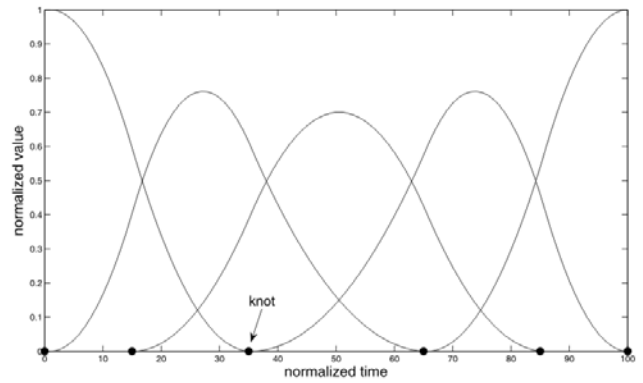


Figure 2: Five basic functions generated with B-splines.

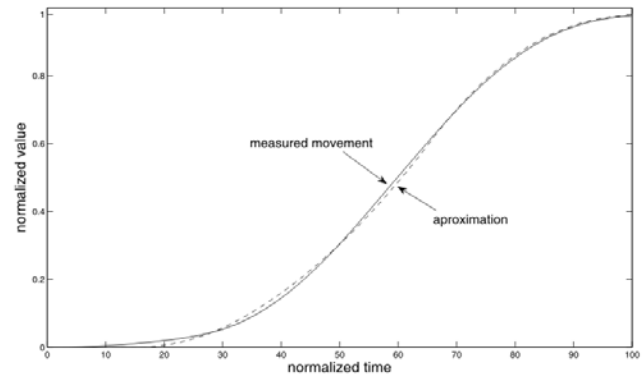


Figure 3: Measured movement and an approximation of arm movement.

D. The haptic trajectory tunnel

The approximated path using B-splines defines central curve line of the trajectory tunnel, linking the pick point and place point. This haptic trajectory tunnel also has the radius along the central curve line. The end point of the robot is haptically presented as a ball. The position of the ball is defined with the position of the robot end point while the size of the ball is minimal. The user can move the ball along the tunnel, as well as in radial direction when the ball diameter is smaller than the diameter of the tunnel. The collision between the object and the tunnel wall is modeled as a spring-damper system with a stiffness and viscous friction. The guidance force along tunnel central line could also be provided with a reference time value that defines the movement duration.

The described model of the haptic trajectory tunnel is designed as an object in the haptic Matlab/Simulink environment. Haptic tunnel is designed to be used as an independent haptic primitive.

III. RESULTS

To show that the human movements are repeatable and that the curvature of the movement depends on the direction and length of the pick to place point movement, we observed differences between the measured points and the linear path between pick and place points. From there were calculated average values of control points and then taken their absolute value for movement in a horizontal plane. These absolute values are differences of the measured control points values and the straight line control points values. The movements were performed by healthy subject in different directions. Fig. 4 shows the absolute values of the middle three control points (d_2, d_3, d_4) for different pick points in the xy plane. The solid black color marks value of the second control point, the grey dotted color marks value of the fourth control point while the white block marks the value of the third control point. The place point of the trajectory was always in the center of the coordinate system. The absolute values of the control points are depicted at pick points in four directions. The second and fourth control point are divided into two parts, showing values in x and y direction respectively. The width of the white block represents the value of the third control point in x direction while the block height represents the value in y direction.

Fig. 5 shows trajectories of movement from pick to place point in zero impedance space. The trajectories were measured in hemiparetic subject performing six pick to place movements and the Fig. 6 shows the trajectories with the haptic trajectory tunnel present.

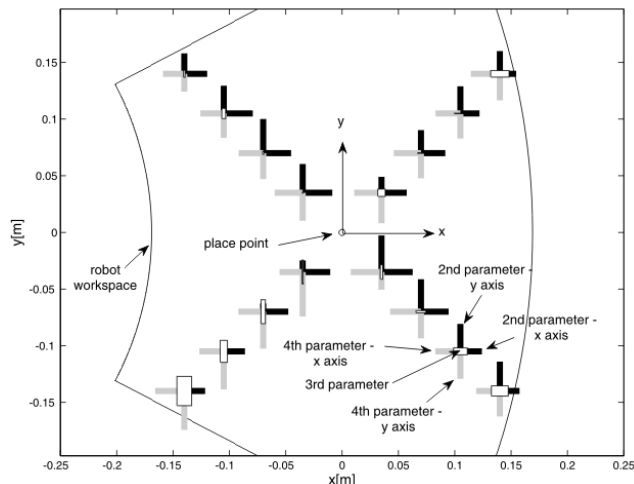


Figure 4: Values of second, third and fourth control point (d_2, d_3, d_4) for movements in the xy plane for different movements in man arm workspace.

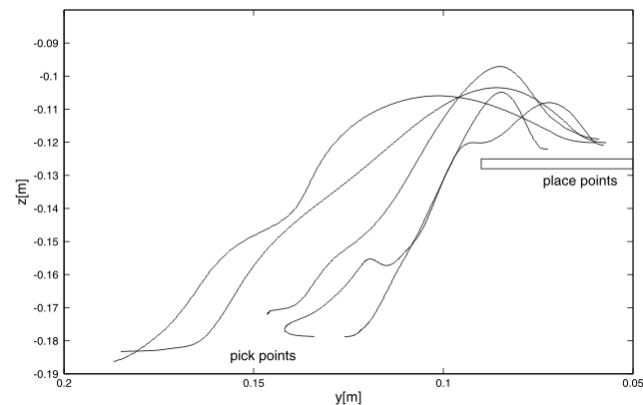


Figure 5: Pick to place movements of the hemiparetic subject in the pick and place task in zero impedance space.

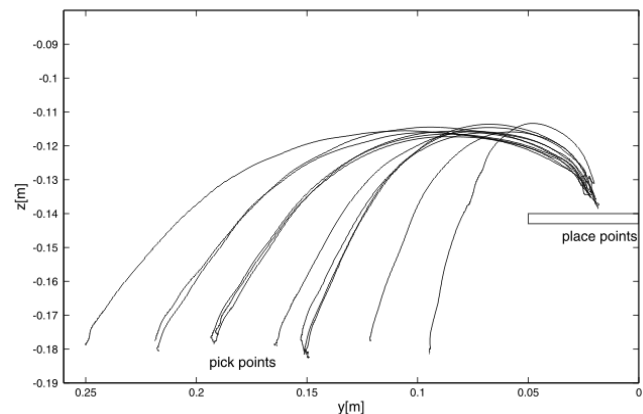


Figure 6: Pick to place movements of the hemiparetic subject in the pick and place task with the haptic trajectory tunnel present.

IV. DISCUSSION

To confirm that the human movements are repeatable, were initially examined the average absolute values of the middle three control points only by taking a number of measurements. Fig. 4 shows that in the same directions values of the control points stay in the same proportion while the values decrease proportional with the length of the movements in all directions. These measurement findings confirmed that for similar pick and place points human movements are repeatable. It can be recognized from Fig. 5 and Fig. 6 that the haptic trajectory tunnel determines the trajectory of the movement from the pick to the place point for a hemiparetic subject. Therefore, with the haptic trajectory tunnel, the patient is guided in cooperative manner to make same pick to place movements as healthy person with only minimal intervention from haptic system.

The big advantage of the presented trajectory planning method is primarily in the fact that the complexity of the movement being approximated does not play an important note. By using more control points, the method could be implemented also for other, much more complex trajectory planning problems, not only the point to point and pick to place movement.

V. CONCLUSIONS

The goal of this study was to create a trajectory planning algorithm and to develop adequate haptic object. The algorithm exploits use of the movements measured in healthy people as a base for further trajectory planning in patients. The results showed that the control points values of the approximated movements stay in the same proportion in the same directions while the values decrease proportional with the length of the movements in all directions. The measurement findings confirmed that for similar pick and place points human movements are repeatable. Further, a haptic object which helps the patient to move along the minimum intervention trajectory was designed. The results of our simple task confirmed that the patient can make same pick to place movements as healthy person when using the trajectory tunnel. These findings show that our model, which uses B-splines and haptic tunnel together with other movement primitives, can be easily implemented in rehabilitation robotics. Our next step is inclusion of the tunnel in an upper extremity robotic therapy system.

ACKNOWLEDGMENT

The authors wish to acknowledge financial support from the Republic of Slovenia Ministry of Higher Education, Science and Technology.

REFERENCES

1. Alho J M (1997) Scenarios, uncertainty and conditional forecast of the world population. *J Roy Stat Soc A Sta* 160:71-85
2. Amer. Heart Assoc. (2008) Heart and stroke statistical update. *Circulation* 117:25-146
3. Erol D, Sarkar N (2008) Coordinated control of assistive robotic devices for activities of daily living tasks. *IEEE T Neural Syst Rehabil Eng* 16:278-285
4. Sunderland A, Tinson D J, Bradley E L et al. (1992) Enhanced physical therapy improves recovery of arm function after stroke. A randomized controlled trial. *J Neurol Neurosurg Ps* 55:530-535
5. Mihelj M, Nef T, Reiner R (2007) A novel paradigm for patient-cooperative control of upper-limb rehabilitation robots. *Adv Robotics* 21:843-867
6. Siciliano B, Khatib O (2008) Springer Handbook of Robotics. Springer, Heidelberg
7. Hogan N, Kerbs H I, Charnnarong J et al. (1992) MIT - MANUS: A workstation for manual therapy and training I. IEEE International Workshop on Robot and Human Communication, Tokyo, Japan, 1992, pp 161-165
8. Lum P S, Burgar C G, Shor P C (2004) Evidence for improved muscle activation patterns after retraining of reaching movements with the MIME robotic system in subjects with post-stroke hemiparesis. *IEEE T Neural Syst and Rehabil Eng* 12:184-194
9. Loureiro R C V, Harwin W S (2007) Reach & Grasp Therapy: Design and Control of a 9-DOF Robotic Neuro-rehabilitation System. IEEE 10th International Conference on Rehabilitation Robotics, Kyoto, Japan, 2007, pp 757-763
10. Deneve A, Moughamir A, Afilal L et al. (2008) Control system design of a 3-DOF upper limbs rehabilitation robot. *Comput Meth Prog Bio* 89:202-214
11. Flash T, Hogan N (1985) The coordination of arm movements: an experimentally confirmed mathematical model. *Journal Neurosci* 5:1688-1703
12. Fitts P M (1992) The information capacity of the human motor system in controlling the amplitude of movement. *J Exp Psychol* 121:262-269
13. Wada Y, Kaneko Y, Nakano E et al. (2001) Quantitative examinations for multi joint arm trajectory planning - using a robust calculation algorithm of the minimum commanded torque change trajectory. *Neural Networks* 14:381-393
14. Simmons G, Demiris Y (2005) Optimal robot arm control using the minimum variance model. *J Robotic Syst* 22:677-690
15. Farin G (2001) Curves and Surfaces for CAGD, Morgan Kaufmann, San Francisco

Author: Jaka Zihel
 Institute: Faculty of Electrical Engineering, University of Ljubljana
 Street: Trzaska 25
 City: Ljubljana
 Country: Slovenia
 Email: jaka.zihel@robo.fe.uni-lj.si

Subretinal Microelectrode Arrays Implanted Into Blind Retinitis Pigmentosa Patients Allow Recognition of Letters and Direction of Thin Stripes

E. Zrenner¹, R. Wilke¹, H. Sachs², K. U. Bartz-Schmidt¹, F. Gekeler¹, D. Besch¹, H. Benav¹, A. Bruckmann¹, U. Greppmaier³, A. Harscher³, S. Kibbel³, A. Kusnyerik⁴, T. Peters⁵, K. Porubská¹, A. Stett⁶, B. Wilhelm⁵, W. Wrobel³ and SUBRET Study Group.

¹Centre for Ophthalmology, University of Tuebingen, Germany

²Klinikum Friedrichstadt, Dresden, Germany

³Retina Implant AG, Reutlingen, Germany

⁴Department of Ophthalmology, Semmelweis University, Budapest, Hungary

⁵STC Autonomous Nervous System and Safety Studies, Offerdingen, Germany

⁶NMI Natural and Medical Sciences Institute, Reutlingen, Germany

Abstract— Eleven patients have received subretinal implants, powered and controlled via a subdermal cable that enters the body retroauricularly and ends in a thin intraocular foil, placed transsclerally between the retinal pigment epithelium and the neuroretina. The tip of this foil carries two distinct arrays, a Multiphotodiode Array (MPDA) with 1500 electrodes, each electrode being controlled by an adjacent photodiode and an amplifier within a 3x3x0.1 mm chip, as well as a second array (1.2x1.2 mm) with 16 electrodes, for direct stimulation (DS) controlled via wires from outside. Safety of the approach has been investigated by means of angiography, OCT and fundus photography. The implant was well tolerated in all patients. Efficacy has been investigated in terms of threshold voltages to elicit phosphenes and the ability to perceive visual information mediated by the MPDA. Patients were tested for 4 weeks and spatial as well as temporal characteristics of repetitive multielectrode-stimulation were investigated. Letters were presented to the 3 most recent patients either by stimulating retinal cells in 10 ms steps via individual electrodes in a sequence patients had learned to write such letters or - via the light sensitive chip - by individual bright letters or stripe patterns steadily presented at a screen in 62 cm distance.

It was shown that active subretinal multielectrode implants with currents close to recognition threshold (10 to 27 nC/electrode) produce retinotopically correct patterns that allow for the first time recognition of individual letters (8 cm high, viewed in appr. 62 cm distance) even at low luminance levels. Stripe patterns of moderate luminance can be resolved up to 0.35 cycles/deg via the subretinal chip. This clearly supports the feasibility of light sensitive subretinal multi-electrode devices for restoration of useful visual percepts in blind patients.

Keywords— Artificial Vision, Subretinal Implants, Retinal Prosthesis, Blindness, Electrode Arrays

I. INTRODUCTION

Several concepts have been developed how to restore vision in blind persons by implanting electronic devices to evoke useful visual sensations. Since 1995, our consortium has developed a so-called “active” subretinal microphotodiode array (MPDA), based on *in vitro* measurements (Stett et al. 2000) and in various animal models (Zrenner et al. 1999, Schwahn et al. 2001). These *in vitro experiments revealed that:*

- (1) charge injections of about 1 nC per electrode are sufficient to excite post-receptoral retinal neurons;
- (2) electrode separation distances of 50-150 μm in the outer retina can be resolved in ganglion cell recordings;
- (3) retinæ with completely degenerated photoreceptors (RCS rats, 160 days and older) can be excited sub-retinally in a proper spatially organized manner;
- (4) surface coating of MPDAs as e.g. with laminins can improve cell adhesion and biocompatibility (Guenther et al. 1999).

In vivo experiments revealed that:

- (1) inner retinal layers are well preserved in the central retina, as shown by comparative histological studies of human and animal forms of degenerative retinal disorders (see Zrenner et al. 1997);
- (2) a safe introduction of the devices via a scleral flap near the limbus through the subretinal space (like in a tunnel) to the back of the eye is possible (Sachs et al. 2005 and ARVO 1999, Shinoda et al. ARVO 2004);
- (3) inner retinal layers are well preserved after subretinal long term implantation (28 months) in pigs;
- (4) MPDAs remain fixated at stable subretinal positions as investigated in both rabbit and pig;
- (5) adequate coating has been developed to protect MPDAs from damage tested for 12 months;

(6) cortical recordings with multielectrodes and optical recording from the visual cortex of cat revealed a spatial resolution for electrical subretinal stimulation of at least 1 degree (Eckhorn et al. 2006).

Based on these findings a subretinal implant was developed that is suited for implantation into the human eye.

Presently, a *clinical study* is ongoing where wire-bound MPDAs are being implanted for four weeks into one eye of 11 blind RP patients. Within a subretinal layer of 1/10 mm there are photodiodes, amplifiers and circuits that adapt the electrical signal to the nerve cell to the strength of the brightness of the object to be seen and its surroundings. This is the first active subretinal chip ever implanted in patients (see Zrenner et al. ARVO 2006, 2007, 2008, 2009 and Sachs et al. ARVO 2006, 2007, 2008, 2009 and Gekeler et al. ARVO 2008).

II. MATERIAL AND METHODS

A. The subretinal implant

The active implant consists of approximately 1500 light-sensitive cells on a surface of 3x3 mm (each cell containing an amplifier and a TiN electrode of 50x50 μm , spaced 70 μm) as well as a 4x4 array of identical electrodes, spaced 280 μm , for direct stimulation (DS), chronically implanted next to the fovea. MPDA (so-called chip) and DS array are positioned on a small subretinal polyimide foil powered via a subretinal transchoroidal, retroauricular transdermal line that provides power and control signals to the chip and stimulation currents to the DS electrode array. Stimulation parameters for each DS electrode and chip activity and sensitivity can be controlled independently by a software tool that allows to transform the orientation of the visual space to the orientation of the electrode field and to set individual stimulation parameters in the stimulation box via a wireless transmitter. Moreover, all stimulation parameters and patient's "yes" or "no" responses to each parameter are recorded automatically by a particular software. (Sailer ARVO 2005). For selection of patients, corneal DTL-electrodes and an alternative forced choice method was used to determine electrical excitability of the retina and of optic nerve transmission in normals and patients with degenerative retinal disease; determination of phosphene threshold with corneal electrodes has turned out to provide an important criterion for the suitability of patients for electrical retinal prostheses (Gekeler et al. 2006).

B. Study design

In the present study, wire-bound MPDAs were implanted for four weeks into one eye of 11 blind RP patients who had no useful vision for more than 5 years and a visual acuity earlier in life $> 20/200$. They were able to perceive corneally elicited electrical phosphenes and had no other serious eye or general diseases.

The implant safely stored in a trocar was guided from a retroauricular skin incision to the region of the upper lid; from there it was fed via a silastic tube into the intraorbital space. After vitrectomy and a small peripheral retinal detachment it was then fed via a flap in the sclera and a transchoroidal access along a guiding foil into the subretinal space and then gently pushed into a final parafoveal position; radiodiathermy and a specially designed implantation instrument were used to penetrate the choroid without causing bleeding; silicone oil was used as a tamponade (Sachs et al. ARVO 2005, 2006, 2007). This transchoroidal procedure was applied to all patients without adverse events such as retinal detachment, bleeding, infection etc. (Sachs et al. ARVO 2008).

C. Stimulation procedures

A battery of computerized, standardized tests for patients with visual prostheses was developed to quantify the functional outcome (Zrenner et al. ARVO 2004, Wilke et al. ARVO 2006, 2007). Visual perception of brightness elicited by applying biphasic voltage impulses to DS electrodes from 1 to 2,5 V ($t = 0.5$ to 6 ms) was assessed using a scale from 5 (very strong) to 0 (none); additionally double impulses with differences up to 0.8 V between two stimuli (10 s interval) as well as pulse trains were applied. For testing the light sensitive chip, letters were presented to the most recent 3 patients either by stimulating retinal cells in 10 ms steps via individual electrodes in a sequence patients had learned to write such letters or - via the light sensitive chip - by individual letters or stripe patterns steadily presented at a screen in 62 cm distance.

III. RESULTS

A. Direct stimulation via the DS-Array

Electrical stimulation of rows, columns and blocks of 4 electrodes allowed some patients of the first 8 patients to clearly distinguish horizontal from vertical lines and positions, respectively. Under optimal conditions, dot alignment (vertical vs horizontal up to 86% correct) and direction of dot movement (4 AFC, up to 91% correct) was properly

recognized, if three or four neighboring electrodes were switched on simultaneously or sequentially at 1 s intervals (Zrenner et al. ARVO 2007).

Brightness perception of spots varied from scale 0 to 5 in a linear manner if voltages between 1.5 and 2.5 were applied (randomly 6 times) to a square of 4 electrodes. This corresponds to a charge increase of approximately $0.23\text{mC}/\text{cm}^2$ for each of the 5 steps. A difference in brightness between two consecutive pulses was discerned, if a difference in charge of at least $16\ \mu\text{C}/\text{cm}^2$ was applied. If equal charges were applied to both conditions, the second flash always was perceived slightly dimmer irrespective of the stimulation level. Subjective brightness amplification phenomena were observed at medium stimulation levels with pulse trains and at certain frequencies. The subjective size of spot perception upon stimulation of a square of 4 electrodes increased from 1 to 5 mm at arm's length, if the voltage was increased from 1,5 to 2,5 V. Interestingly at the offset of current, the spot disappeared in a quick sequence of individual very small pixels.

Recently, a new preoperative planning procedure was implemented to preoperatively define the most appropriate location on the fundus for surgical implantation of the prosthesis (Kusnyerik et al. ARVO 2008).

In the most recent three patients various patterns consisting of 4 x 4 dots were presented, corresponding to letters of approximately 5 cm diameter in 60 cm distance. Pat. 1 correctly (20/24) recognized the direction of the letter "U", presented with the opening in four different directions in a 4 alternative forced choice (4AFC) mode. Pat. 2 correctly (12/12) differentiated letters (e.g. C, O, I, L, Z, V) within few seconds, presented via DS-electrodes in random order (4AFC).

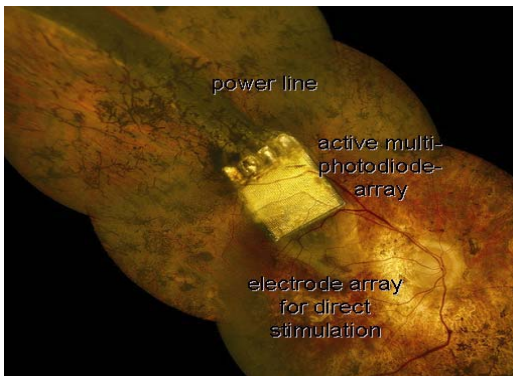


Fig. 1 DS-Array, MPDA and powerline in the subretinal space of a patient suffering from retinitis pigmentosa

B. Light stimulation of the MPDA

Six of eleven patients perceived light projected onto the MPDA. In SLO microperimetry of the MPDA, single light spots down to 100 to 400 μm in diameter were detected. Via the MPDA patients were able to correctly localize a white plate on a black table cloth or a window when freely moving in a room (Zrenner et al. ARVO 2007, 2009). In 2 of the devices there were problems with cable contact stability or encapsulation, in two other cases the retina of patients was degenerated too extensively (blindness > 15y) preventing successful activation of the chip. Of the most recent three patients using the light sensitive subretinal chip, patient 3 correctly (22/24) differentiated without head movements letters (e.g. L,I,T,Z; 8,5 cm high, 1.7 cm line width) steadily presented on a screen at 62 cm distance with a red light (630nm cutoff) of $3.4\ \text{cd}/\text{m}^2$. Pat. 3 recognized (15/20 correct, 4AFC) the direction of lines or stripe patterns with the chip, as did Pat. 1 (11/14, 2AFC) and Pat. 2 (11/12 4AFC) up to 0.35 cycles/deg.

C. Life Quality

The brief symptom inventory (BSI) by Derogatis, a validated 53-item questionnaire was used for the assessment of variations in psychological stress of the patients before and during the four week study. The sum score total Global Severity Index (tGSI) was used for evaluation (Peters et al. ARVO 2007). At screening seven out of eight subjects (mean 50.33, SD 12.17) were in the normal range of the tGSI. In addition, we provided regular psychological support and counseling during study participation. The difference at close out visit compared to screening (t-test: mean diff 6.17, SD 8.95; $p=0.08$) showed a tendency to lower values in a sense of better emotional balance at the end of trial participation.

IV. DISCUSSION

Active, power driven subretinal implants presented here are able to provide useful visual information; passive elements (Chow et al. 2004) cannot provide sufficient energy for electrical neural stimulation. Subretinal active stimulation always yielded spatially confined retinotopic perceptions in form of round whitish or yellowish dots. Spatial dimensions of percepts elicited by single electrodes could be determined to be approximately one degree of visual angle. The size and brightness of such percepts can be modulated with stimulation strength. However, percepts from multiple-electrode stimulation, although still strictly

retinotopic, are somewhat more complex than the mere spatial composite of single electrode stimulation. Several mechanisms leading to this effect will be discussed. Among them, neuronal reorganization (Marc et al. 2003) seems to play a minor role, given the size of retinal area stimulated by individual electrodes and the fact that lateral displacement of neuronal structures does rarely exceed 100 micrometer (Strettoi, pers. comm.). Temporal characteristics of subretinally elicited percepts depend on numerous factors such as pulse amplitude, characteristics of proceeding stimuli, as well as size of retinal area stimulated. These investigations in patients show a window for safety and efficacy of multielectrode stimulation of the retina on the one hand and the necessity of individual adaptation for feasible approaches on the other.

V. CONCLUSION

Subretinal electrical multielectrode stimulation can provide a useful range of localized brightness perceptions in blind patients within a limited range of temporal, spatial and electrical parameters. Nevertheless was shown that active subretinal multielectrode implants with currents close to recognition threshold (10 to 27 nC/electrode) can produce retinotopically correct patterns that allow for the first time recognition of individual letters (8 cm high, viewed in appr. 62 cm distance) even at low luminance levels. Stripe patterns of moderate luminance can be resolved up to 0.35 cycles/deg via the subretinal chip. This clearly supports the feasibility of light sensitive subretinal multi-electrode devices for restoration of useful visual percepts in blind patients.

ACKNOWLEDGMENT

Supported by BMBF project 01K008 and by Retina Implant AG, Pro Retina Deutschland e.V. and Kerstan Foundation

REFERENCES

(other than ARVO abstracts quoted in the text; for ARVO abstracts see www.arvo.org)

- [1] Chow AY, Chow VY, Packo KH, Pollack JS, Peyman GA, Schuchard R. Arch Ophthalmol. 122:460-469 (2004)
- [2] Eckhorn R, M. Wilms, T. Schanze, M. Eger, L. Hesse, U. T. Eysel, Z. F. Kisvarday, E. Zrenner, F. Gekeler, H. Schwahn, K. Shinoda, H. Sachs, P. Walter: Vision Research 46:2675-2690 (2006)
- [3] Gekeler F, A Messias, M Ottinger, K.U Bartz-Schmidt, E Zrenner: IOVS 47: 4966-4974 (2006)
- [4] Gekeler F, Szurman P, Grisanti S, Weiler U, Claus R, Greiner T, Völker M, Kohler K, Zrenner E, Bartz-Schmidt K U: Graefe's Archive for Clinical and Experimental Ophthalmology 245:230-41 (2007)
- [5] Guenther E, Troeger B, Schlosshauer B, Zrenner E.: Vision Research 39:3988-3994 (1999)
- [6] Marc RE, Jones BW, Watt CB, Strettoi E: Progr.Ret.Eye.Res. 22:607-655 (2003)
- [7] H. Sachs, T. Schanze, M. Wilms, A. Rentzos, U. Brunner, F. Gekeler, L. Hesse: Graefe's Arch. Clin. Exp. Ophthalmol. (2005)
- [8] Schwahn HN, Gekeler F, Kohler K, Kobuch K, Sachs H, Schulmeyer F, Jakob W, Gabel VP, Zrenner E: Graefe's Arch Clin Exp Ophthalmol 239:961-967 (2001)
- [9] Stett A, Barth W, Weiss S, Haemmerle H, Zrenner E. Vision Research 40:1785-1795 (2000)
- [10] Stett A, Mai A, Hermann T: Journal of Neural Engineering 4: S7-S16 (2007)
- [11] Zrenner E, Miliczek K-D, Gabel VP, Graf HG, Günther E, Haemmerle H, Höfflinger B, Kohler K, Nisch W, Schubert M, Stett A, Weiss S. Ophthalmic Res: 29, 5:269-280 (1997)
- [12] Zrenner E, Stett A, Weiss S, Aramant RB, Guenther E, Kohler K, Miliczek K-D, Seiler MJ, Haemmerle H. Vision Research 39:2555-2567, (1999)
- [13] Zrenner E: Science 295:1022-1025 (2002)

Prof. Dr. med. Eberhart Zrenner
 University of Tübingen
 Centre for Ophthalmology
 Institute for Ophthalmic Research
 Schleichstr. 12-16
 72076 Tübingen
 Germany
 E-Mail: ezrenner@uni-tuebingen.de

Investigation of the Adaptation to Artificial Damping in Cerebellar Ataxia Using the Myohaptic Technology

M. Manto¹, N. Van Den Braber², J. Meuleman², P. Lammertse², and G. Grimaldi¹

¹ Neurologie Erasme, ULB, Bruxelles, Belgium

² Moog, Nieuw-Vennep, Holland

Abstract— We investigated fast pointing and fast reversal single-joint movements performed under artificial damping conditions applied with the myohaptic technology. Healthy subjects were able to scale the intensity of the agonist and antagonist electromyographic (EMG) activities when damping was added during both types of movements. Cerebellar patients were able to scale the magnitude of the agonist and antagonist EMG activities during pointing movements. For reversal movements, patients could scale the intensity of the initial agonist EMG activity but were unable to modulate the intensities of the second set of EMG discharges associated with the return to the initial position. Patients were able to adopt the appropriate motor strategy for the first phase of reversal movements, but they were unable to implement the suitable sequential strategy for the superimposition of motor plans during artificial damping. The myohaptic technology is the first to allow the detection of deficits in the implementation of sequential motor coding under the mechanical condition of artificial damping.

Keywords— Cerebellum, myohaptics, electromyography, damping, reversal.

I. INTRODUCTION

One of the fundamental parameters underlying the accuracy of fast movements with a bell-shaped speed profile is damping [1]. During a fast movement, muscle damping, one of the factors generating resistance to movement [2], is typically asymmetrical, predominating in the direction of muscle shortening, which renders the encoding of speed more difficult. For hand kinematics in the physiological range of motion, the damping compensation signal (aiming at compensating the asymmetry of the damping parameter) is a crucial element for motor encoding by the primary motor cortex [1]. In other words, the primary motor cortex has to compensate for the muscle's state dependence. Due to technological limitations, the elucidation of the structures of the central nervous system (SNC) controlling the damping compensation signal has remained elusive.

Fast single-joint movements are associated with a triphasic pattern of EMG activity: a first burst in the agonist muscle (providing the launching torque) is followed by a second

burst in the antagonist muscle (providing the braking torque), followed by a second burst in the agonist muscle (to bring the limb accurately to the target) [3]. When cerebellar patients attempt to perform a fast movement, they overshoot the aimed target. This classical sign, called hypermetria, is associated with the following electromyographic (EMG) deficits: a delayed onset latency of the antagonist EMG activity, a prolongation of the first agonist burst, a decreased rate of rise in the antagonist EMG activity, an inability to increase the intensity of the agonist and antagonist EMG activities when the inertia of the moving limb is artificially increased [4-7].

We investigated fast pointing movements (FPM) and fast reversal movements (FRM) in cerebellar patients. The goal of this study was to understand the contribution of the cerebellum in the sequential superimposition of motor plans during the adaptation of damping. Movement was studied before and after addition of mechanical damping using a new myohaptic device—called Wristalyzer—which allows to assess specifically tremor and dysmetria under various inertial or damping conditions [8], to assess rigidity in extrapyramidal disorders and to characterize voluntary muscle force [9]. Moreover the system is able to deliver mechanical oscillations at the wrist at various frequencies and with high accuracy [10]. Using this technique, we have found that neurological patients are more susceptible to contralateral high-frequency oscillations (13.3 Hz) than controls [10]. Abnormal EMG responses to 15 Hz oscillations (amplitude of oscillations: 0.1 rad) has been also observed in a neurological patient exhibiting dysmetria and kinetic tremor due to a severe paraneoplastic syndrome [8]. Cerebellar patients showed a beneficial effect with motion loading during alternate movements [8]. The wristalyzer is not only an assessment device for neurological disorders which allows a better characterization of the control of limbs, but can have other applications as a rehabilitation device.

II. METHODS

A. Description of the wristalyzer

The wristalyzer is a mechatronic myohaptic unit, including a moving unit and its controller, as well as a signal acquisition unit, able to measure in real time the mechanical response. The EMG signal can be used to control the motor and the haptic loop, so that a physiological signal from the muscle (either motor units recorded with needles inserted in the muscle, or EMG activity recorded with surface electrodes) is taken into account to control haptics. The moving unit presents one rotation axis around which it is able to rotate relatively to the haptic device. The system comprises a direct drive brushless motor with a high resolution encoder (the encoder is embedded in the motor casing) and a dedicated 16-bit resolution strain gauge torque sensor integrated into the mechanical interface to the manipulandum. The haptic inner control loop runs on an embedded haptic server computer running a real time operating system on a 2048 Hz interrupt. The haptic server functions and data can be accessed both by a dedicated application program interface (API) and by a web browser. The controlling user application runs on a separate Windows computer. It has a graphical user interface and a file logging capability. Position accuracy is about 0.1 mm, angular accuracy is 0.35 deg, nominal torque is 6 Nm, maximal rotation velocity up to 2000 degrees/s, and range of motion -60 to $+60$ degrees. The system is equipped with a safety button and its range of motion is constrained from -1 rad to $+1$ rad. The inertia of the motor and handgrip is $0.004 \text{ kg} \times \text{m}^2$. The wristalyzer offers several advantages in terms of medical device. It is portable with a dedicated rack including wheels and can be used on the bedside of a patient. Oscillations can be generated while the hand is held either vertically or horizontally with pronation. A safety button has been added to stop the device if necessary. The system can deliver oscillations up to 50 Hz. The wristalyzer controller can be commanded from a host computer with a Ethernet card (100 Mbps). The input voltage range is 230 Volts (VAC), frequency from 50-60 Hz. The power consumption does not exceed 1200W. Adjustable screws are used to ensure stability on the floor.

B. Cerebellar patients

Our 3 patients exhibited a pure cerebellar syndrome. Patient 1 (age: 44, male) presented a spinocerebellar ataxia (SCA2) with a mild cerebellar syndrome. The Ataxia Score was E2D0T1A1H0 (ataxia rating scale; E: eye movements, D: dysarthria, T:tremor/dysmetria in limbs, A: ataxia of

stance/gait, H: hypotonia; 0 to 4: slight to severe) [Manto Ann Neurol 1994] Needle EMG and sensorimotor nerve conduction velocities in upper and lower limbs were normal. Plantar reflexes were flexor. Sensory testing was normal. Muscle tone was normal. He did not exhibit fasciculations, myoclonus, rest tremor, dystonia or choreiform movements. We selected this patient because the study of the SCA2 gene showed a mild expansion with 32 repeats (normal: < 31 repeats) and brain MRI showed atrophy restricted to the cerebellum. Patients 2 and 3 presented a pancerebellar syndrome associated with a pure cerebellar atrophy on brain MRI. The ataxias scores were respectively E2 D2 T2 A2 H0 (age: 28, female) and E2 D2 T2 A2 H0 (age: 50, male), respectively. Search for SCA1, SCA2, SCA3 and SCA6 was negative in these patients. Gluten ataxia and paraneoplastic cerebellar degeneration were excluded.

C. Protocol and parameters

Studies were performed following approval of the institutional ethical committee of the Free University of Brussels.

All our subjects were right-handed and we investigated the right hand. Control group was composed of $n = 8$ healthy subjects with a mean age: 34.8 ± 10.2 years (3 women). Subjects were comfortably seated, with the shoulder relaxed and the elbow at an angle of 90 degrees. The hand and forearm were affixed with straps. The wrist joint was carefully aligned with the motor axis. Movements were performed in the horizontal plane. Subjects performed sets of FPM and FRM over 3 distances (targets: 0.2, 0.3 and 0.4 rad). The targets were horizontal lines displayed on the screen of a computer placed in front of the subject. The origin (0 rad) was defined as the neutral position of the hand. For FPM, subjects were instructed to flex quickly the wrist towards the aimed target (located at 0.2, 0.3 or 0.4 rad). Speed and accuracy were stressed (“you have to perform the movement as quickly and as accurately as possible towards the target displayed on the screen”) [7]. For FRM, subjects were instructed to flex the wrist quickly and accurately towards the first target (located at 0.2, 0.3 or 0.4 rad), and to come back immediately to the starting position at 0 rad (“you have to perform the movement as quickly and as accurately as possible towards the first target, and to get back immediately to the initial position as fast and as accurately as possible”). The instructions were repeated twice to avoid any ambiguity. Each subject practiced 3 to 4 trials before recordings of FPM, and practiced 3 to 4 trials before recordings of FRM (in 2 patients, we assessed specifically the possible consequences of the number of practice trials and found no effect upon the pattern of EMG activities). Subjects performed series of 10 fast movements. Each movement started after a “go” signal. We used the follow-

ing order: 10 fast flexions for each angle (0.2, 0.3 and 0.4 rad from the initial position), followed by 10 FRM for each angle. For each set of recordings, we studied movements in the basal condition and following addition of artificial damping (0.1 Nms/rad or 0.2 Nms/rad). We recorded the surface EMG activities of the flexor carpi radialis and extensor carpi radialis muscles. Surface EMG activities were amplified (X 1000), and full-wave rectified (filter settings: 20-500 Hz; Delsys surface electrodes, USA; electrodes fixed on the skin with tape).

Damping was controlled by multiplying a damping coefficient (mDampCoef) to the velocity of the end effector (mEffectVel). The result was introduced in the Torque command of the device:

$$mOutTor = TorCommand - [mDampCoef * mEffectVel]$$

Friction was compensated via software. Movements were studied in the basal condition (free mode) and with addition of damping: either 0.1 Nms/rad or 0.2 Nms/rad. For comparison, damping of a completely relaxed hand is 0.02-0.03 Nm.s/rad [2].

Due to the anatomic variations and due to the various levels of fat under the skin, calibration of surface EMG activities is critical to compare the intensities of agonist and antagonist EMG activities within subjects and across subjects [6]. To this aim, we developed a novel calibration method specifically adapted to the myohaptic device. We assessed the maximal contraction in an isotonic task (MIC, maximal isotonic contraction; the motor is opposing a controlled force). The calibration area was defined as the integrated area below the averaged EMG trace (traces are first rectified) corresponding to a torque value from 0 Nm up to 6 Nm. Amongst the variables, the following parameters were computed: movement amplitudes, the integrals over the first 80 msec for the antagonist burst in the ECR muscle (Q80ANTA).

III. RESULTS

Figure 1 illustrates a typical observation for the reversal movement and the associated EMG activities in the 3 experimental damping conditions in a control subject and in patient 1. In patient 1 (performing hypometric movements), dysmetria worsened during reversal movements when damping was artificially increased. Dysmetria decreased with damping in patients 2 and 3 (performing hypermetric movements). (see Tables 1 and 2 for the mean movement amplitudes +/- SD during FPM and FRM; aimed target: 0.2 rads). In the 3 patients, we found a major deficit in the adaptation of the activity of the ECR muscle, as confirmed by the lack of increase of the Q80Anta (group by damping

effect: $p < 0.001$). Figure 2 illustrates this inability for the target of 0.2 rad. We made similar observations for the other targets. For the 3 patients, damping modified the features of the pattern of EMG activities. Deficits were more severe with the addition of 0.2 Nms/rad.

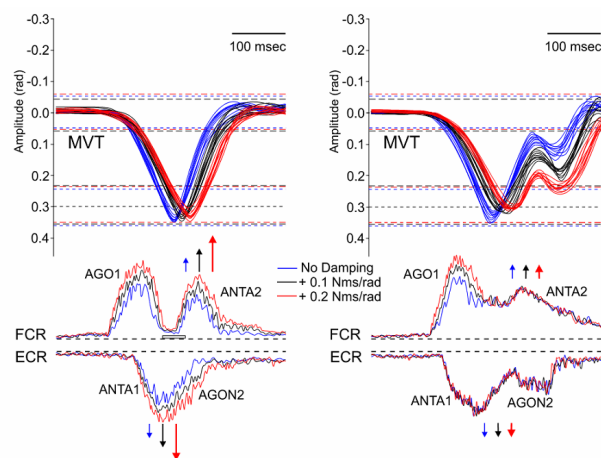


Fig 1. Reversal movements in a control subject (left) and in patient 1 (right). The patient can only adapt the intensity of the first burst in the FCR muscle (AGO1). He cannot adapt the intensity of the ECR muscle. Note also that the 2 bursts in the FCR muscle (AGO1 and ANTA2) are not demarcated. As a consequence of these deficits, the return to the baseline position becomes more hypometric with damping.

Table 1 Movement amplitudes for the aimed target of 0.2 rads (fast pointing movements)

Added damping (Nms/rad)	Controls	Patients
+0	0.2006 +/- 0.01251	0.3232 +/- 0.0903*
+0.1	0.2007 +/- 0.0122	0.3000 +/- 0.0979*
+0.2	0.2005 +/- 0.019	0.2587 +/- 0.0459*

*Significant dysmetria ($p < 0.01$)

Table 2 Movement amplitudes for the aimed target of 0.2 rads (fast reversal movements)

Added damping (Nms/rad)	Controls	Patients
+0	-0.0179 +/- 0.026	-0.0943 +/- 0.1518*
+0.1	0.0358 +/- 0.0233	-0.0681 +/- 0.1564*
+0.2	0.00375 +/- 0.028	-0.0006 +/- 0.1366

*Significant dysmetria ($p < 0.01$)

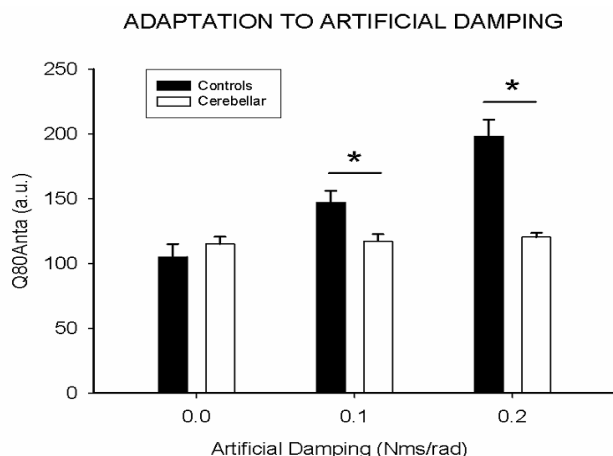


Fig 2. Mean Q80Anta (+/- SD) for the control subjects and the 3 patients.
*: $p < 0.01$

IV. DISCUSSION

A major law governing fast goal-directed movements is the increase in the intensity of the agonist EMG activity (the launching torque) for movements requiring a greater impulse [11]. The deficits that we have observed in reversal movements cannot be a direct consequence of the hypermetria occurring during the first phase of movement, since some patients are able to perform accurate movements during FPM and exhibit an inability to adapt the intensities of EMG discharges during FRM. The capacity of the central nervous system (CNS) to adapt to the variations of passive torques occurring during motion permits the accurate control of angular position parameters. The distorted patterns reported here may be an essential and so far not recognized defect underlying cerebellar dysmetria. When we asked our patients whether addition of damping improved or decreased the accuracy, they all said that it was more difficult to perform FRM with damping, while the accuracy was improved with damping the FPM. This highlights a difference between the adaptation to inertia and the adaptation to damping when cerebellar patients perform pointing movements, since cerebellar hypermetria is larger when the mass is artificially increased [4].

Rehabilitation strategies in patients with cerebellar disorders should take into account the differences in the motor strategies underlying pointing movements and reversal movements in cerebellar disorders. In particular, we show that a given muscle can exhibit a normal behaviour facing mechanical damping during the first part of a motor sequence, but is not able to adapt appropriately for the following part.

V. CONCLUSION

We provide the first demonstration of an inability to adapt to artificial damping in cerebellar disorders. We hypothesize that cerebellar patients might not get access to some specific sections of the motor code under the experimental condition of artificial damping. The code appears to be executed adequately in the first part of a complex movement, but the execution is distorted in the second part. Studies under artificial damping reveal that the estimations of the motoneuronal discharges are wrong.

ACKNOWLEDGMENT

Supported by the FNRS Belgium.

REFERENCES

1. Todorov E. (2000) Direct cortical control of muscle activation in voluntary arm movements: a model. *Nature Neurosci* 3:391-398
2. Gielen CCAM, Houk JC. (1984) Nonlinear viscosity of human wrist. *J Neurophysiol* 52:553-569
3. Hallett M, Shahani BT, Young RR. (1975) EMG analysis of stereotyped voluntary movements in man. *J Neurol Neurosurg Psychiatry* 38:1154-1162
4. Manto M, Godaux E, Jacqy J. (1994) Cerebellar hypermetria is larger when the inertial load is artificially increased. *Ann Neurol* 35:45-52
5. Manto M, Godaux E, Jacqy J. (1995) Detection of silent cerebellar lesions by increasing the inertial load of the moving hand. *Ann Neurol* 37:344-50
6. Manto M, Jacqy J, Hildebrand J, Godaux E. (1995) Recovery of hypermetria after a cerebellar stroke occurs as a multistage process. *Ann Neurol* 38:437-45
7. Manto M, Godaux E, Jacqy J, Hildebrand J. (1996) Cerebellar hypermetria associated with a selective decrease in the rate of rise of antagonist activity. *Ann Neurol* 39:271-4
8. Grimaldi G, Lammertse P, Van Den Braber N, Meuleman J, Manto M. A new myohaptic device to assess wrist function in the lab and in the clinic: the Wristalyzer. *Haptics: Perception, Devices and Scenarios*, 6th International Conference, EuroHaptics. Madrid, 2008, pp 33-42.....
9. Grimaldi G, Lammertse P, Manto M (2007) Effects of wrist oscillations on contralateral neurological postural tremor using a new myohaptic device ('wristalyzer'). 4th IEEE-EMBS Proc. Intern. Summer School Symp. Med. Dev. Biosensors, Cambridge, UK, 2007, pp. 44-48
10. Grimaldi G, Lammertse P, Van Den Braber N et al. (2008) Effects of inertia and wrist oscillations on contralateral neurological postural tremor using the Wristalyzer, a new myohaptic device. *IEEE Trans Biomed Circuits Syst.*, vol 2, pp 269-279
11. Gottlieb GL (1998) Muscle activation patterns during two types of voluntary single-joint movement. *J Neurophysiol* 80:1860-1867

Corresponding author:

Manto Mario
FNRS ULB Erasme
808 Route de Lennik
Bruxelles 1070 - Belgium

Analysis of Parkinson gait based on wavelet packet entropy

Yang Han¹, Zhanhong Ma², Ping Zhou¹ and Zhicheng Liu^{1,*}

¹ School of Biomedical Engineering, Capital Medical University, Beijing, PR China

² Radiology Department, Chaoyang Hospital, Beijing, PR China

* Corresponding author, zcliu@ccmu.edu.cn

Abstract— In this paper we show the possibility of using wavelet packet to analysis and characterize the gait signal of patients with Parkinson disease. Entropy has been defined to help extract the feature from results of wavelet packet decomposition. And the assessment of results has been performed by the means of T-test, showing that control group and PD group are statistically different from each other and our procedure based on wavelet packet could be applied to feature extraction of gait data.

Keywords— Wavelet packet, Parkinson's disease, wavelet entropy

I. INTRODUCTION

The first recorded article of "wavelet" could date back to 1909, which is in a thesis by Alfred Haar. And now the wavelet transform has been increasingly used in the analysis of biological signal, and has proved to be a powerful mathematical tool. This technique is applied in detecting cardio-electrical signals, inducing noise and enhancing and compressing images [1]. In this analysis, we put forward a processing method based on Haar wavelet packet transform to reconstruct the gait signal of Parkinson patients. The Haar transform is one of the earliest examples of what is known now as a compact, dyadic, orthonormal wavelet transform [2, 3]. The Haar wavelet basis, being an odd rectangular pulse pair, is the simplest and oldest orthonormal wavelet with compact support [4].

Parkinson's disease (PD) is a chronic and progressive neurological disorder that results in tremor, rigidity, slowness, and postural instability. A disturbed gait is a common, debilitating symptom; patients with severe gait disturbances are easy to falls and may lose their functional independence [5]. Gait analysis is an excellent method for explaining those disturbances and help further treatment.

II. MATERIALS AND METHODS

A. Data

We used the gait data from 93 patients with idiopathic PD (mean age: 66.3 years; 63% men), and 72 healthy con-

trols (mean age: 66.3 years; 55% men). The data includes the vertical ground reaction force records of subjects as they walked at their usual, self-selected pace. Underneath each foot were 8 sensors that measure force (in Newtons) as a function of time [5]. The sampling rate is 100 Hz and sampling time is 121.1715 s.

Based on original data, we obtain Fig. 1 to observe the original gait signal of PD patients and control subjects. In fig. 1, we can see that compared with normal people, whose gait data is continuous and stable, while that of PD patient is discontinuous and irregular.

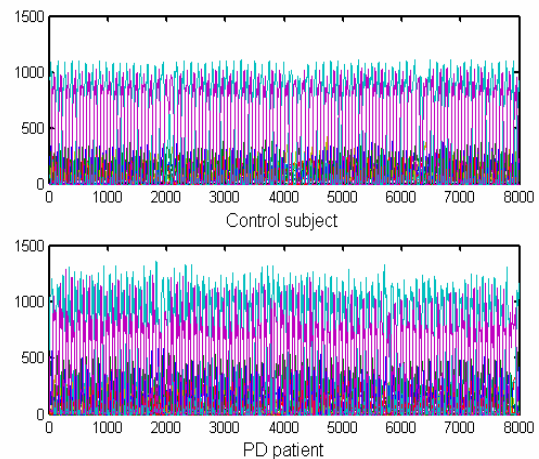


Fig. 1 In this figure we can see that compared with normal people, whose gait data is continuous and stable, while that of PD patient is discontinuous and irregular.

B. Haar wavelet packet transform

In 1910, Alfred Haar [6] pointed out that the following simple function can be transformed by translating and stretching.

$$\varphi(t) = \begin{cases} 1 & \text{if } 0 \leq t < 1/2 \\ -1 & \text{if } 1/2 \leq t < 1 \\ 0 & \text{else} \end{cases} \quad (1)$$

And the result of which is an orthonormal basis of $L^2(\mathbb{R})$.

$$\left\{ \varphi_{j,n}(t) = \frac{1}{\sqrt{2^j}} \varphi\left(\frac{t-2^j n}{2^j}\right) \right\}_{(j,n) \in \mathbb{Z}^2} \quad (2)$$

Arbitrary signal can be expanded based on the orthonormal basis and obtain the following equation.

$$f = \sum_{j=-\infty}^{+\infty} \sum_{n=-\infty}^{+\infty} \langle f, \varphi_{j,n} \rangle \varphi_{j,n} \quad (3)$$

The orthogonal set of Haar wavelets $h_i(t)$ is a group of square waves, which is shown in fig. 2.

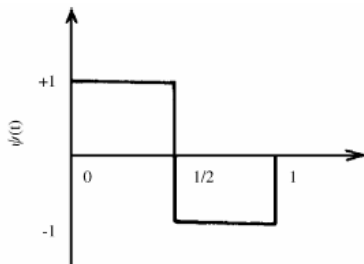


Fig. 2 Haar wavelet basis.

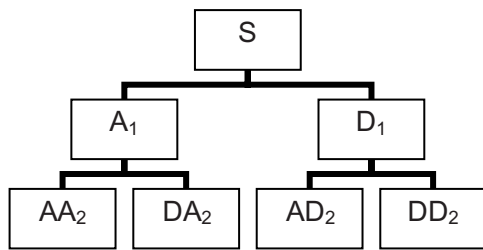


Fig. 3 Two-scale wavelet packet decomposition tree

The wavelet packet method [7, 8] is a generalization of wavelet decomposition that offers a richer signal analysis.

In the wavelet decomposition procedure, the first step is splitting the approximation coefficients into two parts. After splitting, a vector of approximation coefficients and a vector of detail coefficients are obtained. The information lost between two successive approximations is captured in the detail coefficients. The next step consists of splitting the new approximation coefficient vector; successive details are never reanalyzed. However, in wavelet packet situation, each detail coefficient vector is also decomposed into two parts using the same approach as in approximation vector splitting. Compared with wavelet decomposition, wavelet packet offers rich analysis: the complete binary tree is pro-

duced in the one-dimensional case [10]. The binary tree of two-scale wavelet packet decomposition we used is illustrated in Fig. 3.

The Haar wavelet transform yields differences of non-overlapping weighted averages of observations when used with a given one-dimensional time-series. This transform tends to emphasize discontinuities in the raw data set [9].

According to the two-scale wavelet packets decomposition tree in fig.3, while one signal of a sensor is decomposed on a two-scale, 4 coefficient sets.

C. The definition of entropy

Because of the existence of zero items in the data, we give our own definition of entropy, which could help extract feature from the result of wavelet packet transform.

$$E = \frac{\sum_{i=1}^n |x_i|}{n} \quad (4)$$

III. RESULTS

The entropy of different sensors was obtained after Haar wavelet packet decomposition. Table 1 shows a comparison of entropy between Control group and PD patient at level one D_1 . That is based on the vector of detail coefficients, which is the result of the first step in wavelet packet decomposition. Table 2 shows a comparison of entropy between Control group and PD patient at level two DD_2 . That is also based on a vector of detail coefficients DD_2 , which is the result of splitting the D_1 . So DD_2 is a vector of further detail coefficients based on first level vector of detail coefficient D_1 .

The value P, as the result of t-test, has a statistical significance and shows the results of that the entropy was compared using unpaired T-test. The entropy of PD patient and control subject were compared. And the two-tailed value P of some sensors is below 0.05, indicating statistical significance.

In table 1, the value P of Sensor L1, R1, L2, R2, L6 and R6 are below 0.05 and apparently lower than those of other sensors. In table 2, the value P of Sensor L1, R1, L6 and R6 are below 0.05 and lower than those of other sensors. All those values show obvious difference between PD patients and control group at different level of wavelet packet decomposition.

Table 1 Comparison of entropy between Control group and PD patient at level one D₁

	Normal	PD patient	Value P
Sensor L1	4.46 ± 1.49	3.61 ± 2.20	5.92×10 ⁻⁷
Sensor L2	3.36 ± 1.06	2.87 ± 0.86	1.27×10 ⁻⁴
Sensor L3	2.73 ± 1.18	2.53 ± 0.98	0.12
Sensor L4	2.69 ± 0.91	2.52 ± 1.10	0.18
Sensor L5	1.38 ± 1.09	1.46 ± 0.87	0.51
Sensor L6	3.20 ± 0.63	2.85 ± 0.71	6.25×10 ⁻⁴
Sensor L7	3.60 ± 0.77	3.53 ± 1.04	0.56
Sensor L8	2.27 ± 1.21	2.09 ± 1.19	0.20
Sensor R1	4.48 ± 1.43	3.70 ± 2.62	6.40×10 ⁻⁶
Sensor R2	3.19 ± 0.95	2.85 ± 0.80	4.56×10 ⁻³
Sensor R3	2.77 ± 1.20	2.57 ± 0.99	0.13
Sensor R4	2.76 ± 0.79	2.71 ± 1.01	0.64
Sensor R5	1.38 ± 0.78	1.45 ± 0.88	0.54
Sensor R6	3.13 ± 0.60	2.76 ± 0.52	1.82×10 ⁻⁴
Sensor R7	3.70 ± 0.92	3.61 ± 1.14	0.44
Sensor R8	2.34 ± 0.88	2.11 ± 0.60	5.07×10 ⁻²
Total L	14.5 ± 7.82	14.1 ± 7.53	0.24
Total R	14.6 ± 8.87	14.1 ± 6.24	0.15

Table 2 Comparison of entropy between Control group and PD patient at level two DD₂

	Normal	PD patient	Value P
Sensor L1	3.02 ± 0.89	2.36 ± 1.48	7.48×10 ⁻⁷
Sensor L2	1.52 ± 0.26	1.38 ± 0.39	5.65×10 ⁻²
Sensor L3	1.30 ± 0.42	1.25 ± 0.39	0.49
Sensor L4	1.07 ± 0.12	1.01 ± 0.16	0.14
Sensor L5	0.59 ± 0.10	0.66 ± 0.10	9.38×10 ⁻²
Sensor L6	1.28 ± 0.14	1.18 ± 0.12	2.16×10 ⁻²
Sensor L7	1.40 ± 0.17	1.47 ± 0.28	0.24
Sensor L8	1.37 ± 0.53	1.38 ± 0.60	0.37
Sensor R1	2.89 ± 0.82	2.44 ± 1.76	7.52×10 ⁻⁴
Sensor R2	1.47 ± 0.27	1.38 ± 0.34	0.18
Sensor R3	1.31 ± 0.38	1.27 ± 0.40	0.59
Sensor R4	1.15 ± 0.11	1.09 ± 0.13	0.17
Sensor R5	0.64 ± 0.07	0.68 ± 0.11	0.33
Sensor R6	1.28 ± 0.13	1.15 ± 0.12	5.76×10 ⁻³
Sensor R7	1.48 ± 0.21	1.47 ± 0.28	0.95
Sensor R8	1.36 ± 0.66	1.26 ± 0.25	0.27
Total L	6.54 ± 2.04	6.07 ± 3.48	1.86×10 ⁻²
Total R	6.35 ± 2.50	6.12 ± 3.15	0.26

IV. DISCUSSION

According to the coordinate of sensor, the position of sensor can be located in Fig. 4. We assume that the origin (0, 0) is just between the legs and the subject is facing towards the positive side of the Y axis [5].

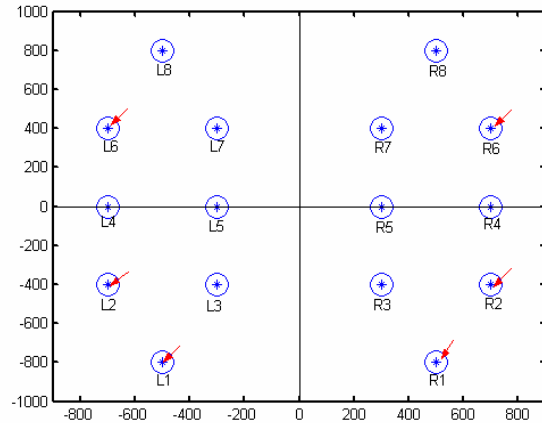


Fig. 4 Location of 16 sensors underneath each subject's feet. We assume that the origin (0, 0) is just between the legs and the subject is facing towards the positive side of the Y axis [5]. Blue spots represent those sensors. And the Sensor L1, R1, L2, R2, L6 and R6, which can be used to differentiate between PD patient and control subject in our study, are marked by red arrows.

In Fig. 4, the Sensor L1, R1, L2, R2, L6 and R6, which can be used to differentiate between PD patient and control subject in our study, are marked by red arrows. All those sensors were located on the lateral plantar side, which accords with the fact that lateral side underneath foot is main force side while walking. Thus, we can hypothesize that those sensors located on the lateral plantar side could reflect the gait feature of PD patient better. As to the Sensor L4 and R4, which are also located on the lateral side, however, they can not help distinguish between two groups. This raises question about the walking feature of PD patient and needs further study.

In this study, original plots of gait signal were observed and checked before processing. Data of 2 subjects were sorted out for the trends of which signal image are totally different from other with large gaps.

V. CONCLUSIONS

In wavelet packet situation, we can make full use of each detail coefficient vector offering the richest analysis. Our study proves that it is feasible to use Haar wavelet packet entropy to extract features from gait signal and distinguish the PD patient from the normal. And it is also a easy but reliable way for the reason that the result of our study shows obvious difference between PD patients and control group.

The sensors located on the lateral plantar side could reflect the feature of gait signal in PD patients better than others.

The study of the applications of wavelet is continuing to expand day by day. Our future work will include the application based on other wavelet bases which are computationally attractive.

ACKNOWLEDGMENT

The data are provided by the web site [5].

This work was supported by the clinical basic cooperation fund of Capital Medical University under Grant 2007JL25.

REFERENCES

1. Li L, Liu Q, Zhang J (2008) Application of Wavelets Transform in Biomedical Signals. *China Med Device Information* , Vol. 14, No. 8: 24-25
2. Castleman KR. *Digital image processing*. Englewood Cliffs: Prentice-Hall; 1996.
3. Moharir PS. *Pattern recognition transforms*. New York: Wiley; 1992.
4. Radomir S, Stankovi, Bogdan J, Falkowski (2003) The Haar wavelet transform: its status and achievements, *Computers and Electrical Engineering* 29: 25-44
5. www.physionet.org
6. Mallat S. (1999) *A Wavelet Tour of Signal Processing*, Second Edition, Academic Press. Translation by Lihua Yang et al , 2002, China Machine Press. P166-188.
7. J. Zarei, J. Poshtan (2007) Bearing fault detection using wavelet packet transform of induction motor stator current, *Tribol. Int.* 40: 763-769.
8. Z. Ge, W. Sha, *Wavelet Analysis Theory and MATLAB R2007 Implementations*, Publishing House of Electronics Industry, Beijing, 2007, pp. 115-126 (in Chinese).
9. Capilla C (2006) Application of the Haar wavelet transform to detect microseismic signal arrivals. *Journal of Applied Geophysics* 59: 36-46
10. Ekicia S, Yildirim S, Poyraz M (2008) Energy and entropy-based feature extraction for locating fault on transmission lines by using neural network and wavelet packet decomposition. *Expert Systems with Applications* 34: 2937-2944
11. Goldberger AL, Amaral LAN, Glass L, Hausdorff JM, Ivanov PCh, Mark RG, Mietus JE, Moody GB, Peng CK, Stanley HE. *PhysioBank, PhysioToolkit, and PhysioNet: Components of a New Research Resource for Complex Physiologic Signals*. *Circulation* 101(23):e215-e220

Medium-Cost Electronic Prosthetic Knee for Transfemoral Amputees: A Medical Solution for Developing Countries

R.R. Torrealba^{1,2}, L.A. Zambrano², E. Andara², G. Fernández-López¹, and J.C. Grieco¹

¹ Simón Bolívar University / Department of Electronics and Circuits, Group of Mechatronics Research, Caracas, Venezuela

² Simón Bolívar University / Department of Mechanics, Group of Biomechanics Research, Caracas, Venezuela

Abstract— There is a very high demand for prosthetic components in developing countries, but this is far to be satisfied because such devices are imported and hence, not affordable by most people with disabilities; however, at the same time, many of these countries have professionals and technology to develop the products they need. This work presents an approach carried out by the Mechatronics and Biomechanics Research Groups of Simón Bolívar University regarding the development of a medium-cost electronic prosthetic knee for transfemoral amputees. The paper describes both the design and manufacture of the prosthesis, as well as the control and instrumentation used by this. The knee prosthesis consists of a monocentric design composed by a chassis unit, a knee joint and a magneto-rheological actuator; in particular, the chassis was manufactured by using rapid prototyping technique and presents human-leg shape as external appearance; also, the chassis was reinforced with a metallic frame and carbon fiber laminated in resin to provide further support to the structure. On the other hand, the prosthesis instrumentation is based on accelerometers and a goniometer, while the control strategy applied is a finite-state approach. The control is based on characterization of gait cycle performed through an accelerometry-based detection algorithm, that allows to determine the gait cycle phase on the prosthesis and apply the corresponding control signal in accordance with the gain-scheduled controller. The prosthesis was proved by a transfemoral amputee walking at 2kph on a treadmill. The performance of the different modules of the control scheme was satisfactory, but the knee angle measured as result of the control applied was irregular. This result brought out the need of carrying out further work to determine the appropriate control to use on the prosthesis.

Keywords— Knee prosthesis, rapid prototyping, magneto-rheological actuator, gait events detection, finite-state control.

I. INTRODUCTION

There is huge need of prosthetic components for people with disabilities due to amputations in the world. According to the World Health Organization, only in low-income countries, the demand of prostheses is estimated to be of 30 millions by 2010 [1]. Prosthetic components are mainly produced by a few manufacturers in the world, whose

products usually result too expensive for people in developing countries. Most of these countries do not produce prosthetic components, even though many of them have the technological and human resources to develop and manufacture their own products. The Mechatronics and Biomechanics Research Groups of Simón Bolívar University in Venezuela have been working in that direction for several years, with the commitment of developing prosthetic components at affordable prices, to make these products available to people who needs them in the country [2-4]. However, we did not want to limit our proposal to rudimentary designs; on the contrary, we want to offer the best of these designs, but always having in mind to keep the cost to the final consumer as low as possible, in order to cover the major part of the demand of such components in the country.

Regarding prosthetic knees, we want to take advantage of a linear commercial magneto-rheological (MR) actuator, whose response is controlled electronically by modulating the current intensity that passes through its magnetic circuit. This allows to adapt the damping offered by the prosthesis at the knee joint along the gait cycle, taking into account the gait speed of the prosthesis user. Furthermore, this MR actuator results relatively inexpensive, which goes according to our purpose of developing affordable products to people in our country. The mechanical prototype of the prosthesis incorporates two features of interest, i. e. human leg shape and polymeric material chassis reinforced with a metallic structure. Also, unlike commercial prosthetic knees that use strain gauges as part of the instrumentation of the prosthesis to perform the characterization of gait cycle on which the control is based, we use accelerometers to perform this task [5]. These sensors result cheap and much easier to install than the strain gauges, though they require particular processing techniques to enable using acceleration signals to characterize the gait cycle. In addition, the prosthesis uses a goniometer to measure the knee angle during walking.

This work shows the development of the prosthetic knee, describing the design and manufacture of the mechanical prototype; then, it presents the control scheme proposed to control the knee during walking, and the first test results with the prosthesis being used by a transfemoral amputee.

II. METHODS

A. Design and manufacture of the prosthesis

The knee prosthesis presents a monocentric design composed of a chassis unit, a knee joint and an actuator. The prosthesis is designed to use standard commercial adaptors to be coupled with the socket and foot-ankle prosthesis that complete the transfemoral prosthesis.

- Chassis unit:

The chassis is an important part of the prosthesis, as it must accomplish three fundamental tasks: 1. To support the patient weight and floor reaction loads applied on the prosthesis during walking, 2. To link together all the pieces of the prosthesis mechanism, and 3. To provide the final appearance to the prosthesis. To satisfy all these requirements, a chassis unit with an anthropomorphic shape was designed, reinforced with a metallic frame that supplies the appropriate strength to the prosthesis and allows to assemble all its parts into a mechanism.

The external surface of the chassis is based on a human shank to provide the prosthesis with a natural and aesthetics form; thus, the chassis results an anthropomorphic case that enables the patient to use the knee prosthesis without wearing any cosmetic cover. The prosthetic knee is intended to be used indistinctively for both right and left sides, so using a CAD software (Solidworks®), the shank features are distributed symmetrically around the chassis axis and the final lower leg form is then achieved as shown in Fig. 1.

Regarding the manufacture, the irregular shape of the shank was very difficult to achieve by means of a conventional machining process, and using some typical metallic material found in the country would increase the prosthesis weight, not to mention the tremendous increase of the manufacturing time in case of making this option. As a solution to overcome this situation, polymers, and more specifically, ABS has proved to have good mechanical properties and a CNC manufacturing process not only faster than conventional machining, but also more precise when creating irregular shapes.

The CAD model was 3D-printed in a rapid prototype machine, resulting a final product ready to use; however, due to the fact that rapid prototyping produces a structure composed of layers, it was considered necessary to reinforce it by means of a metallic frame to share the applied loads. It consists of an aluminum platens arrangement that perfectly fits the internal surface of the ABS cover (see Fig. 1); this material helps to support the loads while keeping low the overall prosthesis weight. Finally, the chassis unit was also coated with carbon fiber laminated in resin,

which not only avoids the ABS to dismember, but also augments the overall mechanical properties of the unit.

- Knee joint:

As seen in Fig. 1, the knee joint consists of an articular base and two axes; the frontal axis is the articular axis that connects the base to the chassis unit, while the posterior axis is the axis that connects the base to the upper end of the actuator. Finally, the mechanism of the prosthesis is closed by the distal axis that joins the lower end of the actuator with the chassis unit, but this is not part of the knee joint.

- Actuator:

The actuator is a commercial MR axial actuator that uses a magneto-rheological fluid that varies the knee resistance by means of magnetic fields. More in detail, this MR fluid allow to modulate its viscosity according to the current intensity that passes through the electromagnetic circuit of the actuator and hence, to modulate the prosthesis response along the gait cycle.

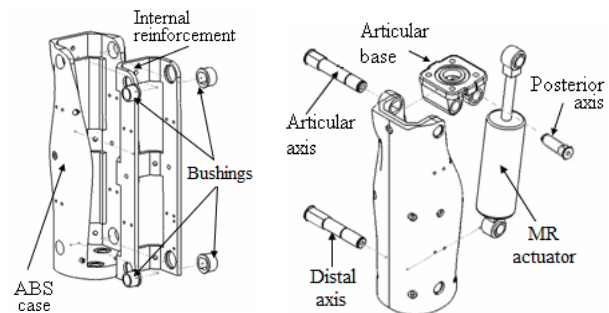


Fig. 1 Knee prosthesis assembly: ABS case and metallic structure of the chassis (left) and mechanism of the knee joint (right)

B. Control and instrumentation of the prosthesis

As a first approach to control the prosthesis, a finite-state scheme have been proposed, which is the typical control architecture used by commercial intelligent prosthesis today [6-9]. This scheme divides the gait cycle in states and determines in which pre-defined state the user is during walking, in order to apply the corresponding control action on the prosthesis actuator. The present state along the gait cycle is determined by the characterization performed from the signals captured through the sensors of the prosthesis; in this case, we have developed an accelerometry-based detection algorithm (ADA) that allows to know the gait cycle phase on the prosthesis [5]. This algorithm uses two bi-axial accelerometers placed at the knee and ankle heights of the prosthetic leg in the sagittal plane, plus a goniometer located directly on the knee axis to measure the knee angle.

Regarding the control scheme, it is shown in Fig. 2. The accelerometers and goniometer signals captured through the DAQ/SC Module goes to a Gait Event Detector (GED), which detects several events spread throughout the gait cycle length applying the ADA. The Gait Cycle Phase Generator (GCPG) receives the events detected and the gait cycle frequency ω_{GC} calculated by the Gait Frequency Estimator (GFE). This GFE estimates the ω_{GC} from the gait cycle periods T_i determined from each of the events detected and finally, the GCPG generates the gait cycle phase ϕ_{GC} that enters into the Gain-Scheduled Controller (GSC). This controller sets a particular gain depending of the actual finite state of gait cycle on the prosthesis; in this case, the GSC output is directly the damping level to be applied by the MR actuator on the prosthesis, in order to enable the user to walk.

A dynamic user interphase was developed in LabVIEW, to manually adjust the damping level of each state, as well as the length of these in terms of percentages of gait cycle; particularly, the GSC applied at the knee divided the gait cycle in five states as follows: the first state goes from 0 to 15% of gait cycle and applies a high damping level to avoid the knee collapse during the load response; the second state reduces the damping from the previous high value to a minimum, going from 15 to 25% of gait cycle; the third state keeps the last value applied from 25 to 65% of gait cycle, in order to offer a minimum support during the mid-stance and allow the knee flexion during the pre-swing; the fourth state goes from 65 to 75% of gait cycle and applies a bell-curve damping to hold the knee flexed during the midswing to guarantee foot clearance on this stage; the fifth state goes from 75 to 100% of gait cycle and returns the knee damping level to its minimum to allow the knee extension during the terminal swing.

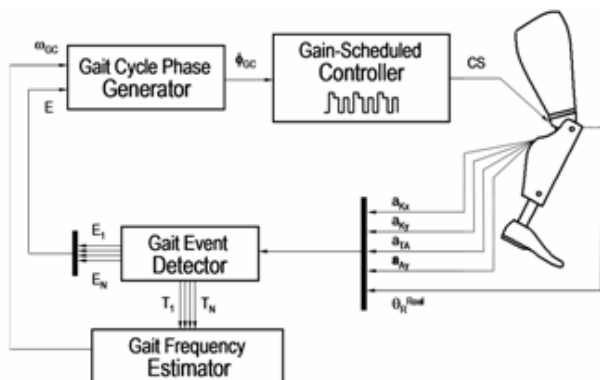


Fig. 2 Control scheme of the prosthetic knee

III. RESULTS

The resulting end-product is a resistant mechanism easy to assemble. As can be seen in Fig. 3, the external shape gives the patient leg a more natural appearance, and the carbon fiber coating not only improves the mechanical strength, but also provides a delicate external surface. From preliminary tests, no interferences were found between the actuator and the chassis, and flexion and extension movements were achieved within the expected range: 0-90°. No extra effort than the usual was required from the patient to make these movements.



Fig. 3 Knee prosthesis mechanism without carbon fiber coating (left) and final knee prosthesis adapted to a user (right)

Most materials employed in the construction of the prototype came from our domestic market; however, the ABS and the carbon fiber were imported, though given the chassis shape, a low amount of these materials was required. As an approximation, the overall cost of the prosthesis is about 5.000US\$, that compared to the cost of a conventional hydraulic knee in our country (whose price is about the same) is very competitive, not to mention that the technology offered by this prosthesis is comparable to the most recent and advanced knee prosthesis designs.

The results of the trials with the prosthesis used by a transfemoral amputee walking at 2kph on a treadmill are shown in Fig. 4. The first plot shows the ADA performance detecting a gait event on one of the accelerations captured at the ankle height on the prosthesis; the second plot shows the gait cycle phase ϕ_{GC} determined by the GCPG, according to the events detected by the ADA; the third plot shows the output of the GSC modulated during walking, in accordance to the gait cycle phase plotted before; the fourth plot presents the knee angle measured on the prosthesis axis, as result of the damping applied by the MR actuator and the loads due to floor reaction and user weight during walking.

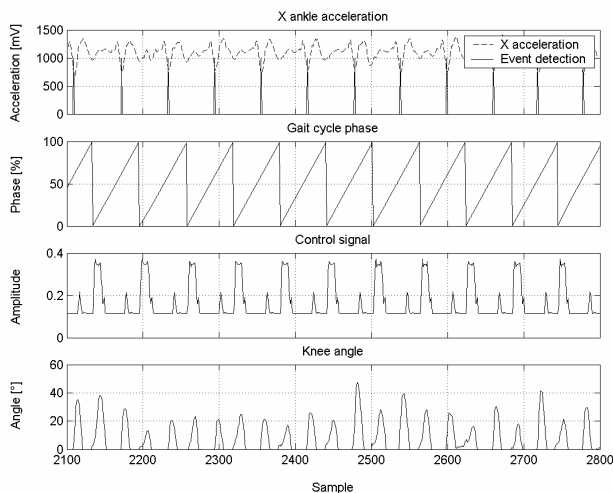


Fig. 4 Results of the trials with the prosthesis used by a transfemoral amputee at 2kph on a treadmill

From Fig. 4, it is observed that the ϕ_{GC} is perfectly coupled with the events detected by the ADA and as a consequence, the control action is similarly synchronized with the gait cycle; however, the knee angle on the prosthesis is quite unstable. During the trials, the walking subject tried to achieve the natural flexion of the knee on each of the gait cycle phases: the flexion corresponding to load response during the stance phase and the flexion corresponding to the pre-swing and swing phase. The stance flexion varies its amplitude widely between gait cycles, due to variations of the load applied by the user during walking and therefore, difficulties to find the adequate damping level to obtain a constant behaviour; the swing flexion occurs rather between the pre-swing and initial swing, due to the MR actuator response that takes the knee to extension immediately after toe-off. The latter makes senseless the damping applied during midswing, as the knee has practically recovered its extension by this moment.

IV. CONCLUSIONS

This work allowed the authors to develop a methodology for the design and manufacture of an electronic prosthetic knee that offers mechanical strength, anthropomorphic shape and easy assembly. The prosthesis was completely built with materials found in the country, though some of them were imported. Likewise, given the manufacture process, it was possible to create a good-quality device at a relatively medium-cost that is competitive in the domestic market.

The characterization of gait cycle from accelerometers data has proved to be robust against perturbations of the prosthesis behavior. Given the gain-scheduled controller applied on the prosthesis, its performance resulted irregular during walking, concluding that it is required further work to determine the appropriate control to use on the prosthesis. The latter task might be divided in two stages: first, to study the convenience of using a finite state control scheme for controlling a prosthetic knee equipped with a linear magneto-rheological actuator as shown in this paper; second, to consider other control schemes different to the finite state strategy to control the knee prosthesis in order to obtain a regular performance.

Herein, it is shown that despite of being a developing country, we count on multidisciplinary professionals in Venezuela, whose knowledge makes possible to develop sophisticated, competitive and high-technology prostheses, able to help lower-limb amputees to perform a more natural gait and thus, improve their quality of life.

REFERENCES

1. Pearlman J, Cooper R, Krizack M et al. (2008) Lower-Limb Prostheses and Wheelchairs in Low-Income Countries: An Overview. *IEEE Engineering in Medicine and Biology* 27(2):12–22
2. Lanza U, Müller-Karger C, Graciano C. (2006) High-tech or solving the needs in developing countries. *Journal of Biomechanics* 39:S524
3. Torrealba R, Müller-Karger C (2007) Proposal of Design, Analysis and Construction of Adaptors for Transtibial Prosthesis, IFMBE Proc. IV Latin American Congress on Biomed. Eng. CLAIB'2007, Margarita Island, Venezuela, 2007, pp 783–787
4. Torrealba R, Fernández-López G, Grieco J (2008) Towards the development of knee prostheses: Review of current researches. *Kybernetes* 37(9/10):1561–1576
5. Torrealba R, Castellano J, Fernández-López G, Grieco J (2007) Characterisation of Gait Cycle from Accelerometer Data. *Electronics Letter* 43(20):1066–1068
6. Bar A, Ishai G, Meretsky P et al. (1983) Adaptive microcomputer control of an artificial knee in level walking. *Journal of Biomedical Engineering* 5:145–150
7. Aeyels B, Peeraer L, Sloten J et al. (1992) Development of an above-knee prosthesis equipped with a microcomputer-controlled knee joint: first test results. *Journal of Biomedical Engineering* 14:199–202
8. Herr H, Wilkenfeld A (2003) User-adaptive control of a magneto-rheological prosthetic knee. *Industrial Robot: An International Journal* 30(1):42–55

Corresponding author:

Author: Lilibeth Zambrano
 Institute: Simón Bolívar University
 Street: MEU Building
 City: Caracas
 Country: Venezuela
 Email: lazambrano@usb.ve

Human Gait Data Mining by Symbol Based Descriptive Features

V. Ergovic¹, S. Tonkovic², and V. Medved³

¹ IBM Croatia / Software Group, Zagreb, Croatia

² Faculty of Electrical Engineering and Computing / ZESOI, Zagreb, Croatia

³ Faculty of Kinesiology / Biomechanics, Zagreb, Croatia

Abstract— Most medical applications which include large dataset require search by example capability. Such similarity-based retrieval has attracted a great deal of attention in recent years. Although several different approaches have appeared, most are not specialized for problems of time series signals, typically found in gait analysis or ECG. This paper proposes an approach for efficient processing of human gait by using symbolization of different features by means of feature description. We evaluated this approach against database that holds limited set of kinematics, kinetic and EMG data, describing simple step (a subset of standard gait variables). The measurement was performed in the Biomechanics Laboratory at the Faculty of Kinesiology, University of Zagreb, using 2002-ELITE system with Kistler platform (40 cm by 60 cm).

Keywords— descriptive features, data mining, gait analysis.

I. INTRODUCTION

Gait analysis and diagnosis are mostly based on limited observations and measurements from parts of the complicated movement system. Inexperienced therapist often does not have a clear understanding of the integrated movement system and, therefore, cannot properly set diagnosis. The learning process takes significant amount of time; it is based on facts and rules. This leads to generation of statements and provides an input which can be used by an expert system. Based on our observation of typical process and deductions performed by the therapist we propose novel approach for times series data mining which imitates therapist approach. We propose a human readable text description of signal just as one used by the therapist. We then map this description to symbols. Each signal is expressed by symbolic word where symbols are alphabetically ordered. This approach greatly improves search across large databases, dimension reduction and interpretation of the results.

A. Background work

Humans have vast amount of cultural and domain knowledge and experience to draw upon, as well as a remarkable ability to recognize similar situation when

making decision about new information, while machine learning methods can only generalize based on the data that has already been seen and even than is in a limited manner. Many machine-learning algorithms rely heavily on mathematics and statistics. There are many different machine-learning algorithms all with different strengths and weaknesses and they are suited to different types of problems. Some, such as decision trees, are so easy to interpret and are among the most widely used methods in medical decision-making. Others, such as neural networks are of a black box type. They produce an answer but it is very difficult to reproduce and understand reasoning behind the mechanism [1]. Decision trees and rule based reasoning are typically used in medical signal analysis especially in ECG analysis [2]. However, in domain of gait analysis there are only few papers which have similar approach. Table 1 shows an excerpt from Winter's table, originally titled Elaborated Strategy of the Clinical Application of Gait Analysis [3].

Table 1 Gait Diagnostic Chart [3]

Observed Abnormality	Possible Causes	Diagnostic Evidence
Foot slap at heel contact approximation	Below normal dorsiflexor activity at heel contact	Below normal tibialis anterior EMG or dorsiflexor moment at heel contact
Forefoot or flatfoot initial contact	(a) Hyperactive plantar-flexor activity in late swing (b) Structural limitation in ankle range (c) Short step-length	(a) above normal plantar-flexor EMG in late swing (b) decreased dorsiflexion range of motion (c) See a,b,c,d below
Short step-length	(a) weak hip push-off prior swing (b) weak hip flexors at toe off and early swing (c) excessive deceleration of leg in late swing (d) Above normal contralateral hip extensor activity during contralateral stance	(a) Below normal plantar-flexor moment or power generation or EMG during push-off (b) Below normal hip flexor moment or power generation or EMG during late push-off and early swing (c) Above normal hamstring EMG or knee flexor moment or power absorption late in swing (d)Hyperactivity in EMG of contralateral hip extensors

Selected statements can be easily stored in a database and used for comparison with other gait signals by leveraging text mining. Text mining, roughly equivalent to text analytics, refers generally to the process of deriving high-quality information from text. High-quality information is typically derived through the dividing of patterns and trends through the means such as statistical pattern learning. Text mining usually involves the process of structuring the input text, deriving patterns within the structured data, and finally evaluation and interpretation of the output [1]. In order to leverage text mining, time series signals are converted to text and stored in database table(s). Basically, input time series datasets are described by words like in a table. However, the area of gait analysis is not so well researched and structured as for example ECG. It is more complex and it can hold much more data (default setup of our system gives over 20 different variables which hold time series data – kinetics and kinematics). Figure 1 shows abnormal pelvic obliquity and tilt. We can apply descriptive approach on the signal level and describe signals with statements (right pelvic obliquity curve is shifted down; left pelvic obliquity curve is shifted up, pelvic tilt curve is shifted down; pelvic tilt has large extreme values; pelvic obliquity degrees are completely out of normal ranges and completely shifted up, multiple deviations on the curves, phase shift, etc.). Those statements, together with selected statements from table can be stored in database for purpose of text mining or construction of decision trees.

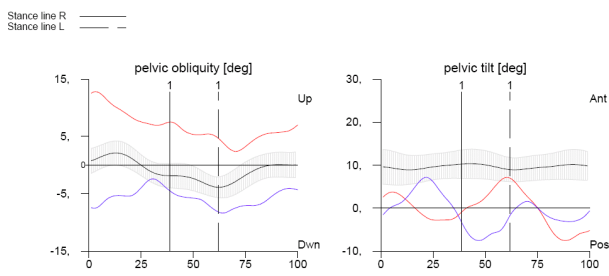


Fig. 1 Normal range and discords - pelvic

For subjects who have walking problems, it would be expected that parts of some of the graphs would be outside the expected range. A skilled clinician requires a considerable amount of time to analyze this data. In addition to this, simply browsing through all possible graphs for a single trial is time consuming [4, 5].

B. Symbolization

Symbolization is the method of representing time series dataset as a set of symbols in the form of one or more symbolic words which brings significant dimension

reduction. The most popular symbolic algorithm in the field of research in recent years is SAX which is an extension to PAA (Piecewise Aggregate Approximation). Real valued time series converted to the SAX word baabccbc [6] are shown with Figure 2. All three possible symbols are approximately equally frequent.

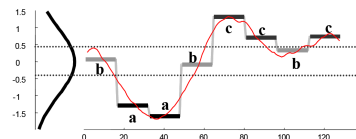


Fig. 2 Time series signal converted to symbolic word [6]

In PAA, each sequence of time series data is divided into k segments with equal length and the average value of each segment is used as a coordinate of a k-dimensional feature vector. PAA is fast and simple for implementation and provides linear time indexing. SAX uses an intermediate representation between the raw time series and the symbolic strings because the first step is transformation of the data into PAA representation. Second step is to symbolize the PAA representation into a discrete string. Time series is discretized by first obtaining a PAA and then, using predetermined breakpoints, PAA coefficients are mapped into SAX symbols. SAX uses MINDIST function that returns the minimum distance between the original time series of two words like shown with formula 1.

$$MINDIST(\hat{Q}, \hat{C}) \equiv \sqrt{\frac{n}{w}} \sqrt{\sum_{i=1}^w (dist(\hat{q}_i, \hat{c}_i))^2} \quad (1)$$

Where n is the length of the string to be reduced to a string of arbitrary length w, (w < n, typically w << n). The alphabet size is also an arbitrary integer a, where a > 2. Q and C are words for distance calculation and q_i and c_i are individual symbols in the words. This function is used to calculate distance between two symbolic words and it is used for classification purposes. Typically this function is implemented via lookup table.

In processing human gait it is very common to process very long time series. Disadvantages of PAA and SAX include inability to deal with significant phase shifts and predetermined alphabet without the possibility for runtime extension. A distance function brings computational overhead during queries when larger alphabet is used. Although there are few initiatives that are dealing with these problems they can not avoid some limitations such as strict order of symbols in the word, compression limitations, and problem with runtime alphabet extension [8, 9].

II. SYMBOL BASED DESCRIPTIVE FEATURE APPROACH

A. Proposed approaches

Our approach introduces a concept of descriptive feature of time series data set such as a signal.

Definition. Descriptive feature is text representation of observed facts stated in human readable and understandable format.

Our approach does not include text mining method which would normally calculate word statistics and relevance in statement. Each descriptive feature can be mapped to a symbol. Symbol does not represent any segment in the curve like SAX does and therefore position in a word is irrelevant (it can be sorted alphabetically). This feature provides fast retrieval by exact match, almost as a hash function and enables additional extensions to the alphabet during the runtime without additional computation costs. Each description can be placed in separate table to provide mapping between symbols which are represented by primary key in description table to descriptive feature. This helps to improve search and classification across complex time series dataset such as human gait variables. The disadvantage is a descriptive feature is that is based on heuristics. Therefore someone should identify and describe the feature before it is stored in repository.

B. Comparison with previous work

Figure 3 represents logical model of the data warehouse with hierarchical lookup tables (summary tables). In this model query is first performed on the first level of the lookup hierarchy table and then based on the similarity, queries are performed on the sub levels until sufficient similarity has been reached or query has not returned a result at all (not found). In ETL (Extract Transform and Load) stage each signal is summarized at a different level of SAX granularity. SAX word generation is performed more than ones with different alphabet size and different word lengths. This idea of hierarchy has been taken from Hierarchical clustering algorithm. Drawback of this solution is a number of queries that have to be performed before results are obtained and for each fact table additional lookup table is required [9]. SAX is also heavily dependant on the alphabet size, word length, segmentation of the input signal, and additional computation during queries when larger alphabet and larger words are used.

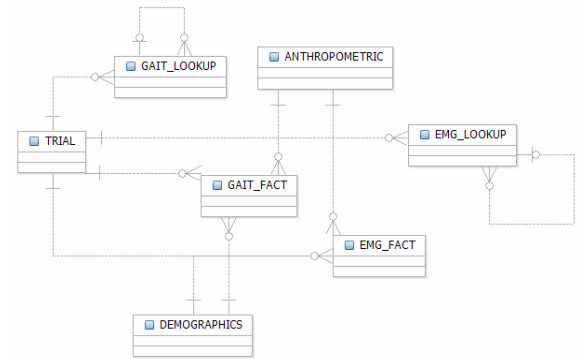


Fig. 3 Logical warehouse model for gait analysis with lookup tables [9]

C. Improvement of the model

Descriptive feature approach requires a table with description (code table which maps symbols to statements). This also enables easier signal interpretation and human understandable query construction. Modified lookup tables point to correct trial which is shown with the Figure 4.

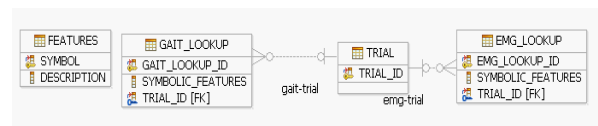


Fig. 4 Feature based lookup tables

In each row of the lookup table symbolic features are inserted as one word, with symbols sorted in ascending order (e.g. abfhlxz). We enforce ordering since position of our symbols is irrelevant. If we look into this model even more we will notice that EMG and gait are only some features of the trial. With that approach we can reduce this model even more by eliminating gait and lookup table, merging them together as shown with Figure 5.

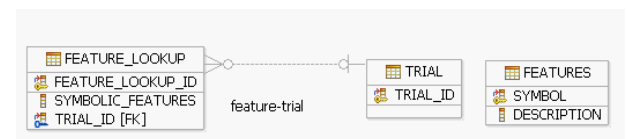


Fig. 5 Final model

Elimination of lookup table increases alphabet, there are more feature descriptions and it is appropriate for alphabets under 200 symbols, not recommended for larger alphabets.

III. RESULTS

We have worked with ground reaction force components (X,Y,Z), sensor marker readings (knee extension and rotation) and EMG. Created dataset tends to be very large. In our case average reading included 10 different parameters sampled at 10 ms for 20 seconds period of movement that produced more than 20000 samples for one movement pattern including five to six steps. Presented results are referring to GAIT_FACT table. Gait fact table was loaded with 7.201.050 rows, each row had 10 columns. Fourier approximation used 44 elements to approximate the signal (22 for magnitude and 22 for phase) as stated by formula 2.

$$f(t) = a_0 + a_1 \cos(w_0 + \varphi_1) + \dots + a_n \cos(nw_0 + \varphi_n) \quad (2)$$

Based on previous work, lengths of symbolic words were set to 4 and 9, with alphabet size of 3 and 6. Each signal was aggregated in 8 words. Average dimensional reduction was 384.61, but reduction in number of rows was 10000 times as summarized in Table 2. Gait fact table populated with 7.201.050 rows was described with less than 720 rows (the worst case scenario - 360 on the level one of the hierarchy and 360 on the level two). Since original data is contained in GAIT_FACT table there were no limitations on the use of additional algorithms after lookups were considered [9]. Similar results were with EMG. We used 10 selected statements regarding our dataset.

Table 2 Dimension reduction and data base rows

Method	Average reduction	Number of rows
Fourier approximation	476.16	171352
SAX hierarchy (2 level)	384.61	360-720
Descriptive features	1996	359

IV. CONCLUSIONS

Like any other approach in expert system diagnostics, this approach should be considered just to offer recommendations and possible indications about the problem. We have identified two major benefits of our approach. In the segment of dimension reduction, descriptive features can be stored in database alone, however in that case we original data are lost and additional algorithms such as clustering support vector machines or regression can not be utilized since original data is lost. The other segment that is affected is the speed of the retrieval during searches performed on the database – in that case our

descriptions are stored in lookup tables to enable fast retrieval. Usage of additional algorithms for drilling down specific subset in that case is supported. Since expert systems in biomechanics tend to contain huge amount of time series data, structural approach and aggregation mechanism are needed. Further research should be oriented towards evaluation of data mining chaining possibilities and domain specific ontologies which should describe diagnostic process and standardize vocabulary which describes signals on description level.

ACKNOWLEDGMENT

The results presented are the product of scientific projects „Noninvasive measurements and procedures in bio-medicine“, „Automated motion capture and expert evaluation in the study of locomotion“ and „Real-life data measurement and characterization“, realized with the support by The Ministry of Science, Education and Sports, Republic of Croatia.

REFERENCES

1. Segaran T, (2007) Programming Collective Intelligence. O'Reilly, Sebastopol, 2007, US
 2. Yanowitz F, ECG Conduction Abnormalities at http://library.med.utah.edu/kw/ecg/ecg_outline/Lesson6/index.html
 3. Winter D (1991), Gangbildanalyse-Stand der Messtechnik und Bedeutung für die Orthopädie-Technik. Duderstadt: Mecke Druck, pp 266-277
 4. The Robert Gordon University (School of Computing) at <http://www.comp.rgu.ac.uk/docs/info/project/ce-humangait-rn.htm>
 5. Noble R.A, White R (2005), Visualisation of gait analysis data, Information Visualization, Proceedings 9th International Conference on Information Visualization, London, UK, 2005 pp 247 - 252
 6. Keogh E, Lonardi S, Ratanamahatana C (2004) Towards Parameter-Free Data Mining, 10th ACM SIGKDD International Conference on Knowledge Discovery and Data Mining, Seattle, US, 2004, pp 206-215
 7. Korn F, Jagadish H, Faloutsos C (1997) Efficiently supporting ad hoc queries in large datasets of time sequences, In Proceedings of SIGMOD, pp 289-300
 8. Ergovic V (2008) Multi Stage Symbolic-Based Shape Indexing and Retrieval, In proceedings of ELMAR 2008, Zadar, Croatia, 2008, pp 87-90
 9. Medved V, Ergovic V, Tonkovic S (2008), Towards a High Performance Expert System for Gait Analysis, IFMBE Proceedings of 4th European Congress for Medical and Biological Engineering 2008, Antwerp, Belgium, 2008, pp 2105-2108
- Author: Vladimir Ergovic
 - Institute: IBM
 - Street: Miramarska 23
 - City: Zagreb
 - Country: Croatia
 - Email: vladimir.ergovic@hr.ibm.com

Novel Control for Ambulation Function Restoration in a Non-invasive Functional Electrical Stimulation System

J.-C. Hsieh¹, C.-C. Chen¹, S.-C. Chen², Y.-L. Chen^{3,*}, Y.-C. Li⁴, Y.-Y. Shih⁴, and T.-S. Kuo⁵

¹Department of Information Management, Hwa-Hsia Institute of Technology

²Department of Rehabilitation Medicine, Taipei Medical University

³Department of Computer Science, National Taipei University of Education (*correspondence)

⁴Department of Rehabilitation Medicine, Chang Gung Memorial Hospital

⁵Department of Rehabilitation Medicine, Chang Gung Memorial Hospital

Abstract -In this study, a patient-driven loop control in a non-invasive functional electrical stimulation (FES) system was designed to restore ambulation function of stroke patients with their residual capabilities.

Keywords -patient-driven loop control, hemiplegic, functional electrical stimulation, electromyographics, ambulation function restoration.

I. INTRODUCTION

Functional electrical stimulation (FES) has been applied to provide control of movements or functions by generating electrical stimuli to nerves or muscles, and it is also helpful to restore lost functions of patients with hemiplegia or quadriplegia. Many researchers have dedicated their efforts to control methods of FES to restore ambulation functions. However, input sources or controller commands of FES remain complicated and inconvenient for patients to use. Because of the initial unfamiliarity with the system, patients certainly need an acceptable and effective control strategy. In addition, after long-term electrical stimuli of the paralyzed extremities, problems of muscle fatigue and force decrement may occur and thereby hinder patients' efforts. If input sources or controller commands combine with an appropriate approach, it will be very helpful for patients to manipulate the assistive devices [1-5].

Owing to the problems described above, the patient-driven loop control was designed for a non-invasive FES system to restore ambulation functions of hemiplegics in this study. The EMG signals from residual muscles still under voluntary control were utilized as triggers and adjustments of the FES system during electrical stimuli. From the aspects of rehabilitation and psychology, patients can benefit from this control strategy because they use their residual capabilities to control the system.

II. MATERIALS AND METHODS

PATIENT-DRIVEN LOOP CONTROL

For coordinating artificial and voluntary control capabilities in a FES system, one possible way is to adjust the stimulus parameters by

the residual capacities of patients. The user can drive the commands to have good posture control of the ambulation and to adjust his contracting force. For example, he changes the control variables so that his lower extremity is closing to contact the ground; and further, he may increase the dorsi-flexion and plantar-flexion to secure the heel stride more firmly by the command controller. The aforementioned is the concept of patient-driven loop control because electrical stimuli are adjusted by the voluntary movements or residual capacities of patients. By this approach, patients are able to influence or even control the stimulation of their paralyzed extremities. Figure 1 shows the block diagram of patient-driven loop control. It can be used as an on/off switch control and serve as a proportional control to the FES system.

Dorsi-flexion and plantar-flexion were chosen in the experiment. The selected muscles (tibialis anterior and gastrocnemius) were utilized to design the motion-oriented modules, which described different states when generating plantar movements including the neural position of the plantar, dorsi-flexion and plantar-flexion, as illustrated in Figure 2(a) and Figure 2(b). The stimulation templates of plantar movements were obtained from the motion-oriented modules in order to find the most suitable stimulus parameters of different plantar movements with minimal computation. The methods to establish the stimulation templates were presented elsewhere [1-5].

EXPERIMENTAL EVALUATION

A non-invasive FES system

Figure 3 illustrates the block diagram of control concepts in this study. A non-invasive FES system [1][2] was employed to validate the patient-driven loop control strategy. This system with a digital signal processor as its kernel showed greater versatility and computing capability. It provided four-channel stimulation with arbitrary currents and biphasic waveforms to excite the paralyzed muscles. Figure 4 depicts an example of electrical stimulation sequences in the FES system. The stimulation sequences were initiated by the digital I/O components in the electrical stimulator. In addition, patients could switch to different states of plantar movements by controlling the channel change point to initiate a new stimulating channel.

The analog-to-digital converters (ADCs) were mounted in the electrical stimulator for recording the bio-signals from the subjects. Residual EMG signals were used to control the stimuli to excite the paralyzed muscles and to trigger the electrical stimulation sequences via four-channel EMG recording amplifiers and ADCs in the electrical stimulator, which had the potential to modify stimulus parameters for avoiding the problems of muscle fatigue or force decrement during long-term electrical stimuli. Furthermore, the FES system's interfaces were written by LabVIEW 7.1 (National Instrument Inc.) [1][2].

A case Report

One patient (male, 41 years old, right-sided hemiplegia) was recruited and gave his formal consent in this study. The patient is at level 2 of Functional Ambulation Category (FAC), and he needs intermittent support from one person to help him with balance or coordination all the time. All levels of FAC are shown in Table 1. The patient had been treated with this new closed-loop FES system for 15 minutes per day, every other day, for a period of 12 weeks. The dynamic EMG and FAC of the patient were both recorded at the end of each training every 3 weeks. After the gait training program (12 weeks training), the patient received a gait motion analysis via a VICON system (Oxford Metrics Limited Company). The VICON system containing six-camera was used to record translational and angular kinematics of the lower segments of disabled limb in the sagittal, frontal, and horizontal planes.

The hemiplegic caused by cerebral hemispheric stroke resulting from infarct or hemorrhage had sufficient cognition to give informed consent to participate in the study and to perform the tasks required in the experiment. The hemiplegic subject without any functional dorsi-flexion and plantar-flexion movement were also noted. The nature of the experimental procedures was explained to him, and he agreed to participate in the study.

Electrode configurations and task evaluations

After skin preparation of the lower extremity, a pen-shaped electrode with the adequate stimulus parameters (20 Hz and biphasic asymmetric current pulses) was used to detect best electrode site to generate plantar movements of main muscle groups. When finding adequate movements, significant marks were added to the areas which the pen-shaped electrode was on. In addition, to avoid the crosstalk effects caused by electrical currents when different stimulation sites were excited simultaneously, the spillover currents should also be recorded. Current given by the stimulator were less than 40mA with 20Hz frequency and 300 μ s pulse-width. These stimulation parameters were used to build the stimulation templates, which were the basis elements in the motion-oriented modules as mentioned in the previous paragraph.

The input sources of patient-driven loop control in this experiment were surface EMG signals from tibialis anterior and gastrocnemius muscles. Recording electrodes were positioned on

the lateral side of lower extremity and arranged perpendicularly to the muscle fibers and firmly fixed with adhesive tapes [2]. Before EMG measurements, the skin sites were abraded and cleaned with alcohol. The EMG signals were amplified and band-pass filtered (10–10k Hz) through the recording device connecting with the FES system for control purposes. The stimulating electrodes were applied on the pre-marked site that selected by the method mentioned in the previous paragraph. The command controller of FES system was triggered and adjusted by EMG signals, and it generated appropriate stimuli via the stimulating electrodes to excite the targeted muscles for motor outcomes.

III. RESULTS

The subject could use one set of their myoelectric signals detected by the surface electrodes to control electrical stimulation sequences successfully. The sequences combined with the motion-oriented modules were triggered by EMG signals to initiate stimulation for motor outcomes, as illustrated in Figure 5. It is revealed that the mean velocity, cadence, stride length, active ankle motion range, and functional ambulation category (FAC) have improved significantly from 0.22 ± 0.17 m/sec, 37.3 ± 15.5 steps/min, 0.32 ± 0.11 m, 10° , level 2 to 0.46 ± 0.23 m/sec, 58.2 ± 19.1 steps/min, 0.73 ± 0.22 m, 35° , level 4 respectively for the patient. A paired t-test indicated that differences in the electromyography (EMG) of the tibialis anterior and the gastrocnemius muscles between patient's disabled (affected-side) foot and normal (unaffected-side) foot are not significant ($p>0.05$) after 12 weeks of training, as showed in Table II.

IV. DISCUSSION AND CONCLUSION

The non-invasive FES system with the strategy of patient-driven loop control was manipulated by subject's residual capabilities to produce appropriate electrical stimuli for ambulation function restoration in this study. We chose the most common and acceptable signals as the input sources, the residual EMG signals, for our system control in the experiment. Several similar studies also utilize the EMG signal as the control source for the FES system [5]. If we tried to maximize the efficiency of EMG controlled system, one must find the properties of EMG signals which may change during different states of the muscle. However, traditional myoelectric-controlled FES systems failed to do that [6]. In this study, the FES system with patient-driven loop control to restore motor functions of the ambulation. Moreover, all subjects could modify the stimulation currents by discriminating the scales of EMG signals they generated as the control sources.

In this study, hemiplegic patient used his residual capabilities to restore ambulation functions (such as dorsi-flexion and

plantar-flexion) by the strategy of patient-driven loop control using a non-invasive FES system. In the experimental results, subject voluntarily controlled and adjusted the plantar positions by himself with the motion-oriented modules. Subject restored ambulation functions by different motion-oriented modules with the strategy of patient-driven loop control in a more natural way because he used his retained voluntary control capabilities.

ACKNOWLEDGEMENTS

This work is supported by the National Science Council, ROC, under Grants 97-2221-E-152-001-MY3.

REFERENCES

1. Wu HC, Young ST, Kuo TS. A versatile multichannel direct-synthesized electrical stimulator for FES applications. *IEEE Transactions on Instrumentation and Measurement* 2002;51:2-9.
2. Chiou YH, Luh JJ, Chen SC, Lai JS, Kuo TS. The comparison of electromyographic pattern classifications with active and passive electrodes. *Medical Engineering and Physics* 2004;26:605-610.
3. Graupe D, Kohn KH. A critical review of EMG-controlled electrical stimulation in paraplegics. *CRC Critical Reviews in Biomedical Engineering* 1988;15:187-210.
4. Scoot TRD, Peckham PH, Kilgore KL. Tri-state myoelectric control of bilateral upper extremity neuroprostheses for tetraplegic individuals. *IEEE Transactions on Rehabilitation Engineering* 1996;4:251-263.
5. Chen YL, Chang WH, Chen SC, Sheu PF, Chen WL. The development of a knee locker with closed-loop functional electrical stimulation (FES) for hemiplegia in gait training. *Disability and Rehabilitation* 2003;25:916-921.

Table I. The results of muscle activities (tibialis anterior and the gastrocnemius),and FAC of affected- side foot experimental subject during four-weeks of gait training

Week	Experimental Group (Tibialis)			Experimental Group (Gastrocnemius)			FAC
	affected-sided	unaffected-sided	P	affected-sided	unaffected-sided	P	
Pre-training	7.88 ± 2.00	12.93 ± 2.74	*	7.83 ± 1.97	11.23 ± 2.16	*	2
Post-training							
3	8.53 ± 1.95	12.21 ± 2.11	*	8.64 ± 1.89	11.43 ± 2.18	*	2
6	9.17 ± 1.01	11.48 ± 2.17	*	9.57 ± 2.59	11.58 ± 2.17	*	3
9	11.23 ± 2.66	12.13 ± 1.79		10.69 ± 2.00	11.78 ± 3.12		3
12	12.38 ± 2.38	12.48 ± 2.15		11.25 ± 2.79	11.33 ± 1.98		4

*: P<0.05

PATIENT-DRIVEN LOOP CONTROL

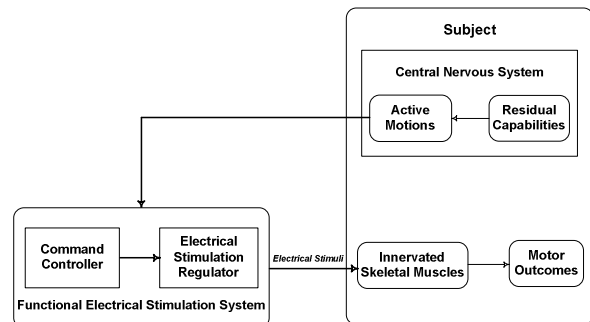


Fig. 1 Block diagram of patient-driven loop control in this study

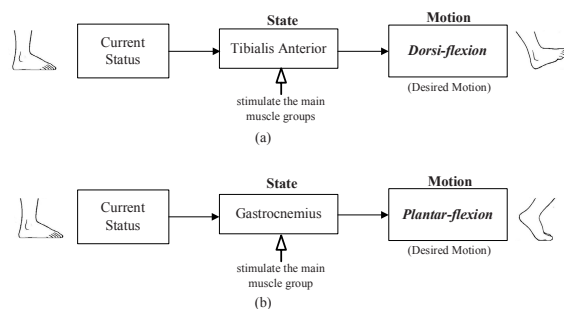


Fig. 2 Motion-oriented modules (a) dorsi-flexion; (b) plantar-flexion.

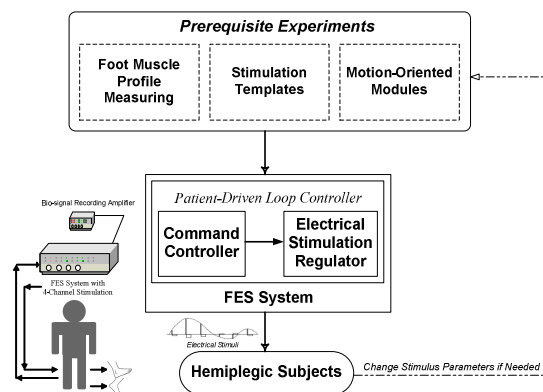


Fig. 3 Block diagram of the strategy of patient-driven loop control in the FES system; the system was a non-invasive electrical stimulator, and it provided 4-channel stimulation with arbitrary currents and biphasic waveforms.

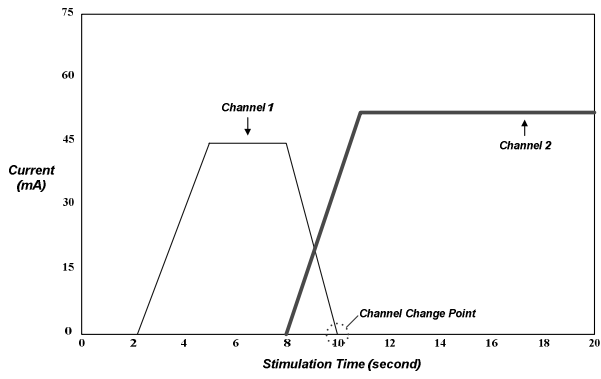


Fig. 4 An example of electrical stimulation sequences in this FES system. Channel 1 and Channel 2 mean the stimulation of tibialis anterior and the gastrocnemius muscles, respectively. Channel change point can be set by the user if he is ready for ambulation.

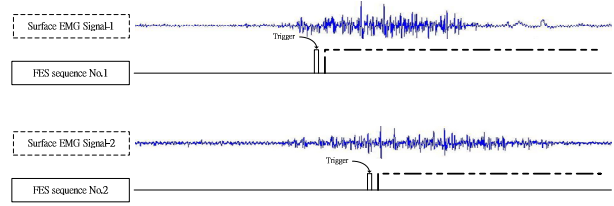


Fig. 5 Different electrical stimulation sequences of lower extremity functions triggered by EMG signals as the control sources for this FES system.(Surface EMG Signal-1 from tibialis anterior muscle and Surface EMG Signal-2 from gastrocnemius muscle)

Design of a Hybrid Powered Upper Limb Orthosis

S. Schulz¹, C. Pylatiuk¹, A. Kargov¹, I. Gaiser¹, O. Schill¹, M. Reischl¹, U. Eck², R. Rupp²

¹ Institute for Applied Computer Science, Forschungszentrum Karlsruhe GmbH, 76344 Eggenstein-Leopoldshafen, Germany,

² Orthopaedic University Hospital, 69118 Heidelberg, Germany

Abstract— The loss of the grasping function in cervical spinal cord injured patients leads to life long dependency on helping persons. At the current state neuroprostheses using Functional Electrical Stimulation (FES) require unrestricted active shoulder and elbow movements which are often not present in high cervical lesioned patients. Therefore this project aims at the development of a non invasive, modular FES-hybrid orthosis for the upper extremity, which combines the advantages of orthotics in mechanically stabilising joints together with the possibilities of FES for actively eliciting muscle contractions. A lightweight, portable system is achieved by the use of miniaturized flexible fluidic actuators that support the movements and that ensure safety by inherent compliance. Thus the system can not only be used for functional restoration but also for training. The integration of novel user interfaces based on residual muscle activities and detection of movement intentions by real-time data mining methods will enable the user to independently control the system in a natural way.

Keywords— Upper limb rehabilitation, flexible fluidic actuators, powered orthosis, FES, paraplegia.

I. INTRODUCTION

In Europe every year 11.000 new patients suffer from a spinal cord injury (SCI) resulting in a life long dependency on caregivers due to loss of motoric functions. Most tetraplegic patients in Europe have - according to data taken from the European Multicenter-Study of Spinal Cord Injury (www.emsci.org) - a lesion of the spinal cord at the level of C4 with functional restriction not only of the hand and fingers but also of the elbows and sometimes of the shoulders. The objective of modern rehabilitation medicine is to at least partly restore the individual functional deficits. Today, in acute patients a task-oriented, function-specific training of high intensity is performed soon after the lesion to restore the function to a certain extent by enhancing neuroplasticity on spinal and supraspinal levels. Up to now most therapeutic systems are stationary floor-mounted robotic systems and their application is limited to the clinical environment due to their size and complexity [1]. Several prototypes of portable home-use training systems for the upper extremity have been presented [2-4]. However, these systems have been designed as exclusive training devices and not for

supporting patients during activities of daily living. Additionally no such system is commercially available yet.

In chronic patients Functional Electrical Stimulation (FES) is - besides physiotherapy and surgical interventions - a major option for restoring the grasping function. However, FES systems have only successfully applied to patients, in which shoulder and elbow have sufficient functional capacity to place the hand voluntarily in space. The reason for this limited use is a premature muscle fatigue and the occurrence of denervated arm muscles in tetraplegic spinal cord injured individuals.

Therefore, a combined therapy and assistive device for the upper limb should be ideally a portable powered orthosis, which is non-invasive and comprising a compact and lightweight design allowing for simple, effective, and safe use.

According to the findings presented in [5], elbow joint moments of 3.1 Nm are needed to hold an average forearm against gravity at a flexion angle of 90 degrees. During activities of daily living, maximum elbow joint moments of 5.8 Nm were recorded [6] with a functional range of movements between 30° and 130° [7]. Finally, safety is an important issue to be considered when designing a rehabilitation device, especially for patients with high spinal cord injuries. The moments exerted at the elbow joint by exclusive FES systems are limited [5]. In order to achieve higher moments and static forces to overcome gravity and to regain independence of helping persons, additional power is needed. Thus, the combination of both FES for neuromuscular activation and for restoration of the grasping function and of artificial muscles to exert the force and the range of motion and to maintain the position of the extremity against gravity overcomes limitations of existing rehabilitation systems and assistive devices.

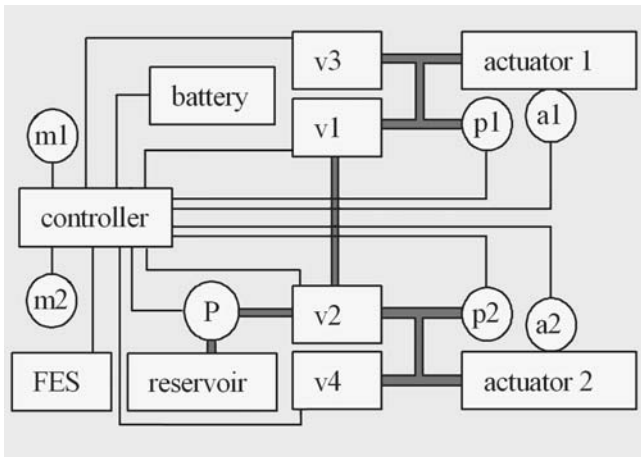


Fig. 1. Diagram of the upper limb training system: m1, m2= myoelectrodes; v1-v4= valves; p1, p2= pressure sensors; a1, a2 – joint positioning sensors; P – hydraulic pump; FES – functional electric stimulation.

II. COMPONENTS OF THE PROTOTYPE OF THE HYBRID ORTHOSIS

In a first step a prototype of a powered orthosis for upper limb training and functional support was developed that comprises the following subsystems: FES, a fluidic actuation system and a controller using biosignals from surface EMG. The basic system structure is illustrated in Fig. 1, a photo of the prototype is presented in Fig. 2. The components are integrated into a lightweight elbow orthosis made of two reinforced half-shells with Velcro® fastener for fixation.

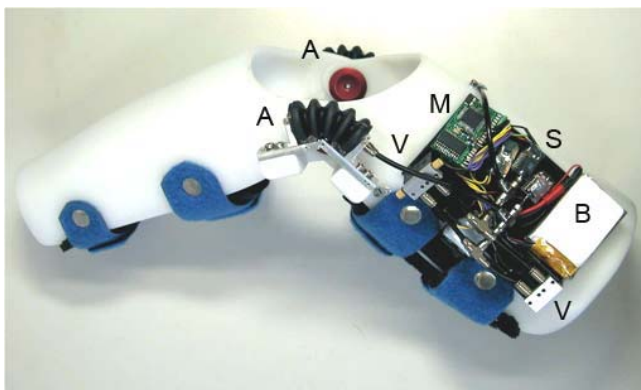


Fig. 2. Components of a hydraulically driven elbow training system prototype. A= flexible actuator, M=microcontroller and electronic drivers, V=valves, B=lithium battery, S= pressure sensors.

A. Functional Electrical Stimulation

In order to perform activities of daily living like holding a spoon a FES system based on surface electrodes is used to regain a lateral grasp pattern [8]. A minimal number of electrodes, which have to be individually placed on a daily basis, is a crucial prerequisite. Grasping can be generated by pairs of surface electrodes for stimulation of the finger extensors (M. ext. digitorum communis EDC), the thumb extensors (M. ext. pollicis longus EPL) and one pair for common stimulation of the finger (M. flex. digitorum superficialis FDS und profundus FDP) and thumb flexors (M. flex. pollicis longus FPL) as depicted in Fig. 3.

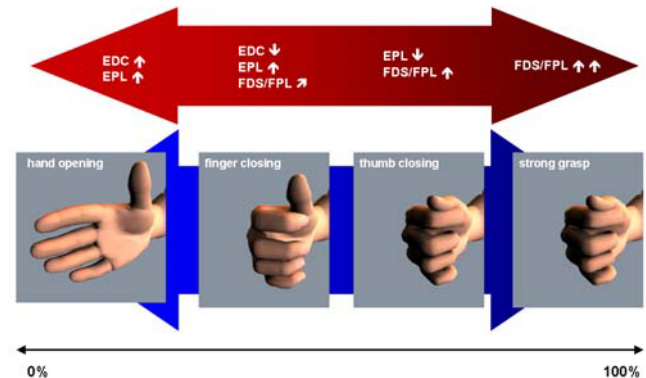
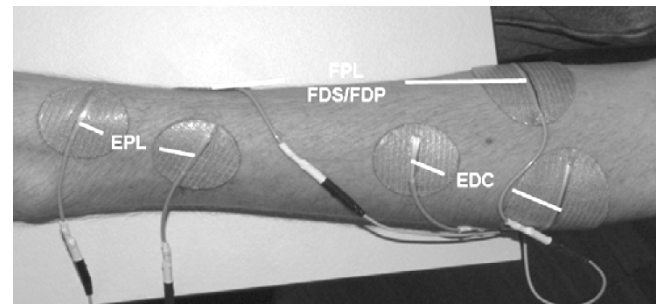


Fig. 3. Stimulation electrodes positions and lateral grasp pattern

Realignment of the custom made (double sided self-adhesive conductive gel) surface electrodes and their connection to the stimulator is simplified by the use of an elastic textile sleeve with integrated cable structures and arrays for contacting the stimulation electrodes [9]. For electrical stimulation a Motionstim 8 stimulator (Krauth & Timmerman Hamburg, Germany) with biphasic constant current pulses with a magnitude of 30 mA, a stimulation frequency of 20Hz and a pulse width of 200µs were used.

B. Flexible Fluidic Actuators

A lightweight, modular miniature fluidic actuation system was designed to fit into the joints of an elbow orthosis. It comprises a custom-made hydraulic pump, miniature valves, and custom-made flexible fluidic actuators (FFAs) (Fig. 2). Each of the two FFAs consists of reinforced flexible bellows that expand during pressurization (expansion principle). When integrated in the levers of a joint, a rotational movement can be achieved. A more detailed description, including a mathematical model to calculate the resulting forces, is given in [10]. The dimension of each actuator is 20 mm in diameter and the maximum torque is 3 Nm, which is determined to be sufficient for a functional support of the patient's elbow, when two actuators are combined, thus working in parallel. The actuators may be driven either hydraulically or pneumatically. The FFAs are characterised by inherent compliance which provides both, safety and comfort compared to conventional stiff actuators [11]. A modification of the first prototype was designed in CAD by adding a second FFA on each side of the elbow joint that works antipodal resulting in an active extension movement of the elbow (Fig. 4).

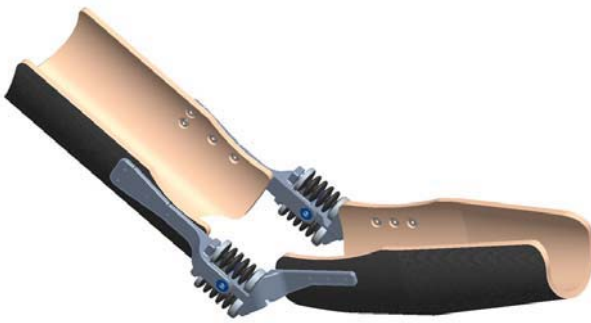


Fig. 4. CAD model of a powered orthosis with two FFAs on each side of the elbow joint to enable both powered flexion and extension of the elbow.

Control of the pressurized fluid is achieved via miniaturized valves. In a hydraulic system only one valve per actuator is needed (v1 and v2 in Fig. 1), because pressurization and deflation are controlled by the same valve. Hence, inlet and outlet are identical. In a pneumatic system the flow rate is much higher, so that a single valve can provide both actuators with pressurized air. However, one valve is needed to control the actuator's inlet for pressurization (v1 or v2 in Fig. 1) and another valve (v3 or v4 in Fig. 1) to open the actuator for deflation. The circuit board comprises a programmable controller (type PIC16F877 by Microchip Technology Inc., USA) with analogue and digital inputs for the sensors a, an A/D converter, and drivers for the valves and the gear pump. Additionally, a wireless Bluetooth™ inter-

face is integrated in the circuit board that allows to change the settings of the controller. The overall weight of the training system, including all components, is 700 grams, with the orthosis accounting for 500 grams.

C. Surface EMG Control

The residual activity of weak muscles can be monitored by the measurement of the surface EMG. A mandatory prerequisite for using the EMG to control a Functional Electrical Stimulation is the possibility to obtain an artefact free signal for real-time processing. This is a technical challenge, since conventional EMG amplifiers react to stimulation pulses with a transient oscillation. Therefore, an existing EMG amplifier has been modified to the requirements of the "OrthoJacket" and is currently miniaturised, being capable of detecting the onset and end of a stimulation pulse generated by stimulation electrodes near the recording site, suppressing the artefacts by switching the amplification factor and the cut-off frequencies of the filters and amplifying the EMG activity within the stimulation pulse pauses [9] (see Fig. 5).

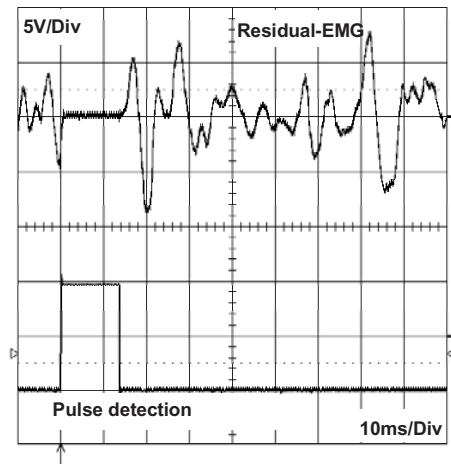


Fig. 5. stimulation artefact detection and suppression .

Recently a setup for a classifier based evaluation scheme based on the analysis of the duration of the electrically induced M-wave has been introduced to determine optimal EMG recording sites and experimentally verified [12]. Additionally an automated selection of the most effective recording sites of an EMG-electrode array is investigated accompanied by software implementations like the introduction of real-time data mining methods for classification of movement intentions and spasticity.

III. CONCLUSIONS

The basic concept for a novel hybrid orthosis for both training and functional support is presented for patients suffering from high spinal cord injury, which will combine both FES and additional external force generating components namely flexible fluidic actuators. Safety is ensured by inherent compliance of the actuators, by mechanical stops and by careful limitation of the maximal moments that are applied to the upper limb. The first prototype of an elbow flexion orthosis serves as a testbed for a modular system to be developed that will also include adjacent upper limb joints, such as shoulder and wrist. The overall aim of the project is to design a portable training device for the whole upper limb that meets the requirements of being lightweight, compact, and inexpensive. The upcoming clinical tests of the device with selected patients with preserved shoulder but missing hand and elbow function will provide information about its basic functionality and usability. This will form the basis for further refinements and improvements of the device.

ACKNOWLEDGMENT

This work is supported by the German Federal Ministry of Education and Research BMBF grant 01EZ-0774.

REFERENCES

1. Riener R, Nef T, Colombo G (2005) Robot-aided neurorehabilitation of the upper extremities, *Med. Biol. Eng. Comput.* 43(1):2-10.
2. Vanderniepen I, Van Ham R, Van Damme M, Lefeber D (2008) Design of a powered elbow orthosis for orthopaedic rehabilitation using compliant actuation. *Proceedings of the IEEE International Conference on Biomedical Robotics and Biomechatronics*, Oct. 19-22, 2008, Scottsdale, AZ, USA, 801-806.
3. Engen TJ (1976) Recent advances in upper-extremity orthotics. In: *The Advance in Orthotics*. London, U.K., Edward Arnold Publishers, 117-128.
4. Kiguchi K, Esaki R, Fukuda T (2005) Development of a wearable exoskeleton for daily forearm motion assist. *Adv Robotics* 19(7):751-771.
5. Pylatiuk C, Schulz S, Vaassen H and Reischl M (2008) Preliminary Evaluation for a Functional Support of the Elbow and Shoulder Joint. *Proc. of the 13th Conf. of the Intl. Functional Electrical Stimulation Society*, Freiburg, Germany, Sep. 21-25 2008, *Biomedical Technology* 53:77-79.
6. Murray IA, Johnson GR (2004) A study of the external forces and moments at the shoulder and elbow while performing every day tasks. *Clin Biomech (Bristol, Avon)*, 19(6):586-594.
7. Bruno RJ, Lee ML, Strauch RJ, Rosenwasser MP (2002) Posttraumatic Elbow Stiffness: Evaluation and Management. *J Am Acad Orthop Surg*, 10(2):106-116.
8. Rupp R, Gerner HJ (2007) Neuroprosthetics of the upper extremity - clinical application in spinal cord injury and challenges for the future. *Acta Neurochir Suppl.* 97(Pt 1):419-426.
9. Rupp R, Eck U, Schill O, Reischl M, Schulz S (2009) OrthoJacket – An active FES-hybrid orthosis for the paralyzed upper extremity. *Proceedings of the 2nd European Conference on Technically Assisted Rehabilitation (TAR 2009)*, Berlin, March 18 - 19, 2009.
10. Kargov A, Pylatiuk C and Schulz S (2007) Development of a Miniaturised Hydraulic Actuation System for Artificial Hands. *Sensors & Actuators A: Physical* 141(2):548-557.
11. Zinn M, Khatib O, Roth B, Salisbury JK (2004) Playing it safe [human friendly robots]. *IEEE Robotics and Automation Magazine*, 11(2):12-21.
12. Schill O, Rupp R, Reischl M (2008) Signal processing concepts for optimal myoelectric sensor placement in a modular hybrid FES orthosis. *Proceedings of the 4th European Congress for Medical and Biomedical Engineering*, Nov. 23-27, 2008, Antwerp, Belgium, 395-399.

Author: Stefan Schulz

Institute: Institute for Applied Computer Science

Street: Hermann-v.-Helmholtz-Platz 1

City: D-76344 Eggenstein-Leopoldshafen, Germany

Email: stefan.schulz@iai.fzk.de

Electrodeposition and characterization of iridium oxide as electrode material for neural recording and stimulation

W. Hasenkamp^{1,3}, S. Musa^{2,3}, A. Alexandru³, W. Eberle³ and C. Bartic^{2,3}

¹ K.U.Leuven, Faculty of Engineering, B-3001 Leuven, Belgium

² K.U.Leuven, Department of Physics, B-3001 Leuven, Belgium

³ IMEC, Kapeldreef 75, B-3001 Leuven, Belgium

Abstract— Electrodeposited iridium oxide films were investigated as electrode material for neural implants. Iridium oxide films were prepared by two electrodeposition protocols: (A) potential cycling in combination with voltage pulsing and (B) constant potential. Both procedures reduced the impedance at 1 kHz more than 30 times and increased the cathodic charge storage capacity up to 35 mC/cm², characteristics desired for neural implants. It was found that the constant potential technique drastically reduced the time needed for deposition, from 7h to roughly 10min. This finding is specially important for large scale fabrication of neural probes.

Keywords— Neuroprosthetics, Electrodes, Electrodeposition, Iridium Oxide.

I. INTRODUCTION

The aim of a neural implant is to provide an interface to the nervous system and help, at least to some degree, to restore the function of defective parts of the brain [1]. To perform this task it is necessary to enable the bidirectional information transfer between neurons and electronic systems with the aid of electrode arrays by means of electrical neural stimulation and recording [2, 3]. Nowadays, the miniaturization permits the fabrication of high density multi-electrode structures that can selectively interact with neuronal tissue on the level of single neurons and also reduce the tissue injury during implantation.

The performance of various electrode materials under physiological conditions is usually given in terms of the frequency-dependent interface impedance and the geometrical charge storage capacity. The down-scaling of electrode dimensions increases the electrode-electrolyte or electrode-tissue impedance and thus can give rise to high current densities and potentially damaging electrode overpotentials during stimulation [4]. One way to solve this problem, is by using electrode materials that are capable of storing more charge at lower electrode potentials.

Currently, platinum is widely used in neuroprosthetic devices but it has a low cathodic charge storage capacity (CSC_c) and therefore cannot safely deliver sufficient charge to ex-

cite neurons. Electrodeposited iridium oxide films (EIROFs), on the other side, can be deposited with large intrinsic surface area and exhibit a much higher CSC_c due to the reversible Faradaic reactions between Ir⁺³/Ir⁺⁴ oxidation states [2]. Iridium oxide films are also stable for long time periods without material degradation [5].

In this work, iridium oxide (IrOx) thin films were electrodeposited on Pt substrate by two techniques: (A) potential cycling in combination with voltage pulsing and (B) constant potential. In both techniques, deposition parameters were optimized such as to achieve an electrode impedance as low as possible and a cathodic charge storage capacity (CSC_c) as high as possible while maintaining a good material quality and stability.

II. EXPERIMENTAL PROCEDURES

A. Electrode fabrication

For this study, platinum-based electrode arrays with electrode dimensions ranging from 5 to 50 μm diameter were fabricated using a similar process flow as previously reported for our neural probe [6]. Fabrication was carried out on 8-inch silicon wafers with 400 nm thermal oxide on both front- and backside. The metal lines and electrode sites were defined by means of lift-off of a layer stack of 20 nm Ti and 200 nm Pt. 1 μm thick Parylene C was used as insulation material and etched in a reactive ion plasma to open the electrode contacts and bondpads. After dicing, the chips were wire-bonded onto custom PCBs and sealed with epoxy. An assembled chip is shown in the Figure 1a and a close-up of one of the platinum electrodes is presented in Figure 1b.

B. Deposition solution

The deposition solution was prepared similarly to the method reported by Yamanaka [7]. The solution was made from iridium tetrachloride (IrCl₄), oxalic acid ((COOH)₂), hydrogen peroxide (H₂O₂) and potassium carbonate (K₂CO₃). It has been reported by Yamanaka [7] that

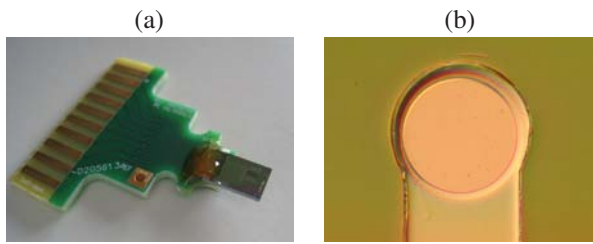


Fig. 1: (a) Assembled chip and (b) an optical microscope image of one of the platinum electrodes (50 μm in diameter).

the addition of hydrogen peroxide to the solution lowers the necessary overpotential for deposition of the oxide. However, the underlying mechanism remains unclear. The potassium carbonate was used to adjust the pH of the solution to 10.5. To guarantee the solution has reached the equilibrium state it was set aside for at least 48h before deposition.

C. Electrodeposition

All electrochemical experiments were performed with a three-electrode cell comprising the microfabricated chip as working electrode, a large area of platinum as counter electrode and Ag|AgCl as reference electrode. They were carried out with a high performance potentiostat/galvanostat (AUTOLAB PGSTAT302N, Eco Chemie, The Netherlands) at room temperature.

The iridium oxide deposition was performed using two methods: (A) potential cycling followed by multiple anodic voltage pulses, as proposed by Meyer *et al.* [2] or (B) by applying a constant potential against the reference electrode for several minutes, as reported by Elsen *et al.* [5]. In method (A), the potential was cycled 200 times with a triangular waveform between 0.00 V and 0.55 V vs. Ag|AgCl at a scan rate of 10 mV/s, followed immediately by 1600 anodic voltage pulses with an amplitude of 0.55 V, pulse width of 0.5 s and period of 1 s. In method (B), the electrode potential was set to a fixed value in the range 0.58-0.7 V vs. Ag|AgCl for a desired time. Immediately after deposition, IrOx films were rinsed with deionized water and dried under stream of nitrogen.

D. Physical Characterization

The surface morphology and microstructure of the electrodes were evaluated by scanning electron microscopy (SEM). The roughness of EIROFs was analyzed by means of atomic force microscopy (AFM). In order to verify the chemical composition the films were characterized by X-ray photoelectron spectroscopy (XPS).

E. Electrochemical characterization

To reproduce the physiological environment, all electrochemical studies were performed in phosphate buffer saline (PBS, 0.15M, pH=7.4) at room temperature. Electrode materials were studied with standard electrochemical techniques, such as cyclic voltammetry (CV) [8] and electrochemical impedance spectroscopy (EIS) [9].

CV provides direct information about the CSC_c of a given material. The CSC_c is the result of both Faradaic reactions represented by cathodic current peaks in the cyclic voltammograms and the current related to the charging of the double layer capacitance which depends on the sweep rate. To determine the CSC_c , assuming every iridium atom is electrochemically active, a CV was performed at a scan rate of 50 mV/s in the water window, i.e. between -0.6 V to 0.8 V vs. Ag|AgCl. The CSC_c was calculated by dividing the total cathodic charge, being the time integral of the cathodic current (Figure 2), by the scan rate.

EIS provides information about the frequency-dependent impedance of the electrode-electrolyte interface which is an important figure of merit for low-noise neural recording and safe stimulation of brain tissue. The impedance spectra were measured using a sinusoidal 10 mV (rms) excitation signal at frequencies from 10 Hz to 100 kHz.

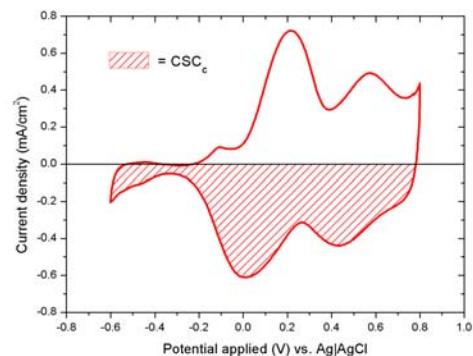


Fig. 2: CV of EIROF performed in PBS at 50 mV/s showing the area used to calculate the CSC_c .

III. RESULTS AND DISCUSSIONS

A. Potential cycling followed by anodic voltage pulses

Two parameters were investigated individually in order to decrease the electrode's impedance: the number of potential cycles and the scan rate. All the other parameters of the original protocol presented by Meyer *et al.* [2] were kept constant.

We observed a decrease in impedance by either increasing the number of potential cycles (Figure 3) or by reducing the scan rate (Figure 4). The impedance of a platinum electrode at 1 kHz was about 500 k Ω and decreased to roughly 40 k Ω by increasing the number of potential cycles, and to approximately 120 k Ω by reducing the scan rate. These results suggest that an overall improvement of the electrode impedance can be achieved by applying more voltage cycles and lower scan rates. The combination of 200 cycles and 10 mV/s scan rate, in a single protocol, resulted in a 30-times reduction of the impedance at 1 kHz.

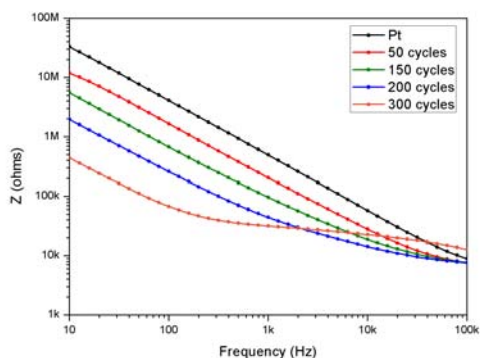


Fig. 3: EIS of Pt electrode in comparison with EIROF electrodes deposited with different number of potential cycles.

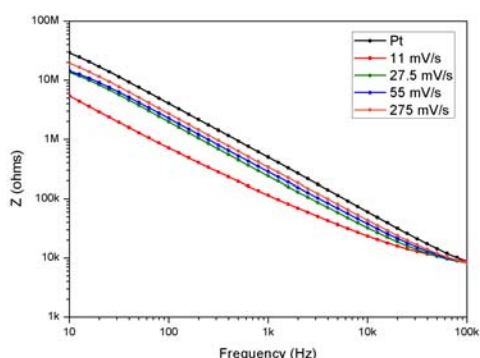


Fig. 4: EIS of Pt electrode in comparison with EIROF electrodes coated with different scan rates.

Our modified procedure created layers of 200-250 nm thickness that were very uniform, mechanically stable and well adherent to the Pt substrate. Figure 5a shows the cross section of an EIROF electrode produced by this protocol. An AFM image of an EIROF surface is presented in Figure 5b. The average roughness calculated from AFM data was

around 3 nm. XPS composition analysis verified the presence of the Ir⁺⁴ oxidation state and of oxygen, thus suggesting the chemical structure of the deposited films to be IrO₂.

Films prepared by this method resulted in a CSC_c of about 40 mC/cm². It was also possible to deposit several electrodes, with different sizes, at the same time without losing the coating homogeneity. This result allows one to use the process for wafer-level and thus large-scale electrodeposition of iridium oxide on various electrode configurations. The main drawback, however, is the long deposition time which can take up to 7h depending on the amount of voltage cycles and the sweep rate.

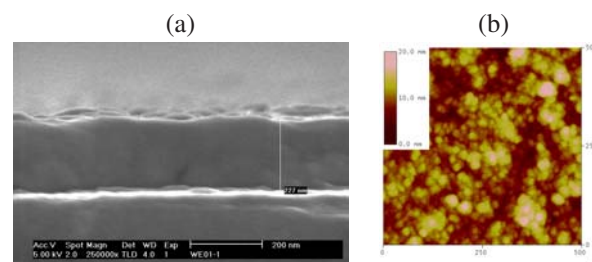


Fig. 5: (a) Cross section SEM image and (b) an AFM image of an EIROF electrode produced by potential cycling followed by voltage pulses.

B. Constant potential electrodeposition

This method offers a way to drastically reduce film-growth times. Here, the electrodes were positively biased (in the range 0.58-0.7 V vs. Ag|AgCl) and the current was monitored for several minutes. We could observe that depositions at higher electrode potentials proceeded faster than at lower potentials, but also were more difficult to control in terms of material quality and adhesion. To improve the film adhesion, the Pt electrodes were first conditioned before plating by performing about six CV cycles (in the water window, i.e. -0.6 V to 0.8 V vs. Ag|AgCl) in PBS.

Although the constant potential method allowed the preparation of thicker IrOx layers we observed that increasing the

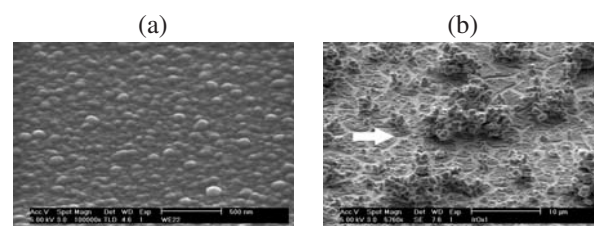


Fig. 6: IrOx films deposited at 0.6 V with distinct deposition times, (a) 500 s and (b) 3000 s.

EIROF thickness progressively rendered the films less uniform and more stressed. The coatings cracked when layers reached thicknesses larger than 300 nm. Figure 6 shows two different coatings, performed at 0.6 V vs. Ag|AgCl, for different deposition times: (a) 500 s and (b) 3000 s. The film deposited for longer time showed cracks, an example being pointed out by the white arrow in Figure 6b. In comparison with the other method, the constant potential procedure was most suitable for a fast preparation of uniform and adherent coatings. With the constant potential method it was possible to coat several electrodes at the same time. However, the layers lacked uniformity when electrodes of different areas were deposited.

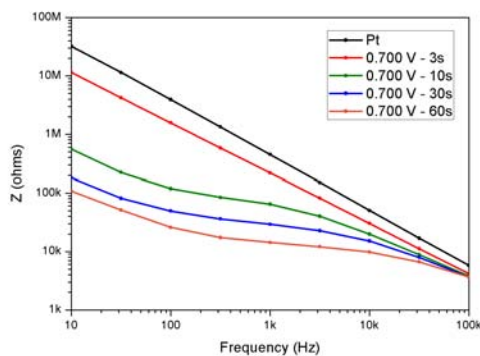


Fig. 7: EIS of EIROF electrodes coated using the constant potential protocol for different deposition times.

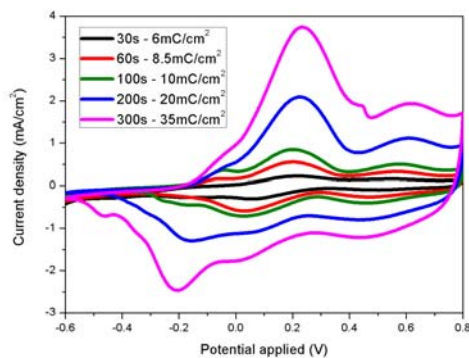


Fig. 8: CV of EIROF electrodes deposited using the constant potential of 0.6 V vs. Ag|AgCl showing the arise of CSC_c with the increasing of deposition times. In all the curves the IrOx films were crack-free.

The impedance spectra of IrOx films grown at 0.7 V for different deposition times by the constant voltage technique are shown in Figure 7. Already after 60 s, the impedance at 1 kHz drops from around 500 k Ω to 15 k Ω which is a factor

30 lower. The impedance drop is even more pronounced at lower frequencies.

The increase of the CSC_c with deposition times was evaluated by CV. Figure 8 shows cyclic voltammograms and corresponding CSC_c of EIROF electrodes deposited at a constant potential of 0.6 V for different times. Up to CSC_c of 35 mC/cm² crack-free IrOx films were obtained, cracks were observed from 60 mC/cm² on. Elsen *et al.* [5] reported cracks on films with CSC_c above 45 mC/cm².

IV. CONCLUSION

Iridium oxide films were prepared by two electrodeposition protocols. Both (A) potential cycling followed by multiple anodic voltage pulses and (B) constant potential reduced the electrode impedance at 1 kHz more than 30 times and increased the cathodic charge storage capacity up to 35 mC/cm². These methods produce electrodes which are more advantageous for neural stimulation and recording. The constant potential technique drastically reduced the time for deposition of comparable films from 7h to roughly 10min. This is especially important for large-scale fabrication of neural probes.

ACKNOWLEDGEMENTS

This work was supported in part by IWT contract ASAP. W. Hasenkamp is grateful to the EMM-Nano program.

REFERENCES

1. Nicolelis M. A. L.. Brain-machine interfaces to restore motor function and probe neural circuits *Nat. Rev. Neurosci.* 2003;4:417–422.
2. Meyer R.D., et al. . Electrodeposited iridium oxide for neural stimulation and recording electrodes *IEEE Trans. NER.*, 2001;9:2–11.
3. Cogan S.F., et al. . Sputtered iridium oxide films (SIROFs) for low-impedance neural stimulation and recording electrodes in *Proc. IEEE EMBS*;2:4153–4156 2004.
4. Lu Yi, et al. . Anodically electrodeposited iridium oxide films microelectrodes for neural microstimulation and recording *Sensors and Actuators B: Chemical.* 2009;In Press, Corrected Proof.
5. Elsen H. A., et al. . Effects of Electrodeposition Conditions and Protocol on the Properties of Iridium Oxide pH Sensor Electrodes *J. Electrochem. Soc.*. 2009;156:F1–F6.
6. Musa S., et al. . Planar 2D-Array Neural Probe for Deep Brain Stimulation and Recording in *Proc. IFMBE*;22:2421–25 2008.
7. Yamanaka K.. Anodically Electrodeposited Iridium Oxide Films (AEIROF) from Alkaline Solutions for Electrochromic Display Devices *Jap. J. Appl. Phys.*. 1989;28:632–637.
8. Robblee L. S., et al. . Electrical stimulation with Pt electrodes - VII. Dissolution of Pt electrodes during electrical stimulation of the cat cerebral cortex *J. Neurosci. Meth.*. 1983;9:301–308.
9. Macdonald J.. Impedance spectroscopy *Ann. Biomed. Engin.*. 1992;20:289–305.

Design and Modeling of an Upper Extremity Exoskeleton

S. Moubarak¹, M.T. Pham¹, T. Pajdla² and T. Redarce¹

¹Laboratoire Ampere UMR CNRS 5005, INSA-Lyon, F-69621, France

²Czech Technical University Prague, Department of Cybernetics, Center of Machine Perception, Czech Republic

Abstract— This paper presents the design and modeling results of an upper extremity exoskeleton mounted on a wheel chair. This new device is dedicated to regular and efficient rehabilitation training for weak and injured people without the continuous presence of a therapist. The exoskeleton being a wearable robotic device attached to the human arm, the user provides information signals to the controller in order to generate the appropriate control signals for different training strategies and paradigms. This upper extremity exoskeleton covers four basic degrees of freedom of the shoulder and the elbow joints with three additional adaptability degrees of freedom in order to match the arm anatomy of different users.

Keywords— Upper extremity exoskeleton, medical robotics, rehabilitation.

I. INTRODUCTION

Elderly people, stroke victims, hemiplegic subjects, paralyzed and spinal cord injured persons suffer from many forms of handicaps for locomotion because of the decline of their physical and muscular strength. Robotic assistance and rehabilitative training have recently become more common, and thus, commercial robotic devices and orthosis are already available and increasingly needed to assist, facilitate and accelerate the training and the recovery of weak and injured people.

Several studies have been carried out on robotic medical training and assistance. For lower limbs, these works not only concentrated on the therapeutic applications of the robotic devices, but also on the development of lower extremity exoskeletons for the augmentation of the load carrying capability and the endurance of the user [1]. However, for the upper limbs, most researchers have paid increasing attention to develop upper extremity exoskeletons for medical assistance and rehabilitation training [2]-[6].

This paper deals with the development and the modeling of an upper extremity exoskeleton mounted on a wheel chair (Fig. 1). Our objectives are to provide an efficient rehabilitative training and physiotherapy for the patient's arm, as well as the possibility for the therapist to apply different training strategies with a variable assistance degree depending on the state of the user and the injury level. Furthermore, this device enables the patient to have a consistent training without the continuous assistance of the therapist; therefore, the latter can work on many patients

simultaneously and the total cost of the therapy can be reduced.

The paper is organized as follows: Section 2 deals with the human arm anatomy. Section 3 describes the different components of our prototype. Section 4 presents the kinematic and dynamic modeling of the exoskeleton. Finally, a brief conclusion highlights the ongoing works but also the perspectives of this project.

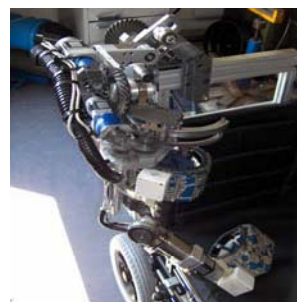


Fig. 1 The upper extremity exoskeleton

II. HUMAN ARM ANATOMY

The shoulder and elbow gather 5 bones of the upper limb: the clavicle, the scapula, the humerus, the ulna and the radius [6] (Fig. 2).

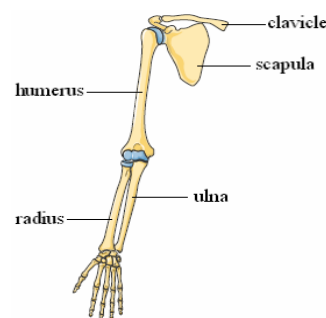


Fig. 2 The shoulder and elbow bones

From a biomechanical point of view, the human anatomy can be represented as a set of rigid bodies connected by joints. In robotic rehabilitation, biomechanical models can be used for the design as well as the control of the prototype

to simplify the interaction mechanism between the human and the robot. Mechanical analyses are carried out to validate the kinematic structure of the robot and its actuators dimensions.

Biomechanical models of the upper limb are also used for evaluation and diagnosis, in order to control the forces and the couples generated by the upper limb movements during a robotic assisted rehabilitation session.

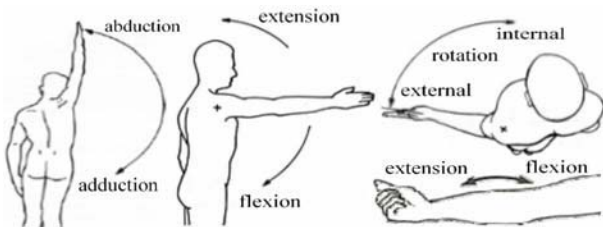


Fig. 3 The four basic degrees of freedom of the arm

The human arm has three complex articulations; the shoulder, the elbow and the wrist. Our prototype, being dedicated to the shoulder and elbow rehabilitation training, covers three shoulder degrees of freedom (DoFs) (abduction / adduction, flexion / extension and internal / external rotation) and one elbow DoF (flexion / extension) (Fig. 3).

Table 1 Human arm characteristics

	Shoulder adduction	Shoulder flexion	Shoulder rotation	Elbow flexion
Range of motion	0°- 180°	-50° - 180°	-80° - 100°	0° - 145°

Table 1 gives the average range of the shoulder and the elbow joints of the human arm [6].

III. A NEW UPPER EXTREMITY EXOSKELETON

This section describes the three prototype's components:

- The mechanical structure
- The actuators and the force sensors
- The control system

The prototype has 4 motorized degrees of freedom; the shoulder abduction / adduction, flexion / extension and internal / external rotation as well as the elbow flexion / extension motion. The shoulder height, the shoulder width and the arm length can be adapted to fit with different body sizes for different users. An arm holder and a wrist holder with 8 integrated force sensors are sending information signals to the controller in order to estimate the state of the user and his motion intentions. Each motor is connected to a drive and can be controlled either by torque or by velocity.

The 4 drives, the force sensors and the adaptability motors are connected to a Dspace card and continuously exchanging information and control signals. Different control schemes can be created and applied using Matlab / Simulink and Dspace -Control Desk interface.

III.1- Mechanical structure:

The main purpose of an exoskeleton is not only to provide efficient motion assistance to the human limbs, but also to guarantee the safety and the comfort of the user. That is why matching the human body anatomy is one of the most important criteria for an exoskeleton design.

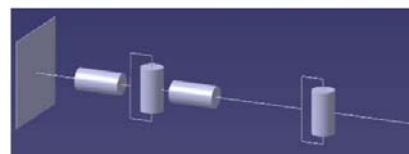


Fig. 4 The mechanical structure of the exoskeleton

The mechanical structure of our prototype (Fig. 4) mainly consists of three links and four revolute joints covering the basic degrees of freedom of the human arm. The motion range of the robot's joints is limited to provide a wide risk-free workspace for the user. The arm is attached to the exoskeleton by external arm and wrist holders with pressure adjustable internal pneumatic holders. The rotation motion is transmitted from the motor axes to the joint axes by rigid and compact spiro-conical gear systems. The prototype is relatively lightweight (10 Kg) with a high ratio of DoFs / weight (Fig. 5).

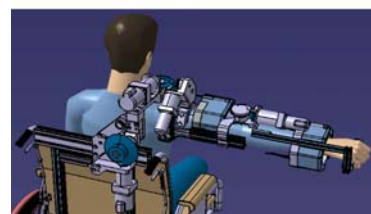
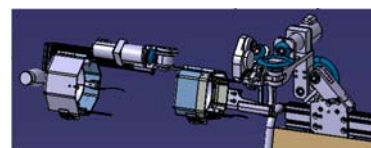


Fig. 5 The gear systems and the arm holders of the exoskeleton

III.2- *Actuators and force sensors:*

The four active DoFs of the prototype are motorized by brushless motors with high torque and relatively small dimensions. The motor torques are amplified by the reducers and the gear systems, to give final output torques of 63 Nm for the shoulder abduction / adduction, 52.5 Nm for the shoulder flexion / extension, 17.1 Nm for the shoulder internal / external rotation, and 13.5 Nm for the elbow flexion / extension motion.

The prototype must be adaptable so it can be used by different patients with different body sizes. The shoulder height, the shoulder width and the arm length can be varied using three DC motors to fit with the users' body dimensions.

The control of the prototype with different training strategies is mainly based on the information feedback signals from the user and the exoskeleton. The motor encoders' feedbacks provide a real time estimation of the position and the velocity of the joints and can be used as feedback information for the kinematic and dynamic models. However, to control an exoskeleton for medical and rehabilitation applications, we need to estimate the state of the user, his interactions with the robot and sometimes we need to predict his motion intentions in order to apply the appropriate robotic assistance. One solution consists in using force sensors. Therefore, depending on the training strategy, we can guide the patient's arm in the correct displacement or modify the exoskeleton's motion to assist him in his desired motion.

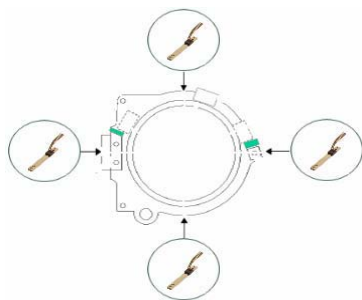


Fig. 6 The arm holder with the force sensors

In our prototype, 4 force sensors are applied in each arm holder. Each sensor can measure any force in the 0 – 125 N interval. The sensors are surrounding the arm and the wrist at 90° on from the other, detecting almost all the possible interactions between the user and the robot (Fig. 6).

III.3- *Control system:*

All brushless motors are equipped with high resolution magnetic encoders for position feedback measurements. Each motor is connected to a drive with a sampling frequency of 5 KHz. The 4 drives, the 3 adaptability DC

motors and the 8 force sensors are connected to the same electronic interface card.

The electronic card exchanges information and control signals with a Dspace controller analyzing all the feedback information and sending the appropriate control signals to the system depending on the training strategy. At this stage, different control schemes and therapy modes are created and applied to the system using Matlab / Simulink software and Controldesk interface.

The complete electrical setup diagram of the system is shown in Fig. 7.

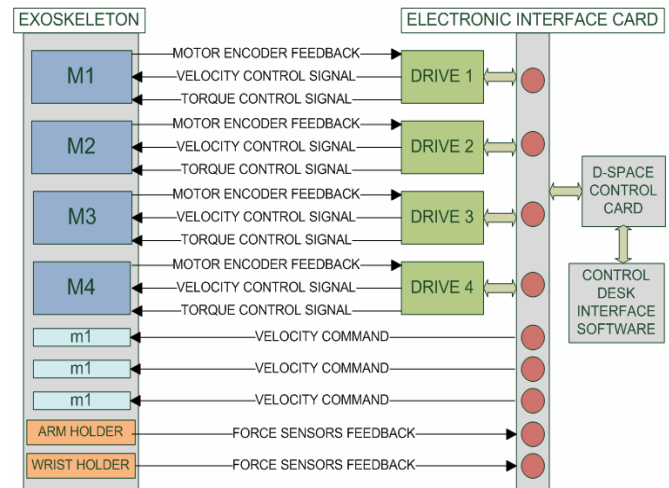


Fig. 7 The electrical setup

IV. MODELING OF THE EXOSKELETON

In order to achieve a compliant controller for the exoskeleton, the kinematic and dynamic models of the structure must be calculated and identification experiments must be carried out to get a better estimation of the dynamic and friction parameters of the robot, and therefore, improve the theoretical models.

IV.1- *Geometric and inertial parameters:*

The mechanical structure of our prototype mainly consists of three links and four joints. The geometric parameters of the robot have been calculated using the Denavit-Hartenberg notations.

The theoretical inertial parameters, used in the dynamic modeling have been calculated based on a complete CATIA model of the prototype.

IV.1- *Kinematic and dynamic models:*

The following models have been calculated using SYMORO+ software (Symbolic Modeling of Robots) and simulated with Matlab/Simulink interface [7]:

- The direct kinematic model (DKM)
- The inverse kinematic model (IKM)
- The direct differential kinematic model (DDKM)
- The inverse differential kinematic model (IDKM)
- The direct dynamic model (DDM)
- The inverse dynamic model (IDM)

The simulation diagram of the kinematic and dynamic models is shown in fig. 8.

A motion generator (MG) creates, for each joint, a 5th degree displacement between two given positions, in a given time, starting and ending with a null acceleration.

q , \dot{q} and \ddot{q} represent the joint position, velocity and acceleration vectors created by the motion generator.

X , \dot{X} and Γ represent the final link position and velocity vectors and the joints torque vector calculated by the direct models.

Q , \dot{Q} and \ddot{Q} represent the joint position, velocity and acceleration vectors calculated by the inverse models.

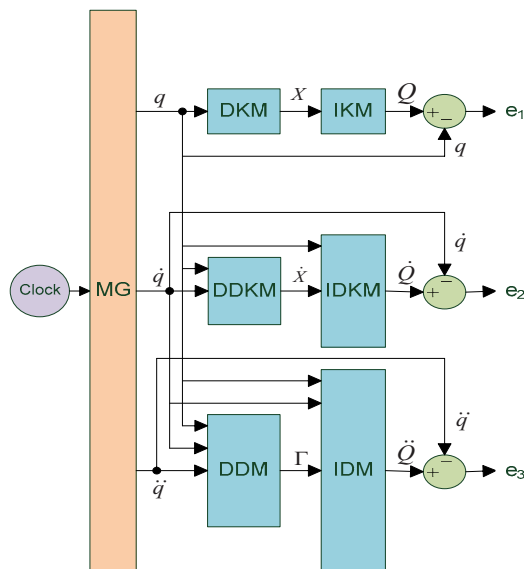


Fig. 8 The modeling and simulation diagram

The six kinematic and dynamic models have been simulated and validated ($e_1 = e_2 = e_3 = 0$).

An important criterion for comfortable rehabilitation training is the efficient gravity compensation of the prototype so that the user can move his arm freely without feeling the mass of the robot. The static component of the inverse dynamic model is applied on the prototype and 90% of the gravity effect of the exoskeleton has been compensated successfully.

Identification experiments are being carried out in order to improve the theoretical estimations of the inertial and the friction parameters of the exoskeleton.

V. CONCLUSION AND FURTHER WORKS

This paper introduces the design and modeling results of an upper extremity exoskeleton mounted on a wheel chair. The key objective of this device is to help users with disabled upper limbs to practice their daily living activities by providing different training levels and therapy modes. It can accelerate the muscle strength development and the recovery of post-stroke and spinal cord injured persons, as well as accident victims and elderly people.

The direct and inverse kinematic, differential kinematic and dynamic models of our prototype have been created based on the Denavit-Hartenberg notations, calculated using SYMORO+ software, simulated and validated with Matlab/Simulink interface.

Another aspect of this work concerns the control strategy. The force sensors feedback will be used in order to estimate the state and the motion intentions of the user; and create efficient training strategies and therapy modes for a better and faster recovery.

ACKNOWLEDGMENT

This work was supported by EC project MEST-CT-2005-021024 WARTHE.

REFERENCES

1. R. Steger, S.H. Kim, H. Kazerooni, "Control scheme and networked control Architecture for the Berkeley lower extremity exoskeleton (BLEEX)", *IEEE International conference on robotics and automation*, Orlando, Florida, Mai 2006, pp.3469-3476.
2. E. Rocon, A.F. Ruiz, F. Brunetti, and J.L. Pons, "On the use of an active wearable exoskeleton for tremor suppression via biomechanical loading", *IEEE International conference on robotics and automation*, Orlando, Florida, Mai 2006, pp.3140-3145.
3. K. Kiguchi, Y. Imada, and M. Lianage, "EMG-Based Neuro-Fuzzy Control of a 4DOF power-assist exoskeleton", *29th IEEE EMBS International conference*, Cité internationale, Lyon, France, August 2007, pp.3040-3043.
4. R. Song, K.Y. Tong, X.L. Hu, S.F. Tsang, and L. Li, "The therapeutic effects of myoelectrically controlled robotic system for persons after stroke-A pilot study", *28th IEEE EMBS International conference*, New York city, USA, August-September 2006, pp.3504-3511.
5. M. Mihelj, T. Nef, and R. Reiner, "ARMin II-7DOF rehabilitation robot: mechanics and kinematics", *IEEE International conference on robotics and automation*, Romania, Italy, April 2007, pp.4120-4125.
6. A. Denève, "Développement et commande d'un robot pour la rééducation des membres supérieurs", Ph.D. dissertation, University of Reims Champagne-Ardenne, France, 2007.
7. W. Khalil, E. Dombre, "Modélisation, identification et commande des robots", PARIS, Hermès, 1999.

Detection of Steady-State Visual Evoked Potentials for Brain-Computer Interfaces Using PCA and High-Order Statistics

S. Pouryazdian and A. Erfanian

Brain-Computer Interface Laboratory, Neural Technology Research Center, Department of Biomedical Engineering, Iran University of Science and Technology (IUST), Tehran, Iran

Abstract— This paper presents a new method for detection of steady-state visual evoked potential (SSVEP) in a 26-class brain-computer interface (BCI) using principal component analysis (PCA). PCA is used to decompose the multi-channel EEG signals into the components which are orthogonal. After PCA processing, the principal components (PCs) can be grouped into components related to SSVEPs and components related to brain activities. A major issue in using PCA to detect the SSVEP is the selection of proper components. In this work, we use high-order statistics to automatically identify the SSVEP components and AR power spectra to detect the frequency of SSVEP. The results of experiments on three subjects and each subject with 8 experiment sessions show that an average detection accuracy between 76.4% and 91.8% can be achieved.

Keywords— Steady-state visual evoked potential, SSVEP, brain-computer interface, BCI, principal component analysis.

I. INTRODUCTION

Steady-state visual evoked potential (SSVEP)-based brain computer interface (BCI) systems have received more and more attention during recent years [1]. The SSVEP is a periodic response elicited by the repetitive presentation of a visual stimulus, at frequencies greater than 6 Hz [2]. The frequency range associated with the SSVEPs normally consists of the fundamental frequency of the visual stimulus as well as its harmonics. Thus, the main part of SSVEP-based BCI is to recognize the frequency of the recorded SSVEP from the scalp. Success in optimizing performance in terms of both speed and accuracy, relies on the accuracy of frequency detection. Several algorithms have been already proposed to improve the accuracy and speed of SSVEP-based BCIs [3]-[12].

Cheng et al. [3] developed a BCI system which was based on frequency-coded SSVEPs to select 10 numbers and 2 controls buttons. An average information transfer rate (ITR) of 27.15 bits/min was reported. To improve the accuracy and ensure more universal applicability of the system, they implemented a preparation experiment before a real practical application [4]. The purpose of the experiment was to find optimal parameters (including *channel location*,

stimulus frequency, and *speed of selection*) for each specific subject. The parameters will be used in his/her further applications. The average ITR was 43 bits/min (range 29–63 bits/min).

In [9], a kernel partial least squares classifier was individually calibrated to map multi-channel frequency bands of the SSVEP signals to right-left or up-down motion of a cursor on a computer display. The best subject's average skill in correct selection of the cursor direction grew from 58% to 88% after 13 training sessions. Friman et al. [10] developed a method for multi-channel detection of SSVEPs. They reported that six different visual stimulation frequencies could be discriminated with an average classification accuracy of 84%. Lin et al. [11] used canonical correlation analysis for detection of nine different visual stimulation frequencies and reported an average accuracy of about 76%.

In this paper, we introduce a new method for detection of 26 different frequencies of frequency-coded SSVEP using principal component analysis (PCA) and high-order statistics.

II. METHODS

A. Subjects and Recording

The experiments were carried out with three able-bodied volunteer subjects with normal or corrected to normal vision. EEG signals were recorded at a sampling rate of 256 Hz from electrode positions Pz, PO1, POz, PO2, O1, Oz, and O2 by Ag/AgCl scalp electrodes placed according to the International 10-20 system using the left mastoid for reference and one electrode on the forehead as a ground electrode. The data were bandpass filtered between 5-40 Hz with a 50-Hz notch filter turned on. The EEG was recorded with a bipolar EEG-amplifier (g.USBamp, g.tec, Guger Technologies, Graz, Austria).

B. Experimental Setup

A stimulator panel with 26 LEDs functioned as the visual stimulator. Each LED flickered at a certain frequency. When a subject gazes at a certain LED, SSVEP would

emerge in the brain. The fundamental frequency of the evoked SSVEP is equal to the flickering frequency of the key. The flicker frequencies were set within 6–18 Hz band with frequency resolution of 0.25 Hz and the flickering frequencies around alpha band (9–11 Hz) were excluded to avoid the interference of spontaneous alpha rhythm.

The experiment consisted of 8 sessions for each subject. Each session was conducted on a different day and consisted of 78 3-s trials.

C. PCA-Based Detection of SSVEP

PCA finds a linear transformation of a data set that maximizes the variance of the transformed variables subject to orthogonality constraints on the transformation and transformed variables. Statistically, PCA decomposes the signals into uncorrelated, but not necessarily independent, components that are spatially orthogonal.

Principal component analysis (PCA) has been already proposed as a method to remove eye artifacts from multi-channel EEG. In this work, we use PCA to decompose the EEG signals into SSVEP responses and brain activity components. One major issue to detection of SSVEP response using PCA is the identification of the SSVEP components. In this work, we employ high-order statistics (i.e., kurtosis) to identify the SSVEP components.

D. Kurtosis as the Marker of SSVEP Component

Kurtosis is fourth-order cumulant of a random variable. The kurtosis of s , denoted by $kurt(s)$, is defined by

$$kurt(s) = E(s^4) - 3[E(s^2)]^2 \quad (1)$$

where E is the statistical expectation. Kurtosis is zero for a Gaussian random variable, positive for super-Gaussian, and negative for sub-Gaussian. Thus, if the kurtosis is highly positive, the activity distribution is highly peaked.

E. Identification of SSVEP Components

First, multi-channel EEG data during each trial of experiment are decomposed by PCA. Then, power spectral density of each component is estimated using AR power spectral estimation by modified covariance method. The kurtosis value of the estimated spectral of each principle component (PC) is computed and component with maximum value is marked as the SSVEP component. To compute the kurtosis, we used the built-in *kurtosis.m* function of Matlab (The Mathworks, R2007b).

To detect the frequency of SSVEP, the peak value of the SSVEP component is detected. The frequency corresponding to this peak is taken as the visual stimulus frequency.

III. RESULTS

Fig. 1(a) shows the AR power spectra of a typical 3-s recorded EEG in response to flicker frequency of 13.25 Hz for different bipolar derivations in subject HK. It clearly observed that the 13.25 Hz can only be recognized at channel Oz-POz. At the other channels, the flicker frequency is dominated by the alpha rhythm (i.e., 12 Hz). The power spectral of the principal components of this trial is shown in Fig. 1(b). It is observed that the SSVEP response is more easily detected in components 2, 5, 6, and 7.

Fig. 2 shows the same information as in Fig. 1 for another trial in subject HK while the flicker frequency is 16.25 Hz. The SSVEP response can only be recognized at channel O2-POz. At the other channels, the flicker frequency is dominated by the alpha rhythm (i.e., 12 Hz). Using PCA, the SSVEP response is decomposed into component 4 with enhanced signal-to-noise ratio.

Interesting point to note is that the optimal channel location during the first trial (i.e., Oz-POz) is different from that during the second trial (i.e., O2-POz).

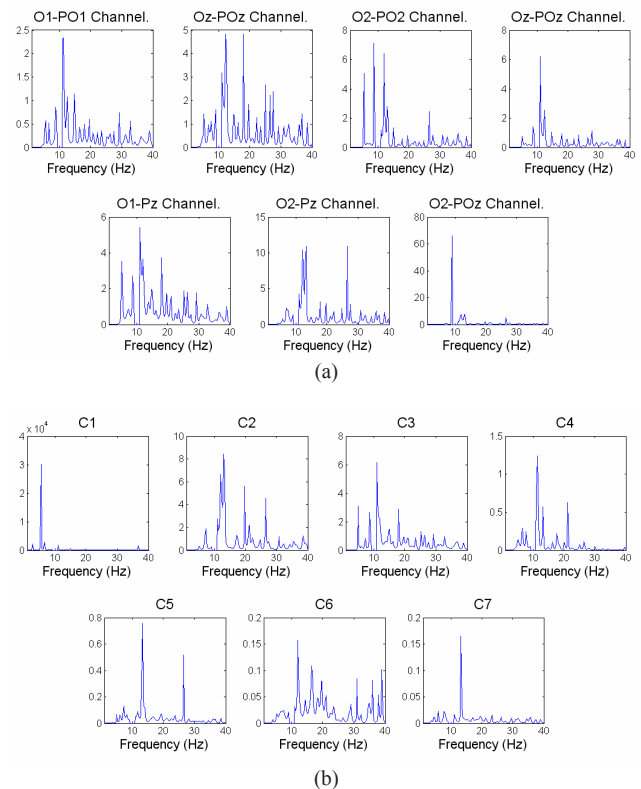


Fig. 1 Power spectra of a typical recorded EEG signals for different bipolar derivations (a) and power spectra of their principal components (b). The flicker frequency is 13.25 Hz.

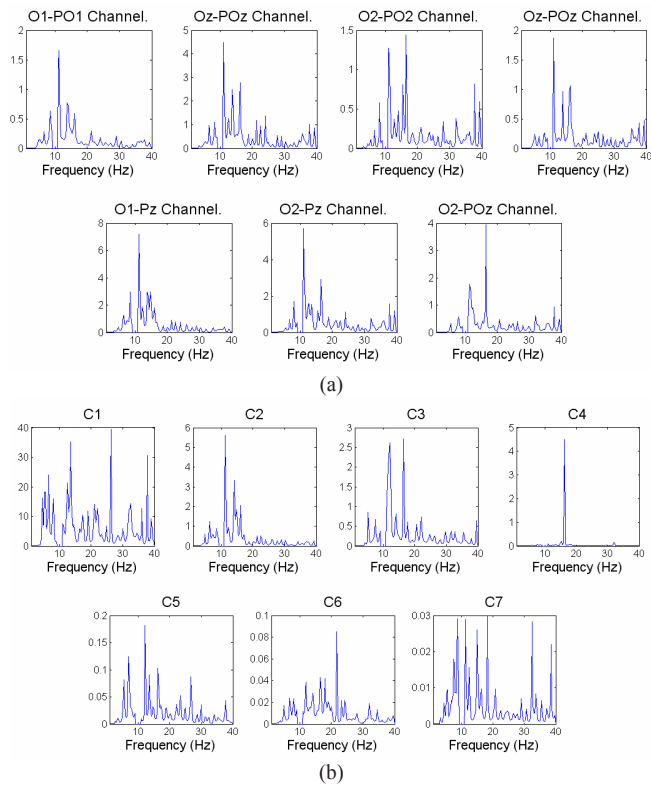


Fig. 2 Power spectra of a recorded EEG epoch during a different trial of experiment for different bipolar derivations (a) and power spectra of their principal components (b). The flicker frequency is 16.25 Hz.

Table 1 Kurtosis values of the spectra of the principal components for two typical trials

Flicker Frequency	Principal Components						
	C1	C2	C3	C4	C5	C6	C7
13.25 Hz	295	52	68	99	170	27	317
16.25 Hz	29	103	55	502	48	47	32

The results indicate that the PCA decomposes the SSVEP contaminated by background EEG signal into SSVEP components and brain activity components. Table 1 summarizes the kurtosis values of the power spectra of the principal components. It is observed that the SSVEP components have the highest value of kurtosis. [component 7 in the first trial (Fig. 1) and component 4 in the second trial (Fig. 2)].

Fig. 3 shows the average recognition accuracy for three subjects during 8 experiment sessions. It is observed that the PCA-based SSVEP detection provides a more robust recognition and improve the accuracy of recognition compared to

the power spectral density based analysis (PSDA) approach. During the first experiment session, using PCA-based approach, average accuracies of 84.6%, 94.9%, and 94.9% were obtained for the subject MA, HK, and AF, respectively, while the average accuracies were 62.8%, 69.2%, and 79.5% using PSDA approach. The subject AF provides a more accurate detection with respect to two other subjects.

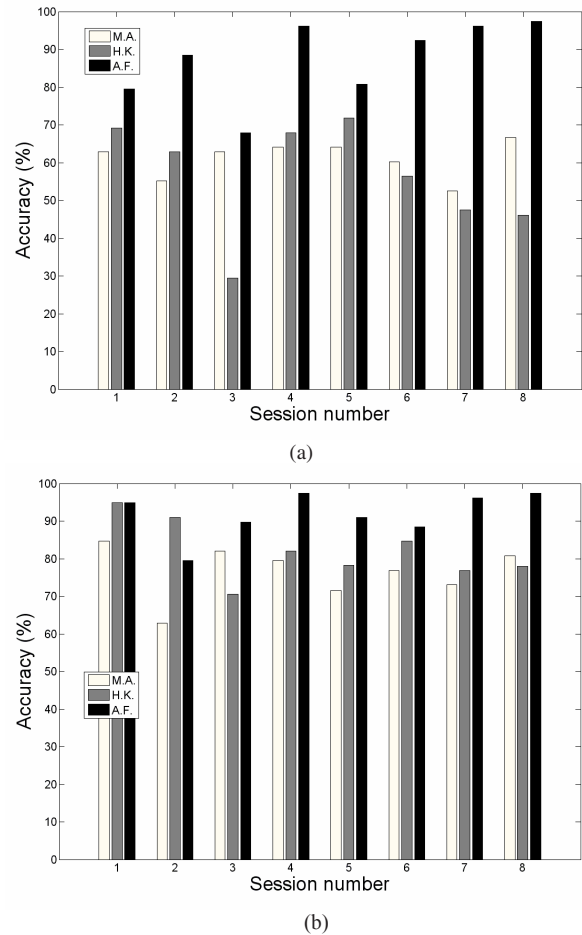


Fig. 3 Average detection accuracy for three subjects during 8 experiment sessions using PSDA (a) and PCA-based (b).

Table 2 summarizes the average accuracy of SSVEP recognition over 8 experiment sessions for three subjects using PSDA and PCA-based approaches. Using PSDA approach, the best average accuracies of 74.5% and 74.0% were obtained for the subject HK and MA, respectively, at the position Oz-POz, while the best accuracy was obtained for subject AF was 87.3% at the location O2-Pz. The best average accuracy over all subjects and all sessions was 68.3% which is obtained at position O2-Pz.

Table 2 Average detection accuracy obtained using PSDA and PCA-based approaches

Subject	O1-PO1	Oz-Pz	O2-PO2	Oz-POz	O1-Pz	O2-Pz	O2-POz	O1-PO1	PCA-Based (Single PC)	PCA-Based (Multiple PCs)
H.K.	61.2±12.1	70.2±11.8	63±12.5	74.5±9.9	55.4±12.9	56.4±14.6	48.4±12.6	75.8±7.2	75.8±7.2	82.0±8.0
M.A.	65.2±8.8	68.6±6.5	68.4±5.5	74±6.8	56.7±10.3	61.1±4.8	60.7±5.2	69.9±8.7	69.9±8.7	76.4±7.1
A.F.	33.5±18.0	62.5±19	56.6±29.8	49.8±20.4	21.2±6.4	87.3±10.4	82.2±15.9	88±6.2	88±6.2	91.8±6.1
Average	53.3±17.3	67.1±4.1	62.7±5.9	66.1±14.1	44.4±20.1	68.3±16.7	63.8±17.1	77.9±9.2	77.9±9.2	83.4±7.8

Table 2 shows that an average detection accuracy of 77.9% was obtained using PCA. In this case, only one selected principal component for detection of SSVEP response was used.

Considering the fact that the signals from several components may improve the performance of detection, we also used the spectra from multiple components with highest kurtosis for detection of SSVEP. The frequency which is detected by the majority of the selected components (i.e., several components with highest value of kurtosis), is considered as the frequency of the SSVEP. Table 2 shows the average accuracy of SSVEP detection using multiple component detection for three subjects. An average accuracy between 76.4% and 91.8% was obtained for a 26-class SSVEP-based BCI system.

IV. CONCLUSION

In this paper we presented a new method for SSVEP response detection which is based on principal components analysis. PCA decomposes the signals into components which are orthogonal. The major motivation of using PCA for detecting SSVEP is that the recorded EEG signal can be intrinsically considered as a mixture of sinusoid waves which are orthogonal. Accordingly, it seems logical that the PCA can decompose the EEG signal into the brain activity and SSVEP components. The results demonstrate that an average detection accuracy of 83.4% was achieved over three subjects and each with 8 experiment sessions.

ACKNOWLEDGMENT

This work was supported by Iran Neural Technology Center (INTC), Iran University of Science and Technology under Grant 160.5261.

REFERENCES

- Middendorf M, McMillan G, Calhoun G, Jones K (2000) Brain-computer interfaces based on the steady-state visual-evoked response. *IEEE Trans Rehabil Eng* 8:211–214
- Regan D (1989) *Human brain electrophysiology: evoked potentials and evoked magnetic fields in science and medicine*. Elsevier, New York
- Cheng M, Gao X, Gao S, Xu D (2002) Design and implementation of a brain-computer interface with high transfer rates. *IEEE Trans Biomed Eng* 49:1181–1186
- Wang Y, Wang R, Gao X, Hong B, Gao S (2006) A practical VEP-based brain-computer interface. *IEEE Trans Neural Syst Rehabil Eng* 14:234–239
- Gao X, Xu D, Cheng D, Gao S (2003) A BCI-based environmental controller for the motion-disabled. *IEEE Trans Neural Syst Rehabil Eng* 11:137–140
- Kelly S, Lalor E, Finucane C, McDarby G, Reilly R (2005) Visual spatial attention control in an independent brain-computer interface. *IEEE Trans Biomed Eng* 52:1588–1596
- Kelly S, Lalor E, Reilly R, Foxe J (2005) Visual spatial attention tracking using high-density SSVEP data for independent brain-computer communication. *IEEE Trans Neural Syst Rehabil Eng* 13:172–178
- Mukesh T, Jaganathan V, Reddy M (2006) A novel multiple frequency stimulation method for steady state VEP based brain computer interfaces. *Physiol Meas* 27:61–71
- Trejo L, Rosipal R, Matthews B (2006) Brain-computer interfaces for 1-D and 2-D cursor control: designs using volitional control of the EEG spectrum or steady-state visual evoked potentials. *IEEE Trans Rehabil Eng* 14:225–229
- Friman O, Volosyak I, Gräser A (2007) Multiple channel detection of steady-state visual evoked potentials for brain-computer interfaces. *IEEE Trans Biomed Eng* 54:742–750
- Lin Z, Zhang C, Wu W, Gao X (2007) Frequency recognition based on canonical correlation analysis for SSVEP-based BCIs. *IEEE Trans Biomed Eng* 54:1172–1176
- Berg P, Scherg M (1994) A multiple source approach to the correction of eye artifacts. *Electroenceph Clin Neurophysiol* 90:229–241

Author: Abbas Erfanian
 Institute: Department of Biomedical Eng., Iran University of Science and Technology (IUST)
 Street: Narmak, Hengam Street
 City: Tehran
 Country: IRAN
 Email: erfanian@iust.ac.ir

Intensive FES therapy and its effect on the upper limb motor recovery after stroke

N. Kawashima^{1,2,3}, V. Zivanovic¹ and M.R. Popovic^{1,2}

¹ Institute of Biomaterials and Biomedical Engineering, University of Toronto, Canada

² Lyndhurst Centre, Toronto Rehab, Canada

³ National Rehabilitation Center for Persons with Disabilities, Tokorozawa, Japan

www.toronto-fes.ca

Abstract— This case report describes a stroke patient who participated in an intensive functional electrical stimulation (FES) therapy program that consisted of task-specific upper arm movements with the combination of pre-programmed electrical stimulation and manual assisted passive motion. The patient was a 22-year-old woman who had suffered a hemorrhagic stroke 2 years earlier. While tactile sensation was only gently impacted by the stroke, motor function of the upper extremity was severely impaired and showed the typical flexor synergy pattern. She demonstrated increased resistance to passive stretch in the distal flexor musculature, and did not use her paretic upper limb for functional activities. The FES therapy was carried out for 12 weeks, two times per day, one hour in each session. The results of the kinematic test indicated a remarkable improvement in dynamic range of motion and coordination of the shoulder and elbow joints. While the motor recovery measured using Chedoke McMaster Stroke Assessment scale and maximal voluntary contraction level of upper arm muscles did not show any changes, a remarkable reduction of the arm spasticity and muscle tone was observed as indicated by the decrease of Modified Ashworth Scale (3 to 2 in the hand and 4 to 3 in the arm) and the reduction of H-reflex in the wrist flexor muscle (82.09% to 45.04% in the Hmax/Mmax). The present results suggest that intensive FES therapy has a capability to improve upper limb function in chronic stroke patients. The improvement of the upper limb motion can be attributed to the enhancement of coordinated muscle activation pattern and the reduction of spasticity and muscle tone.

Keywords— FES therapy, stroke, upper limb, spasticity, reaching, grasping, neurorehabilitation, plasticity

I. INTRODUCTION

According to the American Heart Association there are at least 5.5 million individuals who survived stroke in the US. Stroke survivors usually experience significant deficit in sensorimotor functions [1], and 80 to 85% of them are left with major functional problems in their hand and arm [2]. The paralysis of the arm impairs many daily activities such as dressing and writing, and thus leads to reduction in functional independence.

Neuromuscular electrical stimulation (NMES) is one of the useful therapeutic methods to improve motor function. Previous

studies examining the use of NMES have demonstrated improvements in joint range of motion [3-5], force digits production [6], magnitude of electromyographic (EMG) muscular activity [7], and reduction of muscle tone [8]. While the above studies used NMES for single-segment exercise, more recently, studies have been focused on the effect of electrical stimulation on arm function [5,6,9-12]. Functional electrical stimulation (FES) therapy is a treatment that integrates electrical stimulation of sensory motor systems and repetitive functional movement of the paretic arm in hemiplegic or quadplegic patients [12-14]. In the FES therapy, a preprogrammed electrical stimulation and manual support of joint motion by a therapist are used to help the patient to achieve functional arm motion. With these assistances the patient feels that his/her paralyzed muscles are performing desired contractions in synergistic manner and are accomplishing the desired arm motion. Simultaneously, sensory signals might be generated by the excitation of afferent pathways in the stimulated peripheral nerves. In theory, such neural activity promotes motor re-learning [15]. Recent studies using such sort of novel intervention reported significantly better recovery of upper extremity functions, specifically, in acute stroke patients [10-17]. However, some important questions remain unanswered, for example; what is the neural mechanism underlying an improvement of the sensorimotor function, and if FES therapy is effective in chronic stroke patients.

Improving upper extremity function, specifically arm, hand and finger motion, is the most challenging part for the rehabilitation following stroke. It is well known that most of the sensorimotor recovery occur during the first four weeks after stroke and it is not easy to restore motor function in chronic stroke patients. However, the true potential of chronic stroke patients to improve their upper limb functions is still unknown, although some positive results have been already reported [14]. In the present study, we aimed to address the question to what extent one could improve reaching and grasping functions using intensive FES therapy in chronic stroke patients. The FES therapy consisted of a variety of task-specific multi joint movements with the combination of manual assisted passive motion. To capture the FES therapy-induced improvements of the upper arm function, the following assessments were performed: (1) clinical assessments: Chedoke McMaster Stages of Motor Recovery (CMSMR), Motoricity Index, Maximum Voluntary Contraction (MVC), and Modified Ashworth Scale (MAS), (2) electrophysiological assessment: H-reflex, and (3) kinematical measurements" dynamic range of motion (ROM) test and drawing test.

II. METHODS

A. Patient description

The patient was a 22-year-old woman who suffered an ischemic stroke in the right frontal parietal area two years prior to the participation in this study. When the participant started the inpatient rehabilitation immediately after stroke, the motor recovery status scored by CMSMR for the left side of the body was as follows: arm=1, hand=2, leg=2, and foot=2. After four months of rehabilitation, the CMSMR scores were as follows: arm=2, hand=2, leg=4, and foot=2. While left leg showed good recovery, the left arm was not functional due to high tone. At the beginning of the FES therapy, the patient was independent in activities of daily living with the help of cane and ankle-foot orthosis, but reported that she rarely used her paretic upper limb for functional activities. Movement of the upper extremity was characterized by a flexor synergy pattern. The patient had increased resistance to passive stretching in the distal flexor musculature. We confirmed that the tactile sensation was not severely impaired throughout the upper limb with the use of the two point discrimination test.

The patient signed an informed consent document approved by the Institutional Review Board at Toronto Rehabilitation Institute.

B. Functional electrical stimulation

The Compex Motion electric stimulator was used to deliver FES therapy [18]. In the study the following muscles were stimulated with the surface stimulation electrodes:

- anterior deltoid: aDel (shoulder flexion & abduction)
- posterior deltoid: pDel (shoulder extension & abduction)
- biceps brachialis: BB (elbow flexion)
- triceps brachialis: TB (elbow extension)
- extensor carpi radialis longus and brevis, and extensor carpi ulnaris (wrist extension)
- flexor carpi radialis (FCR) and flexor carpi ulnaris (wrist flexion)

Stimulus parameters used to stimulate the muscles and nerves were symmetrical biphasic current pulses with the pulse duration of 250 μ s and stimulation frequency was 40Hz.

C. FES therapy protocol

The therapy consisted of 2 concurrent components: (1) pre-programmed coordinate muscular stimulation that coincided with the phase and type of arm motion; the stimulation amplitudes were 2 times greater than the motor threshold stimulations; and (2) manual assisted (externally generated) passive motion to establish physiologically correct movement. During the movement, the patient was asked to imagine the movements and to try to carry it out herself. A typical example of task-specific movements that involve all joints of the upper extremity and may be combined with FES is the attempt to touch the nose, reach out, grasp an object, lift it, move it, and release it. The FES therapy was carried out for an hour, twice a day.

During the treatment, a therapist controlled/triggered the arm movements using a pushbutton. During the movements, the physiotherapist guided the arm and assisted the patient with the neuro-prosthesis in performing the desired task. This assistance ensured

that all movements were carried out in a correct physiological way. In the early stages of the treatment, the arm tasks were performed by the combination of muscular stimulation and therapist's assistance. As the patient improved, the assistance was reduced to the necessary minimum. Typically, the stimulation protocols were adjusted weekly or biweekly. The participant was asked to repeat the same arm task 10 times for each motion during a single treatment session. The treatment sessions lasted up to 60 minutes.

D. Motor tasks

The patient was seated with both her arms relaxed in neutral position. The FES was delivered to shoulder and elbow extensor and flexor muscles while the patient (assisted by the therapist) performed specific types of motions. As soon as the patient showed signs of recovery of both the voluntary shoulder and elbow motion, the wrist and hand muscles were stimulated. In this way, the patient was trained to extend the fingers when the arm was fully relaxed. This function is essential to allow patients to voluntarily grasp and release objects. The following six types of movements were prepared for the training.

1. Touch nose: aDel and BB muscles were stimulated simultaneously to produce an arm flexion motion that resembled a feeding movement. Once the hand reached the nose, pDel and TB muscles were stimulated simultaneously to produce arm extension motion and place the arm in a relaxed position next to the body.

2. Touch shoulder: Stimulus pattern was exactly the same as in 1, but the patient was asked to touch her contralateral shoulder. This movement included shoulder inversion motion.

3. Move arm forward: The initial position of the shoulder was slightly extended and elbow was in a flexed position. aDel and TB muscles were stimulated simultaneously to produce the shoulder flexion and elbow extension motion. Once the elbow reached full extension, pDel and BB muscles were stimulated simultaneously to produce shoulder extension and elbow flexion motion and place the arm in the initial position.

4. Lift arm left side up: aDel and pDel muscles were stimulated simultaneously to produce the shoulder abduction motion. Once the upper arm reached horizontal position, TB muscle was stimulated to produce elbow extension motion. The target position was elbow full extended position with upper arm in horizontal position.

5. Grasping large object: With the use of 3 pairs of electrodes, wrist and finger extension motions were produced. Hand grasping motion was produced during shoulder flexion with the elbow fully extended. Once in this position, the three pairs of electrodes were simultaneously stimulated. The cessation of the stimulation enabled the patient to voluntarily grasp a plastic bottle (200ml).

6. Grasping a small object: In addition to palmar and lateral grasps, more precise pinch grasp was trained in the last three weeks of the therapy. Initially, the patient tried to perform reaching motion towards a plastic cassette case (7cm x 5cm x 1.5cm), which was placed in front of her. Once her hand was close enough to the object, the index finger was extended using FES. The cessation of the stimulation enabled the patient to pick up the object.

E. Outcome measures

1. Clinical assessments: CMSMR and the Motricity Index [19] tests for the upper limb were used to assess the participant's arm

and hand functions. The degree of spasticity in the affected upper limb was evaluated using the five-grade MAS.

2. H-reflex and M max: To assess the excitability of the spinal motoneuron pool in FCR muscle, the H-reflex was elicited. The H-reflex was evoked by stimulation of the left median nerve with a monopolar electrode placed in the inside of cubital joint under constant pressure. A rectangular pulse (1ms) was generated by a constant voltage stimulator (DPS-007, Dia Medical System Co.) that was triggered once every 2s. The anode was positioned in the posterior aspect of the cubital joint for selective stimulation of the nerve trunk.

3. Maximal voluntary contraction: The electromyographic (EMG) signals in the following paralyzed upper arm muscles were detected: aDel, pDel, BB, TB, FCR, extensor digitorum longus (EDL), and first distal interosseous muscles (FDI). We used a bipolar differential amplifier (Bortec AMT-8 EMG system; Bortec Biomedical) with upper and lower cut off frequencies of 20 and 1,000Hz, respectively. A pair of surface electrode (BiPole; Bortec Biomedical) was placed along the muscle fibers over the belly in each muscle with an inter-electrode distance (center to center) of 10mm. The recorded EMG signals were amplified 500 times and digitized at a sampling rate of 1,000Hz over a period of 500ms before and 500ms after the onset of the stimulation.

4. Active range of motion test: This test was aimed to evaluate the active range of motion in the shoulder and elbow's combined movement. The patient was asked to move her arm toward following five directions as much as she could: forward, backward, upward, right side, and left side. During the movements, we recorded the position of the shoulder, elbow, and wrist joints, and the second joint of index finger. The patient did three trials for each of the five movements.

5. Circle drawing test: This test was aimed to assess the ability to coordinate shoulder and elbow joints. During a circle drawing task on a table, the subject requires the ability to coordinate shoulder and elbow movements. Specifically for stroke patients, those who have spasm in their elbow joint it is not easy to draw a wide and a properly shaped circle. We recorded the position of the shoulder, elbow, and wrist joints, and the second joint of index finger while the patient drew the circle. The subject was allowed to practice the drawing test in order to get familiarized with this task prior to the assessment. During the assessment the movements were self-paced, and the task continued for 30s.

Originally we planned to assess the patient using tests 1 through 3. However, during the first 6 weeks of training the patient showed remarkable improvement of her shoulder and elbow function, which prompted us to add tests 4 and 5 to further evaluate functional motion of the upper limb.

III. RESULTS

The patient successfully completed all training sessions and assessments. Following 12 weeks of FES therapy, the patient was able to pick a thin object and touch her nose which could not be done prior to the FES therapy sessions. Table 1 summarizes the changes in scores of the clinical assessments, (i.e., CMSMR, Motoricity Index and MAS) during the course of the therapy. H-reflex, which reflects the spinal motoneuron excitability, also showed remarkable reduction with training. Namely, the size of

the H-reflex was quite high at the beginning of the therapy (82.09% Mmax) and as the time passed it decreased considerably (53.65% in 6th week and 45.04% in 12th week). Figure 1 shows the changes in the MVC in the upper arm muscles obtained every two weeks. The MVC level of the affected arm was remarkably smaller than that of the unaffected arm. While there were no consistent changes of the MVC level among all muscles, some muscles showed meaningful changes with the time course of training, for example, the FDI and TB muscle, which did not show any EMG activity at the beginning of the FES therapy, showed a visible EMG as the result of the FES therapy, which patient was able to control voluntarily. Figure 2 shows the shoulder and elbow dynamic range of motion. It is clearly shown that the value of dynamic range of motion for the shoulder and elbow joint at week 12 showed remarkable improvement as compared to those measured at week 6.

IV. DISCUSSION

The purpose of this study was to assess the effect of 12 weeks intensive FES therapy on a chronic stroke patient. Although motor capacity score, i.e., CMSMR and MVC tests did not show any changes, the MAS and the amplitude of H-reflex were reduced as the result of the FES therapy. Additionally, the kinematic results showed a profound improvement in the ability to perform arm movements and to coordinate shoulder and elbow joints. These results suggest that the improvement of the upper arm functional motion can be attributed not only to motor recovery itself, but also to the reduction of muscle tone and/or spasticity.

In this study, FES therapy was used to retrain a chronic stroke patient to voluntarily perform coordinated multi-joint movements with the arm that was previously paralyzed as a result of stroke. Since the stimulus intensity we used was approximately two times larger than the motor threshold, one could not expect that the FES therapy would increase muscle strength. This assumption was confirmed by the results shown in the Figure 1, that is, there were no consistent changes of the MVC.

Although motor score and MVC level did not show any changes with the course of FES therapy, some muscles, i.e., TB and FDI showed remarkable EMG activity as the result of the FES therapy. Because these muscles showed no visible EMG activity at the beginning of the therapy, the contraction level induced by electrical stimulation was sufficient to reactivate the "deactivated" motor command to these muscles.

At the beginning of the FES therapy, the patient's upper limb had high muscle tone. However, the muscle tone of wrist and elbow flexors was remarkably decreased as the result of the FES therapy, which was clearly reflected by the results of MAS and H-reflex. This result was in good agreement with the previous findings that describe the effects of the electrical stimulation on the reduction of the abnormally high muscle tone [8,11]. It should be noted that at the end of the therapy the patient was able to relax her arm and hand and keep the hand relaxed during reaching motion. Therefore, the improvement of the upper arm functional motion can be partly attributed to the reduction of muscle tone and/or spasticity.

In this study we have observed marked changes in the H-reflex and that a number of muscles that the patient was unable to volun-

tarily contract prior to the FES therapy were under her voluntary control at the end of the therapy. This suggests that the functional improvements induced by the FES therapy are in part due to changes that occur in the central nervous system. In other words, we believe that the intensive, repetitive and yet diverse FES therapy is promoting cortical reorganization.

ACKNOWLEDGMENT

This work was supported by the Japanese Society for Promotion of Science, Physician Services Incorporated, Toronto Rehabilitation Institute, Ontario Ministry of Health and Long-Term Care, and Natural Sciences and Engineering Research Council of Canada.

REFERENCES

- Lai SM et al. (2002) Persisting consequences of stroke measured by the Stroke Impact Scale. *Stroke* 33:1840-1844
- Rand D et al. (1999) Does proprioceptive loss influence recovery of the upper extremity after stroke? *Neurorehab. Neural Repair* 13:15-21
- Faghri PD et al. (1994) The effects of functional electrical stimulation on shoulder subluxation, arm function recovery, and shoulder pain in hemiplegic stroke patients. *Arch Phys Med Rehabil* 75: 73-79
- Pandyan AD et al. (1996) Effects of electrical stimulation on the wrist of hemiplegic subjects. *Physiotherapy* 82: 184-188
- Chae J et al. (1998) Neuromuscular stimulation for upper extremity motor functional recovery in acute hemiplegia. *Stroke* 29: 975-979
- Powell J et al. (1999) Electrical stimulation of wrist extensors in poststroke hemiplegia. *Stroke* 30: 1384-1389
- Dimitrijevic MM et al. (1996) Modification of motor control of wrist extension by mesh-glove electrical afferent stimulation in stroke patients. *Arch Phys Med Rehabil* 77: 252-258
- Levin MF, Hui-Chan CW. (1992) Relief of hemiparetic spasticity by TENS is associated with improvement in reflex and voluntary motor functions. *Electroencephalogr Clin Neurophysiol* 85: 131-142
- Cauraugh J et al. (2000) Chronic motor dysfunction after stroke: recovering wrist and finger extension by electromyography-triggered neuromuscular stimulation. *Stroke* 31: 1360-1364
- Popovic MB et al. (2003) Clinical evaluation of functional electrical therapy in acute hemiplegic subjects. *J Rehabil Res Dev* 40: 443-453
- Popovic MB et al. (2004) Functional Electrical Therapy (FET): Clinical Trial in Chronic Hemiplegic Subjects. *Neuromodulation* 7: 133-140
- Popovic MR et al. (2005) Neuroprosthesis for restoring reaching and grasping functions in severe hemiplegic patients, *Neuromodulation* 8 (1):60-74
- Popovic MR et al. (2006) Functional electrical therapy: Retraining grasping in spinal cord injury, *Spinal Cord* 44(3):143-151
- Thrasher TA et al. (2008) Rehabilitation of reaching and grasping function in severe hemiplegic patients using functional electrical stimulation therapy *Neurorehab and Neural Repair* 22(6): 706-714
- Nudo RJ, Milliken GW. (1996) Reorganization of movement representations in primary motor cortex following focal ischemic infarcts in adult squirrel monkeys. *J Neurophysiol.* 75: 2144-2149
- Ring H, Rosenthal N. (2005) Controlled study of neuroprosthetic functional electrical stimulation in sub-acute post-stroke rehabilitation. *J Rehabil Med.* 37: 32-36
- Alon G et al. (2002) Improving selected hand functions using a noninvasive neuroprosthesis in persons with chronic stroke. *J Stroke Cerebrovasc Dis.* 11: 99-106
- Popovic MR and Keller T. (2005) Modular transcutaneous functional electrical stimulation system, *Med. Eng. Phys.* 27(1): 81-92
- Collin C, Wade D. (1990) Assessing motor impairment after stroke: A pilot reliability study. *J Neurol Neurosurg Psychiatry* 53: 576-579

Table 1: The results of clinical assessment scores obtained every two weeks

Type of scale	Pre	2nd	4th	6th	8th	10th	12th
CMSA							
(arm)	2	2	2	2	2	2	2
(hand)	2	2	2	2	2	2	2
Motoricity Index							
(arm pinch grip)	0	0	0	0	0	0	0
(elbow flex)	14	14	14	14	14	14	14
(shoulder abduction)	0	0	0	0	0	0	0
Modified Ashworth Scale							
(arm)	3	3	3	3	3	2	2
(hand)	4	4	4	4	4	4	3

Figure 1: Time course changes of the MVC level of the FDI, FCR, EDL, BB, TB, aDel and pDel muscles. The most left bar fill with black is the data obtained from right (unaffected side) arm.

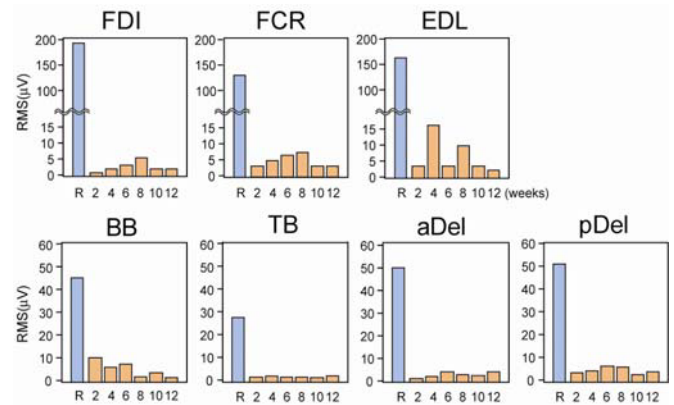
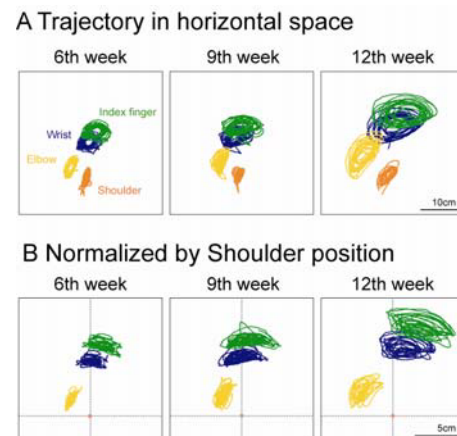


Figure 2: The x-y plot of the shoulder, elbow, and wrist joint, and index finger position during circle drawing test.



Corresponding Author: Dr. Milos R. Popovic
 Institute: University of Toronto and Toronto Rehab
 Country: Canada
 Contact information: www.toronto-fes.ca

Dynamics of the Seizure Engine

O.C. Zalay and B.L. Bardakjian

Institute of Biomaterials and Biomedical Engineering, University of Toronto, Toronto, Canada

Abstract—Epileptiform activity involves abrupt changes in dynamic behaviour of neuronal ensembles, which alternates between higher complexity, possibly chaotic ‘interictal’ dynamics and lower-complexity ‘ictal’ activity characterized by dense, rhythmic firing of the seizing network. This paper aims to investigate some of the dynamical underpinnings of the transition to seizure-like activity, by examining the role of network excitability using complexity analysis and numerical continuation. An asymmetric, bidirectionally coupled oscillator network model – consisting of an accumulator with self-feedback and a dissipator that opposes the activity of the accumulator – was used to generate both seizing and non-seizing activity by varying a single parameter controlling network excitability. The variation of network excitability induced both local and global bifurcations in the dynamics leading to a globally bistable seizure attractor under hyperexcitable conditions.

Keywords— Coupled oscillator, ictal, epilepsy, bifurcation, complexity, nonlinear dynamics

I. INTRODUCTION

Epilepsy is prevalent neurological disorder affecting millions of people around the world. As a disease, epilepsy has a complicated etiology, at times developing as a result of hereditary factors, environmental sensitizers, head trauma, or a combination thereof [1]. In dynamical terms, epilepsy appears to involve pathology in the mechanisms for generating and/or regulating excitability in the affected neuronal networks [2], whether local or global, leading to the appearance of abnormal network activity – characterized by rhythmic, highly-entrained firing of neuronal populations – that interrupts the normal functional activity or rhythms of the brain.

Aberrant reinforcement of recurrent circuitry in certain regions of the brain has also been correlated with the onset and development of epileptiform phenomena, such as mossy-fiber sprouting in temporal lobe epilepsy [3], which purportedly results in an imbalance of network excitation versus inhibition.

We propose that abnormal forms of neural excitability may be perceived in terms of a pathological energy accumulation or dissipation in the network, resulting from one or more of the aforementioned causative factors. Under the assumption that interconnected neuronal populations act as

coupled oscillators, operating in different dynamic regimes depending on network properties and prevailing conditions, we constructed a simple network model of 2 coupled oscillators to study the interplay of accumulation and dissipation resulting from variation in network excitability. The network possesses integrating transfer functionality to portray synaptic coupling, and the parameter governing the decay time of the synaptic impulse function (i.e. the coupling ‘memory’) is the parameter used to vary excitability. Both qualitative and quantitative methods, including bifurcation and complexity analyses, were used to investigate the dynamics of the model in order to relate excitability to epileptiform transitions and the emergence of seizure-like activity.

II. METHODOLOGY

A. Coupled Oscillator Model

The oscillator units are derived from the mapped clock oscillator (MCO) which features dynamic amplitude and phase and an output static nonlinearity that maps the variables to an observable output [4]. Both network oscillators are ‘clocks’, in that they produce a periodic output waveform in their uncoupled, unperturbed state. The coupling between oscillators occurs through transfer functions with exponential (integrating) impulse responses, with the convolution operation dynamically represented by second-order dynamics. Oscillator *A* is designed to be an ‘accumulator’, due to the positive self-feedback; the second oscillator, *B*, is a ‘dissipator’, as its activity generally opposes the action of the first oscillator (Fig. 1). The system of equations defining a single MCO (first 2 equations) and its coupling support (last 2 equations) is as follows:

$$\dot{u}_{1x} = \omega_x \{u_{2x}(1 + S_{\phi,x}) + u_{1x}(1 + S_{\alpha,x} - u_{1x}^2 - u_{2x}^2)\} \quad (1)$$

$$\dot{u}_{2x} = \omega_x \{-u_{1x}(1 + S_{\phi,x}) + u_{2x}(1 + S_{\alpha,x} - u_{1x}^2 - u_{2x}^2)\} \quad (2)$$

$$\dot{u}_{3x} = u_{4x} \quad (3)$$

$$\dot{u}_{4x} = \beta_x F_x(y) - 2\beta_x u_{4x} - \beta_x^2 u_{3x} \quad (4)$$

where $x = \{A, B\}$; ω is the intrinsic angular oscillator frequency; and β is the parameter controlling the decay rate of

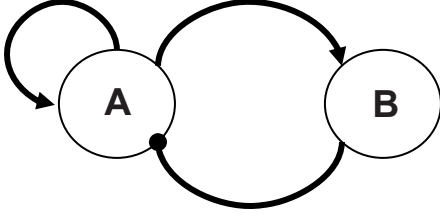


Fig. 1 Coupled network model, consisting of accumulator, A , and dissipator, B .

the coupling response, given by u_3 ($\beta_A = \beta_B = \beta$ for this paper, which is a variable). $F(\cdot)$ is the coupling input function which is written as

$$F_x(y) = c_{Ax}y_A + c_{Bx}y_B \quad (5)$$

such that c_{jk} is the coupling coefficient for the directional connection from the j th to the k th oscillator, and y is the observable oscillator output, given by the static nonlinearity

$$y_x = u_{3x} + \sqrt{u_{1x}^2 + u_{2x}^2} W(\arctan \frac{u_{2x}}{u_{1x}}) \quad (6)$$

where $W(\cdot)$ is the intrinsic output waveform of the oscillator (a neuronal spike) normalized over $(-\pi, \pi]$ with reference to the 4-quadrant arctangent function giving the phase angle. The coupling dynamically modulates the amplitude and phase of the oscillator through portal inputs S_α and S_ϕ respectively in (1) and (2). The generic form of the portal inputs for the coupling as defined is the following:

$$S_{r,x}(u_{3x}) = \varepsilon_{0r,x} + (\varepsilon_{r,x}u_{3x})/\sigma \quad (7)$$

where $r = \{\alpha, \phi\}$, $\varepsilon_{0r,x}$ and $\varepsilon_{r,x}$ are constants and σ is an intrinsic waveform-dependent normalization factor. Table 1 provides the values of the parameters used in the network model.

B. Numerical Continuation

Bifurcation analysis for the parameter β was carried out using the numerical continuation software AUTO, executed from within XPPAUT, a dynamical systems analysis software toolkit developed by B. Ermentrout of the University of Pittsburgh, PA.

C. Complexity Analysis

The relative complexity of the network activity, sampled from the phase-space variable u_{1A} , was determined by estimating the maximum lyapunov exponent (MLE) of the time series as the parameter β was varied. The algorithm to

compute the measure was adapted from the short-time MLE method (STLmax) proposed by Iasemidis *et al.* (1999).

Table 1 Model Parameters

Parameter	Units	Value
ω_A	rad s ⁻¹	2π
ω_B	rad s ⁻¹	2.2π
c_{AA}	s ⁻¹	0.5
c_{BB}	s ⁻¹	0
c_{AB}	s ⁻¹	0.3
c_{BA}	s ⁻¹	-1
$\varepsilon_{0\alpha, \{A,B\}}, \varepsilon_{0\phi, B}, \varepsilon_{\alpha, \{A,B\}}$	—	0
$\varepsilon_{0\phi, A}$	—	-1
$\varepsilon_{\phi, A}$	—	50
$\varepsilon_{\phi, B}$	—	100
σ	[$W(\cdot)$] (mV)	5.815

III. RESULTS AND DISCUSSION

A. Fixed Points and Stability

A single, isolated oscillator of the form given by (1) and (2) has one fixed point at $(u_1, u_2) = (0, 0)$. Taking the Jacobian of the second-order system yields

$$\mathbf{J} = \begin{bmatrix} \omega(1 + S_\alpha - 3u_1^2 - u_2^2) & \omega(1 + S_\phi - 2u_1u_2) \\ \omega(-1 - S_\phi - 2u_1u_2) & \omega(1 + S_\alpha - 3u_2^2 - u_1^2) \end{bmatrix} \quad (8)$$

and solving for the eigenvalues of (8) at $(0, 0)$ gives

$$\lambda_{1,2} = \omega[(1 + S_\alpha) \pm (1 + S_\phi)i]. \quad (9)$$

The eigenvalues reveal that $(0, 0)$ is an unstable focus under unperturbed conditions ($S_\alpha = S_\phi = 0$), at the centre of a limit cycle of radius 1. The limit cycle vanishes when $S_\alpha < -1$; the node becomes a stable focus. Therefore, a supercritical Hopf bifurcation occurs at $S_\alpha = -1$. Varying S_ϕ does not change the stability of the fixed point but the direction of phase rotation reverses as S_ϕ crosses -1 , with the phase sticking at $S_\phi = -1$.

For the coupled case, as presented by equations (1) to (7) with parameters in Table 1, the central fixed point is replaced with at least 3 saddle foci, with the number depending on the value of parameter β . (Saddle-node or fold bifurcations induced by parameter changes can both create or annihilate saddle structures.) Therefore the effect of cou-

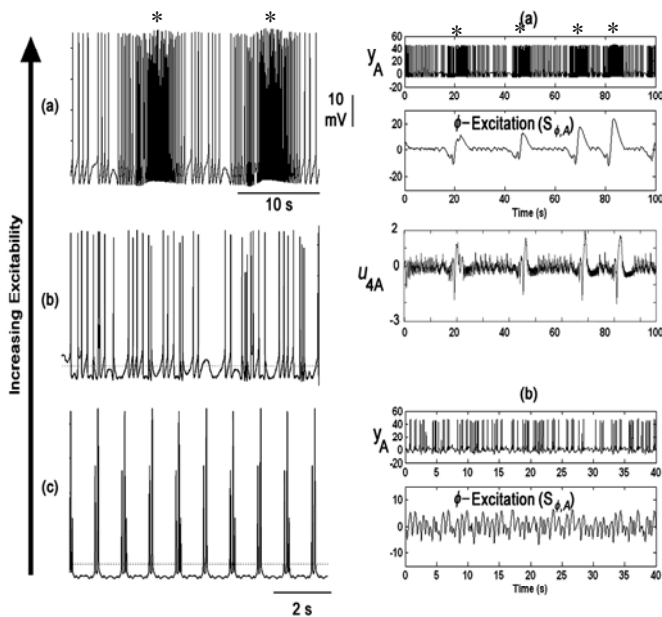


Fig. 2 Effect of varying excitability. (a) $\beta = 1 \text{ s}^{-1}$ (b) $\beta = 10 \text{ s}^{-1}$ (c) $\beta = 60 \text{ s}^{-1}$. The ϕ -excitation level ($S_{\phi,A}$) exhibits large deviations for small β , signalling pathological network regulation of excitability.

pling is to introduce saddle-type objects into the phase space, which enables complex dynamics to emerge. The caveat, however, is that collisions with saddle-type objects also can result in crises or catastrophes that entail very sudden, unexpected shifts in the dynamics, some of which are associated with pathological phenomena and seizure-like transitions in neuronal systems.

B. Effect of Varying Excitability

As the parameter governing network excitability, β , is varied, the model dynamics evolve considerably. As seen in Fig. 2, as β is decreased, the activity goes from rhythmic bursting to high complexity, possibly chaotic spiking to seizure-like activity punctuated by intermittent, high-frequency ictal bursts (asterisks). The interspike intervals within the ictal bursts are actually more regular, and therefore less complex, than the interictal periods. The large, cyclic swings in excitation level for low values of β are an indication of abnormal network regulation of excitability: the mechanisms of energy accumulation and dissipation become unbalanced (partly owing to the inherent asymmetry in network topology), destabilizing the system and leading to cyclic over- and under-compensation of network activity. Once β has reached a critical value, where enough energy has been accumulated to disrupt the dynamic excitation balance, the system behaves similarly to a 'seizure

engine', having attained sufficient momentum to sustain continuous transitions between ictal and interictal states.

C. Local and Global Bifurcations

Numerical periodic-orbit continuation of the system of nonlinear ODEs constituting the model network detected multiple fold and period-doubling bifurcations of orbits as the excitability parameter β was varied. Fold bifurcations of orbits involve a collision between an unstable (or saddle) orbit and a stable one that results in the destruction of both; whereas period-doubling bifurcation occurs with the loss of stability of period N orbit, and the orbit flips to a stable orbit with period $2N$. The latter type of bifurcation offers one route to chaos through a period-doubling cascade. The same bifurcation mechanism run in reverse leads to order through period-halving.

The period-doubling cascade that begins at $\beta = 64.4 \text{ s}^{-1}$ (Fig. 3(a)) as the parameter is decreased gives rise to limited chaos, which resolves after a period-halving cascade. However, around $\beta = 31.5 \text{ s}^{-1}$, the periodic limit-cycle attractor suddenly becomes a chaotic attractor; intermittency is observed very close to the transition. From the inset of Fig. 3 (top row), the stable manifold, $W^{s(1)}$, of the first saddle focus, SF1, forms the basin boundary of the basin of attraction of the limit cycle, which contains the unstable manifold $W^{u(1)}$. Therefore, a boundary crisis occurs whereby the tangency of the stable and unstable manifolds of SF1 results in the birth of a chaotic strange attractor [5]. Interior crises are also observed; the many cyclic fold or saddle-node bifurcations detected by numerical continuation give rise to intermittent chaos followed by periodic windows in the chaotic set. The bottom row inset of Fig. 3 shows numeric continuation of an orbit in one such periodic window for $19.17 \text{ s}^{-1} < \beta < 20.6 \text{ s}^{-1}$. The fold bifurcation at 19.17 s^{-1} leads to disappearance of the chaotic dynamics and the stabilization of a periodic orbit, with maximum lyapunov exponent (MLE) hitting zero (Fig. 4(b)). However, the saddle created by the bifurcation collides with the growing period-doubling orbit which results in an explosion of attractor size, leading to fully developed chaotic dynamics (with positive MLE).

Perhaps what is most relevant and interesting to understanding the evolution of seizure dynamics is what happens when β becomes small, producing pathological excitability in the network: the chaotic attractor undergoes a splitting crisis that results in a bistable epileptiform attractor (as seen from the time-delay reconstructed maps of the u_{1A} attractor in Fig. 4(c)), with ictal and interictal orbits separated in phase space. The large depolarizations associated with runaway excitation during ictal events (Fig. 2) are a manifestation of the trajectory visiting a different region of the phase

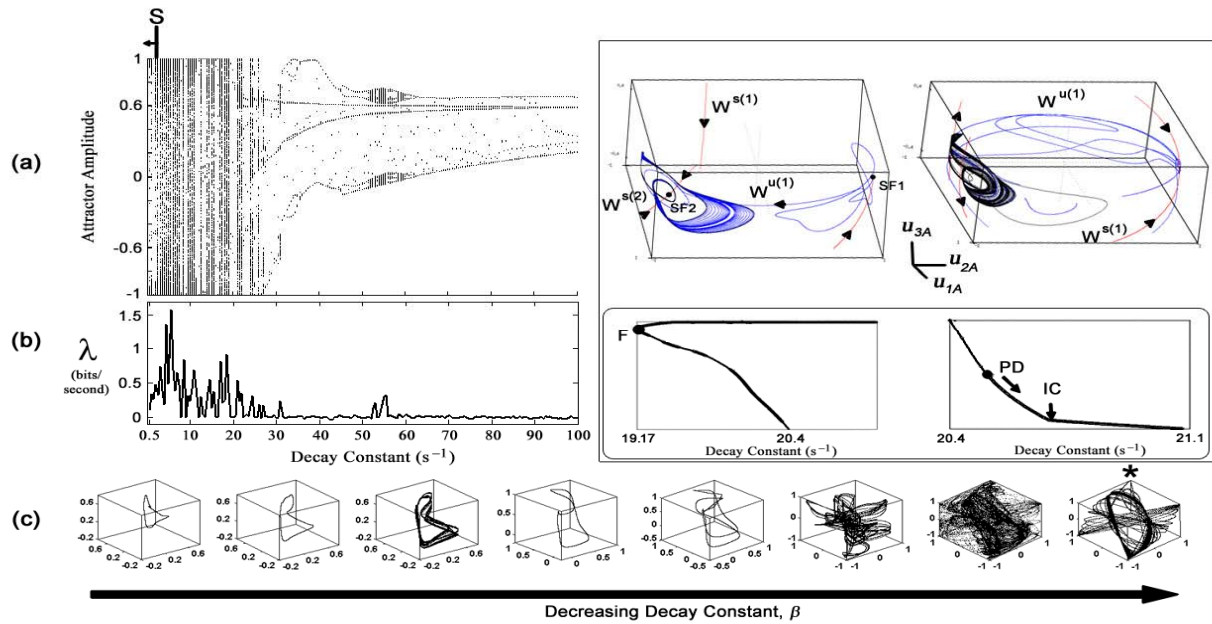


Fig. 3 (a) Orbit diagram (maxima and minima) of u_{1A} as β is varied. Seizure-like region denoted by arrow S . (b) Corresponding maximum lyapunov exponent measure. (c) Time-delay mapping of attractors. From left-to-right, $\beta = \{95, 65, 54, 40, 34, 24, 10, 0.5\} \text{ s}^{-1}$; asterisk identifies bistable epileptiform attractor set. Inset top: pre- (left) and post- (right) boundary crisis attractors (black) with trajectories marking the unstable (blue) and stable (red) manifolds of the saddle foci. (Saddle focus at origin not shown.) Inset bottom: numerical continuation of orbit within a periodic window. PD = period doubling bifurcation/cascade; IC = interior crisis; F = cyclic fold bifurcation.

space than the one during interictal periods. The geometry of the globally bistable attractor promotes intermittent ‘flipping’ between the ictal and interictal regions. The epileptiform attractor is complex (with a positive MLE), though the degree of complexity is lower as compared to the values seen for larger β , as implied by the decreased MLE value for very small β .

IV. CONCLUSION

A wide range of network dynamics was probed by varying a single coupling parameter affecting network excitability. Moderate values of β resulted in high-complexity activity and/or rhythmic bursting, whereas low values of β led to the appearance of a globally bistable, lower-complexity epileptiform attractor. The splitting of the phase space into ictal and interictal regions, visited intermittently, has a physical interpretation in the breakdown of the regulation of network excitation leading to an imbalance in the interplay of accumulative and dissipative network forces; this results in abnormal, cyclical deviations in network excitation – what could be termed a ‘seizure engine’.

ACKNOWLEDGMENT

This work was funded by grants from the Canadian Institutes of Health Research and the Natural Sciences and Engineering Research Council of Canada.

REFERENCES

- Ottman R, Annegers J F, Risch N, Hauser W A, Susser M (1996) Relations of genetic and environmental factors in the etiology of epilepsy. *Ann Neurol* 39:442–449
- Davis G W, Bezprozvanny I (2001) Maintaining the stability of neural function: a homeostatic hypothesis. *Ann Rev Physiol* 64: 847–869
- Sutula T, Cascino G, Cavazos J, Parada I, Ramirez L (1989) Mossy fiber synaptic reorganization in the epileptic human temporal lobe. *Ann Neurol* 26:321–330
- Zalay O C, Bardakjian B L (2008) Mapped clock oscillators as ring devices and their application to neuronal electrical rhythms. *IEEE Trans Neur Sys Rehab Eng* 16:233–244
- Grebogi C, Ott E, Yorke J A (1983) Crises, sudden changes in chaotic attractors, and transient chaos. *Physica D* 7:181–200

Author: Osbert C. Zalay

Institute: Institute of Biomaterials and Biomedical Engineering

Street: 164 College St.

City: Toronto

Country: Canada

Email: oz.zalay@utoronto.ca

Skin properties and the influence on electrode design for transcutaneous (surface) electrical stimulation

Thierry Keller¹ and Andreas Kuhn²

¹ Fatronik Foundation, Mikeletegi Pasealekua, 7, Donostia-San Sebastian, Spain

² Altran AG, CH-8005 Zurich, Switzerland

tkeller@fatronik.com, andreas.kuhn@altran.ch

Abstract— Stimulation electrodes play an important role in interfacing the tissue with an electrical stimulation system. Between the electrode and the excitable tissues a number of obstacles in form of tissue resistivities are present. For transcutaneous electrical stimulation (TES) skin, fat and muscle tissue properties strongly influence current pathways and distribution. Some of these properties can be experimentally measured, but others are more difficult to be correctly assessed. Modeling can help to analyze and differentiate influences of structures and tissue properties on current pathways. However, non-linearities and active behavior of cellular structures need to be considered. Specifically for TES applications with rather high current densities as they occur in selective muscle stimulation active current pathways are important. Homogeneous electrode materials with high resistivities can improve current homogeneity through skin layers.

Keywords— Current density, high impedance stimulation electrodes, Transcutaneous electrical stimulation

I. INTRODUCTION

Skin impedance and other physical properties of the skin tissues have a strong influence on current pathways. Therefore they need to be considered for the design of stimulation electrodes used for transcutaneous electrical stimulation. Current distribution underneath the electrodes affects sensation and can vary between feel of touch, tingling, itching up to strong feeling of burn depending of the number and type of activated receptors [1]. For maximizing stimulation comfort an equal distribution of the current density through its entire path is targeted. For selective stimulation of specific nervous pathways we have to consider skin properties as well, mainly the skin impedance, but also properties of underlying tissues gain importance. Special considerations need to be made for novel emerging FES technologies that are based on multiple small electrodes arranged in an array configuration, which allow dynamic variation of current densities underneath an area of multiple pads [2].

This article aims at summarizing the main skin properties and current pathways important in transcutaneous electrical stimulation and presents results, conclusions and consideration obtained from modeling approaches and measurements

in humans. Not considered in this article are the influences of electrode sizes and shapes. A review of these findings can be found in [3].

II. SKIN PROPERTIES AND PATHWAYS

For the characterization of the electrode-skin interface we need to consider skin properties and current pathways through its layered structure. The skin consists of the epidermis and the dermis. The outer layer of the epidermis, the stratum corneum (SC), consists of a lipid-corneocyte matrix crossed by appendages like sweat glands or hair follicles. The SC has the highest resistance of about $10^5 \Omega\text{cm}^2$ and a capacitance of $\sim 0.03 \mu\text{F}/\text{cm}^2$ [4] when small currents are applied. However, through electroporation, a high increase in permeability of the cell membrane caused by an externally applied electrical field occurs and the skin impedance drops significantly. Electroporation happens when the voltage drop across SC is about 30 V [4].

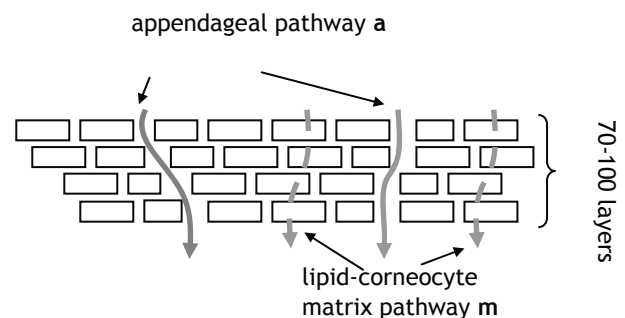


Fig. 1. The stratum corneum (SC) is often modeled as a layered brick model. The impedance of the SC consists mostly of dried out keratin layers with very high impedances. Appendages cross the skin and are preferred pathways for electrical currents [6].

For the epidermis brick structured models are used [5]. An example of such a brick model is depicted in Fig. 1. There are two main pathways: The lipid-corneocyte matrix pathway and the appendageal pathway. These pathways often are modeled as shown in Fig. 2b. The dermis is full of bundles of fibrous connective tissue, blood and lymphic vessels, sensory receptors and related nerves and glands. The electric impedance of the dermis is much lower than the dryer epidermis. It

is modeled either as equipotential area (when the epidermis is modeled in more detail) or as homogeneous volume conductor with a resistivity of about the same as the fat layer. In simplified models (Fig. 2a) the epidermis and dermis are modeled as skin layer using a single volume conductor (e.g. conductivity $\rho=300 \Omega\text{m}$; permittivity $\epsilon\text{r}=6000$).

III. EFFECTS OF SKIN AND ELECTRODES PROPERTIES

A. Non-linearity of skin resistance

For low currents in the μA range (when the applied voltage is lower than 1 V) the voltage-current dependence, hence the impedance, is linear in accordance to measured values [7]. However, for higher currents as needed for TES the skin impedance is a nonlinear function of the current density. Non-linear skin resistivities were measured by Dorgen et. al. for current densities up to 5 mA/cm^2 [8]. For large electrodes (e.g. $5 \times 5 \text{ cm}^2$) such current densities are sufficient. However, when using smaller electrodes (e.g., on array electrodes) even higher current densities can be required. We performed experimental measurements on human volunteers in order to obtain skin resistivities also at higher current densities (up to 15 mA/cm^2). Skin resistivity was determined by using an equivalent network model as shown in Fig. 2a. It consists of a capacitor C_s in parallel with a resistor R_s representing the skin and a series resistor R_c for the plain resistive part (fat, muscle). Polarization voltage V_{Pol} (not depicted) can be neglected in surface electrical stimulation [8].

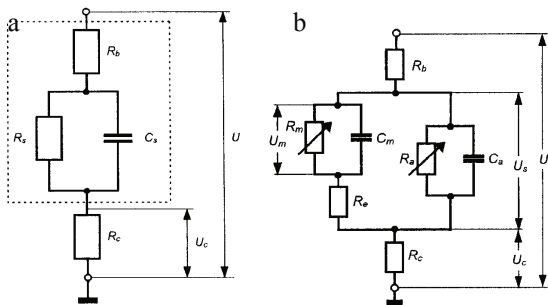


Fig. 2. a) Simplified lumped skin model; b) Slightly more complex model shows the two pathways. R_b = bulk (equipotential) impedance; R_m, C_m = matrix impedance; R_e = epidermis impedance; R_a, C_a = appendagal impedance; R_c = electrode impedance

B. Skin and electrode inhomogeneities

Skin and electrode inhomogeneities have a great influence on the current density distribution. Both affect stimulation efficiency and comfort. As such the design of electrodes is crucial for effective and comfortable stimulation [1]. Localized high current densities can cause discomfort or even skin burns [9]. Such high current densities can have different origins:

- Inhomogeneities of the resistance in the electrode material can cause locally high current densities and worsen stimulation comfort. The size of such inhomogeneities is usu-

ally a couple of millimeters [10].

- Current densities are higher at the edges of electrodes (edge effects) [11].
- The skin layer has a complex structure with local inhomogeneities that lead to resistance changes [12, 13], which cause locally higher or lower current densities. Different sizes of inhomogeneities were identified: Small inhomogeneities from pores and sweat glands which have a size of 50 to $100 \mu\text{m}$ [4, 6]; larger inhomogeneities that are due to different water content and due to different skin structures that have a size of a couple of millimeters [14].

It is hypothesized that high resistance electrodes can improve the homogeneity underneath surface electrodes. Panescu et al. [13] presented a 2D finite element (FE) model with millimeter sized skin inhomogeneities to analyze this hypothesis. They showed that high resistivity electrodes can improve the distribution of the current density underneath surface electrodes. Sha et al. [15] integrated a one pore sized (few μm) skin inhomogeneity in a 2D axis-symmetric FE model. They also found that higher electrode resistivities can reduce high current densities peaks due to the skin inhomogeneities. In the following a more detailed 3D FE model is presented that allowed us the investigation of large (mm) and small (μm) inhomogeneities in the skin and also inhomogeneities in the electrode [16].

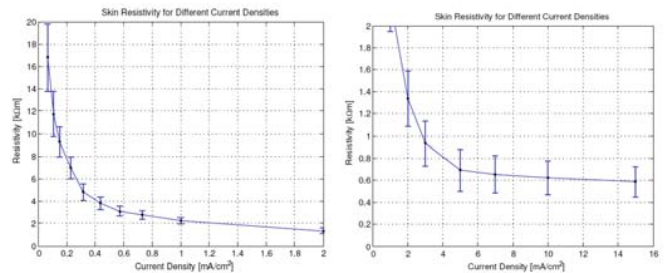


Fig. 3. Non-linear behavior of skin resistivity versus the current density measured experimentally on 7 human volunteers. Two charts are provided for visual clarity where the left one shows the skin resistivity for moderate densities and the right one for high current densities [16].

Besides inhomogeneities the influence of the edge effects on the localized current densities was investigated. The potential and the current density distribution were calculated using a static FE model.

An array of small channels through the skin representing pores and glands (identified as black dots in Fig. 8a) were placed under the electrode surface with a density of 100 per cm^2 and diameters of 50 or $100 \mu\text{m}$ (common values for a human forearm). A small electrode of $0.5 \times 0.5 \text{ cm}^2$ was modeled because larger areas significantly increased the number of finite elements in the FE model. The tissue properties are given in Table 1 and the skin inhomogeneity (e.g. pore) had a resistivity of $1.4 \Omega\text{m}$ [15].

C. Small Skin Inhomogeneities (Pores, Glands)

Fig. 8 shows the geometry that was used to model small inhomogeneities within the skin structure.

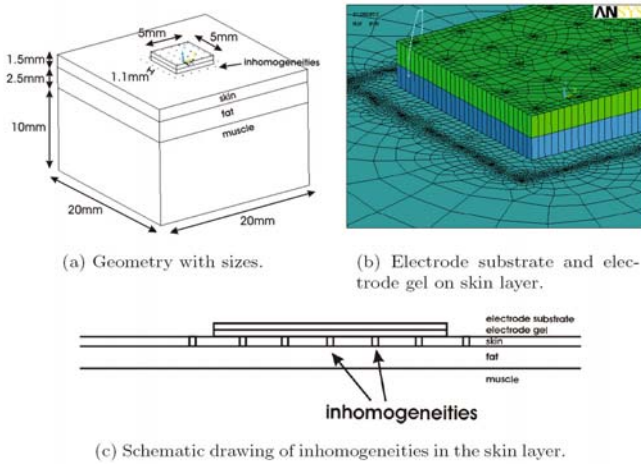


Fig. 8. Geometry and mesh of the model used in [16] to analyze small inhomogeneities.

A current of 5mA was applied between the stimulation electrode and the plane underneath the volume representing muscle.

		Min	Standard	Max
Electrode interface	ρ [Ωm]	1	300	10000
	ϵ_r	1	1	2000000
Skin	ρ [Ωm]	500	700	6000
	ϵ_r	1000	6000	30000
Fat	ρ [Ωm]	10	33	600
	ϵ_r	1500	25000	50000
Muscle (axial)	ρ [Ωm]	2	3	5
	ϵ_r	100000	120000	2500000
Muscle (radial)	ρ [Ωm]	6	9	15
	ϵ_r	33000	40000	830000
Cortical bone	ρ [Ωm]	40	50	60
	ϵ_r	2400	3000	3600
Bone Marrow	ρ [Ωm]	10	12.5	15
	ϵ_r	8000	10000	12000

Table 1. Resistivities and relative permittivities of different tissues. Columns "Min" and "Max" are extreme permittivity values from [14]. The column "Standard" contains properties used in an FE model that was verified with experimental measurements [17].

D. Large Inhomogeneities (Water Content, Structure)

Larger inhomogeneities in electrode and skin were investigated using the same model with slightly changed geometry. The inhomogeneities in the electrode and the skin were assumed to have a factor of 10 lower resistivity than the surrounding electrode gel resistivity or skin resistivity [13]. Either skin inhomogeneities or electrode inhomogeneities were modeled, but the combined effects were not investigated. The inhomogeneities had a diameter of either 0.2 cm or 1 cm [13].

Detailed results from extensive simulations using the above model have been published in [16]. Following conclusions could be made:

- The high current densities at the edge of surface electrodes compared to the center of the electrodes resulting from edge effects can be reduced by using a higher electrode gel resistivity.
- Locally high current densities occurring from large skin inhomogeneities can be decreased with high resistive electrodes. Compared to standard hydrogel electrodes (300 Ωm) a high resistive electrode (70k Ωm) decreased the current density by 50% at the skin-fat interface. These results compare well with [13] where a more even current density distribution was also predicted.
- Inhomogeneities in high resistivity electrodes cause locally high current densities. This effect increases for higher electrode gel resistivities. Therefore, electrode inhomogeneities should be avoided in the production process of high resistivity electrodes.
- The electrode gel resistivity should not be chosen too high. There is trade-off between a more homogeneous current distribution due to a higher electrode gel resistivity and an unequal current distribution due to inhomogeneities in the electrode material. In general electrodes with smaller inhomogeneities in the electrode material can have a higher resistance.
- Our results indicated that that using electrode gel resistivities that are above the values of the skin resistivity ($\rho_{gel} > 700\Omega m$) should be favored. Lower gel resistivities always resulted in a less homogeneous current distribution. Significantly higher resistivities do not improve homogeneity much further and will only cause high voltage drops across the stimulation electrodes.

E. Electrode Edge Effects

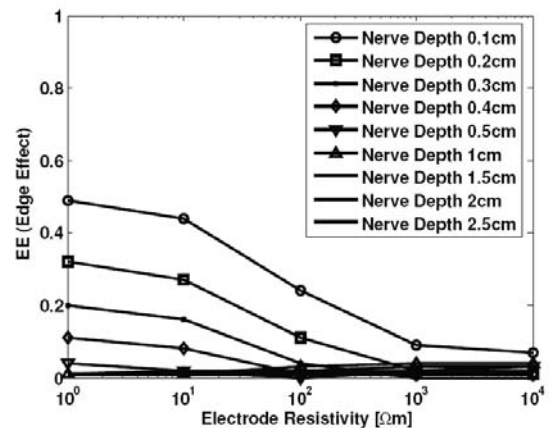


Fig. 7. Edge Effects for different electrode gel resistivities and nerve depths using a 3x3 cm² electrode. The edge effects decrease for higher electrode gel resistivities and deeper nerves.

Electrode edge effects play a significant role in the electrode design for defibrillation. High currents in the Ampere region cause skin damage mainly at the electrode edges because the current density there is higher than in the center. For TES applications electrode edge effects are less dangerous.

ous, however they have been studied intensively. Besides hazardous effects the influence of the electrode edge effects on nerve activation is of interest. The tissue and electrode impedance has a great influence on how the edge effects affect nerve activation. The edge effects on the activation function are shown for an electrode $3 \times 3 \text{ cm}^2$ size for electrode gel resistivities between $1 \Omega\text{m}$ and $10 \text{ k}\Omega\text{m}$.

IV. REQUIREMENTS FOR ELECTRODES

Requirements for conductive stimulation electrodes are fairly simple: They should provide the optimal function with the least pain, not cause permanent skin damage (burns) or irritation. For neuromuscular stimulation optimal performance is actual muscle activation at the desired location. For TENS applications many sensory organs and afferent nerves should be activated without producing much discomfort. This second requirement can be achieved with electrode designs that do not allow currents to enter deep into the tissues as for example proposed by [6].

A. Electrode-skin contact

Good skin contact allows the electrode to interface the skin on the largest area possible. In microscopic images it is obvious that the skin has a very uneven surface with mountains, valleys with loose keratin layers that are breaking off etc. Liquid or sticky gel-type interfaces are used with most success to improve the contact area. Other materials as e.g. conductive hotmelts showed good results, too [16]. A secondary effect of sticky electrodes is that they removably fix the electrode to the skin.

B. Homogeneous current density

The current density should preferably be homogenous over the entire electrode. A gradually lower current density towards the electrode edges will in addition help to reduce edge effects. This can be achieved as e.g. done in latest designs of commercially available hydrogel electrodes by adding a current redistribution layer in a sandwich between two hydrogel layers.

C. High impedance

When the electrode or the interface gel is the dominant impedance, then skin inhomogeneities like the SC layer thickness, partial abraded skin, and more importantly appendages like sweat ducts and hair follicles have theoretically less influence. However, sweat ducts if not dried out are filled with good conducting salty liquid that collect the current from the surroundings and can cause a stinging sensation and pain.

ACKNOWLEDGMENT

The authors would like to thank to the Automatic Control Laboratory, ETH Zurich, Switzerland for the infrastructure to perform most of the presented results. Further we thank

Bischoff Textile AG, St. Gallen, Switzerland, Compex Medical SA, Ecublens, Switzerland, and the Functional Fibers and Textile Group at EMPA St. Gallen, Switzerland for the materials and manufacturing of the textile array electrodes

REFERENCES

1. G. Alon, G. Kantor, and H. S. Ho, "Effects of electrode size on basic excitatory responses and on selected stimulus parameters," *J Orthop Sports Phys Ther*, vol. 20, pp. 29-35, 1994.
2. T. Keller, M. Lawrence, A. Kuhn, and M. Morari, "New multi-channel transcutaneous electrical stimulation technology for rehabilitation," *Conf Proc IEEE Eng Med Biol Soc*, vol. 1, pp. 194-7, 2006.
3. Automatic control journal
4. Y. A. Chizmadzhev, A. V. Indenbom, P. I. Kuzmin, S. V. Galichenko, J. C. Weaver, and R. O. Potts, "Electrical properties of skin at moderate voltages: contribution of appendageal macropores," *Biophys J*, vol. 74, pp. 843-56, 1998.
5. R. Ivanic, I. Novotny, V. Rehacek, V. Tvarozek, and M. Weis, "Thin film non-symmetric microelectrode array for impedance monitoring of human skin," *Thin Solid Films*, vol. 433, pp. 332-336, 2003.
6. S. Grimnes, "Pathways of ionic flow through human skin in vivo," *Acta Derm Venereol*, vol. 64, pp. 93-8, 1984.
7. H. P. Schwan, "Linear and nonlinear electrode polarization and biological materials," *Ann Biomed Eng*, vol. 20, pp. 269-88, 1992.
8. S. J. Dorgan and R. B. Reilly, "A model for human skin impedance during surface functional neuromuscular stimulation," *IEEE Trans Rehabil Eng*, vol. 7, pp. 341-8, 1999.
9. A. Patriciu, K. Yoshida, J. J. Struijk, T. P. DeMonte, M. L. Joy, and H. Stodkilde-Jorgensen, "Current density imaging and electrically induced skin burns under surface electrodes," *IEEE Trans Biomed Eng*, vol. 52, pp. 2024-31, 2005.
10. M. Lawrence and T. Keller, "A transcutaneous electrode measurement system," presented at International Functional Electrical Stimulation Society Conference, Montreal, Canada, 2005.
11. F. Rattay, *electrical nerve stimulation theory, experiments and applications*. Wien: Springer, 1990.
12. D. Panescu, K. P. Cohen, J. G. Webster, and R. A. Stratbucker, "The mosaic electrical characteristics of the skin," *IEEE Trans Biomed Eng*, vol. 40, pp. 434-9, 1993.
13. D. Panescu, J. G. Webster, and R. A. Stratbucker, "A nonlinear finite element model of the electrode-electrolyte-skin system," *IEEE Trans Biomed Eng*, vol. 41, pp. 681-7, 1994.
14. R. B. Reilly, H. Antoni, and M. A. Chilbert, *Applied bioelectricity from electrical stimulation to electropathology*. New York: Springer, 1998.
15. N. Sha, L. P. Kenney, B. W. Heller, A. T. Barker, D. Howard, and M. Moatamedi, "A FE model to identify electrode influence on current distribution in the skin," presented at Vienna International Conference on Functional Electrical Stimulation, Vienna, 2007.
16. A. Kuhn, "Modeling transcutaneous electrical stimulation," Thesis Dr. sc. techn. at Automatic Control Laboratory, ETH Zurich, 2008.
17. A. Kuhn and T. Keller, "A 3D transient model for transcutaneous electrical stimulation," presented at International Functional Electrical Stimulation Society Conference, Montreal, Canada, 2005.

Use macro [author address] to enter the address of the corresponding author:

Author: Thierry Keller
 Institute: Biorobotics Department, Fatronik-Tecnalia
 Street: Paseo Mikeletegi, 7
 City: 20009 Donostia – San Sebastian
 Country: Spain
 Email: tkeller@fatronik.com

Estimation Method of Consumption Energy in Human Activities for Daily Living

T. Sugimoto¹, Y. Yoshida² and I. Yoshida²

¹ College of Science and Technology, Nihon University, Funabashi City, 274-8501, Japan.

² Student of graduate school, Science and Technology, Nihon University, Funabashi City, 274-8501, Japan.

Abstract— Estimation method of consumption energy in human activities for daily living was studied using triple axes attached on the waist bone [1]. It is important to estimate the posture and movement in order to get reliable values of consumption of energy. Further consumption of energy and ECG can estimate on the one chipped small device, it is available to keep our healthy monitoring in a daily living. There are some kinds of sickness especially heart diseases due to consumption energy or amount of quantities for our daily exercise [2]. There are many kinds of postures and movements have obtained in relation to consumption of oxygen during respiration. In our 24 hour daily cycle, the most common postures and movements are walking, running, standing still, standing with a little movement, sitting still, reclining, and sleeping. And consumption of energy for our living depends on the type of movement. Consumption of energy for human movement is varied, but appropriate data could be obtained by accelerometer to estimate consumption of energy. Additionally, type of movement and consumption of energy could be shown to have a correlation.

Keywords— consumption energy, posture, movement, ECG

I. INTRODUCTION

A new medical check up system started in Japan in 2008 that is mandatory for people who are more than 40 years old. This system is to help prevent life style related diseases to decrease medical costs nationwide. Therefore it is important for people to keep appropriate body-mass index (BMI). In order to maintain a suitable BMI, consumption energy has to be estimated for the daily 24 hour cycle. Further, combined measurement consumption energy and ECG on the one chipped IC device, it can be also more widely applied diagnosis due to heart disease [3]. Especially, heart diseases depend on strength or quantities of exercise can be available to diagnosis. There are previous studies for estimating consumption energy [4,5,6]. But the previous studies did not consider the various movements humans make throughout the day, and therefore this study takes a variety of movements into consideration. Consumption energy depends on posture and movement, therefore posture and movement for living have to be estimated appropriately.

II. ESTIMATION METHOD AND CONFIGURATION

(1) Measurement device of consumption energy

A lightweight accelerometer with triple axes on an IC chip was installed on the sternum as shown in Fig. 1. The direction progress was defined as the Z-axis, and transverse to the direction of progress was defined as the X-axis, and direction of gravity was defined as the Y-axis, respectively as shown in Fig.2. The data from the Y-axis 1.0 G during standing still at rest, the data from both the X-axis and the Z-axis should be 0 G. Consumption energy depends on posture and movement, therefore postures and movements have to be estimated first and then the consumption of energy is estimated for each posture and movement. Human posture and movement is very complicated, but it can be calculated using the data from the accelerometer.



Fig. 1 IC chipped 3 axes accelerometer combined ECG on the sternum

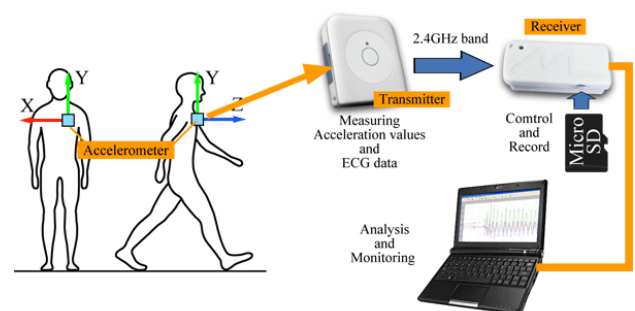
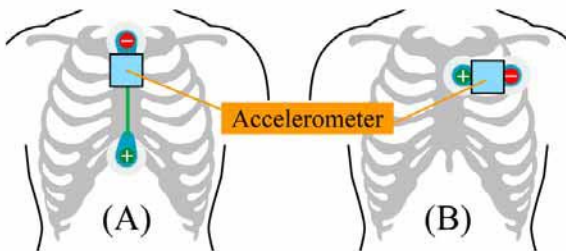


Fig. 2 system configuration and defined axes

(2) Measurement device for ECG

Fig. 1 shows system configuration. The measurement of 3 axes accelerometer combined ECG is installed in the sternum. There are 2 kinds of lead system in the device as shown in Fig.3 (a) and (b). One is called pseudo-MCL1 lead attached along on the 2-nd Sternum. And another lead is called NASA lead or pseudo orthogonal electro cardiograph lead systems. The system provide acceleration values for X, Y, Z axes, ECG data and measured time and body temperature, respectively. And those data are transmitted to receiver with memory attached on the waste bone using 2.4 GHz band. Data is sampling frequency 64 Hz for acceleration values and 256Hz for ECG. After get the data on the receiver is analysis on the analysis software. The Electrode for lead wire used for gel material due to keep constant electric resistance and also electrode are made by waterproofed by special designed seal tape. As a result, during participants are have heavily sweat on the exercised, it can be available used it. And also can available to use 24 hours including sleeping hours. It shows the device may be possible to show the pulse rhythm due to the body movement.



(a) NASA lead method (b) pseudo orthogonal to NASA lead method

Fig.3 Applied electro cardio graphic lead method

3.1. Estimation of posture and movement

The data that was obtained by the accelerometer was compensated for in angle direction of gravity. The progressive and transversal directions were not compensated because there was no baseline. Fig. 4 shows typical average movement data from the accelerometer, processed by 512 data point segments that were sampled at 1/64 seconds increments. Typical data obtained by accelerometer is shown in Fig. 4.

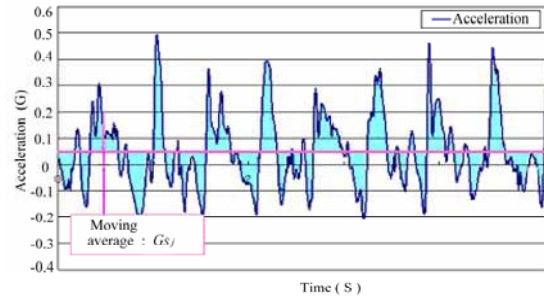


Fig. 4 Data obtained by accelerometer

Gsj shows the data sampled at 1/64 seconds and processed by average movement. The values show the angle of inclination of the body. The data that were obtained from the accelerometer were also processed by FFT in order to get the peak values for the specific frequency for each movement of the body. Typical data processed by FFT is shown in Fig. 5.

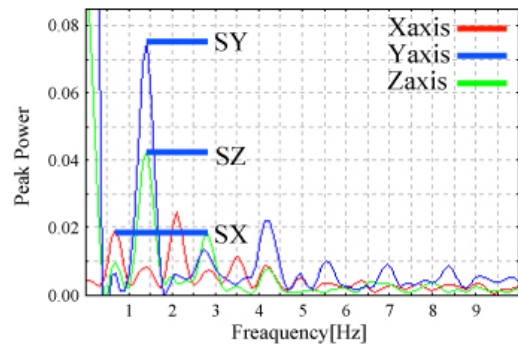


Fig. 5 FFT processed results of the obtained data

The walking cadence was 2 steps/second. The peak values processed by FFT were SY for the direction of gravity, and SZ for the progressive direction, and SX for the transversal direction, respectively. The frequency of SX was decided at 1/2 of SY and SZ, because the frequency of SY and SZ accorded with the steps, but SX accorded with twist frequency. Also the movement data from the accelerometer was sampled at 0.01 second increments. Values for body angle were estimated for standing and reclining positions. The values were estimated as shown in Equation (1).

$$G_{sj} = \left(\sum_{i=1}^{512} (G_j(i)) \right) / 512 \quad (1)$$

The procedure for estimating posture and movement were as follows:

- (1) Discrimination of dynamic and static states. Dynamic and static states were discriminated by using values of SY. Values larger than the threshold value were

determined as dynamic, values below the threshold were determined as static.

(a) If the values were determined dynamic, that movement was walking or running.

Fig. 3 shows the threshold of dynamic and static states. There were plenty of values for dynamic and static measurements for SY, as shown in Fig. 6.

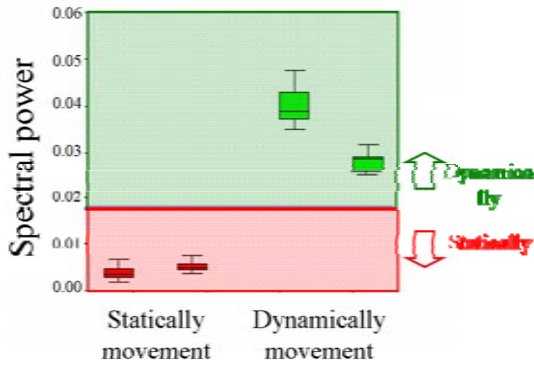


Fig. 6 The strength of spectral power for SY

(b) Values larger than the threshold level are determined as walking, below the threshold is determined as running, as shown in Fig. 7. SY was larger for running than for walking.

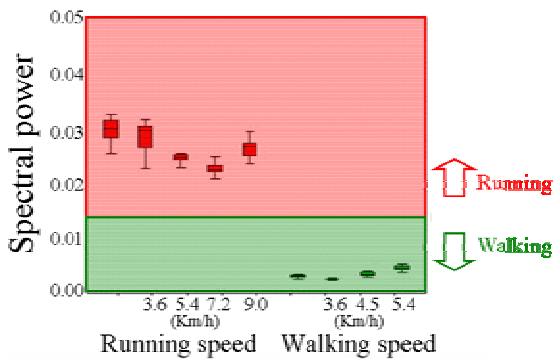


Fig. 7 Discrimination for walking and running movement

(2) Discrimination of standing still, sitting still, and reclining

For static state estimations, there were two positions, standing and reclining, as shown Fig. 8. Standing and reclining were discriminated by using values of the inclination angle. Measurements included standing with a little movement, standing still, and sitting still, as shown Fig. 6. In the next step, the values of SZ were compared to the threshold level. If the value was larger than the threshold

level, it was determined to be standing still or with a little movement, other cases were considered to be sitting still.

(a) Estimation for upright or reclining

Static estimations were for upright or reclining positions. If the inclination angle was larger than 50 degrees from the vertical position was defined as reclining.

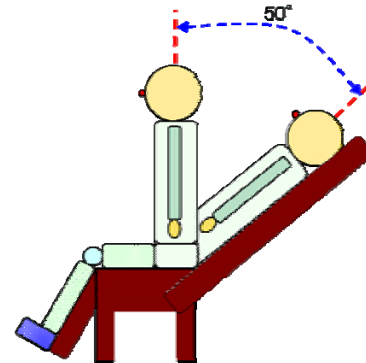


Fig. 8 Definition of the inclination angle of sitting still

(b) Estimation of sitting still and standing still

Although it was hard to estimate values between sitting still and standing still because the measurements were at the sternum, basal energy expenditure could be roughly estimated as the same range, as shown later. However, for standing with a little movement, the consumption of energy had larger values. There were many kinds of standing positions. There were some when the walker is trying to reach a place, but there were other times when the walker was only wandering, such as walking in the office without a place at which to arrive, or a shopper who is looking for something but does not know where it is. Fig. 9 shows differences between standing still and standing with a little movement, when the SY becomes larger than sitting still.

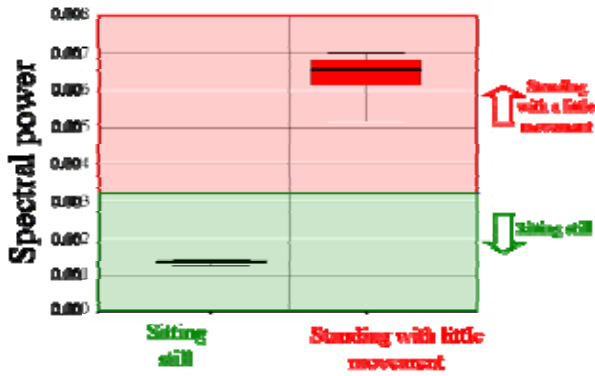


Fig. 9 Discrimination of standing with a little movement and sitting still

To conclude, the procedure for the estimation of postures and movements is shown as a flow chart in Fig. 10, where SY was the 1st peak frequency for Z axes processed by FFT, Gsy was the moving average for Z axes, Th1 was the threshold for dynamic or static postures, Th2 was the threshold to discriminate for reclining, and Th3 was the threshold to discriminate for sitting still.

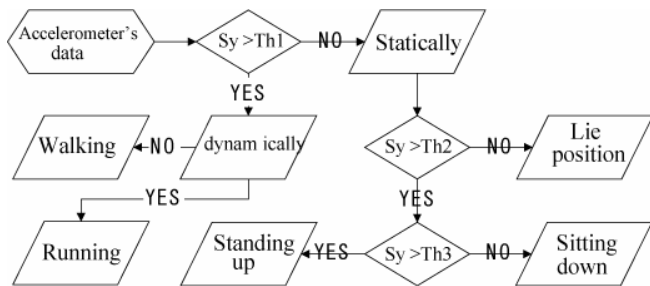


Fig. 10 Flow chart of procedure for discriminating postures and movements

III. RESULT

3.1 Estimation of posture and movement

Fig. 8 shows the results of the estimation for actual posture and movement for horizontal and vertical axes in relation to time, as mentioned above. The participants went through sequences of sitting still in a chair, standing still without moving, walking, standing with a little movement, and after that, walking again. The results show that standing and sitting still could not be discriminated because they were the

same values of Gsy. An accurate estimation could be determined, but from time to time it was indeterminable. For example, the participant in Fig. 11 walked between 0.5 minutes and 2 minutes (illustrated in pink), but around 0.7 minutes was moving only a little. There were a lot of other reasons, such as walking up stairs, walking down stairs, and so on.

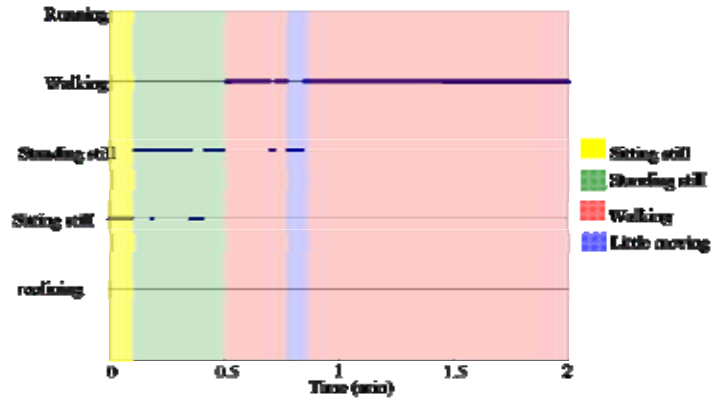


Fig. 11 The result of estimation for posture and movement

3.2 Estimation of consumption energy for daily cycle

There were many kinds of postures in our daily cycle, but mostly they were movements that belong to sleeping, reclining, sitting still, standing still, standing with a little movement, walking, and running. We may have other postures and movements, but they last a short time in the daily cycle. Just to live, our bodies consume energy through basal energy expenditure (BEE). The consumption of energy during the daily cycle was estimated through incremental quantities of BEE. Consumption of energy was measured by the quantity of oxygen intake and carbon dioxide exhaust. These gases were sampled by a 250 liter collection bag. The samples were taken after 4 minutes of warming-up, for 5 to 7 minutes, at the same time of the sampling of the accelerometer data for posture and movement.

(1) Consumption energy during sleeping

Consumption energy BEE is defined by basal energy expenditure during sleeping by the well-known Harris Benedict equation as shown in Equation 2, where BW is bodyweight, Ht is body height, and Yr is age, respectively.

For males:

$$BEE = 66 + (BW \times 13.7) + (Ht \times 5.0) - (Yr \times 6.8)$$

For females:

$$BEE = 665 + (BW \times 9.6) + (Ht \times 1.7) - (Yr \times 7.0)$$

(2) Consumption energy for walking and running

Fig. 12 shows consumption energy for walking. The participants were aged 22 to 26 years old and male. The values were shown without BEE. This shows that consumption energy depends on body weight, the heavier the body, the higher the energy consumed during walking [7]. And Fig.13 shows consumption of energy for running without BEE. In this action, the heavier body weight also consumed more energy. But not enough data could be obtained, therefore the reliability remains uncertain.

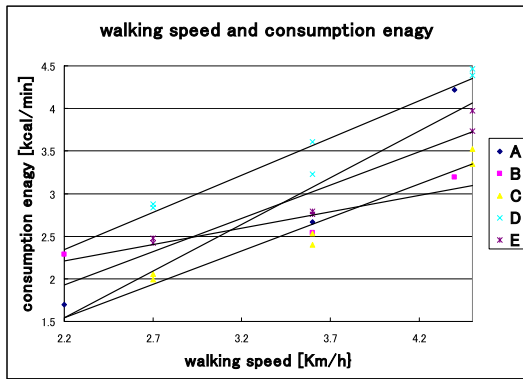


Fig. 12 Consumption energy for walking

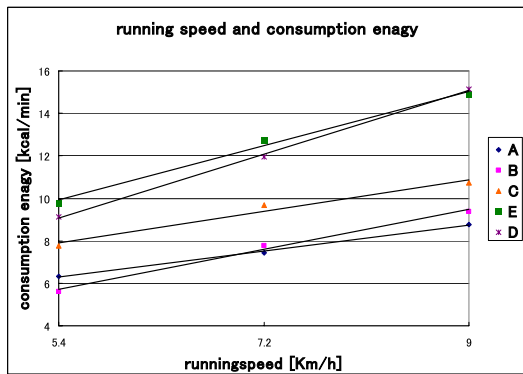


Fig. 13 Energy consumption for running

(3) Dependency on body weight and consumption energy for standing still, standing with a little movement, and sitting still.

Consumption energy between standing still and standing with a little movement had different values. On average, less consumption energy was required for standing still than for standing with a little moving, as shown in Fig. 14. There are many common instances of standing with a little movement in the daily cycle, for example, while lingering

around a desk in the office, or walking sluggishly while shopping.

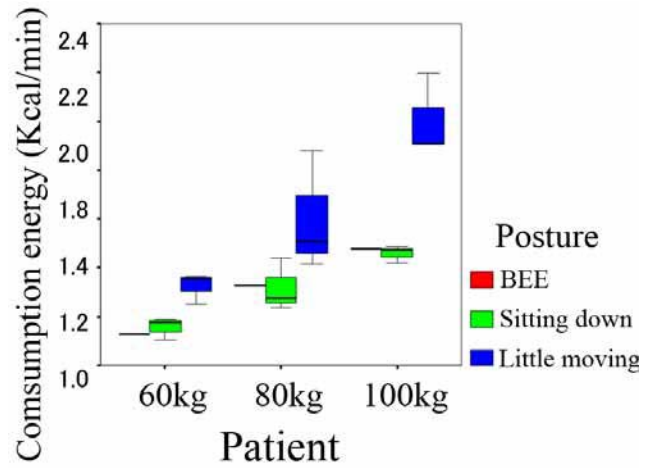


Fig. 14 Dependency of body weight and energy consumption for standing with a little movement, sitting still, and BEE

(4) Consumption energy for BEE and reclining

Fig. 15 shows comparison of consumption energy for BEE and reclining. Consumption energy for both was estimated at almost the same range of values. Likewise, standing still yielded similar values. However, standing still with a little movement resulted in BEE. This means that even when in a static state, some of quantity of energy is consumed in our body.

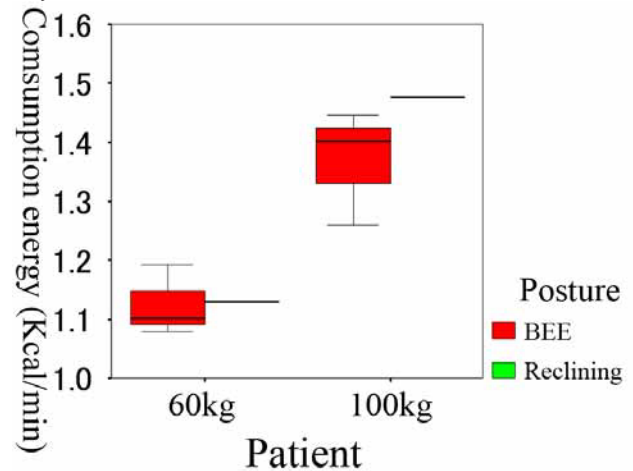


Fig. 15 Comparison of BEE and reclining

3.2 Obtained ECG data

An example of ECG data are shown in Fig.16(a) which is obtained by NASA lead, Fig.17(b) is obtained pseudo orthogonal to NASA lead.

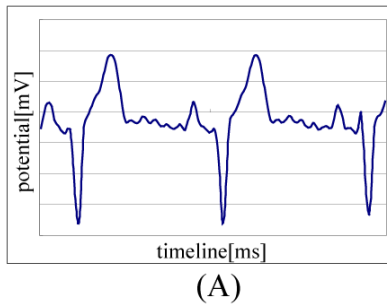


Fig. 16 Obtained by NASA lead

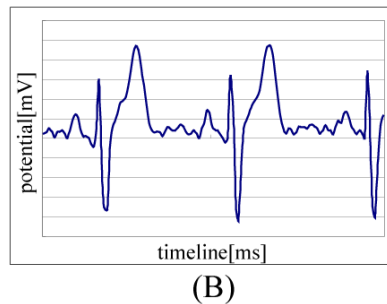


Fig. 17 Obtained ECG data

In this study, medical data for heart diseases or other diseases due to exercises are not yet obtained because of just finished made it.

IV. CONCLUSIONS

Estimation method for consumption energy for the daily cycle of people has been studied with an IC chip attached on the sternum. For estimating consumption energy, posture and movement have to be estimated appropriately. The results of the estimations for this study are as follows:

(1) Estimation method of posture and movement was obtained from an accelerometer and processed by FFT..

(2) Estimation of consumption of energy was processed by FFT from the accelerometer data.

(3) Consumption energy for the daily cycle was estimated but this study should be replicated with a greater number of participants.

REFERENCES

1. T. Sugimoto, et al. "Measurement Method for Activities for Human Daily Living Human without Restriction," *Proceeding of SICE Annual Conference, MP 2-14-2* (Okayama, Japan 2005).
2. Y. Inagaki et al. "Exercise Stress Testing and Systolic Time Intervals" *Japanese circulation journal*, Vol. 43, No. 3 pp.207-213 (1979).
3. J. Hayano "Fitness, Disease and Heart Rate Fluctuation" *The Transportation and Logistics Conference 2002*, No. 11 pp.1-6 (2002).
4. C. James et al. "An investigation of a novel three-dimensional activity monitor to predict free-living energy expenditure" *Journal of Sports Sciences*, Vol. 26 Issue 6, pp. 553-561 (2008).
5. J. Levine et al. "Tracmor system for measuring walking energy expenditure" *European Journal of Clinical Nutrition*, vol. 57, pp. 1176-1180 (2008).
6. S. Rutter "Comparison of Energy Expenditure in Normal-Weight and Overweight Women Using the Caltrac Personal Activity Computer" *International Journal Eating Disorders*, VOL. 15, No. 1, pp. 37 – 42 (1994).
7. T. Ueno, K. Yamahigashi et al. "Study of appropriateness for basal metabolism expenditure for equation of Harris Benedict" *Evaluation and treatment of Nutritiona*, vol. 16, No. 4 pp. 29, (1999).

A Test of Stride Length Measurement with an Accelerometer and a Gyroscope Attached on the Foot

T. Watanabe¹ and Y. Minegishi²

¹ Graduate School of Biomedical Eng., Tohoku University, Sendai, Japan

² Graduate School of Eng., Tohoku University, Sendai, Japan

Abstract— Simplified gait analysis system using wearable sensors based on accelerometers and gyroscopes were focused in this study for rehabilitation of motor function and daily exercise for health. In this paper, a preliminary test of stride length estimation for each step using an accelerometer and a gyroscope attached on the foot was performed with two neurologically intact subjects. Reference signals were obtained from 3D motion analysis system. Although error in stride length estimation varied between subjects and between trials, mean absolute error was acceptable (less than about 10%) except for the 1st step (start of walking) of one subject. For subject B, the mean absolute errors for the 2nd step were less than 5% for all the trials. Experimental results also suggested that precise measurement of tilt angle of the foot and determination of appropriate integration period would realize practical estimation of the stride length using only inertial sensors. Since the sensor unit used in the experiment was not packaged all in one, development of a sensor unit and further tests with the developed sensor would be in the next work.

Keywords— stride length, accelerometer, gyroscope, tilt angle, foot movement.

I. INTRODUCTION

In this study, we aimed to realize simplified gait analysis system using wearable sensors for rehabilitation of motor function and daily exercise for health. Inertial sensors such as accelerometers and gyroscopes have been widely used in many industrial products. In recent years, those inertial sensors have also been used in measurement or analysis of human movements as wearable sensor system because of its shrinking in size and cost. Many studies using these inertial sensors were for detecting gait phase [1-3]. Measurement of joint angle or tilt angle of segment has also been studied using inertial sensors [4-6].

This paper focused on measurement of stride length at every step by using an accelerometer and a gyroscope attached on the dorsum of foot. In order to estimate stride length, a method of using forward acceleration of foot has been studied [7, 8]. In these method, gait phase such as heel-off and foot-flat have to be detected to determine integration period for calculating forward movement velocity

and forward displacement of the foot from acceleration signal, which determines accuracy of the length estimation. Therefore, foot switches or force sensitive registers are sometimes used with inertial sensors for precise estimation. Other methods of stride length estimation use mathematical model with joint angle measurement of lower limb or with acceleration of a different part of the body [9, 10].

In this paper, the method of using an accelerometer and a gyroscope to estimate stride length was tested. The integration period was determined by detecting stationary state of the foot using the accelerometer.

II. STRIDE LENGTH ESTIMATION

The stride length is estimated at each step by using an accelerometer and a gyroscope attached on the foot (Fig.1(a)). Tilt angle of the foot in the sagittal plane, $\theta(t)$, is calculated by the integral of gyroscope output:

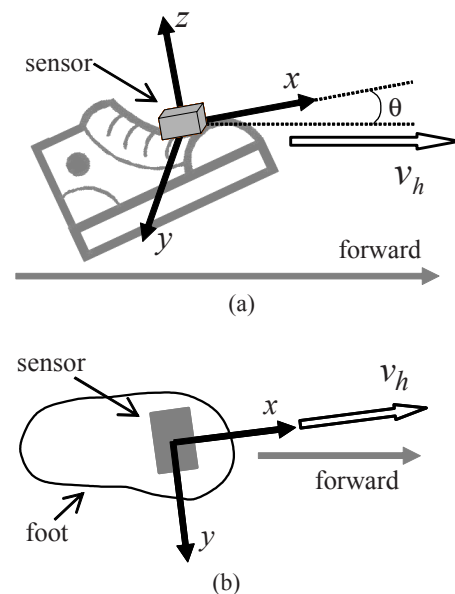


Fig. 1 Attachment of sensors on the foot and velocity in forward direction. Side view (a) and top view (b).

$$\theta(t) = \int_0^t \dot{\theta}(\tau) d\tau + \theta_{init} \quad (1)$$

Here, initial tilt angle θ_{init} is obtained from the accelerometer:

$$\theta_{init} = \arcsin\left(\frac{a_x}{g}\right) \quad (2)$$

Then, the horizontal acceleration can be calculated under the condition that the x and z axes are in the sagittal plane:

$$a_h = a_x \cos \theta - a_z \sin \theta \quad (3)$$

Therefore, traveling distance of the foot can be calculated:

$$L = \int_0^T v_h(\tau) d\tau \quad (4)$$

$$v_h(t) = \int_0^t a_h d\tau + v_{init} \quad (5)$$

Initial value of the integral in eq.(5), v_{init} , can be zero because the integral of sensor signal is calculated during foot movement excluding the stationary state of the foot at the stance phase. In this test, the stationary state was detected by using the accelerometer as follows:

Beginning of the 1st step:

Mean value of acceleration signals of 3-axes is larger than 0.01V (about 0.05G) for three successive samples.

End of the 1st step and the beginning of the 2nd step:

Mean value of acceleration signals of 3-axes is less than or equal to 0.01V (about 0.05G) for six successive samples.

The initial value for calculating the tilt angle of the foot, θ_{init} , is determined by averaging the tilt angle obtained by the accelerometer for those three or six samples.

In the above calculation, the sensors should be attached in exact direction of forward movement. For practical use, misalignment of sensor axis to the traveling direction as shown in Fig.1(b) was corrected in calculating stride length using acceleration signal of the y-axis:

$$L = \sqrt{\left(\int_0^T v_h(\tau) d\tau\right)^2 + \left(\int_0^T v_y(\tau) d\tau\right)^2} \quad (6)$$

In addition, calculated movement velocities of the foot were corrected so as to be 0m/s at the end of the integral by using linear approximation. Because offset level of gyroscope varies during movement causing error in the integral of sensor output, the movement velocities are assumed to be 0m/s at the beginning and at the end of calculation. The

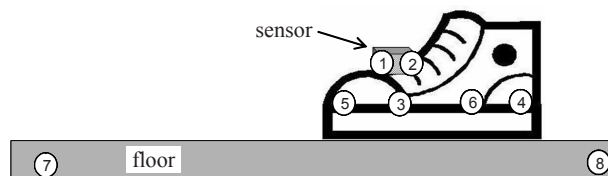


Fig. 2 Positions of markers of 3D motion analysis system.

integral process for the tilt angle, the forward velocity and the forward distance is calculated for each step with their initial values.

III. PRELIMINARY EXPERIMENTAL TEST

A. Method

In order to evaluate the stride length estimation described in the previous section, a 3-axis accelerometer (MM-2860, Sunhayato) and a gyroscope (ENC-03J, Murata) were used. They are packaged separately to measure accelerations and angular velocity of the foot.

The stride length estimated by the sensors was compared with stride length calculated by using marker positions obtained from 3D motion analysis system (OPTOTRAK, Northern Digital). The marker positions are shown in Fig.2. Displacement of the marker No.3 was calculated as the stride length. The sensor signals were acquired by personal computer with marker positions of the 3D motion analysis system simultaneously with a sampling frequency of 120 Hz.

The sensors and markers were attached on the left shoe with adhesive tape. The signals were measured with two neurologically intact subjects and stride length was analyzed off-line after the measurement. The subjects were instructed to start walking with left side step after quiet standing on the level floor. Walking speed was not restricted, but normal speed walking.

B. Result

The results of stride length estimation are shown in Table 1. The ratio of error to its stride length is also shown in this Table as %error. Because of restriction of used motion analysis system, the stride length was evaluated for the 1st and 2nd steps of the left side. A total of 10 trials (5trials for each subject) were analyzed.

Mean absolute error of the 2nd step was smaller than the 1st step for both subjects in comparison of %error. From these results, it was shown that the estimated stride length was acceptable for the 2nd step. Especially, %error was

Table 1 Evaluation results of stride length estimation

(a) subject A								
	3D motion analysis		Sensors		error [cm]		error [%]	
	1st	2nd	1st	2nd	1st	2nd	1st	2nd
1	67.3	137.5	39.1	109.5	-28.1	-28.0	-41.8	-20.3
2	74.3	138.6	65.3	131.2	-9.1	-7.4	-12.2	-5.3
3	80.6	145.1	55.7	127.3	-24.8	-17.8	-30.8	-12.3
4	76.3	156.8	62.1	149.2	-14.2	-7.6	-18.6	-4.9
5	81.7	150.8	70.4	128.6	-11.3	-22.2	-13.8	-14.7
absolute mean					17.5±8.5	16.4±9.0	23.4±12.5	11.5±6.5

(b) subject B								
	3D motion analysis		Sensors		error [cm]		error [%]	
	1st	2nd	1st	2nd	1st	2nd	1st	2nd
1	52.1	134.5	50.0	129.8	-2.2	-4.6	-4.1	-3.5
2	55.7	133.2	59.3	137.0	3.6	3.8	6.5	2.9
3	60.6	139.8	53.2	143.3	-7.5	3.5	-12.3	2.5
4	55.5	129.6	49.8	134.9	-5.6	5.3	-10.1	4.1
5	53.9	134.7	47.3	130.9	-6.6	-3.7	-12.3	-2.8
absolute mean					5.1±2.2	4.2±0.7	9.1±3.6	3.1±0.6

Table 2 Evaluation results of tilt angle measurement of the foot

(a) subject A										
	1st					2nd				
	1	2	3	4	5	1	2	3	4	5
CC	0.974	0.992	0.965	0.990	0.992	0.992	0.994	0.989	0.996	0.990
RMSE	5.84	3.33	7.07	4.40	4.99	6.83	6.62	7.17	7.47	9.42

(b) subject B										
	1st					2nd				
	1	2	3	4	5	1	2	3	4	5
CC	0.999	0.997	0.999	1.000	1.000	0.998	0.999	0.999	0.999	0.994
RMSE	10.00	3.49	16.09	2.18	4.09	8.04	1.55	8.84	16.33	6.93

very small for subject B (less than 5% for all the trials). Although the error varied between trials for Subject A, %error for the 2nd step was about 5% in two trials. As for the 1st step, it was acceptable for Subject B. However, %error of the 1st step was large for Subject A.

IV. DISCUSSION

Error of the stride length estimation varied between subjects and between trials. For subject B, mean absolute error for the 1st and the 2nd steps were less than 10%. For the

2nd step, the mean absolute errors of all the five trials were less than 5%. In the previous work using similar method of stride length estimation with inertial sensors [7], 'mean error' was about 10%. Therefore, by reducing the variability of the error, the method of estimating stride length using inertial sensors described in this paper would be practical.

Mean absolute error [cm] of the stride length estimation was almost same between the 1st and the 2nd steps on both subjects. The stride length of the 1st step was almost half of the length of the 2nd step and there was no large difference in integration period between the 1st and the 2nd steps. That

is, forward movement velocity of the 1st step was smaller than that of the 2nd step. This result suggests that error rate in the length estimation increases in case of slow movements.

Tilt angle obtained by gyroscope was evaluated in order to consider length estimation error. Table 2 shows correlation coefficient (CC) and RMS error calculated by using reference values of the angle obtained from 3D motion analysis system. Strong correlation was found between the estimation error and correlation coefficient of the tilt angle (-0.847), while there was no correlation between the length error and RMSE of the tilt angle (-0.124). It is suggested that pattern of the tilt angle is required to be precise for good length estimation.

However, in the case of the 1st step of Subject B, estimation errors of the trial 3, 4 and 5 were large although their correlation coefficients were very large. This was caused because of tilt angle error and detection error of integration period. For the trial 3, recalculating the stride length using tilt angle obtained from 3D motion analysis system showed that the error reduced to -8.8%. For the trials 4 and 5, the error reduced to -4.6% and -3.8%, respectively, by using tilt angle and different integration period obtained from 3D motion analysis system. For the 2nd step of the subject A, the errors reduced to between -2.1 and 3.6% by using tilt angle obtained by 3D motion analysis system.

In case of Subject A, correlation coefficient was not large for all the trials. Therefore, it is considered that attachment position or attachment method of the sensors for Subject A was not appropriate in the experiment.

V. CONCLUSION

In this paper, a preliminary test of stride length estimation using an accelerometer and a gyroscope attached on the foot was performed. Although error in stride length estimation varied between subjects and between trials, mean absolute error was acceptable (less than about 10%) except for the 1st step of Subject A. For the 2nd step of Subject B, the mean absolute errors were less than 5% for all the trials, which were quite good. It was also suggested that precise measurement of the tilt angle of the foot and determination of appropriate integration period would realize practical estimation of the stride length using only inertial sensors. Since the sensor unit used in the experiment was not packaged all in one, development of a sensor unit and detailed test would be in the next work.

ACKNOWLEDGMENT

This work was supported in part by Miyagi Prefectural Government under the Sendai Advanced Preventive Health Care Services Cluster.

REFERENCES

1. Lau H, Tong K (2008) The reliability of using accelerometer and gyroscope for gait event identification on persons with dropped foot. *Gait Posture* 27(2):248-257
2. Jasiewicz JM, Allum JH, Middleton JW, Barriskill A, Condie P, Purcell B, Li RC (2006) Gait event detection using linear accelerometers or angular velocity transducers in able-bodied and spinal-cord injured individuals. *Gait Posture* 24(4):502-509
3. Selles RW, Formanoy MA, Bussmann JB, Janssens PJ, Stam HJ (2005) Automated estimation of initial and terminal contact timing using accelerometers; development and validation in transtibial amputees and controls. *IEEE Trans Neural Syst Rehabil Eng* 13(1): 81-88
4. Arifin A, Saito H, Watanabe T (2008) An error reduction method of portable, low-cost joint angle sensor system for human movement measurement and control. *IEICE Technic Rep* 108(314): 31-34
5. Findlow A, Goulermas JY, Nester C, Howard D, Kenney LP (2008) Predicting lower limb joint kinematics using wearable motion sensors. *Gait Posture* 28(1): 120-126
6. Dejnabadi H, Jolles BM, Aminian K (2005) A new approach to accurate measurement of uniaxial joint angles based on a combination of accelerometers and gyroscopes. *IEEE Trans Biomed Eng* 52(8): 1478-1484
7. Alvarez JC, Gonzalez RC, Alvarez D, Lopez AM, Rodriguez-Uria J (2007) Multisensor approach to walking distance estimation with foot inertial sensing. *Proc 29th IEEE Eng Med Biol Soc*, 2007, pp 5719-5722
8. Bamberg SJ, Benbasat AY, Scarborough DM, Krebs DE, Paradiso JA (2008) Gait analysis using a shoe-integrated wireless sensor system. *IEEE Trans Inf Technol Biomed* 12(4): 413-423
9. González RC, Alvarez D, López AM, Alvarez JC. (2007) Modified pendulum model for mean step length estimation. *Proc 29th IEEE Eng Med Biol Soc*, 2007, pp 1371-1374
10. Lee SW, Mase K, Kogure K (2005) Detection of spatio-temporal gait parameters by using wearable motion sensors. *Proc 27th IEEE Eng Med Biol Soc*, 2005, pp 6836-6839

Author: Takashi Watanabe
 Institute: Graduate School of Biomedical Engineering, Tohoku University
 Street: 901-7 Complex Build., 6-6-11 Aoba-yama
 City: Sendai
 Country: Japan
 Email: nabet@bme.tohoku.ac.jp

Ankle and Knee Joint Angle Measurements during Gait with Wearable Sensor System for Rehabilitation

Hiroki Saito¹, Takashi Watanabe¹, and Achmad Arifin²

¹Graduate School of Biomedical Engineering, Tohoku University, Sendai, Japan

²Electrical Engineering Department, Institute of Technology Sepuluh Nopember, Surabaya, Indonesia

Abstract— A method of joint angle measurement during gait using wearable sensors for rehabilitation was studied in this paper. The method corrected joint angles measured by gyroscopes using joint angles measured by accelerometers with Kalman filter. Although gyroscopes could measure joint angles, their offset drift caused error in measurement of joint angles. At first, we made up small sensor units consist of a gyroscope and an accelerometer. Then, the method was validated with the developed sensor units in measurement of ankle and knee joint angles of three healthy subjects under walking on short distance pathway and on treadmill for long time. The measured joint angles were compared with reference joint angles measured with optical motion measurement system simultaneously. The result for short distance walking showed low RMS errors and high correlation coefficients (3.19deg and 0.918 for the ankle joint, 2.98deg and 0.993 for the knee joint in average). The result for treadmill walking also showed low RMS errors and high correlation coefficients (3.04deg and 0.960 for the ankle, 4.19deg and 0.994 for the knee in average). Although the measurement accuracy decreased in some of trials of a specific subject because of sensor attachment position, the experimental results suggested that joint angle could be measured with good accuracy independent of measurement period of time, walking speeds and subjects.

Keywords— Gait analysis, Joint angle, Gyroscope, Kalman filter, Accelerometer.

I. INTRODUCTION

A motion measurement system can be effective for objective and quantitative evaluation in rehabilitation of motor function. Optical motion measurement systems (VICON, OPTOTRAK, etc.) and force plates are commonly used in research work and these systems provide accurate motion data. However, these systems have shortcomings that the set-up of the system is not easy, measurement condition is limited and costs of these systems are very high. Therefore, many studies that measured gait parameters with wearable sensors have been reported [1-6]. Since inertial sensors such as a gyroscope and an accelerometer are small, low cost and easy for settings, they are suitable for clinical application.

The purpose of this study is to develop simplified low cost wearable sensor system for gait evaluation with inertial sensors. In this study, we focused on measurement of lower

limb joint angles during gait with gyroscopes. However, unknown initial joint angles and error accumulation in integral value of sensor output caused by offset drift are significant problems on measurement with gyroscopes. In order to reduce the influence of offset drift of gyroscope, Tong et al. [1] applied automatic resetting of the angle in each gait cycle and high-pass filtering. However, automatic resetting cannot reset if the gait is abnormal, and high-pass filtering remove the dc and low frequency information of angles. Applying Kalman filter, Cikajlo et al. [2] corrected shank inclination measured by gyroscope using inclination measured by accelerometer. But they didn't discuss accuracy and didn't show a joint angle because purpose of their study was to determine trigger timing of FES. Findlow et al. [3] estimated ankle, knee and hip joint angles with good accuracy by applying the neural network. But this method needs training for individual settings before measurements in order to estimate good accuracy.

In previous work, we tested the method of using Kalman filter with commercially available tilt sensors based on accelerometer in measurement of knee joint angle [7]. The method could correct offset drift at each time online. It was considered in our additional tests that the accuracy would become better by determining suitable parameter of Kalman filter and by low-pass filtering of accelerometer outputs with very low cut-off frequency. Initial joint angle can also be determined by the accelerometer in this method.

In this paper, we made up small sensor units consist of a gyroscope and an accelerometer. Then, the sensor units were examined in ankle and knee joint angle measurements during gait for short distance of pathway and in treadmill walking for long time comparing with reference angles obtained from optical motion measurement system.

II. METHODS

A. Joint angle estimation using Kalman filter

A gyroscope outputs angular velocity, thus a joint angle is calculated as integral of difference between two sensor outputs, in which the sensors are attached on the adjacent segments. Accelerometer can measure inclination angle of

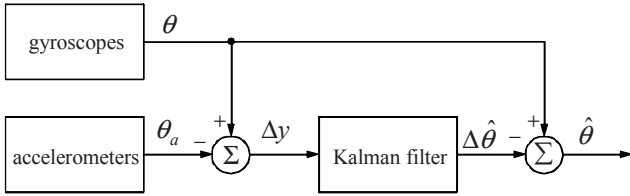


Fig. 1 Block diagram of angle measurement system

segment from inclination of gravitational acceleration. Therefore, a joint angle is calculated from difference of inclination of accelerometers.

Fig. 1 shows the block diagram of the system. θ is the joint angle measured by gyroscopes and θ_a is the joint angle measured by accelerometers. Kalman filter is the method which estimates the state (actual signal) from the observation signal on the system of the state-space model. In our system, Kalman filter estimates the error of the joint angle measured by gyroscopes $\Delta\hat{\theta}$ from difference between angle obtained by gyroscopes and that by accelerometers Δy . Then, estimated joint angle $\Delta\hat{\theta}$ is calculated by subtracting $\Delta\hat{\theta}$ from θ .

The state of the system is represented as the error of the joint angle measured by gyroscopes $\Delta\theta$ and increment of bias offset for one sampling period Δb . That is, the state process is modeled:

$$\Delta\theta_{k+1} = \Delta\theta_k + \Delta b_k + w \quad (1)$$

$$\Delta b_{k+1} = \Delta b_k + w \quad (2)$$

where w is error in measurement with gyroscopes. The state equation is shown by eq. (1) and (2) as follow:

$$\begin{bmatrix} \Delta\theta_{k+1} \\ \Delta b_{k+1} \end{bmatrix} = \begin{bmatrix} 1 & 1 \\ 0 & 1 \end{bmatrix} \begin{bmatrix} \Delta\theta_k \\ \Delta b_k \end{bmatrix} + \begin{bmatrix} w \\ w \end{bmatrix} \quad (3)$$

Observation signal of the system is the difference of two sensors. Therefore observation equation is given as follow:

$$\Delta y_k = \begin{bmatrix} 1 & 0 \end{bmatrix} \begin{bmatrix} \Delta\theta_k \\ \Delta b_k \end{bmatrix} + v \quad (4)$$

where v is error in measurement with accelerometers. On this state-space model, Kalman filter repeats corrections (eq. (5)) and predictions (eq. (6)):

$$\begin{bmatrix} \Delta\hat{\theta}_k \\ \Delta\hat{b}_k \end{bmatrix} = \begin{bmatrix} \Delta\hat{\theta}_k^- \\ \Delta\hat{b}_k^- \end{bmatrix} + \begin{bmatrix} K_1 \\ K_2 \end{bmatrix} (\Delta y_k - \Delta\hat{\theta}_k^-) \quad (5)$$

$$\begin{bmatrix} \Delta\hat{\theta}_{k+1}^- \\ \Delta\hat{b}_{k+1}^- \end{bmatrix} = \begin{bmatrix} 1 & 1 \\ 0 & 1 \end{bmatrix} \begin{bmatrix} \Delta\hat{\theta}_k \\ \Delta\hat{b}_k \end{bmatrix} \quad (6)$$

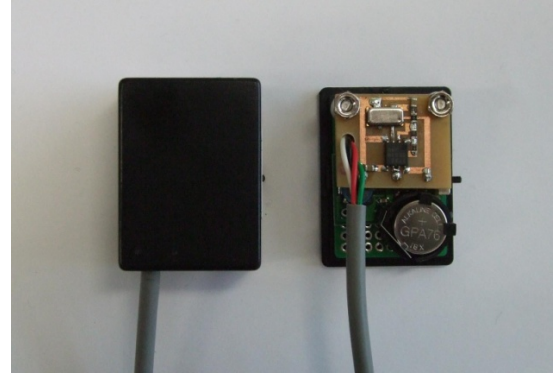


Fig. 2 Sensor unit (30×20×40mm). Outside of sensor unit (left) and inside of sensor unit (right).

where K_1 and K_2 are Kalman gain for $\Delta\theta$ and Δb calculated at each time, respectively. The hat upon a character and the superscript minus represent estimated value and predicted value, respectively. Initial state, $\Delta\hat{\theta}_0^-$ and $\Delta\hat{b}_0^-$, were set 0.

In this paper, we applied stationary Kalman filter instead of normal Kalman filter in order to reduce amount of calculations and to prevent larger error for a while after starting measurement because of the difference of initial state.

B. Sensor unit

Fig. 2 shows the sensor unit made up in our laboratory. Electric power (3.3V) is supplied from inside power source boosted from a button battery (1.5V). The sensor consists of a uniaxial gyroscope (Murata, ENC-03R, Japan) and a 3-axis accelerometer (Freescale, MMA7361L, USA). Two sensors have analogue LPF with cut off frequency of 40Hz and 1500Hz, respectively. Both of the sensors were selected because of low cost and low electric power consumption.

III. EXPERIMENTAL TESTS

A. Experimental Method

The sensor units and the method of using Kalman filter were examined in measurement of ankle and knee joint angles during gait. Three healthy subjects (male, 22-23 years old) participated in this experiment. The sensor units were attached on the foot, shank and thigh of the subject's left leg as shown in Fig. 3. The optical motion measurement system (OPTOTRAK, Northern Digital Inc.) was used to measure reference data for sensor evaluation, and markers were attached on the body as shown in Fig. 3. The sensor signals and marker positions were measured simultaneously by personal computer with a sampling frequency of 200Hz.

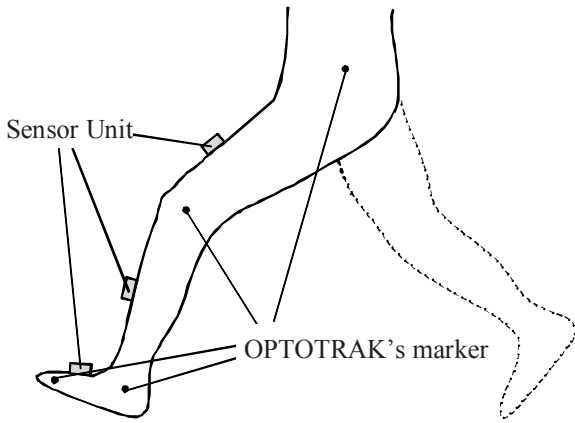


Fig. 3 The attachment location of sensor units and OPTOTRAK's markers

At first, the subjects walked on short distance pathway (about 4m) at 3 speeds (slow, normal, fast). These walking speeds were controlled by themselves. Then, the subjects walked on a treadmill for about 90sec at speeds of 1km/h (slow), 3km/h (normal) and 5km/h (fast). Five trials were performed for each speed of both walking conditions. The parameters of Kalman filter were set for each joint angle with trial and error. Accelerometer outputs were filtered with Butterworth low-pass filter with cut off frequency of 0.5Hz in order to reduce variability caused by differences of walking speeds. For evaluating the accuracy in joint angle measurement of the proposed system, root mean squared error (RMSE) and correlation coefficient (ρ) between measured joint angles and reference values were calculated. All of data processing was implemented with Labview (National Instruments).

B. Results

An example of measured joint angles at the treadmill walking is shown in Fig.4. As seen in Fig. 4, both of ankle and knee joint angle errors due to the offset drift of the gyroscope outputs were reduced by Kalman filter, although the error varied with time (see "Gyroscope only" in Fig.4).

RMSE and ρ are shown in Fig. 5. RMSE and ρ were improved by the proposed method, especially in treadmill walking because measurement time was longer than short distance walking. The standard deviations of RMSE and ρ were also improved. Therefore, it is suggested that the proposed method provides more stable measurement with smaller error. The proposed method showed similar accuracy in both walking conditions. In the short distance walking, average values of RMSE and ρ were 3.19deg and 0.918 for ankle joint angle, and 2.98deg and 0.993 for knee joint angle. In the treadmill walking, they were 3.04deg and 0.960 for ankle joint angle and 4.19deg and 0.994 for knee

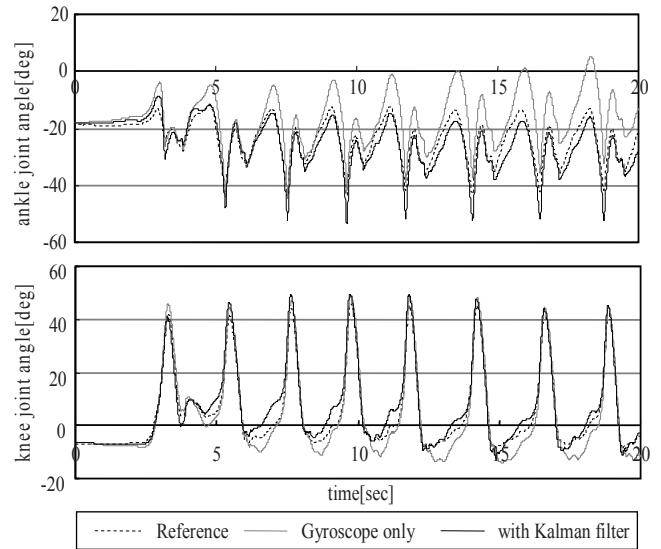


Fig. 4 An example of measured joint angles at treadmill walking (1st trial, slow speed, subject B). In this data, RMSE and ρ were 3.70deg and 0.963 for ankle joint angle and 2.95deg and 0.986 for knee joint angle.

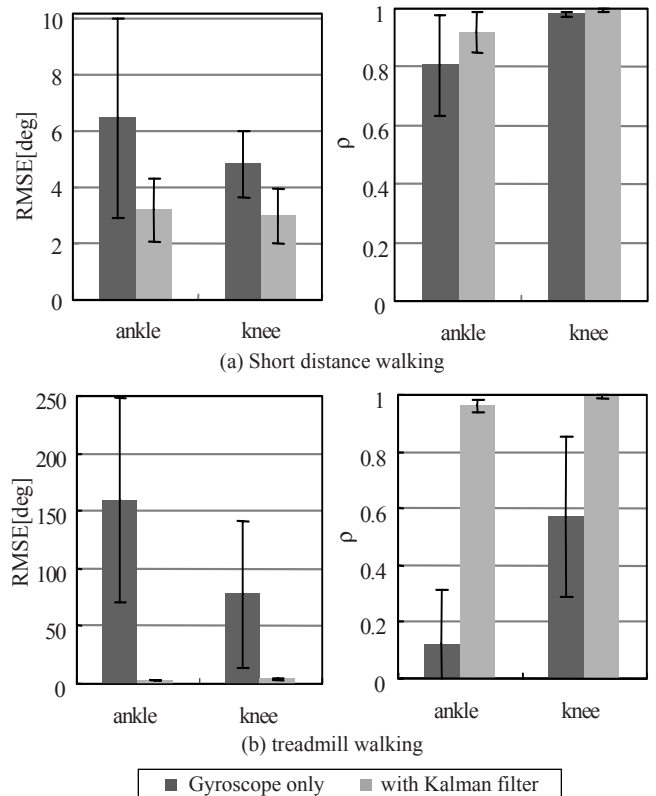


Fig. 5 Evaluation results for measured joint angles. Average and standard deviation obtained from all results of RMSE and ρ are shown.

joint angle. From these data, the proposed method is found to be able to measure without limitation of measurement time.

IV. DISCUSSION

Findlow et al. realized good accuracy on the lower limb joint angle measurement with applying the neural network ($\rho=0.93 - 0.99$, the mean absolute deviation=1.69 - 2.30deg). But the method needs the training of neural network for individual setting, and may not assure the accuracy in irregular gait. The method proposed in this paper could measure joint angles with accuracy of the same level of Findlow's method. Furthermore, our method doesn't need preliminary settings and is able to measure the angles with stable accuracy in any type of gait.

However, some trials showed large error in ankle joint angle measurement. Especially, in the case of slow speed, short distance walking of Subject C, the lowest correlation coefficient was 0.689. We considered that this large error was influenced by attachment location and attachment method of sensor unit on the foot. At the experiment, sensor units were attached directly on the skin with adhesive tape because of preliminary test. There may be the case that the tendon located along the acrotarsium through the ankle joint stands out by toe movements. That is, it seems that the measurement accuracy of the ankle joint angle decreased because the inclination of the sensor was changed by the tendon movements. For the application to rehabilitation, we will make the system to be able to use with shoes and clothes. In that case, it seems that the problem is not caused. However, it is necessary to examine the attachment position and the attachment method of sensor units in the future.

Average values of RMSE and correlation coefficient showed good accuracy even if walking speeds or subjects were different. Therefore, it is expected that the proposed method can measure lower limb joint angles during gait with good accuracy independent of measurement time, walking speeds and subjects.

V. CONCLUSION

In this paper, lower limb joint angle measurements during gait with inertial sensors using Kalman filter were examined. The proposed method successfully reduced joint

angle error caused by offset drift of gyroscope. The results showed that the system could measure joint angles with good accuracy for different measurement conditions and on different subjects. For the application of rehabilitation, it will be necessary to examine the attachment position and the attachment method of sensor units. Additionally, realizing a wireless wearable sensor system with the sensor units and measurement of other gait parameters such as stride length and walking speed is expected.

ACKNOWLEDGMENT

This work was supported in part by Miyagi Prefectural Government under the Sendai Advanced Preventive Health Care Services Cluster.

REFERENCES

1. K. Tong, M.H. Granat (1999) A practical gait analysis system using gyroscopes. *Med. Eng. Phys.*, vol. 21, pp. 87-94
2. I. Cikajlo, Z. matjačić, T. Bajd (2008) Efficient FES triggering applying Kalman filter during sensory supported treadmill walking. *J. Med. Eng. Technol.*, vol. 32, pp. 133-144
3. A. Findlow, J.Y. Goulermas, C. Nester et al. (2008) Predicting lower limb joint kinematics using wearable motion sensors. *Gait & Posture*, vol. 28, pp. 120-126
4. H. Lau, K. Tong (2008) The reliability of using accelerometer and gyroscope for gait event identification on persons with dropped foot. *Gait & Posture*, vol.27, pp. 248-257
5. J.C. Alvarez, R.C. González, D. Alvarez et al. (2007) Multisensor approach to walking distance estimation with foot inertial sensing. *Proc. 29th Annual Conf. IEEE EMBS, Lyon, France, 2007*, pp. 5719-5722
6. S.W. Lee, K. Mase, K. Kogure (2005) Detection of spatio-temporal gait parameters by using wearable motion sensors. *Proc. 27th Annual Conf. IEEE EMBS, Shanghai, China, 2005*, pp. 6836-6839
7. A. Arifin, H. Saito, T. Watanabe (2008) An error reduction method of portable, low-cost joint angle sensor system for human movement measurement and control. *IEICE Technical Report, MBE2008-69, Japan*, pp. 31-34

Author: Hiroki Saito
 Institute: Graduate School of Biomedical Engineering, Tohoku University
 Street: 901-7 Complex Build., 6-6-11 Aoba-yama
 City: Sendai
 Country: Japan
 Email: hiroki.saito@bme.tohoku.ac.jp

Performance of novel dry electrode EEG cap for evoked potential and band-power activity detection.

C. Grozea¹, G. Nolte¹, F. Popescu¹

¹ Fraunhofer Institute FIRST, Berlin, Germany

Abstract— Common applications of electroencephalography (EEG), in both research and clinical practice, are detection of fast, stimulus locked evoked potential (EP) responses and quantification of slower changes in EEG band-power termed event related synchronization/desynchronization (ERD/S). These correspond to categorized electrophysiological phenomena associated with various mental states through prior observations. In this paper we present the technical performance of a dry electrode EEG cap previously introduced for demanding ERD/S applications such as brain-computer interfacing, for trial-averaging applications. Results are shown for N100 auditory evoked potential (AEP) as well as ERD/S EEG spectral estimation. The novel cap can allow for EEG experiments which can be set-up within approx. 5 minutes and provide data of similar quality to those traditionally obtained with gel-based caps, without the need for washing subject's hair or other preparative/follow-up procedures to the experiment.

Keywords— EEG, evoked potential, brain computer interface.

INTRODUCTION

Electroencephalography (EEG) is used as a research tool in brain imaging applications and as a clinical tool, to monitor various mental states, such as alertness, to quantify responsiveness to sensory stimuli, and for biofeedback applications. Typical signal analysis tasks involve the detection of changes in bandpower spectra among physiologically relevant frequency bands (e.g. theta, alpha, beta, gamma), the localization of sources of brain activity, and average responses, time-locked to certain sensory stimuli, which provide average responses (evoked potentials) of varying amplitudes, shapes and latencies. In all of these applications, the set-up of the EEG cap imposes a significant burden of time, support and expertise required, as conductive gel must be expertly applied (and removed by washing after the procedure), the skin sometimes requires slight scratching to improve conductivity, while extra supplies must be inventoried and made available.

In our group, we have developed a dry electrode EEG cap, which was able to achieve high classification accuracies and feedback performance in motor imagination based brain computer interface use [1], which in turn requires accurate, single trial estimation of bandpower changes in

sub-bands in the 8-35 Hz range, whereas the reusable, dry electrodes can render the cap usable within approx. 5 minutes.

An important use of EEG is averaged trial analysis of responses to stimuli, which have been catalogued according to various types of stimuli and the typical shapes of responses (EPs) associated with them [2]. One typical such EP is called the 'N100' auditory stimulus evoked potential (EAP) [3], for which we present results from 2 subjects. Another is Brain Computer Interfacing, which commonly works by single trial detection of subject-specific band-power spatial pattern changes associated with mental states which serve as commands.

METHODS

EEG recording technology

Amplification: A BrainAmp DC 32-channel amplifier setup (BrainAmp, Munich, Germany) was used set for 0.5 μ V resolution. Only 6 channels were used, corresponding to the DryCap's recording channels, with a frontal reference electrode (also dry). No pre-amplification was used (the DryCap being a passive recording device). Hardware filtering for the band 0.1Hz-250Hz was used for recording. The sampling frequency was 1000Hz for EAP determination and 500Hz for BCI use.

Electrodes: The DryCap employs an array of specially plated pins, with 3 for each recording 'arm' (see Figure 1 for picture). The configuration is variable, as the electrodes can be moved along the parietal/central and frontal/occipital directions according to the needs of the experimental protocol. For the EAP detection experiment, the electrodes were more central relative to the BCI set-up. A specially designed plastic molded prototype incorporates the basic design already outlined in [1], with the following enhancements: each electrode arm contains an adjustment screw which may be adjusted by the subject or experimenter as to adjust the pressure on the electrodes as to ensure subjects' comfort and recording quality, and a frontal 'reference' arm slightly above the forehead. Separate, analog measurements of impedance (using a DC current between reference and recording electrode induced by a voltage difference of 4.0 V) has

shown skin to electrode impedances between 60 kΩ and 150 kΩ, with a typical value of 90 kΩ – as opposed to the minimal 1 kΩ impedance that can be achieved with wet electrodes (but is often higher).

Experimental set-ups

EAP experiment: The subjects were seated in front of a computer monitor and table and instructed to relax. Two computer speakers provided a reference tone of 1300 Hz of 45 ms duration at randomly varying intervals between 1.5 and 2.5 seconds at approx. 90dB. 100 such tones were delivered while recording continuously.

BCI: The BCI algorithm and training/testing procedure is the same as in [1] except for the following important modifications: only two types of movement imagination trials were recorded in the training trials (left hand imagination and relaxation), and only 12 trials of each mental task were collected for calibration and classifier training. The entire procedure of Dry-Cap set-up, signal analysis and BCI use (2D control of an open-source computer game “Ibrea-kout2”) lasted approx. 20 minutes per subject. Subjects were given oral and written explanations of the procedures and signed informed consent forms. The live demonstration took place at the Neural Information Processing Systems (NIPS) Conference in December 2008 in Vancouver, Canada.



Fig. 1 Picture of DryCap

RESULTS

The AEP experiment produced EPs shown in Figure 2.

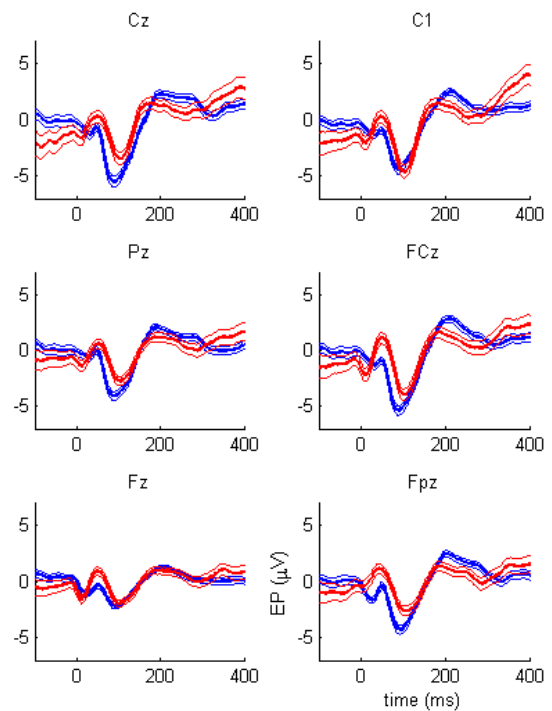


Fig. 2 Results of EP experiment. Evoked potentials averaged over 100 trials. Bracketing top and bottom curves around thick lines indicate +/- standard error of the mean at each time point. Different subjects (N=2) are indicated by different colors.

Power spectra (dB) at O3 electrode for calibration of movement imagination BCI are shown in Figure 3.

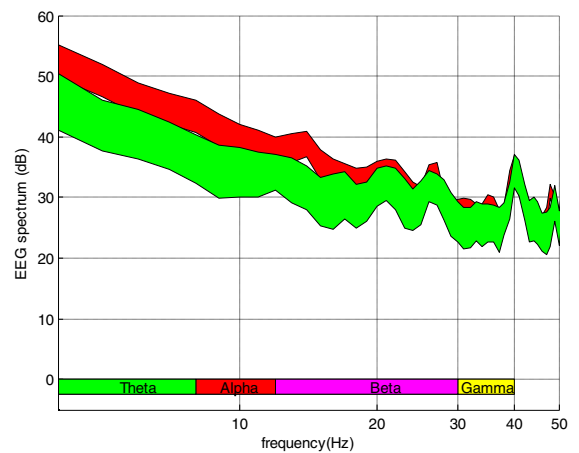


Fig. 3. EEG spectra, averaged over 10 subjects, $\pm\sqrt{2}$ *standard error of the mean of the spectral estimate (the effective std.e. being root mean square of the individual std.e.'s) for left hand movement imagination and relaxation.

The spectra were calculated using an FFT-based, with 1 Hz resolution with averaged 500ms Hamming windows and 250ms overlap.

DISCUSSION

The results shown indicate that despite the dry electrodes having relatively higher impedances, proper digital and analog signal processing yield results comparable to gel-based electrode technology, which may compensate for and may automatically separate recording artefacts. Proper measures being taken, effects of higher impedance have a negligible effect on EP response determination and in determinations of changes in band-power for frequencies below 40 Hz, which is the usual range of interest. In determining absolute spectra further signal processing is necessary.

EEG artefacts can be placed in 6 separate categories: A) muscle artefacts, such as eye, jaw and facial muscles. B) electromagnetic effects of electrostatic charged bodies in motion near the electrodes. C) narrow-band high frequency electrical fields such as 50 or 60 Hz line noise artefact from nearby power lines or similar RF sources D) background electrostatic noise – ‘floating’ random flat spectral noise present in the air E) movement artefact, caused by electrode and/or signal line displacement and F) amplifier noise.

In the case of EP determination, no special treatment is necessary, as long as artefactual signal sources are not locked to the stimulus, the signal to noise ratio being evident in the results shown. In this case, we have obtained signal averages which are entirely consistent with locations, amplitudes and shapes of gel-electrode evoked potentials, in the central and parietal portion of the scalp. Potential clinical applications, where set-up time is of critical importance include intensive care alertness monitoring [4].

Throughout the development of the DryCap, countermeasures to artefact presence have been taken and are continuously being improved upon. Two of the aforementioned artefact sources, muscle artefact and amplifier noise are not specific to dry (higher impedance) electrodes and follow the same treatment otherwise afforded to alternative EEG designs, namely proper recording paradigm design and amplifier/electrode impedance compatibility.

The presence of moving charged bodies can be mitigated by proper grounding, and by further signal conditioning. The results obtained in the live-demo (see spectra in Figure 3) do point out some of the challenges of higher impedance electrodes in determining EEG power spectra. Note that the power spectra obey the ‘ $1/f$ ’ EEG power law [2], while differences in spectra from the two classes are shown poten-

tially in lower frequency ranges (alpha, theta) and more sharply at around 14 Hz. The former effect is likely due to active relaxation and the latter due to the mu-rhythm [5] associated with motor imagination. Note that the ‘wide’ standard error of the mean spectra is mainly due to the fact that each class only contains 12 trials: both inter and intra subject variability in movement imagination ERD/ERS is high [6]. We have already shown smoother ERD/ERS estimates for higher numbers of trials [1] and after linear transformation of EEG data through the Common Spatial Pattern (CSP) algorithm [7] which, by operating on linear combinations of electrodes, is meant to accentuate differences between classes, e.g. between different types of recorded mental activities.

The raw recorded data, in this case, contains a significant 60 Hz peak which is due to the local line noise (not shown). This predictable external narrow band source, once filtered out (with proper anti-alias pre-filtering and tight digital or analog notch-filtering) is not, per se, a significant problem. Other narrow band sources are unlikely, but can occur in ‘noisy environments’: these can be independently measured and accounted for as well. Note that the environment in which this data was obtained, a conference center in a hotel located in a business district, with active demonstration robots nearby, many spectators and attendees using electronic devices is as challenging of an RF and line noise environment as can be reasonably found. Higher impedance generally means higher presence of surrounding (airborne) RF mixed in with the EEG.

Nevertheless 9 of 10 subjects reported that they had some level of control over the cursor in the final ‘feedback’, i.e. game-playing part of the demonstration, while all reported that the cap was comfortable to wear. This follows the basic philosophy of the design: simple, cheap sensors which are more practical than low-impedance designs (i.e. gel electrodes), yet, through the performance of signal processing method, render useful recordings at comparable levels of practical information gained. For ERD/S applications and band-power estimation, simple principles judiciously applied can overcome sources of error. Modulations of EEG spectra from synchronized narrow-band sources are not necessarily problematic in situations where changes in spectra due to different mental activities is needed such as BCI based on movement imagination, or determination of occipital alpha power in applications designed to gage fatigue, as line noise and other synchronized sources are expected to be equally present in recordings of both mental activities, which follow randomized cues. Both external narrow-band, moving charged bodies and muscle artefact have known properties which can help us separate them from EEG, either by their spectral range or by the fact that they are present in all electrodes and emanate from locations outside

the electrode array, rather than having highest amplitude in 'inner' electrodes as mixed EEG sources are, where mixing refers to the recording of single cortical EEG sources in multiple electrodes due to the conductivity of the brain and crania structures. Finally, in our experience, flat, random floating noise has not been a problem at frequencies below 50 Hz except in situations in which skin contact is poor.

The DryCap, as stands, contains 6 recording sites which can be repositioned, frontally, centrally, parietally or occipitally. The basic design, however, allows for simple expansion to 12 or 21 sites which follow standard montage situations. Further signal processing measures, now in development, will be meant to automatically separate EEG from likely artefactual sources, compensate for changing impedances and/or lost contact, and allow for recordings accurate enough for more demanding applications such as real-time inverse modeling of cortical sources. At the present time, detection of band-power modulation below 50 Hz and standard evoked potential determination is well within the potential of the DryCap, which affords the capability of completing important EEG experiments and procedures in a matter of minutes, which is not only a cost and time saving measure, but can also be one of critical clinical importance.

ACKNOWLEDGMENT

This work was funded in part by the European Commission Grant MC-EXT-2004 "Brain2Robot". We thank our colleague Siamac Fazli for his help and support.

REFERENCES

1. F. Popescu, S. Fazli, et al. (2007), Single trial classification of motor imagination using 6 dry eeg electrodes, PLoS ONE 2, no. 7, e637.
2. E. Niedermeyer and F. H. Lopes da Silva, (2005). *Electroencephalography : Basic principles, clinical applications, and related fields*, Lippincott Williams & Wilkins, Philadelphia
3. S. Oray, Z. L. Lu and M. E. Dawson (2002), Modification of sudden onset auditory ERP by involuntary attention to visual stimuli, *Int J Psychophysiol* 43(3): 213-224.
4. P. Tiihonen, J. Kinnunen, et al., A portable device for intensive care brain function monitoring with event-related potentials, (2008) *Comput Methods Programs Biomed* 89(1): 83-92.
5. G. Pfurtscheller, C. Brunner, et. al., (2006), Mu rhythm (de)synchronization and EEG single-trial classification of different motor imagery tasks, *Neuroimage* 31(1): 153-159.
6. S. Fazli, F. Popescu, et al., (2008) Subject independent mental state classification in single trials., *Neural Networks*, In press.
7. B. Blankertz, R. Tomioka, et al. (2008), Optimizing spatial filters for robust EEG single-trial analysis., *IEEE Signal Proc Magazine* 25(1): 41-56.

Development of a shoe-type device for collecting gait information

Yukinobu Sugimura¹, Futoshi Wada², Kenichiro Makino², Taishi Oda², Kenji Hachisuka², Takafumi Ienaga³, Zhimei Yang³, Yoshihiko Kimuro³, Takenori Otawa⁴, Naoto Yukitake⁴, Futoshi Koriyama⁴, Takuro Tsuji⁴ and Chikamune Wada¹

¹ Graduate School of Life Science and Systems Engineering, Kyushu Institute of Technology, Kitakyushu, Japan

² Dept. of Rehabilitation Medicine, School of Medicine, University of Occupational and Environmental Health, Kitakyushu, Japan

³ Institutes of System, Information Technologies and Nanotechnologies, Fukuoka, Japan, ⁴ Logical Product Corporation, Fukuoka, Japan

Abstract— We are developing a measurement device by means of which gait information can be obtained that cannot be obtained by existent devices. We are also evaluating the effectiveness of the device in rehabilitation programs. The final goal of our work is to realize a space where patients can execute their rehabilitation routines at any time. In this paper, we report the outline of our novel measurement device. That is to say, we describe our real-time measurement technique for measuring the position and angle of the feet to obtain the gait information, as well as our method of presenting the gait information.

Keywords— gait analysis, wearable device, center of pressure

I. INTRODUCTION

The doctor and physical therapist combine the 3D motion analyzer and the ground reaction force measurement system to reach an objective judgment of the patient's gait on the hospital site. However, the use of these devices is complicated, and these methods have limitations as to the space required, number of steps required and real-time data collection. So, these devices have limited use, in the hospital and at the rehabilitation site. In addition, it is not possible to give guidance for home use for these devices. Therefore, we are developing a measurement system which obtains the gait information more easily. In past research, a device containing sensors was developed [1]. We intend to develop a shoe-type device for rehabilitation which employs a presentation screen. If we succeed in developing this measurement system, the gait information in various environments can be obtained and guidance at home becomes possible. In this paper, we report the outline of our measurement device.

II. OUTLINE OF OUR MEASUREMENT DEVICE

Figure 1 shows the outline of our system. Our device consists of a shoe-type device onto which sensor units (gyroscope, accelerometer, ultrasonic sensor, pressure sensor), a wireless module, an electronic tag to collect the data from

the shoe-type device, and a display for the gait information are installed. The shoe-type device collects the gait information (step length, step width, pressure, etc.). The collected data are sent to a personal computer by a wireless module. The gait information necessary for rehabilitation is displayed on the screen based on the collected data. The doctor, physical therapist and patient can understand the state of the gait based on the information shown on the screen. In this paper, we describe our trial shoe-type device and the method of displaying the information generated from the data collected by the shoe-type device.

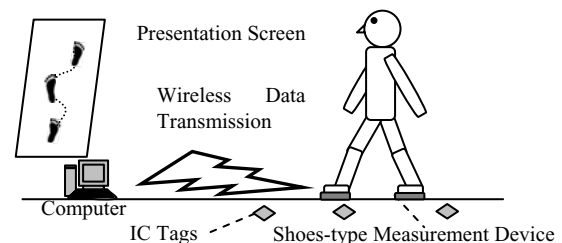


Fig.1 Outline of the system

The specifications of the shoe-type device are described below. In past research, accelerometers, gyroscopes and other types of sensors were used to measure the gait [1]. We are researching the possibility of determining the position of the feet by making measurements in the double-support phase using an ultrasonic sensor and a gyroscope, and in the swing phase using an accelerometer and a gyroscope. In our trial shoe-type device, the range of measurement of the ultra-sonic sensor and the highly accurate gyroscope. The gyroscope was set to measure a maximum foot angle of 300 deg/s during walking. Three ultra-sonic receivers were arranged on the inside of the foot, and two ultra-sonic transmitters were arranged around the heel on each foot, to measure a step length about 0.6 m during walking. We used four pressure sensors, which were sufficient to measure the change in foot sole load during walking. Figure 2 shows the trial shoe-type device. The ultra-sonic sensor and gyroscope set the shoe

for the rehabilitation. The pressure sensor set the insole made of carbon.



Fig.2 The shoe-type device

The method of displaying the gait information obtained from the shoe-type device is described next. The doctor, physical therapist and patient should be able to understand the gait information easily. Conventionally, a second display and a three-dimensional display are considered to be good display methods. But, it is necessary to display the gait information to the doctor, physical therapist and patient at the same time. The opinion of the rehabilitation staff is crucial, and it is important to decide the best method based on their recommendations. We demonstrated in the laboratory (University of occupational and environmental health, JAPAN), and the screen was constructed based on physical therapists' opinions. Figure 3 shows the constructed screen. In Figure 3, the x-axis is the walking direction, the y-axis is the direction perpendicular (right and left) to the walking direction, and the footprints show two left steps and three right steps. Thus, the user easily grasps the position and direction of each foot. The points on the footprints in Figure 3 show the center of pressure in each foot. The present problem is to develop a way of guiding the foot to a pre-set position. In the future, we will develop a display for the swing phase.

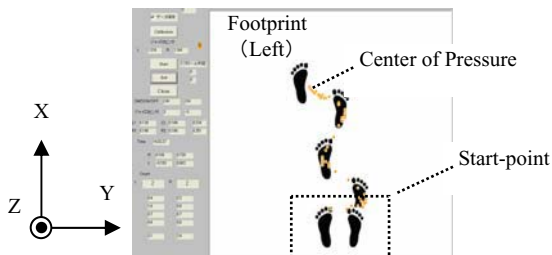


Fig.3 Presentation screen for the gait information, results of the foot position measurement

III. THE RESULTS OF FOOT POSITIONAL MEASUREMENT

We compared the foot positions as given by our device and by the 3D motion analyzer. Figure 4 shows the results of the

foot position measurements. In Figure 4, the circles represent the foot positions given by our device, and the triangles show the foot positions given by the 3D motion analyzer. The step lengths given by our device and by the 3D motion analyzer were almost the same. However, the step widths were different in some cases. Our device is able to measure the step length within the range of 0.1~0.6 m. We will have to improve the accuracy of our device.

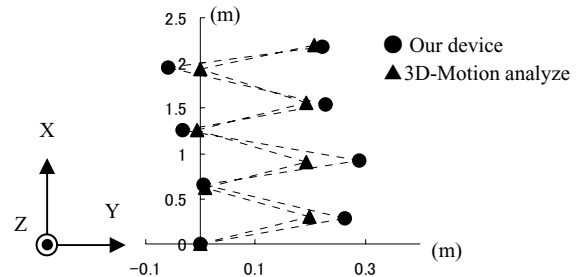


Fig.4 Comparison of the foot position data given by our system and by the 3D motion analyzer

IV. CONCLUSIONS

In this paper, we described the outline of our new gait measurement system and our presentation screen for accessing the gait information. In the future, we must improve the accuracy of the foot position data, and evaluate the swing phase using an acceleration sensor and a gyroscope. Thereafter, we will attempt rehabilitation by means of this system, and examine whether or not the walking ability of the patients improves.

ACKNOWLEDGMENT

This study is supported by the Strategic Information and Communications R&D Promotion Programme (SCOPE) of the Ministry of Internal Affairs and Communications of Japan.

REFERENCES

1. Bamberg, S.J.M., et al. (2008) Gait Analysis Using a shoe-Integrated Wireless Sensor System, IEEE Transactions on Information Technology in Biomedicine, 12(4), 413-423

Author: Yukinobu Sugimura
 Institute: Kyusyu Institute of Technology
 Street: Wakamathu
 City: Kitakyusyu
 Country: Japan
 Email: sugi_kyutech_@live.jp

Optical measurements for guidance during deep brain stimulation surgery

Karin Wårdell¹, Johannes Johansson¹, Johan Richter^{1,2} and Patric Blomstedt³

¹Department of Biomedical Engineering, Linköping University, Sweden

²Department of Neurosurgery, Linköping University Hospital, Sweden

³Department of Neurosurgery, Umeå University Hospital, Sweden

Abstract— Deep brain stimulation (DBS) is an established treatment for Parkinson's disease and related movement disorders. The success of DBS is highly dependent on electrode location, electrical parameter settings and the surgical procedure. In this paper an overview of the current status of optical measurements for intracerebral guidance performed during DBS implantation is presented. Laser Doppler perfusion monitoring and/or reflection spectroscopy measurements have been done in relation to more than 70 DBS lead implantations towards targets in the deep brain structures. The techniques have also been compared with impedance monitoring, and simulation of the measurement depth has been done with Monte Carlo technique. These studies show that grey-white matter boundaries can be determined with a resolution higher than for both impedance measurements and magnetic resonance imaging.

Keywords— Deep brain stimulation, stereotactic neurosurgery, intracerebral guidance, laser Doppler perfusion monitoring, reflection spectroscopy

I. INTRODUCTION

One of the most common and effective procedures for relieving movement related disorders such as Parkinson's disease is deep brain stimulation (DBS) [1]. During the intervention, an electrode is inserted towards a target area along a pre-calculated trajectory determined from magnetic resonance imaging (MRI) or computed tomography (CT). Optimal clinical outcome requires not only safe and accurate navigation towards the target but also a well defined target area specified depending on symptom. Common target areas are the subthalamic nucleus (STN), zona incerta (Zi), globus pallidus internus (GPi) or various parts of the thalamus. Other structures are also currently under investigation and some are found useful for relief of symptoms like pain and psychiatric illness.

Inter- and inpatient variations and displacement of the brain occurring in conjunction with the surgical procedure can result in a deviation of the target during implantation from the pre-planned coordinates determined from a MR or CT batch of images. This can result in a suboptimal effect of the stimulation as well as in stimulation induced side-effects. The introduction of the electrode does further carry

a potential risk of damaging blood vessels with subsequent hemorrhages. Recent studies show a bleeding rate for DBS-implantation between 1-6 % depending on target areas used for the DBS procedure [1, 2].

It is not possible to fully compensate for deviations during probe insertion by the available neuronavigation systems, which are based on pre-operative images. Intracerebral recordings, such as physiological mapping using e.g. micro-electrode recording (MER) [3] or impedance measurements [4] are possible ways to overcome this problem. MER has a very high resolution but may introduce an increased risk of bleeding [5, 6]. Impedance has a limited resolution but can distinguish between cerebral spinal fluid and white fibre tracts. A possible way to increase the precision, accuracy and safety during stereotactic procedures is to use intracerebral recording of optical signals. Giller and colleagues [7] have used diffuse reflectance spectroscopy during stereotactic neurosurgery in patients undergoing DBS implantation and the described technique shows promising results in detecting grey-white matter boundaries. These findings have been confirmed by us and we have also shown that a fixed wavelength e.g. 780 nm, the same wavelength applicable as in laser Doppler systems, can be used for detection of brain tissue boundaries [8]. In this paper an overview of the current status of optical measurements performed by us during DBS implantation is presented.

II. MATERIALS AND METHODS

Recordings have so far been done with laser Doppler perfusion monitoring (LDPM) and/or reflection spectroscopy in more than 70 DBS implantation procedures at the University Hospitals in Linköping and Umeå. The study was approved by the respective local ethics committees (D No. M182-04) and all patients gave their informed consent.

Stereotactic imaging was performed after placement of the Leksell[®] stereotactic frame model G (Elekta Instrument AB, Sweden). Direct anatomical targeting [9] for the STN, GPi and Zi was performed on stereotactic MRI studies using a 1.5 T scanner. During surgery an electrode (l = 190 mm, \varnothing = 1.5 mm) with optical fibres was used to create

tracts for the DBS-electrodes along the pre-calculated trajectory. Measurements of optical signals (LDPM and reflection spectroscopy) were performed along the trajectory from the cortex towards the target area. This was done either continuously while the surgeon manually inserted the electrode with an as even speed as possible (lasting for 1-2 minutes), or in steps ranging from 2-10 mm along the trajectory. A final measurement was always done with both techniques in the target area.

III. RESULTS

These measurements demonstrate that it is possible to distinguish between grey and white matter as well as between different target areas [8, 10, 11]. This has been achieved with both the LDPM and spectroscopy system. Furthermore the LDPM system makes it possible to monitor the microcirculation along the trajectory as well as in the deep brain structures. An example of simultaneous measurements of the total light intensity (representing the grayness of the tissue) and the microvascular blood flow towards the STN is presented in Fig. 1.

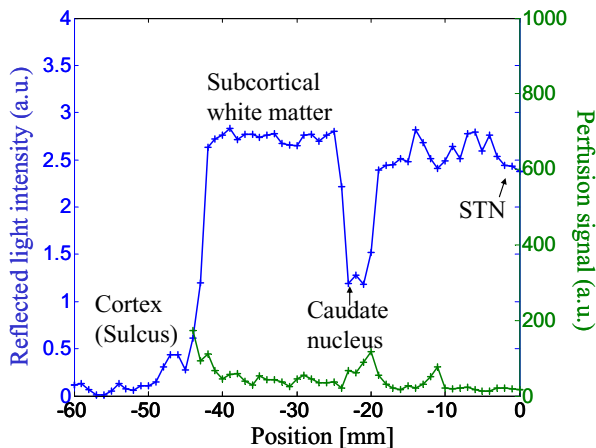


Fig. 1 Recording of microvascular perfusion (green curve) and total light intensity (blue curve) during probe insertion towards STN. Measurements were done in 1 mm steps.

IV. DISCUSSION AND CONCLUSIONS

The techniques have recently also been compared with impedance monitoring [11], and simulation of the measurement depth has been done with Monte Carlo technique [12]. These studies show that the resolution of the optical measurements is higher than for both impedance and magnetic resonance imaging. The next step in the project is to investigate the relation between microvascular blood flow and blood vessels, and to compare the optical technique

with other intracerebral methods such as microelectrode recording. Furthermore, a multi-center study for investigation of the applicability of "bar-codes" to targets commonly used for DBS implantation will be undertaken.

REFERENCES

- [1] A. L. Benabid, S. Chabardes, J. Mitrofanis, and P. Pollak, "Deep brain stimulation of the subthalamic nucleus for the treatment of Parkinson's disease," *Lancet Neurol*, 8; 67-81, 2009.
- [2] D. K. Binder, G. Rau, and P. A. Starr, "Hemorrhagic complications of microelectrode-guided deep brain stimulation," *Stereotact Funct Neurosurg*, 80; 28-31, 2003.
- [3] R. E. Gross, P. Krack, M. C. Rodriguez-Oroz, A. R. Rezai, and A. L. Benabid, "Electrophysiological mapping for the implantation of deep brain stimulators for Parkinson's disease and tremor," *Mov Disord*, vol. 21; S259-S283, 2006.
- [4] L. Zrinzo and M. Hariz, "Impedance recording in functional neurosurgery," in *Textbook of stereotactic and functional neurosurgery*, P. L. Gildenberg, A. M. Lozano, and R. Tasker, Eds., 2008.
- [5] M. I. Hariz, "Safety and risk of microelectrode recording in surgery for movement disorders," *Stereotact Funct Neurosurg*, 78; 146-57, 2002.
- [6] R. S. Palur, C. Berk, M. Schulzer, and C. R. Honey, "A metaanalysis comparing the results of pallidotomy performed using microelectrode recording or macroelectrode stimulation," *J Neurosurg*, 96; 1058-62, 2002.
- [7] C. A. Giller, H. Liu, D. C. German, D. Kashyap, and R. B. Dewey, "A stereotactic near-infrared probe for localization during functional neurosurgical procedures: further experience," *J Neurosurg*, 110; 263-73, 2009.
- [8] J. Antonsson, O. Eriksson, P. Blomstedt, A. T. Bergenheim, M. I. Hariz, J. Richter, P. Zsigmond, and K. Wårdell, "Diffuse reflectance spectroscopy measurements for tissue type discrimination during deep brain stimulation," *J Neural Eng*, 5; 185-190, 2008.
- [9] M. I. Hariz, P. Krack, R. Melvill, J. V. Jorgensen, W. Hamel, H. Hirabayashi, M. Lenders, N. Wesslen, M. Tengvar, and T. A. Yousry, "A quick and universal method for stereotactic visualization of the subthalamic nucleus before and after implantation of deep brain stimulation electrodes," *Stereotact Funct Neurosurg*, 80; 96-101, 2003.
- [10] K. Wårdell, P. Blomstedt, J. Richter, J. Antonsson, O. Eriksson, P. Zsigmond, A. T. Bergenheim, and M. I. Hariz, "Intracerebral microvascular measurements during deep brain stimulation implantation using laser Doppler perfusion monitoring," *Stereotact Funct Neurosurg*, 85; 279-86, 2007.
- [11] J. D. Johansson, P. Blomstedt, N. Haj-Hosseini, A. T. Bergenheim, O. Eriksson, and K. Wardell, "Combined Diffuse Light Reflectance and Electrical Impedance Measurements as a Navigation Aid in Deep Brain Surgery," *Stereotact Funct Neurosurg*, 87; 105-113, 2009.
- [12] J. D. Johansson, I. Fredriksson, K. Wårdell, and O. Eriksson, "Simulation of reflected light intensity changes during navigation and radio-frequency lesioning in the brain," *Submitted, J Biomed Optic*, 2009.

ACKNOWLEDGEMENTS

The study was supported by the Swedish Governmental Agency for Innovation Systems (Vinnova), the Swedish Foundation for Strategic Research (SSF) and the Swedish Research Council (VR).

Author: Karin Wårdell
 Institute: Department of Biomedical Engineering
 Street: Linköping University
 City: 581 85 Linköping
 Country: Sweden
 Email: karwa@imt.liu.se

Trial Study of a Power Presentation Method for Upper-Limb Orthoses

Chikamune Wada¹, Futoshi Wada², Hiroataka Iwata³, Naoki Chidiwa³, Akio Tsutsumi³,
and Kenji Hachisuka²

¹ Graduate School of Life Science and Systems Engineering, Kyushu Institute of Technology, Kitakyushu, Japan

² Rehabilitation Medicine, University of Occupational and Environmental Health, Kitakyushu, Japan

³ ARIZONO ORTHOPEDIC SUPPLIES Co.,Ltd, Kitakyushu, Japan

Abstract— We are developing an upper-limb movement mechanism which is driven by push and pull forces in order to realize human-friendly orthoses. In this paper, we propose a new device which can move the upper limbs without a rotatory center, and describe its feasibility. From the results, it was found that our method can move the upper limbs to some extent.

Keywords— Upper Limb, Orthosis, Motion, Assist.

I. INTRODUCTION

Recently, different kinds of assistive devices for upper-limb movement have been developed. Especially in Japan, robot technology is used to create such devices. The HAL (Hybrid Assistive Limb) [1] and the Muscle Suit [2] are two such forefront technologies.

The HAL has an exoskeleton frame, with motors located on the joints between frame sections. The user wears the exoskeleton frame and his/her arm/leg is moved by the exoskeleton frame due to the movement of the frame by the motors. The important thing when using the HAL is for the rotatory center of the motor to coincide with the rotatory center of the arm, because otherwise the motor-driven frame movement might burden the arm. In order to avoid any discrepancy between the rotary centers, the exoskeleton frame should be constructed by taking the arm length of the user into consideration.

The Muscle Suit is made up of an exoskeleton frame and artificial muscle actuators which are driven by air pressure. The Muscle Suit cannot realize radial flexion and ulnar flexion of the hand and pronation and supination of the forearm. Moreover, some actuators might even be obstacles to certain motions.

Therefore, we would like to construct an assistive device which can move the arm without burdening it or interfering with its movement; our method is expected to realize all the natural arm movements.

In this paper, we introduce our proposed device and describe its feasibility.

II. PROPOSITION OF A NEW METHOD OF DRIVING AN ASSISTIVE DEVICE FOR UPPER-LIMB MOVEMENT

Our planned device is composed of orthoses, an athletic supporter and actuators. The orthoses are linked by actuators which output the necessary driving force through expansion/contraction. We hypothesize that the optimal arrangement of the actuators and the optimal control of the driving force will contribute to the creation of an assistive device without a rotatory center. Figure 1 shows a conceptual diagram showing assisted palmar flexion. The front sides of the hand orthosis and the forearm orthosis are linked by an actuator which contracts. Meanwhile, the reverse sides of the hand orthosis and the forearm orthosis are linked by an actuator which extends. Thus, if the two types of actuators are operated at the same time, it is easy to imagine that our device will bend the hand without burdening the wrist joint, because the load to the hand is supported by two actuators.

An actuator which can output driving force for expansion as well as contraction does not yet exist, but is currently under development. We would like to begin this research on the assumption that this type of actuator will be ready for use in the near future.

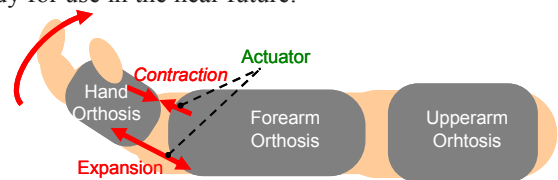


Fig. 1 Example of assisted movement

III. FEASIBILITY STUDY OF OUR DEVICE

First of all, it is important to confirm whether our device can be constructed or not. In this experiment, we had no actuator, so the orthoses were linked by threads, and the examiner pulled the threads to move the orthoses. By pull-

ing the threads, the situation where the actuator contracts and the gap between the orthoses decreases is mimicked. On the other hand, because the threads cannot extend by themselves and the gap between the orthoses cannot be widened by the threads themselves, other threads were pulled in order to mimic the expansion of the gap.

The experimental results show that eight joint motions can be realized: pronation, supination, radial flexion, ulnar flexion, flexion, extension, palmar flexion and dorsiflexion. Figure 2 shows the thread arrangement and the movement of the left arm.

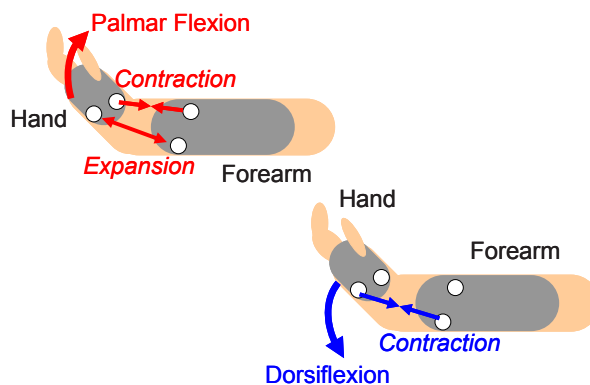
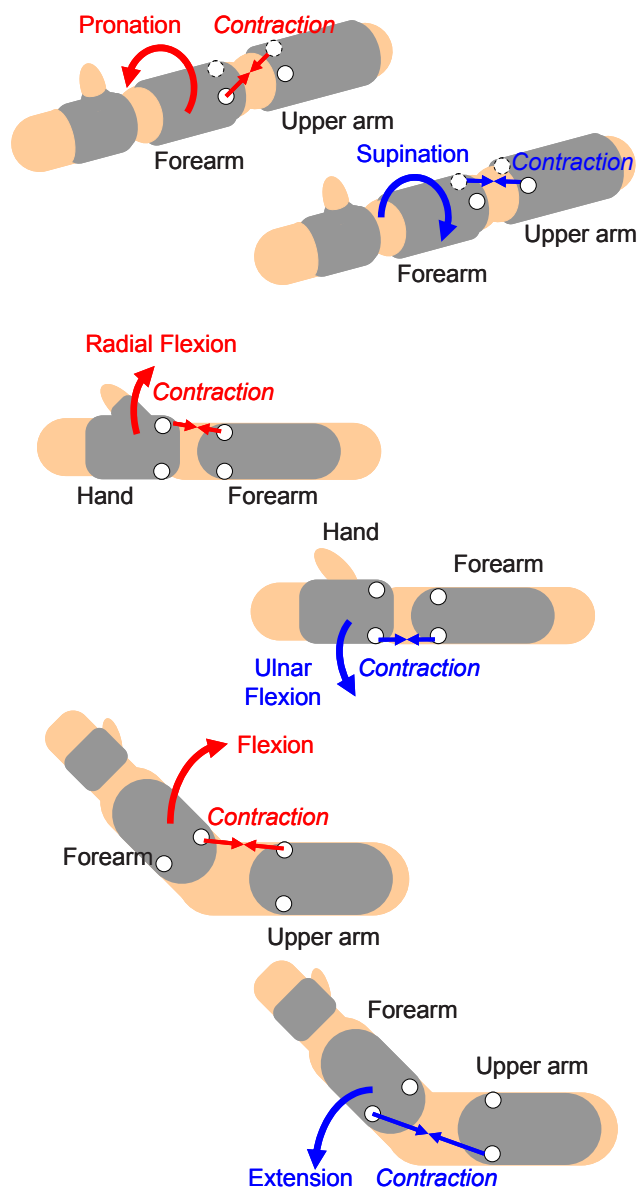


Fig. 2 Examples of joint movement by means of our method

IV. DISCUSSION AND CONCLUSION

The athletic supporter used in this experiment had a certain amount of stiffness. Therefore, the joint was supported to some degree, and one thread (contraction/expansion) was sufficient to move the upper limb. However, in palmar flexion, two threads (contraction and expansion) were necessary. Because of the limitations of the experimental setup, we could not apply two forces via two threads for all arm movements. We believe that joint stiffness could result if two forces were applied in certain cases. We will design a new experimental setup to try to modulate the joint stiffness. Also, we would like to evaluate our method quantitatively by using a motor and an air cylinder.

ACKNOWLEDGMENT

We would like to express our gratitude for contribution of Mr. Nobuyoshi Ujifuku to this research.

REFERENCES

1. Kawamoto H, Sankai Y. (2005) Power assist method based on phase sequence and muscle force condition for HAL. *Advanced Robotics* 19, 7, 717-734
2. Kobayashi H, Suzuki H, Nozaki H et al. (2007) Development of power assist system for manual worked by muscle suit. 16th IEEE International conference on robot and human interactive communication 332-337

Author: Chikamune Wada
 Institute: Kyushu Institute of Technology
 Street: Hibikino 2-4, Wakamatsu-ku
 City: Kitakyushu
 Country: Japan
 Email: wada@life.kyutech.ac.jp

Movement of Lower Extremity – Development of a Portable System for Movement Analysis

H. Grip¹, O. Gustavsson¹, F. Öhberg¹, U. Edström¹, C. Häger-Ross², and R. Lundström¹

¹ Dept of Radiation Sciences, Dept Biomed Engineering and Informatics, Umeå University Hospital, Umeå, Sweden

² Dep. of Community Medicine and Rehabilitation, Umeå University, Umeå, Sweden

Abstract— Today there is no efficient and user friendly method to continuously register, quantify and evaluate human movements. Hip- and knee joint kinematics is an area that has a large clinical interest and a large need of evidence based documentation. There are advanced movement measurement systems, measuring three dimensional movements with a high degree of accuracy. Such systems suffer from limitations when it comes to measurements in a clinic or in a natural setting, for example in the home environment of the patient, since such systems demands a specialised laboratory environment. The systems are also expensive to buy and maintain. Another important factor is the lack of good and easy-to-use tools to analyse and evaluate movements for medical applications.

The long term aim is to develop a portable and easy-to use measurement system to quantify movement ability in upper or lower limbs. In this study, the aim was to evaluate reliability and precision of a custom developed portable system based on gyroscopic sensors.

Keywords— movement analysis, gyroscopic sensors, kinematics, knee.

I. INTRODUCTION

Musculoskeletal disorders (MSD) and pain are among the most common health problem and one of the most common reasons for health consultation in western countries. Symptom of MSD appears in the back, neck, shoulders and the upper limbs as well as in the hip and lower limbs. Movement analysis is a necessary tool in the assessment of such disorders, which gives a greater understanding of musculoskeletal processes in both normal and disease states. Observatory (or functional) movement analysis, is a technique based on visual inspection for qualitative and systematic observation of an individual's movement pattern [1]. It focuses on differences between optimal and abnormal movement patterns, based on body segments relative positions and body orientation in comparison to the global reference system. It is time-consuming and the registration of body movement and postures clearly depend on the observer's observation capacity, skills and motivation. Objec-

tive gait analysis is used as a clinical decision tool for orthopaedic surgery [2] and in the rehabilitation of children with cerebral palsy [3]. The most commonly applied technique in clinical gait laboratories and in research on the musculoskeletal system are optoelectronic cameras and reflective skin markers [2, 4]. Optoelectronic systems provide movement data with very good precision. Although such advanced technology is available, it is rarely used in the assessment of physical handicap and musculoskeletal disorders. There are several reasons: Long-term registration of movements is difficult since measurements must be conducted in a gait laboratory. There is a great lack of standardized protocols and sophisticated tools for movement analysis of other areas than gait, such as head and upper limb movement. Optoelectronic system demands specially trained personnel for executing measurement as well as for data analysis, since the data output is in form of three-dimensional skin marker co-ordinates that need to be transformed into joint angles. Finally, the placement of the markers is essential, since different placements may give a great variation in the joint angle calculations [5].

To overcome these shortcomings, we have developed a novel portable movement analysis system which is based on 3-axial gyroscopes and accelerometers. The advantages of this method is that the movement sensors can easily be attached to the limb that is to be examined, the placement on the limb will not critically effect the calculated joint angle, and that the system is portable so that data registration can be done outside a laboratory.

The aim of this study was to evaluate reliability and precision of a custom developed portable sensor system based on gyroscopic sensors. The sensor system was evaluated by simultaneous measurements with a high precision optical system. Natural movements such as squat were studied.

II. MATERIAL AND METHODS

A. Movement sensor system

The measurement system consists of a battery powered unit with a microprocessor that communicates with up to

four three axial gyroscopic sensors (Analog devices Adis16350). The measured signals can either be stored directly on a memory card or be wirelessly transmitted to a PC or PDA. A custom made PC software visualizes the signals in real time and allow us to store the data in different file formats (c3d or ASCII). The dynamic range of the gyroscopes is ± 300 degrees/s and the data is recorded with a sample frequency of 256 Hz and with a resolution of 14bits.

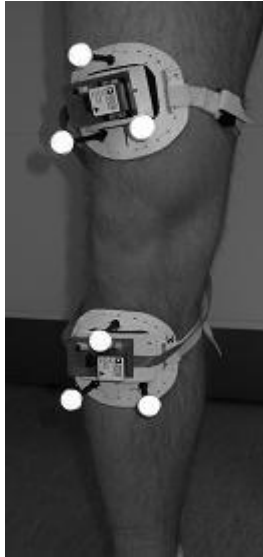


Fig. 1 Illustration of measurement system setup for measurement of knee joint movements. The sensor was placed in the centre of each marker cluster. Two marker clusters were used, one on the thigh and one on the shank.

B. Measurement protocol

Pilot measurements of the knee joint angle were performed on one test subject. Informed consent was obtained from the subject prior to participating, and all procedures were conducted according to the Declaration of Helsinki. Each test person performed ten knee bendings at a comfortable speed. Prior to the knee bendings, two calibration movements were performed: 1) Outward rotation of thigh and shank 2) Flexion of thigh and shank.

C. Measurement setup

Measurements were performed in a movement laboratory with our developed sensor system (Sample frequency 256 Hz) and the optoelectronic system (Sample frequency 240 Hz) simultaneously. The optoelectronic system consisted of five ProReflex cameras, retro-reflective markers, and additional software (Qualisys Track Manager). Two rigid

marker clusters with three markers each were attached on the test person, one on the thigh and one on the shank (Fig 1). The movement sensors were attached in the middle of each cluster to approximately align the co-ordinate systems.

D. Data pre-processing

The movement of the shank relative to the thigh was used to describe the knee joint angle. The Euler convention was used, dividing the angle into three components: flexion/extension, abduction/adduction and inward/outward rotation. The calibration movements were used to align the co-ordinate systems of each measurement system. The helical axis (Grip 2008) for extension and inward rotation was calculated. The helical axis of extension was set to new common X axis and inward rotation was set to new common Z axis. The Y axis was set to the cross product of these two axes.

Angle calculations were different for the two measurement systems. **Optoelectronic system:** Euler angles of the knee joint were obtained from marker cluster co-ordinates using rigid body calculations [4, 6]. Marker data was low-pass filtered using a Butterworth filter with frequency cut-off at 6 Hz prior to angle calculations. **Sensor system:** Euler angles were obtained from the gyroscopic signal (given in degree/s) by transformation to a new common co-ordinate system and use appropriate integration methods [7]. Offset was removed prior to integration.

E. Statistics

To be able to test and visualise the difference between the two systems (i.e., sensor and marker based) a Bland-Altman plot was calculated followed by a paired t-test using the null hypothesis that there are no difference between the two systems. To be able to use the Bland-Altman statistics the optoelectronic signal was resampled to the sample frequency of the sensor signal.

III. RESULTS

Example of the knee angle, measured with the two systems, is shown in Fig 2. The mean difference was 3.6 ± 1.9 SD degrees for flexion/extension.

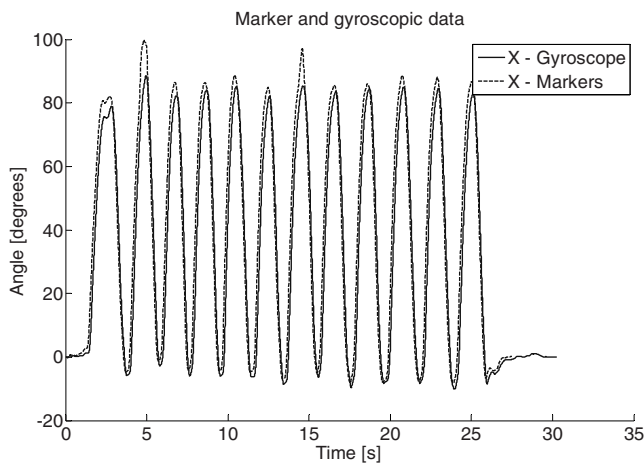
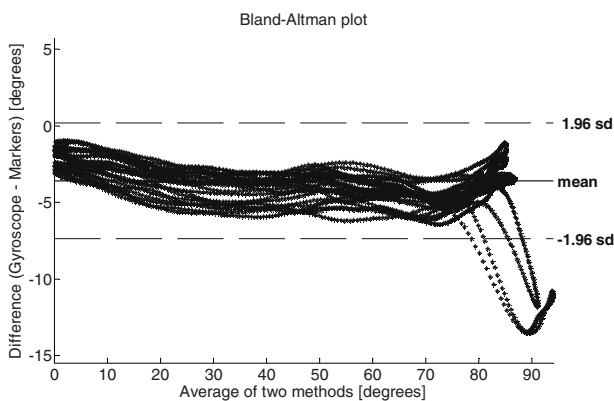


Fig. 2 Flexion of the knee during knee bendings (squat), measured simultaneously with the sensor system (grey) and the optoelectronic system (black).

The result from the Bland-Altman analysis is shown in Fig 3 and the following paired t-test shows that the null hypothesis is rejected at a significant level of 5%.



3 Bland-Altman plot showing the difference between the optoelectronic and sensor system.

IV. CONCLUSIONS

The pilot measurement shows a high agreement between the optoelectronic system and the developed movement sensor system for flexion even though the null hypothesis was rejected. Also there is a systematic difference between the two systems, indicated as a mean difference that deviates from zero in the Bland-Altman plot in Fig 3. Also, there is a tendency that there exists a negative trend in the Bland-Altman plot (seen in Fig 3). However, this can probably be explained by a small drift in the sensor signal

that can be removed using e.g., a static Kalman filter. Another factor that affects the calculations is how the common helical axes are oriented. This can be minimised by using appropriate calibration routines. Measurement on a larger group and test-retest reliability must be performed. Further development of the calibration routines will be performed to improve measurements of adduction and inward/outward rotation. When combining the portable system with a thorough in-depth analysis of body movement and physical activity, it will have a great impact on the assessment of musculoskeletal disorders such as work-related pain conditions, chronic whiplash associated disorders, post-stroke arm, hip replacement after hip arthritis etc.

ACKNOWLEDGMENT

We thank K-G Nilsson, Department of Orthopaedics, University Hospital, Umeå, Sweden for his advice. This project was funded by the European Union's regional development fund Goal 2.

REFERENCES

1. Hirschfeld, H. (1992), On the integration of posture, locomotion and voluntary movement in humans: normal and impaired development. Stockholm, Karolinska Institutet, Thesis
2. Patrick J (1991), Gait laboratory investigations to assist decision making Br J Hosp Med, 1991, 45:35-7
3. Cook RE, Schneider I, Hazlewood ME, Hillman SJ, Robb JE (2003) Gait analysis alters decision-making in cerebral palsy, J Pediatr Orthop, 23:292-5
4. Grip H, Sundelin G, Gerdle B, Karlsson JS (2008), Cervical helical axis characteristics and its center of rotation during active head and upper arm movements-comparisons of whiplash-associated disorders, non-specific neck pain and asymptomatic individuals. J Biomech, 41:2799-805
5. Gorton (2009), Assessment of the kinematic variability among 12 motion analysis laboratories, Gait Posture 29:398-402
6. Zatsiorsky (1998) Kinematics of human motion. Pennsylvania: Human Kinetics Pub.
7. Zhou H, Stone T, Hu H, Harris N, (2008), Use of multiple wearable inertial sensors in upper limb motion tracking, Med Eng Phys, 30:123-33

Author: (Helena Grip)
 Institute: Department of Biomedical Engineering and informatics
 Street: Umeå University Hospital
 City: SE-90185 Umeå
 Country: Sweden
 Email: Helena.grip@vll.se

The role of the sEMG signal processing in the field of the Human Movement Analysis

S. Conforto

Department of Applied Electronics, University Roma TRE, Roma, Italy

Abstract— The role of surface ElectroMyoGraphy in human movement analysis is outlined by using a novel view. As reported in the most recent contributions appeared in the literature sEMG can be used extensively to assess the muscular synergies adopted by the Central Nervous System to control motor tasks. Muscular patterns revealed in agonist, antagonist and synergist muscles give insights on motor control through the use of parameters such as amplitude, timing and spectral characteristics. Modifications of these parameters reveal motor strategies that are implemented by modulating the motor units recruitment process. Recruitment and synchronization, that are further peripheral signs of central mechanisms, can then be assessed by properly processing sEMG signals. These new findings move the use of sEMG signals from the description of the movement to the inferential study about motor learning (re-learning), adaptation and control. Some technical issues on sEMG recording and processing need to be overcome and extensively assessed in order to interpret correctly the information extracted from signals. Several interesting future scenarios for sEMG use are outlined in this paper. If these preliminary proposals will have a future sEMG could be used to propose a new generation of Brain Neural Controlled Interfaces where the Neural contribution, to be interpreted as the motor neural command, will give inferences about the Brain contribution, and will allow to open new scenarios in the assistive technology field.

Keywords— sEMG, Muscular Synergies, Motor control, Human Movement Analysis, BNCI.

INTRODUCTION

Physiologists used for more than two centuries electromyography (EMG) to monitor muscular activity by using the relationship between the mechanical contraction and the current that can be detected when muscles contract (Galvani's revelation) [1]. This current can be recorded both invasively and non-invasively by using respectively wires (or needles) inserted into the muscle, or electrodes placed over the skin surface overlying the muscle investigated. While the invasive techniques provide information about the activity originated in small volumes (few cubic millimeters) of the muscles, the non-invasive one, namely surface EMG (sEMG), refers to large "superficial" mass of muscle tissue (that is mass composed almost exclusively of superficial fibers) and correlates to the mechanical outcome [2].

The diatribe between the two recording techniques fulfilled the scientific literature for years [3]. Nowadays, these techniques are interpreted as complementary instead than in competition, and are adopted on the basis of both the de-

sired information to be extracted and the population to be investigated. sEMG is preferable when dealing with children, elderly, sedentary patients and athletes [4] and for studies and applications belonging to the general framework of the human movement analysis [5].

In this contribution I would like to discuss sEMG and human movement analysis by speculating about the real contribution that sEMG, being influenced by both peripheral (waveforms and durations of the motor unit action potentials) and central factors (neural input) [6], can provide to the field. The movement and the posture of the human body can be studied by using different points of view that jointly contribute to understand the physiological mechanisms driving the movement of body segments. A possible list of these aspects could be: execution of movement, acquisition of motor competencies (that is motor learning or re-learning after damage), implementation of control strategies. The question I would like to deal with is then: may I understand the motor control strategies by observing the execution of motor tasks? In other words: is sEMG a suitable approach to link the execution of movement (i.e. the biomechanics) to the strategies that the Central Nervous System (CNS) implements to realize a well defined motor paradigm? If this is the case, sEMG could become an important driver to increase knowledge on CNS and, from an applicative point of view, could candidate itself as a new actor for a new generation of Brain Neural Controlled Interfaces (BNCI). In these devices sEMG will provide the Neural contribution in terms of motor neural commands and will allow to infer about the Brain mechanisms. The range of applications is large and ranges from rehabilitation protocols to assistive technology tools devoted to patients with residual motor abilities.

I will try to answer to the question by reviewing the drawbacks, the advantages and the future potentialities of sEMG as a driver of information on motor control. The assessment of the muscular patterns for all the muscles (agonist, antagonist and synergist) during the execution of motor tasks can be a signature of the paradigm implemented at the central level and can infer about central processes such as motor learning (or re-learning, occurring during rehabilitation), neuromuscular adaptation and motor control. The muscular co-activation, that is if and how long muscles work together, expresses the muscular synergy implemented to execute the motor task, so that modifications of the co-activation scheme during the exercise can be signs of central control interventions. This can be seen in muscular synergies that occur during gait initiation and represent anticipatory postural adjustments implemented by feed-forward

control strategies [7]. The quantitative assessment of the muscular activation patterns is based on amplitude and timing of the sEMG signal. The amplitude of sEMG gives insights on the force exerted during a task, and the sEMG amplitude of the synergist and agonist muscles represent an implementation of control schemes. In this sense even the assessment of motor unit synchronization by sEMG provides information on force production [8]. The issues related to sEMG processing have to be carefully assessed since they influence the information extraction. The need for processing techniques operator independent, adaptive on signal characteristics, and as much as possible running in real-time is highly requested. This paper will examine some technical issues related to both recording and processing sEMG signals, and then will review some experimental results presented in the literature which appear particularly promising for future scenarios.

TECHNICAL ISSUES

Recording techniques

Even if sEMG signal is mainly related to the number of motor units activated during a motor task and to their discharge rate, various factors can influence the signal and then affect its correct interpretation [9]. Taking apart the physiological factors, such as fiber membrane and motor unit properties, that influence the signal and affect the interpretation of results, other factors related to the experimental setup have to be taken into account. Among the latter, generally known as non-physiological factors, it is worth to remember the crosstalk (contamination by a nearby muscle's electrical activity) and the motion artifacts (induced by the movements of the electrodes and/or cables). Moreover a correct use of sEMG should consider that since the recording comes from a large superficial mass of muscular tissue the information provided lacks in sensitivity. It is possible that this limit will be partially overcome by higher spatial resolution techniques, such as the ones implemented by double differential or Laplacian electrode arrangement [10]. These approaches have shown sensitivity and selectivity levels comparable to invasive recording techniques.

Motion artifacts can be controlled by fixing all the cables carefully, using pre-amplified electrodes, and high-pass filtering of the signal. They have been minimized in the recent wireless acquisition systems. On the other hand, crosstalk is more difficult to counteract even if the use of double differential electrode configuration [11] and a correct positioning of the electrodes on any muscle [12] may reduce it. Linear arrays of electrodes can help in identifying cross-talk components [13]. Moreover, crosstalk is one of the main drawbacks of surface recordings; it becomes destructive when dealing with the assessment of muscular synergies. In fact, in that case it affects the overall signals

and makes a confounding effect on the estimate of muscular co-activations. Besides the techniques based on cross-correlation [14], recent proposals [15] deal with processing data by fuzzy techniques to distinguish cross-talk from co-activation by using soft criteria.

The assessment of co-activation, that is the understanding of coordinated task-specific synergies, implies the need for multichannel recording to provide simultaneous observations of the temporal and spatial distribution of multiple muscle activities [7]. Different subsets of muscles can be chosen on the basis of the motor task.

A further complication in muscular synergies assessment comes from the so called "regionalization effect" [16], that is the occurrence of different muscular patterns in different regions of the same muscle. Regionalization effects are not well known yet but they appear important to understand the muscular patterns of variations with respect to the mechanical load during the exercise. Arrays of surface electrodes can be used to explore these regional variations.

sEMG processing

Information provided by sEMG is strictly related to some parameters which can describe muscular patterns completely. Amplitude, timing and mean spectral frequency of sEMG provide this description and their simultaneous interpretation could infer on central mechanisms driving the muscular synergies. Amplitude of sEMG signals is provided by the estimation of the signal envelope. Techniques used during routine applications lack for generalization and are not operator independent. They are based on rectification and low-pass filtering of the signal, where the cut-off frequency of the filter is set according to the velocity the motor task is executed (typical values proposed in literature are in the range 9-13 Hz [17]). Further approaches are based on RMS values (for the first proposal see [1]) which do not overcome the previous drawbacks. A fully adaptive approach to envelope estimation has been proposed theoretically in [18, 19] and then applied in [20]. This technique allows an automatic determination of the optimal instantaneous cut-off frequency of the smoothing filter and is therefore suitable for non-stationary signals such as the muscular patterns describing dynamic and/or fatiguing protocols. Moreover, the approach is operator-independent, so that a comparison of results among different labs is made easier.

The detection of the timing of muscular patterns is generally based on algorithms that apply a threshold on sEMG envelopes. The results of such a detection are considerably affected by the filtering procedures and give rise, as demonstrated in [21], to muscular activation phases smoother in amplitude and longer in duration as far as the cut-off frequency of the low pass filter is reduced. When the timing information is important, that is for clinical and diagnostic reasons but also for inference about central strategies, more

sophisticated and automatic algorithms [22, 23] have to be chosen. Clinical and experimental studies claim for well defined normalization procedures to obtain muscular activation patterns being independent from both the velocity used to execute the motor task and the maximal level of muscular contraction that different subjects could exert [4, 7].

Spectral information of sEMG signals that historically has been devoted to the assessment of the electrical signs of muscular fatigue, nowadays seems to play a wider role as indicator of the strategies driving the recruitment of motor units. This new and interesting result [24] opens a scenario where sEMG signal, giving information on recruitment, could be used to monitor the learning (re-learning) and adaptation process. The techniques used to extract spectral parameters (e.g. mean and median spectral frequency) are mainly based on FFT approach. When dealing with time-varying characteristics and dynamic physiological phenomena the processing must move toward time-frequency techniques with real-time implementation [25].

As a final remark it is important to outline the importance of an integrated multimodal sEMG information [26] that considering several parameters simultaneously could increase the knowledge and the comprehension of muscular instances of CNS mechanisms. In this direction a first contribution to assess the muscular status during exercise has been proposed in [27] where amplitude and mean spectral frequency are estimated simultaneously and in real-time to code a particular muscular status.

FUTURE SCENARIOS

Recently several works have used sEMG to understand the control mechanisms of CNS driving human movement. This concept can be applied in various contexts ranging from clinical diagnosis, to motor control research, to sport performance assessment. In this paragraph I would like to remember a few recent studies that in my opinion underline some promising scenarios for the future use of sEMG.

In sport sciences, cycling has been often proposed as a means to understand the link between sEMG and muscular synergies. In [28] muscular patterns obtained by sEMG have been evaluated for reference purposes. Chapman and co-workers [29] use muscular patterns as an index to monitor motor learning and adaptation during prolonged pedaling training. The modifications of muscular patterns are proposed as modifications of motor control and recruitment mechanisms. In fact, the acquisition of skilled motor competencies is accompanied by a decrease of: amplitude and duration of muscular patterns [30], amplitude variability [31], co-activation duration [30, 32, 33]. In [4] sEMG multichannel recordings during cycling are used to understand the recruitment strategies and to optimize the training for an optimal performance. sEMG patterns as muscular recruitment indicators have been proposed also in [16] where

modifications of amplitude and timing in different regions of the ankle extensor muscles in man have been quantified to link regional changes in muscle function to a range of mechanical demands. The observed regional changes have been interpreted as signs of motor control and optimization.

The same author in [24] presents sEMG and its spectral characteristics as a novel way to monitor recruitment patterns in motor units populations. This position opens wide scenarios for non-invasive assessment of motor control mechanisms driving mechanical force modulation. A further contribution in this direction is the one proposed by Gronlund and coworkers in [6] where skewness statistic on sub-band filtered monopolar sEMG is used to determine motor unit synchronization. This contribution is worth for at least a pair of physiological reasons: i) functional evaluation of the motoneurons during voluntary contractions; ii) inference on central control mechanisms by linking motor unit synchronization and mechanical force production [8, 34].

sEMG as a balance control indicator as been assessed in [35] with a study about the influence of visual information and adaptation on muscle activity and movement during standing perturbed by calf muscle vibration.

Without any doubt the interpretation of sEMG as a suitable physiological indicator for central paradigms of motor control is the most claimed in the recent literature. To strengthen this point and to conclude these brief remarks, I would like to cite the opinion by Frigo and Crenna who represent influential groups in the field of human movement analysis. In [7] the sEMG characterization of muscle synergies involved in particular phases of gait such as steady-state [36] or initiation and termination [37, 38] is considered as a way of increasing “diagnostic capabilities in gait analysis by enabling deeper insight into locomotor coordination strategies and gait-related postural control mechanisms”.

CONCLUSIONS

This contribution has “explored” a novel point of view about sEMG and its use in human movement analysis. The opinion I have argued about, reflects a recent trend of the scientific literature where sEMG appears as a good candidate to link the way of moving (i.e. the biomechanics) to the motor control paradigms. This recent view increases the importance of sEMG and enlarges its role by adding to the movement description the inference about central mechanisms for motor learning, adaptation and control. The contributions appeared in the literature in the last months present very interesting results and open future promising scenarios for sEMG utilization. If all the signs will be respected, this will open the way for a new generation of BNCI using sEMG as a predictor of central mechanisms. These interfaces will be very useful for assistive technologies and for new rehabilitation protocols: sEMG as a simultaneous indicator of residual motor abilities and control mechanisms could be

used as a means of communication with the environment. An example of this approach is the one presented in the European Project TREMOR where sEMG is used by a multimodal BNCI for tremor control.

ACKNOWLEDGMENT

The Biolab3 group is highly acknowledged for the support in this work and a special thank is addressed to my mentor Prof. Tommaso D'Alessio. Financial support has been provided by the European Union Commission, within FP7 action ICT-2007.7.2 "Accessible and Inclusive ICT", under contract number grant number ICT-2007-224051 TREMOR "An ambulatory BCI-driven tremor suppression system based on functional electrical stimulation".

REFERENCES

- Basmajian JV, De Luca CJ. (1985) Muscle alive (electromyography). Williams & Wilkins, Baltimore.
- Frigo C, Shiavi R. (2004). Applications in movement and gait analysis. *Electromyography: physiology, engineering and noninvasive applications*. Wiley-Interscience, Hoboken.
- Sutherland, D. (2001) The evolution of clinical gait analysis part I, kinesiological EMG. *Gait Posture* 14: 61–70.
- Hug F, Dorel S, (2009), Electromyographic analysis of pedaling: a review. *J Electromyogr Kinesiol* 19(2):182-198.
- Kleissen RF, Buurke JH, Harlaar J, Zilvold G, (1998), Electromyography in the biomechanical analysis of human movement and its clinical application. *Gait Posture* 8(2):143-158.
- Grönlund C, Holtermann A, Roeleveld K, Karlsson JS, (2009), Motor unit synchronization during fatigue: a novel quantification method. *J Electromyogr Kinesiol*. 19(2):242-251.
- Frigo C, Crenna P (2009), Multichannel SEMG in clinical gait analysis: a review and state-of-the-art. *Clin Biomech* 24(3):236-245.
- Yao W, Fuglevand AJ, Enoka RM (2000), Motor-unit synchronization increases EMG amplitude and decreases force steadiness of simulated contractions *J Neurophysiol* 83:441–452.
- De Luca, CJ (1997) The use of surface electromyography in biomechanics. *J. Appl. Biomech.* 13(2): 135–163.
- Huppertz HJ, Disselhorst-Klug C, Silny J, Rau G, Heimann G (1997) Diagnostic yield of non invasive high spatial resolution EMG in neuromuscular diseases. *Muscle Nerve* 20: 1360–1370.
- van Vugt JPP, van Dijk JG (2000) A convenient method to reduce cross talk in surface EMG. *Clin. Neurophysiol.* 112:583–592.
- Hermens HJ, Freriks B, Disselhorst-Klug C, Rau G. (2000) Development of recommendations for SEMG sensors and sensor placement procedures. *J Electromyogr Kinesiol* 10:361–374.
- Merletti R, Farina D, Gazzoni M (2003) The linear electrode array: a useful tool with many applications. *J Electromyogr Kinesiol* 13:37-47
- Morrenhof JW, Abbink HJ, (1985) Cross-correlation and cross-talk in surface electromyography. *Electromyogr Clin Neurophysiol* 25:73–79
- Disselhorst-Klug C, Schmitz-Rode T, Rau G (2009) Surface electromyography and muscle force: Limits in sEMG–force relationship and new approaches for applications *Clin Biomech* 24:225-235.
- Wakeling JM, (2009), The recruitment of different compartments within a muscle depends on the mechanics of the movement, *Biol. Lett.* 5: 30–34.
- Nielsen J, Arendt-Nielsen L, Pedotti A (1994) Power spectrum analysis of the rectified electromyogram during gait for normals and patients. *J. Electromyogr. Kinesiol.* 4:105–115.
- D'Alessio T (1984) Some results on the optimization of a digital processor for surface EMG signals *Electromyogr Clin Neurophysiol.* 24(7):625-43.
- D'Alessio T (1985) Analysis of a digital EMG signal processor in dynamic conditions. *IEEE Trans Biomed Eng.* 32(1):78-82.
- D'Alessio T, Conforto S (2001) Extraction of the envelope from surface EMG signals. *IEEE Eng Med Biol Mag.* 20(6):55-61.
- Kadaba M, Wooten M, Gainey J, Cochran G (1985) Repeatability of phasic muscle activity, performance of surface and intramuscular wire electrodes in gait analysis. *J. Orthopaed. Res.* 3: 350–359.
- Bonato P, D'Alessio T, Knaflitz M (1998) A statistical method for the measurement of muscle activation intervals from surface myoelectric signal during gait. *IEEE Trans. Bio-Med. Eng.* 45: 287–299.
- Staude G (2001) Onset detection in surface EMG signals: a systematic comparison of methods. *Eur. J. Appl. Signal Proc.* 1: 67–81.
- Wakeling JM (2009) Patterns of motor recruitment can be determined using surface EMG. *J Electromyogr Kinesiol* 19: 199–207.
- Conforto S, D'Alessio T (1999) Real time monitoring of muscular fatigue from dynamic surface myoelectric signals using a complex covariance approach, *Med Eng Phys.* 21:225-34.
- Conforto S, D'Alessio T (2001) An integrated tool for EMG signal processing in movement analysis, in *Computer Methods in Biomechanics & Biomedical Engineering – 3* (J. Middleton, M. L. Jones, N.G. Shrive e G. N. Pande eds.), Gordon and Breach Science Publishers, pp. 251-253.
- Conforto S, Schmid M, Bibbo D, D'Alessio T (2008) Assessment of muscular status from surface electromyography during dynamic protocols, *Proceedings of XVII ISEK Congress, Niagara Falls, Ontario, Canada, 2008.*
- Balasubramanian V, Jayaraman S (2009) Surface EMG based muscle activity analysis for aerobic cyclist. *J Bodyw Mov Ther.* 13(1):34-42.
- Chapman AR, Vicenzino B, Blanch P, Hodges PW (2008) Patterns of leg muscle recruitment vary between novice and highly trained cyclists *J Electromyogr. Kinesiol.* 18(3):359-71.
- Osu R, Kamimura N, Iwasaki H, Nakano E, Harris CM, Wada Y, et al. (2004) Optimal impedance control for task achievement in the presence of signal-dependent noise. *J Neurophysiol* 92:1199–215.
- Schneider K, Zernicke RF, Schmidt RA, Hart TJ (1989) Changes in limb dynamics during the practice of rapid arm movements. *J Biomech* 22:805–17.
- Milner TE (2004) Accuracy of internal dynamics models in limb movements depends on stability. *Exp Brain Res* 159:172–84.
- Osu R, Franklin DW, Kato H, Gomi H, Domen K, Yoshioka T, et al. (2002) Short- and long-term changes in joint co-contraction associated with motor learning as revealed from surface EMG. *J Neurophysiol* 88:991–1004.
- Halliday DM, Conway BA, Farmer SF, Rosenberg JR (1999) Load-independent contributions from motor-unit synchronization to human physiological tremor. *J Neurophysiol* 82:664–75.
- Patel M, Gomez S, Lush D, Fransson PA (2009) Adaptation and vision change the relationship between muscle activity of the lower limbs and body movement during human balance perturbations *Clin Neurophysiol.* 120(3):601-609.
- Jonkers I, Stewart C, Spaepen A (2003) The complementary role of the plantarflexors, hamstrings and gluteus maximus in the control of stance limb stability during gait. *Gait Posture* 17: 264–272.
- Crenna P, Do MC, Brénière Y (2001) Motor programmes for the termination of gait in humans, organisation and velocity-dependent adaptation. *J. Physiol. London* 537:1059–1072.
- Mickelborough J, van der Linden ML, Tallis RC, Ennos AR (2004) Muscle activity during gait initiation in normal elderly people. *Gait Posture* 19:50–57.

Author: Silvia Conforto
 Institute: Department of Applied Electronics
 Street: Via della Vasca Navale 84
 City: Rome
 Country: Italy
 Email: conforto@uniroma3.it

Effects of Acupuncture in the Ischemic Model of Diabetes Mellitus Rats

S. Choi^{1,2}, G.-J. Lee^{1,2}, C.-S. Yin³, S.-K. Choi⁴, S.-W. Kang², S.-J. Chae^{1,2}, J.-H. Park^{1,2}, K.-S. Kim^{1,2},
Y.-H. Park^{1,2}, and H.-K. Park^{1,2,5}

¹ Department of Biomedical Engineering, School of Medicine, Kyung Hee University, #1 Hoeki, Dongdaemun-gu, Seoul, 130-702, Korea

² Healthcare Industry Research Institute, Kyung Hee University, Seoul, 130-702, Korea

³ Acupuncture and Meridian Science Research Center, Kyung Hee University, Seoul, 130-702, Korea

⁴ Department of Neurosurgery, Kyung Hee Medical Center, Seoul, 130-702, Korea

⁵ Program of Medical Engineering, School of Medicine, Kyung Hee University, Seoul, 130-702, Korea

Abstract— Acupuncture has been a time honored therapy to be effective for emergency conditions as an ischemic stroke. Glutamate excitotoxicity is seen as the major mechanisms for neuronal death, ischemic injury. An eleven vessel occlusion (11VO) was used as a diabetes mellitus rat model of global ischemia. Changes of the extracellular glutamate releases, cerebral blood flow and electroencephalogram were observed using real time monitoring system with a sampling frequency of 256 Hz and three periods including control of 10 min, occlusion of 10 min and reperfusion of 40 min. Animals were divided into two groups as control and acupuncture. Acupuncture group was stimulated manually with acupunctures on GB34 and GB39 acupuncture sites on both hind limbs during the occlusion period. While reduction level of blood flow during the occlusion period and hyperemia during the reperfusion period was not different between groups, peak concentration of extracellular glutamate levels were significantly lower in the acupuncture group ($p < 0.01$). This study revealed that acupuncture stimulation showed glutamate moderating effect in such a devastating ischemic condition as 11VO model, which maybe a possible mechanism of acupuncture effect for ischemic stroke.

Keywords— Acupuncture, eleven vessel occlusion, diabetes mellitus, glutamate, cerebral blood flow.

I. INTRODUCTION

Ischemic stroke is one of the leading causes of death and dependency. Global aging calls for more attention to stroke than ever, considering its impact on health and increasing prevalence. Acupuncture therapy has been one of main modalities applied to stroke patients in Korea with anecdotal reports in the acupuncture medicine field. A recent review recommended further acupuncture research for stroke rehabilitation based on its widespread use, promising results, lower cost and the insufficient quality of the past researches [1]. In ischemia, neuronal survival is dependent on the process of energy deprivation and resupply. Accumulated extracellular glutamate aggravates and amplifies the impact of ischemic injury [2]. Real time *in-vivo* monitoring of glutamate has been tried using amperometric biosensor

technology with successful application in the field of research. Electro-acupuncture has been reported to attenuate glutamate excess in ischemic injury in common carotid artery occlusion model when acupuncture sites of GV11 and GV16. In this study, we observed the effects of manual acupuncture on neurotransmitter releases using devastating ischemic condition, a ten minutes eleven vessel occlusion (11VO) model. Glutamate releases were monitored along with electroencephalography (EEG) and two-channel cerebral blood flows (CBFs).

II. MATERIALS AND METHODS

A. Animal preparation

Male Sprague-Dawley (SD) rats with the averaged body weight of 300 ± 50 g were used. Animal experiment was conducted in accordance with the animal experimentation guidelines of Kyung Hee University along with the government regulation. Diabetes mellitus (DM) was induced by a single intraperitoneal injection of 60 mg/kg streptozocin. Blood glucose levels with blood samples taken from tail vein and body weight were measured two days after injection. Rats with blood glucose concentration > 300 mg/dl were selected as a DM. Six DM rats were used for real time monitoring of the neuronal damage by cerebral ischemia with and without acupuncture treatments. DM animals were randomly assigned to acupuncture group and control group with three animals each.

B. Experimental setup

In our experiments, the body and brain temperatures were maintained at $36.5 \pm 0.5^\circ\text{C}$ and $37.5 \pm 1^\circ\text{C}$. Four burr holes on the cranium were made for the real time measurement of brain temperature, glutamate, two-channel CBFs. Blood flows of cerebral cortex were monitored with laser Doppler flowmetry. The general 20-10-4-4 type microdialysis electrode for glutamate monitoring was inserted into motor cortex at coordinates A 1: L 4: V 4 mm through a small incision in the dura, after the sensor calibration procedure with the correlation coefficient for linear regression

($R^2 = 0.99$). EEG was monitored on the parietal bones with three electrodes connected with AC Amplifier. Basilar artery, pterygopalatine arteries, occipital arteries, and superior thyroid arteries were coagulated in the meanwhile. External carotid arteries and common carotid arteries were exposed. Rubber rings were put around the exposed arteries for later transient compression of the arteries. After a control period for 10 min, a 10 min 11VO cerebral ischemia was initiated by hanging weights the rubber rings put around the external carotid and common carotid arteries. Weights were released and withdrawn after 10 min and the reperfusion was performed for 40 min.

C. Acupuncture stimulation

In acupuncture group, acupuncture was stimulated during the ischemic period. Four acupuncture needles with a length of 40 mm and a diameter of 0.25 mm were manually inserted about 5 mm deep into acupuncture sites GB34 and GB39.

D. Analysis and statistics

Data obtained from laser Doppler flowmetry, EEG and potentiostat for glutamate were displayed with data acquisition system and were analyzed with Matlab 6.5. Statistical analysis was performed to compare the changes of %CBF and glutamate release between two groups using the two-tailed Student's t-test with a significance level of 0.05.

III. RESULTS AND DISCUSSIONS

The pattern of ischemic response in 11VO DM rat model was similar to both groups. After the onset of ischemia, CBF declined rapidly to near zero levels, concurrently with the development of a flat EEG signal. And CBF greatly increased by initiation of reperfusion and then declined to pre-ischemic levels, along with accompanying changes of EEG activity. CBF changes during ischemic and reperfusion period did not show statistically significant differences between the two groups. Thus 11VO global ischemia model was successfully established.

The elevation in glutamate release in control group began after the onset of ischemic episode and continued to rise throughout the entire ischemic period. Then the glutamate level was rapidly declined to pre-ischemic levels during reperfusion. In acupuncture group, the pattern of glutamate release was similar to control group. However, the elevation in glutamate release was suppressed in the acupuncture group. The maximum change of glutamate concentration was $159.51 \pm 26.25 \mu\text{M}$ in control group and $69.16 \pm 4.01 \mu\text{M}$ in acupuncture group during ischemic period ($p = 0.0059$). The maximum change of glutamate concentration

was $178.49 \pm 12.53 \mu\text{M}$ in control group and $82.31 \pm 7.96 \mu\text{M}$ in acupuncture group during reperfusion period ($p = 0.0002$). The parameters for glutamate release showed statistically significant differences between the two groups.

This study showed acupuncture effect on extracellular glutamate level under devastating acute ischemic condition, 11VO global ischemic model. Glutamate levels were observed to be attenuated with acupuncture stimulation during occlusion and reperfusion periods, using a real-time in-vivo monitoring system of EEG, CBF, and extracellular glutamate. This monitoring system was well established and offers fast and precision measurement data. Effects of acupuncture under more severe and acute condition than previously reported rather mild ischemia model were observed. Ischemia model of 11VO in this study was well established as global ischemia. In line with preliminary observation, acupuncture and control groups showed significant difference in extracellular glutamate level when real-time monitored, while reduction of blood flow and reperfusion hyperemia were not significantly different between two groups. Glutamate release modulation might be an important mechanism of acupuncture effect on ischemic stroke considering glutamate excitotoxicity was major mechanism and probable targets of therapeutic intervention.

In spite of limitations such as small number of cases observed and only one style of acupuncture stimulation method on four acupuncture sites, this study showed the glutamate moderating effect of acupuncture stimulation under acute global ischemic condition using real time monitoring system.

ACKNOWLEDGMENT

This research was supported by the research fund from Seoul R&BD (grant # CR070054).

REFERENCES

1. Wu H, Tang J, Lin X, Lau J, Leung PC, Woo J, Li Y (2008) Acupuncture for stroke rehabilitation, *Stroke*, 39:517-518
2. Abramov, AY, Duchon, MR (2008) Mechanisms underlying the loss of mitochondrial membrane potential in glutamate excitotoxicity, *Biochim Biophys Acta*, 1777:953-964

The corresponding author:

Author: Hun Kun Park
 Institute: Kyung Hee University
 Street: #1 Hoeki-dong, Dongdaemun-gu
 City: Seoul
 Country: Korea
 Email: hpark@khmc.or.kr

The Mechanism of Electro-Acupuncture(EA) Treating Cerebral Ischemia: Whether EA Administered to Mobilization of EPCs?

S.X. Cai¹, S.J. Chen¹, W.J. Yu¹, and Y. Zhao²

¹ College of Bioengineering, Chongqing University, Chongqing, china

² School of Life Sciences, Chongqing Normal University, Chongqing, China

Abstract—Objective To explore the favourable effect of EA in ischemic rehabilitation, which was observed by the changes of endothelial progenitor cells (EPCs) ratio in blood, vascular endothelial growth factor (VEGF) level and nitric oxide synthase (NOS) activity in serum. **Methods** Male rats were randomly and evenly assigned to normal group, sham-operation group, model group and EA group. Each group was divided into 24hr, 48hr and 72hr time points. Model group and EA group were taken the model of acute focal cerebral ischemia and reperfusion by occluding middle cerebral artery(MCAO). EA(2/15Hz, 1mA, one time a day, 30min per time)was delivered via acupuncture needles inserted into “quchi” and “zusanli”. Cerebral IR model was established by occlusion of the middle cerebral artery for 120min. Peripheral blood was obtained from abdominal aorta at every time point. EPCs quantity was displayed using flow cytometry. Blood serum was assembled. VEGF level was measured using enzyme-linked immunosorbent assay (ELISA). The activity of the different isoforms of NOS was measured by spectrophotometry. **Results** EPCs quantity in blood, total NOS(tNOS) and inducible nitric oxide synthase (iNOS) activity in blood serum were increased significantly in model group in IR-24hr; while in IR-48hr, EPCs quantity in EA group was significantly higher than other groups ($P<0.01$, $P<0.05$). In this group, iNOS activity in blood serum was lower than model group, and had no significant difference with normal group or sham-operation group. VEGF levels in EA group were significantly higher than any other groups at different time points ($P<0.01$, $P<0.05$).

Keywords—Electro-acupuncture, Endothelial Progenitor Cells, Cerebral Ischemia-Reperfusion.

I. INTRODUCTION

Nowadays, ischemic stroke gradually become a major cause of morbidity and mortality. Further more, the hotspot and difficulty on vascular repair research is looking for new and effective intervention strategy. Chinese acupuncture, can be regarded as one kind of mechanical stimulation. Many reports have shown its curative effect in the ischemia repair[1-2]. Despite intense efforts to determine the mechanism of the repair, this process remains poorly understood. It has been needed to explore the mechanism of the repair from multiple pathways and angles of view.

Endothelial progenitor cells (EPCs) derived from bone marrow circulate in the peripheral blood and have been implicated in neoangiogenesis after tissue ischemia has occurred. Under physiological conditions EPCs are basically present in bone marrow and rarely in peripheral blood. EPCs can be defined as progenitor cells with the capacity to differentiate into mature endothelial cells when grown under appropriate conditions [3]. Endothelial progenitor cells (EPCs) are capable of proliferating and differentiating into endothelial cells and are therefore ideal candidates for vascular regeneration[4-6]. Recent reports suggest that local or systemic administration of EPCs enhances ischemic neovascularization and improves the function of ischemic tissues in animals with hindlimb or myocardial ischemia [7-8].

Considering the special role of EPCs in the progress of angiogenesis and repair of vascular injury, we attempt to study whether the acupuncture could mobilize EPC from the marrow into circulation and then start the repair process.

II. MATERIALS AND METHODS

Healthy adult male Sprague – Dawley rats (200 – 250g) were randomly and evenly assigned to normal group, sham-operation group, model group and EA (electro-acupuncture) group. Each group was divided into 24hr, 48hr and 72hr time points. Model group and EA group were taken the model of acute focal cerebral ischemia and reperfusion (IR) by occluding middle cerebral artery (MCAO). EA (2/15Hz, 1mA, one time a day, 30min per time) was delivered via acupuncture needles inserted into “quchi” and “zusanli” (acupuncture points were arranged according to “Atlas of Experimental Animal Acupoints” made by Hua’s). Cerebral IR model was established by occlusion of the middle cerebral artery for 120min. We investigated the EPCs ratios in blood, the expression of nitric oxide synthase (NOS), vascular endothelial growth factor (VEGF) in blood serum of the rats in different groups. The EPCs ratios was measured by fluorescence activated cell sorting (FACS) analysis. The activity of the different isoforms of NOS was measured by spectrophotometry. VEGF level was

measured using enzyme-linked immunosorbent assay (ELISA).

III. RESULTS

A. EPCs quantity in peripheral blood.

The number of EPCs in peripheral blood are different from groups and has the fluctuation with the time(Figure1). The EPCs quantity in the peripheral blood of the rats elevated obviously in the Model group in 24hr. The EPCs ratios in the EA group were higher than the ones in the other groups in 48hr. The Model group were again significantly higher than other groups in 72hr.

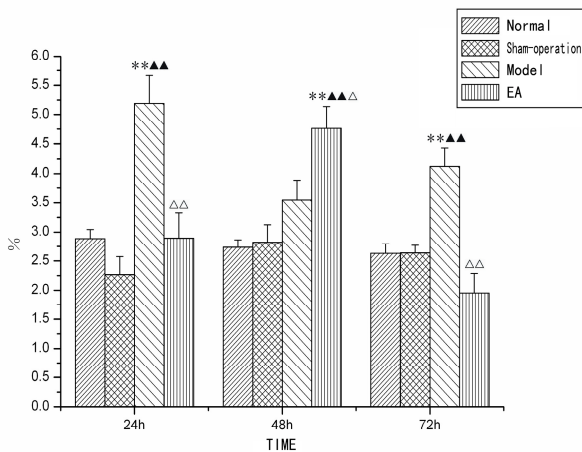


Fig. 1 EPCs quantity in peripheral blood from each group at different time points. vs normal group at the same time point $**P<0.01$; vs sham-operation group at the same time point $\blacktriangle\blacktriangle P<0.01$; vs model group at the same time point $\Delta P<0.05$, $\Delta\Delta P<0.01$; $n=6$ per time point, $\bar{X} \pm S$.

B. The TNOS activity in blood serum.

In addition to the normal group, other groups has slightly fluctuation along with the time(Figure 2).TNOS activity in blood serum were increased significantly in model group in 24hr. TNOS activity in model group were decreased in 48hr and 72hr, and there is no significant difference in other groups.

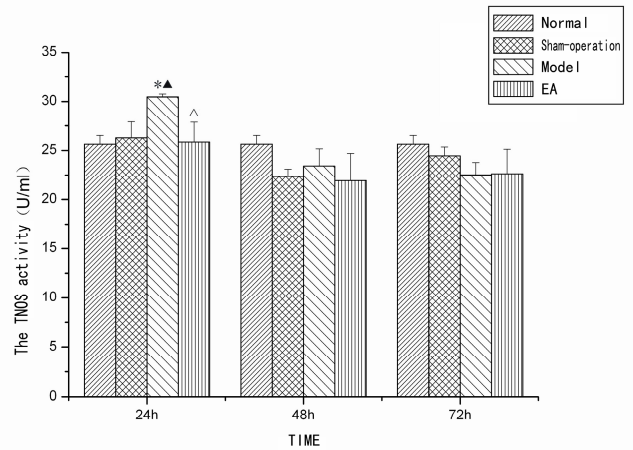


Fig. 2 The TNOS activity in blood serum from each group at different time points. vs normal group at the same time point $*P<0.05$; vs sham-operation group at the same time point $\Delta P<0.05$; vs model group at the same time point $\Delta P<0.05$; $n=6$ per time point, $\bar{X} \pm S$.

C. The iNOS activity in blood serum.

Besides the normal group, other groups has slightly fluctuation. iNOS activity in blood serum were increased significantly in model group and EA group in 24hr; while in 48hr, iNOS activity in model group also higher than other groups. There is no significant difference in 72hr(Figure 3).

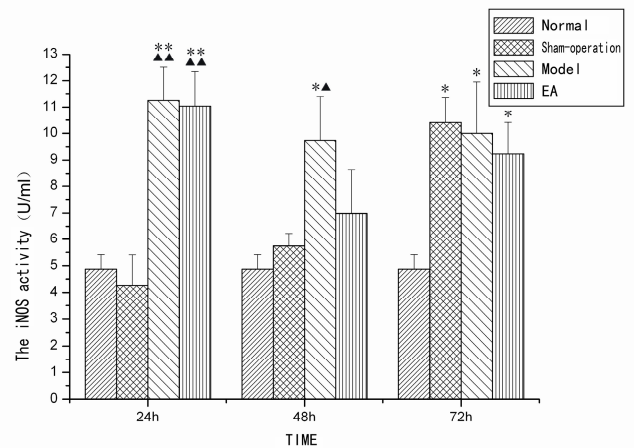


Fig. 3 The iNOS activity in blood serum from each group at different time points. vs normal group at the same time point $*P<0.05$ $**P<0.01$; vs sham-operation group at the same time point $\blacktriangle P<0.05$ $\blacktriangle\blacktriangle P<0.01$; $n=6$ per time point, $\pm S$

D. The iNOS activity in blood serum.

In addition to the normal group, other groups has some fluctuation(Figure 4). VEGF level in EA groups were

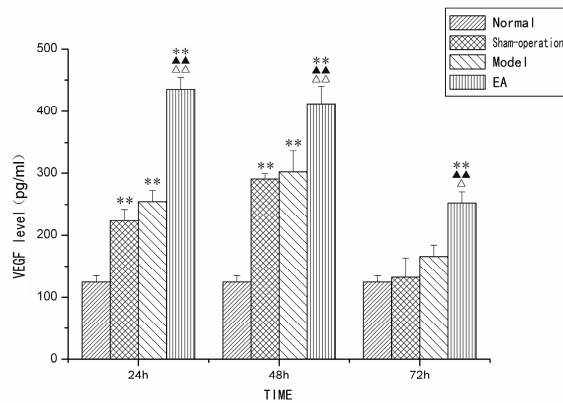


Fig. 4 VEGF level in blood serum from each group at different time points. vs normal group at the same time point** $P < 0.01$; vs sham-operation group at the same time point▲▲ $P < 0.01$; vs model group at the same time point Δ $P < 0.05$, ΔΔ $P < 0.01$; $n = 6$ per time point, $\pm S$. significantly higher than any other groups at different time points. In EA group, VEGF level were reduced in 72hr.

IV. CONCLUSIONS

More recent studies have shown that EPCs contribute to the regeneration and maintenance of endothelium[9]. It was discovered that some markers characterize the functional endothelial precursor cell:CD31, CD133, CD34, and the vascular endothelial growth factor receptor-2 (VEGFR-2), and so on[10]. Data regarding the number of endothelial progenitors in the peripheral circulation of healthy adults are scanty[11].After ischemic stroke and injury,EPCs have the ability to home to sites of ischemia or endothelial injury and differentiate to mature endothelial cells[12]. To date,it was discovered that VEGF is one of most potential factors in the process of mobilizing and homing EPCs.

NOS is one kind of enzyme which directly related to the production of NO. TNOS divides into neuronal nitric oxide synthase(nNOS),endothelial nitric oxide synthase(eNOS) and inducible nitric oxide synthase(iNOS). The former two kinds express continually in organism.In case of inflammation, the expression of iNOS can be induced by inflammatory cells.The iNOS is involved in produces a large number of NO,and then causes the cytotoxicity function.The eNOS is essential for neovascularization.It may contribute to impaired regeneration processes in cerebral ischemia disease patients, who are characterized by a reduced systemic NO bioactivity.

The former results have shown that, acupuncture could release and ameliorate the injury caused by ischemia in many pathways significantly[13-14]. Angiogenesis may be one of

the important pathways. EPCs play an important role in angiogenesis. And acupuncture can influence the factors which can mobilize EPCs. However, the mechanism of acupuncture has not yet been reported.Our research embarks upon this question and studied on the changes in cerebral ischemia rats treated by EA. The results showed the acupuncture can change the number of EPCs in the peripheral blood.

The data showed the number of EPCs in the peripheral blood were all have increased after cerebral ischemia.The EPCs ratios in the blood of the rats in the EA group were higher than the ones in the model group on 48hr after reperfusion. In this group, iNOS activity in blood serum was lower than model group, and had no significant difference with normal group or sham-operation group.It suggested that EPCs mobilization could have a quick response to thread insertion in a short time.

The injury after IR could increase EPCs quantity in blood and iNOS activity in blood serum. This phenomenon may be related with inflammation. According to existing studies, ischemia and vascular injury would lead to the inflammatory response, and then reach a peak in 24hr[15].EA stimulation could not only release inflammation[16-17], but also affect endogenous EPCs. This effect could be related with up-regulating VEGF expression. The VEGF concentration in rat serum has increased after the cerebral ischemia, consistent with the clinical results[18-19].VEGF level in EA group were significantly higher than any other groups at different time points ($P < 0.01$, $P < 0.05$). It suggested that the acupuncture

possibly through promoting expression of VEGF to mobilize EPCs.At the same time, It has reported that the increased expression of VEGF can also promote EPCs homing ater infarction[20]. Then Speculated that the reduction of EPCs quantity in 72hr EA group related with high expression of VEGF. In addition, iNOS activity in EA group was lower than the model group in 48hr, while the TNOS activity had no significant difference with normal group.We presumed that eNOS activity had raised,and then play a favourable role in mobilizing.

So far we have not clarified whether such a decrease is related with the homing of EPC to the lesion location in brain. We are confirming the co-effect of other factors, such as the expression of SDF-1, to promote the studies on the mechanism of acupuncture.

ACKNOWLEDGMENT

This research was funded by National Natural Science Foundation of China (Grant No. 10872224).

REFERENCES

1. Peng Xm, Jin R, Zhang Jw et al (1998) The effect of acupuncture on blood fat, blood rheology and superoxide dismutase (SOD) in cerebral thrombosis patients. *Zhongguo Zhen Jiu (Chinese Acupunct Moxi)* 18 (1):12-14.
2. Chen J, Chen Hp, Cheng Js (2001) Ischemic cerebral injury and treatment with acupuncture and medication at super-early stage. *Zhongguo Zhen Jiu (Chinese Acupunct Moxi)* 21(1):37-39.
3. Hristov M, Weber C (2004) Endothelial progenitor cells: characterization, pathophysiology, and possible clinical relevance. *J Cell Mol Med* 8:498-508
4. Murasawa S, Asahara T (2004) Endothelial progenitor cells for vasculogenesis. *Physiology* 20(2):36-42.
5. Jujo K, Ii M, Losordo Dw (2008) Endothelial progenitor cells in neovascularization of infarcted myocardium. *J Mol Cel Cardiology* 45:530-544
6. Hur J, Yoon Ch, Kim Hs, et al (2004) Characterization of two types of endothelial progenitor cells and their different contributions to neovascularogenesis. *Arterioscler Thromb Vasc Biol* 24 (2):288-293
7. Qian C, Tio R A, Roks Aj et al (2007) A promising technique for transplantation of bone marrow-derived endothelial progenitor cells into rat heart. *Cardiovascular Pathology* 16(3):127-135.
8. Kawamoto A, Gwon Hc, Iwaguro H, et al (2001) Therapeutic potential of ex vivo expanded endothelial progenitor cells for myocardial ischemia. *Circulation* 103:634-637
9. Asahara T, Murohara T, Sullivan A, et al (1997) Isolation of putative progenitor endothelial cells for angiogenesis. *Science* 275 (5302) : 964-967.
10. Hristov M, Weber C (2004) Endothelial progenitor cells: characterization, pathophysiology, and possible clinical relevance. *J Cell Mol Med* 8(4):498-508.
11. Mutin M, Canavy I, Blann A, et al (1999) Direct evidence of endothelial injury in acute myocardial infarction and unstable angina by demonstration of circulating endothelial cells. *Blood* 93:2951-2958.
12. Shintani S, Murohara T, Ikeda H, et al (2001) Mobilization of endothelial progenitor cells in patients with acute myocardial infarction. *Circulation* 103(6):897-903.
13. Zhang Hm, Fei Yt, Shi Yj, et al (2006) Effects of acupuncture of “Baihui” (GV 20) and “Taiyang” (EX-HN 5) on functions of vascular endothelial cells in cerebral ischemia injury rats. *Zhen Ci Yan Jiu (Acupuncture Res)* 31(2):67-73.
14. Guan L, Shi X, Du Yh (2002) Effect of acupuncture on cerebral microcirculation in acute cerebral ischemia rats. *Zhen Ci Yan Jiu (Acupuncture Res)* 27(1):29-32.
15. Xiao Y C, Zheng A (1999) Inflammatory reaction and acute cerebral infarction. *Nao Yu Shen Jing Ji Bing Za Zhi (Journal of Brain and Nervous Diseases)* 7(4):252-254.
16. Cheng L, Luo Mj, Ming Jk, et al (2003) Effect of electroacupuncture on the expression of IL-1 β mRNA and TNF-mRNA of cerebral neurons in cerebral ischemia-reperfusion rats. *Zhen Ci Yan Jiu (Acupuncture Res)* 28(3):174-177.
17. Huo Zj, Zhang L, Qian Rq (2002) The effect of acupuncture on peripheral blood WBC and cell factors in cerebral ischemia reperfusion. *Shanghai Zhen Jiu Za Zhi (Shanghai J Acu-mox)* 21(2):41-43.
18. Slevin M, Krupinski J, Slowik A, et al (2001). Serial Measurement of Vascular Endothelial Growth Factor and Transforming Growth Factor-b1 in Serum of Patients With Acute Ischemic Stroke. *Stroke* 32(1):1863-1870.
19. Kaeng Wl, Gregory Yh, Andrew D (2004) Blann. Plasma Angiopoietin-1, Angiopoietin-2, Angiopoietin Receptor Tie-2, and Vascular Endothelial Growth Factor Levels in Acute Coronary Syndromes. *Circulation* 110:2355-2360.
20. Abbott, Jd et al (2004) Stromal cell-derived factor-1alpha plays a critical role in stem cell recruitment to the heart after myocardial infarction but is not sufficient to induce homing in the absence of injury. *Circulation* 110:3300-3305.

Use macro [author address] to enter the address of the corresponding author:

Author: S.X. Cai
 Institute: College of Bioengineering, Chongqing University,
 Street: Shazheng Street
 City: Chongqing
 Country: China

PERFORM: Building and Mining Electronic Records of Neurological Patients Being Monitored in the Home

R. Greenlaw¹, M. Garcia Robledo², J.J. Estrada³, M. Pansera³, S. Konitsiotis⁴, D. Baga⁴, P. Maziewski⁵, M. Pastor⁶, A. Papsava⁷, D. Chaloglou⁸, and F. Zanichelli⁹

¹ Oxford Computer Consultants Ltd, UK

² Siemens S.A., Spain

³ Universidad Politecnica de Madrid, Spain

⁴ Medical Technology and Intelligent Information Systems Unit, University of Ioannina, Greece

⁵ Gdansk University of Technology, Poland

⁶ Centre for Applied Medical Research, University of Navarra, Spain

⁷ Michalis Papasavas A.E., Greece

⁸ Anco, Greece

⁹ Dipartimento di Ingegneria dell'Informazione, Universita' di Parma, Italy

Abstract— The PERFORM project is building a novel application for the home-based monitoring and assessment of people with neurologically based movement disorders such as Parkinson's disease (PD) and Amyotrophic Lateral Sclerosis (ALS). PERFORM includes a hospital-based EHR data-analysis and mining system compatible with HL7. For EHR to include monitoring data an alert-based system of data reduction is used which supports both patient management and modelling. Pilots will be started in Spain, Greece and Italy in 2009. PERFORM is in the early stages of development and is an FP7 integrated project.

Keywords—Digital homecare, EHR, neurology, data mining, home monitoring.

I. INTRODUCTION

There is a clinical deficit of objective data on which neurologists can base the assessment and care of patients with chronic neurologically-based movement disorders. The natural response is to develop digital home monitoring but there is a corresponding lack of experience in storing such data in EHR and in using it to present a coherent view of the patient. The PERFORM project (<http://www.perform-project.com/>) aims to develop a complete home monitoring system using data gathered by the patient themselves wearing sensors in and outside the home and fusing this into EHR. A home-based wireless unit will pre-process the data before it is transferred to a hospital-based system for fusion, mining and integration with EHR. The strategy for preparing monitoring data for inclusion in EHR is based upon a system of alerts, described below - such systems will always be specific to disease groups. PERFORM is particularly looking at disorders such as Parkinson's disease (PD) and

Amyotrophic Lateral Sclerosis (ALS); a type of motor neurone disease. People with PD have symptoms which typically vary throughout the day. It is disempowering not to be able to present the clinician with an objective picture of your disease. Since PERFORM is driven by the patient, they can choose when to be monitored and so can capture the symptoms that most concern them in an objective manner the doctor can exploit. Development of the system is ongoing with pilots in 2009. PERFORM is an integrated project receiving support under Framework Programme 7.

II. CLINICAL DATA DEFICIT, ACQUISITION AND REDUCTION

Assessment for neurological disorders such as PD and ALS is largely based on intermittent clinical visits and subjective reports by patients and carers. In Europe neurologists and GPs normally care for 50 to 800 patients with PD[1] (fewer with ALS). The range in workload is a result of diversity both in national health systems and in the availability of clinical resources across Europe. Even at 50 patients per clinician this represents a serious challenge to homecare monitoring for specialised conditions. Patients with neurological diseases such as Parkinson's disease and ALS normally visit their specialised clinician or GP every 4-6 months. As a result, any changes in the patient's condition may not be recognised for several months, unless the patient themselves makes contact. Certainly for PD there is the additional complication of symptoms which vary throughout the day (swinging between "on" and "off" phases). It is disempowering for the patient to be asked to present a true picture of their disease in a pre-scheduled one hour appointment. There is therefore a critical need for home monitoring in this class of diseases. The monitoring

system itself should empower the patient so that they choose when they are monitored. They are effectively in the position of being able to write part of their own EHR.

Home monitoring systems such as PERFORM process patient data on a daily basis and integration with EHR is a challenge. A major objective of home-based monitoring therefore is data reduction by analysing raw data and passing on to the hospital only notifications of events that are of clinical relevance. The correct processing and reduction of data locally is critical to building home-based monitoring EHR of value. The PERFORM strategy is to process the raw data locally and from this develop a system of alerts which are raised when features of clinical relevance are found. This massively reduces the data set and produces data which integrate well with EHR at the expense of making the system specific to a disease family.

In the case of PERFORM data is gathered by wearable sensors; typically five triaxial 50Hz accelerometers, plus gyroscopes, pressure and optionally blood-oxygen and electroculogram (during sleep) sensors. Symptoms of general clinical interest in neurologically-based motion disorders such as Parkinson's disease are tremor, *dyskinesia* (poorly constrained movement) *bradykinesia* (slow movement), *akinesia* (no movement), and falls.[2] Tremor needs to be distinguished between tremor at rest (*rest tremor*) and in activity (*action tremor*). In Parkinson's disease, the fluctuation of the patient between "on" phases of well managed symptoms and "off" phases of poorly managed symptoms is important as is the occurrence of "freezing" (sudden-onset akinesia).[2]

III. PATIENT MANAGEMENT AND MODELLING

PERFORM passes no raw data on to the EHR repository. Instead data is locally processed and notifications (alerts) of clinical events are raised. The event data flowing into the central hospital EHR need to support two distinct objectives: patient management and modelling.

For patient management, events are detected which are known to be of importance to the condition being treated. Patient Management sub-modules are dedicated to supporting the clinician in the management of a specific disease. For example, for a patient with Parkinson's disease it is essential to recognize when an "off" state is appearing earlier than expected, if a fall is connected to a freezing or if recognized tremor is action tremor. Algorithms for the detection of bradykinesia, dyskinesia, tremor and freezing are available in the literature and are not described here.[3-5] Since the PERFORM system is (de)activated by the patient themselves they can guide their own management by using

home monitoring to objectively show their doctor the nature of their most difficult symptoms.

Conversely, the patient model is used by the system to capture the patient-specific characteristics of the disease. Commonly in chronic neurological diseases patients do not present the same constellation of symptoms, and even universal symptoms are expressed quite differently across patients. Typical examples would be Parkinson's dyskinesia (the exact pattern of movement is not static and is different for each patient), or tremor (which can appear on different sides of the body and evolve differently during the disease)[1]. For each such symptom, the patient model represents the current expression of the symptom for each specific patient. This provides EHR which can be used to immediately recognize differences in the way a symptom is expressed and trigger corresponding alerts. If the challenge of building an alert-based patient management system and model can be met, EHR based on home-monitoring becomes far more manageable. In PERFORM one metric of the success of the alert-based architecture will be the ability to data mine the EHR.

IV. PILOTS

The PERFORM project will be conducting pilots at three sites managed by University of Navarra (Spain) and University of Ioannina (Greece). In each clinical environment different EHR management systems are operative but fundamental clinical information can be exchanged via standard interfaces. The major variables are (where *inbound* denotes flow *into* PERFORM):

- General patient information (demographic data) : *inbound/outbound*
- Patient anamnesis: *inbound*
- Reports on patient pathology: *outbound*
- Medication types and schedule: *outbound*

The exchange of information between the PERFORM Central Hospital Unit and external Clinical Information Systems will be based on the XML-based HL7 version 3. PERFORM will be tested for accessibility since it must be usable by patients whatever their condition.

V. SUMMARY

A fundamental problem in digital homecare is the inclusion of monitoring data in EHRs. The PERFORM project is building an innovative homecare monitoring system for people with neurological diseases such as PD and ALS.

PERFORM puts the patient at the centre of their own disease management. PERFORM solves the EHR problem by processing the monitoring data before EHR storage by reducing the data to a series of events and this can only be done on the basis of clinical knowledge about the diseases. Therefore this is an approach to EHR which is specific to disease groups. The stream of monitoring event data in a digital homecare system must be constructed with the different objectives of patient management and modelling in mind. PERFORM will be running pilots in Spain, Greece and Italy starting in 2009.

ACKNOWLEDGMENT

PERFORM is supported by EU Framework Programme 7, Agreement 215952.

REFERENCES

1. D3.2 Review of Technologies, System Architecture & Functional Specification, PERFORM Project, January 2009, based on interviews with neurologists.
2. A.Samii, J.Nutt, B.Ransom, Parkinson's disease, *The Lancet* 9423 (2004), 1783-1793
3. .I.Hoff, V. van der Meer, J.J. van Hilten, Accuracy of Objective Ambulatory Accelerometry in Detecting Motor Complications in Patients With Parkinson Disease, *Clin Neuropharmacol* 27 (2004), 53-57
4. G Wu, S Xue, "Portable Pre-impact Fall Detector With Inertial Sensors", *IEEE Transactions on Neural Systems and Rehabilitation Engineering* 16 (2008), 178-183
5. J Gour, R Edwards, S Lemieux, Movement patterns of peak-dose levodopa-induced dyskinesias in patients with Parkinson's disease, *Brain Research Bulletin* 74 (2007), 66-74

Author: Reynold Greenlaw
Institute: Oxford Computer Consultants Ltd
Street: 23-38 Hythe Bridge Street
City: Oxford
Country: UK
Email: reynold.greenlaw@oxfordcc.co.uk

Real-Time Adaptive Neural Predictors for Upper Limb Gestures Blind Recognition

M. Gneo, R. Muscillo, M. Goffredo, S. Conforto, M. Schmid, and T. D'Alessio

University Roma Tre, Applied Electronics Department, Rome, Italy

Abstract— A real-time system based on artificial neural networks (ANNs) for time series prediction is proposed. For each movement the prediction errors are used *both* to train the ANNs *and* to estimate a measure of the unlikelihood of the specific gesture occurrence. The first repetition of each gesture trains the related ANNs bank and the current motion is recognized after a few successive repetitions. Neither a priori assumptions nor signal pre-processing is performed (*blindness*). The training is performed at the beginning and can be repeated during the running (*adaptability*). Each procedure is strictly physically realizable (*real-time feasibility*).

Four gestures performed by three healthy volunteers are selected by a set of upper limb motor tasks contained in the rehabilitation scale known as Wolf motor function test (WMFT). Two accelerometers placed on the upper arm and on the forearm respectively, constitute the sensors set. Even in very challenging test settings, the proposed method shows a correct recognition rate higher than 83%.

Keywords— Neural networks, time series prediction, accelerometers, gesture recognition.

I. INTRODUCTION

The aim of this work is to prove the feasibility of a real-time limb gesture recognition system based on artificial neural networks (ANNs). The system is integrated with a simplified sensor set of only two accelerometers placed on the upper limb and the recognition rate is assessed on real data. Due to their pattern classification and pattern recognition capabilities and their property to learn from and generalize from experience, ANNs have been mainly applied to data regression and classification problems. As a particular regression task, ANNs have been also widely used for time series prediction [1][2][3][4].

The rationale of the proposed method is to use ANNs as real-time neural predictors (RTNPs) in order to utilize the prediction errors to *both* continuously train the ANNs *and* to recognize the current motion using wearable sensors. The latter ones are being increasingly used in many applications related to the monitoring and the recognition of daily living activities in healthy people [5]. Being these sensors easy to use and wear, they can be used in home environment allowing to implement tele-rehabilitation programs able to remotely monitor gesture performance [6], and eventually to quantify the progress of rehabilitation in people recovering

from pathologies. Thus, they are also being used to analyse and quantify human motion, for both lower limb and upper limb applications [7][8]. Accelerometers are also often used in combination with magnetometers, cameras and gyroscopes to study tremor and balance, and for pose reconstruction [9]. The related signals are analysed by various processing methods, ranging from classic frequency analysis, to HMM-based techniques, to different types of Template Matching [10].

In this work, for each gesture a different RTNP is trained to predict each of the time series of the accelerometers channels, constituting a bank of RTNPs. After few consecutive motion repetitions, the recognition system guesses the gesture category referred to the RTNPs bank exhibiting the best predictions. The use of ANNs and of the on-line learning scheme gives the system a powerful ability to learn different gestures and to be adaptive in learning the way different subjects perform the same gestures.

Although very challenging test conditions were considered in this work (the RTNPs banks are not specialized to the related gesture, only the first gesture trains the ANNs, no signal processing is performed) an encouraging mean value of the percentage recognition rate greater than 83% is obtained, proving the robustness and the recognition power of the proposal, which will be detailed in the following.

II. MATERIALS AND METHODS

A. The proposed real-time neural predictor (RTNP)

ANNs are a neurologically inspired computational paradigm using many simple elaboration units (neurons) highly interconnected. A set of significant inputs and corresponding desired output couples (*training set*) is used to *train* the ANNs connections strengths (*weights*) minimizing the distance between the desired outputs and the actual outputs. According to the neurological long-term potentiation principle – the efficacy of synapses change as a result of experience providing both memory and learning to the brain – the training reinforces or depresses the connections giving the ANN the capability to learn the knowledge and the behavior contained in the training set. Thus, ANNs have been mainly applied to data regression and classification tasks.

Table 1 Time series forecasting: generally used training set

Item No	Inputs	Desired output
1	$x[1], x[2], \dots, x[L]$	$x[L+1]$
2	$x[2], x[3], \dots, x[L+1]$	$x[L+2]$
...
N-L	$x[N-L], x[N-L+1], \dots, x[N-1]$	$x[N]$

A particular regression task is the time series prediction: L delayed samples $\{x[n-\ell]; \ell=0, 1, \dots, L-1\}$ of the series are provided as L inputs to the ANN; the ANN H outputs give the predictions of the H future values $\{\hat{x}[n+h]|n; h=1, 2, \dots, H\}$. A non linear AR(L) model is thus assumed for the series (eq. 1) [1][2][3].

$$x[n+1] = f(x[n-L+1], \dots, x[n-1], x[n]) \quad (1)$$

Assuming N previous samples of the series are available and considering a one-step-ahead prediction, the ANN training set is schematized in Table 1 [1].

An essential feature of ANNs is the option to train them continuously even during functioning. The so called *on-line training* is conceptually opposite to the generally used *batch training* method, referred to the off-line ANN training.

A basis of this proposal is to use ANNs as RTNPs. Referring to Figure 1, at each time n the RTNP stores the last N samples, predicts the H future values and uses the H prediction errors $e_h[n]$ (eq. 2) to concurrently perform the training during the prediction phase, according to Table 1.

$$e_h[n] = x[n] - \hat{x}[n] \quad h = 1, 2, \dots, H \quad (2)$$

These prediction errors will serve as inputs for the performance measurement step, described in the following.

B. Performance measurements

Although the crucial performance measurement for predictors is the prediction accuracy, based on the prediction error (eq. 2), a suitable figure for any given problem is not defined [1][4].

There are absolute performance measurements, which are used to compare the performances of different predictors operating on the same dataset:

- the mean squared error (MSE) = $(\sum_n e^2[n])/N$
- the root mean squared error (RMSE) = $MSE^{1/2}$
- the mean absolute deviation (MAD) = $(\sum_n |e[n]|)/N$

and normalized performance measurements, which are in turn used to compare performances related to different data sets:

- the mean absolute percentage error (MAPE)

$$MAPE = \frac{100}{N} \cdot \sum_n \left| \frac{e[n]}{x[n]} \right| \quad (3)$$

- the symmetric mean absolute percentage error (SMAPE)

$$SMAPE = \frac{100}{N} \cdot \sum_n \frac{|x[n] - \hat{x}[n]|}{|x[n] + \hat{x}[n]|/2} \quad (4)$$

As in this proposal the several RTNPs prediction performances are compared to recognize gestures, a normalized performance measurement has to be used. Moreover, since the accelerometer signals used in this work have zero mean, the use of the MAPE would lead to very large values when $x[n]$ is close to zero. On the other hand the SMAPE is used for positively defined series. A corrected SMAPE (cSMAPE) (eq. 5) is thus proposed.

$$cSMAPE = \frac{1}{N} \cdot \sum_n \frac{|x[n] - \hat{x}[n]|}{(|x[n]| + |\hat{x}[n]|)/2} \quad (5)$$

The performance measurement of the recognition system is the correct recognition percentage rate (CRPR).

C. Application: the accelerometers signals

The signals were recorded using two different accelerometers (ADXL202): a three-axis one, placed on the inside of the forearm (Acc1), and a dual-axis one placed on the upper arm (Acc2). The axes are oriented as in Figure 2.

For each subject 100 time series (5 repetitions \times 5 channels \times 4 gestures) were recorded. Signals were sampled at 400 samples/s and have a duration ranging from 2.5 s to 6.5 s (RP and SP task, respectively).

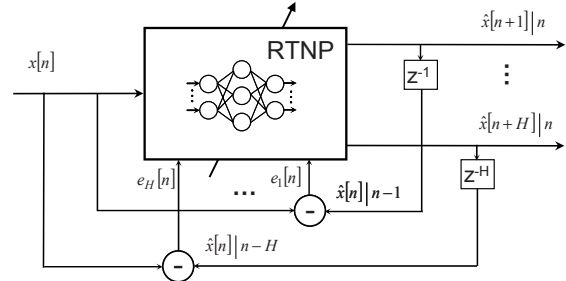


Fig. 1 Real-time neural predictor (RTNP)

D. Application: experimental setup and protocol

Three healthy subjects were recruited to execute five repetitions of each exercise. The gesture categories are selected from a set of exercises listed in the WMFT which is generally used to monitor the improvement of functional movements in people recovering from stroke. The following

four exercises are selected as they are more similar to the gestures performed during daily living:

- *SP* - *stack pieces* – stack up 3 different draughts pieces,
- *LD* – *lock the door* – reach, grasp and turn the keys as if locking a door three times,
- *RJ* – *raise jar* – reaching and raising a jar and bring it to the mouth, mimicking drinking,
- *RP* – *raise pencil* – reaching and then raising a pencil at a distance of 20 cm from the subject.

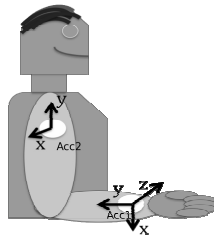


Fig. 2 Placement of the accelerometers

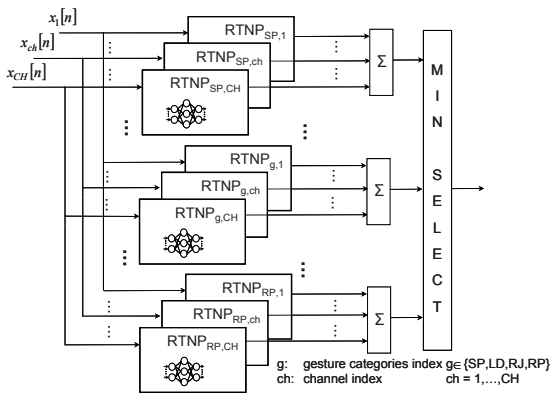


Fig. 3 Real-time gesture recognition system

E. The proposed real-time gesture recognition system

In this section a real-time implementation of the use of RTNPs cSMAPEs to recognize gestures is detailed.

A multi-layer neural network (MLNN) with one hidden layer is considered is used for the RTNP. The standard backpropagation training algorithm is used and the transfer functions for the hidden and the output layer units are the hyperbolic tangent (tanh) and the linear function, respectively. The selection of the main MLNNs factors is essentially problem-dependent and none of the existing methods can be assumed as superior to the others [3]. Given the real-time feasibility requirement, an heuristic trial-and-error approach in modeling the RTNPs is so applied.

For each gesture category a different bank of RTNPs is trained with the different accelerometer output channels (a

RTNP for each channel). Four gesture categories are considered and five motion repetitions are totally available from the 3+2 channels of the two used accelerometers. With reference to Figure 3, the proposed system is composed of 4 RTNPs banks, each being formed by 5 RTNPs.

Only the single initial repetition of each gesture trains the RTNPs of the related bank and then the signals given by the 5 accelerometer channels are simultaneously provided to all the RTNPs banks so that $H=40$ series of the prediction errors $e_h[n]$ (eq. 2) are evaluated. After 4 movement repetitions of the same gesture, the mean cSMAPE for each RTNPs bank is evaluated averaging both in the 5 different channels and in the prediction directions $h=20, 21, \dots, 40$. The bank with the minimum mean cSMAPE provides the system guess about the gesture category. The finally settled RTNPs model uses a training size of 5000 samples (the first repetition of each gesture, with $N=1200$ in Table 1), 600 input nodes, 2 hidden units and 40 output nodes.

As other authors found ([1][2][3]), it was confirmed that: the number of input nodes is the most critical factor for prediction and recognition task; a large training data set may overcome the overfitting problem; parsimonious models have both the best recognition performance and the highest generalization capability.

III. RESULTS AND DISCUSSION

Figure 4 shows the predictions for the 5th accelerator channel of a SP gesture during the on-line training. The first repetition of each gesture is used twice during the training.

Figure 5 shows the cSMAPE for each of the 4 accelerometer channel RTNPs when RJ is performed: the minimum cSMAPE is found in the RTNP trained with RJ. Moreover, the higher is the prediction step, the higher is the cSMAPE but the higher is the system discrimination power. It is also worth highlighting that:

- for each subject the RTNPs are re-initialized; only the first gesture repetition is used for the training; the train is never again repeated,
- the different RTNP bank structure is not optimized for the specific related gesture category,
- for each bank the different cSMAPEs of the related RTNPs are simply averaged over the channels,
- neither any assumption nor any pre-processing or normalization of the data is performed.

Table 2 Correct recognition percentage rate

Subject \ Gesture	Gesture correct detection percentage rate				
	SP	LD	RJ	RP	Mean
Mean	100%	66.7%	66.7%	100%	83.3%

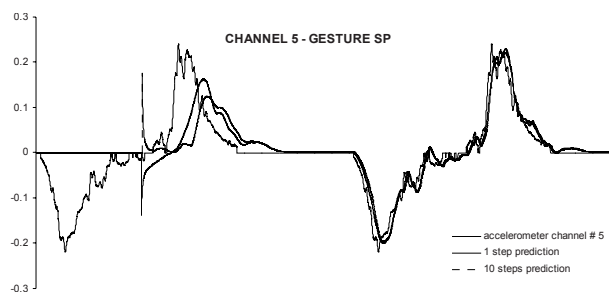


Fig. 4 Real time prediction during the on-line training

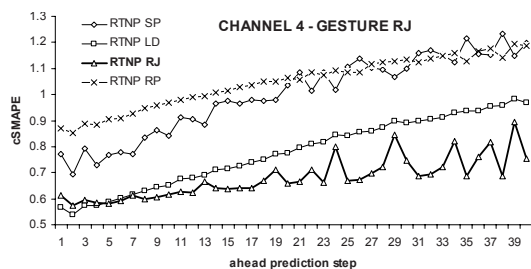


Fig. 5 Different gestures RTNPs - cSMAPE vs. prediction step

Even in these very challenging test settings, a mean CRPR higher than 83% is obtained, proving the robustness and the recognition power of the proposed system (Table 2).

IV. CONCLUSIONS

An implementation of a real-time gesture recognition system based on the use of time series neural predictors is proposed. The CRPR is measured on real data obtained from two inertial sensors placed on the upper limb. The accelerometer sensors, the ANNs architecture, and the prediction accuracy block are assembled in the system.

The use of ANNs and of the on-line learning scheme gives the system a powerful ability to learn different gestures and to be adaptive in learning the way different subjects perform the same gestures. As the learning can be repeated during the functioning, the system is also able to learn the change in performing movements for the same subject, suggesting applications in remote monitoring of gesture performance, and in adaptive rehabilitation programs. The lack of both a priori assumptions and signal pre-processing makes the system prone to recognize different kind of gestures and, in general, of data patterns.

Even in the described test conditions, results obtained in this preliminary version of the system prove both the correctness and the robustness of the inspiring principles and the feasibility of a real-time implementation.

To improve the recognition ability allowing the system to recognize motions at the end and even during the single gesture repetition, the following future works are planned:

- to specialize each RTNPs bank architectures for the related specific gesture category,
- to sophisticate the ANNs (e.g. recurrent networks),
- to automatize the ANNs modeling (e.g. generating more than a model and selecting the winning one [3])
- to use more than one gesture repetition to train each RTNPs and periodically refreshing the training (e.g. using the trusted current recognition).

ACKNOWLEDGMENT

The research work presented in this paper has been carried out with the financial support of the European Union Commission, within FP7 action ICT-2007.7.2 "Accessible and Inclusive ICT", under contract number ICT-2007-224051 TREMOR "An ambulatory BCI-driven tremor suppression system based on functional electrical stimulation".

REFERENCES

1. Zhang G, Patuwo B E, Hu M Y (1998), Forecasting with artificial neural networks: The state of the art. *J Forecasting* 14:35–62
2. Zhang G, Patuwo B E, Hu M Y (2001), A simulation study of artificial neural networks for nonlinear time-series forecasting. *Comput. Oper. Res.* 28:381-396
3. Crone S (2005), Stepwise selection of artificial neural network models for time series prediction. *J Intell. Syst.* 14(2-3):99-122
4. <http://www.neural-forecasting-competition.com>
5. Pentland A (2005), *Healthwear: medical technology becomes wearable*. *Stud. Health Technol. Inform.* 118:55-65, 2005.
6. Schasfoort F C, Bussmann J B J, Stam H J (2002), Ambulatory measurement of upper limb usage and mobility-related activities during normal daily life with an Upper Limb-Activity Monitor: a feasibility study. *Med. Biol. Eng. Comput.* 40(2):173-82
7. Mathie M J, Coster A C, Lovell N H et al. (2004), Accelerometry: providing an integrated, practical method for long-term, ambulatory monitoring of human movement. *Physiol. Meas.*, vol. 25, pp. R1-20.
8. Veltink P H, Bussmann H B, de Vries W et al. (1996), Detection of static and dynamic activities using uniaxial accelerometers. *IEEE Trans. Rehabil. Eng.*, vol. 4, pp. 375-85.
9. Giansanti D, Macellari V, Maccioni G et al (2003). Is it Feasible to Reconstruct Body Segment 3-D Position and Orientation Using Accelerometric Data. *IEEE Trans. on Biomed. Eng.*, vol. 50, no. 4
10. Muscillo R, Conforto S, Schmid M et al. (2007), Resolving ADL Activities Variability through Derivative Dynamic Time Warping applied on Accelerometer Data. *IEEE EMBS Proc. 29th Intern. Conf.* 2007: 4930-33.

Author: Massimo Gneo
 Institute: University Roma Tre, Applied Electronics Department
 Street: Vasca Navale, 84
 City: Rome
 Country: Italy
 Email: massimo.gneo@uniroma3.it

The European R&D Project RISE - Use of Electrical Stimulation to Restore Standing in Paraplegics with Long-Term Denervated Degenerated Muscles (DDM)

Winfried Mayr¹, Christian Hofer², Helmut Kern², Manfred Bijak¹,
Hermann Lanmüller¹, Dietmar Rafolt¹, Ewald Unger¹, Hans Stöhr³

¹ Center for Biomedical Engineering and Physics, Medical University Vienna, Austria

² Department of Physical Medicine and Rehabilitation, Wilhelminenspital Wien, Vienna, Austria

³ Center for Biomedical Research, Medical University Vienna, Austria

Abstract

RISE was funded in Framework Program (FP5). The consortium included 13 European partners from Austria, United Kingdom, Italy, Slovenia, Germany and Iceland and six subcontractors from Austria and Germany. Nine of the nineteen were SCI centres. The project started with November 1, 2001 and ended with December 31, 2006. Within RISE a novel rehabilitation method for patients with long-term flaccid paraplegia and no chance of recovery of the nervous system, was developed. It restores their muscle fibres and mass, muscle function and thus in selected cases their ability to rise and maintain a standing posture. Based on the results from animal experiments on rabbit and pig and a patient study the associated technology was developed and finally an initiative to gain compliance with current and future regulatory affairs was part of the project. One basic intention was to provide European industry with a novel product family to support broad clinical application of the method that addresses the needs of about twenty new patients per million EU inhabitants per year. In addition to stimulation equipment for home based training, measurement equipment to support patient supervision was developed, to monitor the biomechanical and electrophysiological muscle conditions – transfer to industry is in progress.

1 Introduction

Practically all established clinical FES applications are based on direct excitation of neural structures and - in case of muscle functions - indirect activation of the muscles. For reactivation of denervated and especially denervated degenerated muscles (DDM) the technical demands are completely different. Due to the absence of the neuromuscular junction and decomposition of motor units, muscular contractions can only be elicited by depolarizing the cellular membrane of each single muscle fibre.

Until recently there were only few published studies giving evidence in both animal and clinical experiments that functional reactivation of denervated muscles by FES is possible in principle and in the long-term even in case of severe degeneration. Our own preliminary studies confirmed that FES could be a powerful tool for regeneration, functional restoration and maintenance of denervated muscles with the potential to serve as a novel rehabilitation method for patients with muscle denervations of various origins and especially after injury of the cauda equina. Working out of a firm scientific basis for a later clinical routine treatment was the main goal of the European project RISE, "Use of electrical stimulation to restore standing in paraplegics with long-term denervated de-

generated muscles". The project was funded by the European Union within the 5th Framework Program and involved nineteen European partner institutions. The consortium included 13 European partner institutions from Austria (4), United Kingdom (1), Italy (3), Slovenia (1), Germany (3) and Iceland (1) and additional six subcontractors from Austria (5) and Germany (1). Nine out of the nineteen were spinal cord injury centres. RISE started with November 1, 2001 and ended with all nationally co-financed extensions projects in December 31, 2006.

2 Methods

RISE has aimed in developing a novel clinical rehabilitation method for patients with long-term flaccid paraplegia (denervated degenerated muscles - DDM) and no chance of recovery of the nervous system, a problem that concerns about twenty new patients per million EU inhabitants per year, and to develop the associated technical equipment. The project work was organised in 5 work-packages: an animal study on rabbits (denervation up to one year), a second one on pigs (denervation up to three years), a technical work-package on stimulation equipment for home based therapy, a second one on test- and measurement

equipment and finally a patient study with an observation time of 2 years.

3 Results

The rabbit experiments have provided us with new knowledge about the course of denervation in the rabbit tibialis anterior (TA) and extensor digitorum longus (EDL) over observation periods of up to one year. Comprehensive electrophysiological, biomechanical, histological and biochemical data of 70 rabbits were obtained. Battery powered single-channel implants and epifascial stainless steel electrodes were applied and various training strategies and safety issues were addressed. The denervation period of one year led to atrophy not yet degeneration. Muscle mass and histological appearance were sufficiently restored with daily electrical stimulation of 30 minutes with a stimulation frequency of 20-25 Hz inducing fused contractions. More stimulation did not show improvements but also did not cause tissue damage. Despite this muscle restoration a remaining force and endurance deficit compared to controls was observed in the terminal assessment sessions [6, 7].

The study on Göttinger Minipigs was performed in 9 animals and denervation periods of up to 3 years (isolated unilateral denervation of EDL and TA). Data on histological, electrophysiological and biomechanical changes were obtained, confirming that the model shows a very similar time course of post-denervation atrophy and later degeneration in comparison to humans. 4 of the animals were treated with patient stimulation equipment (surface electrodes) and protocols and the results were comparable to those from the human study.

In the technical work packages we have developed stimulation and measurement equipment for the animal experiments and the patient study [1, 2, 3]. An implantable battery powered stimulator including epifascial muscular electrodes [5], a versatile bench stimulator for both manual and PC-based control, measurement setups for rabbit and pig experiments and the patient study, two generations of prototype stimulation equipment for pig and human experiments and various prototype garments for improved electrode application in the patient study are now available [1]. A patent for a novel electrode minimising the risk of skin burns [10] and the developed dual channel stimulator were licensed to the Austrian company Schuhfried (Mödling). The equipment is in a final phase of certification and market introduction. The parameters of a suitable stimulator cover biphasic rectangular impulses with constant voltage (CV) amplitude up to ± 80 V (current delivery up to ± 250 mA), impulse width between 15 ms and 200 ms per phase and interpulse intervals down to 5 ms to achieve fused contractions in well trained patients. Multiple safety features are included to avoid electrical dangers and potential skin burns. CC output sources and large surface electrodes are important to

avoid excessive current density spots in the contact surface. The critical electrode edges, where the risk of burns is the highest are unloaded by a special patented shape modification [10] that obviously solved the problem, as our tests showed.

The patient study was completed with finally 20 patients. 5 of them achieved standing-up, 3 walking in mobile parallel bars up to 36 m [4].

The data collected during the project have increased our knowledge about degeneration, regeneration and restoration of denervated human muscle substantially. CT-scans of the thigh showed changes in muscle size and tissue composition. Morphology was analysed with reference to the Hounsfield scale. The assessment included biopsies from vastus lateralis at the beginning and end of the two years study. Histological, biochemical and electronmicroscopical analysis showed functional degeneration and restoration of the muscle cells. Furthermore single-fiber conduction velocity measurements showed nearly normalisation as well as near normal refractory behaviour (measured with a double impulse protocol using the same setup) [2]. Furthermore biomechanical assessment: oscillation tonometry, patella twitch sensor and isometric knee torque measurement were used to quantify the FES related functional improvements [3].

Clinically initial atrophy turns to degeneration within the second year after denervation. Not surprisingly FES training turned out to be most efficient if started within the first year post denervation. It is possible to restore muscle mass, histology and even ultra structure almost completely and provide an effective tissue cushioning to prevent pressure sores. Successful restoration of already long-term denervated degenerated muscles seems possible but takes by far longer and restoration was clearly less efficient at least within the limited therapy time we were able to follow within the RISE study [8, 9].

4 Discussion and Conclusions

Though the appearance of the FES restored muscle looks normal in many respects we have observed a remaining force and endurance deficit in experimental and clinical data. To explain this discrepancy and survey the underlying mechanisms will be main topics of our future work. Other plans concern an extension of the method to incomplete lesions and partly intact sensibility and the development of an implantable stimulation system for FES of denervated muscles. For patients with intact sensibility we need to experiment with various impulse shapes to find a compromise between effective muscle contraction and unpleasant skin sensation. Some potential in this direction can be expected from exponential and ramp shaped impulses. Implantable solutions need novel technical approaches in comparison to contemporary implants for nerve or cardiac muscle stimulation. Electrodes have to be large in size and placed very close to the muscle fibers, meaning a large foreign

body within moved soft tissue with all related problems. A further problem is power supply control as the delivered energy is by far higher than for nerve stimulation. One approach is suggested in patent [11]. The basic idea is to attach all technical components to the skeleton to avoid biological, chemical and mechanical interaction of implant components and soft tissue as far as possible. In combination with power supply by inductive coupling the whole system could provide fully automatised muscle training for prevention of pressure sores without substantial demands on the compliance of the patient. The patent is owned by the Austrian company Medel (Innsbruck).

For now – with the end of RISE – we are able to provide a clinical method and associated technology that is capable of reducing substantially the risk of pressure sores in patients with flaccid paraplegia and thus contributing to an improved quality of live for those patients. Part of the patients is able to stand-up with muscle power with the additional benefit of cardiovascular training.

A safe and effective set of stimulation equipment for home based training is in transfer to industry. The Austrian medical company Schuhfried has licensed the safety electrode [10] and the developed stimulator. The company aims to make to make the electrodes and a dual-channel stimulator available on the European market within the year 2008. A 4-channel version is planned for 2009.

5 References

- [1] Mayr W, Hofer C, Bijak M, Rafolt D, Unger E, Sauermann S, Lanmueller H, Kern H. Functional Electrical Stimulation (FES) of denervated muscles: existing and prospective technological solutions *Basic Appl Myology*. 2002;12(6):287-290
- [2] Hofer C, Forstner C, Mödlin M, Jager H, Mayr W, Kern H. In vivo assessment of conduction velocity and refractory period of denervated muscle fibers. *Artif Organs* 2005 Jun;29(6):436-9
- [3] Gallasch E, Rafolt D, Kinz G, Fend M, Kern H, Mayr W. Evaluation of FES-induced knee joint moments in paraplegics with denervated muscles. *Artif Organs*. 2005 Mar;29(3):207-11
- [4] Kern H, Rossini K, Carraro U, Mayr W, Vogelauer M, Hoellwarth U, Hofer C. Muscle biopsies show that FES of denervated muscles reverses human muscle degeneration from permanent spinal motoneuron lesion. *J Rehabil Res Dev*. 2005 May-Jun;42(3 Suppl 1):43-53.
- [5] Lanmüller H, Ashley Z, Unger E, Sutherland H, Reichel M, Russold M, Jarvis J, Mayr W, Salmons S. Implantable device for long-term electrical stimulation of denerv. muscles in rabbits. *Med Biol Eng Comput* 2005 Jul;43(4):535-40.
- [6] Ashley Z, Sutherland H, Lanmüller H, Russold MF, Unger E, Bijak M, Mayr W, Boncompagni S, Protasi F, Salmons S, Jarvis JC. Atrophy, but not necrosis, in rabbit skeletal muscle denervated for periods up to one year. *Am J Physiol Cell Physiol*. 2007 Jan;292(1):C440-51.
- [7] Ashley Z, Salmons S, Boncompagni S, Protasi F, Russold M, Lanmüller H, Mayr W, Sutherland H, Jarvis JC. Effects of chronic electrical stimulation on long-term denervated muscles of the rabbit hind limb. *J Muscle Res Cell Motil*. 2007;28(4-5):203-17. Epub 2007 Sep 29
- [8] Kern H, Hofer C, Mödlin M, Mayr W, Vindigni V, Zampieri S, Boncompagni S, Protasi F, Carraro U. Stable muscle atrophy in long-term paraplegics with complete upper motor neuron lesion from 3- to 20-year SCI. *Spinal Cord*. 2008 Apr;46(4):293-304. Epub 2007 Oct 23.
- [9] Boncompagni S, Kern H, Rossini K, Hofer C, Mayr W, Carraro U, Protasi F. Structural differentiation of skeletal muscle fibers in the absence of innervation in humans. *Proc Natl Acad Sci U S A*. 2007 Dec 4;104(49):19339-44. Epub 2007 Nov 27.
- [10] WO2007131248 – Winfried Mayr: “Surface electrode” (avoiding skin burns in transcutaneous electrostimulation, electrotherapy or electro-surgery), published Nov. 22, 2007-12-07 Priority date Mai 16, 2006
- [11] R 49626 – Winfried Mayr “Implant for functional electrical stimulation of denervated muscles”
Filed March 21, 2007, pending

Acknowledgements

This research was supported by EU Commission Shared Cost Project RISE (contract QLG5-CT-2001-02191) and the Austrian Ministry of Science (GZ 8.130/6-VI/1/2003).

Modulation of stimulation frequency of spinal cord afferents with unchanged intensity and electrode site can induce a variety of movements

Winfried Mayr¹, Christian Hofer², Karen Minassian¹, Ursula Hofstötter¹, Helmut Kern², Manfred Bijak¹, Ewald Unger¹, Frank Rattay³ and Milan Dimitrijevic⁴

¹ Center for Biomedical Engineering and Physics, Medical University Vienna, Austria

² Department of Physical Medicine and Rehabilitation, Wilhelminenspital Wien, Vienna, Austria

³ TU-BioMed Association for Biomedical Engineering, Vienna University of Technology, Vienna, Austria

⁴ Baylor College of Medicine, Houston, Texas

Abstract

In this report we shall review the finding that selective stimulation of tibial nerve large afferents and selective stimulation of lumbar sacral afferents to the spinal cord can elicit modification of motor output only by changing of the rate of the train of stimuli without changing the stimulus strength or site of stimulation. After a brief description of the applied methods in reported studies of suppression of sustained anti-clonus by train of stimuli of large afferents of tibial nerve at the sensory level, we shall point out that this “anti-clonus” effect depends from a particular frequency range. Other study in which we shall illustrate dependence from frequency rate of motor output it is epidural or transcutaneous stimulation of lumbar posterior roots; and how the frequency of applied stimulation trains can induce two completely different functional outputs of paralysed lower limbs (standing and locomotor-like movement) due to upper motor neuron lesion.

At the end we shall discuss underlying mechanisms of this artificial “coding” in order to induce movement by afferent FES. Finally we shall discuss the significance of these findings for clinical practice of FES in upper motor neuron disorders.

1 Introduction

From the early beginning of FES frequency of stimulation of peripheral nerves in order to elicit functional movement by activating paralyzed muscles has been focused towards elicitation of sufficient muscle power. Therefore the used frequency was determined by fusion of muscle twitches to the steady and strong movement [1]. However, it has been noticed that stimulation of peripheral nerve trunks in addition to depolarisation of motor axons and induced proprioceptive muscle input by contraction of otherwise paralyzed muscles was also effect of stimulation of the largest diameter sensory fibers of the nerve trunk with lowest threshold for depolarisation by a train of stimuli [2]. This observations, that peripheral nerve trunk stimulation can have direct motor effect and indirect reflex afferent (sensory) – efferent (motor) effects, led researchers to study optimal frequency for muscle force generation and optimal frequency for augmentation of neural control. In this presentation we shall focus on “sensitivity” of central nervous system and its sensory – motor mechanisms to modulation of frequency while modifying movement.

We shall use two examples to illustrate the main point

of our presentation dependence of movement modification by changing frequency of the train of stimuli.

Example 1: Clonus is a term describing repetitive stretch reflex of any muscle group of the human body with a frequency between 6 and 7 Hz. Clonus can be present in adult persons with intact nervous system after setting volitionally or by extraneous muscle exercise in healthy people it is a known observation that clonus will appear after hours of mountain climbing. However in patients with neurological conditions, after stroke, head and spinal cord injury, multiple sclerosis and others, clonus can be an obstacle for those patients standing, walking and other daily activities, even for use of wheelchair.

From neuro-physiological point of view the underlying mechanism for clonus is an increased central state of excitability of segmental mechanisms involved in motor cells, motor nuclei and functional disbalance in reciprocal inhibition between agonist and antagonist muscle. In case of ankle clonus motor cell excitability of triceps sure muscle group is higher than motor cell excitability of dorsal flexors of the ankle (tibial anterior and other muscles).

Fig. 1 is showing a sketch of described agonist and antagonist segmental levels of leg muscles and illus-

trate an attempt to suppress ankle clonus by increasing reciprocal inhibition by stimulating at the threshold for large afferents of peripheral nerve and causing the increase of reciprocal inhibition to the motor neurons of hyper-excitible triceps sure muscle.

Effect of this stimulation is illustrated in Fig. 2. Anti-clonus effect was clear and repetitive when applied train of stimuli of 75 V with 1ms duration of the single stimulus within a 50 Hz train of 0,4 s. Nevertheless such clear effect was absent when frequency of train was of the same strength but lower frequency of 30 or 40 Hz [3, 4].

“Anti-clonus effect” depends from different stimulation parameters. Naturally this effect will not be present in every testing subject with same parameters since this is not a “wired” sensory motor integration activity but a dynamic response to externally controlled input. What we are learning is if our attempt is to induce reciprocal inhibition and establish equilibrium between antagonistic motor nuclei we should not only examine the effect of one frequency, but at least several of them within a range of 30 to 100Hz.

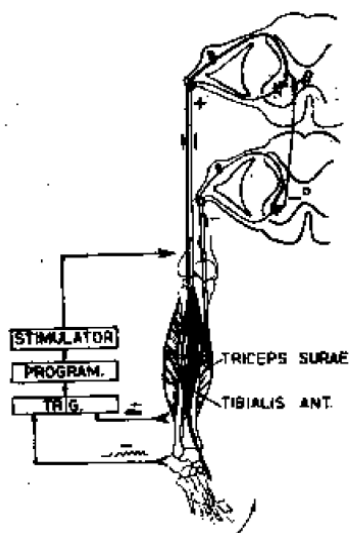


Fig. 1 Anit-clonus model. Clonus in triceps surae (detected by electromechanical or bioelectrical clonus detector) triggers stimulator, which delivers stimuli to afferent fibers of peroneal nerve. These evoke slight contraction in tibialis anterior muscle, and at the same time inhibit clonic activity in antagonistic triceps surae muscle [3, 4].

Example 2: Another reported illustrative example is selective stimulation of lumbar-sacral posterior roots in people with chronic posttraumatic spinal cord injury and known as a ASIA A or B between clinicians. Placement of multi-site epidural electrode can elicit selective stimulation of posterior roots and such studies of Vienna group for restoration of locomotion in Otto Wagner Hospital, Wilhelminenspital and Center of Biomedical Engineering and Physics [5, 6, 7, 8] demonstrate that application of different frequencies of train at the same stimulus site and strength it is

possible to elicit movement of paralysed lower limbs similar to strong standing are locomotor-like movement. Fig. 3 is illustrating this finding.

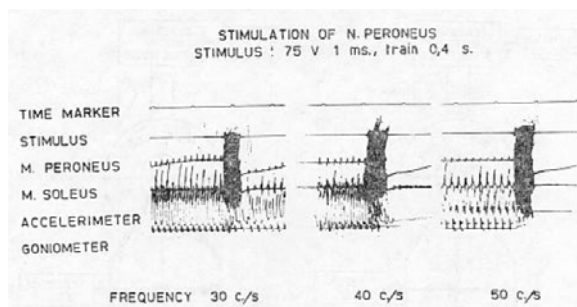


Fig. 2 Dependency of the anti-clonus effect upon frequency of the stimuli within the train. This proves that the effect of stimulation is highly specific [3, 4].

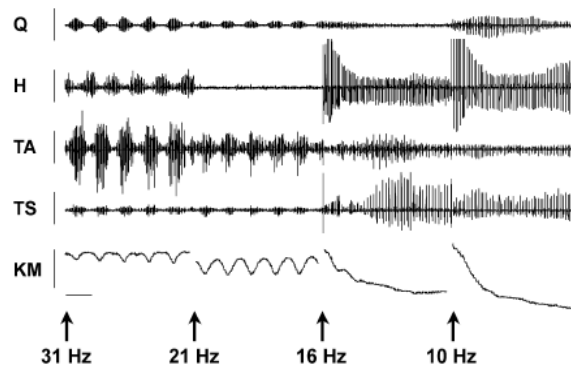


Fig. 3 Surface electrode recording from lower limb muscles of a paraplegic patient while stimulating epidurally posterior roots L2-S1. We are showing in the same subject without changing site and strength of stimulation we can modify feature of motor output from locomotor-like to extending lower limbs of standing-like posture [5, 6]; Vertical markers: 500 μ V (Q, H, TA, TS); 45° (KM knee movement). Horizontal marker: 1 s

We can see that rhythmical and tonic EMG activity of paralyzed lower limbs induced by spinal cord stimulation can be elicited and 31 and 21 Hz can induce strikingly different motor outputs of rhythmical activity when compared to 16 and 10 Hz of tonic activity [7, 8]. Moreover the goniometer traces illustrate the corresponding rhythmical and extension movements, respectively. We would like to emphasise that stimulation parameters (site and strength) were never changed during the recording session. Note that during the “flexion phases” induced at 31–21 Hz the amplitudes in quadriceps and tibialis anterior are larger than the ones in hamstring and triceps surae, respectively. This dominance is reversed in response to stimulus frequencies of 16–10 Hz. Recorded in a complete SCI subject (estimated segmental level of stimulation: L4/5); stimulation parameters: 10 V, 210 μ s pulse width.

2 Discussion and Conclusion

Let us initiate discussion and conclusion by analysing Fig. 4 which is a sketch of interneuron human lumbar grey matter network and superimposed drawing of spinal reflex pathways with different numbers of interposed inter-neurons between afferent and efferent parts of the reflex arc.

Described finding led us to develop the working hypothesis that depolarised primary afferent fibers have connectivity with monosynaptic, polysynaptic and interneuron networks. When changing the repetition rate of input parameters, the interneuron network can respond with different configuration of subunits of the motor output generator. Therefore “coupling” and “decoupling” of human lumbar cord interneurons by different frequencies is at present proposed mechanisms under testing. Further work should demonstrate how much functional movement can be elicited by modifying frequencies in interaction with human motor control with intact or impaired CNS in order to become useful in the clinical practise.

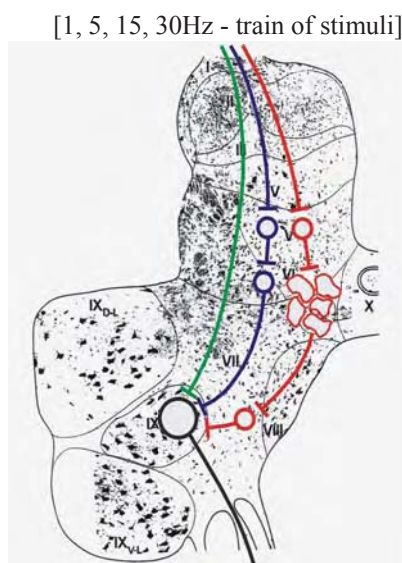


Fig. 4 Histological preparation of the L2 segment of the human lumbar cord with borders of Rexed-zones. This combined sketch illustration of interneuron cells and motor cells distribution within grey matter from smallest size interneurons in Rexed-segment I and II to for us relevant segments IV, V and VI and finally largest cells of motor nuclei of segment VIII is bringing to our attention possibility that different input of different frequencies can engage different population of interneurons.

3 Literature

- [1] Liberson WT. Brains, Nerves, Muscles and Electricity: My Life in Science. Cohen R (ed). Smirna Press, ISBN-10: 0918266386, June 1999.
- [2] Dimitrijevic MR. Use of physiological mechanisms in the electrical control of paralyzed extremities. In: Advances in External Control of Human Extremities, Dubrovnik, Yugoslav Committee for Electronics, Telecommunication, Automatic, and Nuclear Sciences (ETAN) Belgrade, Yugoslavia. 1967: 27-41.
- [3] Dimitrijevic MR, Gracanin F: Control of release phenomena in hemiplegics by means of afferent electrical stimulation. International Meeting on Electromyography, Glasgow, 1967
- [4] Gracanin F, Marincek I: Development of new systems for functional electrical stimulation In: Advances in External Control of Human Extremities, Dubrovnik, Yugoslav Committee for Electronics, Telecommunication, Automatic, and Nuclear Sciences (ETAN) Belgrade, Yugoslavia. 1970: 495-502.
- [5] Jilge B, Minassian K, Rattay F, Pinter MM, Gerstenbrand F, Binder H, Dimitrijevic MR. Initiating extension of the lower limbs in subjects with complete spinal cord injury by epidural lumbar cord stimulation. *Exp Brain Res.* 2004; 154: 308-326.
- [6] Jilge B. Neurocontrol of standing and walking: Analysis of the electrically stimulated lumbar generator for extension in paraplegic human. Doctoral Thesis, Vienna University of Technology, 2003
- [7] Minassian K, Jilge B, Rattay F, Pinter MM, Binder H, Gerstenbrand F, Dimitrijevic MR. Stepping-like movements in humans with complete spinal cord injury induced by epidural stimulation of the lumbar cord: electromyographic study of compound muscle action potentials. *Spinal Cord* 2004; 42: 401-416.
- [8] Minassian K. Modeling of a human spinal pattern generator for locomotion and its activation by electrical epidural stimulation. Doctoral Thesis, Vienna University of Technology, 2004.

Acknowledgements

The author would like to acknowledge the support of the Foundation for Movement Recovery, Oslo, Norway, and the Wings for Life Spinal Cord Research Foundation, Salzburg, Austria.

A biofeedback based portable device to support elderly mobility in the home environment

M. Mancini¹, E. Farella², L. Rocchi¹, C. Tacconi², L. Benini² and L. Chiari¹

¹ Biomedical Engineering Unit, DEIS, University of Bologna, Bologna, Italy

² Micrel Lab, DEIS, University of Bologna, Bologna, Italy

Abstract— We present a device to support elderly balance and mobility in the home environment based on the sensory augmentation principle. We designed and tested an audio-biofeedback system that is wireless and lightweight, and can be easily worn and operated by elderly subjects. Having in mind wearability and unobtrusiveness, it is based on a palmtop computer, a stereo headset, and body sensors networks. Preliminary validation was performed on a sample of 6 older people with Parkinson's Disease and 3 age-matched control subjects. Promising results were obtained, both in terms of ease-of-use and users' acceptability of the device, and in terms of postural improvement induced by the use of the biofeedback system.

Keywords— ambient assisted living, assistive technologies, telemedicine, biofeedback.

I. INTRODUCTION

Balance disorders may be a critical health problem, because they seriously affect the activity of daily life, and they may originate even more serious problems, related to falls and disabilities. Annual costs associated with falls, particularly in an elderly population, are exceeded only by those associated with motor vehicles injuries [1]. In fact, one-third to one-half of the population over age 65 reports some difficulty with balance or ambulation [2, 3]. In Europe, approximately one-third of community-dwelling adults over 65 years and 50% of those over 80 years fall at least once a year [4]. Twenty to thirty percent of those who fall suffer injuries that reduce mobility and independence and increase the risk of premature death [5, 6].

The improvement of balance ability and consciousness is an important point for reducing falls and increasing the quality of life. Increased body awareness and position sense is necessary to compensate functional limitation in balance disorders. Balance improvements may be achieved by adding artificial sensory information (sensory augmentation or substitution) that enlightens the brain about actual body posture and movements. This information may be coded into an appropriate sensory signal and provided in real-time; in this case, brain and muscle activities, that are not nor-

mally controlled voluntarily, may be changed accordingly to the new information available. This is a typical example of biofeedback (BF), a training technique in which people are taught to improve their health and performance by using signals from their own bodies [7].

It has been demonstrated that physical activity based interventions, including biofeedback therapies, can improve functioning in older people. In specific elderly populations, such as older fallers and patients with Parkinson's disease, there is evidence that interventions may improve both cognitive and motor functions. Available results suggests higher efficacy when interventions take place over longer time periods, when they are individually tailored, and include exercises in the home environment [8].

Due to recent technological advances, it is now possible to use body-fixed sensors in combination with advanced ICT solutions to effectively monitor older people in their home environment and to introduce BF-like interventions that are tailored to individual needs. This new approach allows, e.g., tele-rehabilitation solutions where, from a distance, medical professionals monitor and assist older people.

In this paper we present a portable wireless system for BF user-tailored rehabilitation for balance disorders, and its preliminary application in six subjects with Parkinson's Disease (PD) and three control subjects.

II. SYSTEM ARCHITECTURE

The portable and wireless BF system was designed to include modular hardware architecture for diverse sensors integration and wireless communications, and a modular software design to allow easy and optimized integration of different sensors, communication protocols and BF algorithms. The hardware architecture was designed to potentially include a network of sensing nodes, and is capable to drive different actuators as BF generators (e.g. audio, tactile, and visual). In its simplest release, the body area network consists of an inertial sensor (3D accelerometer and/or 3D gyroscope), a headset, a processing node, and a PDA. This minimal configuration was chosen to comply with users' acceptability of the system.

The software architecture has been designed to best accomplish real-time data processing, I/O synchronization, trouble-free integration of further BF algorithms, independence from sensor node(s) characteristics and set-up. Furthermore, the software allows the detection of possible radio communication problems (packet losses), notifying the user in case of misuse of the system. The processing node manages the data from the body sensor, to estimate the user's posture and to provide adequate audio BF [9]. Such features have been combined with a friendly graphical interface for non-expert users (leftmost window presented in Fig.1). An advanced set of dialogue windows offers the caregiver or training supervisor the possibility to select the appropriate BF algorithm and user-specific options, and to perform a spot-check on the correct functioning of the sensing node (right side of Fig.1).

enabling the communication between the wireless sensor and the handheld device (e.g. open the communication port, selection of the protocol, configuration of main parameters such as baud-rate, etc.) and of extracting meaningful data (the payload) from the packet received; ii) a data processing module implementing the BF algorithm and generating the corresponding feedback (e.g. the sound); iii) a data manager, which is the module handling the communication with the actuator and the storage of data on the palmtop computer; iv) a graphical user interface to easily handle basic functionalities (e.g. to start and stop the application) and advanced configuration for expert user (e.g. algorithm selection, advanced user profiling, algorithm parameters set-up, etc.).

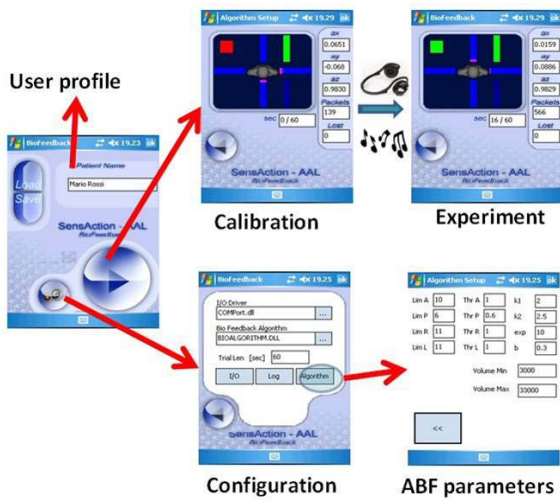


Fig. 1 Graphical user interface – basic and advanced windows

The functioning principles of the system and its architecture are illustrated in Fig.2.

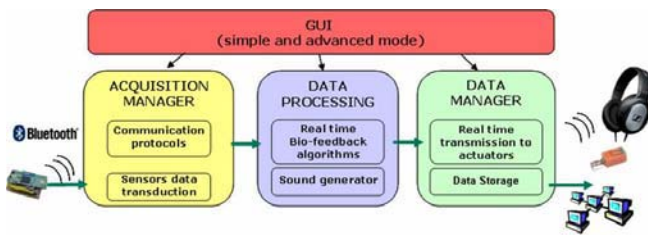


Fig. 2 System architecture

In summary, the main building blocks of the software architecture consist on: i) an acquisition manager in charge of

III. CASE STUDY

A. Participants and Protocol

The system was preliminarily tested on a sample of elderly volunteer population of 6 patients with PD (Hoehn & Yahr, II-III), and 3 age-matched control subjects. The patients were not in their chronic stage of the trunk abnormalities typical of late-stage PD, but still in an early phase, where correction of the trunk position was still possible, with an intentional effort. The experimental set-up used for this test is shown in Fig. 3.



Fig. 3 Experimental Setup

Subjects stood quietly with eyes closed prior (CONDITION: pre), during (ABF), and after (post) the delivery of the ABF. During the trials with ABF, subjects were asked to correct their sway according to the feedback, by keeping the volume as low and as balanced as possible.

A preliminary analysis to study the efficacy of ABF in reducing the postural sway was carried out with a main focus on the following indexes, computed from the bidi-

mensional trunk acceleration: 1) JERK, indicating the smoothness of sway, 2) RMS, that estimates the extent of sway, 3) F95%, that represents the frequency below which the 95% of the power of the signal is included.

B. Preliminary results

PD subjects found the system easy-to-use and adequate, and they were able to correctly follow the audio information when available. Figure 4 shows bidimensional trunk acceleration in the 3 aforementioned conditions for a representative subject with PD. The extent of sway was smaller in ABF and post conditions with respect to pre condition.

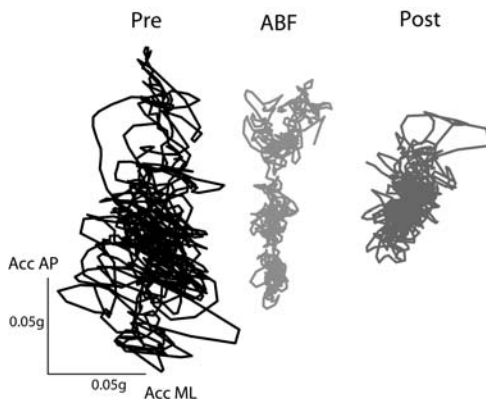


Fig. 4 Trunk acceleration in a representative PD subject in the 3 conditions

JERK in the subjects with PD is larger with respect to control subjects (Fig. 5), even if no statistical analysis was possible due to the paucity of subjects included in the study. The observed decrease in JERK in 5 among 6 PD subjects, with ABF treatment, reflects an increased smoothness of movement; this is preserved even (shortly) after the end of the ABF.

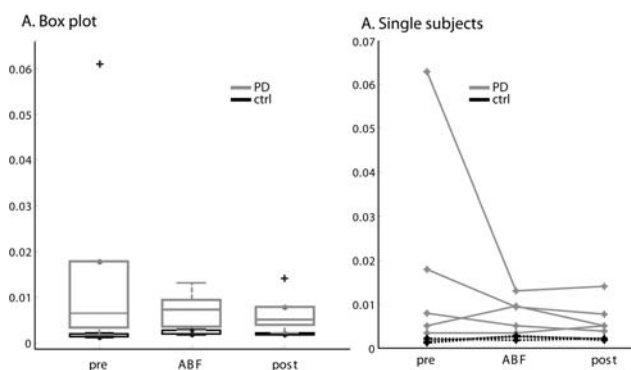


Fig. 5 JERK of postural sway

In addition, RMS, which reflects extent of sway, and F95% tend to be reduced in PD during ABF with respect to the pre condition. This suggests that ABF might act to improve regularity of trunk sway.

IV. CONCLUSIONS

In this paper we presented a wireless, portable device to support elderly mobility in the home environment which is suitable for a ubiquitous use. The device affects balance and mobility by taking advantage of the essential principles of biofeedback-based interventions. Moreover, it has been designed with both a hardware and software modular architecture to allow an easy interoperability and a wide versatility. The preliminary validation process is showing an adequate behavior of the system and a good acceptability by PD subjects which were able to correctly follow the audio information, and to properly extend the trunk toward a more physiological position, during trials of 60 seconds in a quiet-standing position.

Such results, whereas preliminary, are promising and an extended campaign for the clinical validation of the device is in progress among the clinical partners of the SENSATION-AAL project after adequate approval from the local Ethical Committees.

ACKNOWLEDGMENTS

This work was supported by the EU-funded project SENSATION-AAL (FP6-IST-2005-2.6.2-045622).

REFERENCES

1. Loughlin P, Redfern M (2003). Analysis and modeling of human postural control. *IEEE Eng. Med. Biol. Mag* 22(2): 18.
2. Coogler C (1992). Falls and imbalance. *Rehab Management* 53.
3. Hausdorff JM, Rios DA, Edelberg HK (2001). Gait variability and fall risk in community-living older adults: a 1-year prospective study. *Arch. Phys. Med. Rehabil.* 82(8):1050-1056.
4. Halter M (2000). Falls in the older population: a pilot study to assess those individuals who are attended to by the London Ambulance Service as a result of a fall but are not conveyed to an accident and emergency department. London Ambulance Service NHS Trust.
5. Tinetti ME, Speechley M (1989). Prevention of falls among the elderly. *New Engl. J. Med.* 19:1055-1059.
6. Freeman C (2002). Quality improvement for people with hip fracture: experience from a multi-site audit. *Qual. Saf. Health Care* 11:239-245.
7. Huang H, Wolf SL, He J (2006). Recent developments in biofeedback for neuromotor rehabilitation. *J Neuroeng Rehabil.* 21:3-11.

8. Ashburn A, Fazakarley L, Ballinger C et al. (2007). A randomised controlled trial of a home based exercise programme to reduce the risk of falling among people with Parkinson's disease. *J. Neurol. Neurosurg. Psychiatry* 78:678-684.
9. Chiari L, Dozza M, Cappello A et al. (2005). Audio-biofeedback for balance improvement: an accelerometry-based system. *IEEE Trans. Biomed. Eng.* 52:2108-2111.

Martina Mancini, MS
DEIS, University of Bologna
Via Venezia, 52 47023
Cesena (FC)
Italy
martina.mancini@unibo.it

Measurement System of Hand Tapping Capacity for Quantitative Diagnosis of Parkinson's Disease

Sang Kyong Kim¹, Hyo Seon Jeon¹, Jonghee Han¹, Yoon Jae Choi², Beom Seok Jeon²,
Won Jin Yi³, and Kwang Suk Park⁴

¹ Interdisciplinary Program of Bioengineering, Seoul National University, Seoul, Korea

² Dept. of Neurology, Seoul National University Hospital, Seoul, Korea

³ Dept. of Oral and Maxillofacial Radiology, College of Dentistry, Seoul National University

⁴ Dept. of Biomedical engineering, College of Medicine, Seoul National University, Seoul, Korea

Abstract—The Unified Parkinson's Disease Rating Scale (UPDRS) is commonly used to measure the patients' disorder in clinical therapeutics. However, UPDRS scores can be somewhat variable and subjective. Especially, there are only 5 scales at each item. It is necessary to develop a quantitative measurement of movement ability in PD patients. Hand Tapping test system was developed in this purpose.

Here, we present hand tapping test system and some test such as simple reaction test and random response test. Twelve PD patients (7 men and 5 women) were evaluated. The result of tests show us good correlation between movement time and UPDRS part III score (0.84, 0.72). On the other hand, the reaction time and UPDRS part III score was not related to each other. Thus, we conclude that movement time of hand tapping test can be one of the feasible quantitative measurement methods of PD patients' movement.

Keywords— Hand Tapping Capacity Measurement System, Unified Parkinson's Disease Rating Scale, Simple reaction test, Random response test, movement time, reaction time.

I. INTRODUCTION

Parkinson's disease (PD) is the most common progressive and degenerative movement disorder which middle age and elderly people get. The major symptoms are characterized by tremor, rigidity, bradykinesia and gait disturbance. Such symptoms are related to dopaminergic loss. The major treatment of PD is pharmacotherapy with L-dopa, and so on [1]. For dosage of the drugs, quantitative diagnostic methods are important.

Unified Parkinson Disease Rating Scale (UPDRS) was currently standard and widely used scale for Parkinson's disease diagnosis or research. However, the scores could be somewhat variable, subjective and may not be as reproduc-

ible. It was, therefore, necessary to develop a quantitative diagnostic method [2].

Hand tapping test could be simple, easy and accurate to assess ability of upper limb. Actually until a recent date, some classical methods of physical capacity test of PD patients are used. For example, doctors draw two points at interval of about 30cm on the board, and ask the patients to move and to press the points alternately for 1 min. All the while, they were watching the stop watch and record how many points are pressed with patient's finger. These methods are cumbersome and not accurate.

In connection with hand tapping test, many previous studies about finger tapping movement were reported. Finger tapping movement analyses were about finger taps movement acceleration, velocity, finger taps accuracy, finger tapping force, and so on. [3-4] On the other hand, study about web-based and lab-based hand tapping test was reported.[5] However, reported studies about hand tapping movement were not plenty yet.

The purpose of this study was to develop the hand tapping capacity measurement system which can be used simply and easily and to analyze the significance of the hand tapping test.

II. METHODS

A. Subjects

There were 12 Parkinson's disease patients (7 men and 5 women) in the present study. The PD patients ranged from 34 to 75 years (mean age: 57.78 years, S.D: 10.94). All patients were tested UPDRS part III. UPDRS part III scores ranged from 0 ~ 22 (Mean: 11.75, S.D: 7.08). All patients tested had relatively mild or moderate symptoms. Patients with severe symptoms moved their hands very difficultly, or could not move as intended. For that reason, they could not

press button well, and not be tested. Thus, severe patients were not included in this study.

B. Hand-Tapping Capacity Measurement System

Fig. 1 shows the hand tapping capacity measurement system. This system was made use of ATmega128 microcontroller, 6 switch buttons and computer. The distance between red button and yellow button was 25cm, which was designed for subjects to use their whole arm. We thought that high resolution timing was the most important to accurate test. Thus, it was made in order to record time in 1 millisecond. Red button was used as "Home Key", or start point. And it was fan-shaped in order not to conceal yellow button with participant's arm while the subject were pressing the red button.

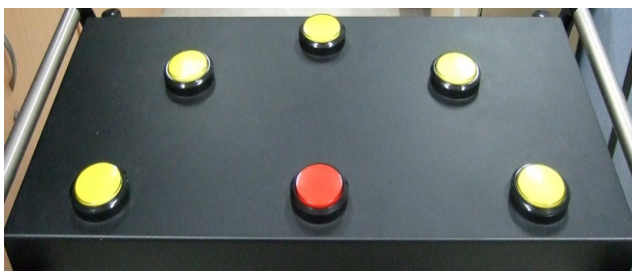


Fig. 1 Hand-Tapping Capacity Measurement System.

C. Simple Reaction Test

Simple reaction test used right and left yellow buttons. The instructions emphasized speed of performance. Subjects pressed the left and right button alternately as quickly as possible. 20 trials are administered at each test. And total 3 trials of the same test are conducted and both hands were tested. The best result which had fastest movement time and lowest S.D was chosen. Result file included pressed button number and movement time expressed in millisecond. Movement time represented intervals from one released button to the other pressed button. So that result file showed the movement time of each direction. Therefore, we could guess what muscles around the arms were damaged.

D. Random Response Test

Random response test used red button and all yellow buttons. Red button was used as "Home Key". After starting the test, red button light up. If participants keep the lighted red button pressing, yellow button would be lighted up, then they should press the yellow button as quickly as possible. Such processes were repeated 20 times. In the same way of

Simple reaction test, both hands were tested and total 3 trials were conducted. The best result of 3 trials was chosen. Result file included pressed yellow button number, reaction time and movement time. Reaction time represented the intervals from yellow button lighted up to red button pressed down. And movement time represented the intervals from red button released to yellow button pressed down. The delays of yellow button lighted up from red button pressed down are randomly arranged in the range of 1700 to 2700 milliseconds.

III. RESULTS

A. Simple Reaction Test

Fig.2 shows a result of Simple reaction test. The result was chosen among total 3 trials of test. Each point represented not the mean value of movement time but the value at each movement. Thus, the bundle of points could be the result of one participant. However, some participants had the different result between the right direction and the left direction movement time. The results of such participants looked like split bundles.

The correlation coefficient between movement time and UPDRS Part III score was 0.84, quite high. This test was similar to the classical diagnostic method referred to Introduction, so that such high correlation meant that classical method could be significant. On the other hand, movement time of one direction of one participant was quite uniform in comparison with the result of random response test.

B. Random Response Test

Fig.3 shows a result of random response test. In this test, two types of results were recorded. One was the reaction time the other was the movement time. Each point represents the value at each trial like Fig.2. Because both hands were all tested, the number of bundle of points was twenty-four. The correlation between reaction time and UPDRS Part III score was 0.35. And the correlation between movement time and UPDRS Part III score was 0.72. Thus, in view of the results so far achieved, we could interpret that in mild or moderate PD patients, as the symptoms get worse movement capacity gets worse faster than reactionary delay of certain stimulus.

In this test, significance of intraindividual variability, that is S.D. in each participant, was not found. However, we could found that intraindividual variability slightly tends to increase as UPDRS Part III score get higher. If the participants with severe symptoms were tested, we could find such tendency clearly.

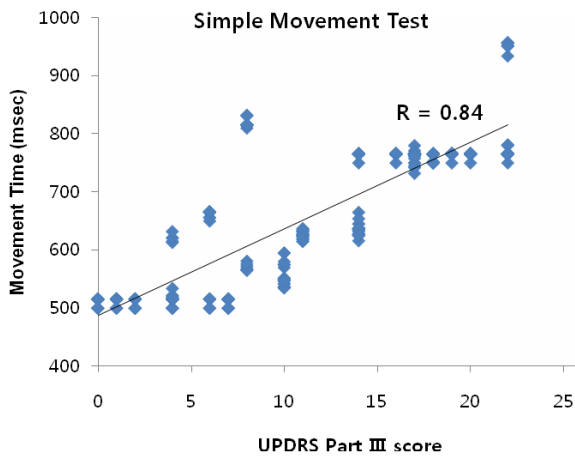


Fig. 2 The result of Simple Movement Test

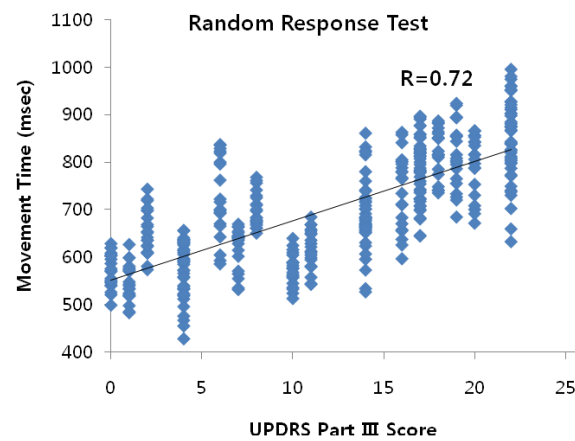
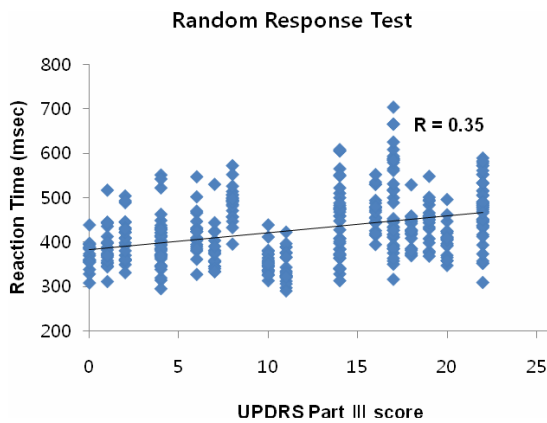


Fig. 3 The result of random response test. The correlation between reaction time and UPDRS Part III score was 0.35. The correlation between movement time and UPDRS Part III score was 0.72.

IV. DISCUSSION & CONCLUSIONS

The study has shown that the quantitative measurement of hand tapping test is valid measure of motor disability in Parkinson's disease, especially in PD patients with mild or moderate symptoms.

Movement time recorded in both simple movement test and random response test was in close correlation with UPDRS Part III score. On the other hand, reaction time in random movement test didn't seem to be related to UPDRS Part III score. Thus, it was thought that relation between seriousness of PD symptoms and reaction time was not significant, and that PD patients' reactionary start point didn't get slower significantly although their symptoms got worse.

In the random response test, we could find some patients who had different movement abilities between right direction and left direction. Although differences between right direction and left direction were not referred specially to this study, it might be the other important value.

Although we intended to find the significance of intra-individual variability as other reported paper related this study, we could not find the significant feature [1]. However, in random response test we could find that intra-individual variability of movement time had a slight tendency to get larger as UPDRS Part III score. It seems that intraindividual variability could be used as a point of reference whether patients were mild or not.

Severe PD patients could not move their hands or press the button down well as intended, so that they were difficult to be tested. Thus, this study has made progress with an exception of them.

Hand tapping test was very easy and simple to assess their symptoms in clinic as well as in patients, therefore, it was thought that patients could tested and checked easily by themselves on occasion.

ACKNOWLEDGEMENT

This work was supported by a grant from the Advanced Biometric Research Center (ABRC) and the Korea Science and Engineering Foundation (KOSEF).

REFERENCES

1. Richard M. Camicioli, Marguerite Wieler, Cindy M. de Frias, W.R. Wayne Martin (2008) Early, untreated Parkinson's disease patients show reaction time variability. *Neuroscience Letters* 441:77~80

2. Ryuhei Okuno, Masaru Yokoe, Kenzo Akazawa, Kazuo Abe and Saburo Sakoda (2006) Finger Taps Movement Acceleration Measurement System for Quantitative Diagnosis of Parkinson's disease, NIBIO
3. Ana Lisa Taylor Tavares, MB, BS, Gregory S.X.E. Jefferis, PhD, Mandy Koop, MS, Bruce C. Hill, PhD, Trevor Hastie, PhD, Gary Heit, MD, PhD, and Helen M. Bronte-Stewart, MD, MSE (2005) Quantitative Measurements of Alternating Finger Tapping in Parkinson's Disease Correlate with UPDRS Motor Disability and Reveal the Improvement in Fine Motor Control From Medication and Deep Brain Stimulation. *Movement Disorders* Vol.20, No. 10 : 1286~1298
4. R. Arunachalam, V. S. Weerasinghe, and K.R.Mills (2005) Motor Control of Rapid Sequential Finger Tapping in Humans. *J Neurophysiol* 94 : 2162-2170
5. George V. Kondraske, Fellow IEEE and R. Malcolm Stewart (2008) Web-based Evaluation of Parkinson's Disease Subjects : Objective Performance Capacity Measurements and Subjective Characterization Profiles. 30th Annual International IEEE EMBS Conference Vancouver, British Columbia, Canada, August 20-24, 2008

Author: Kwang Suk Park
Institute: Dept. of Biomedical engineering, Seoul National University
Street: College of Medicine, Seoul National University Hospital,
110-799, 28, Yeongeon-dong, Jongno-gu, Seoul, Republic
of Korea
City: Seoul
Country: Korea
Email: kspark@bmsil.snu.ac.kr

Optimization of Sensomotoric Insoles

J. Subke¹, S. Kolling², J. Griesemann¹, P. Kleinau¹, and M. Staudt³

¹ Biomechanics Lab, University of Applied Sciences Giessen-Friedberg, Giessen, Germany

² Laboratory of Mechanics, University of Applied Sciences Giessen-Friedberg, Giessen, Germany

³ Footpower, Giessen, Germany

Abstract— In orthopaedics the adaption of insoles is a complex task. The sensomotoric concept of Jahrling [1-4] is a procedure which allows the improvement of the gait without an operation. The experience is excellent, but there is a need to build up the scientific background of the sensomotoric procedure. The aim of our work is to investigate the properties of the used materials of the sensomotoric insoles to improve the adaption of the insoles to the patients.

Keywords— Sensomotoric Insole, Dynamics Streifenlichttopometrie, Pressure, Material Testing, Material Modelling.

I. INTRODUCTION

Insoles are employed to improve the gait of patients and to avoid further damages of the joint structures of the patients.

In orthopaedics there are different concepts to build up insoles. The concept of the sensomotoric insole is to change directly the muscle length and for this reason the stimulation pattern of the gait [1- 4]. With this concept many patients could improve their gait without an operation of their musculo-skeletal system. During the therapy the task of the orthopaedic shoe specialist is the recognition of the pathologies, the choice of the shore hardness of the material, the creation of the surface of the insole and the adaption of the insole to the patient.

In this complex procedure the behavior of the material must be well known to provide the patients with well-designed insoles.

The state of the art is, that the properties of the used materials are dependent of the charge and the loading conditions during wearing the insoles.

For this reason the aim of the project is to investigate the properties of the materials, the creation and the adaption of the insoles and beyond it the change of the properties during wearing the insoles.

II. METHOD

In our investigation we use a 3-dimensional gait analysis system and a 3-dimensional surface measuring method

(dynamic SLT) to document the gait of the patient and the deformation of the feet. To analyse the vertical ground reaction forces on the feet we use a Zebris pressure platform. With the data of the above described measuring methods the insoles are created and adapted by the orthopaedic shoe experts.

The gait of the patients is documented by means of a gait analysis system, which was developed in our lab.

The deformation of the feet is measured by a surface measuring method. SLT is a method for the optical 3D measurement. A recent development, the dynamic SLT, makes it possible to investigate the dynamic behaviour of surfaces by the 3D documentation and measurement of objects in motion [5, 6].

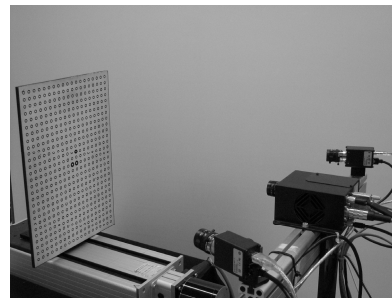


Fig. 1 Dynamic SLT equipment; projector Minirot® and two video cameras (100 Hz).

The SLT method consists of two working steps, the measurement and the analysis. SLT is an optical measurement method based on the projection, recording and analysis of coded sets of stripes of light on the object to be measured. Physical principles of the method are the triangulation and the light sectioning. [7, 8]

There are a new element of the measurement process which is called the multiple wavelength phase shift and new algorithms for the “unwrapping” of the data sets [7]. These replace the Graycode sequence and the phase shift in the measurement of stationary objects.

For this kind of measurement we use a new type of projector developed by ABW GmbH, Frickenhausen, Germany which is called the “MiniRot”®.

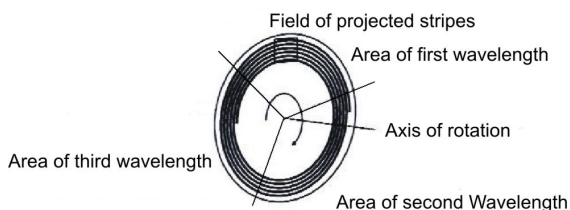


Fig. 2 Rotating slide of the Minirot® Projector.

The projector is equipped with a special rotating slide. On this slide there are three different grid patterns, representing the three wavelengths. The projector can be synchronised to different types of cameras.



Fig. 3 Recording of the changing surface of the foot; frame 32 of the video sequence of the dynamic SLT.

The result of the measurement process is a 3D film showing the deformation of the object. In the data procedure a choice of significant stages of the movement is submitted to the actual data analysis.

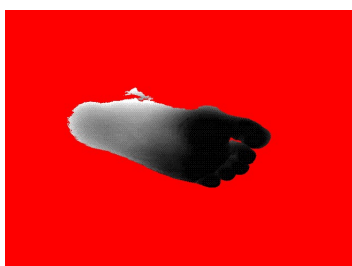


Fig. 4 Recording of the changing surface of the foot; frame 32 of the 3D-film of the dynamic SLT; deepness z is grey coded.

To obtain the vertical ground reaction force a pressure platform of Zebris is used (FDM 1.5 platform; dimensions 158 x 60.5 x 2.5 cm (L x W x H); sensor area 149 x 54 cm; Number of sensors 11264; sampling rate 100 Hz).

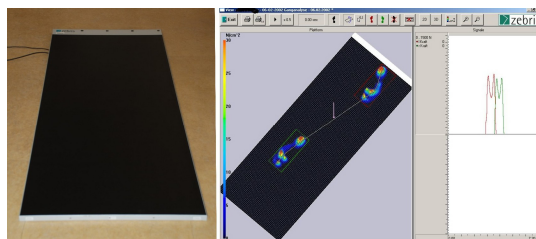


Fig. 5 Zebris FDM 1.5 pressure platform.

In the next step the orthopaedic shoe specialist designs the surface of the insole by means of the measured data of the gait analysis. He must recognize the pathologies of the anatomy of the feet and the sensible area where the sensomotoric insoles should actuate the feet. In this adapting process the material of the insole must have the appropriate properties.



Fig. 6 Sensomotoric insole.

The material consists of rubber-like latex foam that determines the overall properties of the insole. In order to measure the dynamic behavior of this, the 4a Impetus II pendulum test system is used. Impetus II represents a fast and efficient experimental setup for dynamic testing of foam-like materials.



Fig. 7 Material testing device Impetus II.

For the material testing, cube-like specimens of 30x30x30mm have been used. A maximum compression of 50% for an impact velocity of 4m/s has been reached. Some selected results of the obtained engineering stress-strain relation of the insole material for impact velocities of 1m/s, 2.5m/s and 4m/s are shown in Fig. 8. The stress values are normalized for confidentiality reasons. The material shows the typical behavior of rubber-like foams. Apart from the expected visco-elastic response, the material also exhibits a small amount of permanent deformation.

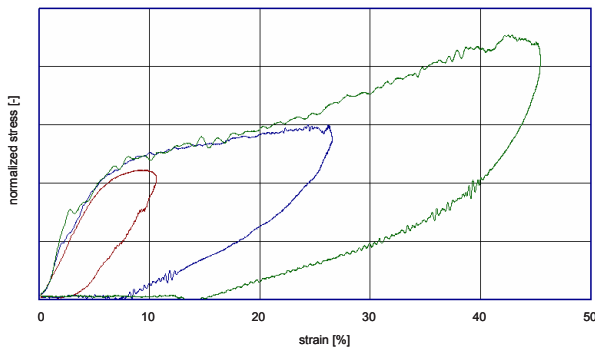


Fig. 8 Stress-strain relation for 1m/s, 2.5m/s and 4m/s.

In Fig. 9, the true strain-rate is depicted over engineering strain for different impact velocities. As can be seen a wide range of strain rates up to 150/s are realized. This range of strain rates can be used very efficiently for the validation and verification of the test data by the including Impetus II software package.

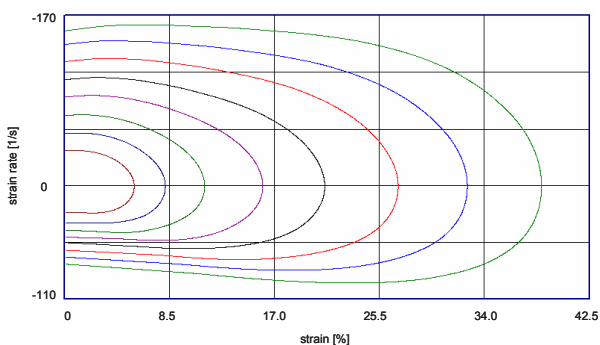


Fig. 9 Strain-rate over strain for different impact velocities.

For the material modelling of this dynamic behaviour, a strain-rate dependent hyper-elastic formulation is used [9]. Additionally, an elastic damage formulation is used for the simulation of the unloading path. Fig. 10 shows the result of a uniaxial quasi-static compression test and the corresponding results of the finite element simulation. This modelling

technique is also capable to describe the change of the material properties during wearing the insoles.

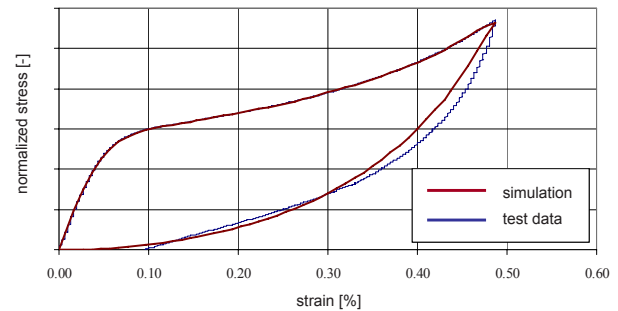


Fig. 10 Simulation vs. test data using an elastic damage formulation.

III. CONCLUSIONS

First steps towards an optimization scheme for sensomotoric insoles under dynamic loading are presented. A new SLT-technique for the measurement and digitalization of dynamic processes is shown. This can also be used for scanning human feet and for converting this data to a finite element model for numerical simulations. In addition, pressure platforms are used to measure the vertical ground reaction forces. With these “ingredients” all required data is available for a proper validation and verification process of the foot-insole-interaction via numerical analysis. In the next step, the finite element modeling of the patient’s foot including the corresponding biomaterials will be performed and the foot-insole interaction will then be investigated in detail.

ACKNOWLEDGMENT

We thank Dr. Wolf of the company ABW GmbH (<http://www.abw-3d.de>) Frickenhausen, Germany for the support of the 3D-surface measurement equipment.

REFERENCES

1. Jahrling, L. (1999): Propriozeptive Einlagen für Spastiker. OST – Sonderheft Propriozeption, S.52-55.
2. Jahrling L (2001) Propriozeptiv oder „klassisch“? Medizin & Technik, Orthopädieschuhtechnik 7/8/2001
3. Brinckmann F (2005) Ganganalytische Untersuchung zur therapeutischen Effizienz der sensomotorischen Einlagen nach Jahrling bei zentralnervösen Erkrankungen. Diplomarbeit im Studiengang Orthopädie- und Rehathechnik, FH Gießen-Friedberg

4. Jahrling, L.; B. Rockenfeller (2007): Der Einsatz von sensomotorischen Einlagen zur Steigerung koordinativer Leistungsfähigkeit nach Patellaspitzensyndrom. http://www.footpower.de/downloads/assets/Sonderheft_Sensomotorik_2006.pdf
5. Subke J, Umbach O, Griesemann J, Nissels V (2007) Dynamische 3D-Oberflächenmessung in der Biomechanik. Proceedings 41. DGBMT-Jahrestagung 26.-29. September 2007
6. Subke J (2005) Digitale 3D-Messmethoden für die individuelle Patientenversorgung. 32. Fachtagung des Fachbereichs Krankenhaus- und Medizintechnik, Umwelt- und Biotechnologie der Fachhochschule Gießen-Friedberg, Gießen, 15-16. März
7. Wolf K (2004) Absolute dreidimensionale Vermessung dynamischer Objekte mit Phasenshiftverfahren. Dissertation der Fakultät für Informations- und Kognitionswissenschaften der Eberhard-Karls-Universität Tübingen. Tübingen
8. Wolf K (2003) 3d measurement of dynamic objects with phase shifting techniques. In Proceedings of Vision, Modelling and Visualization (VMV 2003), pages 537–544, Munich, Germany Nov
9. Kolling S, Du Bois P.A, Benson DJ, Feng WW (2007): A tabulated formulation of hyperelasticity with rate effects and damage. Computational Mechanics 40 (5): 885-899.

Author: Prof. Dr. Jörg Subke
Institute: Biomechaniklabor, Zentrum für Medizin- und
Krankenhaustechnik, Fachhochschule Gießen-Friedberg
Street: Wiesenstr. 11
City: D-35390 Giessen
Country: Germany
Email: joerg.subke@tg.fh-giessen.de

Modeling the dynamics of recovery in robot-assisted rehabilitation

M. Casadio^{1,2}, P. Morasso^{1,3}, and V. Sanguineti^{1,3}

¹ Dept Informatics, Systems and Telematics, University of Genoa, Genoa, Italy

² Sensorimotor Performance Program, Rehabilitation Institute of Chicago, USA

³ Italian Institute of Technology, Genoa, Italy

Abstract— The mechanisms of action of physical assistance in promoting motor recovery after stroke are poorly understood. To explicitly model the process of recovery of motor functions in impaired subjects, while they move with the assistance of a therapist, or a robot, might help to understand how to make recovery faster and/or more effective. Here we use a linear dynamical system to describe the trial-by-trial dynamics of the training process, with robot-generated assistance as input and subject's motor performance as output. To test the feasibility of this approach, we focused on two robot therapy experiments with chronic stroke survivors, which involved a hitting and a tracking task. The model correctly reproduced the observed evolution of performance over sessions. A comparison of the estimated parameters with clinical scales (Fugl-Meyer arm portion and Ashworth), and their modifications indicated that the time constant of the recovery process is predictive of the retention of the recovery (assessed after 3 months from completion of the protocol). Moreover, in subjects with little or no spasticity, recovery is mediated by motor error; in contrast, in subjects with high spasticity, recovery is more influenced by performance.

Keywords— robot therapy, stroke, rehabilitation

I. INTRODUCTION

In stroke survivors, exercise promotes the recovery of motor functions[1] over a time horizon of days. Intensity and frequency of practice are a major determinant of motor recovery [2, 3], but skill acquisition or motor learning are required to achieve functional reorganization. Clinical studies have suggested [4, 5] that robot therapy may be effective in accelerating the recovery of stroke survivors[6].

A few studies have addressed the way assistive forces affect motor performance and/or motor learning [7]. Are there 'optimal' ways to provide assistance, and to continuously regulate it? If this is the case, do they depend on the specific task, or do they obey to general principles, valid for a wide range of motor learning problems? While optimal solutions have been proposed for simple, specific tasks, it would be desirable to derive general principles and methods, that can (in principle) be applied to any motor learning/re-learning task.

Linear dynamical models have been used to characterize a variety of motor learning tasks and motor learning situa-

tions, in both healthy subjects[8-10] and in subjects with neuromotor impairments[11, 12] can be extended to the modeling of the recovery process.

Here we show that the formalism used in the study of sensorimotor adaptation may be adequate for describing the (trial-by-trial) dynamics of the training process during a robot therapy protocol. To test the feasibility of this approach, we apply the technique to data from two robot therapy trials, respectively involving a hitting [13] and a tracking task.

II. MATERIALS AND METHODS

A. Mathematical model

Similar to sensorimotor adaptation[14], we assumed that the trial-by-trial evolution of the recovery process is described by a linear dynamical system, in which performance (system output, y) is determined by the sum of a voluntary component and an assistive component. The voluntary component of performance is taken as the system state (voluntary control, x). The assistive component is assumed to be proportional to the degree of assistance, e.g. the magnitude of the assistive force (w), which is taken as one of the system's inputs. The quantity y should be a task-relevant measure of performance.

We also assumed that the evolution of voluntary control is modeled as a linear equation, and is driven by a performance error u , which is taken as an additional system input. For the i -th trial, the model can be summarized as follows:

$$\begin{aligned} y^i &= x^i + D \cdot w^i + r^i \\ x^{i+1} &= A \cdot x^i + B \cdot u^i + q^i \end{aligned} \quad (1)$$

Model parameters A and B denote, respectively, the forgetting and learning rate of the degree of voluntary control. Parameter D accounts for the dependence of performance on the degree of assistance. If w is a force magnitude and y is a kinematic performance measure, D can be seen as a fluidity term (the reciprocal of viscosity). A, low D would indicate that speed is little affected by assistive force.

The degree of voluntary control may be interpreted as the subject's performance when no assistance is provided ($w=0$). In this case, zero or negative voluntary control

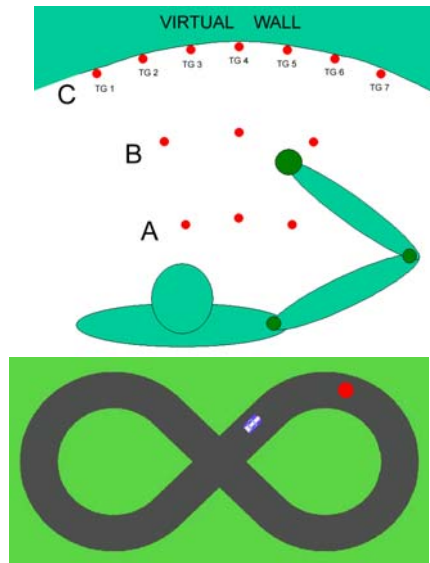


Figure 1. Top: Hitting task. Targets are arranged on three layers: A, B, C. Bottom: Tracking task

would mean that subjects cannot complete task without assistance. If recovery takes place, voluntary control is expected to gradually increase up to a maximum (i.e., the ‘peak’ performance). The quantities r and q are noise terms (performance noise and recovery or process noise).

B. Experimental data

We used the model to analyze the recovery processes taking place within two robot therapy trials which involve two different exercises, whose outcomes have been reported elsewhere: (i) hitting a target[13], and (ii) visual tracking of a moving object[15]; see Fig. 1. In both cases, subjects sat on a chair and grasped the handle of a planar manipulandum with 2 degrees of freedom (‘Braccio di Ferro’, see [16] for details). In both cases, the rehabilitation protocol consisted of 8 to 10 rehabilitation sessions (about 1 hr each, twice a week).

Hitting task

Subjects had to hit a target by extending completely their impaired arm, starting from targets on layer A (fig. 1, top) until targets on the outer (C) layer. Reaching the outer targets required an almost full arm extension. There were no explicit spatial or timing requirements. The robot generated a constant assistive force directed toward the target, whose initial magnitude was set by the therapist to the minimum amount that evoked a functional response, i.e. a (possibly

incomplete) movement in the intended direction. During each session, force magnitude was manually reduced if subjects improved their performance. At the beginning of every session, the initial force magnitude was reset to the initial magnitude set for that subject at the beginning of the first session. Therefore, during every session, subjects explored an (increasingly large) range of forces that decreased from the initial magnitude to a minimum amount that still allowed the subject to successfully hit the outer targets.

Tracking task

Subjects had to continuously track a moving visual target, moving on a figure-of-eight trajectory; see Fig. 1, bottom. The target was represented visually as a small red circle, and haptically, as an attractive force field defined by $F = K \cdot \sqrt{d}$, where d is the distance of the hand from the target. The current position of the hand was continuously displayed (as the picture of a small car). For each subject, the scale factor, K , was initially selected as the minimum level capable to induce the initiation of movement. The moving target stopped if the distance from the cursor was greater than 2 cm. Within each block, half of the trials were clockwise and half were counterclockwise.

In both cases, we alternated block of trials with and without vision. Subjects were evaluated with the Fugl-Meyer score (arm part, FMA) and the Ashworth scale for spasticity, before and just after completion of the trial. In the case of the hitting task, we also evaluated the FMA score three months later.

C. Model parameters

To adapt the general model to the specific tasks, we need to specify suitable indicators for performance (and therefore the interpretation of the ‘voluntary control’ variable), assistance and the error signal which drives recovery.

For the hitting task, as performance measure we took the average speed of the outward movement, which is greater in presence of assistance and is expected to increase while recovery proceeds. As the ‘assistance’ variable in the model, we took the magnitude of the constant assistive force.

For the tracking task, as performance measure we took the fraction of time during which the hand was actually moving during a complete eight-turn. As ‘assistance’, we took the average force level during the same interval.

The rehabilitation protocol included trials with and without vision of the hand. As a simplifying assumption, we treated ‘vision’ (v) as an additional assistance input, so that Eq. 1 becomes:

$$y^i = x^i + D_1 \cdot w^i + D_2 \cdot v^i + r^i \quad (2)$$

Another important modeling choice is the selection of the error signal, u , which drives recovery. Recovery may be either driven by (i) performance, i.e. a better performance results in a greater recovery, or (ii) error, i.e. larger errors elicit greater changes in voluntary control. In the hitting task we took the endpoint error, i.e. the distance from the target after the first submovement as the error signal which drives recovery. In the tracking task we took the fraction of time during which the hand was not moving (this corresponds to $1 - \text{performance}$).

It should be noted that looking at the sign of the resulting estimate of parameter B would allow to test whether recovery is error- or performance-driven.

In addition, motivated by earlier observations [13] that the rates of recovery may be different in the vision and no-vision trials, we took two separate learning rates, one for vision trials and the other for the no-vision trials:

$$x^{i+1} = A \cdot x^i + B_1 \cdot u^i \cdot v^i + B_2 \cdot u^i \cdot (1 - v^i) + q^i \quad (3)$$

Where B_1 and B_2 are, respectively, the ‘vision’ and ‘no vision’ rates of recovery.

D. Identification procedure and analysis of results

For each subject and each task, we took the recorded time series of assistance, presence of vision and performance (for each movement repetition: single movement or single eight-turn) as the inputs of an identification procedure based on an Expectation-Maximization (EM) algorithm [14]. We estimated the model parameters A , B_1 , B_2 , D_1 and D_2 , noise covariances Q and R , and the expected initial state, x_0 , and the initial state covariance, V , as well as the predicted evolution of the state variable.

III. RESULTS

Fitting was generally satisfactory, in the sense that the predicted performance closely followed the experimentally observed time series. We examined whether the model parameters could tell us about the different amounts and modalities of recovery that we observed in the different subjects.

A. Initial state and initial degree of assistance

As an initial check for consistency of the results, we first looked at the relationship between the estimated initial value of voluntary control and the initial magnitude of assistive force. In fact, these quantities turned out to be highly correlated in both the hitting ($r=-0.82$) and the tracking task ($r=-0.81$). Subjects who needed greater assistive force turned out to have lower initial magnitudes of voluntary control.

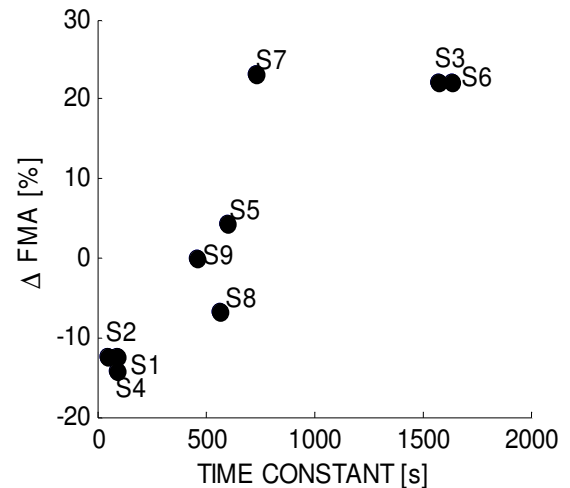


Figure 2. Hitting task: the forgetting time constant correlates with the percent change of the FMA during the 3 months after completion of the rehabilitation trial

B. Time constants of the recovery process

We then looked at the time constants of the recovery process, which may be related to the forgetting rate as $\tau=1/(1-A)$. The time constant describes how fast forgetting takes place. If recovery is durable, τ should be large. In contrast, a small τ would indicate little or no build-up of voluntary control while training proceeds.

To account for that different subjects may need different amounts of time to complete one block of trials, we expressed the time constants in seconds by multiplying τ (which is expressed in number of movement repetitions) by the average duration of a movement (different in different subjects). Different subjects turned out to have very different τ 's, ranging from short-term (49 s) to much longer-term effects (1639 s). Do these differences predict the amount of recovery (percent increase of the FMA score), as well as its stability (percent change of the FMA score from the end of the trial to the 3-months follow-up time)?

In the hitting task, we found (see fig. 2) that subjects with a lower time constant display a degradation of their FMA score at follow-up. In subjects with an intermediate time constant, the FMA score remained almost stationary, whereas subjects with a large time constant displayed a slight increase of the FMA score at follow-up. In summary, we found a strong correlation ($r=0.88$) between FMA change at follow-up and the recovery time constant.

C. Learning rate and learning modalities

As regards the learning rates (parameters B_1 and B_2), only in few subjects we found very different rates for vision and no-vision movements, so we first looked at B_1 (learning rate with vision) alone. The magnitude of this parameter turned

out to be highly variable across subjects. Some subjects revealed a large negative B_1 , thus indicating that in these subjects performance, not motor error triggers the increase of the degree of voluntary control. In contrast, other subjects displayed a positive magnitude, suggesting that recovery is mediated by motor error. It has been suggested that in more severely impaired subjects, robot therapy may be beneficial in that assistance allows completing the task. However, in subjects that are less impaired, error may have a greater effect on recovery. Therefore, it is conceivable that the learning rate – in particular, its sign – is somehow related to the severity of the impairment. To test for this, we looked at the relationship (if any) between B_1 and the initial FMA and Ashworth scores. In the hitting task, we found that B_1 is large and negative in subjects with small FMA (more impaired) and large Ashworth score (more spasticity). In contrast, B_1 is positive in subjects with large FMA (less impaired) and a lower Ashworth score (less spasticity). We found a strong correlation between B_1 and the Ashworth score ($r=-0.83$). The correlation with the initial FMA score turned out to be much smaller ($r=0.52$). Similar results were found in the tracking task. Here the correlation between learning rate and clinical scales was greater in no-vision trials (no-vision learning rate, B_2). More specifically, we found a strong correlation between B_2 and the Ashworth score ($r=-0.73$), and a smaller (but still significant) correlation with the FMA score ($r=0.64$). Again, these results can be interpreted as indicative of different mechanisms of recovery in less severe vs more severe subjects.

IV. DISCUSSION

When analyzing the process of recovery of stroke survivors in robot therapy trials, most studies focus on quantitative indicators of performance and on clinical scales. However, correlation between these two measures is usually rather poor. One possible explanation is that in subjects with different types and/or degrees of impairment, the same type of rehabilitation exercise may have very different effects. An explicit model of the recovery process may help identifying the causes of such variability in the outcomes. Ultimately, it might be used to personalize the rehabilitation exercises. Although preliminary, these results suggest that the modeling framework originally proposed for characterizing the trial-by-trial dynamics of sensorimotor adaptation may be appropriate for describing the complex, subject-dependent recovery process which takes place during robot-assisted exercise. The model could provide a better description of the mechanisms underlying recovery. In addition, it could be used to make predictions on the potential of different subjects for recovery. In perspective, such a model

might be used to derive more advanced strategies for supporting such recovery.

ACKNOWLEDGMENT

This work is partly supported by the EU grant FP7-ICT-271724 HUMOUR.

REFERENCES

1. Nudo, R.J., *Mechanisms for recovery of motor function following cortical damage*. *Curr Opin Neurobiol*, 2006. **16**(6): p. 638-44.
2. Kwakkel, G., *Impact of intensity of practice after stroke: issues for consideration*. *Disabil Rehabil*, 2006. **28**(13-14): p. 823-30.
3. Kwakkel, G., B. Kollen, and J. Twisk, *Impact of time on improvement of outcome after stroke*. *Stroke*, 2006. **37**(9): p. 2348-53.
4. Prange, G.B., et al., *Systematic review of the effect of robot-aided therapy on recovery of the hemiparetic arm after stroke*. *J Rehabil Res Dev*, 2006. **43**(2): p. 171-84.
5. Kwakkel, G., B.J. Kollen, and H.I. Krebs, *Effects of Robot-Assisted Therapy on Upper Limb Recovery After Stroke: A Systematic Review*. *Neurorehabil Neural Repair*, 2007.
6. Volpe, B.T., et al., *Robot training enhanced motor outcome in patients with stroke maintained over 3 years*. *Neurology*, 1999. **53**(8): p. 1874-6.
7. Emken, J.L., et al., *Motor adaptation as a greedy optimization of error and effort*. *J Neurophysiol*, 2007. **97**(6): p. 3997-4006.
8. Smith, M.A., A. Ghazizadeh, and R. Shadmehr, *Interacting adaptive processes with different timescales underlie short-term motor learning*. *PLoS Biol*, 2006. **4**(6): p. e179.
9. Waincott, S.K., O. Donchin, and R. Shadmehr, *Internal models and contextual cues: encoding serial order and direction of movement*. *J Neurophysiol*, 2005. **93**(2): p. 786-800.
10. Kording, K.P., J.B. Tenenbaum, and R. Shadmehr, *The dynamics of memory as a consequence of optimal adaptation to a changing body*. *Nat Neurosci*, 2007. **10**(6): p. 779-86.
11. Smith, M.A. and R. Shadmehr, *Intact ability to learn internal models of arm dynamics in Huntington's disease but not cerebellar degeneration*. *J Neurophysiol*, 2005. **93**(5): p. 2809-21.
12. Casadio, M., et al., *Abnormal sensorimotor control, but intact force field adaptation, in multiple sclerosis subjects with no clinical disability*. *Mult Scler*, 2008. **14**(3): p. 330-42.
13. Casadio, M., et al., *Minimally assistive robot training for proprioception enhancement*. *Exp Brain Res*, 2009.
14. Cheng, S. and P.N. Sabes, *Modeling sensorimotor learning with linear dynamical systems*. *Neural Comput*, 2006. **18**(4): p. 760-93.
15. Vergaro, E., et al. *Robot-therapy of hemiparetic patients with a minimally assistive strategy for tracking movements*. in *3rd International Symposium on Measurement, Analysis, and Modeling of Human Functions (ISHF07)*. 2007. Lisbon, Portugal.
16. Casadio, M., et al., *Braccio di Ferro: a new haptic workstation for neuromotor rehabilitation*. *Technol Health Care*, 2006. **13**: p. 1-20.

Author: Vittorio Sanguineti
 Institute: University of Genoa
 Street: Via Opera Pia 13
 City: 16145 Genoa
 Country: Italy
 Email: vittorio.sanguineti@unige.it

Position of the Head Measured by Digital Photograph Analysis

Cerny R.¹, Hozman J.², Charfreitag J.², Kutilek P.²

¹ Charles University in Prague, Clinic of Neurology (2nd Faculty of Medicine), Prague, Czech Republic

² Czech Technical University in Prague, Faculty of Biomedical Engineering, Kladno, Czech Republic

Abstract— Many diseases of the nervous, visual and vestibular systems can cause abnormal head position in the space. Thus the need for non-invasive, precise and reliable measurement of the head posture is obvious. We have described an originally developed method of head posture measurement by digital picture analysis. Pictures of the head marked on tragus and outer eye canthus are taken simultaneously by two digital cameras aligned by laser beam. Head position is measured with precision of 0,5° in all three space dimensions (rotation -yaw, flexion-pitch and inclination-roll). Mean values of head position from a group of 100 healthy subjects: retroflexion 21,7°, inclination to the right 0,2°, and head rotation to the left 1,7°.

Keywords— head posture, head position measurement, digital image analysis

I. INTRODUCTION

According the definition, natural head position (NHP) is measured on a comfortably standing man looking straight ahead [1]. In this situation, Frankfurt horizontal and sella turcica-nasion line are considered horizontal (see Fig. 1). NHP gained most attention in orthodonty and anthropology. Less is known about head posture in diseases of the nervous system, visual and vestibular senses – e.g. compensatory head positions in oculomotor palsies and tilt reaction in vestibular failure. In practice, head posture is assessed roughly using protractors, plumb line and/or subjective guesses. Quantitative measurement is not possible in routine practice. In our experience, deviations less than 10 ° are hardly noticed by naked eye. NHP can be measured by X-ray cephalometry [2], using of inclinometer [3], by optical method based on divergence of line of sight from physical straight ahead and by picture analysis (photometry). Available methods are limited to measurement of certain planes only and/or are invasive in nature. Angle measurements are relatively easy in the sagittal and frontal planes, where pictures taken by levelled camera are sufficient. In contrast, measurement of head turn in horizontal plane is more complicated, because pictures taken from are needed. Indeed, these results are not frequently cited in literature. Available methods for head rotation measurement are optical – estimation of straight ahead gaze line and pictures taken using mirror above the subject's head [4, 5].

From the point of view of the limitations of the available methods for head position measurement we have decided to design the new equipment for its analysis from digital pictures. Main requirements for the method were: precise evaluation in all 3 dimensions (including head turn), ease of use with open or closed eyes and in different head positions. The measurement should be totally non-invasive and shouldn't influence the holding of the head.

Precision and reliability of the method was assessed on a mechanical head model. Normal values from a group of healthy controls are further presented.

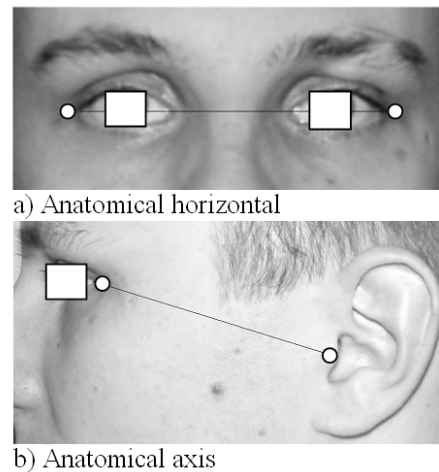


Fig. 1 Anatomical horizontal and axis



Fig. 2 Tripod with camera and laser collimator

II. PROBLEM SOLUTION

Following anatomical landmarks are signed on each subjects prior to the photographing: tragus and outer eye canthus (located by palpation) on both sides. Head diameter at the level of tragus is measured by cephalometer.

Head position is calculated from three digital pictures (left-profile and right-profile, frontal) taken by two digital cameras placed parallel with subject's frontal plane. Cameras are set on the same optical axis using laser beam on specially designed tripods (Fig. 2, Fig. 3). Exact alignment is signalized by LED diode when the laser beam is detected. Pictures are taken in comfortably standing person with closed eyes from both sides at same time. Picture taking and analysis is controlled by computer program, which concurrently controls both cameras. Deviations of anatomical from physical planes (defined by level of the device) are measured.

Sagittal plane value: angle between line canthus-tragus and horizontal; frontal value: angle between line connecting both eye canthi and horizontal.

After evaluating coordinates of tragus in captured images, the angle of the head rotation is calculated as follows (1):

$$\varphi_c = \arcsin \frac{(a - (s - b)) \cdot c}{d}, -\frac{\pi}{2} \leq \varphi_c \leq \frac{\pi}{2}, [\text{rad}] \quad (1)$$

where $a[\text{pixel}]$ is x-axis coordinate of the tragus in the left-profile image, $b[\text{pixel}]$ is x-axis coordinate of the tragus in the right-profile image, $s[\text{pixel}]$ is x-axis size of the image, $d[\text{mm}]$ is diameter of the head and $c[\text{mm/pixel}]$ is a constant converting the distance between tragus coordinates from pixels to millimetres calculated as follows (2):

$$c = \frac{ccd \cdot z}{f \cdot s} [\text{mm/pixel}] \quad (2)$$

where ccd [mm] is width of the CCD sensor given by the camera's manufacturer, z [mm] is distance between the subject and the CCD sensor (camera), f [mm] is the focal length of the camera lens and s [pixel] is the x-axis size of the image.

Rotation (turning) of the head is calculated from the difference between tragus coordinates in the left- and right-profile images. This method is based on circle movement approximation – see Fig. 4, which shows the geometry used for measuring the head rotation (d [mm] is diameter of the head, x [mm] is distance between left and right tragus and φ [deg] is the result angle).

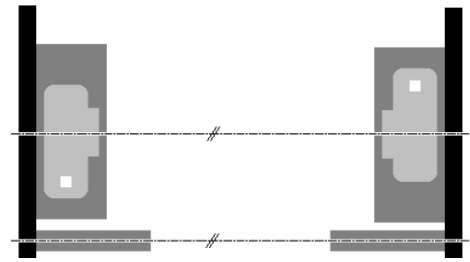


Fig. 3 Identification of the digital cameras optical axes by means of laser transmitter and receiver including collimator and special preparation with digital cameras (top view)

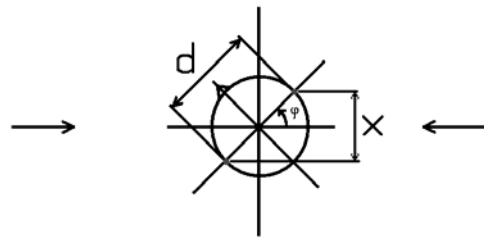


Fig. 4 Geometry used for measuring of head rotation

Control group consisted from 112 healthy volunteers (54 women and 58 men, mean age 25 years). The institutional ethical committee approved all experiments and written informed consent was obtained from all participants.



Fig. 5 Model of the head and stepper motor including planet gearbox (verification of rotation measurement)

III. RESULTS

In the first phase the method was tested on a head model positioned in steps under $1,0^\circ$ (Fig. 5). The mean error of measurement in all three planes was $0,5^\circ$.

Method's error in real situation was assessed by repeated evaluation of the same picture set and expressed as RMS: $0,65^\circ$ in yaw and $1,96^\circ$ in pitch.

Results from a control group are summarized in Table 1.

Table 1 Values in degrees, negative means rotation or inclination to the left

Plane	Mean	SD
Frontal	$0,2^\circ$	$\pm 2,99$
Sagittal	$21,7^\circ$	$\pm 5,62$
Horizontal	$-1,7^\circ$	$\pm 3,85$

In our group of young normal subjects the head is held in slight rotation to the left, without significant inclination in the frontal plane. It means, that the eyes are exactly leveled.

IV. DISCUSSION

Our results are in agreement with that of other authors, particularly in the frontal plane. Clearly, the eye level is of great biological importance and as such is precisely regulated. In healthy human it is precisely horizontal with little variation and is independent from the spine position. In our series the eye position is horizontal within several degrees, as found by others as well [4, 6]. Inclination of the eye line is an important sign of acute vestibular failure (ocular tilt) and ocular muscle palsy [7, 8].

Head position in the sagittal plane is much dependent on the position of the cervical spine and is more variable in consequence [9, 10]. It changes with body position (tends to increase in standing versus sitting) [6]. Actual values depend on the landmarks used for its measurement. High values in our series are mainly effect of choosing the eye canthus as point of reference. This line deviates from the horizontal considerably. Ferrario showed, that location of infraorbital foramen is less variable than lower orbital margin and better corresponds to horizontal than classical Frankfort line [6].

Slight leftward rotation in the horizontal plane could be explained by prevalent right eye fixation in right-handed population. Presumably, this value will be affected by unilateral vestibular failure, but there are no references to our knowledge at present. Gross head turns in horizontal plane are caused by oculomotor palsies [4, 5]. As an

example, we have measured one subject with loss of vision of the left eye, on whom compensatory head rotation $8,4^\circ$ to the left, not apparent clinically was demonstrated.

As expected, both eyes are held precisely horizontal, with minimal inclination in frontal plane. Our values confirm relatively high variability of head posture, particularly in sagittal plane [11, 12].

V. CONCLUSIONS

We have presented a new method of estimation of the head position in 3D from digital photography.

Measurement is easy, semiautomatic and non-invasive. It is done on distance and has no influence on the head position.

Precision of the method is $0,5^\circ$ in the mechanical model and $1-2^\circ$ in the real setting.

Variability of the head position measurement is explained by variation of stand, head movements, and variability of anatomical landmarks.

The method has potential important application in the evaluation of vestibular, ophthalmological and cervical spine diseases.

Technical development will continue in order to increase precision and simplify the mechanical part of the device.

ACKNOWLEDGMENT

This is the work of the Clinic of Neurology, 2nd Medical Faculty, Charles University in Prague and Department of Biomedical Technology, Faculty of Biomedical Engineering, Czech Technical University in Prague in the frame of the research program No. MSM 6840770012 "Transdisciplinary Biomedical Engineering Research II" of the Czech Technical University sponsored by the Ministry of Education, Youth and Sports of the Czech Republic. The study has been supported by the Czech Ministry of Health grant No: NR8261-3/2005 as well.

REFERENCES

1. Solow B., Tallgren A. (1976) Head posture and craniofacial morphology. *American Journal of Physical Anthropology* 44: 417-435
2. Houston W.J. (1991) Bases for the analysis of cephalometric radiographs: intracranial reference structures or natural head position. *Proc Finn Dent Soc* 87: 43-49
3. Usumez S. et al. (2006) Relationship between static natural head position and head position measured during walking. *Am J Orthod Dentofacial Orthop* 129: 42-47
4. Young J.D. (1988) Head posture measurement. *J Pediatr Ophthalmol Strabismus*. 25: 86-89

5. Spierer A., Barak A. (1997) Measurement of head-turn in ocular torticollis. *Ophthalmic Surg Lasers* 28: 424-425
6. Ferrario V. et al. (1993) Craniofacial morphometry by photographic evaluations. *Am J Orthod Dentofacial Orthop* 103: 327-337
7. Brandt, T., Strupp M. (2005) General vestibular testing. *Clinical Neurophysiology* 116: 406-426
8. Getman, I., Goldstein J.H. (1983) Diagnosis of an isolated vertical muscle palsy. *Acta Ophthalmol (Copenh)* 61: 85-93
9. Garrett T.R., Youdas J.W., Madson T.J. (1993) Reliability of measuring forward head posture in a clinical setting. *Journal of Orthopaedic and Sports Physical Therapy* 17: 155-160
10. Kylamarkula S., Huggare J. (1985) Head posture and the morphology of the first cervical vertebra. *European Journal of Orthodontics* 7: 151-156
11. Pancherz, H., Gokbuget K. (1996) The reliability of the Frankfort Horizontal in roentgenographic cephalometry. *European Journal of Orthodontics* 18: 367-372
12. Leitao P., Nanda R. (2000) Relationship of natural head position to craniofacial morphology. *Am J Orthod Dentofacial Orthop* 117: 406-417
13. Hozman J., Zanchi V., Cerny R., Marsalek P., Szabo Z. (2007) Precise Advanced Head Posture Measurement, In: *The 3rd WSEAS International Conference on Remote Sensing*. Venice, Italy, 2007, pp 18-26

- Author: Jiri Hozman
- Institute: FBMI CTU in Prague
- Street: Sq. Sitna 3105
- City: Kladno
- Country: Czech Republic
- Email: hozman@fbmi.cvut.cz

IS THE BOTTLENECK IN MULTITASKING OF COGNITIVE ORIGIN?

TAPPING AS AN EXPERIMENTAL ASSESSMENT TOOL

M. T. Tarata*, C. K. Dung**, D. Georgescu*, D. Alexandru*, G. Staude**, W. Wolf**

*Medical Informatics, University of Medicine and Pharmacy, Craiova, Romania

**Institut für Informationstechnik, Universität der Bundeswehr München, Neubiberg, Germany

mihai@umfcv.ro

Abstract

The paper discusses the bimanual dual-task interference, demonstrated through tapping experiments where periodic dominant hand tapping was shown to strongly interact with single stimulus evoked discrete taps of the non-dominant hand. As a consequence, it proposes the progressive combination hypothesis (which states that computation from sensory input to motor output could be generated progressively) to be reconsidered within this context.

Introduction

While musicians are trained to perform more than one task, normal individuals dealing with some dual tasking (DT) or multi-tasking (MT) are usually troubled; indeed, bimanual interference is found when two manual tasks are conducted concurrently [1]. DT interference has been widely studied in terms of ideomotor compatibility and psychological refractory effect [2,3] as well as in different tandems of tasks [4,5,6,7]. A broad range of sensorimotor or mental tasks ranging from complex task combinations to simple task pairs has been used and DT costs (i.e. signs of decreased performance in comparison to isolated execution of the tasks) were evaluated. In simpler cases [8], latencies and mutual dependencies of two tasks were often analysed as a function of a varied stimulus onset asynchrony (SOA), mostly in speeded choice reaction time (RT) experiments [4,9]. Favouring a serial organization of sensorimotor transformation stages (perception, cognition and action) within a single channel, [5,8,9] postulated a central bottleneck due to limited central processing capacity at the response selection stage, whereas others [10,11] addressed the limitations of strategic allocation of central resources in DT paradigms [12,13].

According to the generic bottleneck models (which are based on a generic nature of central processing being independent of stimulus and response modalities [14]), interference in DT is expected if the central resources have to be shared between two competing tasks. Indeed, strong interferences in dual-tasking have been clearly demonstrated more recently in bimanual finger tapping [15, 16,17,18].

In this study, a DT paradigm required participants to perform repetitive tapping (down-up) [19] by the index finger of the dominant hand, while they also had to respond as fast as possible to randomly interspersed stimuli with a discrete single tap of the other (non-dominant) index finger (RT condition). It was found that the rhythmic task affected the timing of the discrete response and vice versa (Fig. 1).

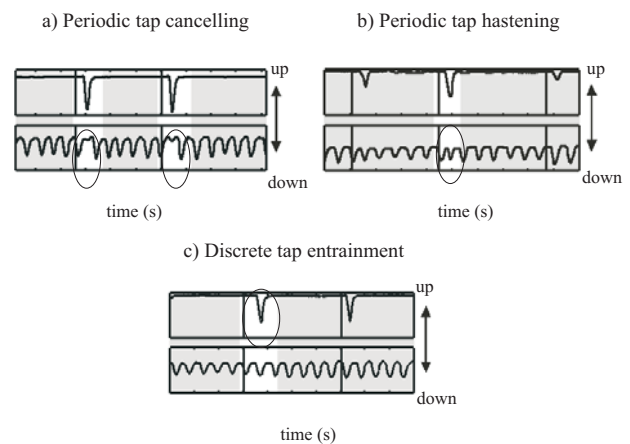


Figure 1. In bimanual DT experiments, the affected discrete and rhythmic events are marked with the ovals (according to [17]); position of the index finger tip is shown. (a) periodic tap cancelling: the execution of the discrete tap interrupts the periodic tapping; (b) periodic tap hastening: the actual intertap interval of the periodic tapping is shortened due to the discrete tap; (c) entrainment of the discrete tap: its onset is delayed for a synchronized execution of both the discrete tap and the next (undisturbed) periodic tap. Upper trace shows the discrete taps executed in response to a go-signal (indicated by the vertical line ahead), and the lower trace depicts the periodic tapping (self-paced mode).

On "what is the mechanism which ensures a correct timing of all single and multiple actions during the daily activity but shows such bottleneck effects in very simple multitasking", several influential and widely discussed theories about a motor timing coordinator were suggested: an internal clock which successively provides relevant intervals and triggers motor commands [20, 21,22], or effector-specific multiple timers being responsible for continuous event timing [23].

For the latter case, apart from the basal ganglia [24,25], the cerebellum [26] was proposed to be a primary site being responsible for motor event timing as well as for perceptual timing; moreover, the cortical Supplementary Motor Area was also suggested to be an “internal clock” candidate [27]. As an alternative to the clock-based concepts for motor timing, the so-called nonlinear coupled oscillators model was also suggested [28].

Tapping revealed to be a simple but effective paradigm to study motor coordination in dual-tasks [15,16,17]. Thus, an experimental setup was established to obtain some observation about system behaviour in bottle neck situations.

Materials and methods

Nineteen subjects participated in a dual task interaction paradigm, performing bimanual tapping (Figure 2 and 3). While the dominant hand was required to perform periodic tapping, the other hand had to respond to a discrete acoustic stimulus. Tapping was instructed as an down-up movement of the index finger with resting in the upper position. The experimental session consisted of 24 trials, each with a synchronization phase and a continuation phase. The go signals were presented at random intervals (3000 to 5000 ms).

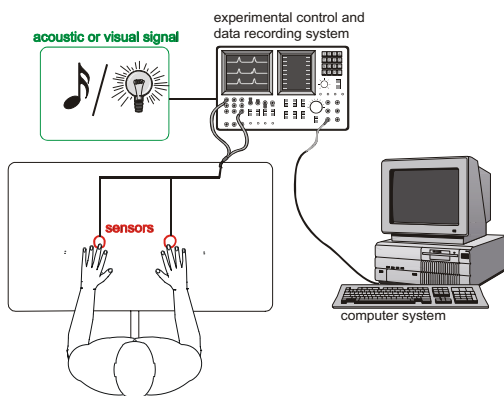


Figure 2. Bimanual tapping setup.

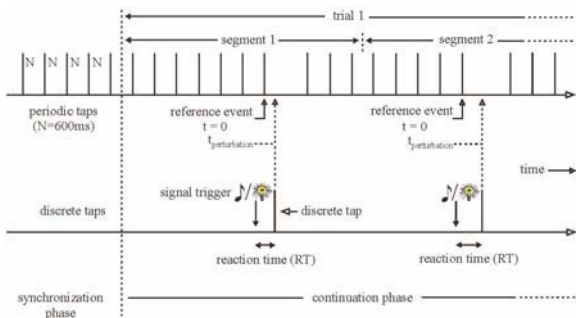


Figure 3. Bimanual tapping experimental paradigm.

All signals were digitized by an ADC (National Instruments Inc.- PCI-MIO-16-4) at a sampling rate of 1 kHz and stored on computer disk. The command signals to the subject were issued acoustically. The experiment was controlled by a DIAdem® (NI Inc.) configuration on a Pentium IV-PC.

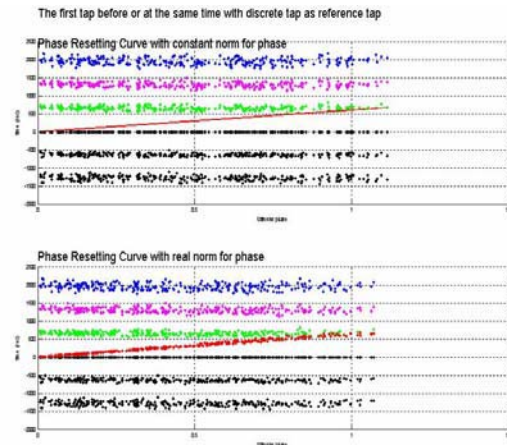


Figure 4. Marginal tapping interaction (MTI). The straight horizontal formation of the dots in the PRC indicates almost no perturbation of the periodic tapping of the right hand due to the concurrent discrete tap of the left hand.

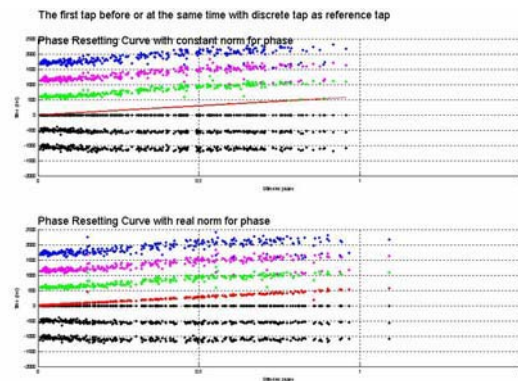


Figure 5. Periodic tap retardation (PTR). The inclined formation of the dots (somehow in parallel with the dashed line) after the perturbation indicates a resetting of the periodic tapping process to the starting phase.

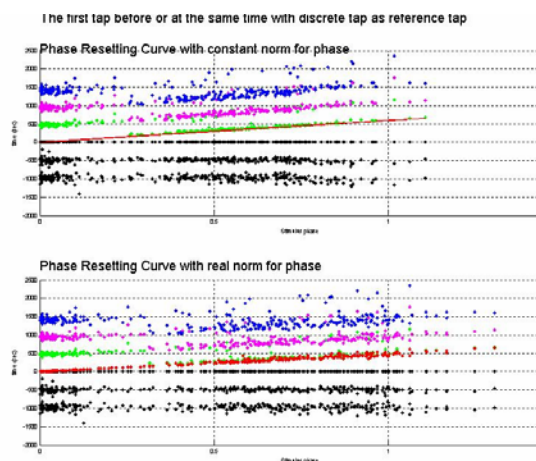


Figure 6. Periodic tap hastening (PTH). The dot ‘lines’ after the perturbation due to the discrete tap show an inclined orientation, but there is an additional branch starting around $\Phi = 0.25$. Dots on this line represent periodic right hand taps simultaneously executed with the discrete left hand tap.

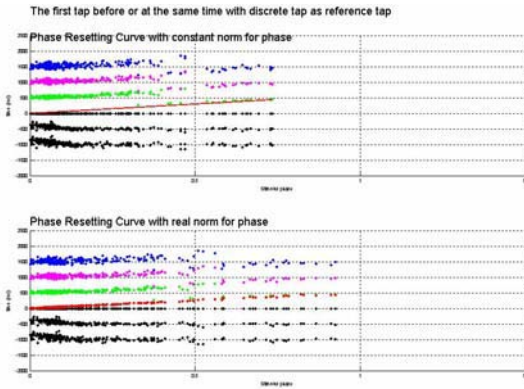


Figure 7. Discrete tap entrainment (DTE). The density of dots is extremely raised in the range Φ from 0 to 0.4

Results

Four distinct types of interaction resulted and are documented through the experiments according to [17]:

- Marginal tapping interaction (MTI) – Figure 4
- Periodic tap retardation (PTR) – Figure 5
- Periodic tap hastening (PTH) – Figure 6
- Discrete tap entrainment (DTE) – Figure 7

Results are shown by so-called Phase-resetting-Curves (PRC) according to [15].

Discussion and conclusions

Besides the four specific types of interaction already mentioned (i) marginal tapping interaction (MTI) – Figure 4, (ii) periodic tap retardation (PTR) – Figure 5, (iii) periodic tap hastening (PTH) – Figure 6 and (iv) discrete tap entrainment (DTE) – Figure 7, in a few subjects peculiar interaction was noticed.

Figure 8 shows a moderate PTR with a low density of dots in the range of Φ from 0 to 0.2.

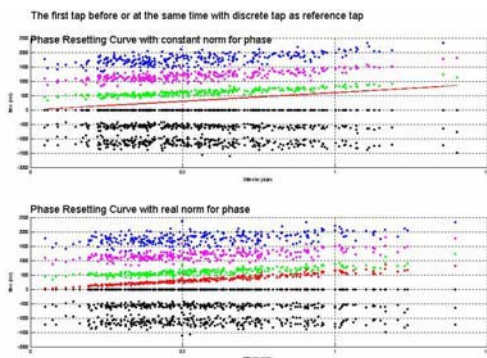


Figure 8. Periodic tap retardation (PTR). The density of dots is low in the range Φ from 0 to 0.2

Figure 9 shows a moderate PTR with an extremely low density of dots in the range of Φ from 0 to 0.4.

Figure 10 shows MTI with an extremely low density of dots in the range of Φ from 0.25 to 0.75.

These exceptions raise the question whether the coordinated bimanual movements are based on a non-linear system of coupled oscillators, or it is rather a matter of reciprocal biasing between the operational neural structures.

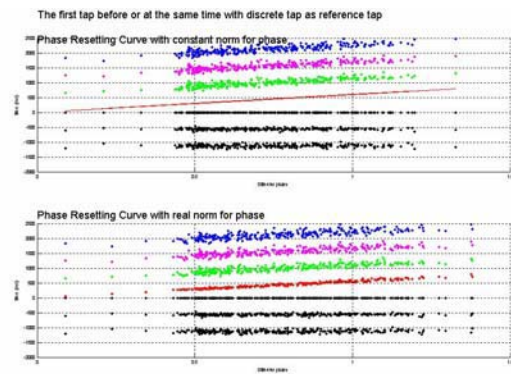


Figure 9. Periodic tap retardation (PTR). The density of dots is extremely low in the range Φ from 0 to 0.4

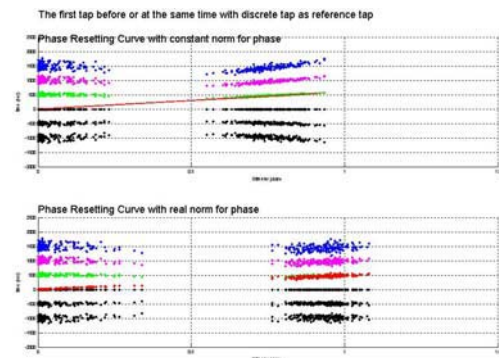


Figure 10. Marginal tapping interaction (MTI). The density of dots is extremely low in the range Φ from 0.25 to 0.75

As an alternative, we would be inclined to consider the progressive combination hypothesis [29] which states that computation from sensory input to motor output could be generated progressively, i.e. information percolates through the units and motor command gradually emerges and is refined through a gradient of functional properties and anatomical connections.

In this sense, peculiar intrinsic connectivity or specific loads of the neural structures would make the tap impossible in certain instances, e.g. when the discrete stimulus is closer to the periodic tap, or when it is within an uncertainty phase range (Φ from 0.25 to 0.75).

Under this hypothesis, the bottleneck encountered through different experimental paradigms, leading to bimanual interference, may not occur at the cognitive level, as suggested.

Further research is necessary to explore this possibility.

Acknowledgement

The authors are greatly indebted to their lab staff which supports the experimental setup, organizes the experiments and performed some tedious data evaluation. The study was partly supported by DFG grant CoTeSys #301 to W. Wolf (Excellence Cluster).

References

- [1] Swinnen S, Wenderoth N. Two hands, one brain: cognitive neuroscience of bimanual skill. *TICS* 8, 2004, 18–25.
- [2] Greenwald AG. On doing two things at once: III. Confirmation of perfect timesharing when simultaneous tasks are ideomotor compatible. *J. Exp. Psychol. Hum. Percept. Perform.* 29, 2003, 859–868.
- [3] Lien MC, Proctor RW, Allen PA. Ideomotor compatibility in the psychological refractory period effect: 29 years of oversimplification. *J. Exp. Psychol. Hum. Percept. Perform.* 28, 2002, 396–409.
- [4] Pashler H. Processing stages in overlapping tasks: Evidence for a central bottleneck. *J. Exp. Psychol. Hum. Percept. Perform.* 10, 1984, 358–377.
- [5] Pashler H. Dual-task interference in simple tasks: Data and theory. *Psychol. Bull.* 116, 1994, 220–244.
- [6] Brass M, Bekkering H, Wohlschlaeger A, Prinz W. Compatibility between observed and executed finger movements: Comparing symbolic, spatial, and imitative cues. *Brain Cogn.* 44, 2000, 124–143.
- [7] Sigman M, Dehaene S. Brain mechanisms of serial and parallel processing during dual-task performance. *J. Neurosci.* 28, 2008, 7585–7598.
- [8] Welford AT. Single channel operation in the brain. *Acta Psychol.* 27, 1967, 5–22.
- [9] Pashler H, Johnston JC. Chronometric evidence for central postponement in temporally overlapping tasks. *Q. J. Exp. Psychol. A* 41, 1989, 19–45.
- [10] Logan GD, Gordon RD. Executive control of visual attention in dual-task situations. *Psychol. Rev.* 108, 2001, 393–434.
- [11] Navon D, Miller J. Queuing or sharing. A critical evaluation of the single-bottleneck notion. *Cogn. Psychol.* 44, 2002, 193–251.
- [12] Byrne MD, Anderson JR. Serial modules in parallel: the psychological refractory period and perfect time-sharing. *Psychol. Rev.* 108, 2001, 847–848.
- [13] Hazeltine E, Ruthruff E. Modality pairing effects and the response selection bottleneck. *Psychol. Res.* 70, 2006, 504–513.
- [14] Hazeltine E, Ruthruff E, Remington RW. The role of input and output modality pairings in dual-task performance: Evidence for content-dependent central interference. *Cogn. Psychol.* 52, 2006, 291–345.
- [15] Yoshino K, Takagi K, Nomura T, Sato S, Tonoike M. MEG responses during rhythmic finger tapping in humans to phasic stimulation and their interpretation based on neural mechanisms. *Biol. Cybern.* 86, 2002, 483–496.
- [16] Wachter C, Gerisch H, Nave PRW, Staude G, Wolf W. Synchronization of periodic movements with external events and interlimb coordination: phase entrainment or phase resetting? *Measur. Sci. Rev.* 4, 2004, 20–28.
- [17] Wachter C, Cong DK, Staude G, Wolf W. Coordination of a discrete response with periodic finger tapping: additional experimental aspects for a subtle mechanism. *J. Motor Behav.* 40, 2008, 417–432.
- [18] Cong DK, Staude G, Tarata M, Wolf W. Event Detection: Basic Timing Concepts for the Execution of Multiple Motor Tasks, Tagungsband “Biosignalverarbeitung – Innovation bei der Erfassung und Analyse bioelektrischer und biomagnetischer Signale”, Universität Potsdam, Germany, Juli 16–18, 2008, 102–105, 2008.
- [19] Repp BH. Sensorimotor synchronization: a review of the tapping literature. *Psychon. Bull. Rev.* 12, 2005, 969–992.
- [20] Treisman M. Temporal discrimination and the indifference interval: implications for a model of the “internal clock”. *Psychol. Monogr.* 77, 1963, 1–31.
- [21] Wing AM. Voluntary timing and brain function: An information processing approach. *Brain Cogn.* 48, 2002, 7–30.
- [22] Spencer RM, Zelaznick HN, Diedrichsen J, Ivry RB. Disrupted timing of discontinuous but not continuous movements by cerebellar lesions. *Science* 300, 2003, 1437–1439.
- [23] Ivry RB, Richardson TC. Temporal control and coordination: The multiple timer model. *Brain Cogn.* 48, 2002, 117–132.
- [24] Ivry RB, Spencer RM. The neural representation of time. *Curr. Opin. Neurobiol.* 14, 2004, 225–232.
- [25] Buhusi CV, Meck WH. What makes us tick? Functional and neural mechanisms of interval timing. *Nat. Rev. Neurosci.* 6, 2005, 755–765.
- [26] Dreher JC, Grafman J. The roles of the cerebellum and basal ganglia in timing and error prediction. *Eur. J. Neurosci.* 16, 2002, 1609–1619.
- [27] Halsband U, Ito N, Tanji J, Freund HJ. The role of premotor and the supplementary motor area in the temporal control of movement in man. *Brain* 116, 1993, 243–266.
- [28] Mauk, M.D., Buonomano, D.V., 2004. The neural basis of temporal processing. *Annu. Rev. Neurosci.* 27, 307–340.
- [29] Wise SP, Boussaoud D, Johnson PB, Caminiti R, PREMOTOR AND PARIETAL CORTEX: Corticocortical Connectivity and Combinatorial Computations, *Annu. Rev. Neurosci.* 1997. 20:25–42

Superimposition of 2D Pressure Data and 3D Surface Data to Optimize Seat Shells in Rehabilitation

J. Subke, P. Mischke, and J. Griesemann

Biomechanics Lab, University of Applied Sciences Giessen-Friedberg, Giessen, Germany

Abstract—The individual adaptation of seat shells is a very difficult task, especially in the case of disabled patients who are unable to articulate their requirements [1]. Besides the individual body geometry the amount of pressure has to be considered particularly with regard to the patients who use the seat shells all day. Congestion has to be reduced to prevent decubitus [2]. Typically the pressure load is measured by a sensor mats that deliver a 2-dimensional result [3]. To optimize a seat shell under geometrical and pressure aspects the 2-dimensional data of the pressure measurement have to be superimposed with the 3-dimensional surface data of the seat shell.

Keywords— Data Superimposition, 3D-Surface Measurement, 2D-Pressure Measurement, Congestion, Seat shell.

I. INTRODUCTION

In rehabilitation technology and in particular in the adaptation of orthopaedic devices like seat shells there is an increasing use of 3D-scan technologies like SLT (Streifenlichttopometrie) [4,5] and CAD/CAM systems for the acquisition and processing of data. It stands to reason that modern CAD devices can increase the quality of the individual adaptation of seat shells and the cost efficiency of the production process [6].

3D Scan technologies provide minute measurements of the patient's body geometry. The pressure loads acting on the patient's body can be estimated with force sensor mats.

In order to effect an efficient adaptation of the seat shells the data sets (3D data of SLT Scan and 2D pressure measurement data) have to be superimposed. The correct superimposition requires the definition of reference points on the seat shell's surface as well as on the force sensor mat. Once the superimposition of the data sets is completed critical high pressure areas where a congestion of tissue can lead to decubitus can easily be identified and the seat shell's surface can be altered to minimize pressure loads.

II. METHOD

The method can be described with the following working steps:

1. Creation of a mould of the patient in a sitting position
2. 3D-measurement of the mould,
3. measurement of the pressure loads with the patient,
4. superimposition of the data sets,
5. analysis of the seat shell's surface considering the critical pressure areas,
6. reworking of the seat shell's surface and rescan of the pressure situation,
7. repetition of 6. to obtain an optimized pressure situation and patient's comfort.

In the first working step a mould of the patient in a sitting position is created with the help of a vacuum moulding system. The moulding system basically consists of a large latex cushion that is filled with fine plastic granulate and that is equipped with a vacuum valve. The patient is seated upon the cushion observing a number of measurement parameters : width, depth angle and incline of the seat and incline and height of the backrest. With the help of a vacuum pump the air is extracted from the cushion and an impression of the patient's body is embedded in the plastic granulate (fig. 1).



Fig. 1 Vacuum moulding system with impression of patient's body

It is of this mould that the patient’s body geometry is measured with the help of the 3D Scan system SLT (fig. 2). The SLT measurement procedure basically consists in the projection recording and measurement of a sequence of stripes of light on the object to be measured. The distortion of the stripes of light indicates the surface geometry of the object. With the help of the Graycode sequence and the Phaseshift the 3D coordinates of the surface points can be calculated within a very short time. The local resolution can be adjusted during the calibration of the system by the selection of the camera’s sensor pixels and the dimension of the image section in relation to the focal width.

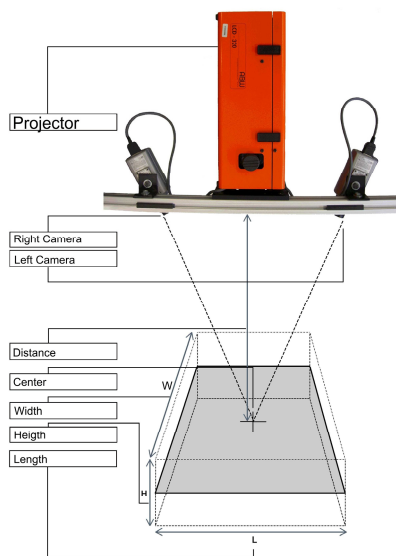


Fig. 2 SLT system with the defined measuring volume

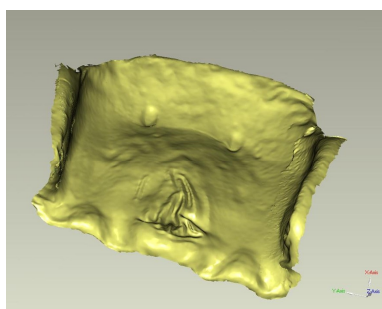


Fig. 3 Result of the SLT measurement; 3D-surface of the seat shell

In the next step the patient is seated on a force sensor mat that is placed on the mould taken previously. In the present

study we refer to the measurement system Pliance® by Novel® with the following technical specification [7]:

- sensor matrix: 16 lines x 16 columns
- measurement rate: 20k sensors/sec.
- calibration in 240 steps from 0 to 60k PA

The patients were advised to shift their positions slightly during the measurement process (3 to 5 minutes). Thus it was intended to take into account the effect of minor deviations of the position in relation to the pressure situation.

The results of the pressure measurement are presented in a colour coded map (fig.4) that is imported into a bitmap format for the superimposition with the 3D SLT data.

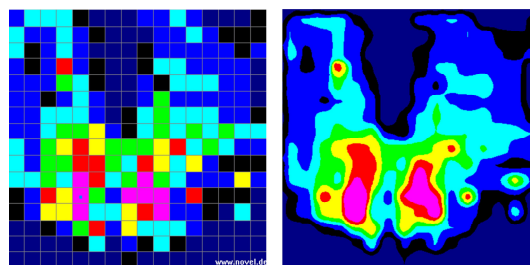


Fig. 4 Result of the pressure measurement (colour coded: high pressure red; low pressure blue)

In order to effect the superimposition and matching of the data sets, the 3D data of the mould in STL-format and the 2D data of the pressure measurement in Bitmap-format are imported into the CAD/CAM system Inventor 10® by Autodesk® (fig. 5). The Bitmap data are added to the STL data as a sketch plane and adjusted to the 3D surface (fig. 6). Distinctive anatomical landmarks serve a reference points and enhance the orientation and adjustment of the two surfaces. The colour coded pressure map is matched to the seat’s surface by means of the function *Aufkleber* [8]. This function suggests that the 2D Bitmap data can be matched to the 3D surface like an adhesive sticker. This is misleading as the function works more or less like a projection of the 2D pressure map on the 3D surface. Therefore the 2D map becomes too much distorted on the raises and depths of the 3D topography. To avoid inaccuracies the pressure data map must be cut according to the 3D surface topography. After this matching process the correct fit of the seat can be easily analysed with the help of the colour coded pressure data (fig. 7).

The mould can be altered and overworked to enhance the patient’s comfort. The procedure of pressure measurement and data superimposition has in this case to be repeated until an optimal solution is found.

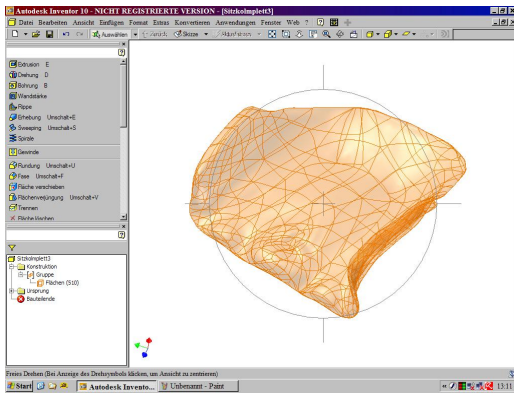


Fig. 5 CAD/CAM system (Autodesk Inventor 10); import of the 3D surface

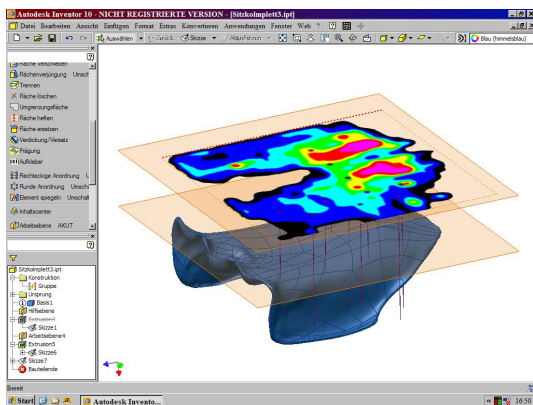


Fig. 6 Superimposing of the 2D pressure data and the 3D surface data

III. DISCUSSION

A necessary precondition for the optimization procedure is the superimposition and matching of the different 2D and 3D data sets. This crucial exchange of data and their processing in the Cad/CAM system Inventor® is possible without problems. The program interfaces are completely functional.

The correct adjustment of the data sets and the orientation with the help of reference points on the 2D pressure map and the 3D surface do not pose any problems. On the whole the digital methods are reliable and manageable tools to optimize the workflow and the production of orthopedic devices like seat shells. Thus it is possible to increase the quality of the individual adjustment and to increase the comfort of the patient.

The actual match with the function “Aufkleber” has to be optimized by dividing the pressure map in a series of cuts in order to avoid the distortion of the surface data.

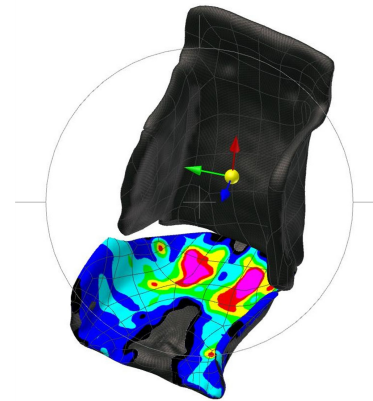


Fig. 7 Result of the superimposed data

ACKNOWLEDGMENT

We thank the companies ABW, Frickenhausen and Novel, Munich for the support.

REFERENCES

1. Strobl W, Dauter G (2000) Sitzhilfen für körper- und mehrfachbehinderte Menschen, Pathophysiologie, Indikationen und Fehler, Orthopädie-Technik 12/2000, 1042-1051
2. Hochmann D, Diesing P, Boenick U (2003) Extrinsic Faktoren der Dekubitus-entstehung – Ein Rückblick auf die Erkenntnisse der letzten 80 Jahre, Orthopädie-Technik 09/2003, 620-627
3. Grady JH (1997) Druckmesssysteme für das Sitzen und ihre klinische Bedeutung, Orthopädie-Technik 12/1997, 1000-1007
4. Subke J, Wehner H-D, Wehner F, Wolf H (1998) "Wundtopographie mittels Streifenlichttopometrie," Rechtsmedizin Supplement I zu Band 8, 1998.
5. Subke J, Wehner H-D, Wehner F, Szczepaniak S (2000) "Streifenlichttopometrie (SLT). A New Method for a 3-Dimensional Photorealistic Forensic Documentation in Color," Forensic Sci. Int., 113, 289-295, 2000.
6. Tschanz H-P (2003) CAD-Sitzschalenmodellierung und CNC-Frästechnik, Orthopädie-Technik 06/2003, 447-448
7. Novel GmbH, Novel pliance-m – Handbuch, Novel GmbH, München, 03/2005
8. Autodesk, AutoCAD Inventor 10 Series – Handbuch Erste Schritte, Autodesk, Inc., München, 2005

Author: Prof. Dr. Jörg Subke
 Institute: Biomechaniklabor, Zentrum für Medizin- und
 Krankenhaustechnik, Fachhochschule Gießen-Friedberg
 Street: Wiesenstr. 14
 City: D-35390 Giessen
 Country: Germany
 Email: joerg.subke@tg.fh-giessen.de

Spatiotemporal pixelization method based on vertical sub-sampling to improve reading ability for visual prosthesis

H. S. Kim¹, J. H. Shin¹ and K. S. Park²

¹ Interdisciplinary Program of Bioengineering, Seoul National University, Seoul, Korea

² Department of Biomedical Engineering, College of Medicine, Seoul National University, Korea

Abstract— We proposed the spatiotemporal pixelization method based on vertical sub-sampling to improve reading ability for visual prosthesis. To evaluate proposed method, we simulated a test of reading performance of visual prosthesis with five different frame rates at 8×8 pixel arrays. The proposed method showed better reading performance than static pixelization method. The maximum reading speed was found at 50Hz of spatiotemporal pixelization method.

Keywords— Visual Prosthesis, Spatiotemporal, Vertical Sub-Sampling, Reading Speed, Frame Rate.

I. INTRODUCTION

Many research groups have studied about visual prosthesis which restores sight of blind people by implanting microelectrode arrays into visual pathway. Recently, chronic human trials of visual prosthesis were performed few groups and acquired meaningful data [1-4].

Reading ability is the important in the rehabilitation of blind people. Many researchers have investigated psychophysics of pixelized reading with various methods and parameters to find adequate parameters and overcome the limited number of microelectrode array [5-7]. However, the previous research has tended to focus on spatial information rather than temporal information. Spatiotemporal image processing techniques of visual prosthesis remained unexplored.

The main purpose of this study is to propose a spatiotemporal pixelization method based on vertical sub-sampling to improve reading ability. The experiment was performed to verify the reading speed of proposed spatiotemporal pixelization method compared with a conventional static pixelization method.

II. METHODS

A. Experimental set up

Experiment platform consisted of a camera, a laptop computer, and a head-mounted display (HMD). The camera (FL2-03S2M/C, 80 FPS, 1/3" CCD, IEEE1394) was used

to capture printed reading materials with fixed focal length lens. The camera was installed to a table perpendicularly. Captured image by camera was processed by self-developed image processing software and the processed images were seen through the HMD (Z800 3DVisor, 800x600 resolution, 40° diagonal total field of view, refresh rate 60Hz, eMagin Co., Bellevue, WA, USA). Subjects were scanning the reading materials by controlling printed paper.

B. Image processing method

The original image captured by camera was converted into binary image by polarity reversing and contrast stretching using manually selected threshold values.

Conventional static pixelization method: The pre-processed binary image was sampled with the same resolution of microelectrode array using the block averaging algorithm. The block averaging algorithm reduced the resolution of original image by dividing it into $n \times n$ blocks and replacing the pixel values of each block by the means of the corresponding values. Finally, the phosphene image was generated by multiplying the block averaged image by square phosphene map which had Gaussian typeface. (Fig. 1(a))

Spatiotemporal pixelization method based on vertical sub-sampling: Compared with the previous method, the block averaging algorithm converted the pre-processed binary image into a block averaged image of $2n \times n$ blocks. And the block averaged image was vertical sub-sampled into two different images that consisted of $n \times n$ blocks. After generating two phosphene images as previous method, they were seen through HMD in turns by varying frame rates (stimulus frequency).

C. Subjects

Three volunteers participated in this experiment. All subjects had normal or corrected-to normal visual acuity and aged from 23 to 28. They were Korean graduate students and also good at English with at least 6 years of English education. Before experiments, we informed them of purpose of this study as well procedure of experiments and obtained their approval.

The reading speed of spatiotemporal pixelization method was affected by variation of frame rate. The reading speed was on an increasing trend as the frame rate increases.

Training effect was founded by difference result of static pixelization method that was performed at start and end. The second result of static pixelization method showed a 22% increase over first one.

Fig. 1 The procedures of pixelization method. (a) Static pixelization method (b) Spatiotemporal pixelization method using vertical sub-sampling

D. Experimental Design

The Reading ability was evaluated by measuring a reading speed. Experiment was performed to compare the spatiotemporal pixelization method with the conventional static pixelization method and to find optimal stimulus frequency of spatiotemporal pixelization. Before experiment, HMD was fitted to the subjects and angular substance of pixelized image was fixed at visual field of $6.2^\circ \times 6.2^\circ$ on the HMD. Reading materials were from MNREAD [8]. For all subjects, static pixelization method was experimented prior to spatiotemporal pixelization method. After test of spatiotemporal pixelization by varying stimulus frequency (10, 20, 30, 40 and 50Hz), static pixelization method was tried again to investigate a training effect. Subjects were instructed to read 5 sentences loudly as quickly as possible. While experiment, we measured reading speed of each sentence and number of correct words. Each sentence consisted of six to nine words.

III. RESULTS

Three normal subjects were requested to read English sentences to evaluate proposed spatiotemporal pixelization method by reading speed. Reading speed was computed by the number of correctly read words per minute.

Fig.2 shows reading speed of both methods at 8×8 pixel arrays. There was difference of reading speed between the static pixelization method and the spatiotemporal pixelization method. The result of spatiotemporal pixelization is lower than static pixelization between 10Hz and 30Hz. The maximum reading speed of 16.7 words/min was discovered at 50Hz of the spatiotemporal pixelization method.

Fig. 2 Reading speed of English at 8×8 pixel arrays. Static (1) is result of static pixelization method that performed at start of experiment. Static (2) is result of static pixelization method that performed at end of experiment. Spatiotemporal pixelization method was experimented with five frame rates (10, 20, 30, 40, and 50Hz). Error bars indicate standard deviation

Fig. 3 Reading speed of each subject at 8×8 pixel arrays. Static (1) is result of static pixelization method that performed at start of experiment. Static (2) is result of static pixelization method that performed at end of experiment. Spatiotemporal pixelization method was experimented with five frame rates (10, 20, 30, 40, and 50Hz). Error bars indicate standard deviation

Fig. 3 shows reading speed of each subject at 8×8 pixel arrays. There was a difference in reading speed among subjects, but there was a similar changing tendency in comparison with Fig.2. All subjects scored maximum reading speed at 50Hz of the spatiotemporal pixelization method.

IV. DISCUSSION

The most important finding is that variation of frame rates of spatiotemporal pixelization method based on vertical sub-sampling affected reading speed. Because of the low frame rates seem not enough to update fast moving of paper, gaze stayed at specific region longer than high frame rates. On the other hand, fast scanning have influenced on the maximum reading speed with high frame rates. The variance of reading speed among subjects may be vanishing by longer and systematic training.

The limitation of this study is that we did not experiment in similar circumstance of visual recipients. In the future study, we will develop more realistic apparatus, and investigate another effect of spatiotemporal image processing techniques.

ACKNOWLEDGMENT

This study was supported by a grant from the Korea Health 21 R&D Project, Ministry of Health & Welfare, and from the Advanced Biometric Research Center (ABRC) of the Korea Science and Engineering Foundation (KOSEF), Republic of Korea (A05-0251-B20604-05N1-00010A).

REFERENCES

1. Humayun MS, de Juan E Jr, Weiland JD et al. (1999) Pattern electrical stimulation of the human retina. *Vision Res* 39:2569–2576
2. Dobbelle WH (2000) Artificial Vision for the Blind by Connecting a Television Camera to the Visual Cortex. *ASAIO J* 46:3-9
3. Troyk P, Bak M, Berg J et al (2003) A Model for Intracortical Visual Prosthesis Research. *Artif Organs* 27:1005–1015
4. Humayun MS, Weiland JD, Fujii GY et al (2003) Visual perception in a blind subject with a chronic microelectronic retinal prosthesis. *Vision Res* 43:2573-2581
5. Fornos AP, Sommerhalder J, Rappaz B et al (2005) Simulation of Artificial Vision, III: Do the spatial or Temporal Characteristics of Stimulus Pixelization Really Matter?. *Invest Ophthalmol Vis Sci* 46:3906-3912
6. Fu L, Cai S, Zhang H et al (2006) Psychophysics of reading with a limited number of pixels: Towards the rehabilitation of reading ability with visual prosthesis. *Vision Res* 46:1292-1301
7. Dagnelie G, Barnett D, Humayun MS et al (2006) Paragraph text reading using a pixelized prosthetic vision simulator: Parameter dependence and task learning in free-viewing conditions. *Invest Ophthalmol Vis Sci* 47:1241-1250
8. Legge GE, Ross JA, Luebker A et al (1989) Psychophysics of reading, VII. The Minnesota Low-Vision Reading Test. *Optom Vis Sci* 66:843-853

Address of the corresponding author:

Author: Kwang Suk Park
 Institute: Seoul National University
 Street: 28 Yongon-dong, Chongno-gu
 City: Seoul
 Country: Korea
 Email: kspark@bmsil.snu.ac.kr

Optimizing Visual Cues for Brain-Computer Interfaces

L.R. Jacinto, N.S. Dias, and J.H. Correia

Dept. of Industrial Electronics, University of Minho – Campus Azurem, 4800-058 Guimaraes, Portugal

Abstract— Brain-Computer Interfaces (BCI) based on event related potentials (ERP) have been successfully developed for applications like virtual spellers and navigation systems. This study tests the use of visual stimuli unbalanced in the subject's field of view to cue movement imagery tasks (left vs. right hand movement) and elicit early transient visual ERPs. These cues were compared with balanced cues on classification accuracy. Subject-specific ERP spatial filters were calculated for optimal group separation. The unbalanced cues improved movement imagery discrimination achieving errors as low as 3%. The unbalanced cues appear to enhance visual ERPs related to primary visual processing that reduce the classification error to a minimum soon after the cue presentation. This work suggests that the use of such visual interfaces may be of interest not only for the overall performance improvement of BCI application but also for its use on validation of control decisions.

Keywords— brain-computer interface, spatial filter, event-related potentials, feature selection, visual stimuli.

I. INTRODUCTION

Brain-Computer Interfaces (BCI) allow subjects to control a computer cursor or an electronic device with signals extracted from their brains. [1]. A non-invasive BCI typically uses electroencephalogram (EEG) signals recorded via electrodes placed on the scalp. Some implementations of this interface rely on the detection of sensory-motor rhythms in response to movement imagery tasks in order to control a cursor on the screen [2]. Others utilize brain potentials in response to mental tasks or attention shift events which are denominated event related potentials (ERP) to write words on a virtual speller [3]. However, the EEG patterns that best describe movement imagery or ERP are subject-dependent and the translation algorithm needs to be trained on an individual basis. The employment of feature selection methods is a way of identifying the subject-specific EEG features that provide the best task detection accuracy [4]. Alternatively, EEG data may be spatially filtered by creating virtual channels as linear combinations of the original EEG channels. Spatial filters specifically designed for the classification of ERPs can achieve improved performance [6].

The spatial arrangement of visual stimuli on a screen affects ERP amplitudes and latencies [7]. Additionally, shifting visual attention between different regions on a screen may enhance early visual evoked potentials [8]. The possibility of utilizing specific visual interfaces to elicit such ERPs may be used to estimate subject attention, validate control decisions and increase overall BCI performance [9].

This study proposes the use of graphical cues in the form of unbalanced arrows presented to the subject's visual field as mental task cues. The classification accuracy of spatially filtered ERPs, early after cue presentation, was assessed for balanced vs. unbalanced cues. Spatial filters that enhanced discrimination of responses to visual cues for left vs. right movement imagery tasks were optimized for each subject.

II. METHODS

A. Paradigms

Four healthy human subjects, two male and two female, ages 20 to 30, participated in the study. Two different experiments were run each presenting a paradigm where arrows indicated the imagination tasks to be performed (left vs. right arm movement imaginations).

The subjects were seated approximately 60 cm from a computer screen. The timeline of the trials was the same for all experiments. Each trial started with a fixation cross, which remained on screen for the entire trial period, at the center of which the subjects were instructed to focus their gaze and attention. An arrow indicating the direction of the imagination task appeared 3 seconds after the cross was made visible. The arrow remained on screen for 4 seconds, i.e. for the duration of the imagination period which started at the appearance of the arrow. Then, both the cross and the arrow disappeared, leaving a blank screen. The length of the inter-trial period was randomly set between 3 and 4.5 seconds to avoid subject adaptation.

The paradigms differed in the type of arrows presented and their position in the subject's visual field. Figure 1 illustrates an example of each of the two paradigms. In Experiment 1 (Fig 1-A), the arrows appeared centered on a fixation cross (balanced), where both ends of the arrow were equidistant from the cross's origin and had both a head and a tail. In Experiment 2 (Fig. 1-B), the arrows appeared in a non-centered fashion (unbalanced) with the total length of each arrow appearing on just one side of the cross's origin and having only a head, but no tail.

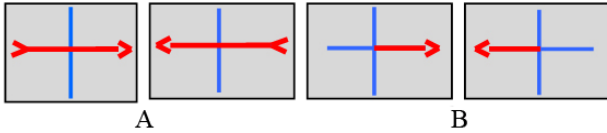


Fig. 1 Visual cues employed in both experiments. A. right and left cues for the balanced arrows paradigm; B. right and left cues for the unbalanced arrows paradigm

Two sessions of Experiment 1 and two sessions of Experiment 2 were conducted in a total of 4 sessions per subject. Each session consisted of 2 experimental runs of 40 trials with an equal number of each type of cue being presented (i.e. 20 left and 20 right).

B. Recording

EEG signals were recorded from 19 electrodes (FP1, FP2, F7, F3, Fz, F4, F8, T7, C3, Cz, C4, T8, Pz, P3, Pz, P4, P8, O1 and O2), according to the 10-20 system, all referenced to the linked earlobes. Data were sampled at 256 Hz and band-pass filtered between 0.05 and 60 Hz with a fourth order zero phase Butterworth filter. An ocular artifact removal algorithm was applied to the data [10] to eliminate eye movement related artifacts. The peripheral frontal and temporal electrodes (i.e. FP1, FP2, F7, F8, T7 and T8) were also excluded from subsequent analyses to further reduce remaining eye movement artifacts that could misguide the calculation of the spatial filters and classification. In order to obtain reference independent signals, all EEG channels were referenced to the common average of all electrodes.

C. Post-processing and epoch extraction

Data were first low-pass filtered to 8 Hz. Trials (500 ms pre-stimulus to 600 ms post-stimulus) with sample-to-sample gradients larger than $40 \mu\text{V}$, absolute amplitudes larger than $50 \mu\text{V}$ or maximum-minimum amplitude differences of $80 \mu\text{V}$ were considered artifacts and flagged for removal. The epochs were extracted from a window

starting 200 ms before the stimulus up to 600 ms after the stimulus. The mean value of the pre-stimulus period was subtracted from the activity of the post-stimulus interval. To reduce the computational complexity the data were finally downsampled to 20 samples per second. Each final epoch thus contained 12 points representing the 0-600 ms post-stimulus activity. All epochs previously flagged for artifacts were excluded from further processing and analysis.

D. Spatial Filtering and Classification

With the purpose of determining the EEG electrodes that best represent the ERPs in response to stimuli on a subject basis, spatial filters suitable for ERP discrimination were optimized for each subject according to the approach proposed in [11]. Spatial filters f can be optimally determined from training data by maximizing criterion J in equation (1) which can be interpreted as a measure of separation between two groups of feature vectors. Each group represents the EEG epochs recorded in response to either left or right cues. S_B and S_W are the between and within group scatter matrices respectively.

$$J(f) = \frac{f^T S_B f}{f^T S_W f} \quad (1)$$

The eigenvectors V and the eigenvalues are the solution of the generalized eigenvalue problem S_B / S_W where the eigenvectors may be used as spatial filters and the eigenvalues represent the discriminative power of the filters. The feature vectors Y_i resultant from the spatial filtering of the data epochs X_i ($m \times n$ dimensional vectors with electrodes as rows and samples points in a epoch as columns) are calculated in (2).

$$Y_i = V^T X_i + v_o \quad (2)$$

The unidimensional projections (rows of Y_i) are unbiased by the use of the term $v_o = -V^T M$ where M is the time average of all data epochs X_i . The calculated projections may be considered as virtual channels that optimize group discrimination by minimizing the variance of the data along the projection while maximizing the difference between the projected group means.

A form of Fisher Discriminant Analysis was applied to discriminate the projected samples in Y and epoch group membership was predicted as in [12].

The spatial filters were calculated for each session and their accuracy was tested on the data of the same session. Discrimination performance was assessed through the mean prediction error rate calculated over 10 repetitions of a 10-fold cross-validation scheme.

III. RESULTS

Table 1 presents the classification results of 100 cross-validation folds for each subject. The classification accuracy for the paradigm with balanced arrows (sessions 1 and 2) shows minima for all subjects with latencies between 400 and 550 ms after the stimulus presentation. The classification accuracy for the paradigm with unbalanced arrows (sessions 3 and 4) shows the existence of early minima with latencies between 150-300 ms post-stimulus for all subjects except for the fourth session of subject C. Additionally, the minimum error rate found for the unbalanced arrows sessions (3%-20%) is almost always lower than the error found for the balanced arrows sessions (9%-26%). Figure 2 illustrates the classification results and minimal latencies for subject A. The early error minima for the unbalanced arrows' sessions (sessions 1 and 2) are in contrast to the later error minima for the balanced arrows' sessions (sessions 3 and 4).

Figure 3 shows the topographical maps of two spatial filters calculated for sessions 1 (balanced) and 3 (unbalanced) of subject A as well as examples of the spatially filtered group mean projections. Figure 3-A refers to session 1 and shows an increased filter weights for frontal and central electrodes in the topographical map. Instead, Figure 3-C (session 3) shows the highest weights on parietal and occipital electrodes. The projected group means using the illustrated filter for session 1 (Figure 3-B) reveal clear group separation in the latency range 400-550 ms post-stimulus with maximum difference occurring at 500 ms.

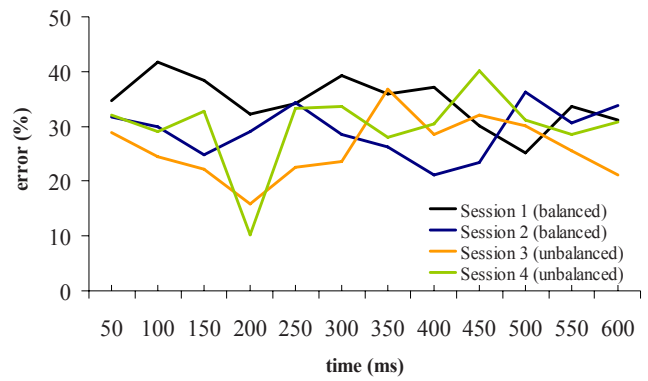


Fig. 2 Average classification error rate for subject A for the balanced arrows paradigm (sessions 1 and 2) and for the unbalanced arrows paradigm (sessions 3 and 4)

The projected group means for session 3 (Figure 3-D) show increased group separation for the latency period 100-250 ms with maximum difference occurring at 200 ms.

IV. DISCUSSION AND CONCLUSIONS

The present work proposes the use of specific visuospatial stimulation to enhance early visual ERP responses leading to successful discrimination between tasks early on after stimulus onset. The arrows unbalanced in the subject visual field were employed as an example of such stimulation. The proposed approach identified an early latency range between 150-300 ms post-stimulus with high group discrimination. The classification errors achieved by the filters at those instants ranged from 3% up to 20%. In contrast, sessions that implemented balanced arrow cues presented later minima with latencies between 400-550 ms post-stimulus and higher classification errors (9%-26%).

Table 1 Classification results and respective latencies

Subject	Session 1		Session 2		Session 3		Session 4	
	Error (%)	Latency (ms)	Error (%)	Latency (ms)	Error (%)	Latency (ms)	Error (%)	Latency (ms)
A	26	500	20	400	16	200	11	200
B	23	500	20	450	20	200	20	200
C	16	450	9	550	3	200	5	450
D	15	400	14	400	9	300	19	150

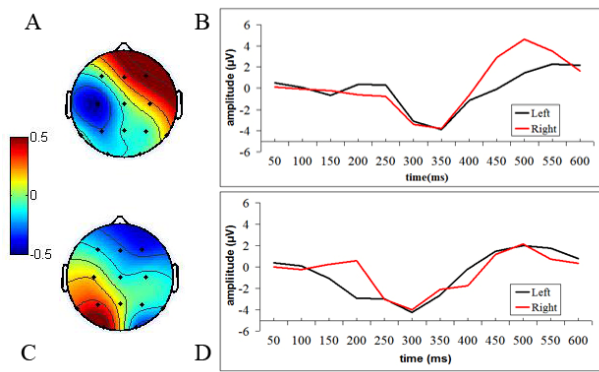


Fig. 3 Topographical maps and spatially filtered group mean projections for subject A. A and B present the electrode weights and the group mean projections for session 1 (balanced arrows paradigm) respectively. C and D illustrate the electrode weights and the group mean projections for session 3 (unbalanced arrows paradigm) respectively.

The differences encountered in the responses to the balanced vs. unbalanced cues suggest that the unbalanced arrows display is responsible for triggering the observed early discriminative response (150-300 ms). Previous studies have shown that non-centered cues tend to generate enlarged early visual ERP as a result of attention allocation in visual space due to stimulus position [8]. These enhanced potentials may have led to high classification accuracy during the early time period.

The spatial distribution of the calculated filters for unbalanced arrow cues show activation of vision-related brain regions, suggesting that the early minima are most likely related with an early visuospatial processing of the cue. In opposition, the spatial distribution of the filters for the balanced arrow cues suggests the activation of motor-related brain regions. From our results, it remains unclear whether these early ERP reflect any attention orientation mechanism or simple visual evoked responses. Our future work will address this issue. In either case, the findings suggest that such visual interfaces may be used in BCI systems for validation of control decisions calculated from other EEG features (e.g. mu and beta rhythms) and overall improvement of performance.

ACKNOWLEDGEMENT

L.R. Jacinto is supported by the Portuguese Foundation for Science and Technology (FCT) under grant SFRH/BD/40459/2007. N. S. Dias is supported by FCT under grant SFRH/BD/21529/2005.

REFERENCES

1. G Pfurtscheller G, Neuper C (2001) Motor imagery and direct brain-computer communication. *IEEE Proc*, vol. 89, no. 7, pp. 1123-1134
2. Wolpaw JR, McFarland DJ, Vaughan T M (2000) Brain-Computer Interface Research at the Wadsworth Center. *IEEE Trans Rehabil Eng*. 8(2):222-6
3. Nijboer F, Sellers, E W, Mellinger J et al. (2008) A P300 based brain-computer interface for people with amyotrophic lateral sclerosis. *Clin Neurophysiol* 119(8):1909-1916
4. Dias NS, Mendes PM, Correia JH (2009) Variable subset selection for brain-computer interface. *Biodevices Proc.*, Porto, Portugal, 2008, pp. 35-40
5. Müller-Gerking J, Pfurtscheller G, Flyvbjerg H (1999) Designing optimal filters for single-trial EEG classification in a movement task. *Clin. Neurophysiol.*, 10:787-798
6. Hoffmann, U, Vesin J, Ebrahimi T (2006) Spatial filters for the classification of event-related potentials. *Proc ESANN*, pp. 47-52, Bruges, Belgium, 2006
7. Yamaguchi S, Tsuchiya H, Kobayashi S (1994) Electroencephalographic activity associated with shifts of visuospatial attention. *Brain*, 117(Pt 3):553-562
8. Müller M M, Hillyard S (2000) Concurrent recording of steady-state and transient event-related potentials as indices of visual-spatial selective attention. *Clin Neurophysiol*, 111(9):1544-52
9. Reddy B S, Basir O A, Leat S J (2007) Estimation of driver attention using visually evoked potentials. *Proc IEEE Intelligent Vehicles Symposium*, pp. 588-593, Istanbul, Turkey, 2007
10. Gratton G, Coles M G H, Donchin E (1982) A new method for the off-line removal of ocular artifact. *Electroencephalogr Clin Neurophysiol* 55(4):468-84
11. Liao X, Yao D, Wu D et al (2007) Combining spatial filters for the classification of single-trial EEG in a finger movement task. *IEEE Trans Biomed Eng* 54(5):821-831
12. Schiff S J, Sauer T, Kumar R et al (2005) Neuronal spatiotemporal pattern discrimination: The dynamical evolution of seizures. *Neuroimage* 28: 1043-1055

Video Game-Based Exercise for Improvement of Calf Muscle Properties: A Case Study

D.G. Sayenko¹, M. Milosevic², K. Masani¹, E.G. Sanin¹, K.M. McConville², and M.R. Popovic^{1,3}

¹ Rehabilitation Engineering Laboratory, Toronto Rehabilitation Institute, Toronto, Canada

² Electrical Engineering Department, Ryerson University, Toronto, Canada

³ Institute of Biomaterials and Biomedical Engineering, University of Toronto, Canada

Abstract— A video game-based training system was designed to integrate functional electrical stimulation (FES) technology and visual feedback therapy as means to regain strength and aerobic capacity of muscles. We believe that the inclusion of interactive gaming component in the muscle training process can increase individuals' motivation to perform their exercises and therefore result in improved muscle properties. The system allows the subjects to perform isotonic plantarflexion and dorsiflexion with utilization of FES against different levels of resistance, while controlling video games. The control of the game is performed based on the visual feedback representing the ankle joint angle. Participant was a man with chronic complete paraplegia at the level of T4. The participant indicated that he enjoyed the video game-based tool, and that he would like to continue the treatment. The game was easy to control and at the same time provided a challenging environment for the player. We believe that video game-based FES training program might be effectively used to motivate subjects to practice with the FES system more frequently and by doing so improve and/or maintain muscle properties after SCI. It is anticipated that such training protocol could be used to minimize the occurrence and severity of secondary complications in individuals with SCI. We believe that the improvement of muscle strength will help individuals with incomplete SCI to participate in other rehabilitation programs designed to improve functional tasks.

Keywords— SCI, FES, visual feedback, muscle training.

I. INTRODUCTION

A decrease in skeletal muscle function has been described as one of the most significant problems impacting the health and quality of life of persons after spinal cord injury (SCI) [11]. Pressure sores [6], fractures [4], and deep venous thrombosis [8] are all thought to be at least partially related to musculoskeletal atrophy and disuse in these individuals.

It has been hoped that the re-institution of forceful muscle contractions utilizing functional electrical stimulation (FES) training would counteract musculoskeletal atrophy in individuals with SCI, and thus, decrease the likelihood of costly secondary complications [11]. However, optimal protocols of FES for the recovery of both muscle strength and endurance in individuals with SCI are not well established. Besides, existing FES applications often require participation of skilled medical or technical staff to supervise the training. Moreover, even when these technical problems are addressed, one needs to ensure that the participants maintain

their interest and adhere to the therapy over long periods of time. This provides a strong rationale for the development of simpler training systems that individuals with SCI will likely use and keep using it for longer time periods.

Recent advances in technology have resulted in availability of the application of video games and virtual reality in rehabilitation [3,13]. For example, video games were used by O'Connor et al. [9] in an attempt to increase the physiologic responses of people using manual wheelchairs and to examine their effects on the motivation of the people to perform their exercises. The observations showed that 87% of the subjects found that the games motivated them to perform their exercises [9]. Additionally, the motivational benefits of game-based exercises with visual feedback [2] and virtual reality [7] were observed during sitting balance training in individuals with SCI. The results of these studies demonstrated that the interactive gaming intervention can motivate patients to practice dynamic movement tasks, and can provide the patients and the therapist with instantaneous feedback about performance and goal attainment during the training [2,7].

We therefore proposed a video game-based training system that is designed to integrate FES technology and visual feedback therapy as means to regain strength and aerobic capacity of muscles, as well as joint mobility. We believe that the inclusion of interactive gaming component in the muscle training process increases the individuals' motivation to perform their exercises and therefore will result in improved muscle properties. Our system allows the subjects to perform isotonic plantarflexion and dorsiflexion with the help of FES against different levels of resistance while controlling video games. The control of the game is performed based on the visual feedback representing the ankle joint angle. Thus, the purpose of our study was to evaluate the concept of the new training system using the following criteria: (1) the system must include an entertaining component, and be easy to control and operate; (2) characteristics of the FES and resultant movements recorded during training must correspond to the general muscle training criteria identified in the literature; (3) the designed system must be adjustable and provide optimal training even for individuals with the lowest degree of preserved muscle function; and (4) the system must be safe.

II. MATERIAL AND METHODS

Positioning equipment: During the training, the participant was seated on a padded bench with a backrest support; the positions of the hip and knee joints were set to 90° of flexion. The feet were firmly strapped to the foot platform. The platform was attached to the main shaft which was inserted into the side bearings. The bearings bolted to the base plate held the foot platform in place. The main shaft had two sections: one supporting the foot platform and the other one with a notch that served as the lock for the inverted pendulum which length was 1 m and was in an upright position (Fig. 1A).

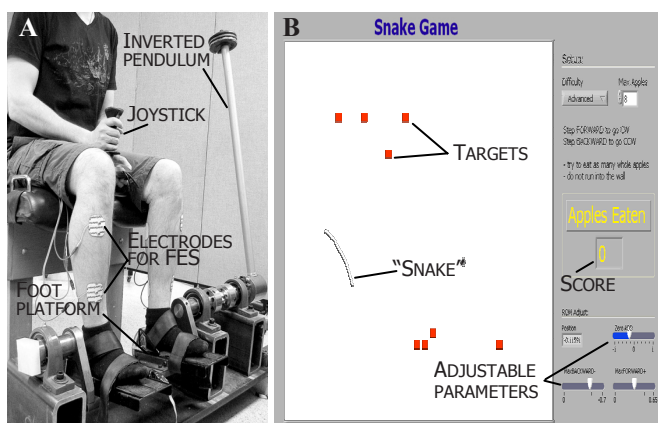


Fig. 1. (A) Foot platform with the inverted pendulum locked in place on the end of the main shaft. (B) Interface of game-based exercise.

The pendulum was used to provide resistance during exercise. Varying amounts and numbers of lifting weights might be added onto the pendulum according to preserved muscle function of the particular participant. The neutral position of the ankle joints (0° dorsiflexion/plantarflexion) corresponded to 4° of the backward inclination of the pendulum. It created higher load on plantarflexors (PF) than on dorsiflexors (DF). The Reaction Torque Sensor (Model TS11-200 (Germany) with a capacity of 200 Nm was amounted to the main shaft to measure the torque produced during training. The range of angular displacement of the foot platform was mechanically restricted within the range of 25° plantarflexion and 15° dorsiflexion to prevent excessive motions during the training. The stoppers were covered by a soft surface to absorb possible mechanical shocks when the platform stopped moving.

Tilt sensor: Tilt of the foot platform was registered by a differential capacitance Micro-Electro-Mechanical System 3-axial accelerometer with a range of ± 2.0 g (KXM52-1050, Kionix Inc., USA), which was securely attached to the platform. Signals were sampled using a 12-bit resolution data

acquisition system (National Instruments, Austin, TX, USA). Real-time data acquisition, processing, visualization, and storage were performed using the LabVIEW 8.6 software package (National Instruments, Austin, TX, USA).

Functional Electrical Stimulation: A programmable 4-channel neuromuscular electrical stimulator (Compex Motion, Compex SA, Switzerland) was used to deliver transcutaneous FES to the calf muscles. Two pairs of self-adhesive gel electrodes (ValuTrove, Denmark) of different size (9×5 cm and 5×5 cm) were placed over two different stimulation sites of each leg, i.e., the surface of PF and DF, respectively. The stimulation waveform was a rectangular, biphasic, monopolar pulse waveform, with pulse duration of $300 \mu\text{s}$. The stimulation was delivered with a frequency of 40 Hz. The maximal amplitude (intensity) of the stimulation was set to 80% of the intensity required to produce a maximum torque.

Joystick: The stimulation intensity was controlled by the participant himself in response to the videogame prompts using an analog joystick controller, connected through an analog input port to the electrical stimulator. Inclination of the joystick forward corresponded to the stimulation of PF, whereas its inclination backward to the stimulation of DF. The intensity of the stimulation increased proportionally with the joystick input. For the participant, intensity of FES was defined before the training session and varied from 30 and 20 mA (motor threshold for PF and DF, respectively) to 80 and 70 mA (80% of the intensity required to produce a maximum torque by PF and DF, respectively).

Game-based exercise: Visual feedback of the foot platform tilt (which was correspondent to the ankle joint angle) during the training was provided by the 37" LCD monitor placed in front of the participant. The goal of the game was to navigate the moving "snake" around the screen over the randomly appearing targets (Fig. 1B). To produce clockwise or counterclockwise turns of the snake, the participant performed plantar- or dorsiflexions, respectively with the use of FES. With the ankle joints in the neutral position, the snake moved straight. To motivate the participant to improve his performance, a score representing the number of collected targets was displayed. The trial was restarted every time the snake got out of bounds of the screen. The game parameters were adjustable, namely, speed of the snake and number of targets. The amount of additional weights added to the pendulum impacted the resistant force (torque) during movements in the ankle joint. The adjustable weight of the inverted pendulum allowed us to increase the difficulty of the tasks performed and made the game more challenging which made it more attractive for the participant and more relevant for the training that we were trying to accomplish.

Outcome measurements: Intensity and duration of FES for each muscle group, angular displacement of the foot

platform, and torque produced in the ankle joints were recorded during one training session. All data were sampled at 500 Hz and stored on a personal computer for subsequent analysis. Obtained signals were low-pass filtered using a fourth-order, zero-phase-lag Butterworth filter. The cutoff frequency of the filter was set to 5 Hz. In addition to the aforementioned recordings, an open-question interview was carried to assess motivational aspects of training, as well as the participant's demands and suggestions to improve the training system.

Participant: Participant was a 57-year-old man with chronic complete paraplegia (American Spinal Injury Association (ASIA) classification A) at the level of T3/4 resulted from an industrial accident 4 years before recruitment into the study. At the time of initial assessment, he demonstrated complete motor and sensory loss below the T4 level. His primary treatment goal was to prevent secondary complications associated with impaired blood circulation and bone demineralization.

III. RESULTS

In Fig. 2 an example of recordings obtained during the training session is presented. It can be seen that FES applied to calf muscles resulted in ankle joints rotation. As the inverted pendulum was coupled with the foot platform, which movements were restricted by the stoppers, the maximal torque was exerted at the moment when the pendulum was moved from its initial position on the stoppers (these parts are indicated by arrows on the gray bold line). With increment of plantarflexion or dorsiflexion the magnitude of torque decreased since the inverted pendulum approached to the upright position. After the pendulum reached the vertical point, it continued to move under the force of gravity until the rotation of the foot platform was arrested by the stoppers. The subject maintained a constant level of stimulation in his muscles until an opposite rotation of the foot platform was required to control the game.

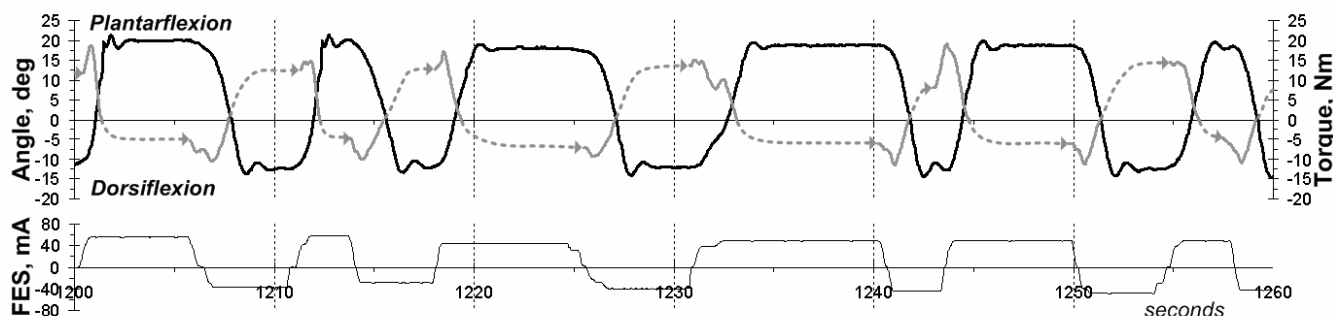


Fig. 2. Example of recordings obtained on the twentieth minute of the training session. The training was performed with weight of 3 kg on the pendulum. The thin black line indicates intensity of FES, whereas the bold black line indicates the angular displacement and the bold gray line – torque produced in the ankle joints during rotation of the foot platform. The dotted portions of the bold gray line indicate motion of the pendulum driven by force of gravity.

It has been found that the optimal weight on the pendulum that the subject could control using FES was 3 kg. With this weight, plantarflexion and dorsiflexion could be performed within the range of motion (ROM) throughout the whole training session which was 45 min long. Table 2 represents average values of the recorded parameters during first, twentieth, and fortieth minutes.

Table 1. Average values of intensity and duration of FES for each muscle group, angular displacement of the foot platform, and torque produced in the ankle joints during one training session.

Parameter	Training session			
	1 st min	20 th min	40 th min	
Intensity of FES, mA	PF	44.9±6.2	50.2±5.1	49.2±6.8
	DF	44.5±5.6	39.8±6.5	48.6±6.1
Duration of FES, s	PF	5.9±1.4	6.5±2.1	6.1±1.8
	DF	5.1±1.2	4.4±1.1	4.9±0.7
Angular displacement, deg	PF	19.7±0.3	19.1±0.8	19.1±0.6
	DF	-12.5±0.4	-12.4±0.6	-9.4±1.3
Peak torque, Nm	PF	15.3±1.3	16.1±1.9	16.4±1.5
	DF	-9.2±0.5	-10.0±0.9	-9.9±0.8
Repetitions	7	6	7	

It can be seen that the ROM and resultant torque at the end of the session were very close to those in the beginning of the training session. The parameters of the stimulation also stayed similar throughout the training session. During the training session approximately 300 repetitions of plantarflexions and dorsiflexions were performed.

The subject reported that he had fun controlling the video game-based training. He stated that the video game was challenging to play but was easily adjusted to meet the needs of the subject. The subject also reported that the instruction to maximize his score during each trial motivated him to play, and keep his attention to the game throughout the whole session. The subject was very encouraged to participate in this training program on a regular basis, and he continues to do so to the present time.

IV. DISCUSSION

The main observation in this case study was that the interactive gaming FES intervention can motivate a person with chronic SCI to practice muscle training exercise. Our participant indicated that he enjoyed the video game-based tool, and that he would like to continue the treatment. The game was easy to control and at the same time provided a challenging environment for the player.

To the best of our knowledge, there is no conventional protocol or device aimed to regain calf muscle properties in SCI individuals. Existing training systems include training during isometric contractions, i.e., with a constant muscle length and fixed ankle joints [10]. However, such condition introduces a high risk of bone fracture [1], decreased blood circulation [5], and restrained ankle joints' mobility. We therefore suggested a system which allows the subjects to perform dynamic plantarflexion and dorsiflexion against different levels of resistance, and thus, decreases the probability of the aforementioned risks. To eliminate the risk of excessive and unsafe motions in the ankle joints during the training, our system is secured with mechanical stoppers which provide a safe rotation of the foot platform within the individual's range of motion.

During the training session the main pattern of the electrical stimulation was intermittent, that is consisted of cycles with approximate 6 s of plantarflexion followed by 6 s of dorsiflexion. This agonist-antagonist work ratio provided long muscle performance without signs of fatigue.

During the training session the forces imposed upon the calf muscles implied primarily concentric action (that is muscle contraction in which the muscles shorten while the generate force). However, the system may be adjusted to incorporate eccentric muscle actions which are believed to be more effective in generating muscle hypertrophy and increasing muscle strength [12].

It has been noted earlier that a regular training program might not be available or might be too difficult to participate in, either physically and/or psychologically [9]. Our approach was applied to an individual with complete SCI, and thus, with a severe impairment of leg muscles' function. However, the system parameters were easily adjustable permitting the participant to successfully train while progressively increasing the challenge of the game. Moreover, characteristics of the system allow individuals with even less preserved muscle function to participate in this training program.

Thus, we believe that our video game-based training program might be effective in motivating subjects to train more frequently and adhere to otherwise tedious training protocols. It is expected that such training will not only improve properties of their muscles, but also decrease the severity and frequency of the secondary complications that result

from SCI. In addition we believe that the improvement in muscle strength may be instrumental in helping individuals with incomplete SCI to increase their participation in other rehabilitation programs and activities designed to improve function.

REFERENCES

1. Belanger M, Stein RB, Wheeler GD et al. (2000) Electrical stimulation: can it increase muscle strength and reverse osteopenia in spinal cord injured individuals? *Arch Phys Med Rehabil* 81:1090-1098.
2. Betker AL, Desai A, Nett C, et al. (2007) Game-based exercises for dynamic short-sitting balance rehabilitation of people with chronic spinal cord and traumatic brain injuries. *Phys Ther* 87:1389-1398.
3. Bryanton C, Bosse J, Brien M et al. (2006) Feasibility, motivation, and selective motor control: virtual reality compared to conventional home exercise in children with cerebral palsy. *Cyberpsychol Behav* 9:123-128.
4. Chantraine A, Nusgens B, Lapiere CM (1986) Bone remodeling during the development of osteoporosis in paraplegia. *Calcif Tissue Int* 38:323-327.
5. Crameri RM, Cooper P, Sinclair PJ et al. (2004) Effect of load during electrical stimulation training in spinal cord injury. *Muscle Nerve* 29:104-111.
6. Garber SL, Krouskop TA (1982) Body build and its relationship to pressure distribution in the seated wheelchair. *Arch Phys Med Rehabil* 63:17-20.
7. Kizony R, Raz L, Katz N et al. (2005) Video-capture virtual reality system for patients with paraplegic spinal cord injury. *J Rehabil Res Dev* 42:595-608.
8. Merli GJ, Herbison GJ, Ditunno JF et al. (1988) Deep vein thrombosis: prophylaxis in acute spinal cord injured patients. *Arch Phys Med Rehabil* 1988; 69: 661-664.
9. O'Connor TJ, Cooper RA, Fitzgerald SG et al. (2000) Evaluation of a manual wheelchair interface to computer games. *Neurorehabil Neural Repair* 14:21-31.
10. Petrofsky JS, Phillips CA (1984) The use of functional electrical stimulation for rehabilitation of spinal cord injured patients. *Cent Nerv Syst Trauma* 1:57-74.
11. Ragnarsson KT (2008) Functional electrical stimulation after spinal cord injury: current use, therapeutic effects and future directions. *Spinal Cord* 46: 255-274.
12. Roig M, O'Brien K, Kirk G et al. (2008) The effects of eccentric versus concentric resistance training on muscle strength and mass in healthy adults: a systematic review with meta-analyses. *Br J Sports Med* *in press*.
13. Schultheis MT, Rizzo AA (2001) The application of virtual reality technology for rehabilitation. *Rehabil Psychol*. 46:296-311.

Implanted Myo-neural Interface for Upper Limb Prosthesis

N.R. Prabhav, S.R. Devasahayam, and R. Ojha

Department of Bioengineering, Christian Medical College, Vellore, India

Abstract— The wide use of powered prosthetic hands is hampered by the availability of good human-machine interfaces. Current interfaces using electromyography suffer from stringent requirements of electrode placement and limited multi-functionality.

An implanted EMG acquisition system with a transcutaneous packet-radio link and power transfer addresses the problems with electrode placement. It also makes possible the use of sophisticated classification algorithms to address the issue of multi-function control. We have developed an implantable EMG acquisition system with transcutaneous data transfer for prosthesis control. The system has provision for data transmission from the prosthesis to the implanted unit for sensory feedback to the user. The radio link is immune to occasional power interruptions; data corruption due to noise can be detected without deterioration of the SNR. We also propose that EMG classification will be improved by independent suturing of each electrode to the muscle to avoid time scaling of EMG signal shape.

The system has been built and tested successfully. Implantations in animals for long-term testing have been started.

Keywords— Prosthesis Control, EMG, Implanted Electrodes, Human-Machine Interface, Myo-neural Interface.

I. INTRODUCTION

Upper limb prosthesis can improve the quality of life of an amputee dramatically. The two main types of upper limb prostheses are body powered and self-powered. Body powered prostheses typically use a cable to transfer power from the shoulder to the prosthetic hand. Self-powered prostheses usually use batteries for powering electric motors. Such powered prostheses are less physically demanding of the user, but the “human-machine interface” is usually the bottle-neck. Even technologically educated people often choose body-powered prostheses instead of self-powered prostheses owing to the awkward and tedious control interface [1]. A variety of control strategies are used to enable the user to control a prosthetic hand. EMG based control systems are available commercially and use very basic EMG amplitude thresholding for generating the control signals. Alternatively, the EMG can be used by pattern classifiers to decipher the intended movement and generate control signals based on the intention. Such methods, which use one or more channels of EMG,

have been described in the literature and have been very successful in the laboratory [2]. Their use in commercially available hands, however, is still awaited. The sensitivity of classifiers to electrode placement and other factors affecting the quality of EMG may be the reasons for such difficulty in deployment [3]. Moreover, changes in the soft tissue over time (such as change in fat content) would affect the classifier performance.

In our experience with the fitting of the Bombay-Vellore Artificial hand, a small switch embedded in the prosthesis socket and actuated by muscle movement in the residual limb provides the human-machine interface (see Fig. 3) [4]. This interface has been received with unexpected enthusiasm as the users have sensory awareness of skin contact with the switch and can feel the switch press. Multi-function control is achieved by converting a sequence of switch-presses to parallel data; but this can be slow and tedious for large number of functions. The present research has been undertaken to enable multi-function control using simple EMG acquisition coupled with sophisticated signal analysis and classification.

An important issue in EMG acquisition and classification is that a combination of classifier training and user training is used to achieve the optimal performance. Kuiken and others at Northwestern University have simplified the aspect of user training by using targeted reinnervation of easily accessible muscle by nerves from the amputated limb [5]. However, their use of surface EMG pickup is likely to reduce the

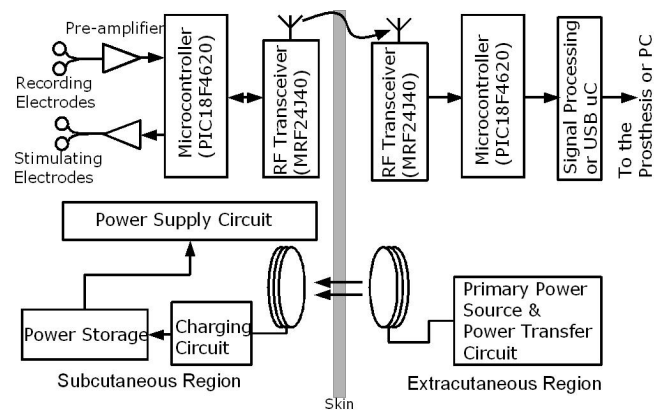


Fig. 1 The block diagram of the implanted myo-neural interface.

reliability of the EMG signal. An allied group at Northwestern University has recently proposed an implanted EMG system to provide good quality EMG for prosthetic control [6].

The usefulness and acceptability of a prosthesis among amputees will be enhanced with sensory feedback from the prosthesis. An often heard complaint about the myoelectric hand vis-a-vis the mechanical hand is that the myoelectric hand doesn't afford any sensory feedback, which would enable the user to know when the hand is operational. In addition, other information from the hand (position, hardness of objects, temperature etc.) will enhance the functionality of the hand.

We have developed a system over the last two years, that addresses many of the shortcomings of current EMG classification based prostheses control. Our approach is based on the following: (i) minimum channels of reliable EMG with robust classification is preferred to multi-channel EMG with thresholding, (ii) standard packet radio networks will provide noise-free reliable EMG in a radio dense environment, (iii) sensory feedback coupled with the EMG pickup will provide a terminal function awareness of the prosthesis and help in mental integration.

II. SYSTEM DESCRIPTION

The block diagram of the system is shown in Fig. 1. The system can be divided into the following subsystems: a) the data recording system, b) the wireless link, c) the power transfer system, d) the stimulating system and, e) the EMG classification system. The subsystems are described below.

Data Recording System: A pair of gold ring electrodes, sutured individually to the muscle, is used to record the EMG. This EMG is amplified and digitized at a sampling rate of 1 kHz and 8-bit quantization by the internal ADC of the PIC18F4620. The microcontroller arranges the data into packets of 64 bytes and sends it across the wireless link, along with an appropriate header.

Wireless Link: The wireless link is designed around the MRF24J40 from Microchip Technology Inc., a IEEE 802.15.4 standard compliant 2.4 GHz RF transceiver. Each RF device consists of a microcontroller and the MRF24J40. The network is configured in a star topology with one coordinator (called the master) that configures the network and sits external to the body in the artificial hand. The nodes (called slaves) are implanted into the body and communicate with the master. The protocol used for the wireless transmission network was designed in the lab for recording of physiological signals, where the network configuration is known a priori and does not change for the duration the RF link is used. The addresses of all devices in the network are hard coded in each RF device making the system more robust and able to reject packets that may come from other

sources. To reduce the power consumed by the circuit, the slaves are put into sleep whenever possible. External interrupts generated using CMOS clocks, time the sampling of the EMG data at each slave. When a sufficient number of samples to form a packet are obtained, the microcontroller (in the slave device) wakes up the RF transceiver and transmits the packet through it. The packets from the master to the RF slaves carries information about the stimulus to be given to the user. The parameters of the stimulation are decided by the external device and transmitted in.

Power Transfer System: The power transfer is achieved by means of an inductive link (a pair of coupled inductors) in a discontinuous flyback topology. The primary to secondary turns ratio was 1:4. We used a high and low side driver, IR2110, for driving the MOSFETs used as switches for driving the primary coil. On the secondary side the coil charges up a supercapacitor (0.47 F, Aerogel capacitor). A 3.3 V switched capacitor voltage regulator provides regulated power.

Stimulating System: The stimulator output stage uses an inductor which is charged through a switch. When the switch is thrown open the current in the inductor discharges through the stimulating electrodes. The switch is controlled by the microcontroller which can deliver pulses of varying widths and frequencies depending on the incoming stimulation command that comes from the RF master.

EMG Processing and Classification: The processing of the raw EMG and the pattern classification algorithm to decipher the intended motion is being refined on a desktop PC and will be implemented on a dsPIC, a range of microcontrollers from Microchip, having a DSP engine in it.

III. RESULTS AND DISCUSSION

Electrode System for Recording EMG: Reliable classification of the EMG requires that the recorded EMG is independent of changes in body position. Usually with surface EMG recording the inter-electrode distance is fixed, but the muscle length changes underneath during movement. Changes in limb position can change the muscle length and thereby alter the geometry of the muscle relative to the recording electrodes resulting in altered EMG even if the neural input is unchanged. If the geometry can be kept stable, then the recorded EMG can be classified more consistently. In order to illustrate the effect of electrode geometry on the recorded EMG we simulated motor-unit action potentials recorded with different electrode spacing. This is the obverse of fixed electrode spacing while muscle length changes, and is thus, equivalent. The MUAP model used in the simulation is adapted from [7]. The simulated motor end plate distribution for two motor units is shown in Fig. 2. The resulting motor unit action potentials for the two motor units are shown. The changes in the MUAP shape are clearly visible.

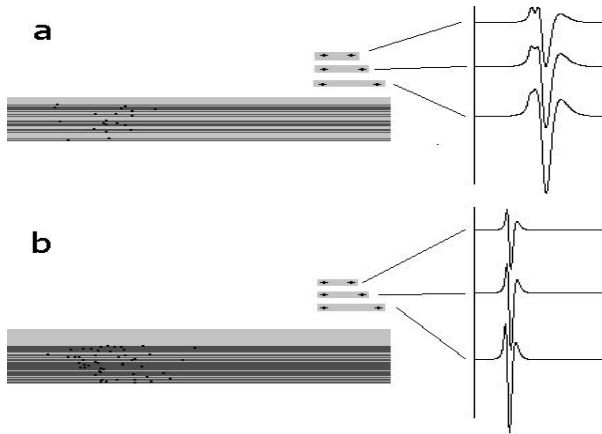


Fig. 2 Changes in the MUAP shape as the interelectrode spacing changes for two motor units. The fibers in the MU was 20 and 50, the conduction velocity 5 m/s and 6 m/s, the muscle depth 2mm and 5mm from the electrodes, respectively. Electrode spacing of 5mm, 7.5mm, and 10mm were simulated, and the resulting motor unit action potentials are shown (the sweep time is 40ms). The left side of each figure shows the motor unit muscle fibers and the end plate distribution. The location of the bipolar electrodes relative to the innervation zone is also shown.

The changes in the shape of the MUAP due to muscle position will result in changes in the features extracted from the EMG and confound the classification of the user's pure intention. This problem is exacerbated in the case of an amputee where the muscles in the residual limb is not anchored. The changes in the length of the muscle may be as much as 50%. See, for example, the muscle in Fig. 3a. We propose, therefore, to independently suture the electrodes on the muscle. By doing this the interelectrode spacing changes proportional to the length of the muscle, maintaining the MUAP shapes.

Wireless Link: The wireless link was tested by giving various artificially generated signals as well as transmitting EMG recorded from surface electrodes. Transmission of sinusoids was used to check the integrity of the RF data link. Fig. 4 shows the transmission of a sinusoid across the link with and without noise in the radio environment. Noise was generated keeping: a) a

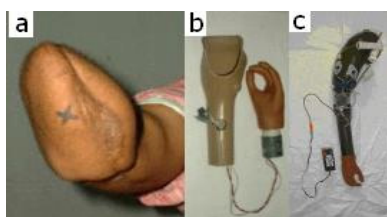


Fig. 3 The Bombay Vellore Hand [4]. It is controlled by one or two switches (depending on the number of functions) fixed on the socket over muscle bulges in the residual limb. **a** shows the muscle bulge for an amputee which may be used to press a switch to control the hand. **b** shows the hand and the socket with the holes for placing the switches. **c** shows a fully connected transhumeral hand.

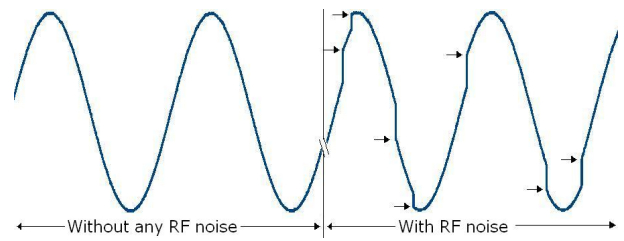


Fig. 4 Trace of a sinusoid transmitted across the wireless link in conditions without noise and with radio noise. The error in transmission results in packet loss and not in data corruption. The arrows denote the places where there is a packet loss.

2.4GHz IEEE 802.15.4 compliant RF transmitter, and b) a Bluetooth network, in close proximity (about 10 cm) to the test network. Whenever there is an error in transmission, the entire packet (consisting of 64 samples of data) is lost. This packet loss can be detected easily, by looking at the packet numbers, and appropriate steps taken to account for the loss in the classification algorithm. Although packets can be resent on request, the additional overhead is not considered worthwhile in this case. The loss of data packets is different from the data corruption seen in analog RF links (AM or FM links), where there is no easy way of determining that the data has not been corrupted during transmission. Various rules for sharing the bandwidth available are a part of the IEEE 802.15.4 standard. Using a standard protocol instead of a proprietary digital radio link, therefore, allows for optimal sharing of resources in a crowded radio environment.

Fig. 5 shows a trace of EMG that was recorded using surface electrodes and transmitted across the link. The spectrum of the EMG is typical of surface EMG and shows no aberration.

Power Transfer System: The RF slave operates at 3.3 V and requires an average current of 10 mA. The power transfer system needs to supply this power to the implanted electronics. A

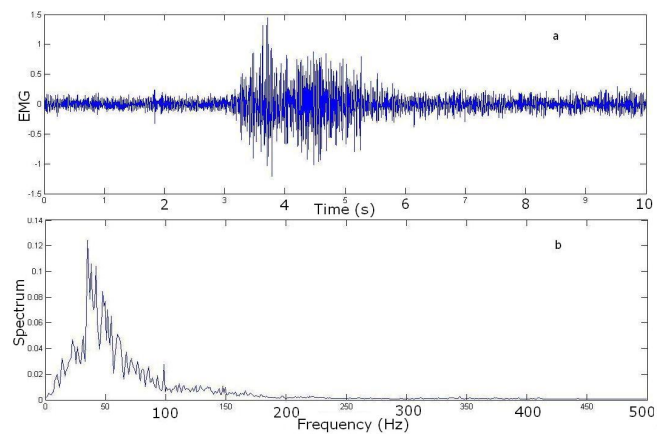


Fig. 5 Surface EMG recorded and transmitted across the RF link. a) shows the raw EMG data. b) shows the spectrum of the EMG recorded.

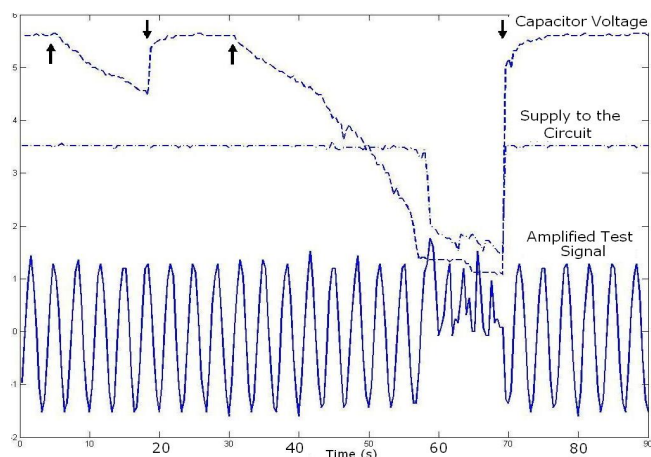


Fig. 6 The response of the circuit when the power supplied to the secondary storage element (the supercapacitor) is interrupted. The arrows show the interruption and subsequent restoration of power supply to the capacitor.

secondary storage element in the implanted circuit would enable the system to tolerate the failure of the power transfer link without disrupting the EMG data transfer. Fig. 6 shows how the data transfer across the wireless link is affected when the charging of the secondary storage element is stopped. The disruption can be detected and intimated to the user, enabling corrective action. A supercapacitor (aerogel capacitor) is used as the secondary storage element. It was chosen because it remains operational for a large number of charge-discharge cycles (a few million cycles), ensuring that the prosthesis remains in operation for a very long duration (a few decades in contrast to electrochemical accumulators which have about 1000 charge cycles).

The efficiency of the power transfer, which is around 5% now, is being improved.

Stimulating System: While doing intramuscular EMG using fine wire electrodes, stimulation is used to locate the electrodes inside the body and to see if they are placed correctly in the muscle of interest. When the stimulus strength is kept very low so that it doesn't cause any contraction of the muscle, and the electrodes are kept very superficially, subjects have reported sensations correlating with the stimulus pulses (unpublished data from our lab). This shows a possibility of using this modality for sensory feedback, however more study needs to be done before any conclusion can be arrived at.

EMG Processing and Classification: EMG classification for prosthesis control has been an ongoing research topic for many years. Many algorithms have been designed that perform very well, even in real time applications. The algorithm used in our testing was picked from [2] and compares favorably with others methods of classification. We have used the Daubechies 4 filter to extract features from the raw EMG and used only one channel of EMG, with one electrode placed on the biceps and the

other on the triceps. With preliminary data we have achieved 100% classification accuracy for a two-class case and 50% for a five class case. More work on the classification is in progress.

IV. CONCLUSIONS

A myo-neural interface for prosthesis control has been developed. The interface involves a wireless link which transmits the EMG recorded using implanted electrodes outside the body. Another set of electrodes is used to give stimulus pulses which can be used to code sensory feedback from the artificial hand to the user. A novel electrode placing scheme has been proposed which will enable us to record EMG whose characteristics do not change with change in muscle length.

The entire system has been tested on the bench and animal trials of the system have been initiated. This interface provides a means of bringing the large amount of work done on EMG classification for prosthesis control into clinical practice.

ACKNOWLEDGEMENTS

We thank the Dept. of Biotechnology, Govt. of India for funding this work. We thank Dr. Srinivasa Babu, Dr. Suranjan Bhattacharji and Dr. Niranjana Khambete for their ideas and inputs at different stages of the project.

REFERENCES

1. Kuniholm J (2009) Open arms: What prosthetic-arm engineering is learning from open source, crowdsourcing, and the video-game industry. *IEEE Spectrum* 46:36-41
2. Englehart K, Hudgins B, Parker P A (2001) A Wavelet-based continuous classification scheme for multifunction myoelectric control. *IEEE Trans Biomed Eng* 48:302-311
3. Kampas P (2001) The optimal use of myoelectrodes. *Medizinisch-Orthopdische Technik* 21-27
4. Devasahayam S R, Bhattacharji S (2005) The Bombay-Vellore Artificial Hand: Recent Developments. *Indian Conference on Medical Informatics & Telemedicine (ICMIT) 2005*
5. Kuiken T A, Miller L A, Lipschutz R D, et al. (2007) Targeted reinnervation for enhanced prosthetic arm function in a woman with a proximal amputation: A case study. *Lancet* 369:371-380
6. Weir R F, Troyk P R, DeMichele G A, et al. (2009) Implantable myoelectric sensors (IMESs) for intramuscular electromyogram recording. *IEEE Trans Biomed Eng* 56:159-172
7. Devasahayam S R (2000) *Signals and Systems in Biomedical Engineering: Signal Processing and Physiological Systems Modeling*. Kluwer Academic/ Plenum Publishers

Author: Suresh R. Devasahayam
 Institute: Christian Medical College, Vellore
 Street: Bagayam
 City: Vellore
 Country: India
 Email: surdev@cmcvellore.ac.in

Closed-loop control of epileptic seizures via deep brain stimulation in a rodent model of chronic epilepsy

L.D. Iasemidis¹, S. Sabesan², L. B. Good², K. Tsakalis³ and D.M. Treiman²

¹ The Harrington Department of Bioengineering, Arizona State University, Tempe, Arizona 85287 USA, Mayo Clinic, 5777 E. Mayo Boulevard, Phoenix, AZ 85054 USA

² Barrow Neurological Institute/Neurology Research, St. Joseph's Hospital and Medical Center, Phoenix, Arizona 85013 USA

³ Department of Electrical Engineering, Arizona State University, Tempe, Arizona 85287 USA

Abstract— We have designed and implemented an automated, just-in-time seizure control scheme using a seizure prediction method coupled with deep brain stimulation in the centromedial thalamic nuclei of epileptic rats. The scheme was tested in terms of its efficacy to control seizures, as well as its effect on synchronization of brain dynamics. The proposed technique of just-in-time stimulation resulted to a significant (50%) reduction of seizure frequency as compared to a baseline period with no stimulation. Importantly, we show that successful seizure control was highly correlated with desynchronization of brain dynamics. This study provides initial evidence for the efficacy of closed-loop feedback control systems in epileptic seizures combining methods from seizure prediction and deep brain stimulation.

Keywords— seizure prediction, deep brain stimulation, desynchronization, feedback control

I. INTRODUCTION

Epileptic seizures are manifestations of intermittent spatiotemporal transitions of the brain from chaos to order. Measures of chaos, namely maximum Lyapunov exponents (STLmax), estimated from dynamical analysis of the electroencephalograms (EEGs) at critical sites of the epileptic brain, progressively converge (diverge) before (after) epileptic seizures, a phenomenon we have called dynamical entrainment (disentrainment) [1]. This phenomenon has already constituted the basis for the design and development of systems for long-term (tens of minutes), on-line, prospective prediction of epileptic seizures [2][3].

More recently, in patients with focal temporal lobe epilepsy (TLE), it was shown that the observed preictal dynamical entrainment (synchronization) of normal brain sites with the focus irreversibly resets in the immediate postictal period [4][5]. Furthermore, recent studies on dynamical analysis of seizure control via drug-based stimulation in rodent models of chronic epilepsy, as well as clinical data from patients treated with anti-epileptic drugs (AED), have shown a significant increase in the brain dynamical disentrainment

(desynchronization) immediately after drug administration [6]. In particular, it appears that the applied stimulation dynamically resets the brain (disentrains the prior to the stimulation entrained brain sites). This constitutes evidence that drug-based stimulation can actually reset the spatio-temporal dynamics of the brain, and hence could be used as actuation in a control scheme for epileptic seizure prevention [6][7]. Also, in computer simulations of biologically plausible models, that consist of networks of coupled chaotic oscillators and exhibit seizure-like behaviors, we have shown that seizures can be avoided only if an applied stimulus successfully resets the dynamically entrained sites ([8][9]).

Motivated by the above findings in humans, epileptic rats and simulation models, in this study, a stand-alone closed-loop automated seizure prediction and just-in-time (JIT) stimulation control system is developed. The feasibility and efficacy of such an automated JIT stimulation control scheme is herein shown when applied to a rat with chronic epilepsy. Results show that the automated JIT stimulation control scheme was significantly effective with respect to reduction of seizure frequency. In terms of brain dynamics, it was found that successful seizure control was highly correlated with the ability of JIT to reset dynamically synchronized brain sites, whereas unsuccessful seizure control was correlated with the failure of stimulation to desynchronize the brain.

The organization of the rest of this paper is as follows. The employed methodology to generate seizures in rats, the seizure prediction methods utilized, as well as the design and implementation of the automated JIT stimulation system are discussed in Section II. In Section III, results from the application of this system to one epileptic animal are shown. Conclusions of this study are given in Section IV.

II. MATERIALS AND METHODS

A. Recording Procedures and EEG data

A male Sprague-Dawley rat (225 g), obtained from Harlan Labs (Madison, WI), was used for the study. The exper-

iment and data collection were conducted in the Laboratory for Translational Epilepsy Research at Barrow Neurological Institute and approved by the Institutional Animal Care and Use Committee. The algorithms for the analysis of the data were developed in the Brain Dynamics Lab at Arizona State University. An episode of acute SE in the rat, utilizing the Lithium-Pilocarpine (LP) model, was used to generate a subsequent state of chronic epilepsy with spontaneous recurring seizures. We refer the reader to [10] for further details about the procedures involved in developing chronic epilepsy in this animal model.

Three to four weeks after the insult of SE, the rat (by then weighing 350 g) was implanted with a six-microwire monopolar electrode array targeted for EEG recording in: a) four cortical locations (from Bregma: A-P 2.0-mm, lateral 3.0-mm and A-P -4.0, lateral 3.0-mm to depth 1.0-mm), and b) two hippocampal locations (A-P -5.6-mm, lateral 4.5-mm, to depth of 5.0-mm). Two Teflon coated tungsten bipolar twisted stimulating electrodes were also inserted, targeting the centromedial thalamic nucleus (A-P -2.5-mm, lateral 1.5-mm, to depth 5.9-mm under a 10° lateral angle). During the surgical implantation of the electrodes, the rat was anesthetized with an intramuscular injection of an anesthetic cocktail consisting of 50 mg/kg ketamine, 10 mg/kg xylazine, and 1 mg/kg acepromazine, and maintained with a 20% booster dose of the cocktail every 45-minutes during the surgery or as necessary.

All electroencephalographic (EEG) data in the study were recorded on a Beehive Millenium LTM EEG machine (Grass-Telefactor Inc., West Warwick, RI). Referentially recorded EEG data, with the electrode over the olfactory bulb as the reference, were band-pass filtered at 0.3 to 70Hz, including a 60 Hz notch filter. The EEG was continuously recorded over days, with concurrent real-time nonlinear dynamical analysis of the recorded EEG on an adjacent personal computer.

B. Automated just-in-time (JIT) control scheme

The seizure prediction scheme described by Iasemidis et al.[2][3][11] was used in this study. This scheme follows the amount of dynamical entrainment of brain sites over time. This dynamical entrainment is characterized by a progressive convergence of STL_{max} estimated at multiple brain sites over time and is quantified by a statistical measure of synchronization of the dynamics between two electrodes i and j , namely, the T-index. Specifically, the T-index T_{ij} between electrode sites i and j for a measure of dynamics (e.g., STL_{max}) at time t is defined as:

$$T_{ij}^t = \frac{|\overline{D}_{ij}^t|}{\hat{\sigma}_{ij}^t \sqrt{m}} \quad (1)$$

where \overline{D}_{ij}^t and $\hat{\sigma}_{ij}^t$ denote the sample mean and standard deviation respectively of all m differences between a measure's values at electrodes i and j within a window $w_t = [t, t-m*10.24 \text{ sec}]$ moving over the measure's profiles. The seizure prediction algorithm continuously follows the average T-index of all entrained electrode pairs, using sequential 10 min sliding windows on the STL_{max} profiles created per electrode site. The average T-index values are continuously compared to a preset statistical threshold value (T_{th}), defined as the value below which the average difference of STL_{max} values in the corresponding time window is not significantly different from 0 ($p = 0.01$). When the average T-index becomes less than T_{th} , the pairs are considered to be entrained and a warning is issued [for details see [3]]. The Epileptic Seizure Warning Program (ESWP) software was developed on a .NET framework to operate in a Windows based environment. The ESWP software can analyze more than 90 channels of EEG data in real time.

A software module to interface with an external stimulator was also created within the ESWP software. This software module triggered an A-M Systems Model 2300 stimulator unit (Calsborg, WA) and provided a stimulus of predetermined pulse width, frequency and duration, to the stimulation electrodes at the time points that ESWP issues seizure warnings. The steps in the combined automated seizure prediction with deep brain electrical stimulation are depicted in the flow chart of Figure 1. The entire experiment was conducted in three phases:

Phase 0: Optimization of Stimulus parameters. In phase 0, a search over a wide range of parameters of the electrical stimulus (amplitude and frequency), that are extensively used in animal studies of deep brain stimulation[12][13], was conducted (frequency range from 50 to 230 Hz, bipolar constant current pulse duration range from 30 to 1000 μsec). The optimal set of stimulus parameters were selected to be the ones that produced maximal resetting of the previously entrained (critical) tuples of brain sites [For further details about the steps involved in selection of the optimal stimulus parameters, we refer the reader to [10]]. Maximal resetting of brain dynamics was achieved by a high frequency (130-200 Hz) stimulus pulse over a short range of stimulus amplitudes (100-600 μA , that is up to well below the 30 $\mu\text{C}/\text{cm}^2$ charge density limit for non-damaging stimulation in neural tissues given the size of our stimulating electrodes, which were 170 μm in diameter). The stimulus was administered for 1 minute, its pulse-width was kept constant at 100 μsec , and was delivered in a charge-balanced bipolar cathodic form across the centromedial thalamic electrodes. We then used the optimal parameters of the electrical stimulus from Phase 0 for control of seizures in Phase 2.

Phase 1: Baseline EEG Recording (no stimulation). Baseline EEG recording for a period of 11 days was performed to evaluate the frequency of seizures occurring spontaneously in the rat. The presence of seizure activity was recorded by visual inspection of the EEG. During this period, evaluation of the performance of the seizure prediction scheme with respect to its sensitivity and specificity was conducted.

Phase 2: Automated Seizure Prediction combined with JIT Deep Brain Stimulation. (A closed-loop seizure control scheme.) During this phase of the experiment the ESWP software was programmed to deliver a one-minute stimulation train to the centromedial thalamic nucleus electrodes at seizure warnings. The frequency of seizure warnings and delivered stimulations were recorded. This phase lasted for 11 days following completion of Phase 1.

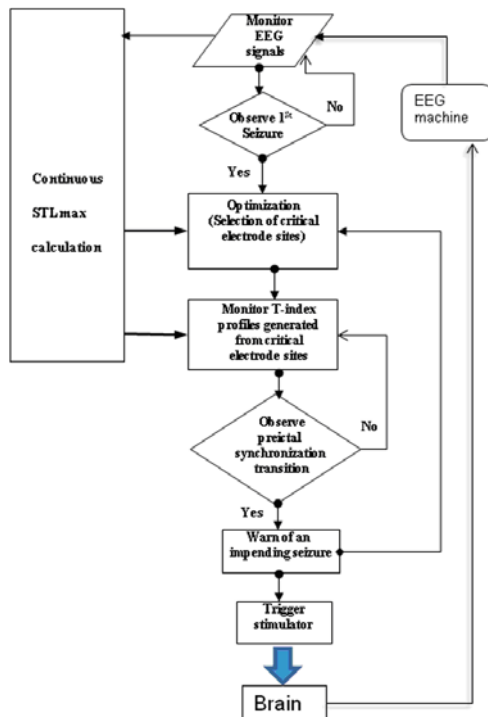


Fig. 1: Flow chart of automated seizure prediction and control in the JIT stimulation system. Continuous real-time estimation of STL_{max} from EEG data is performed. Global optimization is employed to select the critical electrode sites at the first seizure and at seizure warnings thereafter. At seizure warning, the stimulator is triggered to deliver a predetermined stimulus.

III. RESULTS

The performance of the JIT control scheme was evaluated by comparing the mean seizure frequency per day and seizures duration during Phase 2, to the ones in the baseline

(Phase 1). The sensitivity and specificity of the seizure prediction algorithm during Phase 1 was 81.2% and 0.07 false positives/hour respectively, with a mean prediction time of 64 minutes. Using this prediction algorithm to trigger the control stimulus in Phase 2, we observed a 57.37% reduction in seizure frequency, from 54.0 ± 3.12 seizures during Phase 1 to 22.91 ± 4.29 in Phase 2 ($p = 0.01$, Wilcoxon signed-rank test). Interestingly, the seizure duration increased from a mean of 47.88 ± 0.80 seconds during Phase 1 to 53.83 ± 1.41 seconds in Phase 2 ($p = 0.05$, Wilcoxon signed-rank test). Further, to test the repeatability of the results, we repeated Phase 1 and 2 of the experiment. Phase 2 resulted again to a 46.5% reduction in seizure frequency compared to Phase 1 ($p = 0.05$, Wilcoxon signed-rank test).

Subsequently, a comparative analysis of dynamical synchronization and seizure frequency during control phase was performed off-line. In Phase 2, we first estimated the global brain synchronization via a global T-index (average of T-indices of all pairs of available electrode sites within 2-hour non-overlapping running windows) over time. We then compared the resulting global T-index curve with the one generated from the number of seizures that occurred within the corresponding windows over time. Such a comparison over time in Phase 2 is shown in Figure 2(a). From this figure it is evident that: a) when seizure frequency was significantly decreased during the JIT stimulation (e.g., in days 2 and 3 was almost zero), T-index assumed its highest values, denoting significant desynchronization of brain dynamics and b) when seizure frequency was high, T-index assumed low values, denoting synchronization of brain dynamics. We went one step further and estimated the cross-correlation coefficient between the two curves in Figure 2(a). The value of this coefficient across the whole record was -0.72 with a p-value of 0.001. This result means that the global T-index is significantly and inversely correlated with the seizure frequency, and therefore desynchronization of brain dynamics significantly correlates with effective seizure control. Interestingly, based on the opposite assumption of desynchronization of dynamics prior to seizures, it was recently proposed that DBS should be designed to “synchronize the epileptic brain in order to prevent seizures” [14], despite the generation of mixed results. The results from our current study suggest that the key for prevention of seizures through stimulation is the desynchronization of the synchronized epileptic brain (re-setting). This conjecture is in agreement with Durand et al. [15] and our theory of synchronization of dynamics as precursor to seizures, and of seizures as the natural means for the brain to reset [4][5]. In Figure 2(b), we show the actual JIT stimulation rate (number of stimuli per 2 hour running windows) over time for this rat in this period. It shows that stimulation was ON across all days in Phase 2, and therefore

we cannot base the failure of maintaining seizure control after day 4 on lack of stimulation. However, combining all the results shown in Figure 2, we can conclude that lack of seizure control was most probably due to inability of the stimulation to reset the brain.

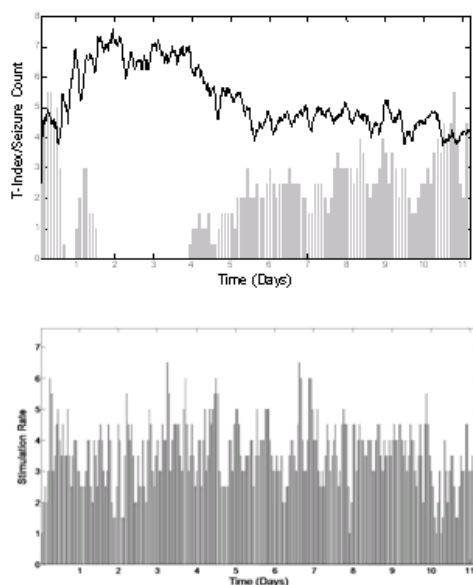


Fig. 2: Brain dynamics of JIT seizure control during Phase 2. (a) Top panel: The global T-index (solid black line) and the seizure frequency (# seizures in two-hour non-overlapping running windows - grey bars) are shown over time. It is observed that when brain desynchronization (higher T-index values) exists, seizures are controlled (e.g. in days 1 to 4). However, when synchronization is higher (lower T-index values), seizure frequency is higher, which is indicative of ineffective seizure control. (b) Bottom panel: The delivered stimulus rate (#stimuli per 2 hour windows) over time.

IV. CONCLUSION

In this small-scale, real-time, in-vivo closed-loop DBS study in one epileptic rodent, we have shown that: 1) The development of an effective closed-loop seizure control system, that has the recorded EEG as input and electrical stimulation as output, is feasible and promising for the control of epileptic seizures 2) It appears that the concept of brain's dynamical desynchronization or resetting is central to the success of such a seizure control system. It was found that successful seizure control was highly correlated with the ability of JIT stimulation to reset dynamically synchronized brain sites, whereas unsuccessful seizure control was correlated with the failure of stimulation to desynchronize the brain. Conduct of larger scale studies to shed more light on these important con-

jectures for epileptogenesis, ictogenesis and the treatment of epilepsy is currently underway.

ACKNOWLEDGEMENTS

Support for this study has been provided in part by the Epilepsy Research Foundation of America and Ali Paris Fund for LKS Research, the National Science Foundation grant No. 0601740, and the Science Foundation Arizona (Competitive Advantage Award CAA 0281-08).

REFERENCES

1. Iasemidis LD. Epileptic seizure prediction and control *IEEE Transactions on Biomedical Engineering*. 2003;50:549–558.
2. Iasemidis LD, Shiau DS, Chaovalitwongse W., Pardalos PM, Carney PR, Sackellares JC. Adaptive seizure prediction system *Epilepsia*. 2002;43:264–265.
3. Iasemidis LD, Shiau D.S., Chaovalitwongse W., et al. Adaptive epileptic seizure prediction system *IEEE Transactions on Biomedical Engineering*. 2003;50:616–627.
4. Iasemidis LD, Shiau D.S., Sackellares JC, Pardalos PM, Prasad A.. Dynamical resetting of the human brain at epileptic seizures: application of nonlinear dynamics and global optimization techniques *IEEE Transactions on Biomedical Engineering*. 2004;51:493–506.
5. Sabesan S., Chakravarthy N., Tsakalis K., Pardalos P., Iasemidis L.. Measuring resetting of brain dynamics at epileptic seizures: application of global optimization and spatial synchronization techniques *Journal of Combinatorial Optimization*. 2009;17:74–97.
6. Good LB, Sabesan S., Iasemidis LD, Tsakalis K., Treiman DM. Brain dynamical disentrainment by anti-epileptic drugs in rat and human status epilepticus *26th Annual International Conference of the Engineering in Medicine and Biology Society, 2004*. 2004;1:1-4.
7. Tsakalis K., Iasemidis L. D. Control aspects of a theoretical model for epileptic seizures *International Journal of Bifurcation and Chaos*. 2006;16:2013-2027.
8. Tsakalis K., Chakravarthy N., Sabesan S., Iasemidis L. D., Pardalos P. M.. A feedback control systems view of epileptic seizures *Cybernetics and Systems Analysis*. 2006;42:483-495.
9. Chakravarthy N., Sabesan S., Iasemidis L. D., Tsakalis K.. Controlling synchronization in a neuron-level population model *International Journal of Neural Systems*. 2007;17:123-138.
10. Good LB. *Automated Seizure Prediction and Control in a rat model of chronic Epilepsy*. Phd dissertation Arizona State University 2007.
11. Iasemidis LD, Shiau DS, Pardalos PM, et al. Long-term prospective online real-time seizure prediction. *Clin Neurophysiol*. 2005;116:532–44.
12. Vercueil L., Benazzouz A., Deransart C., et al. High-frequency stimulation of the subthalamic nucleus suppresses absence seizures in the rat: comparison with neurotoxic lesions. *Epilepsy research*. 1998;31:39.
13. Lado F.A., Velíšek L., Moshé S.L.. The effect of electrical stimulation of the subthalamic nucleus on seizures is frequency dependent *Epilepsia*. 2003;44:157–164.
14. Schindler K., Elger C.E., Lehnertz K.. Increasing synchronization may promote seizure termination: Evidence from status epilepticus *Clinical Neurophysiology*. 2007;118:1955–1968.
15. Durand D.M., Warman E.N.. Desynchronization of epileptiform activity by extracellular current pulses in rat hippocampal slices *The Journal of Physiology*. 1994;480:527–537.

Recognition of Arm-Movement Electroencephalography (EEG) Using Motor-Related Intrinsic Mode Functions Filtering and Cross Mutual Information

C.F. Lu^{1,2}, C.Y. Hung^{1,2}, P.J. Tseng³, L.T. Lin¹, Z.Y. Wang^{1,2},
and Y.T. Wu^{1,2,3}

¹ Department of Biomedical Imaging and Radiological Sciences, National Yang-Ming University, Taipei, Taiwan, ROC

² Integrated Brain Research Laboratory, Department of Medical Research and Education, Taipei Veterans General Hospital, Taipei, Taiwan, ROC

³ Institute of Brain Science, National Yang-Ming University, Taipei, Taiwan, ROC

Abstract—In this paper, we propose trial-specific and subject-specific filters to extract the motor-related compartment for the recognition of EEG signals induced by the left- or right-arm movement. Such motor-related filters are the intrinsic mode functions (IMF), which were produced by the decomposition of signals in C3 or C4 motor channels using the empirical mode decomposition (EMD), with the peak frequency pertaining to the mu rhythm within alpha band (8-12Hz) or beta band (16-25Hz). After these trial-specific and subject-specific filters were applied on all channels, the cross mutual information (CMI) of filtered signals between any two channels was computed. The average classification rates for five healthy subjects obtained from the proposed filters related to the alpha and beta bandpass filtering with whole-brain CMI maps were 77.4% and 88.3%, respectively, which were superior to the 72.2%, and 77.7% obtained from the same filtering but with only CMI vectors related to motor signals in C3 and C4, respectively.

Keywords— Electroencephalography, intrinsic mode functions, cross mutual information.

I. INTRODUCTION

In this paper, the empirical mode decomposition (EMD) [1] developed in the HHT method was employed to extract the motor-related brain signal trial by trial induced by the left and right arm movement. We first applied EMD on signals collected from motor-related channel, namely C3 and C4, to produce the so-called intrinsic mode functions (IMFs). The IMFs whose main frequency bands were close to the alpha band (8~12 Hz) or beta band (16-25 Hz) were recognized and used as an impulse response (kernel) to circularly convolve with the signals from other EEG channels. In doing so, we anticipate to filter out the motor-related components from other channels which can facilitate the subsequent trial-by-trial classification of left or right arm movement. Since the motor-related IMFs resulted from signals in C3 and C4 channel vary not only from trial to trial but also from subject to subject, such IMFs are termed as trial-specific and subject-specific impulse responses.

After the trial-specific kernel was circularly convolved with EEG from all channels (except C3 and C4) for a subject, the cross mutual information (CMI) [2] of filtered signals between any two channels was computed. The channel-to-channel, or whole-brain, CMI maps were compressed using principal component analysis (PCA) followed by the Fisher linear discriminate (FLD) [3] that searched for optimal directions for efficient discrimination.

It has been reported that the brain functions were coupled by complex network of interrelation brain regions, such as the frontal-parietal attention network, the resting state network, and the motor network [4]. Accordingly, it would be useful to make use of the task-related features as many as possible for the improvement of recognition rates.

II. MATERIALS AND METHODS

A. Subjects and data acquisition

Five healthy subjects, three males and two females, participated in our EEG experiments. Their average age is 27.0 years old and they habitually use the right hand. All subjects had not exercised in similar experiments before. The EEG was recorded from 28 scalp electrodes (QuickAmp amplifier, Brain Products GmbH, Munich, Germany). The EEG was also filtered between 0.5 and 55 Hz and sampled at 500 Hz. Horizontal and vertical electro-oculograms (EOGs) were recorded to reject eye-movements.

B. Experiments

The experiment was to perform the right and left arm movement (elbow flexing). The subjects sat in an armchair and stared at the computer monitor placed approximately 90 centimeters away from the subject at eye level. Meanwhile, they were asked to keep their arms and hands relax and comfortable, and avoid eye movements during the recordings.

The length of each trial was 10 seconds. Subjects were free to blink their eyes during the first second and then pay

attention on the cross mark shown on the screen in the next 9 seconds. A visual arrow cue was performed at 5 second, referring to as the onset time, to instruct subjects performing right or left motor movement (Fig. 1).

Signals on the time interval from -3 to 4 second relative to movement onset time were clipped as an epoch for subsequent analysis. Each subject performed 140 trials of right movement and 140 trials of left movement.

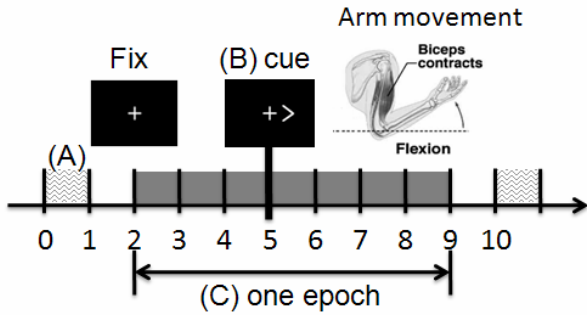


Fig. 1 The experimental paradigm of right or left arm movement. The time interval A (0~1) meaning eyes blinking is allowable. There is a visual cue, cross sign, shown on the screen, and a visual arrow cue represent the onset time B. Time interval C (2~9, from -3 to +4 sec relative to movement onset time) is considered as an epoch.

C. Empirical mode decomposition (EMD)

Empirical mode decomposition (EMD), the fundamental part of the Hilbert-Huang transformation [1], is a procedure to decompose signals, which can be non-linear and non-stationary, into a finite number of components, referred to as the intrinsic mode functions (IMFs). After the EMD process, the signal $x(t)$ is decomposed to a residue $r_n(t)$, which is a mean trend or a constant, and a collection of n IMFs, denoted by $c_i(t)$ ($i=1,2,\dots,n$). The original $x(t)$ can be reconstructed exactly via the residue $r_n(t)$ and IMFs $c_i(t)$ as follows [1]:

$$x(t) = \sum_{i=1}^n c_j(t) + r_n(t) \quad (1)$$

In our study, each motor signal from C3 or C4 surviving from the eye movement rejection was decomposed by EMD to generate its IMFs trial by trial.

D. Feature extraction using cross mutual information (CMI)

In our experiment, each trial of EEG raw data consisting of 3501 samples (from -3 to +4 sec relative to movement onset time) was first filtered by the alpha-related/beta-related IMFs using the circular convolution [5]. Let the filtered signal at the i -th channel be denoted by a random

variable F_i and its density function (pdf) be denoted by $p(F_{i,b})$. The entropy, which is the average amount of information reflecting the measure of uncertainty, of F_i is denoted by $H(F_i)$ and given by:

$$H(F_i) = -\sum_{b=1}^{N_b} p(F_{i,b}) \ln p(F_{i,b}) \quad (2)$$

where the $b=1,2,\dots,N_b$ was the index of sampling bins for the construction of approximated pdf via the data histogram. Similarly, let the joint probability density function (jpdf) between the i -th and j -th channels be denoted by $p(F_{i,b}, F_{j,b})$ and the joint entropy be denoted by $H(F_i, F_j)$ with the following form,

$$H(F_i, F_j) = -\sum_{b=1}^{N_b} p(F_{i,b}, F_{j,b}) \ln p(F_{i,b}, F_{j,b}) \quad (3)$$

Then the CMI between two random variables F_i and F_j can be calculated by

$$CMI(F_i, F_j) = H(F_i) + H(F_j) - H(F_i, F_j) \quad (4)$$

It is noted that the value of CMI represents degree of functional connectivity, or coupling strength, between any two channels. Accordingly, the resulting 28×28 CMI map encoded whole brain connectivity. In the following discussion, we denote the CMI maps, which were created by filtering each channel using alpha-related IMF and beta-related IMF, by alpha-IMF-CMI and beta-IMF-CMI maps, respectively. Since each CMI map was symmetric, we can either use the upper or lower triangular part (excluding the diagonal terms which were normalized to ones) as features which can be further rearranged into a 1×378 vector. Four different sets of features based on the CMI maps were created. The first feature vector was a concatenation of two row vectors, which represent mutual information between C3/C4 and other 27 signals, extracting from the alpha-IMF-CMI map, resulting in a 1×54 feature vector. The second one was the same as the first one except that alpha-IMF-CMI map was replaced by the beta-IMF-CMI map. It is noted that the motor-related feature vector (1×54) can also be represented by two topographical maps, one stands for coupling strengths between C3 and other channels, and the other stands for that between C4 and other channels. The third one was a concatenation of two upper triangular parts of alpha-IMF-CMI maps generated from the alpha-related IMFs in the C3 and C4, resulting in a 1×756 feature vector. The last one was the same as the third one except that alpha-related IMFs were replaced by the beta-related IMFs.

E. Linear classification of right or left arm movement

Once the feature vectors were created, we employed the principle component analysis (PCA) to reduce the feature

vector from size 1×54 or 1×756 to $1 \times d$ while kept 99% variance compare to the total variance. Following PCA, the FLD and the Bayes classifier [3] was used to automatically determine the threshold for two-class classification.

III. RESULTS

A. Spectrum analysis of the IMF filter and Butterworth band pass filter

To illustrate the difference between alpha-related/ beta-related IMF filters and the Butterworth band pass filter with alpha/beta band (8-12Hz/16-25 Hz), their power spectra were computed and display in Figure 1. The alpha-related IMF filter (solid curve in Figure 1.(a)) and beta-related IMF filter (solid curve in Figure 1.(b)) both exhibit distributed spectra with different magnitudes over frequencies. The major frequency for the former and latter is at 9 Hz and 17.5 Hz, respectively. It is worth noting that the spectrum of such motor-related IMF filters not only distinct from subject to subject, but also varies from trial to trial.

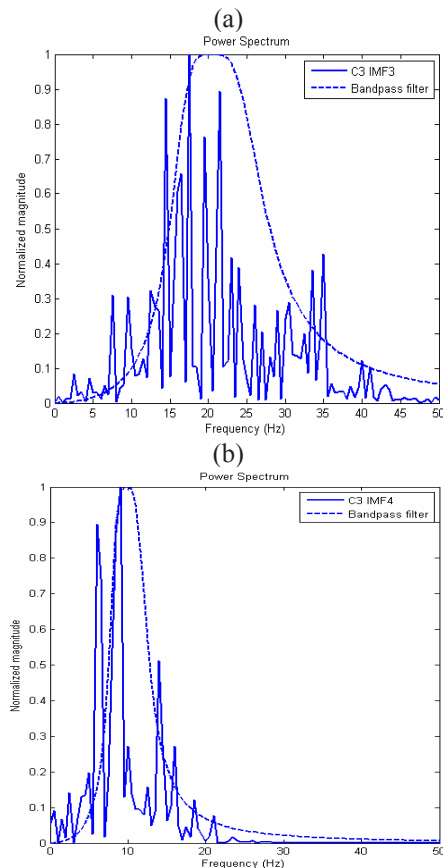


Fig. 2 The spectra of the filters. (a) The power spectrum of the bandpass filter (dashed curve, alpha band 8-12 Hz) and that of the alpha-related IMF filter generated from C3 (solid curve, main frequency = 9 Hz). (b) The power spectrum of the bandpass filter (dashed curve, beta band 16-25 Hz) and that of the alpha-related IMF filter generated from C3 (solid curve, main frequency = 17.5 Hz).

B. The classification rates

The average classification rates obtained from the alpha-related and beta-related IMF filters with the whole-brain CMI maps, and from the alpha-related and beta-related IMF filters with the motor-related CMI vectors were 72.2%, 77.7%, 77.4%, and 88.3%, respectively. The classification rate for each subject and feature is presented in Table 1.

Table 1 The classification rates resulted from different features for five health subjects.

	C3- and C4-related CMI vectors		Whole-brain CMI maps	
	α -related IMF	β -related IMF	α -related IMF	β -related IMF
Subject1	81.0%	84.3%	86.6%	90.3%
Subject2	57.4%	68.1%	60.8%	84.8%
Subject3	70.6%	82.4%	79.9%	91.7%
Subject4	72.4%	70.0%	77.1%	82.9%
Subject5	79.5%	83.8%	82.4%	91.9%
Average	72.2%	77.7%	77.4%	88.3%

C. The difference of the feature patterns

To illustrate the superiority of whole-brain CMI maps, we compared the difference between the left- and right-arm whole-brain CMI maps to the difference between the left- and right-arm CMI vectors. Fig. 2(a) and 2(b) illustrate the topographical maps obtained from averaging over CMI vectors for left-arm movement where C3 and C4 were used to derive the beta-related IMF filters and as reference channels, respectively. Fig. 2(c) and 2(d) exhibit the topographical maps obtained from averaging over CMI for right-arm movement where C3 and C4 were used to derive the beta-related IMF filters and as reference channels, respectively. Fig. 2(e) to (h) shows the similar arrangement to Fig. 2(a) to (d) but derived from the whole-brain beta-IMF-CMI maps. Specifically, the averaged topographical map was resulted from summing over each row (or column) in the whole-brain beta-IMF-CMI maps (28×28) for the left- or right-arm movements. By doing this, the value in each channel

represents the accumulated coupling strength between the filtered signal in that channel and filtered signals in other 27 channels. The squared bi-serial correlation coefficient was adopted to compute the difference of coupling strength between the left- and right-arm movement [6]. We found that larger difference (3400.8) between the left- and right-arm movement feature vectors were resolved by using the whole-brain beta-IMF-CMI maps than that (2572.9) by using beta-IMF-CMI vectors. As a result, the whole-brain CMI maps provided better discrimination between left- and right-arm movement for achieving higher classification rates.

Fig. 3 (a) to (d) The averaged topographical maps illustrating the coupling strength (value of mutual information) between reference channel C3 (or C4) with filtered signals in other 27 channels. (e) to (h) The averaged topographical map obtained from summing over each row (or column) in the whole-brain beta-IMF-CMI maps for the left- or right-arm movements to illustrate the accumulated coupling strength for each channel.

IV. CONCLUSIONS

We propose trial-specific and subject-specific IMFs impulse response derived from the signals induced by left- and right arm movements to circularly convolve with EEG signals over the whole brain followed by the feature extraction using the CMI, PCA and FLD, and the Bayes classification. Results show that the whole-brain CMI maps were better features than the motor-related CMI vectors. The averaged classification rates obtained from alpha-related and beta-related IMF filters using the whole-brain CMI maps were 77.4% and 88.3%, which were 5% to 10% higher than using the motor-related CMI vectors.

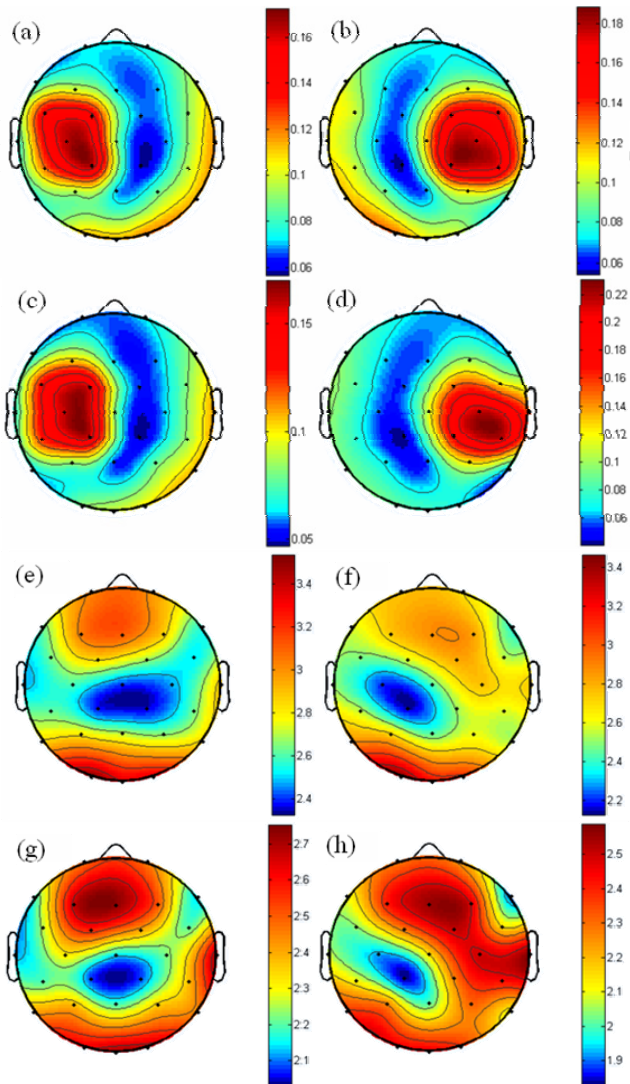
ACKNOWLEDGMENT

The study was funded in part by the National Science Council NSC96-2221-E-010-003-MY3.

REFERENCES

1. Huang NE, Shen Z, Long SR, Wu MC, Shih HH, Zheng Q, Yen NC, Tung CC, Liu HH. (1998) The empirical mode decomposition and the Hilbert spectrum for nonlinear and non-stationary time series analysis. *Proc R Soc Lond A*, 454: 903-995.
2. Chen CC, Hsieh JC, Wu YZ, Lee PL, Chen SS, Niddam D, Yeh TC, Wu YT. (2008) Mutual-information based approach for neural connectivity during self-paced finger lifting task. *Human brain mapping*, 29(3):265-80.
3. Duda RO, Hart PE, Stork DG. (2001) *Pattern Classification*, 2nd Ed, John Wiley & Sons, Inc., pp.117-120.
4. Toro R, Fox PT, Paus T. (2008) Functional coactivation map of the human brain. *Cerebral Cortex*, 18:2553-2559.
5. Oppenheim AV, Schaffer RW. (1989) *Discrete-time Signal Processing*, Prentice-Hall International, Inc., pp.542-546.
6. Müller KR, Krauledat M, Dornhege G, (2004) Machine learning techniques for brain computer interfaces. *Biomed Tech*, 49:11-22.

Author: Yu-Te Wu
 Institute: Department of Biomedical Imaging and Radiological Sciences, National Yang-Ming University
 Street: No.155, Sec.2, Linong Street
 City: Taipei
 Country: Taiwan
 Email: ytwu@ym.edu.tw



Author Index

A

Abatti, P.J. 227
Abe, Yosuke 211
Abellard, A. 219
Abellard, P. 219
Afshinjavid, S. 418
Ahi, S.T. 432
Ahmad, S.A. 231
Akai, M. 201
Akazawa, K. 55
Alexandru, A. 472
Alexandru, D. 566
Amsüss, S. 351
Andara, E. 456
Andersen, O.K. 84
Andersson, Björn 146
Aoki, H. 312
Arifin, Achmad 506
Arras, K.O. 283
Aruga, Masahiro 247
Arzt, C. 190
Åström, Mattias 331

B

Bach, M. 283
Bächle, T. 52
Bacsó, P. 9
Baga, D. 533
Baiden, D. 88
Bang, E.-J. 255
Bardakjian, B.L. 488
Bartic, C. 154, 239, 472
Bartsch, U. 107
Bartz-Schmidt, K.U. 444
Belloso, Aitor 64
Ben Khelifa, M. 219
Benav, H. 444
Bendtsen, J.D. 84
Benfenati, F. 327
Benini, L. 546
Benz, M. 190
Besch, D. 444
Bifulco, P. 343
Bijak, Manfred 540, 543
Bittner, R.C. 135
Blau, A. 327

Blomstedt, Patric 516
Bogdan, M. 339
Boos, R. 124
Boretius, T. 32, 100
Borghs, G. 154, 239
Borton, D.A. 384
Breitbach-Faller, N. 24
Brotons-Mas, J. 104
Bruckmann, A. 444
Brunsch, Thomas 271
Bull, C.W. 384
Burdet, E. 381
Buurke, J. 92

C

Cai, S.X. 529
Carabalona, R. 309
Casadio, M. 381, 558
Castiglioni, P. 309
Cendon, R.V. 362
Cerny, R. 57, 562
Cesarelli, M. 343
Chae, S.-J. 527
Chaloglou, D. 533
Chang, Hsiang-Chih 215
Chang, Walter -H. 5
Chappell, P.H. 231
Charfreitag, J. 57, 562
Chen, Albert 395
Chen, C.-C. 5, 464
Chen, S.-C. 5, 464
Chen, S.J. 529
Chen, S.W. 410
Chen, Y.-L. 5, 464
Chiari, L. 546
Chidiwa, Naoki 518
Chiu, Y.H. 44
Cho, Dong-Seok 306
Choe, B.-Y. 255
Choe, Bo-Young 275
Choi, C.-B. 255
Choi, Chi-Bong 275
Choi, S. 527
Choi, S.-K. 527
Choi, Yoon Jae 550
Chung, K.C. 44
Cikajlo, Imre 20

Comani, S. 61
Conforto, S. 170, 523, 536
Copiluși, C. 223
Correia, J.H. 576
Couronné, R. 190

D

D'Alessio, T. 170, 536
Danesh, A.A. 76
Daskalakis, Zafiris J. 138
Dautermann, C. 327
De Angelis, G. 319
Demosthenous, A. 353
Devasahayam, S.R. 584
Dewald, Jules P.A. 392
Dewald, Julius P.A. 374, 395
de Wild, M. 436
Dias, N.S. 576
Díaz, M. 398
Dimitrijevic, Milan 543
Disselhorst-Klug, C. 24
Doerge, T. 323, 366
Doi, Kouki 235, 243
Donaldson, N. 353
Donoghue, J.P. 384
Donoghue, M.F. 425
Došen, S. 302
Dresselaers, T. 239
Dumitru, N. 223
Dung, C.K. 566
Dupré, Marc André 80
Đurić-Jovičić, M. 299
Duschau-Wicke, Alexander 166, 271

E

Eberle, W. 154, 239, 472
Eck, U. 468
Eckermann, Claus 80
Edelvik, Fredrik 146
Edlinger, G. 174
Edström, U. 520
Edwards, D. 388
Egert, D. 96
Ellis, Michael D. 374, 392
Emborg, J. 84

Endo, T. 55
 Erfanian, A. 480
 Ergovic, V. 460
 Esteller, R. 398
 Estrada, J.J. 533

F

Farella, E. 546
 Farjadian, A.B. 295
 Felsenstein, Simon 271
 Fernández-López, G. 456
 Franke, M. 339
 Fratini, A. 343
 Fujimoto, Hiroshi 235, 243
 Fujimoto, T. 142
 Fujiwara, T. 312

G

Gaiser, I. 468
 Galera, S.R.G.P. 131
 Gargiulo, P. 370
 Gefen, A. 28
 Gekeler, F. 444
 Gener, T. 104
 Georgescu, D. 566
 Giacomozzi, C. 319
 Gielen, G. 154
 Głowacka-Kwiecień, A. 13
 Gneo, M. 170, 536
 Goetz, S.M. 72
 Goffredo, M. 170, 536
 Golz, M. 388
 Good, L.B. 588
 Greenlaw, R. 533
 Greppmaier, U. 444
 Grieco, J.C. 456
 Griesemann, J. 554, 570
 Grimaldi, G. 448
 Grip, H. 520
 Grönegress, C. 174
 Grozea, C. 510
 Guarnieri, B.M. 61
 Gudmundsdottir, V. 370
 Guger, C. 104, 174
 Guidali, Marco 127, 166
 Gustavsson, O. 520
 Guttmann, J. 283
 Gzik, M. 13, 68
 Gzik-Zroska, B. 68

H

Haas, H.-D. 88
 Hachisuka, Kenji 514, 518

Haeberle, S. 158
 Häger-Ross, C. 520
 Han, Jonghee 550
 Han, Seongho 406
 Han, Yang 452
 Hanauer, M. 323
 Hanke, S. 428
 Haque, M.M. 207
 Hariz, Marwan I. 331
 Harscher, A. 444
 Hasenkamp, W. 472
 Hassler, C. 119
 Haueisen, J. 61
 Havlik, J. 421
 Hayakawa, Yasuhiro 1
 Heikkilä, T.J. 316
 Heinze, F. 24
 Hekman, Edsko E.G. 392
 Helgason, T. 370, 377
 Hemm, S. 436
 Henle, C. 100
 Herwik, S. 107
 Hesse, S. 150
 Heuschkel, M. 327
 Higashi, Y. 142
 Himmelreich, U. 239
 Hochmann, D. 194
 Hofer, Christian 540, 543
 Hoffmann, K.-P. 162, 323
 Hofstötter, Ursula 543
 Holzner, C. 174
 Hong, Sung-Tak 275
 Horcik, Z. 421
 Hosono, M. 287
 Hozman, J. 57, 562
 Hsieh, J.-C. 5, 464
 Hsu, H.Y. 410
 Huang, F.C. 335
 Hung, C.Y. 592
 Hwang, S.H. 259, 358
 Hwang, S.J. 17
 Hyttinen, J. 267
 Hyttinen, J.K. 316

I

Iasemidis, L.D. 588
 Ibrahim, W.Md. Azhar Wan 186
 Ichimura, S. 312
 Ienaga, Takafumi 514
 Ingvarsson, P. 370
 Ino, S. 287
 Ivlev, O. 88
 Iwata, Hirotaka 518
 Izumi, T. 287

J

Jacinto, L.R. 576
 Jahed-Motlagh, M.R. 295
 Jakobsson, Stefan 146
 Janda, P. 347
 Janssen, P. 107
 Jantek, B. 9
 Jeon, Beom Seok 550
 Jeon, Hyo Seon 550
 Jobbágy, Á. 9
 Jochymczyk, K. 13
 Johansson, Johannes 516
 Jovičić, N. 299
 Jureczko, P. 13

K

Kambara, H. 432
 Kamibayashi, K. 201
 Kang, S.-W. 527
 Kargov, A. 468
 Kato, Shuichi 247
 Kauff, D.W. 366
 Kawanabe, M. 279
 Kawashima, N. 484
 Kawashima, R. 115
 Keim, A. 124
 Keller, Thierry 64, 291, 492
 Kenntner, J. 107
 Kern, Helmut 540, 543
 Kibbel, S. 444
 Kim, G. 414
 Kim, H. 414
 Kim, H.D. 17
 Kim, H.S. 573
 Kim, Hwi-Yool 275
 Kim, J.Y. 17
 Kim, K.-H. 255
 Kim, K.-S. 527
 Kim, S.-S. 255
 Kim, S.-Y. 255
 Kim, Sang-Young 275
 Kim, Sang Kyong 550
 Kim, Y.H. 17, 259, 358
 Kim, Youngho 265
 Kimuro, Yoshihiko 514
 Kinouchi, Y. 76
 Kisban, S. 107
 Kitamura, T. 201
 Kiyooka, S. 312
 Klamroth-Marganska, Verena 127
 Klasen, S. 52
 Kleinau, P. 554
 Knútsdóttir, S. 370

- Kneist, W. 323, 366
 Ko, A.R. 259
 Kobori, Satoshi 211
 Koch, C. 88
 Koch, K.P. 162, 366
 Kohn, A.F. 197
 Koike, Y. 432
 Kolling, S. 554
 Konitsiotis, S. 533
 Koopman, B. 92
 Koriyama, Futoshi 514
 Koshiji, K. 312
 Koźlak, M. 68
 Kraemer, S. 323
 Kraft, M. 135, 194
 Krajewski, J. 388
 Krishnan, Sridhar 36
 Kristal, A. 28
 Krupicka, R. 347
 Kuhn, Andreas 492
 Kuiken, Todd 123
 Kuo, T.-S. 464
 Kusnyerik, A. 444
 Kutilek, P. 562
 Kuwae, Y. 142
- L**
- La Gatta, A. 343
 Lai, K.H. 410
 Lai, K.Y. 410
 Laiwalla, F. 384
 Lamadé, W. 323, 366
 Lammertse, P. 448
 Lanmüller, Hermann 540
 Lappalainen, R. 316
 Larsson, Stig 146
 Larysz, D. 68
 Laskoski, G.T. 227
 Lee, G.-J. 527
 Lee, Hyun-Sung 275
 Lee, MyoungHo 406
 Lee, Po-Lei 215
 Lee, S.-H. 255
 Lee, S.H. 259
 Lee, Sung-Ho 275
 Lee, Y.H. 259
 Li, Y.-C. 5, 464
 Li, Yvonne 203
 Liang, J.I. 410
 Lim, D.H. 17
 Limousin, Patricia 331
- Lin, L.T. 592
 Liu, Sinwu 247
 Liu, Zhicheng 452
 Łosień, T. 13
 Lu, C.F. 592
 Lucas, C. 295
 Lundström, R. 520
- M**
- Ma, Zhanhong 452
 Macellari, V. 319
 Makino, Kenichiro 514
 Malmivuo, J. 267
 Mancini, M. 546
 Mander, M. 68
 Mansor, Md. Shuhaibul Fadly 186
 Manto, M. 448
 Marchena, P. 398
 Marin, M. 223
 Martínez, I. 398
 Martínez-Torres, Irene 331
 Martins, L.D.L. 227
 Masani, K. 580
 Masia, L. 381
 Matjačić, Zlatko 20
 Mayr, W. 428
 Mayr, Winfried 540, 543
 Maziewski, P. 533
 McConville, K.M. 580
 Mecheri, A.S. 154
 Medved, V. 460
 Meier, W. 100
 Melendez-Calderon, A. 381
 Metzen, R.P. von 96
 Metzen, R.v. 107
 Meuleman, J. 448
 Mikkonen, J. 316
 Milosevic, M. 580
 Milovanović, I. 299
 Minassian, Karen 543
 Minegishi, Y. 502
 Mischke, P. 570
 Miyoshi, T. 251
 Möller, J. 283
 Möller, K. 283
 Montaseri, Gh. 295
 Moosdijk, S. van de 158
 Morasso, P. 558
 Moser, D.C. 428
 Mostofi, N. 295
 Motoi, K. 142
- Moubarak, S. 476
 Munih, M. 440
 Murr, A. 327
 Musa, S. 154, 239, 472
 Muscillo, R. 170, 536
 Mussa-Ivaldi, F.A. 335
- N**
- Nagai, Mary K. 138
 Nagashino, H. 76
 Nakajima, S. 287
 Nakajima, T. 201
 Nakazawa, K. 201
 Narkilahti, S. 316
 Nascimento, L.F.C. 131
 Natorigawa, A. 111
 Nazaradeh, Denis 80
 Nazaradeh, Fridun 80
 Nef, Tobias 127
 Nishida, Naoki 1
 Nohama, P. 362
 Nolte, G. 510
 Norbahiyah, S. 207
 Nurmikko, A.V. 384
 Nuttin, B. 239
- O**
- O'Malley, Marcia K. 203
 O'Reilly, D. 425
 Oblak, Jakob 20
 Oda, Taishi 514
 Oehler, S. 194
 Ogawa, M. 142
 Öhberg, F. 520
 Ojha, R. 584
 Okuno, R. 55
 Oskarsdóttir, A. 377
 Osypka, P. 366
 Ottawa, Takenori 514
- P**
- Pachnis, I. 353
 Pajdla, T. 476
 Pandya, A.S. 76
 Pansera, M. 533
 Paolizzi, M. 319
 Papsava, A. 533
 Park, H.-K. 527

- Park, J.-H. 527
 Park, K.S. 573
 Park, Kwang Suk 550
 Park, S. 384
 Park, S.W. 259, 358
 Park, Y.-H. 527
 Pasquariello, G. 343
 Pastor, M. 533
 Patoglu, Volkan 203
 Patterson, W.R. 384
 Patton, J.L. 335
 Paul, O. 107
 Peng, Y.C. 410
 Perry, Joel C. 64, 291
 Persson, Mikael 146
 Peters, T. 444
 Pham, M.T. 476
 Pichorim, S.F. 227
 Pittaccio, S. 178, 182
 Podolak, C. 190
 Popescu, F. 510
 Popović, D.B. 299, 302
 Popović, M.B. 302
 Popovic, M.R. 484, 580
 Popovic, Milos R. 138
 Poppendieck, W. 162, 366
 Portnoy, S. 28
 Porubská, K. 444
 Pouryazdian, S. 480
 Prabhav, N.R. 584
 Prodanov, D. 239
 Pylatiuk, C. 468
- R**
- Rafolt, Dietmar 540
 Ramanantsizehena, P. 219
 Randria, I. 219
 Rattay, Frank 543
 Redarce, T. 476
 Redl, H. 351
 Reischl, M. 468
 Rensch, S. 52
 Rhim, H.-S. 255
 Richter, J. 124
 Richter, Johan 516
 Riener, Robert 127, 166, 271
 Robledo, M. Garcia 533
 Rocchi, L. 546
 Rosahl, S. 40
 Rosahl, S.K. 40, 48
 Rulsch, M. 190
 Rupp, R. 468
 Rusu, L. 223
 Ruther, P. 96, 107
- Ryu, K.H. 259
 Ryu, M. 414
- S**
- Sabesan, S. 588
 Sachs, H. 444
 Saito, Hiroki 506
 Sakoda, S. 55
 Sanchez-Vives, M.V. 104
 Sanguinetti, V. 558
 Sanin, E.G. 580
 Sato, M. 287
 Sayenko, D.G. 580
 Schaffelhofer, S. 104
 Schanze, Th. 261
 Schenka, A. 388
 Schill, O. 468
 Schkommodau, E. 436
 Schmid, M. 170, 536
 Schmidhammer, R. 351
 Schmitz-Rode, T. 24
 Schneider, U. 52, 124
 Schnupp, T. 388
 Schuettler, M. 100
 Schultheisz, J. 9
 Schulz, S. 468
 Schumacher, A. 158
 Schumann, S. 283
 Seemann, G. 267
 Seki, T. 115
 Seo, Jong-Mo 306
 Serio, A. 61
 Shabshin, N. 28
 Shibata, Y. 251
 Shih, Y.-Y. 5, 464
 Shin, J.H. 573
 Shin, Y. 414
 Shiraishi, Y. 115
 Shirvany, Yazdan 146
 Siev-Ner, I. 28
 Silvestri, S. 319
 Simons, C. 92
 Slater, M. 174
 Sohn, R.H. 259, 358
 Son, J.S. 17
 Son, Jongsang 265
 Song, Y.-K. 384
 Song, Yongsoo 406
 Sołtys, M. 13
 Spaich, E.G. 84
 Spieth, S. 158
 Staude, G. 566
 Staudt, M. 554
 Stegmaier, F. 124
- Steinisch, M. 61
 Steltenkamp, S. 162, 323
 Stett, A. 444
 Stieglitz, T. 32, 96, 100, 107, 119
 Stienen, Arno H.A. 392
 Stöhr, Hans 540
 Su, F.C. 410
 Suaste, E. 402
 Subke, J. 554, 570
 Sugimoto, T. 496
 Sugimura, Yukinobu 514
 Szabo, Z. 347
 Szemán, J. 9
- T**
- Tacconi, C. 546
 Tadano, S. 111
 Takagi, Kiyotaka 247
 Takagi, M. 251
 Takashima, M. 115
 Takeda, R. 111
 Tanaka, S. 142
 Taniguchi, S. 142
 Tanskanen, J.M.A. 316
 Tarata, M.T. 566
 Tejszerska, D. 68
 Telles, H. 124
 Teodoro, E.C.M. 131
 Terán, O. 402
 Tettke, M. 135
 Thomas, U. 261
 Ting, Y.T. 410
 Todoh, M. 111
 Tomazini, J.E. 131
 Tonkovic, S. 460
 Torrealba, R.R. 456
 Toyoda, Wataru 243
 Treiman, D.M. 588
 Trelenkamp, S. 327
 Tripoliti, Elina 331
 Tsai, M.S. 44
 Tsakalis, K. 588
 Tseng, P.J. 592
 Tsuji, Takuro 514
 Tsutsumi, Akio 518
- U**
- Uhlir, J. 421
 Ulmer, Ch. 323, 366
 Unger, Ewald 540, 543
 Uplegger, C. 52

V

Väisänen, J. 267
Vallery, Heike 166, 271
van Asseldonk, E.H.F. 92
Van Den Braber, N. 448
van der Kooij, Herman 92, 392
Vatnsdal, B. 370
Vidaurre, C. 279
Viscuso, S. 178, 182

W

Wada, Chikamune 514, 518
Wada, Futoshi 514, 518
Wada, Tsutomu 235, 243
Wakugawa, M. 142
Walsh, M.T. 425
Wang, P.R. 44
Wang, Z.Y. 592
Watanabe, Takashi 502, 506
Welkenhuysen, M. 239
Wendel, K. 267
Werner, C. 150
Weyh, Th. 72
Wiest, G. 428
Wilhelm, B. 444
Wilke, R. 444
Wilkening, A. 88

Wolański, W. 68
Wolf, W. 566
Wolff, S. 327
Woo, D.-C. 255
Woo, Dong-Cheol 275
Wrobel, W. 444
Wu, Chi-Hsun 215
Wu, Y.T. 592
Wu, Yunfeng 36
Wuesten, J. 327
Wårdell, Karin 331, 516

Y

Yamakoshi, K. 142
Yamamoto, S. 251
Yamamoto, S-I. 201
Yamashita, K. 287
Yambe, T. 115
Yang, Y. 414
Yang, Zhimei 514
Yao, Jun 395
Yi, Won Jin 550
Yin, C.-S. 527
Yizhar, Z. 28
Ylä-Outinen, L. 316
Yngvason, S. 370
Yokoe, M. 55
Yoshida, I. 496

Yoshida, Y. 496
Yoshinari, S. 111
Youseffi, M. 418
Yu, W.J. 529
Yuji, T. 142
Yukitake, Naoto 514
Yun, H. 414

Z

Zabaleta, Haritz 64
Zalay, O.C. 488
Zambrano, A. 398
Zambrano, L.A. 456
Zanichelli, F. 533
Zariffa, José 138
Zeitlhofer, J. 428
Zengerle, R. 158
Zhao, Y. 529
Zhong, J. 190
Zhou, Ping 452
Ziegler, C. 327
Ziherl, J. 440
Zimmermann, D. 32
Zivanovic, V. 484
Zrenner, E. 444
Zrinzo, Ludvic U. 331